Tactical Missile Design

Second Edition

Eugene L. Fleeman
Lilburn, Georgia

EDUCATION SERIES
Joseph A. Schetz
Series Editor-in-Chief
Virginia Polytechnic Institute and State University
Blacksburg, Virginia

Published by
American Institute of Aeronautics and Astronautics, Inc.
1801 Alexander Bell Drive, Reston, VA 20191-4344

AIAA Education Series

Editor-in-Chief

Joseph A. Schetz
Virginia Polytechnic Institute and State University

Editorial Board

Takahira Aoki
University of Tokyo

Edward W. Ashford

Karen D. Barker
The Brahe Corporation

Robert H. Bishop
University of Texas at Austin

Claudio Bruno
University of Rome

Aaron R. Byerley
U.S. Air Force Academy

Richard Colgren
University of Kansas

Kajal K. Gupta
NASA Dryden Flight Research Center

Rikard B. Heslehurst
Australian Defence Force Academy

David K. Holger
Iowa State University

Rakesh K. Kapania
Virginia Polytechnic Institute and State University

Brian Landrum
University of Alabama Huntsville

Tim C. Lieuwen
Georgia Institute of Technology

Michael Mohaghegh
The Boeing Company

Conrad F. Newberry
Naval Postgraduate School

Mark A. Price
Queen's University Belfast

James M. Rankin
Ohio University

David K. Schmidt
University of Colorado Colorado Springs

David M. Van Wie
Johns Hopkins University

To my family, especially my grandchildren Nicholas and Christopher

Foreword

We are delighted to present the second edition of *Tactical Missile Design* by Eugene Fleeman formerly of Georgia Tech. The first edition was very well received in the aerospace community. This new edition has updated material and expanded coverage, and we anticipate that it will be equally well received. The current volume has nine chapters and six appendices in more than 450 pages covering all of the topics relevant to this subject. One appendix has good homework problems and another contains an extensive bibliography. In addition, a CD with PowerPoint slides suitable for a short course is included.

Eugene Fleeman is superbly qualified to write this book because of his long and productive career in the tactical missile area. His command of the material is excellent, and he is able to organize and present it in a clear manner.

The AIAA Education Series aims to cover a very broad range of topics in the general aerospace field, including basic theory, applications, and design. The philosophy of the series is to develop textbooks that can be used in a university setting, instructional materials for continuing education and professional development courses, and also books that can serve as the basis for independent study. Suggestions for new topics or authors are always welcome.

Joseph A. Schetz
Editor-in-Chief
AIAA Education Book Series

Table of Contents

Preface . . . . . **xvii**

Chapter 1. Introduction/Key Drivers in the Design Process **1**
1.1 Introduction. 1
1.2 Tactical Missile Characteristics 1
1.3 Conceptual Design Process 4
1.4 Examples of State-of-the-Art Missiles 7
1.5 Aerodynamic Configuration Sizing Parameters 9
1.6 Example of Alternatives in Establishing Mission Requirements 10
1.7 Use of a Baseline Missile 14
1.8 Summary 18
Problems. 18

Chapter 2. Aerodynamic Considerations in Tactical Missile Design . **21**
2.1 Introduction. 21
2.2 Missile Diameter Tradeoff. 21
2.3 Nose Fineness Tradeoff 29
2.4 Boattail 34
2.5 Lifting Body Versus Axisymmetric Body 34
2.6 Static Stability 38
2.7 Body Aerodynamic Center 40
2.8 Flare Stabilizer. 41
2.9 Wings Versus No Wings. 43
2.10 Normal Force Prediction for Surfaces (e.g., Wing, Tail, Canard) 44
2.11 Aerodynamic Center Prediction for Surfaces (e.g., Wing, Tail, Canard) 47
2.12 Hinge Moment Prediction. 48
2.13 Thin Surface (e.g., Wing, Tail, Canard) Drag Prediction. 49
2.14 Surface Geometry Tradeoffs 51
2.15 Flight Control Alternatives 55
2.16 Maneuver Alternatives 69
2.17 Roll Orientation 72
2.18 Trim 73
2.19 Tail Area Sizing 74
2.20 Stability and Control Conceptual Design Criteria 76
2.21 Body Buildup 77

2.22 Summary 79
Problems. 79

Chapter 3. Propulsion Considerations in Tactical Missile Design . . . 81
3.1 Introduction. 81
3.2 Propulsion Alternatives Assessment 81
3.3 Turbojet Propulsion Temperature Technology Limit 86
3.4 Turbojet Thrust Prediction 92
3.5 Turbojet Specific Impulse Prediction 94
3.6 Ramjet Propulsion Alternatives 95
3.7 Ramjet Specific Impulse Prediction. 97
3.8 Ramjet Thrust Prediction 98
3.9 Ramjet Temperature Technology Limit. 100
3.10 Ramjet Engine/Booster Integration 105
3.11 Ramjet Missile Drag 108
3.12 Ramjet Inlet Options 109
3.13 Supersonic Inlet/Airframe Integration 112
3.14 Fuel Alternatives. 120
3.15 Ducted Rocket Design Considerations 121
3.16 Rocket Motor Performance 122
3.17 Solid Propellant Grain Alternatives 128
3.18 Solid Rocket Thrust Magnitude Control 130
3.19 Solid Propellant Alternatives 132
3.20 Motor Case Material Alternatives 134
3.21 Rocket Nozzle Material Alternatives 136
3.22 Summary 137
Problems. 137

Chapter 4. Weight Considerations in Tactical Missile Design 141
4.1 Introduction. 141
4.2 Benefits of a Lightweight Missile 141
4.3 Subsystem Weight Sensitivity to Flight Performance 141
4.4 Missile Weight Prediction. 143
4.5 Center-of-Gravity and Moment-of-Inertia Prediction 146
4.6 Structure Factor of Safety 149
4.7 Airframe Manufacturing Processes 150
4.8 Airframe Material Alternatives. 153
4.9 Structure/Insulation Trades. 158
4.10 High-Temperature Insulation Materials. 160
4.11 Aerodynamic Heating/Thermal Response Prediction. 162
4.12 Localized Aerodynamic Heating and Thermal Stress 172
4.13 Structure Design. 175
4.14 Seeker Dome 186
4.15 Power Supply and Actuators 190
4.16 Summary 193
Problems. 194

Chapter 5. Flight Performance Considerations in Tactical Missile Design . . . 197
5.1 Introduction . . . 197
5.2 Flight Performance Envelope . . . 197
5.3 Equations of Motion Modeling . . . 199
5.4 Driving Parameters for Flight Performance . . . 201
5.5 Cruise Flight Performance . . . 202
5.6 Steady-State Flight . . . 204
5.7 Flight Trajectory Shaping . . . 205
5.8 Turn Performance . . . 206
5.9 Coast Flight Performance . . . 210
5.10 Ballistic Flight Performance . . . 212
5.11 Boost Flight Performance . . . 214
5.12 Intercept Lead Angle and Velocity . . . 215
5.13 Comparison with Performance Requirements . . . 216
5.14 Summary . . . 217
Problems . . . 217

Chapter 6. Measures of Merit and Launch Platform Integration . . . 219
6.1 Introduction . . . 219
6.2 Robustness . . . 219
6.3 Warhead Lethality . . . 241
6.4 Miss Distance . . . 257
6.5 Carriage and Launch Observables . . . 274
6.6 Other Survivability Considerations . . . 277
6.7 Reliability . . . 281
6.8 Cost . . . 283
6.9 Launch Platform Integration . . . 295
6.10 Summary . . . 309
Problems . . . 309

Chapter 7. Sizing Examples . . . 313
7.1 Introduction . . . 313
7.2 Standoff Range Requirement . . . 313
7.3 Wing Sizing Requirement . . . 329
7.4 Multi-Parameter Harmonization . . . 332
7.5 Lofted Range Comparison . . . 335
7.6 Ramjet Missile Range Robustness . . . 338
7.7 Ramjet Propulsion/Fuel Alternatives . . . 350
7.8 Velocity Control . . . 351
7.9 Examples of Computer-Aided Conceptual Design Sizing Tools . . . 353
7.10 Soda Straw Rocket Design, Build, and Fly . . . 358
7.11 Summary . . . 375
Problems . . . 376

Chapter 8. Development Process . . . 379
8.1 Introduction . . . 379

8.2 Technology Assessment/Roadmap 379
8.3 Phases of Development/Design Maturity 380
8.4 Tactical Missile Follow-on Programs 383
8.5 Subsystem Integration 384
8.6 Example of Technology Development 390
8.7 Examples of State-of-the-Art Advancement. 393
8.8 New Technologies for Tactical Missiles 395
8.9 Summary 397
Problems 397

Chapter 9. Summary and Lessons Learned 399
9.1 Introduction. 399
9.2 Evaluate Alternatives and Iterate the System-of-Systems Design 399
9.3 Exploit Diverse Skills 399
9.4 Utilize Creative Skills 401
9.5 Identify and Quantify the High-Payoff Measures of Merit. 401
9.6 Start with a Good Baseline Design 402
9.7 Conduct Balanced, Unbiased Tradeoffs 403
9.8 Evaluate Many Alternatives. 404
9.9 Search a Broad Design Solution Space (Global Optimization Versus Local Optimization). 404
9.10 Evaluate and Refine as Often as Possible 405
9.11 Provide Balanced Emphasis of Analytical Versus Experimental 406
9.12 Use a Design, Build, and Fly Process for Feedback that Leads to Broader Knowledge 406
9.13 Evaluate Technology Risk. 407
9.14 Maintain Real-Time Documentation 408
9.15 Develop Good Documentation 408
9.16 Utilize Group Skills. 410
9.17 Balance the Tradeoff of Importance Versus Priority. 411
9.18 Iterate the Configuration Design 412
9.19 Configuration Sizing Conceptual Design Guidelines 412
9.20 Wrap-Up. 415

Appendix A. Homework Problems/Classroom Exercises 417

Appendix B. Example of Request for Proposal 427

Appendix C. Nomenclature 437

Appendix D. Acronyms 447

Appendix E. Conversion Factors 451

Appendix F. Example of a Syllabus 453

References 455

Bibliography 457

Index 461

Supporting Materials 469

Preface

The material in this book is oriented toward the needs of aerospace engineering students, missile engineers, and missile program managers. One objective is to provide a reference text for the aerospace engineering curriculum of universities. Although the tactical missile community is large, receives a significant amount of funding, and has many technical and system problems to address, few universities offer courses in missile design. This introduction to tactical missiles will hopefully spark the interest of young engineers to make a career in the missile community. Also, the text is a reference for missile engineers and missile program managers.

The text is a summary of information that I have collected during my 40-plus years of experience in the development of tactical missiles and their technologies. It distills the technical knowledge that I have gathered into an integrated handbook method for missile design. Generally used are simple, closed-form, analytical, physics-based equations to provide insight into the primary driving parameters. Closed-form analytical equations are a throwback to the way missile design was conducted more than thirty years ago. The text also provides example calculations of rocket-powered and ramjet-powered baseline missiles, typical values of missile parameters, examples of the characteristics of current operational missiles, discussion of the enabling subsystems and technologies of tactical missiles, and the current/projected state-of-the-art of tactical missiles.

In recent years we have seen increased usage of tactical missile systems for military operations. Tactical missiles are expected to have an even larger share of military operations in the future. A key contributor to the increased effectiveness is the advancement in technology. Examples of advancement in missile system effectiveness include improved range, firepower, maneuverability, accuracy, lethality, and adverse weather capability.

A historical example of the value of guided weapons is the attack on the Thanh Hoa Bridge in Vietnam. For more than six years, a total of 871 aircraft sorties dropped unguided bombs but failed to close the bridge. However, the first operational application of laser-guided bombs on 13 May 1972 resulted in direct hits on the supporting piers, dropping the center span and closing the bridge. Eleven aircraft had been lost in the 871 previous sorties. No aircraft were lost in the four sorties using precision guided munitions. A more recent example is the use of precision strike weapons in Desert Storm, Kosovo, and Enduring Freedom. In the year 1991 Desert Storm operation, 9% of the strike weapons were guided weapons. In Kosovo 35% of the strike weapons were guided weapons. In the

year 2002 Enduring Freedom operation, 69% of the strike weapons were guided weapons.

The organization of the material in this text is as follows: Chapter 1 gives an overview of the missile design process. Chapter 2 discusses aerodynamic design methods and the technologies of low aspect ratio wing and wingless configurations. Conceptual design methods and technologies for rocket, ramjet, and turbojet propulsion are included in Chapter 3. Chapter 4 addresses conceptual design weight considerations. Topics include weight prediction, aerodynamic heating prediction, technologies for lightweight materials and subsystems, and low-cost manufacturing processes. Conceptual design methods for predicting flight range, velocity, time to target, maneuverability, and off boresight are given in Chapter 5. Chapter 6 provides measures of merit and launch platform integration considerations. It includes conceptual design methods and technologies in the areas of robustness, warhead lethality, miss distance, carriage and launch observables, other survivability considerations, reliability, cost, firepower, store separation and carriage, and storage environment. Conceptual design sizing examples and computer-aided sizing tools are presented in Chapter 7. Sizing examples are for a rocket-powered missile, a ramjet-powered missile, and a soda straw rocket. An example of an electronic spreadsheet sizing tool based on the methods of this textbook is presented. Chapter 8 discusses the missile development process. A summary of this text and lessons learned in missile development are given in Chapter 9.

The appendices in the back of the book have a set of homework problems/classroom exercises, an example of a request for proposal for a missile design study, a list of nomenclature, a list of acronyms, a table for conversion of English to metric units, selected figures from the text that are in color, and an example of a syllabus for a course curriculum in Tactical Missile Design. I wish to express my appreciation to the Boeing Company for providing the funding to print the color figures.

References for the data and methods used in this text and a bibliography of other reports and Web sites that are related to tactical missiles are provided in the back of the book.

A compact disk (CD) is included with this book. It includes a Microsoft PowerPoint presentation of a short course based on this book. The slides are in color and have embedded tabular data. Embedded in the slides are 29 videos illustrating missile design considerations, development testing, manufacturing, and technologies. The CD includes a tactical missile design spreadsheet in Microsoft Excel format. The spreadsheet models the configuration sizing methods of this text. Also on the CD are six tactical missile design case studies. These were conducted by Georgia Tech students over the years 1999 to 2005. Finally, the CD includes a presentation entitled Soda Straw Rocket Science. It is an aerospace engineering outreach program for elementary and middle school students.

I would like to thank the faculty and students at the Georgia Institute of Technology for their support for this textbook. Special appreciation is expressed to Dr. Dimitri Mavris, Director of the Georgia Tech Aerospace Systems Design Laboratory.

I would like to also express my appreciation to the following persons who have supported my work in the areas of missile design, advanced weapon

concepts, and advanced weapons technologies: Bill Lamar and Charles Westbrook of the United States Air Force Research Laboratory and Thad Sandford of the Boeing Company Phantom Works. Again, I wish to thank the Boeing Company for sponsoring the color figures at the back of the back.

Finally, I would appreciate receiving your comments and corrections on this text, as well as any data, examples, or references that you may offer. E-mail to: GeneFleeman@msn.com, or visit the Web site: http://genefleeman.home.mindspring.com.

Eugene L. Fleeman
April 2006

1
Introduction/Key Drivers in the Design Process

1.1 Introduction

The primary area of emphasis in the text is the methods and technology for aerodynamic configuration sizing (Fig. 1.1). Aerodynamic configuration sizing is conducted to develop the configuration geometry and the dimensions of the missile. The output of aerodynamic configuration sizing includes the missile diameter, length, nose geometry, stabilizer size and geometry, and the control surface size and geometry. The configuration sizing methods of this text are physics-based methods to allow analytical sizing of the missile configuration. Areas that also receive primary emphasis are aerodynamic stability and control, aerodynamic flight performance, propulsion, structure, and weight. Other areas that receive secondary emphasis are warhead, miss distance, cost, additional measures of merit, and launch platform integration. These are addressed to a level that is consistent with their impact on the aerodynamic configuration sizing. Tertiary emphasis is given to the areas of seeker, sensors, electronics, and power supply. The areas of safe, arm, and fuzing are not addressed in this text. Although these areas are important at the system level, they generally have lesser impact on the aerodynamic design.

1.2 Tactical Missile Characteristics

Tactical missiles are different from other flight vehicles, such as combat aircraft, and are a technical specialty in their own right. Figure 1.2 is a state-of-the-art comparison of tactical missile characteristics with the current state of the art (SOTA) of fighter aircraft. Examples are shown where missiles are driving technology. Also shown are other areas where the missile is not driving technology.

As an example, the lateral and longitudinal acceleration SOTA of missiles exceeds that of combat aircraft. Missile lateral maneuverability of $30g^+$ and longitudinal acceleration of $30g^+$ have been demonstrated. Notable examples of missiles with high acceleration and maneuverability include the AGM-88 HARM and the AA-11 Archer missiles. Developmental missiles have demonstrated lateral maneuverability of $100g^+$ and longitudinal acceleration of $400g^+$. Missile speed and altitude may be greater than that of combat aircraft. An example of a high-speed endo-atmospheric missile is the MM-3 hypervelocity

Area	Emphasis
Aero Configuration Sizing	●
Aero Stability & Control	●
Aero Flight Performance	●
Propulsion	●
Structure	●
Weight	●
Warhead	◒
Miss Distance	◒
Cost	◒
Additional Measures of Merit	◒
Launch Platform Integration	◒
Seeker, Sensors, and Electronics	○
Power Supply	○
Safe, Arm, and Fuzing	○

Primary Emphasis ●
Secondary Emphasis ◒
Tertiary Emphasis ○
Not Addressed -

Fig. 1.1 Emphasis of this text is on physics-based, analytical sizing of the aerodynamic configuration.

missile. An example of a high-speed exo-atmospheric missile is the SM-3 standard missile. Another difference is the dynamic pressure loading on a missile, which is usually greater than that of combat aircraft. For example, the PAC-3 missile operates at much higher dynamic pressure than that of aircraft. Another

Tactical Missile Characteristics	Example of State of the Art	Comparison With Fighter Aircraft
Axial Acceleration	AGM-88	●
Maneuverability	AA-11	●
Speed / altitude	SM-3	●
Dynamic pressure	PAC-3	●
Size	Javelin	●
Weight	FIM-92	●
Production cost	GBU-31	●
Observables	AGM-129	○
Range	AGM-86	–
Kills per use	Storm Shadow	–
Target acquisition	LOCAAS	–

● Superior ◒ Better ○ Comparable – Inferior

Fig. 1.2 Tactical missiles are different from fighter aircraft.

difference is the relatively small size and lighter weight of missiles in comparison to combat aircraft, examples including the Stinger and Javelin man-portable missiles. Related to cost, missiles are a throwaway. As a result, they are more cost driven than combat aircraft. Development cost is lower for missiles, and the difference in production cost is even more dramatic. An example is the GBU-31 JDAM, with unit cost on the order of $10,000 to $20,000, compared to a cost of tens of millions of dollars for typical combat aircraft.

Cruise missiles such as AGM-129 can have radar cross section (RCS) comparable to that of low observable aircraft. A cruise missile can achieve low RCS without the same limitations for aircraft such as pilot integration and cockpit, windshield, and fire control sensors. However, a design limitation for cruise missiles is launch platform integration, which may limit the amount of low RCS configuration shaping and tailoring that is practical with a span constraint.

Areas where the combat aircraft generally have superior capability include range, targets killed per use, and target acquisition. Although the conventional version of the AGM-86 cruise missile (CALCM) has a flight range that can exceed 700 n miles, combat aircraft can have a much longer range. In the area of target kill capability, precision strike missiles have become more efficient in recent years, with a single target kill probability approaching one and a capability for multiple target kills. The Storm Shadow and Scalp are examples of efficient precision strike missiles. Precision strike missiles have high accuracy and are capable of dispensing submunitions, exhibiting high firepower. However, the same missiles are load-outs on combat aircraft, and so the enhancement in missiles also enhances the combat aircraft effectiveness and firepower. Finally, although missiles such as Brimstone and smart powered submunitions such as the Low Cost Autonomous Attack Submunition (LOCAAS) have demonstrated a capability for automatic target recognition (ATR), a combat aircraft with a human pilot continues to have superior capability for target recognition, discrimination, and acquisition. Autonomous target acquisition by missiles is a relatively immature technology that will improve in the future with new technologies such as multimode and multispectral seekers. A lower risk, but more human logistical intensive alternative to autonomous target acquisition is to use real-time two-way data links.

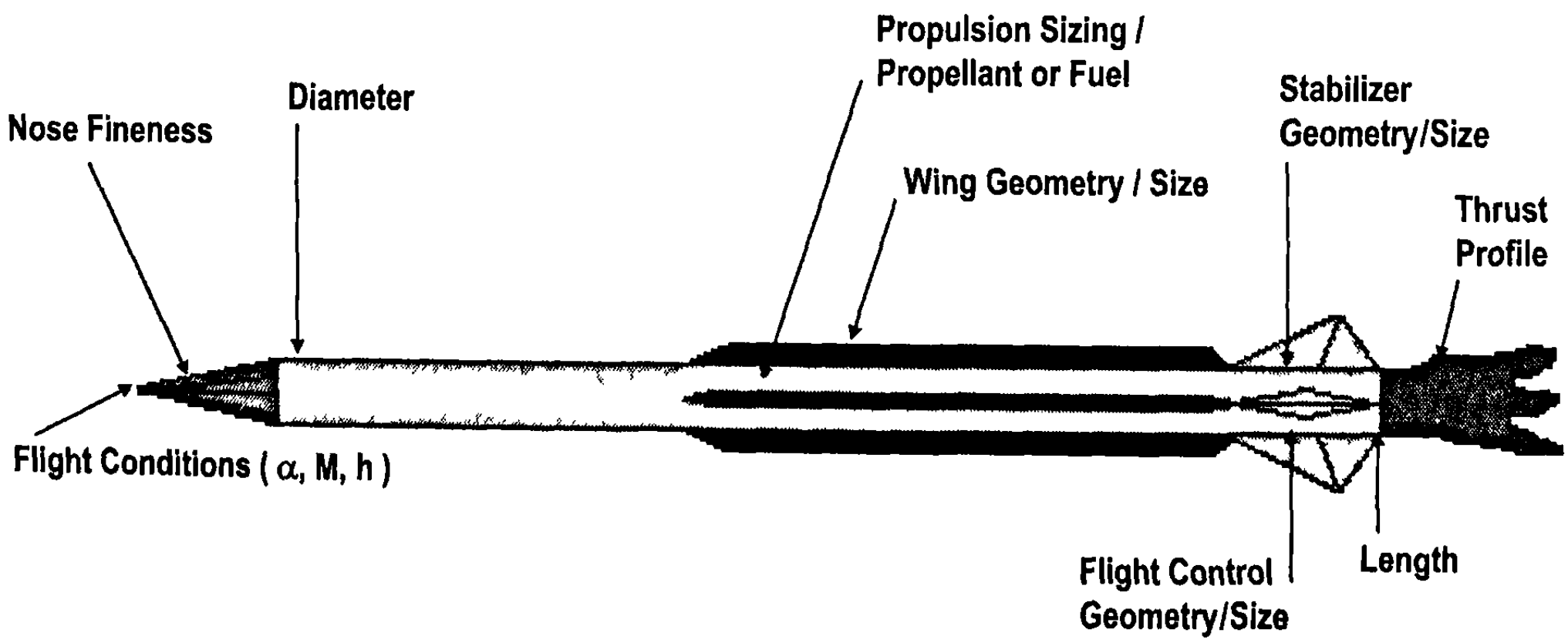

Fig. 1.3 Aerodynamic configuration sizing parameters emphasized in this text.

Figure 1.3 is a summary of the aerodynamic configuration sizing parameters emphasized in this text. These are flight conditions (α, M, h), nose fineness, diameter, propellant/fuel type and weight, wing geometry/size, stabilizer geometry/size, flight control geometry/size, length, and thrust profile. Flight condition parameters that are most important in the design of tactical missiles are angle of attack α, Mach number M, and altitude h. For the aerodynamic configuration, the missile diameter and length have a first-order effect on characteristics such as missile drag, subsystem packaging available volume, launch platform integration, seeker and warhead effectiveness, and body bending. Another configuration driver is nose fineness, an important contributor to the drag of supersonic missiles. Nose fineness also affects seeker performance, available propellant length, and missile observables. Another example is missile propellant/fuel type and weight, which drive flight performance range and velocity. The aerodynamic configuration wing geometry and size are often set by maneuverability requirements and aerodynamic efficiency. Stabilizer geometry and size are often established by static margin requirements. In the flight control area, the geometry and size of the flight control surfaces determine the maximum achievable angle of attack and the resulting maneuverability. Finally, the thrust profile determines the missile velocity time history.

1.3 Conceptual Design Process

Figure 1.4 shows a typical conceptual design process for missiles. Conceptual design is an iterative process, requiring a number of design iterations to achieve a balance of emphasis from the diverse inputs and outputs. The major tasks of conceptual design are 1) mission/scenario definition; 2) weapon requirements, trade

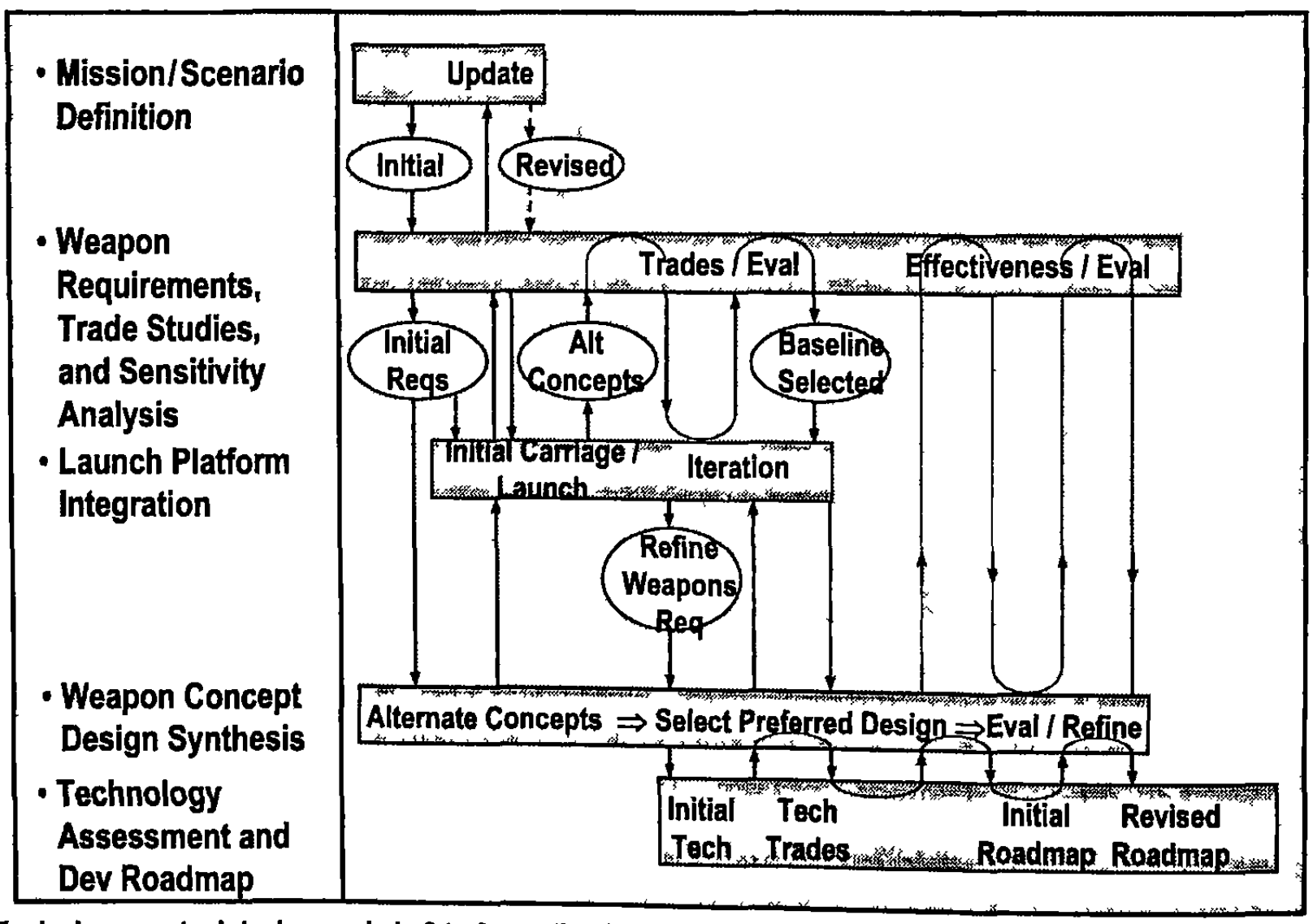

Note: Typical conceptual design cycle is 3 to 9 months. House of quality may be used to translate customer requirements to engineering characteristics. DOE may be used to efficiently evaluate the broad range of design solutions.

Fig. 1.4 Conceptual design process requires evaluation of alternatives and iteration.

studies, and sensitivity analysis; 3) physical integration of the missile with the launch platform; 4) weapon concept design synthesis; and 5) technology assessment and technology development roadmap. The initial design process begins with a general definition of the mission/scenario. The input is a "requirements pull" of the desired capability from the military customer. The customer input for mission requirements is usually not changed during the design study. However, sometimes the mission requirements may be changed by the customer during the design study. Examples are if they are found to be too demanding, too expensive, or the "technology push" of potential technology availability that is provided by the technical community shows that a new technology can be better utilized by different mission requirements. A house of quality may be used to relate the customer requirements and their relative weighting to the engineering design characteristics. The weapon requirements, trade studies, and sensitivity analysis task provide the high level requirements on the missile such as range, time to target, and other measures of merit. This task is oriented toward an operations analysis of a system-of-systems, including command, control, and communication (C^3) targeting. The high level requirements that were initially provided by the military customer are refined through computer modeling. The system-level computer models may be characterized as campaign, raid, or engagement models. In a campaign model many different types of systems are interacting over a simulated time interval from days to weeks. A raid model has multiple platforms engaging multiple targets during a single raid. An engagement model may be that of a single launch platform and missile engaging a single target or threat. The third task, physical integration of the missile with the launch platform, provides constraints such as the length, span, and weight. This task is oriented toward systems integration. The fourth task, weapon concept design synthesis, is the most iterative and arguably the most creative. Characteristics such as the aerodynamic shape, propellant or fuel type and weight, flight trajectory range, time to intercept, maneuverability, seeker detection range, accuracy, lethality, and cost are evaluated; and the missile is resized and reconfigured in an iterative process. For example, the tail stabilizers and flight control surfaces may be resized for improved stability or maneuverability. Another example is adding propellant or fuel to match the flight range requirement. As the design matures and becomes better defined through iteration, the number of alternative solutions is reduced from a broad range of possibilities to a smaller set of preferred candidates that are more reasonable and cost effective. More in-depth information is provided for the design subsystems as the design matures. Finally, a technology assessment task further defines the subsystems and selects the best technologies from the candidate approaches. The technology trades lead to a set of preferred, enabling technologies. A technology roadmap documents the development plan for maturing the enabling technologies.

A typical duration for a conceptual design activity is three to nine months. The products of the missile design activity include refined mission/scenario definitions, system-of-systems definition of the missile requirements, and the interface of the missile with other system elements such as targeting, launch platform compatibility compliance, advanced missile concepts, identification of the enabling technologies, and a technology roadmap.

Figure 1.5 shows the evaluation of alternatives and the iterative process used for conceptual design synthesis. Based on mission requirements, an initial baseline from an existing missile with similar propulsion is established. It is used as a starting point to expedite the design convergence. Advantages of a baseline missile include the prior consideration of balanced system engineering for the subsystems and the use of an accurate benchmark based on existing test data (e.g., wind-tunnel data). Changes are made in the baseline missile aerodynamics, propulsion, weight, and flight trajectory to reflect the new requirements of the new missile concept. The new conceptual design is evaluated against its flight performance requirements (e.g., range, time to target, maneuver footprint). The aerodynamics portion of the conceptual design process is an investigation of alternatives in configuration geometry. The output of the aerodynamics calculation is then inputted to the propulsion system design to size the propulsion system. Propulsion sizing includes providing sufficient propellant or fuel to meet the range and time-to-target requirements. The next step is to estimate the weight of the new missile with its modified aerodynamics and propulsion. Much of this activity is focused on structural design, which is sensitive to changes in flight performance. Following the weight sizing, flight trajectories are computed for the new missile. The range, terminal velocity, maneuverability, and other flight performance parameters are then compared with the mission flight performance requirements. If the missile does not meet the flight performance requirements, it is resized and reiterated. After completing a sufficient number of iterations to meet the flight performance requirements, the next step

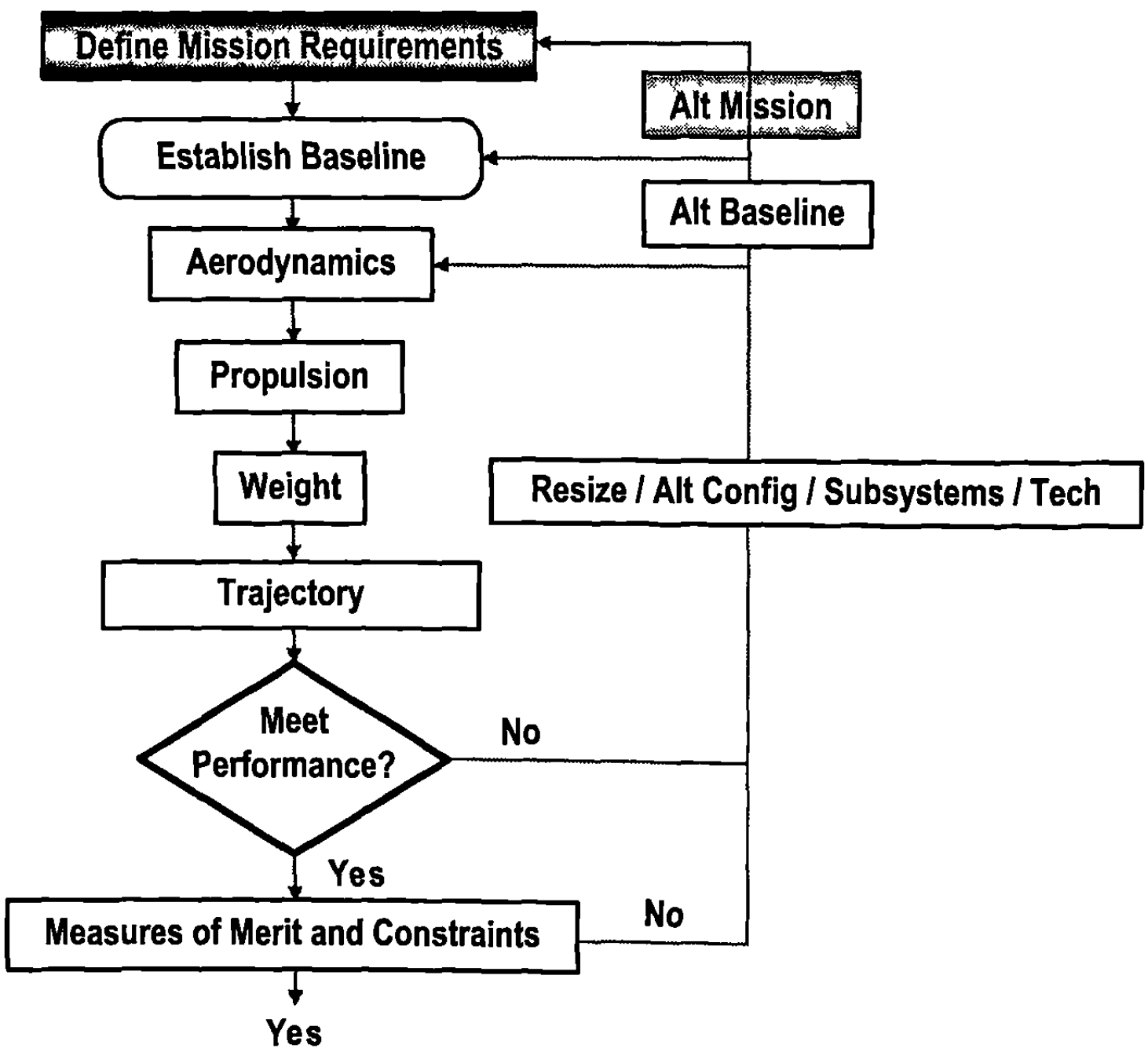

Fig. 1.5 Missile concept synthesis requires evaluation of alternatives and iteration.

is evaluating the new missile against the other measures of merit and constraint requirements. If the missile does not meet the requirements, the design is changed (alternative configuration, subsystems, technologies) and resized for the next iteration and evaluation.

A synthesized missile will differ from the starting point baseline in several respects. For example, the wing area may have been resized to meet the maneuverability requirement. The tail area may have been resized to meet static margin and maximum trim angle-of-attack requirements. The rocket motor or the ramjet engine may have been modified to improve its efficiency at the selected design altitude or Mach number. Additionally, the length of the propulsion system may have been changed to accommodate additional propellant/fuel necessary to satisfy flight range requirements. The design changes are reflected in revisions to the mass properties, configuration geometry, thrust profile, and flight trajectory for the missile. Typically, three to six design iterations are required before a synthesized missile converges to meet the flight performance requirements.

Although a missile design may meet performance requirements and satisfy the other measures of merit and launch platform constraints, it is not necessarily an optimum missile design. It is good design practice to evaluate as many design alternative concepts as possible within the time duration of the design study. A design of experiments (DOE) is an efficient approach to evaluate the broad set of alternatives.

Following conceptual design, the missile is further refined in preliminary design. Preliminary design activities include parameter optimization and ground tests.

1.4 Examples of State-of-the-Art Missiles

Shown in Figs. 1.6 and 1.7 are examples of state-of-the-art missiles for the mission areas of air to air, air to surface, surface to surface, and surface to air. Reference 1 was a source for the missile drawings. Each mission area has examples of short-, medium-, and long-range missiles. Short-range missiles operate within visual range engagements, less than about 3 n miles, have rocket propulsion, and are usually guided by an electro-optical (e.g., infrared, laser) seeker, with seeker lock-on before launch. Medium-range missiles can operate beyond visual range engagements out to the earth's horizon, about 20 n miles, have rocket propulsion, and are usually guided by a radar seeker. Most medium-range missiles also have an inertial reference system and are capable of seeker lock-on after launch. Long-range missiles have ranges greater than the earth's horizon. Long-range missiles have combined inertial/seeker guidance and are capable of seeker lock-on after an inertial midcourse fly-out to the vicinity of the target. Long-range tactical missiles may have rocket, ducted rocket, ramjet, or turbojet propulsion, depending upon their speed and range requirements. Tactical ballistic missiles are rocket powered, while cruise missiles have air-breathing propulsion.

Three examples are shown in the top of Fig. 1.6 of the state-of-the-art drivers of air-to-air missiles. The selected drivers are air-to-air maneuverability, performance with light weight, and range. An example of a short-range air-to-air missile is the highly maneuverable AA-11 Archer. An example of a medium-range missile

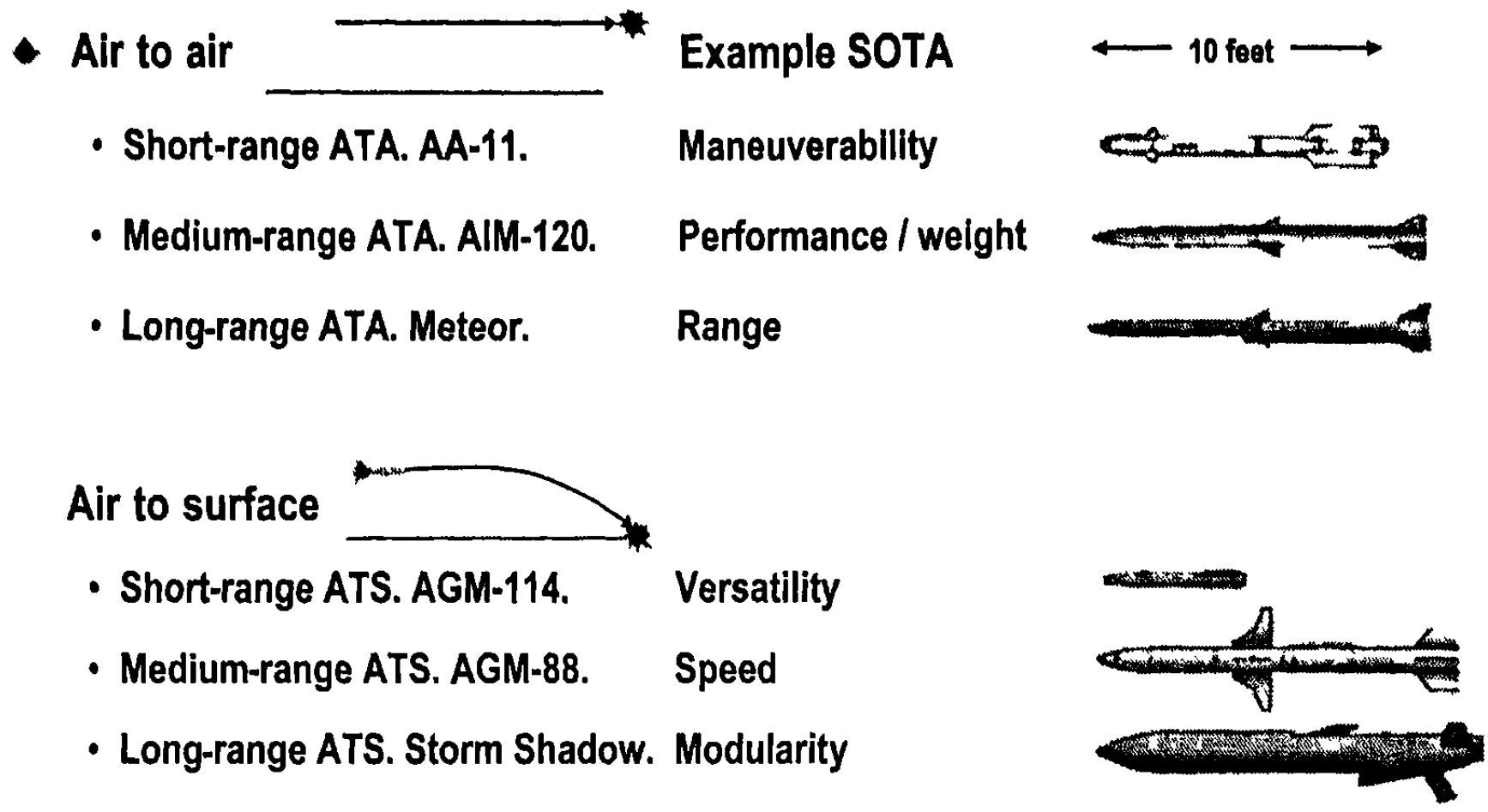

Permission of Missile Index. Copyright 1997©Missile.Index All Rights Reserved

Fig. 1.6 Examples of air-launched missile missions/types.

is the high-performance/lightweight AIM-120 AMRAAM. Finally, an example of a long-range missile is the ducted rocket Meteor.

Three examples are shown in the bottom of Fig. 1.6 of the state-of-the-art drivers for air-to-surface missile types. The selected drivers are air-to-surface versatility, speed, and modularity. The examples are a short-range air-to-surface missile represented by the versatile AGM-114 Hellfire, a medium-range missile represented by the high-speed radar defense suppression AGM-88

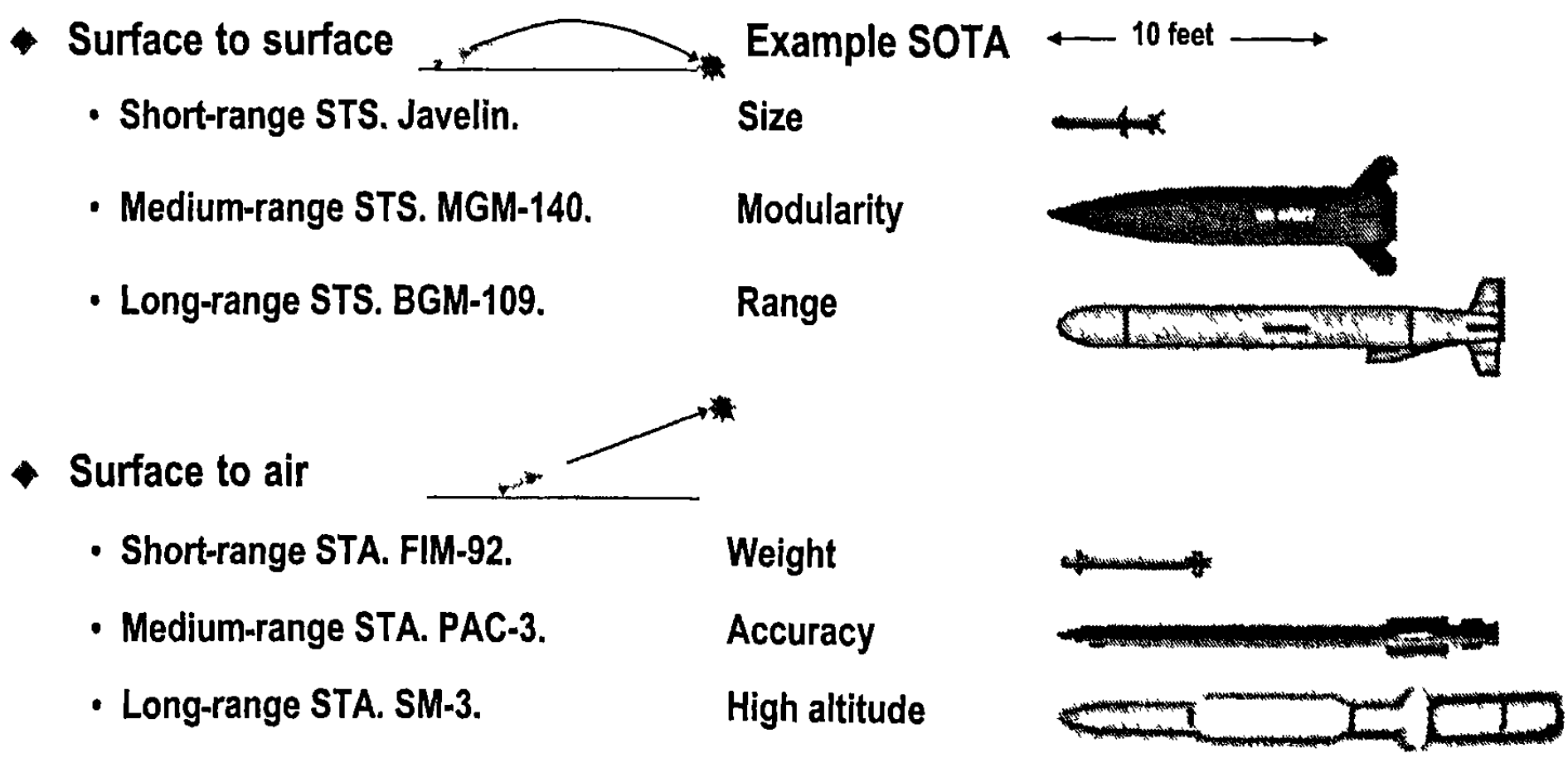

Permission of Missile.Index. Copyright 1997©Missile.Index All Rights Reserved

Fig. 1.7 Examples of surface-launched missile missions/types.

HARM, and a long-range missile represented by the precision strike modular Apache/Storm Shadow/Scalp.

Examples are shown in the top of Fig. 1.7 of tactical surface-to-surface missiles that illustrate the state-of-the-art drivers. The selected drivers are surface-to-surface size, modularity, and range. The example missiles are the man-portable Javelin anti-tank missile, the medium-range modular payload (e.g., dumb submunitions, smart submunitions, unitary surface warhead, penetrator warhead) MGM-140 ATACMS, and the long-range BGM-109 Tomahawk.

Surface-to-air missile state-of-the art drivers are shown in the bottom of Fig. 1.7. The selected drivers are surface-to-air weight, accuracy, and altitude. The missiles shown are the short-range lightweight FIM-92 Stinger, medium-range hit-to-kill PAC-3, and the long-range high-altitude SM-3 Standard Missile.

1.5 Aerodynamic Configuration Sizing Parameters

Aerodynamic configuration sizing parameters have an impact on missile requirements. Figure 1.8 is an assessment of the relative impact of aerodynamic configuration sizing parameters on flight performance measures of merit (e.g., weight, range, maneuver footprint, time to target). Also shown is the impact of aerodynamic configuration sizing parameters on other measures of merit (e.g., robustness, lethality, miss distance, observables, survivability, cost), as well as their impact on constraints (e.g., launch platform integration weight, length, and span constraints).

The aerodynamic configuration sizing parameters that are addressed in this text are listed on the left side of the figure. These are nose fineness, diameter, length, wing geometry/size, stabilizer geometry/size, flight control

Aero Configuration Sizing Parameter	Impact on Weapon Requirement									
	Aero Measures of Merit			Other Measures of Merit						Constraint
	Weight	Range / Maneuver	Time to Target	Robust-ness	Lethality	Miss Distance	Observ-ables	Survivability	Cost	Launch Platform
Nose Fineness	●	●	●	○	●	●	●	●	◒	○
Diameter	●	●	●	○	●	◒	○	○	●	●
Length	●	●	◒	○	◒	◒	○	○	●	●
Wing Geometry / Size	●	●	◒	○	●	●	◒	◒	◒	●
Stabilizer Geometry / Size	●	●	○	○	●	●	◒	◒	◒	●
Flight Control Geometry / Size	●	●	○	○	●	●	◒	◒	◒	●
Propellant / Fuel	●	●	●	○	◒	◒	◒	●	◒	◒
Thrust Profile	●	●	●	○	◒	◒	●	●	◒	–
Flight Conditions (α, M, h)	●	●	●	●	●	●	●	●	●	○

● Very Strong ◒ Strong ○ Moderate – Relatively Low

Fig. 1.8 Aerodynamic configuration sizing has high impact on mission requirements.

geometry/size, propellant/fuel, thrust profile, and flight conditions (angle of attack, Mach number, altitude). Note from the figure that the parameters have very strong impact on missile requirements in the areas of weight, range, and maneuverability. The aerodynamic configuration sizing parameters also have a strong impact in the areas of lethality, miss distance, and cost.

1.6 Example of Alternatives in Establishing Mission Requirements

Figure 1.9 is an example of alternative approaches that should be considered in establishing future mission requirements. It illustrates an assessment of alternative approaches for precision strike. The assessment includes the approaches that are used today by current systems, as well as a projection of capabilities that may be used in the future for new missile systems. Three measures of merit are assumed in comparing future precision strike missiles with the current systems. These are cost per shot, number of launch platforms required, and the effectiveness against time-critical targets (TCTs). For the current systems, two approaches are used: 1) penetrating aircraft with relatively short range subsonic precision guided munitions or missiles and 2) standoff platforms (ships, submarines, or aircraft) using subsonic cruise missiles. The penetrating aircraft systems include the F-117 with subsonic precision guided munitions such as JDAM. As shown, penetrating aircraft/subsonic precision guided munitions have an advantage of low cost per shot, about $10,000 to $20,000. However, the experience in Desert Storm showed that subsonic penetrating

Alternatives for Precision Strike	Measures of Merit		
	Cost per Shot	Number of Launch Platforms Required	TCT Effectiveness
Future Systems			
◆Standoff platforms / hypersonic missiles	○	●	◒
◆Overhead loitering UCAVs / hypersonic missiles	◒	◒	●
◆Overhead loitering UCAVs / lightweight PGMs	●	○	◒
Current Systems			
◆Penetrating aircraft / subsonic PGMs	●	–	–
◆Standoff platforms / subsonic missiles	○	●	–

Note: ● Superior ◒ Good ○ Average – poor

Note: C4ISR targeting SOTA for year 2010 projected to provide sensor-to-shooter/weapon connectivity time of less than 2 m and TLE of less than 1 m for motion-suspended target.

Fig. 1.9 Example of assessment of alternatives to establish future mission requirements.

aircraft do not have the capability to counter TCTs such as theater ballistic missiles (TBMs). Another current approach using standoff platforms such as ships, submarines, and large aircraft outside the threat borders requires fewer launch platforms, resulting in lower logistics costs. However, standoff platforms with subsonic cruise missiles (e.g., Tomahawk, CALCM) are also ineffective against TCTs.

Also shown in the figure are future missile system alternatives for precision strike. Technology development work is under way in all three of the areas; the best approach has yet to be demonstrated. One approach is based on a standoff platform, with an aircraft, ship, or submarine standing off outside the threat country border. Hypersonic long-range precision strike missiles would provide broad coverage, holding a large portion of the threat country at risk. This approach is attractive because only a small number of launch platforms are required and there is good effectiveness against TCTs. Based on current technology programs, the cost of future hypersonic missiles is projected to be comparable to that of current cruise missiles.

Another potential alternative approach is to use overhead loitering unmanned combat air vehicles (UCAVs) with small hypersonic missiles. The number of UCAVs required is dependent upon the speed and range of their onboard missiles and the loiter altitude. A high loiter altitude tends to reduce the available payload weight/firepower. This approach would probably provide the fastest response time against TCTs because of the shorter required flight range of the missile.

A third approach is overhead loitering UCAVs with advanced lightweight precision guided munitions. Again, a design consideration is the loiter altitude required for survivability versus the weapon payload. This approach would have the lowest cost per shot but would also require a larger number of UCAVs.

An enabling synergistic capability for precision strike is the application of near-real-time, accurate targeting from either overhead tactical satellite or overhead unmanned air vehicle (UAV) sensors. It is projected that an advanced command, control, communication, computers, intelligence, surveillance, reconnaissance (C4ISR) network will be available around the year 2010 to support near-real-time and high accuracy targeting of TCTs. The C4ISR network could be used by all types of launch platforms (e.g., fighter aircraft, bombers, helicopters, UCAVs, ships, submarines, and ground vehicles). Illustrated in Fig. 1.10 are examples of a ground station, overhead satellite sensors and satellite relays, and the overhead UAV sensor platform elements of the assumed C4ISR architecture. The assumed C4ISR of the year 2010 is projected to have a capability for a target location error (TLE) of less than 1 m (1σ) for a motion suspended target and a sensor-to-shooter/weapon connectivity time of less than 2 min (1σ). A two-way data link from the launch platform to the missile will allow in-flight target updates and battle damage indication/battle damage assessment (BDI/BDA). An enabling capability for a lightweight/low-volume missile data link is phased array antenna technology. A phased array antenna can be conformally mounted on the missile airframe.

Figure 1.11 is an illustration of system-of-systems analysis. The example is a system analysis to develop mission requirements for precision strike in the year 2010 timeframe. A comparison is made of a subsonic cruise missile versus a

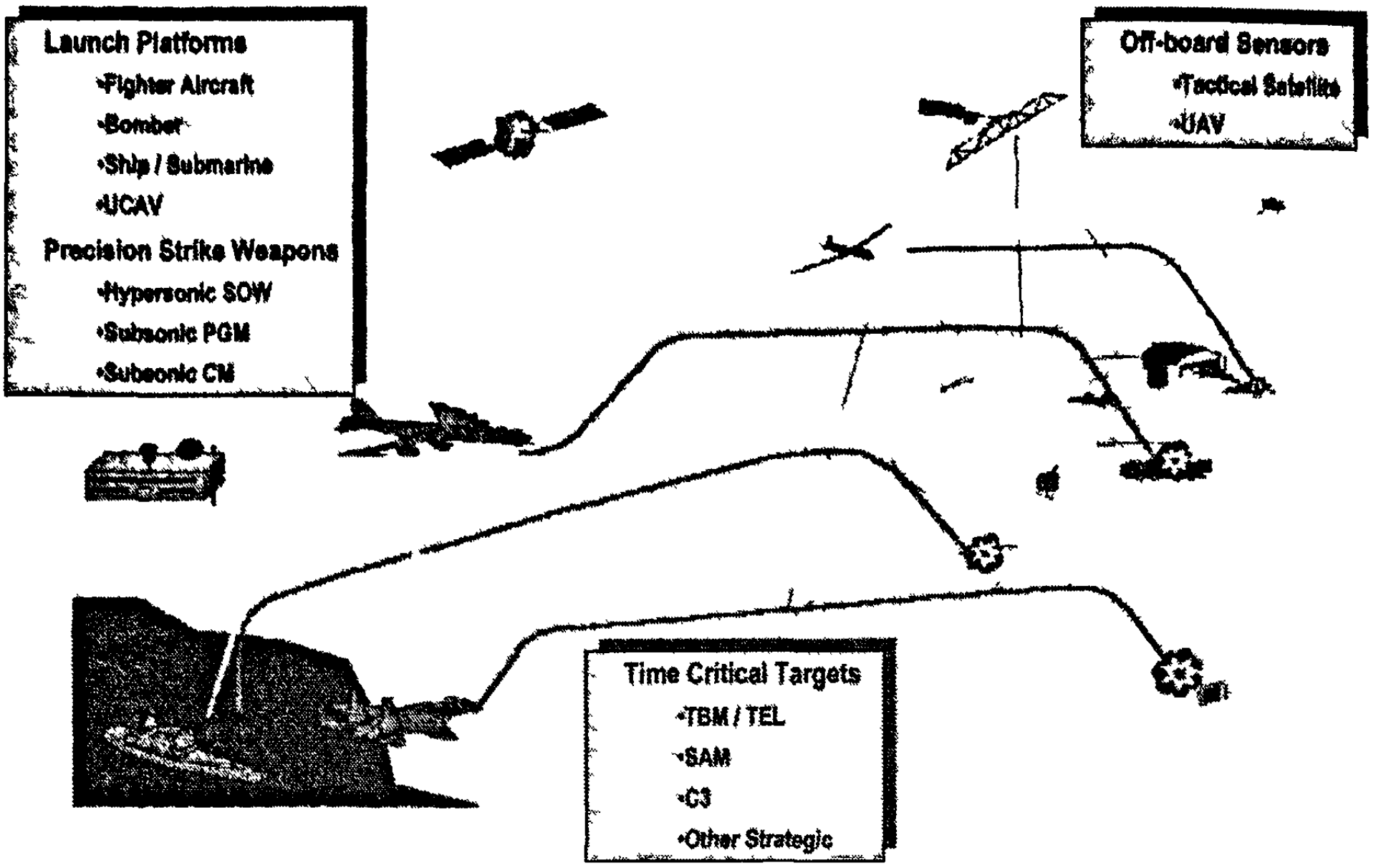

Note: C4ISR targeting state-of-the-art for year 2010 projected to provide sensor-to-shooter / weapon connectivity time of less than 2 m and target location error (TLE) of less than 1 m for motion suspended target.

Fig. 1.10 C4ISR tactical satellites and UAVs have high impact on mission capability. Figure also in color section.

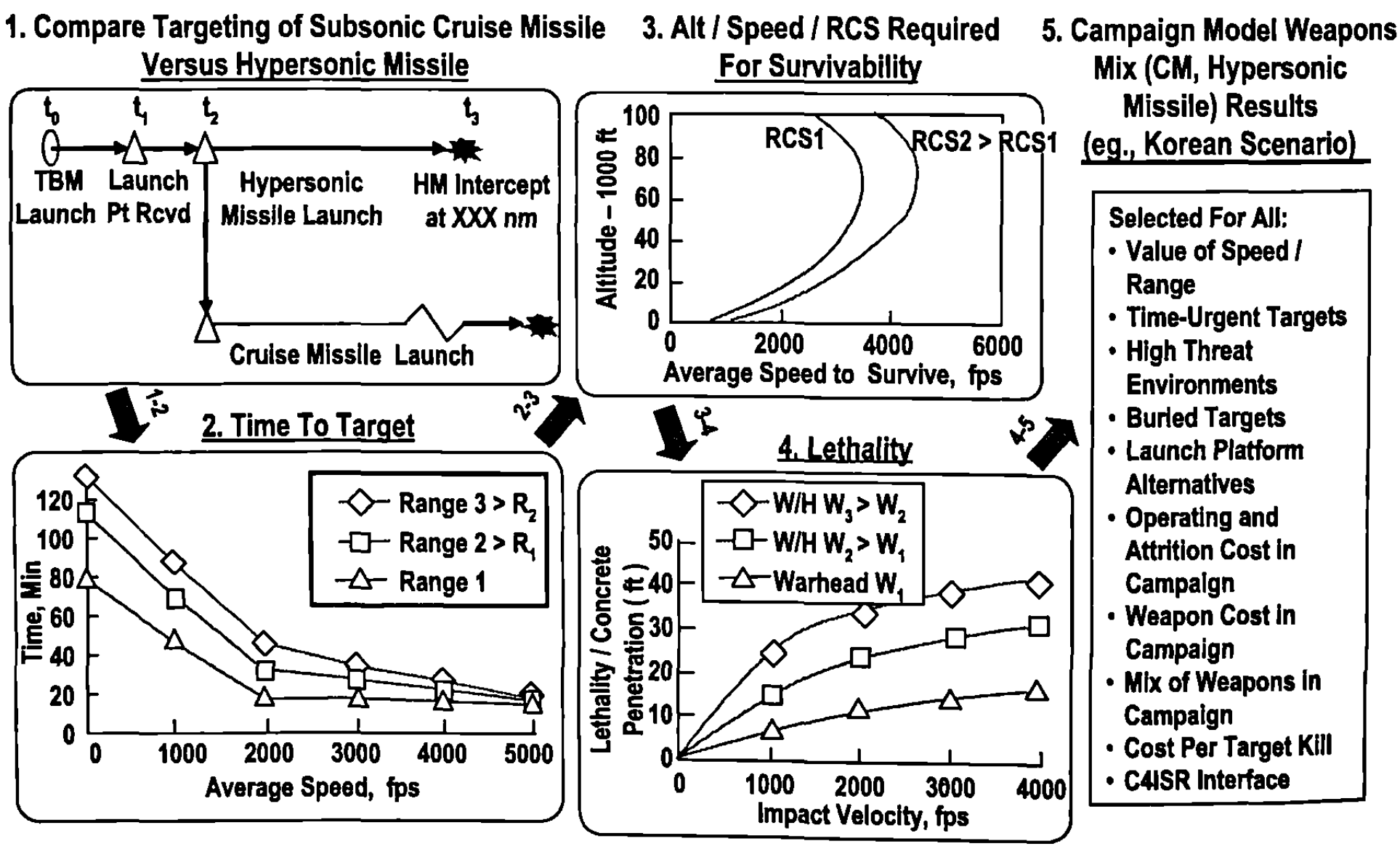

Fig. 1.11 Example of system-of-systems analysis to develop future mission requirements.

hypersonic missile. In the initial activity, requirements are defined for the targeting time of the two missiles. In the example both missiles rely on receiving the target location in near real time, with a fast response capability for launch. The second activity (shown in the lower left section of the figure) develops a solution matrix of time-to-target versus average speed. Shown in the figure are three assumptions of a relatively short-range R_1 for standoff against a relatively small country (e.g., North Korea), medium-range standoff R_2, and long-range standoff R_3 against a relatively large country (e.g., Iran). Based on the knee of the curve of standoff range versus speed, an average speed is selected and a third activity is initiated, involving tradeoffs of flight attitude versus the level of reduced observables required for survivability. In the fourth activity (lower right section of the figure) a tradeoff is made of the missile lethality. In the example the impact velocity required for penetration of a buried target is evaluated as a function of warhead weight. Finally, a system-of-systems analysis campaign modeling activity is initiated (upper right section of the figure) to derive the weapon system-of-systems requirements such as the best mix of cruise missiles and hypersonic missiles for a representative scenario (e.g., Korean scenario). Measures of merit include the value of speed and range, capability against time-urgent targets, survivability in a high-threat environment, effectiveness against buried targets, launch platform alternatives (e.g., ship, aircraft, submarine), operating and attrition cost during the assumed campaign, cost of the number of weapons used during the campaign, mix of weapons (e.g., long-range hypersonic missile, long-range cruise missile, shorter range weapons), cost per target kill, and the requirements for the C4ISR interface.

Figure 1.12 is another illustration of the impact of mission requirements on missile design. It shows an example of technological surprise driving immediate mission requirements. The example is mission requirements for short-range air-to-air missiles. A comparison is made of the older technology AIM-9L Sidewinder with the technological surprise of the newer technology from the highly maneuverable Archer AA-11/R-73 missile. As a result of the technological surprise of the AA-11, there was a sudden mission requirement for the United States to develop the AIM-9X missile.

Shown on the left side of the figure are the off-boresight and flight range capability of the AIM-9L Sidewinder. The initial operational capability (IOC) for AIM-9L was the year 1977. The performance of the AIM-9L is +/−25 deg off boresight and approximately 6.5 n miles range. Contrasting with AIM-9L is a more recent missile, the Archer AA-11/R-73. The Archer is described in the right section of the figure. The Archer has a more recent IOC, 1987. Its performance is about +/−60 deg off boresight and 20 n miles range. New technologies developed for the Archer missile include thrust vector control, split canard, near-neutral static margin, +/−90 deg gimbaled seeker, and integration with a helmet-mounted sight. Archer also has forward vanes that weathercock, providing information on the missile angle of attack. In summary, Archer has higher maneuverability, greater off boresight, and longer range than AIM-9L.

Also shown at the bottom of the figure is a video illustrating the off-boresight advantage of a highly maneuverable missile such as Archer versus a relatively low maneuverable missile such as AIM-9L. In the video large off-boresight conditions and intensive pilot activities are required for short-range air-to-air

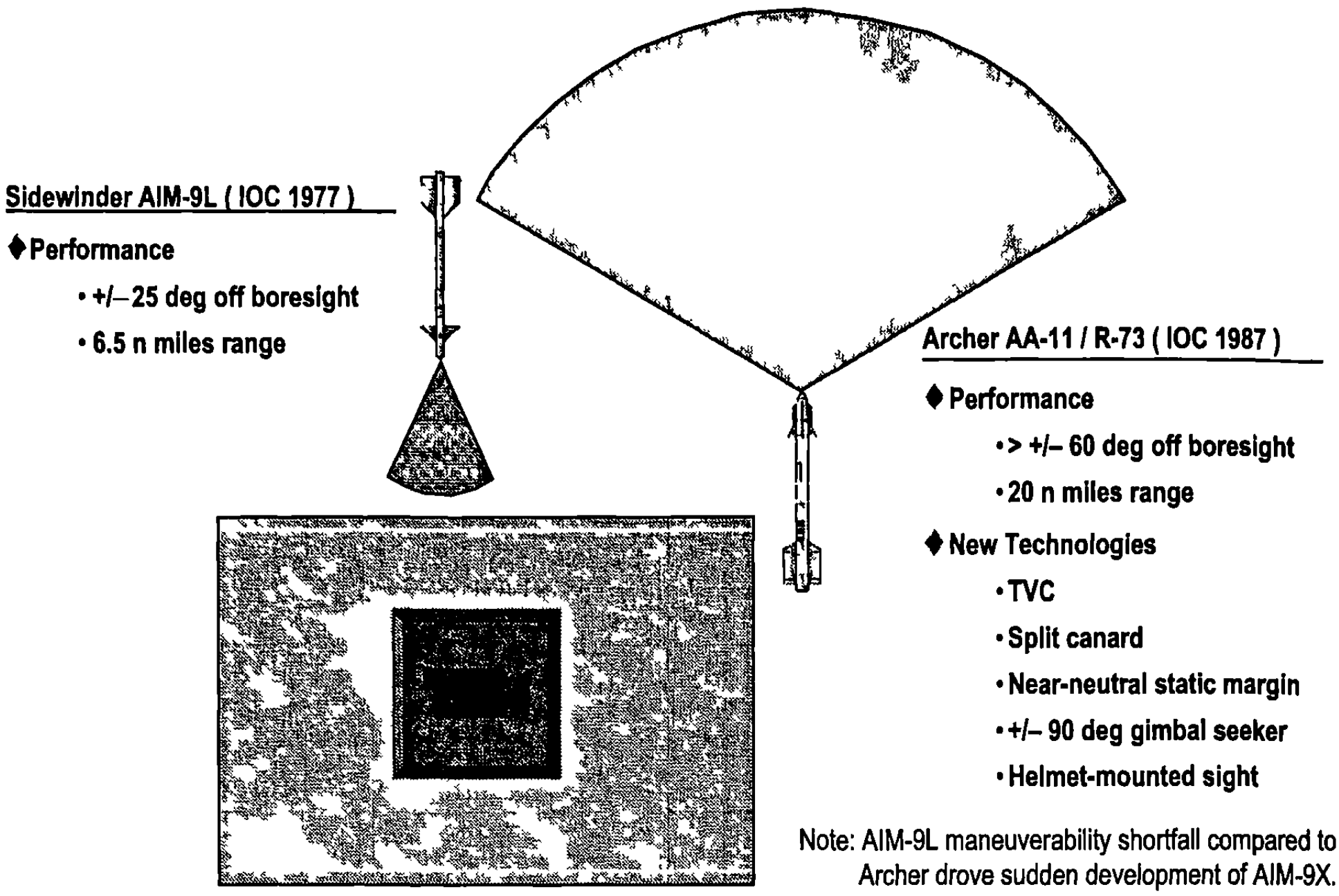

Fig. 1.12 Example of technological surprise driving immediate mission requirements. Video is in the CD included with this textbook.

combat. A highly maneuverable missile such as Archer can be launched at much larger off boresight than a low maneuverable missile such as AIM-9L, allowing an earlier launch in a short-range air-to-air engagement. Because an Archer-type missile has a superior short-range air-to-air capability, an older, relatively low maneuverability aircraft that uses a highly maneuverable, such as Archer, missile may be able to defeat a more modern, highly maneuverability aircraft that has an older, lower technology missile such as AIM-9L. The shortfall of AIM-9L maneuverability compared to the Archer was an immediate driver in the sudden development of AIM-9X. Like the Archer AA-11/R-73, AIM-9X has high maneuverability [through thrust vector control (TVC) and near-neutral static margin] and large off boresight (through a large gimbal angle seeker and integration with a helmet-mounted sight). In addition, AIM-9X has a high-resolution imaging infrared seeker for improved accuracy and countermeasures resistance.

1.7 Use of a Baseline Missile

Missile conceptual design synthesis is an evaluation of alternatives through an iterative process. Alternative configurations, alternative subsystems, and alternative technologies are evaluated in sizing the missile. As shown in Fig. 1.13, following the definition of mission requirements, a baseline missile is selected. For the purpose of this text, two alternative baselines are available for conceptual design, a rocket-powered medium-range missile based on the AIM-7 Sparrow

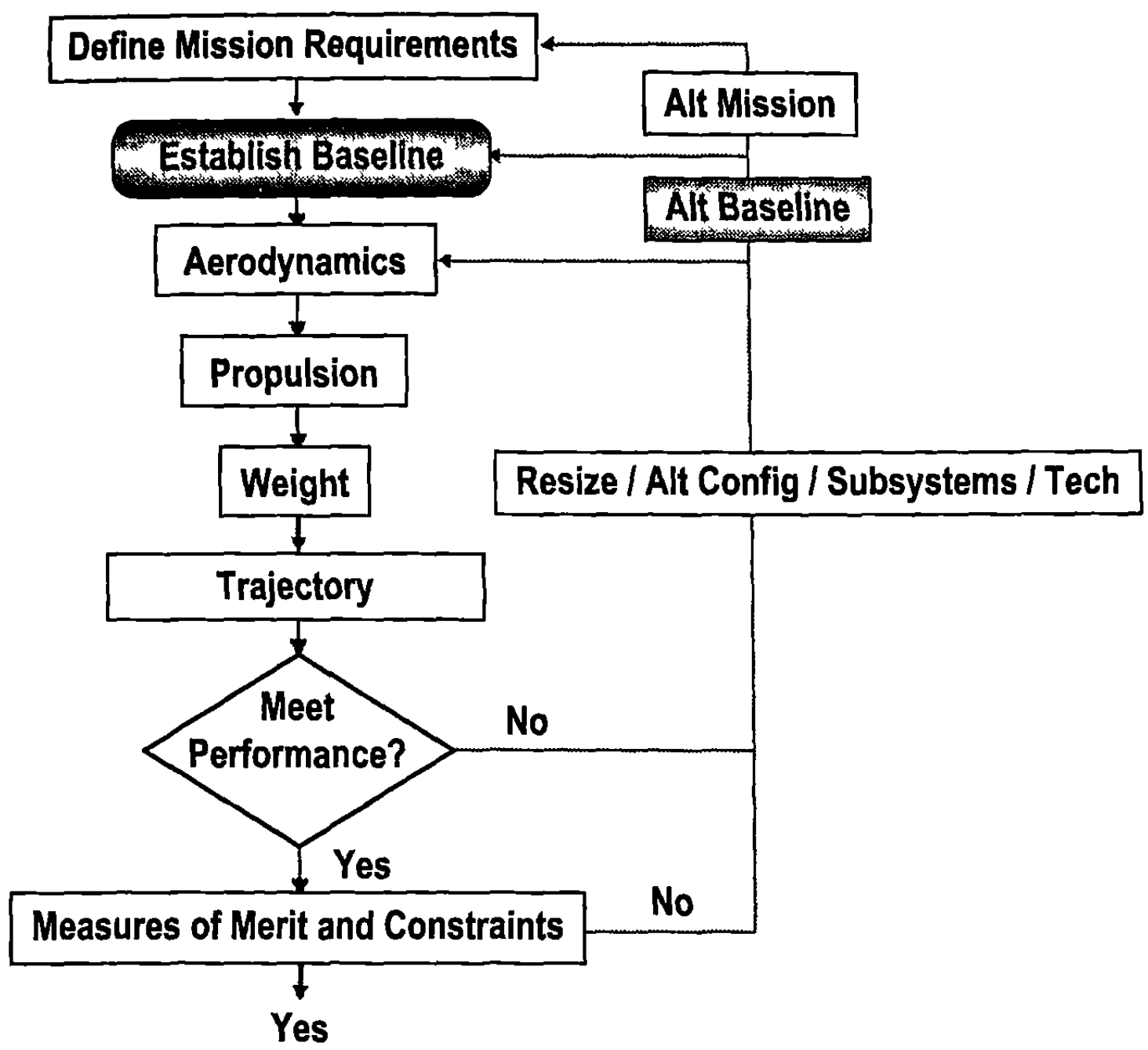

Fig. 1.13 Missile concept synthesis requires evaluation of alternatives and iteration.

and a ramjet-powered long-range missile based on the Advanced Strategic Air Launched Missile (ASALM). Detailed information on the baseline missiles is provided in Chapter 7.

Using a baseline missile to initiate the design process has benefits that include a faster design process and a more accurate design. Because a baseline missile is a real missile that is anchored with test data, it allows simple conceptual design methods to be used with reasonable accuracy. The existing documentation and the configuration control of a baseline missile provide traceability between cause and effect as the conceptual design process is conducted. System engineering has already been applied to the baseline missile, providing a benchmark for balanced subsystems. The startup time for conceptual design is greatly reduced by using a baseline missile. The default values for the conceptual design missile are the baseline missile. Sensitivity trends for the baseline missile indicate changes that would provide an improved design. However, note that one baseline cannot cover all of the range of possible solutions. The more data that are available for missile baselines, the better. Typically the propulsion system of the new conceptual missile should be the same type as that of the baseline missile. The baseline missile flight performance (e.g., range, Mach number, maneuverability) should also be comparable to that of the conceptual design missile. The baseline missile characteristics can usually be extrapolated about $+/-50\%$ with reasonable accuracy.

Note that, when using a baseline missile, it is important not to get locked in by the baseline but to be creative in exploring design alternatives. Also, because the baseline is an existing missile, whereas the conceptual design usually involves a

missile projected for the future, the SOTA must often be projected into the future, particularly for the electronic and sensor subsystems.

Shown in Fig. 1.14 is an example of baseline missile data for conceptual design sizing. The example is based on the chin inlet, integral rocket ramjet baseline described in Chapter 7. In the upper left of the figure is an illustration of a configuration drawing of the baseline missile. The configuration drawing is a dimensioned layout with an inboard profile showing the major subsystems (guidance, warhead, fuel, booster/engine, and flight control surfaces). In the upper center of the figure are examples of tables for a missile weight statement and geometry data. Missile weight and center-of-gravity location are provided for launch, booster burnout, and engine burnout flight conditions. Weight and geometry data are also provided for the major subsystems. The upper right corner of the figure is an illustration of a description of the ramjet internal flowpath geometry. The internal flowpath geometry data include the inlet design capture area and the internal areas of the inlet throat, diffuser exit, flame holder plane, combustor exit, nozzle throat, and nozzle exit. Examples of aerodynamic data plots are illustrated in the left center section of the figure. The aerodynamic data of the ramjet baseline cover angles of attack up to 16 deg and Mach numbers up to 4.0. Aerodynamic coefficients and derivatives include zero-lift drag coefficient C_{D_0}, normal force coefficient C_N, pitching moment coefficient C_m, pitching moment control effectiveness derivative C_{m_δ}, and normal force control effectiveness derivative C_{N_δ}. Examples of ramjet propulsion thrust T and the ramjet specific impulse I_{SP} are shown in the center of the figure. Thrust of the ramjet baseline is a function of Mach number, altitude, and fuel-to-air ratio. Specific impulse of the ramjet baseline is primarily a

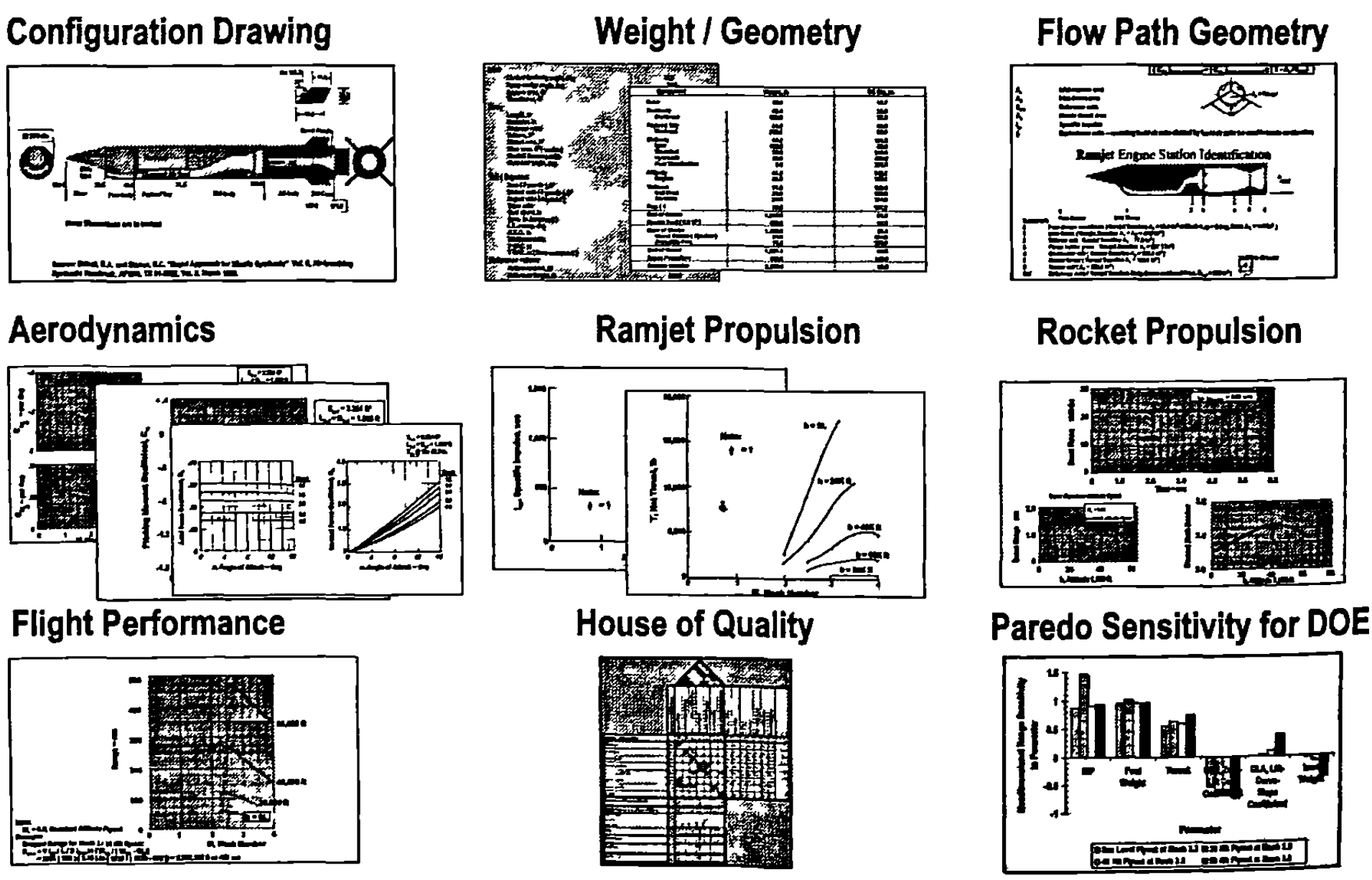

Fig. 1.14 Example of missile baseline data. Figure also in color section.

function of Mach number for fuel-to-air ratios less than stochiometric. Rocket booster propulsion thrust, boost range, and burnout Mach number are illustrated in the right center of the figure as a function of launch Mach number and altitude. The left bottom section of the figure shows the maximum flight range of the ramjet baseline. Maximum flight range is a function of the launch Mach number, launch altitude, cruise Mach number, and the cruise altitude. In the left bottom center section is an example of a house of quality which includes a most important requirements weighting. The house of quality is developed through a consensus with the customer on the most important requirements and their relative weighting. It is used to map the "voice of the customer" to the "voice of the engineer." The weighting from the house of quality is a tool for the downselect of the preferred concept alternative. Finally, the right bottom section of the figure is an example of a Paredo (ranking) sensitivity of design parameters to a measure of merit (e.g., maximum flight range). The Paredo sensitivity study is used to define a DOE set of alternative concepts for the design study. The sensitivity study in the example was conducted for cruise flight conditions ranging from Mach 2.3, sea level to Mach 3.0, 60,000 ft in altitude.

Shown in Fig. 1.15 is the process of using baseline missile data to provide enhanced accuracy to prediction methods. The predicted values of the design parameters from the conceptual design prediction methods are corrected by the baseline missile data. First, an uncorrected prediction is made of a notional conceptual design parameter $P_{CD,U}$. Second, an uncorrected prediction is made of the baseline missile notional parameter $P_{B,U}$. The correction in the prediction for the baseline missile $P_{B,C}/P_{B,U}$ provides a correction to the

$$P_{CD,C} = (P_{B,C} / P_{B,U})\, P_{CD,U}$$

- $P_{CD,C}$ — Parameter of conceptual design, corrected
- $P_{B,C}$ — Parameter of baseline, corrected (actual data)
- $P_{B,U}$ — Parameter of baseline, uncorrected (computed)
- $P_{CD,U}$ — Parameter of conceptual design, uncorrected (computed)
- Example
  - Ramjet Baseline with RJ-5 fuel (heating value = 11,300,000 ft-lbf / lbm)
  - Advanced Concept with slurry fuel (40% JP-10 / 60% boron carbide = 18,500,000 ft-lbf/lbm)
  - Flight conditions: Mach 3.5 cruise, 60k ft altitude, combustion temperature 4,000 R
  - Calculate specific impulse $(I_{SP})_{CD,C}$ for conceptual design, based on corrected baseline data
    - $(I_{SP})_{B,C} = 1{,}120$ s
    - $(I_{SP})_{B,U} = 1387$ s
    - $(I_{SP})_{CD,U} = 2{,}271$ s
    - $(I_{SP})_{CD,C} = [(I_{SP})_{B,C} / (I_{SP})_{B,U}]\,(I_{SP})_{CD,U} = [(1120) / (1387)]\,(2271) = 0.807\,(2271) = 1{,}834$ s

Fig. 1.15 Baseline design data allows the correction of computed parameters in conceptual design.

prediction method. Finally, the corrected conceptual design parameter $P_{CD,C}$ is computed by

$$P_{CD,C} = (P_{B,C}/P_{B,U})P_{CD,U} \tag{1.1}$$

In the example the ramjet baseline fuel is RJ-5, with a heating value of 11,300,000 ft-lbf/lbm (14,525 BTU/lbm). The assumed fuel of the more advanced conceptual design missile is a high-density slurry fuel consisting of 40% JP-10 and 60% boron carbide. It has a higher heating value of 18,500,000 ft-lbf/lbm. The assumed cruise condition of this example is Mach 3.5, 60,000 ft in altitude. The ramjet combustion temperature is assumed to be 4,000°R. Finally, the uncorrected specific impulse predicted for the high-density fuel $[(I_{SP})_{CD,U} = 2{,}271\ \text{s}]$ is corrected by the ratio of the assumed actual specific impulse of the baseline $[(I_{SP})_{B,C} = 1{,}120\ \text{s}]$ to the predicted specific impulse of the baseline $[(I_{SP})_{B,U} = 1{,}387\ \text{s}]$, giving a factor of 0.807 correction to the specific impulse for the high-density fuel. The corrected specific impulse is

$$\begin{aligned}(I_{SP})_{CD,C} &= [(I_{SP})_{B,C}/(I_{SP})_{B,U}](I_{SP})_{CD,U} \\ &= (1120/1387)(2271) = 0.807(2271) = 1{,}834\ \text{s}\end{aligned} \tag{1.2}$$

1.8 Summary

This chapter provided an overview of the missile design process. Also included were examples of tactical missile characteristics. A comparison was made of tactical missile capabilities with those of combat aircraft. In many cases tactical missiles drive the SOTA more than combat aircraft. The aerodynamic configuration sizing parameters of tactical missiles were identified. It was shown the aerodynamic configuration sizing parameters have a strong impact on the missile system measures of merit and constraints. The chapter also gave examples of the process and considerations for establishing mission requirements. Included was an example of defining the mission requirements for a hypersonic strike missile based on an analysis of a mix of hypersonic strike missiles with subsonic cruise missiles. Another example was the sudden development of a mission requirement for a highly maneuverable air-to-air missile based on a technology surprise that pointed out the shortfall in current capability. Finally, Chapter 1 presented a process for correcting design predictions using baseline missile data. The following chapters of this text will address the specific methods and technologies for tactical missile design.

Problems

1.1 The missile design team should address the areas of mission/scenario definition, weapon requirements, launch platform integration, design, and t_____ a _____.

1.2 The steps to evaluate missile flight performance require computing aerodynamics, propulsion, weight, and flight t_____.

1.3 Air-to-air missile characteristics include light weight, high speed, and high m_____.

1.4 Air-to-surface missiles are often versatile and m_____.

1.5 Four aeromechanics measures of merit are weight, range, maneuverability, and t___ to target.

1.6 The launch platform often constrains the missile span, length, and w_____.

1.7 An enabling capability for hypersonic strike missiles is fast and accurate C____.

1.8 An enabling capability for large off-boresight air-to-air missiles is a h_____ m_____ sight.

1.9 A baseline design improves the accuracy and s____ of the design process.

2
Aerodynamic Considerations in Tactical Missile Design

2.1 Introduction

This chapter addresses aerodynamic considerations for tactical missile design. The conceptual design methods, design tradeoffs, design criteria, and technologies emphasize low-aspect ratio wing and wingless configurations. Consideration is given to missile diameter tradeoffs; nose fineness tradeoffs; boattail considerations; lifting body versus axisymmetric body; calculation of body and surfaces normal force, lift-to-drag ratio, zero-lift drag coefficient, and center-of-pressure location; wings versus no wings; surface planform geometry alternatives; flight control alternatives; maneuver alternatives; roll orientation; static stability; tail area sizing; stability and control conceptual design criteria; and body buildup aerodynamics.

As shown in Fig. 2.1, aerodynamic configuration synthesis follows the initial activities of defining mission requirements and establishing a baseline missile. Aerodynamic configuration synthesis requires consideration of alternative configurations, aerodynamic technology, and the process for resizing the missile. The output of aerodynamic configuration synthesis includes the missile diameter, length, nose geometry, wing size and geometry, stabilizer and control surfaces size and geometry, and the aerodynamic coefficients and derivatives. The output of the aerodynamic configuration synthesis is an input to the propulsion system design.

2.2 Missile Diameter Tradeoff

Missile diameter tradeoff has drivers toward a small diameter as well as drivers toward a large diameter. These must be harmonized. The drivers toward a small diameter missile include lower drag and smaller lateral dimensions for improved launch platform compatibility. However these must be harmonized with the other drivers toward a large diameter missile. These include 1) increased range, higher resolution, better tracking, and higher signal-to-noise for the seeker; 2) increased warhead effectiveness from higher fragment velocity and higher blast overpressure for a blast fragmentation warhead or a longer and faster jet for a shaped charge warhead; 3) increased body bending frequency, which reduces aeroelasticity and improves flight control performance; 4) improved subsystem packaging for diameter limited subsystems; and 5) shorter length for launch platform compatibility.

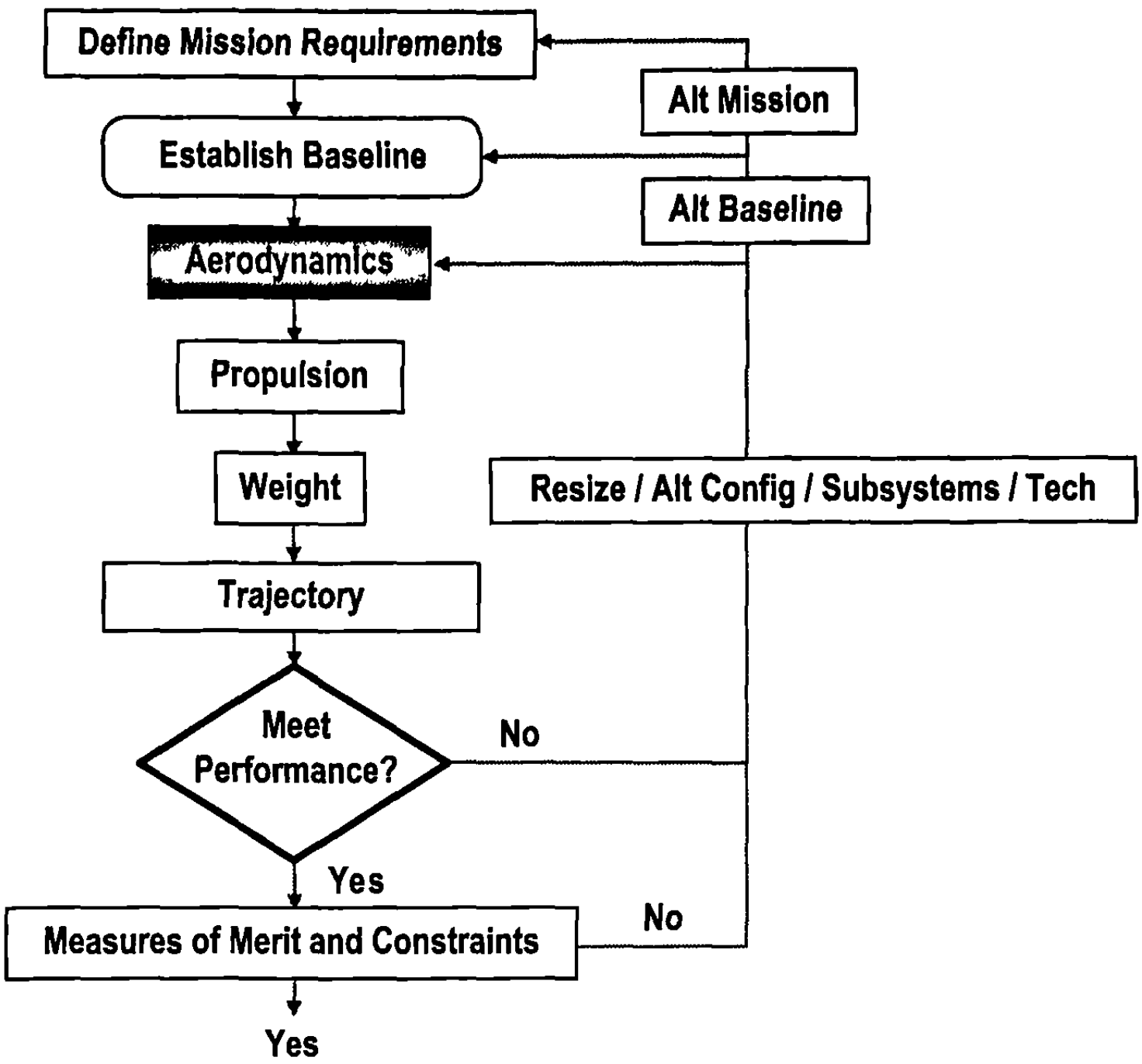

Fig. 2.1 Missile concept synthesis requires evaluation of alternatives and iteration.

The typical range in missile body fineness ratio (length-to-diameter ratio) is

$$5 < l/d < 25 \tag{2.1}$$

An example of a low-fineness missile is the Javelin man-portable anti-armor missile, which has an $l/d = 42.6\text{ in}/5\text{ in} = 8.5$. Javelin is a small subsonic missile with relatively low drag. An example of a high-fineness missile is the AIM-120 AMRAAM supersonic air-to-air missile, which has an $l/d = 144\text{ in}/7\text{ in} = 20.5$.

Drag is a major design parameter in satisfying the flight range requirement of tactical missiles, especially supersonic missiles. It is a function of drag coefficient, dynamic pressure, and reference area, given by the equation

$$D = C_D q S_{\text{Ref}} \tag{2.2}$$

For a missile configuration, the reference area is the body cross-sectional area. Substituting missile diameter for a typical circular cross section gives

$$D = C_D q(\pi/4)d^2 = 0.785\, C_D q d^2 \tag{2.3}$$

Shown in Fig. 2.2 is D/C_D as a function of diameter and dynamic pressure for a typical range in the values of these parameters for tactical missiles.

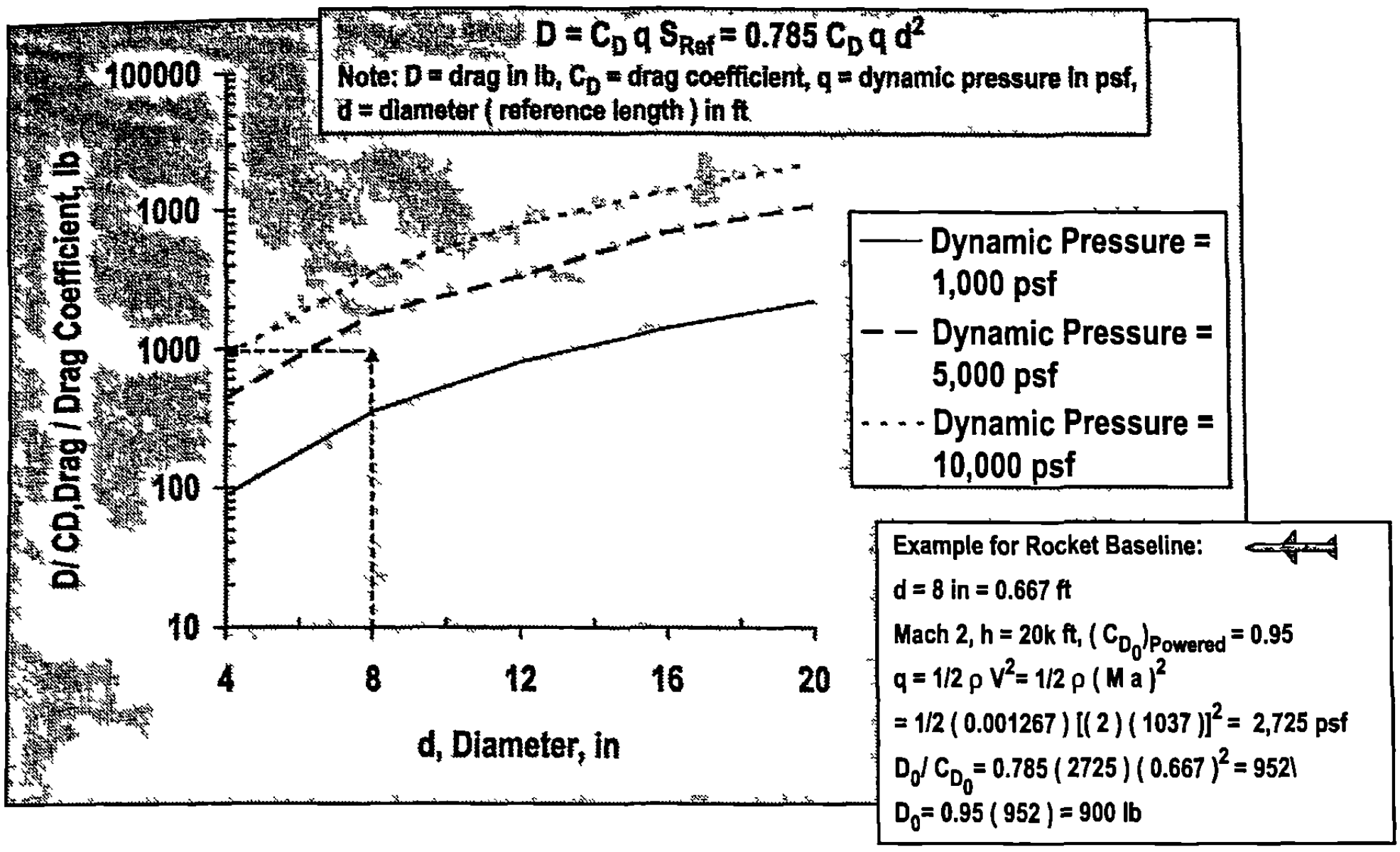

Fig. 2.2 Small diameter missiles have low drag.

As an example of missile drag, consider the rocket baseline missile. The rocket baseline missile has a reference area of 0.349 ft^2 and a reference length (diameter) of 8 in. At a typical flight condition of Mach 2 and flight altitude of 20,000 ft, the dynamic pressure $q = 2725$ psf. Also, at Mach 2, the rocket baseline zero-lift drag coefficient for powered flight $C_{D_0} = 0.95$. Substituting into the drag equation, the zero-lift powered flight drag of the rocket 8-in diameter baseline is $D_0 = 900$ lb. A missile with configuration geometry similar to the rocket baseline, but with one-half the diameter (4 in) would have one-fourth the drag (225 lb). A similar configuration with twice the diameter (16 in) would have four times the drag (3600 lb).

Figure 2.3 shows the benefit of a large diameter in enhancing seeker detection range and resolution. It is based on the two-way radar range equation for an active radfar seeker, given by

$$R_D = \{\pi\sigma \mathrm{n}^{3/4}/[64\,\lambda^2 kTBFL(S/N)]\}^{1/4}\, P_T^{1/4} d \tag{2.4}$$

Assumptions are a uniformly illuminated circular aperture, noncoherent radar with integration of only the pulse signal amplitude, negligible clutter, negligible interference, negligible atmospheric attenuation, and thermal noise-limited receiver sensitivity. In regard to pulse integration, the efficiency of integrating the number of pulses (n) can vary from $n^{1/2}$ to n. Coherent radar, which integrates both the signal amplitude and phase, can have an integration efficiency approaching an ideal value of n^1. For a noncoherent radar, which integrates only the signal amplitude, a typical value of the integration efficiency is $n^{3/4}$. Although a coherent radar seeker is usually more efficient, most tactical radar missiles use noncoherent seekers, which integrate only the pulse amplitude. A noncoherent

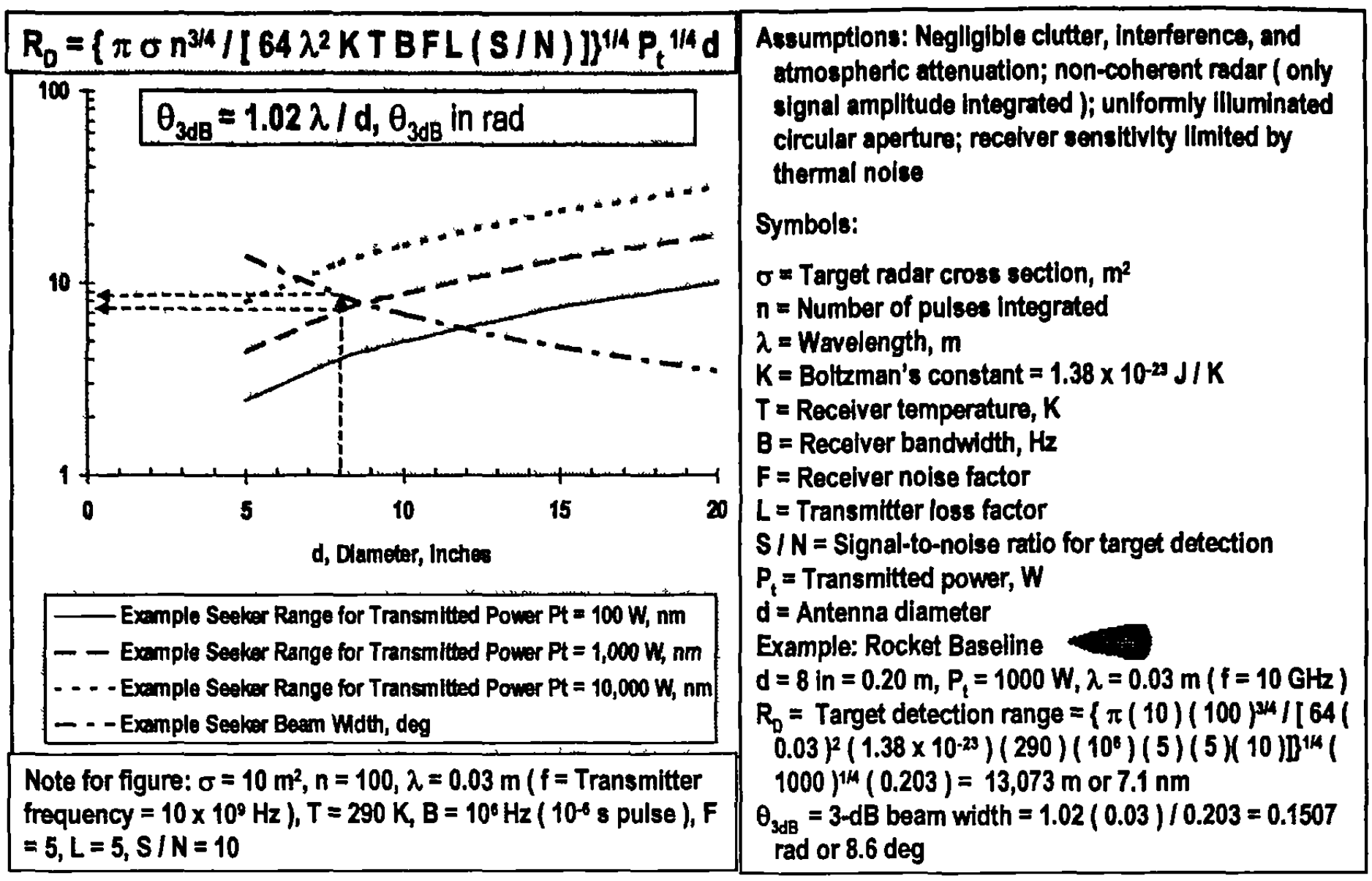

Fig. 2.3 Large diameter radar seeker provides longer detection range and better resolution.

seeker is usually preferred for tactical missiles because it is lower cost. Referring back to the radar range equation of the figure, the receiver threshold sensitivity P_r (in Watts) is given by the equation $P_r = kTBF$. Assumptions are a nominal receiver temperature $T = 290$ K, bandwidth B $= 10^6$ Hz (pulse width of about 10^{-6} s), and noise factor $F = 5$. Boltzman's constant is the term $k = 1.38 \times 10^{-23}$ J/K. Substituting,

$$P_r = 1.38 \times 10^{-23}(290)(10^6)(5) = 2.0 \times 10^{-14}\,\mathrm{W} \tag{2.5}$$

Other assumptions for the example plotted in the figure are a target radar cross section $\sigma = 10$ m^2, number of pulses integrated $n = 100$, transmitter frequency $f = 10$ GHz, transmitter loss factor $L = 5$, and target detection signal-to-noise ratio $S/N = 10$. The assumed value of $S/N = 10$ provides a false alarm of about 1% for a probability of detection of 90%. For a typical transmitter duty cycle of 20% and a loss factor of 5, the average output power is about 20% of the peak power and the input power is comparable to the peak power. The maximum allowable transmitted power by the seeker is limited by the transmitter technology, power available from the battery, maximum allowable temperature because of heating, and signal processing technology (such as pulse compression).

As an example, assume that the rocket baseline missile has an antenna diameter of about $d = 8$ in and a transmitted power $P_T = 1000$ W. Detection range is computed to be $R_D = 13{,}073$ m or 7.1 n miles.

Beamwidth of a radar seeker is given by the equation

$$\theta_{3\,\mathrm{dB}} = 1.02\lambda/\mathrm{d} \tag{2.6}$$

The 3-dB beamwidth for a frequency of 10 GHZ and a diameter of 8 in is

$$\theta_{3\,\mathrm{dB}} = 1.02(0.03)/0.203 = 0.151 \text{ rad or } 8.6\,\mathrm{deg} \tag{2.7}$$

A larger antenna diameter or a higher transmission frequency provides longer range, more precise tracking, and finer resolution. For example, an increase of 100% in diameter (to 16 in) provides an increase in the seeker range of 100% (to 14.1 n miles) and a decrease in the seeker beamwidth of 50% (to 4.3 deg). Also, a longer pulse width would provide longer detection range, with disadvantages of degraded range measurement accuracy, higher false alarm rate, and potentially receiving overlapping pulses. Pulse modulation (e.g., chirp) can be used to avoid range ambiguity for a long duration pulse. Pulse compression is another approach to improve range. Processing provides the equivalence of an increase in the pulse width. Pulse compression has advantages of not degrading the range measurement accuracy, the pulse nonambiguity, or the false alarm rate.

There is a similar benefit of a large diameter in enhancing the detection range and resolution of a passive infrared (IR) seeker. It is based on the one-way IR range equation

$$R_D = \{(\mathrm{I_T})_{\Delta\lambda}\eta_\mathrm{a}\mathrm{A_o}\{\mathrm{D}^*/(\Delta\,\mathrm{f_p}^{1/2}\mathrm{A_d}^{1/2})\}(\mathrm{S/N})^{-1}\}^{1/2} \tag{2.8}$$

As shown in the equation, there are seven drivers for IR seeker range: radiant intensity of the target within the upper and lower wavelength cutoffs of the seeker $(\mathrm{I_T})_{\Delta\lambda}$, atmospheric transmission efficiency for the total distance from the target to the seeker η_a, seeker optics aperture area A_o, pixel specific detectivity D^*, pixel bandwidth $\Delta\mathrm{f_p}$, detector total area A_d, and signal-to-noise ratio required for detection S/N.

Referring to the seeker range equation, the second term is atmospheric transmission efficiency η_a. It accounts for the attenuation over the total distance from the target to the seeker. The transmission can range from perfect transmission ($\eta_\mathrm{a} = 1$) for exo-atmospheric conditions to almost no transmission ($\eta_\mathrm{a} \approx 0$) through clouds. The effect of atmospheric transmission on detection range is shown in Fig. 2.4. A typical value of atmospheric humidity of 7.5 g/m^3 results in an atmospheric attenuation of -0.2 dB per km for an IR signal, or an atmospheric transmission of 0.955 per km. Increasing the range reduces the received signal. As an example, an atmospheric attenuation of 0.955 per km results in 95% transmission at a range of 1 km but only 63% transmission at a range of 10 km ($0.955^{10} = 0.63$). Adverse weather results in less transmission. As an example, moderate rainfall (4 mm/h) has an atmospheric attenuation of -2 dB per km for an IR signal, or an atmospheric transmission of 0.631 per km. It reduces the transmission to 63% at a range of 1 km. There is only 1% transmission at a range of 10 km.

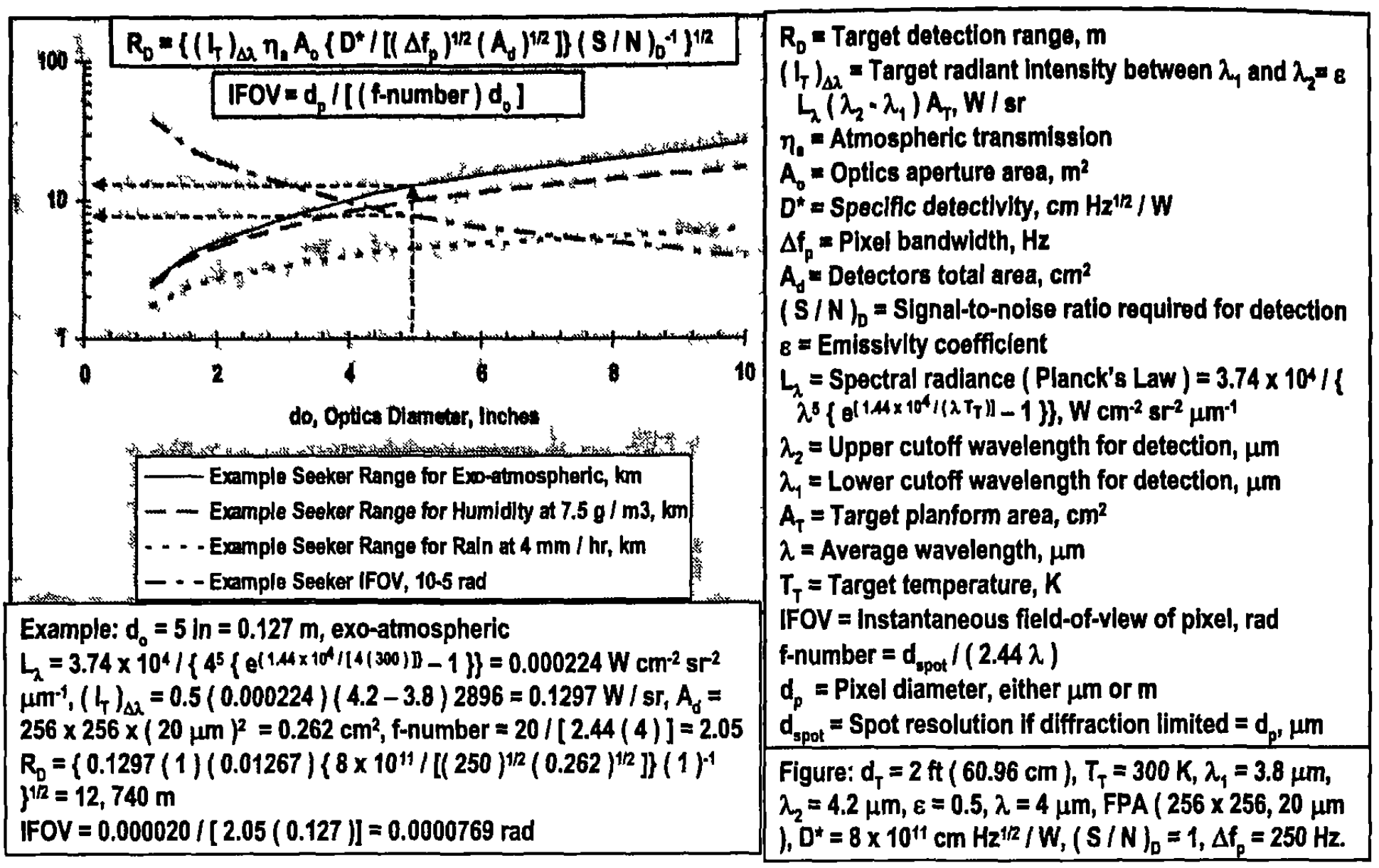

Fig. 2.4 Large diameter IR seeker provides longer detection range and better resolution.

The third term in the seeker range equation is seeker optics aperture area, which is a major configuration design parameter. A larger aperture delivers more optical energy to the detectors, providing longer detection range. It also provides better resolution. For a strap-down seeker, the seeker optics diameter can be almost as large as the diameter of the missile. For a gimbaled seeker, the seeker optics diameter is limited to about one-half of the missile diameter. Shown in the figure is the effect of seeker optics diameter on detection range. A small optics diameter of 1 in, representative of a small diameter missile such as a Stinger, has a detection range of only a few km and the detection range can be less than 1 km against a low-signature target in adverse weather. A larger IR sensor diameter of 10 in, such as a FLIR on an aircraft or unmanned air vehicle (UAV), has ranges that can greatly exceed 10 km against moderate signature targets in favorable weather.

As an example, the seeker detection range will be calculated for a 5 in diameter aperture in an exo-atmospheric intercept. The seeker is assumed to operate over a wavelength range of 3.8 to 4.2 μm, with an average wavelength of $\lambda = 4$ μm. The target characteristics are assumed to be 2 ft diameter ($A_T = 2896$ cm^2), temperature $T_T = 300$ K, and emissivity $\varepsilon = 0.5$. The spectral radiance (Planck's law) of the target is

$$
\begin{aligned}
L_\lambda &= 3.74 \times 10^4 / \{ \lambda^5 \{ e^{[1.44 \times 10^4 / (\lambda T_T)]} - 1 \}\} \\
&= 3.74 \times 10^4 / \{ 4^5 \{ e^{\{1.44 \times 10^4 / [4(300)]\}} - 1 \}\} \\
&= 0.000224 \, \mathrm{Wcm^{-2}\, sr^{-2}\, \mu m^{-1}}
\end{aligned} \tag{2.9}
$$

Substituting into the equation for target radiant intensity gives

$$(I_T)_{\Delta\lambda} = \varepsilon L_\lambda(\lambda_2 - \lambda_1)A_T = 0.5(0.000224)(4.2 - 3.8)(2896)$$
$$= 0.1297\,\mathrm{Wsr}^{-1} \tag{2.10}$$

The detector is assumed to be a diffraction limited 256 × 256 focal plane array with 20 μm pixels. Detector area is therefore $A_d = 256(256)(0.002) = 0.262\ \mathrm{cm}^2$. A $Hg_{0.67}Cd_{0.33}Te$ detector is assumed, which has a specific detectivity $D^* = 8 \times 10^{11}\ \mathrm{cmHz}^{1/2}\mathrm{W}^{-1}$ at a detector temperature of 77 K (liquid nitrogen) when it is optimized for the $\lambda = 4$ μm application. The pixel detector bandwidth for best signal-to-noise ratio (S/N) is assumed to be $\Delta f_p = 250$ Hz and the S/N for detection is assumed to be $(S/N)_D = 1$. Finally, substituting into the IR seeker range equation gives

$$R_D = \{(I_T)_{\Delta\lambda}\eta_a A_o\{D^*/(\Delta f_p^{1/2}A_d^{1/2})\}(S/N)^{-1}\}^{1/2}$$
$$= \{0.1297(1)(0.01267)\{8 \times 10^{11}/[(250)^{1/2}(0.262)^{1/2}]\}(1)^{-1}\}^{1/2}$$
$$= 12{,}740\,\mathrm{m} \tag{2.11}$$

The figure also shows the benefit of optics diameter on instantaneous field of view (IFOV), which is the field of view of a single pixel. The equation is

$$\mathrm{IFOV} = d_p/[(\text{f-number})d_o] \tag{2.12}$$

Note from the preceding equation that the IFOV becomes smaller (better resolution) as the diameter increases.

A diffraction limited system is assumed, with the minimum spot size equal to the size of a single pixel detector. The Rayleigh criterion for the limiting angular resolution of the optics results in the equation

$$\text{f-number} = d_p/(2.44\,\lambda) \tag{2.13}$$

As an example, we will assume an optics aperture diameter d_o=5 in (12.7 cm) diameter, a system that is diffraction limited, pixel size $d_p = 20$ μm, and wavelength $\lambda = 4$ μm. The f-number is given by the equation f-number = 20 μm/[2.44(4 μm)] = 2.05. Substituting into the equation for instantaneous field of view,

$$\mathrm{IFOV} \approx 20 \times 10^{-6}/[2.05(0.127] = 0.0000769\,\mathrm{rad} \tag{2.14}$$

Missile fineness ratio is a design consideration that may limit the missile diameter. Figure 2.5 illustrates that high-fineness missiles may be limited by aeroelasticity problems from the body bending frequency. Shown is the nondimensional first mode body bending frequency as a function of body fineness ratio. The equation is

$$\omega_{BB} = 18.75\{Et/[W(l/d)]\}^{1/2} \tag{2.15}$$

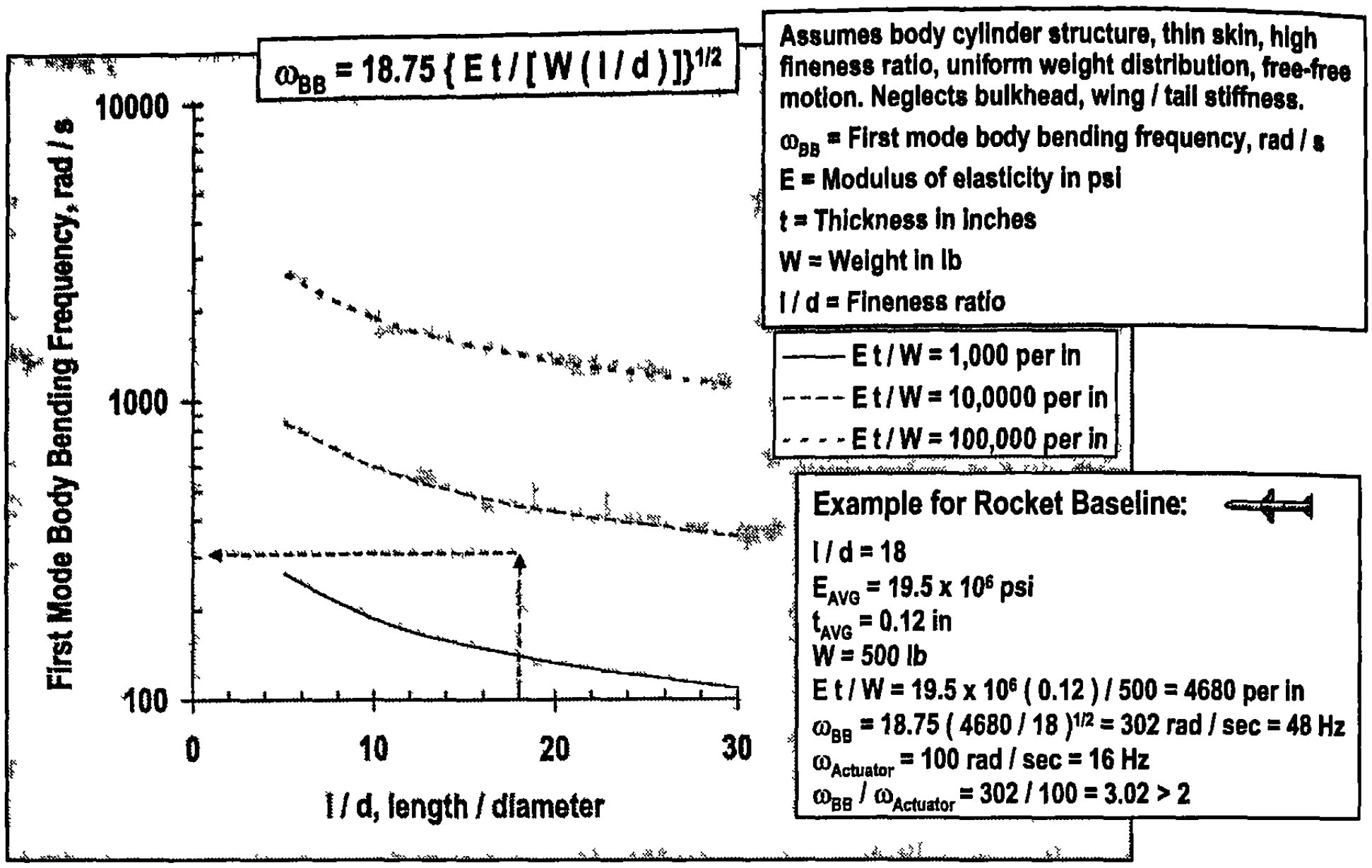

Derived from: AIAA Aerospace Design Engineers Guide, American Institute of Aeronautics and Astronautics, 1993.

Fig. 2.5 Missile fineness ratio may be limited by the impact of body bending modes on the flight control system.

It is derived from Ref. 2. The assumptions are a thin wall cylinder structure with no stiffening from surfaces or bulkheads, uniform weight distribution, and free-free motion. Note that the body bending frequency is highest for a missile that has low fineness ratio, light weight, high modulus of elasticity, and large airframe skin thickness.

An example is given for the rocket baseline missile. The contribution from the wing is neglected. The rocket missile body is a combination of the pyroceram dome, aluminum airframe structure (including the aft body structure that shrouds the rocket nozzle), and the steel motor case. The modulus of elasticity of the steel motor case is 29.5×10^6 psi, the thickness of the case is 0.074 in, and the length of the case is 59.4 in. The modulus of elasticity of the aluminum body structure is 10.5×10^6 psi, thickness is 0.16 in, and the total length is 65.3 in. The contribution from the radome is neglected for this conceptual analysis because of its relatively short length and the geometric stiffness of the tangent ogive radome. Using a weighted average based on length, the average modulus of elasticity is $E_{AVG} = 19.5 \times 10^6$ psi and the average thickness $t_{AVG} = 0.12$ in. The rocket baseline missile launch weight is 500 lb, and the body fineness ratio is 18. Substituting into the equation, the first mode body bending frequency is computed to be 302 rad/s or 48 Hz. As a rule of thumb, the first mode body bending frequency should be at least twice the actuator bandwidth of the flight control system. For the rocket baseline missile, the actuator frequency is 100 rad/s, providing a design margin in body bending frequency for the fineness ratio $l/d = 18$.

Adding a stiff bulkhead, such as a welded interface between rocket motor case and the airframe, usually adds stiffness and increases the body bending frequency. However, a bulkhead interface using fittings may have a poor mechanical attachment and could decrease the stiffness, resulting in lower body bending frequency.

2.3 Nose Fineness Tradeoff

Shown in Fig. 2.6 are the nose fineness tradeoff drivers toward high-fineness ratio versus low-fineness ratio. These must be harmonized. A high-fineness nose, such as $l_N/d = 5$, is ideal aerodynamically and has low observables. A low-fineness nose, such as an $l_N/d = 0.5$ spherical nose, is ideal electromagnetically and allows more propellant length and volume for a length-limited missile. For supersonic missiles, a moderate nose fineness compromise dome is a nose length-to-diameter ratio of about 2.

Alternative dome geometry includes tangent ogive, faceted or pyramidal, flat window, and multilens domes. A tangent ogive dome has a circular arc surface. Although a tangent ogive dome has lower supersonic drag and low radar cross section, the curved surface results in high error slope for a seeker tracking the target. An alternative dome is a faceted dome. A faceted dome is typically composed of six to eight triangular surfaces that form a pyramid. A faceted dome has the advantage of low error slope because of the flat surfaces. The bond line between the facets must be small to minimize optical distortion. A disadvantage of a faceted dome for an IR seeker is the solar energy reflection off the facets into the seeker. A third type of dome is a window dome composed of a single flat surface. The window dome also has an advantage of low dome error slope.

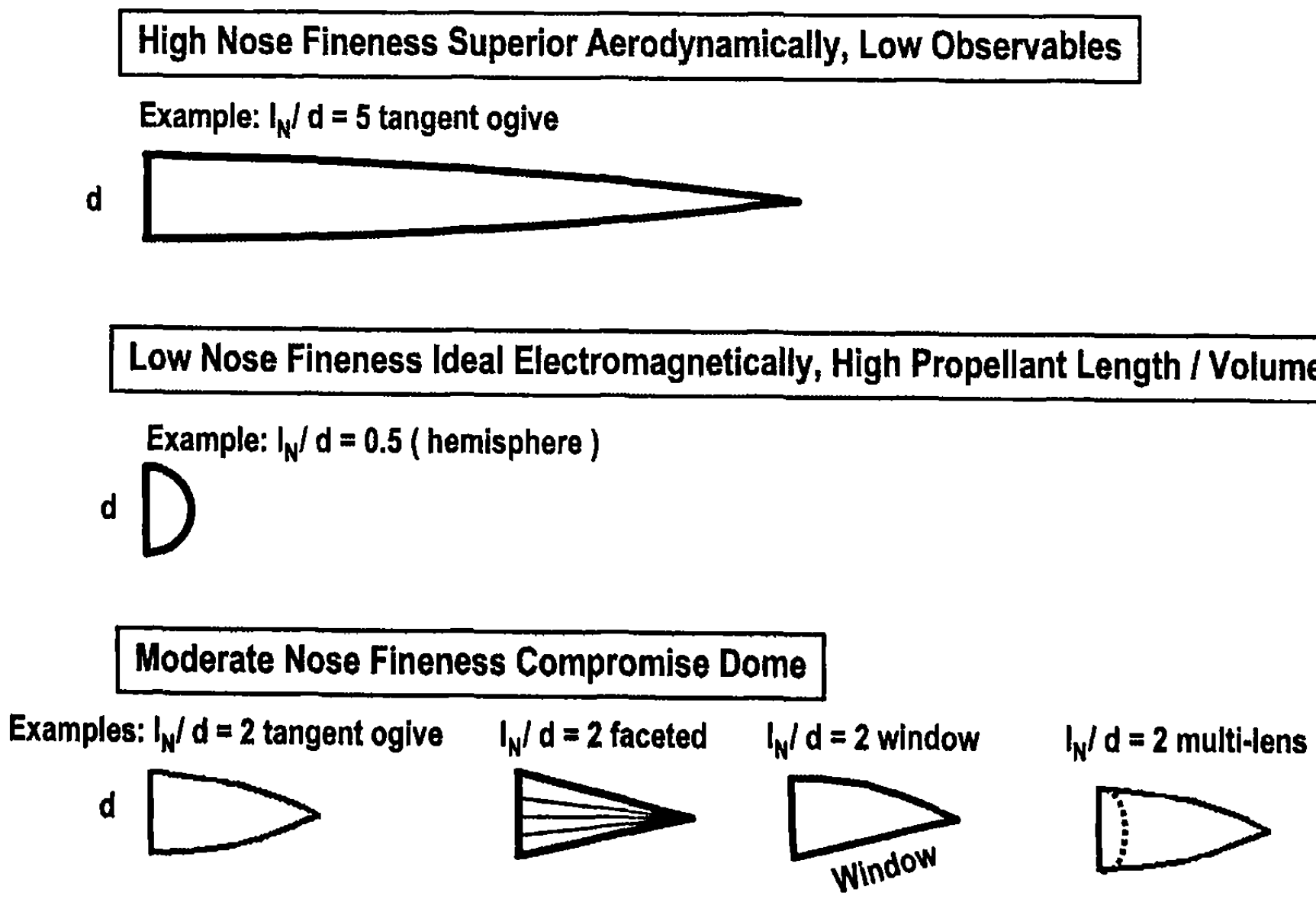

Fig. 2.6 Nose fineness tradeoff.

A disadvantage of a window dome is that it limits the field of regard of the seeker, which may limit the ability of the seeker to acquire an off-boresight target. Finally, a multilens dome is composed of two or more concentric domes, with a high-fineness outer dome. A multilens dome can provide compensation that reduces the dome error slope. The interior dome(s) provide optical correction to the dome error slope induced by the low drag/low radar cross section (RCS) exterior dome.

Shown in Fig. 2.7 are current missiles with IR domes that are high-fineness ratio and also have low dome error slope. Faceted dome technology has been applied to supersonic surface-to-air and air-to-air missiles to provide low drag combined with low dome error slope. Two supersonic missiles that have a high-fineness faceted dome are the United Kingdom Firestreak and the French Mistral. A concern with faceted domes is multiple reflections of the facets. Background reflections into the detector increase the background clutter, reducing target contrast. Solar reflections off the facets can result in false "hot spots." A video of a sea-launched application of Mistral is in the upper right section of the figure. Faceted and window dome technology has also been applied to cruise missiles to provide low radar cross section combined with low dome error slope. Cruise missiles that have high-fineness IR domes are the U.S. SLAM-ER missile and the JASSM missile. SLAM-ER has a two-facet IR dome. JASSM has a window dome. The JASSM seeker has a limited field of regard and is biased downward to look through the window. Finally, the U.S. THAAD anti-missile missile dome is a high-fineness window for low drag and low dome error slope. Because the THAAD seeker is biased to look through the side window, there is a limited field of regard. Shown in the bottom right

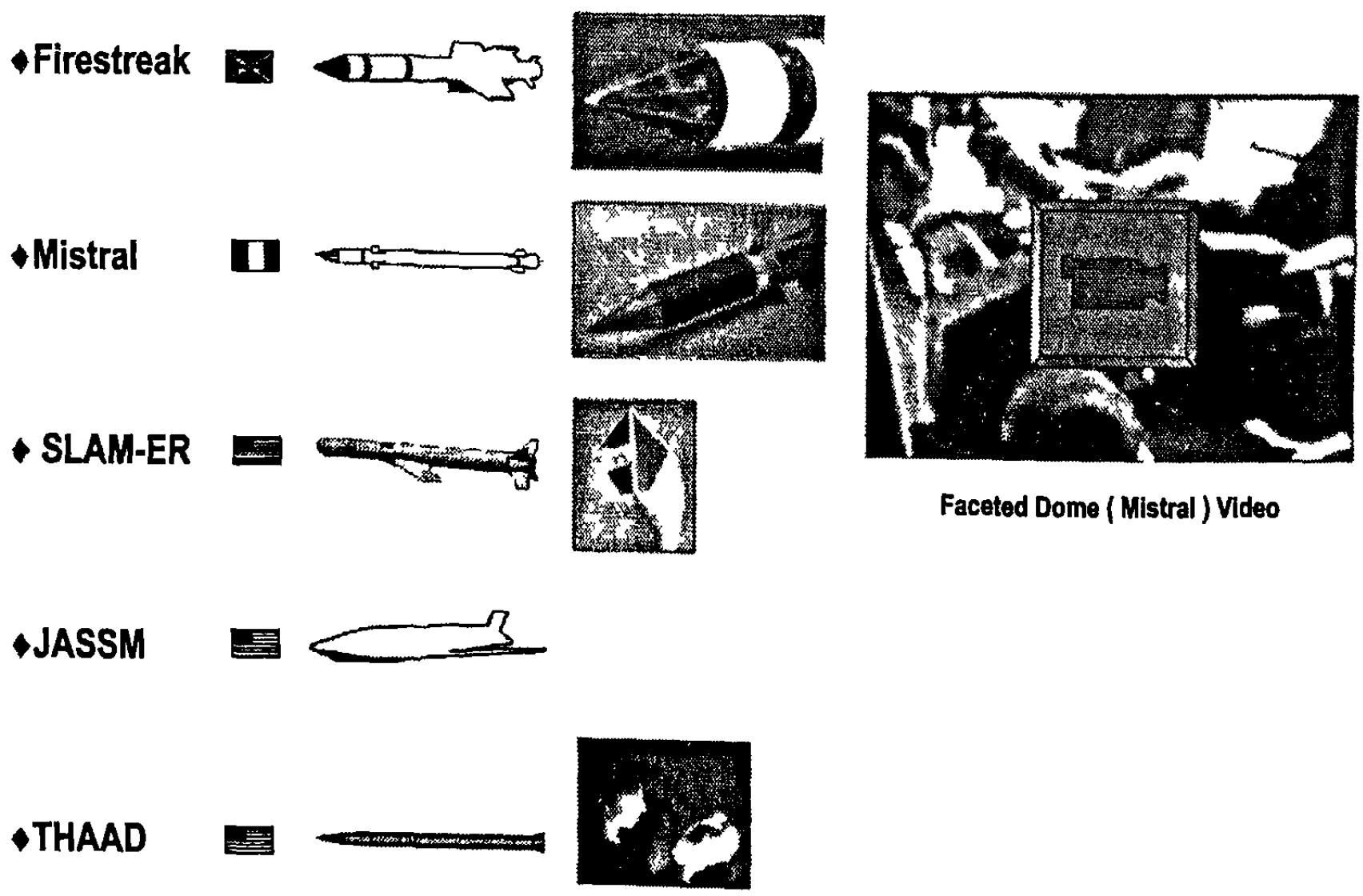

Fig. 2.7 Faceted and flat window domes can have low dome error slope, low drag, and low RCS. Figure also in color section. Video is in the CD included with this textbook.

section of the figure is a photograph of developmental hardware for a cooled window dome similar to THAAD.

The total zero-lift drag coefficient of a body is the combination of the skin friction drag, base drag, and wave drag (if supersonic). It is given by the equation

$$(C_{D_0})_{\text{Body}} = (C_{D_0})_{\text{Body,Friction}} + (C_{D_0})_{\text{Base}} + (C_{D_0})_{\text{Body,Wave}} \tag{2.16}$$

In the case of wave drag, Fig. 2.8 shows the benefit of a high-fineness nose to reduce supersonic drag. For supersonic missiles, the drag from the shock wave on the nose may be comparable to or even larger than skin friction drag and base drag. $(C_{D_0})_{\text{Body,Wave}}$ is a function of nose fineness and Mach number. The equation for body wave drag coefficient based on Bonney[3] is

$$(C_{D_0})_{\text{Body,Wave}} = (1.586 + 1.834/\text{M}^2)\{\tan^{-1}[0.5/(\text{l}_\text{N}/\text{d})]\}^{1.69} \tag{2.17}$$

In the above equation the value of the inverse tangent is in radians. Note from the figure that $(C_{D_0})_{\text{Body,Wave}}$ decreases with increasing nose fineness ratio. The figure also shows body base drag coefficient during coasting flight $(C_D)_{\text{Base,Coast}}$ as a function of Mach number. Body base drag can be a major contributor to the total drag during coasting flight because of the low pressure in the base. Base drag is caused by flow separation at the base, which forms a low pressure wake. For a high-fineness nose, the base drag can be larger than the wave drag. The base drag for coasting flight at supersonic Mach number can be approximately correlated as

$$(C_D)_{\text{Base,Coast}} = 0.25/M \tag{2.18}$$

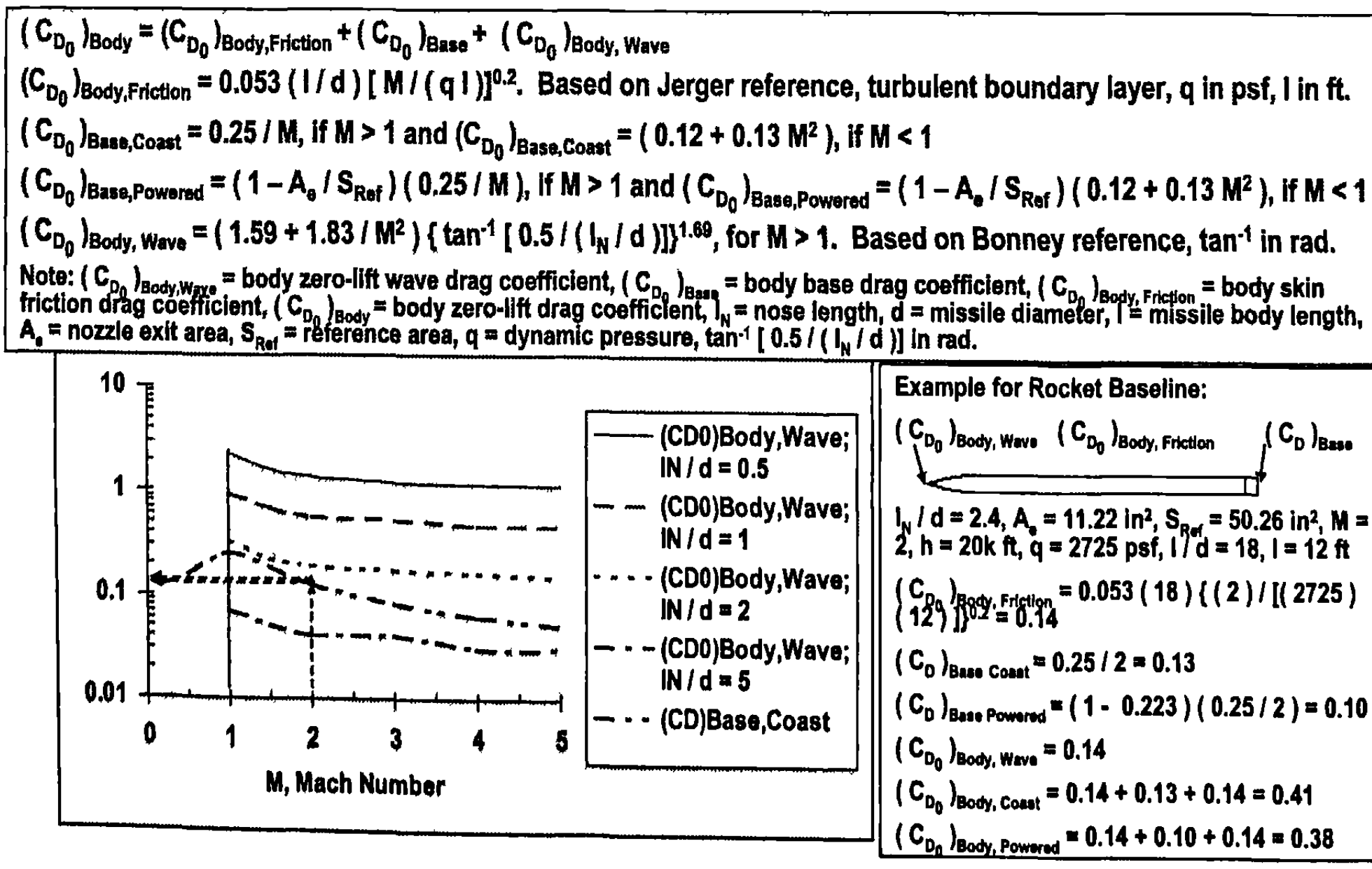

Fig. 2.8 Supersonic body drag driven by nose fineness while subsonic drag driven by wetted area.

A correlation for coasting flight at subsonic Mach number is

$$(C_D)_{\text{Base,Coast}} = 0.12 + 0.13\,M^2 \tag{2.19}$$

During powered flight the base drag is reduced by the factor $(1 - A_e/S_{\text{Ref}})$. If the nozzle exit area is nearly as large as the missile base area, the base drag may be negligible during powered flight. Finally, skin friction drag is a major contributor to subsonic drag. $(C_{D_0})_{\text{Body,Friction}}$ is primarily driven by body fineness ratio. It is also a weak function of Mach number, dynamic pressure, and body length. The equation for the body skin friction drag coefficient, based on Jerger[4], is

$$(C_{D_0})_{\text{Body,Friction}} = 0.053(l/d)[M/(ql)]^{0.2} \tag{2.20}$$

Assumptions in the above equation are that the body wetted area of a noncircular lifting body can be approximated by the wetted area of an equivalent circular cross-section cylinder, the variation in the free stream speed of sound and viscosity with altitude is relatively small, and a turbulent boundary layer. The assumption of a turbulent boundary layer is most in error for a short length missile at very low Mach number (e.g., $M < 0.2$) and very high altitude (e.g., $h > 80{,}000$ ft). Note that for the same flight conditions, a circular cross section body has less skin friction drag because it has less wetted area than a lifting body.

As an example, we will calculate the body zero-lift drag coefficient of the rocket baseline missile, which has a nose fineness ratio of $l_N/\text{d} = 2.4$, body fineness $l/d = 18$, and body length $l = 12$ ft. At a nominal Mach number $M = 2$, the predicted zero-lift wave drag coefficient is $(C_{D_0})_{\text{Body,Wave}} = 0.14$. The base drag coefficient during coasting flight at Mach 2 is $(C_D)_{\text{Base,Coast}} = 0.13$, which is comparable to $(C_{D_0})_{\text{Body,Wave}}$. During powered flight at Mach 2, the base drag coefficient is smaller, $(C_D)_{\text{Base,Powered}} = 0.10$. The skin friction drag coefficient at Mach 2 and a nominal altitude of 20,000 ft (corresponding to a dynamic pressure of $q = 2725$ psf) is $(C_{D_0})_{\text{Body,Friction}} = 0.14$. Note that this is also comparable to the value of $(C_{D_0})_{\text{Body,Wave}}$. Finally, the body total power-off drag coefficient is computed as the sum of the contributions from the wave drag plus the base drag plus the skin friction drag. At Mach 2 and 20,000 ft in altitude, the predicted body drag coefficient during coasting flight of the rocket baseline missile is $(C_{D_0})_{\text{Body,Coast}} = 0.41$. The body drag coefficient in powered flight is slightly lower, $(C_{D_0})_{\text{Body,Powered}} = 0.38$.

A small amount of nose tip bluntness is usually desirable for a tactical missile. Nose tip bluntness alleviates problems of localized stress concentration and nose tip heating, usually with a negligible change in drag. Figure 2.9 illustrates the process of calculating the effect of nose tip bluntness on zero-lift wave drag. First, the blunted nose geometry is described as a spherical nose tip. Next, the zero-lift wave drag coefficient is calculated for a sharp nose, based on the equation

$$(C_{D_0})_{\text{Wave,SharpNose}} = (1.59 + 1.83/M^2)\{\tan^{-1}[0.5/(l_N/d)]\}^{1.69} \tag{2.21}$$

- **Steps to Calculate Wave Drag of a Blunted Nose**
  1. Relate blunted nose tip geometry to pointed nose tip geometry

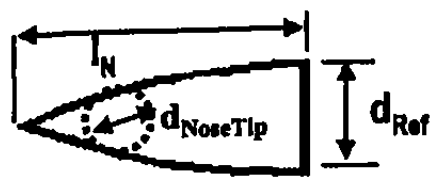

  2. Compute $(C_{D_0})_{Wave,SharpNose}$ for sharp nose, based on the body reference area

     $(C_{D_0})_{Wave,SharpNose} = (1.59 + 1.83 / M^2)\{\tan^{-1}[0.5 / (l_N / d)]\}^{1.69}$
  3. Compute $(C_{D_0})_{Wave,Hemi}$ of the hemispherical nose tip ($l_{NoseTip} / d_{NoseTip} = 0.5$), based on the nose tip area

     $(C_{D_0})_{Wave,Hemi} = (1.59 + 1.83 / M^2)\{[\tan^{-1}(0.5 / (0.5)]\}^{1.69} = 0.665(1.59 + 1.83 / M^2)$
  4. Finally, compute $(C_{D_0})_{Wave,BluntNose}$ of the blunt nose, based on the body reference area

     $(C_{D_0})_{Wave,BluntNose} = (C_{D_0})_{Wave,SharpNose}(S_{Ref} - S_{NoseTip}) / S_{Ref} + (C_{D_0})_{Wave,Hemi} S_{NoseTipi} / S_{Ref}$
- **Example Rocket Baseline ($d_{Ref} = 8$ in) with 10% Nose Tip Bluntness at Mach 2**
  - $(C_{D_0})_{Wave,SharpNose} = [1.59 + 1.83 / (2)^2][\tan^{-1}(0.5 / 2.4)]^{1.69} = 0.14$
  - $d_{NoseTip} = 0.10(8) = 0.8$ in
  - $S_{NoseTip} = \pi d_{NoseTip}^2 / 4 = 3.1416(0.8)^2 / 4 = 0.503 \text{ in}^2 = 0.00349 \text{ ft}^2$
  - $(C_{D_0})_{Wave,Hemi} = 0.665[1.59 + 1.83 / (2)^2] = 1.36$
  - $(C_{D_0})_{Wave,BluntNose} = 0.14(0.349 - 0.003) / 0.349 + (1.36)(0.003) / (0.349) = 0.14 + 0.01 = 0.15$

Fig. 2.9 Moderate nose tip bluntness causes a negligible change in supersonic drag.

Next, the zero-lift drag wave coefficient of the hemispherical nose tip ($l_{NoseTip}/d_{NoseTip} = 0.5$) is calculated. The equation is

$$(C_{D_0})_{Wave,Hemi} = 0.665(1.59 + 1.83/M^2) \tag{2.22}$$

In the above equation $(C_{D_0})_{Wave,Hemi}$ is based on the nose tip cross-sectional area. Finally, the zero-lift wave drag coefficient of a missile with a blunt nose tip is the summation of the wave drag coefficient of the sharp nose plus the wave drag coefficient of the hemispherical nose tip, scaled by their areas. The equation is

$$\begin{aligned}(C_{D_0})_{Wave,BluntNose} = {} & (C_{D_0})_{Wave,SharpNose}(S_{Ref} - S_{NoseTip})/S_{Ref} \\ & + (C_{D_0})_{Wave,Hemi}\, S_{NoseTip}/S_{Ref}\end{aligned} \tag{2.23}$$

As an example, the wave drag coefficient of the rocket baseline with a sharp nose of fineness ratio $l_N/d = 2.4$ and flying at Mach 2 has a nose zero-lift wave drag coefficient $(C_{D_0})_{Wave,SharpNose} = 0.14$. The wave drag coefficient of a hemispherical nose tip is given by $(C_{D_0})_{Wave,Hemi} = 1.36$, where $(C_{D_0})_{Wave,Hemi}$ is based on the nose tip cross-sectional area. Finally, the rocket baseline missile ($d = d_{Ref} = 8$ in) with an assumed 10% nose tip bluntness at Mach 2 has a predicted zero-lift wave drag coefficient of $(C_{D_0})_{Wave,BluntNose} = 0.15$, which is only slightly larger than that of a sharp nose.

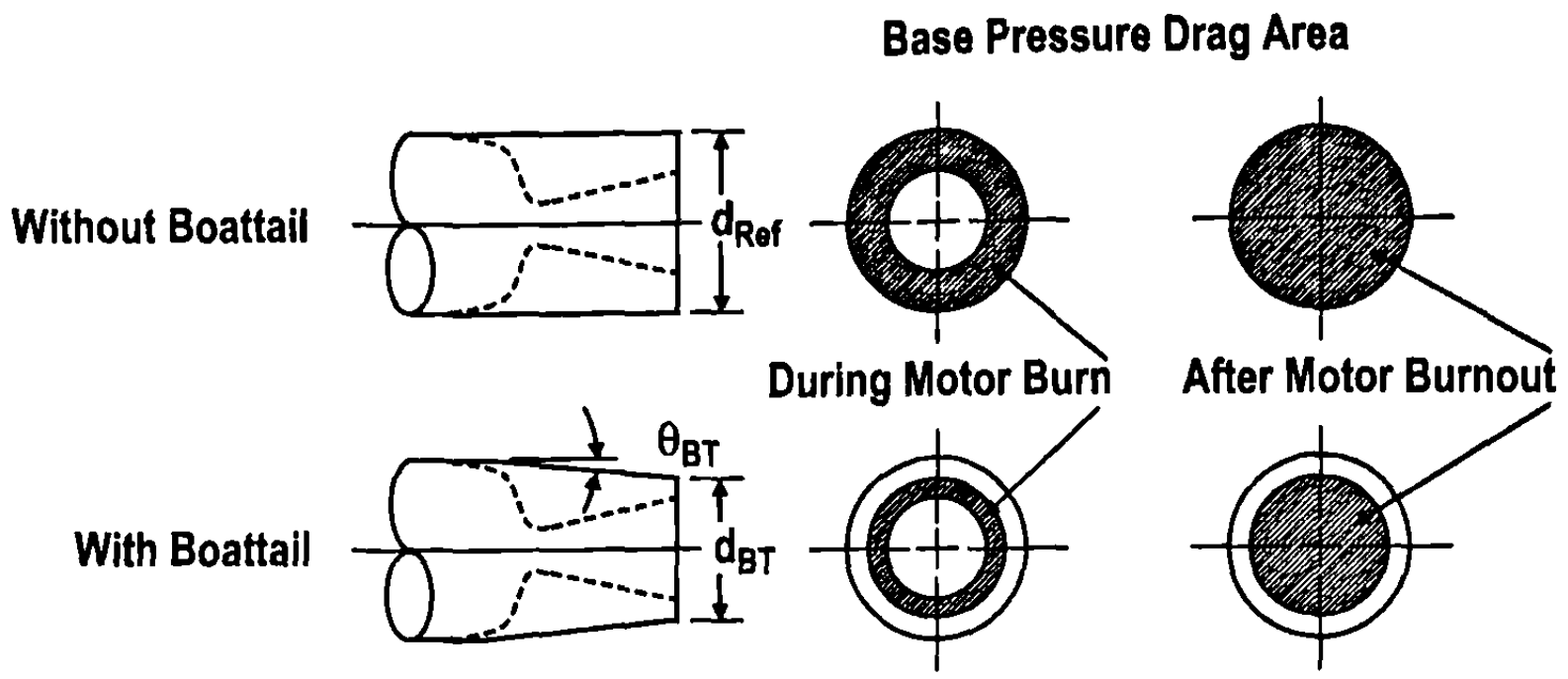

Note: Boattail angle θ_{BT} and boattail diameter d_{BT} limited by propulsion nozzle packaging, tail flight control packaging, and flow separation

Reference: Chin, S. S., *Missile Configuration Design*, McGraw-Hill Book Company, New York, 1961

Fig. 2.10 Boattail decreases base pressure drag area.

2.4 Boattail

Boattailing has its best payoff for subsonic missiles; supersonic missiles are susceptible to aft flow separation from boattailing. Figure 2.10 from Chin[5] illustrates the benefit of a moderate amount of boattailing. Without a boattail, during motor burn the base area that is outside the nozzle has a pressure less than that of the free stream, causing base drag. After motor burnout, the entire base area causes base drag. However, with boattailing the area occupied by the boattail has a larger base pressure, reducing the base drag in the area of the boattail. A design consideration if the missile has a boattail is that there is less volume available to package subsystems such as tail control actuators.

Figure 2.11 from Ref. 6 shows that the payoff for boattailing is greatest for subsonic missiles. The example body has an overall fineness ratio of 10.5, a nose fineness ratio of 3.00, a center body fineness ratio of 6.00, and a boattail fineness ratio 1.50. Note that for subsonic Mach number, boattailing reduces the drag by more than 50%. However, at supersonic to hypersonic Mach number there is only a slight reduction in drag with moderate boattailing, and large boattailing actually causes an increase in drag. From the figure, note that at Mach 5.0 the C_{D_0} for $d_{BT}/d_{Ref} = 0.6$ (boattail half-angle = 7.6 deg) is larger than the C_{D_0} for $d_{BT}/d_{Ref} = 0.8$ (boattail half-angle = 3.8 deg). At high Mach number, a large boattail angle can cause flow separation over the boattail, resulting in increased drag. As a rule of thumb, the boattail half-angle should be less than 10 deg.

2.5 Lifting Body Versus Axisymmetric Body

As shown in Fig. 2.12, the maximum normal force of a lifting body is higher than that of an axisymmetric body. The equation for normal force

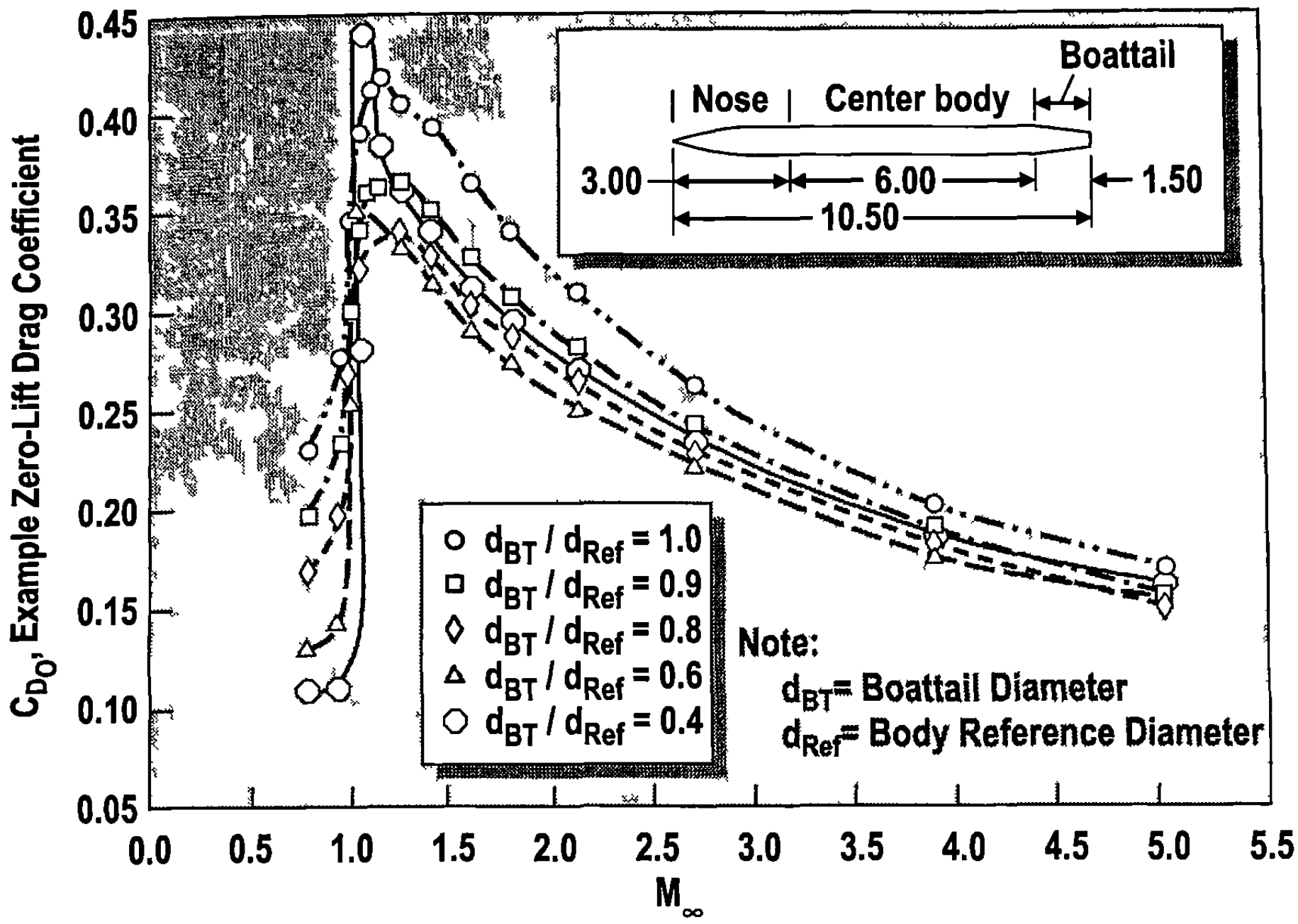

Note: Boatail half angle should be less than 10 deg, to avoid flow separattion.
Source: Mason, L.A., Devan, L. and Moore, F.G., "Aerodynamic Design Manual for Tactical Weapons," NSWC TR 81-156, July 1981

Fig. 2.11 Boattailing reduces drag for subsonic missiles.

$$\boxed{|C_N| = [|(a/b)\cos^2\phi + (b/a)\sin^2\phi|][|\sin(2\alpha)\cos(\alpha/2)| + 2(l/d)\sin^2\alpha]}$$

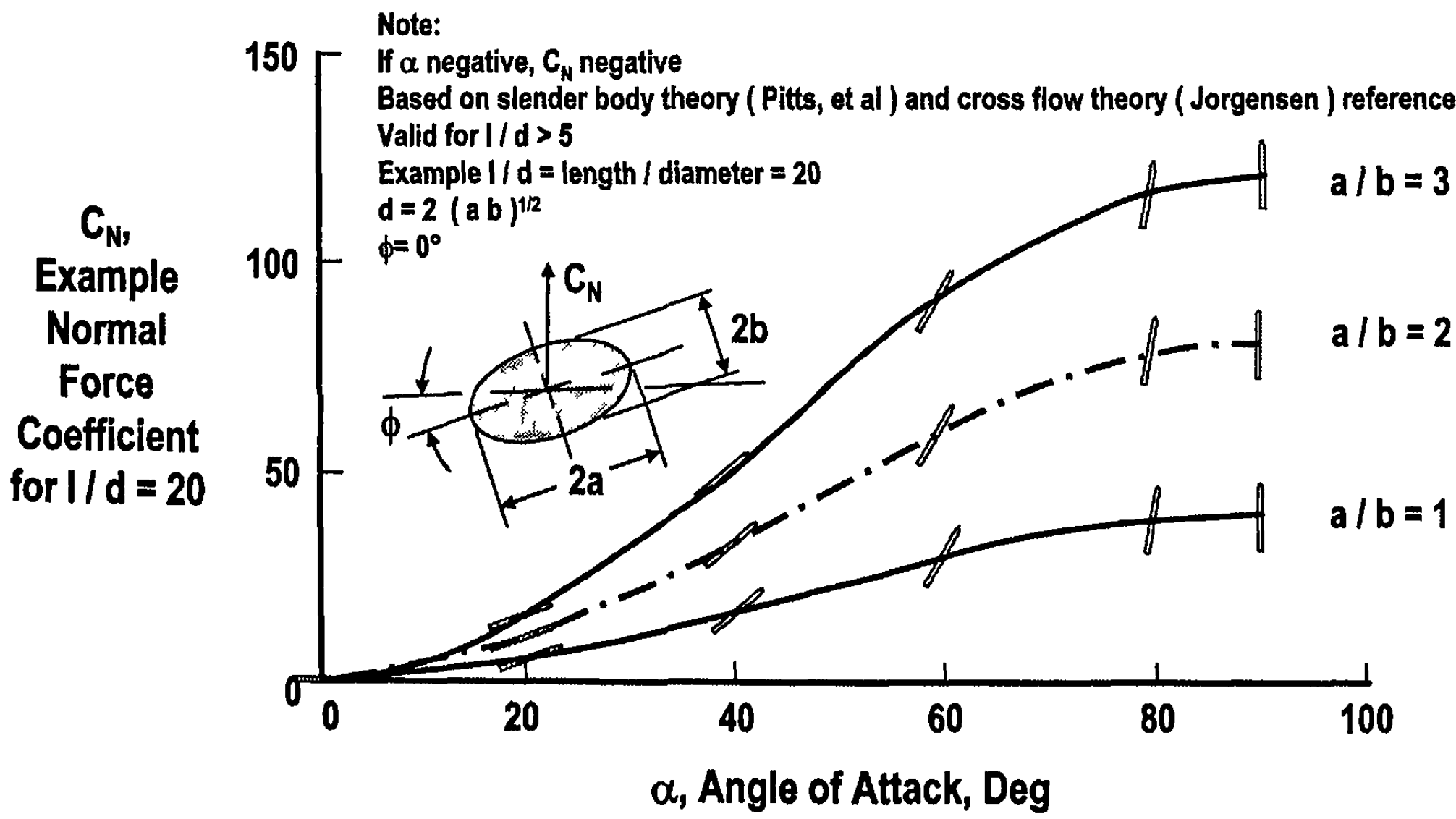

Fig. 2.12 A lifting body has higher normal force.

coefficient of a body is

$$|C_N| = [|(a/b)\cos^2\phi + (b/a)\sin^2\phi|][|\sin(2\alpha)\cos(\alpha/2)| + 2(l/d)\sin^2\alpha] \tag{2.24}$$

The normal force coefficient of a slender body is a function only of angle of attack and body geometry and is independent of Mach number. The normal force prediction is based on combining slender body theory (Ref. 7) and body crossflow theory (Ref. 8). It is valid for a body fineness ratio $l/d > 5$. For an elliptical cross section, an equivalent diameter is based on a circular cross section of the same area. The figure shows normal force coefficient increases with α (up to $\alpha = 90$ deg) and a/b. As an example, at a 90-deg angle of attack, the normal force coefficient for an elliptical cross section with a major-to-minor axis ratio of $a/b = 2$ is twice that of a circular cross section.

The body normal force curve slope from angle of attack is used in sizing the tail (or in some cases a flare) to meet the static stability requirement. $(C_{N_\alpha})_{Body}$ is the derivative of the equation for body normal force coefficient. At low angle of attack, $(C_{N_\alpha})_{Body} = 2[(a/b)\cos^2\varphi + (b/a)\sin^2\varphi]$, with the units of per rad.

A measure of aerodynamic efficiency is the ratio of lift-to-drag (L/D). The equation for aerodynamic efficiency is

$$L/D = C_L/C_D = (C_N\cos\alpha - C_{D_0}\sin\alpha)/(C_N\sin\alpha + C_{D_0}\cos\alpha) \tag{2.25}$$

For a lifting body missile without wings, the equation for the normal force coefficient is $|C_N| = [(a/b)\cos^2\phi + (b/a)\sin^2\phi|][\sin(2\alpha)\cos(\alpha/2)| + 2(l/d)\sin^2\alpha]$. Again, C_N for a body is based on combining slender body theory with crossflow theory. As shown in Fig. 2.13, an increase in L/D is achievable by reducing the zero-lift drag coefficient, increasing the body fineness, or by providing a lifting body configuration ($a/b > 1$). Also shown is that as a higher L/D is achieved, the angle of attack in which $(L/D)_{Max}$ is achieved is decreased. Note that other design considerations, such as launch platform lateral and length constraints, may limit the aerodynamic shaping that is practical. Also note that for 1-g constant altitude flight the angle of attack is usually much lower than the angle of attack for $(L/D)_{Max}$. As a result, the L/D during the flyout of most rocket powered missiles is usually much lower than $(L/D)_{Max}$.

Although a lifting body configuration has a higher $(L/D)_{Max}$ than a circular cross-sectional configuration, for 1-g flight at low angles of attack a circular configuration provides comparable L/D. Figure 2.14 compares the L/D of a lifting body configuration ($a/b = 2$) with that of a circular cross-sectional ($a/b = 1$) configuration. Typical values are given for a precision strike missile configuration of 2 ft^2 cross-sectional area and 2000 lb weight. As before, the L/D is based on combining slender body theory with crossflow theory. Maximum L/D for the lifting body configuration occurs at a dynamic pressure $q \approx 500$ psf. At $q = 500$ psf, the lifting body L/D is 40% higher than the circular cross-sectional body ($L/D = 3.37$ vs 2.40). However, note that the circular body cross-sectional configuration provides comparable L/D if the dynamic pressure is greater than 5000 psf. At $q = 5000$ psf, the lifting body L/D is only 5% higher than the circular cross-sectional body ($L/D = 0.96$ vs 0.91).

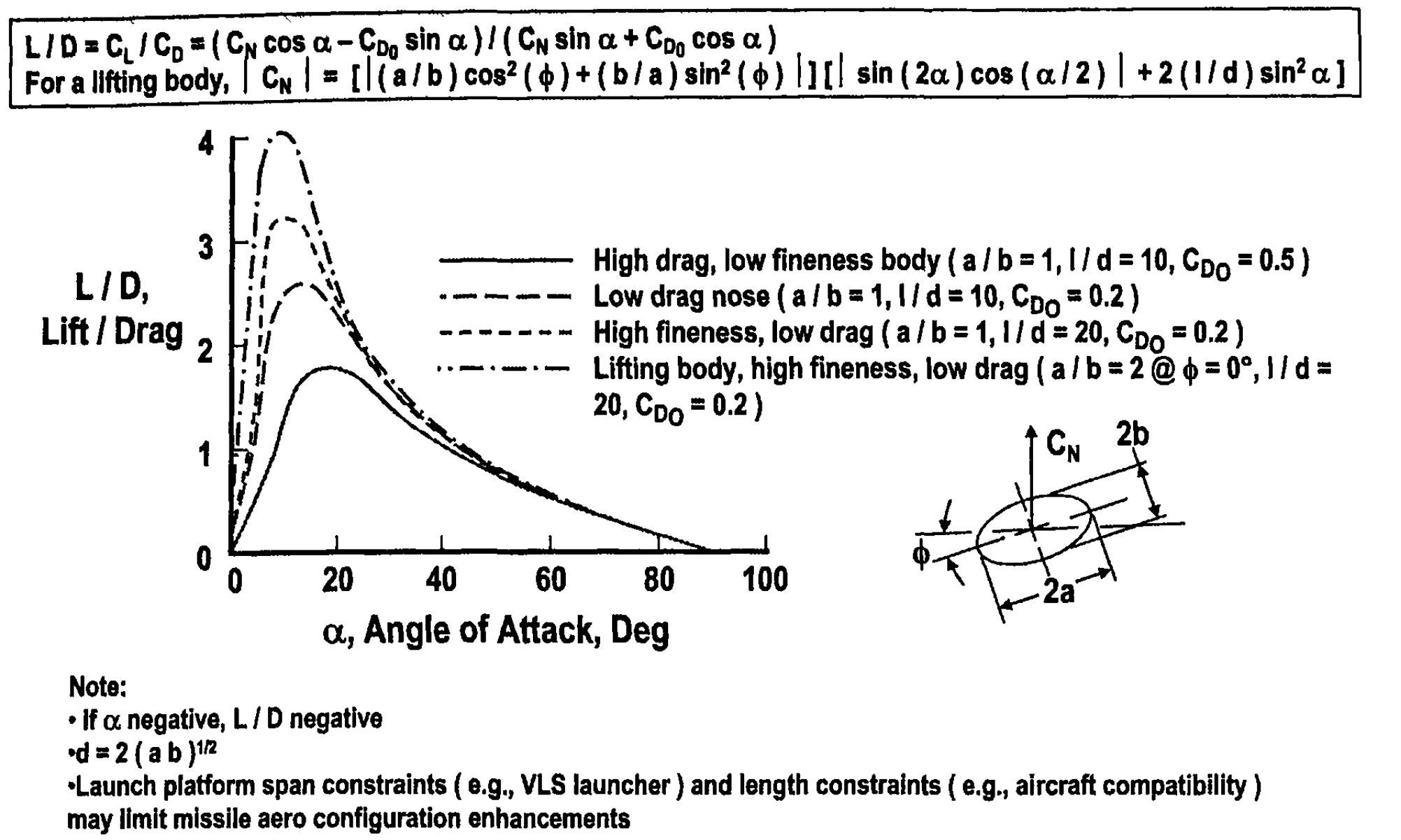

Fig. 2.13 ***L/D*** **is impacted by** C_{D_0}**, body fineness, and lifting body cross section geometry.**

A tailored lifting body (e.g., $a/b > 2$) or adding a wing increases $(L/D)_{\text{Max}}$, reduces $\alpha_{(L/D)\text{Max}}$, and reduces $q_{(L/D)\text{Max}}$. For example, the rocket baseline has a relatively high L/D because of its wing. At Mach 0.8, $(L/D)_{\text{Max}} = 6.2$, $\alpha_{(L/D)_{\text{Max}}} = 4.5$ deg, and $q_{(L/D)_{\text{Max}}} = 350$ psf. Supersonic missiles usually fly at a

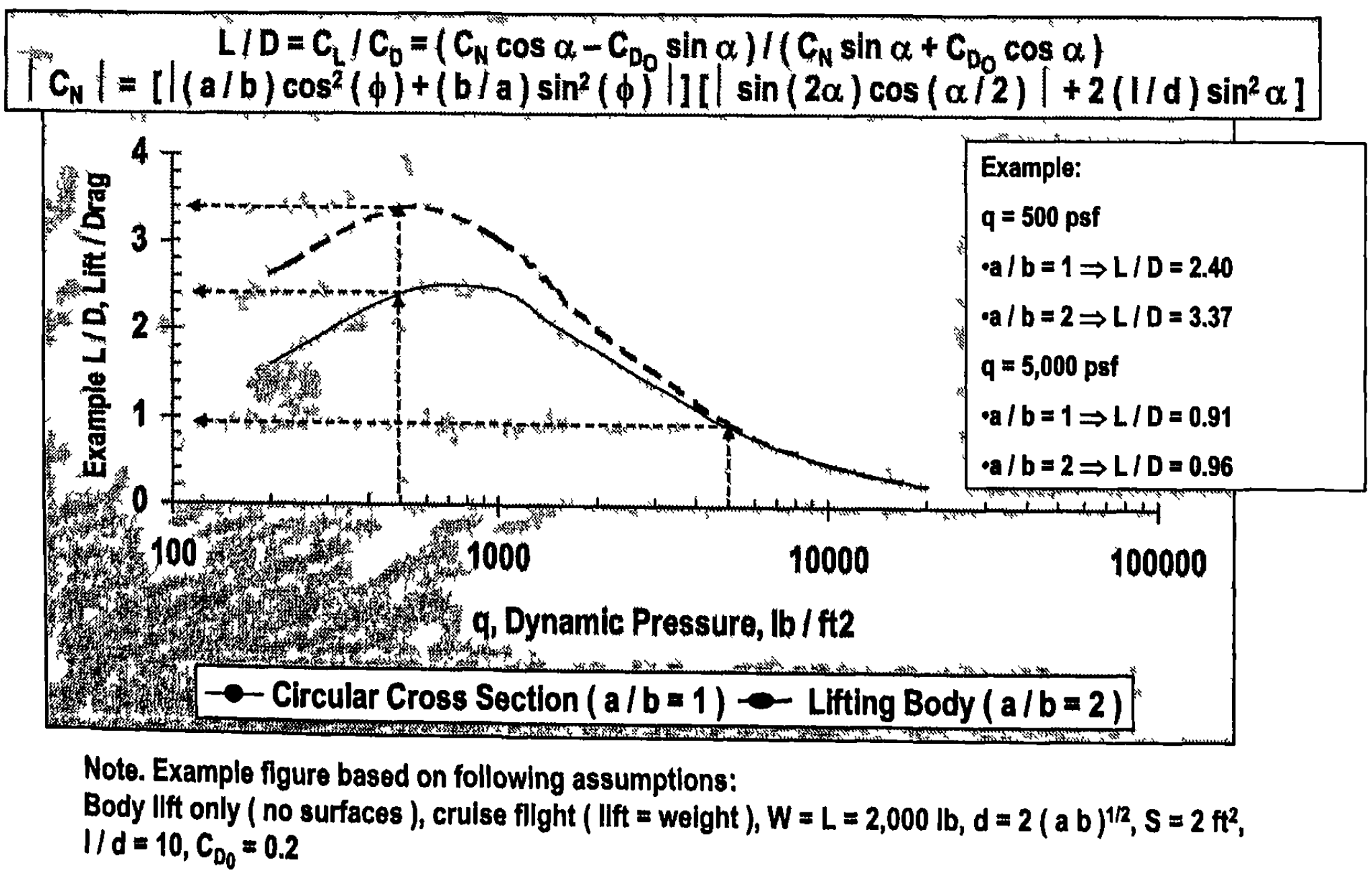

Fig. 2.14 A lifting body requires flight at low dynamic pressure to achieve high aerodynamic efficiency.

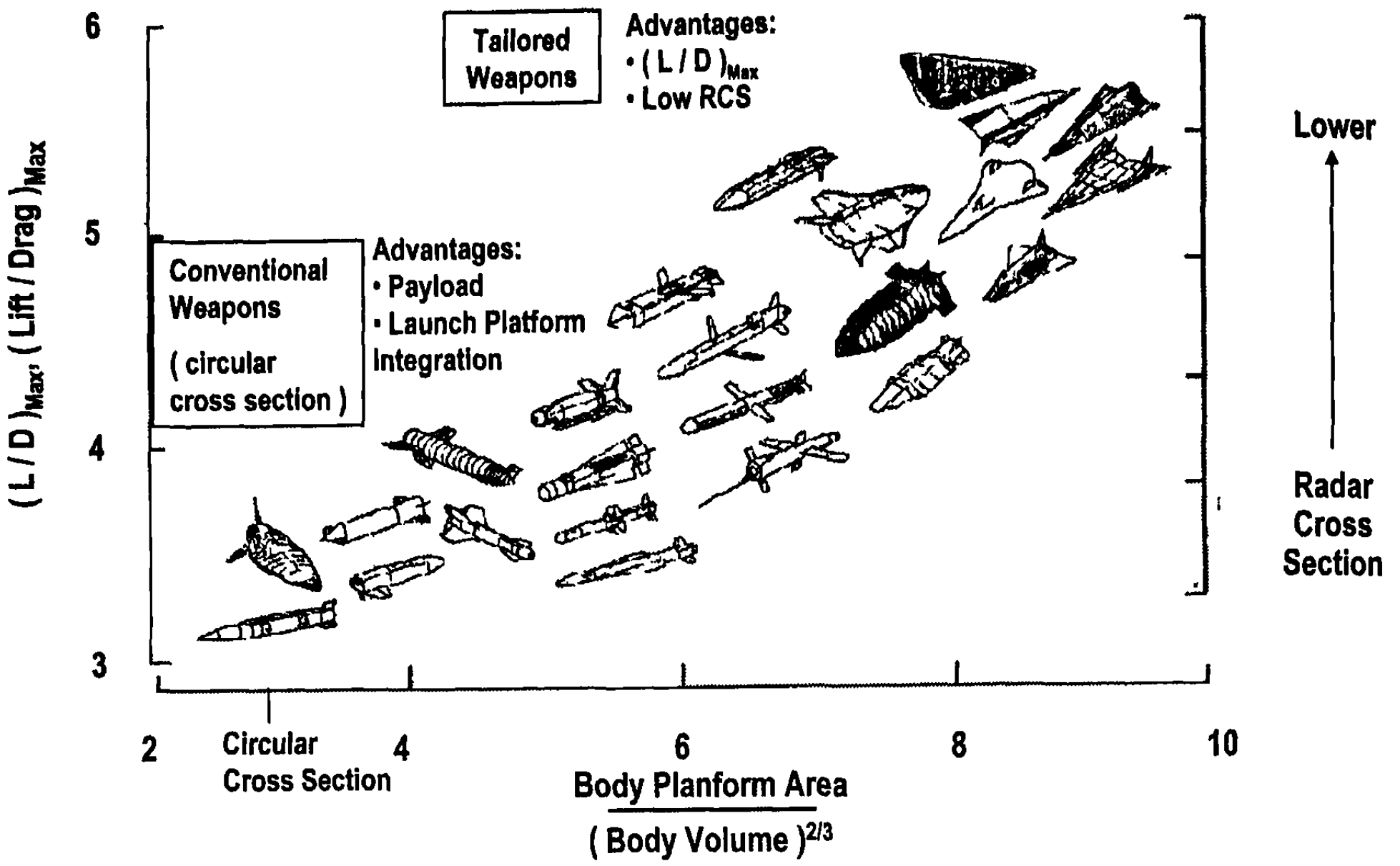

Fig. 2.15 Trade-off of low observables and $(L/D)_{\text{Max}}$ vs volumetric efficiency.

dynamic pressure greater than 1000 psf. The L/D for a supersonic missile in 1-g flight is usually much less than $(L/D)_{\text{Max}}$. As an example, the rocket baseline during 1-g powered flight at Mach 2, 20,000 ft altitude has an $L/D = 0.41$.

Figure 2.15 compares weapon configurations that have conventional cylindrical bodies of circular cross section to other weapons that are highly tailored, using aerodynamic shaping of their lifting body configurations. An indication of subsystems packaging efficiency is the ratio of body planform area to the 2/3 power of the body volume ($S_P/V^{2/3}$). For a circular cross-sectional body, this parameter has a value of about 3. As shown in the figure, a highly tailored missile could have a value of the subsystems packaging efficiency parameter $S_P/V^{2/3} > 9$. An advantage of a tailored lifting body missile is higher aerodynamic efficiency L/D (lift-to-drag ratio) for extended range cruise performance and enhanced maneuverability. Also shown is the synergy of tailored missiles with reduced radar cross section. Tailored missiles are also synergistic with ramjets in areas such as inlet integration and liquid hydrocarbon fuel packaging. Disadvantages of tailored missiles include their relative inefficiency for solid subsystems packaging and an adverse impact on launch platform integration because of a larger span. Improved methods and tests are required for the prediction of the aerodynamics and the structural loads of nonaxisymmetric weapons. This includes more extensive wind tunnel tests, computational fluid dynamics (CFD) predictions, and finite element modeling (FEM) of structural integrity.

2.6 Static Stability

Static stability in pitch is defined by the slope of the pitching moment coefficient versus angle of attack $\Delta C_m/\Delta\alpha = C_{m_\alpha}$. Shown in the top left portion of Fig. 2.16 is an example of the pitching moment coefficient versus angle of

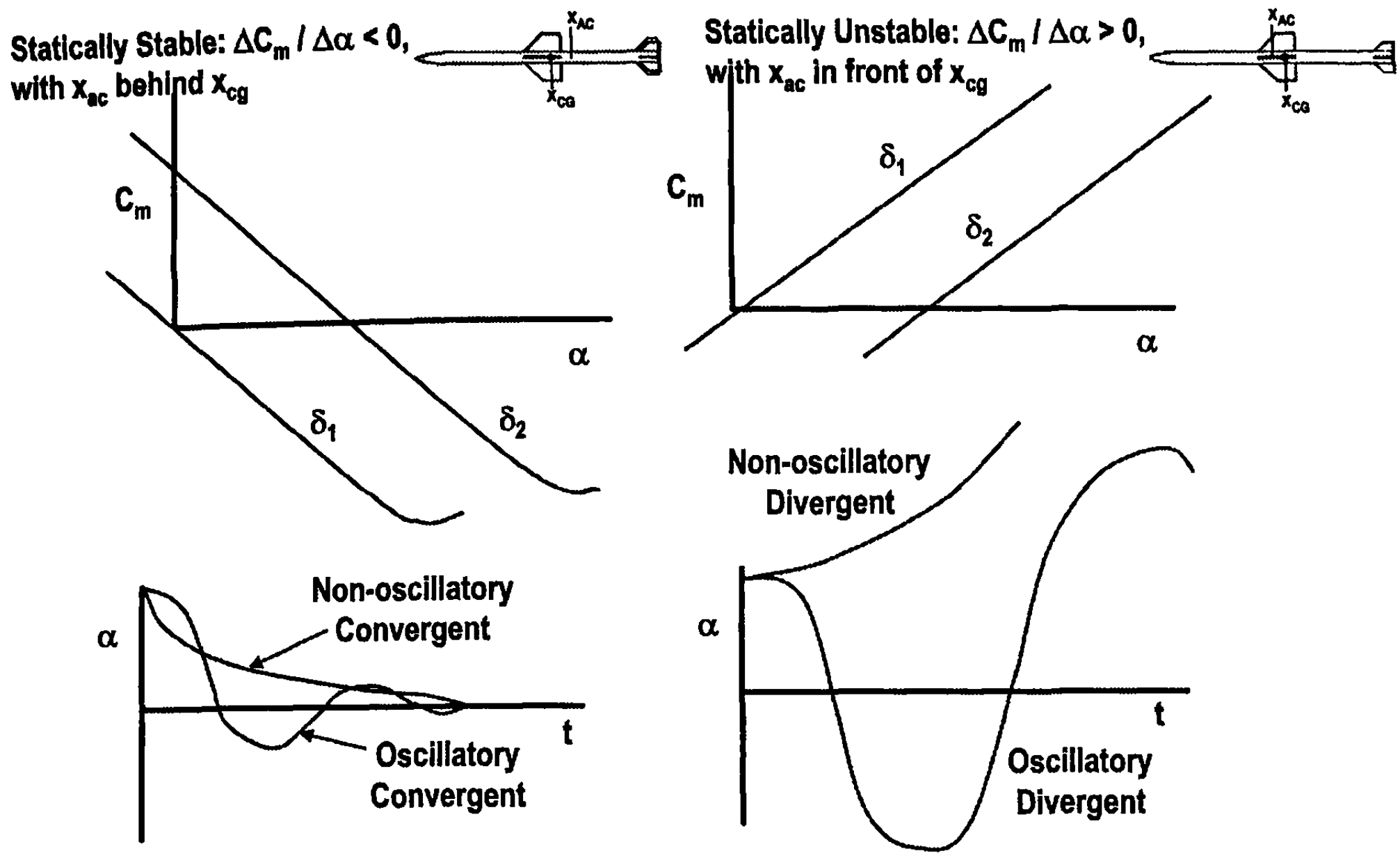

Note: Statically unstable missile requires high bandwidth autopilot.

Autopilot negative rate feedback provides stability augmentation.

Fig. 2.16 $\Delta C_m/\Delta\alpha$ and static margin define static stability.

attack curve for a statically stable missile. For a statically stable missile, the slope of the pitching moment coefficient versus angle of attack is negative, with the aerodynamic center aft of the center of gravity. An increase in angle of attack (nose up) causes a negative incremental pitching moment (nose down), which then tends to decrease the angle of attack. Control surface deflections allow the missile to trim ($C_m = 0$) at the desired angle of attack. The bottom left portion of the figure shows the decay of an incremental disturbance in the angle of attack as a function of time. It assumes a statically stable missile without an autopilot correction. For a highly stable, highly damped missile, the convergence is usually nonoscillatory. Most missiles have small tail surfaces, small static margin, and are lightly damped during free flight if there is no autopilot feedback (e.g., their unguided flight trajectory during store separation). The lightly damped missiles have an oscillatory convergence from a disturbance in angle of attack. The ideal damping for autopilot feedback is $\zeta \approx 0.7$.

As shown in the upper right of the figure, a statically unstable missile has the opposite trend. The slope of the pitching moment coefficient versus angle of attack is positive, with the aerodynamic center forward of the center of gravity. An increase in angle of attack causes an increase in pitching moment, which tends to cause a further increase in angle of attack. The rate of divergence is a function of dynamic pressure, with rapid divergence occurring at high dynamic pressure. If the autopilot has a high bandwidth and is sufficiently fast, it is possible to trim and control a statically unstable missile. Negative rate feedback from the gyros provides the required stability augmentation. A statically unstable missile might be desirable to improve the responsiveness and

maneuverability. The bottom right portion of the figure shows the divergence of a statically unstable missile without an autopilot correction. A highly unstable missile will diverge monotonically. A statically unstable missile that is slightly unstable will tend to oscillate with increasing divergence.

2.7 Body Aerodynamic Center

Aerodynamic center is defined as the location for neutral static margin. If the center of gravity is located at the aerodynamic center, the pitching moment does not change with angle of attack. The aerodynamic center location for the body $(x_{AC})_B$ depends mostly on three parameters, angle of attack, nose fineness, and aft body fineness. For conceptual design, the effect of Mach number on $(x_{AC})_B$ may be neglected. As shown in Fig. 2.17, for a body without a flare at low angle of attack, $(x_{AC})_B$ is located at about 63% of the nose length. At angles of attack approaching 90 deg, $(x_{AC})_B$ approaches the center of the body. Results in the figure are shown as a function of the body-length-to-nose-length ratio l_B/l_N and the angle of attack α. As before, results are based on combining slender body theory with crossflow theory, giving the equation

$$(x_{AC})_B/l_N = 0.63(1 - \sin^2\alpha) + 0.5(l_B/l_N)\sin^2\alpha \tag{2.26}$$

As an example, the rocket baseline missile has a nose length of 19.2 in and a total body length of 143.9 in. The ratio of body length to nose length is $l_B/l_N = 7.49$. For an angle of attack of $\alpha = 13$ deg, the center of pressure of the body $(x_{cp})_B$ is located at 81% of the length of the nose.

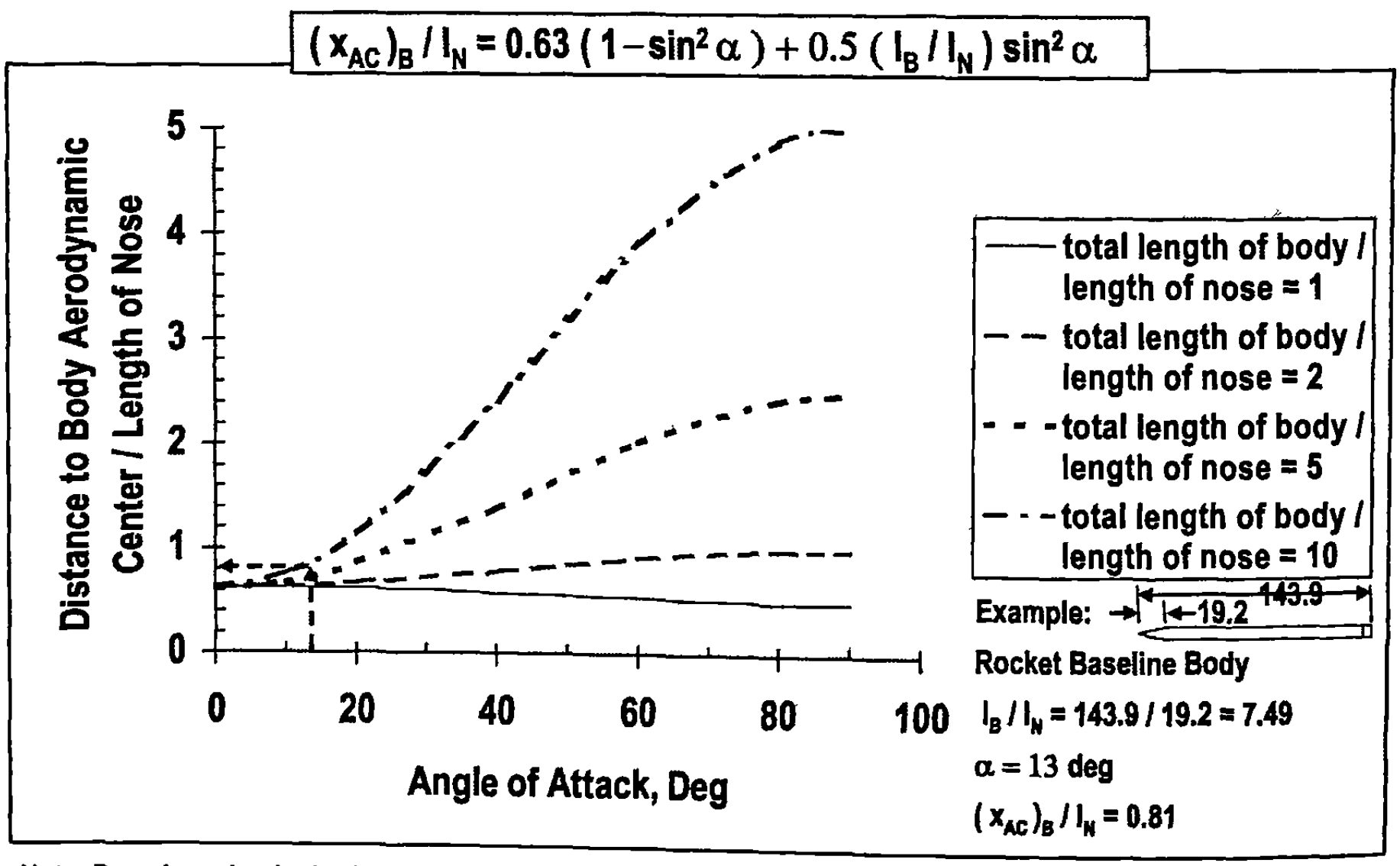

Note: Based on slender body theory (Pitts, et al) and cross flow theory (Jorgensen) references. No flare.
$(x_{AC})_B$ = Location of body aerodynamic center, l_N = length of nose, α = angle of attack, l_B = total length of body.

Fig. 2.17 Body aerodynamic center is a function of angle of attack, nose fineness, and body length.

2.8 Flare Stabilizer

A flare may be added to the aft end of a body to increase the static stability. Typically the flare half-angle is less than 10 deg to avoid flow separation. Figure 2.18a illustrates a process to calculate the static margin of a body-flare configuration. It is based on the locations of the normal force coefficient derivative contributors to pitching moment. As shown previously, at low angle of attack, the normal force coefficient derivative contribution and its location for a circular cross-sectional body, based on slender body theory are

$$(C_{N\alpha})_B = 2 \text{ per rad} \tag{2.27}$$

$$(x_{ac})_B = 0.63 l_N \tag{2.28}$$

Also for low angle of attack, the flare normal force coefficient derivative contribution and its location, based on slender body theory[8] are

$$(C_{N\alpha})_F = 2[(d_F/d)^2 - 1] \tag{2.29}$$

$$(x_{ac})_F = x_F + 0.33 l_F[2(d_F/d) + 1]/[(d_F/d) + 1] \tag{2.30}$$

The static margin of a body-flare missile, such as THAAD, is given by the equation

$$(x_{AC} - x_{CG})/d = -\{(C_{N\alpha})_B\{[x_{CG} - (x_{AC})_B]/d\} + (C_{N\alpha})_F\{[x_{CG} - (x_{AC})_F]/d\}\}/[(C_{N\alpha})_B + (C_{N\alpha})_F] \tag{2.31}$$

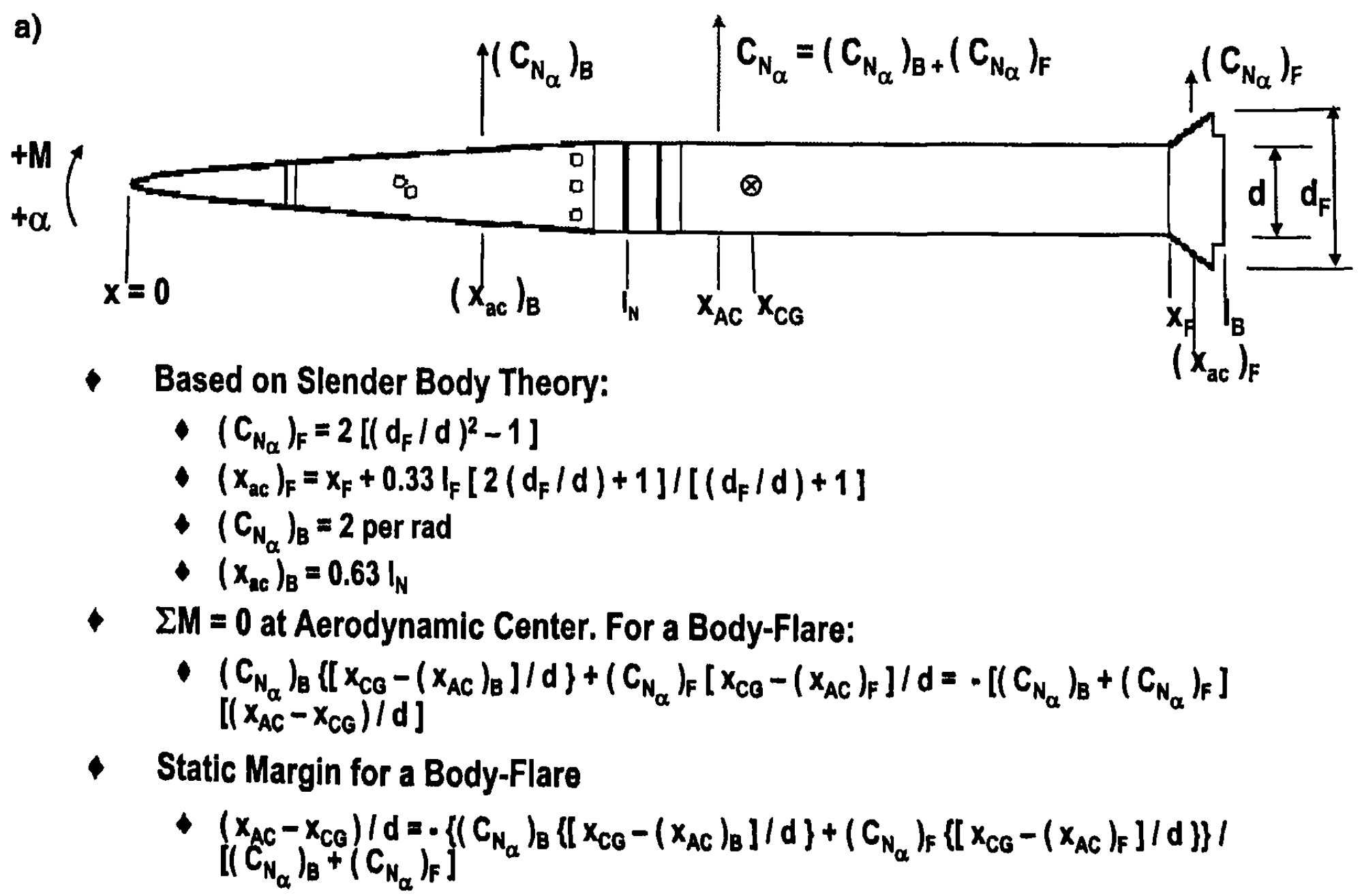

Fig. 2.18a Flare increases static stability.

b)

Example of Static Margin for THAAD (Statically Unstable Missile)

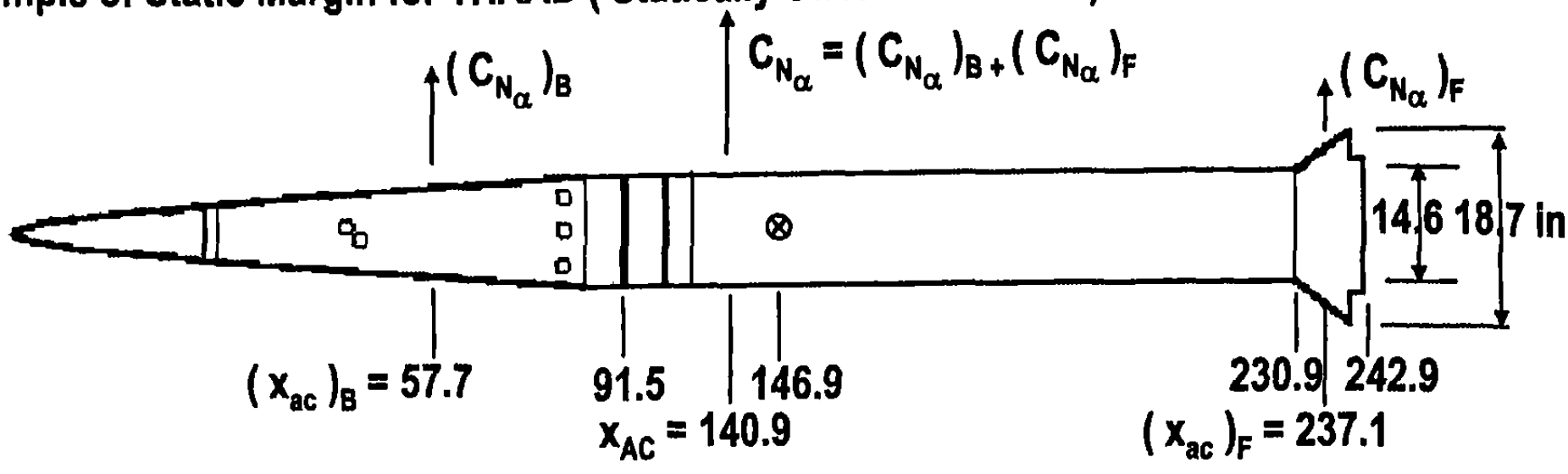

- $(C_{N_\alpha})_F = 2\,[(18.7/14.6)^2 - 1] = 2\,[(1.28)^2 - 1] = 1.28$ per rad
- $(x_{ac})_F = 230.9 + 0.33\,(12.0)[2\,(18.7/14.6) + 1]/[(18.7/14.6) + 1] = 237.1$ in
- $(x_{ac})_B = 0.63\,(91.5) = 57.7$ in
- $x_{CG_{Launch}} = 146.9$ in
- $(x_{AC} - x_{CG})_{Launch}/d = -\{2\{[146.9 - 57.7]/14.6\} + 1.28\{[146.9 - 237.1]/14.6\}\}$ $/[2 + 1.28] = -0.41$

Fig. 2.18b Flare increases static stability (Continued).

Figure 2.18b further illustrates the process of calculating static margin for a body-flare configuration, using the THAAD missile as an example. The flare somewhat compensates for the statically unstable body. As shown in the example, for a flare-to-body diameter ratio of $d_F/d = 18.7$ in$/14.6$ in $= 1.28$, THAAD is predicted to be statically unstable at launch, with a static margin of

$$(x_{AC} - x_{CG})/d = -0.41 \tag{2.32}$$

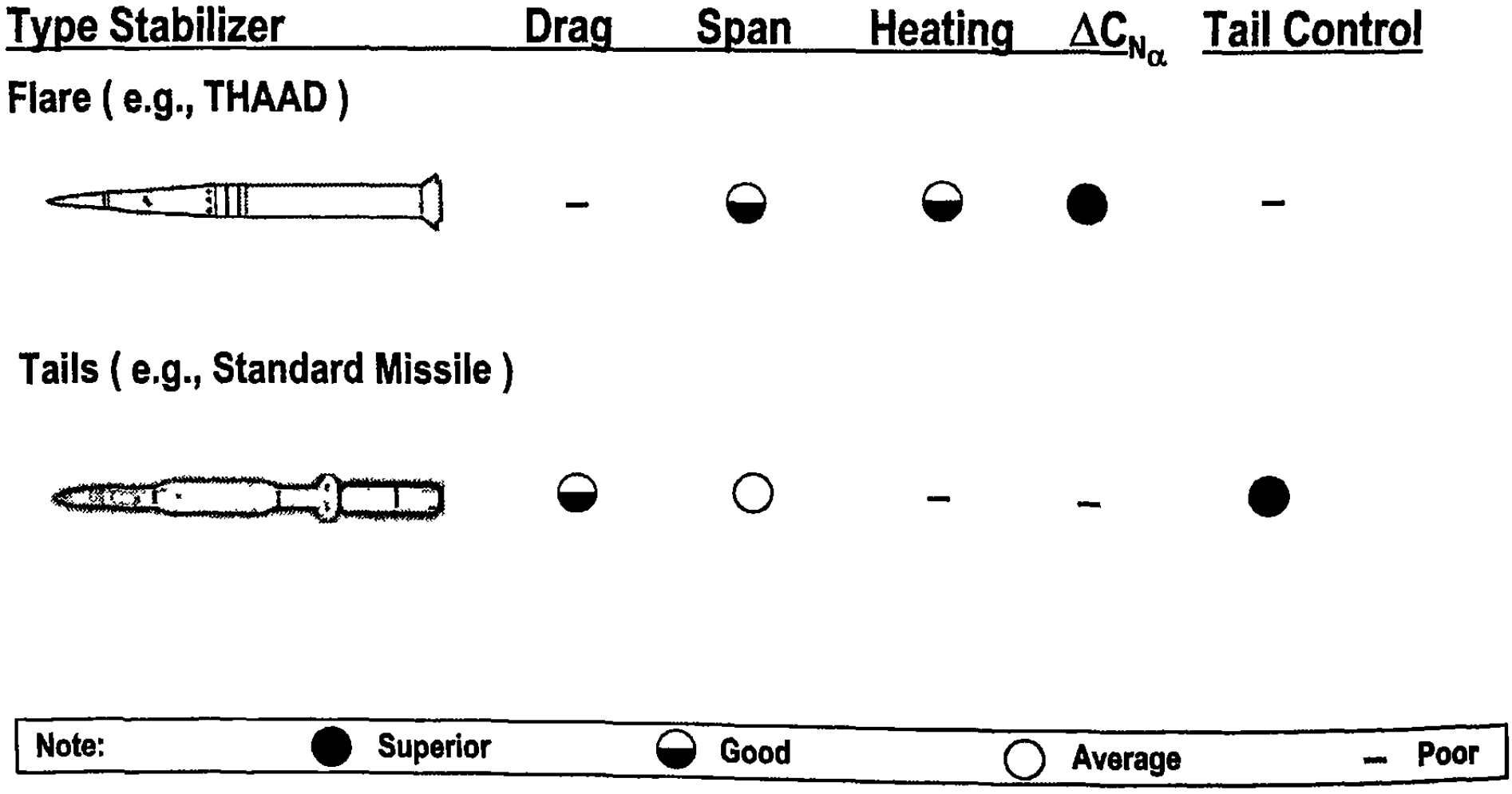

Fig. 2.19 Tail stabilizers have lower drag while flares have lower aerodynamic heating and changes in stability.

The flare half-angle of THAAD is 9.7 deg to avoid flow separation (and the separation pressure drag) in front of the flare.

Figure 2.19 is a comparison of a flare stabilizer with conventional tail stabilizers. A flare-stabilized missile, such as THAAD, has advantages of lower required span for the stabilizer, lower aerodynamic heating, and less variation in its aerodynamics with Mach number. Reduced aerodynamic heating is particularly beneficial for a hypersonic missile such as THAAD. Reentry vehicles also use flares to provide static stability while minimizing aerodynamic heating. An example of a missile that uses conventional tail surfaces for static stability is the Standard Missile. Compared to flares, conventional tails have benefits of lower drag and the availability of the tail surfaces for flight control in addition to stability. THAAD relies entirely on thrust vector control (TVC) and reaction jet control. Compared to aerodynamic control, a disadvantage of TVC and reaction jet control is a weight penalty because of the additional weight of propellant.

2.9 Wings Versus No Wings

There are many considerations in the tradeoff of a small wing/strake/no wing versus a larger wing. A small wing, a strake, or no wing has advantages of range in high supersonic flight, range in high dynamic pressure, maximum angle of attack (stability and control is better at high angles of attack, with less induced roll and delayed stall), launch platform compatibility, lower radar cross section, and volume and weight available for propellant/fuel in a volume- or weight-limited missile. A larger wing has advantages of range in subsonic flight, range in low dynamic pressure, lower guidance time constant, normal acceleration, high-altitude intercept, body stiffness, seeker tracking (less dome error slope error from lower angle of attack), less wipe velocity for the warhead at impact (lower angle of attack), and lower gimbal angle requirement for the seeker. Note that some of the disadvantages of a wingless missile can be alleviated by unconventional flight control (e.g., TVC, reaction jet/jet interaction control). It is possible for a wingless missile to achieve small guidance time constant, high normal acceleration or maneuverability, and a high-altitude intercept capability at low dynamic pressure through unconventional flight control.

Because supersonic missiles generally operate at relatively high dynamic pressure, body lift may be sufficient for the required aerodynamic efficiency (L/D) and maneuverability. Shown in Fig. 2.20 are examples of supersonic missiles that do not have wings. Many of these missiles are highly maneuverable and are capable of operating at high angle of attack. Wingless missiles that use canard control may have enhanced maneuverability from the additional lift of the canard surface. The majority of the wingless missiles (the first 15 of 28) in the figure use canard control, while the remaining 13 missiles have either tail control or thrust vector control. Unconventional flight control may also be used if additional maneuverability is required to supplement the body lift. Examples of supersonic wingless missiles that use TVC are THAAD, Archer AA-11 (TVC combined with canard control), Sidewinder AIM-9X (TVC combined with tail control), and Standard Missile (TVC combined with tail control).

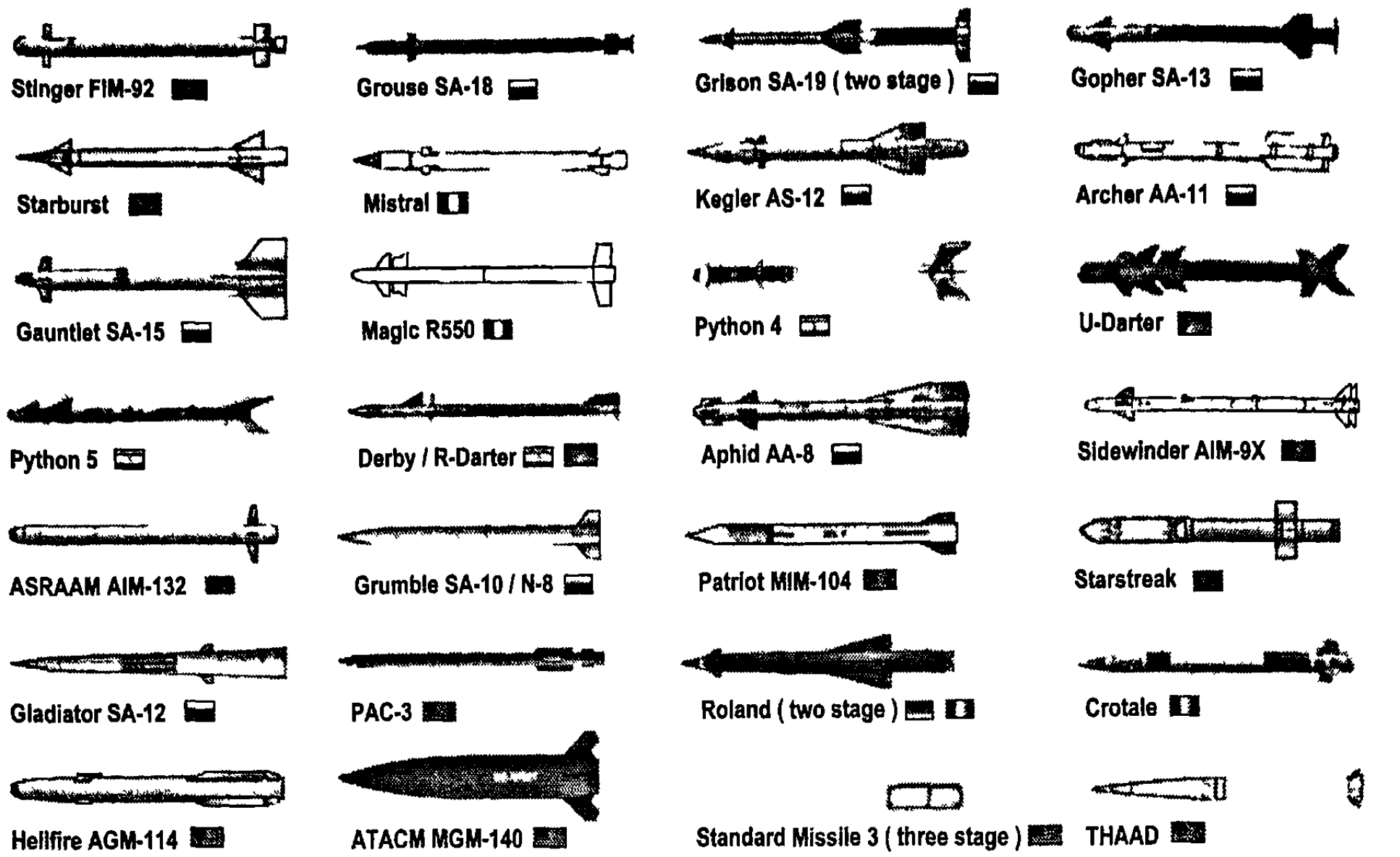

Permission of Missile Index. Copyright 1997©Missile.Index All Rights Reserved

Fig. 2.20 Most supersonic missiles are wingless. Figure also in color section.

2.10 Normal Force Prediction for Surfaces (e.g., Wing, Tail, Canard)

Wing, tail, and canard surfaces may be characterized by their location relative to the center of gravity, cg. Wing surfaces are located near the cg. Tail surfaces are located aft of the cg. Canard surfaces are located forward of the cg. Strake surfaces have very low aspect ratio ($A < 1$). Strakes may be located forward, aft, or near the center of gravity. Wing, tail, and canard surfaces may be fixed or movable (i.e., control surfaces). The methodology described here to predict the normal force on the wing is also applicable to other surfaces, such as tails and canards. As shown in the equations of Fig. 2.21, the surface normal force coefficient $(C_N)_{\text{Surface}}$ is a function of Mach number, local angle of attack, aspect ratio, and the surface planform area. $(C_N)_{\text{Surface}}$, which is based on the missile reference area, decreases with increasing supersonic Mach number and increases with angle of attack and the surface area. The prediction is based on the method of Ref. 9. In the figure, linear wing theory plus Newtonian impact theory are applied at high supersonic Mach number, with the requirement that

$$M^2 > 1 + [8/(\pi A)]^2 \tag{2.33}$$

The linear wing theory plus Newtonian impact theory equation is

$$|(C_N)_{Surface}| = [4|\sin\alpha' \cos\alpha'|/(M^2 - 1)^{1/2} + 2\sin^2\alpha'](S_{\text{Surface}}/S_{\text{Ref}}) \tag{2.34}$$

Note that $(C_N)_{\text{Surface}}$ based on linear wing theory is independent of aspect ratio. For the rocket baseline missile wing with an aspect ratio of $A_W = 2.82$, linear

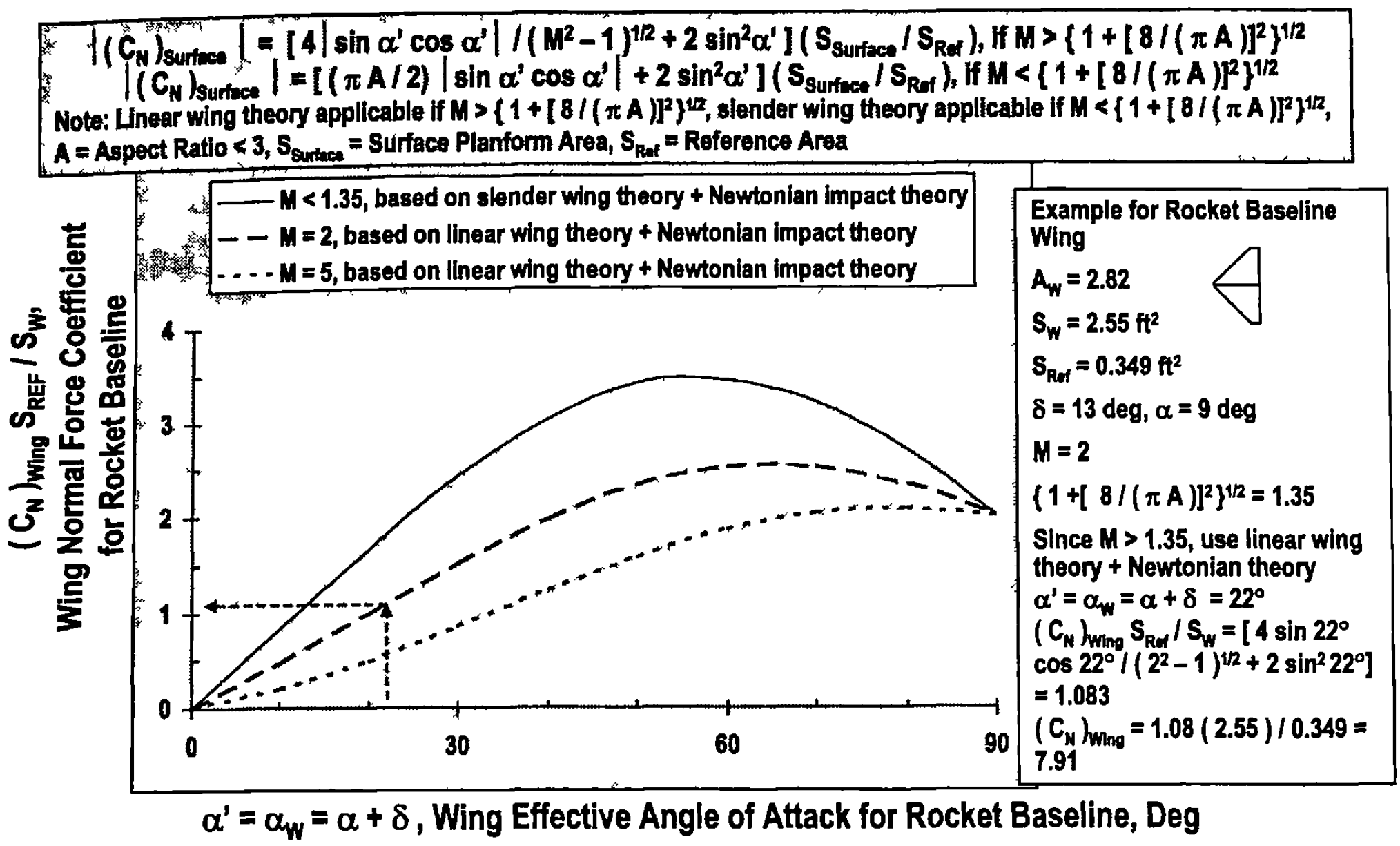

Fig. 2.21 Wings, tails, and canards with large area and at high angle of attack have high normal force.

wing theory is applicable for Mach numbers greater than 1.35. An alternative approach, slender wing theory plus Newtonian impact theory, is more applicable at subsonic and low supersonic Mach number, with the requirement that

$$M^2 < 1 + [8/(\pi A)]^2 \tag{2.35}$$

The slender wing theory plus Newtonian impact theory equation is

$$|(C_N)_{\text{Surface}}| = [(\pi A/2)|\sin\alpha' \cos\alpha'| + 2\sin^2\alpha'](S_{\text{Surface}}/S_{\text{Ref}}) \tag{2.36}$$

Note that $(C_N)_{\text{Surface}}$, based on slender wing theory, is independent of Mach number. Slender wing theory is accurate for low aspect ratio wings ($A < \approx 3$). As a comparison with lifting surface theory, which is most applicable to high aspect ratio surfaces, at an aspect ratio of $A = 3$, slender wing theory overpredicts normal force by about 25% compared to lifting surface theory. For the rocket baseline missile wing ($A_W = 2.82$), slender wing theory is applicable for Mach numbers less than 1.35.

As an example, we shall evaluate the rocket baseline missile wing at Mach 2. Because the Mach number is greater than 1.35, the prediction is based on linear wing theory plus Newtonian impact theory. The rocket baseline missile wing is limited to a maximum local angle of attack of 22 deg because of stall of the wing. For a typical cg location, this results in a maximum angle of attack of 9.4 deg for a maximum wing control deflection of 12.6 deg. For this condition, the normal force coefficient of the wing, based on wing area $S_W = 2.55$ ft^2, is equal to 1.08. Finally, the normal coefficient of the wing,

based on the body reference cross-sectional area $S_{Ref} = 0.349$ ft^2, is computed to be $(C_N)_{Wing} = 7.91$. Because the rocket baseline missile has a relatively large wing, most of the normal force for the missile comes from the wing.

The rocket baseline has fixed tail surfaces with an exposed tail aspect ratio $A_T = 2.59$ and a tail planform area $S_T = 1.54$ ft^2. At Mach 2 and an angle of attack $\alpha = 9.4$ deg, the normal force coefficient of the tail is computed to be $(C_N)_{Tail} = 0.425$, based on the tail surface planform area. Based on the missile reference area, $(C_N)_{Tail} = 1.88$. Note that for the trimmed flight condition of Mach 2 and $\alpha = 9.4$ deg, the tail normal force is relatively small compared to that of the deflected wing $[(C_N)_{Tail}/(C_N)_{Wing} = 1.88/7.91 = 0.24]$.

The total normal force coefficient of the wing-tail-body configuration is assumed to be the sum of the contributions from the wing plus the tail plus the body. As shown previously, the body normal force coefficient is a function of angle of attack, fineness ratio, and cross section geometry. The rocket baseline has a circular cross section ($a/b = 1$) and a fineness ratio $l/d = 17.99$. At an angle of attack of $\alpha = 9.4$ deg, the body normal force coefficient is computed to be

$$(C_N)_{Body} = \sin(2\alpha)\cos(\alpha/2) + 2(l/d)\sin^2\alpha = 1.28 \tag{2.37}$$

Note that the body normal force coefficient is only 16% of that provided by the deflected wing. Substituting, the total trimmed normal force coefficient at Mach 2, $\alpha = 9.4$ deg, and $\delta = 12.6$ deg is

$$C_N = (C_N)_{Wing} + (C_N)_{Tail} + (C_N)_{Body} = 7.91 + 1.88 + 1.28 = 11.1 \tag{2.38}$$

A similar approach can be used to determine the wing normal force curve slope from angle of attack. $(C_{N\alpha})_{Surface}$ is used in sizing the tail to meet the static stability requirement. It is the derivative of the equation for surface normal force coefficient. At low angle of attack, $(C_{N\alpha})_{Surface} = 4/(M^2 - 1)^{1/2}$, if the parameter $M^2 > 1 + [8/(\pi A)]^2$. If the parameter $M^2 < 1 + [8/(\pi A)]^2$, then the appropriate equation is $(C_{N\alpha})_{Surface} = \pi A/2$. Note that $(C_{N\alpha})_{Surface}$ in these equations is based on the surface planform area and has the units per rad.

The total normal force curve slope from angle of attack is assumed to be the sum of the contributions from the wing plus the tail plus the body. As shown previously, the body normal force curve slope at low angle of attack is $(C_{N\alpha})_{Body} = 2[(a/b)\cos^2\varphi + (b/a)\sin^2\varphi]$. For the rocket baseline with a circular cross section ($a/b = 1$), $(C_{N\alpha})_{Body} = 2$ per radian. At Mach 2, the total normal force curve slope at low angle of attack, based on body cross-sectional reference area is

$$\begin{aligned} C_{N\alpha} &= (C_{N\alpha})_{Wing}(S_W/S_{Ref}) + (C_{N\alpha})_{Tail}(S_T/S_{Ref}) + (C_{N\alpha})_{Body} \\ &= 4/(2^2 - 1)^{1/2}(2.55/0.349) + 4/(2^2 - 1)^{1/2}(1.54/0.349) + 2 \\ &= 16.9 + 10.2 + 2 = 29.1 \text{ per rad} \end{aligned} \tag{2.39}$$

As a comparison, the total normal force curve slope from angle of attack (Chapter 7), which is based on wind tunnel data, is $C_{N\alpha} = 34.4$ per rad. The predicted value of $C_{N\alpha}$ has an error of 14%.

The normal force prediction is likely to be optimistic for very low Mach number (e.g., $M < 0.2$) and for very high altitude (e.g., $h > 80{,}000$ ft). For these flight conditions, boundary-layer transition from laminar to turbulent is delayed, resulting in a thicker boundary layer. The boundary-layer thickness on the aft body may blanket a significant portion of the tails, reducing the stability and control effectiveness of the tails.

2.11 Aerodynamic Center Prediction for Surfaces (e.g., Wing, Tail, Canard)

Shown in Fig. 2.22 is the variation of aerodynamic center $(x_{AC})_{\text{Surface}}$ of a thin surface (e.g., wings, tails, canards) with Mach number and aspect ratio. Results are applicable at low angles of attack ($\alpha < 10$ deg). At low Mach number, $(x_{AC})_{\text{Surface}}$ is located near 25% of the mean aerodynamic chord C_{MAC}. At hypersonic Mach number $(x_{AC})_{\text{Surface}}$ shifts to 50% of C_{MAC}. Compressed carriage missiles with relatively long chord surfaces, such as AMRAAM AIM-120C, usually have a disadvantage of a larger supersonic hinge moment. The prediction at supersonic Mach number and low angle of attack is based on linear wing theory[5], giving

$$(x_{AC}/C_{\text{MAC}})_{\text{Surface}} = [A(M^2 - 1)^{1/2} - 0.67]/[2A(M^2 - 1)^{1/2} - 1] \qquad (2.40)$$

The rocket baseline missile wing has an exposed aspect ratio of 2.82, a mean aerodynamic chord length of 13.3 in, and a location of the leading edge of the

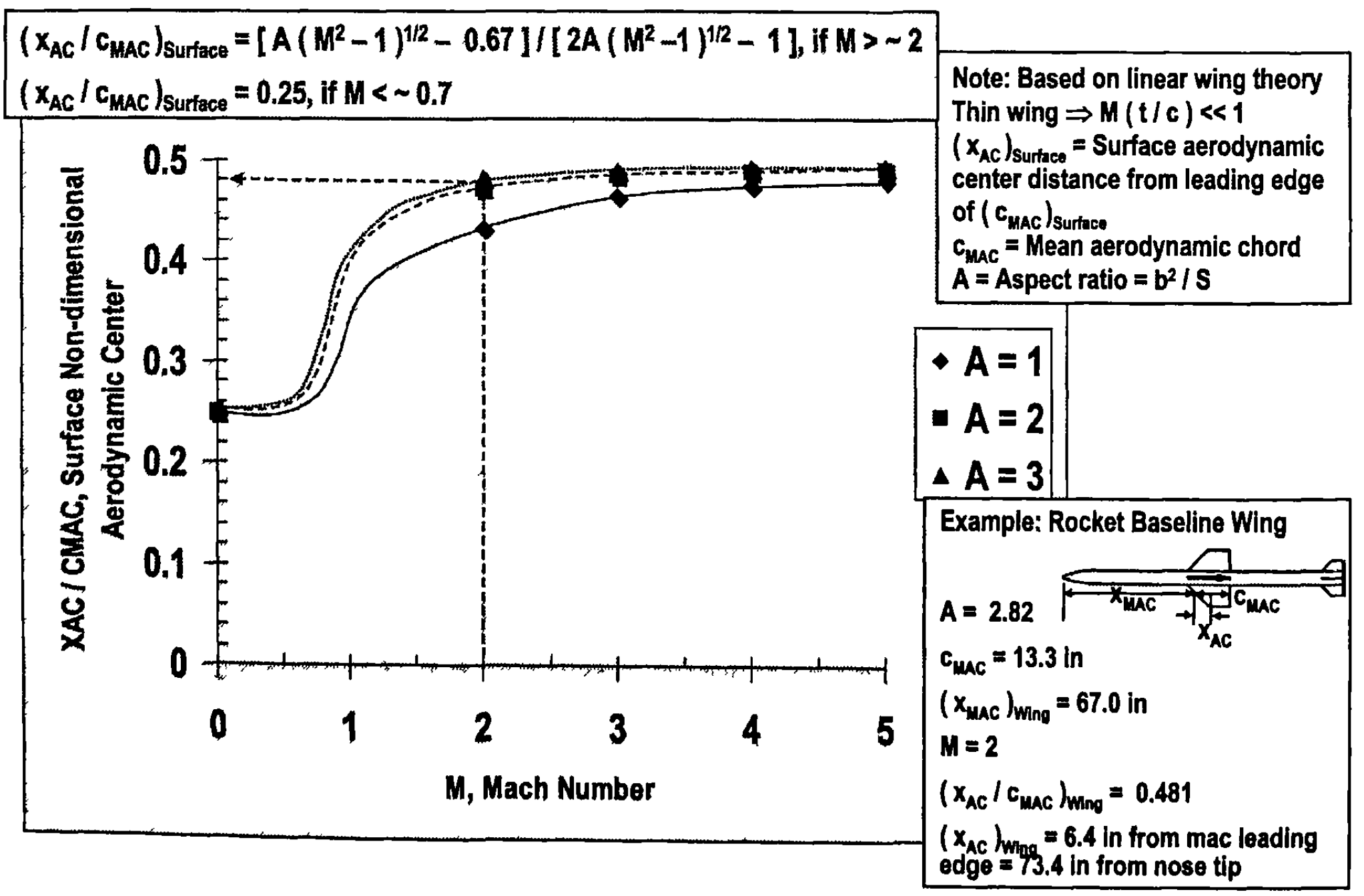

Fig. 2.22 Aerodynamic center of a thin surface (e.g., wing, tail, canard) varies with Mach number.

mean aerodynamic chord at 67.0 in from the nose tip. As shown in the figure, at Mach 2 the predicted aerodynamic center of the exposed wing is located at 48% of the length of the mean aerodynamic chord, providing a location of $(x_{AC})_{\text{Wing}} = 73.4$ in from the nose tip. At subsonic Mach number the wing aerodynamic center is located at approximately 25% of the mean aerodynamic chord, providing a location of $(x_{AC})_{\text{Wing}} = 70.3$ in from the nose tip. The center-of-gravity location of the rocket baseline missile is 84.6 in from the nose tip at launch and 76.2 in at burnout. Because the distance between the wing aerodynamic center and the missile center of gravity is always relatively small (less than 14.3 in) for all flight conditions, the deflection of the wing control causes a relatively small change in missile angle of attack. If either tail control or canard control were used for the rocket baseline missile instead of wing control, the change in angle of attack with control surface deflection would be larger because of the larger moment arm of a tail or canard control.

2.12 Hinge Moment Prediction

The hinge moment (HM) of an aerodynamic control surface is a function of the normal force N_{Surface} on a surface times the moment arm between the aerodynamic center and the hinge line of the control surface $(x_{AC} - x_{HL})_{\text{Surface}}$. The equation is

$$HM = N_{\text{Surface}}(x_{AC} - x_{HL})_{\text{Surface}} \tag{2.41}$$

Shown in Fig. 2.23 is the variation of the HM with dynamic pressure and effective angle of attack for the rocket baseline missile. An assumed flight altitude is

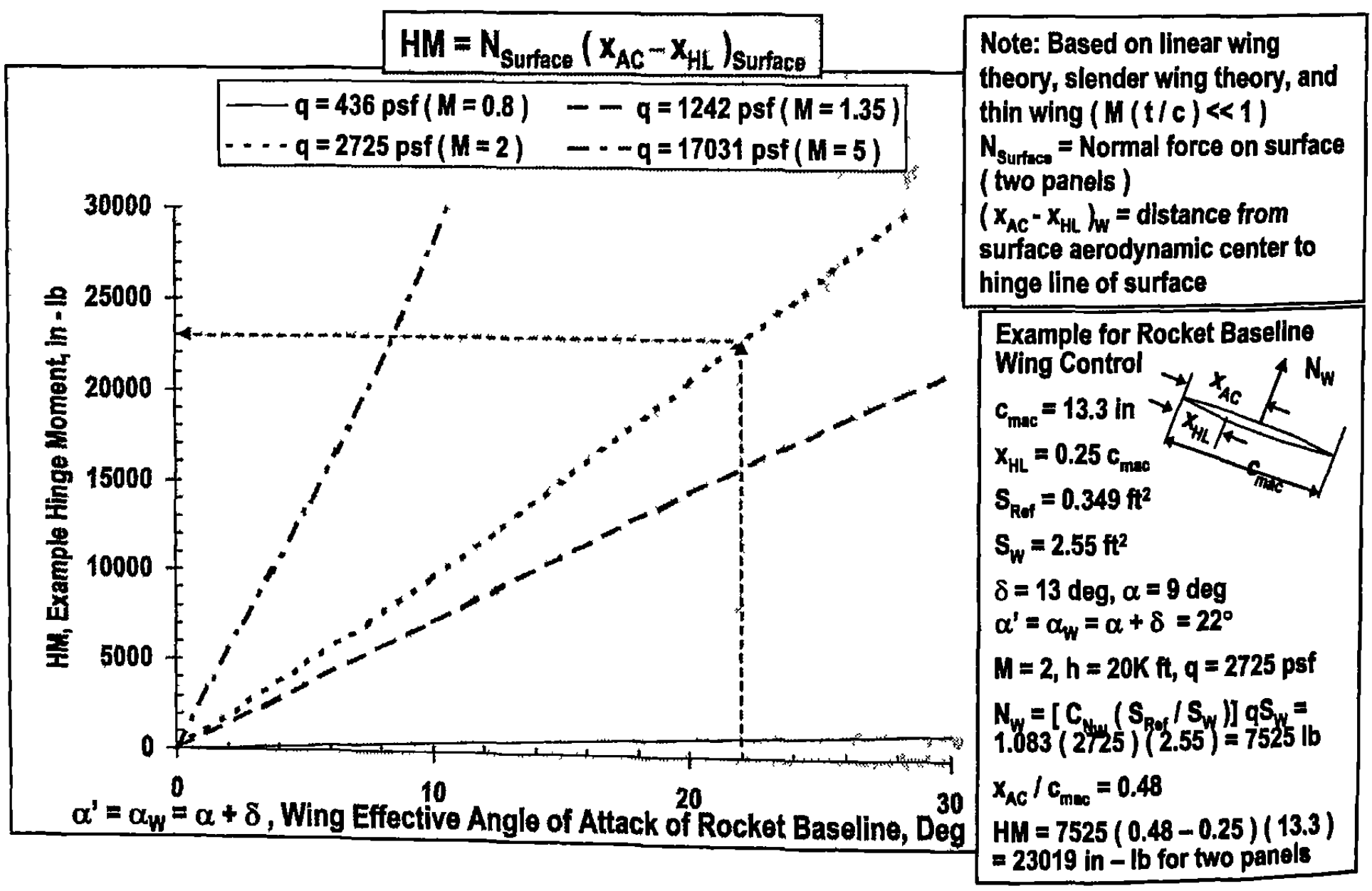

Fig. 2.23 Hinge moment increases with dynamic pressure and effective angle of attack.

$h = 20{,}000$ ft altitude. As previously, the prediction of N_{Surface} is based on linear wing theory at high supersonic Mach number and on slender wing theory at subsonic and low supersonic Mach number. It is also assumed that the surface section is thin $[M(t/c) \ll 1]$. At low subsonic Mach number, the aerodynamic center is located at the quarter chord of the mean aerodynamic center ($x_{AC} = 0.25C_{\text{mac}}$). For this example, the hinge line of the control surface of the rocket baseline is also assumed to be located at the quarter chord of the mean aerodynamic center ($x_{HL} = 0.25C_{\text{mac}}$). The hinge must be located either at or forward of the aerodynamic center to avoid unstable feedback through the flight control system.

An example is shown for the rocket baseline wing control at a maximum effective angle of attack $\alpha' = \alpha_{\text{W}} = 22$ deg. For this condition, the control deflection $\delta = 13$ deg and the body angle of attack $\alpha = 9$ deg. The total normal force on the two panels that comprise the wing is $N_{\text{Wing}} = [C_{\text{N}}S_{\text{Ref}}/S_{\text{W}}]qS_{\text{W}} = 1.083(2725)(2.55) = 7525$ lb. Also, from a previous calculation, the aerodynamic center is located at 48% of the mean aerodynamic center ($x_{AC} = 0.48\,C_{\text{mac}}$). Finally, calculating the HM of the rocket baseline wing control at Mach 2, 20,000 ft altitude with maximum wing control deflection, $HM = 7525(0.48 - 0.25)(13.3) = 23{,}019$ in-lb for the two panels that comprise the wing. Each actuator of the two panels has an individual HM of 11,510 in-lb. Control surface actuators are sized by the highest HM flight condition, which usually occurs at the maximum maneuverability requirement for the highest dynamic pressure flight condition.

2.13 Thin Surface (e.g., Wing, Tail, Canard) Drag Prediction

Equations for predicting thin surface drag coefficient are shown in Fig. 2.24. The surface skin friction drag prediction, based on Ref. 4, is the equation

$$(C_{D_0})_{\text{Surface,Friction}} = n_{\text{Surface}}[0.0133[M/(qC_{\text{mac}})]^{0.2}](2S_{\text{Surface}}/S_{\text{Ref}}) \tag{2.42}$$

In the equation the units of dynamic pressure q and mean aerodynamic chord C_{mac} are psf and ft respectively. Major contributors to the skin friction drag coefficient are the number of surface planforms N_{Surface} and the surface planform area S_{Surface}. The total wetted area for surface skin friction drag is equal to $2N_{\text{Surface}}S_{\text{Surface}}$. Surface skin friction drag coefficient is a weak function of Mach number, dynamic pressure, and the length of the mean aerodynamic chord. Assumptions for the equation are that the variation in the free stream speed of sound and viscosity with altitude is relatively small, and a turbulent boundary layer.

A second contributor to surface drag is wave drag. The wave drag prediction is based on modified Newtonian theory, described in Ref. 8, with the equation

$$\begin{aligned}(C_{D_0})_{\text{Surface,Wave}} = {} & \text{n}_{\text{Surface}}[2/(\gamma \text{M}^2_{\Lambda\text{LE}})]\{\{[(\gamma+1)\text{M}^2_{\Lambda\text{LE}}]/2\}^{\gamma/(\gamma-1)} \\ & \times \{(\gamma+1)/[2\gamma\text{M}^2_{\Lambda\text{LE}} - (\gamma-1)]\}^{1/(\gamma-1)} - 1\} \\ & \times \sin^2\delta_{\text{LE}}\cos\Lambda_{\text{LE}}\text{t}_{\text{mac}}\text{b}/\text{S}_{\text{Ref}} \quad \text{if } \text{M}_{\Lambda\text{LE}} > 1\end{aligned} \tag{2.43}$$

$(C_{D_0})_{Surface,Friction} = n_{Surface}\{0.0133[M/(q\,c_{mac})]^{0.2}\}(2S_{Surface}/S_{Ref})$, q in psf, c_{mac} in ft
$(C_{D_0})_{Surface,Wave} = n_{Surface}(1.429/M_{\Lambda_{LE}}^2)\{(1.2M_{\Lambda_{LE}}^2)^{3.5}[2.4/(2.8M_{\Lambda_{LE}}^2 - 0.4)]^{2.5} - 1\}\sin^2\delta_{LE}\cos\Lambda_{LE}$
$t_{mac}b/S_{Ref}$, based on Newtonian impact theory
$(C_{D_0})_{Surface} = (C_{D_0})_{Surface,Wave} + (C_{D_0})_{Surface,Friction}$

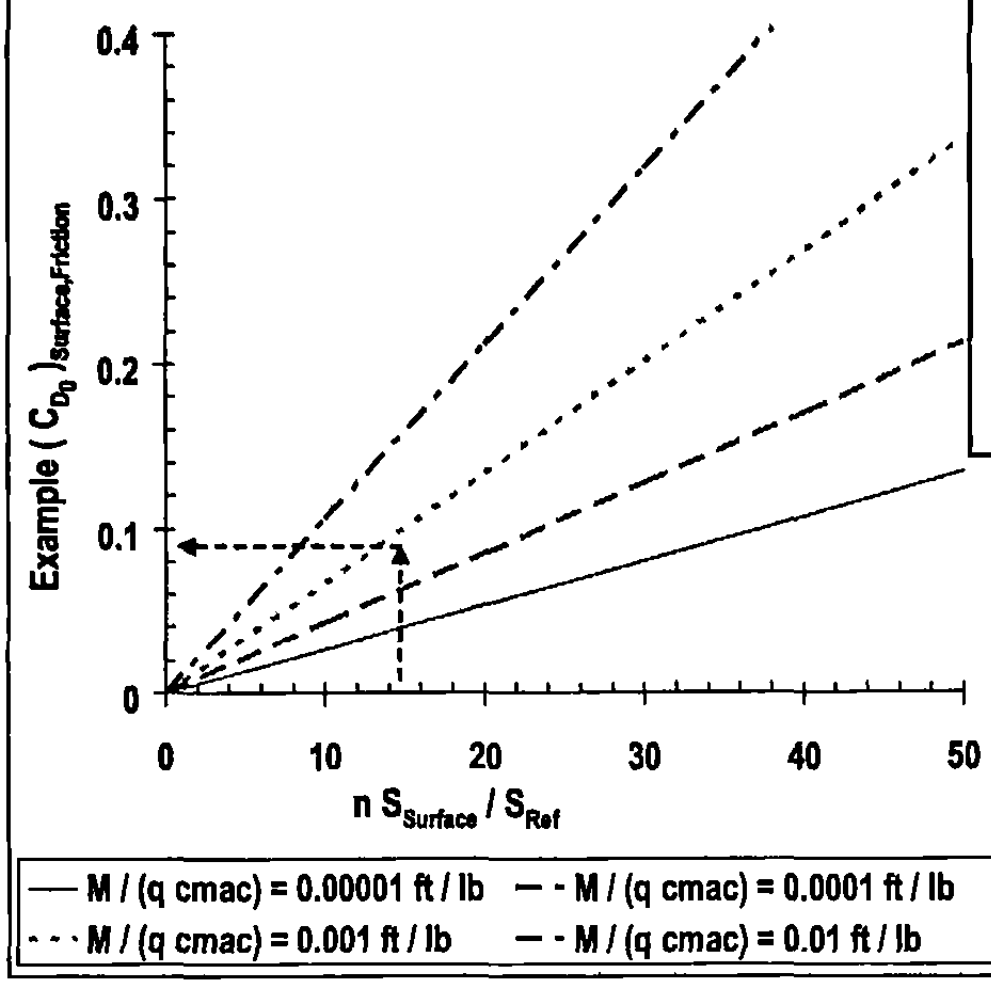

$n_{Surfaces}$ = number of surface planforms (cruciform = 2)
q = dynamic pressure in psf
c_{mac} = length of mean aero chord in ft
γ = Specific heat ratio = 1.4
$M_{\Lambda_{LE}} = M\cos\Lambda_{LE}$ = Mach number ⊥ leading edge
δ_{LE} = leading edge section total angle
Λ_{LE} = leading edge sweep angle
t_{mac} = max thickness of mac
b = span

Example for Rocket Baseline Wing:

$n_W = 2$, M = 2, h = 20K ft (q = 2,725 psf), c_{mac} = 1.108 ft, S_{Ref} = 50.26 in², S_W = 367 in², δ_{LE} = 10.01 deg, Λ_{LE} = 45 deg, t_{mac} = 0.585 in, b = 32.2 in, $M_{\Lambda_{LE}}$ = 1.41 (M = 2)

$M/(qc_{mac})$ = 2 / [2725 (1.108)] = 0.000662 ft / lb

n $S_{Surface}$ / S_{Ref} = 2 (367) / 50.26 = 14.60

$(C_{D_0})_{Wing,Friction}$ = 0.090

$(C_{D_0})_{Wing,Wave}$ = 0.024

$(C_{D_0})_{Wing}$ = 0.024 + 0.090 = 0.11

Fig. 2.24 Wings, tails, and canards usually have greater skin friction drag than shock wave drag.

Newtonian theory is modified by calculating the pressure across the normal shock as a function of Mach number. Substituting $\gamma = 1.4$ for air gives

$$(C_{D_0})_{\text{Surface,Wave}} = n_{\text{Surface}}(1.429/M_{\Lambda LE}^2)\{(1.2M_{\Lambda LE}^2)^{3.5} \times [2.4/(2.8M_{\Lambda LE}^2 - 0.4)]^{2.5} - 1\} \times \sin^2\delta_{LE}\cos\Lambda_{LE}t_{mac}b/S_{Ref} \tag{2.44}$$

A thin surface with a small leading edge section angle has smaller wave drag than a surface with a blunt leading edge. Also, leading edge sweep reduces the effect of Mach number by the factor of $\cos\Lambda_{LE}$, maintaining a subsonic leading edge until $M\cos\Lambda_{LE} = 1$.

A third potential contributor to surface drag is the base drag from flow separation on the trailing edge of the surface. For a thin surface with a sharp trailing edge, there is negligible flow separation. Base drag can be neglected for most missile surfaces, which are usually thin.

As an example, the rocket baseline missile has cruciform wings ($n_W = 2$), exposed planform area of each wing $S_W = 2.55$ ft^2, reference area based on the body cross-sectional area of $S_{Ref} = 0.349$ ft^2, length of the mean aerodynamic chord $C_{mac} = 1.108$ ft, wing leading edge sweep angle of $\Lambda_{LE} = 45$ deg, leading edge section total angle $\delta_{LE} = 10.01$ deg, maximum thickness of the mean aerodynamic chord $t_{mac} = 0.585$ in, and an exposed span $b = 32.2$ in. At a typical flight condition of Mach 2/20,000 ft altitude, the wing skin friction

contribution to zero-lift drag, based on two wings with four panels, is $(C_{D_0})_{\text{Wing,Friction}} = 0.090$. The wing wave drag contribution to zero-lift drag, based on two wings with four panels, is $(C_{D_0})_{\text{Wing,Wave}} = 0.024$. The total wing zero-lift drag coefficient is

$$(C_{D_0})_{\text{Wing}} = 0.09 + 0.02 = 0.11 \tag{2.45}$$

Note from above that 82% of the wing zero-lift drag is because of skin friction. Also note that the rocket baseline missile wing has a zero-lift drag coefficient that is only 27% of the body coast zero-lift drag coefficient (0.11 vs 0.41).

The rocket baseline has cruciform tail surfaces ($n_T = 2$), tail leading edge sweep angle of $\Lambda_{LE} = 57$ deg, exposed tail planform area of $S_T = 1.54\ \text{ft}^2$, leading edge section total angle $\delta_{LE} = 6.17$ deg, mean aerodynamic chord $C_{mac} = 1.025$ ft, maximum thickness of the mean aerodynamic chord $t_{mac} = 0.33$ in, and exposed span $b = 24.0$ in. At Mach 2 and an altitude of 20,000 ft, the zero-lift drag coefficient of the tail surfaces, based on the missile reference area, is computed to be

$$(C_{D_0})_{\text{Tail}} = (C_{D_0})_{\text{Tail,Wave}} + (C_{D_0})_{\text{Tail,Friction}} = 0.003 + 0.048 = 0.051 \tag{2.46}$$

The zero-lift drag of the tail is much smaller than that of the wing. This is because of the smaller leading edge section angle (6.17 deg vs 10.01 deg) and the smaller planform area. Note that for the flight condition of Mach 2 and 20,000 ft altitude, the tail provides only 12% of the zero-lift drag compared to that of the body.

Finally, the total zero-lift drag coefficient is assumed to be the sum of the contributions from the body plus the wing plus the tail. Substituting, the total zero-lift drag coefficient of the rocket baseline during coasting flight at Mach 2 and 20,000 ft altitude is computed to be

$$C_{D_0} = (C_{D_0})_{\text{Body}} + (C_{D_0})_{\text{Wing}} + (C_{D_0})_{\text{Tail}} = 0.41 + 0.11 + 0.05 = 0.57 \tag{2.47}$$

2.14 Surface Geometry Tradeoffs

Shown in Fig. 2.25 are examples of alternative surface panel geometries for missile tails, canards, and wings. The figure is a comparison of a triangular (delta), conventional trapezoidal with an aft swept leading edge, "bow tie" trapezoidal with a forward swept leading edge and an aft swept trailing edge, a double swept leading edge, and a rectangular surface planform geometry. The comparison is based on the same planform area because roughly the same area is required to provide the same static stability and maneuverability. The comparison also assumes that there is a span constraint, which is often the case for launch platform compatibility. Note from the figure that the double swept leading edge geometry has a major advantage of minimizing the shift in aerodynamic center. As a wing, the double swept leading edge geometry has more nearly constant static margin. As a control surface, the double swept leading edge geometry has reduced HM, allowing lighter weight, smaller size, and lower cost actuators. In addition to a

Parameter	Triangle (Delta)	Aft Swept LE Trapezoid	Bow Tie	Double Swept LE	Rectangle
Variation x_{AC}	–	○	○	●	◒
Bending Moment / Friction	●	◒	–	○	–
Supersonic Drag	●	◒	◒	○	–
RCS	●	◒	●	○	–
Span Constraint	–	◒	●	◒	●
Stability & Control	○	●	◒	●	○
Aeroelastic Stab.	●	◒	–	◒	○

λ = Taper ratio = c_T / c_R
A = Aspect ratio = $b^2 / S = 2b / [(1+\lambda) c_R]$
y_{CP} = Outboard center-of-pressure = $(b/6)(1+2\lambda)/(1+\lambda)$
c_{MAC} = Mean aerodynamic chord = $(2/3) c_R (1+\lambda+\lambda^2)/(1+\lambda)$

Note: ● Superior ◒ Good ○ Average – Poor
Based on equal surface area and equal span.
Surface area often has more impact than geometry.

Fig. 2.25 Examples of wing, tail, and canard panel geometry alternatives.

low variation in the location of aerodynamic center, the double swept leading edge geometry has superior control effectiveness (especially at subsonic Mach number), good aeroelastic stability, and no major weaknesses in the other design considerations. Standard Missile and HARM are examples of missiles with double delta wings. Both are high-speed missiles that benefit from the reduced static margin shift of a double swept leading edge wing. Examples of missile that have control surfaces with double swept leading edges are Super 530, Standard Missile, Crotale, AIM-91, Magic, and U-Darter. All are high speed missiles that benefit from the reduced HM and lighter weight actuators of a double swept leading edge. Another example of a relatively new aeromechanics technology is the bow tie geometry, with a forward swept leading edge and an aft swept trailing edge. This is beneficial for missiles that require low radar cross section (RCS) or have small span requirements for aircraft compatibility. The smaller span also provides a smaller roll moment of inertia, allowing higher roll acceleration. A bow tie surface has low RCS because of the combination of the wing sweep and the attenuation of backscatter bouncing off the adjacent body. In addition to a low RCS and a smaller span requirement, the bow tie geometry has low supersonic drag and good control effectiveness. An inherent disadvantage of a bow tie is the increased potential for aeroelastic instability. Composite structure is synergistic with a bow tie surface because the higher stiffness of composites mitigates aeroelastic instability and facilitates aeroelastic tailoring of the wing. Composite material may also be used in radar absorbing structure. Another disadvantage of a bow tie surface is a larger bending moment, which increases shaft friction and requires more actuator torque to maintain bandwidth. The U.S. AGM-129 Advanced Cruise Missile and the Russian AA-10 are examples of missiles with forward swept wings. A third

alternative of a triangular (delta) surface geometry is a candidate if the span can be accommodated within the launch platform span constraint. A delta surface has strengths of low bending moment/less required thickness for structural integrity (which results in lighter weight), low supersonic drag (because of the larger sweep angle), low radar cross section, and high structural stiffness. A disadvantage of delta geometry is a large variation in aerodynamic center. AGM-65 and AIM-54 are examples of missiles with triangular wings. A fourth alternative, a trapezoidal surface with an aft swept leading edge, is often selected for missile wing, canard, and tail surfaces because it has high control effectiveness and does not have any serious weaknesses in the other attributes. Patriot and AIM-9X are examples. Finally, rectangular surfaces have many disadvantages and are used less often, but a superior characteristic of a rectangular surface is that it has the largest surface area that can be accommodated within launch platform chord and span constraints. A rectangular planform also has a small shift in aerodynamic center because of the relatively small required chord. The AGM-130, AGM-65, and AIM-54 are examples of missiles with rectangular tails.

The surface planform geometry parameters shown in the figure include taper ratio, aspect ratio, outboard location of the center of pressure, and the mean aerodynamic chord. The planform geometry is based on two panels joined at the root chord. Taper ratio is the ratio of the tip chord to the root chord ($\lambda = C_T/C_R$). Aspect ratio is defined as the square of the surface span divided by the surface area ($A = b^2/S$). For a conventional planform with straight leading and trailing edges,

$$A = 2b/[(1 + \lambda)C_R] \tag{2.48}$$

The outboard location of the mean aerodynamic chord, or center-of-pressure location, of a straight leading/trailing edge planform is given by

$$y_{CP} = (b/6)(1 + 2\lambda)/(1 + \lambda) \tag{2.49}$$

Note from the equation for y_{CP} that $\lambda = 0$ (delta wing) provides the benefit of a small value of the lateral center of pressure ($y_{CP} = b/6$), resulting in lower bending moment, while $\lambda = 1$ (rectangular wing) gives the adverse effect of a larger value of the lateral center-of-pressure location ($y_{CP} = \mathrm{b}/4$) and a larger bending moment.

The equation for the length of the mean aerodynamic chord of a trapezoidal planform is

$$C_{MAC} = (2/3)C_R(1 + \lambda + \lambda^2)/(1 + \lambda) \tag{2.50}$$

The aerodynamic center, which is the same as the center of pressure for a surface with a symmetrical noncambered cross section, is located on the mean aerodynamic chord.

Surface area usually has a greater impact on aerodynamic stability, control, and performance than surface geometry. Because missiles are usually span limited, they usually cannot take advantage of high aspect ratio geometry.

Wing, stabilizer, and control surface integration alternatives are shown in Fig. 2.26 for a number of surfaces (two to eight), folding arrangements (folded, wraparound, extended), control surface deflection (balanced actuation control, flap control), and tandem surface orientation (interdigitated, inline).

At least three tail surfaces are required for static stability. An example of a missile with three tails is the AGM-69 SRAM missile. For most missiles, the wings, tails, and canards are comprised of four surfaces (cruciform). This works best with skid-to-turn maneuvering. For bank-to-turn maneuvering missiles, two wing surfaces are usually used, with at least three tail surfaces. If a missile has more than four tail surfaces, the reasons are often either a span limit imposed by the launch platform or an attempt to reduce the rolling moment from vortices. A high angle of attack missile may have six or more tail surfaces that are uncoupled from the airframe and are on bearings that are free to roll. The free-to-roll tails provide the required static stability, but with low induced roll.

Surfaces may be folded to reduce the span requirement for compressed carriage with the launch platform. A folded surface usually has either a ballistic actuator or a spring that deploys the surface after separation from the launch platform. An example of a missile with folded tail surfaces is the AGM-86 cruise missile. Another approach to compressed carriage is wraparound surfaces. These are particularly suited for tube launch. A third approach is surfaces that are extended laterally after launch, such as switchblade wings and diamondback wings. The BGM-109 Tomahawk cruise missile has a switchblade wing. Enhanced range JDAM has a diamondback wing. Finally, reduced span surfaces provide compressed carriage. An example is compressed carriage AMRAAM.

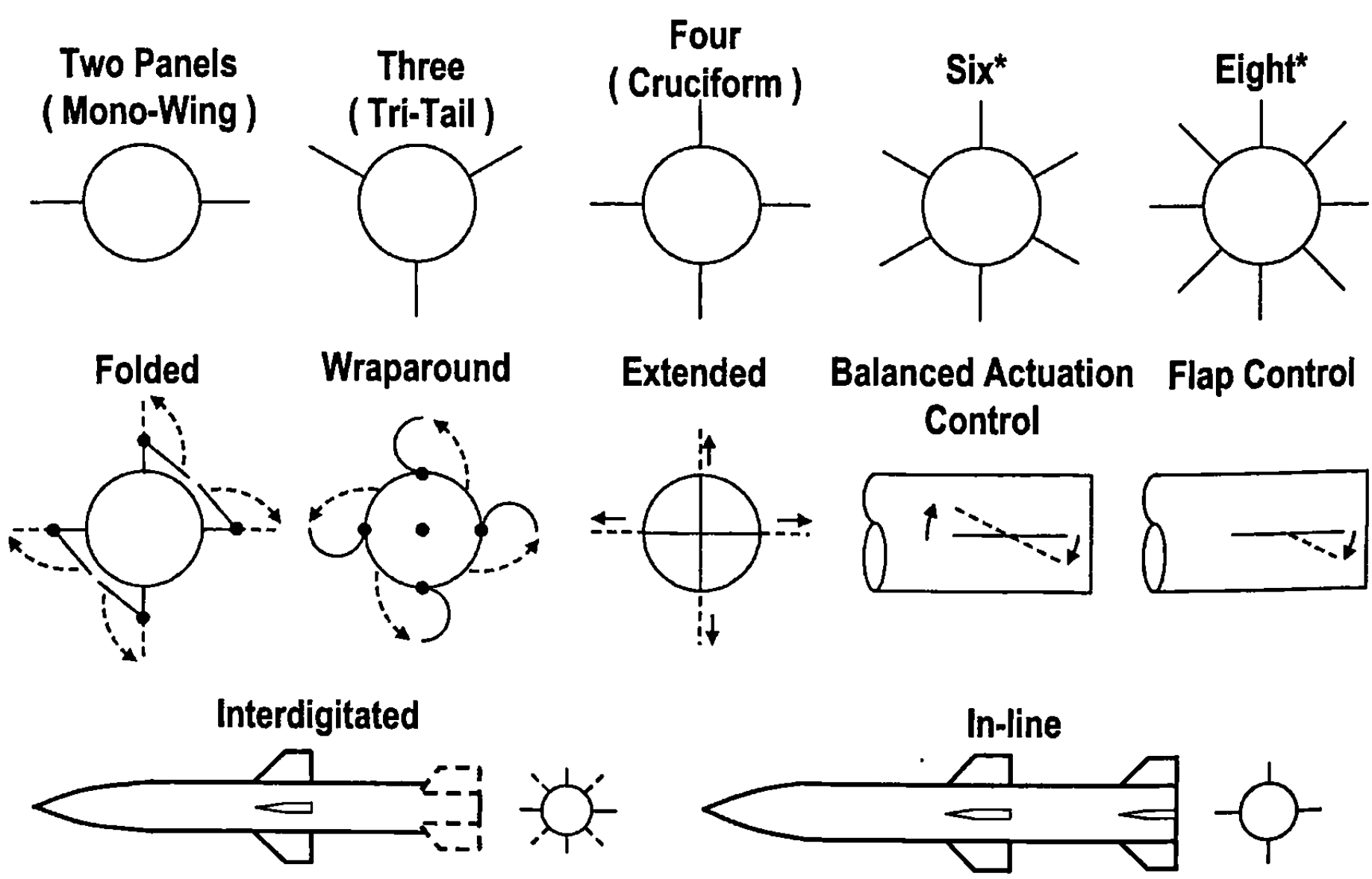

Fig. 2.26 Examples of surface arrangement and aerodynamic control alternatives.

Alternatives for the location of the hinge line/control shaft of flight control actuators are either near the aerodynamic center of the surface (balanced actuation control) or near the trailing edge of the surface (flap control). Balanced actuation control, using an all movable surface, has advantages of lower HM and lower drag. Flap control has advantages of a stable HM and generally has a lower radar cross section.

Tandem surfaces include canard-tail and wing-tail planforms. Alternative orientation arrangements of the surfaces are either inline or interdigitated. Interdigitated surfaces may have advantages of less induced roll ($C_{l\phi}$) and launch platform compatibility. However, inline surfaces are usually preferred because of lower drag and RCS.

2.15 Flight Control Alternatives

Most missiles use four aerodynamic control surfaces to provide combined integrated control of all three axes (pitch/yaw/roll). However, a few missiles use only two control surfaces to fly with combined two-axis control (either pitch/yaw or pitch/roll) and a few missiles use more than four control surfaces to fly with independent, dedicated control of each axis. Other missiles have combined control of the pitch/yaw axes with independent roll control. Figure 2.27 is a comparison of the control integration approaches. Advantages of missiles that use only two-axis control (pitch/yaw, pitch/roll) are lower cost of the flight control actuators (only two actuators required) and ease of packaging only two actuators. Stinger is a free-to-roll missile with two

Control Integ	Control Surfaces	Example	Control Effect	Cost	Packaging
♦Pitch / Yaw	2	Stinger FIM-92	–	●	●
♦ Pitch / Roll	2	ALCM AGM-86	–	●	●
♦Pitch / Yaw / Roll	3	SRAM	–	◒	◒
♦Pitch / Yaw / Roll	4	Adder AA-12	○	○	○
♦Pitch + Yaw + Roll	5	Kitchen AS-4	●	–	–
♦Pitch / Yaw + Roll	6	Derby / R-Darter	◒	–	–

Note: ● Superior ◒ Good ○ Average – Poor

Fig. 2.27 Most missiles use four control surfaces with combined pitch/yaw/roll control integration.

control surfaces for combined pitch/yaw control, but no control of the roll axis. The ALCM cruise missile is a bank-to-turn missile with combined pitch/roll control, but no control of the yaw axis. A disadvantage of two-axis control is that it does not provide precision maneuvering. Combined three-axis control requires at least three or four surfaces. The control effectiveness is typically less for a missile with three control surfaces. Another disadvantage of a combined control missile with three control surfaces, such as SRAM, is a larger induced rolling moment. Also, it is more difficult to design an efficient autopilot. Another potential approach, to use independent control surfaces for each axis, is uncommon for a missile. In this case, the missile flight control is similar to an aircraft. The Russian Kitchen AS-4, which has five control surfaces (two for pitch, two for roll, one for yaw) is an example of independent axis control. Although independent axis control has high control effectiveness and a relatively simple autopilot, it is more expensive because of the larger number of actuators, and it requires more volume for the actuators. Another example of flight control integration that is most appropriate for high angle of attack, highly maneuverable missiles, is the approach used by R-Darter. It has six control surfaces (four surfaces for combined pitch/yaw control plus two surfaces for dedicated roll control). Because vortex shedding and induced roll are problems for high angle of attack missiles, dedicated roll control provides more roll control effectiveness at high angle of attack.

Exo-atmospheric interceptors such as SM-3 and THAAD have dedicated control for each axis. Four divert thrusters (up, down, left, right) provide direct forces to change the flight trajectory, while eight attitude control thrusters [pitch up, pitch down, yaw right, yaw left, roll clockwise (two thrusters), roll counterclockwise (two thrusters)] provide independent stabilization in the three axes.

The types of flight control (tail, canard, wing, thrust vector/reaction jet control) and the alternative approaches for design and integration with fixed surfaces are shown in Fig. 2.28. For tail control, the control surface design alternatives include the number of tails (usually four) and the launch platform integration (no compressed carriage, folded, wraparound, extended). A tail control missile may also have forward surfaces (fixed wings, strakes, canards). The forward fixed surfaces may be either inline or interdigitated with the tail controls. The forward surfaces of a tail control missile may consist of two surfaces (usually used with bank-to-turn maneuvering), three surfaces (usually used with a tri-tail), or four (cruciform) surfaces.

For canard control, there are similar control alternatives. Canard control has an additional design alternative of two control surfaces for a rolling airframe missile. Using only two control surfaces reduces cost and subsystem volume. Examples of missiles with two control surfaces are the 5-in-diameter Rolling Airframe Missile (RAM) and the 2.75-in-diameter Stinger missile. The number of tail surfaces for a canard control missile may be tri-tail (three), cruciform (four), or more (six, eight) surfaces. The missile may have free-to-roll tails to minimize the rolling moment at high angle of attack. An example of a highly maneuverable canard control missile with free-to-roll tails is the Python 4.

Wing control requires three or more tail surfaces for static stability, similar to canard control. Although a wing control could have fixed forward surfaces

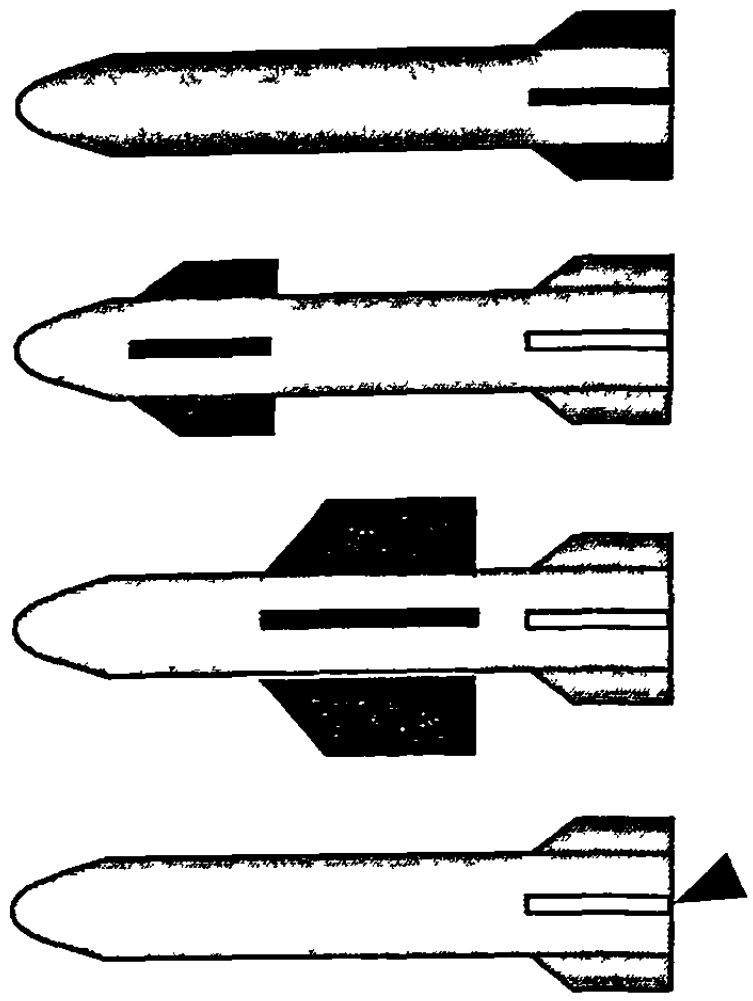

Control	Control Design Alternatives	Fixed Surface Alternatives
Tail	Cruciform (4) Tri-tail (3) Not Compressed Folded Wraparound Switchblade	Wingless Wing Strake / Canard In Line with Controls Interdigitated with Controls Number (2, 3, 4)
Canard	Above Rolling Airframe (2)	Tail (3, 4, 6, 8) Tail + Wing In Line with Controls Interdigitated with Controls
Wing	Above	Tail (3, 4, 6, 8) Strake / Canard & Tail In Line with Controls Interdigitated with Controls
TVC or Reaction Jet Control	Movable Nozzle Jet Tab Jet Vane Axial Plate Secondary Injection Normal Jet / JI Spanwise Jet / JI	Tail (3, 4, 6, 8) Tail + Canard / Strake Tail + Wing

Fig. 2.28 There are many flight control alternatives.

(canards/strakes), it has not been used because of problems at high angle of attack from vortex shedding.

Finally, unconventional flight control includes TVC and jet interaction/ reaction jet control. There are a number of approaches to unconventional flight control, with considerations including performance, cost, weight, packaging, and the capability for roll control. Thrust vector/reaction jet control is used when aerodynamic control has either insufficient control effectiveness or an excessive response time. Unconventional flight control is usually augmented by aerodynamic control for flight at higher dynamic pressure and long duration. Fixed surfaces used with thrust vector/reaction jet control include tails (three or more), tails plus canards/strakes, and tails plus wings.

Advantages and disadvantages of tail control are illustrated in Fig. 2.29. Typical advantages of tail control include an efficient packaging of the subsystems around a blast tube, a low HM and a low actuator torque because of the small local angle of attack, low induced rolling moment because the vortices shed by tail deflection trail behind the missile, and good efficiency at high angle of attack. Note from the figure that for a statically stable tail control missile, the control surface deflection to trim the missile reduces the local angle of attack at the control surface. A disadvantage of tail control is decreased normal force and lift for a statically stable missile because of the negative incremental normal force/lift from the control surface deflection. As shown in the figure, for a statically stable tail control missile, the control deflection force is opposite that of the force on the body. Conversely, for a statically unstable missile, the control deflection force adds to the force on the body.

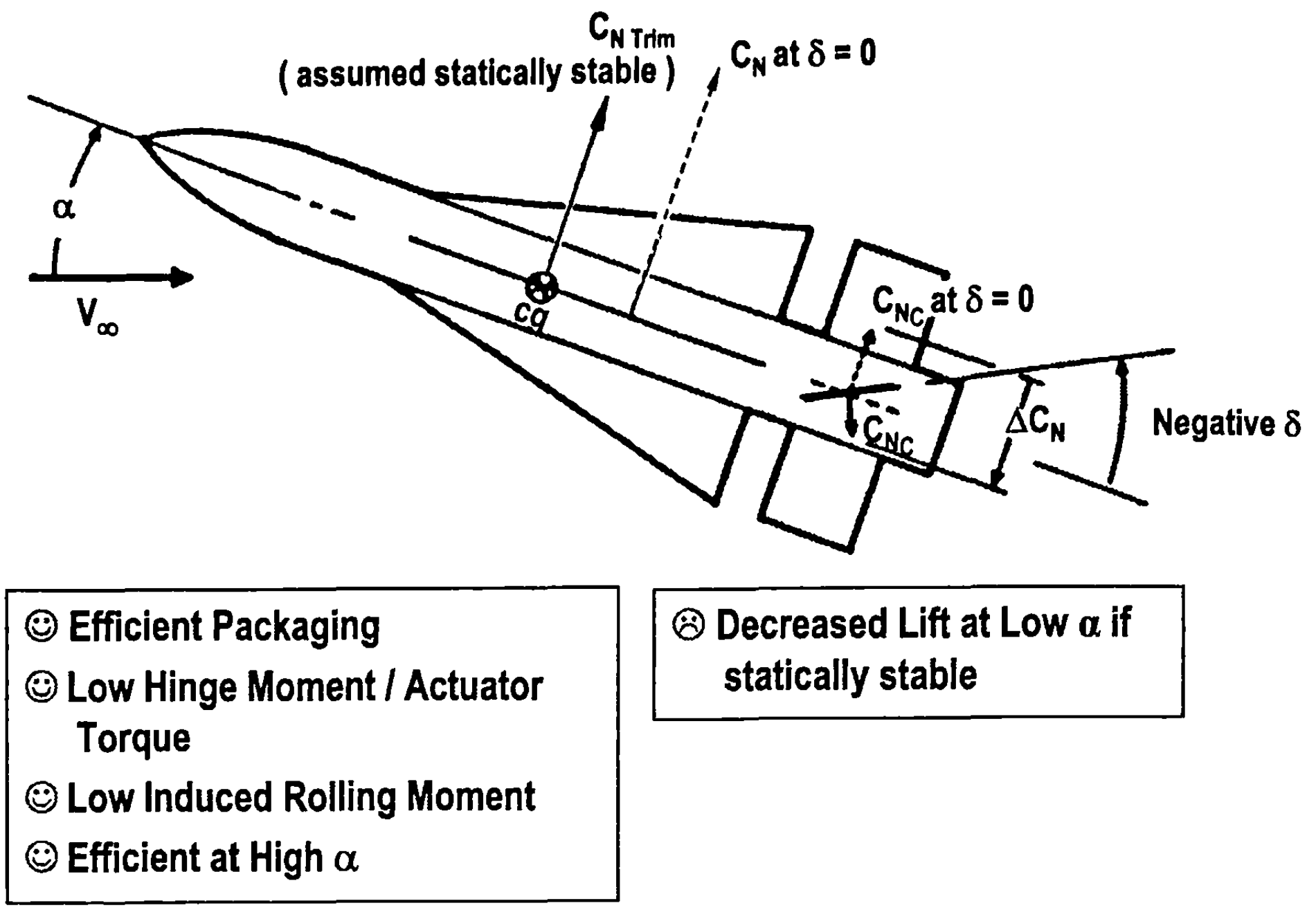

Fig. 2.29 Tail control is efficient at high angle of attack.

For a statically stable missile, tail control is usually more effective than conventional canard control at high angle of attack. As shown in Fig. 2.30, the deflection of the tail to trim the missile reduces the local angle of attack at the tail. As a result the tail can be deflected to a high deflection angle without stall. In the case of conventional canard control, the deflection of the canard to trim the missile increases the local angle of attack at the canard. The canard can be deflected only to relatively small angles before stalling. Also, the vortices shed by the canard can interact with the tail, resulting in a loss of roll control and large induced roll.

Note that a fixed forward surface in front of the movable canard (such as the split canards of Python 4) alleviates the problems of stall, loss of roll control, and induced roll at high angle of attack. Also, free-to-roll tails (such as the free-to-roll tails of Python 4) alleviate the problems of loss of roll control and induced roll at high angle of attack. The Python 4 free-to-roll tails are mounted on roll bearings that are decoupled from the airframe. Another approach to improve roll control effectiveness at high angle of attack is dedicated roll control surfaces, such as the Derby and R-Darter missiles. Dedicated roll control surfaces avoid the problem of control surface deflection saturation and simplify the autopilot design. Finally, a statically unstable missile alleviates the problem of canard stall. The required deflection of the canard for trim is opposite the angle of attack, reducing the local angle of attack at the canard.

About 70% of tail control missiles have low aspect ratio wings. Wings can provide greater aerodynamic efficiency (L/D) and higher maneuverability. Shown in Fig. 2.31 are examples of 24 subsonic and supersonic missiles that

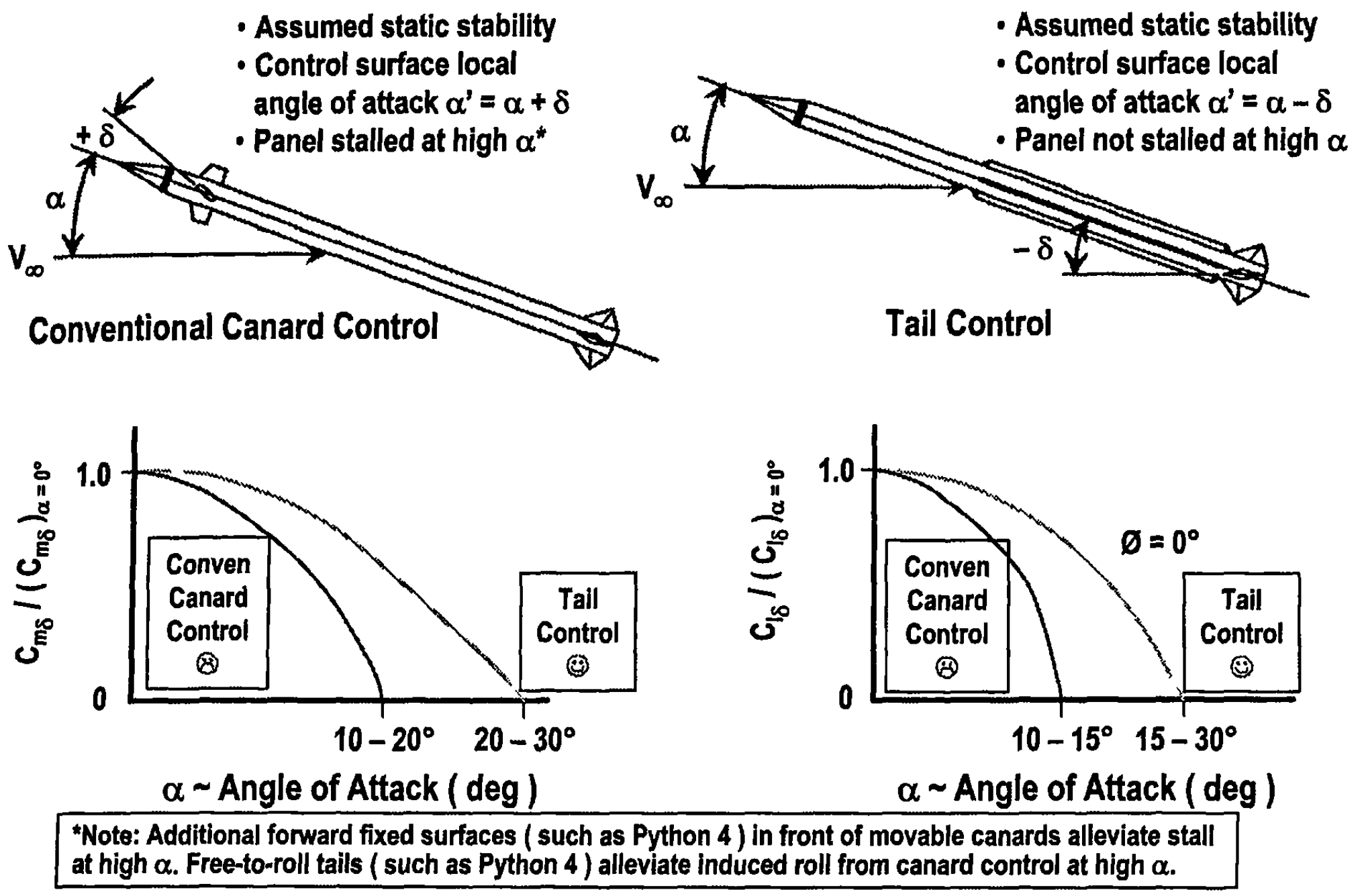

Fig. 2.30 Tail control is more effective than conventional canard control at high angle of attack.

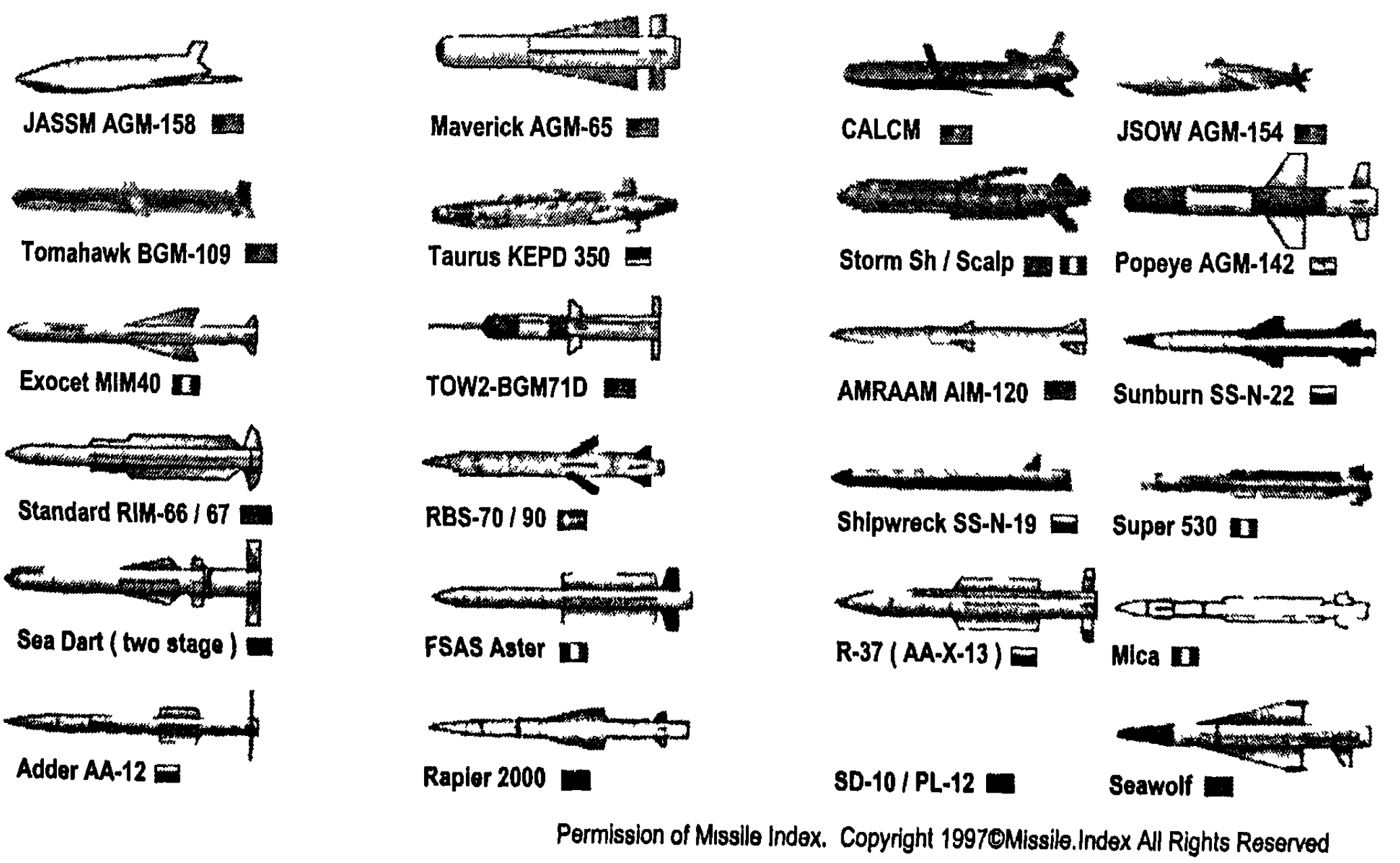

Permission of Missile Index. Copyright 1997©Missile.Index All Rights Reserved

Fig. 2.31 About 70% of tail control missiles also have wings. Figure also in color section.

have wings and use tail control. The first 10 missiles are subsonic missiles. Subsonic missiles with wings, such as cruise missiles, generally have higher wing aspect ratio. The remaining 14 missiles in the figure are supersonic missiles. For supersonic missiles, the wing aspect ratio is generally less than 2.

An example of a new aeromechanics technology is lattice tail control. Lattice fins have advantages of lower HM and higher control effectiveness. Figure 2.32 shows a comparison of lattice tail control with two conventional approaches to tail control, balanced actuation fin and flap control. Except for RCS, lattice tail control has good-to-superior performance. RCS is particularly high when there is a resonance of a lattice dimension with the radar wavelength. For example, a lattice with individual compartments of 1 × 1×1 in will have high RCS if it is illuminated by an X-band (10 GHz frequency or 1-in wavelength) radar. Also shown in the figure are examples of missiles with the tail control alternatives of lattice tail control (Adder AA-12/R-77), conventional balanced actuation fin control (ASRAAM AIM-132), and flap tail control (Hellfire AGM-114). The vertical arrangement of surfaces and the smaller chord length of lattice control result in greater control effectiveness and less variation in the location of the center of pressure of the tail, leading to a lower HM.

Lattice fins, such as the fins shown in the top right section of Fig. 2.33, are most appropriate for either subsonic or high supersonic missiles. The bottom right section of the figure shows the flow through the lattice at a subsonic, transonic, a low supersonic, and a high supersonic Mach number. At subsonic Mach number the drag of lattice fins is comparable to that of traditional fins. At transonic Mach number, lattice fins have higher drag and lower control

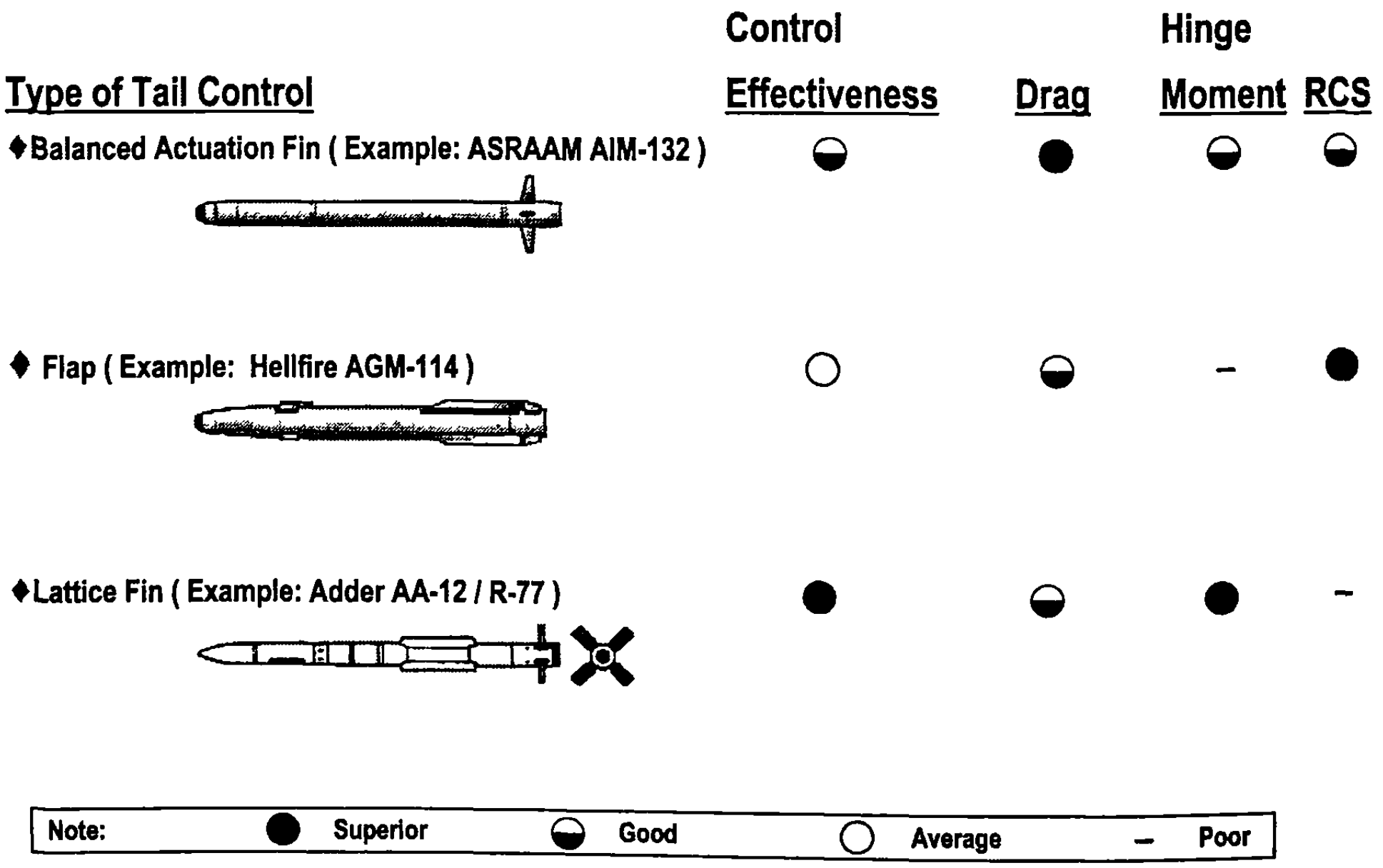

Fig. 2.32 Tail control alternatives: conventional balanced actuation fin, flap, and lattice fin.

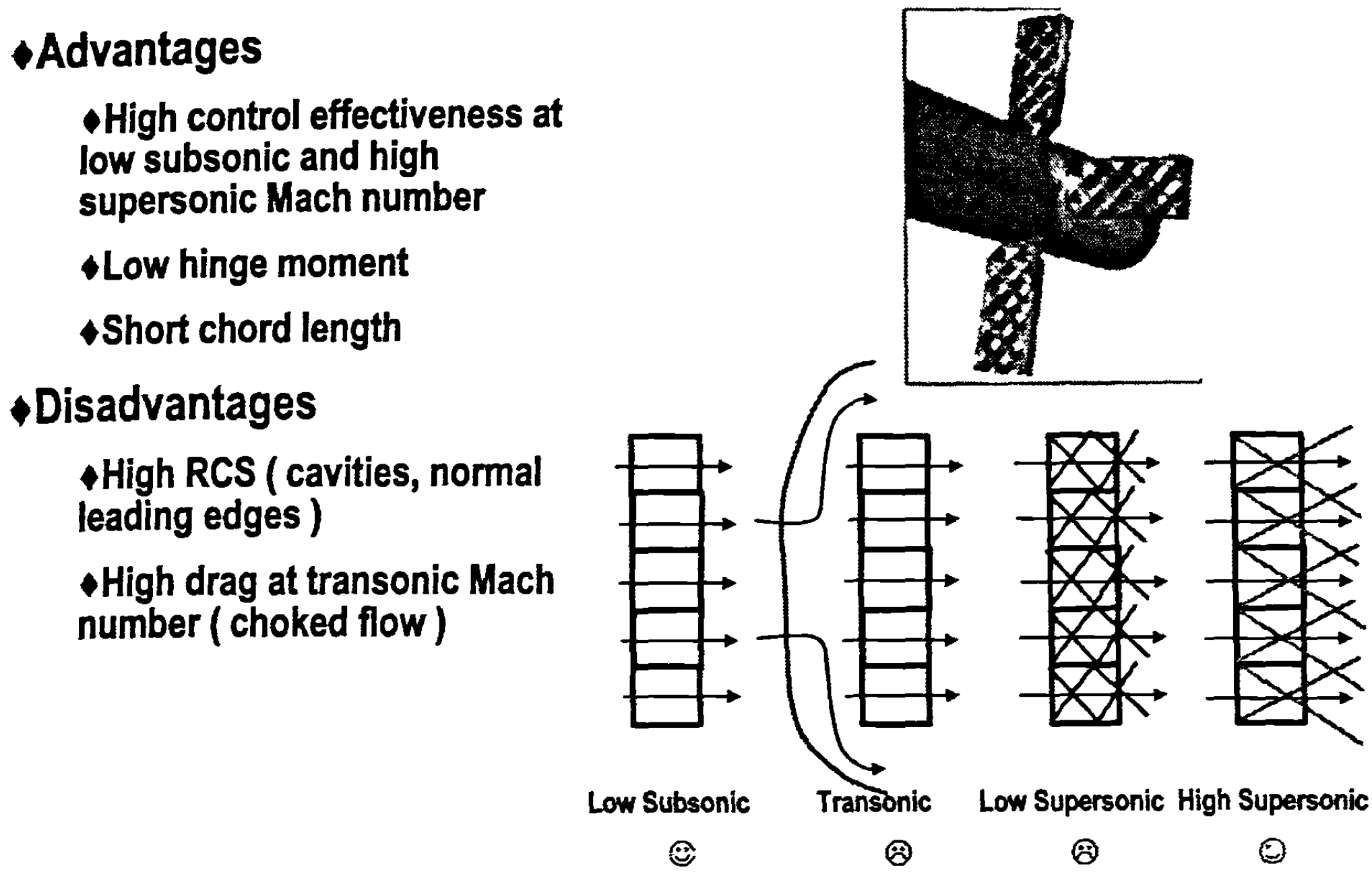

Fig. 2.33 Lattice fins have advantages for low subsonic and high supersonic missiles. Figure also in color section.

effectiveness than traditional fins. At a low transonic freestream Mach number less than 1, the local flow through the lattice can accelerate to Mach 1 because of the thickness of the surface and the thickness of the boundary layer. For a transonic freestream Mach number slightly greater than 1, the flow through the lattice remains choked. A detached, normal shock wave in front of the lattice spills excess air flow around the lattice. The lattice remains choked until the Mach number is sufficiently high to allow the lattice to swallow the shock. An oblique shock is then formed on each leading edge of the surfaces of the lattice. At low supersonic Mach number the oblique shock angle of each leading edge is large, and the oblique shocks are reflected downstream off the lattice surfaces. The large number of reflected shocks results in a relatively high drag. At higher Mach number the oblique shock angle of each leading edge is smaller, passing through the lattice without intersecting a lattice surface, resulting in low drag. The leading edge angles of the lattice can be small because of the efficiency of the box structure. The small angle and thickness provide low drag.

A disadvantage of lattice fins is high RCS. There are numerous cavities, with dimensions comparable to the threat radar wavelength (e.g., 1 in), providing resonance. Also, the numerous leading edges are not swept, resulting in large backscatter.

In summary, lattice fins have advantages of high control effectiveness, low HM, and short chord length. Their best application is at low subsonic or high supersonic Mach number, where the drag is comparable to conventional fins. A disadvantage of lattice fins is high RCS.

Figure 2.34 shows the advantages and disadvantages of conventional canard control. Advantages of canard control include 1) efficient packaging of the

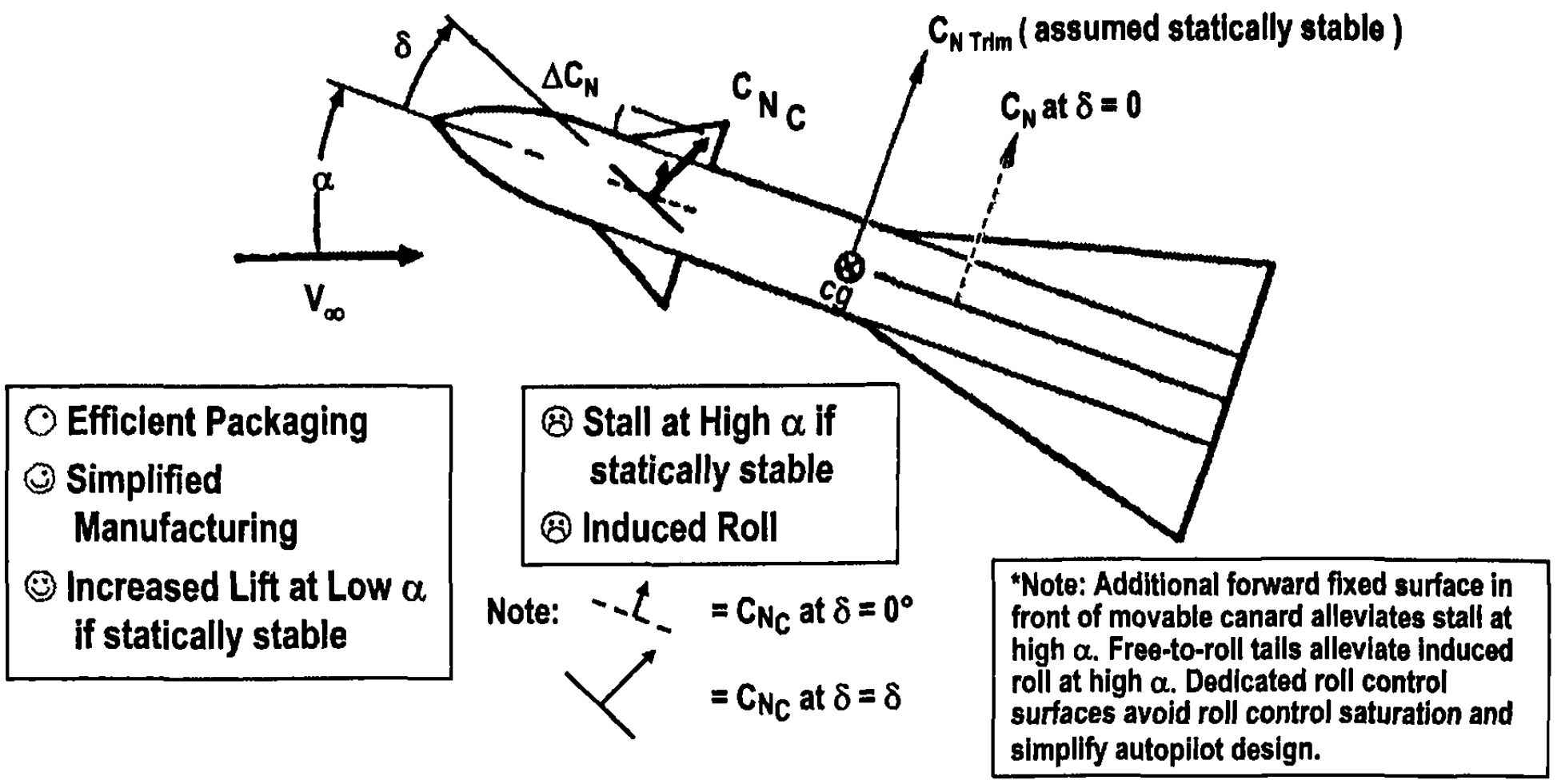

Fig. 2.34 Conventional canard control is efficient at low angle of attack but stalls at high alpha. Figure also in color section.

guidance, navigation, and control subsystems in the same location; 2) simplified manufacturing and ease of integration of the guidance, navigation, and control subsystems; and 3) for a statically stable missile, increased lift at low angle of attack. The figure illustrates the incremental normal force from the canard to trim the missile, providing additional lift. Disadvantages of conventional canard control include 1) a tendency to stall at high angles of attack for a statically stable missile and 2) a large induced roll at high angles of attack. As noted previously, these problems are alleviated by the use of split canards, free-to-roll tails, and dedicated roll control surfaces.

Shown in Fig. 2.35 are examples of operational missiles that have canard control. Canard control missiles do not have wings because the induced rolling moment from the vortex shedding from the canard makes it difficult to integrate a wing. Also, the additional surface area of the canard and the larger tail required for stability usually provide sufficient aerodynamic efficiency (L/D) and maneuverability. Because location of the canard is forward of the center of gravity, the canard is destabilizing, requiring a larger tail for stability. Shown in the figure are 20 operational wingless missiles that use canard control. Fifteen of the 20 missiles are air intercept missiles (SAM or AAM). Sixteen of the 20 missiles, including the Kegler AS-12, are supersonic missiles. Four are subsonic laser-guided bombs (GBU-12, 22, 27, and 28).

A split canard has a smaller local angle of attack, enhancing the maneuverability at high angle of attack. Modern highly maneuverable missiles use split canards for flight control. Split canard control has a fixed surface in front of the movable canard. Shown in Fig. 2.36 is a schematic of the local flow that illustrates the advantage of split canards. The incremental normal force coefficient (ΔC_N) in the figure is the difference between the normal force coefficient of the deflected control surface and the normal force coefficient of an undeflected control surface. Note that the forward surface reduces the local effective angle

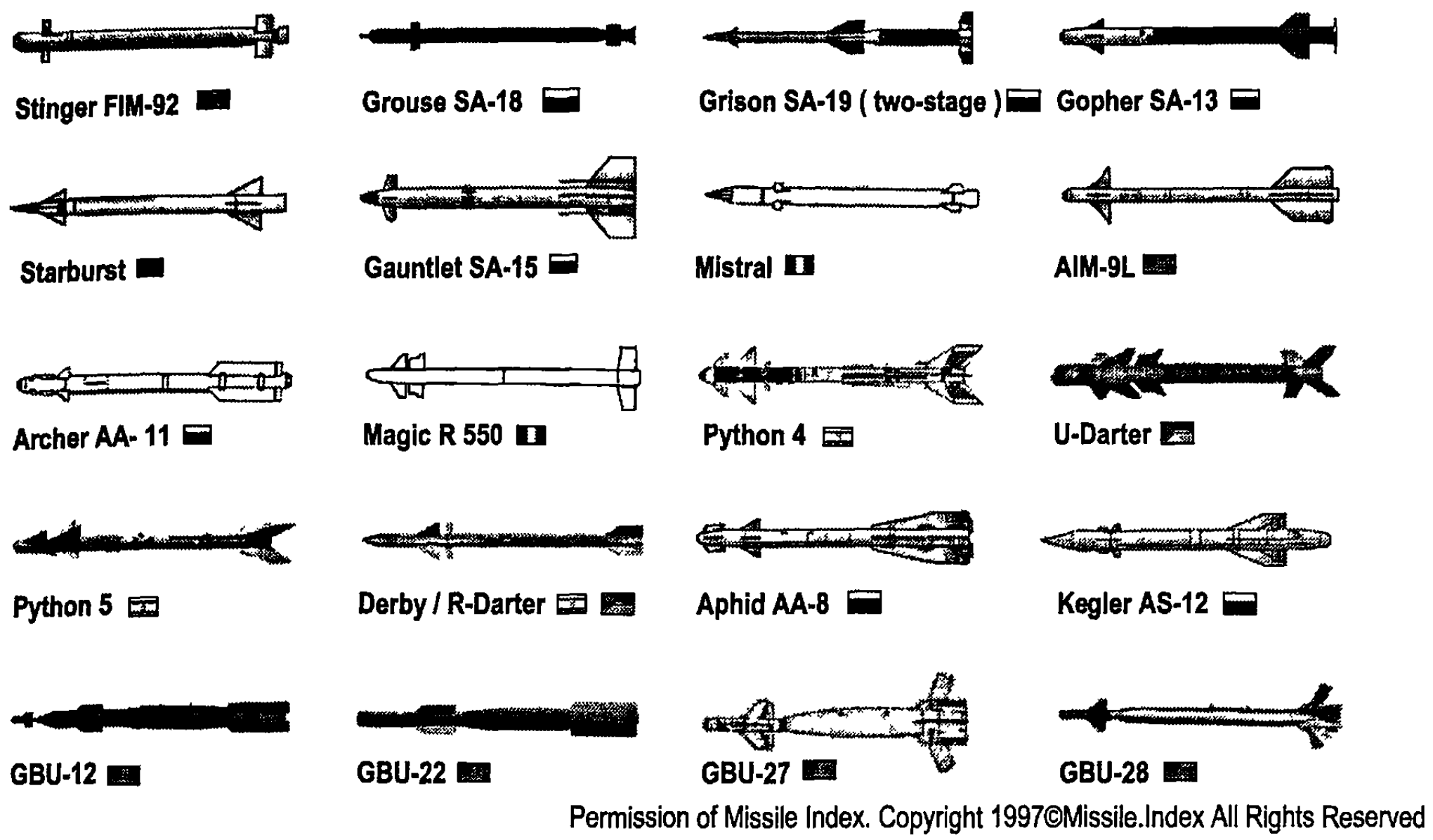

Fig. 2.35 Canard control missiles are wingless and most are supersonic. Figure also in color section.

of attack α'. Because the trailing canard control surface has a smaller local angle of attack, it is more effective at high control surface deflection δ and high angle of attack α, operating without stall. Another benefit of a fixed forward surface is that the location of the vortex shedding is fixed, reducing the uncertainty in the

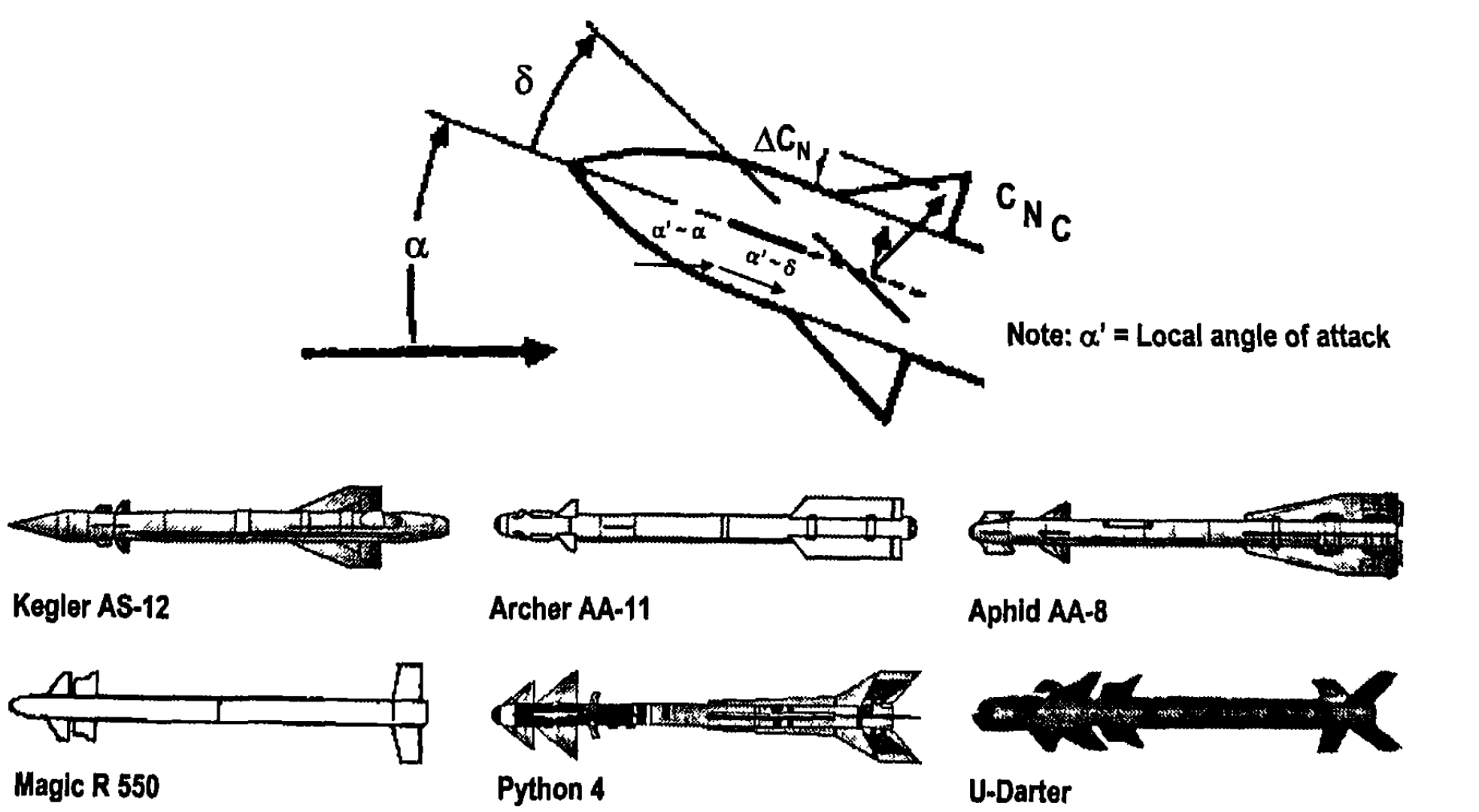

Note: Forward fixed surface reduces local angle of attack for movable canard, providing higher stall angle of attack. Forward surface also provides a fixed, symmetrical location for vortex shedding from the body.

Python 4 also has free-to-roll tails and separate roll control ailerons.

Fig. 2.36 Missiles with split canards have enhanced maneuverability at high angle of attack.

aerodynamics. In addition to a fixed forward surface, some canard control missiles (e.g., AA-11) also have a weather-cocking surface to sense angle of attack. The measured angle of attack is fed into the autopilot to improve the missile maneuverability. Most modern canard control missiles use split canard control, including the Kegler AS-12, Archer AA-11, Aphid AA-8, Magic R-550, Python 4, and U-Darter. In addition to split canards for high angle-of-attack maneuverability, Python 4 has dedicated roll control surfaces and free-to-roll tails for enhanced maneuverability.

Figure 2.37 shows advantages and disadvantages of wing control. The advantages of wing control are few and the disadvantages are many. One advantage of wing control is that only a small body rotation is required to maneuver. This results in smaller seeker tracking error because of the lower dome error slope. A second advantage is fast response for maneuverability, particularly for skid-to-turn maneuvers. As shown in the figure, most of the missile lift is derived from deflecting the wing. Because the wing can usually be deflected faster than body rotation, the time required to achieve maneuver g is shorter.

A major disadvantage of wing control is the limited space available for packaging of the large actuators. For a high-performance missile, the wing may be located over the motor case. Another disadvantage is the larger HM required to deflect the wing. A third disadvantage is that the wing must be larger; it must be sized for maneuverability in addition to aerodynamic efficiency (L/D). A fourth disadvantage is the large induced roll produced by the wing. Finally, a wing-control missile usually has a higher aspect ratio, contributing to a wing stall at a relatively low angle of attack.

The strong vortex shedding for a wing control missile often has adverse effects on missile stability and control. The top right portion of Fig. 2.38 from Ref. 10 illustrates wing and body vortex shedding for a body-wing-tail configuration at

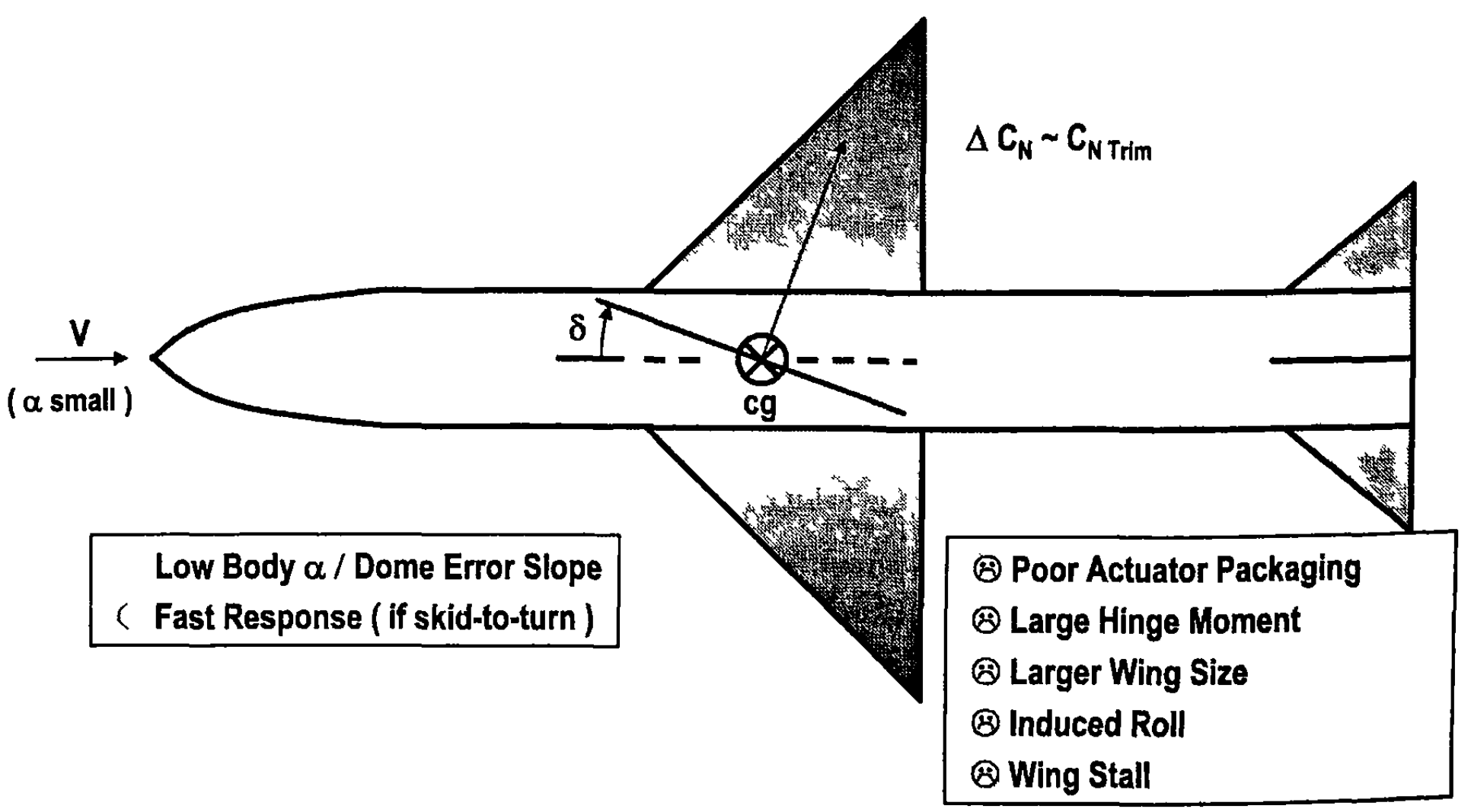

Fig. 2.37 Wing control requires less body rotation but exhibits high hinge moment, induced roll, and wing stall.

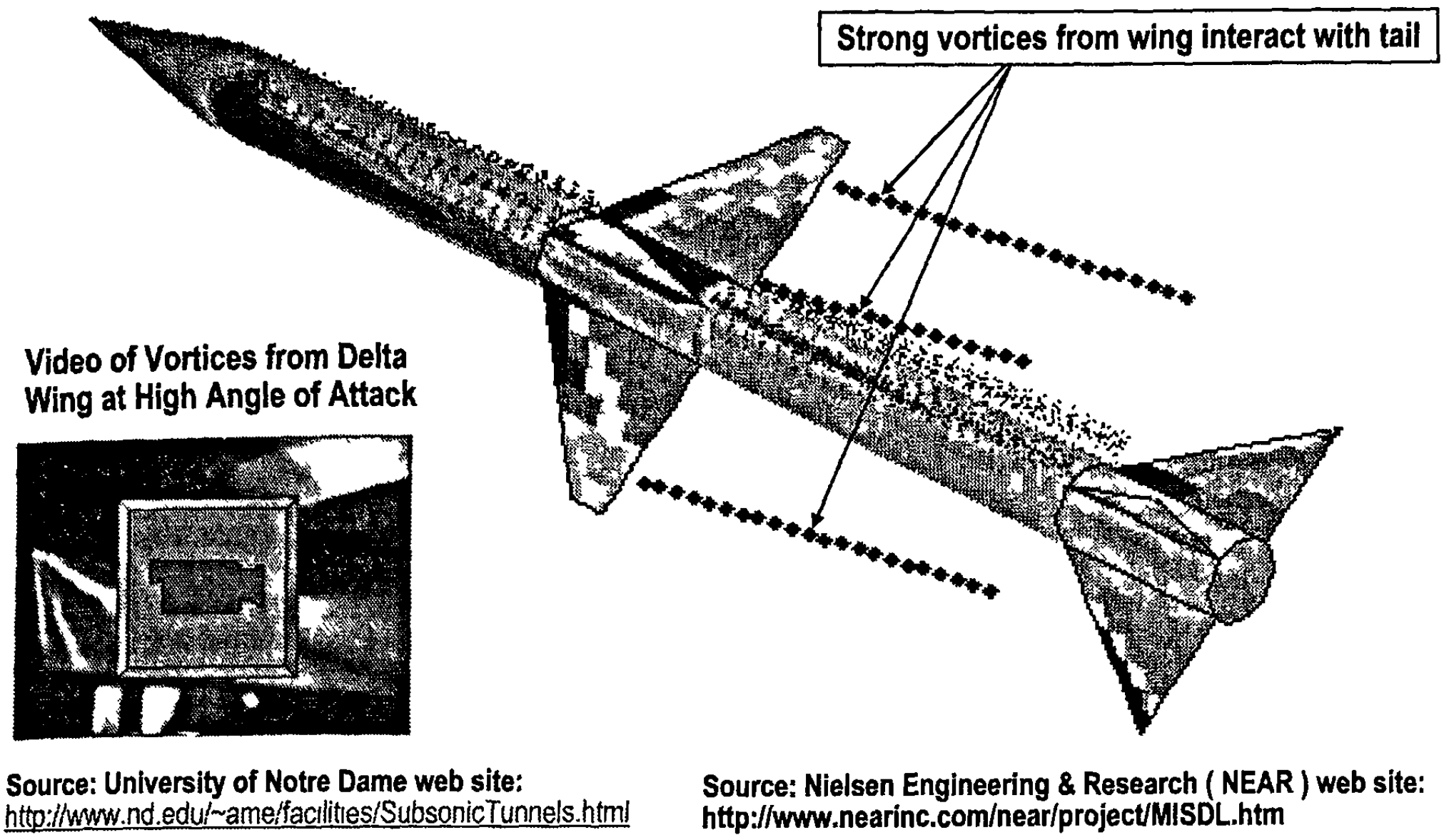

Fig. 2.38 Wing control missile susceptible to high vortex shedding. Figure also in color section. Video is in the CD included with this textbook.

high angle of attack. As shown in the figure, wing vortices are shed near the wing tips, trailing back with the free stream. Body vortices are shed near the nose center of pressure, approximately two-thirds of the length of the nose. At high angles of attack, additional body vortices may be shed from the cylindrical body downstream of the nose. Surfaces aft of the wing, particularly aft surfaces with a span comparable to that of the wing, are susceptible to the strong vortices shed from the wing, and the missile may have large adverse induced roll, a loss in stability, and a loss in control effectiveness. Shown in the bottom left portion of the figure is a wind tunnel video of a highly swept wing pitching over an angle of attack range from 0 to 90 deg. The source of the video was the University of Notre Dame School of Aerospace and Mechanical Engineering. Note that the vortices are relatively weak at low angle of attack. As the angle of attack increases, the vortices increase in strength up to an angle of attack of about 60 deg. For angles of attack greater than about 60 deg, the flow detaches from the leading edge of the wing and there is a wake over the entire rear surface of the wing.

Examples of operational missiles that use wing control are shown in Fig. 2.39. Note that the wings are generally large and located near the center of gravity. The configurations of Skyflash, HARM, and Aspide are similar to that of the Sparrow missile, which was developed in 1956. The AA-10/R-27 Alamo configuration is different from Sparrow. It has a fixed forward strake surface and a "bow tie" forward swept movable wing. The Alamo geometry of a fixed, forward strake may have more predictable vortex shedding at high angle of attack because it tends to fix the location of vortex shedding. Also, the bow tie wing requires less wing span, which enhances the fitment in exterior carriage. The HARM missile wing is somewhat different from the Sparrow wing because of a

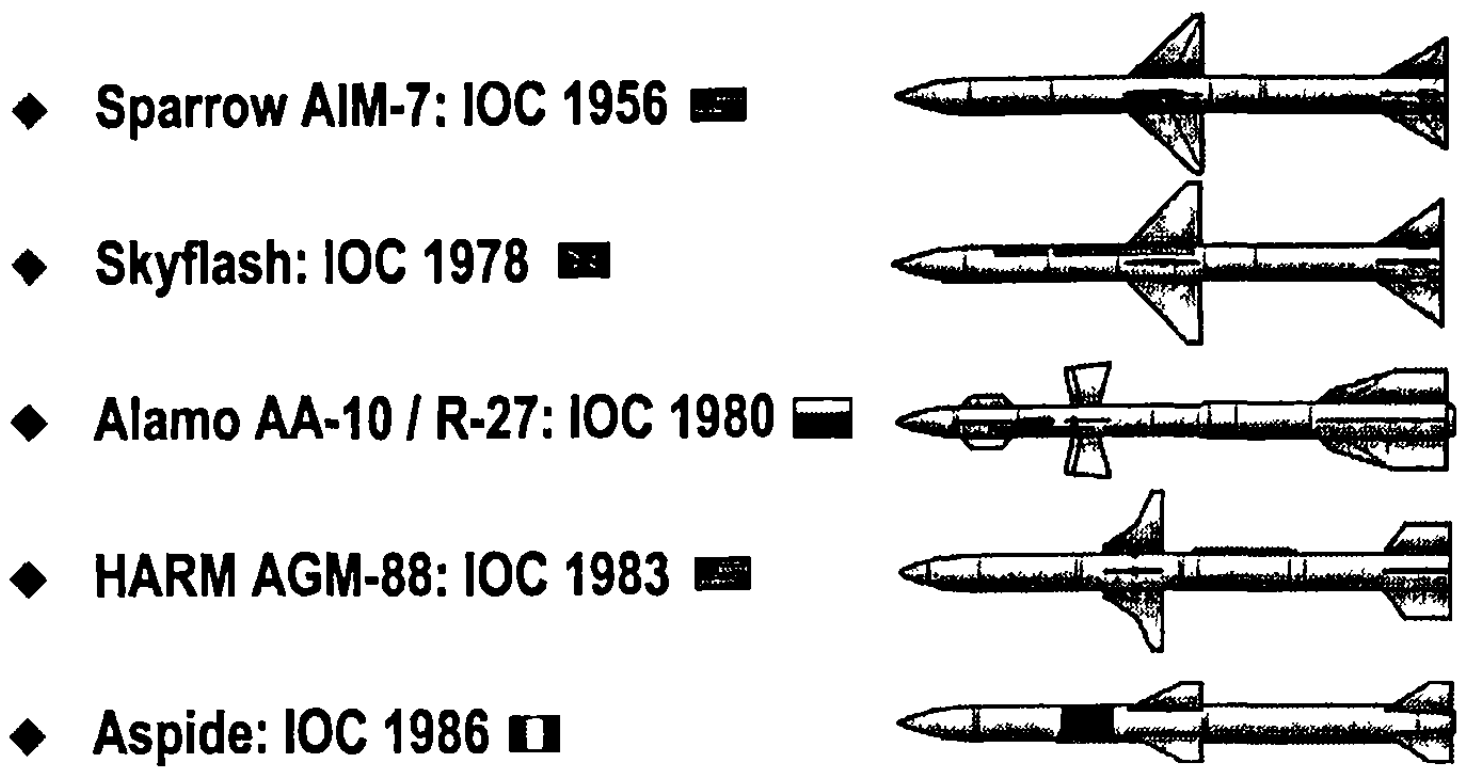

Permission of Missile Index. Copyright 1997©Missile.Index All Rights Reserved

Fig. 2.39 Wing control missiles are old technology. Figure also in color section.

double swept leading edge. The double swept leading edge reduces the variation in aerodynamic center, providing a lower HM.

Because of deficiencies such as actuator packaging, HM, wing size, and angle of attack limitations from wing stall/induced roll, no wing control missile has been developed in recent years. Modern missiles use tail, canard, or unconventional flight control. Although the wing control Sparrow has been largely replaced by the tail control AMRAAM as a preferred medium-range air-to-air missile, the Sparrow was selected as a rocket baseline for this text because of the availability of unclassified data for the Sparrow missile.

TVC and reaction jet control alternatives are illustrated in Fig. 2.40. The figure is a schematic of seven different types of unconventional flight control. It also shows a relative deflection of the thrust for each of the flight control types. Liquid injection TVC uses a fluid such as freon, injected normal to the local stream, which causes a bow shock wave inside the nozzle. Deflection is of the order of +/−7 deg. Another type is hot gas injection TVC, which ducts hot gas products from the motor chamber into the nozzle. The injection of the hot gas into the nozzle causes a bow shock, similar to that of liquid injection TVC. Hot gas injection has high deflection, although there may be problems for the high temperature valves, which must operate with gas products up to 5500° F. A third type is jet vanes, which are control surfaces inside the nozzle. Jet vanes have an advantage in that differential deflection also provides roll control. Jet vanes can also share common actuators with aerodynamic control. However, jet vanes are continually exposed to the rocket exhaust plume, which results in about 3–5% loss in specific impulse even if they are not deflected. Axial plate thrust vector control is a fourth type, consisting of a plate that extends back and forth. When the plate is fully extended, the plume attaches to the plate because of the Coanda effect. A fifth type is jet tabs, which are simple devices that switch in and out of the plume. The jet tab sets up a bow shock inside the nozzle, similar to that of liquid injection TVC. A sixth type of TVC is movable nozzle. Although movable nozzle TVC is often used with

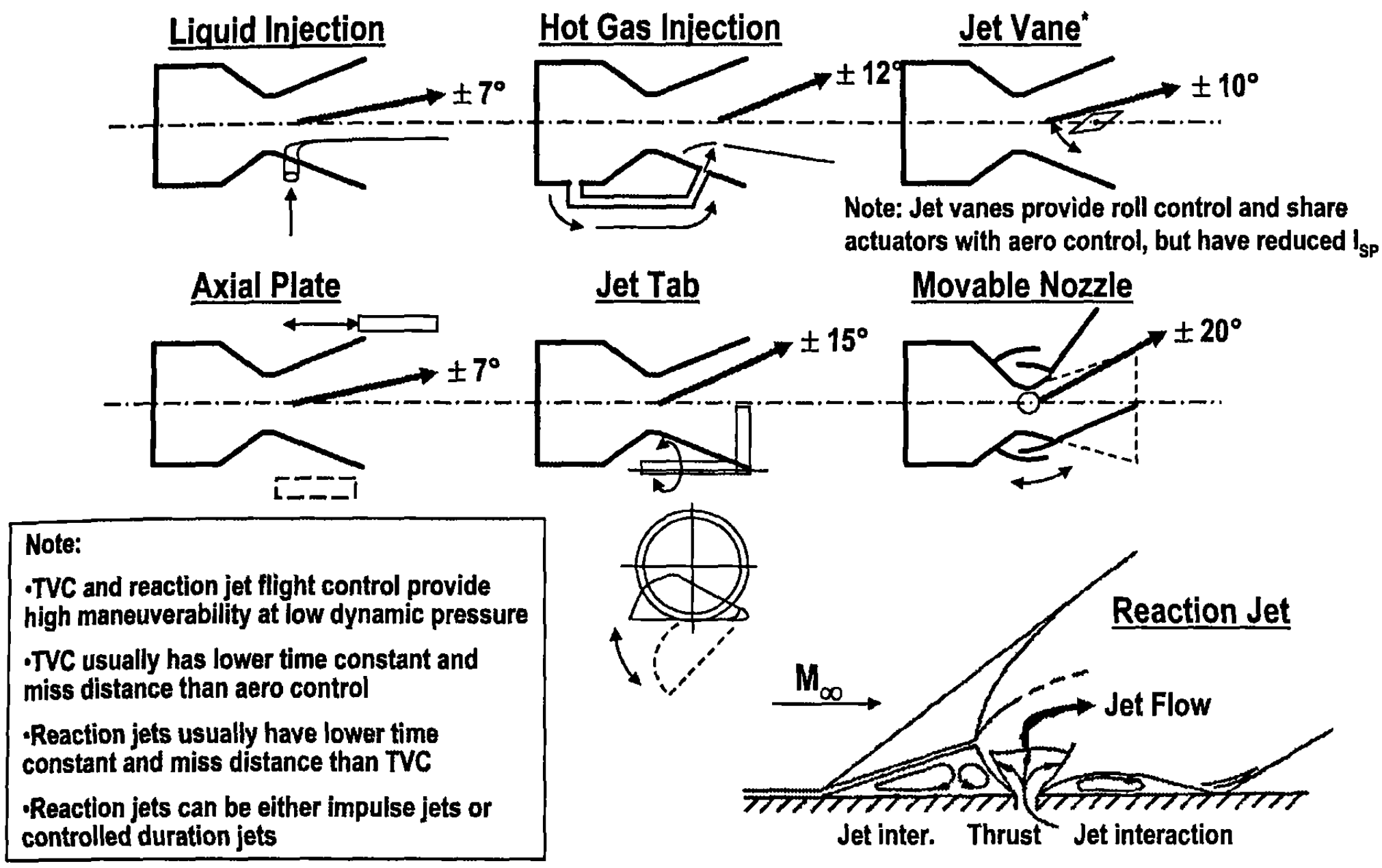

Fig. 2.40 TVC and reaction jet flight control alternatives.

strategic ballistic missiles, its application to tactical missiles, because of its high cost, is primarily limited to expensive, high-performance missiles such as Standard Missile and THAAD. A seventh type of unconventional flight control is reaction jet control. Reaction jet control can be based on either short-duration impulse, "shotgun shell-type" jets similar to PAC-3, or longer duration controlled jets similar to SM-3 or THAAD. During endo-atmospheric flight, reaction jet control interacts with the free stream air. The total force is a combination of the thrust force and the jet interaction force. The jet interaction force results from the pressure distribution on the airframe surface. As illustrated in the figure, the free stream flow separates from the airframe surface because of the obstruction of the jet. This causes a higher local pressure in the separated flow region in front of the nozzle and a lower local pressure in the separated flow region behind the nozzle. Although the jet interaction force usually augments the thrust force, there are relatively high uncertainty and risk in the magnitude of the jet interaction force.

Most unconventional flight control usually provides higher maneuverability and faster response than aerodynamic control. In general, reaction jet control has faster response and smaller miss distance than TVC, enabling hit-to-kill guidance. Unconventional flight control is especially suited for short duration operation to enhance the maneuverability and response of aerodynamic control. Cost, weight, subsystem packaging, risk, and the capability for roll control are design considerations.

Shown in Fig. 2.41 are examples of operational tactical missiles that use either TVC or reaction jets for flight control. Jet vane plus aerodynamic control is the most popular type of TVC. As mentioned previously, jet vanes can provide roll

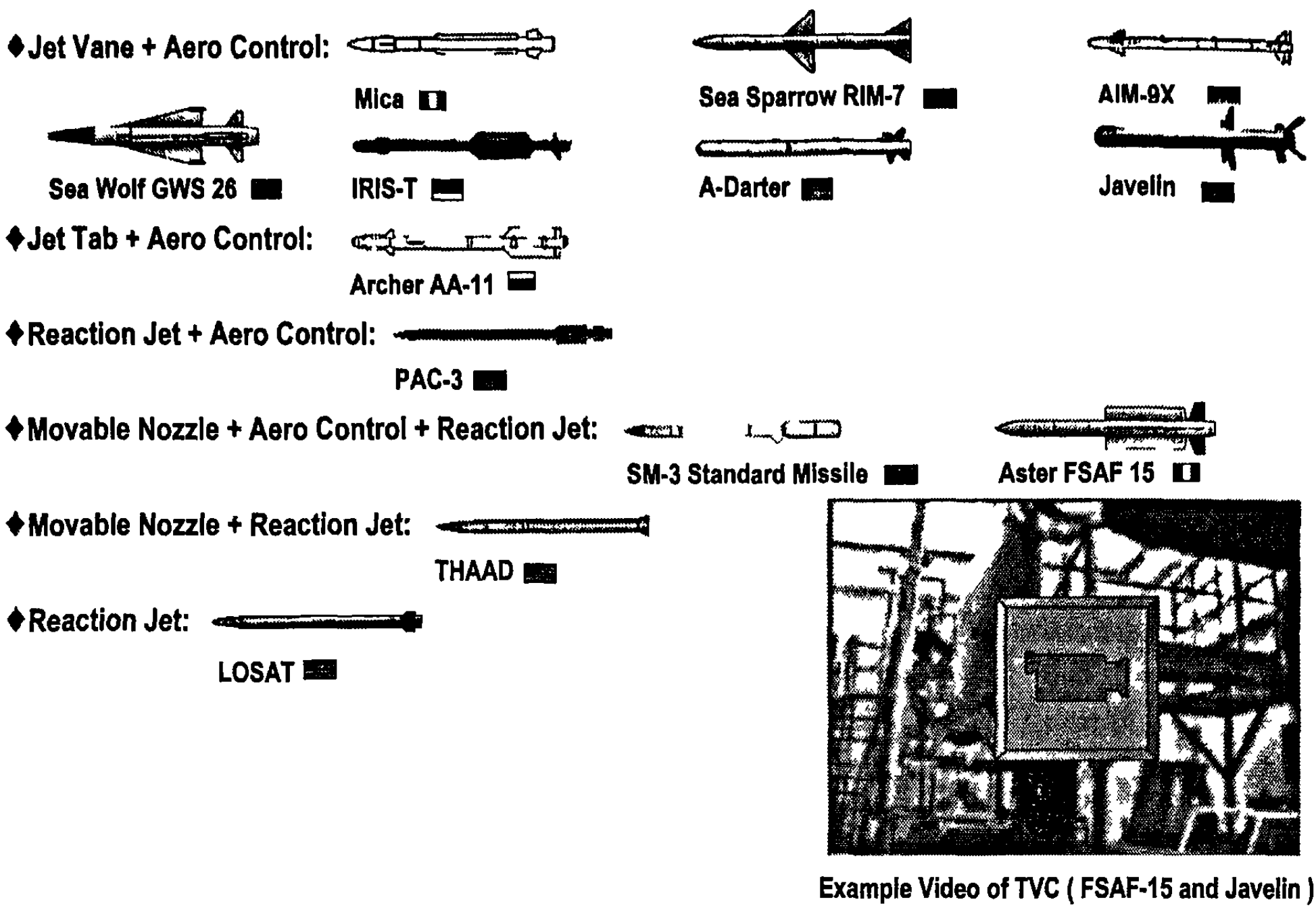

Fig. 2.41 Most tactical missiles with TVC or reaction jet control also use aerodynamic control. Figure also in color section. Video is in the CD included with this textbook.

control and can also share actuators with aerodynamic control. Examples of missiles that use jet vane plus aerodynamic control include the French Mica; the U.S. Sea Sparrow RIM-7, Sidewinder AIM-9X, and Javelin; the U.K. Seawolf GWS 26; the German IRIS-T; and the South African A-Darter. A disadvantage of jet vanes is weight. Because jet vanes operate in the high temperature nozzle plume, they must be constructed from materials with high temperature capability, such as tungsten, molybdenum, or carbon-carbon. For a missile flight control system that consists of combined jet vane plus aerodynamic control, the jet vanes provide the large off-boresight maneuvering that is often required after launch, while aerodynamic control provides the required trim and maneuvering after motor burnout.

An example of a missile that uses jet tab plus aerodynamic control is the Russian Archer AA-11. Jet tabs have advantages of higher pitch/yaw vectoring and lighter weight than jet vanes, but have a disadvantage in that they cannot provide roll control.

An example of missiles that use reaction jet plus aerodynamic control is the U.S. PAC-3 surface-to-air missile defense missile. Reaction jets are usually required for hit-to-kill anti-missile missiles because their smaller time constant ($\sim$ms) is necessary for the smaller required miss distance.

Examples of complex missiles that combine movable nozzle TVC, aerodynamic control, and reaction jet control are the U.S. SM-3 Standard Missile and the French Aster FSAF 15. Movable nozzle TVC is used for launch stabilization

and off-boresight maneuvering following launch. Following launch, aerodynamic control provides midcourse trim and maneuvering. Divert and attitude control thruster reaction jets provide terminal maneuvering during the hit-to-kill intercept.

The last two missiles in the figure are examples of missiles that do not use any aerodynamic control. THAAD has movable nozzle TVC for stabilization and off-boresight maneuverability during launch and midcourse. Similar to SM-3, THAAD uses divert and attitude control thruster reaction jets for the exo-atmospheric hit-to-kill intercept. Shown at the bottom left of the figure is LOSAT. LOSAT uses only reaction jet control to provide the fast response time necessary for hit-to-kill accuracy of the hypersonic missile. The weight of the LOSAT reaction jet control system is relatively low because of the short time of flight.

Shown in the bottom right of the figure is a video of examples of TVC (FSAF-15 and Javelin). FSAF-15 has sophisticated dual TVC nozzles, which allow full axis control (roll control in addition to pitch/yaw control). A mission for FSAF-15 is defense against low-altitude sea-skimming missiles. Because its active radar seeker is not effective at a low grazing angle, FSAF-15 flies a lofted flight trajectory, impacting the target from above. Also shown in the video is a Javelin lofted trajectory flight test against a T-72 tank at 2.5 km range. Javelin has the option of either a lofted trajectory for a top impact or a line-of-sight trajectory for a horizontal impact. Note that the missile has high maneuverability and top impact kill, even at short range.

2.16 Maneuver Alternatives

Figure 2.42 compares missile maneuver alternatives of skid-to-turn maneuvering, bank-to-turn maneuvering, and rolling airframe maneuvering. Bank-to-turn maneuvering is a relatively new technology for tactical missiles. Missiles using bank-to-turn will first roll until the wings (or the major axis of a lifting body) are oriented perpendicular to the target line of sight. Following the roll maneuver, the missile then conducts a pitch maneuver, maintaining the preferred roll orientation. A benefit of bank-to-turn maneuvering is higher maneuverability for a lifting body, which has a noncircular cross section, or for a missile with wings. Another benefit is a smaller sideslip angle for missiles with inlets. Bank-to-turn is particularly suited for midcourse guidance maneuvers prior to seeker lock-on to the target. A disadvantage of bank-to-turn maneuvering is slower response in terminal maneuvers that could degrade guidance accuracy, increasing the missile miss distance. Alternative approaches to alleviate this problem include faster actuators for roll control, faceted or multilens dome to decrease dome error slope, and switching from bank-to-turn maneuvering to skid-to-turn maneuvering for terminal flight. Bank-to-turn missiles often have high greater miss distance because of dome error slope. The seeker looks through a dome with a large variation in radial angle in addition to the variation in off-boresight angle.

Most missiles use skid-to-turn maneuvering. Skid-to-turn is particularly applicable to axisymmetric, cruciform missiles with low aspect ratio surfaces.

- Skid-to-Turn (STT)
  - Advantage: Fast response
  - Features
    - Does not require roll commands from autopilot
    - Works best for axisymmetric cruciform missiles
- Bank-to-Turn (BTT)
  - Advantage: Provides higher maneuverability for planar wing, noncircular / lifting bodies, and airbreathers
  - Disadvantages
    - Time to roll
    - Requires fast roll rate
    - May have higher dome error slope
  - Features
    - Roll attitude commands from autopilot
    - Small sideslip
- Rolling Airframe (RA)
  - Advantage: Requires only two sets of gyros / accelerometers / actuators (packaging for small missile)
  - Disadvantages for aero control
    - Reduced maneuverability for aero control
    - Requires high rate gyros / actuators
    - Requires precision geometry and thrust alignment
  - Features
    - Bias roll rate and roll moment
    - Can use impulse steering (e.g., PAC-3, LOSAT)
    - Compensates for thrust offset

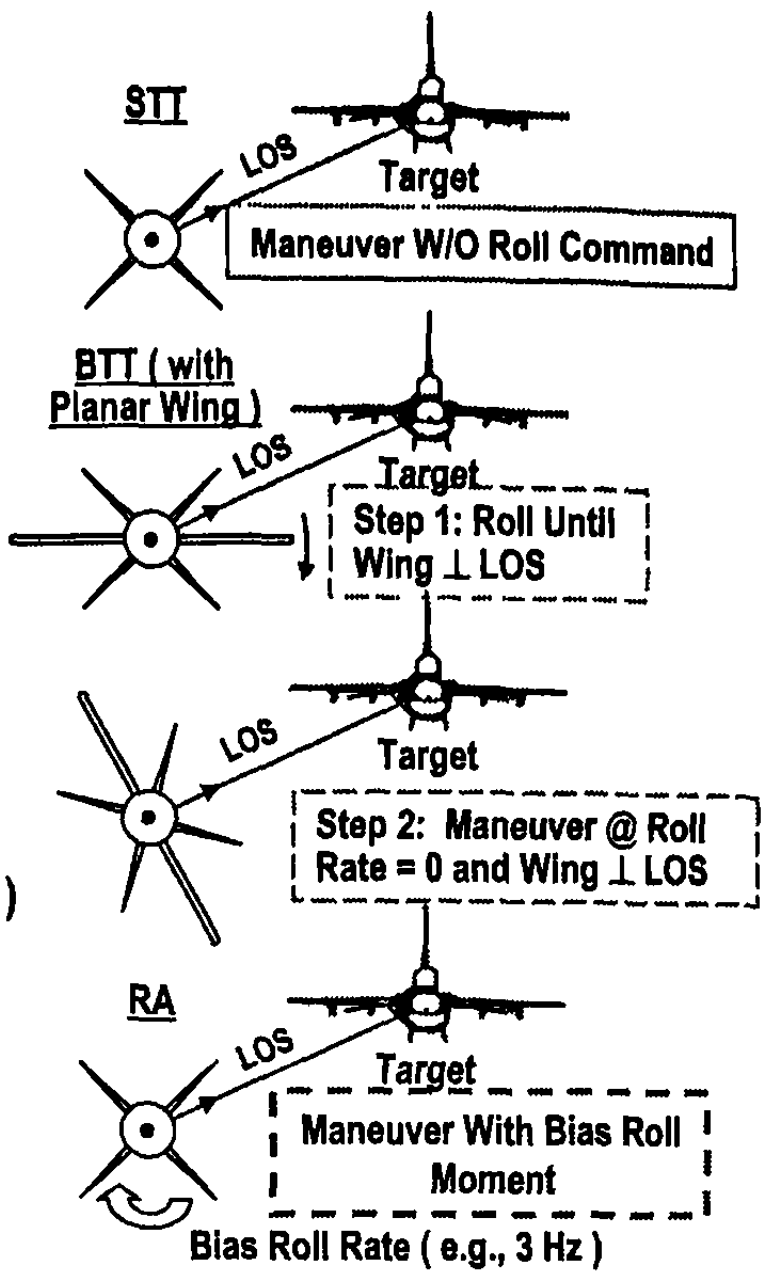

Fig. 2.42 Skid-to-turn is the most common maneuver law.

As shown in the figure, a skid-to-turn maneuver is a commanded maneuver along the line of sight of the seeker, without a roll command. An advantage of skid-to-turn is fast response because the maneuver is immediately made along the line of sight without delay.

A third type of maneuver is a rolling airframe maneuver. Rolling airframe maneuvering is similar to skid-to-turn, except the missile also has a rolling moment bias input to provide a bias roll rate. The rolling moment bias may be provided either by thrust offset, tail incidence, canard incidence, or a combination of approaches. Advantages of rolling airframe missiles include lower cost because of fewer flight control gyros, accelerometers, and actuators; lower volume to package less flight control hardware; compensation for thrust misalignment; and compatibility with reaction jet impulse control. The 5-in-diameter Rolling Airframe Missile (RAM) and the 2.75-in-diameter Stinger missile are examples of small-diameter rolling airframe missiles. RAM and Stinger use two-axis flight control, requiring less flight control hardware packaging within the small diameter. PAC-3 and LOSAT are examples of hypersonic rolling airframe missiles that use impulse reaction jet control. Disadvantages of an aerodynamic controlled rolling airframe include reduced maneuverability from using fewer controls, a requirement for high rate gyros and actuators, and a requirement for precision geometry with precision thrust alignment. The maximum roll rate of a rolling airframe missile is about 3 Hz because most actuators are limited to a maximum rate of about 1000 deg/s. Another potential problem is susceptibility to roll-pitch-yaw cross-coupling instability. Roll-pitch-yaw cross coupling tends to occur from roll resonance when the roll rate

is comparable to the missile natural frequency in pitch or yaw. Designing a rolling airframe missile requires consideration of the precession and nutation modes of motion. Note that the miss distance from the seeker dome error slope may be reduced because of the averaging effect of roll rate. However, the miss distance may also be increased because of susceptibility to roll resonance.

Twin and single inlet air-breathing missiles usually require bank-to-turn maneuvering to avoid loss of inlet efficiency from sideslip. Figure 2.43 shows examples of air-breathing missiles that use bank-to-turn maneuvering. The French ASMP is an example of an operational ramjet missile with twin side inlets that are separated by a radial angle of 180 deg. Also shown are two developmental missiles, HSAD and Meteor, with twin cheek inlets. The cheek inlets are in tandem with the bottom cruciform tails and are separated by a radial angle of 90 deg. A major difference between the U.S. HSAD and the U.K. Meteor is the propulsion system. The HSAD is a variable flow solid hydrocarbon ducted rocket. An advantage of a hydrocarbon ducted rocket is a low observable plume. The Meteor engine is a variable flow boron fuel ducted rocket. Boron fuel provides longer range. Compared to liquid fuel ramjets, ducted rockets have simpler logistics and higher acceleration capability. Shown in the bottom of the figure are examples of bank-to-turn missiles with a single inlet. An example of a developmental ramjet missile with a chin inlet is the U.S. Advanced Strategic Air Launched Missile (ASALM). ASALM uses angle of attack α and angle of sideslip β feedback in the flight control system to provide a coordinated turn in bank-to-turn maneuvering. The ASALM was selected as a ramjet baseline for this text because of the availability of unclassified data and its high performance. The BGM-109 Tomahawk and the Storm Shadow/Scalp are examples of bank-to-turn turbojets with a single bottom inlet. Finally, the AGM-86 ALCM

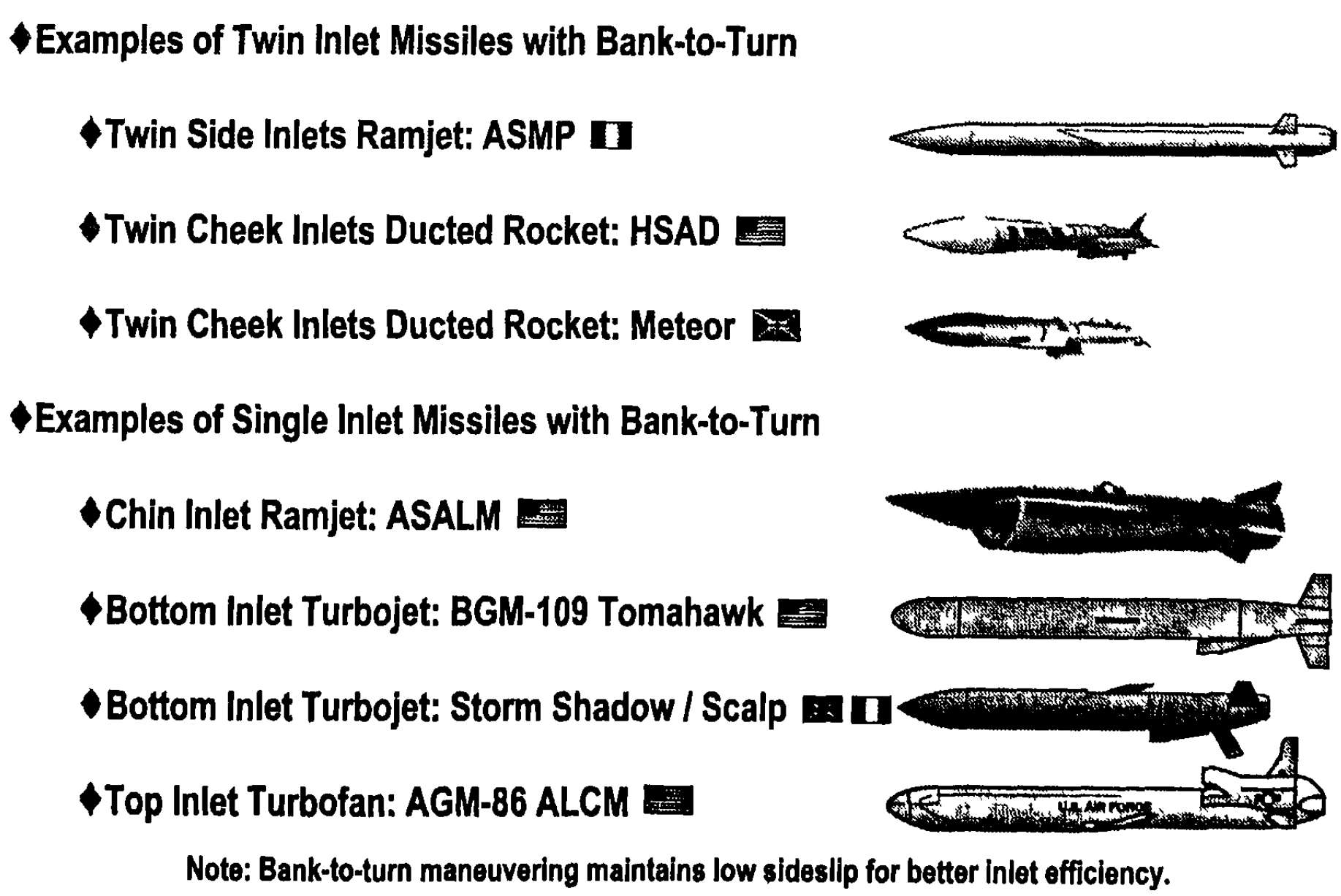

Fig. 2.43 Asymmetric inlets require bank-to-turn maneuvering. Figure also in color section.

is an example of a single top inlet. An advantage of locating the inlet on top is reduced RCS against ground-based radars because of the shielding of the body. A disadvantage is reduced specific impulse at high angles of attack because of inlet flow distortion. Inlet flow distortion occurs at high angle of attack because of crossflow, a thicker boundary, and a tendency for flow separation.

2.17 Roll Orientation

Figure 2.44 compares roll attitude and maneuver control deflection alternatives for a cruciform missile. Approaches to symmetric roll orientation during missile flight, with no induced roll, are + roll orientation and x roll orientation. Each has advantages and disadvantages. The + orientation has the simplest control mechanization. For a pitch command using conventional control with four tail surfaces, the trailing edges of the two horizontal surfaces are deflected upward to cause a positive pitch-up moment. Similarly for a yaw command using conventional tail control, the trailing edges of the two vertical surfaces are deflected to the right to cause a positive yaw right moment. For a roll command, the trailing edges of all four surfaces may be deflected to provide either positive clockwise (roll right) or negative counterclockwise (roll left) roll. The + roll configuration usually has an advantage of lower trim drag. A disadvantage is that it usually has a statically unstable rolling moment derivative ($C_{l\phi} > 0$). The + roll configuration has less static stability and less control effectiveness in pitch and yaw.

An alternative approach of the x roll orientation during missile flight is somewhat more complex in its control mechanization. For a pitch command, all four surfaces are deflected to provide a pitching moment without side force. For a yaw

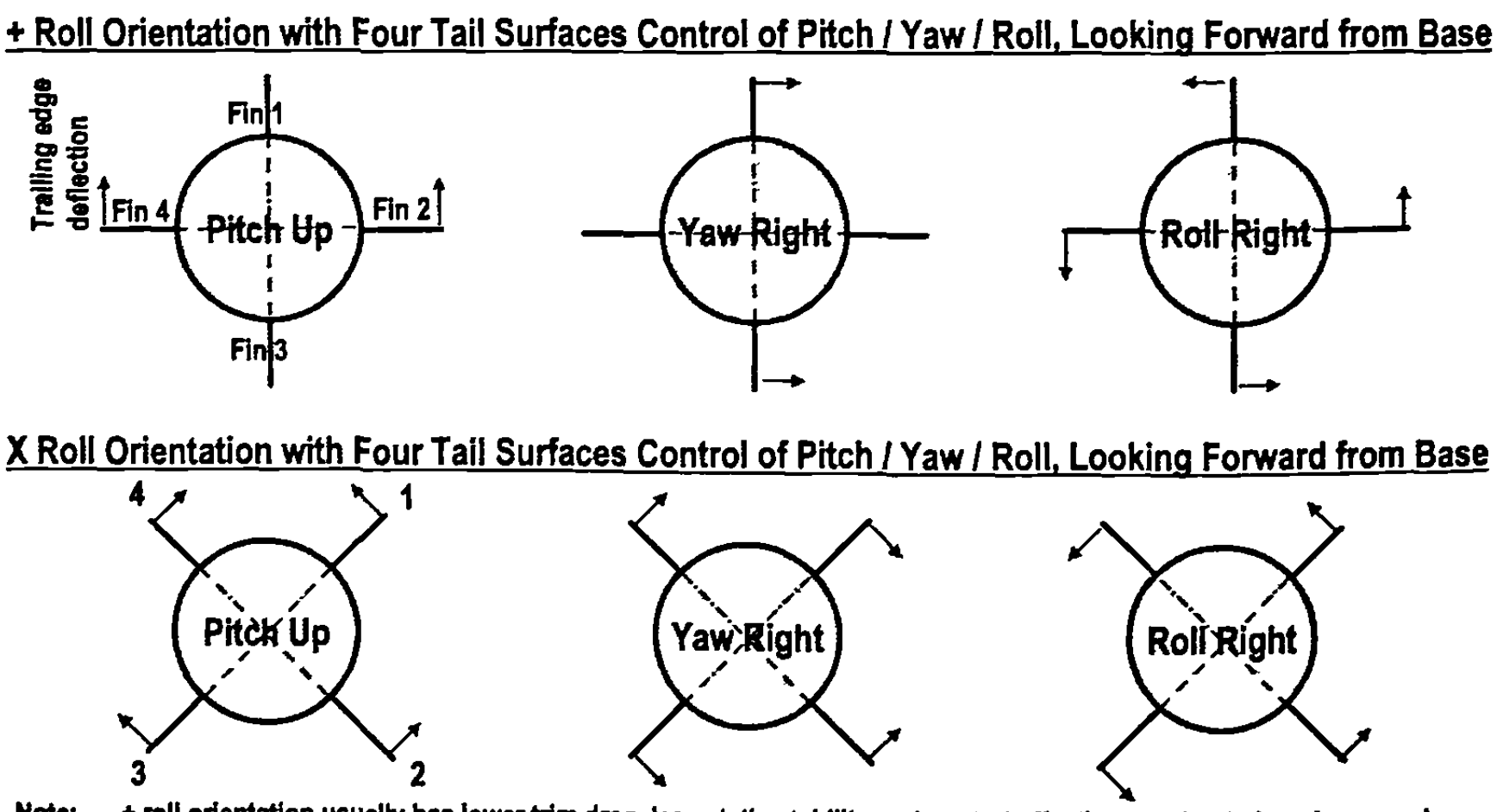

Note: + roll orientation usually has lower trim drag, less static stability and control effectiveness in pitch and yaw, and statically unstable roll moment derivative ($C_{l\phi} > 0$)
X roll orientation has better launch platform compatibility, higher L / D, higher static stability and control effectiveness in pitch and yaw, and statically stable roll moment derivative ($C_{l\phi} < 0$)

Fig. 2.44 X roll orientation is usually better than + roll orientation.

command, all four surfaces are deflected to provide a yawing moment without normal force. The roll command is similar to that of the + orientation. For roll control, all four surfaces are deflected to provide either clockwise roll or counter-clockwise roll. The x roll orientation often has advantages of better fit for launch platform compatibility, higher aerodynamic efficiency (L/D), and a statically stable rolling moment derivative ($C_{l\phi} < 0$). Also, the x roll orientation has higher static stability and control effectiveness in pitch and yaw. Generally, the x orientation is preferred over the + orientation.

2.18 Trim

Trim is defined at zero pitching moment. As shown in Fig. 2.45, the normal force at a trimmed flight condition is lower for either a statically stable missile using tail control or a statically unstable missile using canard control. Conversely, the trimmed normal force is higher for a statically unstable missile using tail control or a statically stable missile using canard control. A rule of thumb for conceptual design of a tail or canard control missile is that the change in angle of attack from control deflection should be greater than 1 ($|\alpha/\delta| > 1$). Most control surfaces have deflection limits less than $+/-30$ deg. $|\alpha/\delta| > 1$ usually allows a trim angle of attack up to about 30 deg.

Relaxed static margin allows the missile to trim at higher angle of attack, providing higher maneuverability. Shown in Fig. 2.46 is the benefit of relaxed static stability for the rocket baseline missile. The rocket baseline missile has excessive static margin (e.g., 0.88 diameter at Mach 2), resulting in a relatively low maximum angle of attack ($\alpha = 9.4$ deg) and a relatively low maximum trimmed normal force ($C_N = 9$). Reducing the static margin increases the maximum angle of attack and the maximum trimmed normal force. In the

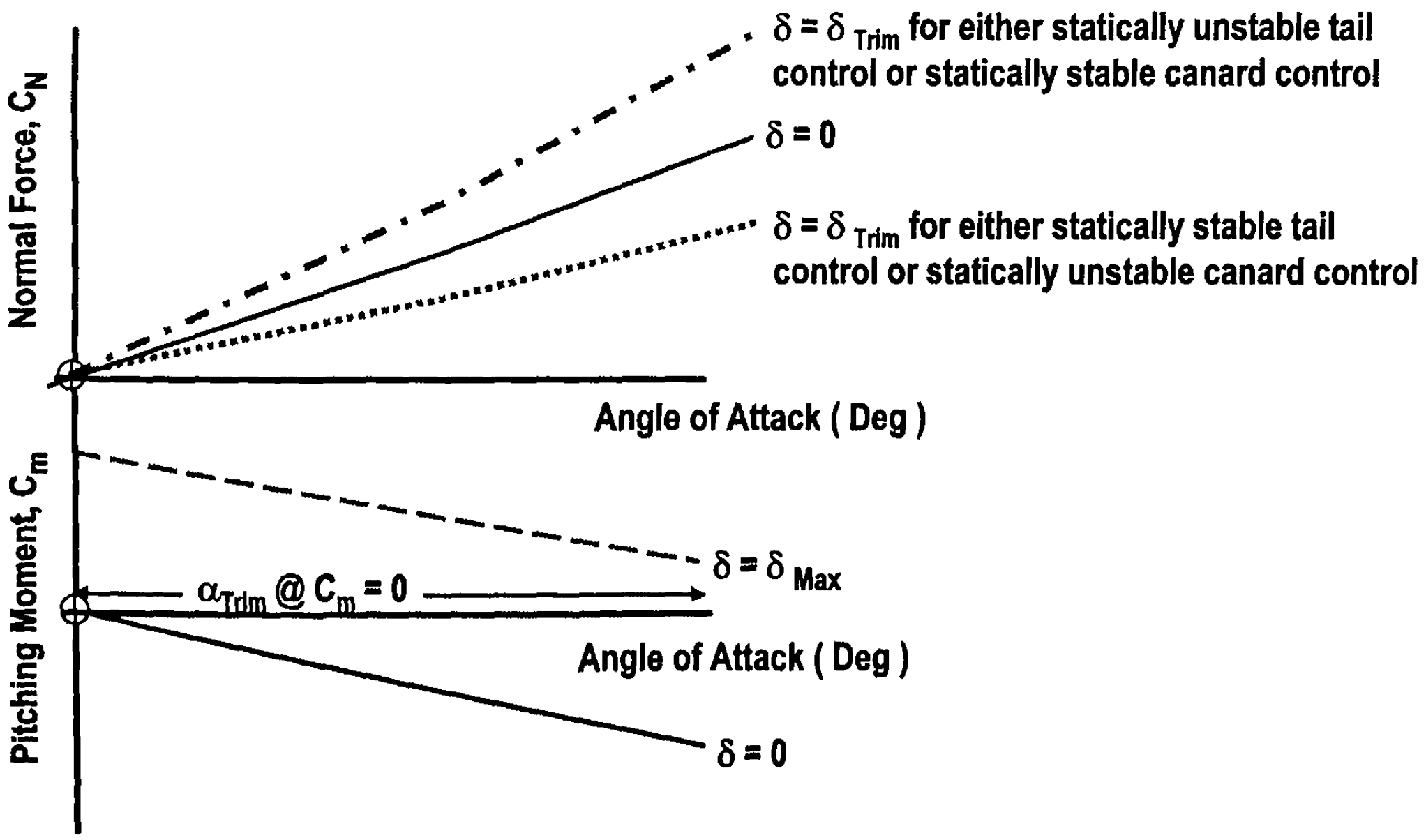

Fig. 2.45 Trimmed normal force is defined at zero pitching moment.

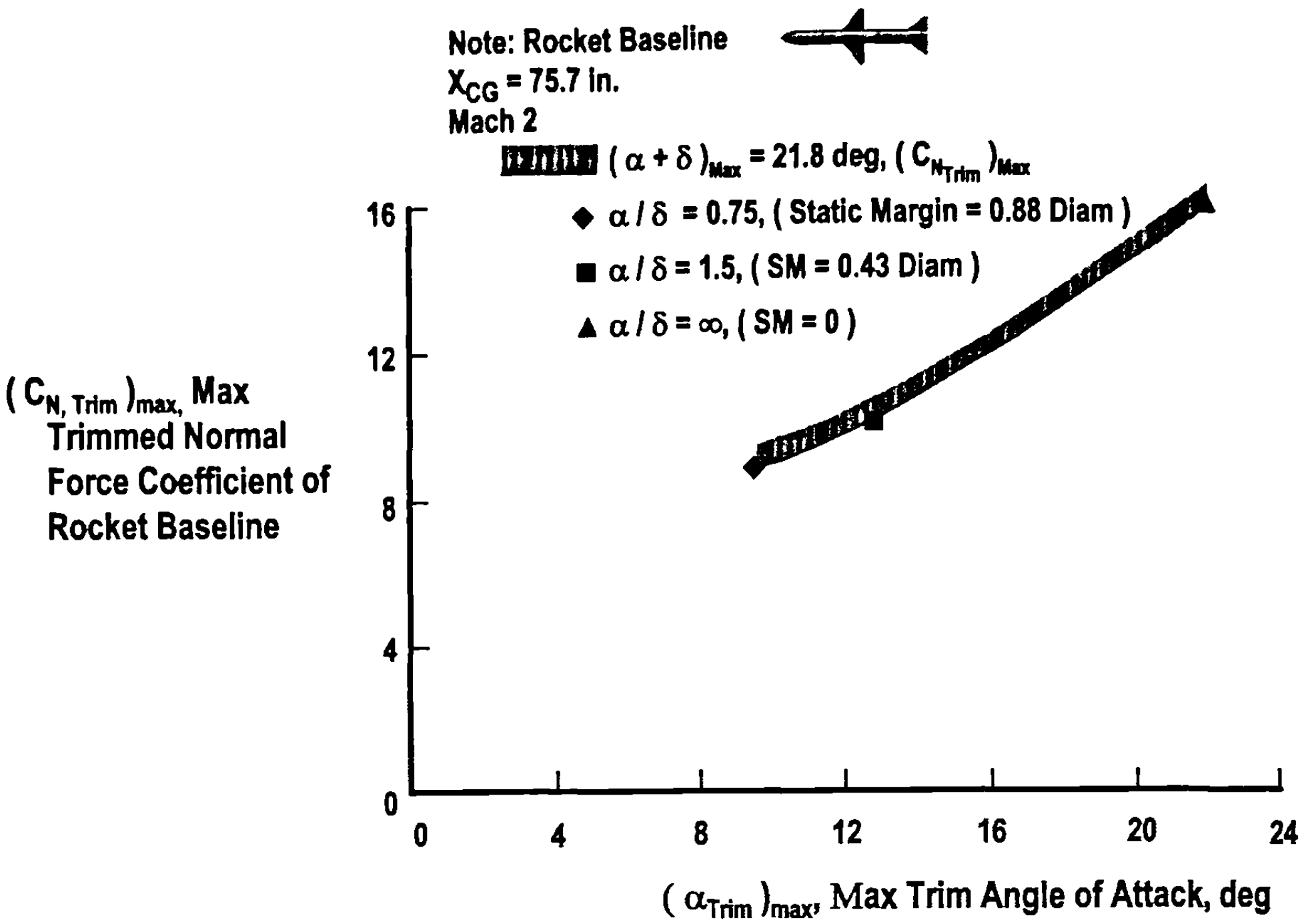

Fig. 2.46 Relaxed static margin allows higher trim angle of attack and higher normal force.

example, a neutrally stable missile ($\alpha/\delta = \infty$ or static margin $= 0$) has a 130% increase in maximum angle of attack ($\alpha = 9.4$ to 21.8 deg) and an 80% increase in maximum available normal force ($C_N = 9$ to 16).

2.19 Tail Area Sizing

Much of the conceptual design configuration sizing process is oriented toward tail sizing. Because missiles are usually volume limited and the subsystems are of comparable density, the center-of-gravity location is usually near 50% of the length of the missile. Because the nose and any forward surfaces (strakes/canards) are destabilizing, the tails must be sized to provide static stability. Figure 2.47 illustrates the process for tail sizing. The tail contribution to pitching moment stability, provided by the tail normal force effectiveness $(C_{N\alpha})_T(S_T/S_{\text{Ref}})$ times its moment arm to the center of gravity $[(x_{\text{AC}})_T - x_{\text{CG}}]$, must balance the contributions to pitching moment from the nose and wing. Shown in the figure is the equation for the static margin, given a specified tail area. Also shown in the figure is the equation for the required tail area, given a specified static margin.

Of particular interest is the required tail area for neutral stability. The equation is

$$\begin{aligned} S_{\text{T}} = \{&(C_{N\alpha})_{\text{B}}[x_{\text{CG}} - (x_{\text{AC}})_{\text{B}}]/d \\ &+ (C_{N\alpha})_W\{[x_{\text{CG}} - (x_{\text{AC}})_W]/d\}(S_W/S_{\text{Ref}})\} \\ &\times \{d/[(x_{\text{AC}})_T - x_{\text{CG}}]\}S_{\text{Ref}}/(C_{N\alpha})_T \end{aligned} \tag{2.51}$$

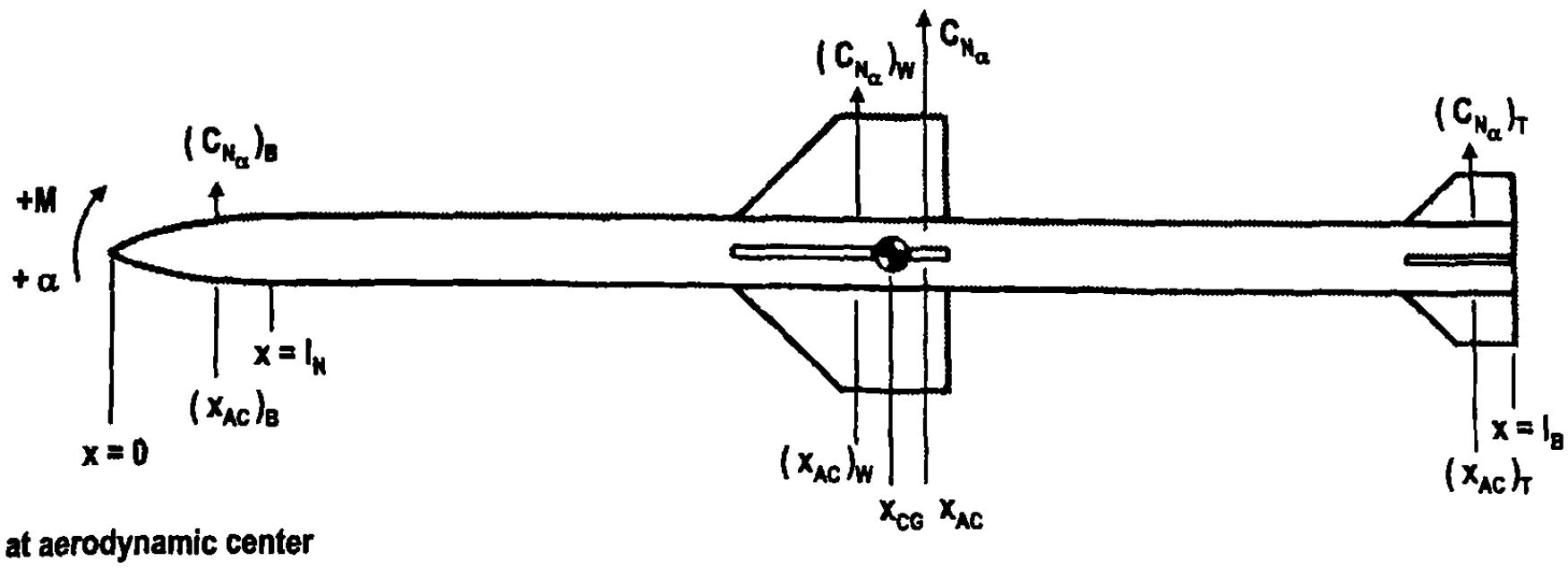

ΣM = 0 at aerodynamic center

$$(C_{N_\alpha})_B \{[x_{CG} - (x_{AC})_B]/d\} + (C_{N_\alpha})_W \{[x_{CG} - (x_{AC})_W]/d\} S_W/S_{Ref} + (C_{N_\alpha})_T \{[x_{CG} - (x_{AC})_T]/d\} S_T/S_{Ref}$$
$$= -[(C_{N_\alpha})_B + (C_{N_\alpha})_W S_W/S_{Ref} + (C_{N_\alpha})_T S_T/S_{Ref}][(x_{AC} - x_{CG})/d]$$

Static margin for a specified tail area is

$$(x_{AC} - x_{CG})/d = -\{(C_{N_\alpha})_B \{[x_{CG} - (x_{AC})_B]/d\} + (C_{N_\alpha})_W \{[x_{CG} - (x_{AC})_W]/d\} S_W/S_{Ref} + (C_{N_\alpha})_T \{[x_{CG} - (x_{AC})_T]/d\} (S_T/S_{Ref})\} / [(C_{N_\alpha})_B + (C_{N_\alpha})_W S_W/S_{Ref} + (C_{N_\alpha})_T S_T/S_{Ref}]$$

Required tail area for a specified static margin is

$$S_T/S_{Ref} = (C_{N_\alpha})_B \{[x_{CG} - (x_{AC})_B]/d\} + (C_{N_\alpha})_W \{[x_{CG} - (x_{AC})_W]/d\} (S_W/S_{Ref}) + \{[(C_{N_\alpha})_B + (C_{N_\alpha})_W S_W/S_{Ref}][(x_{AC} - x_{CG})/d]\} / \{(C_{N_\alpha})_T [(x_{AC})_T - x_{CG}]/d - (x_{AC} - x_{CG})/d\}$$

Fig. 2.47 Tails are sized for desired static margin.

Figure 2.48 shows the rocket baseline required tail area for neutral static margin as a function of Mach number and wing location. It is based on predicted aerodynamics. Note that the required tail area for neutral static stability must be larger as the Mach number increases toward hypersonic. The tail loses aerodynamic

$$(S_T)_{Neutral}/S_{Ref} = \{(C_{N\alpha})_B [x_{CG} - (x_{AC})_B]/d + (C_{N\alpha})_W \{[x_{CG} - (x_{AC})_W]/d\} (S_W/S_{Ref})\} / \{\{[(x_{AC})_T - x_{CG}]/d\} (C_{N\alpha})_T\}$$

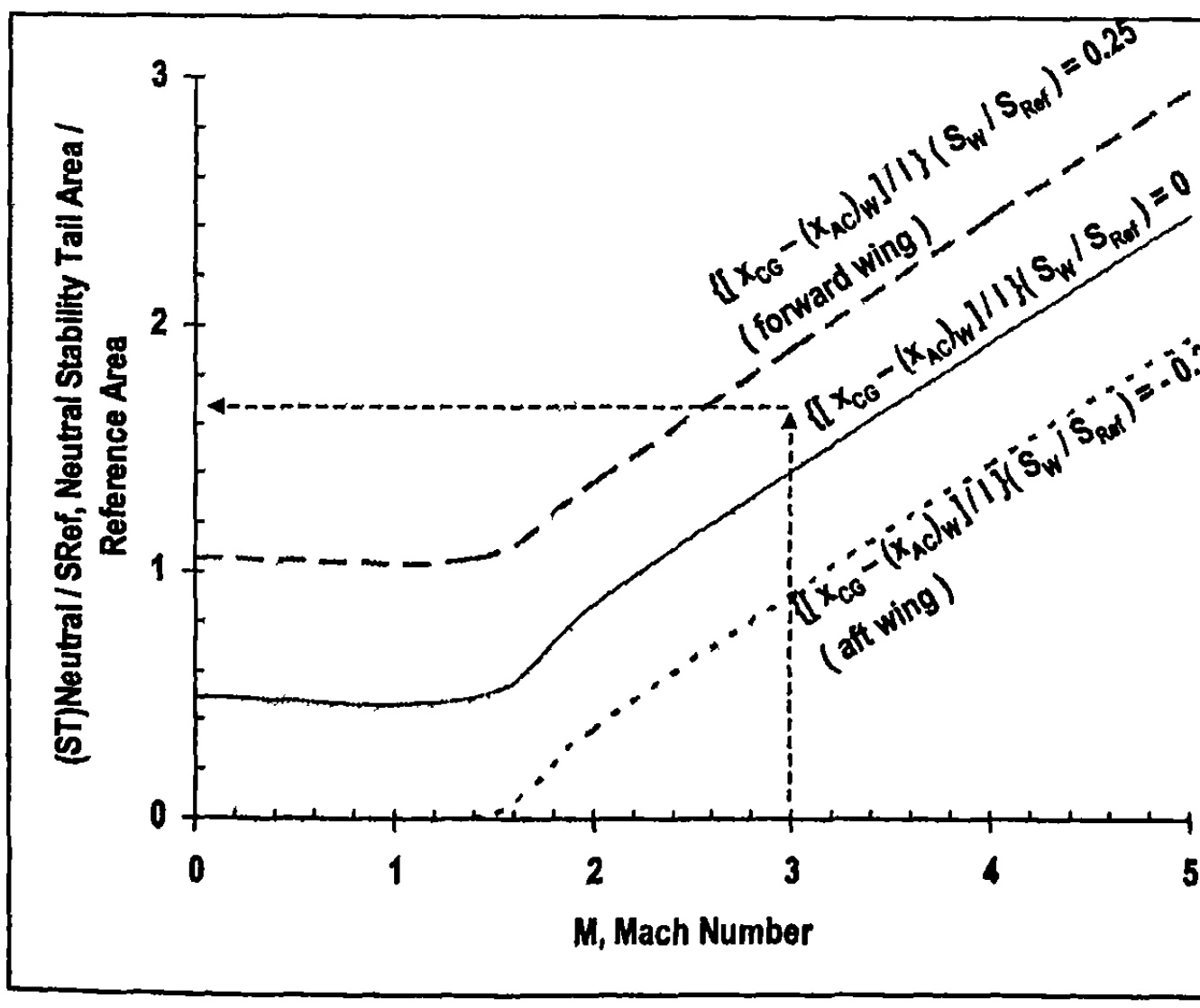

Assumptions for figure:

- $X_{CG} \approx l/2$, $(X_{AC})_B \approx d$, $(X_{AC})_T \approx l - d$
- $\alpha < 6$ deg, turbulent boundary layer
- $(C_{N\alpha})_B = 2$ per radian
- $(C_{N\alpha})_T = (C_{N\alpha})_W = 4/[M^2 - 1]^{1/2}$, if $M > \{1 + [8/(\pi A)]^2\}^{1/2}$
- $(C_{N\alpha})_T = (C_{N\alpha})_W = \pi A/2$, if $M < \{1 + [8/(\pi A)]^2\}^{1/2}$

Example Rocket Baseline:

l = 144 in, d = 8 in, S_W = 2.55 ft², S_{Ref} = 0.349 ft², A_W = 2.82, $(c_{MAC})_W$ = 13.3 in, x_{MAC} = 67.0 in from nose tip, burnout (X_{CG} = 76.2 in from tip), M_{max} = 3

$(x_{AC})_W$ = 0.49 (13.3) = 6.5 in from leading edge of MAC

$(x_{AC})_W$ = 6.5 + 67.0 = 73.5 in from nose

{[x_{CG} − $(x_{AC})_W$]/ l } (S_W / S_{Ref}) = 0.14 (forward wing)

$(S_T)_{Neutral}$ / S_{Ref} = 1.69 provides neutral stability

$(S_T)_{Neutral}$ = 1.69 (0.349) = 0.59 ft²

Fig. 2.48 A Larger tail area is required for neutral stability at high Mach number.

efficiency as Mach number increases. Also note that placing the wing such that its aerodynamic center is forward of the center-of-gravity location is destabilizing, requiring a larger tail area for compensation. The rocket baseline wing aerodynamic center is forward of the center of gravity, and therefore the rocket baseline requires a larger tail. Placing the wing aft of the center of gravity is stabilizing, allowing a smaller tail area to meet the static margin requirement. Note that for a typical missile wing without camber, the location of the wing aerodynamic center is the same as the wing center-of-pressure location.

The figure is based on analytical prediction of aerodynamics from slender body theory [$(C_{N\alpha})_B = 2$ per rad and $(x_{CP})_B \approx d$] for the body. For the wing and tail, linear wing theory [$(C_{N\alpha})_W = (C_{N\alpha})_T = 4/[M^2 - 1]^{1/2}$] is used at high Mach number and slender wing theory [$(C_{N\alpha})_W = \pi A_W/2$, $(C_{N\alpha})_T = \pi A_T/2$] is used at subsonic and low supersonic Mach numbers. It is assumed that the moment arm from the tail aerodynamic center location to the missile center of gravity is approximately equal to the moment arm from the body (nose) aerodynamic center to the center of gravity. Another assumption is low angle of attack ($\alpha < 6$ deg). Still another assumption is a turbulent boundary layer with small boundary layer thickness. Note that for flight conditions with a laminar boundary layer over much of the body (e.g., $M < 0.2$ or $h > 80{,}000$ ft), the body boundary-layer thickness at the tails may blanket a significant portion of the tails, reducing the tail effectiveness.

In the example for the rocket baseline at Mach 3, the predicted tail area must be 0.59 ft^2 for neutral static stability. The predicted tail area is 1.69 times the reference body cross-sectional area. The actual rocket baseline missile has a tail area that is more than four times the reference body cross-sectional area. This is an indication that the rocket baseline missile has excessive static margin from a tail that is unnecessarily large. Also, the wing aerodynamic center location of the rocket baseline is in front of the missile center of gravity, requiring a larger tail area.

2.20 Stability and Control Conceptual Design Criteria

Stability and control have an impact on the aerodynamic configuration design, particularly tail sizing, and should be considered early in conceptual design. Because tactical missiles tend to have near-neutral static stability and use combined pitch/yaw/roll controls, it may be difficult to accurately predict static margin and control effectiveness. Although the actual stability and control derivatives prediction may have large error, it is often possible to size the canard, wing, or tail surfaces with less than 10% error in the surface area. Predicting stability and control derivatives usually requires iteration as the surfaces are resized and the center-of-gravity location changes during the design convergence. It is helpful to start with a baseline missile, such as the rocket and ramjet baselines in this text, which have a balance of system engineering in their stability and control derivatives. It is useful to compare stability and control derivatives with wind tunnel data to assess the accuracy of prediction methods. Conceptual design criteria are also useful, providing a "sanity check" and facilitating design convergence. Figure 2.49 shows conceptual design criteria for roll cross coupling (rolling moment from rudder deflection $C_{l\delta_r}$), yaw cross coupling (yawing

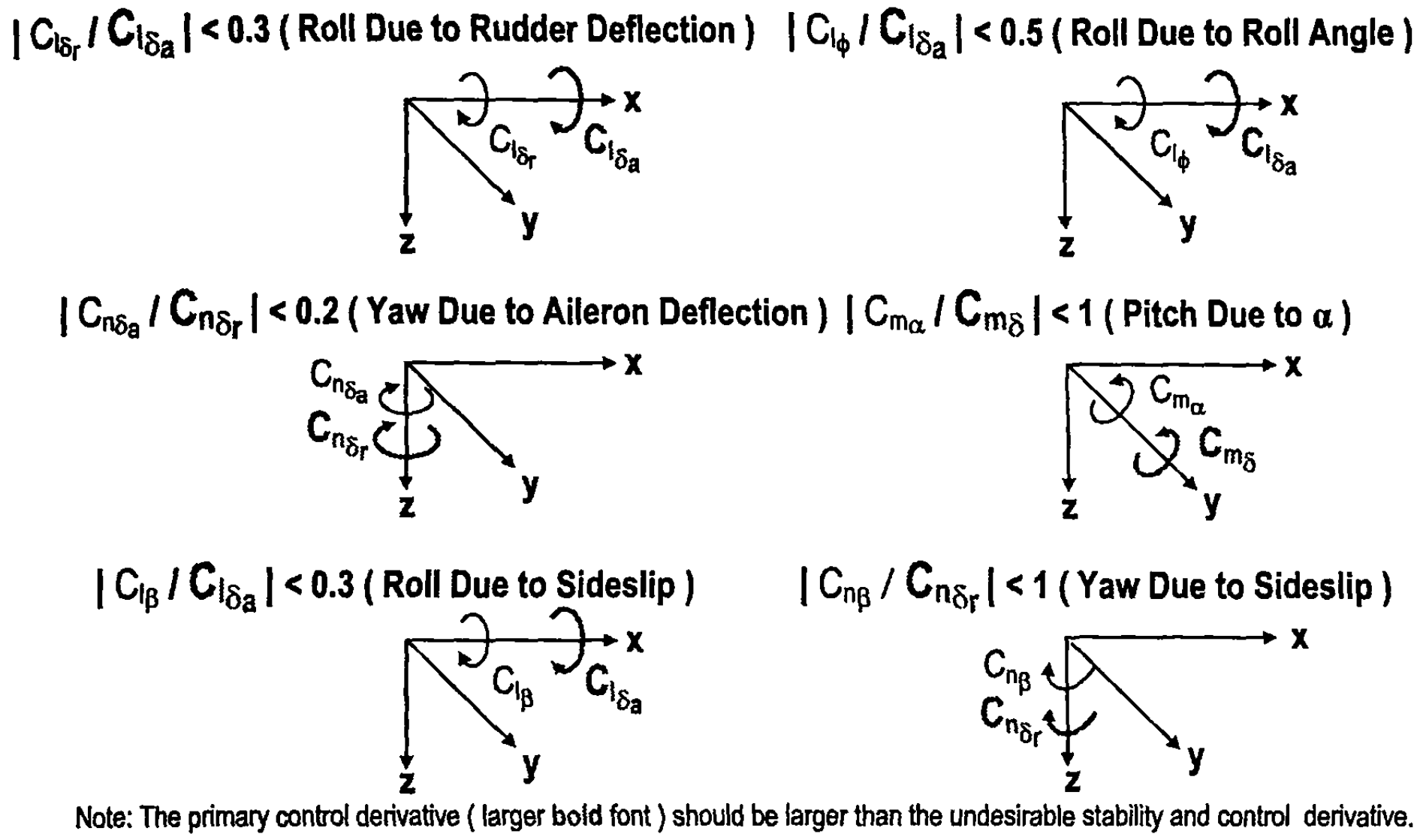

Fig. 2.49 Stability and control derivatives conceptual design criteria. Figure also in color section.

moment from aileron deflection $C_{n\delta_a}$), roll control effectiveness $C_{l\delta_a}$ to compensate for the rolling moment from sideslip C_{l_β}, roll control effectiveness $C_{l\delta_a}$ to compensate for induced roll from roll attitude C_{l_ϕ}, pitch control effectiveness C_{m_δ}, and yaw control effectiveness $C_{n\delta_r}$. Stability and control cross coupling or out-of-plane moments should generally be less than 30% of the "pure" in-plane moments, to maximize the control power and minimize the time constant for maneuvers. Examples of stability and control conceptual design criteria are:

1) $|C_{l\delta_r}| < 0.3\ |C_{l\delta_a}|$, rolling moment from rudder deflection should be less than 30% of the aileron control effectiveness to have adequate control margin

2) $|C_{n\delta_a}| < 0.2|C_{n\delta_r}|$, yawing moment from aileron deflection should be less than 20% of the rudder control effectiveness to have adequate control margin

3) $|C_{l_\beta}| < 0.3\ |C_{l\delta_a}|$, rolling moment from sideslip should be less than 30% of the aileron control effectiveness to have adequate control margin

4) $|C_{l_\phi}| < 0.5\ |C_{l\delta_a}|$, rolling moment from roll orientation should be less than 50% of the aileron control effectiveness to have adequate control margin

5) $|C_{m_\alpha}| < |C_{m_\delta}|$, pitching moment from angle of attack should be less than the elevator control effectiveness to have adequate control margin

6) $|C_{n_\beta}| < |C_{n\delta_r}|$, yawing moment from sideslip should be less than the rudder control effectiveness to have adequate control margin

2.21 Body Buildup

A first-order estimate of total normal force, suitable for conceptual design, is to assume a body buildup of the configuration, which consists of the contribution from the body plus the contribution from each surface. As an example, for a

wing-body-tail conceptual design, it is assumed that the total normal force is the summation of that of an isolated body + wing (exposed) + tail (exposed). The effects of wing-body, body-wing, tail-body, body-tail, and wing-tail interference are assumed to be small when compared to the contributions from the isolated configuration geometries. For a wing-body-tail configuration the equation is

$$(C_N)_{\text{Total}} = (C_N)_{\text{Wing-Body-Tail}} \approx (C_N)_{\text{Body}} + (C_N)_{\text{Wing}} + (C_N)_{\text{Tail}} \tag{2.52}$$

Figure 2.50 shows a body buildup of the normal force coefficient of the rocket baseline missile. The body buildup in the figure is based on undeflected control surfaces. Note that for the rocket baseline missile most of the normal force is provided by the wing contribution. Deflecting the wing control provides an additional contribution to normal force. The second largest contributor to normal force is from the tail. As mentioned previously, the rocket baseline has a large tail and a large static margin. Finally, the body provides a relatively small contribution to normal force. This has an implication in the design for maneuverability. The maneuverability requirements of the rocket baseline missile are satisfied through sizing the wing.

The body buildup approach based on summing the isolated contributions from the body plus each surface is used in the conceptual design prediction of normal force, drag, and pitching moment. For preliminary design, more accurate methods based on including the effects from wing-body, body-wing, tail-body, body-tail, and wing-tail interface are used. Body buildup wind tunnel tests are also normally conducted during preliminary design. For the conceptual design prediction methods of this text, the conceptual design predictions without

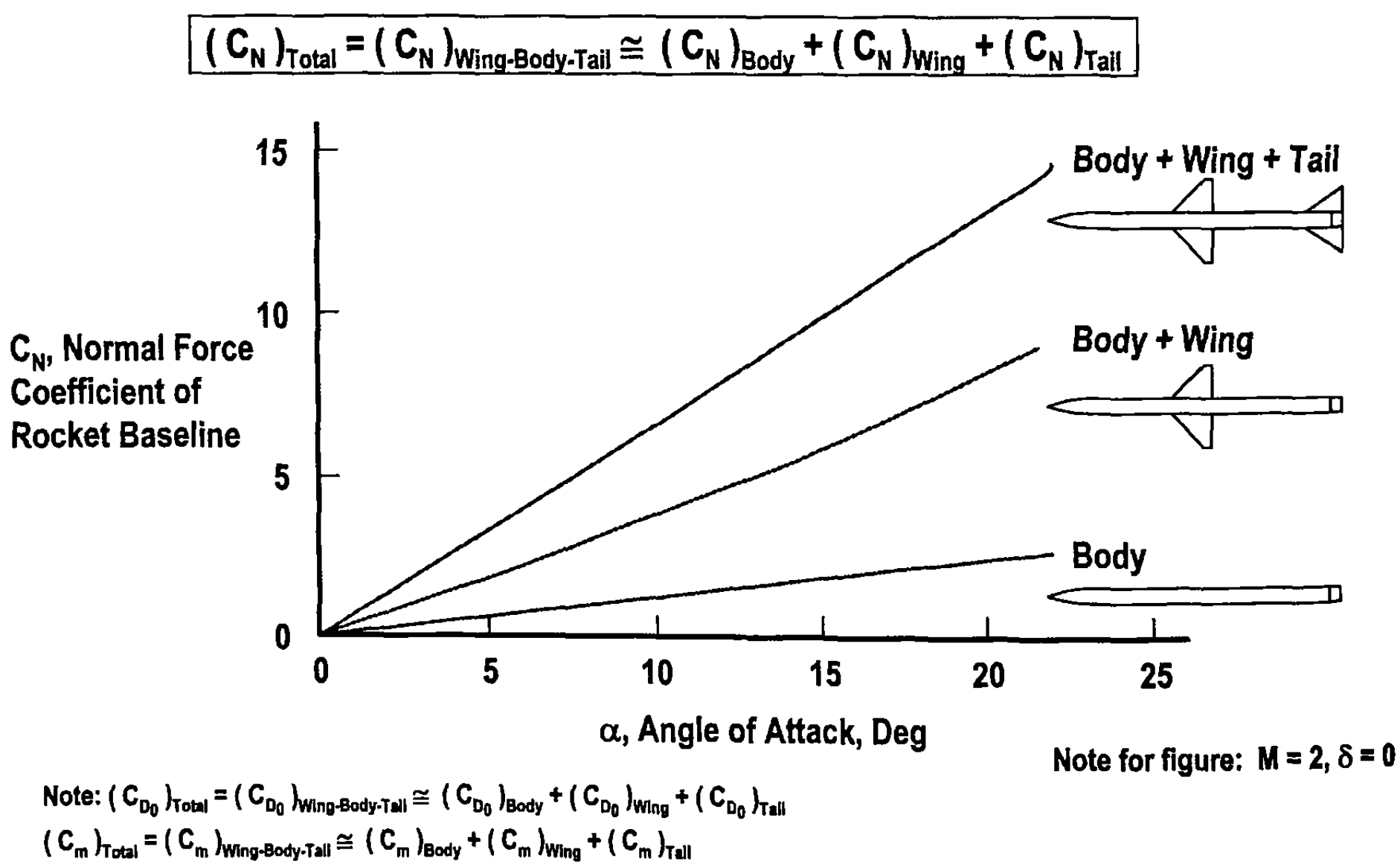

Fig. 2.50 Most of the rocket baseline body buildup normal force is provided by the wing.

interference effects are corrected by the baseline missile aerodynamics, which include interference effects.

2.22 Summary

Chapter 2 provided conceptual design methods, design tradeoffs, design criteria, and technologies for the aerodynamics of tactical missiles. The emphasis was on the aerodynamics of low aspect ratio wing and wingless missiles. The conceptual design methods of this text addressed the prediction of the normal force coefficient, the drag force coefficient, and the aerodynamic center/pitching moment coefficient of bodies and surfaces and the hinge moment of surfaces. Design tradeoffs addressed missile diameter, nose fineness, boattail, lifting body versus axisymmetric body, wings versus no wings, tails versus flares, surface planform geometry, flight control alternatives, maneuver alternatives, roll orientation, and static margin. A process was given for tail area sizing. Stability and control design criteria were provided for static stability, control effectiveness, and cross coupling. A process to compute the total forces and moments based on the summation of the individual contributions (e.g., body, wing, tail) was demonstrated. New aerodynamic technologies were identified that have high payoff for tactical missiles. These include faceted/window/multi-lens domes, bank-to-turn maneuvering, lifting body airframe, forward swept surfaces, neutral static margin, lattice tails, split canard control, and free-to-roll tails.

Problems

2.1. Missile diameter tradeoffs include consideration of seeker range, warhead lethality, structural mode frequency, and d___.

2.2. Benefits of a high-fineness nose include lower supersonic drag and lower r____ c____ s_____.

2.3. Three contributors to drag are base drag, wave drag, and s___ f_____ drag.

2.4. To avoid flow separation, a boattail or flare angle should be less than__ deg.

2.5. A lifting body is most efficient at a d_____ p_____ of about 700 psf.

2.6. At low angle of attack the aerodynamic center of the body is on the n___.

2.7. Subsonic missiles often have w____ for enhanced range.

2.8. The aerodynamic center of the wing is between 25% and 50% of the m___ a_____ c____.

2.9. Hinge moment increases with the local flow angle from control surface deflection and the a____ o_ a_____.

2.10. Increasing the surface area increases the s___ f_____ d___.

2.11. Leading edge sweep reduces drag and r____ c____ s_____.

2.12. A missile with six control surfaces, four surfaces providing combined pitch/yaw control plus two surfaces providing roll control, has an advantage of good c_____ e_____.

2.13. A missile with two control surfaces providing only combined pitch/yaw control has advantages of lower c____ and good p_____.

2.14. A tail control missile has larger trim normal force if it is statically u_____.

2.15. Lattice fins have low h____ m_____.

2.16. Split canards allow higher maximum angle of attack and higher m_____.

2.17. Two types of unconventional control are thrust vector control and r_____ j__ control.

2.18. The most common type of TVC for tactical missiles is j__ v___ control.

2.19. Three maneuver laws are skid to turn, bank to turn, and r_____ a_____.

2.20. Bank-to-turn maneuvering is usually required for missiles with a single wing or with a_____ inlets.

2.21. A missile is statically stable if the aero center is behind the c_____ o_ g_____.

2.22. Tail stabilizers have low drag while a f____ stabilizer has low aero heating and a relatively small shift in static stability.

2.23. If the moments on the missile are zero the missile is in t___.

2.24. Total normal force on the missile is approximately the sum of the normal forces on the surfaces (e.g., wing, tail, canard) plus normal force on the b___.

2.25. Increasing the tail area increases the s_____ m_____.

3
Propulsion Considerations in Tactical Missile Design

3.1 Introduction

Tactical missile propulsion considerations that are addressed in this text emphasize conceptual design methods, design trades, and technologies for rocket, ramjet, and turbojet propulsion. Consideration is given to propulsion system alternatives, turbojet compressor and turbine temperature limits, turbojet specific impulse and thrust prediction, ramjet Mach number and temperature limits, ramjet specific impulse and thrust prediction, ramjet engine/booster integration options, ramjet inlet options, inlet spillage prediction, inlet shock loss, inlet start Mach number, ramjet missile drag from booster integration, fuel alternatives, propellant fraction required for an incremental velocity, solid rocket burn area requirement, solid rocket throat area requirement, solid rocket specific impulse and thrust prediction, solid rocket grain alternatives, solid rocket thrust magnitude control, solid propellant alternatives, motor case material alternatives, and rocket nozzle material alternatives.

Figure 3.1 shows that, after aerodynamic configuration design, the next step in the missile configuration synthesis process is propulsion system design. Propulsion system design is an iterative process requiring consideration of alternative propulsion systems, alternative propulsion subsystems, alternative technologies, and propulsion system resizing. The propulsion sizing output includes the thrust, specific impulse, and the propellant/fuel weight of the propulsion system.

3.2 Propulsion Alternatives Assessment

Figure 3.2 compares the efficiency of tactical missile propulsion alternatives across the Mach number ranges of subsonic through hypersonic. Shown is a typical specific impulse envelope and typical constraints for the alternatives of turbojet, ramjet, ducted rocket, scramjet, and solid rocket propulsion.

Subsonic turbojet/turbofan propulsion is a relatively mature technology. It is most suited for subsonic cruise missiles, providing high efficiency against non-time-critical targets. Beyond Mach 2, there is a technology challenge of the maximum allowable temperature of current turbine materials. Other problems include increasingly complex inlet systems to match the inlet airflow to the

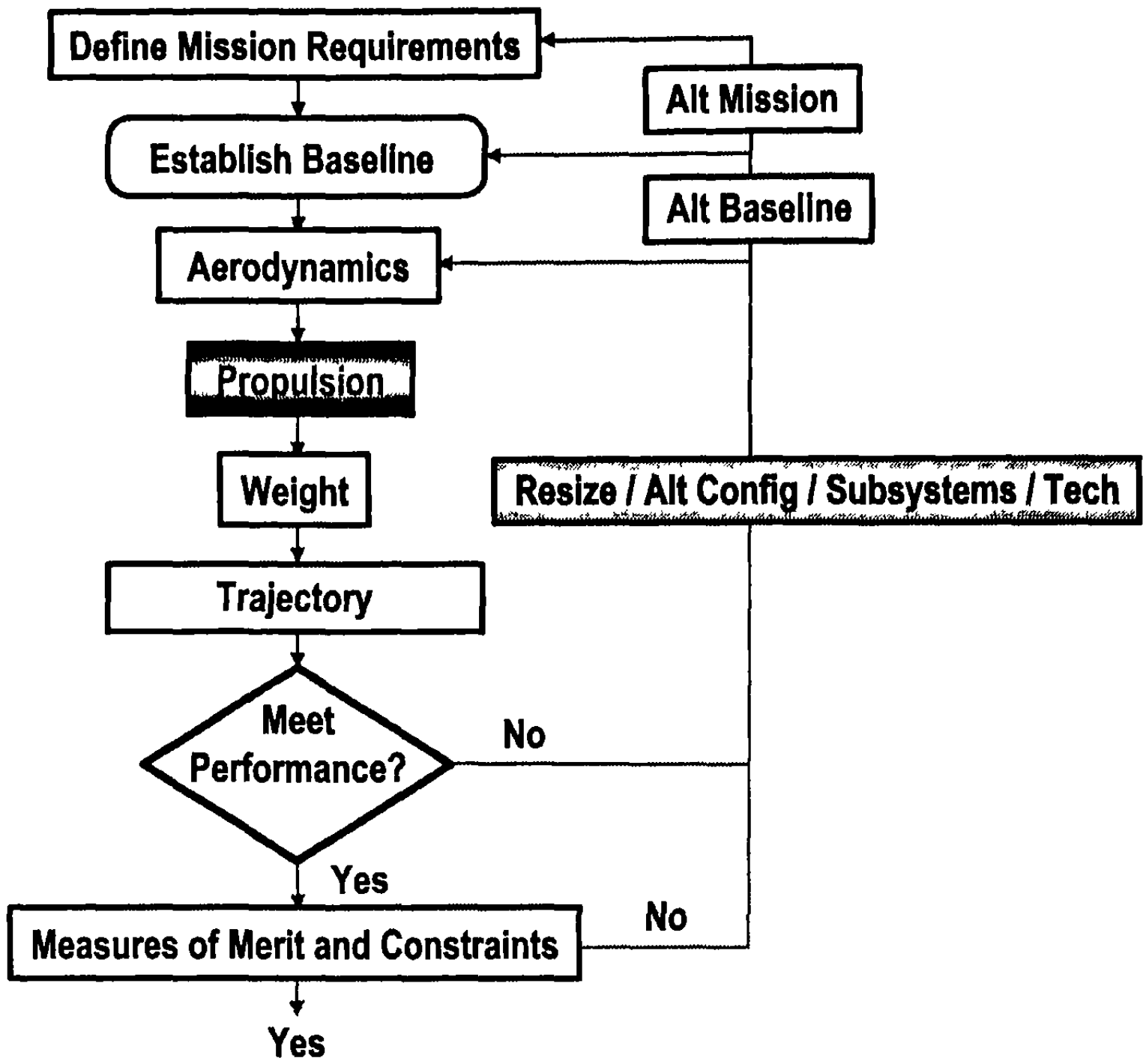

Fig. 3.1 Missile concept synthesis requires evaluation of alternatives and iteration.

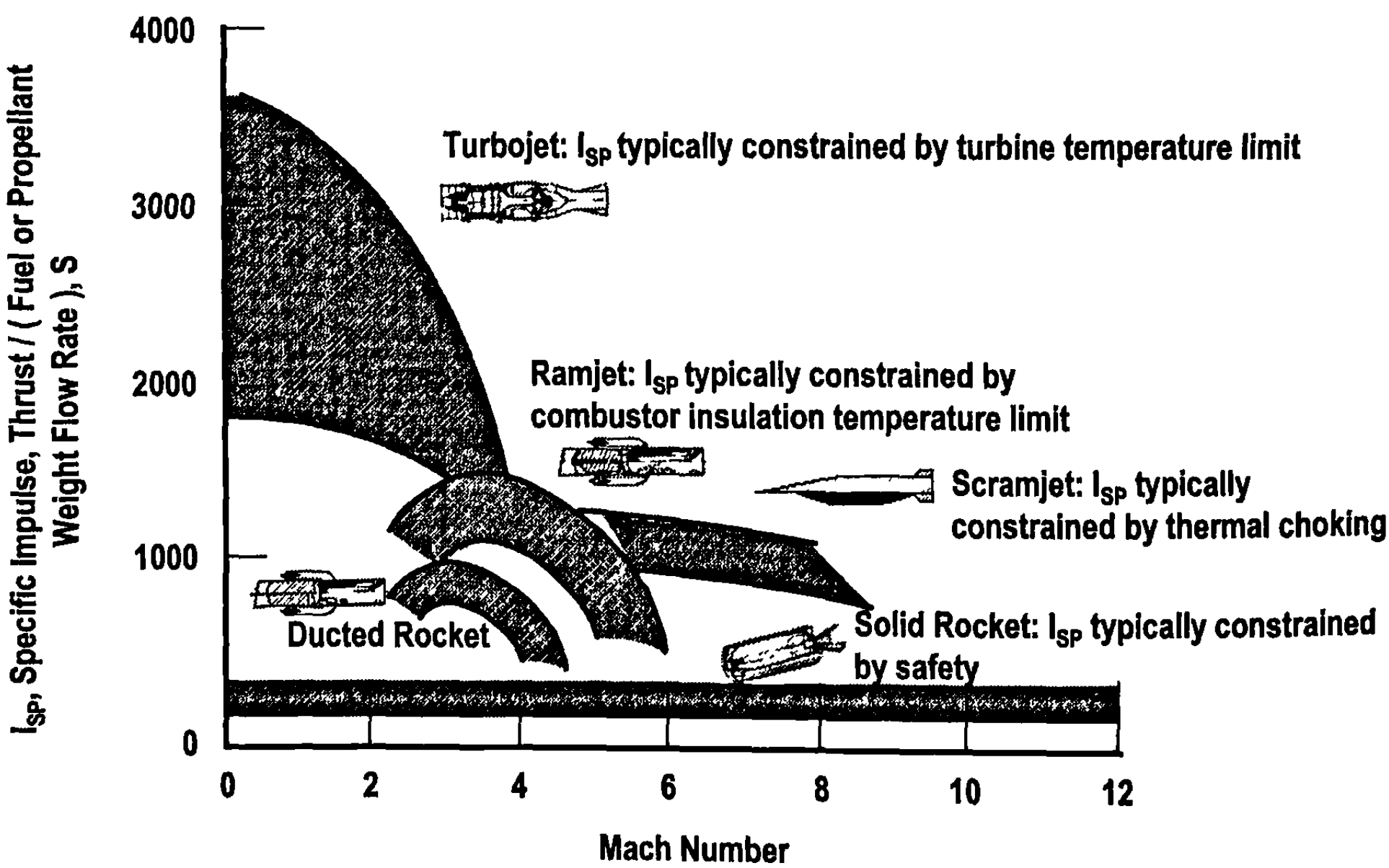

Fig. 3.2 High specific impulse is indicative of lower fuel/propellant consumption.

compressor and expensive cooling to avoid exceeding the current material temperature limit of about 2500° F at the turbine.

A ramjet is efficient from Mach 2.5 to 5. Above Mach 5, the combustor maximum material temperature limits the achievable exit velocity and thrust. Also, deceleration of the inlet airflow to subsonic velocity results in chemical dissociation of the air, which absorbs heat and negates a portion of the energy input of the combustor. For a subsonic launch platform, a rocket boost is required to achieve the ramjet thrust takeover at about Mach 2.5.

The maximum specific impulse of ducted rocket propulsion is about 800 to 1000 s, which is intermediate to that of a solid rocket and a ramjet. Ducted rockets are most efficient for a Mach number range from about 2.5–4. Ducted rockets have higher acceleration capability (higher thrust) than ramjets and generally have longer range capability (higher specific impulse) than solid propellant rockets.

Scramjet propulsion has supersonic flow through the entire flowpath, including supersonic combustion. Efficient cruise is about Mach 6, 100,000 ft altitude. A typical limit in scramjet specific impulse at lower Mach number is thermal choking. A larger inlet is required to avoid thermal choking for Mach numbers less than Mach 6. Scramjet propulsion challenges include fuel/air mixing, efficient combustion, airframe integration, and sufficient thrust to overcome the drag. Compared to a ramjet, a longer combustion chamber is required because of the mixing time for supersonic combustion. An enabling technology to enhance supersonic combustion is endothermic fuels. Endothermic fuels decompose at high temperature into lighter weight molecular products that burn more readily, providing higher specific impulse and permitting shorter combustor length. An endothermic fuel also acts as a heat sink, cooling the adjacent structure. Because scramjet thrust is less than drag for Mach numbers less than about 4, a scramjet requires a large rocket motor to boost it to a high takeover speed. Due to its relatively low thrust, a scramjet may not have sufficient thrust to accelerate or even maintain a cruise condition of thrust equal to drag.

A dual-combustion ramjet/scramjet (DCR) has some of the higher Mach number capability of a scramjet and some of the relatively higher thrust capability and lower takeover Mach number of a ramjet. DCR propulsion separates the inlet airflow into two streams. The main airflow remains supersonic. The smaller airflow is decelerated to subsonic speed for fuel-rich combustion, after which it accelerates through a nozzle. Efficient flight is Mach 3 to Mach 7.

Solid propellant rockets are capable of providing thrust across the entire Mach number range. Safety concerns of explosive sensitivity and toxicity provide constraints on the practical specific impulse of tactical rocket propellants. Although the specific impulse of tactical rockets is relatively low, on the order of 250 s, rockets have an advantage of much higher acceleration capability than air-breathing propulsion. Also, because a rocket can operate at any altitude, a boost-climb-glide trajectory can provide extended range by minimizing drag in high-altitude flight.

Figure 3.3 compares four propulsion alternatives for a long-range precision strike missile. The propulsion alternatives are subsonic cruise turbojet, supersonic cruise liquid hydrocarbon fuel ramjet, hypersonic cruise liquid hydrocarbon fuel scramjet, and supersonic cruise solid propellant rocket. All four propulsion types are held to a missile launch weight of 2000 lb, a representative weight limit

$$R = (L/D)\, I_{sp}\, V \ln[W_L/(W_L - W_P)]\text{, Breguet Range Equation}$$

Parameter	Typical Value for 2,000 lb Precision Strike Missile			
	Subsonic Turbojet Missile 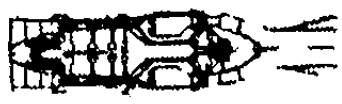	Liquid Fuel Ramjet Missile 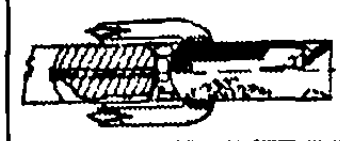	Hydrocarbon Fuel Scramjet Missile	Solid Rocket
L / D, Lift / Drag	10	5	3	5
I_{sp}, Specific Impulse	3000 s	1300 s	1000 s	250 s
V_{AVG}, Average Velocity	1000 ft / s	3500 ft / s	6000 ft / s	3000 ft / s
W_P / W_L, Cruise Propellant or Fuel Weight / Launch Weight	0.3	0.2	0.1	0.4
R, Cruise Range	1800 nm	830 nm	310 nm	250 nm

Note: Ramjet and Scramjet missiles booster propellant for Mach 2.5 to 4 take-over speed not included in W_P for cruise. Rockets require thrust magnitude control (e.g., pintle, pulse, or gel motor) for effective cruise. Max range for a rocket is usually a semi-ballistic flight profile, instead of cruise flight. Multiple stages may be required for rocket range greater than 200 nm.

Fig. 3.3 Cruise range is driven by L/D, I_{sp}, velocity, and propellant or fuel weight fraction.

for carriage on a small fighter aircraft such as the F-18C. The predicted cruise range is based on the Breguet range equation

$$R = (L/D)I_{sp}Vln[W_L/(W_L - W_P)] \tag{3.1}$$

Note from the figure that subsonic cruise turbojet propulsion is the preferred approach for long-range strike against targets that are not time critical. Subsonic cruise turbojet propulsion has 120% greater range than the next best alternative, a supersonic cruise liquid-fuel ramjet (1800 vs 830 n miles). An examination of the Breguet range equation explains the difference in performance. The subsonic cruise turbojet missile is superior to the supersonic cruise ramjet missile in the maximum lift-to-drag ratio ($L/D = 10$ vs 5), specific impulse ($I_{SP} = 3000$ vs 1300 s), and available fuel for a specified launch weight of 2000 lb (600 vs 400 lb of fuel). The ramjet missile has less available weight for fuel because it requires a rocket to boost the missile up to about Mach 2.5 for transition to ramjet propulsion. However, a ramjet missile has an advantage of a shorter response time against time-critical targets. It may also have an advantage in survivability because of the higher flight altitude and higher speed. If time-critical targets are of utmost importance, scramjet propulsion may be preferred. As shown in the figure, the scramjet missile example is 70% faster than the ramjet (6000 vs 3500 ft/s). However, the maximum range of a scramjet missile that is limited to 2000 lb launch weight is only 37% that of a liquid-fuel ramjet (310 vs 830 n miles). Again, examining the Breguet range equation is instructive. The liquid-fuel ramjet missile is superior to the scramjet in its aerodynamic efficiency ($L/D = 5$ vs 3), specific impulse ($I_{SP} = 1300$ vs 1000 s),

and available fuel for a missile limited to 2000 lb launch weight (400 vs 200 lb of fuel). The scramjet missile has less available weight for fuel because it requires a larger rocket booster for a higher takeover Mach number (Mach 4 vs 2.5), requires a longer combustor for efficient combustion, and requires more insulation. Finally, the supersonic cruise rocket has a maximum flight range of 250 n miles. The most efficient cruise condition for the long-range rocket was found to be Mach 3 cruise at high altitude. The solid propellant rocket example uses thrust magnitude control from a pintle motor for more efficient acceleration and cruise. Although it is not shown, a semiballistic flight trajectory (e.g., launch, pitch-up, ballistic climb, glide) would have provided a more efficient flight trajectory for the rocket. For ranges greater than about 200 n miles, a rocket may benefit from multiple stages.

Based on an examination of the Breguet range equation, new technology development has payoff in the areas of high cruise velocity, aerodynamic efficiency (lift/drag), specific impulse, lightweight structure, lightweight/low volume subsystems, and high density fuel/propellant.

Shown in Fig. 3.4 is a comparison of tactical missile propulsion alternatives based on acceleration capability. It is a typical envelope of the maximum thrust-to-weight ratio. The comparison is shown as a function of Mach number. Note that the solid rocket has the highest thrust-to-weight ratio. This is because of high exit velocity, the independence of the exit velocity from that of the freestream velocity, and the capability for high mass flow rate. The exit velocity of a solid rocket is about 6000 ft/s, much higher than that of a typical ramjet (exit velocity about 4500 ft/s) or a typical turbojet (exit velocity about 2000 ft/s). Note from the maximum thrust equation for air-breathing propulsion

$$T_{\text{Max}} = (\pi/4)d^2\rho_0 V_0^2[(V_e/V_0) - 1] \tag{3.2}$$

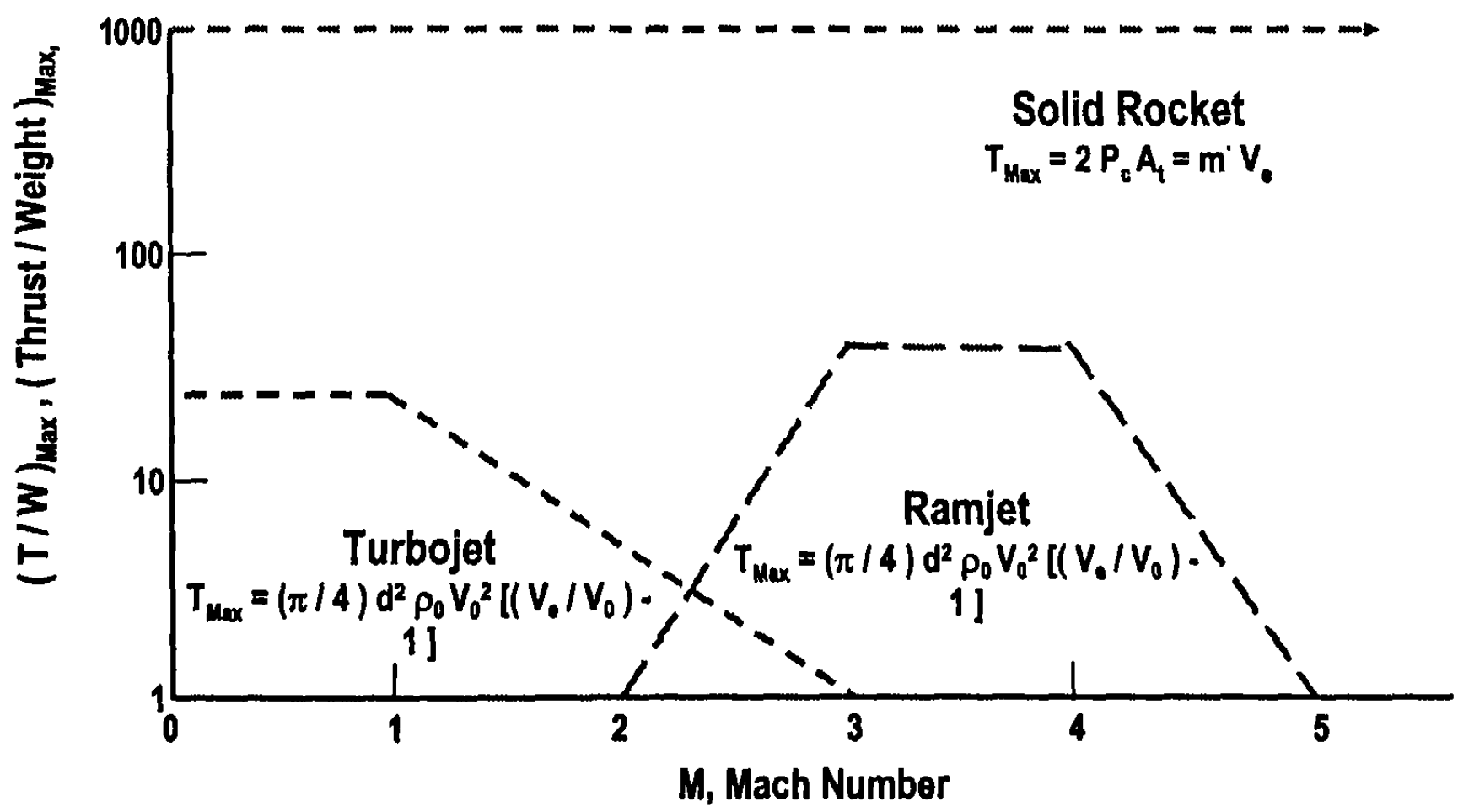

Note:
P_c = Chamber pressure, A_t = Nozzle throat area, $\dot{m}$ = Mass flow rate
d = Diameter, ρ_0 = Free stream density, V_0 = Free stream velocity,
V_e = Nozzle exit velocity (Turbojet: V_e ~ 2000 ft / s, Ramjet: V_e ~ 4500 ft / s, Rocket: V_e ~ 6000 ft / s)

Fig. 3.4 Solid rockets have high acceleration capability.

Turbojets and ramjets produce thrust only if the exit velocity is greater than the freestream velocity ($V_e > V_0$). The maximum velocity of an air-breathing missile is less than the exit velocity.

3.3 Turbojet Propulsion Temperature Technology Limit

The material temperature limits of the turbojet combustor and turbine usually limit the specific impulse and thrust of a turbojet, particularly for high-speed flight. Figure 3.5 is a schematic of the flow through a turbojet. The flow path consists of the initial free stream (station 0), inlet entrance (station 1), inlet exit/compressor entrance (station 2), compressor exit/combustor entrance (station 3), combustor exit/turbine entrance (station 4), and turbine exit/nozzle entrance (station 5). For a theoretical, ideal turbojet, the thermodynamic cycle consists of an isentropic compression of the flow by the inlet, isentropic compression by the compressor, constant pressure combustion in the combustor, isentropic expansion through the turbine, and isentropic expansion through the nozzle to freestream static pressure. For an ideal turbojet, the work extracted from the flow by the turbine is equal to the work that is required in driving the compressor.

Figure 3.6 shows the impact of the compressor pressure ratio and the flight Mach number on the compressor exit temperature T_3. Note from the figure that the compressor has high temperatures for high compressor pressure ratios and high freestream Mach Numbers. An assumption is low subsonic flow through the compressor such that the static temperature is nearly equal to the total temperature ($T_3 \approx T_{3t}$). For an ideal compressor, with isentropic flow, the compressor exit temperature is

$$T_3 \approx T_0\{1 + [(\gamma_0 - 1)/2]M_0^2\}(p_3/p_2)^{(\gamma_3-1)/\gamma_3} \tag{3.3}$$

If the temperature of air is less than 800 R, it behaves as a calorically perfect gas with a constant specific heat ratio of $\gamma = 1.4$. If the temperature of air is

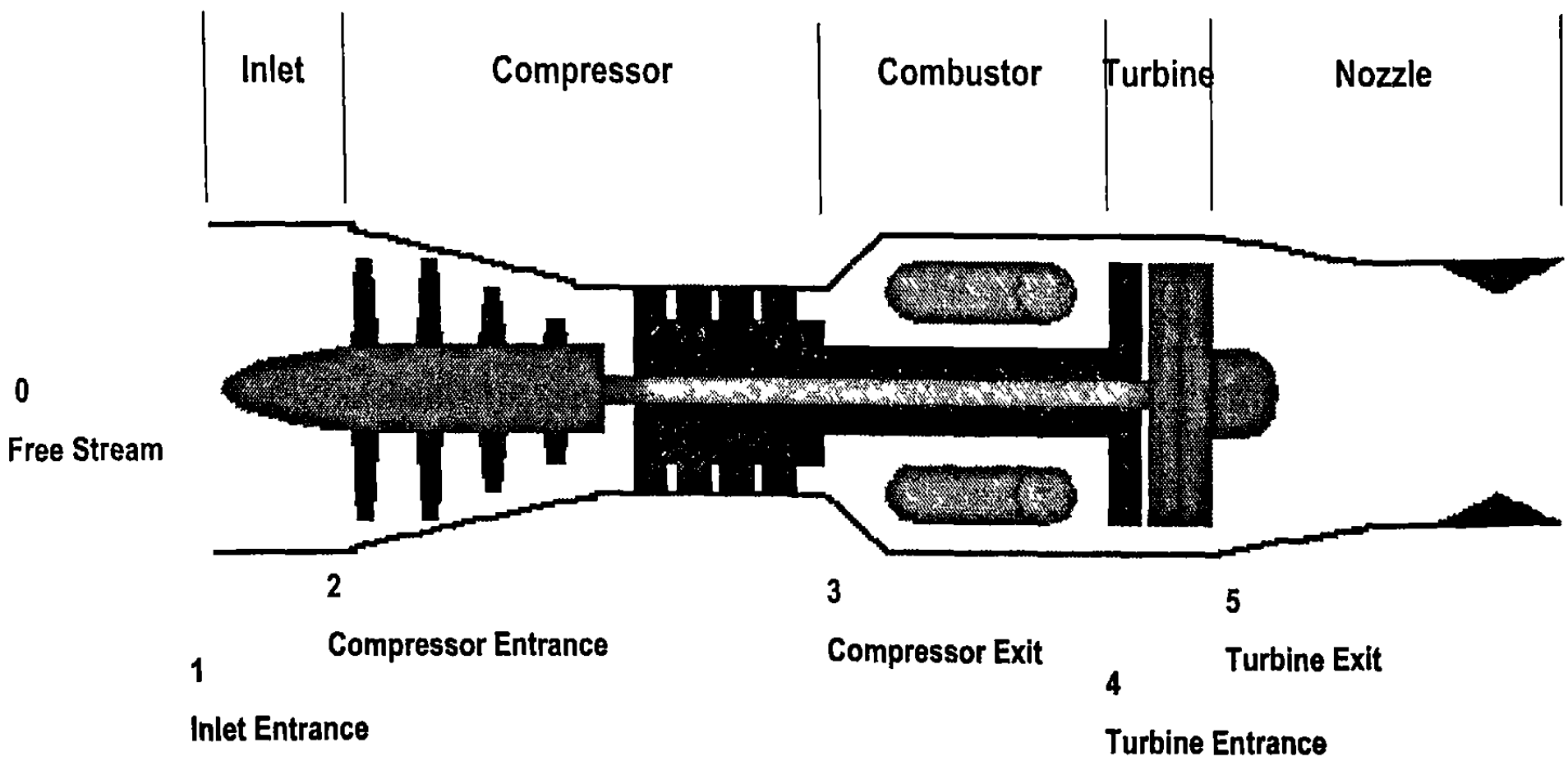

Fig. 3.5 Turbojet nomenclature.

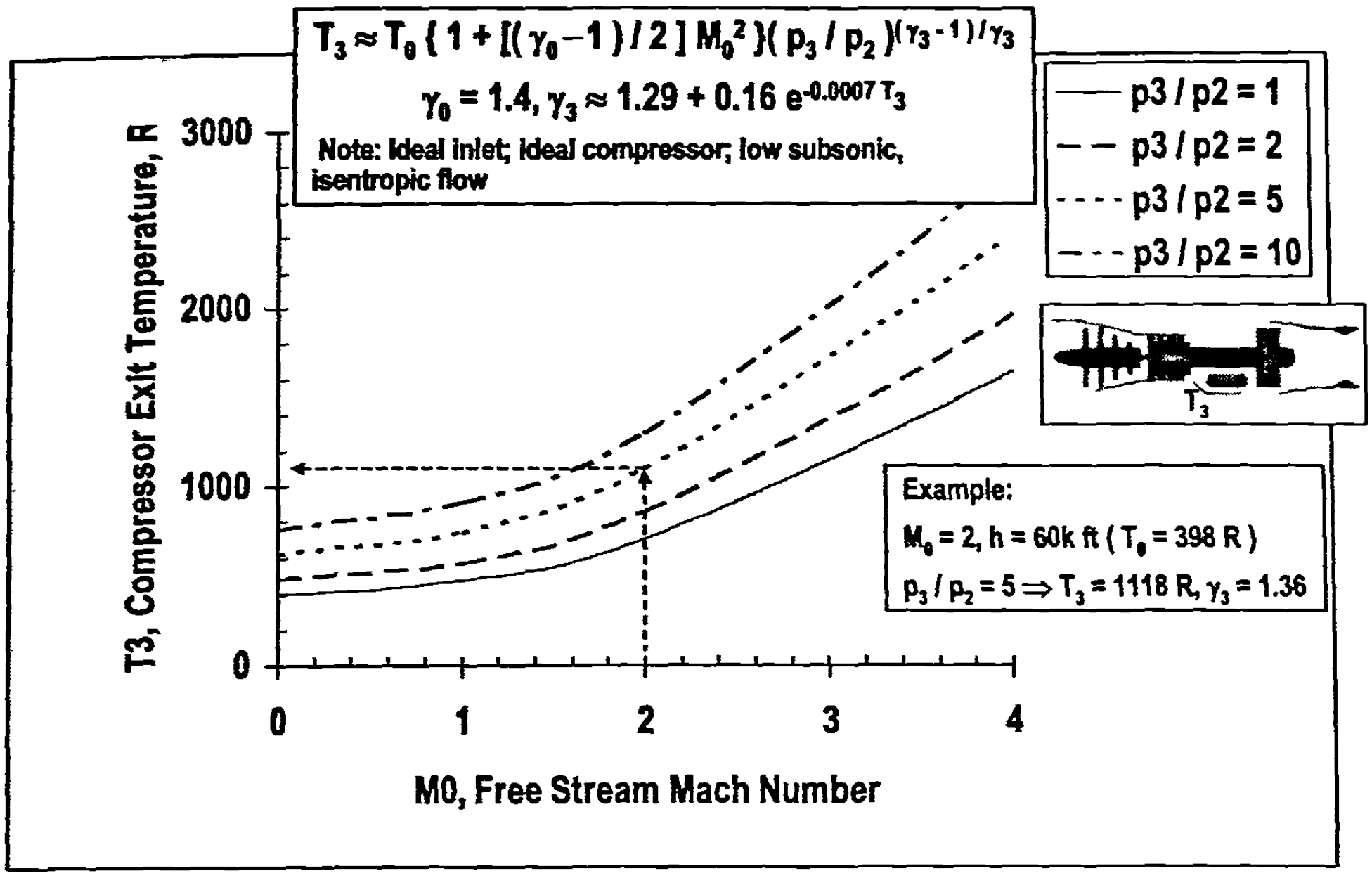

T_3 = Compressor exit temperature in Rankine, T_0 = freestream temperature in Rankine, γ = specific heat ratio, M_0 = free stream Mach number, p_3 = compressor exit pressure, p_2 = compressor entrance pressure

Fig. 3.6 High-temperature compressors are required to achieve high pressure ratio at high speed.

greater than 800 R but less than 5000 R, the vibration states of oxygen and nitrogen molecules affect the specific heat ratio. The air behaves as a thermally perfect gas with the specific heat ratio a function of temperature. If the temperature of air is greater than 5000 R, the oxygen molecules of the air chemically react to form dissociated atomic oxygen. An equation for γ for air temperatures up to 5000 R is

$$\gamma \approx 1.29 + 0.16\, e^{-0.0007T} \tag{3.4}$$

As an example, assume a flight number of $M_0 = 2$, a flight altitude of $h = 60{,}000$ ft, and a compressor pressure ratio of $p_3/p_2 = 5$. Substituting into the equations for compressor exit temperature and specific heat ratio gives $T_3 = 1118$ R for a value of $\gamma_3 = 1.36$.

Figure 3.7 shows the impact of compressor exit temperature and fuel-to-air ratio on the turbine entrance temperature. It is assumed that the turbine entrance temperature is the same as the combustor exit temperature. Note from the figure that the turbine temperature is high for high values of compressor temperature and fuel-to-air ratio. An assumption is low subsonic flow into the turbine, such that the static temperature is nearly equal to the total temperature ($T_4 \approx T_{4t}$). For an ideal turbine, the turbine entrance temperature T_4 is equal to the sum of the compressor exit temperature T_3 plus the temperature rise from combustion. The equation is

$$T_4 \approx T_3 + (H_f/c_p) f/a \tag{3.5}$$

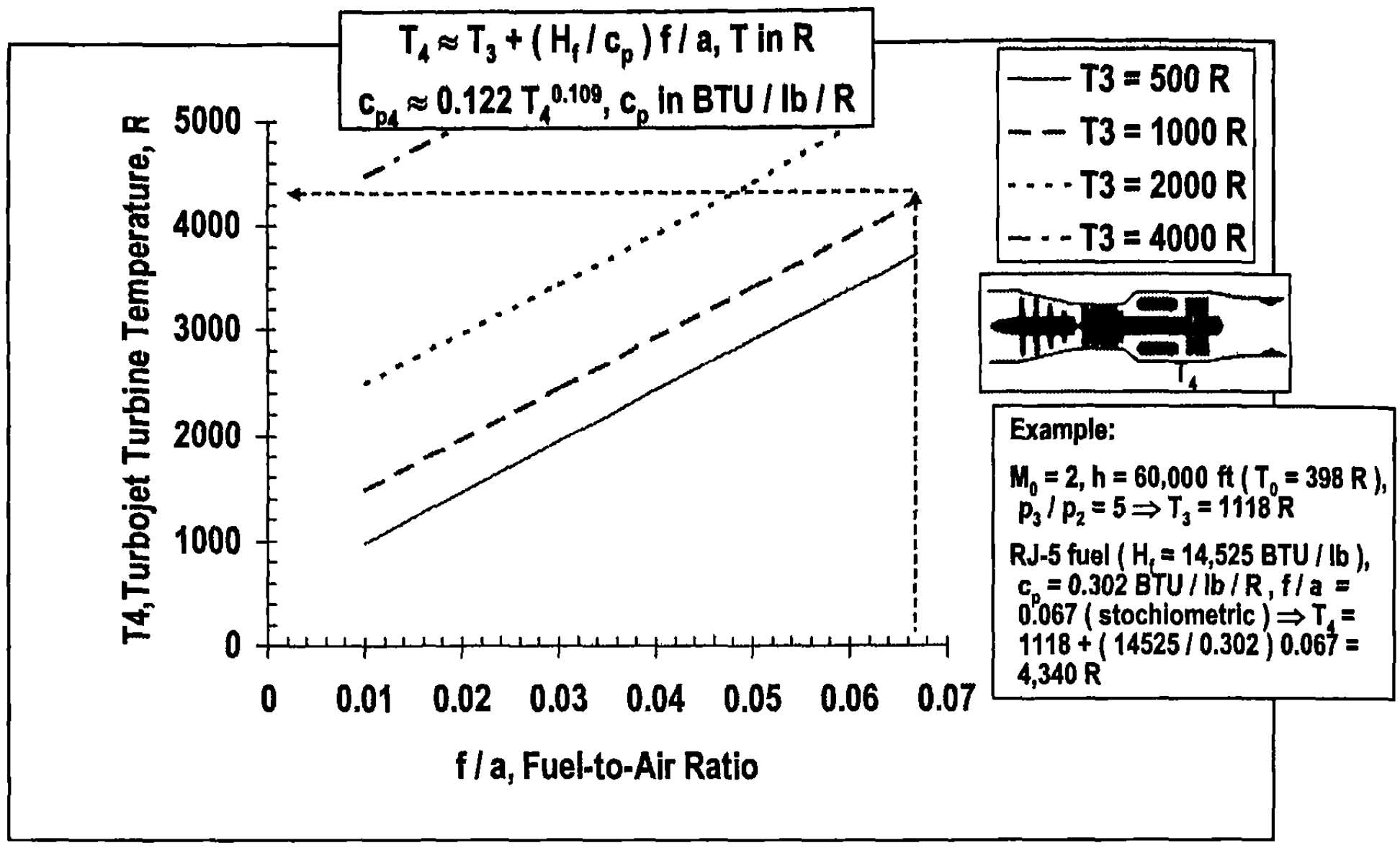

T_4 = Turbojet turbine entrance temperature in Rankine, T_3 = compressor exit temperature in Rankine, H_f = heating value of fuel, c_p = specific heat at constant pressure, f / a = fuel-to-air ratio

Fig. 3.7 High turbine temperature is required for high-speed turbojet missiles.

In the above equation H_f = heating value of fuel, c_p = specific heat at constant pressure, and f/a = fuel-to-air ratio. The specific heat at constant pressure is a function of temperature, given by the equation

$$c_p \approx 0.122T^{0.109} \tag{3.6}$$

The units of c_p are Btu/lb/R.

The range of fuel-to-air ratio shown in the figure is from $f/a = 0.01$, which is a lean typical lower limit of combustor blowout, to $f/a = 0.067$, which is stochiometric combustion.

As an example, let us calculate the turbine entrance temperature for flight at Mach 2 and $h = 60{,}000$ ft altitude. Assume a compressor pressure ratio $p_3/p_2 = 5$; RJ-5 hydrocarbon fuel, which has a heating value of $H_f = 14525$ Btu/lb; and stochiometric combustion, which has a fuel-to-air ratio $f/a = 0.067$. Substituting into the previous equation for compressor exit temperature gives $T_3 = 1118$ R. Substituting into the equations for turbine entrance temperature and specific heat at constant pressure gives $T_4 = 4340$ R for a value of $c_p = 0.302$ Btu/lb/R.

Hypersonic turbojet propulsion is not currently practical because of the turbine material temperature limits. An assessment is given in Table 3.1 of the achievable specific impulse at Mach 4 cruise for current and advanced materials. Nickel-based super alloys such as Inconel, Rene, Hastelloy, and Haynes have a maximum temperature limit of about 3000 R for short-duration turbines. For Mach 4 cruise, limiting the turbine temperature to 3000 R has a large negative impact on the specific impulse I_{SP}. Limiting the compressor ratio to less than

Table 3.1 Turbine material temperature limit is a constraint for a high-speed turbojet missile

Max Short Duration Temp	Turbine Material	Temperature Constrained Turbines for Mach 4 Cruise	I_{SP} for Mach 4 Cruise
≈3000R	Nickel Super Alloys	Very Highly Constrained Turbojet, Air Turbo Rocket, Turbo Ramjet	≈1000s
≈3000R	Titanium Aluminides (lighter weight than nickel super alloys)	Very Highly Constrained Turbojet, Air Turbo Rocket, Turbo Ramjet	≈1000s
≈3500R	Single Crystal Nickel Aluminides	Highly Constrained Turbojet	≈1200s
≈4000R	Ceramic Matrix Composites	Moderately Constrained Turbojet	≈1500s
≈4500R	Rhenium Alloys	Moderately Constrained Turbojet	≈2000s
≈5000R	Tungsten Alloys	Slightly Constrained Turbojet	≈2500s

Note: Constrained turbojet for Mach 4 cruise imposes a limit on turbine temperature that is less than ideal. Constraints could consist of a combination of:

- Constraint on compressor pressure ratio to limit turbine temperature
- Constraint on fuel-to-air ratio to limit turbine temperature
- Use of afterburner to limit turbine temperature

optimum, limiting the fuel-to-air ratio to less than optimum, or using an afterburner can constrain the turbine temperature, but with reduced I_{SP}. For a turbine temperature limit of 3000 R, a very highly constrained turbojet has an I_{SP} of about 1000 s for Mach 4 flight, about 33% of the subsonic I_{SP}. Other potential turbine-based propulsion systems, such as an air turbo rocket or a turbo ramjet, would also have a Mach 4 I_{SP} of about 1000 s. Another advanced high-temperature material is titanium aluminide. Titanium aluminide is a more expensive but lighter weight alternative to nickel super alloys. The temperature limit of a titanium aluminide turbine is also about 3000 R, giving a Mach 4 I_{SP} of about 1000 s. As before, the turbine-based Mach 4 propulsion alternatives would be a very highly constrained turbojet, an air turbo rocket, or a turbo ramjet. Another advanced material, with a higher temperature capability, is single crystal nickel aluminide. The maximum short-duration turbine temperature is about 3500 R, which would provide a Mach 4 I_{SP} of about 1200 s for a highly constrained turbojet, with about 40% of the subsonic I_{SP}. For a turbine temperature of 3500 R, a turbojet is preferred over the alternatives of an air turbo rocket or a turbo ramjet because of its higher I_{SP}. A higher temperature but higher risk turbine material is ceramic matrix composite. A concern is fracture sensitivity. Short-duration maximum turbine temperature is about 4000 R, which would provide a Mach 4 I_{SP} of about 1500 s for a moderately constrained turbojet, about 50% of the subsonic I_{SP}. As before, the turbojet would be preferred over either an air turbo rocket or a turbo ramjet. Rhenium would allow a short-duration turbine temperature of about 4500 R, allowing a Mach 4 turbojet

I_{SP} of about 2000 s, about 67% of the subsonic I_{SP}. Disadvantages of rhenium are high cost and weight. However, rhenium has good potential for high-temperature applications, and its cost should decrease in the future. The SM-3 Standard Missile Third Stage Rocket Motor (TSRM) is an example of an application of rhenium. Finally, the highest temperature turbine material is tungsten, which has a maximum temperature of about 5000 R for a short-duration application. The I_{sp} of a Mach 4 turbojet using a tungsten-based turbine is about 2500 s, which is 83% of the subsonic I_{SP}. Although a tungsten-based turbine would only slightly constrain a Mach 4 turbojet, tungsten has a risk of fracture sensitivity, is difficult to fabricate to precision tolerance, and is very heavy. However, the relatively small constraint of limiting a tungsten turbine to a temperature of 5000 R, a value that is somewhat lower than ideal temperature for Mach 4 cruise, would result in a compressor pressure ratio slightly less than ideal and a fuel-to-air ratio slightly less than stochiometric, or it would require a small amount of afterburning.

It was previously shown that a turbine-based missile has longer range than a ramjet. Another advantage is a capability to loiter over the target area. Although a turbine-based missile is capable of subsonic through supersonic cruise, to date there are few examples. These are shown in Fig. 3.8. Examples of supersonic turbojets are the low supersonic Firebee II, the low supersonic Regulus II, and the higher supersonic SS-N-19 Shipwreck. There are no examples of a turbo ramjet missile. Turbo ramjets are complicated, requiring variable bypass air, and may be too expensive for missile applications. The high supersonic SR-71 has turbo ramjet propulsion. An air turbo rocket is a relatively new technology. The relatively low temperature gas from a fuel-rich gas generator drives the turbine, which drives the compressor. Freestream air is compressed by the compressor and then flows into the combustor, where it mixes with the fuel-rich gas from the gas generator. Secondary combustion occurs, followed by

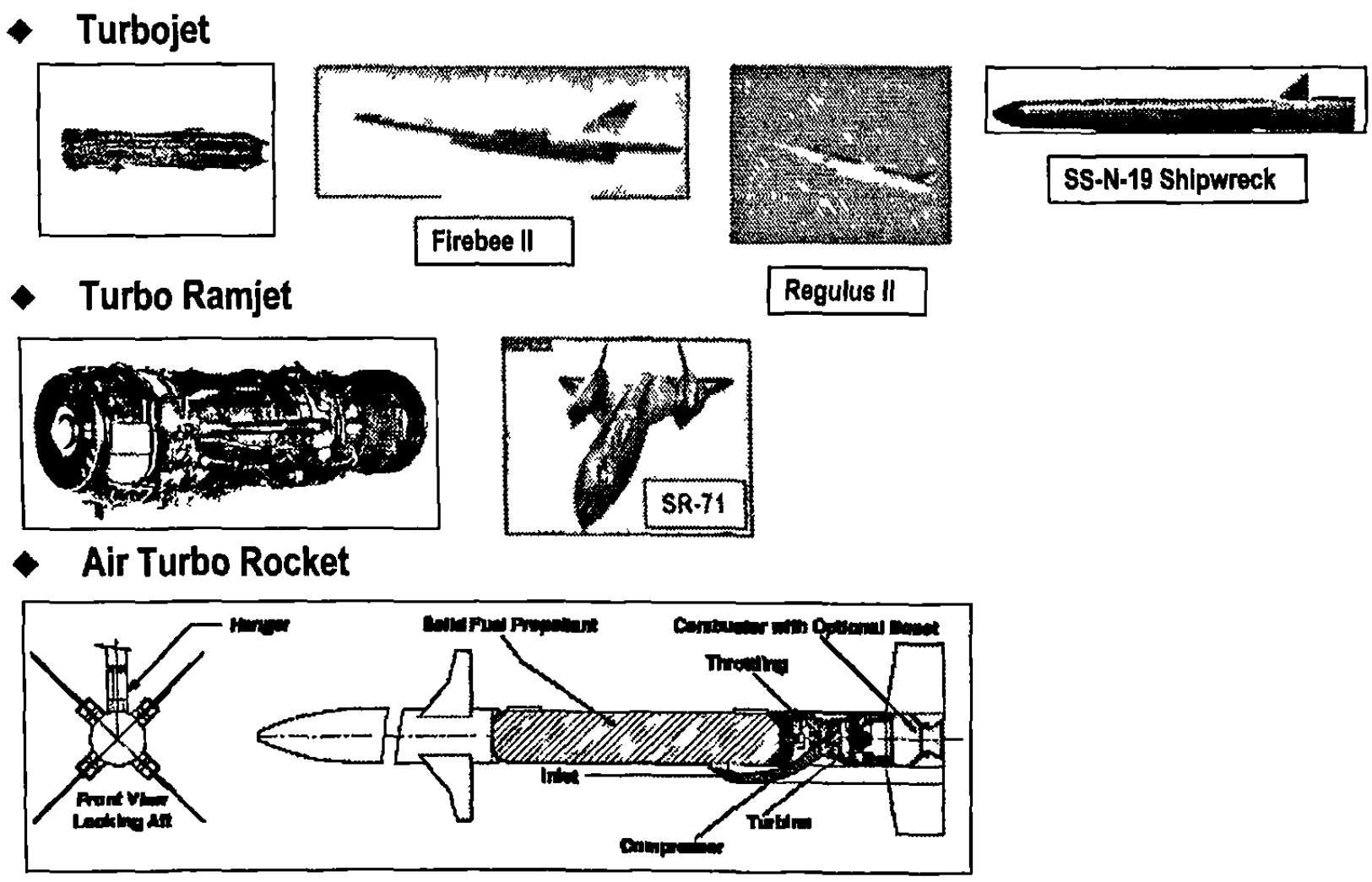

Fig. 3.8 Turbine-based missiles are capable of subsonic to supersonic cruise. Figure also in color section.

expansion through the nozzle. An advantage of an air turbo rocket is the turbine is not exposed to the high temperature of secondary combustion in the combustion chamber. An air turbo rocket has a higher I_{SP} than a ducted rocket but a lower I_{SP} than an unconstrained turbojet.

A multimission strike missile using turbine-based propulsion has high potential. It could counter both conventional targets and time-critical targets. Benefits of a turbine-based propulsion system could include 1) subsonic cruise efficiency against long-range targets that are not time critical; 2) fast response (e.g., Mach 4 cruise) against time-critical targets; 3) subsonic loiter capability; and 4) reduced logistics/cost of a multimission missile.

Turbojet thrust is usually limited by the turbine temperature. For a specified turbine temperature, there is an optimum value of the compressor ratio that gives maximum thrust. For an ideal turbojet, from Ashley[11]

$$(p_3/p_2)_{@T\max} \approx \{(T_4/T_0)^{1/2}/\{1+[(\gamma_0-1)/2]M_0^2\}\}^{\gamma_4/(\gamma_4-1)} \tag{3.7}$$

The assumptions in the above equation are isentropic inlet, compressor, turbine, and nozzle; low subsonic flow through the compressor ($p_3 \approx p_{3_t}$, $p_2 \approx p_{2_t}$); low subsonic flow and constant pressure through the combustor; and the nozzle exit pressure equal to the freestream pressure.

Figure 3.9 shows that at subsonic Mach number the ideal pressure ratio for maximum thrust is very high [e.g., $(p_3/p_2)_{@T\max} \gg 10$]. A technology limit at low Mach number is achieving high compressor ratios. At the other extreme, the figure shows that at high supersonic Mach numbers, low values of p_3/p_2 are optimum for maximum thrust. Considering the limit for the practical use of a

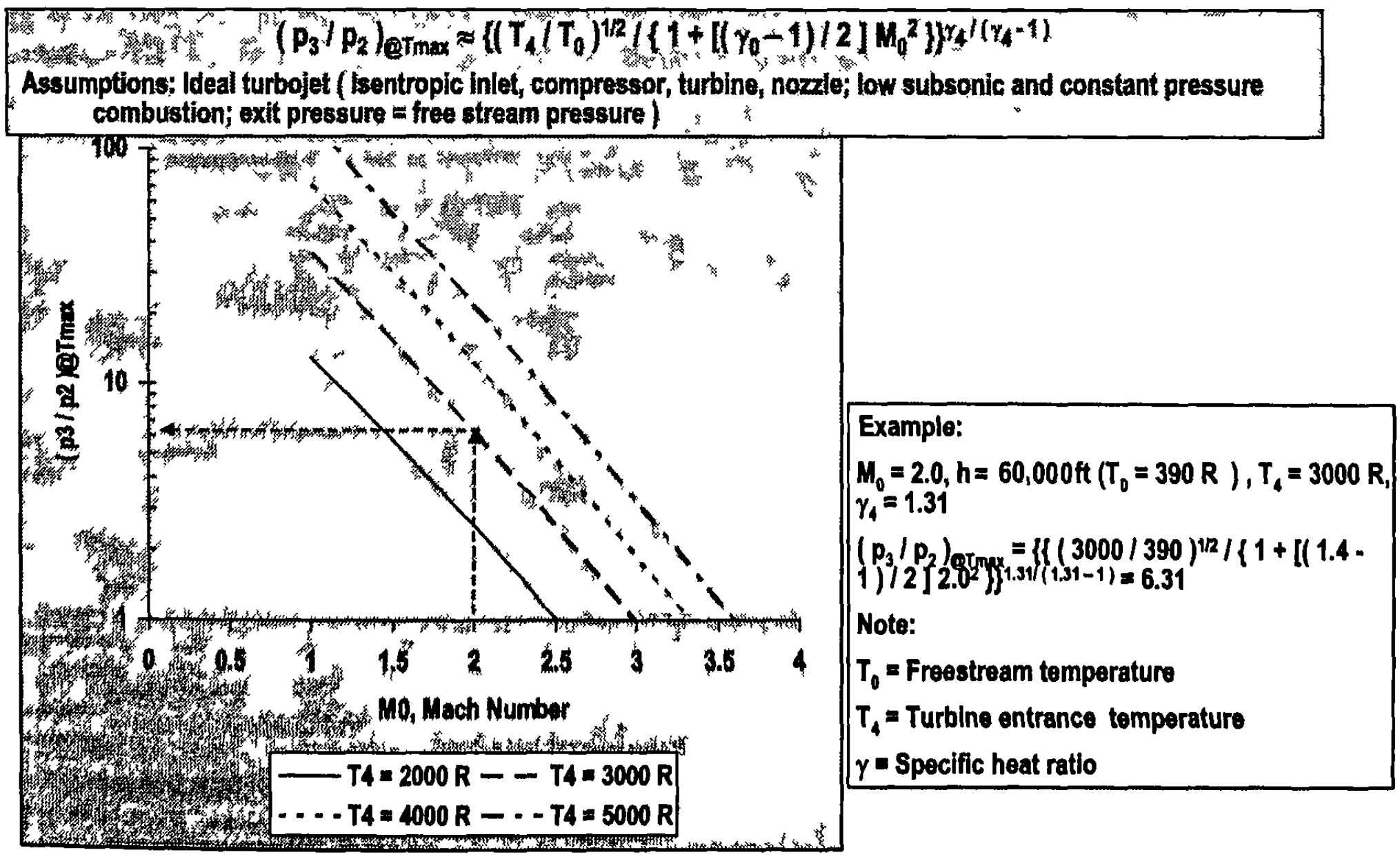

Source: Ashley, H., *Engineering Analysis of Flight Vehicles*, Dover Publications, Inc., New York, 1974

Fig. 3.9 Compressor pressure ratio for a maximum thrust turbojet is limited by turbine temperature.

turbojet, at very high supersonic Mach numbers the ideal pressure ratio approaches 1 (ramjet operation). Turbojet operation at very high supersonic Mach number, with $p_3/p_2 > 1$, requires high-temperature combustion/high-temperature turbine.

As an example calculation of $(p_3/p_2)_{@T\max}$, assume $M_0 = 2$, $h = 60{,}000$ ft altitude ($T_0 = 390$ R), $T_4 = 3000$ R, and $\gamma_4 = 1.31$. Calculate

$$(p_3/p_2)_{@T\max} = \{\{(3000/390)^{1/2}/\{1 + [(1.4 - 1)/2]2^2\}\}^{1.31/(1.31-1)} = 6.31 \tag{3.8}$$

3.4 Turbojet Thrust Prediction

Shown in Fig. 3.10 is the nondimensional thrust of an ideal turbojet. The equation is

$$T_{\text{IdealMax}}/(p_0 A_0) = (\gamma_0 M_0/a_0)(T/\dot{m})_{\text{IdealMax}} \tag{3.9}$$

Assumptions are isentropic flow through the inlet, compressor, turbine, and nozzle; low subsonic flow through the compressor; low subsonic flow and constant pressure through the combustor; and nozzle exit pressure equal to the freestream pressure. The thrust equation is derived from the momentum equation

$$T = \dot{m}(V_e - V_0) \tag{3.10}$$

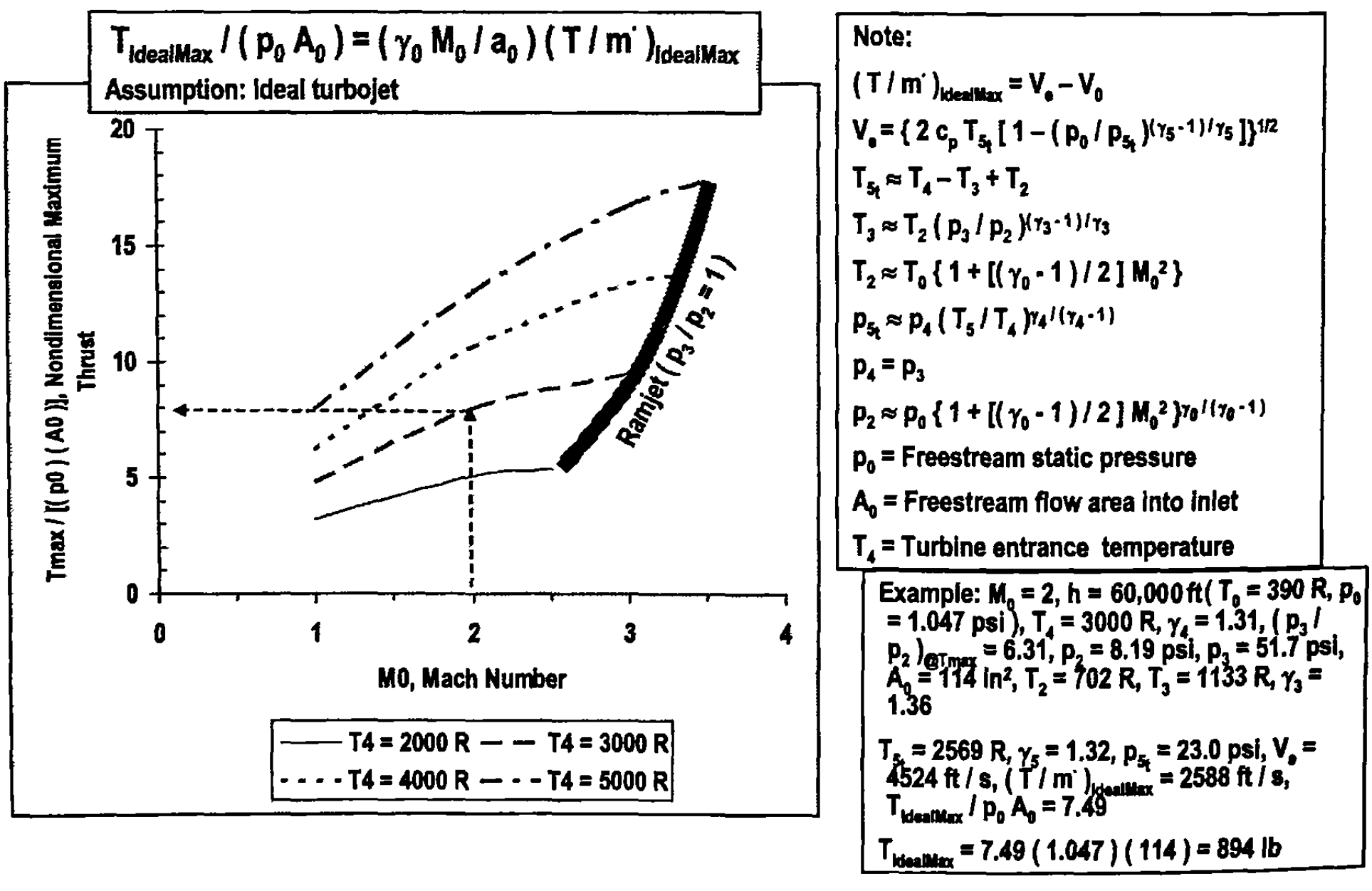

Fig. 3.10 Turbojet thrust is limited by the turbine maximum allowable temperature.

The equation for the exit velocity of an ideal turbojet is

$$V_e = \{2c_p T_{5_t}[1 - (p_0/p_{5_t})^{(\gamma_5-1)/\gamma_5}]\}^{1/2} \tag{3.11}$$

The primary terms to be determined in the above equation are the turbine exit total temperature T_{5_t} and the turbine exit pressure p_{5_t}. The equation for the turbine exit total temperature of an ideal turbojet is $T_{5_t} \approx T_4 - T_3 + T_2$. The temperatures in this equation are the combustor temperature T_4, compressor exit temperature T_3, and the compressor entrance/inlet ext temperature T_2. In this analysis the combustor temperature T_4 is specified. For the ideal turbojet, the compressor exit temperature is

$$T_3 \approx T_2(p_3/p_2)^{(\gamma_3-1)/\gamma_3} \tag{3.12}$$

The compressor entrance temperature is

$$T_2 \approx T_0\{1 + [(\gamma_0 - 1)/2]M_0^2\} \tag{3.13}$$

Next, the term p_{5_t} in the exit velocity equation can be solved from

$$p_{5_t} \approx p_4(T_{5_t}/T_4)^{\gamma_4/(\gamma_4-1)} \tag{3.14}$$

We will assume constant pressure combustion ($p_4 = p_3$). In this analysis, the compressor pressure ratio p_3/p_2 is specified. Compressor entrance/inlet exit pressure p_2, for adiabatic flow through the inlet, is

$$p_2 \approx p_0\{1 + [(\gamma_0 - 1)/2]M_0^2\}^{\gamma_0/(\gamma_0-1)} \tag{3.15}$$

Note from the figure that high thrust for an ideal turbojet occurs for high atmospheric pressure p_0 (low altitude), large inlet capture area A_0, high freestream Mach number M_0, and high combustor exit/turbine entrance temperature T_4. Also note the boundary at the right side of the figure (ramjet operation, with a compressor pressure ratio $p_3/p_2 = 1$).

As an example calculation of the maximum thrust of an ideal turbojet, assume $A_0 = 114\ \text{in}^2$, $T_4 = 3000$ R, $M_0 = 2$, and $h = 60{,}000$ ft altitude ($T_0 = 390$ R, $p_0 = 1.047$ psi, $a = 968$ ft/s). From the previous example, $\gamma_4 = 1.31$ and $(p_3/p_2)_{@\text{Tmax}} = 6.31$. Calculate

$$p_2 = 1.047\{1 + [(1.4 - 1)/2]2^2\}^{1.4/(1.4-1)} = 8.19 \text{ psi} \tag{3.16}$$

$$T_2 = 390\{1 + [(1.4 - 1)/2]2^2]\} = 702 \text{ R} \tag{3.17}$$

Solve for

$$p_3 = p_4 = 6.31(8.19) = 51.7 \text{ psi} \tag{3.18}$$

$$T_3 = 702(6.31)^{(1.36-1)/1.36} = 1133 \text{ R} \tag{3.19}$$

$$\gamma_3 = 1.29 + 0.16\,\mathrm{e}^{-0.0007(1133)} = 1.36 \tag{3.20}$$

Substituting the values of the T_4, T_3, and T_2 temperatures gives

$$T_{5_t} = 3000 - 1133 + 702 = 2569 \text{ R} \tag{3.21}$$

$$\gamma_5 = 1.32 \tag{3.22}$$

Substituting the values of p_4, T_{5_t}, T_4, and γ_4 into the equation for the turbine exit total pressure gives

$$p_{5_t} = 51.7(2569/3000)^{1.31/(1.31-1)} = 23.0 \text{ psi} \tag{3.23}$$

Also, substituting the values of c_{p_5}, T_{5_t}, p_{5_t}, p_0, and γ_5 in into the exit velocity equation gives

$$V_e = 4524 \text{ ft/s} \tag{3.24}$$

Thrust per unit mass flow rate (also the incremental velocity), is then

$$\mathrm{T}/\dot{\mathrm{m}} = 4524 - 1936 = 2588 \text{ ft/s} \tag{3.25}$$

All of the required terms are now available to substitute in the nondimensional thrust equation, giving

$$T_{\mathrm{IdealMax}}/(p_0 A_0) = [1.4(2)/968](2588) = 7.49 \tag{3.26}$$

Substituting the freestream static pressure p_0 and inlet capture area A_0 into the above equation gives the thrust

$$T_{\mathrm{IdealMax}} = 7.49(1.047)(114) = 894 \text{ lb} \tag{3.27}$$

3.5 Turbojet Specific Impulse Prediction

Figure 3.11 shows the nondimensional specific impulse of an ideal turbojet. It is based on the equation

$$(I_{\mathrm{SP}})_{\mathrm{Ideal@T_{max}}} g_c c_p T_0/(a_0 H_f) = T_{\mathrm{IdealMax}} T_0/[(p_0 A_0 \gamma_0 M_0)(T_4 - T_3)] \tag{3.28}$$

Assumptions are maximum thrust; isentropic flow through the inlet, compressor, turbine, and nozzle; low subsonic flow through the compressor ($T_3 \approx T_{3_t}$);

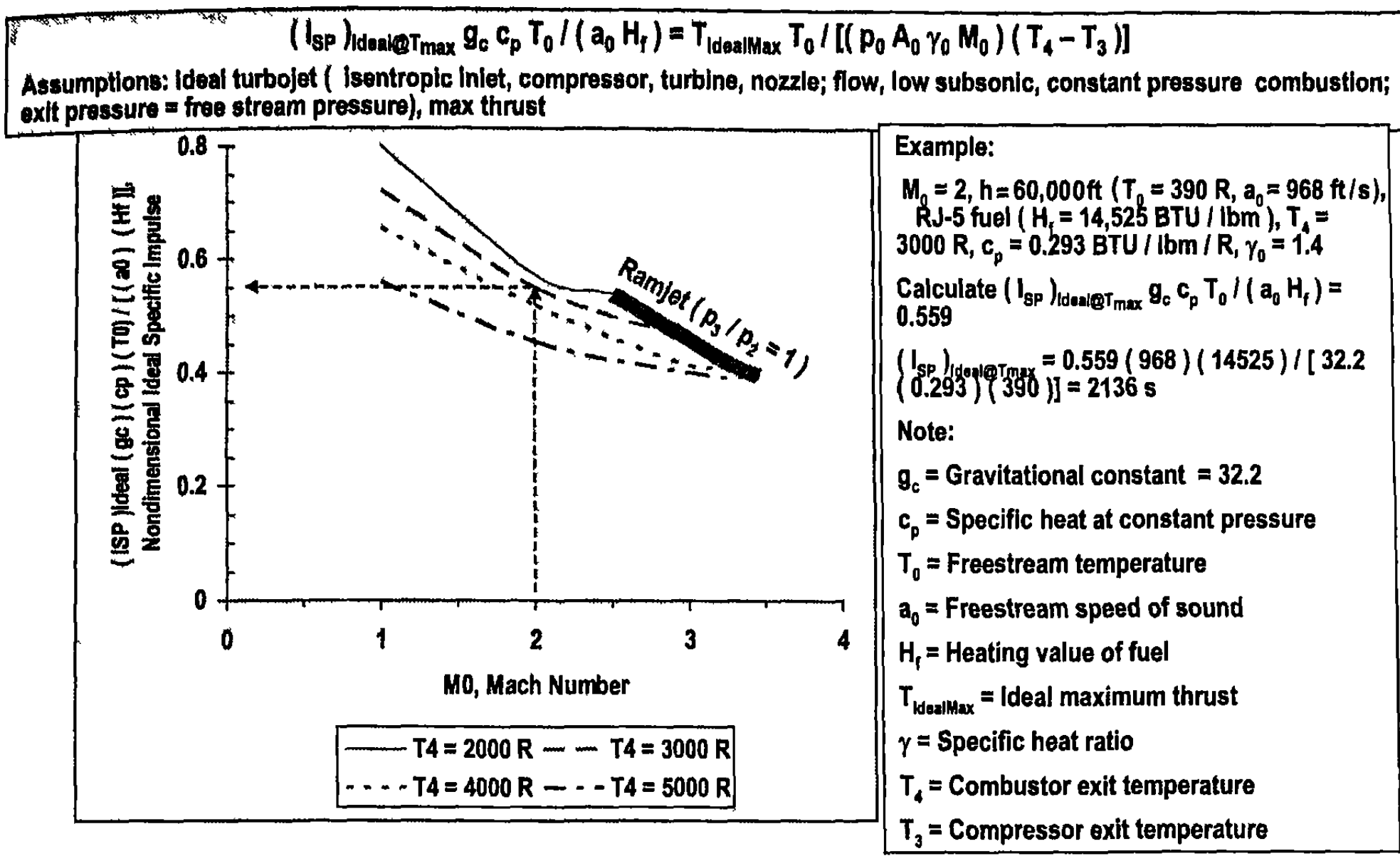

Fig. 3.11 Turbojet specific impulse decreases with supersonic Mach number.

combustor has low subsonic flow ($T_4 \approx T_{4_t}$) and constant pressure ($p_4 = p_3$); and nozzle exit pressure equal to the freestream pressure.

The example calculation of turbojet specific impulse will be based on the same conditions as the previous example calculation of turbojet thrust, which were $A_0 = 114\,\text{in}^2$, $T_4 = 3000\,\text{R}$, $M_0 = 2$, and $h = 60{,}000$ ft altitude ($T_0 = 390\,\text{R}$, $p_0 = 1.047$ psi, $a = 968$ ft/s). Also, from the previous example, $T_3 = 1133$ R, $c_p = 0.293$ Btu/lbm/R, and $T_{\text{IdealMax}} = 894$ lb. We shall assume the fuel is RJ-5, which has a heating value $H_f = 14{,}525$ Btu/lbm/R. Substituting, the non-dimensional specific impulse is

$$(I_{SP})_{\text{Ideal@}_{T\max}} g_c c_p T_0/(a_0 H_f) = 894(390)/[1.047(114)(1.4)(2)(3000 - 1133)] = 0.559 \tag{3.29}$$

Substituting the values of the freestream speed of sound a_0, heating value of RJ-5 fuel H_f, gravitational constant g_c, specific heat at constant pressure c_p, and freestream temperature T_0 gives the specific impulse

$$(I_{SP})_{\text{Ideal@}_{T\max}} = 0.559(968)(14525)/[32.2(0.293)(390)] = 2136 \text{ s} \tag{3.30}$$

3.6 Ramjet Propulsion Alternatives

Figure 3.12 illustrates tactical missile ramjet propulsion alternatives of liquid-fuel ramjet, solid-fuel ramjet, and ducted rocket. The examples are based on an integral rocket ramjet, with the rocket booster occupying the same volume as the ramjet engine combustor. Shown in the upper portion of each example is the

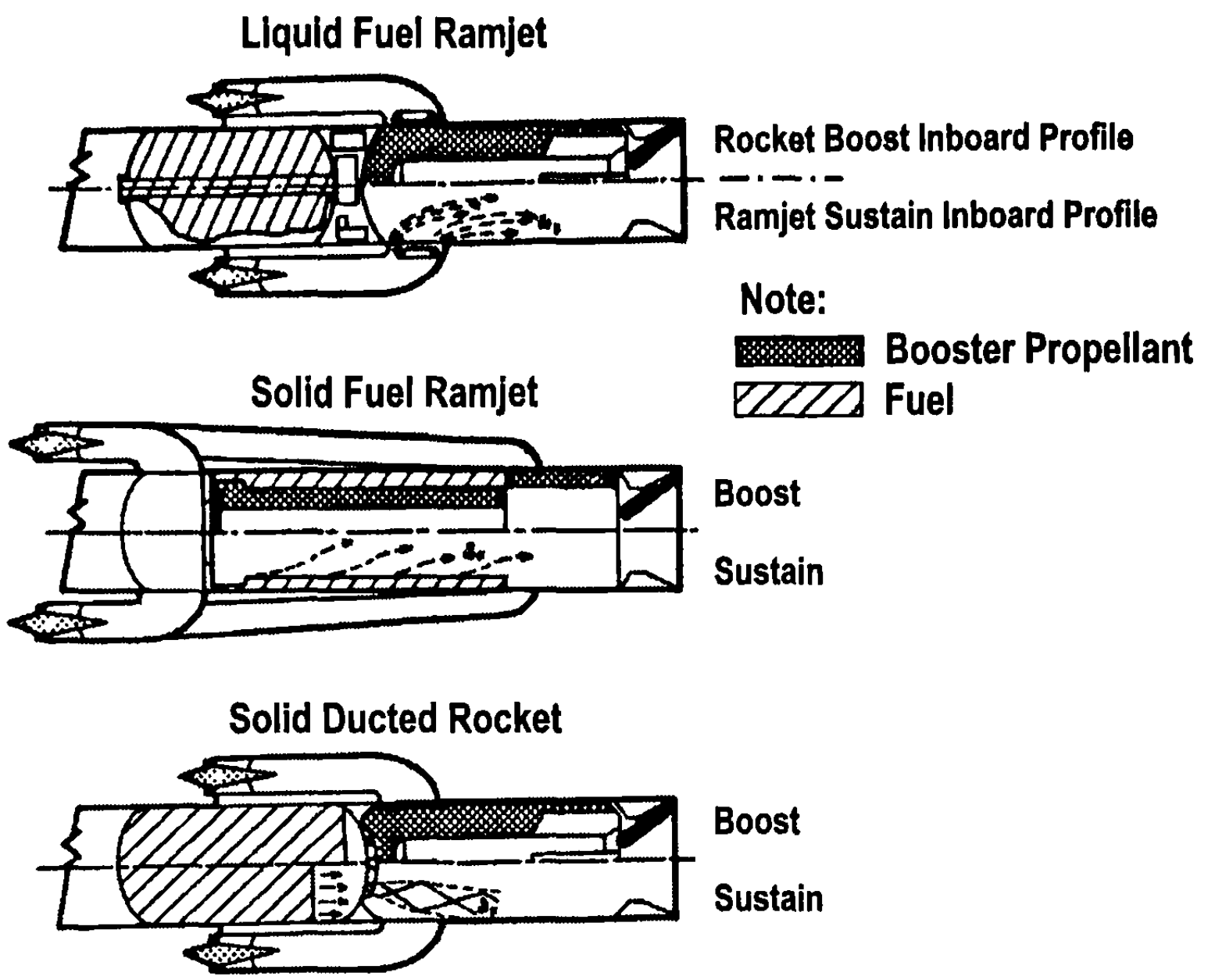

Fig. 3.12 Tactical missile ramjet propulsion alternatives.

rocket booster configuration during boost. The bottom portion of each example shows the ramjet engine configuration during sustain. Ramjet propulsion is relatively simple compared to turbojet propulsion; it has no moving parts. Air enters the inlet at supersonic velocity and is decelerated to low subsonic speed (e.g., Mach 0.2) at the combustor entrance. Downstream of the combustor is a convergent-divergent nozzle, which accelerates the airflow back to supersonic velocity. The maximum specific impulse of a hydrocarbon liquid-fuel ramjet is about 1500 s, much higher than the specific impulse of a solid rocket. An efficient cruise condition for a liquid-fuel ramjet is about Mach 4, 80,000 ft altitude. As mentioned previously, the maximum Mach number is about 5. Because a ramjet is inefficient at low supersonic Mach number, a rocket is required for subsonic launch to boost the missile to the ramjet thrust takeover at about Mach 2.5. Liquid-fuel ramjets are synergistic with noncircular, lifting body airframes because fuel can be stored in noncircular tanks. Liquid-fuel ramjets can be throttled for efficient matching of the fuel with the inlet airflow over a broad flight envelope of Mach number and altitude.

A variation on the traditional liquid-fuel ramjet is the solid-fuel ramjet. The solid-fuel ramjet has a fuel grain with a hollow center core for the inlet airflow. An advantage of the higher density solid fuel is its volumetric performance. Disadvantages are limited throttle capability, reduced volumetric loading of the fuel because of the hollow center grain, and lower combustion efficiency. Some passive fuel flow compensation is achieved from changing flight conditions. If a larger variation in fuel flow rate is required, shaping of the fuel grain is needed, at a loss in volumetric loading. Other means of thrust management, such as variable geometry inlets or nozzles, are not cost effective for tactical missiles.

As mentioned previously, a ducted rocket has a specific impulse of about 500–800 s, intermediate to that of a solid rocket and a ramjet. Ducted rockets are most efficient for Mach 2.5 to 4. Ducted rockets have higher acceleration (higher thrust) than ramjets and longer range (higher specific impulse) than solid rockets. A gas generator provides fuel-rich products to the combustor. The gas generator flow rate can be controlled, providing a throttle capability for thrust magnitude control.

The integration of the ramjet booster impacts the missile compatibility for launch platform length and diameter constraints. Integral boosters that occupy the combustor case improve volumetric efficiency and reduce weight, enhancing integration with the launch platform. Another integration challenge for the booster is to minimize fratricide by having no ejecta. A nozzleless booster with a common booster case/ramjet combustor avoids nozzle and booster ejecta. A nozzleless booster has a cast propellant grain that maintains the throat and divergence geometry during motor burn.

3.7 Ramjet Specific Impulse Prediction

Shown in Fig. 3.13 is the nondimensional specific impulse of an ideal ramjet.[11] The equation is

$$(I_{SP})_{Ideal} g_c c_p T_0/(a_0 H_f) = \{M_0\{\{(T_4/T_0)/\{1+[(\gamma_0-1)/2]M_0^2\}\}^{1/2}-1\}/ \{\{1+[(\gamma_0-1)/2]M_0^2\}\{(T_4/T_0)/ \{1+[(\gamma_0-1)/2]M_0^2\}\}-1\} \tag{3.31}$$

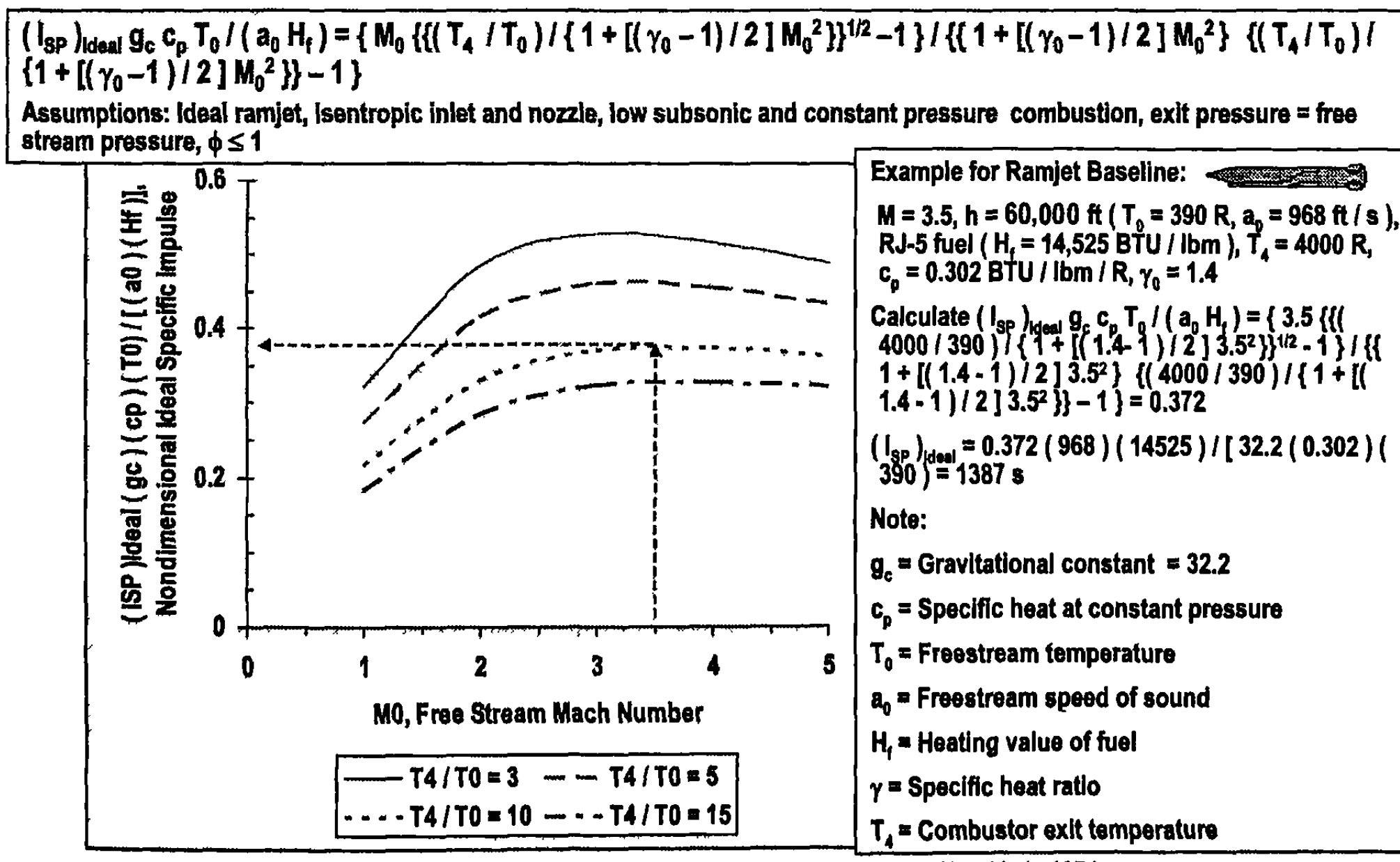

Source: Ashley, H., *Engineering Analysis of Flight Vehicles*, Dover Publications, Inc., New York, 1974

Fig. 3.13 High specific impulse for a ramjet occurs when using high heating value fuel at Mach 3 to 4.

Note that ideal specific impulse is a function of freestream Mach number M_0, heating value of fuel H_f, combustion temperature T_4, freestream temperature T_0, specific heat at constant pressure c_p, freestream speed of sound a_0, and the freestream specific heat ratio γ_0. Results for the ideal ramjet are based on assumptions of isentropic inlet and nozzle, low subsonic combustion with the combustor static temperature approximately equal to the combustor total temperature, constant pressure combustion, ideal expansion to freestream pressure at the nozzle exit, and an equivalence ratio less than 1. It is also assumed that the ramjet combustor is sufficiently long to provide complete combustion. This may be a problem for flight at a dynamic pressure less than 500 psf and an altitude above 60,000 ft. A design guideline for a typical length-limited combustor with subsonic combustion is that the pressure inside the combustor should be greater than 5 psi to ensure complete combustion.

The ideal specific impulse from the above equation may be corrected to account for losses in efficiency. A typical ramjet has an overall specific impulse efficiency of about of 81%. The typical efficiencies of the combustor, nozzle, and inlet are about 0.86, 0.96, and 0.83 respectively.

An example will be calculated for the ramjet baseline at Mach 3.5 and an altitude $h = 60{,}000$ ft ($T_0 = 390$ R, $a_0 = 968$ ft/s). The assumed fuel is RJ-5 fuel (heating value $H_f = 14{,}525$ Btu per lbm of fuel). The assumed combustion temperature is $T_4 = 4000$ R. From the equation, the nondimensional specific impulse is calculated to be

$$\begin{aligned}(I_{SP})_{Ideal} g_c c_p T_0/(a_0 H_f) = {} & \{3.5\{\{(4000/390)/\{1+[(1.4-1)/2]3.5^2\}\}^{1/2}-1\}/ \\ & \{\{1+[(1.4-1)/2]3.5^2\}\{(4000/390)/ \\ & \{1+[(1.4-1)/2]3.5^2\}\}-1\} = 0.372 \end{aligned} \tag{3.32}$$

The specific impulse, after substituting the values of freestream speed of sound $a_0 = 968$ ft/s, heating value of RJ-5 fuel $H_f = 14525$ Btu/lbm, gravitational constant $g_c = 32.2$, specific heat at constant pressure $c_p = 0.302$ Btu/lbm/R, and freestream temperature $T_0 = 390$ R, is

$$(I_{SP})_{Ideal} = 0.372(968)(14525)/[32.2(0.302)(390) = 1387 \text{ s} \tag{3.33}$$

3.8 Ramjet Thrust Prediction

Shown Fig. 3.14 is the thrust of an ideal ramjet.[11] The nondimensional thrust equation is

$$T_{Ideal}/\phi p_0 A_0 = \gamma_0 M_0^2\{\{[T_4/T_0]/\{1+[(\gamma_0-1)/2]M_0^2\}\}^{1/2}-1\} \tag{3.34}$$

Note that the ideal thrust is a function of the equivalence ratio ϕ, combustion temperature T_4, freestream flow area into the inlet A_0, freestream Mach number M_0, freestream static pressure p_0, freestream temperature T_0, and ratio of specific heat γ_0. For typical values of the parameters, maximum thrust

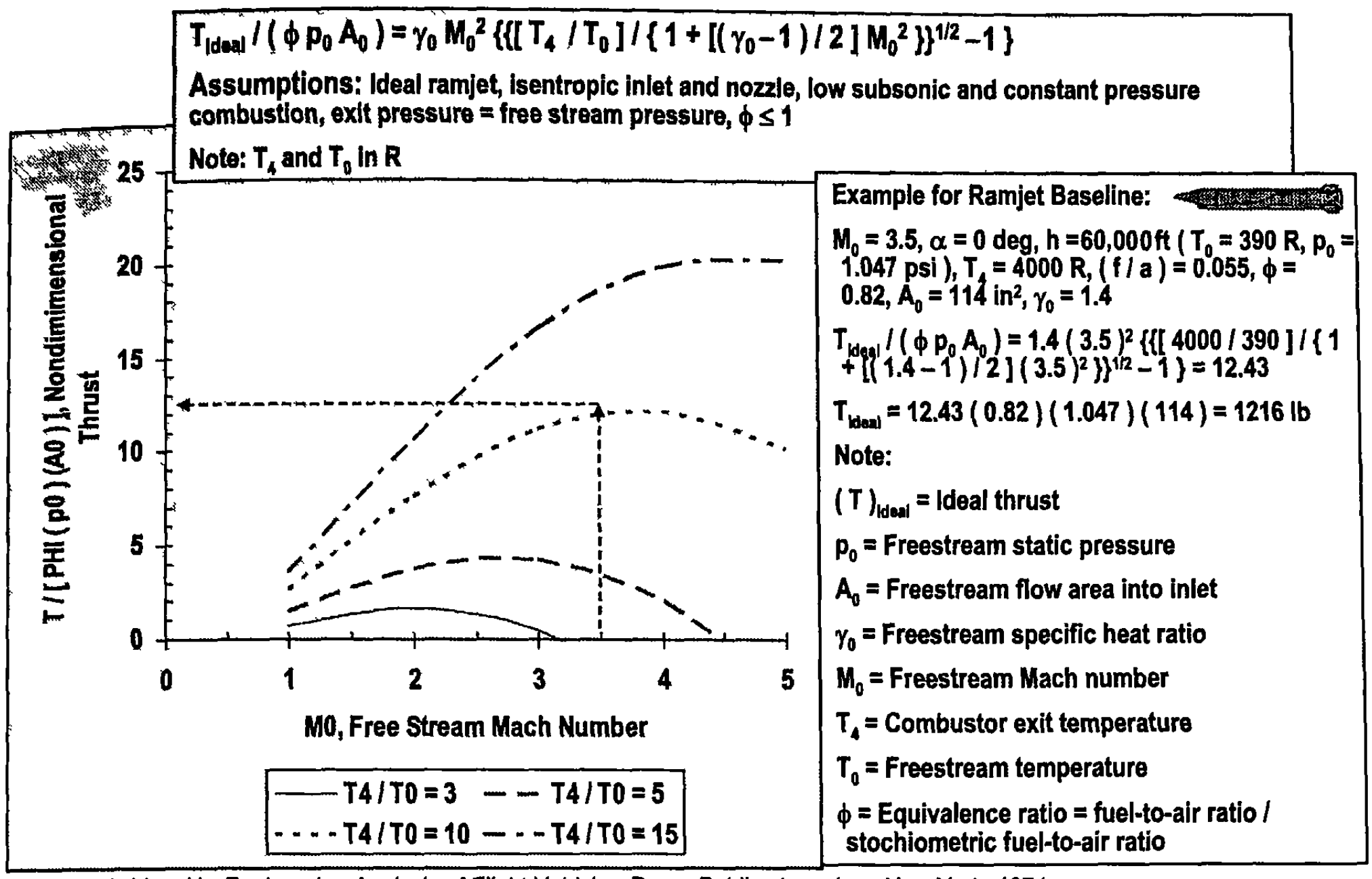

Source: Ashley, H., *Engineering Analysis of Flight Vehicles*, Dover Publications, Inc., New York, 1974

Fig. 3.14 High thrust for a ramjet occurs from Mach 3 to 5 with high combustion temperature.

occurs at a Mach number between Mach 3 to 5. Results are based on an ideal ramjet with isentropic inlet and nozzle, low subsonic and constant pressure combustion, fuel-to-air equivalence ratio ϕ less than stochiometric combustion, and ideal expansion of the nozzle exit pressure to the freestream static pressure.

As an example, assume that the ramjet baseline is at a flight condition of Mach 3.5/60,000 ft altitude ($T_0 = 390$ R, $p_0 = 1.047$ psi). Also assume a combustion temperature $T_4 = 4000$ R and a fuel-to-air ratio $f/a = 0.055$ (which gives an equivalence ratio of $\phi = 0.82$ and provides a combustion temperature $T_4 = 4000$ R). The freestream flow area is assumed to be equal to the inlet capture area, $A_0 = 114$ in^2. Substituting in the nondimensional thrust equation

$$T_{\text{Ideal}}/(\phi p_0 A_0) = 1.4(3.5)^2\{\{[4000/390]/\{1 + [(1.4-1)/2](3.5)^2\}\}^{1/2} - 1\}$$
$$= 12.43 \tag{3.35}$$

Substituting equivalence ratio $\phi = 0.82$, freestream pressure $p_0 = 1.047$, and freestream flow area $A_0 = 114$ in^2 in the thrust equation gives

$$T_{\text{Ideal}} = 12.43(0.82)(1.047)(114) = 1216 \text{ lb} \tag{3.36}$$

Note that the actual thrust is lower because of combustor, nozzle, and inlet efficiency losses and because of the inlet capture efficiency.

The fuel-to-air ratio for stochiometric combustion is a function of the type of fuel. For typical liquid hydrocarbon fuels such as RJ-5, JP-4, and kerosene the fuel-to-air ratio for stochiometric combustion is $f/a \approx 0.067$. For lighter weight hydrocarbon fuels, stochiometric f/a values are somewhat lower. The general equation for combustion of a hydrocarbon fuel of composition C_xH_y with oxygen (O_2) is

$$C_xH_y + (x + y/4)O_2 \rightarrow xCO_2 + (y/2)H_2O \tag{3.37}$$

Because air is approximately 21% oxygen and 79% nitrogen, the equation for combustion of a hydrocarbon fuel in air is $C_xH_y + (x + y/4)(0.21O_2 + 0.79\,N_2) \rightarrow xCO_2 + (y/2)H_2O + [(x + y)/4](0.79/0.21)N_2$. Substituting the molecular weight of hydrogen (1), carbon (12), oxygen (16), and nitrogen (14) gives a fuel-to-air ratio equation for stochiometric combustion of a hydrocarbon fuel as

$$f/a = (12x + y)/\{(x + y/4)[32 + (0.79/0.21)28]\} \tag{3.38}$$

As an example, octane (C_8H_{18}) has a stochiometric fuel-to-air ratio

$$f/a = (96 + 18)/\{(8 + 18/4)[32 + (0.79/0.21)28]\} = 0.066 \tag{3.39}$$

For methane (CH_4), which is a lightweight gas, the stochiometric fuel-to-air ratio is

$$f/a = (12 + 4)/\{(1 + 4/4)[32 + (0.79/0.21)28]\} = 0.058 \tag{3.40}$$

3.9 Ramjet Temperature Technology Limit

Figure 3.15 shows ramjet combustor exit temperature T_4 as a function of freestream Mach number M_0 and fuel-to-air ratio f/a. The equation used to develop the figure is

$$T_4 \approx T_0\{1 + [(\gamma_0 - 1)/2]M_0^2\} + (H_f/c_p)(f/a) \tag{3.41}$$

In the equation, T_0 is the freestream temperature, γ_0 is the freestream specific heat ratio, H_f is the fuel heating value, and c_p is the specific heat of air at constant pressure in the combustor. Assumptions are low subsonic combustor, no heat transfer through the inlet (isentropic flow), and fuel-to-air ratio less than stochiometric. The figure is based on the heating value of RJ-5 fuel ($H_f = 14{,}525$ Btu/lbm/R).

Note that the ramjet combustor temperature exceeds 4000 R for flight conditions of high Mach number and fuel-to-air ratios approaching stochiometric flow [$(f/a)_{\varphi=1} = 0.067$ for RJ-5 hydrocarbon fuel]. Operation at less than stochiometric ($\phi < 1$), with excess inlet air, may be required to avoid exceeding the temperature limit of the combustor and its insulation. The state-of-the art of ramjet combustor insulation technology is often a limiting factor in achieving the thrust and specific impulse that are required for efficient flight at hypersonic Mach number.

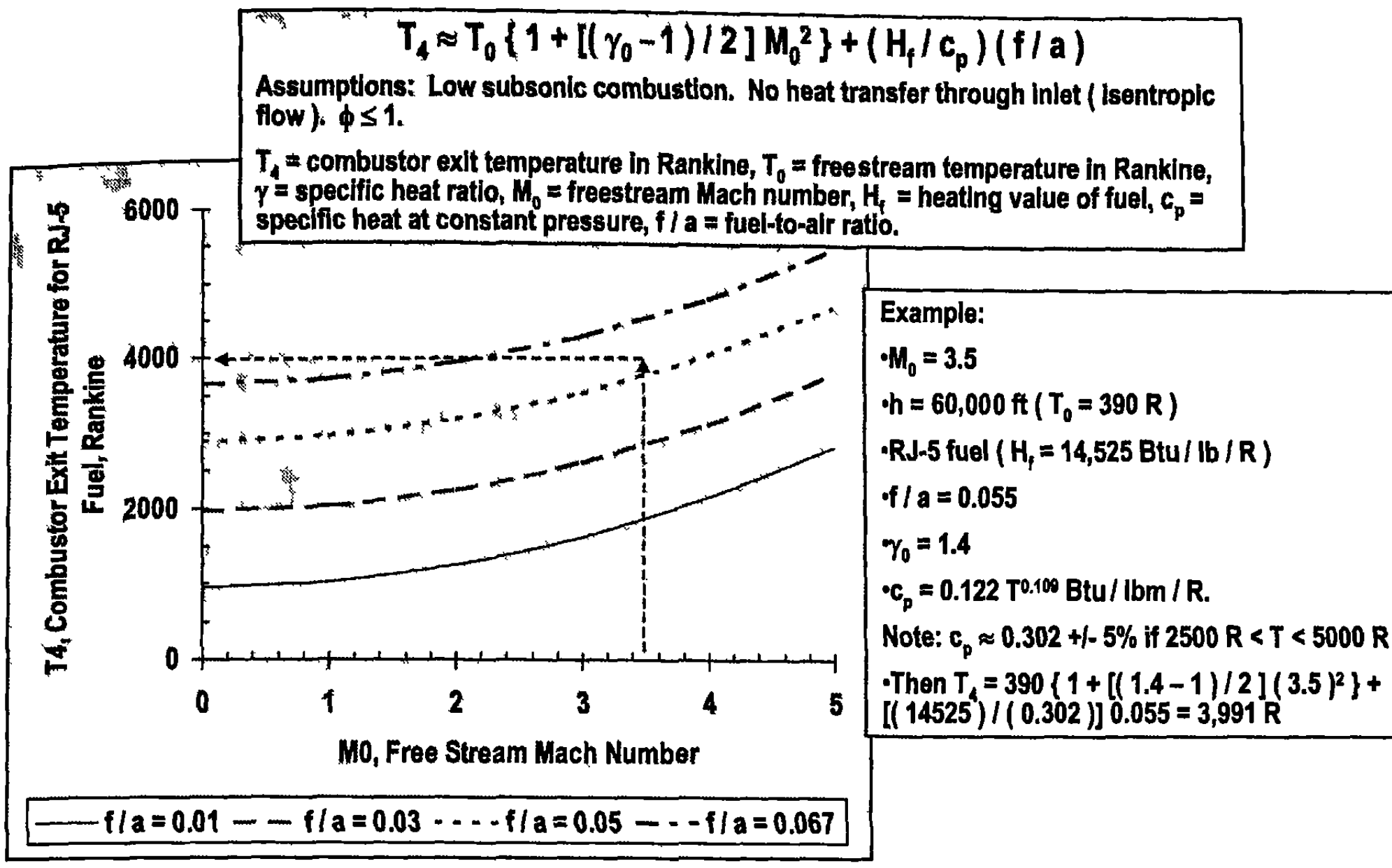

Fig. 3.15 Ramjet combustor temperature increases with Mach number and fuel flow.

As an example, assume a subsonic combustion ramjet flying at a flight Mach number $M_0 = 3.5$ and an altitude $h = 60{,}000$ ft ($T_0 = 390$ R). The assumed fuel is RJ-5 fuel ($H_f = 14{,}525$ Btu/lb) and the assumed fuel-to-air ratio $f/a = 0.055$. It is also assumed that $\gamma_0 = 1.4$. The specific heat at constant pressure is approximately $c_p \approx 0.302$ Btu/lbm/R for the flow through the combustor at typical temperatures. A previous equation showed that c_p is a weak function of temperature, $c_p = 0.122\ T^{0.109}$ Btu/lbm/R. For the typical temperature range,

$$c_p = 0.302 \pm 5\% \quad \text{if } 2500\text{ R} < T < 5000\text{ R} \tag{3.42}$$

Substituting into the equation for combustion temperature gives

$$T_4 \approx T_0\{1 + [(\gamma_0 - 1)/2]M_0^2\} + (H_f/c_p)(f/a) = 390\{1 + [(1.4 - 1)/2] \times (3.5)^2\} + (14525/0.302)(0.055) = 3991\,\text{R} \tag{3.43}$$

The assumption of constant pressure combustion in a constant area combustor can have significant error if there is a high combustor entrance Mach number or if there is high heating. A limiting condition occurs when the local Mach number in the combustor is increased from the subsonic entrance Mach number M_3 to a thermally choked combustion Mach number $M_4 = 1$. Shown in Fig. 3.16 is the thermally choked combustor entrance Mach number $(M_3)_{TC}$ versus freestream Mach number M_0 and the ratio of the combustor total temperature to freestream static temperature (T_{4_t}/T_0). The figure is based on

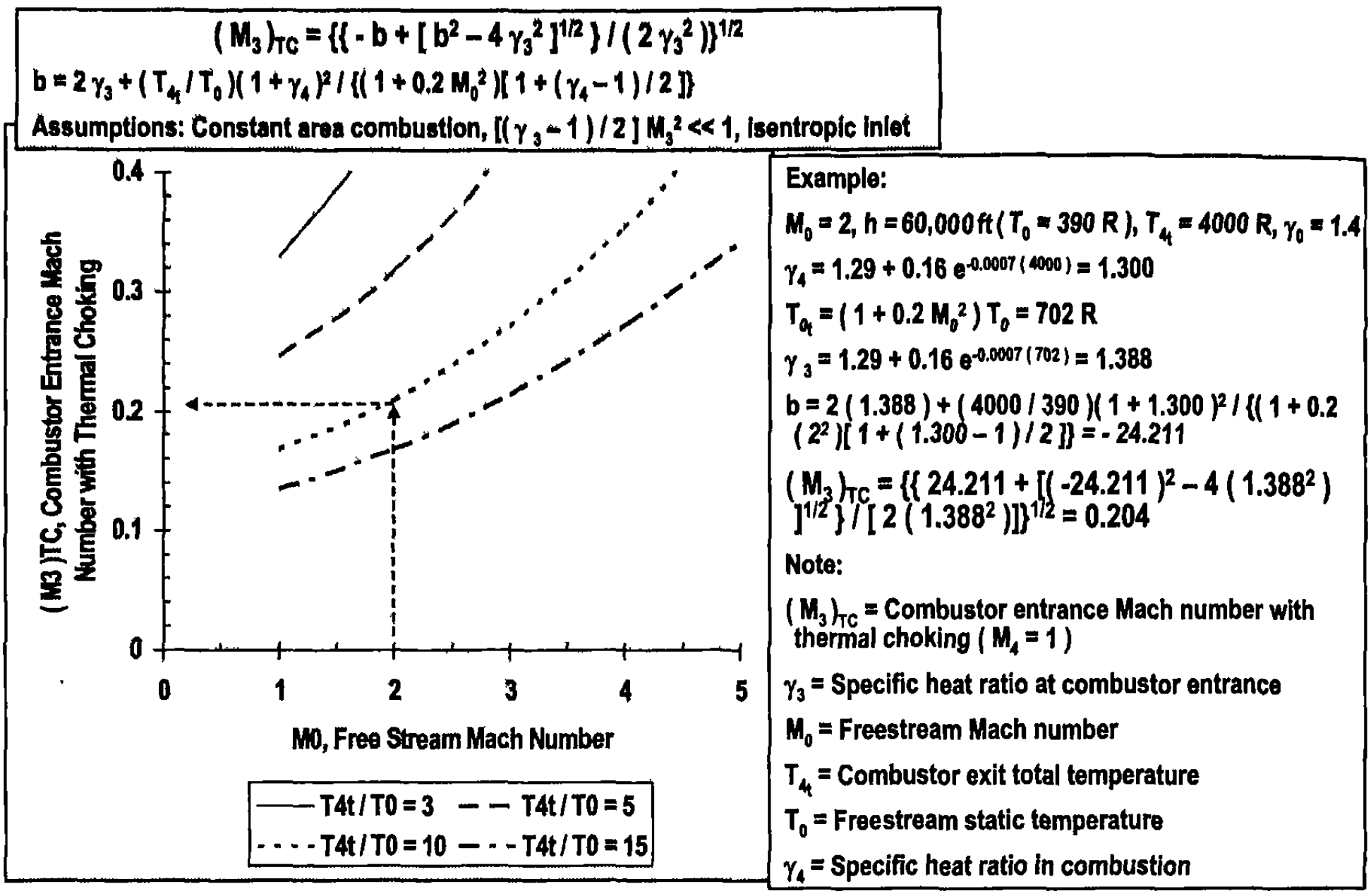

Fig. 3.16 Ramjet combustor entrance Mach number should be low to avoid thermal choking.

the equation

$$(M_3)_{TC} = \{\{-b + [b^2 - 4\gamma_3^2]^{1/2}\}/(2\gamma_3^2\}^{1/2} \tag{3.44}$$

where $b = 2\gamma_3 + (T_{4t}/T_0)(1+\gamma_4)^2/\{(1+0.2M_0^2)[1+(\gamma_4-1)/2]\}$.

Terms in the above equations are $(M_3)_{TC}$ = combustor entrance Mach number with thermal choking ($M_4 = 1$), γ_3 = specific heat ratio at the combustor entrance, M_0 = freestream Mach number, T_{4t} = combustor exit total temperature, T_0 = freestream static temperature, and γ_4 = specific heat ratio in combustion. Assumptions are constant area combustion with negligible skin friction (Rayleigh flow), $[(\gamma_3 - 1)/2]M_3^2 \ll 1$, and isentropic flow from the freestream to the combustor entrance (i.e., isentropic inlet). A source for the generalized Rayleigh flow equation is Ref. 12. Note from the figure that a low subsonic combustor entrance Mach number is required to avoid thermal choking, particularly for high values of combustor temperature ratio T_{4t}/T_0 and low supersonic freestream Mach number (e.g., booster-to-ramjet transition).

As an example, assume $M_0 = 2$, $h = 60{,}000$ ft ($T_0 = 390$ R), and $T_{4t} = 4000$ R. For this case, the freestream specific heat ratio $\gamma_0 = 1.4$. Calculate

$$\gamma_4 = 1.29 + 0.16\,e^{-0.0007(4000)} = 1.300 \tag{3.45}$$

$$T_{0t} = (1 + 0.2M_0^2)T_0 = 702 \text{ R} \tag{3.46}$$

$$\gamma_3 = 1.29 + 0.16\,e^{-0.0007(702)} = 1.388 \tag{3.47}$$

Solving for the term b in the $(M_3)_{TC}$ equation,

$$b = 2(1.388) + (4000/390)(1 + 1.300)^2/\{[1 + 0.2(2^2)][1 + (1.300 - 1)/2]\}$$
$$= -24.211 \tag{3.48}$$

Then for this case, the maximum combustor entrance Mach number to avoid thermal choking is

$$(M_3)_{TC} = \{\{24.211 + [(-24.211)^2 - 4(1.388^2)]^{1/2}\}/[2(1.388^2)]\}^{1/2}$$
$$= 0.204 \tag{3.49}$$

Reference 12 also gives the static pressure at thermal choking relative to the static pressure at the combustor entrance as

$$(p_4/p_3)_{M_4=1} = [1 + \gamma_3(M_3)^2]/(1 + \gamma_4) \tag{3.50}$$

Substituting into the above equation, the decrease in static pressure is

$$(p_4/p_3)_{M_4=1} = [1 + 1.388(0.204)^2]/(1 + 1.300) = 0.46 \tag{3.51}$$

For this case, thermal choking would result in a large decrease (54%) in combustor pressure. A design consideration to minimize the pressure drop and avoid thermal choking during constant area combustion is to have a relatively small inlet throat area (low value of A_{IT}/A_3). This results in a low subsonic Mach number at the combustor entrance ($M_3 \ll 1$).

The inlet entrance Mach number M_3 for a supersonic ramjet can be obtained comparing the cross-sectional area at the combustor entrance to the cross-sectional area at the inlet throat.

Downstream of the normal shock, the inlet subsonic Mach number is a function of the ratio of the local cross-sectional area to the inlet sonic throat area A_{IT}. From Ref. 12, the combustor entrance Mach number M_3 can be obtained from the equation

$$A_{IT}/A_3 = [(\gamma + 1)/2]^{(\gamma+1)/[2(\gamma-1)]} M_3[1 + (\gamma - 1)/2]\, M_3^2]^{-(\gamma+1)/[2(\gamma-1)]} \tag{3.52}$$

For $\gamma = 1.4$,

$$A_{IT}/A_3 = (216/215)M_3(1 + M_3^2/5)^{-3} \tag{3.53}$$

Assumptions are an isentropic inlet, $M_{IT} = 1$, and $\gamma = 1.4$. Figure 3.17 shows the combustor entrance Mach number M_3 versus the ratio of inlet throat area to combustor area (A_{IT}/A_3).

As an example, for the ramjet baseline $A_{IT} = 41.9$ in^2 and $A_3 = 287$ in^2. Assume sonic flow ($M = 1$) at the inlet throat. Calculate

$$A_{IT}/A_3 = 41.9/287 = 0.1459 \tag{3.54}$$

$$A_{IT} / A_3 = [(\gamma + 1) / 2]^{(\gamma+1)/[2(\gamma-1)]} M_3 [1 + (\gamma - 1) / 2] M_3^2]^{-(\gamma+1)/[2(\gamma-1)]} = (216 / 215) M_3 (1 + M_3^2 / 5)^{-3}$$

Assumptions: Isentropic inlet, $M_{IT} = 1$, $\gamma = 1.4$

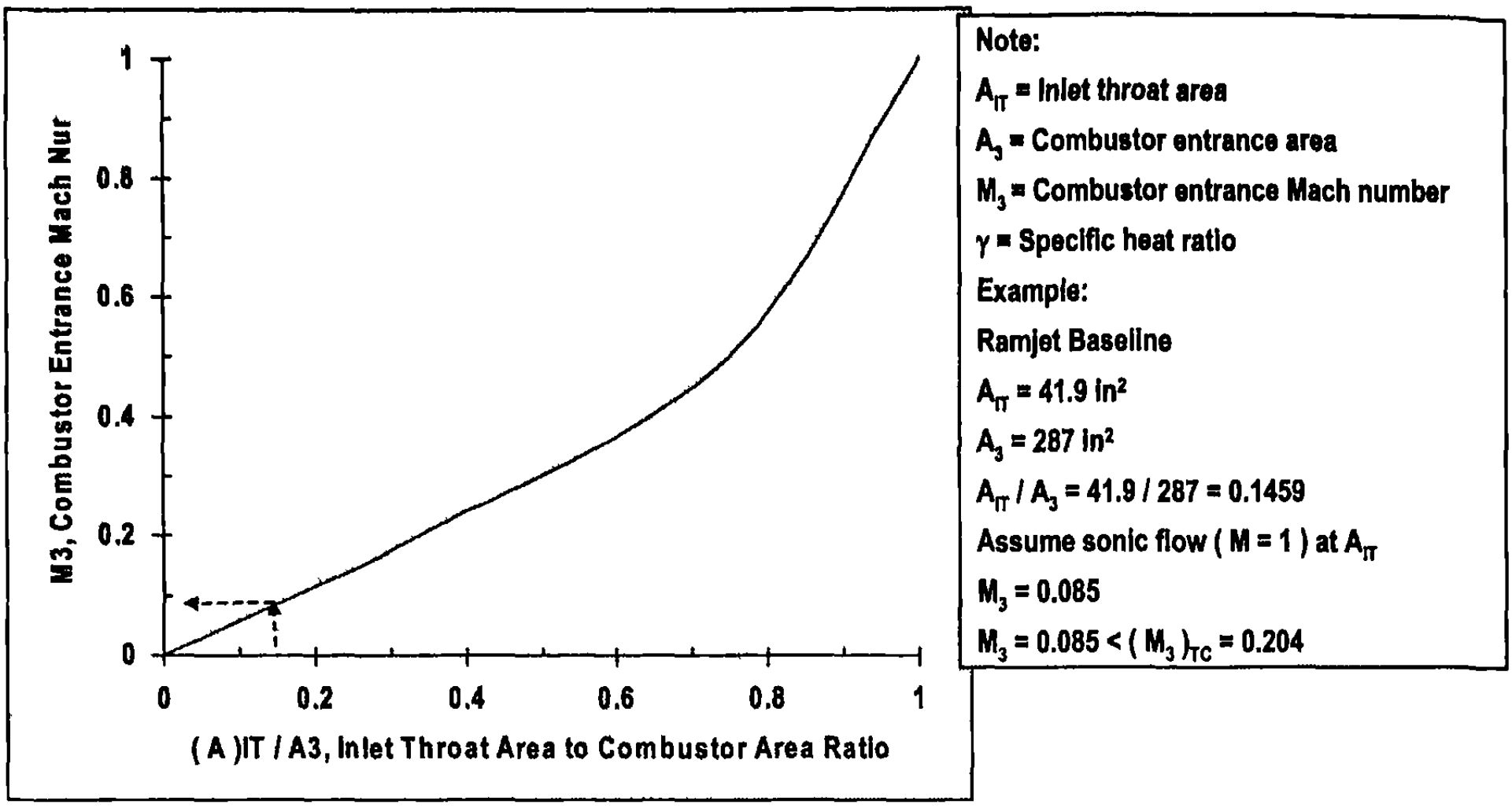

Fig. 3.17 A ramjet combustor with a low entrance Mach number requires a small inlet throat area.

Substituting into the above equation gives

$$M_3 = 0.085 \tag{3.55}$$

Comparing to the prior example, note that $M_3 = 0.085 < (M_3)_{TC} = 0.204$. Since the ramjet baseline has sonic flow at its throat and $M_3 < (M_3)_{TC}$, the flow is not thermally choked.

From Ref. 12, the pressure loss in the combustor, assuming Rayleigh flow, is given by the equation

$$p_4/p_3 = (1 + \gamma_3 M_3^2)/(1 + \gamma_4 M_4^2) \tag{3.56}$$

The Rayleigh flow temperature equation is

$$T_{4t}/T_0 = [(1 + \gamma_3 M_3^2)/(1 + \gamma_4 M_4^2)]^2 (M_4/M_3)^2 \{1 + [(\gamma_4 - 1)/2] M_4^2\}/\{1 + [(\gamma_3 - 1)/2] M_3^2\} \tag{3.57}$$

Assumptions for Rayleigh flow are heat addition at a constant combustor cross-sectional area and negligible friction. An approximate equation for the Rayleigh flow combustion Mach number is

$$M_4 \approx \{[-b - (b^2 - 4ac)^{1/2}]/(2a)\}^{1/2} \tag{3.58}$$

The terms in the above equation are

$$a = (T_{4t}/T_0)\gamma_4^2 M_3^2 \tag{3.59}$$

$$b = 2(T_{4t}/T_0)\gamma_4 M_3^2 - \gamma_3 M_3^2 - 1 \tag{3.60}$$

$$c = (T_{4t}/T_0)M_3^2 \tag{3.61}$$

Assume the conditions from the prior example, $M_0 = 2$, $h = 60{,}000$ ft ($T_0 = 390$ R), $T_{4t} = 4000$ R, $\gamma_0 = 1.4$, $\gamma_4 = 1.300$, and $\gamma_3 = 1.388$. Also assume the ramjet baseline with a sonic inlet throat flow condition. Then for

$$A_{IT}/A_3 = 41.9/287 = 0.1459, M_3 = 0.085 \tag{3.62}$$

Solving for the terms in the combustion Mach number equation,

$$a = 10.256(1.300)^2(0.085)^2 = 0.1252 \tag{3.63}$$

$$b = 2(10.256)(1.300)(0.085)^2 - 1.388(0.085)^2 - 1 = -0.8174 \tag{3.64}$$

$$c = 10.256(0.085)^2 = 0.0741 \tag{3.65}$$

Substituting into the equation for combustion Mach number gives

$$M_4 \approx 0.304 \tag{3.66}$$

Solving for the pressure ratio loss in the combustor,

$$p_4/p_3 = [1 + 1.388(0.085)^2]/[1 + 1.300\,M_4^2] = 0.902 \tag{3.67}$$

Note that there is a 10% reduction in combustion pressure for this example, indicating that the assumption of constant pressure combustion is reasonably accurate for conceptual design (10% error).

3.10 Ramjet Engine/Booster Integration

The integral rocket ramjet (IRR) engine is the most popular type of ramjet. After rocket booster burnout, the rocket booster motor case is used as the ramjet engine. Typically the booster case length is sufficiently long to provide efficient combustion as a ramjet engine. Shown in Fig. 3.18 is the minimum length of the combustor for complete combustion as a function of time required for combustion and the velocity of the airflow through the combustor. The equation is

$$(l_{comb})_{min} = t_{comb} V_{comb} \tag{3.68}$$

A subsonic combustion ramjet has a typical combustion time $t_{comb} \approx 0.002$ s and a combustion velocity $V_{comb} \approx 200$ ft/s. The minimum length of the combustor for efficient combustion is $(l_{comb})_{min} \approx 0.4$ ft. For a typical ramjet with

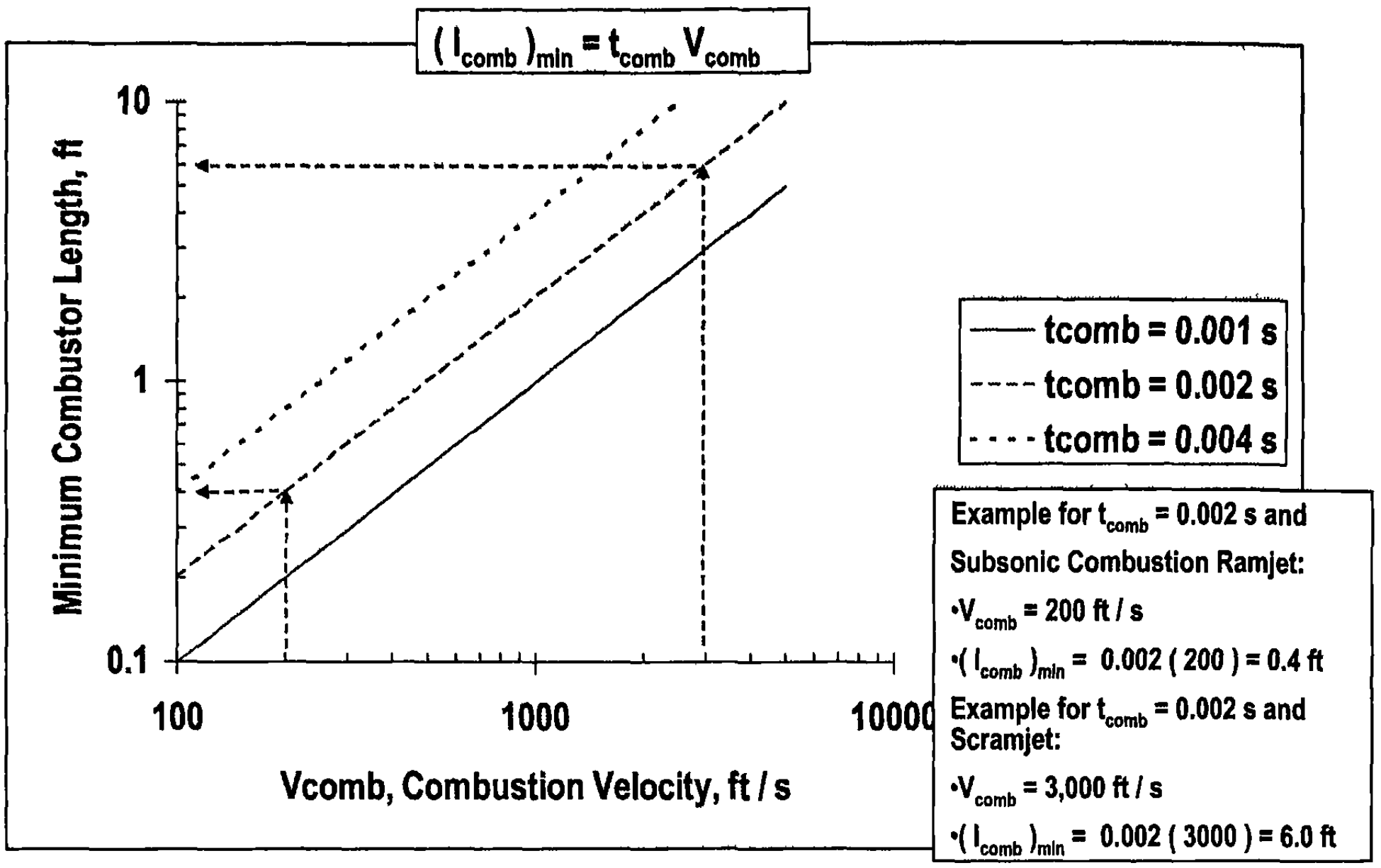

Fig. 3.18 Minimum length for the combustor is a function of combustion velocity.

a diameter greater than 1 ft and a total fineness ratio greater than 10, the impact of the minimum combustor length is relatively small, less than 4% of the length of the missile. For an IRR, the typical booster length is much longer than the minimum combustor length, easily accommodating the combustor.

A supersonic combustion ramjet also has a typical combustion time $t_{comb} \approx 0.002$ s. However, a typical combustion velocity is $V_{comb} \approx 3000$ ft/s. The minimum length of the combustor for efficient combustion is $(l_{comb})_{min} \approx$ 6 ft. In the case of the scramjet, the impact of the minimum combustor length is large, requiring a much longer and heavier missile.

Figure 3.19 from Ref. 13 characterizes ramjet engine/booster integration options according to their cruise drag. Low cruise drag ramjets are tandem IRR, aft drop-off booster, forward-located booster, and podded drop-off booster. The high cruise drag ramjets shown in the figure are the podded ramjet, podded IRR, and the podded ramjet with a drop-off booster. Most modern ramjets have low cruise drag. The IRR is particularly attractive. As noted previously, after booster burnout, an IRR uses the booster case as the combustion chamber for the ramjet. The IRR is often preferred because of advantages of low cruise drag, low volume, light weight, and small diameter.

A further comparison of ramjet engine/booster integration options is given in Fig. 3.20 based on Ref. 13. Note that the integral rocket-ramjet engine has above-average-to-superior characteristics for the selection factors of length, diameter, weight, no ejecta, cruise drag, launch platform carriage drag, cost, compatibility of the ramjet engine with the booster, and compatibility of the ramjet engine with the inlet. The other candidate engines are below average in one or more of the selection factors. However, depending upon the weighting of the selection factors and the mission, one or more of the other candidate engines may be

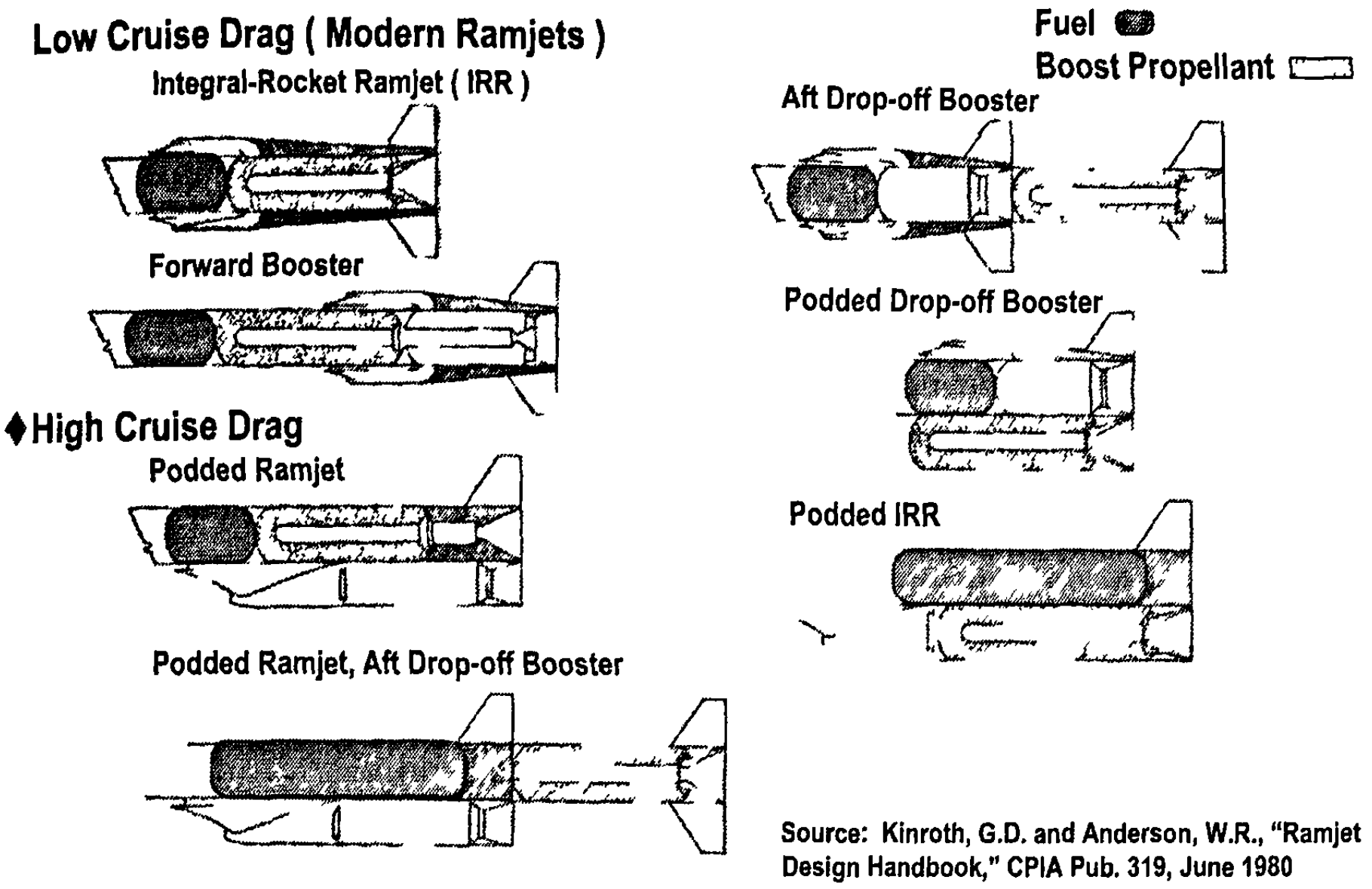

Fig. 3.19 Ramjet engine/booster integration options.

acceptable, or even preferable. The strengths and potential weaknesses of the other candidate ramjet engine alternatives to an IRR include the following:

1) Aft drop-off booster attractive features include small diameter, low cruise drag, low cost, and compatibility of the engine with the inlet. Disadvantages of an aft drop-off booster include long length and ejecta.

	Selection Factors								
	Length	Diameter	Weight	Ejectables	Cruise Drag	Carry Drag	Cost	Cycle Compatibility	Inlet Compatibility
Integral Rocket – Ramjet (IRR)	◒	●	●	◒	●	●	◒	◒	●
Aft Booster (Drop-off)	–	●	○	–	●	◒	●	◒	●
Forward Booster	–	●	○	●	◒	●	○	○	○
Podded Booster (Drop-off)	●	–	○	–	●	○	●	◒	◒
Podded Ramjet	◒	–	○	●	–	○	◒	○	–
Podded IRR	●	–	●	◒	–	○	○	○	–
Podded Ramjet Aft Booster (Drop-off)	○	–	–	–	–	–	◒	○	–

● Superior ◒ Above Average ○ Average – Below average

Source: Kinroth, G.D. and Anderson, W.R., "Ramjet Design Handbook," CPIA Pub. 319, June 1980

Fig. 3.20 Ramjet engine/booster integration trades.

2) Forward booster has attractive features of small diameter, no ejecta, and low launch platform carriage drag. A disadvantage is long length.

3) Podded drop-off booster has attractive features of short length, low cruise drag, and low cost. Disadvantages include a large diameter and ejecta.

4) Podded ramjet has an attractive feature of no ejecta. Disadvantages of a podded ramjet include a large diameter, high cruise drag, and a potential problem of inlet compatibility. The disadvantages make it unsuitable for most modern applications.

5) Podded IRR has attractive features of short length and lighter weight. Disadvantages include large diameter, high cruise drag and a potential problem of inlet compatibility. The disadvantages make it unsuitable for most modern applications.

6) Podded ramjet with a drop-off booster has disadvantages of large diameter, heavy weight, ejecta, high cruise drag, high carriage drag, and a potential problem of inlet compatibility. The disadvantages make it unsuitable for most modern applications.

3.11 Ramjet Missile Drag

A first-order estimate of ramjet zero-lift drag, based on Ref. 13, is given in Fig. 3.21. Results are applicable to ramjets that have a high fineness nose ($l_N/d \geq 2.25$) with small bluntness ($d_{NoseTip}/d \leq 0.2$). The examples of ramjets that have low cruise drag are wingless ramjets based on one of the following: an IRR, an aft drop-off booster, a forward-located booster, or a podded drop-off booster. As an example, the wingless low-drag ramjet missiles have a zero-lift drag coefficient at Mach 2 of $C_{D_0} \approx 0.3$ to 0.6. Adding wings to the low drag ramjets increases the drag. At Mach 2, the value of the zero-lift drag coefficient is $C_{D_0} \approx 0.6$ to 0.9. Examples of the older high drag configurations are the

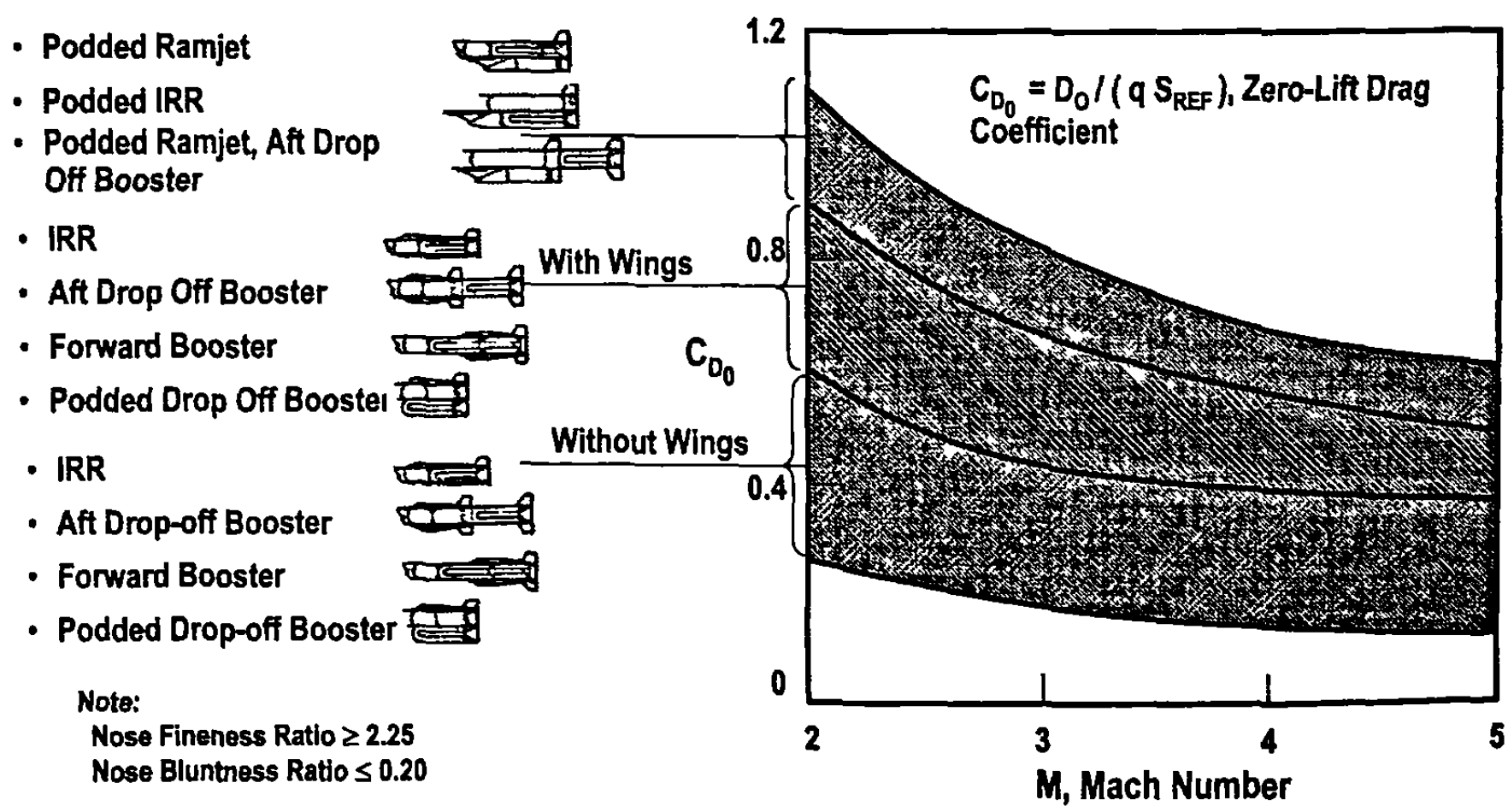

Source: Kinroth, G.D. and Anderson, W.R., "Ramjet Design Handbook," CPIA Pub. 319, June 1980

Fig. 3.21 Ramjets with internal boosters and no wings have low drag.

podded ramjets. The figure shows that at Mach 2, the zero-lift drag coefficient for podded ramjets is the highest, $C_{D_0} \approx 0.9$ to 1.1. As stated previously, the high drag podded ramjets are unsuitable for most modern applications.

3.12 Ramjet Inlet Options

Ramjet inlet design considerations include the type of opening, the location of the inlet on the body, and the number of inlets. Figure 3.22 from Ref. 13 shows the inlet placement and geometry of the following nine ramjet inlet options:

1) Annular nose inlet. The inlet surrounds the body. It may rely only on the cowl lip oblique shock for the initial compression, or it may also have a center spike for compression.

2) Chin inlet located forward underneath the nose. The nose compression angle provides an oblique shock in front of the inlet. The ramjet missile baseline of this textbook has a chin inlet.

3) Forward cruciform axisymmetric inlet. The nose compression angle provides an oblique shock in front of each inlet. The inlets are usually in tandem with cruciform fins.

4) Aft cruciform axisymmetric inlet. There are four inlets located near the center of the missile. The inlets are usually in tandem with cruciform fins.

5) Underwing axisymmetric inlet. There are two inlets located near the center of the missile, under a planar wing. The wing provides an initial compression.

6) Twin two-dimensional inlet. This concept has two inlets near the center of the missile. They are usually located on the lower portion of the body, separated by a radial angle of about 90 deg. The inlets are usually in tandem with the bottom cruciform tails.

Type Inlet	Sketch	Placement
Nose		Nose-full axisymmetric
Chin		Forward underside in nose compression field-partial axisymmetric
Forward Cruciform Axisymmetric		Forward in nose compression field-cruciform (four) axisymmetric
Aft Cruciform Axisymmetric		Aft-cruciform (four) axisymmetric
Under Wing Axisymmetric		In planar wing compression field-twin axisymmetric
Twin Two-dimensional		Aft-twin cheek-mounted two dimensional
Underslung Axisymmetric		Aft underside-full axisymmetric
Underslung Two-dimensional		Aft underside-belly mounted two dimensional
Cruciform Two-dimensional		Aft-cruciform (four) two dimensional

Source: Kinroth, G.D. and Anderson, W.R., "Ramjet Design Handbook," CPIA Pub. 319, June 1980.

Fig. 3.22 Ramjet inlet options.

7) Underslung axisymmetric inlet. The underslung inlet is located near the center of the missile.

8) Underslung two-dimensional inlet. Similar to the above.

9) Cruciform two-dimensional inlet. Similar to the aft cruciform axisymmetric inlet.

Tradeoff considerations of inlet alternatives are shown in Fig. 3.23 from Ref. 13. The selection factors are:

1) High pressure recovery. The chin inlet and the forward cruciform axisymmetric inlet benefit from relatively high recovery pressure provided by an oblique shock from the forebody in front of the inlet. Another benefit of the oblique shock is a lower Mach number at the inlet entrance, which allows the inlet to swallow the shock at lower flight Mach number. Other inlets that also have relatively good pressure recovery are the nose inlet, underwing axisymmetric inlet, and the twin two-dimensional inlet. The underwing axisymmetric inlet benefits from the wing compression, whereas the twin two-dimensional inlet benefits from the underbody compression.

2) Small carriage envelope on the launch platform. The annular inlet and the chin inlet require only a small inlet height to capture airflow because of the large wraparound angle.

3) High angle of attack capability. The chin inlet and the underwing axisymmetric inlet allow high positive angles of attack, providing a relatively high recovery pressure for bank-to-turn maneuvering.

4) Lightweight. The underwing axisymmetric inlet and the underslung axisymmetric inlet, located aft on the missile body, require less material for structure.

Type Inlet	Selection Factors									
	Pressure Recovery	Carriage Envelope	Alpha Capability	Weight	Drag	Warhead Shrouding	Inlet Cost	Preferred Steering	Preferred Control	Prime Mission Suitability
	◒	●	○	◒	●	–	◒	STT	W, C	ATS, STA
	●	●	●	○	●	○	○	BTT	T	ATS, ATA, STA
	●	○	◒	–	○	–	–	STT	T	ATS, ATA, STA
	○	◒	○	◒	○	●	○	STT	T	ATS
	◒	–	●	●	○	●	◒	BTT	T	ATS, ATA, STA
	◒	○	◒	◒	◒	◒	○	BTT	T	ATS, ATA, STA
	○	–	○	●	○	◒	●	BTT	T	ATS
	–	–	◒	◒	◒	◒	◒	BTT	T	ATS, ATA, STA
	–	○	○	◒	◒	●	○	STT	T	ATS

Note:
BTT = Bank to Turn
STT = Skid to Turn
W = Wing C = Canard
T = Tail

● Superior ◒ Above Average ○ Average – Below average

Source: Kinroth, G.D. and Anderson, W.R., "Ramjet Design Handbook," CPIA Pub. 319, June 1980

Fig. 3.23 Ramjet inlet concept trades.

5) Low drag. The annular nose inlet and the chin inlet have reduced drag on the nose.

6) Does not shroud the warhead. The aft cruciform axisymmetric inlet, aft twin axisymmetric inlet, and the aft cruciform two-dimensional inlet, as shown in the figure, are located aft of the warhead section of the missile.

7) Low cost. The lowest cost, simplest fabrication inlet is probably an underslung axisymmetric inlet.

8) Preferred steering approach (skid to turn, bank to turn). Cruciform inlets are consistent with skid-to-turn maneuvering, whereas chin, twin, or underslung inlets are consistent with bank-to-turn maneuvering.

9) Preferred flight control (tail, canard, wing). An annular inlet has volume available for the forward packaging of the flight control actuators for canard or wing control. The other inlets are more compatible with tail control.

10) Preferred mission application (air to surface, air to air, or surface to air). The air intercept mission requires high maneuverability and high angle of attack, which is especially consistent with the capability of the chin inlet and underwing axisymmetric inlets. These inlets require bank-to-turn maneuvering.

There is no single inlet that is best for all missions. The selection factors must be weighted for the mission as part of the inlet selection.

The current supersonic/hypersonic airbreathing missiles are shown in Fig. 3.24. Except for the SS-N-19 Mach 2.5 turbojet, the missiles use ramjet propulsion. These missiles have either a nose inlet (U.K. Sea Dart, Russian

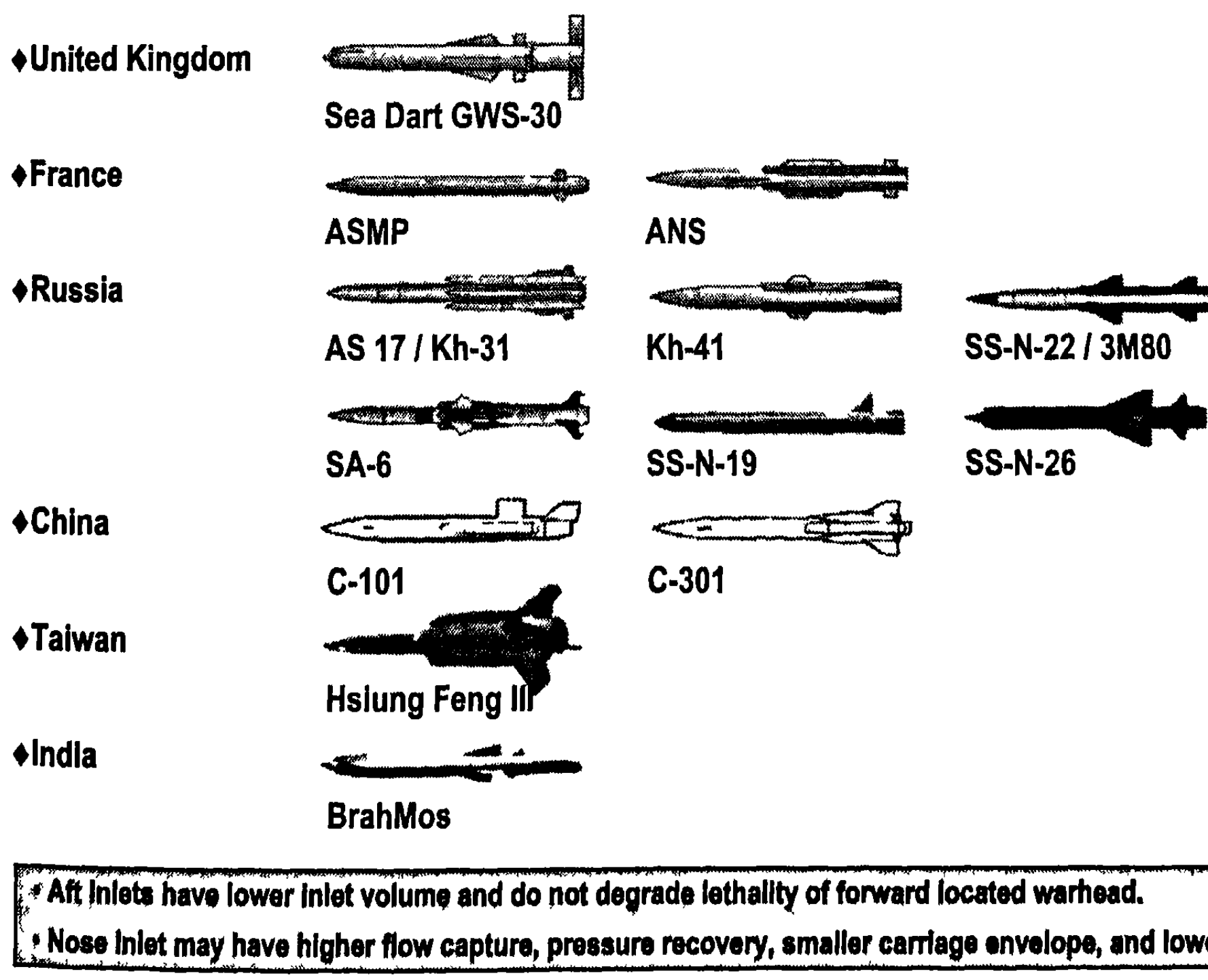

Fig. 3.24 Current supersonic airbreathing missiles have either a nose inlet or have axisymmetric aft inlets.

SS-N-19 and SS-N-26, and Indian BrahMos) or aft axisymmetric inlets (France ANS and ASMP, Russian AS-17/Kh-31, Kh-41, SS-N-22/3M80, and SA-6, China C-101 and C-301, and Taiwan Hsiung Feng III). A nose inlet has advantages of low drag and small carriage envelope and may have higher flow capture and pressure recovery at low supersonic Mach number. Aft axisymmetric inlets have advantages of light weight and low volume, and they do not shroud/degrade the warhead. Note that the flight control for all of these missiles is based on tail control surfaces. The tail flight control actuators are packaged around the throat of the nozzle.

3.13 Supersonic Inlet/Airframe Integration

Inlet design and integration for a supersonic or hypersonic tactical missile involve a host of considerations, including matching the flow delivered to the ramjet nozzle, swallowing capacity, and inlet start. There may not be sufficient time to consider all of these in the initial conceptual design. The inlet design considerations that are addressed in this text are those that are considered to have a large effect on the aerodynamic configuration.

Figure 3.25 shows the shock wave location for an inlet without external compression compared to the shock wave location for an external compression inlet. The external compression inlet has a body deflection angle in front of the inlet. The inlet without external compression, shown at the top of the figure, has an advantage in that it swallows 100% of the oncoming air, with no spillage. A disadvantage is that it may have lower pressure recovery, particularly at high

- Inlet w/o External Compression
  - Inlet Swallows 100% of the Free Stream Flow
  - External Compression Required for Efficient Pressure Recovery if Mach Number > 2 and Inlet Start at Low Supersonic Mach number
- External Compression Inlet (with Spillage)
  - Shocks Converge Outside Inlet Lip (Results in Spillage Air)
- External Compression Inlet (w/o Spillage)
  - Inlet Swallows 100% of the Free Stream Flow
  - Shocks Converge at Inlet Lip (Inlet Captures Maximum Free Stream Flow)

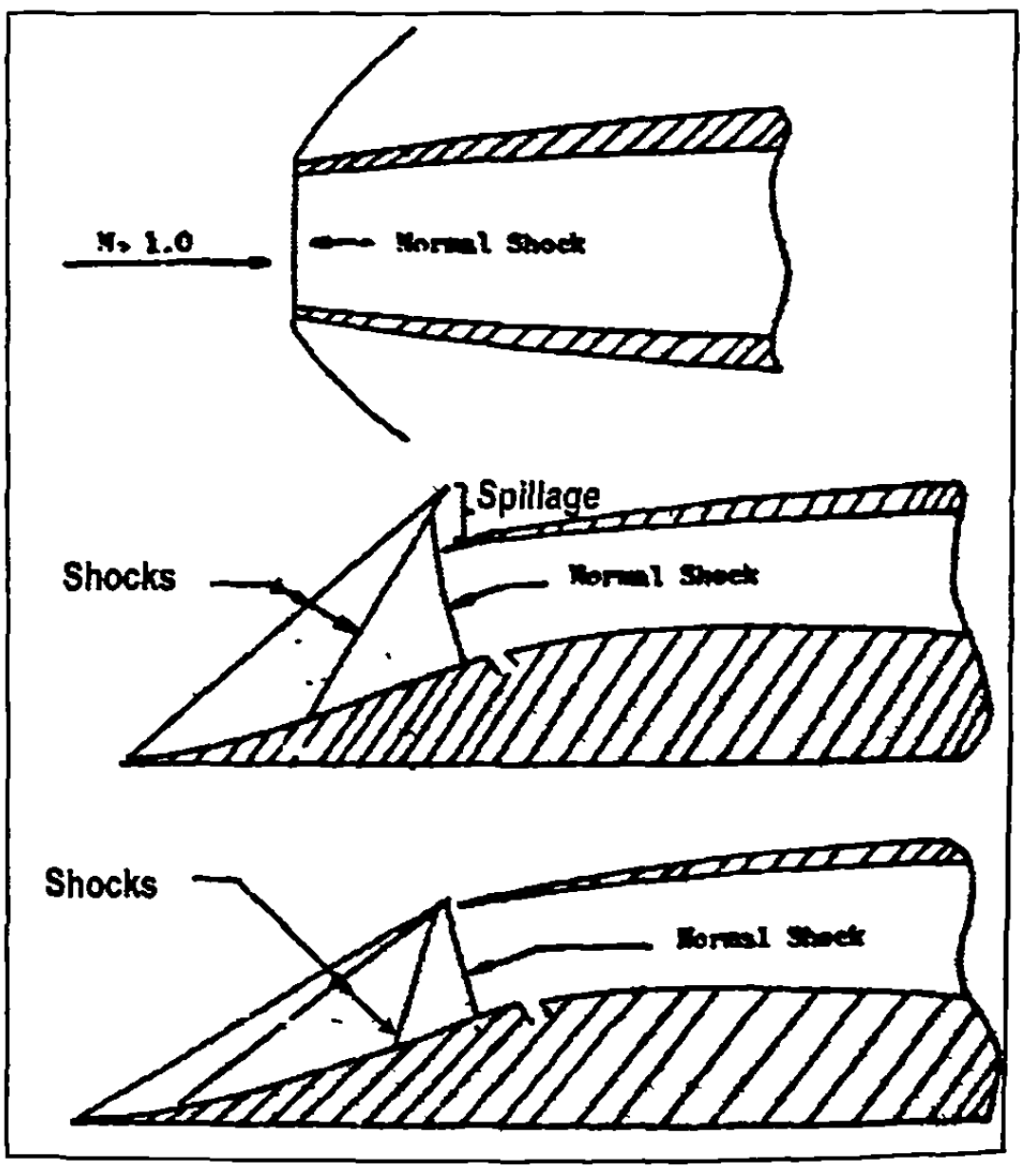

Fig. 3.25 Shock on inlet cowl lip prevents spillage.

Mach number, because of a strong normal shock inside the inlet. External compression (e.g., external compression spike) is usually required for efficient pressure recovery at a Mach number greater than 2. External compression is also usually required to swallow the shock and have an inlet start at low supersonic Mach number. External compression reduces the problem of a strong normal shock but adds an additional concern of matching the airflow of the inlet with the requirement of the engine. An external compression inlet is illustrated at the middle and bottom of the figure, operating in two conditions. The first condition, shown in the middle of the figure, is a lower Mach number where the external shocks have high shock wave angles, passing over the inlet. The inlet captures less of the freestream air and has spillage, which results in lower thrust and tends to increase the drag. The second condition for the external compression inlet is shown at the bottom of the figure. It is a higher Mach number condition with the shocks converging on the inlet lip. In this condition the external compression inlet swallows 100% of the oncoming air, providing greater thrust.

The forebody oblique shock wave angle provides a guideline for the inlet height that is required to achieve a shock-on-lip condition. Shown in Fig. 3.26 is the relationship of the oblique shock wave angle θ to the flow deflection angle $(\alpha + \delta)$ and Mach number M. The equation is

$$\tan(\alpha + \delta) = 2\cot\theta_{2D}(M^2 \sin^2\theta_{2D} - 1)/[2 + M^2(\gamma + 1 - 2\sin^2\theta_{2D})] \quad (3.69)$$

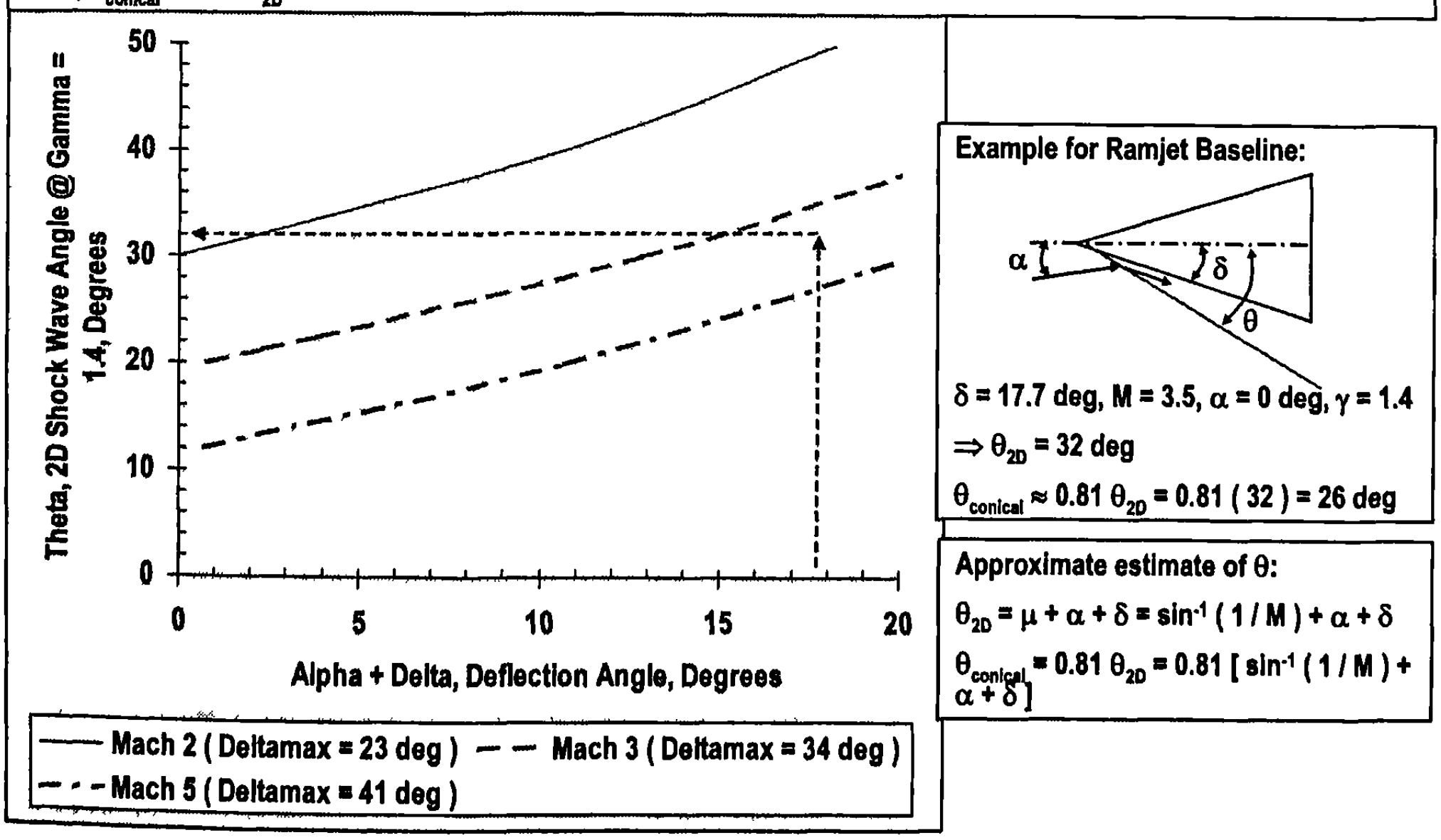

Fig. 3.26 Shock wave angle increases with deflection angle and decreases with Mach number.

The prediction is based on assumptions of two-dimensional flow of a perfect gas. Note that the shock wave angle increases with body deflection angle and decreases with Mach number. As a result, the inlet height to avoid air spillage must be larger for a missile with a low fineness nose at a low supersonic Mach number. Also, the maximum allowable flow deflection increases with Mach number. For example, at Mach 2 the maximum allowable flow deflection angle for an attached two-dimensional oblique shock with $\gamma = 1.4$ is $(\alpha + \delta)_{max} =$ 23 deg. At Mach 5, the maximum allowable flow deflection angle is greater, $(\alpha + \delta)_{max} = 41$ deg.

A first-order estimate of the two-dimensional shock wave angle, suitable for conceptual design, is to assume that the shock wave angle θ_{2D} is the sum of the Mach angle μ plus the flow deflection angle $\alpha + \delta$. The approximate equation is

$$\theta_{2D} \approx \mu + \alpha + \delta = \sin^{-1}(1/M) + \alpha + \delta \tag{3.70}$$

The approximate equation for θ_{2D} becomes less accurate for lower supersonic Mach number and body deflection angle $\delta > 20$ deg.

For conical flow around a conical nose, the shock wave angle is

$$\theta_{conical} \approx 0.81\theta_{2D} \tag{3.71}$$

As an example for the ramjet baseline, which has a body deflection angle $\delta = 17.7$ deg (from its conical nose), assume Mach 3.5 and an angle of attack $\alpha = 0$ deg. The exact equation with $\gamma = 1.4$ gives a two-dimensional shock wave angle $\theta_{2D} = 32$ deg. The approximate equation gives $\theta_{2D} = 34.3$ deg, an error of 7%. The conical shock wave angle for the ramjet baseline is $\theta_{conical} = 26$ deg (81% of a two-dimensional shock wave angle).

Supersonic inlets are designed for shock-on-lip operation at the highest Mach number cruise condition. For a shock-on-lip design, a higher flight Mach number should be avoided. A higher Mach number would result in the shock wave entering the inlet, causing shock-wave boundary-layer interaction, flow separation, a large loss in total pressure, and a large loss in thrust. For a shock-on-lip design, operating at a lower Mach number results in a larger shock wave angle, streamlines spilling outside the inlet, a reduction in the captured air, a reduction in thrust, and spillage drag.

Inlet capture efficiency can be determined by tracing the shockwave and the streamlines back to the inlet lip. For a two-dimensional (wedge) nose, tracing the shock wave and streamlines shown in the right side of Fig. 3.27 results in the following two-dimensional inlet capture efficiency equation

$$(A_0/A_c)_{2D} = (h/l)(1 + \delta M + \alpha M)/[(1 + \alpha M)(\delta + h/l)] \tag{3.72}$$

For a conical nose, a similar tracing gives the following conical inlet capture efficiency equation

$$(A_0/A_c)_{conical} = (h/l)(1 + \delta M + \alpha M)/[(1 - 0.23\delta M + \alpha M)(\delta + h/l)] \tag{3.73}$$

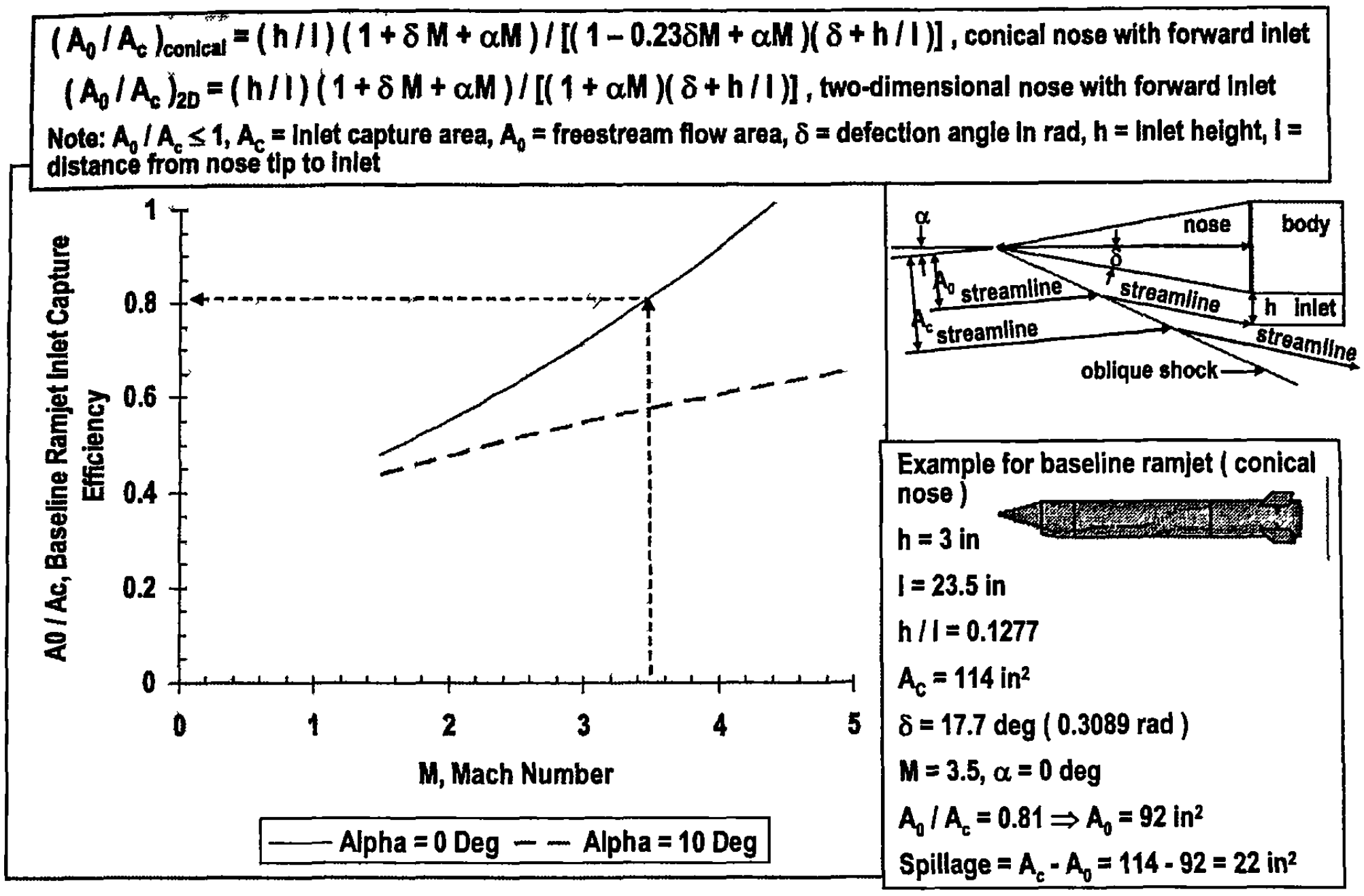

Fig. 3.27 Capture efficiency of an inlet increases with Mach number.

At a given Mach number, a conical shock wave has a smaller shock angle ($\theta_{\text{conical}} = 0.81\theta_{2D}$), resulting in higher capture efficiency for a given body deflection angle δ.

The ramjet baseline capture efficiency is shown in the figure as a function of Mach number ($2 < M < 5$) and angle of attack ($\alpha = 0$, 10 deg). Note from the figure that the ramjet baseline has 100% capture efficiency (shock-on-lip operation) at the cruise design maximum Mach number $M = 4$. Lower capture efficiency and spillage occur at lower Mach number because of the larger value of the shock wave angle θ.

The ramjet baseline will be used as an example calculation of inlet capture efficiency. The chin inlet ramjet baseline has an inlet height $h = 3$ in, a distance from the nose tip to the inlet of $l = 23.5$ in, capture area $A_C = 114$ in^2, and a conical nose half angle $\delta = 17.7$ deg $= 0.309$ rad. For an assumed flight condition of $M = 3.5$ and an angle of attack $\alpha = 0$ deg, the ramjet baseline inlet capture efficiency is computed

$$\begin{aligned}(A_0/A_c) &= (3/23.5)[1 + 0.309(3.5) + 0(3.5)]/ \\ &\quad \{[1 - 0.23(0.309)(3.5) + 0(3.5)](0.309 + 3/23.5)\} \\ &= 0.128(2.08)/[0.751(0.437)] = 0.81 \end{aligned} \tag{3.74}$$

The freestream flow area is computed $A_0 = 0.81(114) = 92$ in^2 and the air spillage is given by $A_C - A_0 = 114 - 92 = 22$ in^2. For the ramjet baseline, a greater value of inlet height would be required for shock-on-lip operation at Mach 3.5.

The equation for the nondimensional inlet throat area that is required to start a two-dimensional supersonic inlet with ideal (isentropic) compression is

$$A_{IT}/A_0 = (M_{IE})_{start}[(\gamma+1)/2]^{(\gamma+1)/[2(\gamma-1)]}$$
$$\{[1+(\gamma-1)/2](M_{IE})_{start}{}^2\}^{-(\gamma+1)/[2(\gamma-1)]} \tag{3.75}$$

The terms in the equation are A_{IT} = inlet throat area, A_0 = freestream flow area, $(M_{IE})_{start}$ = inlet start Mach number, and γ = specific heat ratio. Substituting $\gamma = 1.4$ for air gives

$$A_{IT}/A_0 = 1.728(M_{IE})_{start}(1+0.2(M_{IE})_{start}{}^2)^{-3} \tag{3.76}$$

Another extreme is a two-dimensional supersonic inlet with a single, normal shock compression ($n = 1$). The equation for the nondimensional inlet throat area that is required to start the inlet is

$$A_{IT}/A_0 = (M_{IE})_{start}\{[0.4(M_{IE})_{start}{}^2+2]/[2.4(M_{IE})_{start}{}^2]^{3.5}$$
$$\{[2.8(M_{IE})_{start}{}^2-0.4]/2.4]^{2.5}\{[1.2/[1+0.2(M_{IE})_{start}{}^2]\}^3 \tag{3.77}$$

Figure 3.28 shows $(M_{IE})_{start}$ versus A_{IT}/A_0. Note that $A_{IT} = A_0$ for $(M_{IE})_{start} = 1$ and that for values of $A_{IT} < A_0$, $(M_{IE})_{start} > 1$. Also note that an inlet with a single, normal shock requires a larger Mach number to start the inlet.

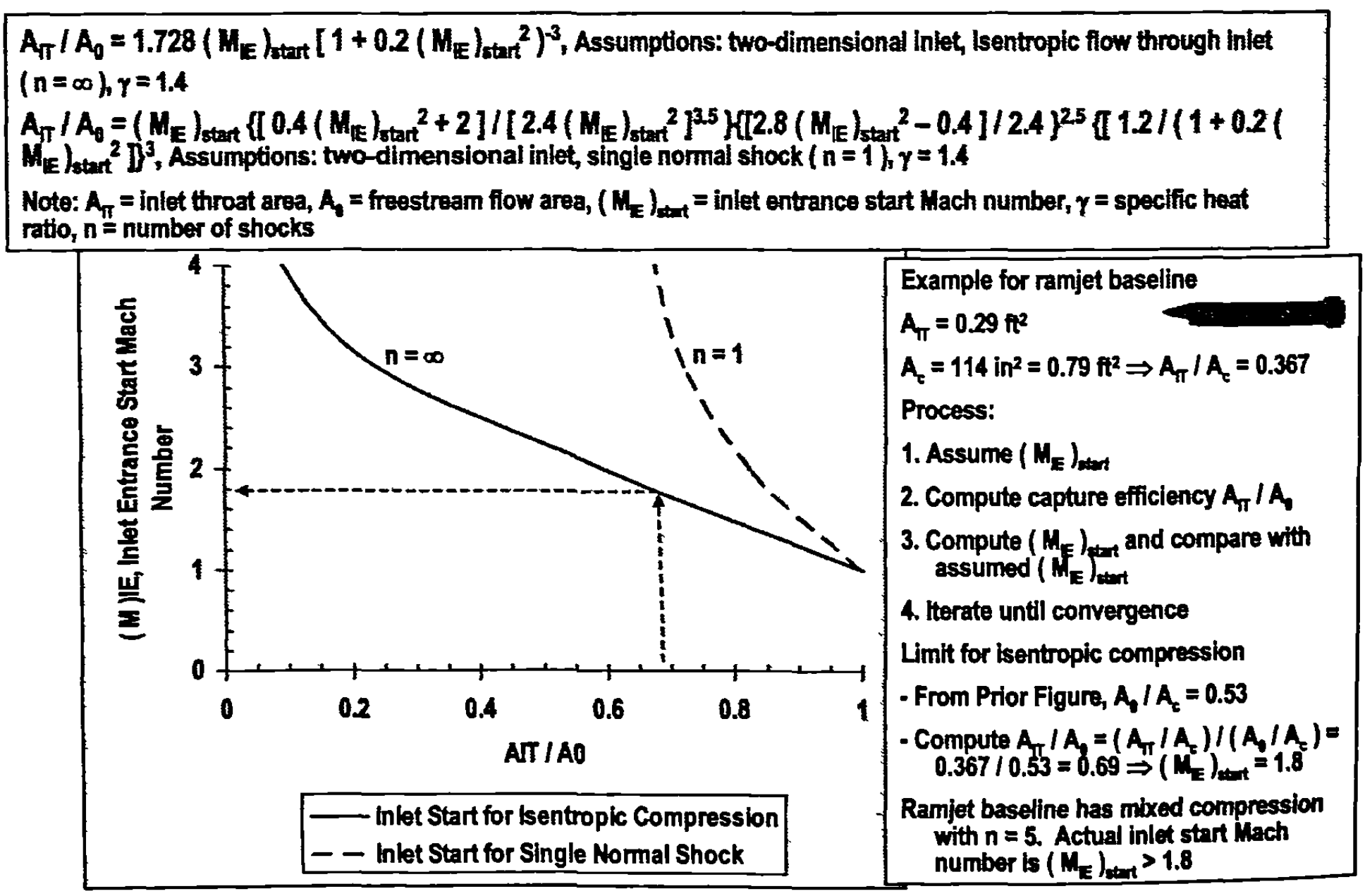

Fig. 3.28 Isentropic compression allows inlet start at lower Mach number.

As an example calculation, assume the ramjet baseline is at an angle of attack $\alpha = 0$ deg. The ramjet baseline inlet throat area is $A_{IT} = 0.29$ ft^2 and its inlet capture area is $A_c = 114$ in$^2 = 0.79$ ft^2. Compute $A_{IT}/A_c = 0.29/0.79 = 0.367$. The inlet start Mach number is obtained by iteration. The process is to 1) assume a value of $(M_{IE})_{start}$; 2) compute the capture efficiency A_{IT}/A_0; 3) compute $(M_{IE})_{start}$ and compare with the assumed $(M_{IE})_{start}$; and 4) iterate until convergence. For this example, assume an ideal isentropic inlet with $(M_{IE})_{start} = 1.8$. From the previous figure, for $(M_{IE})_{start} = 1.8$ and $\alpha = 0$ deg, the inlet capture efficiency is $A_0/A_c = 0.53$. Calculate

$$A_{IT}/A_0 = (A_{IT}/A_c)/(A_0/A_c) = 0.367/0.53 = 0.69 \tag{3.78}$$

Substituting into the inlet start equation $A_{IT}/A_0 = 0.69 = 1.728(1.8)[1 + 0.2(1.8)^2]^{-3}$ verifies $(M_{IE})_{start} = 1.8$.

The ramjet baseline has a mixed compression inlet, with a total of $n = 5$ shocks (four compressions prior to the normal shock inside the inlet). The actual inlet entrance start Mach number is greater than the isentropic inlet start Mach number of $(M_{IE})_{start} = 1.8$. Also, a typical design criteria for a supersonic air-breathing missile is a minimum cruise Mach number of $(M_0)_{MinCruise} \approx 1.2 \times (M_0)_{InletStart}$, to overcome inlet buzz and to have sufficient design margin for the inlet to swallow the shock. Inlet buzz is caused by a transient start and unstart of the inlet. Also, a ramjet needs a thrust/drag design margin following inlet start to accelerate under ramjet thrust to the cruise Mach number. The minimum design Mach number for transition from booster to ramjet flight is $(M_0)_{RamjetTransition} \approx 1.2 \times (M_0)_{InletStart}$.

As discussed previously, it is usually desirable for a ramjet to have a low value of inlet entrance Mach number M_{IE}, which reduces the required start Mach number, which reduces the required size/weight of the booster. A mixed compression inlet provides forebody compression, and the shock wave(s) reduce M_{IE}. The equation for the inlet entrance Mach number for a single oblique shock wave is

$$M_{IE} = \{\{36M_0^4 \sin^2\theta_{2D} - 5[M_0^2 \sin^2\theta_{2D} - 1][7M_0^2 \sin^2\theta_{2D} + 5]\}/ \{[7M_0^2 \sin^2\theta_{2D} - 1][M_0^2 \sin^2\theta_{2D} + 5]\}\}^{1/2} \tag{3.79}$$

The oblique shock wave angle θ_{2D} can be determined from the equation

$$\tan(\alpha + \delta) = 2\cot\theta_{2D}(M_0^2 \sin^2\theta_{2D} - 1)/[2 + M_0^2(2.4 - 2\sin^2\theta_{2D})] \tag{3.80}$$

Terms in the above equations are M_0 = freestream Mach number, α = angle of attack, and δ = body deflection angle. Assumptions are a single shock, two-dimensional flow, perfect gas, and specific heat ratio $\gamma = 1.4$. Figure 3.29 shows M_{IE} for a flow deflection angle $\alpha + \delta$ up to the maximum value for attached flow. Freestream Mach number range shown in the figure is $2 < M_0 < 5$. Note the large effect of flow deflection on reducing M_{IE}.

$$(M_{IE})_{2D} = \{\{36 M_0^4 \sin^2\theta_{2D} - 5[M_0^2 \sin^2\theta_{2D} - 1][7 M_0^2 \sin^2\theta_{2D} + 5]\} / \{[7 M_0^2 \sin^2\theta_{2D} - 1][M_0^2 \sin^2\theta_{2D} + 5]\}\}^{1/2}$$

$$\tan(\alpha + \delta) = 2 \cot\theta_{2D} (M_0^2 \sin^2\theta_{2D} - 1) / [2 + M_0^2 (2.4 - 2\sin^2\theta_{2D})]$$

Assumptions: two-dimensional flow, perfect gas, γ = specific heat ratio = 1.4

Note: M_{IE} = inlet entrance Mach number, M_0 = freestream Mach number, θ = oblique shock angle, α = angle of attack, δ = body deflection angle

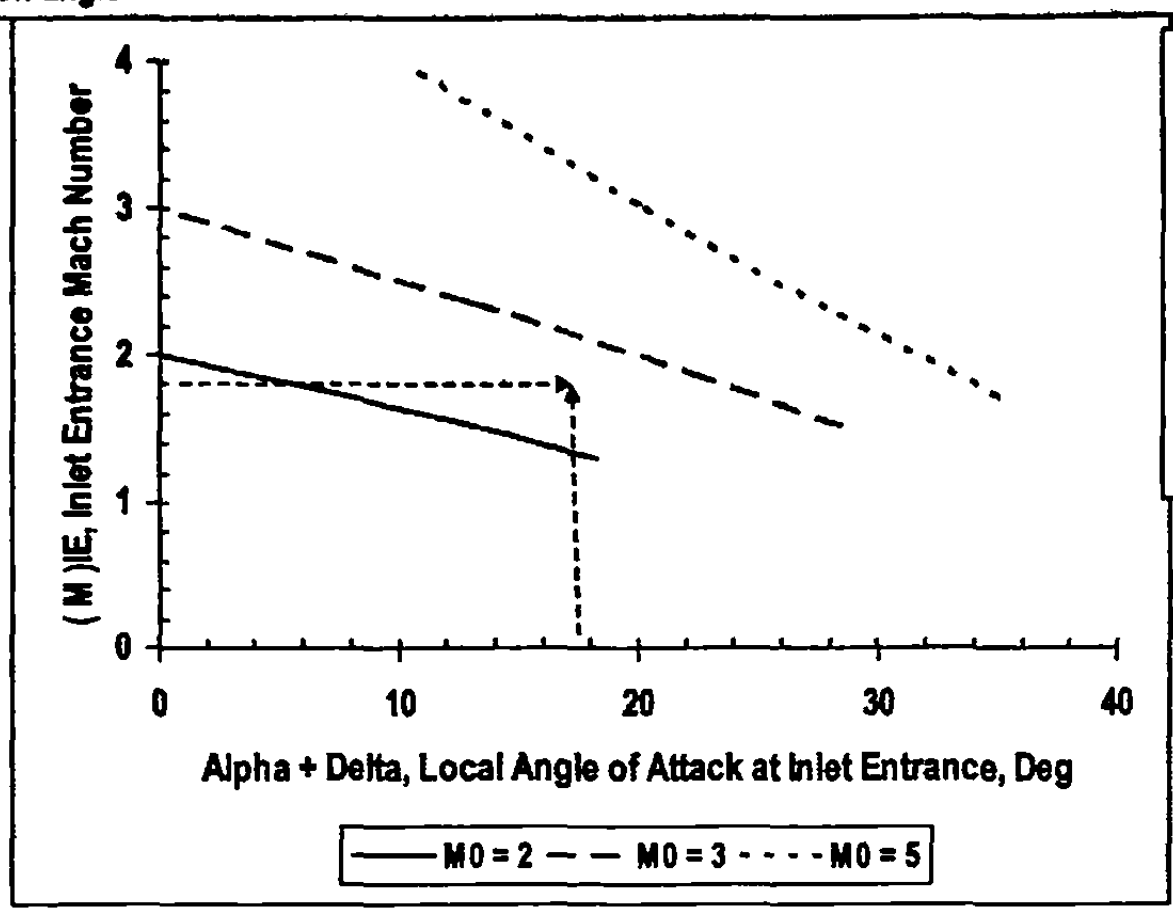

Example for ramjet baseline

δ = 17.7 deg

$(M_{IE})_{start}$ = 1.8 (from prior example)

Compute M_0 = 2.55

Note: Ramjet baseline forebody is conical, not two-dimensional

Fig. 3.29 Forebody shock compression reduces the inlet entrance Mach number.

As an example, assume that the ramjet baseline conical forebody can be approximated as a two-dimensional deflection. Then for $\alpha = 0$ deg, $\alpha + \delta = 17.7$ deg. From the prior example, the inlet start Mach number is $(M_{IE})_{Inletstart} \approx 1.8$. Substituting into the above equations and neglecting the difference between a conical deflection versus a two-dimensional deflection, the ramjet baseline booster must be sized for a ramjet transition Mach number of approximately $(M_0)_{RamjetTransition} \approx 2.55$.

Figure 3.30, derived from Ref. 14 presents the optimum deflection angles of wedge forebodies to give the highest value of total pressure ratio following a normal shock. Oswatitsch[15] showed that the optimum forebody deflection angles for maximum total pressure behind a normal shock provide equal loss in total pressure across each shock wave. Note from the figure that the required deflection angle(s) for optimum pressure recovery increases with Mach number. For freestream Mach numbers greater than 4, the optimum deflection angle(s) increases slowly with increasing Mach number. The figure also shows that two external shocks have smaller optimum deflection angles than the optimum deflection angle of a single external shock. Also note that the sum of the deflections (total turning angle) for two optimum external shocks is greater than the deflection angle of a single optimum external shock. Similarly, three optimum external shocks have smaller deflection angles than two optimum external shocks and the total turning angle of three optimum external shocks is greater than the total turning angle of two optimum external shocks. The advantage of multiple shocks over one shock is higher total pressure recovery. A disadvantage of multiple external shocks prior to the inlet normal shock is the flow is deflected more away from the centerline. As a rule of thumb, the total turning angle of the flow should be less than about 45 deg to avoid flow separation inside the inlet.

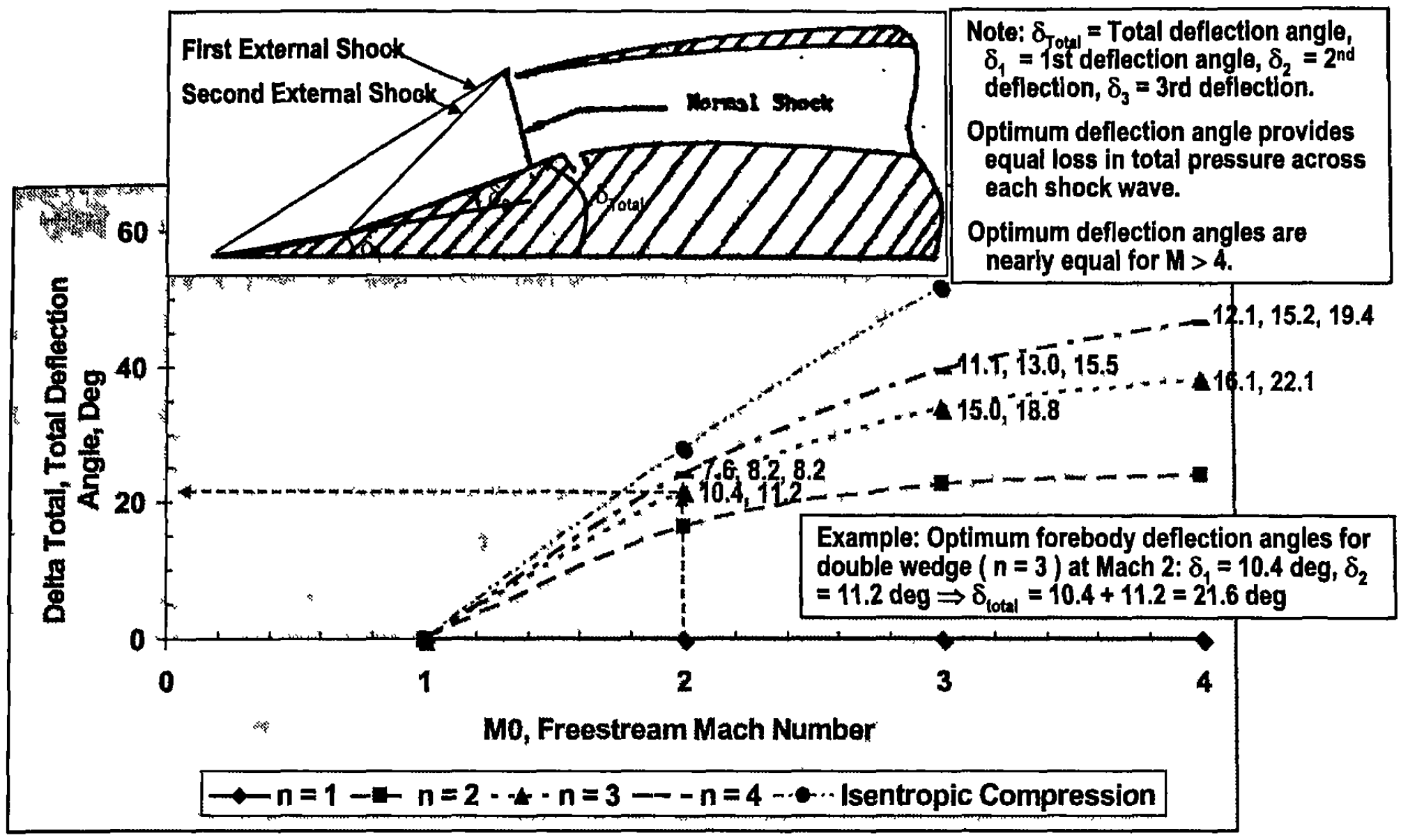

Reference: "Technical Aerodynamics Manual," North American Rockwell Corporation, DTIC AD 723823, June 1970.

Fig. 3.30 Optimum forebody deflection angle(s) for best pressure recovery increases with Mach number.

As an example, at Mach 2 the forebody optimum total deflection angle for a double-wedge forebody is 21.6 deg, with two oblique shocks prior to a normal shock of 10.4 deg half-angle for the first deflection and 11.2 deg half-angle for the second deflection.

Because ramjet combustion is subsonic, there must be an inlet normal shock to provide subsonic flow into the combustor. Small oblique shocks prior to the normal shock alleviate the problem of total (stagnation) pressure loss across the inlet normal shock. Figure 3.31, based on Ref. 14, compares the military specification MIL-E-5008B total pressure recovery requirement with that of a single normal shock as well as one, two, and three optimum two-dimensional oblique shocks prior to the normal shock. The requirement of MIL-E-5008B, which is a reasonable pressure recovery for a well designed inlet, is given by the equation

$$p_{t_{Inlet}}/p_{t_0} = 1 - 0.075(M-1)^{1.35} \tag{3.81}$$

As stated previously, from Oswatitsch[15] we know that the maximum pressure recovery occurs for an equal loss in total pressure across each shock wave. Note from the figure that for hypersonic missiles, a mixed compression inlet with three or more oblique shocks is required to satisfy MIL-E-5008B. For the ramjet baseline, inlet/airframe integration consists of 1) an external forebody compression (conical nose); 2) a ramp leading up to the cowl; 3) an inlet cowl lip angle; 4) internal turning; and 5) an internal normal shock. A mixed compression inlet reduces excessive flow turning away from the axial direction.

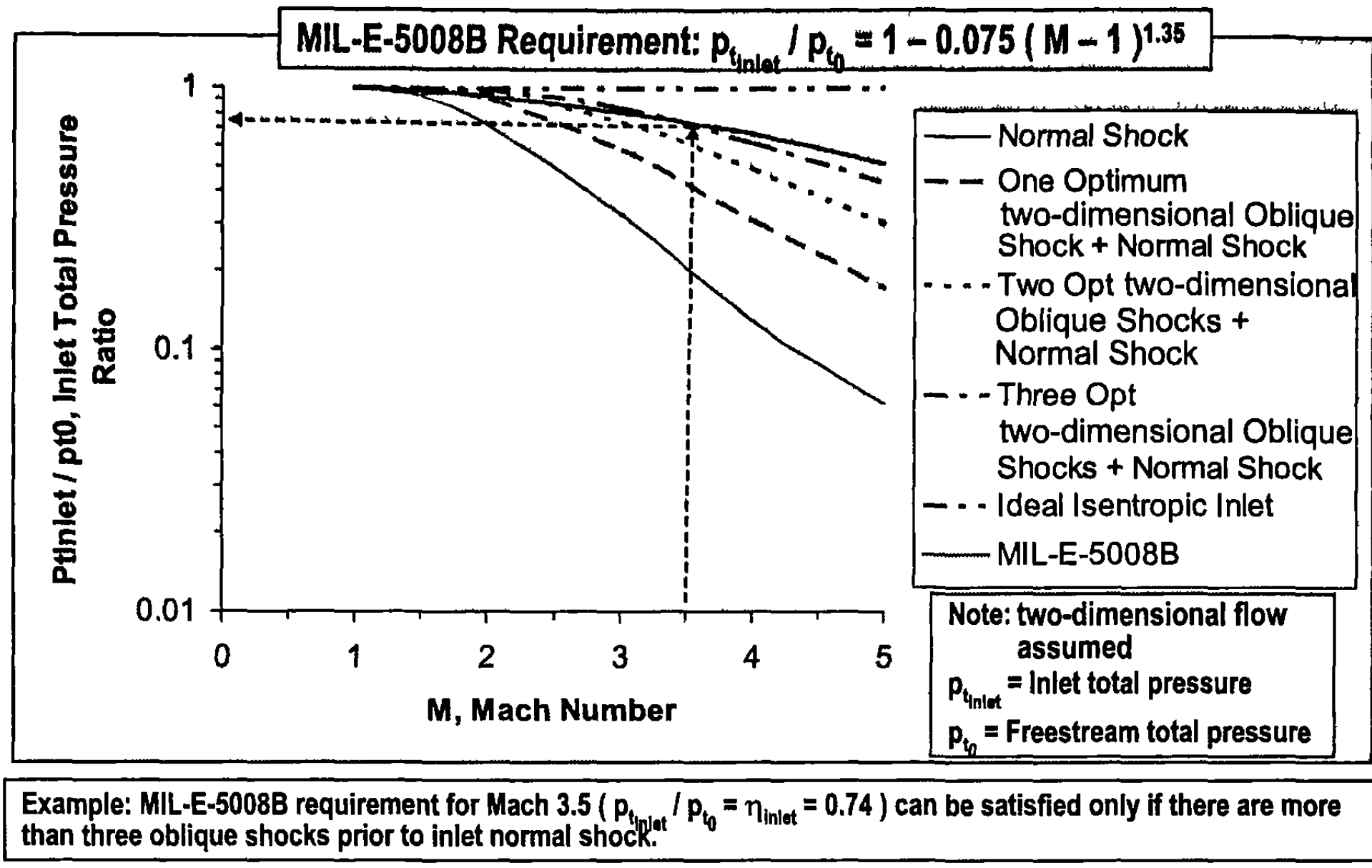

Source for Optimum 2D Shocks: Oswatitsch, K.L., "Pressure Recovery for Missiles with Reaction Propulsion at High Supersonic Speeds", NACA TM - 1140, 1947.

Fig. 3.31 Oblique shocks prior to the inlet normal shock are required to satisfy MIL-E-5008B.

An example is shown in the figure. The MIL-E-5008B Mach 3.5 requirement is compared with the Mach 3.5 total pressure recovery for three optimum oblique shocks plus a normal shock. From Ref. 13, at Mach 3.5 the optimum deflection angles are $\delta_1 = 11.9$ deg, $\delta_2 = 14.1$ deg, and $\delta_3 = 17.2$ deg. As shown in the figure, the stagnation pressure recovery from three optimum oblique shocks at Mach 3.5 is $\eta_{\text{inlet}} = 0.72$. The requirement from MIL-E-7008B for Mach 3.5 is

$$\eta_{\text{inlet}} = p_{\text{tInlet}}/p_{\text{t0}} = 1 - 0.075(3.5 - 1)^{1.35} = 0.74 \tag{3.82}$$

Therefore, more than three oblique shocks are required to satisfy the military standard for Mach 3.5.

3.14 Fuel Alternatives

An area of high payoff for airbreathing missiles is that of high-density fuels. As shown in Fig. 3.32, the high-density fuels provide high volumetric performance, which is especially beneficial for volume-limited missiles. Current turbojet fuels such as JP-4, JP-5, JP-7, and JP-10 have relatively low density, on the order of 0.028 lb/in^3, and low volumetric performance, on the order of 559 BTu/in^3. Liquid-fuel ramjet hydrocarbon fuels such as RJ-4, RJ-5, RJ-6, and RJ-7 have somewhat higher density (0.040 lb/in^3) and higher volumetric performance (581 BTu/in^3). Binder fuels, such as hydroxyl-terminated polybutadiene (HTPB), have an advantage of slightly higher volumetric performance (606 BTu/in^3) with

Type Fuel	Density, lb / in³	Volumetric Performance, BTU / in³	Low Observables
Turbine (JP-4, JP-5, JP-7, JP-8, JP-10)	~ 0.028	○ 559	●
Liquid Ramjet (RJ-4, RJ-5, RJ-6, RJ-7)	~ 0.040	○ 581	●
HTPB	~ 0.034	○ 606	○
Slurry (40% JP-10 / 60% carbon)	~ 0.049	◒ 801	○
Solid Carbon (graphite)	~ 0.075	● 1132	–
Slurry (40% JP-10 / 60% aluminum)	~ 0.072	◒ 866	–
Slurry (40% JP-10 / 60% boron carbide)	~ 0.050	● 1191	–
Solid Mg	~ 0.068	● 1200	–
Solid Al	~ 0.101	● 1300	–
Solid Boron	~ 0.082	● 2040	–

● Superior ◒ Above average ○ Average – Below average

Fig. 3.32 High-density fuels provide higher volumetric performance but have higher observables.

a disadvantage of increased visual observables. The density of HTPB is 0.034 lb/in^3. Slurry fuels, such as JP-10 with carbon slurry, and solid carbon fuels, such as graphite, have much higher volumetric performance. High volumetric performance is also achievable with high-density solid metal fuels such as magnesium, aluminum, and boron. For example, solid boron fuel, if it could be packaged with a theoretical solids loading of 100%, would provide more than three times the volumetric performance of a liquid hydrocarbon fuel. Disadvantages of solid metal fuels are high visual observables from their plumes and reduced volumetric loading/packaging efficiency.

3.15 Ducted Rocket Design Considerations

Ducted rockets combine the higher specific impulse of a ramjet with some of the simplicity and acceleration capability of a solid rocket. If there is a relatively small amount of excess fuel (e.g., 30% of the propellant weight) discharged by the gas generator, the ducted rocket behaves more like a rocket, with a higher burn rate and a higher temperature but a lower specific impulse. Conversely, if the gas generator discharges a relatively large amount of excess fuel (e.g., 70% of the propellant weight), the ducted rocket behaves more like a ramjet, with a higher specific impulse and a lower burn rate/temperature. The fuel fraction of a ducted rocket varies from about 30 to 80% of the propellant weight. Fuel fractions greater than 80% are not practical for ducted rocket propulsion because the reduced combustion temperature for a high fuel fraction severely reduces the fuel flow rate, resulting in an unacceptably low thrust.

Ducted rocket fuels are either a metal fuel such as boron, aluminum, and magnesium or a carbon-based fuel such as graphite carbon or hydrocarbon HTPB binder. Metal fuels have an advantage of higher specific impulse. Also, the higher density of metal fuels is beneficial for a volume-limited missile. Disadvantages of metal fuels include deposits and higher observables. Metal fuel deposits downstream of the gas generator are a particular problem for a high fuel fraction ducted rocket because of the reduced combustion temperature. A carbon-based fuel has an advantage of lower observables and a higher reliability from reduced deposits. A disadvantage is lower maximum specific impulse compared to a metal fuel (e.g., 800 vs 1,000 s).

The choice of oxidizer is a primary trade of performance versus reduced observables. Ammonium perchlorate (AP) has advantages of higher burn rate and lower hazards classification. However, AP provides an HCl contrail, particularly at high altitude. Minimum smoke oxidizers, such as Her Majesty's Explosive (HMX) and Royal Demolition Explosive (RDX) have reduced observables but have disadvantages of lower performance and are more hazardous.

The most popular approach for thrust magnitude control is to partially block the gas generator throat with a pintle or valve. Partially blocking the gas generator throat reduces the throat area, resulting in an increase in the chamber pressure. The increased chamber pressure increases the gas flow rate, which provides increased thrust. The thrust variation using this approach is about 10:1. A concern is deposits on the pintle or valve that may clog the gas generator throat. Another approach incorporates retractable wires in the gas generator propellant grain. The burn area of the gas generator propellant grain is a function of the retraction speed of the wires. A disadvantage of this approach is the maximum variation in thrust is only about 4:1.

3.16 Rocket Motor Performance

Figure 3.33 shows the relationship of the maximum incremental velocity of a rocket as a function of the propellant weight fraction and the specific impulse. The equation is

$$\Delta V = -g_c I_{sp} ln(1 - W_p/W_i) \tag{3.83}$$

An assumption for the equation is a high-thrust motor, with thrust much larger than drag. It is also assumed that the thrust is much greater than the component of the missile weight in the thrust direction, which is applicable for either high thrust-to-weight ratio or horizontal flight. Also, the flight path angle is assumed to be constant. Note from the figure that hypersonic Mach number can be achieved for a low-speed launch only if the propellant weight is more than one-half of the missile initial weight. Also note that higher specific impulse also gives higher burnout velocity.

For the rocket baseline missile, the initial boost (launch) weight is $W_{i,boost} = W_L = 500$ lb, the boost propellant weight is $W_p = 84.8$ lb, and the specific impulse during boost is $I_{SP} = 250$ s. Computing the maximum theoretical incremental velocity from boost

$$\Delta V = -32.2(250) ln(1 - 84.8/500) = 1496 \text{ ft/s} \tag{3.84}$$

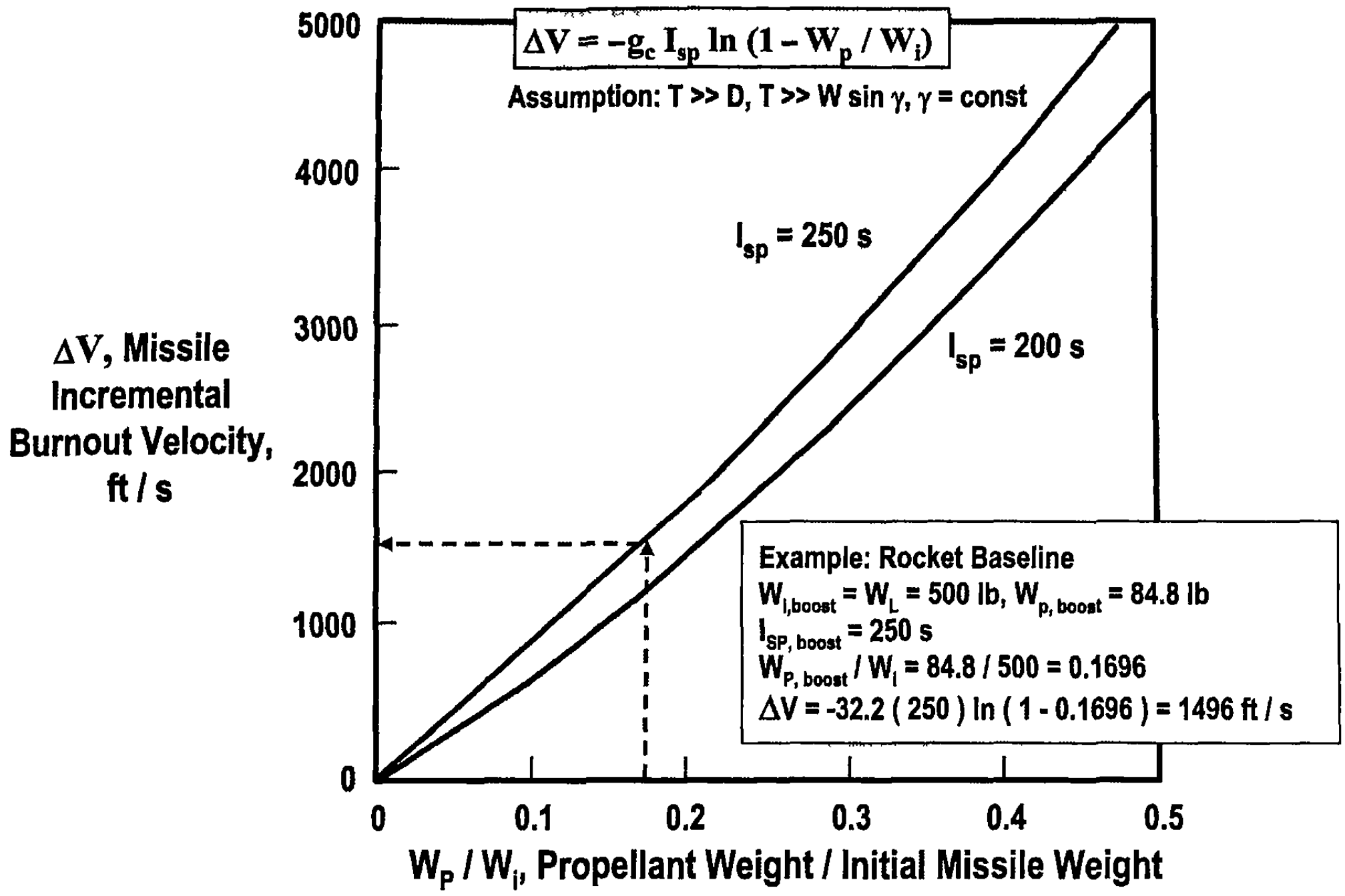

Fig. 3.33 High propellant fraction increases burnout velocity.

For a typical launch condition of Mach 0.8/20,000 ft altitude, the launch velocity is 820 ft/s, resulting in a theoretical end-of-boost velocity of

$$V_{\mathrm{EB}} = 820 + 1496 = 2316 \text{ ft/s} \tag{3.85}$$

The actual end-of-boost velocity would be lower because of drag.

Specific impulse and thrust are primary considerations in the motor sizing process. Assuming isentropic flow, the equations are

$$\begin{aligned} I_{\mathrm{SP}} &= c_{\mathrm{d}}\{\{[2\gamma^2/(\gamma-1)][2/(\gamma+1)]^{(\gamma-1)/(\gamma+1)}[1-(p_{\mathrm{e}}/p_{\mathrm{c}})^{(\gamma-1)/\gamma}]\}^{1/2} \\ &\quad + (p_{\mathrm{e}}/p_{\mathrm{c}})\varepsilon - (p_0/p_{\mathrm{c}})\varepsilon\}c^*/g_{\mathrm{c}} \end{aligned} \tag{3.86}$$

$$\begin{aligned} T &= \dot{w}_{\mathrm{p}} I_{\mathrm{SP}} = (g_{\mathrm{c}}/c^*)p_{\mathrm{c}}A_{\mathrm{t}}I_{\mathrm{SP}} \\ \varepsilon &= \{[2/(\gamma+1)]^{1/(\gamma-1)}[(\gamma-1)/(\gamma+1)]^{1/2}\}/ \\ &\quad \{(p_{\mathrm{e}}/p_{\mathrm{c}})^{1/\gamma}[1-(p_{\mathrm{e}}/p_{\mathrm{c}})^{(\gamma-1)/\gamma}]^{1/2}\} \end{aligned} \tag{3.87}$$

Specific impulse of the rocket baseline is shown in Fig. 3.34 as a function of nozzle expansion ratio and chamber pressure. These results are based on typical values of specific heat ratio ($\gamma = 1.18$), discharge coefficient ($c_{\mathrm{d}} = 0.96$), propellant characteristic velocity ($c^* = 5200$ ft/s), and $h = 20{,}000$ ft altitude ($p_0 = 6.75$ psi). The assumed characteristic velocity of 5200 ft/s is a representative value for a propellant. For a low-performance, minimum smoke propellant, c^* may be less than 4800 ft/s. It may be greater than 5600 ft/s for a high-performance, high-smoke propellant. Referring again

$$I_{SP} = c_d \{\{[2\gamma^2/(\gamma-1)][2/(\gamma+1)]^{(\gamma+1)/(\gamma-1)}[1-(p_e/p_c)^{(\gamma-1)/\gamma}]\}^{1/2} + (p_e/p_c)\varepsilon - (p_0/p_c)\varepsilon\} c^*/g_c$$

$$T = \dot{w}_p I_{SP} = (g_c/c^*) p_c A_t I_{SP}$$

$$\varepsilon = \{[2/(\gamma+1)]^{1/(\gamma-1)}[(\gamma-1)/(\gamma+1)]^{1/2}\} / \{(p_e/p_c)^{1/\gamma}[1-(p_e/p_c)^{(\gamma-1)/\gamma}]^{1/2}\}$$

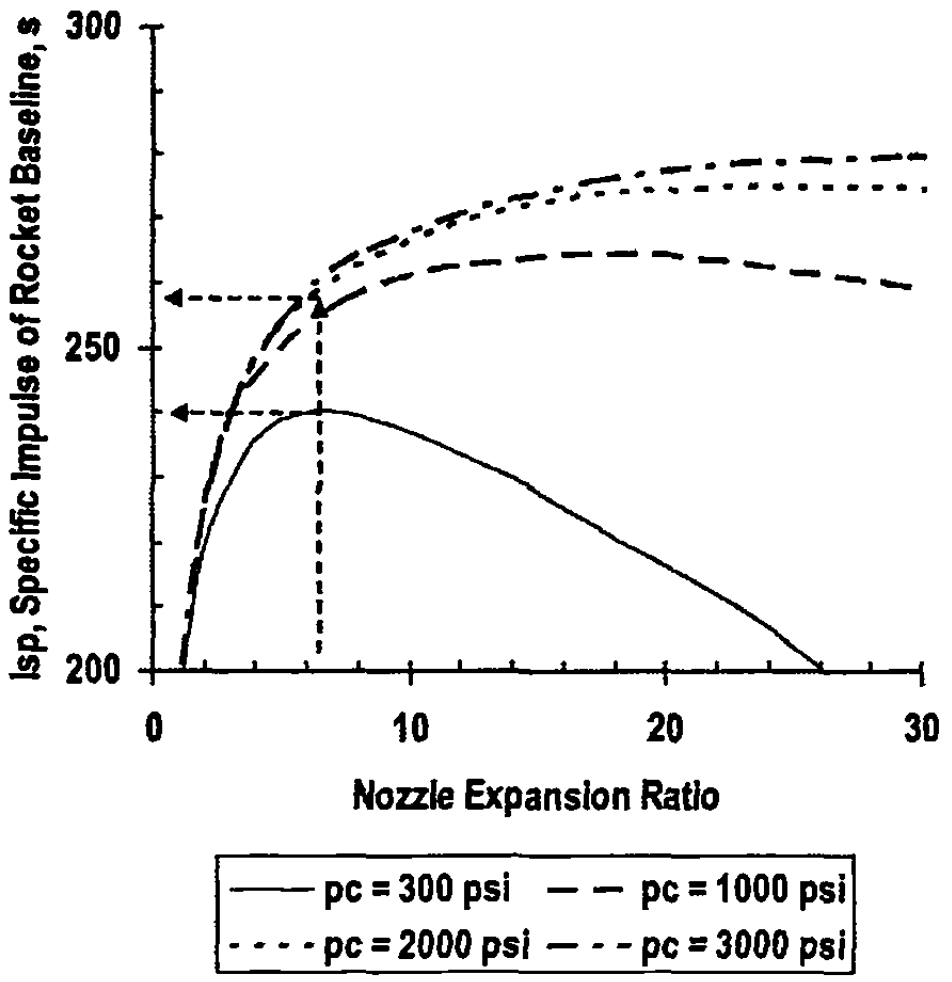

Note:
ε = nozzle expansion ratio
p_e = exit pressure
p_c = chamber pressure
p_0 = atmospheric pressure
$\dot{w}_p$ = propellant weight flow rate
A_t = nozzle throat area (minimum, sonic, choked)
γ = specific heat ratio = 1.18 in figure
c_d = discharge coefficient = 0.96 in figure
c^* = characteristic velocity = 5,200 ft / s in figure
h = 20,000 ft, p_0 = 6.75 psi in figure

Example for Rocket Baseline:
$\varepsilon = A_e / A_t = 6.2 \Rightarrow p_e / p_c = 0.02488$, $A_t = 1.81$ in^2
$(p_c)_{boost} = 1769$ psi, $p_e = 44$ psi, $(I_{SP})_{boost} = 257$ s
$(I_{SP})_{\varepsilon=6.2} / (I_{SP})_{\varepsilon=1} = 257 / 200 = 1.29$
$(T)_{boost} = (32.2 / 5200)(1769)(1.81)(257) = 5096$ lb
$(p_c)_{sustain} = 301$ psi, $p_e = 7.49$ psi, $(I_{SP})_{sustain} = 239$ s
$(I_{SP})_{\varepsilon=6.2} / (I_{SP})_{\varepsilon=1} = 240 / 200 = 1.20$
$(T)_{sustain} = (32.2 / 5200)(301)(1.81)(240) = 810$ lb

Fig. 3.34 High specific impulse requires high chamber pressure and optimum nozzle expansion.

to the figure, note that a high chamber pressure requires a high nozzle expansion ratio for maximum specific impulse. Also note that for a low chamber pressure, a relatively small value of nozzle expansion is desired. At high-altitude flight conditions and high chamber pressure, a large expansion ratio is desirable for the nozzle, within the limit of the missile diameter and length constraints. For a length-limited missile, a tradeoff is a large expansion nozzle with higher I_{SP} versus a lower expansion nozzle and shorter nozzle length. Although the lower expansion nozzle has lower I_{SP}, the shorter nozzle length allows more length for propellant for a length-limited missile. Another possible design approach for a length-limited missile would be to use two or more adjacent nozzles instead of a single nozzle, such as the TOW missile. Multiple nozzles can be designed for optimum expansion and higher I_{SP} in a shorter length.

As an example calculation of specific impulse and thrust, the rocket baseline has a nozzle exit-area-to-throat-area expansion ratio of $\varepsilon = 6.2$ and a nozzle throat area (minimum flow area with sonic, choked flow) $A_t = 1.81$ in^2. At an altitude of 20,000 ft, the specific impulse and thrust during boost ($p_c = 1{,}769$ psi) are computed to be $I_{SP} = 257$ s and $T = 5096$ lb respectively. During the lower chamber pressure sustain ($p_c = 301$ psi), the computed specific impulse and thrust are $I_{SP} = 239$ s and $T = 810$ lb. Note from the figure that for the rocket baseline during sustain flight, its expansion ratio provides maximum I_{SP}.

A purpose of using nozzle expansion is to provide increased specific impulse and thrust. For the rocket baseline, nozzle expansion increases the specific impulse by 29% during boost (257 s for $\varepsilon = 6.2$ vs 200 s for $\varepsilon = 1$). During

sustain, the nozzle expansion increases the specific impulse by 20% (239 s with the nozzle vs 200 s if there were no nozzle expansion).

The actual specific impulse of the rocket baseline is about 3% lower than prediction (250 vs 257 s during boost and 230 vs 239 s during sustain). The actual thrust of the rocket baseline is about 20% higher than prediction (5750 vs 5096 lb during boost and 1018 vs 810 lb during sustain). The predicted burn time is about 20% longer than the actual burn time. A possible contributor to the differences between prediction and data is the assumed value of specific heat ratio γ of the nozzle gases. Although the gases experience a large variation in temperature, the prediction is based on an assumption of a constant $\gamma = 1.18$ during the expansion of the gases through the nozzle.

Shown in Fig. 3.35 are the chamber pressure and the area of the nozzle throat that are necessary to provide a required propellant weight flow rate. The equation is

$$A_t = c^* \dot{w}_p / (g_c p_c) \tag{3.88}$$

Note from the figure that the necessary throat area A_t and chamber pressure p_c increase with increased values of the design propellant burn rate $\dot{w}_p$ and characteristic velocity c^*. Also note that the necessary throat area decreases with an increased value of the design chamber pressure. The range of values shown are the figure are typical values of A_t, $\dot{w}_p$, c^*, and p_c for tactical missiles.

As an example, the rocket baseline has a propellant characteristic velocity of $c^* = 5200$ ft/s. At the boost condition the motor chamber pressure is $p_c = 1769$

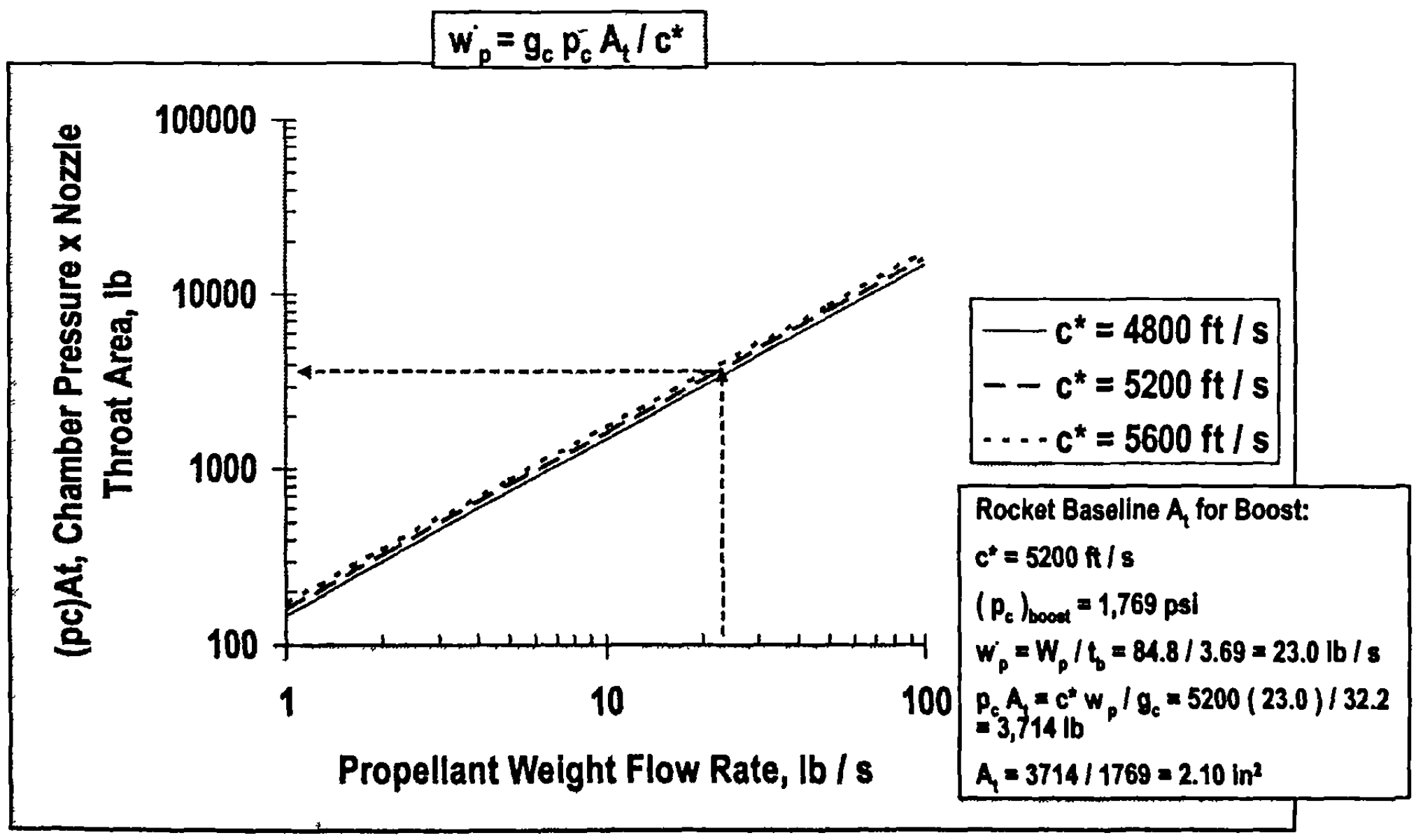

Note: A_t = nozzle throat area, c^* = characteristic velocity, w_p = propellant weight flow rate, g_c = gravitational constant, p_c = chamber pressure

Fig. 3.35 High propellant weight flow rate requires a high chamber pressure and a large nozzle throat

psi and the propellant weight flow rate is $\dot{w}_p = 23.0$ lb/s. The necessary nozzle throat area is computed to be

$$A_t = 5200(23.0)/[32.2(1769)] = 2.10 \text{ in}^2 \tag{3.89}$$

The computed nozzle throat area is 16% higher than the actual nozzle throat area of the rocket baseline (2.10 vs 1.81 in^2).

Nozzle exit area and nozzle throat area define the nozzle expansion ratio ($\varepsilon = A_e/A_t$). It may not be possible to use the value of expansion ratio that gives the maximum value of specific impulse and thrust. The expansion ratio that provides $(I_{SP})_{max}$ and T_{max} may not allow sufficient volume for packaging subsystems around the nozzle, it may result in an excessively long nozzle, or it may exceed the diameter of the missile. A lower value of the design ε may be required, reducing the value of the achievable specific impulse and thrust.

Figure 3.36 shows a relationship of the propellant burn area to the chamber pressure of the rocket baseline. The equations are

$$A_b = g_c p_c A_t/(\rho c^* r) \tag{3.90}$$

$$r = r_{p_c=1000 \text{ psi}}(p_c/1000)^n \tag{3.91}$$

Note that the required burn area A_b is a function of the chamber pressure, throat area, propellant density, characteristic velocity, and the propellant burn rate. To achieve a high chamber pressure, a large propellant burn area and a small nozzle throat are required. Burn rate r is a function of the propellant

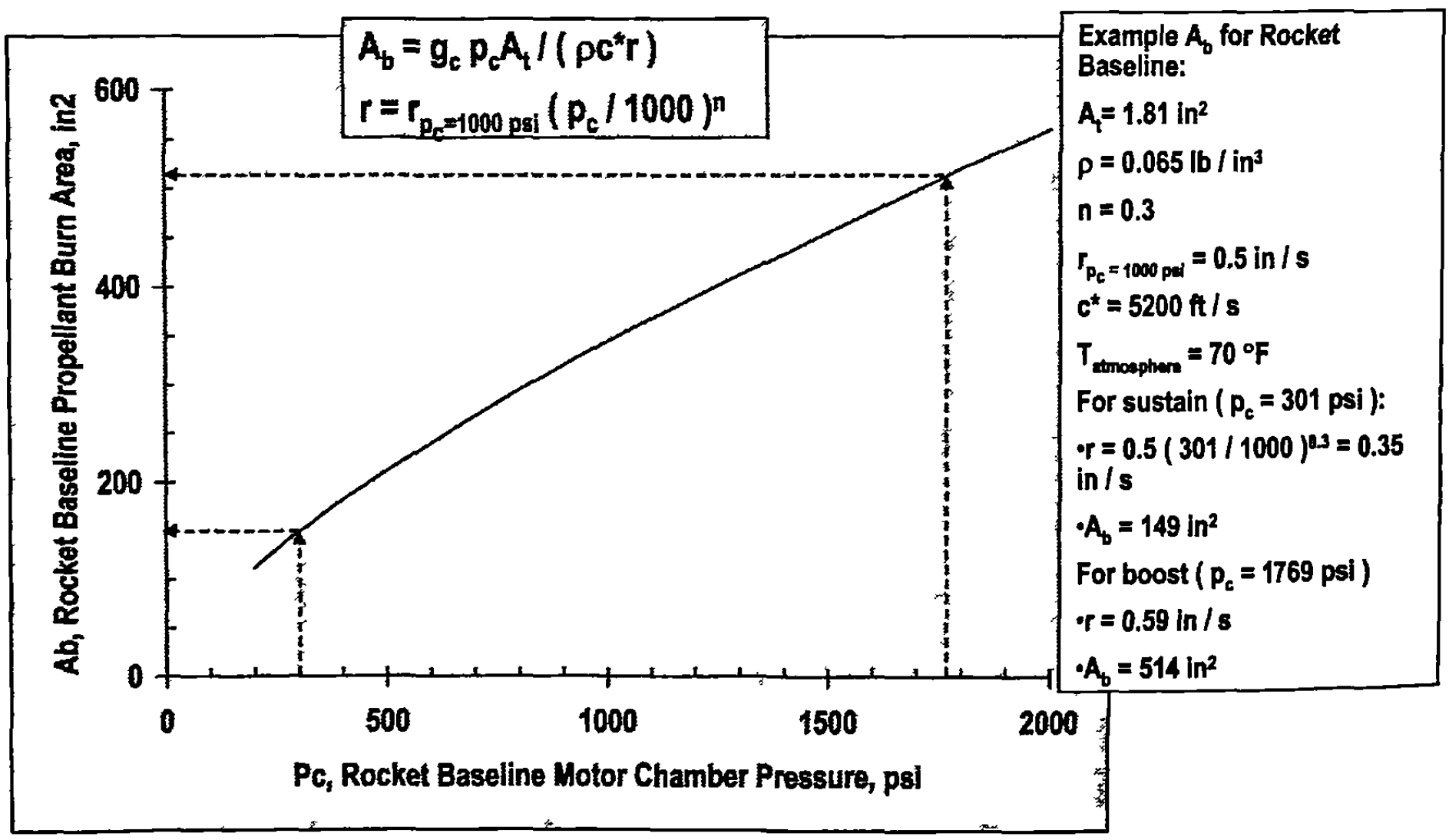

Note: A_b = propellant burn area, g_c = gravitation constant, A_t = nozzle throat area, ρ = density of propellant, c^* = characteristic velocity, r = propellant burn rate, $r_{p_c=1000 \text{ psi}}$ = propellant burn rate at p_c = 1,000 psi, p_c = chamber pressure, n = burn rate exponent

Fig. 3.36 High chamber pressure requires large propellant burn area and a small nozzle throat.

reference burn rate at a reference chamber pressure of 1000 psi ($r_{p_c=1000\text{ psi}}$), chamber pressure p_c, and burn rate exponent n. For statically stable combustion, $n < 1$. For a boost-sustain motor, it may be desirable for the value of n to approach 1. This allows a large change in burn rate, mass flow rate, and thrust with a small change in chamber pressure and burn area.

For a solid rocket, the oxidizer and fuel are all already mixed in the propellant. As a result, combustion occurs nearly instantaneously at the burning surface. For air-breathing or liquid-propellant propulsion, combustion occurs downstream of the mixing of the fuel and oxidizer. As a result, air-breathing propulsion and liquid-propellant rocket propulsion require additional length and volume to complete combustion compared to a solid rocket.

The rocket baseline has a throat area $A_t = 1.81$ in^2, a propellant density $\rho = 0.065$ lb/in^3, and a characteristic velocity $c^* = 5200$ ft/s. The burn rate exponent is $n = 0.3$, referenced to a nominal chamber pressure $p_c = 1000$ psi and a nominal atmospheric temperature $T = 70°$ F. The nominal burn rate at standard conditions is $r = 0.5$ in/s. During sustain, with a chamber pressure of $p_c = 301$ psi, the burn rate is $r = 0.5(301/1000)^{0.3} = 0.35$ in/s. The required burn area for sustain is

$$A_b = 32.2(301)(1.81)/[0.065(5200)(0.35)] = 149 \text{ in}^2 \tag{3.92}$$

For the 8-in diameter rocket baseline, the body cross-sectional area is 50 in^2. An end-burning grain for the rocket baseline, constrained by its nozzle geometry, propellant burn rate exponent, and propellant burn rate, would not provide the required chamber pressure. Therefore a center cavity grain, with three radial slots, is used for the rocket baseline to obtain the required burn surface area for boost and sustain thrust. For the rocket baseline boost chamber pressure $p_c = 1769$ psi, the burn rate during boost is $r = 0.5(1769/1000)^{0.3} = 0.59$ in/s. The required burn area for boost is larger,

$$A_b = 32.2(1769)(1.81)/[0.065(5200)(0.59)] = 514 \text{ in}^2 \tag{3.93}$$

Figure 3.37 summarizes the rocket motor sizing process for conceptual design. It is a highly iterative process that harmonizes a large number of design parameters and constraints. The process begins by 1) specifying an altitude and assuming a desired thrust-time profile. In the next step, 2) assumptions are made for the type of propellant, the desired chamber pressure, the burn area(s), and the nozzle geometry. These are used in step 3) to calculate an initial estimate of the thrust and specific impulse. If the thrust and specific impulse are acceptable, the process continues to the next step. However, if the initial estimate of thrust and specific impulse are not acceptable, we go back to step 2 and try again with a different combination of propellant, chamber pressure, burn area, and nozzle geometry. If we still cannot get an acceptable specific impulse and thrust after iterating in step 2, we may have to go back to step 1 and change the desired thrust-time profile. Assuming that the desired specific impulse and thrust are achievable, we next go to step 4) and calculate of the propellant weight flow rate and the weight of the propellant used. If this is acceptable, we

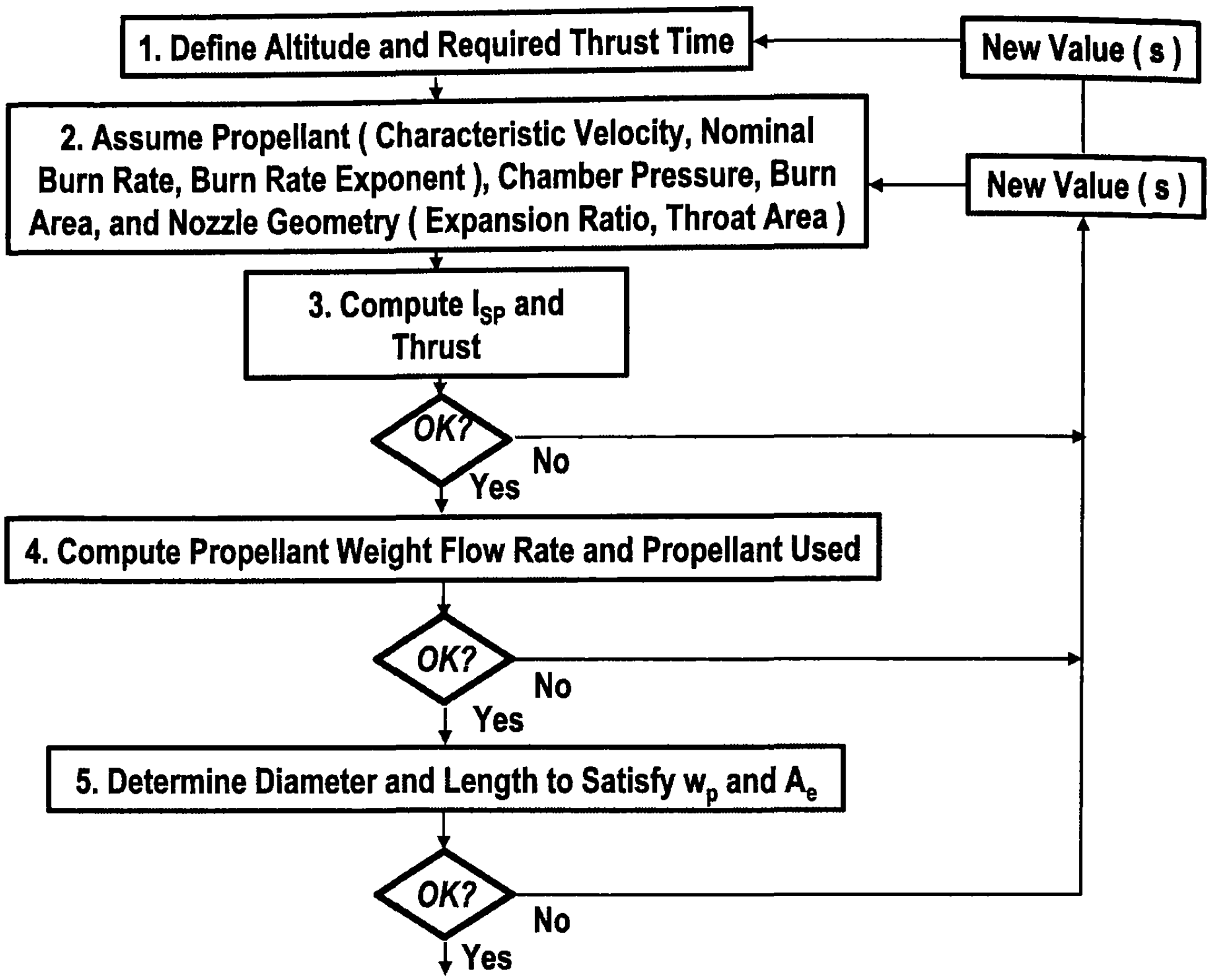

Fig. 3.37 Conceptual design sizing process for a rocket motor.

go to the next step. If not, we go back and iterate step 2 until we reach a convergence. Again, if there is no convergence, we may have to go back to step 1 and change the desired thrust-time history. Assuming that there is a convergence, we next go to step 5), determining the diameter and length to satisfy the propellant weight and nozzle exit area. If this is acceptable, we have completed one of the possible design solutions. If it is not acceptable, we have to go back and iterate until there is a solution.

3.17 Solid Propellant Grain Alternatives

To define a varying thrust-time profile, a cavity through the center of the propellant grain can be used to provide the required burning surface area time profile. As shown in Fig. 3.38, a variety of shapes (e.g., wagon wheel, star, dendrite, end-burner, radial slotted tube) provide larger or smaller burn area and thus more or less hot gas, providing more or less thrust. The change in the burn area as a function of time provides the desired thrust-time profile. If the thrust increases with burn time, it is referred to as progressive burning. If the grain design produces a decrease in thrust with burn time, the rocket motor is said to have regressive burning characteristics. Shown in the figure are typical volumetric loadings for grain design. The volumetric efficiency of the propellant

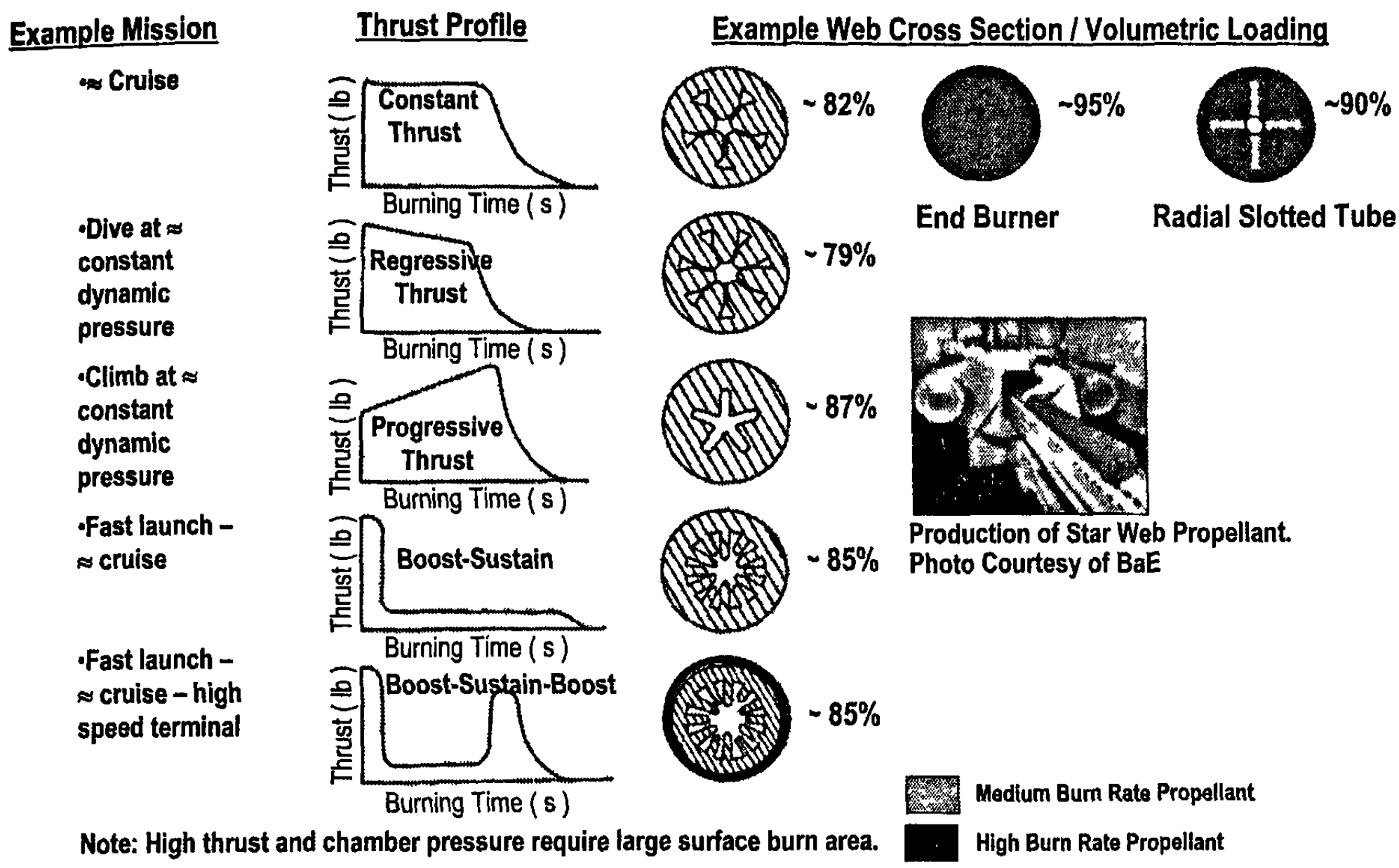

Fig. 3.38 Conventional solid rocket thrust-time design alternatives are a function of the propellant cross section.

grain cavity loading for operational missiles varies from about 79 to 87%. High volumetric efficiency is desirable to maximize the amount of propellant and to minimize the weight of the motor case. A disadvantage of high volumetric loading of the propellant grain cavity is that there may be problems of localized stress and cracks in the the grain.

For a propellant grain with radial burn, the length of the radial-burn motor affects the thrust. A longer motor has more burn area, which provides higher thrust.

Shown in the top section of the figure is an end-burner. An end-burner has no cavity, only the end of the grain burns. An end-burning grain has nearly constant burning area, and if the throat area is constant, provides nearly constant thrust. An advantage of an end-burner is high volumetric loading. A potential disadvantage is relatively low thrust.

Another popular type of cross section is a radial slotted tube, shown in the top right section of the figure. Compared to a web cross section, a radial slotted motor has an advantage of higher volumetric loading. A radial slotted tube has broad application; it can be designed to provide nearly constant, regressive, progressive, and boost-sustain thrust profiles. The most common type of slotted tube provides a boost-sustain thrust profile. For boost-sustain, high burn rate propellant in the aft section of the motor provides an initial high thrust while a different, slower burn rate propellant in the forward section provides the follow-on sustain thrust.

Shown in the middle of the figure is a five-point star cross section. It provides progressive thrust. Volumetric loading is fairly high, about 87%, for this cross section. The middle section of the figure is a photograph of a three-point star cross section extrusion of a double-base propellant. Following extrusion, the propellant can be loaded into the motor case as a free-standing cartridge. A second

approach to loading propellant is to directly pour propellant slurry into the motor case. The loaded motor case is then placed in an oven for curing/bonding.

3.18 Solid Rocket Thrust Magnitude Control

Shown in Fig. 3.39 are conventional solid propellant motor concepts, which have a single burn, compared to pulse motor concepts that have thrust magnitude control. At the top of the figure are examples of single burn boost concepts based on end-burning and radial-burning grain designs. The radial-burning grain has higher burn area, providing higher thrust. In the center of the figure are two examples of single-burn concepts capable of a boost-sustain-coast thrust profile. The left middle concept has a radial-burn boost using a high burn rate propellant, continuing with an end-burning sustain using a lower burn rate propellant. The right middle concept has concentric radial burn, with a high burn rate propellant for boost, followed by a low burn rate propellant for sustain. The bottom concepts in the figure are examples of thrust magnitude control, with a controlled time delay between pulses. The left bottom concept is a pulse motor with a radial-burn boost using a high burn rate propellant. A barrier is provided (either mechanical or chemical) for a controlled time delay in initiating the second burn. Following coast, the second burn in the example is a sustain thrust using an end-burning grain and a low burn rate propellant. The right

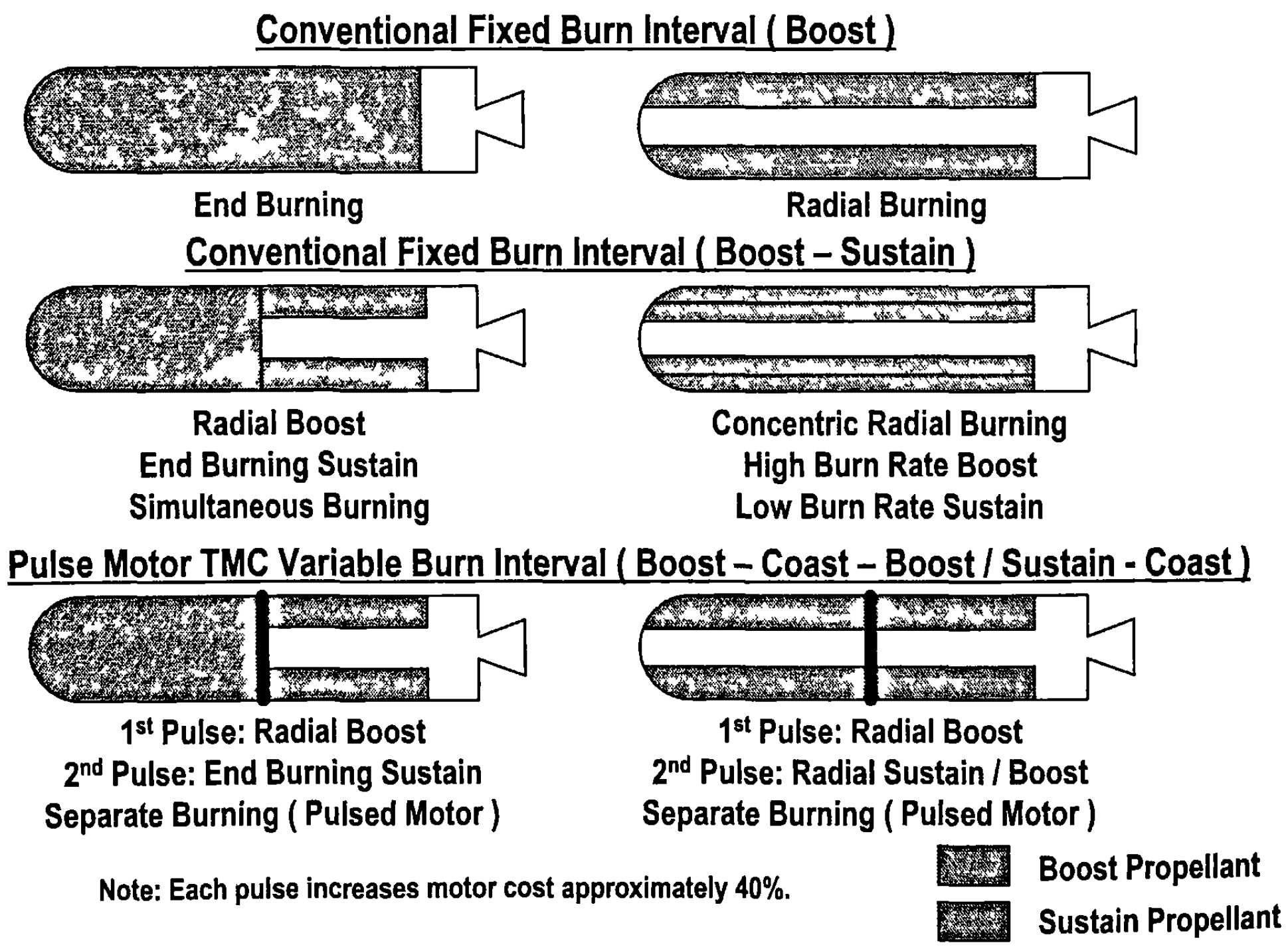

Fig. 3.39 A conventional rocket has a fixed burn, while a thrust magnitude control rocket can vary the burn interval.

bottom concept in the figure is another pulse motor concept based on a radial grain for boost (with high burn rate propellant), followed by second radial grain for either sustain (with lower burn rate propellant) or a second boost (with a high burn rate propellant).

A design concern of layering a high burn rate propellant on top of a low burn rate propellant is the difference in the thermal expansion of the two different propellants. Localized stress and cracks can develop because of thermal expansion.

Potential advantages of a pulse motor include longer range, longer flight duration, and reduced aerodynamic heating (from lower velocity at burnout). Pulse motors are more expensive than conventional single-burn motors. Each pulse of a pulse motor increases the motor production cost by about 40%. Examples of missiles with a pulse motor are the AGM-69 SRAM two-pulse rocket motor and the SM-3 Standard Missile two-pulse TSRM.

Approaches to rocket propulsion energy management for tactical missiles include pulsed, pintle, and gel rocket motors. Figure 3.40 shows these alternatives for thrust magnitude control.

As mentioned previously, the solid pulse motor uses thermal or mechanical barriers to provide separate motor pulses. It is usually limited to two or three pulses. Because the motor can be designed for an optimum combustion pressure, a pulse motor can be designed for maximum specific impulse. Another advantage is that the time delay between pulses can be controlled to optimize the flight trajectory profile. As a result, a boost-coast-boost-coast pulse motor can have longer range and reduced aerodynamic heating compared to conventional single-burn boost-coast and boost-sustain-coast motors.

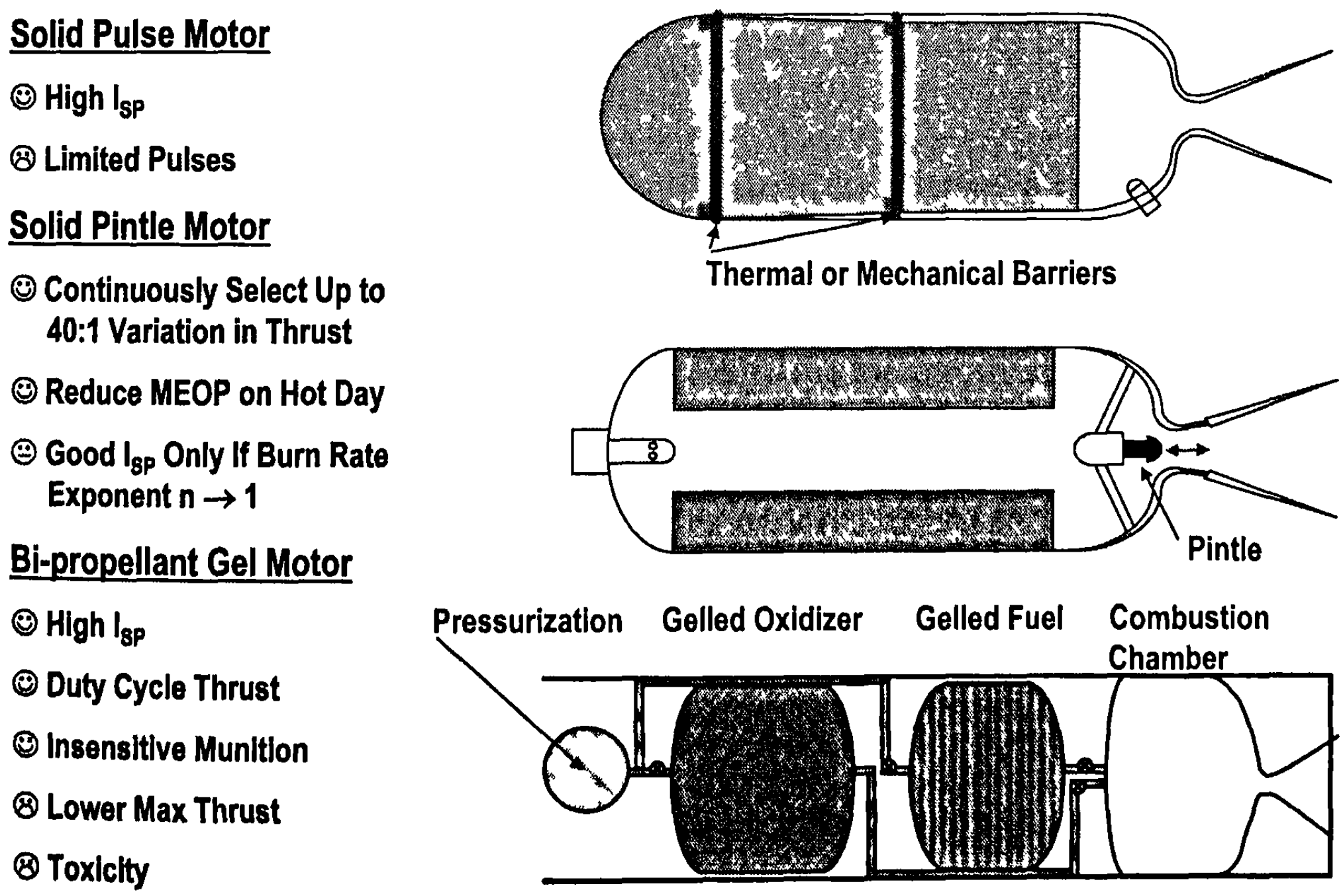

Fig. 3.40 Tactical rocket motor thrust magnitude control alternatives.

The second approach to thrust magnitude control, a solid pintle motor, has a pintle plug that is moved in and out of the throat area. The pintle is constructed from a material with a very high temperature capability, such as tungsten or carbon carbon. Moving the pintle into the throat area increases the chamber pressure, providing higher burn rate and higher thrust. Moving the pintle out of the throat area decreases the chamber pressure, reducing the burn rate and thrust.

One advantage of a pintle motor is that it can be used to reduce the maximum effective operating pressure (MEOP) on a hot day. This capability allows a smaller factor of safety and a lighter weight motor case.

For a typical value of propellant burn rate exponent (e.g., $n = 0.3$), there is a large penalty in specific impulse for the motor to operate over a wide range in chamber pressure. It is desirable for a pintle motor to use a propellant with a high burn rate exponent (e.g., $n \rightarrow 1$), to allow a large change in burn rate/mass flow rate/thrust with only a small change in chamber pressure. Pintle motors have demonstrated maximum-to-minimum thrust ratios of greater than to 40:1. Combustion can be sustained down to a chamber pressure that is the minimum for a sonic throat, allowing an "idle" mode similar to that of a pulse motor.

A technology opportunity is the development of propellants with burn rate exponents that approach the value of one, allowing a large change in burn rate (and thrust) with a relatively small change in chamber pressure. Propellants with $n \rightarrow 1$ require high bandwidth and tight control of the position of the pintle to avoid the hazard of combustion instability if $n > 1$.

A third alternative for thrust magnitude control of a tactical rocket is a gel propellant rocket using a low-toxicity gelled fuel such as alcohol and a low-toxicity gelled oxidizer such as hydrogen peroxide. The gelled propellant is nearly solid at atmospheric pressure but flows like a liquid when it is pumped at high pressure. The thrust is controlled by the rate at which the fuel and oxidizer are pumped into the combustion chamber. The specific impulse of a low-toxicity gel-propellant rocket can be higher than that of a solid-propellant rocket. The specific impulse of a higher toxicity gel propellant could be comparable to that of a liquid-propellant rocket. A disadvantage of a gel-propellant rocket compared to a solid-propellant motor is lower maximum thrust. A second disadvantage is concern for toxicity, particularly for naval platforms. Although a gel-propellant rocket is much less toxic than a liquid-propellant rocket, it is probably unacceptable in a closed environment storage with humans, such as below deck of a ship. In regard to insensitive munitions, a gel-propellant rocket is superior to a solid propellant motor. The gelled fuel and gelled oxidizer are stored in separate tanks, reducing their sensitivity. The U.S. Army has been a leader in the development of gel-propellant rockets. For example, gel propellant is used in the THAAD divert and attitude control system (DACS).

3.19 Solid Propellant Alternatives

Figure 3.41 is a comparison of solid-propellant alternatives based on tradeoffs of rocket motor visual observable versus performance and safety. In high smoke and reduced smoke motors, the solid propellant is a composite consisting of a fuel and an oxidizer blended together and mixed into a binder, or polymer. The mixture is cast (poured) into the motor case and cured. The highest performance

Type	I_{SP}, Specific Impulse, s	ρ, Density, lb / in³	Burn Rate @ 1000 psi, in / s	Safety	Observables
• ***Min Smoke***. No Al fuel or AP oxidizer. Either Composite with Nitramine Oxidizer (CL-20, ADN, HMX, RDX) or Double Base. Very low contrail (H_2O).	– 220–255	– 0.055–0.062	○ 0.25–2.0	–	◒
• ***Reduced Smoke***. No Al (binder fuel). AP oxidizer. Low contrail (HCl).	○ 250–260	○ 0.062	◒ 0.1–1.5	○	○
• ***High Smoke***. Al fuel. AP oxidizer. High smoke (Al_2O_3).	◒ 260–265	◒ 0.065	● 0.1–3.0	◒	–

● Superior ◒ Above Average ○ Average – Below Average

Fig. 3.41 Solid rocket propellant alternatives.

solid propellants are composite propellants based on binding a metal fuel with an oxidizer such as ammonium perchlorate. Powdered aluminum is the metallic fuel most widely used in solid rocket propellants. Benefits of a metal fuel include 1) increased combustion temperature, resulting in an increase in specific impulse; 2) increased density of the propellant, resulting in improved volumetric performance; and 3) improved combustion stability. Binders have been based on both natural and man-made materials. The organic prepolymers have rubbery properties following cure and form a strong binding within the inorganic fuels and chemical oxidizers. The most commonly used liquid polymers cure much like rubber. Prepolymers used as binders in composite propellants are initially liquid, so that the fuel and oxidizer can be blended more easily prior to the start of the polymerization cure. Unfortunately, metal fuels such as aluminum have high observable smoke particles (e.g., Al_2O_3).

An initial approach that was used to reduce the plume observables was reduced smoke motors. Reduced smoke motors replace the metal fuel with a binder fuel, such as HTPB binder. The performance and insensitive munition capability of reduced smoke motors are somewhat lower than that of high smoke motors. Reduced smoke propellants can still have visual observables from a hydrogen chloride contrail, particularly at low atmospheric temperature.

A third type of propellant is minimum smoke propellant. Minimum smoke propellants eliminate the HCl contrail by eliminating ammonium perchlorate as an oxidizer, resulting in lower visual observables. However, the performance and safety of the current minimum smoke propellants are not as good as that of high smoke propellants. Current minimum smoke propellants are either composite propellants with a nitramine oxidizer or cross-linked double base (XLDB) propellants. In the older minimum smoke double-base propellants, the propellant

consists generally of cotton (cellulose) combined with nitric acid to form nitrocellulose (guncotton), which in turn is combined with nitroglycerin, another fuel oxidizer. In double-base propellant, the nitrocellulose serves as the binder, and the nitroglycerin causes it to solidify. A nitramine oxidizer contains the radical group $NHNO_2$. Examples of the nitramine oxidizer of current minimum smoke composite propellants are HMX (cyclotetramethylene tetranitramine, $C_4H_8N_8O_8$) and RDX (cyclotrimethylene trinitramine, $C_3H_6N_6O_6$). An example of a new minimum smoke propellant is the U.S. Navy China Lake CL-20 propellant. CL-20 is a cyclic polynitramine with a unique caged structure that provides higher crystal density, higher heat of formation, and higher oxidizer-to-fuel ratio. CL-20 propellant has 10–20% higher performance than HMX and RDX. CL-20 also has reduced shock sensitivity (Class 1.3 vs 1.1) and milder cookoff reaction than either HMX or RDX. A disadvantage of CL-20 propellant is high cost (currently more than $400 per lb). The relatively high performance of CL-20 is primarily from its high flame temperature. As a first-order estimate, to illustrate the benefit of high flame temperature, specific impulse can be calculated from the equation

$$I_{SP} \approx 25(T_f/MW)^{1/2} \tag{3.94}$$

In the above equation T_f is the flame temperature in Kelvin and MW is the molecular weight.

Another example of a relatively new minimum smoke propellant developed by Russia is ammonium dinitramine (ADN). ADN performance is superior to HMX and RDX and somewhat less than that of CL-20. ADN is lower density and has a lower flame temperature than CL-20.

3.20 Motor Case Material Alternatives

Primary design considerations in selecting the materials for the motor case are shown in Fig. 3.42. These are high maximum temperature, high volumetric efficiency, light weight, ease of attachment (e.g., bolt, weld, bond) to the airframe or launcher, and low cost. Other considerations include manufacturing, handling, storage, and the environment (e.g., sea salt corrosion in a naval environment).

The most common types of motor cases are conventional quench and temper steel (hardened by heating then plunging into liquid to cool suddenly) and nickel precipitation-hardening alloy steel. Other types include aluminum alloys, strip metal/epoxy laminate (e.g., steel/epoxy laminate), titanium alloys, and composite (e.g., fiberglass-reinforced plastics). If a combination of high performance and low cost is required, steel is often the best material. Although steel has high strength, it is susceptible to localized bucking and may require a thicker wall to avoid localized buckling. If the motor has relatively low heating (e.g., a small rocket motor usually has low heating), aluminum may be the best material. Because the maximum allowable temperature of aluminum is lower than steel, it requires more insulation. A strip metal/epoxy laminate may be the best choice of moderate performance and cost. Another good feature of a strip metal/laminate motor case is it is often easier to qualify as an insensitive

Type	Temper-ature	Volumetric Efficiency	Weight	Airframe and Launcher Attachment	Cost
♦ Steel	●	●	○	●	●
♦ Aluminum	–	–	○ ◒	◒	◒ ●
♦ Strip Steel / Epoxy Laminate	○	●	◒	–	◒
♦ Composite	○	–	●	–	–
♦ Titanium	◒	◒	◒	–	–

● Superior ◒ Above Average ○ Average – Below Average

Fig. 3.42 Steel is the most common motor case material.

munition. Composite and titanium cases have had relatively little application to date because of their high cost. However, the cost of a composite motor case is expected to decrease in the future, resulting in increased application of composite motor cases. Current applications of composite cases include LOSAT, PAC-3, and the SM-3 third stage rocket motor. The fifth candidate material, titanium, is rarely used in motor cases because of its higher cost. Molten titanium requires an expensive vacuum manufacturing process to avoid oxidation.

For a volume-limited missile, such as a missile packaged inside a Vertical Launch System (VLS) canister that has a diameter limit, the volumetric efficiency of the material may be as important as the weight efficiency. As an example, a composite motor case may have the lightest weight but also a greater thickness. The thickness of the composite case may limit the available volume for propellant, resulting in a reduction in flight range.

Internal insulation protects the motor case from the high flame temperature (e.g., 5200° F) of combustion. For a typical case-bonded propellant, the internal insulator also provides the bonding of the propellant to the motor case and must have sufficient strength to prevent the propellant from debonding. Most of the internal motor case insulators are rubber-based materials such as hydroxyl terminated polybutadiene or ethylene propylene dimethyl monomer (EPDM). Reinforcing erosion-resistant fibers such as silica are usually added. Upon exposure to the combustion flame temperature, the insulator chars. A design consideration is the required insulation thickness to compensate for the recession and the change in thermal conductivity as a result of char. Another design consideration is the potential debonding from the motor case because of outgassing.

3.21 Rocket Nozzle Material Alternatives

The rocket nozzle is an attachment to the end of the motor case. It is shaped to control the flow of gases and to convert the chemical energy released from combustion into kinetic energy. Figure 3.43 shows material alternatives for the rocket nozzle components (i.e., housing, dome closeout, blast tube, throat, and exit cone).

The housing is the overall structure of the nozzle. It may be made of high temperature steel for a high heating motor case or lower temperature materials such as cellulose/phenolic or aluminum for a low heating motor. The inside of the housing usually must be insulated to maintain structural integrity.

The dome closeout is a convergent section of the nozzle that is downstream of the motor case and upstream of the throat. In the dome closeout the flow area is reduced, and the speed of the subsonic exhaust gas is increased as it is channeled to the throat. For a high heating motor with a high chamber pressure and long burn duration, an insulation insert is required in the dome closeout housing. The candidate dome closeout insulation materials include silica/phenolic, graphite/phenolic, and silicone elastomer. For a relatively low heating motor, low-cost glass/phenolic is a candidate insulation material for the dome closeout. For a very low heating motor, it may not be necessary to have an insulation insert in the housing of the dome closeout.

A blast tube may be downstream of the dome closeout if it is necessary to package subsystems, such as flight control actuators, around the nozzle. Ideally, the blast tube should have a small diameter to allow maximum packaging volume for the surrounding subsystems. However, as the blast tube diameter

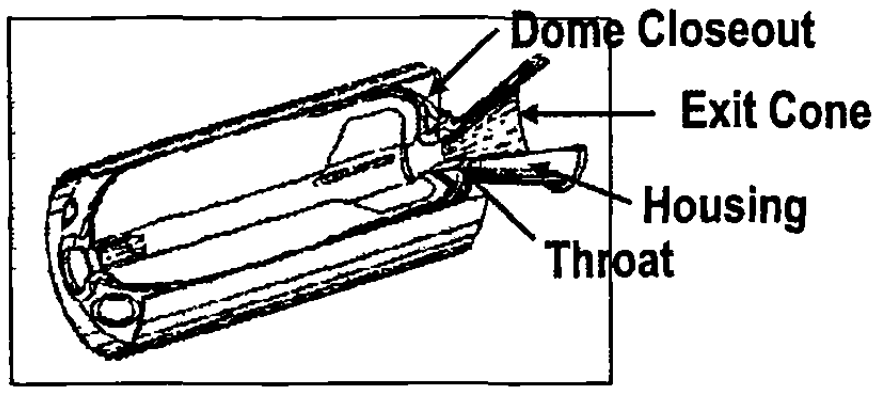

Rocket Nozzle Element	High Heating (High Chamber Pressure or Long Burn) ⇒ High Cost / Heavy Nozzle	Low Heating (Low Chamber Pressure or Short Burn) ⇒ Low Cost / Light Weight Nozzle
♦ Housing Material Alternatives	♦ Steel	♦ Cellulose / Phenolic ♦ Aluminum
♦ Throat Material Alternatives	♦ Tungsten Insert ♦ Rhenium Insert ♦ Molybdenum Insert	♦ Cellulose / Phenolic Insert ♦ Silica / Phenolic Insert ♦ Graphite Insert ♦ Carbon – Carbon Insert
♦ Exit Cone, Dome Closeout, and Blast Tube Material Alternatives	♦ Silica / Phenolic Insert ♦ Graphite / Phenolic Insert ♦ Silicone Elastomer Insert	♦ No Insert ♦ Glass / Phenolic Insert

Fig. 3.43 Heat transfer drives rocket nozzle materials, weight, and cost.

approaches the throat diameter, the local gas Mach number approaches Mach 1. Because of severe erosion from the hot gas at Mach 1, the blast tube diameter is usually significantly larger than the throat diameter, such that the local Mach number is less than Mach 0.8.

The nozzle throat is the smallest internal diameter of the nozzle assembly. At the nozzle throat the exhaust gas passes through the minimum flow area and reaches the speed of sound. Because of high heat transfer at the throat, it may be necessary to have a refractory metal insert at the throat of a high-performance motor to prevent erosion. Examples of low-eroding refractory materials are tungsten, rhenium (used in SM-3 third-stage rocket motor and the Harpoon booster), and molybdenum. For a low heating motor, a lighter weight insert such as cellulose/phenolic, silica/phenolic, graphite, or carbon/carbon may be used.

Downstream of the throat the gases expand in the exit cone to supersonic speed. The exit cone may be contoured or conical. A contoured nozzle provides higher specific impulse, whereas a conical nozzle is shorter length, lighter weight, and lower cost. Most tactical missiles use conical nozzles. Finally, the exit plane is at the end of the exit cone, where the static pressure of the gas is ideally nearly equal to the atmospheric pressure. As shown in the figure, the material selection for the exit cone is driven by heating and cost considerations.

3.22 Summary

Chapter 3 provided conceptual design methods, discussed design trades, and identified high-payoff technologies for tactical missile propulsion. Conceptual design methods were provided for predicting the thrust and specific impulse of turbojet, ramjet, and rocket propulsion. Design trades for turbine-based propulsion include turbine material, compressor pressure ratio, and the propulsion cycle. Design trades for ramjets include combustor material alternatives, ramjet engine/booster integration alternatives, ramjet inlet options, and ramjet fuel alternatives. Desired trades for rockets include rocket propellant burn area required to provide the desired chamber pressure, nozzle throat area required to provide the desired mass flow rate, nozzle expansion ratio required for maximum specific impulse and maximum thrust, rocket motor grain alternatives, thrust magnitude control alternatives, solid-propellant alternatives, motor case material alternatives, and nozzle material alternatives. New propulsion technologies that have high payoff for tactical missiles were identified. These include hypersonic turbojets, ramjets, ducted rockets, scramjets, combined cycle propulsion, high-temperature turbine materials, high-temperature combustor, oblique shock airframe compression, mixed compression inlet, low-drag inlet, high-density fuel/propellant, ramjet throttle fuel control, endothermic fuel, solid rocket thrust magnitude control, high burn exponent propellant, and low observable fuel/propellant.

Problems

3.1. An advantage of turbojets compared to ramjets is s_____thrust.

3.2. The specific impulse of a turbojet is often limited by the maximum allowable temperature of the t_____.

3.3. The specific impulse of a ramjet is often limited by the maximum allowable temperature of the c_____.

3.4. Ducted rockets are based on a fuel-rich g__ g_____.

3.5. A safety advantage of solid-rocket propulsion over liquid propulsion is less t_____.

3.6. A rocket boost to a takeover Mach number is required by ramjets and s_____.

3.7. Parameters that enable the long range of subsonic cruise turbojet missiles are high lift, low drag, available fuel volume, and high s_____ i_____.

3.8. High thrust and high acceleration are achievable with s____ r_____propulsion.

3.9. In a turbojet the power to drive the compressor is provided by the t_____.

3.10. The compressor exit temperature is a function of the flight Mach number and the compressor p_____ r____.

3.11. Compressor exit temperature, fuel heating value, and fuel-to-air ratio determine the turbojet t_____ temperature.

3.12. Three types of turbine based propulsion are turbojet, turbo ramjet, and a__ t____ r_____.

3.13. Mach number and fuel-to-air ratio determine the ramjet c_____ temperature.

3.14. An example of a ramjet with low drag and light weight is an i_____ r_____ ramjet.

3.15. Russia, France, China, United Kingdom, Taiwan, and India are the only countries with currently operational r_____ missiles.

3.16. 100% inlet capture efficiency occurs when the forebody shock waves intercept the i____ l__.

3.17. Excess air that does not flow into the inlet is called s_____air.

3.18. Starting a ramjet inlet at lower supersonic Mach number requires a larger area of the inlet t_____.

3.19. Optimum pressure recovery across shock waves is achieved when the total pressure loss across each shock wave is e____.

3.20. The specific impulse and thrust of a ramjet are a function of the efficiency of the combustor, nozzle, and i____.

3.21. High-density fuels have high payoff for v_____ limited missiles.

3.22. The specific impulse of a ducted rocket with large excess fuel from the gas generator can approach that of a r_____.

3.23. High-speed rockets require large p_____ weight.

3.24. At the throat, the flow area is minimum, sonic, and c_____.

3.25. For an optimum nozzle expansion the nozzle exit pressure is equal to the a_____ pressure.

3.26. High thrust and chamber pressure are achievable through a large propellant b___ area.

3.27. Three approaches to solid rocket thrust magnitude control are pulse motor, pintle motor, and g__ motor.

3.28. A high burn exponent propellant allows a large change in thrust with only a small change in chamber p_____.

3.29. Three tradeoffs in selecting a solid propellant are safety, observables, and s_____ i_____.

3.30. A low-cost motor case is usually based on steel or aluminum material while a lightweight motor case is usually based on c_____ material.

3.31. Rockets with high chamber pressure or long burn time may require a t_____ throat insert.

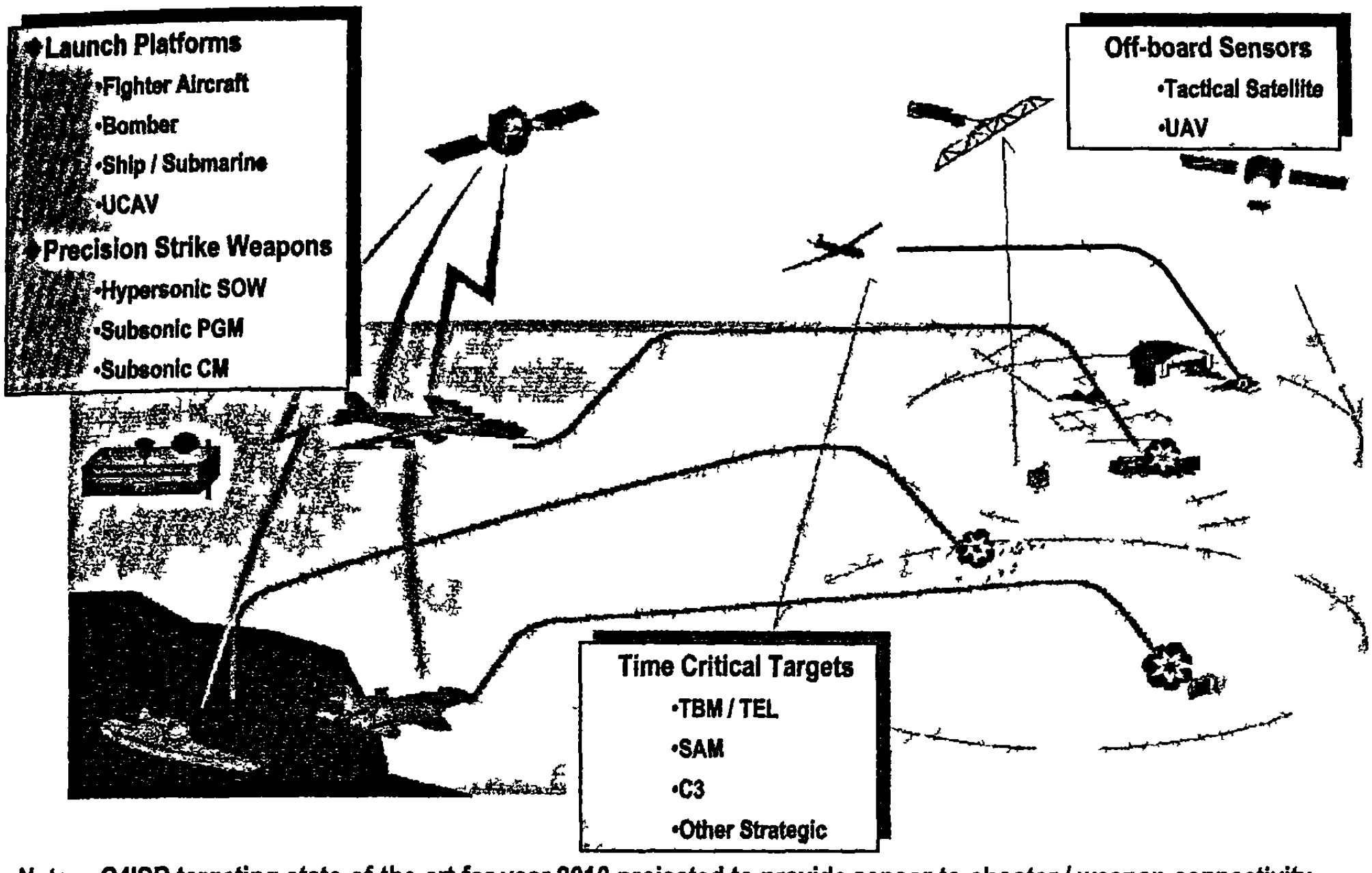

Note: C4ISR targeting state-of-the-art for year 2010 projected to provide sensor-to-shooter / weapon connectivity time of less than 2 m and target location error (TLE) of less than 1 m for motion suspended target.

Fig. 1.10 C4ISR tactical satellites and UAVs have high impact on mission capability.

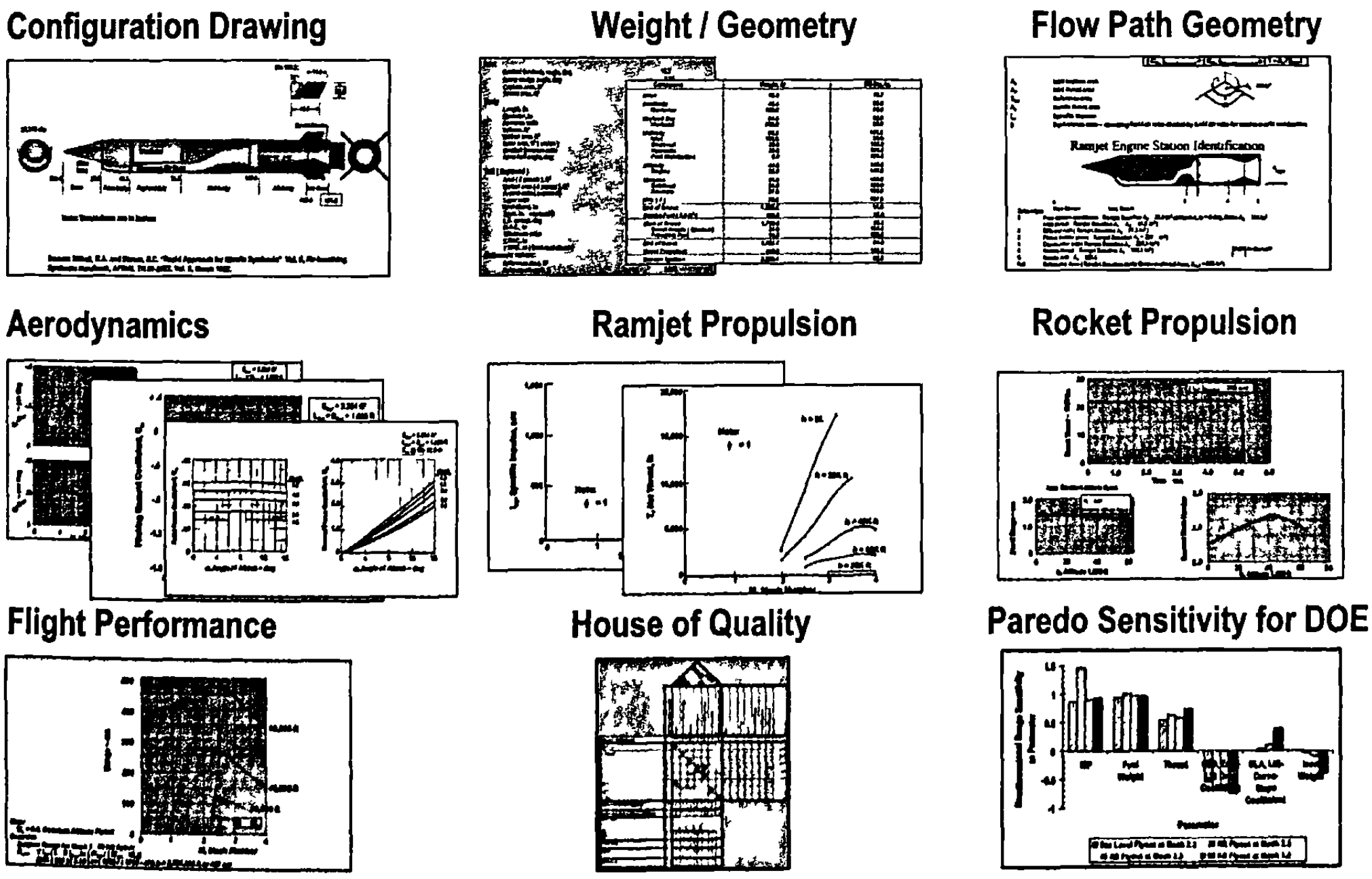

Fig. 1.14 Example of missile baseline data.

COLOR FIGURE SECTION

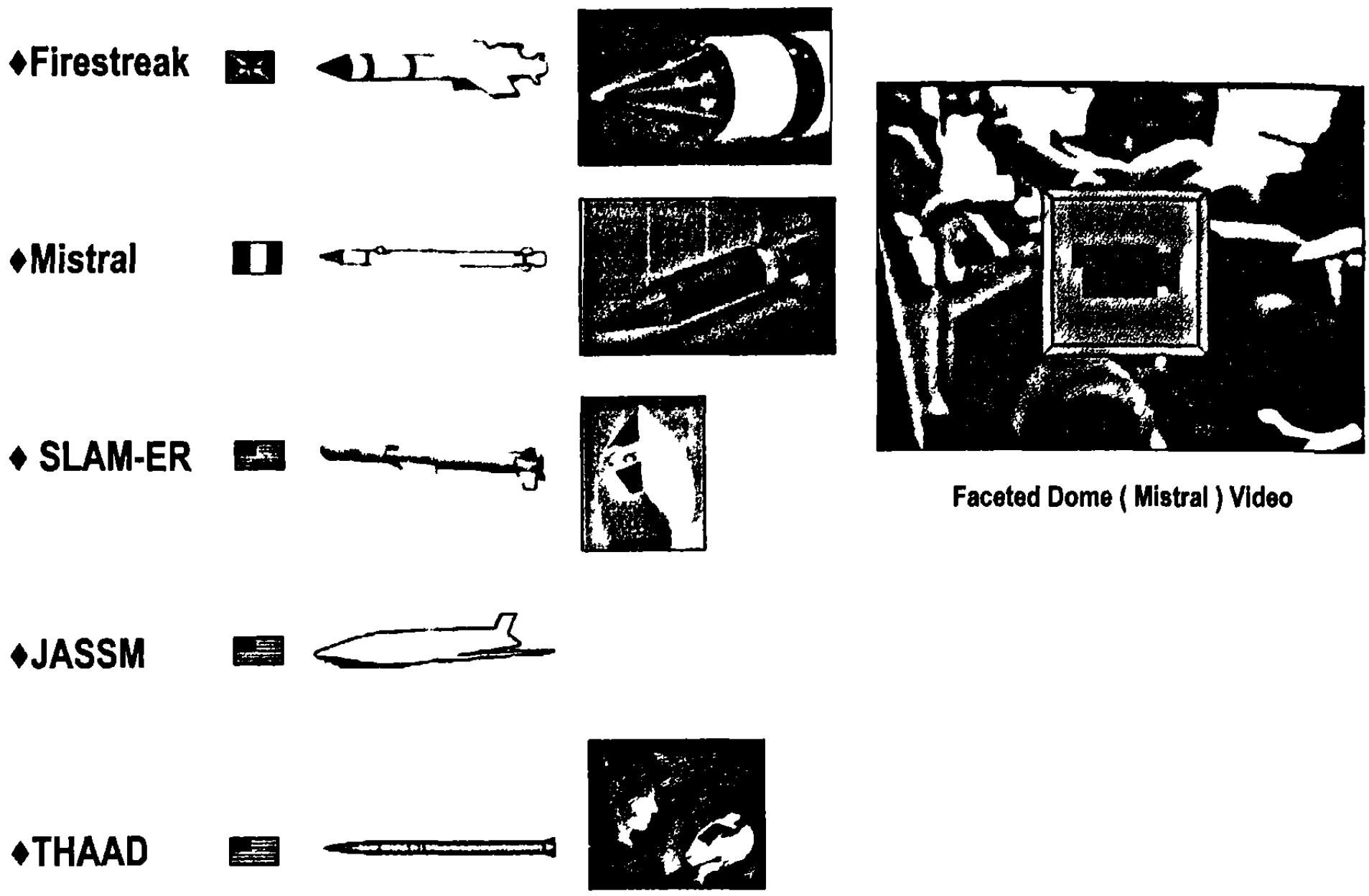

Fig. 2.7 Faceted and flat window domes can have low dome error slope, low drag, and low RCS.

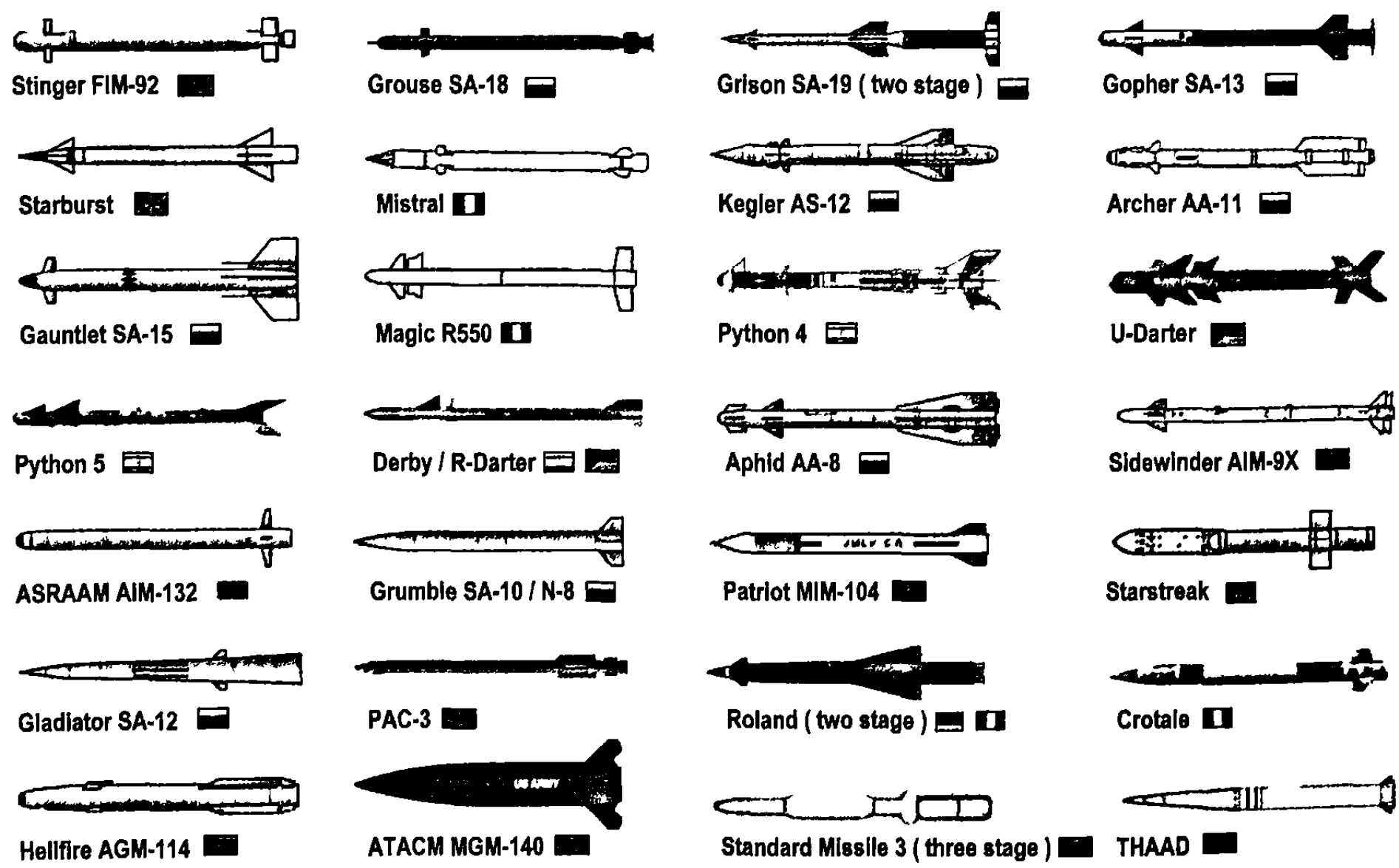

Permission of Missile Index. Copyright 1997©Missile.Index All Rights Reserved

Fig. 2.20 Most supersonic missiles are wingless.

COLOR FIGURE SECTION

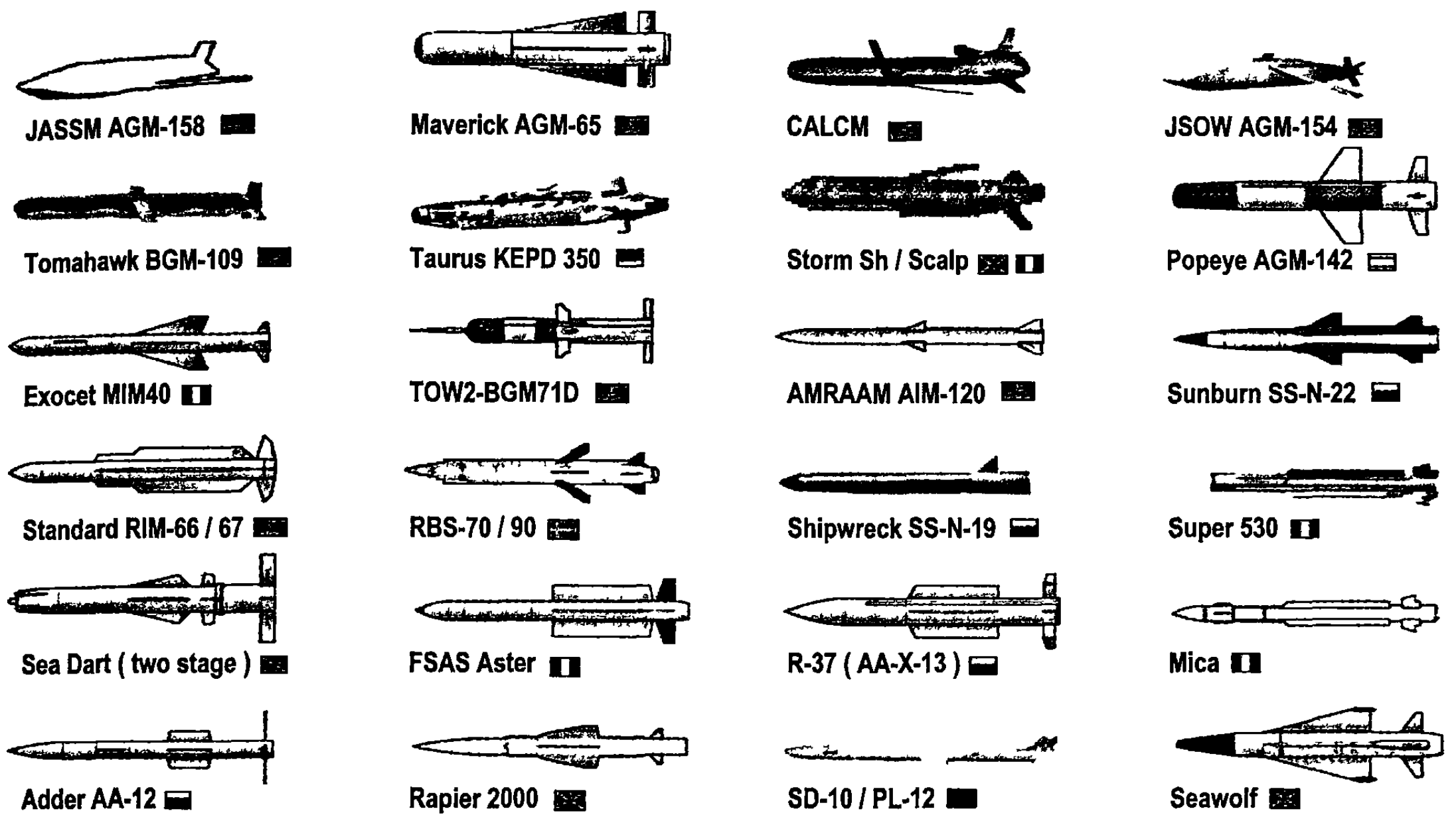

Permission of Missile Index. Copyright 1997©Missile.Index All Rights Reserved

Fig. 2.31 About 70% of tail control missiles also have wings.

- ♦Advantages
  - ♦High control effectiveness at low subsonic and high supersonic Mach number
  - ♦Low hinge moment
  - ♦Short chord length
- ♦Disadvantages
  - ♦High RCS (cavities, normal leading edges)
  - ♦High drag at transonic Mach number (choked flow)

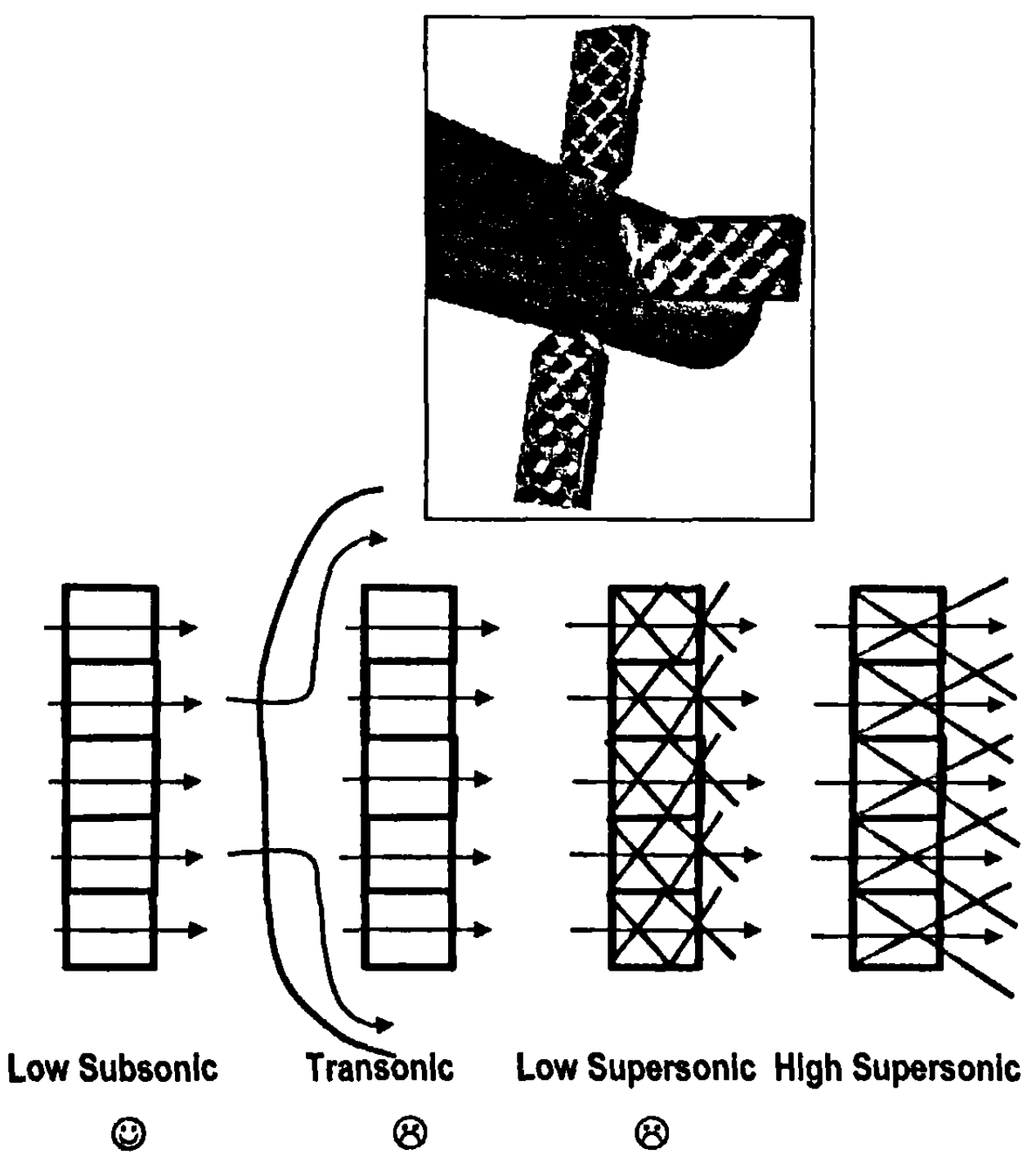

Fig. 2.33 Lattice fins have advantages for low subsonic and high supersonic missiles.

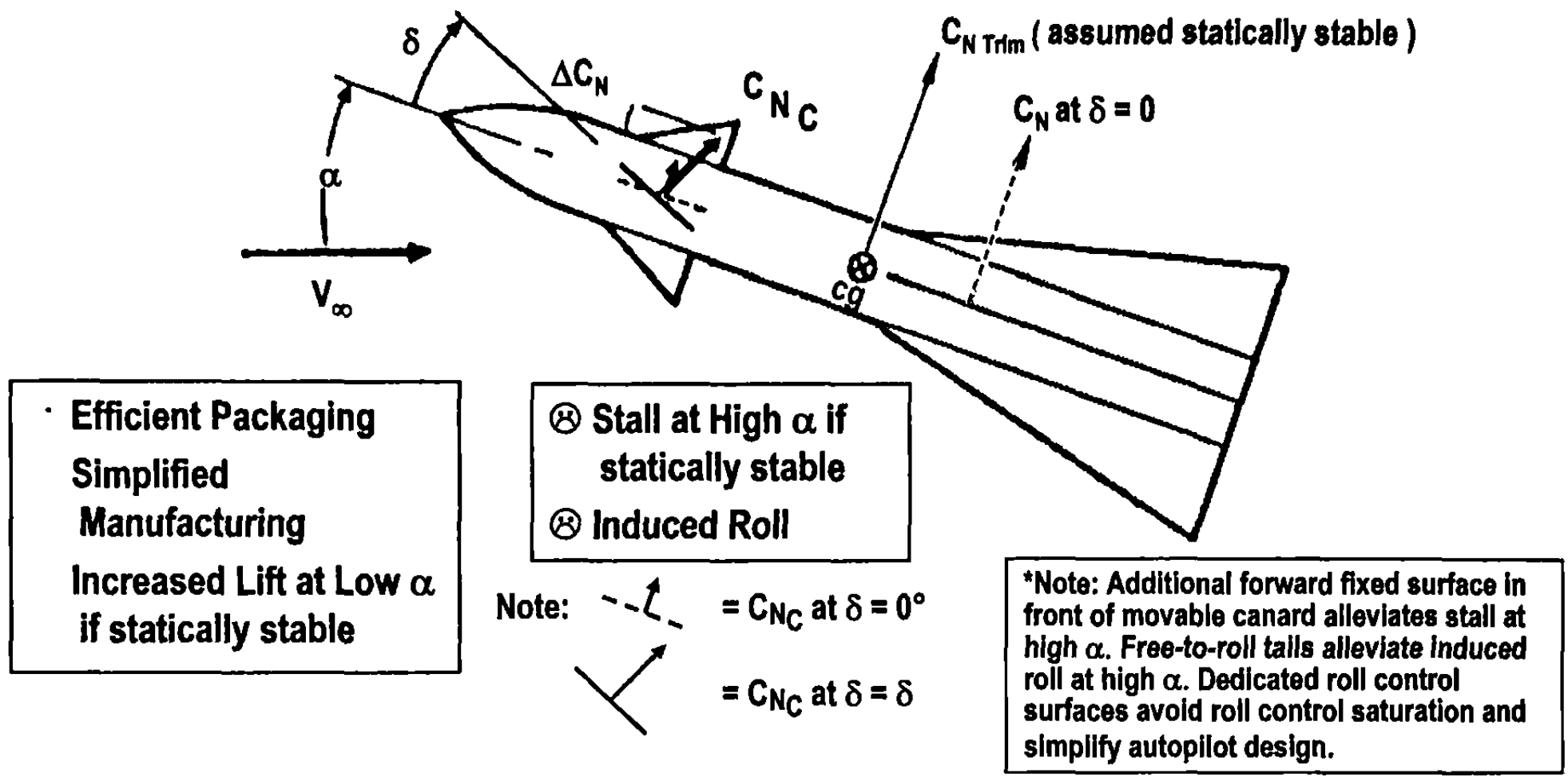

Fig. 2.34 Conventional canard control is efficient at low angle of attack but stalls at high alpha.

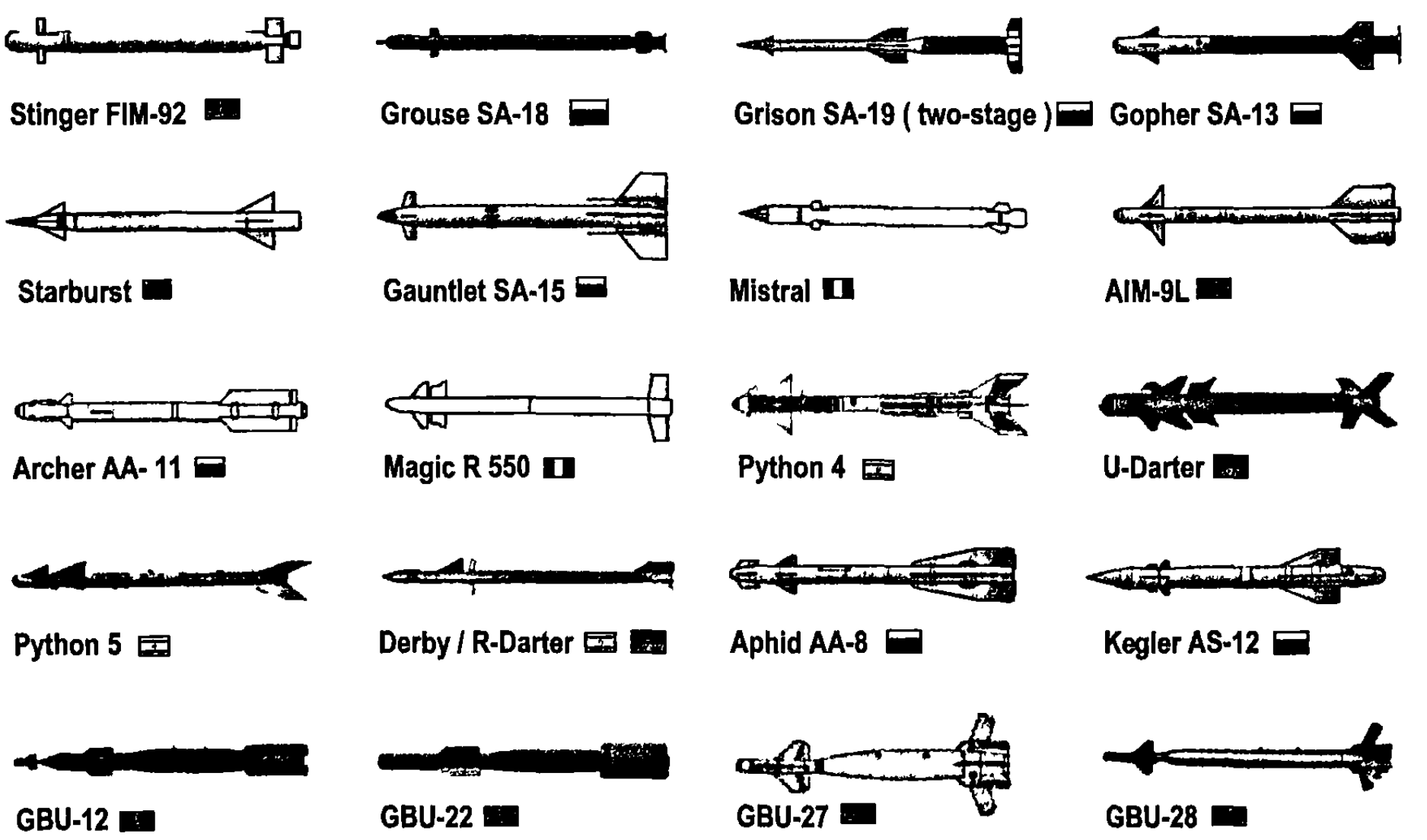

Permission of Missile Index. Copyright 1997©Missile.Index All Rights Reserved

Fig. 2.35 Canard control missiles are wingless and most are supersonic.

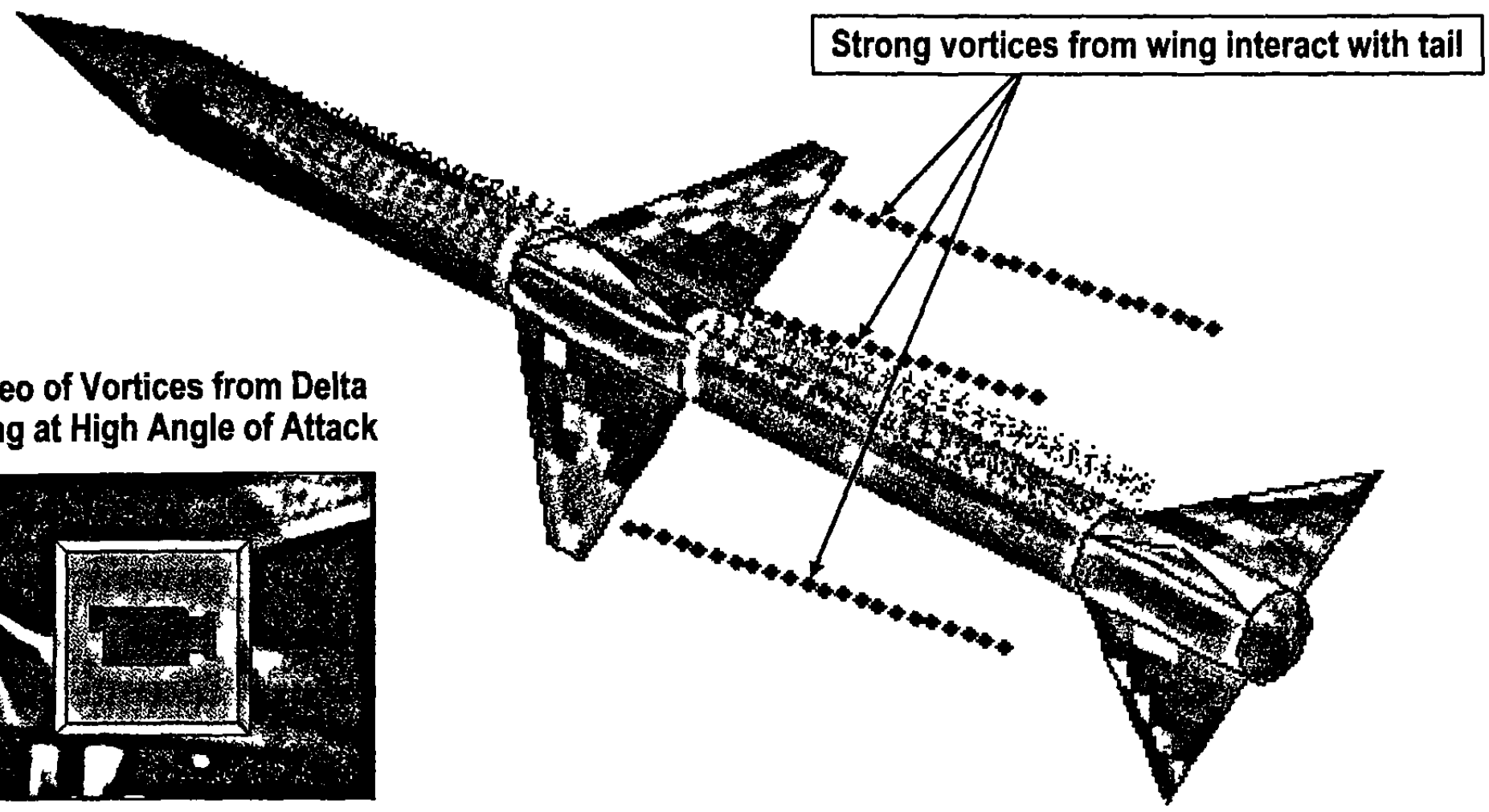

Source: University of Notre Dame web site: http://www.nd.edu/~ame/facilities/SubsonicTunnels.html

Source: Nielsen Engineering & Research (NEAR) web site: http://www.nearinc.com/near/project/MISDL.htm

Fig. 2.38 Wing control missile susceptible to high vortex shedding.

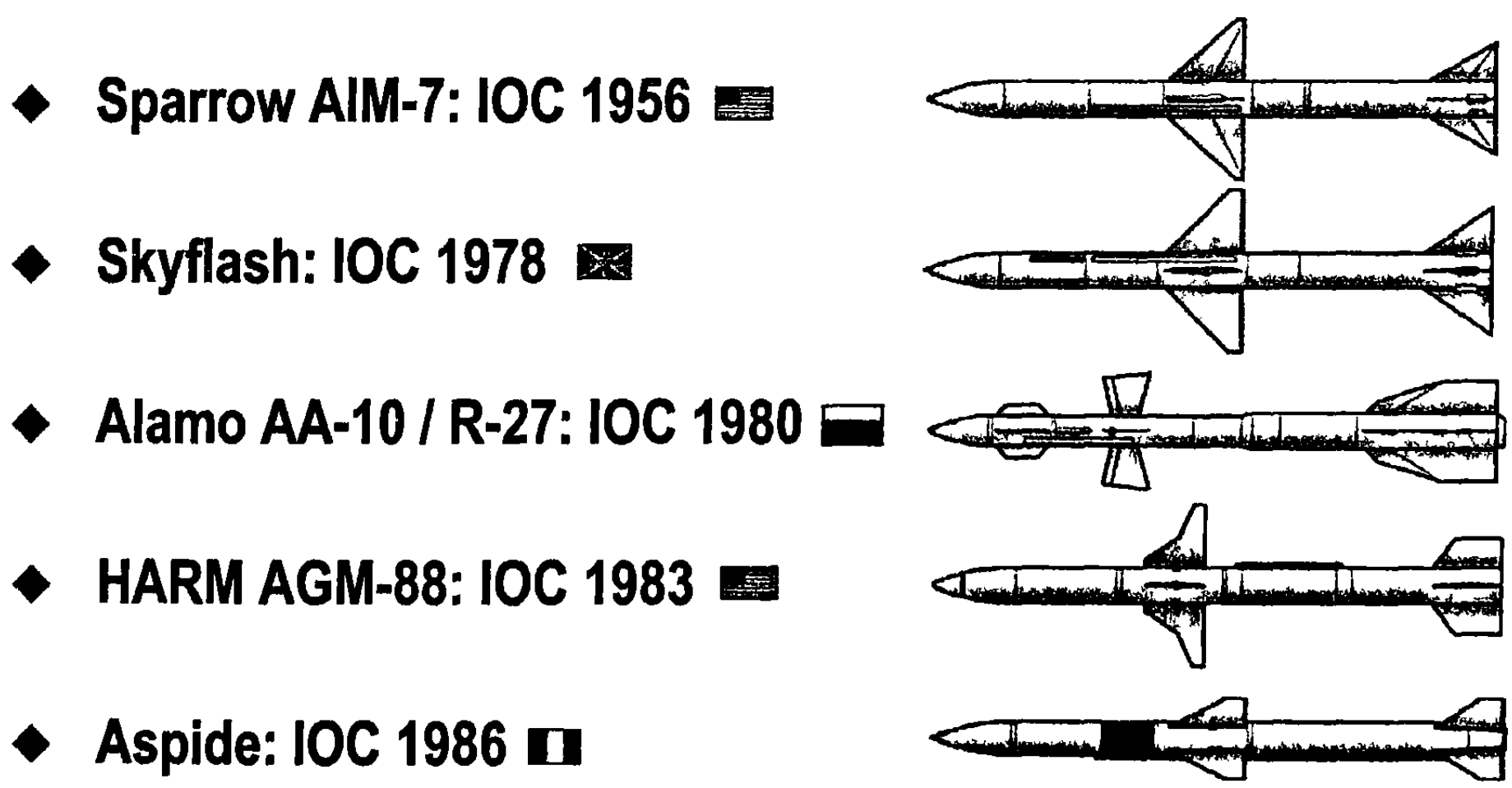

Permission of Missile Index. Copyright 1997©Missile.Index All Rights Reserved

Fig. 2.39 Wing control missiles are old technology.

COLOR FIGURE SECTION

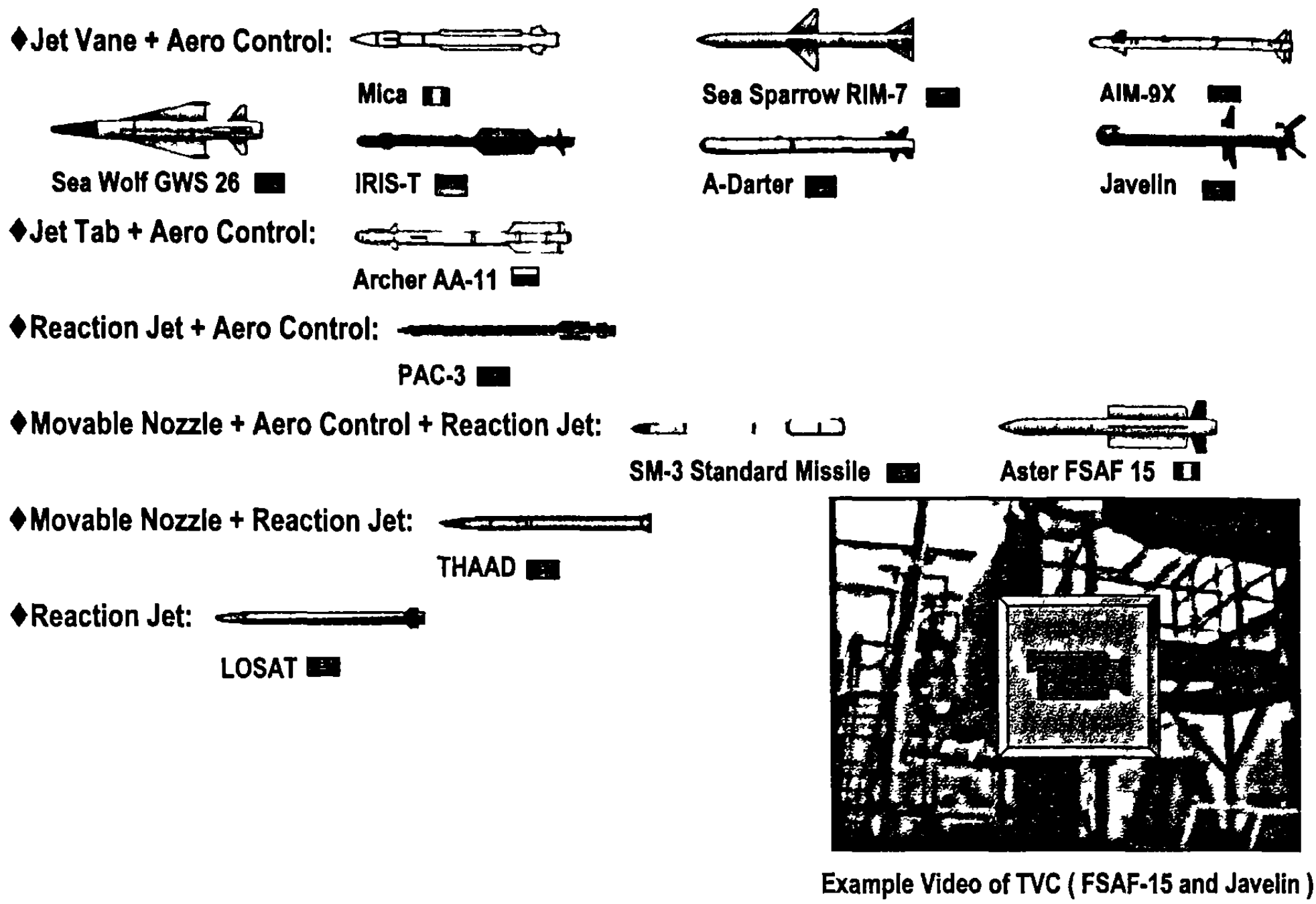

Fig. 2.41 Most tactical missiles with TVC or reaction jet control also use aerodynamic control.

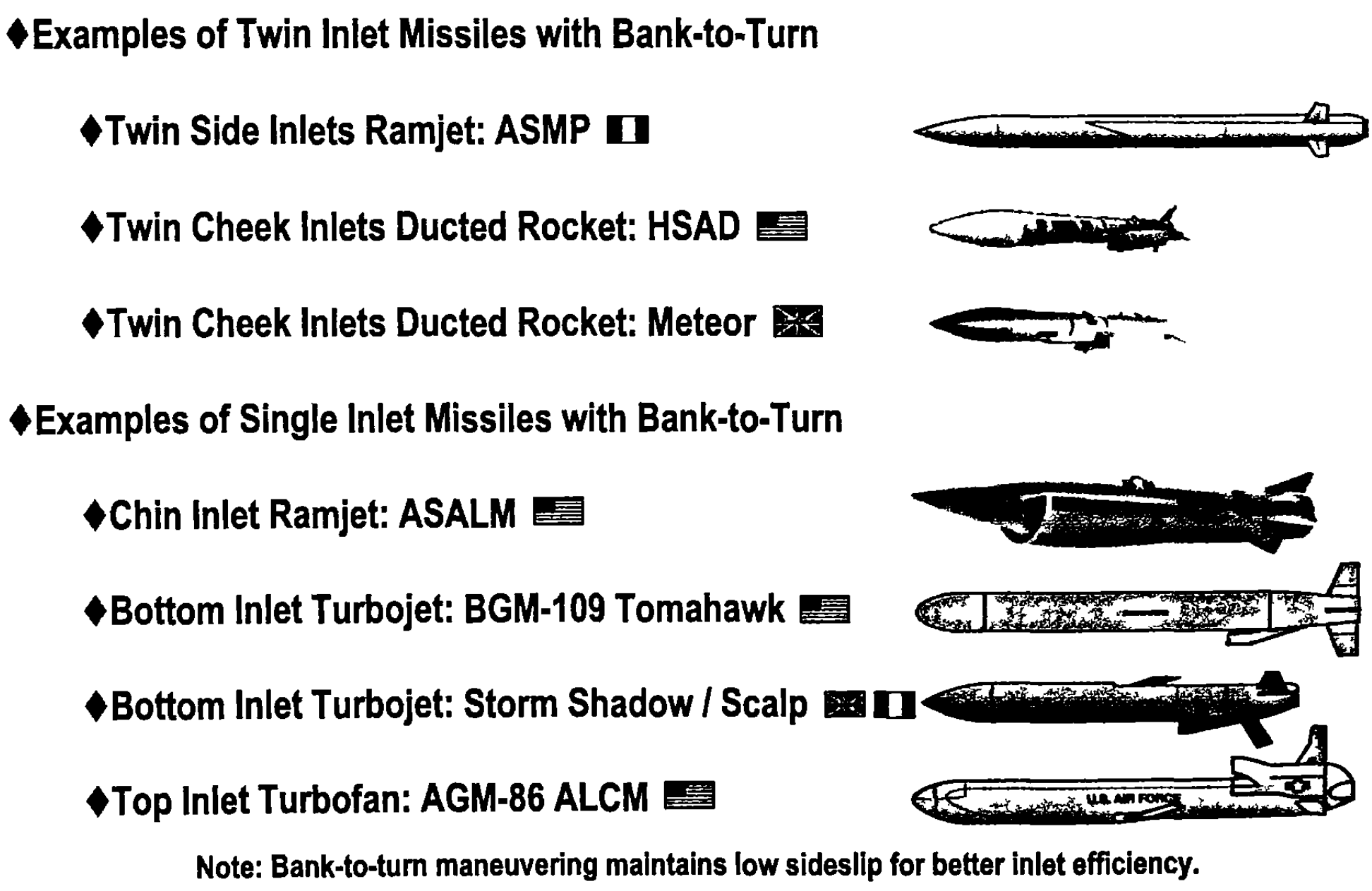

Fig. 2.43 Asymmetric inlets require bank-to-turn maneuvering.

COLOR FIGURE SECTION

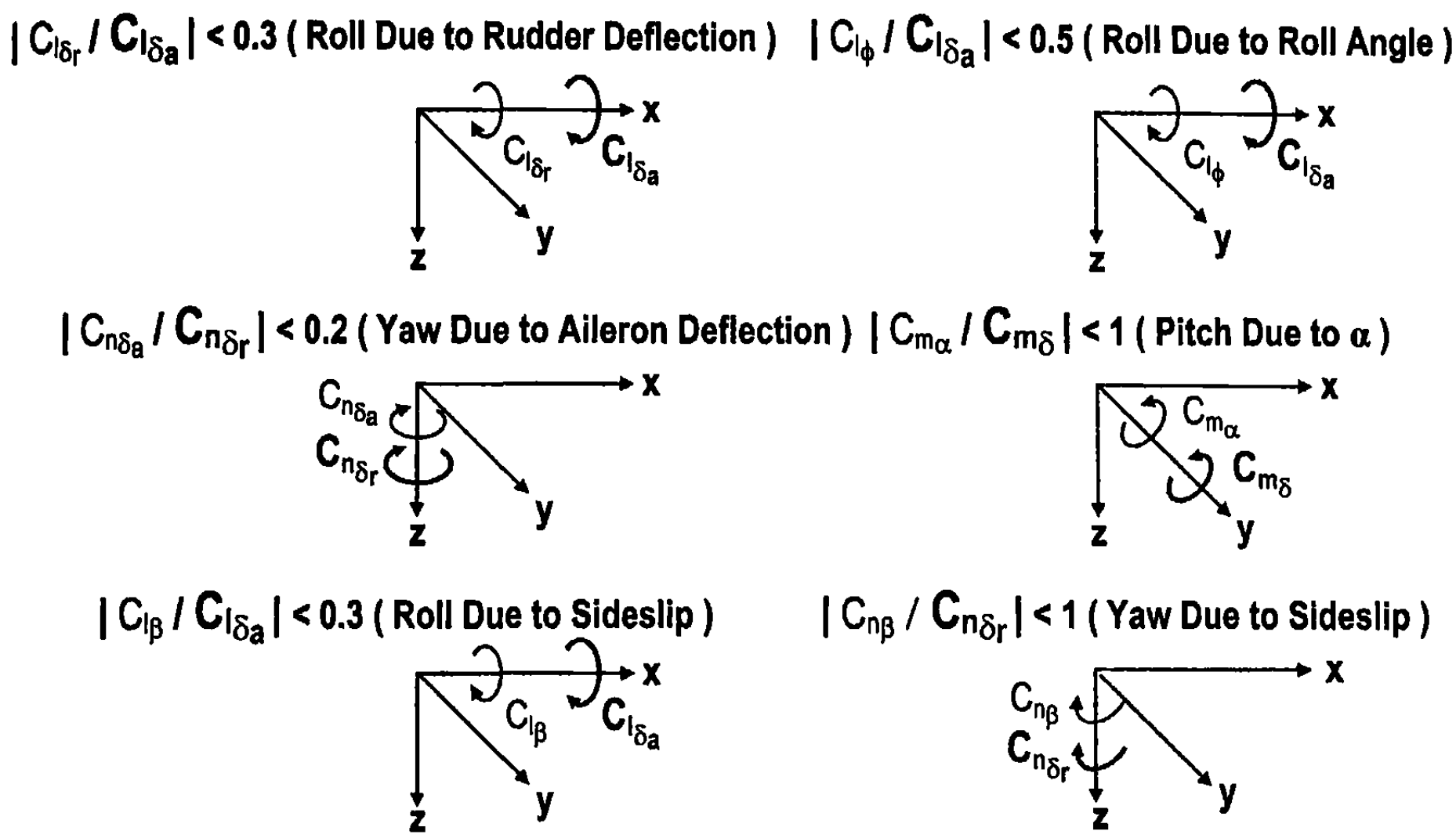

Note: The primary control derivative (larger bold font) should be larger than the undesirable stability and control derivative.

Fig. 2.49 Stability and control derivatives conceptual design criteria.

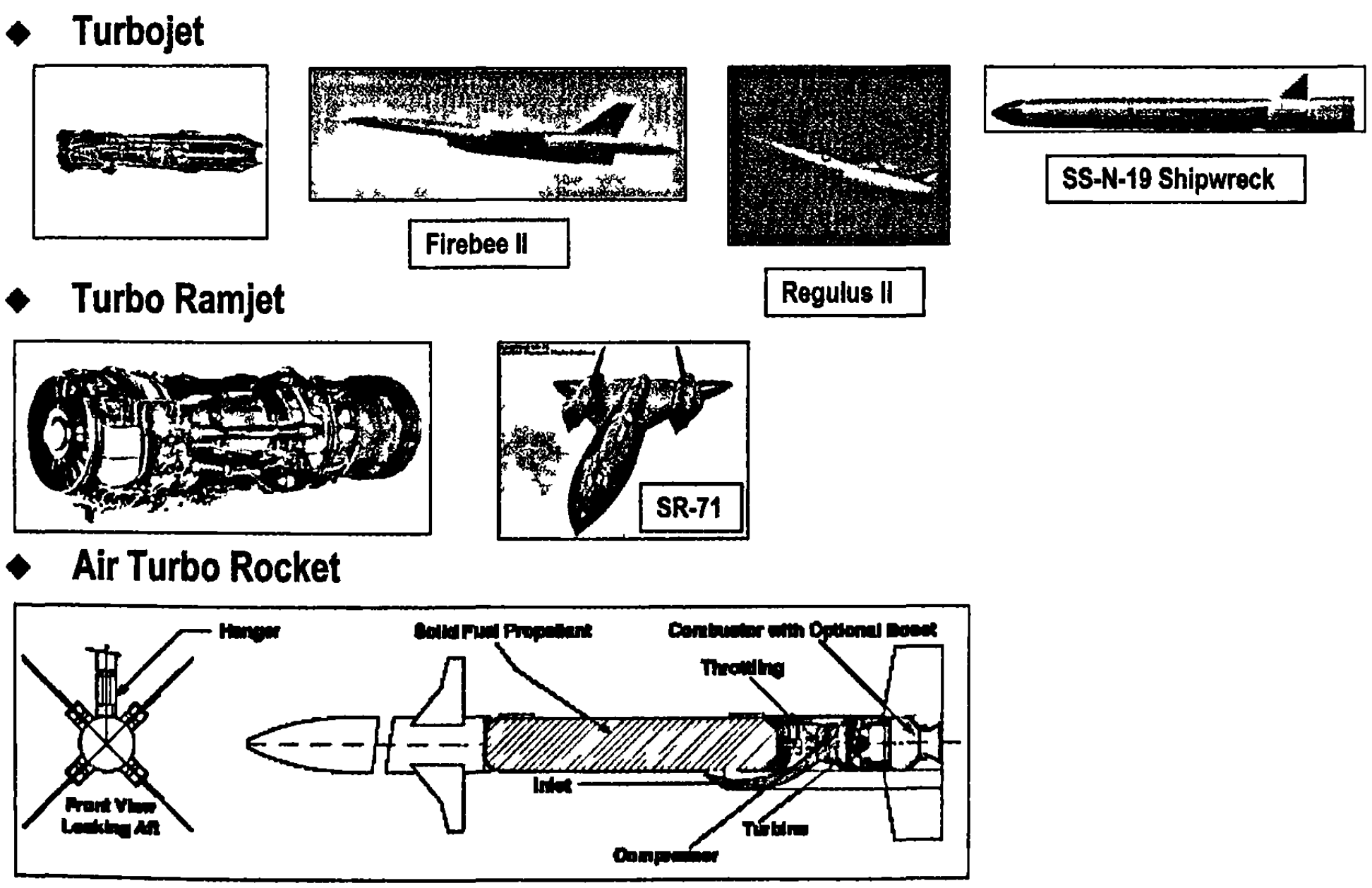

Fig. 3.8 Turbine-based missiles are capable of subsonic to supersonic cruise.

COLOR FIGURE SECTION

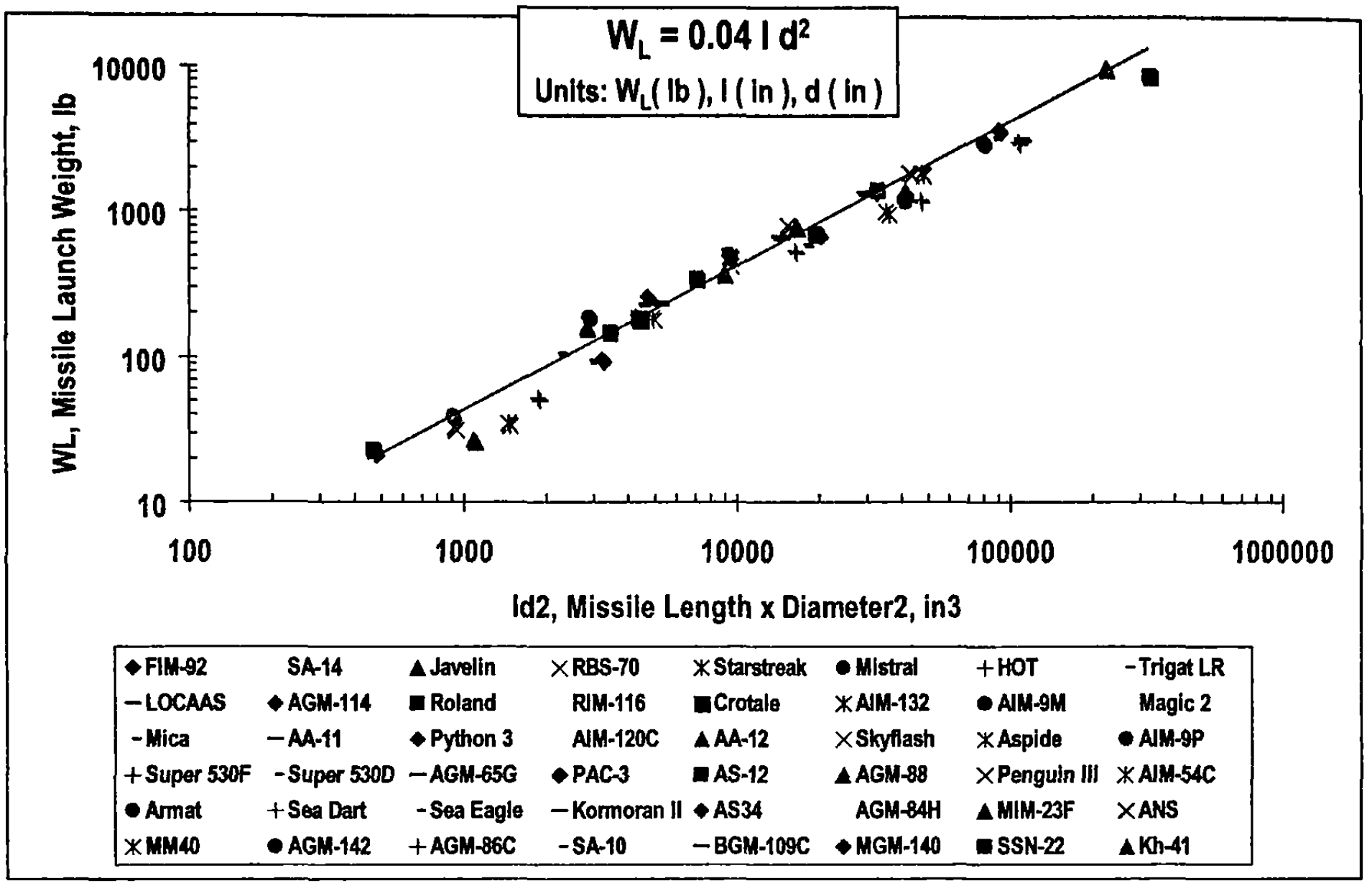

Fig. 4.4 Missile weight is a function of diameter and length.

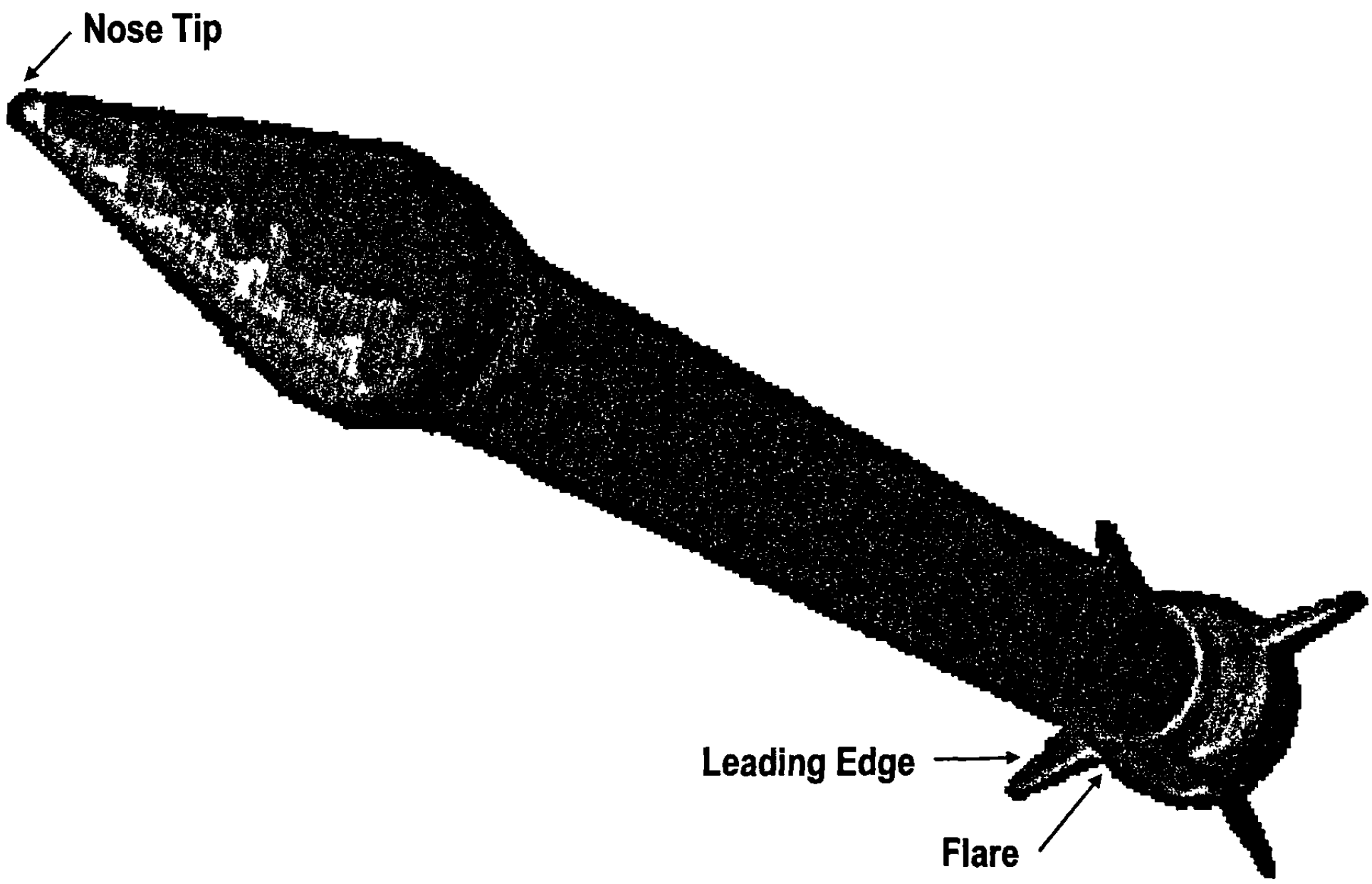

Fig. 4.24 Examples of aerodynamic hot spots.

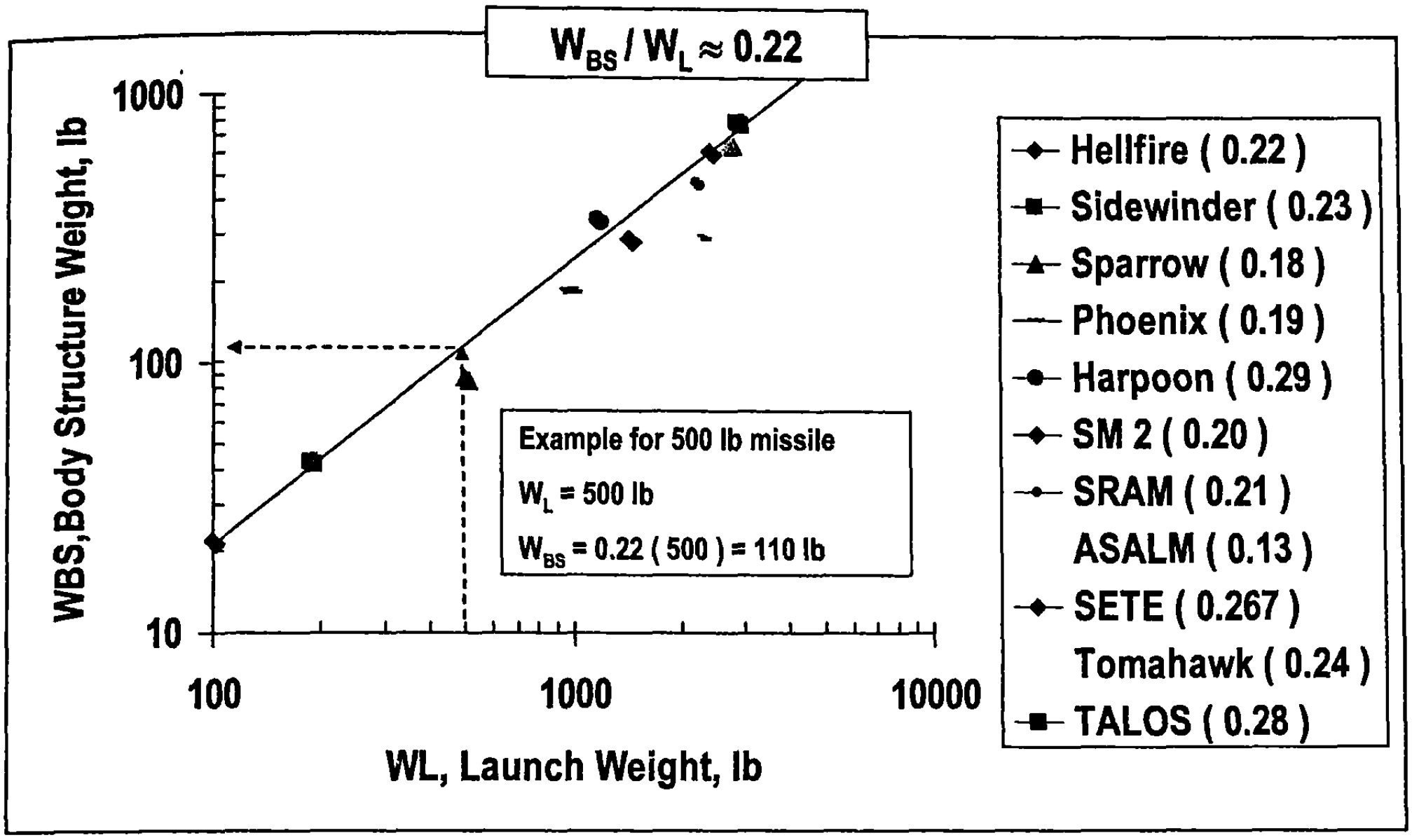

Note: W_{BS} includes all load carrying body structure. If motor case, engine, or warhead case carry external loads then they are included in W_{BS}. W_{BS} does not include tail, wing, or other surface weight.

Fig. 4.25 Tactical missile body structure weight is about 22% of the launch weight.

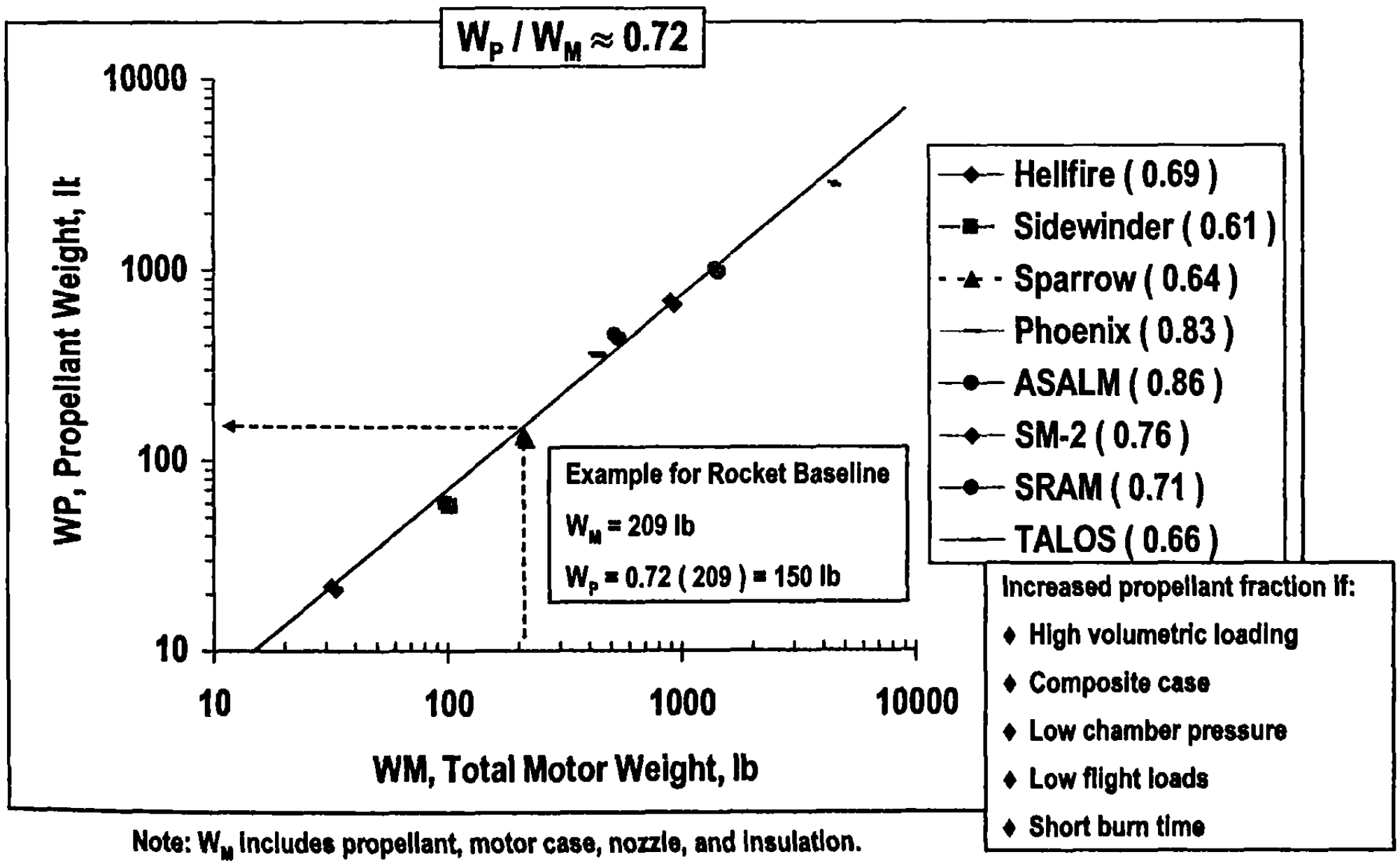

Note: W_M includes propellant, motor case, nozzle, and insulation.

Fig. 4.30 Tactical missile propellant weight is about 72% of the rocket motor weight.

COLOR FIGURE SECTION

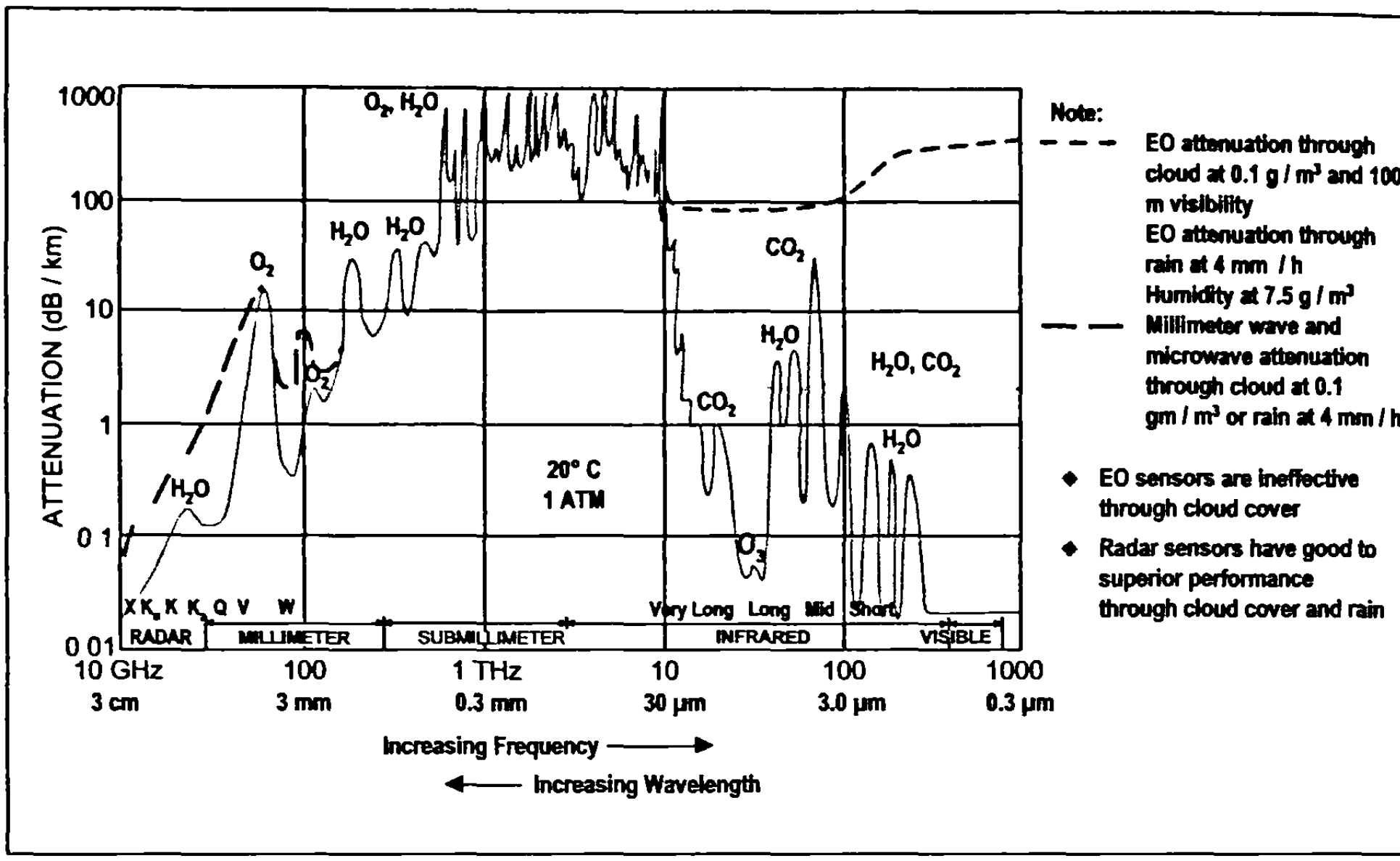

Source: Klein, L.A., *Millimeter-Wave and Infrared Multisensor Design and Signal Processing*, Artech House, Boston, 1997

Fig. 6.4 Radar seekers are robust in adverse weather.

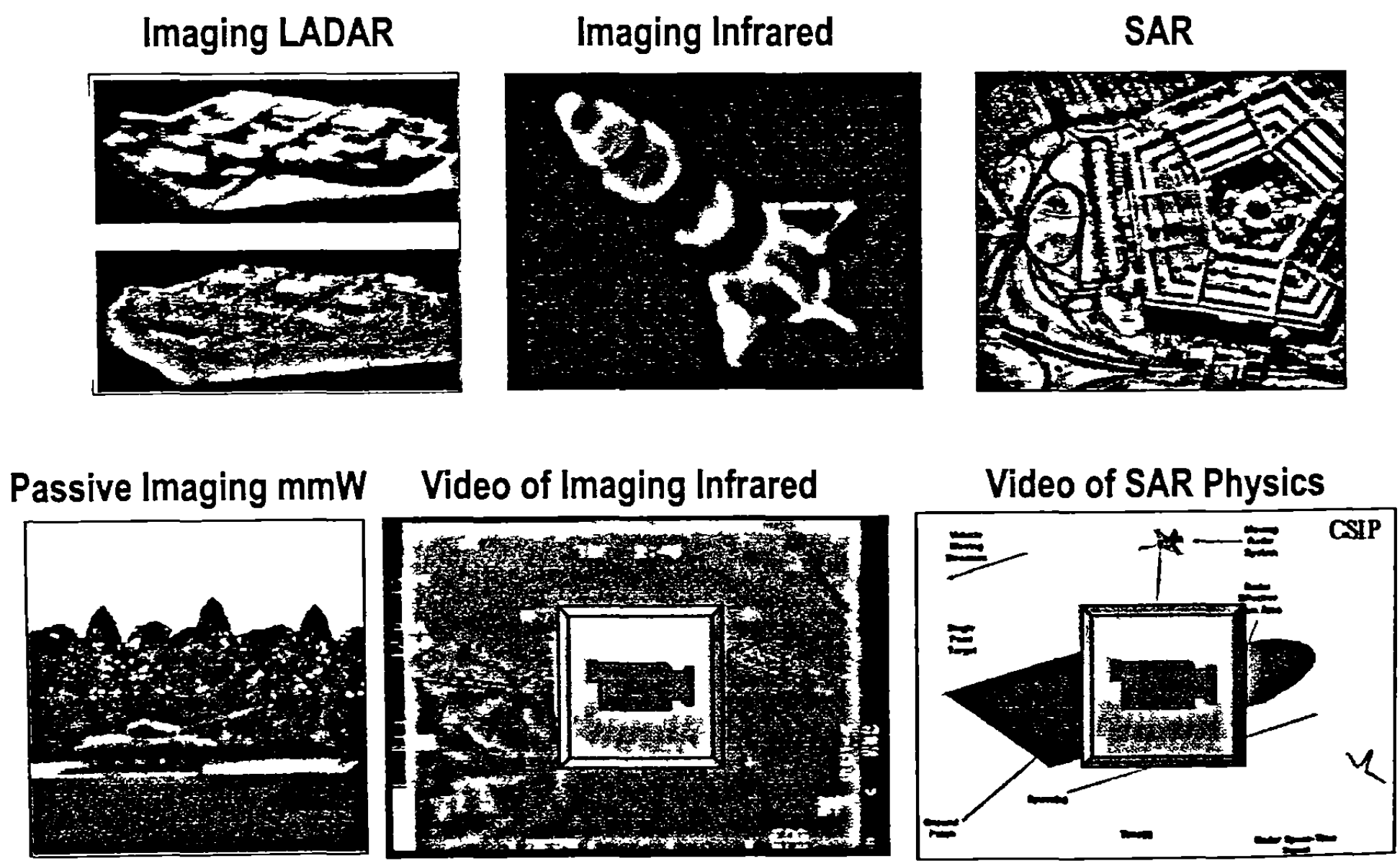

Fig. 6.7 Imaging sensors enhance target acquisition/discrimination.

COLOR FIGURE SECTION

Examples of CM (Threat)

- EOCM
  - directed laser
  - flare
  - smoke
- RFCM
  - active radar
  - jammer
  - chaff
- Decoy
- Low Observables
- Speed
- Altitude
- Maneuverability
- Lethal Defense

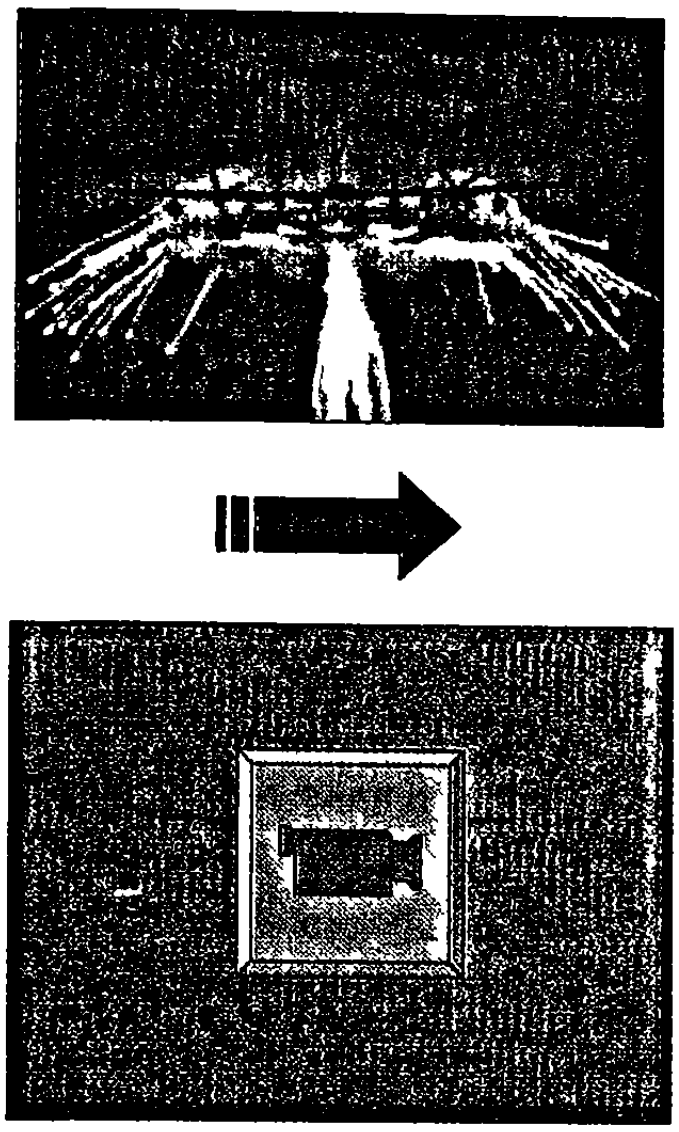

Examples of CCM (Missile)

- Imaging Seeker
- Multi-spectral / Multi-mode Seeker
- Temporal Processing
- Hardened GPS / INS
  - standoff acquisition
  - Integrated GPS / INS
  - directional antenna
  - pseudolite / differential GPS
- ATR / ATA
- Speed
- Altitude
- Maneuverability
- Low Observables
- Saturation

Fig. 6.16 Counter-countermeasures by missile enhance design robustness.

IIR (I^2R AGM-130) .....

Two Color IIR (Python 5)

Acoustic - IIR (BAT) .....

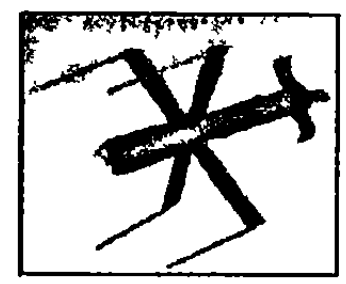

IIR – LADAR (LOCAAS) .....

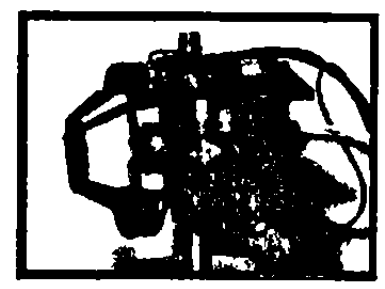

ARH – mmW (AARGM)

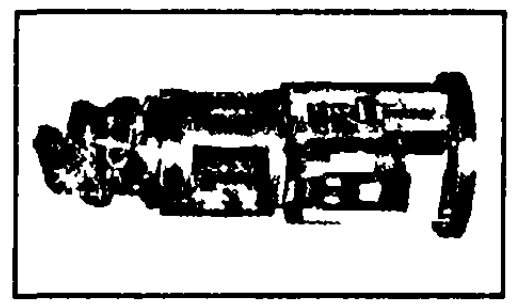

ARH - IIR (Armiger) .....

Fig. 6.17 Examples of countermeasure-resistant seekers.

COLOR FIGURE SECTION

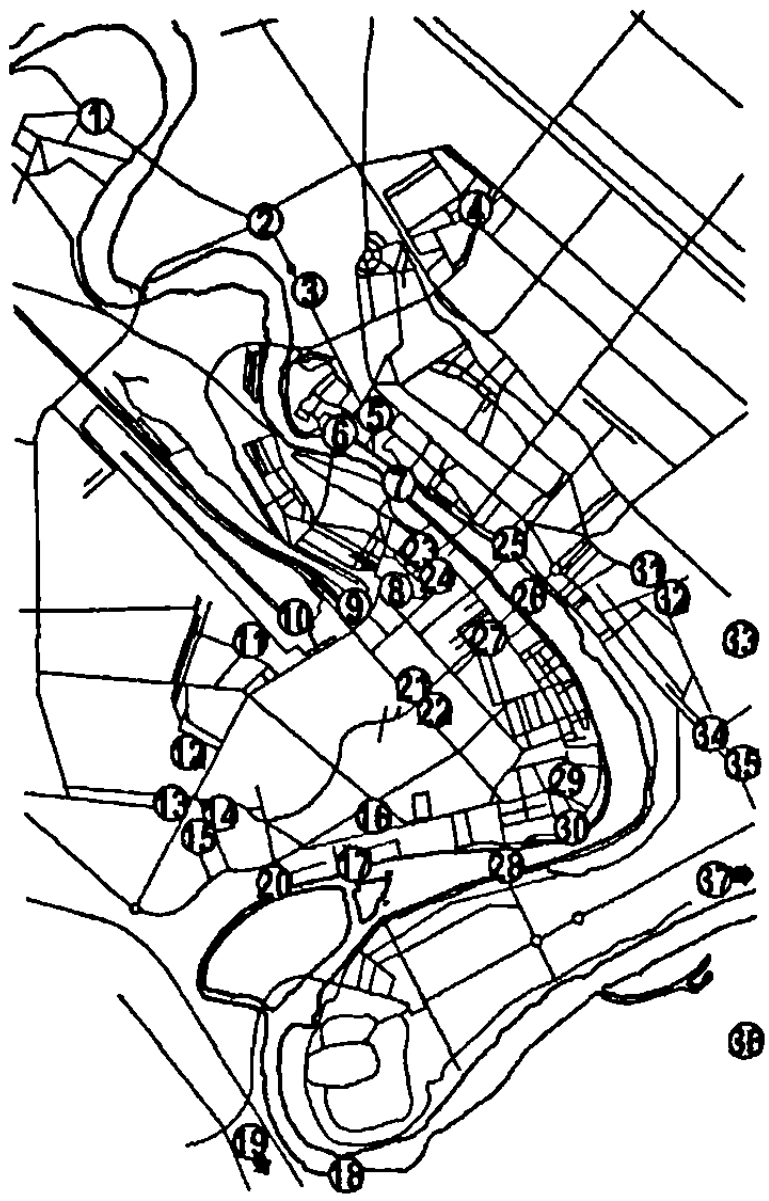

Targets: 1 Directorate of Military Intelligence; 2, 5, 8, 13, 34. Telephone switching stations; 3. Ministry of Defense national computer complex; 4. Electrical transfer station; 6. Ministry of Defense headquarters; 7. Ashudad highway bridge; 9. Railroad yard; 10. Muthena airfield (military section); **11. Air Force headquarters; 12. Iraqi Intelligence Service; 14. Secret Police complex;** 15. Army storage depot; **16. Republican Guard headquarters; 17. New presidential palace; 18. Electrical power station;** 19. SRBM assembly factory (Scud); **20. Baath Party headquarters; 21. Government conference center;** 22. Ministry of Industry and Military Production; **23. Ministry of Propaganda; 24. TV transmitter; 25, 31. Communications relay stations;** 26. Jumhuriya highway bridge; **27. Government Control Center South;** 28. Karada highway bridge (14th July Bridge); **29. Presidential palace command center; 30. Presidential palace command bunker; 32. Secret Police headquarters; 33. Iraqi Intelligence Service regional headquarters; 35. National Air Defense Operations Center;** 36. Ad Dawrah oil refinery; **37. Electrical power plant**

Source: AIR FORCE Magazine, 1 April 1998

Fig. 6.19 76% of Baghdad targets struck first night of Desert Storm were C^3 time-critical targets.

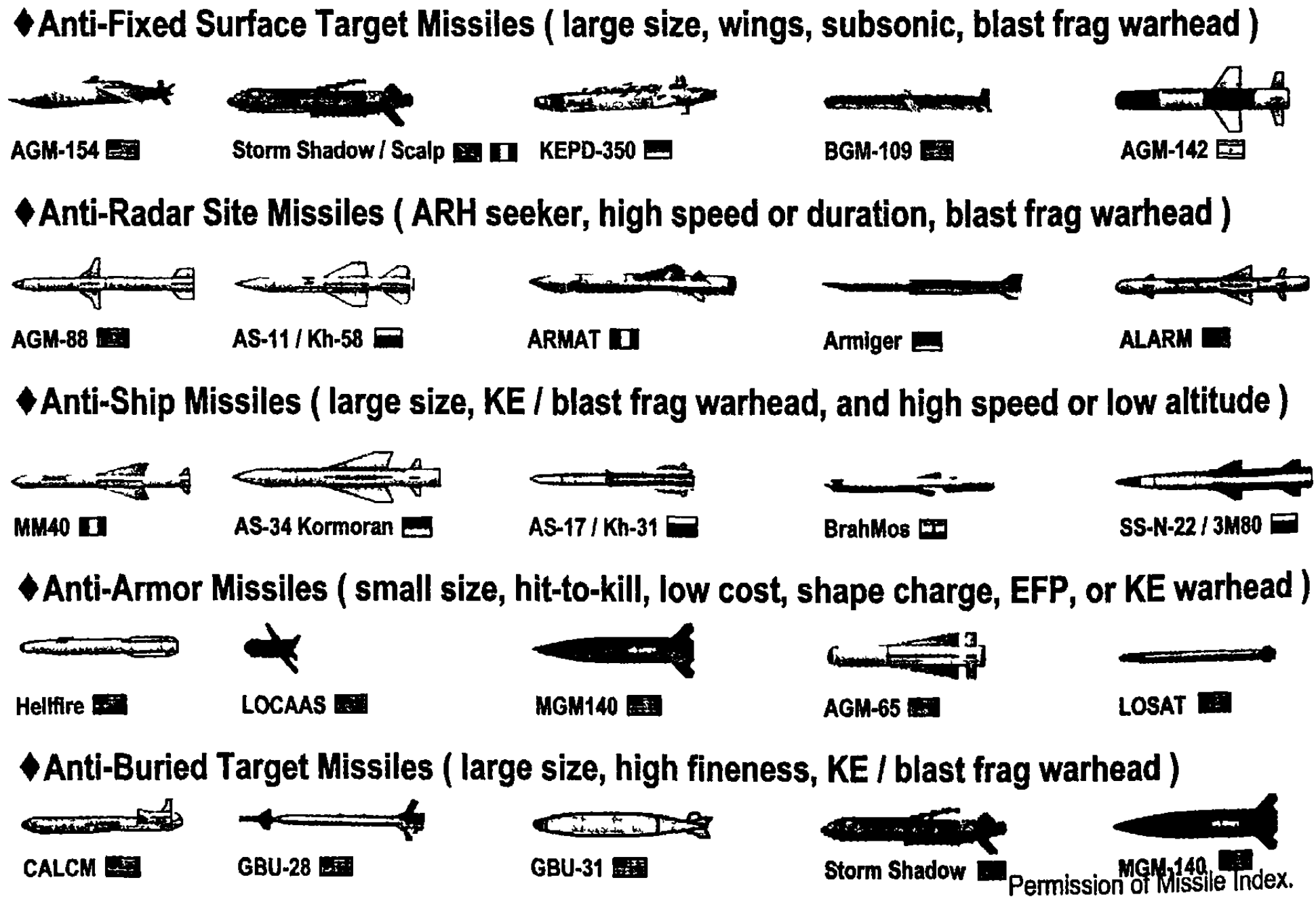

Fig. 6.20 Type of target drives precision strike missile speed, cost, seeker, and warhead.

COLOR FIGURE SECTION

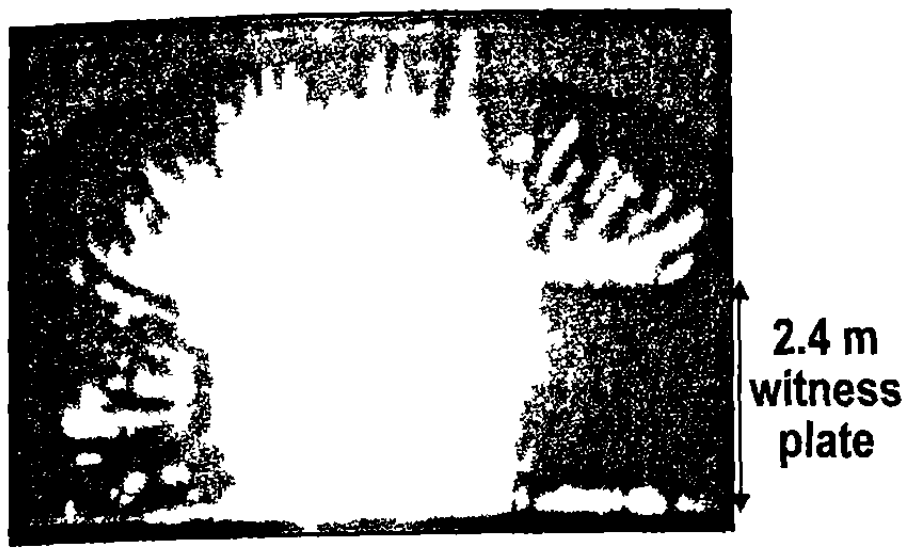

Hellfire 24 lb shaped charge warhead fragments are from natural fragmenting case

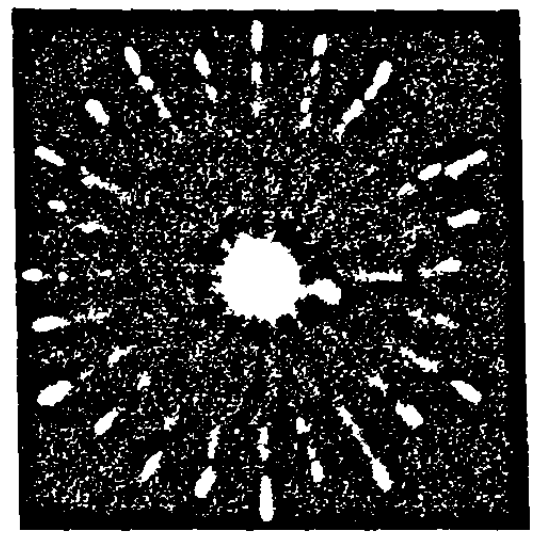

Roland 9 kg explosively formed warhead multi-projectiles are from preformed case

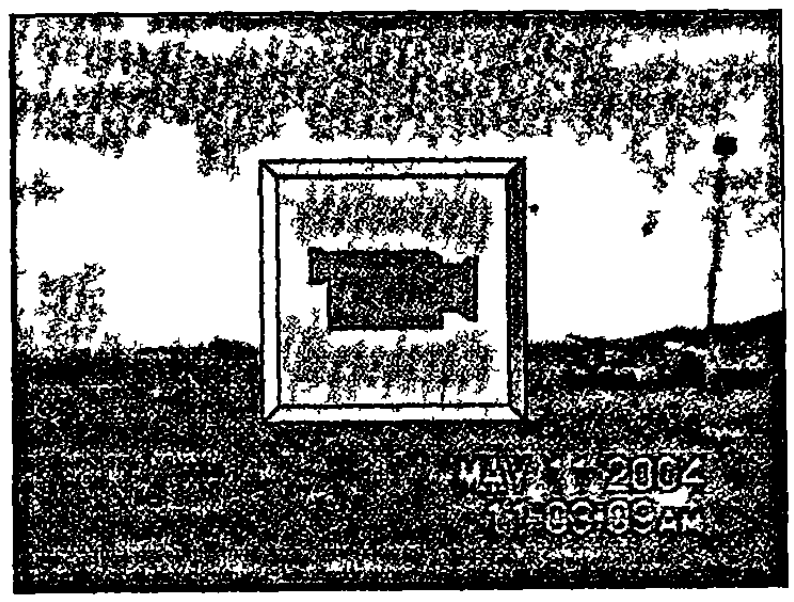

Video of Guided MLRS 180 lb blast fragmentation warhead

Fig. 6.24 Warhead blast and fragments are effective at small miss distance.

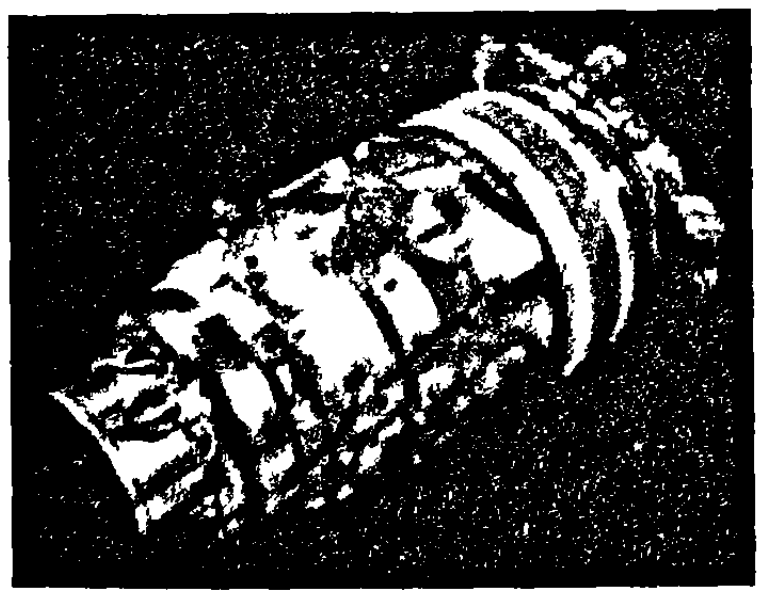

Standard Missile 3 (NTW)

PAC-3

THAAD

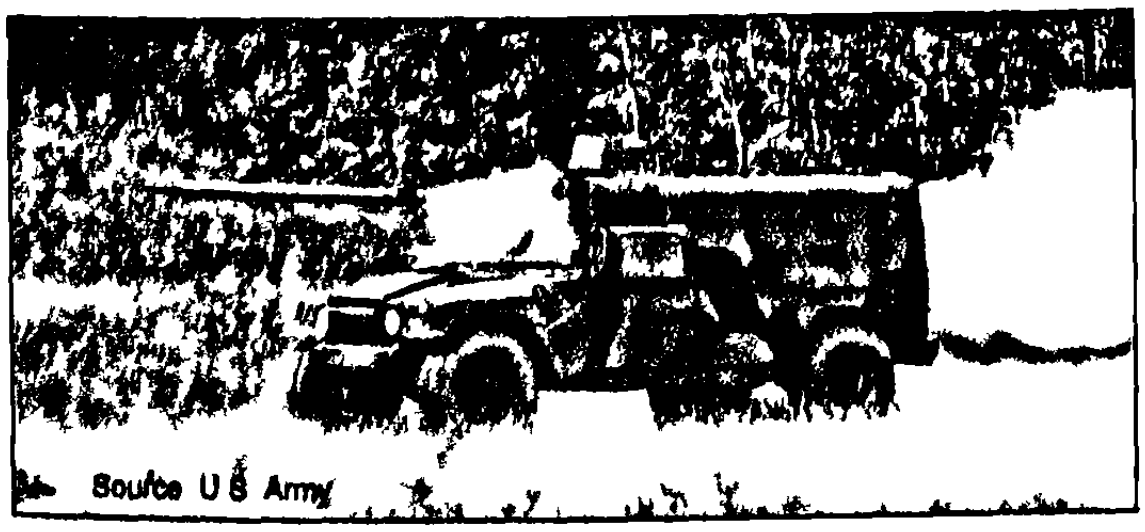

LOSAT

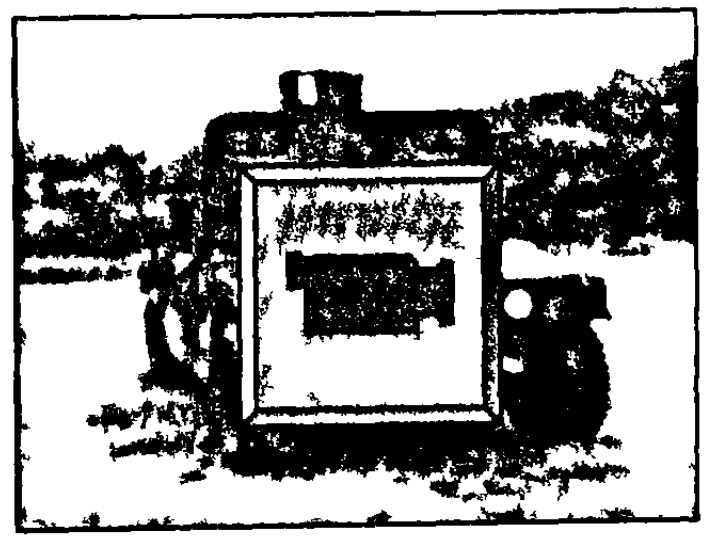

LOSAT Video

Fig. 6.32 Examples of kinetic-kill missiles.

COLOR FIGURE SECTION

Center Weapon Bay Best for Ejection Launchers

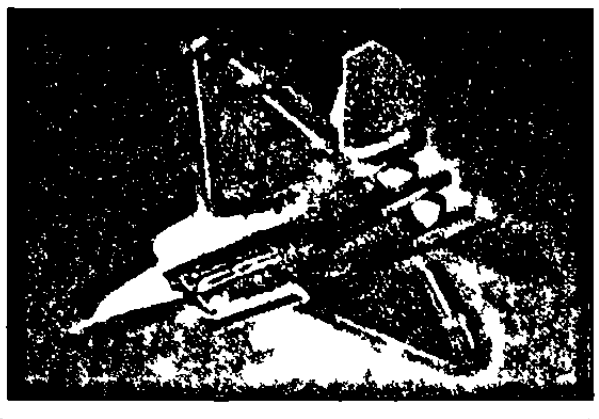

F-22 Bay Loadout: 3 AIM-120C, 1 GBU-32

F-117 Bay Loadout: 1 GBU-27, 1 GBU-10

B-1 Bay Loadout: 8 AGM-69

Video

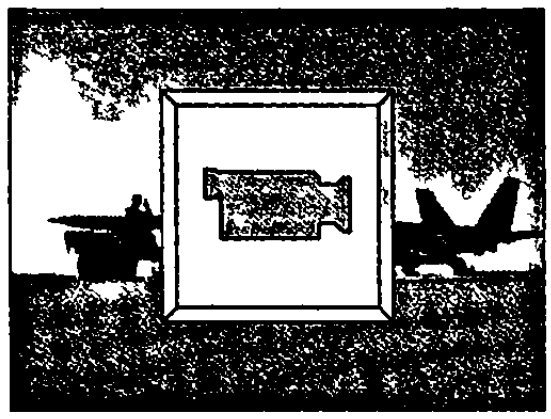

AMRAAM Loading in F-22 Bay

Side Weapon Bay Best for Rail Launchers

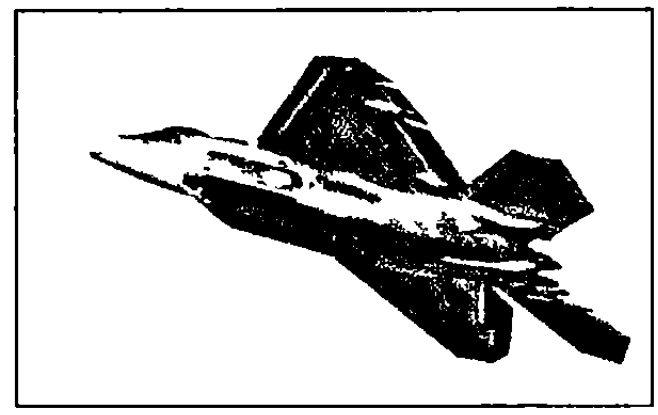

F-22 Side Bay Loadout: 1 AIM-9 Each Side Bay

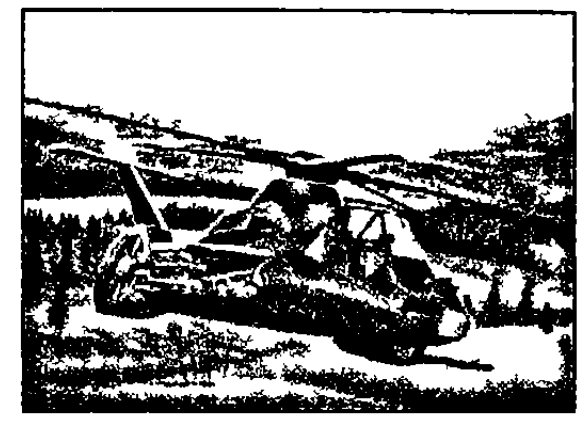

RAH-66 Side Bay Loadout: 1 AGM-114, 2 FIM-92, 4 Hydra 70 Each Side Bay

Fig. 6.47 Examples of weapon bay internal carriage and load-out.

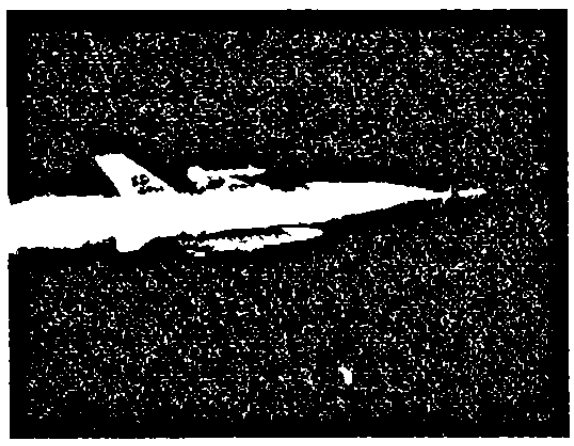

High Smoke Example: AIM-7

Particles (e.g., metal fuel) at all atmosphere temperature.

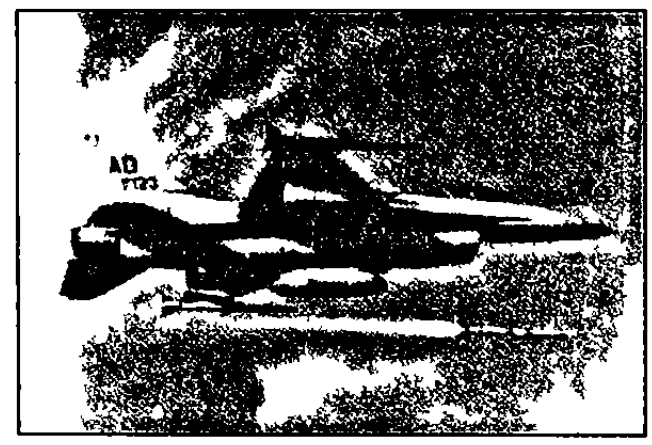

Reduced Smoke Example: AIM-120

Contrail (HCl from AP oxidizer) at < -10° F atmospheric temperature.

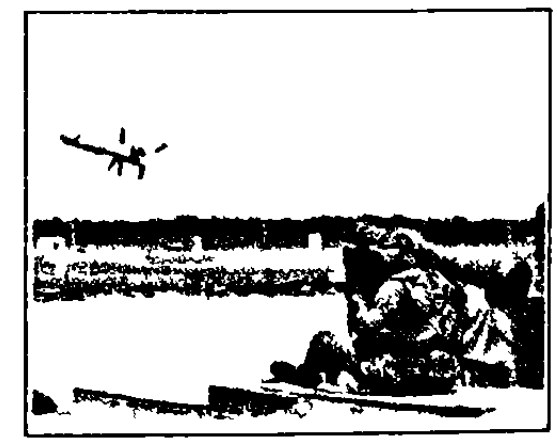

Minimum Smoke Example: Javelin

Contrail (H_2O) at < -35° F atmospheric temperature.

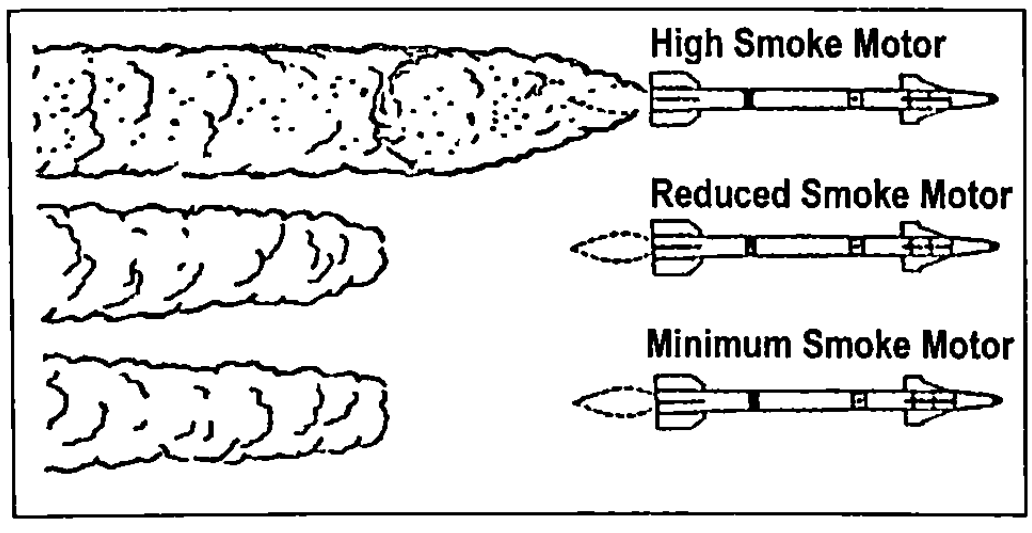

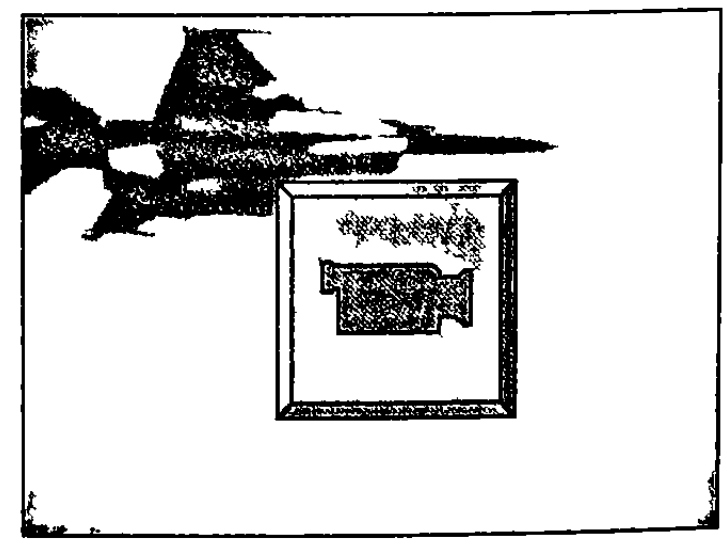

Fig. 6.48 Minimum smoke propellant has low observables.

Example: Derby / R-Darter Missile

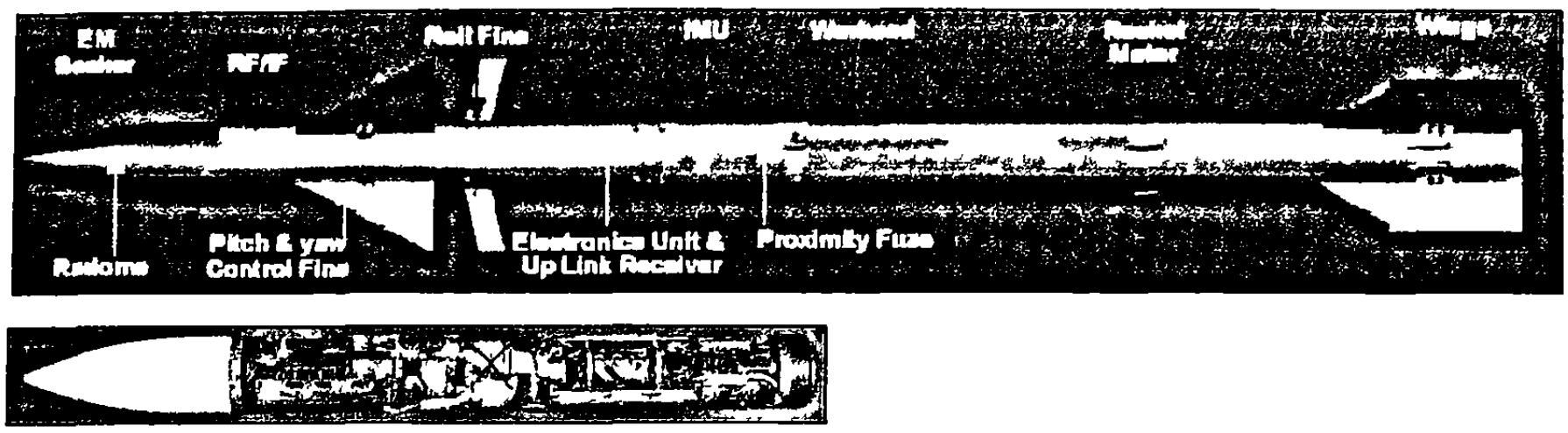

Source: http://www.israeli-weapons.com/weapons/missile_systems/air_missiles/derby/Derby.html

Fig. 6.54 Sensors and electronics occupy a large portion of a high-performance/ high-cost missile.

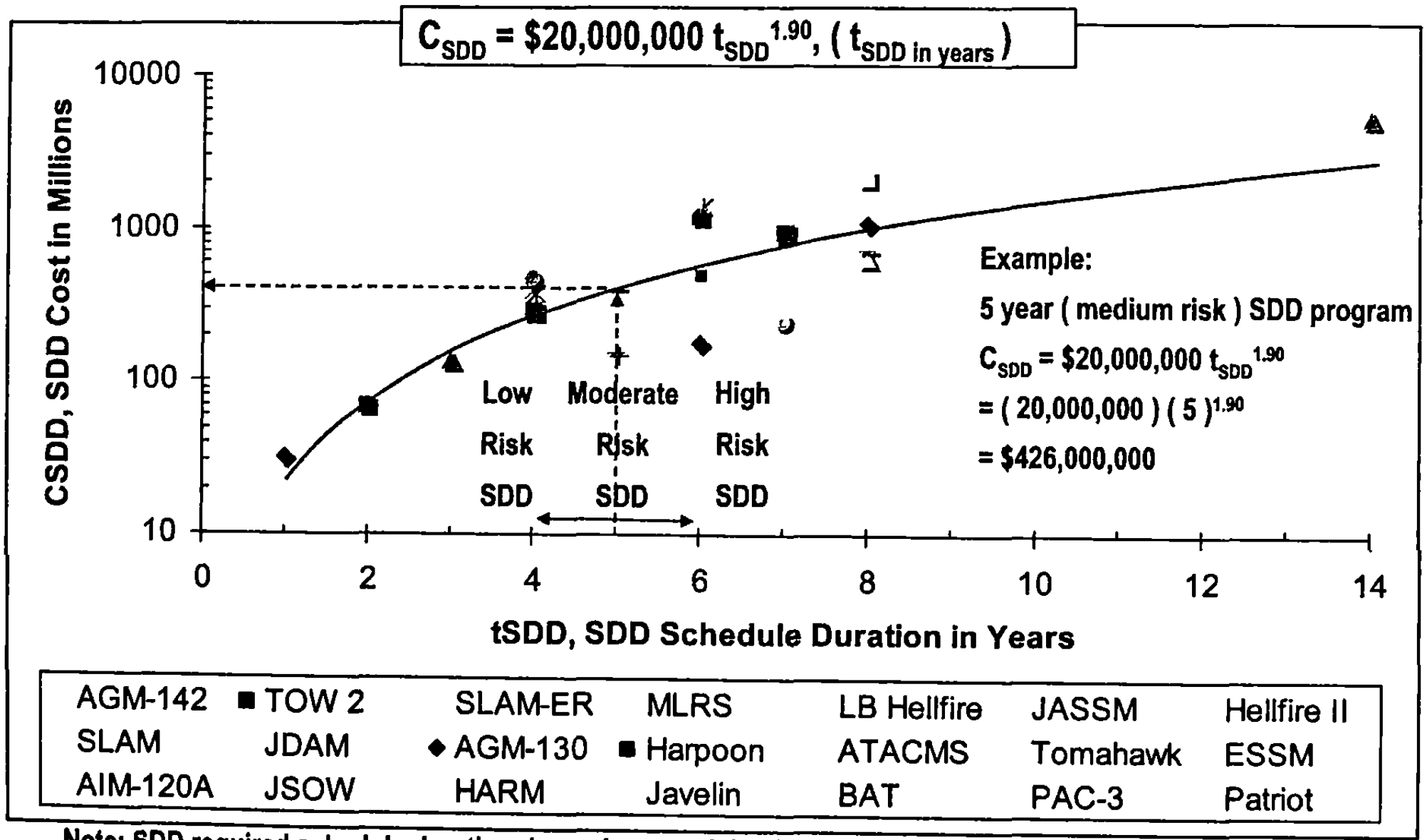

Note: SDD required schedule duration depends upon risk. Should not ignore risk in shorter schedule.
- Source of data: Nicholas, T. and Rossi, R., "U.S. Missile Data Book, 1999," Data Search Associates, 1999
- SDD cost based on 1999 US$

Fig. 6.55 SDD cost is driven by schedule duration and risk.

COLOR FIGURE SECTION

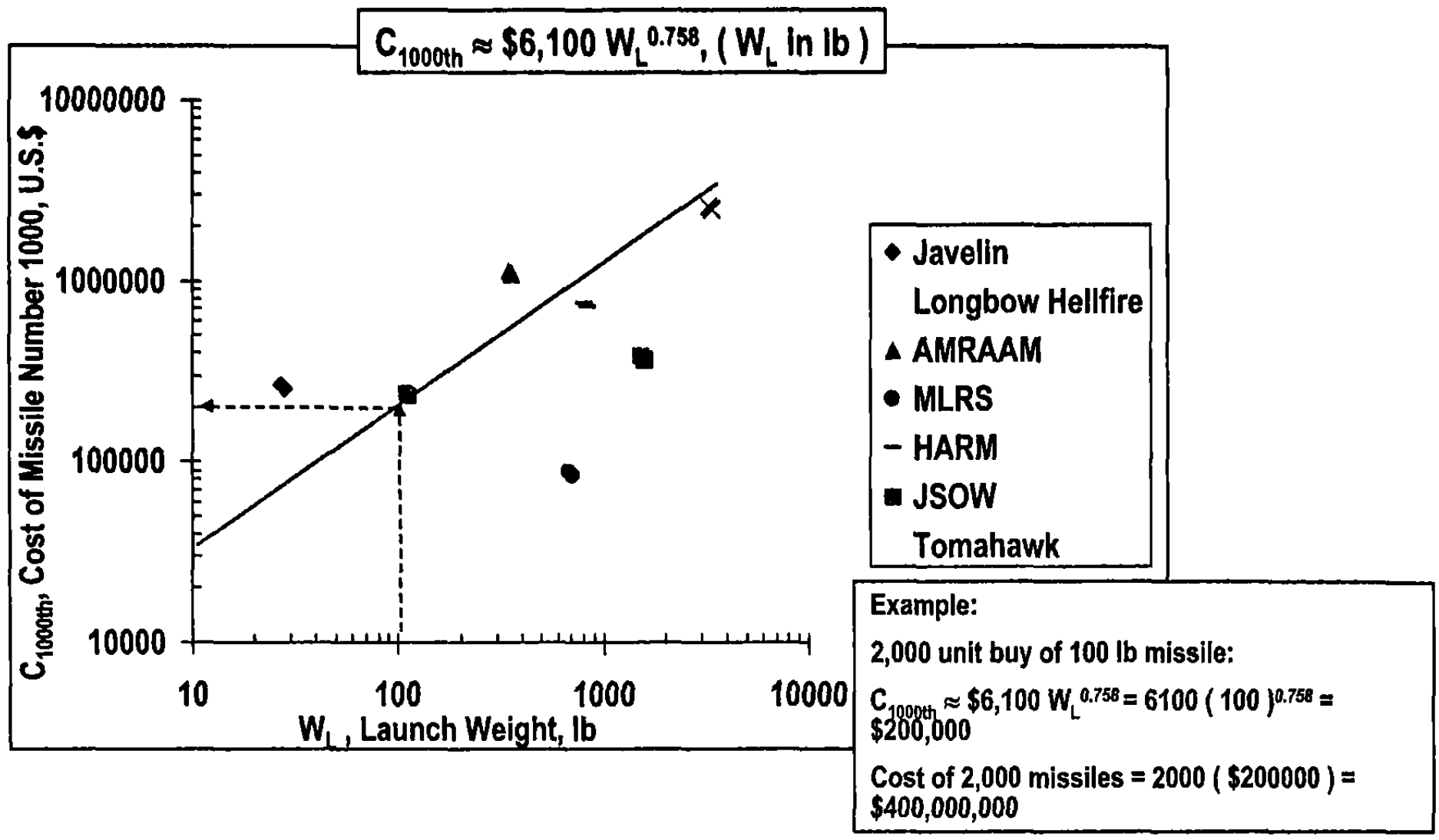

Note:
- Source of data: Nicholas, T. and Rossi, R., "U.S. Missile Data Book, 1999," Data Search Associates, 1999
- Unit production cost based on 1999 US$

Fig. 6.56 Lightweight missiles have low unit production cost.

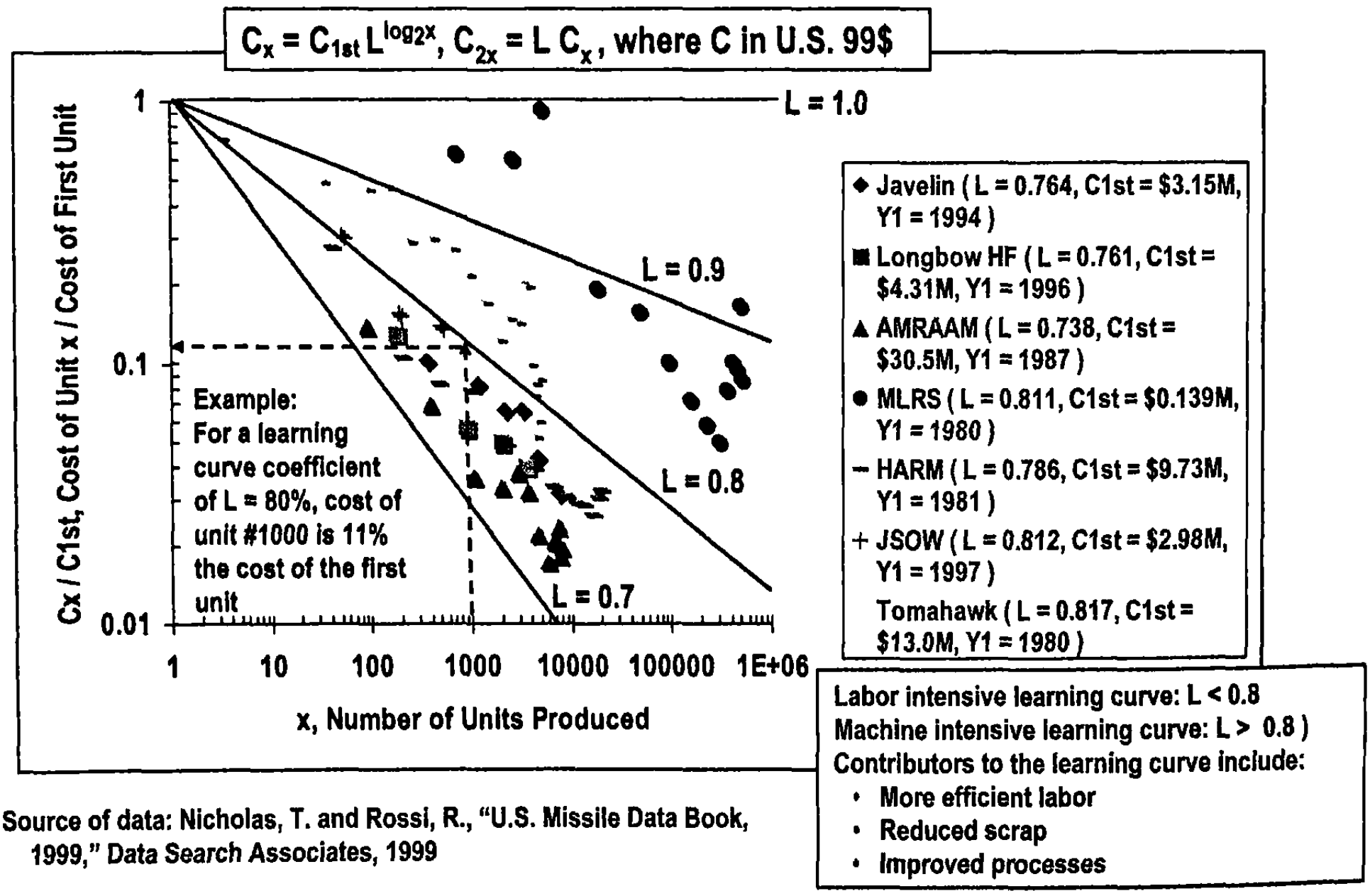

Source of data: Nicholas, T. and Rossi, R., "U.S. Missile Data Book, 1999," Data Search Associates, 1999

Fig. 6.57 Learning curve and large production reduce unit production cost.

COLOR FIGURE SECTION

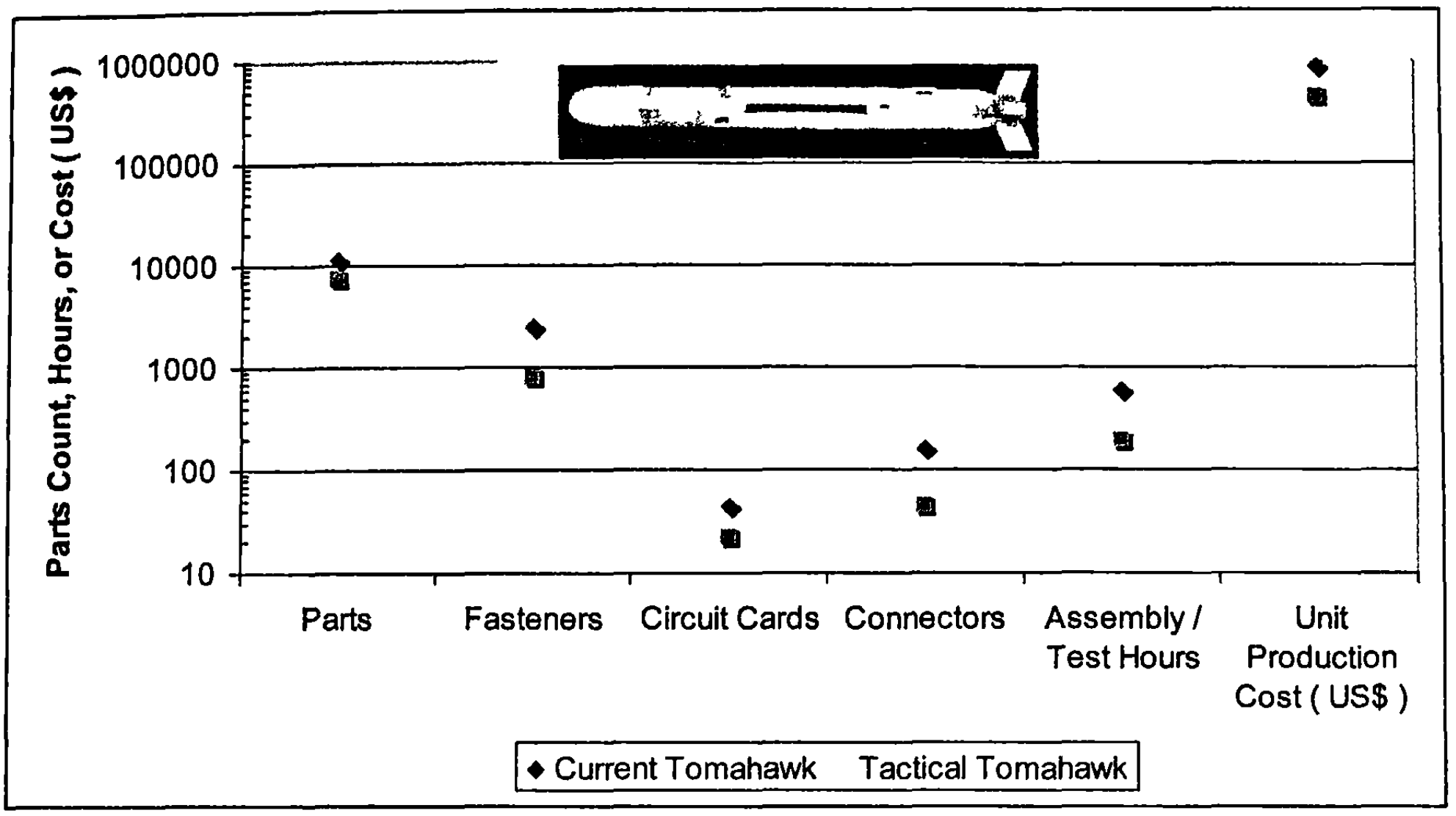

Note: Tactical Tomahawk has superior flexibility (e.g., shorter mission planning, in-flight retargeting, BDI / BDA, modular payload) at lower parts count / cost and higher reliability. Enabling technologies for low parts count include: casting, pultrusion / extrusion, centralized electronics, and COTS.

Fig. 6.58 Low parts count reduces missile unit production cost.

Copperhead Seeker and Electronics Production

Patriot Control Section Production

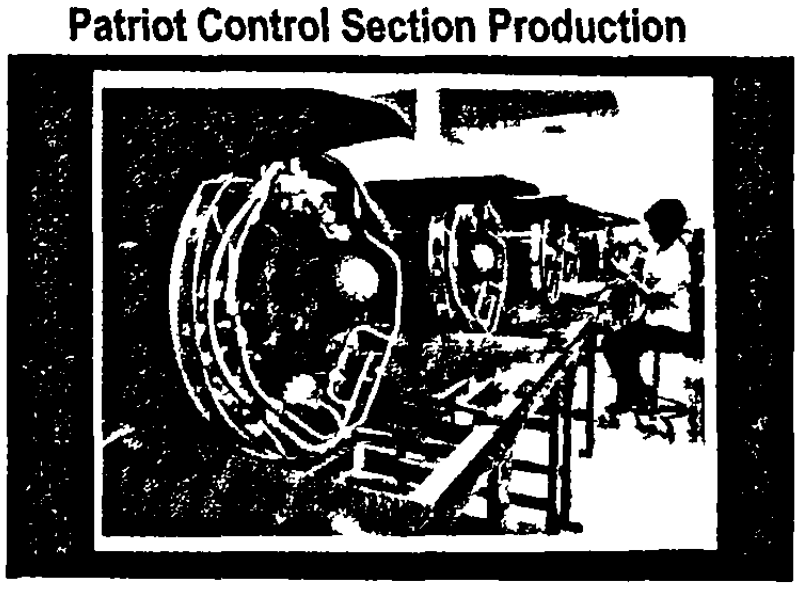

Video of Hellfire Seeker and Electronics Production

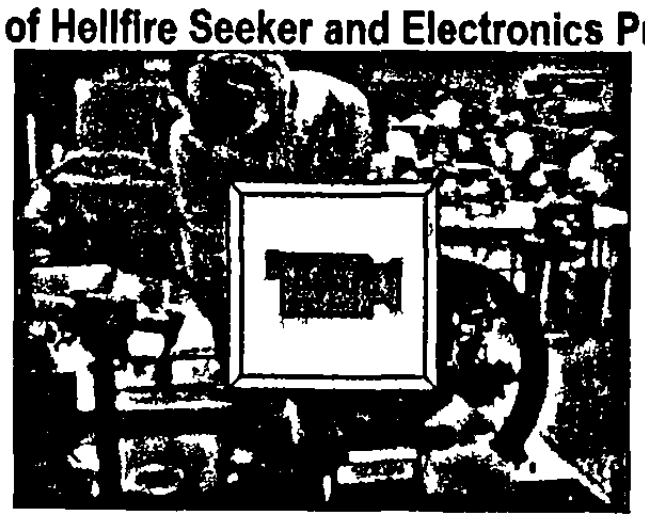

Fig. 6.59 Tactical missile culture is driven by rate production of sensors and electronics.

COLOR FIGURE SECTION

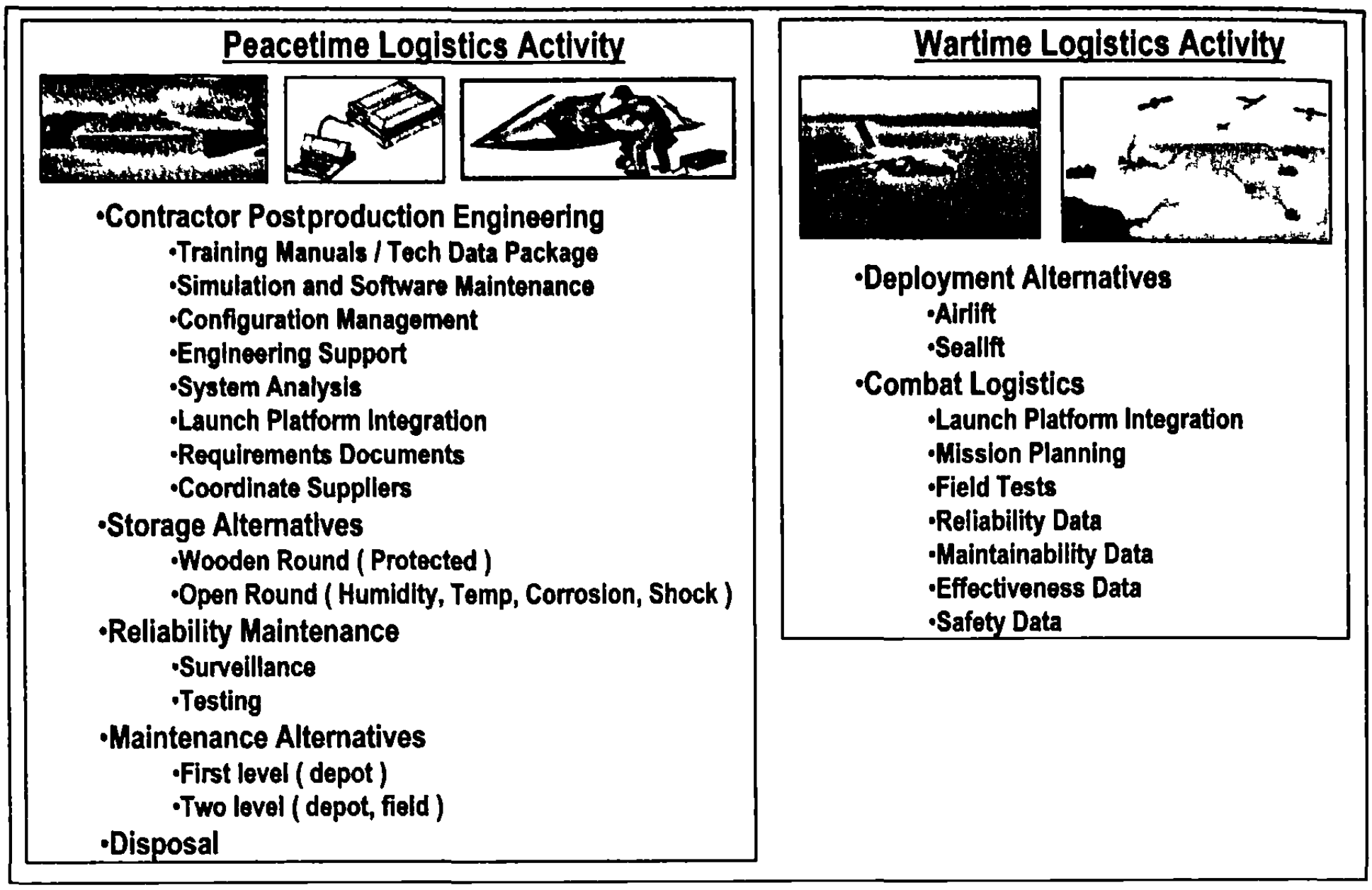

Fig. 6.60 Logistics cost considerations.

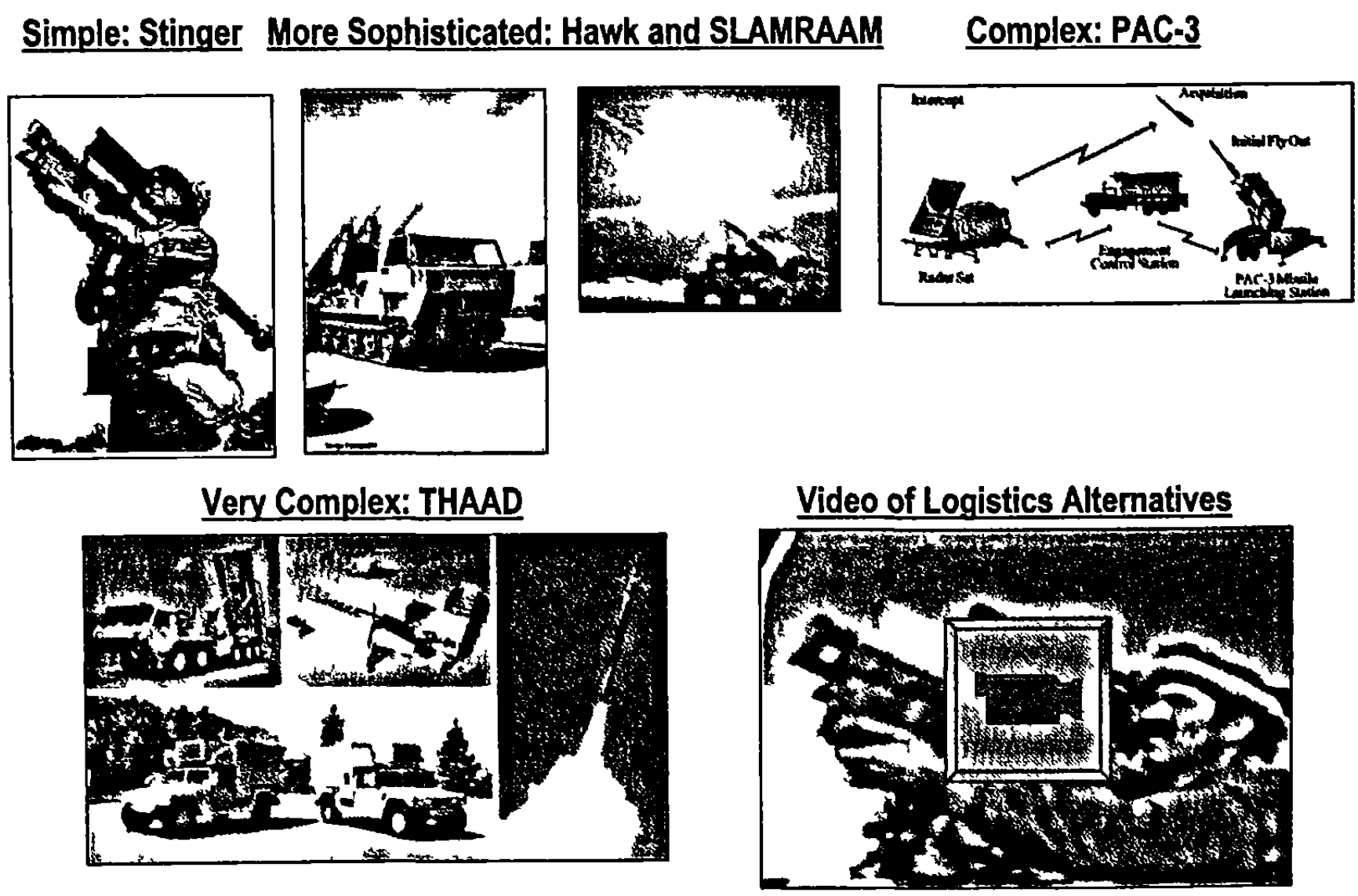

Fig. 6.61 Logistics cost is lower for simple missile systems.

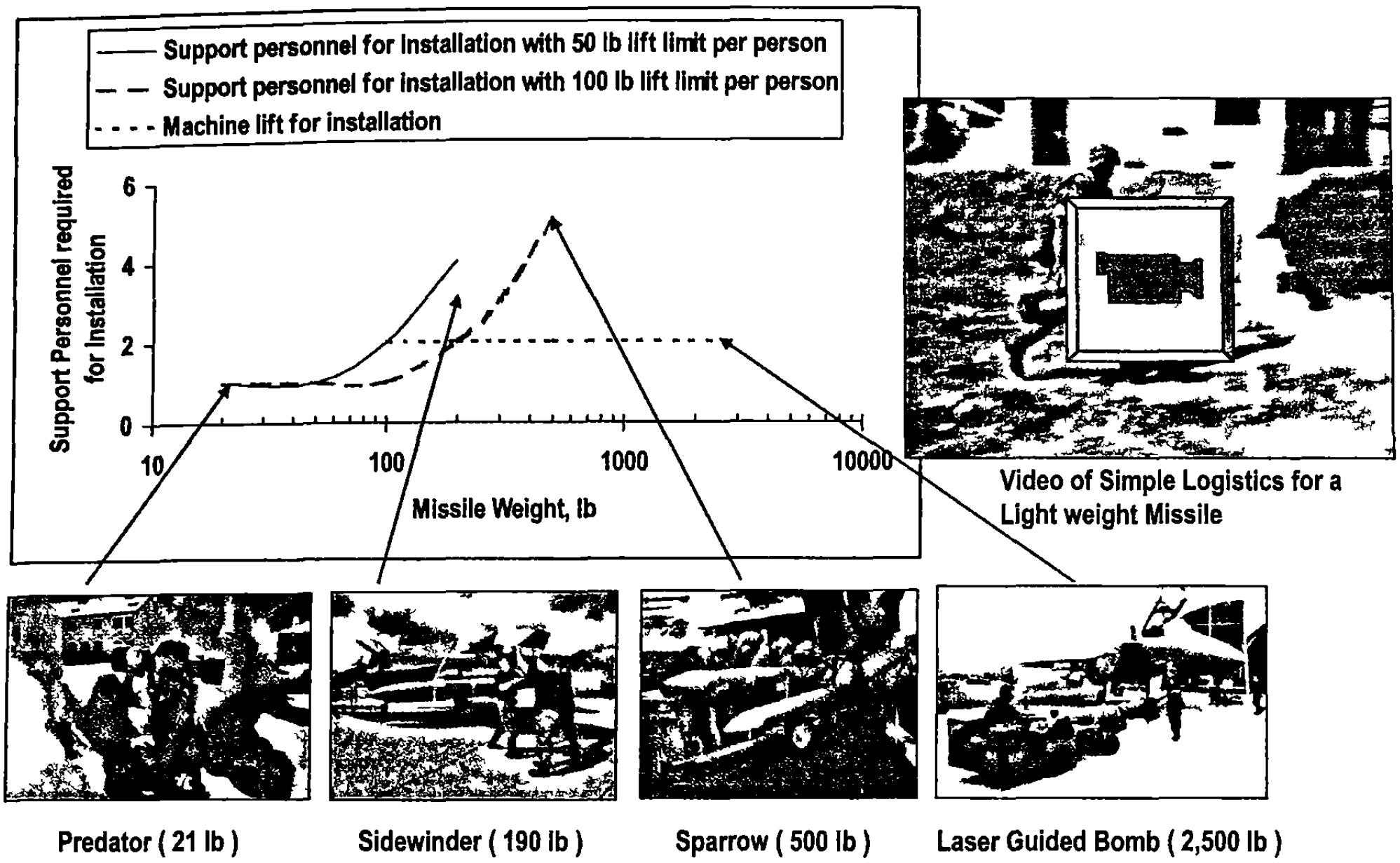

Fig. 6.62 Logistics is simpler for lightweight missiles.

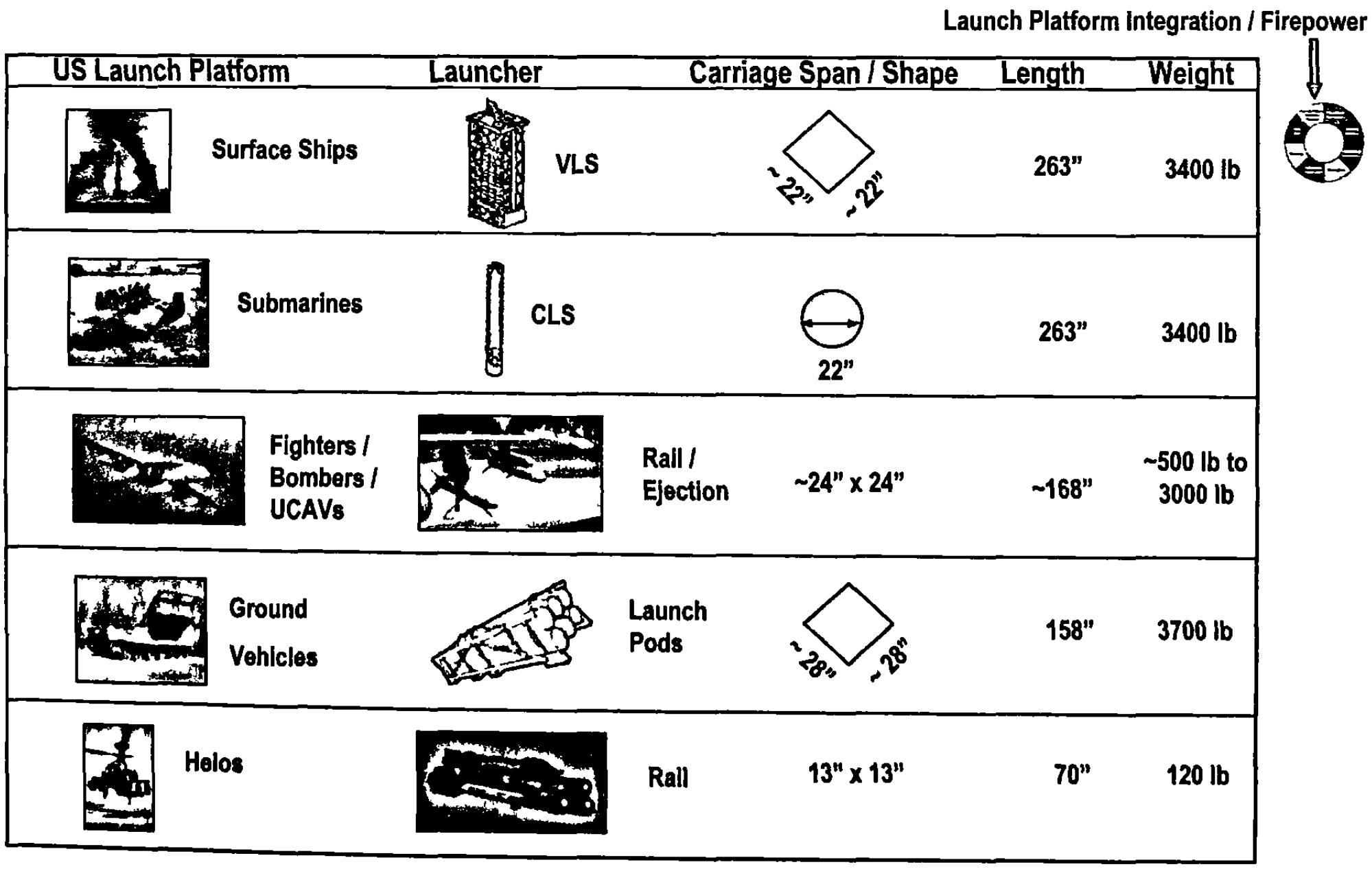

Fig. 6.64 Missile carriage size, shape, and weight are driven by launch platform compatibility.

COLOR FIGURE SECTION

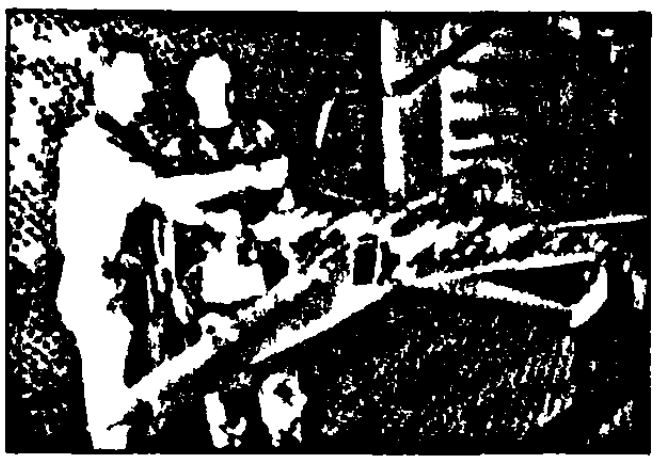

F-18 Store Compatibility Test In AEDC 16T

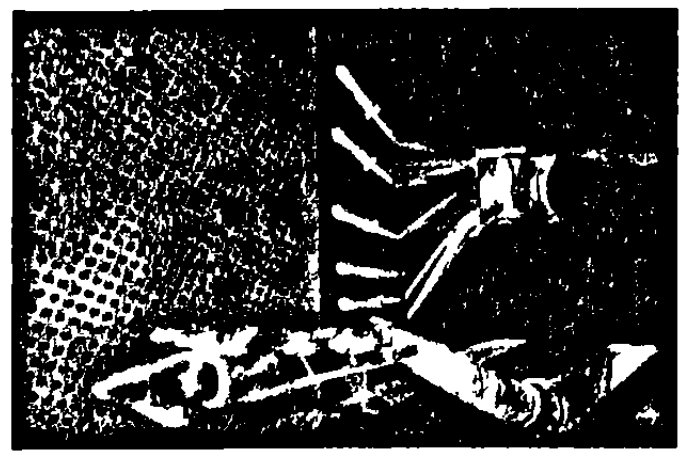

AV-8 Store Compatibility Test in AEDC 4T

Types of Wind Tunnel Testing for Store Compatibility

- Flow field mapping with probe
- Flow field mapping with store
- Captive trajectory simulation
- Drop testing

Example Stores with Flow Field Interaction: Kh-41 + AA-10

Fig. 6.66 Store separation wind tunnel tests are required for missile/aircraft compatibility.

Example Rail Launcher: Hellfire / Brimstone

Example Ejection Launcher: AGM-86 ALCM

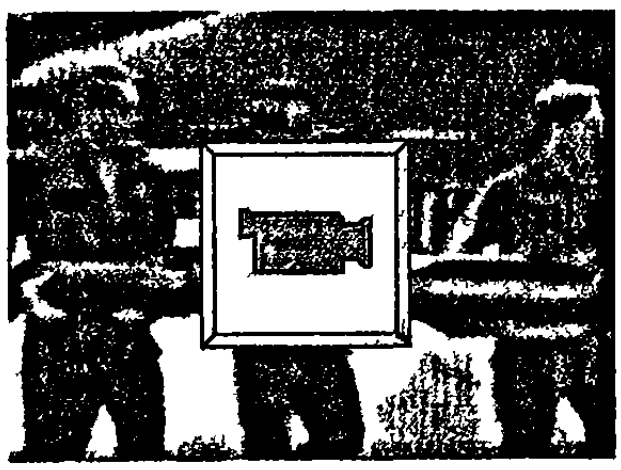

Video of Hellfire / Brimstone Carriage / Launch

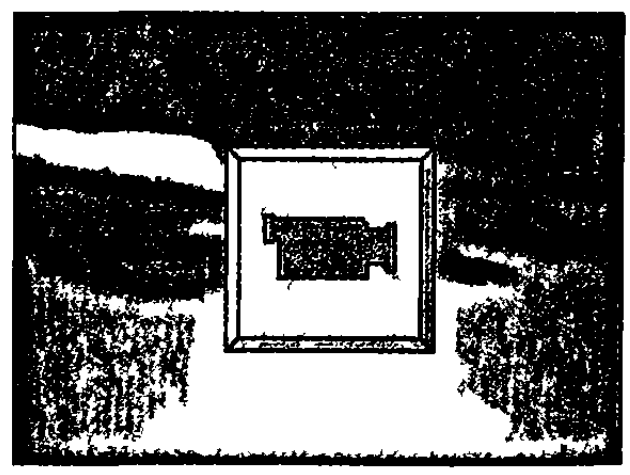

Video of AGM-86 Carriage / Launch

Fig. 6.67 Examples of rail-launched and ejection-launched missiles.

COLOR FIGURE SECTION

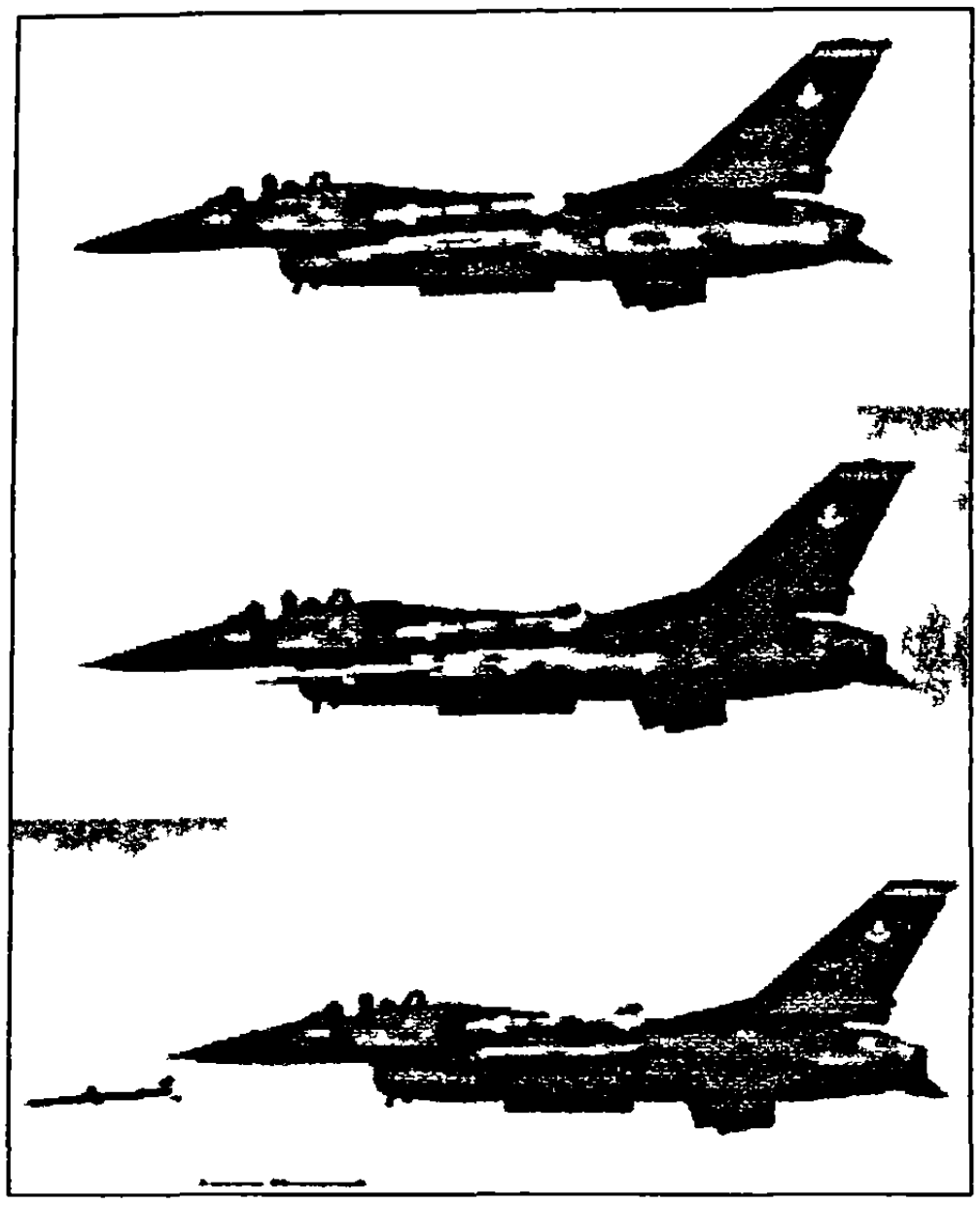

AMRAAM Rail Launch from F-16

Laser Guided Bombs Drop from F-117

Video of Rapid Drop (16 Bombs) from B-2

Fig. 6.68 Examples of safe store separation.

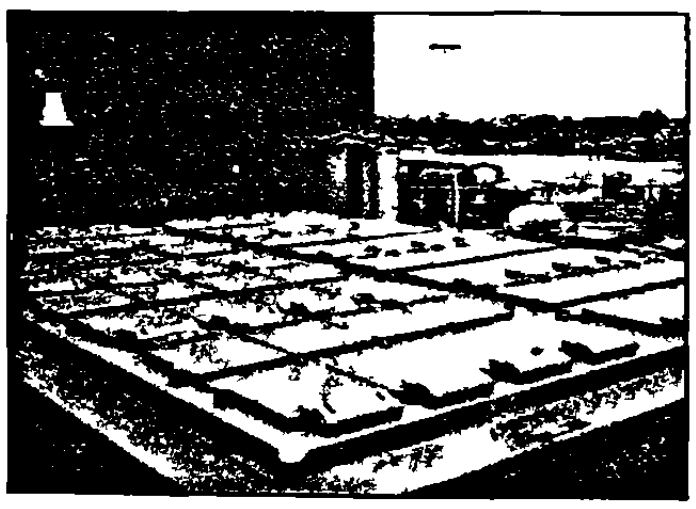

8 Modules / Magazine

Tomahawk Launch

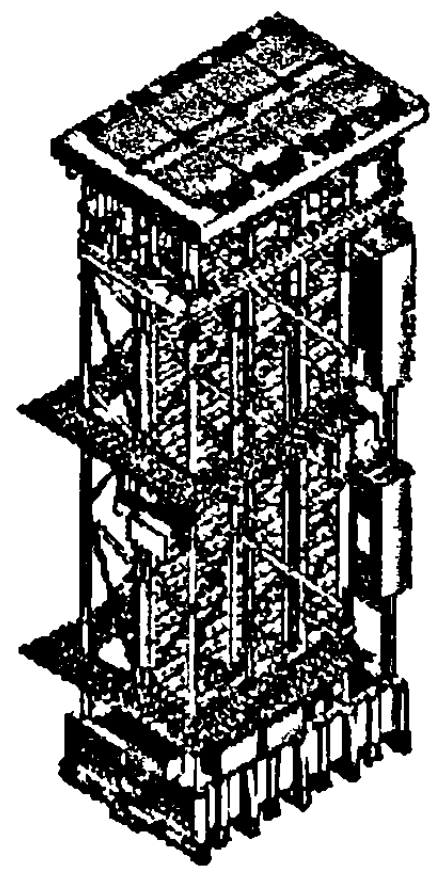

8 Canister Cells / Module

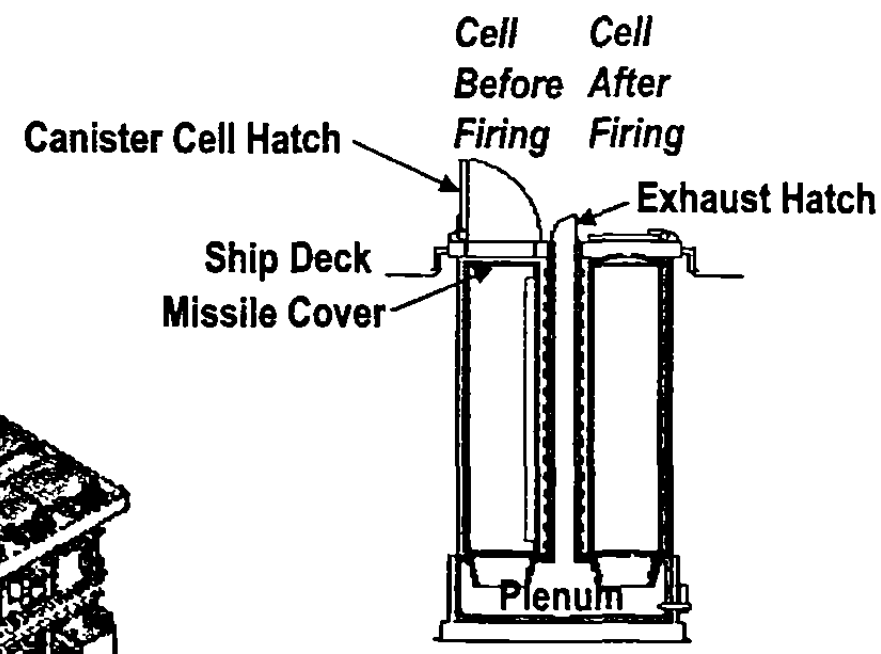

Module Gas Management

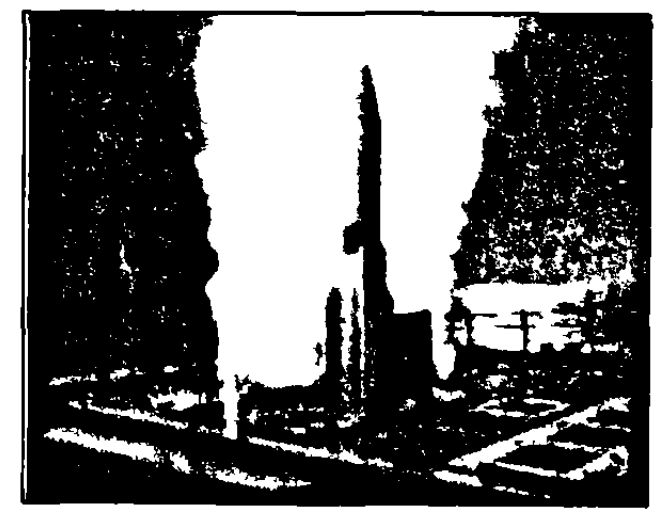

Standard Missile Launch

Fig. 6.74 Example of ship weapon carriage and launcher, Mk41 VLS.

COLOR FIGURE SECTION

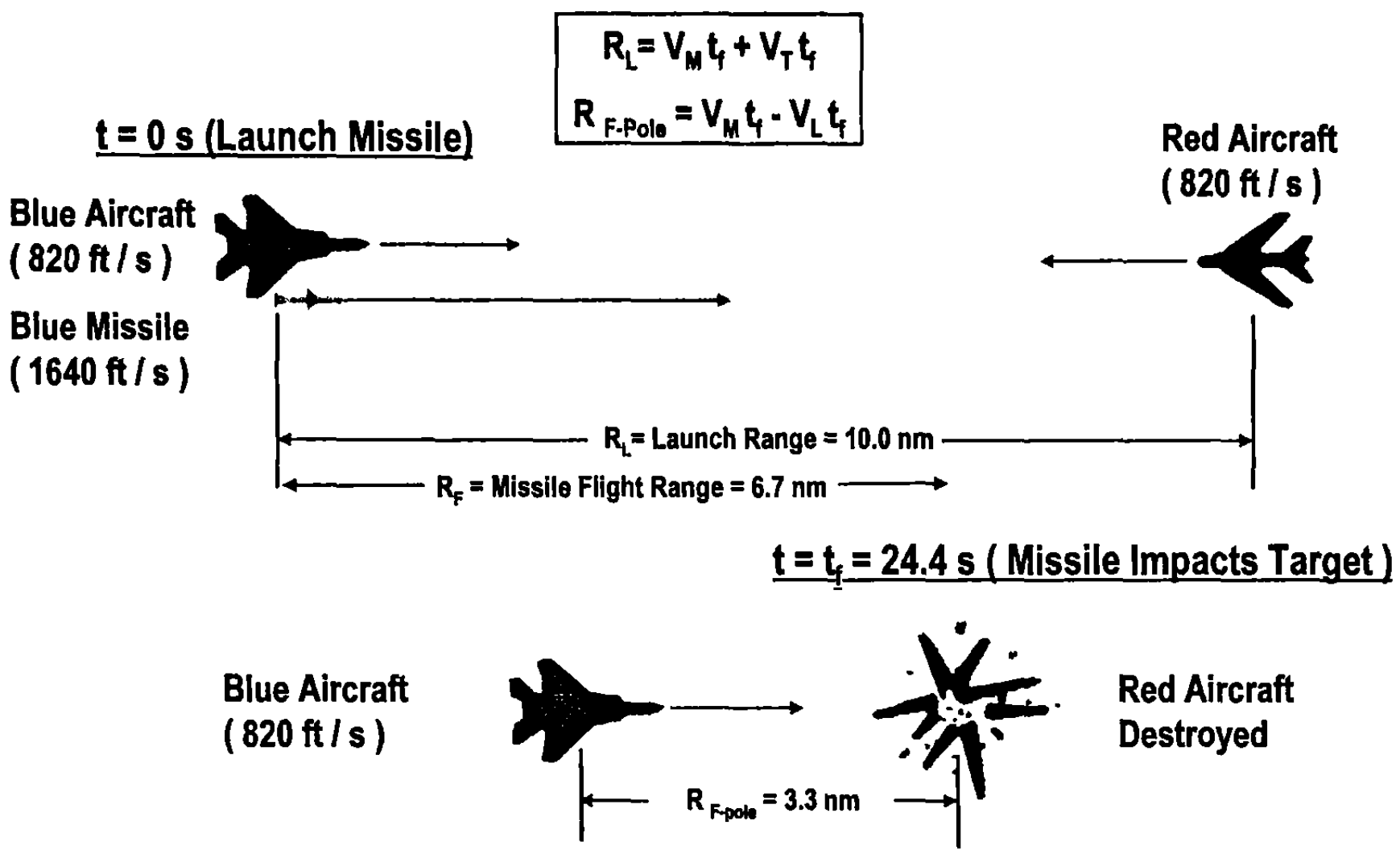

Fig. 7.1 Assumed air-to-air engagement scenario for head-on intercept.

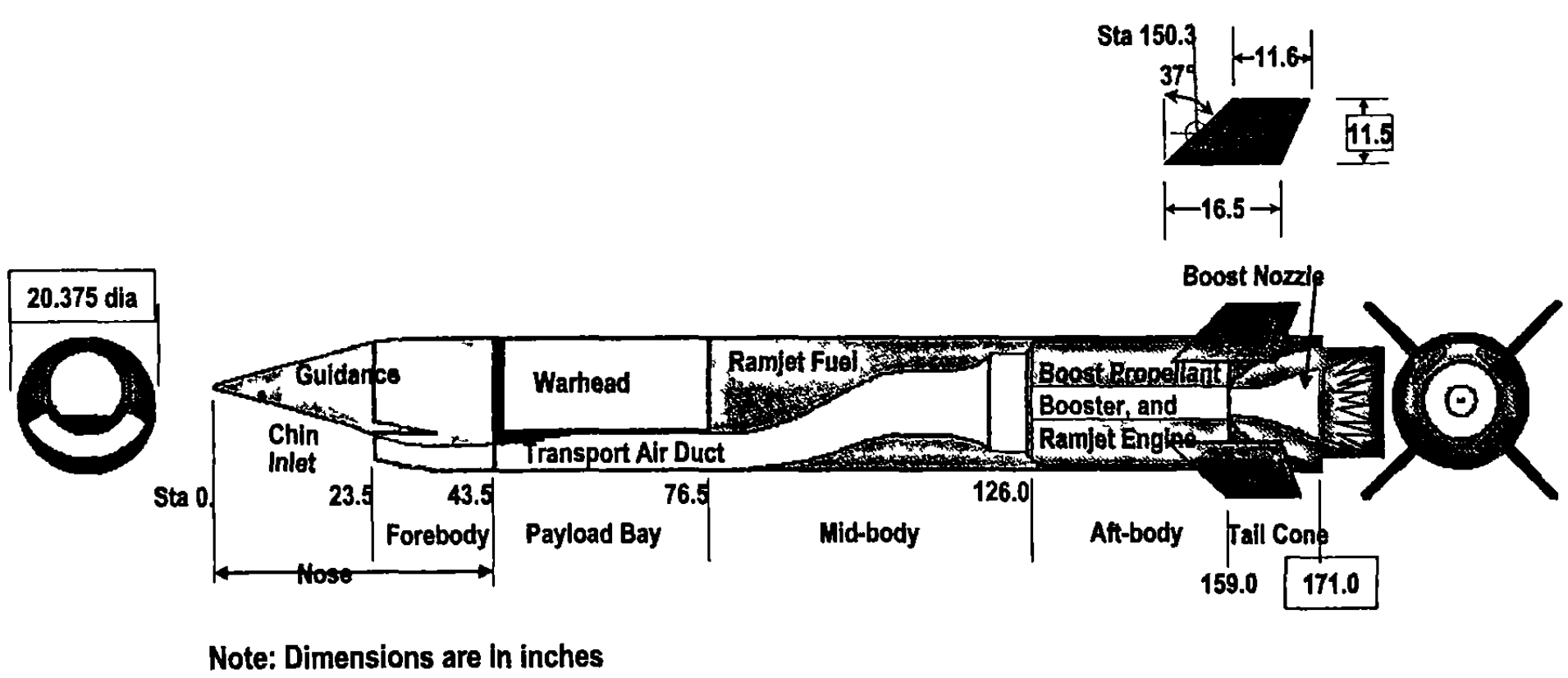

Source: Bithell, R.A. and Stoner, R.C. "Rapid Approach for Missile Synthesis", Vol. II, Air-breathing Synthesis Handbook, AFWAL TR 81-3022, Vol. II, March 1982.

Fig. 7.17 Ramjet baseline is a chin inlet integral rocket ramjet (IRR).

COLOR FIGURE SECTION

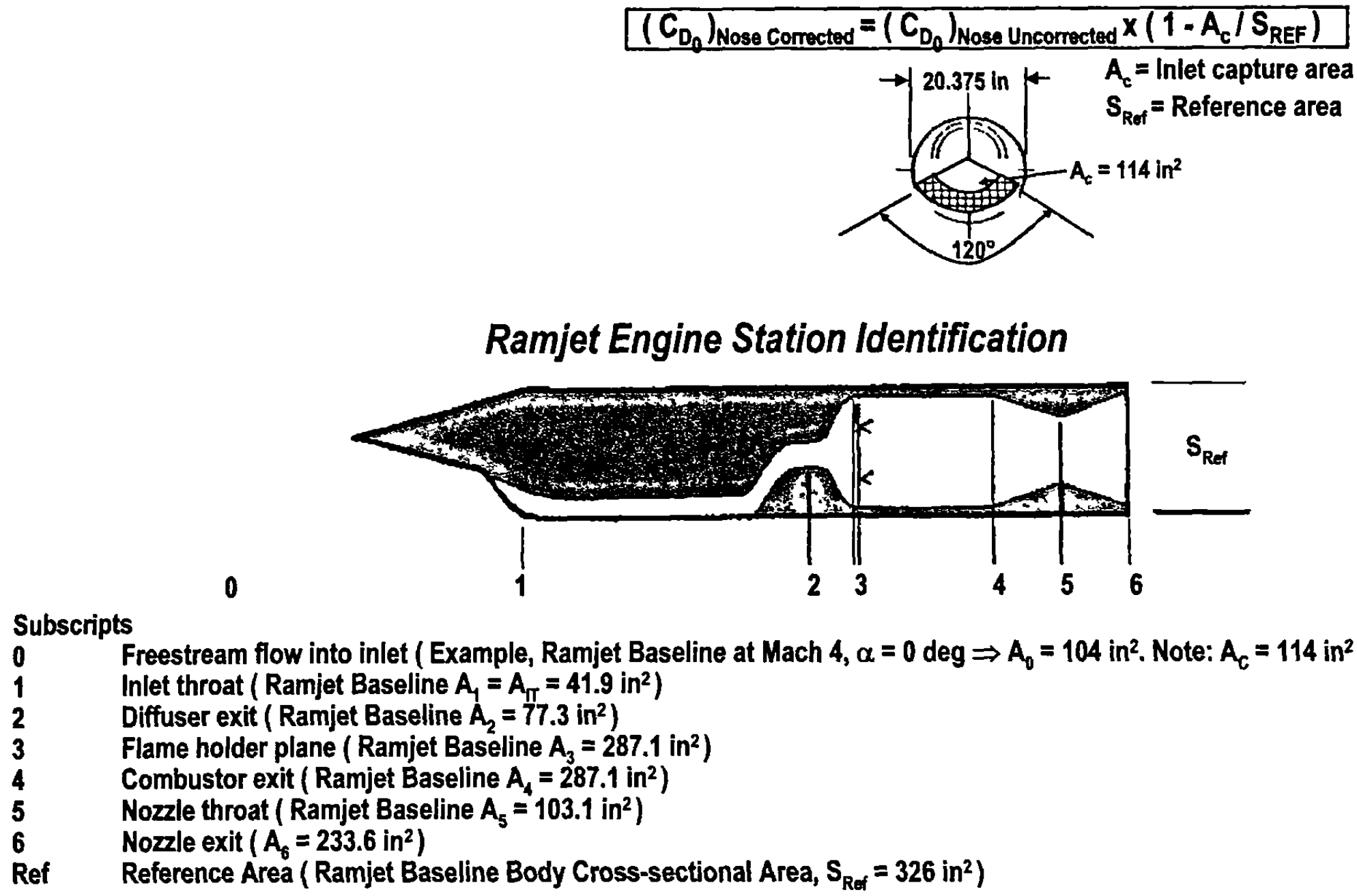

Fig. 7.18 Engine nomenclature and flowpath geometry for ramjet baseline.

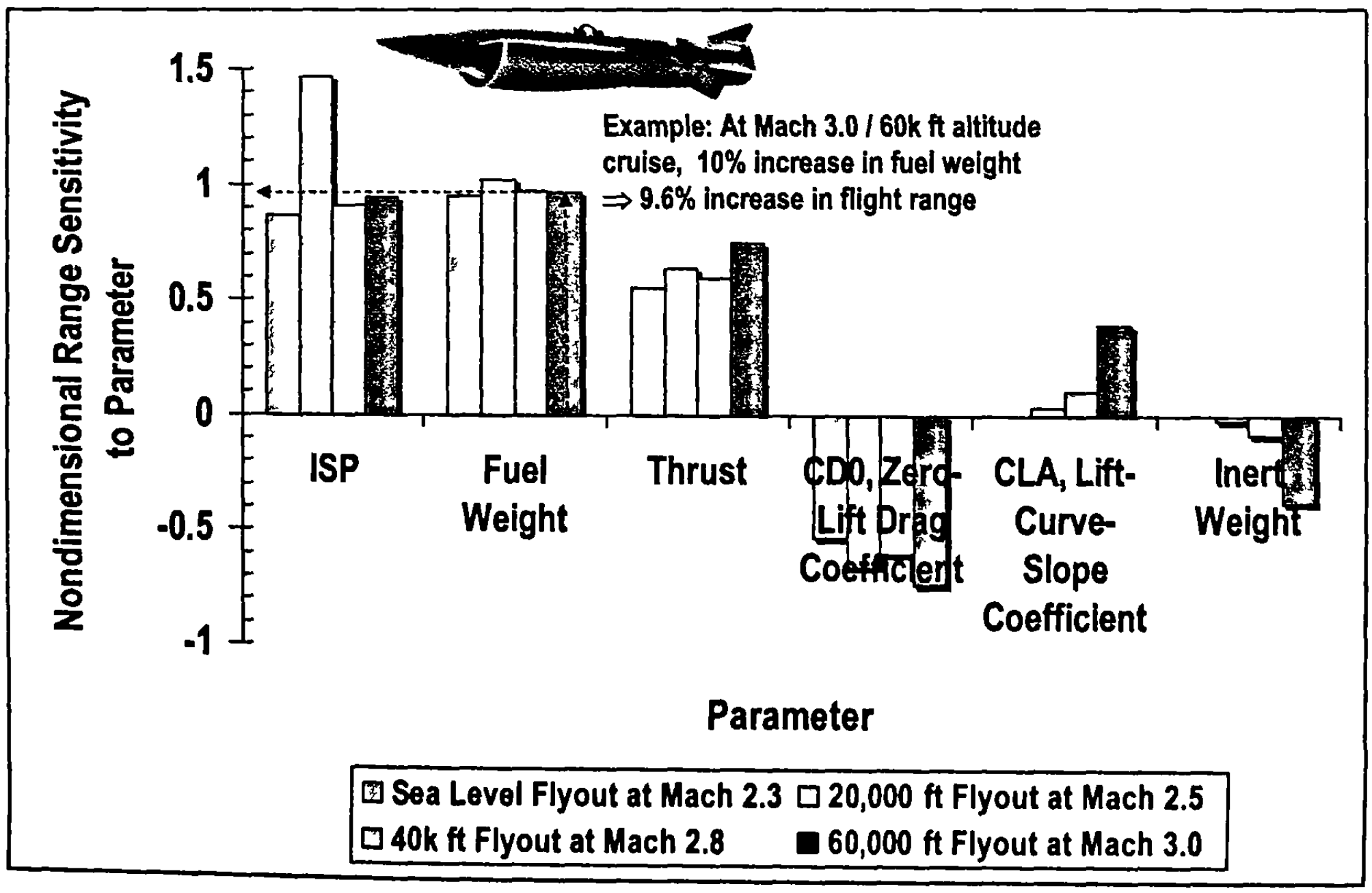

Fig. 7.24 From paredo sensitivity, ramjet baseline range is driven by specific impulse, fuel weight, thrust, and zero-lift drag coefficient.

COLOR FIGURE SECTION

Propulsion / Configuration	Fuel Type / Volumetric Performance (Btu / in3) / Density (lb / in3)	Fuel Volume (in3) / Fuel Weight (lb)	ISP (s) / Cruise Range at Mach 3.5, 60,000 ft (nm)
Liquid Fuel Ramjet	RJ-5 / 581 / 0.040	11900 / 476	1120 / 390
Ducted Rocket (Low Smoke)	Solid Hydrocarbon / 1132 / 0.075	7922 / 594	677 / 294
Ducted Rocket (High Performance)	Boron / 2040 / 0.082	7922 / 649	769 / 366
Solid Fuel Ramjet	Boron / 2040 / 0.082	7056 / 579	1170 / 496
Slurry Fuel Ramjet	40% JP-10, 60% boron carbide / 1191 / 0.050	11900 / 595	1835 / 770

Note: ■ Flow Path □ Available Fuel $R_{cruise} = V\, I_{SP} (L / D) \ln [W_{BC} / (W_{BC} - W_f)]$

Fig. 7.25 Slurry fuel and efficient packaging provide extended range ramjet.

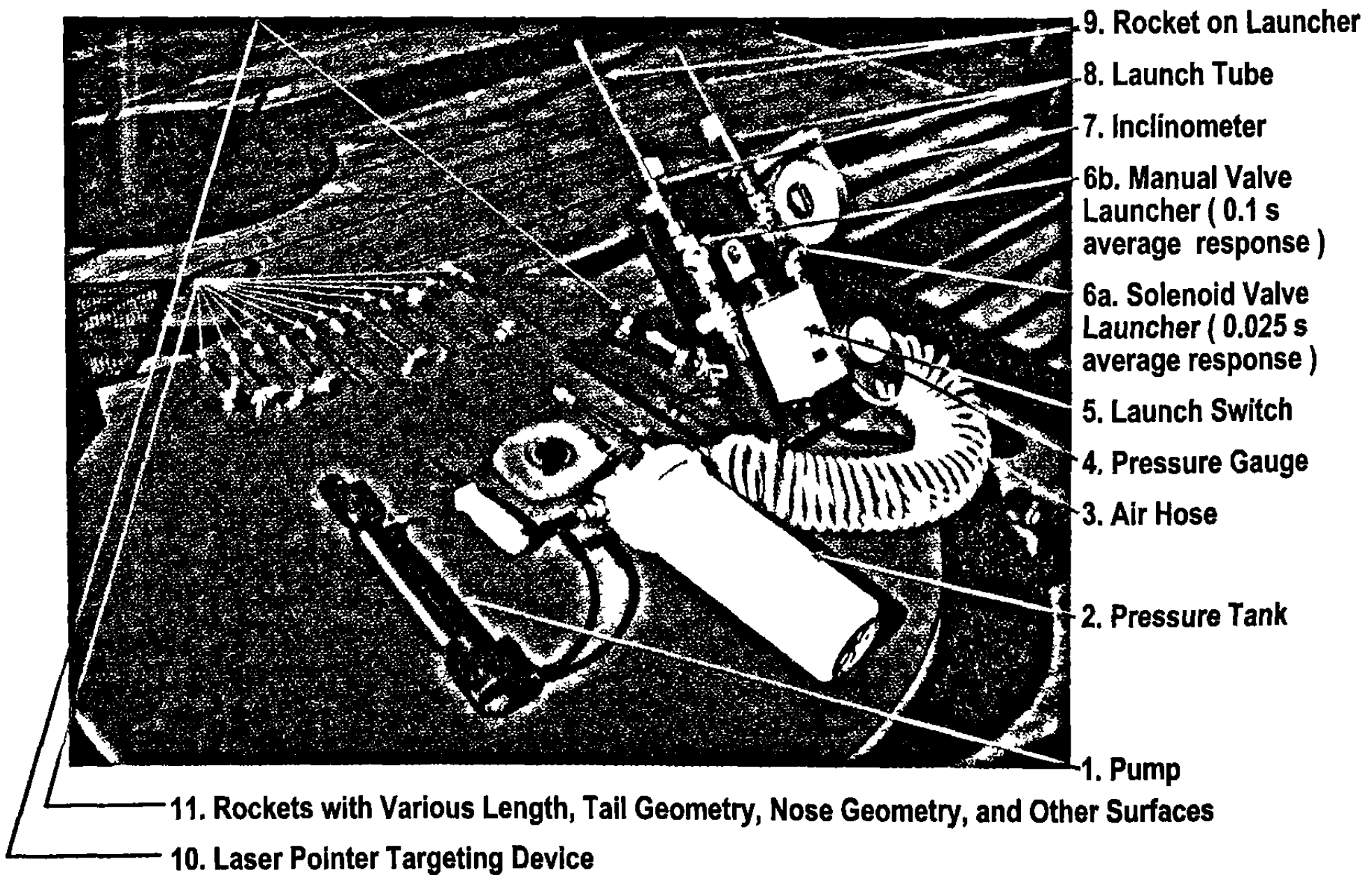

Fig. 7.28 Soda straw rocket launcher and targeting.

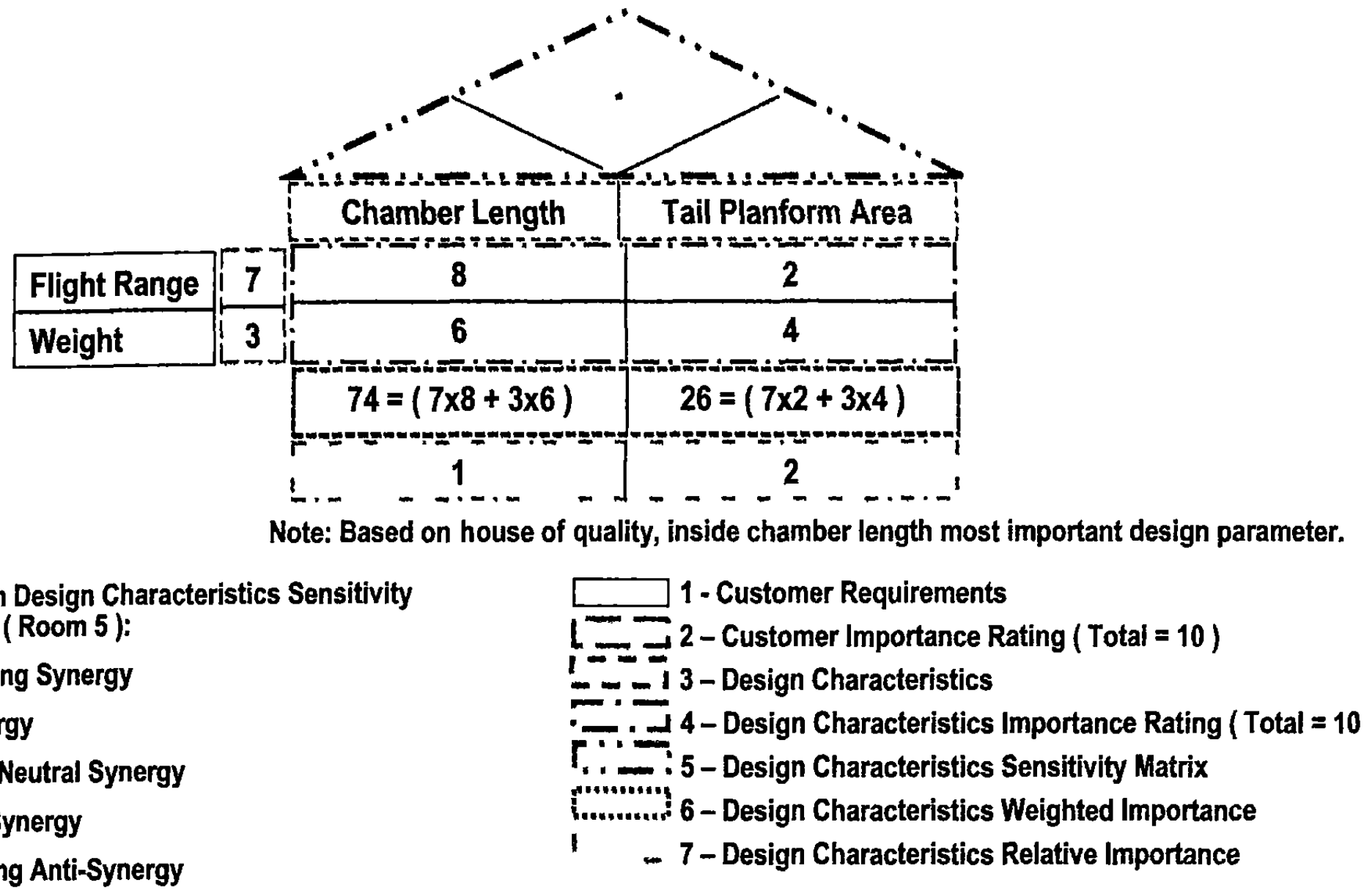

Fig. 7.36 House of quality translates customer requirements into engineering emphasis.

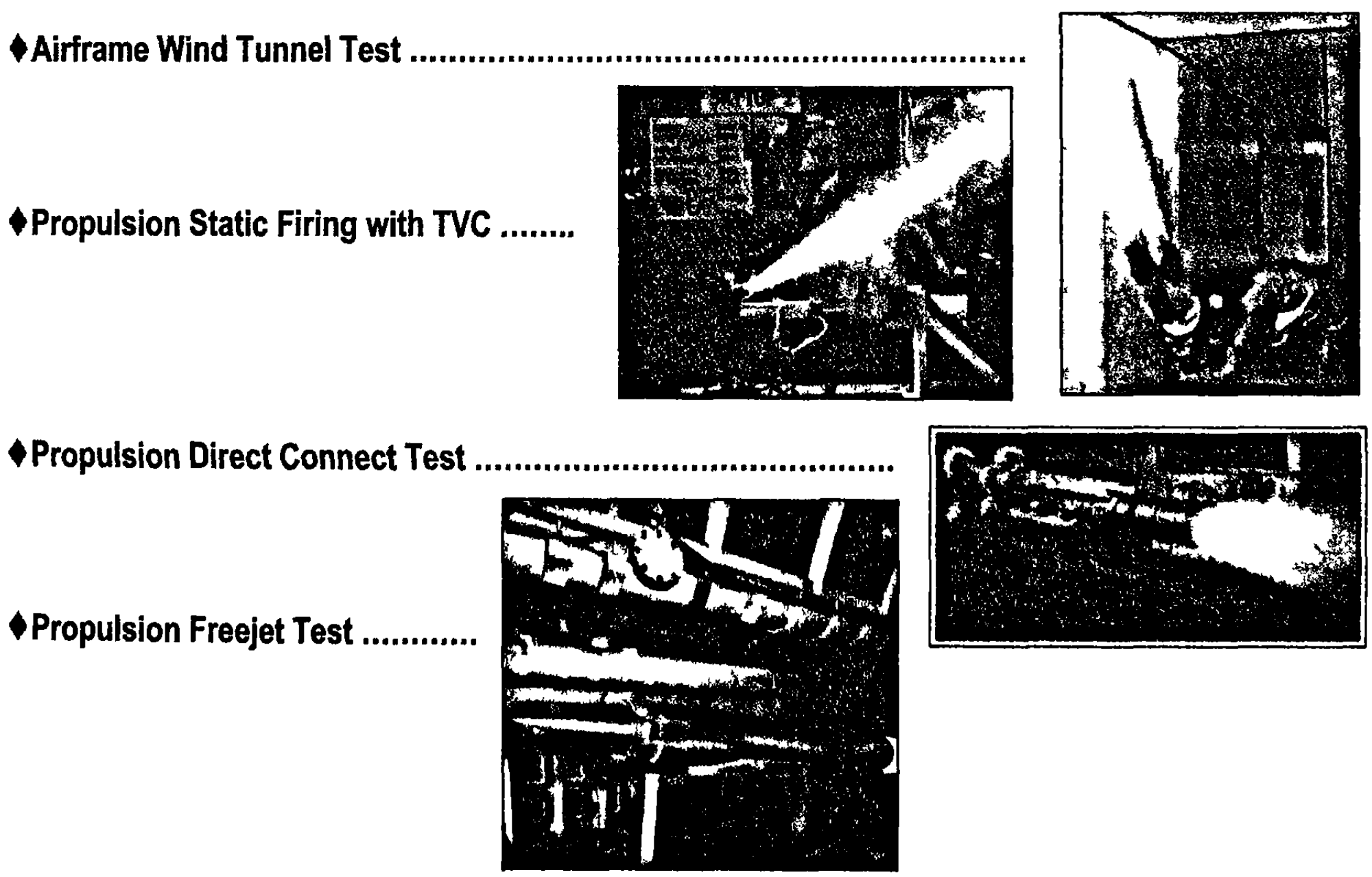

Fig. 8.6a Examples of missile development tests and facilities: aerodynamics and propulsion.

COLOR FIGURE SECTION

◆ **Warhead Arena Test** .....

◆ **Warhead Sled Test** .....

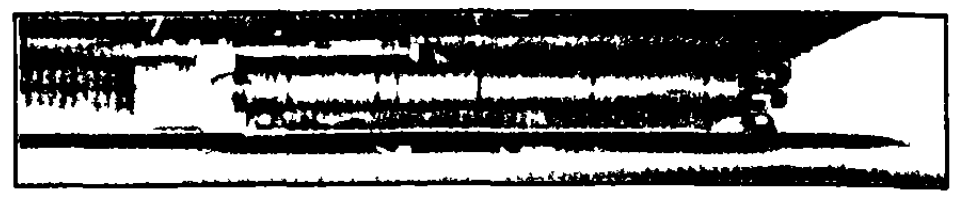

Insensitive Munition Test .....

◆ **Structure Test** .....

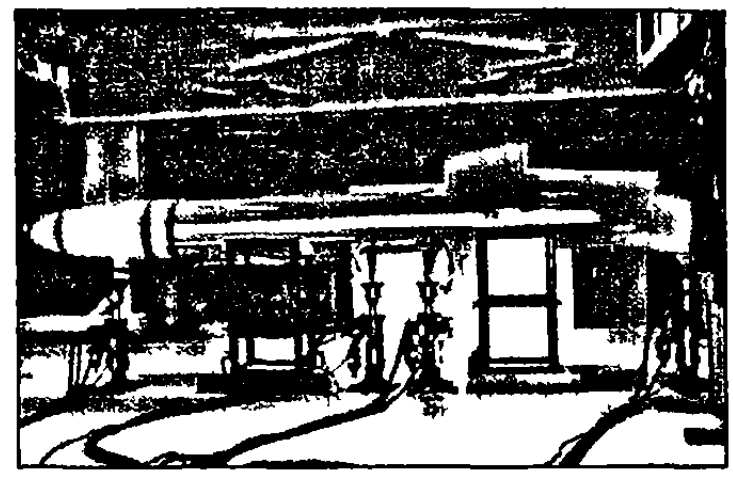

Fig. 8.6b Examples of missile development tests and facilities: warhead and structure.

Seeker Test .....

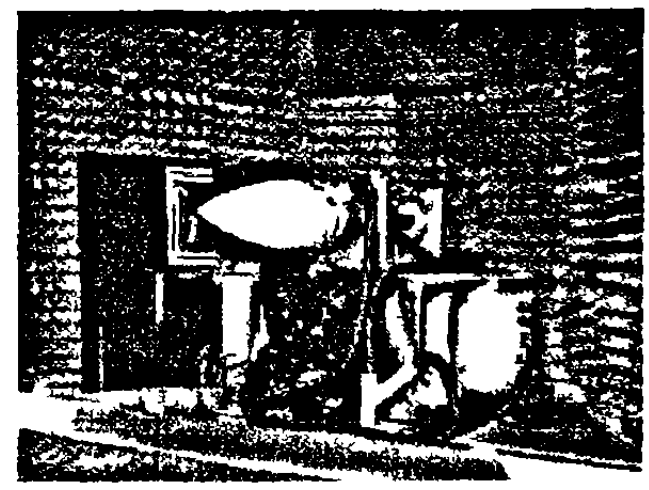

◆ **Hardware In Loop** .....

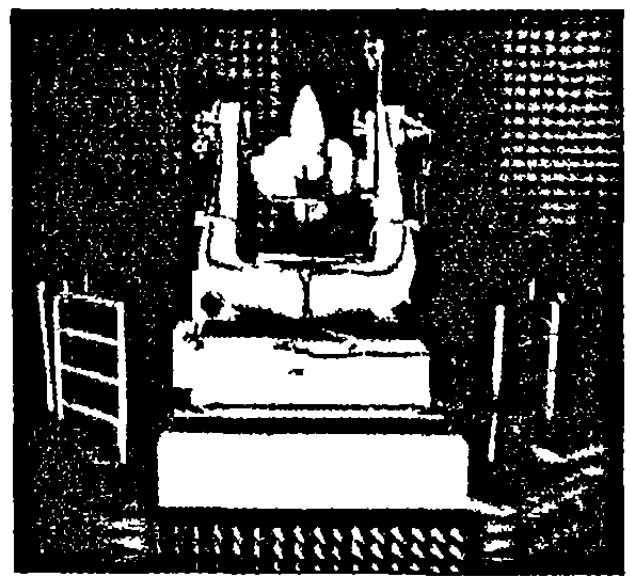

◆ **Environmental Test** .....

Submunition Dispenser Sled Test .....

Fig. 8.6c Examples of missile development tests and facilities: seeker, hardware-in-loop, environmental, and submunition.

COLOR FIGURE SECTION

♦RCS Test .....

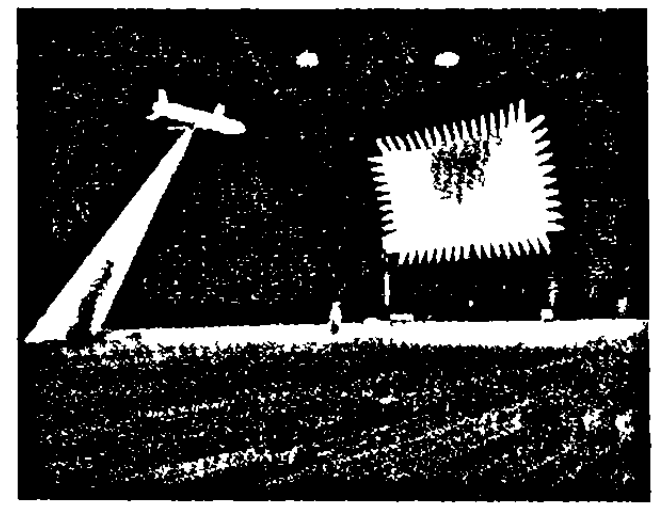

♦Store / Avionics Test

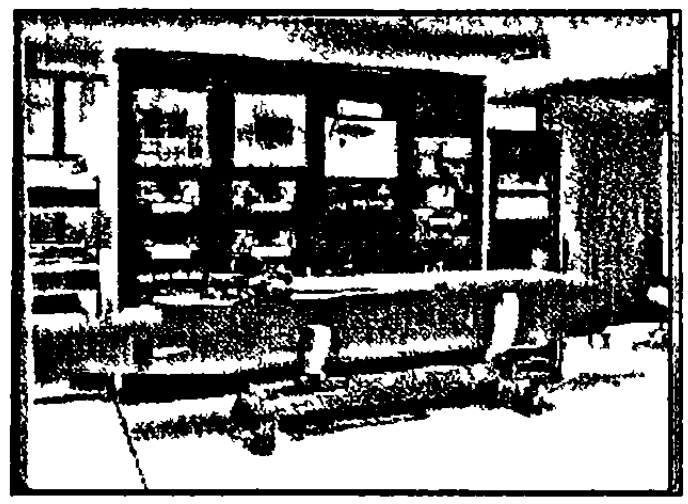

♦Flight Test .....

♦Video of Facilities and Tests

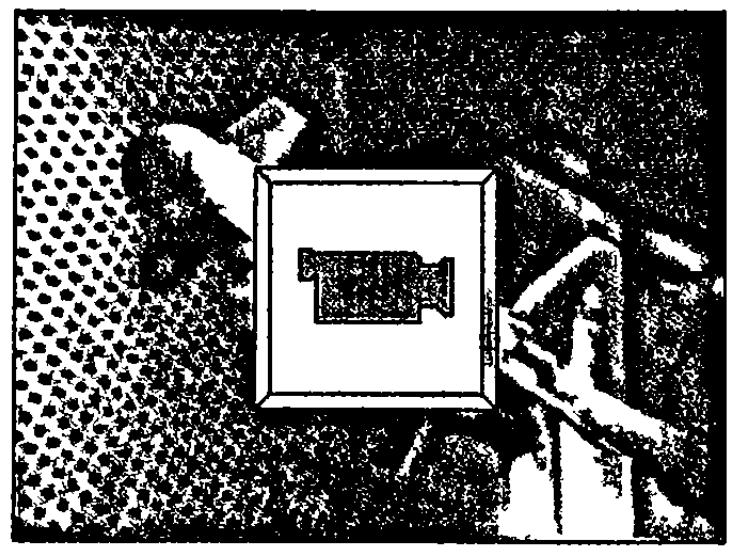

Fig. 8.6d Examples of missile development tests and facilities: RCS, avionics integration, flight test, summary video.

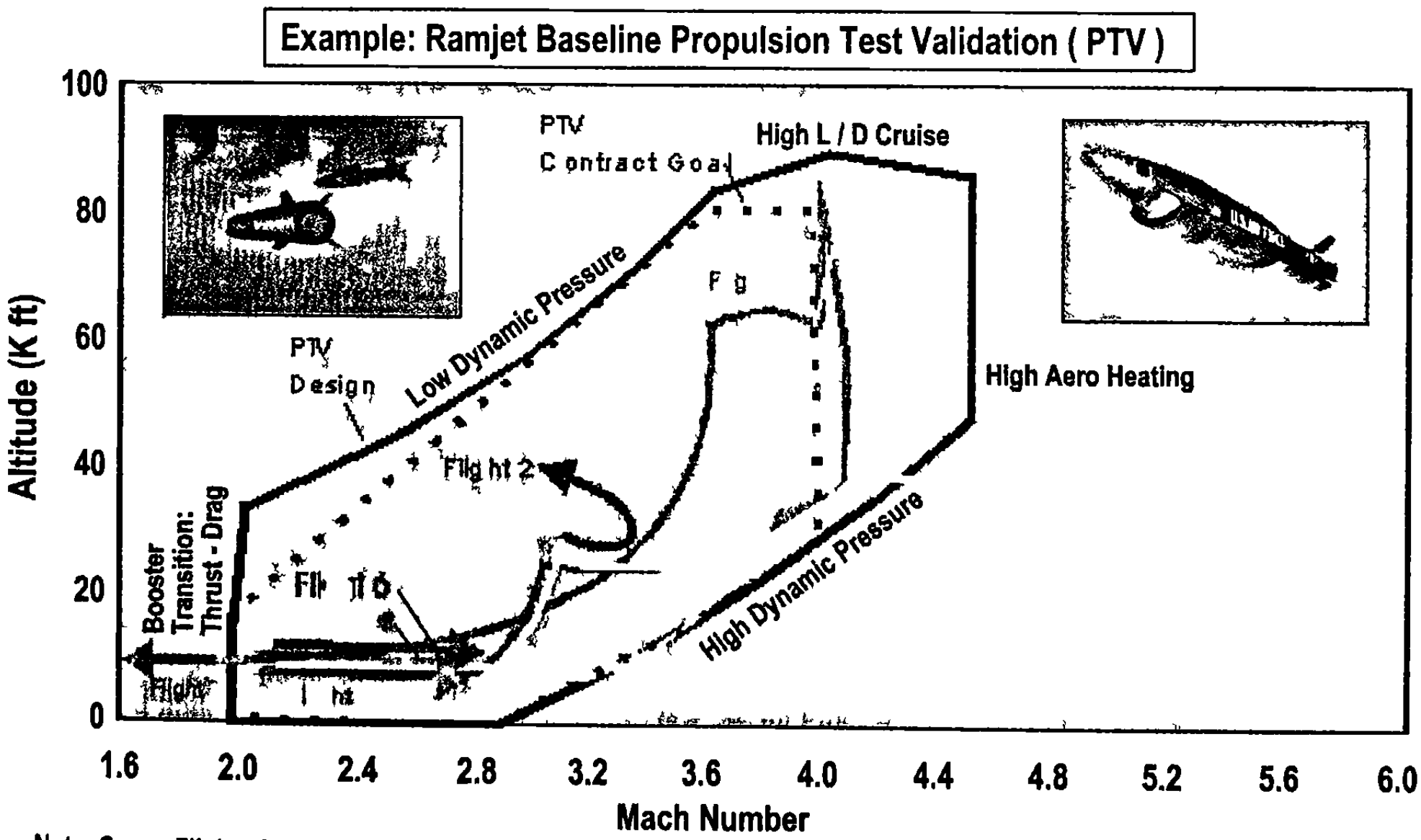

Note: Seven Flights from Oct 1979 to May 1980.

Flight 1 failure of fuel control. As a result of the high thrust, the flight Mach number exceeded the design Mach number.

Fig. 8.7 Missile flight test should cover the extremes of the flight envelope.

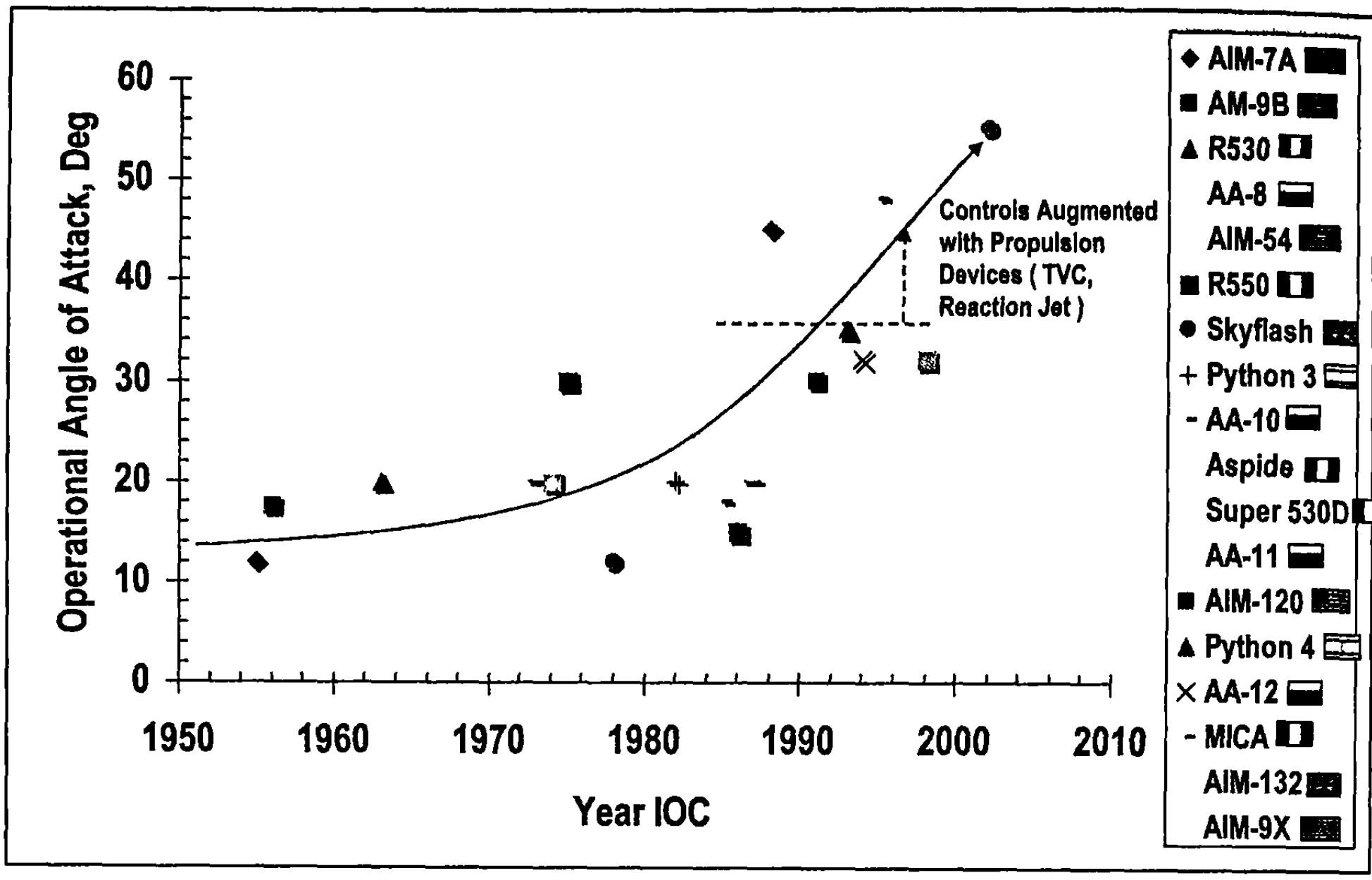

Fig. 8.8 Example of missile technology state-of-the-art advancement: air-to-air missile maneuverability.

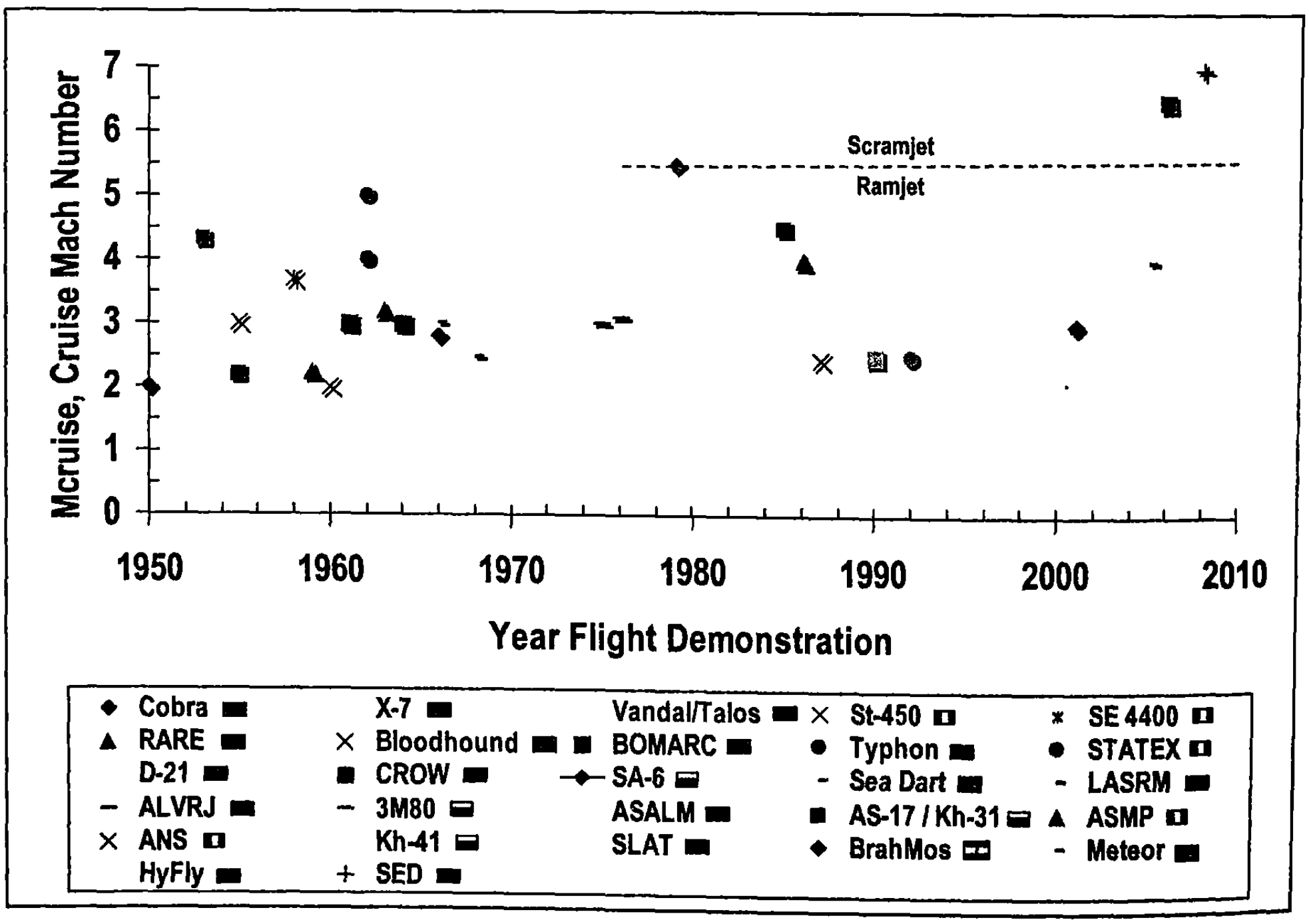

Fig. 8.9 Example of missile technology state-of-the-art advancement: ramjet propulsion.

4
Weight Considerations in Tactical Missile Design

4.1 Introduction

Conceptual design methods and technologies for tactical missile weight are addressed in this chapter. Emphasis is on low-cost, lightweight, and high-temperature/short-duration structure. Weight considerations include the benefits of designing a lightweight missile, subsystem weight sensitivity to flight performance, missile system and subsystem weight prediction, methodology for center-of-gravity and moment-of-inertia prediction, structure weight fraction, guidelines for factors of safety, airframe manufacturing processes and technology, airframe material alternatives, aerodynamic heating prediction, thermal stress concerns and areas of localized aerodynamic heating, airframe structure/insulation trades and insulation material alternatives, structure design, seeker dome material trades, dome weight, power supply alternatives and weight, and flight control actuation system alternatives and weight.

Figure 4.1 shows that the next step in the missile synthesis process following propulsion sizing is estimating and optimizing the missile weight. Weight estimation and optimization are iterative processes that includes alternative materials and subsystems, subsystem packaging, weight and balance bookkeeping, and structure weight prediction/optimization.

4.2 Benefits of a Lightweight Missile

The benefits of designing a lightweight missile are numerous. They include lower production cost, lower logistics cost, smaller size, higher firepower for a weight-limited/volume-limited launch platform, reduced observables, better mission flexibility (from the capability of carriage on multiple launch platforms, e.g., bombers, fighter aircraft, helicopters, unmanned combat air vehicles (UCAVs), ships, submarines, ground vehicles), and synergy with expeditionary warfare. The rapid force deployment requirement of expeditionary warfare requires lightweight missiles.

4.3 Subsystem Weight Sensitivity to Flight Performance

As shown in Fig. 4.2, the weight of most missile subsystems is sensitive to flight performance requirements such as range, speed, and maneuverability.

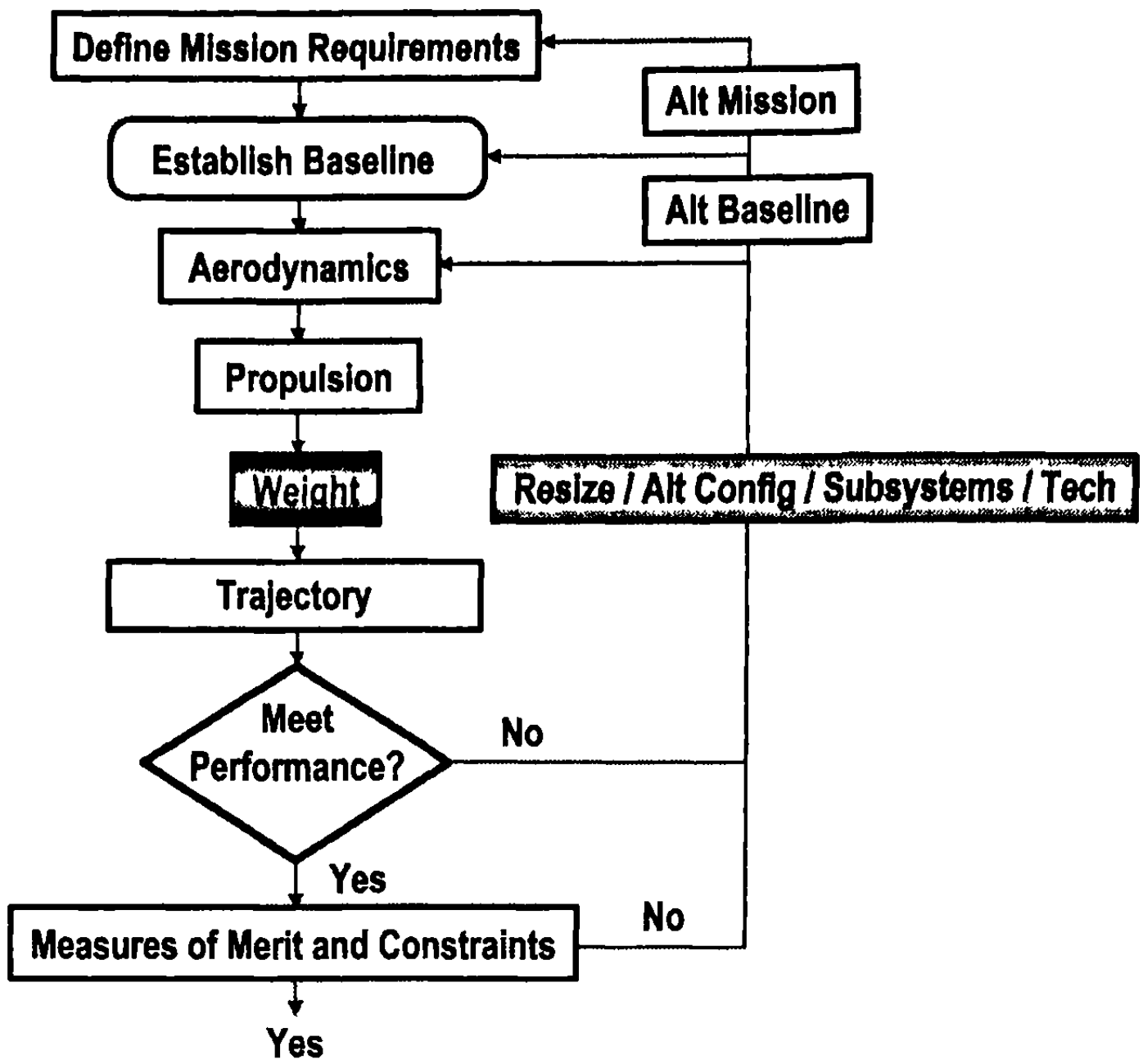

Fig. 4.1 Missile concept synthesis requires evaluation of alternatives and iteration.

Missile subsystem weights that are highly impacted by flight performance are propulsion, structure, flight control hardware, surfaces (e.g., wings, canards, tails), power supply, and aerothermal insulation. Warhead weight has a relatively low sensitivity to changes in flight performance. Subsystem weights that are relativity insensitive to changes in flight performance are the seeker dome, seeker, guidance and control, and the data link.

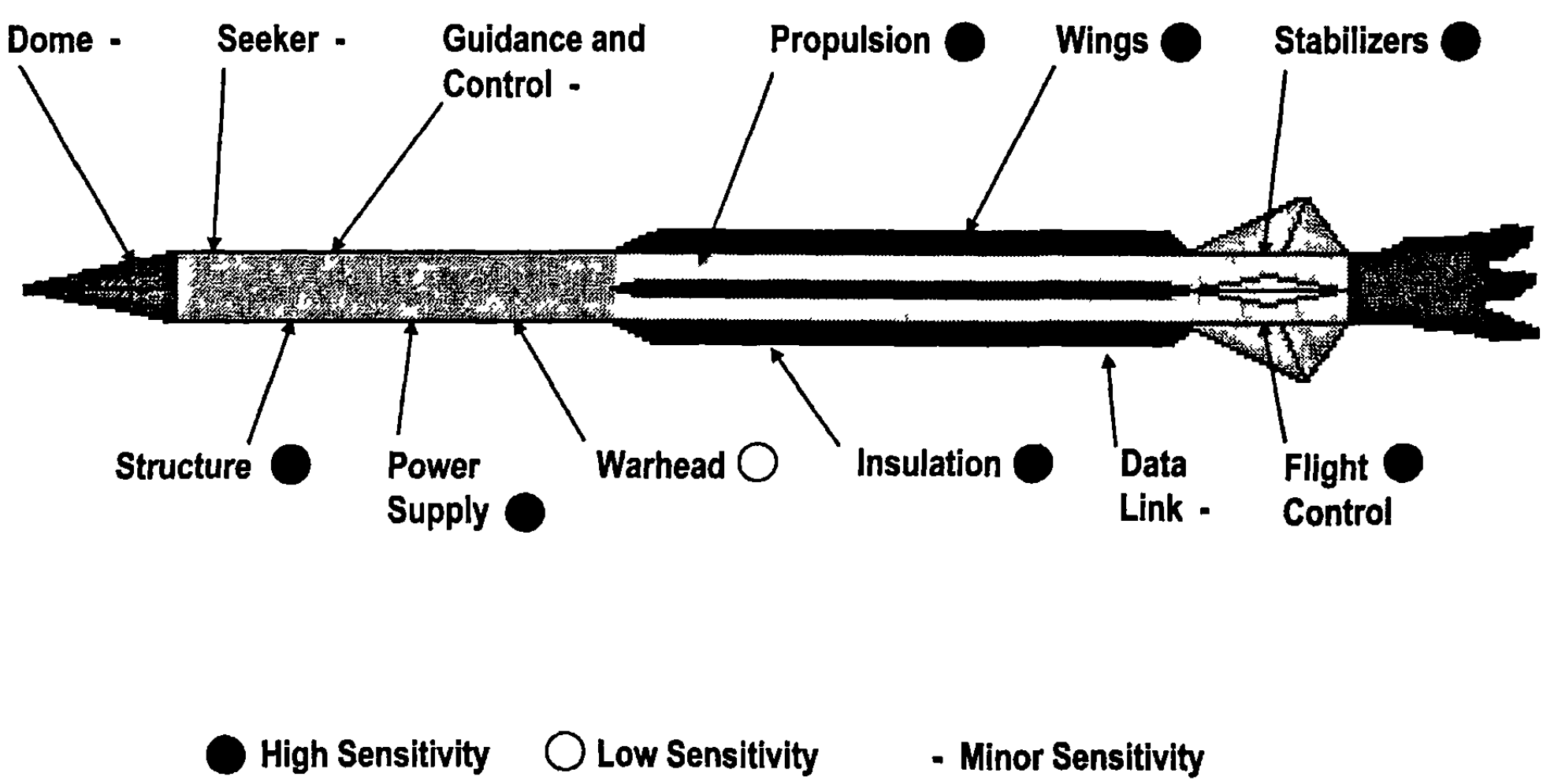

Fig. 4.2 Flight performance (range, speed, maneuverability) is sensitive to subsystem weight.

4.4 Missile Weight Prediction

A first-order approach to missile weight prediction can be based on the burnout velocity equation from the previous chapter,

$$\Delta V \approx -g_c I_{sp} \ln(1 - W_{Propellant}/W_i) \tag{4.1}$$

The parameters that define the missile velocity are the propellant weight $W_{Propellant}$, the initial (launch) weight W_i, and the specific impulse I_{SP}. Integrating the velocity equation and assuming an optimum launch angle gives a first-order estimate of flight range

$$R \approx V^2/g_c \tag{4.2}$$

Note the same primary parameters of propellant weight $W_{Propellant}$, initial weight W_i, and specific impulse I_{SP} also define the missile flight range. The above equations are based on the assumptions that thrust is larger than drag and weight; negligible drag after burnout; and a flat, nonrotating earth.

Figure 4.3 is based on the above equations. It shows missile range versus launch weight based on typical values of payload weight ($W_{Payload} = 500$ lb), specific impulse ($I_{SP} = 250$ s), and inert weight-to-propellant weight fraction ($W_{Inert} = 0.2\ W_{Propellant}$). Payload weight is the portion of the missile weight that is relatively insensitive to changes in flight range. The payload typically

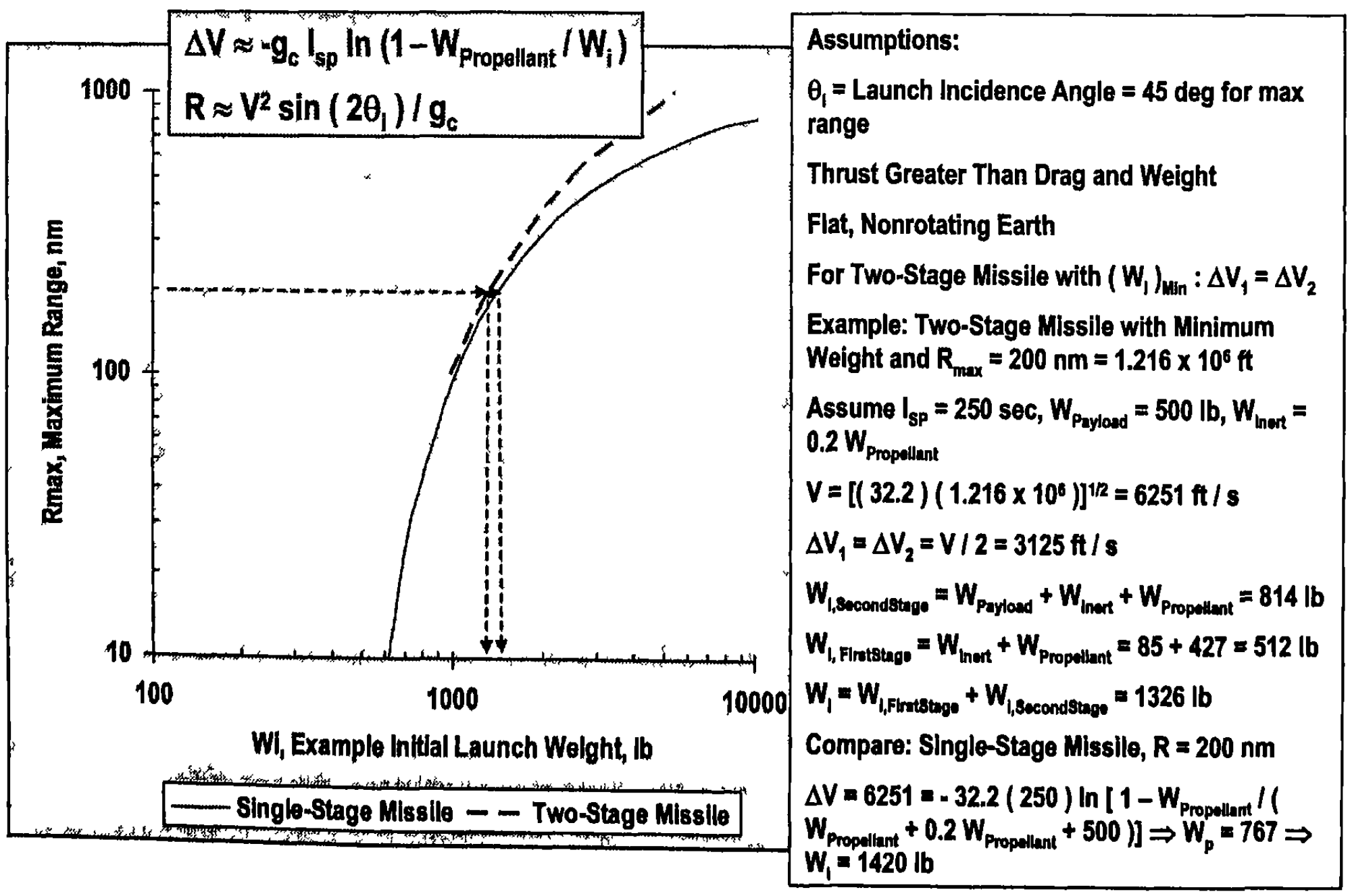

Fig. 4.3 Missile range is a function of launch weight, propellant weight, and specific impulse.

includes the missile warhead, seeker dome, seeker, guidance and control, and data link. Inert weight consists of the missile subsystems that are sensitive to flight range. For rocket propulsion, inert weight is the total weight of the subsystems that are impacted by propellant weight. The total weight of the rocket motor case and nozzle, structure, flight control hardware, surfaces (e.g., wings, canards, tails), power supply, and insulation comprise the inert weight. For a typical tactical missile using solid rocket propulsion, the relationship is

$$W_{\text{Inert}}/W_{\text{Propellant}} \approx 0.2 \tag{4.3}$$

As an example, assume a two-stage ballistic missile with a launch angle $\theta_1 = 45$ deg (for maximum range) and a desired flight range $R_{\max} = 200$ nm $= 1.216 \times 10^6$ ft. For a two-stage missile, equal velocity increments for each stage provide minimum weight

$$(W_i)_{\text{Min}} : \Delta V_1 = \Delta V_2 \tag{4.4}$$

The total burnout velocity to achieve $R_{\max} = 200$ nm is

$$V = (g_c R)^{1/2} = [(32.2)(1.216 \times 10^6)]^{1/2} = 6251 \text{ ft/s} \tag{4.5}$$

The incremental velocity for each stage is $\Delta V_1 = \Delta V_2 = V/2 = 3125$ ft/s. Assume $W_{\text{Payload}} = 500$ lb, $I_{\text{SP}} = 250$ s, and $W_{\text{Inert}} = 0.2\, W_{\text{Propellant}}$. Solving the ΔV equation, the initial weight of the second stage is

$$\begin{aligned} W_{\text{i,SecondStage}} &= W_{\text{Payload}} + W_{\text{Inert}} + W_{\text{Propellant}} = 500 + 52 + 262 \\ &= 814 \text{ lb} \end{aligned} \tag{4.6}$$

Similarly, the initial weight of the first stage is

$$W_{\text{i, FirstStage}} = W_{\text{Inert}} + W_{\text{Propellant}} = 85 + 427 = 512 \text{ lb} \tag{4.7}$$

Total launch weight for a two-stage missile is

$$W_i = W_{\text{i,FirstStage}} + W_{\text{i,SecondStage}} = 512 + 814 = 1326 \text{ lb} \tag{4.8}$$

For a single-stage missile with a flight range $R_{\max} = 200$ nm, $\Delta V = 6251$ ft/s. Assume $W_{\text{Payload}} = 500$ lb, $I_{\text{SP}} = 250$ s, and $W_{\text{Inert}} = 0.2\, W_{\text{Propellant}}$. Then

$$\begin{aligned} \Delta V &= 6251 \\ &= -32.2(250)\, ln\,[1 - W_{\text{Propellant}}/(W_{\text{Propellant}} + 0.2\, W_{\text{Propellant}} + 500)] \end{aligned} \tag{4.9}$$

Solving for the propellant weight, $W_{\text{Propellant}} = 767$ lb. Substituting,

$$W_i = W_{\text{Propellant}} + 0.2 W_{\text{Propellant}} + 500 = 767 + 153 + 500 = 1420 \text{ lb} \tag{4.10}$$

In summary, for a typical single-stage missile using solid-propellant rocket propulsion, a launch weight $W_i = 1420$ lb is required to achieve a flight range of 200 nm. For a typical two-stage rocket, the launch weight would be somewhat lighter, $W_i = 1325$ lb. Although the range equation $R \approx V^2/g_c$ is strictly applicable to ballistic missiles, the equation can be used as a first-order tool to predict the range of other types of missiles. For missiles other than ballistic missiles, the term V in the equation $R \approx V^2/g_c$ is not the actual burnout velocity but instead represents the total energy available from the propulsion system. If a missile is dominated by propulsion and inertia forces with relatively low drag, such as a ballistic missile, the results are fairly accurate. However, if a missile has good aerodynamic efficiency, such as a cruise missile, the results can be in error by a factor of 2 or more.

The average subsystem density of a tactical missile is about 0.05 lb/in^3. Except for the nose section, most missile bodies can be represented as a cylinder of diameter d and length l. The equation for the volume of a cylinder is $V = (\pi/4)d^2$. Neglecting the geometry difference of the missile nose from that of a cylinder and neglecting the weight of the surfaces, the missile weight correlates as the average density times the volume of a cylindrical body

$$W_L = \rho_M V \approx 0.05(\pi/4)ld^2 \approx 0.04ld^2 \tag{4.11}$$

Figure 4.4, which is based on the weight of 48 tactical missiles, shows the correlation of the predicted weight with the actual weight. The scatter in the data includes the effects of differences in the launch environment, maneuverability, subsystem density, nose fineness, body cross-sectional geometry, boattailing, and the surface planform geometry. Note from the figure that the lightest

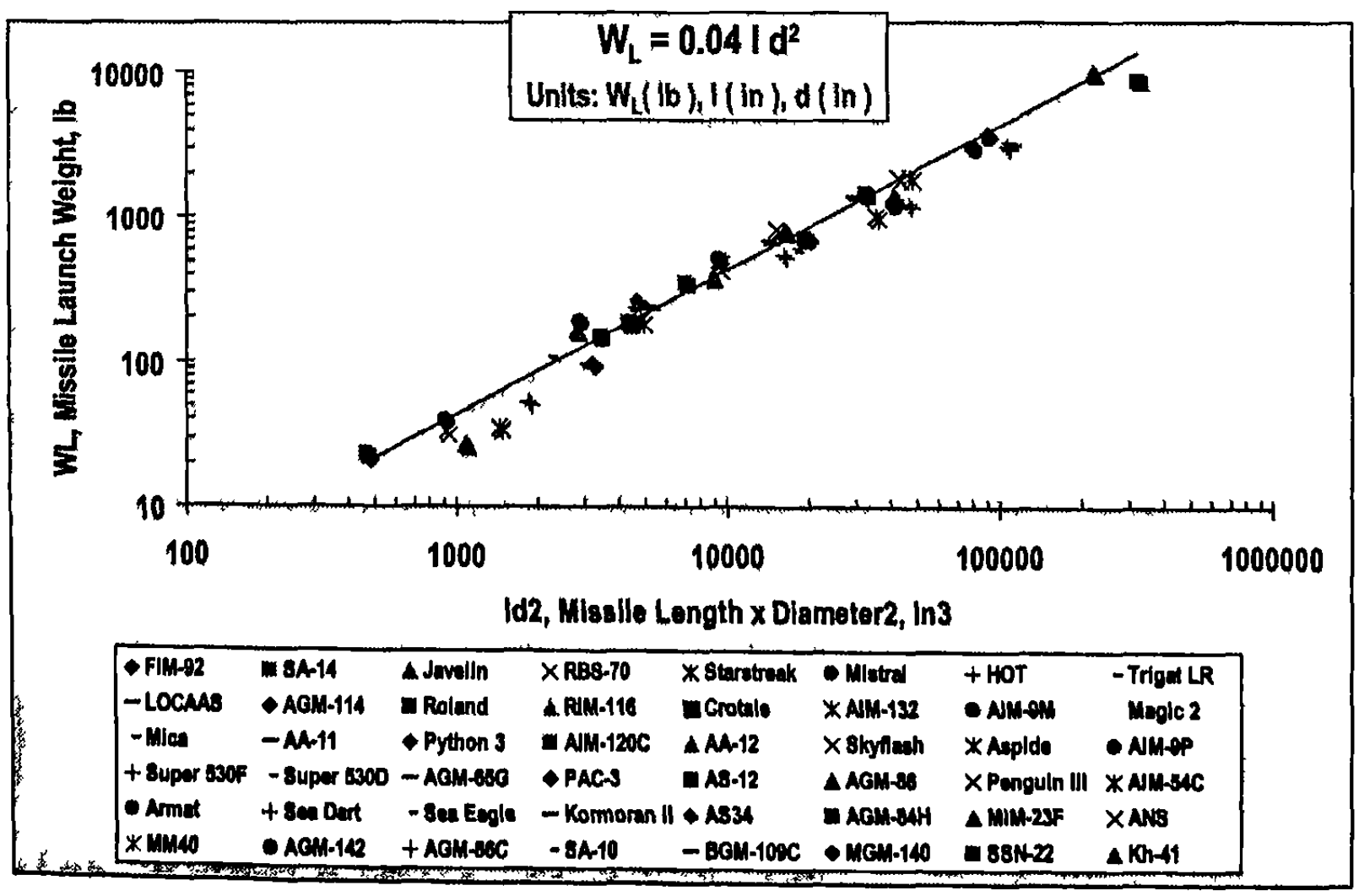

Fig. 4.4 Missile weight is a function of diameter and length. Figure also in color section.

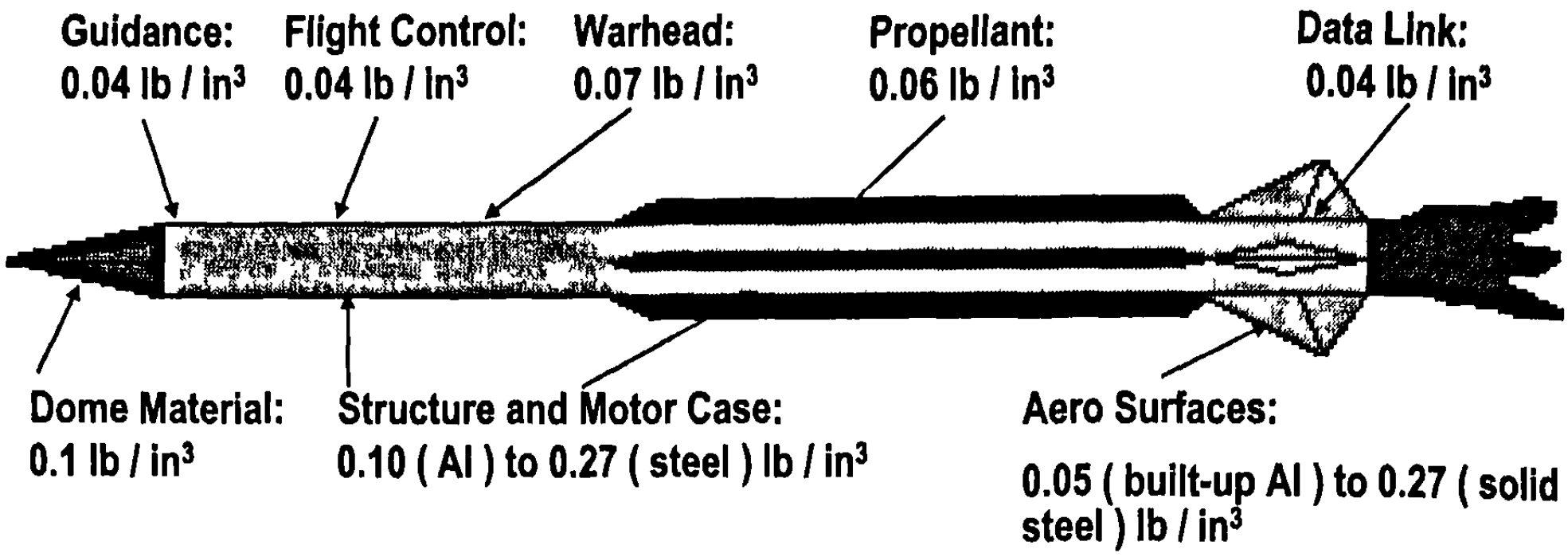

Fig. 4.5 Most subsystems for tactical missiles have a density of about 0.05 lb/in^3.

weight missiles (FIM-92, SA-14, Javelin, RBS-70, Starstreak, Mistral) are man-portable, tube-launched missiles with a relatively benign launch environment, a relatively small warhead, and small surfaces.

A more detailed description of missile weight at the subsystem level is shown in Fig. 4.5. Shown are typical values of subsystem density for rocket-powered missiles. Except for the monolithic (solid) components (dome material, structure, motor case, monolithic aerodynamic surfaces), the subsystem density varies from 0.04 to 0.07 lb/in^3. A more accurate estimate of missile weight is obtained by estimating the individual subsystem volumes, densities, and weights through a missile weight statement.

4.5 Center-of-Gravity and Moment-of-Inertia Prediction

The methodology for missile weight, balance, and moment-of-inertia prediction is shown in Fig. 4.6. Missile weight is the summation of the individual weights of the subsystems, structure, surfaces, and fuel/propellant. Launch weight and burnout weight estimates are required for analysis of the missile flight performance. The missile center of gravity is important in determining stability and control and tail sizing. The moment-of-inertia is used to estimate the missile time constant and its effect on miss distance.

The center of gravity is estimated by summing each subsystem weight times its distance from the nose tip, divided by the total weight. As an example, the longitudinal location of the center of gravity is

$$x_{CG} = \Sigma(x_{\text{subsystem1}} W_{\text{subsystem1}} + x_{\text{subsystem2}} W_{\text{subsystem2}} + \cdots)/W_{\text{total}} \qquad (4.12)$$

Again, x_{CG} must be calculated for launch and burnout conditions.

The moment of inertia about the missile center of gravity is calculated by summing the local moment of inertia of each subsystem about its center of gravity, plus the weight of each subsystem times the square of the distance of the subsystem from the missile center of gravity. As an example, the

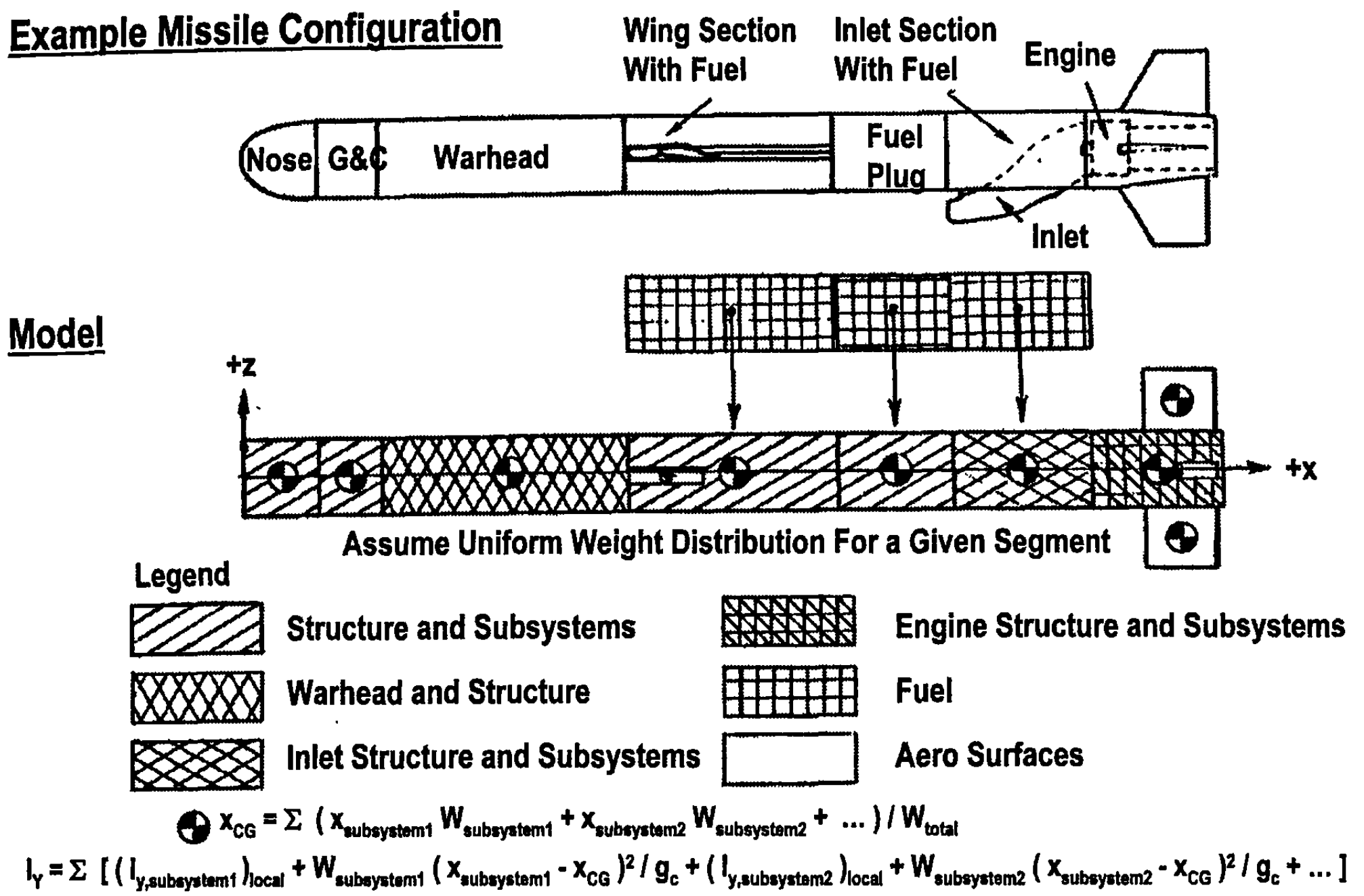

Fig. 4.6 Modeling weight, balance, and moment-of-inertia is based on a buildup of subsystems.

moment-of-inertia about the y axis is

$$I_y = \Sigma[(I_{y,\text{subsystem1}})_{\text{local}} + W_{\text{subsystem1}}(x_{\text{subsystem1}} - x_{\text{CG}})^2/g_c + (I_{y,\text{subsystem2}})_{\text{local}} + W_{\text{subsystem2}}(x_{\text{subsystem2}} - x_{\text{CG}})^2/g_c + \cdots] \tag{4.13}$$

Moment of inertia is calculated for both the launch and burnout conditions.

The yaw and pitch moments of inertia are factors in determining missile maneuverability and miss distance. For a typical tactical missile with symmetric, circular cross section and cruciform surfaces, the center of gravity is on the centerline of the missile, and the yaw and pitch moments of inertia can be assumed to be equal ($I_y = I_z$). Figure 4.7 shows the yaw local moment of inertia $(I_y)_{\text{local}}$ variation with body fineness ratio l/d for cylindrical and conical bodies. The equation for the local moment of inertia of a cylinder is

$$(I_{y,\text{cylinder}})_{\text{local}} = [Wd^2/g_c][1/16 + (1/12)(l/d)^2] \tag{4.14}$$

The equation for the local moment of inertia of a cone is

$$(I_{y,\text{cone}})_{\text{local}} = [Wd^2/g_c][3/80 + (3/80)(l/d)^2] \tag{4.15}$$

Note from the figure that there is a large increase in the moment of inertia with increasing fineness ratio.

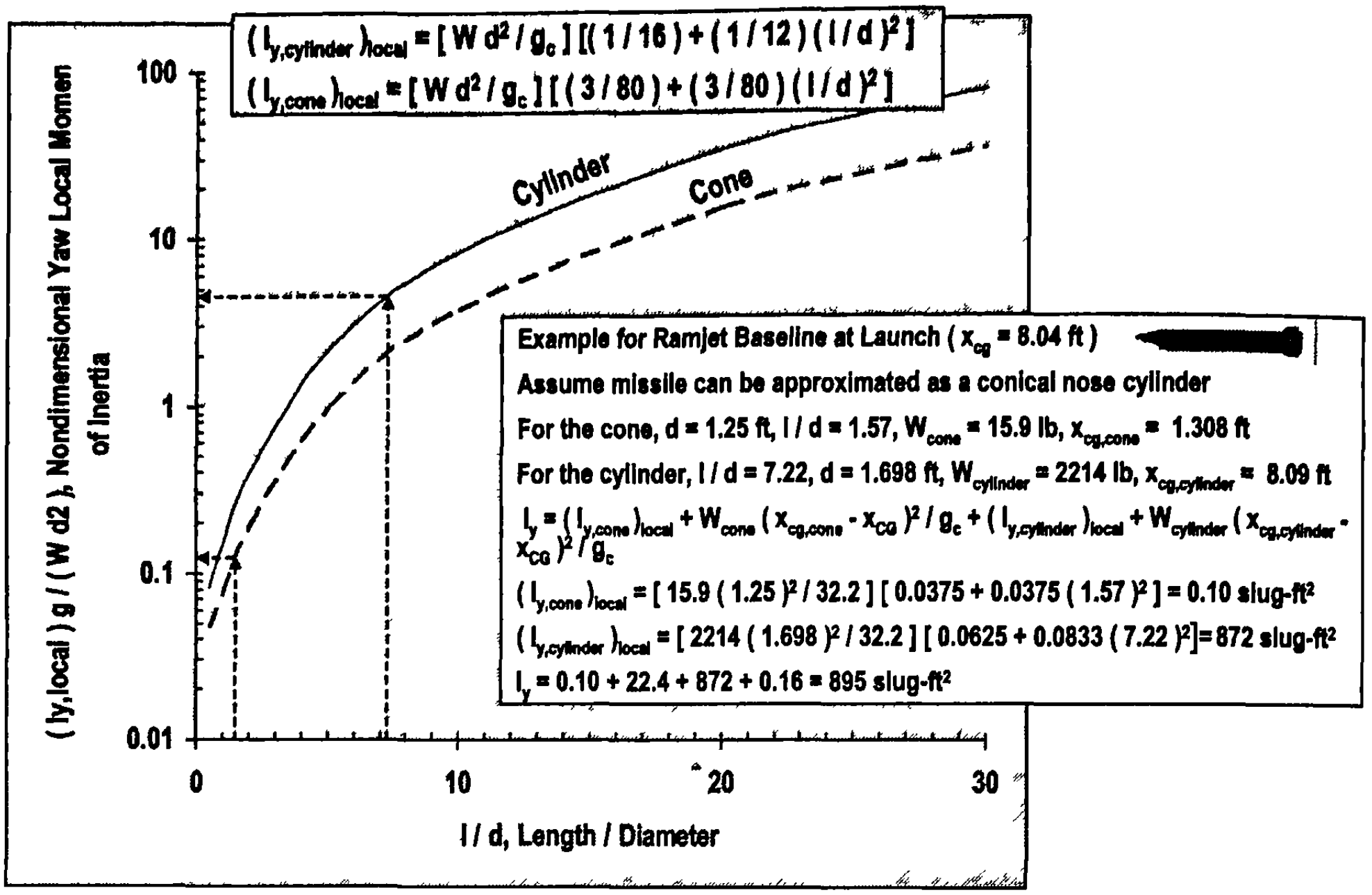

Fig. 4.7 Moment-of-inertia is higher for a high-fineness ratio body.

As an example, the ramjet baseline can be approximated as a cone-cylinder configuration for the moment-of-inertia calculation. For the cone, $d = 1.25$ ft, $l/d = 1.57$, $W_{\text{cone}} = 15.9$ lb, $x_{\text{cg,cone}} = 1.308$ ft. The yaw local moment of inertia of the conical nose about its center of gravity is

$$(I_{\text{y,cone}})_{\text{local}} = [15.9(1.25)^2/32.2][0.0375 + 0.0375(1.57)^2] = 0.10 \text{ slug-ft}^2.$$

For the cylinder, $l/d = 7.22$, $d = 1.698$ ft, $W_{\text{cylinder}} = 2214$ lb, $x_{\text{cg,cylinder}} = 8.09$ ft. The yaw local moment of the cylindrical approximation about its center of gravity is

$$(I_{\text{y,cylinder}})_{\text{local}} = [2214(1.698)^2/32.2][0.0625 + 0.0833(7.22)^2] = 872 \text{ slug-ft}^2.$$

The total yaw moment of inertia about the missile center of gravity is given by

$$I_{\text{y}} = (I_{\text{y,cone}})_{\text{local}} + W_{\text{cone}}(x_{\text{cg,cone}} - x_{\text{CG}})^2/g_{\text{c}} + (I_{\text{y,cylinder}})_{\text{local}} + W_{\text{cylinder}}(x_{\text{cg,cylinder}} - x_{\text{CG}})^2/g_{\text{c}} \tag{4.16}$$

Substitution gives the total yaw moment of inertia of the ramjet baseline at launch as

$$I_{\text{y}} = 0.10 + 22.4 + 872 + 0.16 = 895 \text{ slug-ft}^2$$

Note that for this example, the nose section contributes only 3% to the total moment of inertia. For conceptual design, estimating the moment of inertia based only on the cylindrical body usually provides sufficient accuracy.

4.6 Structure Factor of Safety

Typical structure factors of safety for tactical missiles are shown in Fig. 4.8. The required factor of safety of a missile tends to be high where there is a danger of fratricide. As an example, pressure bottle ultimate and yield factors of safety are typically 2.5 and 1.5, respectively. Missile gas bottles are hazardous, with pressures up to 10,000 psi. Because gas bottles require periodic logistics maintenance and inspection by ground personnel, the required factor of safety is high. Another area where the required factor of safety is high is ground handling, such as cross-country transportation. Factors of safety for ground handling loads are about 1.5 for ultimate loads and 1.15 for yield loads. Other examples of high factor of safety are launch platform carriage and separation. During carriage or during separation, missile factors of safety are required to be about 1.5 for ultimate and 1.15 for yield. The motor case is designed not only for conditions of environmental extremes, such as a hot day, but also for consideration of safety. The ultimate and yield factors of safety for the motor maximum effective operating pressure are about 1.5 and 1.1, respectively. The required factors of safety are lower for flight conditions where the missile is safely away from the launch platform. For example, missile free-flight ultimate and yield loads factors of safety are about 1.25 and 1.1, respectively and the thermal loads, which occur near the end of flight, are just design considerations with a factor

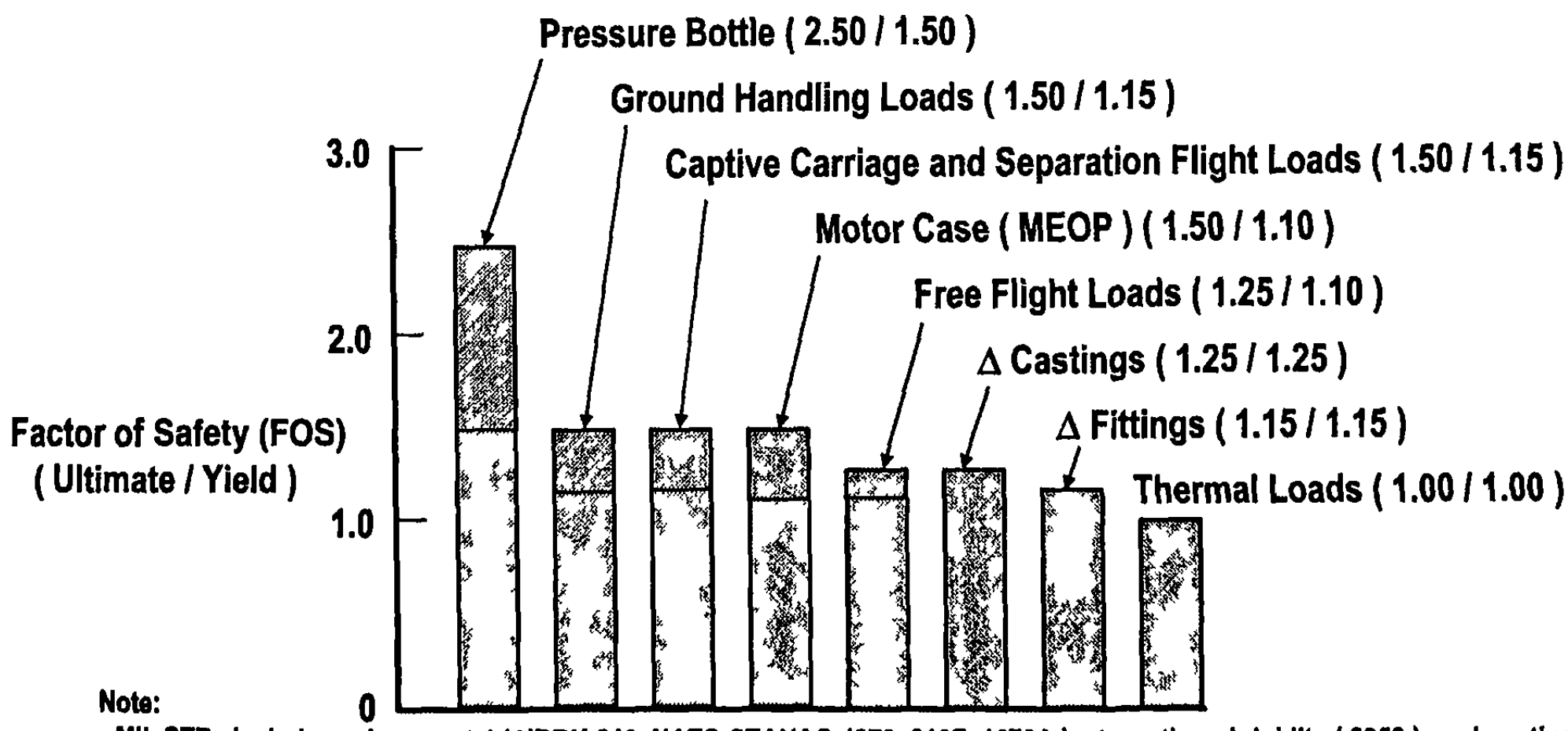

Note:
- MIL STDs include environmental (HDBK-310, NATO STANAG 4370, 810F, 1670A), strength and rigidity (8856), and captive carriage (8591).
- The entire environment (e.g., manufacturing, transportation, storage, ground handling, captive carriage, launch separation, postlaunch maneuvering, terminal maneuvering) must be examined for driving conditions in structure design.
- FOS Δ for castings is expected to be reduced in future as casting technology matures.
- Reduction in required FOS is expected as analysis accuracy improves will result in reduced missile weight / cost.

Fig. 4.8 Structure design factor of safety is greater for hazardous subsystems/flight conditions.

of safety of 1.0. A distinguishing characteristic of tactical missiles is a lower factor of safety compared with manned aircraft or even unmanned air vehicles (UAVs). Because missiles are a throwaway, the factor of safety can be reduced if there is little danger involved to friendly forces or neutrals. This contributes to lighter weight and lower cost compared with an aircraft or a UAV. An additional factor of safety is required for structural areas where there is a relatively large design uncertainty. An example is castings, which can have hidden voids. Castings typically require an incremental factor of safety of about 1.25 in addition to the normal design factors of safety. Fittings also typically require an additional factor of safety of about 1.15 because of the uncertainty in the analysis for attachment integrity. The applicable military standards in the United States that are considered in factors of safety include environmental (HDBK-310, NATO STANAG 4370, MIL-STD-810F, MIL-1670A), strength and rigidity (MIL-STD-8856), and captive carriage (MIL-STD-8591) military standards. A broad range of environmental and load conditions must be examined to determine the driving conditions for structure design. As an example, the conditions to be considered for structure design could include manufacturing, transportation, storage, ground handling, launch platform carriage, launch, post-launch maneuvering, and terminal maneuvering.

A technology opportunity to reduce missile weight is to develop more accurate predictions of the missile environment, loads, and strength. This would allow a reduction in the required factor of safety (which is really a factor of ignorance). Another approach to reduce the required factor of safety is to conduct structural tests to the ultimate load conditions.

4.7 Airframe Manufacturing Processes

Figure 4.9 shows examples of structure concepts and manufacturing processes that are used for tactical missile airframes and surfaces. Two types of airframes are shown, a lifting body airframe and an axisymmetric airframe. An airframe structure design concept may be a monocoque, integrally hoop stiffened (bulkhead), integrally longitudinally stiffened (stringer), or stiffened with both bulkheads and stringers. Also shown are the structure design and manufacturing alternatives for surfaces, such as wings, canards, and tails. Surfaces may be either solid, monolithic structure or a lighter weight sandwich structure stiffened with ribs and spars.

A driving consideration for a low-cost missile airframe is to minimize the parts count. Examples of manufacturing processes that reduce the parts count include vacuum-assisted resin transfer molding (RTM), filament winding, pultrusion, casting, vacuum bag/autoclave forming, metal forming, strip laminate, and compression molding.

Examples of low-cost manufacturing processes that are particularly applicable to complex shapes are precision casting and vacuum-assisted RTM. Precision casting is applicable to metal structure. It has high payoff for reducing the cost of air-breathing hypersonic missiles, which have high-temperature metal airframes with complex shape. A historical limitation in applying castings to

Geometry Alternatives	Structure Concept Alternatives	Structure Manufacturing Process Alternatives									
		Composites						Metals			
		Vacuum Assist RTM	Compression Mold	Filament Wind	Pultrusion	Thermal Form	Vacuum Bag / Autoclave	Cast	High Speed Machine	Forming	Strip Laminate
Lifting Body Airframe 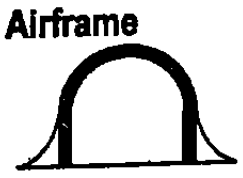	Monocoque	●	◒	●	●	◒	◒	●		◒	
	Integrally Hoop Stiffened	●	◒				◒	●	–		
	Integrally Longitudinal Stiffened	●	◒		●		◒	●	–		
Axisymmetric Airframe 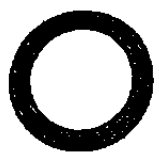	Monocoque	●		●	●		●	●		●	●
	Integrally Hoop Stiffened	●					◒	●	◒		
	Integrally Longitudinal Stiffened	●			●		◒	●	◒		
Surface	Monocoque	●	●			●	●	●	●	●	
	Sandwich	◒	◒				◒			○	

Note: Manufacturing process cost is a function of recurring cost (unit material, unit labor) and nonrecurring cost (tooling).

Note: ● Very Low Parts Count ◒ Low Parts Count ○ Moderate Parts Count – High Parts Count

Fig. 4.9 Structure concepts and manufacturing processes for low parts count.

complex configurations is the tight manufacturing tolerances required for the complex configurations. However, new technology such as nonreactive ceramic tooling allows low-cost precision castings suitable for complex airframe configurations such as ramjets and turbojets. Castings reduce the parts count, with a resulting cost savings. A one-piece cast airframe integrates all of the secondary structure. Precision casting minimizes subsequent machine and hand finishing of mating surfaces by achieving a precision surface finish "as-cast." Fuel tanks can be an integral part of the structure and not require bladders. Structural attachment points (e.g., ejector attachments, payload supports, booster attachments) and self-indexing/aligning features can be integral to the structure. This minimizes or eliminates mating, alignment, and assembly tooling and test/inspection requirements. Aluminum, titanium, and steel precision castings have been demonstrated for missile airframes, motor cases, and combustors. A disadvantage of a casting is that it must usually be heavier and thicker than a conventionally forged metal because of its lower strength compared to that of a work-hardened process.

Shown in Fig. 4.10 are schematics of different low-cost airframe manufacturing processes. The examples are vacuum-assisted RTM, composite filament winding, composite pultrusion, and metal casting. As stated previously, these processes provide cost benefits from reduced parts count and reduced labor.

The vacuum-assisted RTM process consists of inserting a fiber cloth into a mold, pulling a vacuum, injecting resin into the fibers, and curing the part. The vacuum-assisted RTM process has advantages of high production rate, good tolerances (e.g., +/−0.005 in), the capability for a three-dimensional weave,

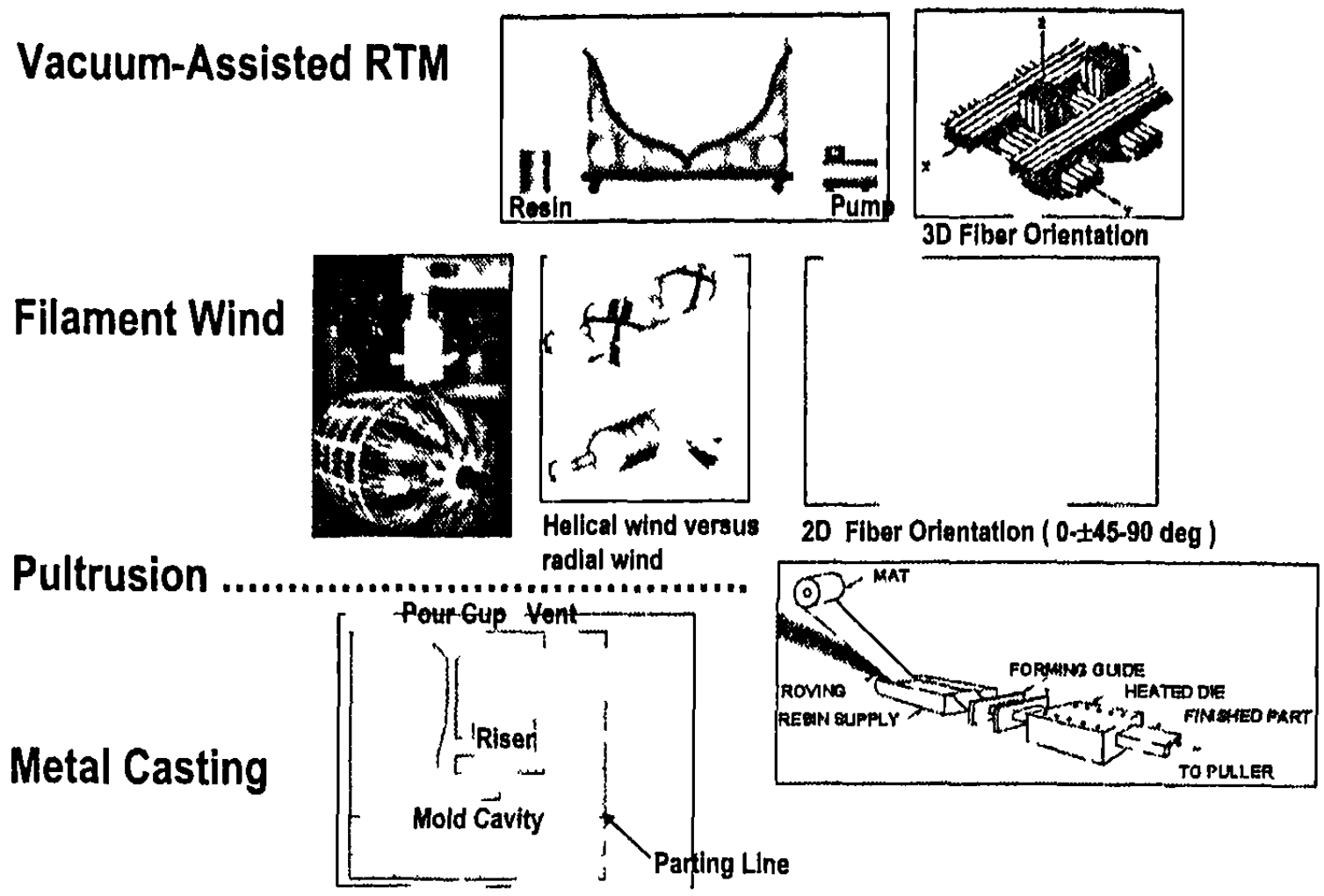

Fig. 4.10 Low-cost airframe manufacturing processes.

and improved mechanical properties. The improved mechanical properties are because of the lower required injection pressure for a vacuum-assisted RTM, which eliminates voids and blisters inside the part. Either a two-dimensional or three-dimensional fiber cloth may be used in the mold. A three-dimensional fiber cloth provides more freedom to tailor the preform fiber type, direction, spacing, and volume fraction to the desired properties. Shown in the top right section of the figure is an example of three-dimensional orthogonal fiber orientation, which provides omni-directional strength. An example of a missile that uses vacuum-assisted RTM with three-dimensional fiber cloth is the AGM-158 JASSM.

Filament winding is an automated process that is suited to circular and elliptical cross-sectional shapes such as airframes and motor cases. The filament fibers are pulled through a resin bath and wound around a mandrel. The resin is usually worked into the fibers by roll coaters or by breaker bars in dip tanks. Cycle time is about 1 h for winding and about 3 h for oven curing. Because the winding action itself will compact the laminate, vacuum bagging or other compaction methods are not necessary. Filament winding is limited to a two-dimensional fiber orientation. Shown in the left section of the figure is a photograph of filament winding. The middle section of the figure illustrates a helical wind of a motor case. A helical wind provides both longitudinal and radial strength. The middle section of the figure also illustrates a radial wind. The right section of the figure shows an example of a two-dimensional fiber weave orientation of 0 deg, ± 45 deg, and 90 deg.

Pultrusion is a continuous, automated closed-molding process that is cost effective for high-volume production of nonaxisymmetric cross-sectional shapes. The process pulls the fiber and resin continuously through a heated die that has the same cross-sectional geometry as that of the part. The part cures into its shape as it passes through the die. After passing through the die, the part is cut to the desired length. An advantage of pultrusion is high-speed,

low-cost production. A disadvantage is that it is limited to parts with a cross-sectional geometry that does not change with length.

Metal casting is particularly suited to reducing the parts count and cost of complex, nonaxisymmetric airframes, such as ramjets and turbojets. It is also applicable to surfaces. Precision casting uses a permanent nonreactive precision die, such as a ceramic die. A ceramic die minimizes metal oxides at the die interface, which improves dimension tolerances. The mold cavity is filled with molten metal by gravity pouring. As the metal cools, the mold cavity, riser, and pour cup become one solid casting. When the metal has cooled and solidified, the die is opened at the parting line and the part is removed by techniques such as vibration and water blasting. Although it is more expensive, a hot isostatic press (HIP) process using an inert gas such as argon also can be used to improve the dimensional tolerances and mechanical properties (e.g., strength) of castings. HIP eliminates internal shrinkage and gas voids. An Argon HIP process is often used for titanium casting, because hot titanium is reactive with the oxygen and nitrogen gases of the atmosphere.

An example of a missile that uses a large metal casting to reduce parts count and cost is the aluminum cast structure of the Tactical Tomahawk missile.

4.8 Airframe Material Alternatives

Examples of tactical missile alternative airframe materials and their tradeoffs are shown in Fig. 4.11. Metallic airframe material alternatives of Aluminum 2219, Steel PH 15-7Mo, and Titanium 6Al-4V are shown in the order of increasing cost. Similarly, composite airframe material alternatives of S994 glass/epoxy and S994 glass/polyimide, glass or graphite reinforced molding, and graphite/epoxy and graphite/polyimide are shown in the order of increasing cost.

Type	Material	Tension (σ_{TU}/ρ)	Buckling Stability ($\sigma_{Buckling}/\rho$)	Max Short – Life Temp	Thermal Stress	Joining	Cost	Weight
Metallic Increasing Cost	Aluminum 2219	○	◒	–	–	◒	●	○
	Steel PH 15-7Mo	◒	–	●	○	●	●	–
↓	Titanium 6Al-4V	◒	○	●	◒	○	–	○
Composite Increasing Cost	S994 Glass / Epoxy and S994 Glass / Polyimide	◒	○	○	◒	○	●	◒
	Glass or Graphite Reinforced Molding	–	○	○	◒	○	○	◒
↓	Graphite / Epoxy and Graphite Polyimide	●	○	◒	●	–	–	●

Note: ● Superior ◒ Above Average ○ Average – Below Average

Fig. 4.11 Tactical missile airframe material alternatives.

Design considerations for airframe materials are maximum allowable stress, susceptibility to localized buckling, maximum temperature for the short-duration flight of tactical missiles, sensitivity to thermal stress, ease of joining (e.g., weld, bond, bolt) to adjacent structure/subsystems, susceptibility to corrosion, low cost, and light weight.

For a lightweight tactical missile airframe at moderate temperature, graphite/epoxy and graphite/polyimide materials may be preferred. For a high-temperature airframe, titanium or steel materials are often preferred. For a low-cost airframe the preferred materials are usually aluminum, steel, S994 glass/epoxy, or S994 glass/polyimide.

Figure 4.12 shows the strength of typical airframe materials. The relationship of tensile stress σ_t to strain ε is the equation

$$\sigma_t = P/A = E\varepsilon \tag{4.17}$$

In the preceding equation P is the tensile load, A is the loading area, and E is the modulus of elasticity. Shown are the tensile strength and the stress–strain curves of small-diameter graphite, Kevlar, and glass fibers (without a composite matrix); high-strength steel (such as precipitation hardening stainless steel); titanium alloy; and aluminum alloy material alternatives. Note that the strength capability of advanced small-diameter fibers is very high. For example, as shown in the figure, the unidirectional tensile strength of a small diameter graphite (carbon) fiber is more than 400,000 psi. Small-diameter Kevlar and glass fibers may have comparable strength to graphite or carbon fiber, but also exhibit a lower modulus of elasticity and exhibit relatively high strain under

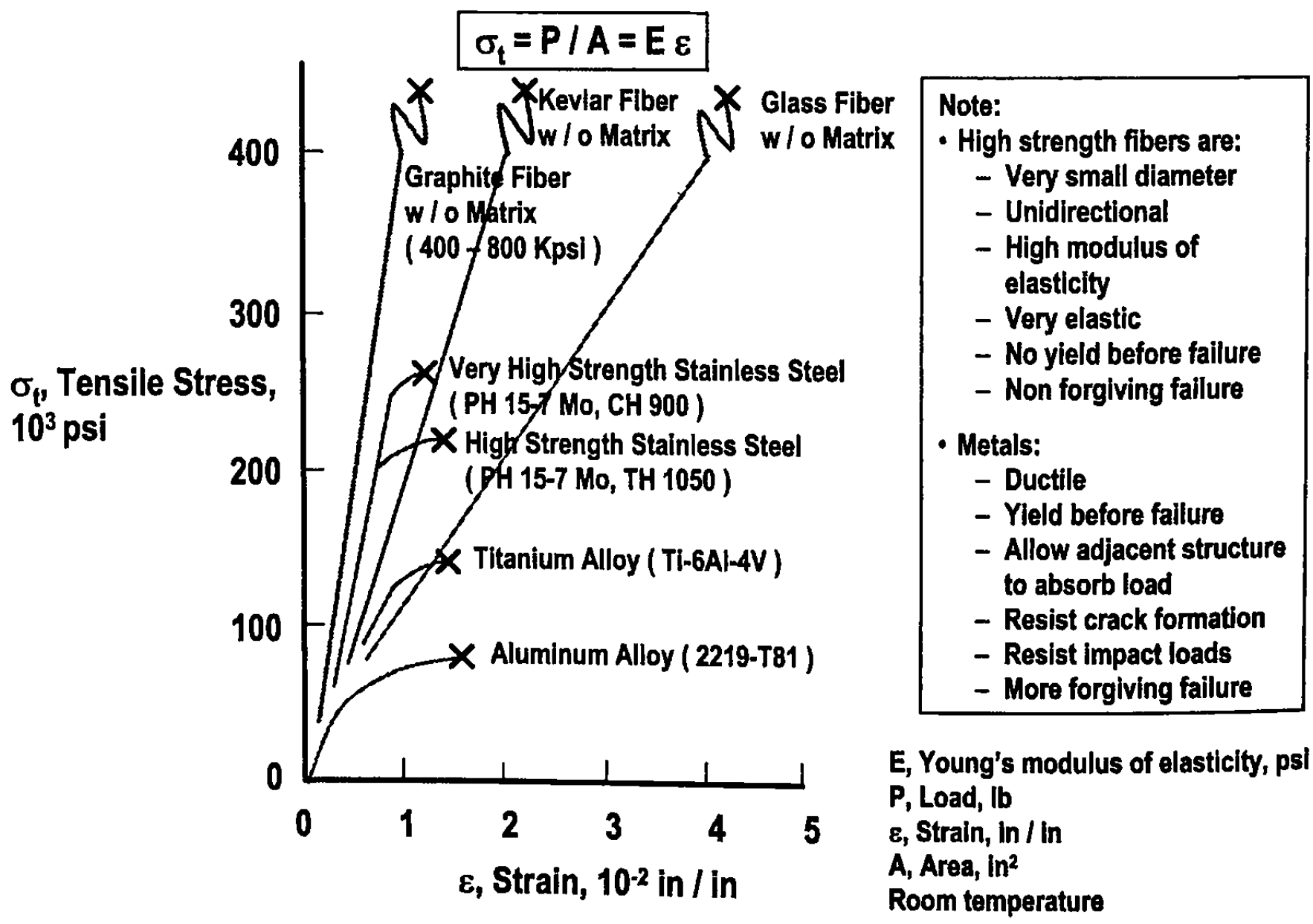

Fig. 4.12 Strength – elasticity of airframe material alternatives.

load. In addition to small-diameter fibers, advanced composite structures have long, continuous fibers (e.g., longer than 4 in) and a fiber/matrix ratio that is greater than 50% fibers by volume. Fibers can be graphite (carbon), Kevlar, glass, boron, ceramic, silicon carbide, quartz, polyethylene, and others. As an example of strength at the structure level, a 50% volume graphite composite structure can have strength in a tailored laminate that is above 200,000 psi, much greater than that of aluminum or even most steels. Also, the low density of composites further reduces the weight compared to metals. Advantages of graphite fiber composite materials include an extremely high modulus of elasticity, resulting in low strain and deflection compared to metals, and the conversion of incident radar energy into thermal energy (increased temperature), resulting in reduced radar cross section. However, note with caution that composites are not fault-tolerant. The fiber has a nearly linear stress–strain curve out to the ultimate load, at which it suddenly fails. Unlike most metals that generally yield gracefully before ultimate failure, composite fibers generally fail suddenly without yield. Other disadvantages of composites include susceptibility to impact damage and the possibility that a failure the structure may be hidden inside the laminate. Microcracks can spread through the matrix, decreasing the ability of the fiber to transfer load.

Figure 4.13 shows the structural efficiency advantage of laminate composites compared to conventional materials. The example is based on a 0–±45–90 deg orientation tailoring of the laminate. For short-duration temperatures up to about 500° F, laminate graphite/epoxy is a good candidate material because of its characteristics of high strength and low density. An epoxy resin that is filled with metallic or ceramic particles has a higher temperature capability. Examples

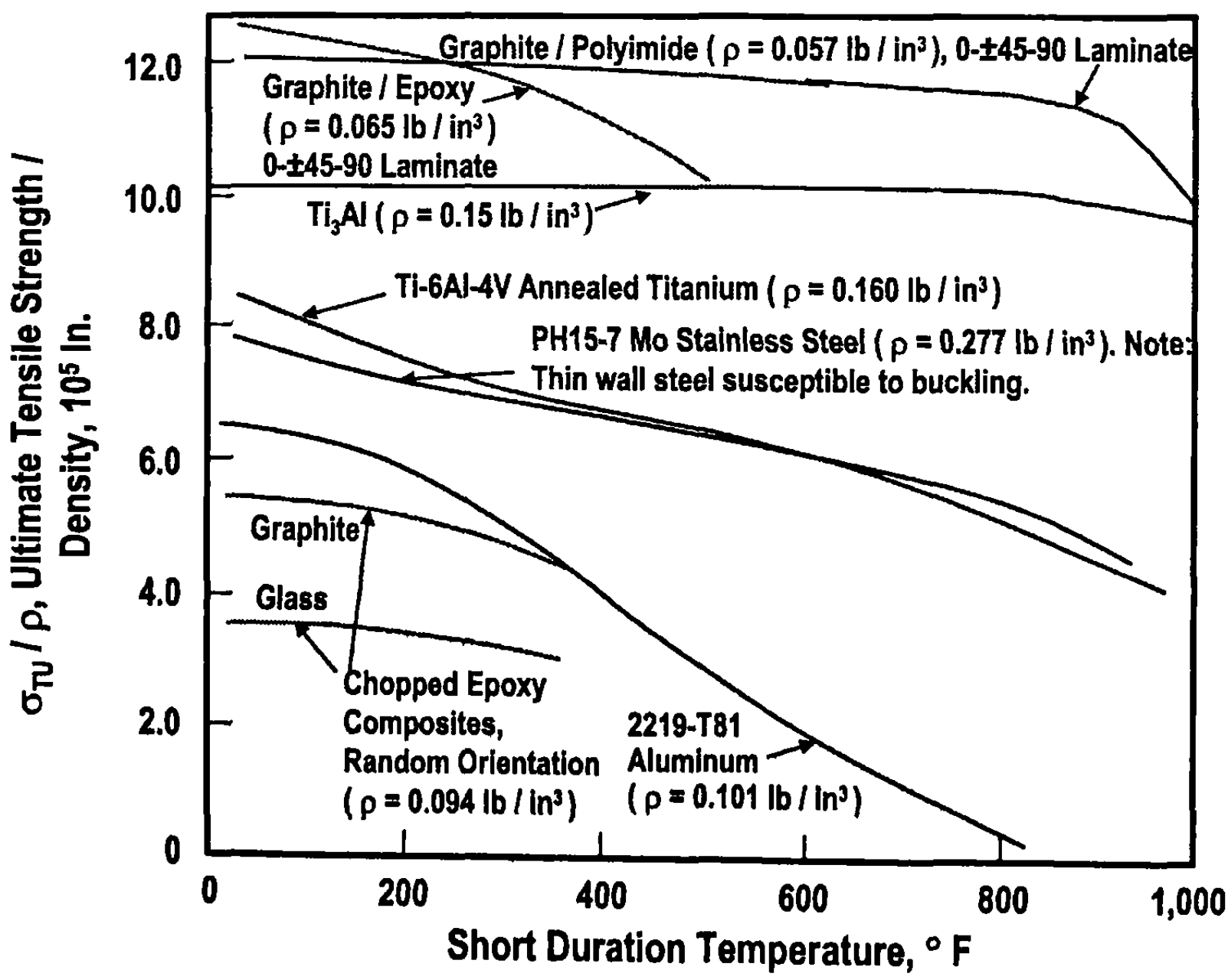

Fig. 4.13 Structural efficiency at high temperature of short-duration airframe material alternatives.

of missiles with rocket motor cases that are graphite epoxy are PAC-3, LOSAT, THAAD, and SM-3 TSRM. Laminate graphite/polyimide can be used at higher temperatures, up to about 1100° F short-duration temperature. Above 1100° F, titanium and steel alloys are better materials based on strength-to-weight ratio. A disadvantage of a polyimide resin compared to an epoxy resin is higher cost because of the higher processing temperature and pressure and carcinogenic volatiles. Another candidate resin is bismaleimide. The maximum short-duration temperature of bismaleimide is about 700° F. Advantages of bismaleimide include a relatively low cost and it is nontoxic at room temperature. Epoxy, polyimide, and bismaleimide matrices are thermoset polymer matrices. Thermosets require a chemical curing agent. Thermosets have relatively high temperature capability, good dimensional stability, and solvent resistance, but they require a relatively long cure time. A common high-temperature thermoset resin is phenolic. Phenolics are based on phenol (carbolic acid) and formaldehydes. An alternative low-cost polymer matrix with a shorter processing time is thermoplastic. Thermoplastics are most suitable to subsonic missiles because of a relatively low temperature capability. Examples of thermoplastic polymer matrices include polyetheretherketone (PEEK), polyphenylene (PPE), and polyetherketone (PEK).

A consideration in developing a design based on laminate composites is complexity. In addition to the material itself having greater complexity, the structures are not as straightforward as metal or chopped epoxy composite structures. The designer of a metal or chopped epoxy composite structure has two primary design considerations: material choice and the geometric configuration. Laminate composites require another design consideration, the composite matrix orientation. Two structures of identical geometric configuration, weight, and composite material, but with different lay-up, will have different stress-strain and failure modes as a function of orientation. The failure modes of laminate composites, which include exploding laminate, fibers pulling free from a matrix, first-ply failure, matrix cracking, and delamination, are difficult to predict.

Metal matrix composites and ceramic matrix composites are in development for strategic missile, space system, UAV, and aircraft applications. An example is titanium matrix/silicon carbide. Although the performance is very high, the cost is very high. Metal matrix and ceramic matrix composites are not yet cost effective for most tactical missiles.

The strength of a material is a function of the duration of the exposure to high temperature. An advantage of a one-way tactical missile is that it can be designed for higher temperature in its short-duration flight. Because aircraft and UAVs operate over many cycles of flight, they must be designed for lower temperature.

Examples of uninsulated structure materials that are cost effective for the short-duration flight of tactical missiles are shown in Fig. 4.14. An assumption is that the heat conducted to the airframe is large compared to the heat radiated by the airframe. This assumption is most applicable at low altitude/high atmospheric density. The airframe temperature would be slightly lower at high altitude because of radiation from the airframe. A second assumption is short-duration flight, but of sufficient duration (e.g., 1–30 m) that the structure is thermally soaked to the recovery temperature. The example airframe materials selected for the figure are based on the consideration of weight, cost, and maximum

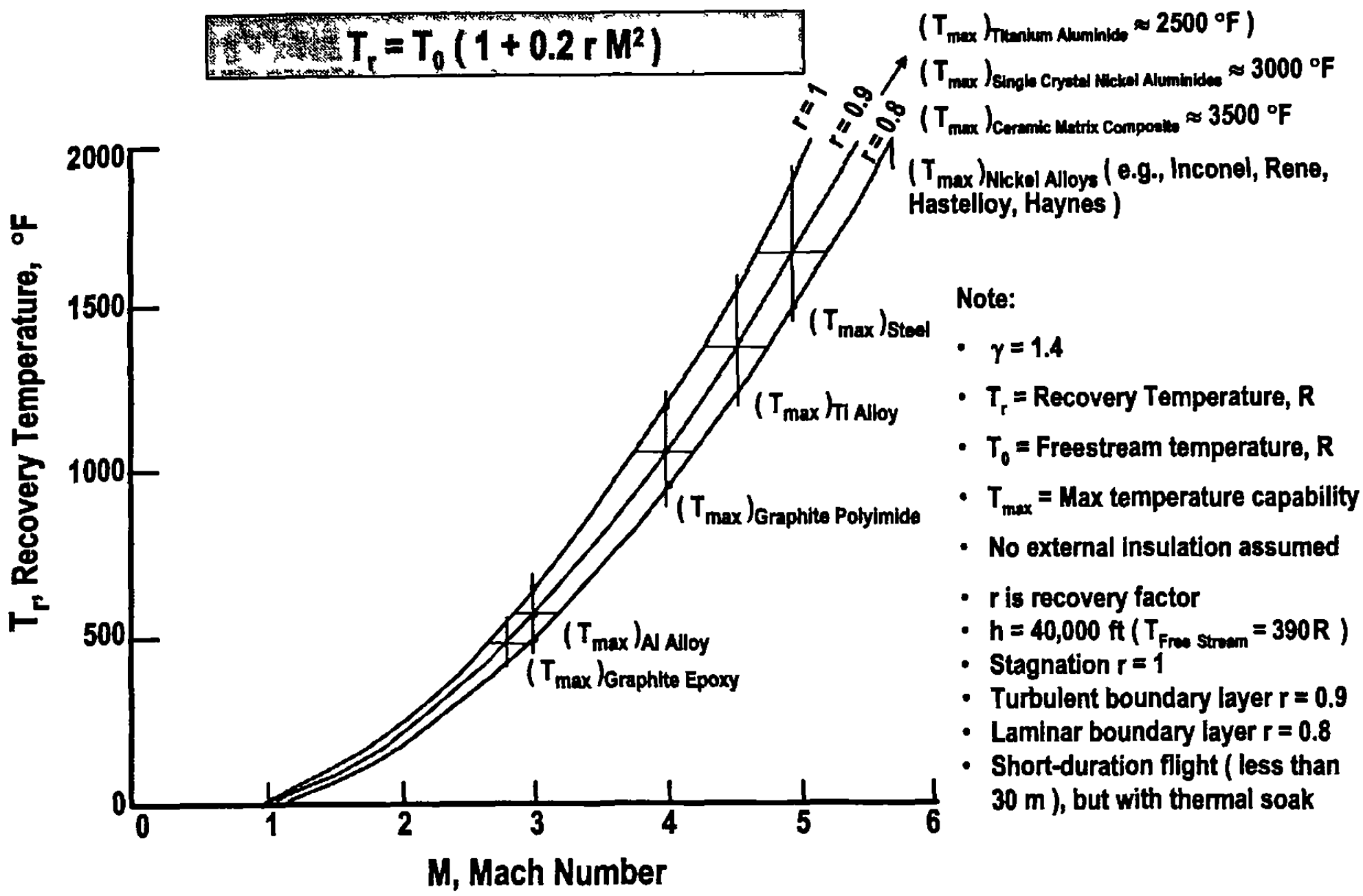

Fig. 4.14 Hypersonic missiles without external insulation require high temperature structure.

temperature capability. Composite materials are a new technology that will find increased use in new missile airframe structure. High-temperature composites have particular benefits for hypersonic missiles, providing weight reduction. Titanium alloy technology also enables lighter weight missiles in a hypersonic, high-temperature flight environment.

As shown in the figure, at subsonic and supersonic Mach number, graphite/epoxy and aluminum or aluminum alloys are attractive choices for a lightweight structure without external insulation. Graphite/epoxy and aluminum alloys have high strength-to-weight ratio, are easily fabricated, have good corrosion resistance, and are low cost. For higher Mach number, graphite/polyimide composite structure has an advantage of high structure efficiency at higher temperature for short-duration flight at Mach numbers to about Mach 4. For flight to about Mach 4.5 without external insulation, titanium structure and its alloys are preferred. A disadvantage of a titanium structure is higher material and machining cost. For example, the material cost of a titanium part can be up to 18 times that of an aluminum part and the machining cost can be up to 13 times that of aluminum. However, the cost to cast a part made of titanium is closer to the cost to cast an aluminum part. Small tolerance (e.g., +/−0.001 in) in casting is required to avoid expensive touchup machining. Up to Mach 5.7 without external insulation (about 2000° F), super nickel alloys such as Inconel, Rene, Hastelloy, and Haynes must be used. Precision castings can be used to minimize the expensive machining and material cost associated with super alloys. Above Mach 5.7 the material alternatives for a hot structure require the use of highly immature

and very expensive materials such as titanium aluminide ($T_{max} \approx 2500°$ F), single crystal nickel aluminides ($T_{max} \approx 3000°$ F), and ceramic matrix composites ($T_{max} \approx 3500°$ F).

Alternatives to a hot structure include active cooling and the use of external insulation. For short-duration tactical missiles, external insulation is usually the best approach to minimize the temperature of the structure. Active cooling is usually not cost effective for tactical missiles.

The Mach number and temperature application relationships are dependent upon the recovery temperature T_r. Recovery temperature is the maximum temperature of a surface after the temperature rises to an equilibrium temperature. The equation for recovery temperature is

$$T_r = T_0(1 + 0.2rM^2) \tag{4.18}$$

At stagnation regions, such as the nose or leading edges, the recovery factor r is about 1, resulting in the highest (stagnation) temperature. A turbulent or laminar boundary layer downstream of the nose or leading edge will have temperature recovery factors of about r =0.9 and r = 0.8 respectively, with the local temperatures less than stagnation.

4.9 Structure/Insulation Trades

Thermal insulators provide short-duration protection of structural materials from aerodynamic and propulsion heating. Tactical missiles use passive thermal protection (no active cooling) to save cost and to minimize the structural volume. Airframe structure/insulation trades for tactical missiles include a hot structure with no external insulation, a hot structure with internal insulation, external insulation over a "cold" structure, and a one-piece self-insulating composite structure. These are shown in Fig. 4.15. A consideration for a volume-limited missile is the total thickness of the structure/insulation. Large thickness means less volume for fuel or propellant, resulting in less range. An uninsulated metal structure has the smallest thickness at low Mach number/low recovery temperature. However as discussed previously, at high Mach number the temperature of most uninsulated structures will rapidly approach the recovery temperature because of the relatively low heat storage capacity and high thermal conductivity of most thin wall metal structures. This can be delayed by the use of a thermal sink below the skin, such as a fuel tank for a ramjet missile, and by the use of composite structure, which has a relatively low thermal conductivity. For short-duration flight at very high Mach number/recovery temperature, an external insulator/ablator over a metal airframe with internal insulation is usually the lightest weight approach, at the expense of larger thickness. The external insulation maintains the airframe below its maximum allowable temperature and the internal insulation maintains subsystems (e.g., warhead, electronics, sensors, batteries, propellant/fuel) below their maximum allowable temperature. A typical maximum temperature for subsystems is about 160° F. At intermediate (supersonic) Mach number, the lightest weight approach for a relatively short duration flight is usually

Example Structure / Insulation Concepts	Mach Increasing	T_{max}	k	c	ρ	α
Hot Metal Structure (e.g., Al) without Insulation		600	0.027	0.22	0.101	0.000722
Hot Metal Structure (e.g., Al)		600	0.027	0.22	0.101	0.000722
Internal Insulation (e.g., Min-K)		2000	0.0000051	0.24	0.012	0.00000106
Self-insulating Composite Structure (e.g., Graphite Polyimide)		1100	0.000109	0.27	0.057	0.00000410
Ext Insulation (e.g., Micro-Quartz Paint)		1200	0.0000131	0.28	0.012	0.00000226
Cold Metal Structure (e.g., Al)		600	0.027	0.22	0.101	0.000722
Internal Insulation (e.g., Min-K)		2000	0.0000051	0.24	0.012	0.00000106

Note:
- Tactical missiles use passive thermal protection (no active cooling)
- Small thickness allows more propellant / fuel for diameter constrained missiles (e.g., VLS launcher)
- Weight and cost are application specific
- T_{max} = max temp capability, ° F; k = thermal conductivity, Btu / s / ft² / ° F / ft; c = specific heat or thermal capacity, Btu / lbm / ° F; ρ = density, lbm / in³; α = thermal diffusivity = k / (ρ c), ft² / s

Fig. 4.15 Structure / insulation trades for short duration flight.

either an uninsulated metal airframe with internal insulation (to protect the subsystems) or a self-insulating composite structure.

The figure also shows typical values of the insulation parameters for the alternative insulation approaches. Values of maximum allowable temperature T_{max}, thermal conductivity k, specific heat or thermal capacity c, density ρ, and diffusivity α for a typical metal structure (aluminum), composite structure (graphite/polyimide), internal insulation (Min-K), and external insulation (microquartz paint) are shown. As an external insulator, microquartz paint provides a high temperature capability ($T_{max} = 2000°$ F). It protects a low-temperature airframe such as aluminum ($T_{max} = 600°$ F) in a short-term, high-temperature environment. Similarly the low conductivity of Min-K ($k = 0.0000051$ Btu/s/ft^2/°F/ft) as an internal insulator protects the warhead, electronics, and other subsystems. As a combined structure and insulator material, graphite/polyimide has good characteristics of maximum temperature ($T_{max} = 1100°$ F) and thermal conductivity ($k = 0.000109$ Btu/s/ft/°F). The thickness that is required for insulation is a design consideration. Thermal diffusivity is a measure of the insulation thickness efficiency of a material. It is a function of the thermal conductivity, heat capacity, and the density of the material, given by the equation

$$\alpha = k/(\rho c) \tag{4.19}$$

As a comparison, the thermal diffusivity of Min-K is 0.1% that of aluminum. Microquartz paint and graphite/polyimide also have low thermal diffusivity compared to aluminum (0.3 and 0.6%, respectively).

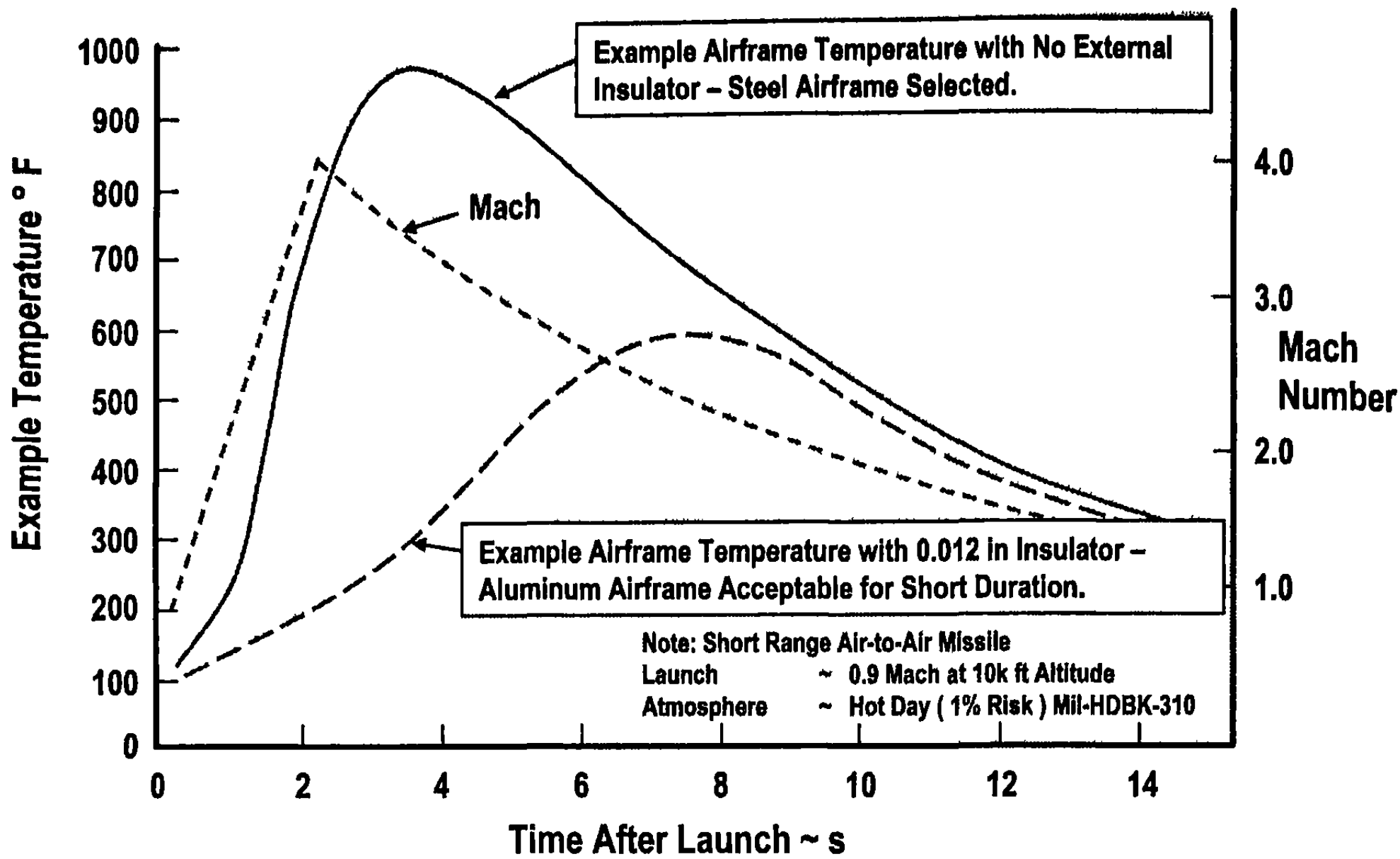

Fig. 4.16 External insulation has high payoff for short duration flight.

Mentioned previously, for environmental control of a tactical missile, an actively cooled (refrigerator) approach is usually not cost effective. Passive insulation using the thermal inertia of an insulator is usually the best approach for the short-duration flight of a tactical missile. In the case of a ramjet, the fuel can provide a thermal sink that reduces the rate of increase in the missile skin temperature.

Figure 4.16 compares the temperature for an insulated airframe versus an uninsulated airframe for short-duration flight. The example is based on a short-range air-to-air missile launched on a hot day at Mach 0.9 and 10,000 ft in altitude. The missile motor burnout is at 2.5 s, providing a burnout Mach number of 4.0. Note from the figure that for an uninsulated airframe, a steel structure was selected because of the high maximum temperature (950° F). An alternative is to use a lighter weight aluminum airframe that is protected by a thin layer of spray-on insulation. The peak temperature on the insulated structure is only 600° F, allowing the use of aluminum in the short-duration flight at high Mach number.

4.10 High-Temperature Insulation Materials

Figure 4.17 shows the maximum temperature capability and short-duration insulation efficiency of structure insulation materials. The insulation efficiency of the figure is based on the time that is required to reach 300° F at the back wall of the insulator. The assumed surface area application of the insulator is 1 lb/ft^2. Note that composite materials are good lightweight insulators. For insulating high-speed airframes, engines, and motor cases, the medium-density

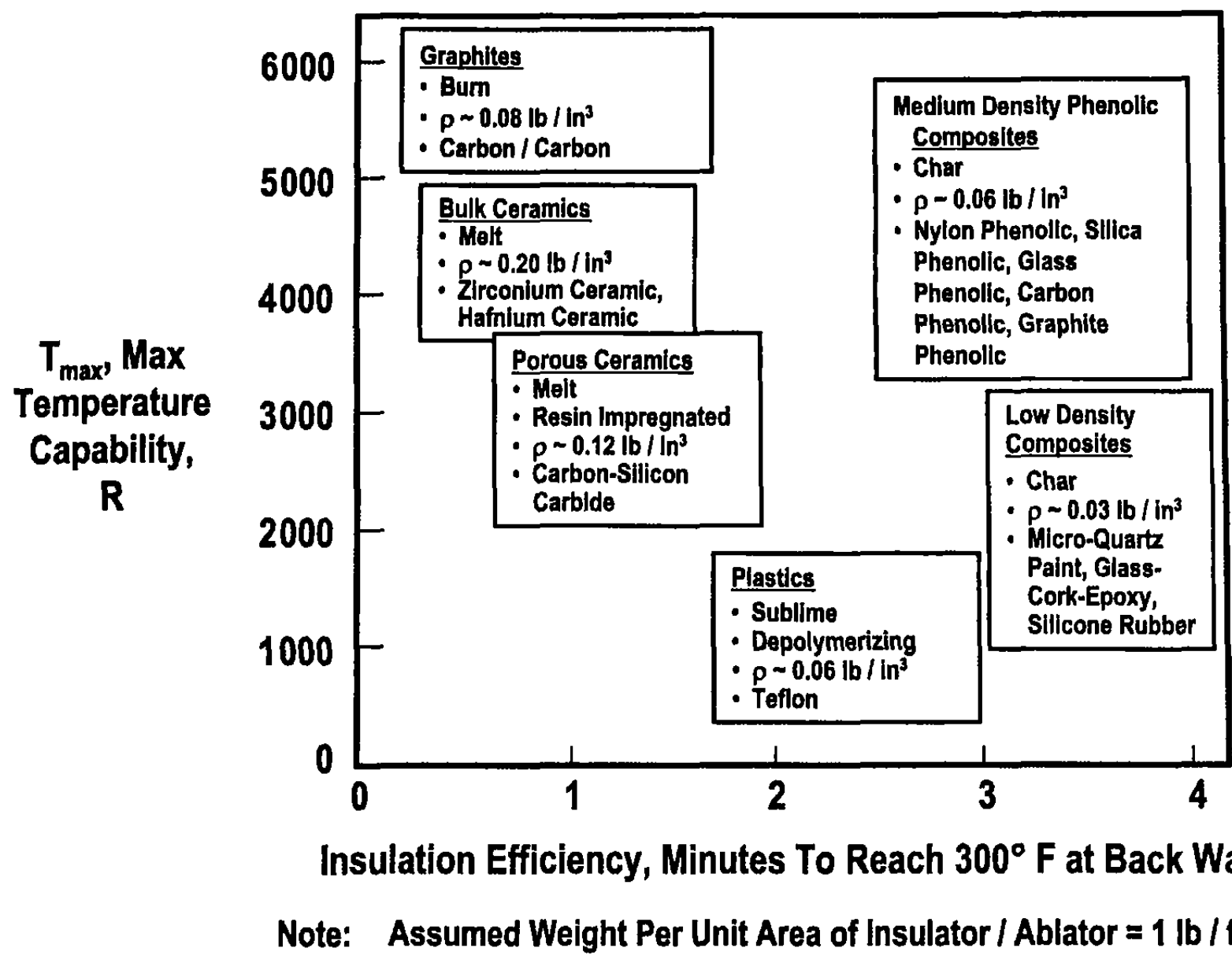

Fig. 4.17 Phenolic composites are good insulators for high-temperature structure and propulsion.

plastic composites are often used. An example is reinforced phenolic resin containing nylon, silica, graphite, or carbon. Phenolics have good resistance to erosion, allow high surface temperatures greater than 5000 R, and exhibit good insulation performance. These materials char at high temperature but generally maintain their thickness and aerodynamic shape. They are usually fabricated by wrapping tape over a metal form mandrel, so that the grain of the finished unit is oriented for minimum erosion. Another example of a good insulator at somewhat lower temperatures is low-density composites. Low-density composites such as microquartz paint, glass-cork-epoxy composite, or rubber polymers such as silicone rubber may be used for temperatures up to about 3000 R. These also char at high temperature. A disadvantage is periodic maintenance touch-up. A third approach based on plastics such as teflon is rarely used for hypersonic missiles. Plastics have a disadvantage of decomposing at high temperature into gas, resulting in decreased thickness and changes in the aerodynamic shape.

Ceramic refractory materials and graphite materials are also candidate insulators for high-speed airframes, engines, and motor cases. Although ceramic refractory materials and graphites have high temperature capability and very small erosion, the insulation efficiency for a given weight of material is not as good as that of plastic composite materials. Another disadvantage of ceramics is susceptibility to impact load failure. An example of a porous ceramic, with a maximum temperature up to about 3500 R, is resin impregnated carbon/silicon carbide. At high temperatures the resin melts, providing cooling for the structure. Examples of bulk ceramics are zirconium ceramic and hafnium ceramic. Bulk ceramics are capable of withstanding temperatures up to 5000 R, but like porous ceramics, they have relatively poor insulation efficiency. Bulk ceramics

are more often used as an external coating for erosion protection. Graphite insulators such as carbon/carbon provide the highest temperature capability. Graphite is capable of withstanding temperatures greater than 5000 R. However, graphite has relatively poor insulation efficiency and it is brittle.

Because missiles have volume and weight constraints, high-density materials for convection heating insulation of the airframe, engine, and motor case structure are in development. High-density insulation materials permit more fuel/propellant for a volume-limited missile, resulting in longer range.

4.11 Aerodynamic Heating/Thermal Response Prediction

Because most tactical missiles have a relatively short time of flight, the heat transfer is usually in a transient, not a steady-state, condition. Aerodynamic heating/thermal response prediction requires consideration of two different types of prediction methods applicable to two different types of surfaces, thermally thin and thermally thick. We will first consider the aerodynamic heating/thermal response of a thermally thin surface, such as a high-conductivity metal airframe. A thermally thin surface can be approximated as one-dimensional heat transfer with nearly uniform internal temperature that increases with time, eventually approaching the recovery temperature.

Figure 4.18 shows the effect of flight Mach number and altitude on the initial temperature rate of the rocket baseline airframe. The figure is based on the method from Jerger[4], beginning with the equation

$$(dT/dt)_{t=0} = (T_r - T_{\text{initial}})h/(c\rho z) \tag{4.20}$$

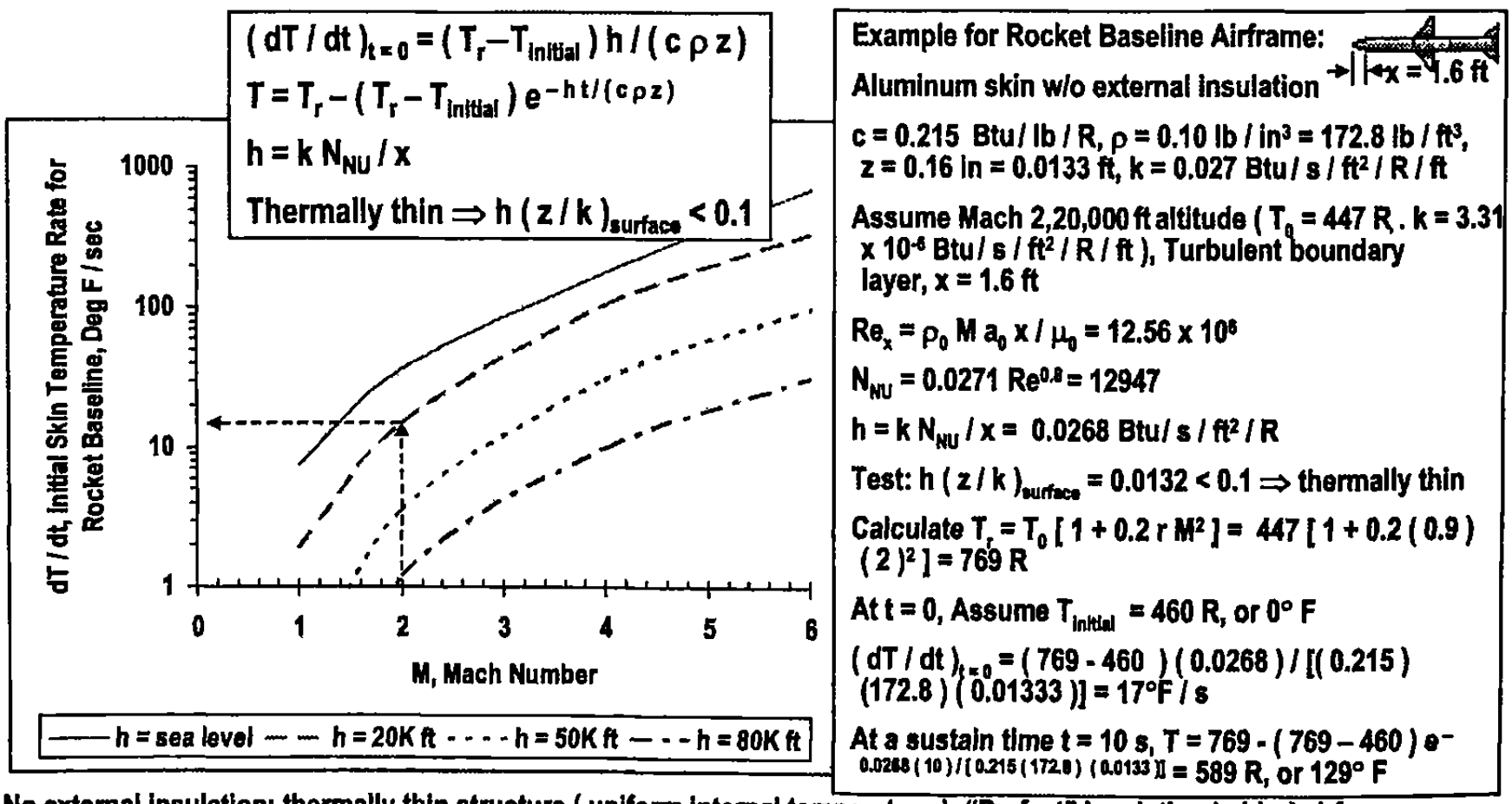

Note: No external insulation; thermally thin structure (uniform internal temperature); "Perfect" insulation behind airframe; one-dimensional heat transfer; Turbulent boundary layer; Radiation neglected; dT / dt = Temperature rate, R / s; T_r = Recovery (max) temperature, R; h = Convection heat transfer coefficient, Btu / s / ft² / R; c = Specific heat, Btu / lb / R; ρ = Density, lb / ft³; z = Thickness, ft; k = Conductivity, Btu / s / ft² / R / ft; Re = Reynolds number; N_{NU} = Nusselt number

Reference: Jerger, J.J., *Systems Preliminary Design Principles of Guided Missile Design*, D. Van Nostrand Company, Inc., Princeton, New Jersey, 1960

Fig. 4.18 A "thermally thin" surface (e.g., metal airframe) has uniform internal temperature.

In the above equation the initial temperature rate $(dT/dt)_{t=0}$ is a function of the recovery (maximum) temperature T_r, the initial temperature $T_{initial}$, heat transfer coefficient h, specific heat c, density ρ, and the thickness z. Note from the figure that the airframe temperature rate is highest at high Mach number and low altitude. The Sparrow missile rocket baseline has an aluminum airframe ($c = 0.215$ Btu/lb/R and $\rho = 0.10\ \text{lb/in}^3 = 172.8\ \text{lb/ft}^3$) without external insulation, an airframe thickness $z = 0.16$ in $= 0.0133$ ft, and "nearly perfect" (Min-K) insulation behind the airframe (i.e., adiabatic wall). It is also assumed that radiation from the airframe may be neglected. At Mach 2 and 20,000 ft altitude, the Reynolds number at the beginning of the aluminum airframe (aft of the radome), which is 1.6 ft aft of the nose tip, is $Re = \rho_0 V_0 x/\mu_0 = 12.56 \times 10^6$. The heat transfer coefficient h of air is a function of the thermal conductivity k, Nusselt number N_{NU}, and the boundary-layer distance from the nose x, given by the equation

$$h = kN_{Nu}/x \tag{4.21}$$

The conductivity of air is a function of the freestream static temperature T_0, given by the equation from Jerger[4]

$$k = 3.58 \times 10^{-6}[717/(T_0 + 225)](T_0/492)^{3/2} \tag{4.22}$$

For altitudes greater than 36,000 ft, $T_0 = 392$ R, giving

$$k = 2.95 \times 10^{-6}\ \text{Btu/s/ft/R} \tag{4.23}$$

For a standard atmosphere altitude of 20,000 ft, $T_0 = 447$ R and the conductivity of air is

$$k = 3.31 \times 10^{-6}\ \text{Btu/s/ft/R} \tag{4.24}$$

Nusselt number is a dimensionless parameter that repesents the heat transfer coefficient and the temperature gradient at the surface. It is a function of the type of boundary layer (laminar, transitional, turbulent) and the Reynolds number. Parameters that affect boundary-layer transition from laminar flow to turbulent flow include Reynolds number, pressure gradient, surface temperature, Mach number, and surface roughness. Boundary-layer transition usually occurs at a higher Reynolds number for a flight test than for a wind tunnel test. It also usually occurs at a higher Reynolds number for conditions of no pressure gradient, hypersonic Mach number, and a cold, smooth surface. For a missile body, the pressure gradient on the nose usually induces boundary-layer transition prior to the end of the nose section[5]. Also from Chin[5], the transition Reynolds number for subsonic through supersonic ($M < 4$) Mach number is at Reynolds number of $Re \approx 1 \times 10^6$. For the example, the Reynolds number is $Re = 12.6 \times 10^6$. It is anticipated that the boundary layer is turbulent. Based on Jerger[4], the approximate Nusselt number for a turbulent boundary layer is given

by the equation

$$N_{\mathrm{NU}} \approx 0.0271 Re^{0.8} = 12{,}947 \tag{4.25}$$

Substituting the values of N_{NU} and x into the heat transfer coefficient equation gives

$$h = 3.31 \times 10^{-6}(12{,}947)/(1.6) = 0.0268 \text{ Btu/s/ ft}^2\text{/R} \tag{4.26}$$

The testing of the assumption that the rocket baseline uninsulated airframe is a thermally thin surface is that

$$h(z/k)_{\mathrm{surface}} < 0.1 \tag{4.27}$$

The lumped parameter $h(z/k)_{\mathrm{surface}}$ is the Biot number. It represents the relative importance of the surface internal thermal resistance compared to boundary-layer thermal resistance. If the Biot number $h(z/k)_{\mathrm{surface}} \ll 1$, the conductance within the surface is much greater than the conductance within the boundary layer. If $h(z/k)_{\mathrm{surface}} \ll 1$, we can assume a uniform temperature within the surface.

For our example, $h(z/k)_{\mathrm{surface}} = 0.0268(0.0133)/0.027 = 0.0132$, which satisfies the test. The recovery temperature at Mach 2, 20,000 ft altitude for a turbulent boundary layer ($r = 0.9$) is

$$T_{\mathrm{r}} = T_0(1 + 0.2\mathrm{r}M^2) = 447[1 + 0.2(0.9)(2)^2] = 769\,\mathrm{R} \tag{4.28}$$

Then for this flight condition, the airframe initial temperature rate is computed to be

$$(d\mathrm{T}/dt)_{\mathrm{t}=0} = (769 - 460)(0.0268)/[(0.215)(172.8)(0.01333)] = 17 \text{ R/s} \tag{4.29}$$

The equation for the temperature of a thermally thin airframe is

$$T = T_{\mathrm{r}} - [T_{\mathrm{r}} - T_{\mathrm{initial}}]\, \mathrm{e}^{-\mathrm{ht}/(\mathrm{c}_p \mathrm{z})} \tag{4.30}$$

Note from the above equation that for a short-duration time of flight, the term $ht/(c\rho z) < 1$ and the airframe will not reach thermal equilibrium. Assuming an airframe initial temperature of $T_{\mathrm{initial}} = 460$ R and a rapid boost to a sustain Mach number, the temperature after 10 s exposure at Mach 2/20,000 ft altitude is

$$\begin{aligned} T &= 769 - (769 - 460)\mathrm{e}^{-0.0268(10)/[0.215(172.8)(0.0133)]} \\ &= 769 - 309\mathrm{e}^{-0.542} = 589 \text{ R, or } 129^\circ \text{ F} \end{aligned} \tag{4.31}$$

We will next consider the transient aerodynamic heating of a thermally thick surface. A thermally thick surface can be approximated as one-dimensional heat transfer through an infinite slab. As before, the temperature increases with time, eventually approaching the recovery temperature. From Jerger[4], the equation for the nondimensional temperature of a thermally thick surface that is suddenly subjected to a freestream with a constant recovery temperature is

$$[T(z,t) - T_{\text{initial}}]/[T_{\text{r}} - T_{\text{initial}}]$$
$$= erfc\{z/[2(\alpha t)^{1/2}]\} - e^{(hz/k)+h^2\alpha t/k^2} erfc\{z/[2(\alpha t)^{1/2}] + h(\alpha t)^{1/2}/k\} \quad (4.32)$$

The surface temperature ($z = 0$) is

$$[T(0,t) - T_{\text{initial}}]/[T_{\text{r}} - T_{\text{initial}}] = 1 - e^{h^2\alpha t/k^2} erfc[h(\alpha t)^{1/2}/k] \quad (4.33)$$

In the above equations $T(z,t)$ is the temperature as a function of the internal distance z and the time t. T_{initial} is the initial temperature, T_{r} is the recovery temperature, *erfc* is the complementary error function, α is thermal diffusivity, h is convection heat transfer coefficient, and k is thermal conductivity. The test for applicability of the thermally thick equation is

$$z/[2(\alpha t)^{1/2}] > 1 \quad (4.34)$$

Figure 4.19 shows the nondimensional temperature $[T(z,t) - T_{\text{initial}}]/[T_{\text{r}} - T_{\text{initial}}]$ versus nondimensional time $h(\alpha t)^{1/2}/k$.

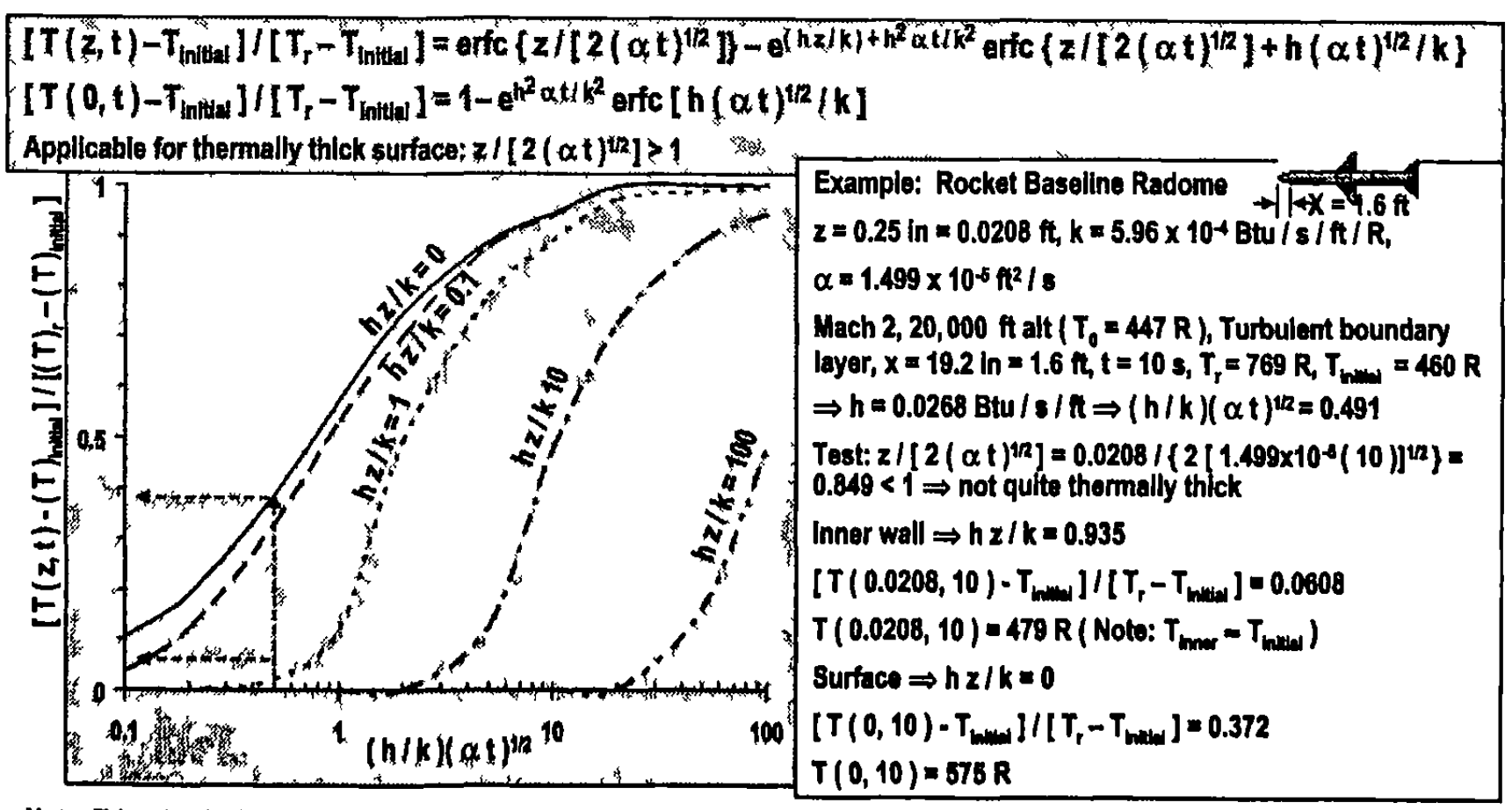

Note: $T(z,t) - (T)_{\text{initial}}$; one-dimensional heat transfer; Radiation neglected; Turbulent boundary layer; T_r = Recovery temperature, R; h = Heat transfer coefficient, Btu / ft² / s / R; k = Thermal conductivity of material, Btu / s / ft² / R / ft; α = Diffusivity of material, ft² / s; z_{max} = Thickness of material, ft; erfc = Complementary error function

Reference: Jerger, J.J., *Systems Preliminary Design Principles of Guided Missile Design*, D. Van Nostrand Company, Inc., Princeton, New Jersey, 1960

Fig. 4.19 A "thermally thick" surface (e.g., radome) has a large internal temperature gradient.

The complementary error function is defined as

$$erfc(x) = (2/\pi^{1/2}) \int_x^{\infty} e^{-u^2}\, du \tag{4.35}$$

Approximate solutions to the complementary error function are

$$x < 0.1,\ erfc(x) \approx 1 - 1.128x \tag{4.36}$$

$$0.1 < x < 2,\ erfc(x) \approx (1 + 0.2784x + 0.2304x^2 + 0.000972x^3 + 0.07811x^4)^{-4} \tag{4.37}$$

$$x > 2,\ erfc(x) = e^{-x^2}/(2\pi^{1/2}) \tag{4.38}$$

The time required to approach the recovery temperature is of interest. If the parameter $h(\alpha t)^{1/2}/k > 5$, a simplified equation for the nondimensional surface temperature after a long duration time, as the surface temperature approaches the recovery temperature, is

$$[T(0, t) - T_{\text{initial}}]/[T_r - T_{\text{initial}}] \approx 1 - k/[h(\alpha t)^{1/2}] \tag{4.39}$$

From the above equation, the time required for the nondimensional surface temperature to achieve 90% of the recovery temperature is

$$t_{90\%} \approx 0.718k^2/(\alpha h^2) \tag{4.40}$$

A simplified equation gives the surface temperature for small values of the parameter $h(\alpha t)^{1/2}/k$. The simplified equation for the nondimensional surface temperature at the beginning of the temperature rise is

$$[T(0, t) - T_{\text{initial}}]/[T_r - T_{\text{initial}}] \approx (2^{1/2}/\pi^{1/4})[h(\alpha t)^{1/2}/k] = 1.06[h(\alpha t)^{1/2}/k] \tag{4.41}$$

Note from the above equation that initially the surface temperature increases as $t^{1/2}$.

As an example, we will calculate the temperature of the rocket baseline radome. The assumed location is at the end of the radome, which is at a distance from the nose tip of $x = 19.2$ in $= 1.6$ ft. The radome is made of pyroceram, which has a conductivity $k = 5.96 \times 10^{-4}$ Btu/s/ft and a diffusivity $\alpha = 1.499 \times 10^{-5}$ ft^2/s. The radome thickness is $z = 0.25$ in $= 0.0208$ ft. Assume a flight condition of $M = 2$, 20,000 ft altitude, and an initial temperature $T_{\text{initial}} = 0°$ F $= 460$ R, as before. From the previous example, the heat transfer coefficient $h = 0.0268$ Btu/s/ft and the recovery temperature $T_r = 769$ R. Testing for applicability to the thermally thick equation, $z/[2(\alpha t)^{1/2}] = 0.0208/\{2[1.499 \times 10^{-5}(10)]^{1/2}\} = 0.849 < 1$, which does not satisfy the criteria. As a second test, we will calculate the inner wall temperature and compare it with

the initial temperature. For a thermally thick surface, the inner wall temperature is approximately equal to the initial temperature. At the time $t = 10$ s, the inner wall nondimensional temperature is

$$
\begin{aligned}
&[T(0.0208, 10) - T_{\text{initial}}]/[T_{\text{r}} - T_{\text{initial}}] \\
&\quad = erfc\{0.0208/\{2[1.499 \times 10^{-5}(10)]^{1/2}\}\} \\
&\qquad - e^{0.0268(0.0208)/(5.96\times10^{-4})+0.0268^2(1.499\times10^{-5})(10)/(5.96\times10^{-4})^2} \\
&\qquad \times erfc\{0.0208/\{2[1.499 \times 10^{-5}(10)]^{1/2}\} \\
&\qquad + 0.0268[1.499 \times 10^{-5}(10)]^{1/2}/(5.96 \times 10^{-4})]\} = 0.0608
\end{aligned} \tag{4.42}
$$

Substituting $T_{\text{r}} = 769$ R and $T_{\text{initial}} = 460$ R in the above equation gives the radome internal temperature

$$T(0.0208, 10) = 479 \text{ R} \tag{4.43}$$

Note that $T_{\text{inner}} \approx T_{\text{initial}}$, which is consistent with the assumption of a thermally thick surface.

As a comparison, we will calculate the temperature near the surface. At the same time $t = 10$ s, the nondimensional surface temperature for the same location ($x = 19.2$ in $= 1.6$ ft) is

$$
\begin{aligned}
&[T(0, t) - T_{\text{initial}}]/[T_{\text{r}} - T_{\text{initial}}] \\
&\quad = 1 - e^{0.0268^2(1.499\times10^{-5})(10)/(5.96\times10^{-4})^2} \\
&\qquad \times erfc\{0.0268[1.499 \times 10^{-5}(10)]^{1/2}/(5.96 \times 10^{-4})]\} = 0.372
\end{aligned} \tag{4.44}
$$

The surface temperature is

$$T(0, 10) = (769 - 460)(0.372) + 460 = 575 \text{ R} \tag{4.45}$$

Note that the radome surface has about the same rise in temperature as the aluminum airframe.

The time required for the nondimensional surface temperature to achieve 90% of the recovery temperature is

$$t_{90\%} = 0.718(5.96 \times 10^{-4})^2/[1.499 \times 10^{-5}(0.0239)^2] = 29.8 \text{ s} \tag{4.46}$$

Estimating the required thickness and weight of internal insulation is part of the conceptual design process. The internal insulation thickness is sized to ensure that the maximum internal temperature is limited to an acceptable maximum value (e.g., $<160°$ F) for the missile subsystems. From Ref. 16, an equation

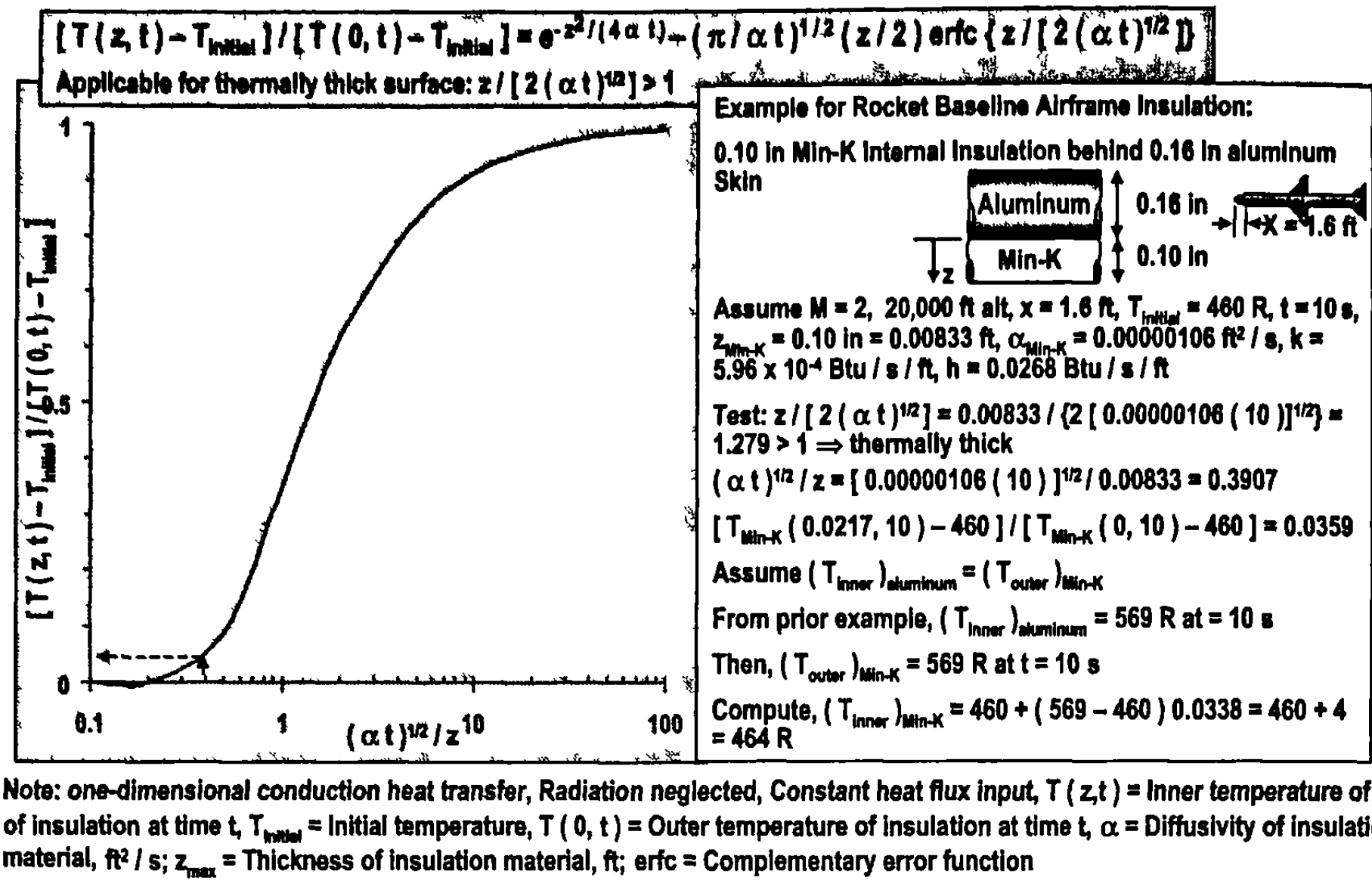

Fig. 4.20 Internal insulation temperature can be predicted assuming constant flux conduction.

for the nondimensional temperature of the insulation behind the airframe is

$$[T(z,t) - T_{\text{initial}}]/[T(0,t) - T_{\text{initial}}]$$
$$= e^{-z^2/(4\alpha t)} - (\pi/\alpha t)^{1/2}(z/2)erfc\{z/[2(\alpha t)^{1/2}]\} \tag{4.47}$$

The assumptions are one-dimensional conduction heat transfer, constant heat flux, negligible radiation, and thermally thick insulation ($z/[2(\alpha t)^{1/2}] > 1$). Figure 4.20 shows the nondimensional temperature $[T(z,t) - T_{\text{initial}}]/[T(0,t) - T_{\text{initial}}]$ versus the nondimensional time $(\alpha t)^{1/2}/z$. As before the temperature increases with time, eventually approaching the recovery temperature.

As an example, the rocket baseline has Min-K internal insulation ($z = 0.10$ in $= 0.0217$ ft, $\alpha = 0.00000106$ ft^2/s, and $k = 0.0000051$ BTU/s/ft^2/R/ft) behind its 0.16 in thick aluminum airframe. As in the previous examples, assume $M = 2$, 20,000 ft altitude, $t = 10$ s, $x = 1.6$ ft, and $T_{\text{initial}} = 460$ R. Assume that the insulation is flush with the airframe, such that there is no temperature discontinuity between the airframe and the insulation, $(T_{\text{inner}})_{\text{aluminum}} = (T_{\text{outer}})_{\text{Min-K}}$. From the previous example, the heat transfer coefficient $h = 0.0268$ BTU/s/ft^2/R and at time $t = 10$ s the airframe temperature is $(T_{\text{inner}})_{\text{aluminum}} = 569$ R. Testing for a thermally thick insulator, $z/[2(\alpha t)^{1/2}] = 0.00833/\{2[0.00000106(10)]^{1/2}\} = 1.279 > 1$, which satisfies the criteria. Substituting $z/[2(\alpha t)^{1/2}] = 1.279$ into the nondimensional temperature equation gives

$$[T(0.00833, 10) - 460]/[T(0, 10) - 460]$$
$$= e^{-1.2792} - 1.279\pi^{1/2}erfc(1.279) = 0.1944 - 0.1585 = 0.0359 \tag{4.48}$$

Substituting $T(0, 10) = 569$ R into the above equation gives

$$T = T(0.00833, 10) = 460 + (569 - 460)0.0359 = 460 + 4 = 464 \text{ R} \quad (4.49)$$

Note that the internal insulation is highly effective, with only a 4° F increase in temperature.

As discussed previously, selecting the nose tip bluntness requires considerations such as drag, localized stress, seeker performance, and the localized aerodynamic heating. A blunted nose is usually required at high supersonic/hypersonic Mach numbers. Allen and Eggers[17] developed the following equation for the convection heat transfer coefficient

$$h_r = N_{NU} k_{air,stagnation} / d_{NoseTip} \quad (4.50)$$

Based on Ref. 17, the equation for Nusselt number of a laminar boundary layer over a blunt nose is

$$N_{NU_r} = 1.321 Re_{d_{NoseTip}}^{0.5} P_{r_r}^{0.4} \quad (4.51)$$

Prandtl number is given by

$$P_{r_r} = c_{p_r} \mu_r / k_r \quad (4.52)$$

The viscosity can be obtained from Sutherland's law[4],

$$\mu_r = 1.147 \times 10^{-5} [708/(T_r + 216](T_r/492)^{3/2} \quad (4.53)$$

Similarly, the conductivity of air[4] is

$$k_r = 3.58 \times 10^{-6} [717/(T_r + 225)](T_r/492)^{3/2} \quad (4.54)$$

Assumptions for the nose tip heat transfer coefficient equation are one-dimensional conduction heat transfer, a laminar boundary layer, stagnation heating, and negligible radiation.

Figure 4.21 shows the heat transfer coefficient of the rocket baseline for a Mach number range of $M = 1$ to 6 and a nose bluntness range of $d_{NoseTip}/d_{Ref} = 0.01$ to 0.10. The assumed altitude is 20,000 ft. Note that a large value of bluntness is required to achieve low values of heat transfer.

An example calculation of the rocket baseline nose tip heat transfer is based on the assumed sustain (M = constant, T_r = constant) flight conditions of $M = 2$, 20,000 ft altitude, $T_{initial} = 460$ R, and $t = 10$ s. For an assumed nose tip with 1% bluntness, $d_{NoseTip}/d_{Ref} = 0.01$. The nose tip diameter is $d_{NoseTip} = 0.01 \times 8$ in $= 0.08$ in $= 0.00667$ ft. The Reynolds number based on the nose tip diameter is $Re_{dNoseTip} = \rho_0 V_0 d_{NoseTip}/\mu$. The stagnation recovery

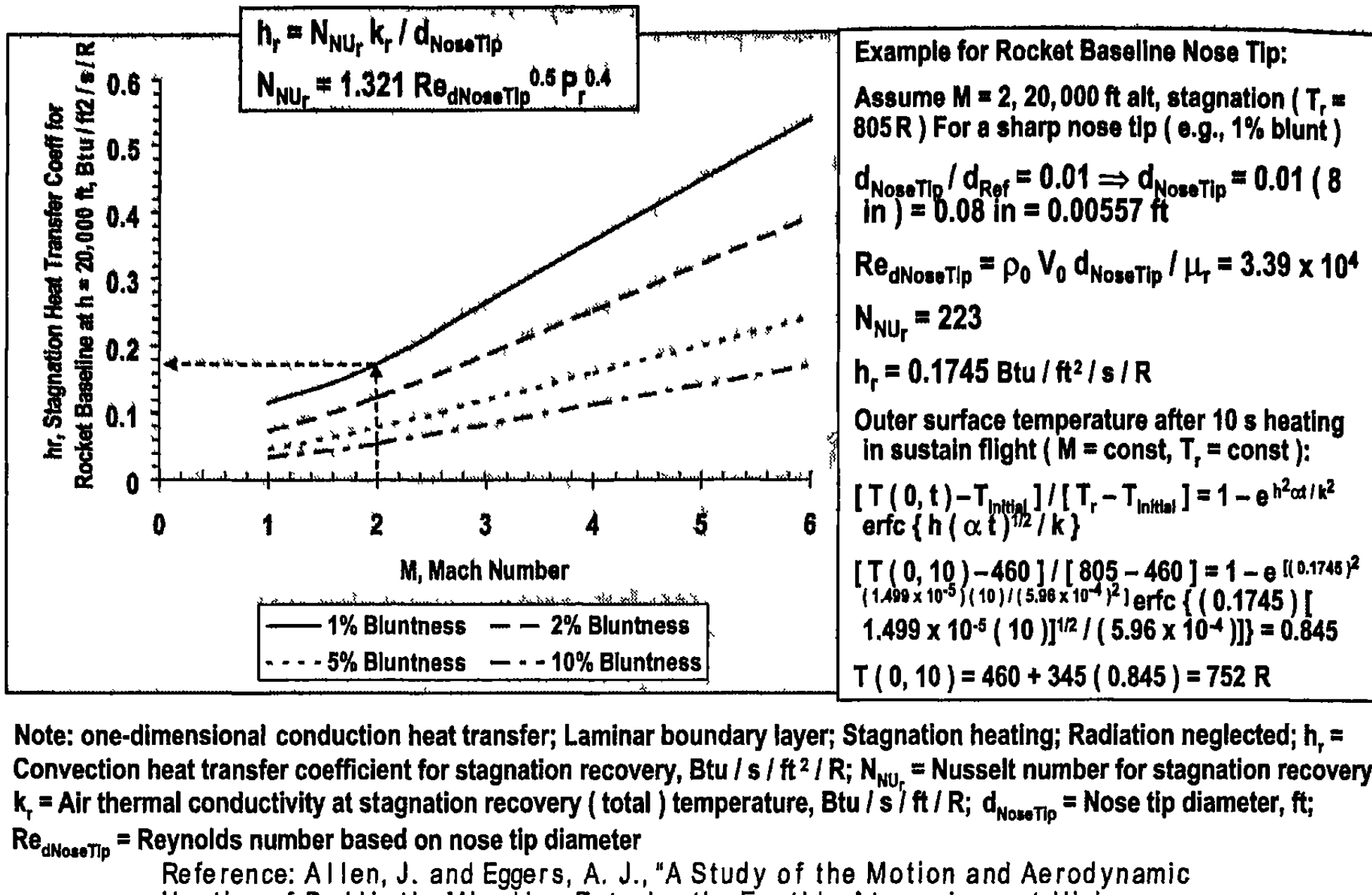

Fig. 4.21 A sharp nose tip has high aerodynamic heating.

temperature ($r = 1$) is

$$T_r = T_0\{1 + r[(\gamma - 1)/2]M^2\} = 447\{1 + (1)[(1.4-1)/2](2)^2\} = 805 \text{ R} \quad (4.55)$$

Substituting into Sutherland's law gives

$$\mu_r = 1.147 \times 10^{-5}[708/(T_r + 216](T_r/492)^{3/2} = 1.665 \times 10^{-5} \text{ lb/s/ft} \quad (4.56)$$

Substituting into the Reynolds number equation

$$\begin{aligned} Re_{d_{NoseTip}} &= 32.2(0.001267)(2074)(0.00667)/1.665 \times 10^{-5} \\ &= 3.39 \times 10^4 \end{aligned} \quad (4.57)$$

The thermal conductivity of the air at the stagnation condition is

$$\begin{aligned} k_r &= 3.58 \times 10^{-6}[717/(T_r + 225)](T_r/492)^{3/2} \\ &= 5.22 \times 10^{-6} \text{ Btu/s/ft}^2\text{/R/ft} \end{aligned} \quad (4.58)$$

Substituting into the Prandtl number equation

$$P_{r_r} = 0.253(1.665 \times 10^{-5})/(5.22 \times 10^{-6}) = 0.807 \quad (4.59)$$

Substituting the value of the Reynolds number and the value of the Prandtl number into the Nusselt number equation

$$N_{\mathrm{NUr}} = 1.321 Re_{\mathrm{d_{NoseTip}}}^{1/2} P_{\mathrm{r_r}}^{2/5} = 1.321(3.39 \times 10^4)^{1/2}(0.807)^{2/5} = 223 \quad (4.60)$$

Finally, the heat transfer coefficient is

$$h = 223(5.22 \times 10^{-6})/0.00667 = 0.1745 \text{ Btu/ft}^2\text{/s/R} \quad (4.61)$$

From the previous example calculations, note that the 1% bluntness nose tip heat transfer coefficient is 7.3x the heat transfer coefficient of a location 1.6 ft downstream of the nose tip. The radome nose tip nondimensional outer surface temperature, after 10 s of heating is

$$\begin{aligned}
&[T(0, \mathrm{t}) - T_{\mathrm{initial}}]/[T_{\mathrm{r}} - T_{\mathrm{initial}}] \\
&\quad = 1 - e^{\mathrm{h}^2 \alpha \mathrm{t}/\mathrm{k}^2} erfc\{h(\alpha t)^{1/2}/k\} \\
&\quad = 1 - \mathrm{e}^{[(0.1745)^2(1.499\times10^{-5})(10)/(5.96\times10^{-4})^2]} \\
&\qquad \times erfc\{(0.1745)[1.499 \times 10^{-5}(10)]^{1/2}/(5.96 \times 10^{-4})]\} = 0.845 \quad (4.62)
\end{aligned}$$

Substituting $T_{\mathrm{initial}} = 460$ R and $T_{\mathrm{r}} = 805$ R gives

$$T(0, 10) = 460 + (805 - 460)(0.845) = 752 \text{ R} \quad (4.63)$$

Note that after 10 s of flight, the nose tip outer surface temperature is only 53 R less than the stagnation recovery temperature (752 vs 805 R). From the previous calculations, also note that at a location 1.6 ft downstream of the nose tip, the outer surface temperature is 236 R less than the stagnation recovery temperature (569 vs 805 R). Again, the figure shows that a blunt nose (e.g., 10% bluntness) is preferable, with much lower heat transfer.

The previous methods for predicting aerodynamic heating/thermal response are based on a constant value of heat transfer coefficient, which is characteristic of sustain flight (e.g., constant Mach number, constant altitude, and constant recovery temperature). The methods can be applied to tactical missiles with varying Mach number and altitude by using a time-averaged value of the heat transfer coefficient of each flight phase. As an example for a boost-sustain-coast missile, the average heat transfer coefficient would be computed from the time-averaged values of the launch, end-of-boost, end-of-sustain, and end-of-coast heat transfer coefficients.

We will next consider radiation heat transfer. Figure 4.22 shows the thermal radiation heat loss Q_{Rad} versus Mach number M for values of emissivity $\varepsilon = 0.1$ and 1. Assumptions for the figure are 1) steady-state, equilibrium heating, 2) a free stream static temperature $T_0 = 390$ R, and 3) a turbulent

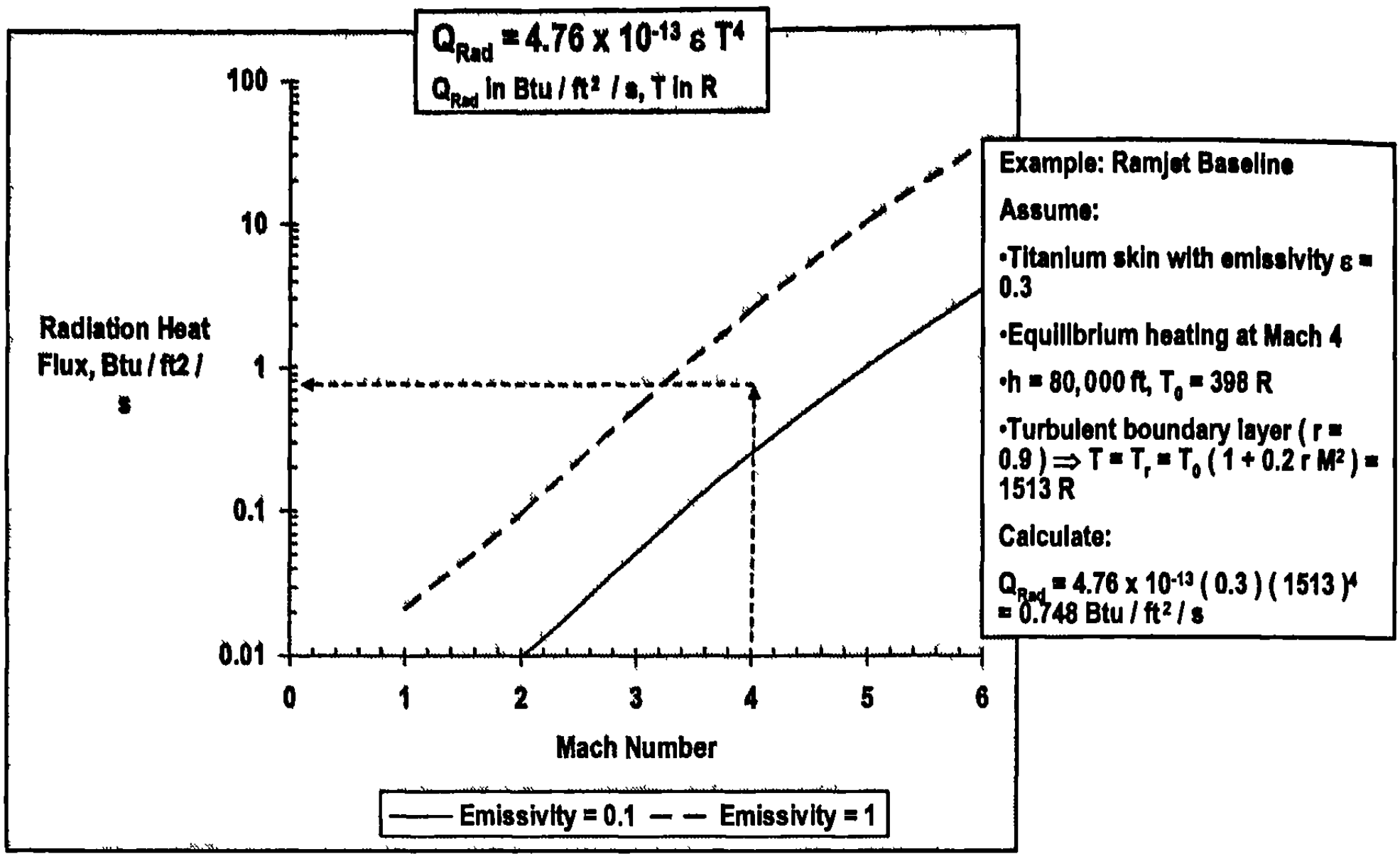

Fig. 4.22 Tactical missile radiation heat flux loss is small compared to convective heat flux input.

boundary layer, with a recovery factor $r = 0.9$. The equation for radiation heat loss is

$$Q_{\text{Rad}} = 4.76 \times 10^{-13} \varepsilon T^4 \tag{4.64}$$

The units of Q_{Rad} are Btu/ft^2/s and the unit of T is R. The steady-state, equilibrium temperature T is assumed to be equal to the recovery temperature equation, giving $T = T_r = T_0(1 + 0.2rM^2)$. Note from the figure that that the radiation heat flux is relatively low for Mach number less than 5.

An example calculation for the ramjet baseline at Mach 4 and an altitude of 80,000 ft ($T_0 = 398$ R) gives $T = T_r = 1513$ R for a turbulent boundary layer ($r = 0.9$). For the titanium airframe, assume an emissivity $\varepsilon = 0.3$. Substituting $T_r = 1513$ R and $\varepsilon = 0.3$ in the radiation heat flux loss equation gives

$$Q_{\text{Rad}} = 4.76 \times 10^{-13}(0.3)(1513)^4 = 0.748 \text{ Btu/ft}^2\text{/s} \tag{4.65}$$

4.12 Localized Aerodynamic Heating and Thermal Stress

Figure 4.23 illustrates design concerns for localized aerodynamic heating trouble spots such as the dome, joints, corner flow, and leading edges.

As an example, radomes and infrared (IR) domes often have thermal stress problems at the attachment of the dome to the metal airframe because of differences in temperature and thermal expansion. Domes have their material selection

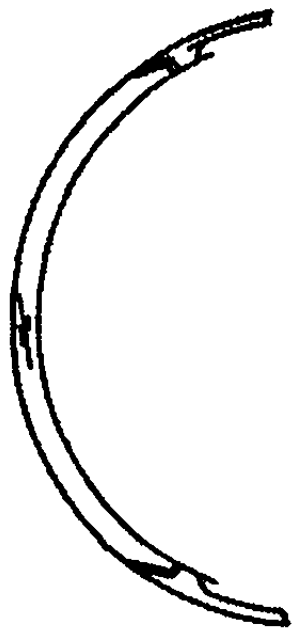

Body Joints
- Hot missile shell
- Cold frames or bulkheads
- Causes premature buckling

Flare / Wedge Corner Flow
- Shock wave – boundary layer interaction
- Separated Flow
- High heating at reattachment

IR Domes / RF Radomes
- Large temp gradients due to low thermal conduction
- Thermal stress at attachment
- Low tensile strength
- Dome fails in tension

Leading Edges
- Hot stagnation temperature on leading edge
- Small radius prevents use of external insulation
- Cold heat sink material as chord increases in thickness leads to leading edge warp
- Shock wave interaction with adjacent body structure

Note: σ_{TS} = Thermal stress from restraint in compression or tension = $\alpha E \Delta T$

α = coefficient of thermal expansion, E = modulus of elasticity, $\Delta T = T_2 - T_1$ = temperature difference.

Example: Thermal Stress for Rocket Baseline Pyroceram Dome, $\alpha = 3 \times 10^{-6}$, $E = 13.3 \times 10^6$ psi

Assume M = 2, h = 20,000 ft alt, t = 10 s. Based on prior figure, $\Delta T = T_{OuterWall} - T_{InnerWall} = 102$ R

Then $\sigma_{TS} = 3 \times 10^{-6} (13.3 \times 10^6)(102) = 4{,}070$ psi

Fig. 4.23 Design concerns for localized aerodynamic heating and thermal stress.

and thickness set by electromagnetic or electro-optical (EO) considerations in addition to structural considerations. Because many dome materials have low strength, domes are susceptible to failure.

Body joints are also susceptible to local stress concentration. For a supersonic or hypersonic missile, the difference in temperature of the hot outer airframe (from aerodynamic heating) and the relatively cold inner bulkhead (from the thermal heat sink of the interior bulkhead material) may lead to high local thermal stress at the body joint. This may cause premature buckling.

Corner flow such as flares and wedges may have localized aerodynamic heating because of shock-wave–boundary-layer interaction. The flow may separate and then reattach. High heating rates approaching stagnation heating occur at reattachment.

Leading edges contribute to high localized aerodynamic heating for hypersonic missiles. The leading edges are subjected to stagnation heating and could erode. Downstream of the hot leading edge, the additional thickness of the wing, canard, or tail surface provides a heat sink, and as a result it is relatively cold. The difference in temperature may cause the leading edge to warp. Another concern is the impingement of the shock wave from the leading edge on an adjacent surface. Shock-wave–boundary-layer interaction causes localized high heating.

Thermal stress occurs if a structure is restrained. For a rigid restraint in compression or tension, the equation for thermal stress is

$$\sigma_{TS} = \alpha E \Delta T \tag{4.66}$$

In the above equation σ_{TS} is the thermal stress, α is the coefficient of thermal expansion, E is the modulus of elasticity, and ΔT is the temperature difference.

As an example of thermal stress, consider the rocket baseline pyroceram radome, which has a coefficient of thermal expansion $\alpha = 3 \times 10^{-6}$ and a modulus of elasticity $E = 13 \times 10^6$ psi. For a typical flight condition of Mach 2, 20,000 ft altitude, and 10 s time of flight, a prior example showed that the temperature difference between the radome outer and inner walls is $\Delta T = 575 - 477 = 98$ R. The thermal stress of the radome if it is rigidly clamped to the airframe is approximately

$$\sigma_{TS} = \alpha E \Delta T = 3 \times 10^{-6}(13 \times 10^6)(98) = 3822 \text{ psi} \tag{4.67}$$

Although the thermal stress for this example is less than the strength of pyroceram (25,000 psi), it does add to the other contributors to radome stress, such as maneuver load. Dome thermal stress is usually not a driving concern for missiles with a maximum Mach number less than 3. However for Mach 4 or greater missiles, dome thermal stress is a concern.

Shown in Fig. 4.24 are examples of aerodynamic hot spots for a supersonic or hypersonic tactical missile. Note the high aerodynamic heating that exists at the nose tip, leading edge of surfaces, corner flow at the cylinder-flare junction, and the reattachment of the separated boundary layer downstream of the cylinder-flare junction. Also note that the aerodynamic heating is somewhat higher on the windward side of the missile, particularly on the bottom of the nose. The flow expansion region aft of the hammer-head bulge is a relatively cool region

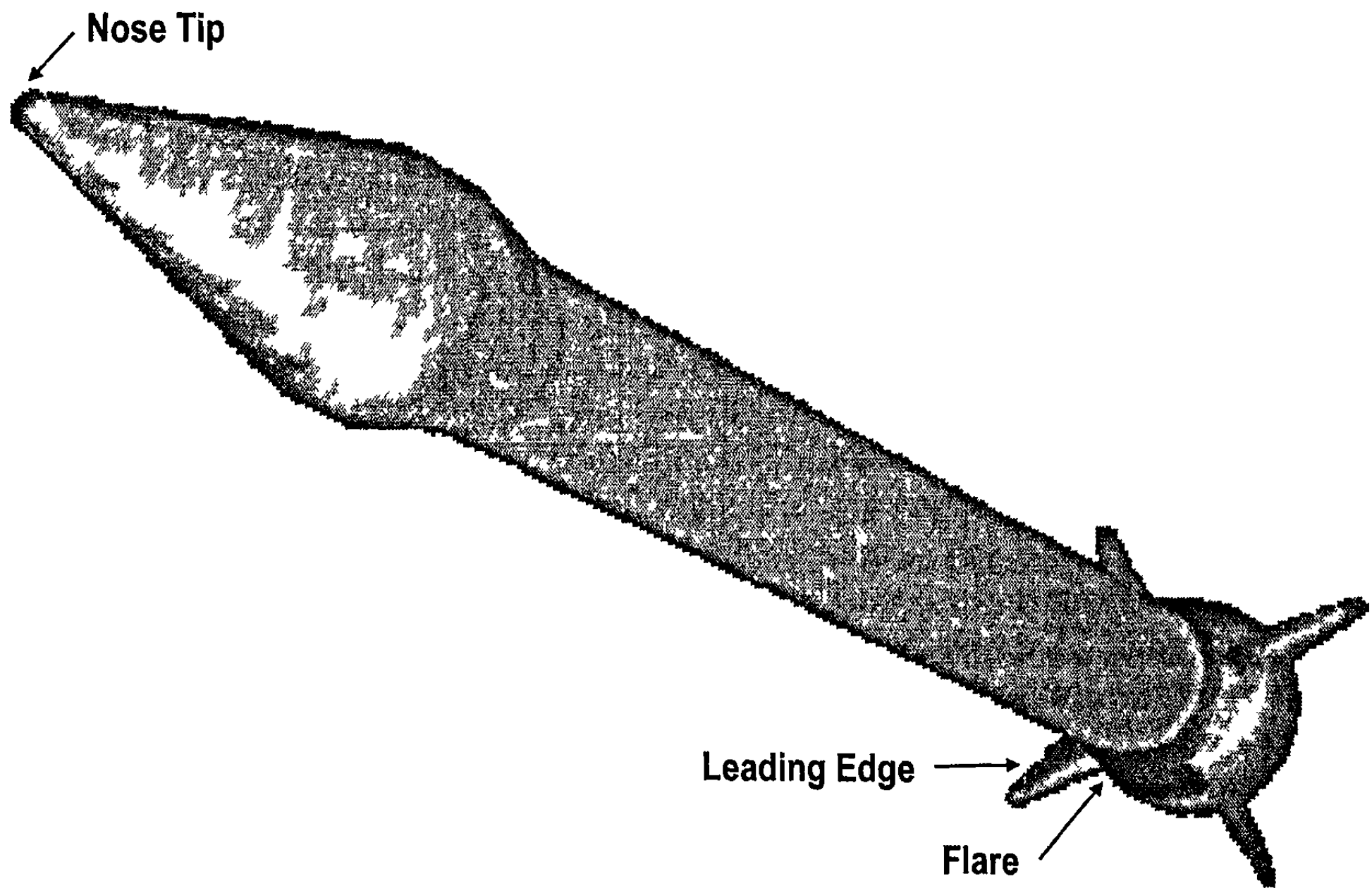

Fig. 4.24 Examples of aerodynamic hot spots. Figure also in color section.

of low aerodynamic heating. Most tactical missiles use acreage insulation, with a constant thickness over the entire airframe. However, aerodynamic hot spots may require local treatment, such as additional local insulation or the local use of a high-temperature airframe material.

4.13 Structure Design

Missile structure weight estimation is major activity in conceptual design. Figure 4.25 is a correlation of the body structure weight of 11 tactical missiles. It covers a broad range in launch weight, from $W_L = 100$ to 2858 lb. Note that the average body structure weight W_{BS} is 22% of the launch weight W_L. The correlation of body structure weight is based on load-carrying structure. If a motor case, engine, or warhead case carries external loads it is included in W_{BS}. W_{BS} does not include the weight of the tail, wing, or other surfaces. Note that all of the body structures for the 11 missiles are metal structures. A composite structure would be lighter, with a smaller structure weight fraction.

As an example, the rocket baseline has a launch weight $W_L = 500$ lb. The predicted body structure weight is $W_{BS} = 0.22(500) = 110$ lb.

A number of structure design conditions may drive the required thickness of the airframe. These include manufacturing, transportation, carriage on the launch platform, launch, fly-out, and maneuvering. For a conventional cylindrical body structure, there are simplified equations to estimate the required thickness for each design condition. The first design condition, minimum gage for

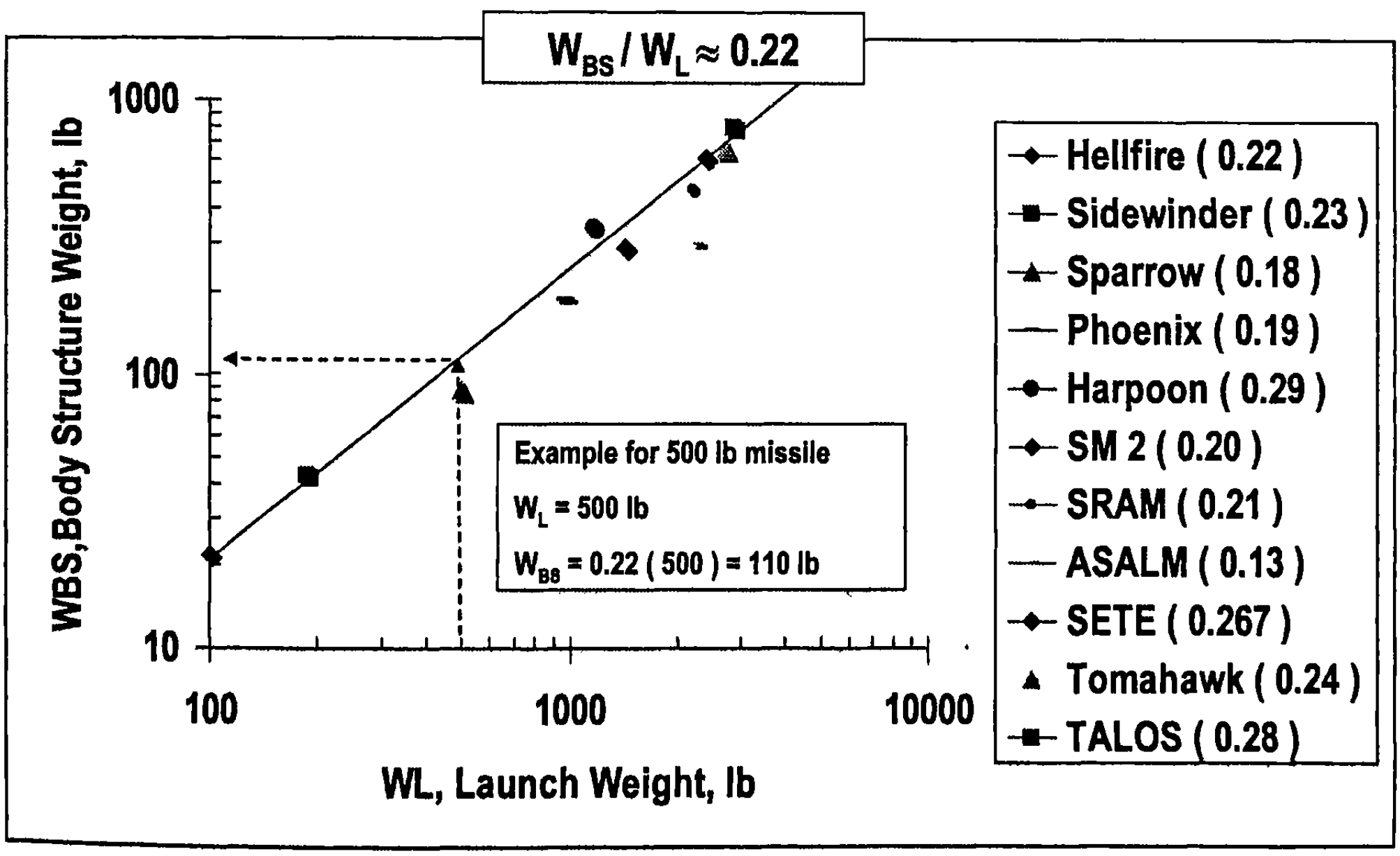

Note: W_{BS} includes all load carrying body structure. If motor case, engine, or warhead case carry external loads then they are included in W_{BS}. W_{BS} does not include tail, wing, or other surface weight.

Fig. 4.25 Tactical missile body structure weight is about 22% of the launch weight. Figure also in color section.

manufacturing, requires sufficient thickness for the manufacturing operations such as drilling, machining, and bending. These operations can be represented as an equivalent external overpressure. The equation for minimum gage thickness is

$$t = 0.7d[(p_{\text{ext}}/E)l/d]^{0.4} \tag{4.68}$$

For an equivalent external overpressure $p_{\text{ext}} \approx 10$ psi, the minimum gage of conventional airframe materials (e.g., aluminum, steel) is $t \approx 0.06$ in.

For the second design condition, the equation for the required thickness to counter localized buckling from bending is

$$t = 2.9r\sigma/E \tag{4.69}$$

For the third design condition, the equation for the required thickness for localized buckling from axial compression (e.g., thrust) is

$$t = 4.0r\sigma/E \tag{4.70}$$

For the fourth design condition, the required thickness from thrust force is

$$t = T/(2\pi\sigma r) \tag{4.71}$$

For the fifth design condition, the required thickness from bending moment is

$$t = M/(\pi\sigma r^2) \tag{4.72}$$

Finally, the required thickness from internal pressure (e.g., motor chamber pressure) is

$$t = pr/\sigma \tag{4.73}$$

The critical design condition is usually a combination of different types of structure loads. However, there is usually insufficient time in conceptual design to find the combined loads critical condition. Three simplified approaches may be used. The first approach, which can be characterized as high-risk approach, has no consideration of combined loads. The thickness is the factor of safety (FOS) times the maximum value of the largest thickness considering each load condition

$$1)\ t = \text{FOS} \times \text{Max}(t_{\text{MinGage}}, t_{\text{Buckling,Bending}}, t_{\text{Buckling,AxialCompression}}, t_{\text{AxialLoad}}, t_{\text{Bending}}, t_{\text{InternalPressure}}) \tag{4.74}$$

The second approach is a moderate-risk approach, which uses a root-sum-of-the-squares (RSS) to select the airframe thickness

$$2)\ t = \text{FOS} \times (t^2_{\text{MinGage}} + t^2_{\text{Buckling,Bending}} + t^2_{\text{Buckling,AxialCompression}} + t^2_{\text{AxialLoad}} + t^2_{\text{Bending}} + t^2_{\text{InternalPressure}})^{1/2} \tag{4.75}$$

The third approach is a low-risk approach, but which usually results in an over-designed/heavy airframe. It assumes that the required airframe thickness is the sum of the thicknesses for each of the loads,

$$3)\ t = \text{FOS} \times (t_{\text{MinGage}} + t_{\text{Buckling,Bending}} + t_{\text{Buckling,AxialCompression}} + t_{\text{AxialLoad}} + t_{\text{Bending}} + t_{\text{InternalPressure}}) \tag{4.76}$$

Approach 2 is often the best approach for conceptual design.

The most important structure design conditions for tactical missiles are usually localized buckling, bending moment loads, and motor case pressure loads. The equation for localized buckling stress from bending is

$$\sigma_{\text{Buckling,Bending}}/E \approx 0.35(t/r) \tag{4.77}$$

The equation for localized buckling stress from axial compression is

$$\sigma_{\text{Buckling,AxialCompression}}/E \approx 0.25(t/r) \tag{4.78}$$

The actual buckling stress can vary as much as $+/-50\%$, 3σ because of typical imperfections in geometry and a slight asymmetry in the loading. Localized non-dimensional buckling stress σ/E in bending and compression are shown in Fig. 4.26 as a function of thickness ratio t/r. Note that for small thickness the allowable stress for localized buckling is very low. Localized buckling may occur in a thin wall structure prior to exceeding the yield stress.

An example is shown of the required motor case wall thickness to avoid localized buckling. It is based on the rocket baseline missile. The rocket baseline motor case is 4130 steel, with a modulus of elasticity $E = 29.5 \times 10^6$ psi. The case thickness $t = 0.074$ in and the case radius $r = 4$ in. For a value of $t/r = 0.074/4 = 0.0185$, the maximum allowable localized buckling stress from bending is

$$\sigma_{\text{Buckling,Bending}} \approx 29.5 \times 10^6(0.35)(0.0185) = 191{,}000 \text{ psi}$$

The above localized buckling stress $\sigma_{\text{Buckling,Bending}} \approx 191{,}000$ psi is comparable to the yield stress $\sigma_{\text{yield}} = 170{,}000$ psi and is within the typical uncertainty of buckling stress.

Considerations in selecting the type of steel for a rocket motor case include tradeoffs of strength, buckling stability, joining/welding, and cost. An example is 4130 steel versus PH 15-7 Mo stainless steel for a rocket motor case. An advantage of 4130 steel is less susceptibility to buckling than PH 15-7 Mo steel,

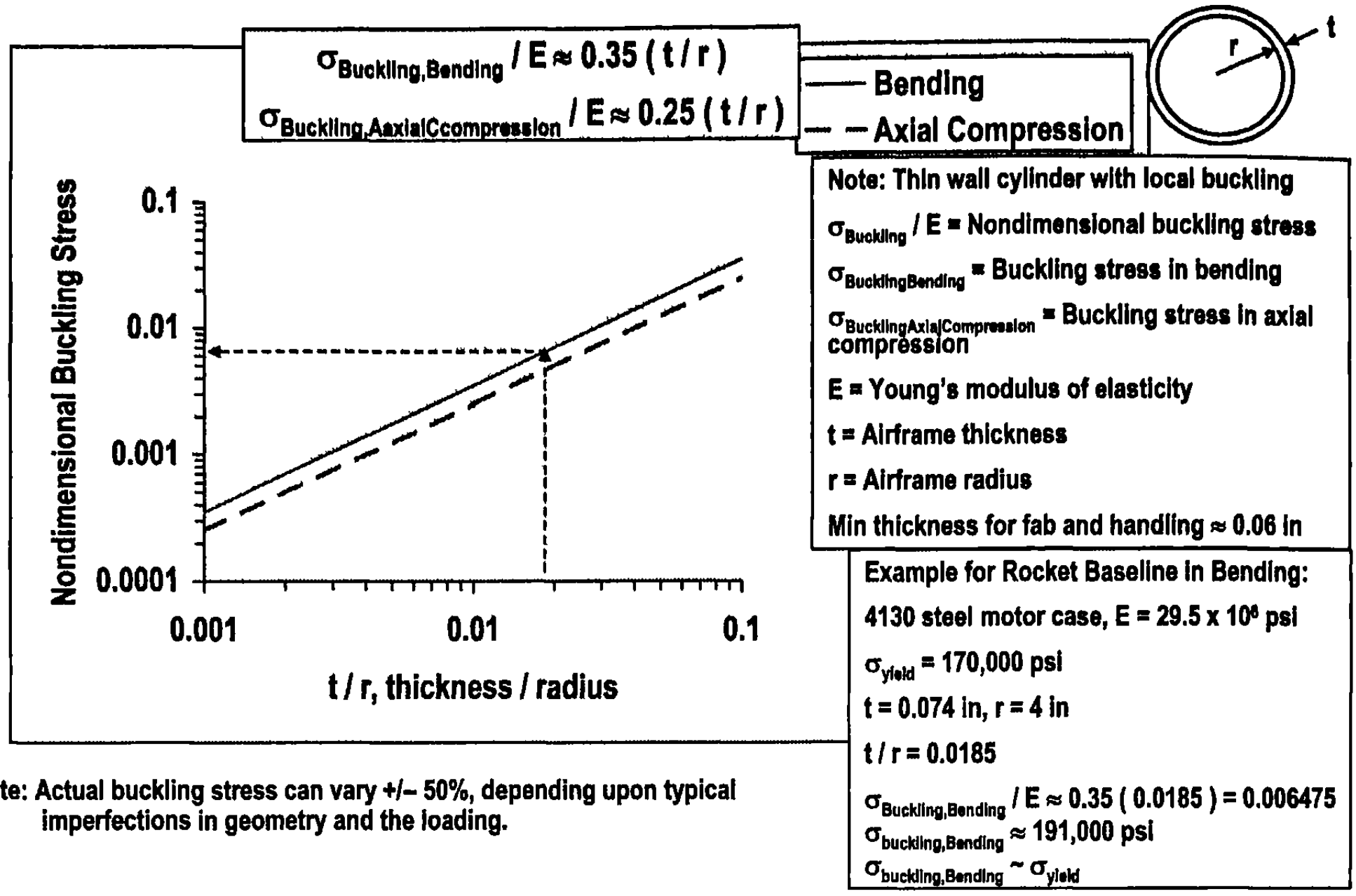

Fig. 4.26 Localized buckling may be a concern for thin wall structure.

because it requires a thicker motor case. Other advantages of 4130 steel are that it is easier to weld and it is lower cost. An advantage of PH 15-7 Mo steel is higher strength (yield strength of 200,000 to 265,000 psi, depending on the heat treatment) than 4130 steel. PH 15-7 Mo steel is more applicable to a very high chamber pressure motor case, where the required motor case thickness is set by strength and not set by buckling. For a very high chamber pressure motor case, the weight savings of very high strength steel may be worth the higher cost.

Noted previously, a consideration is the minimum gage thickness for fabrication and handling loads. Manufacturing processes such as vacuum molding and machining exert loads on the missile section. Handling loads include consideration of the impact load of dropping tools on the structure. Based on the aluminum shell thickness of typical missiles that have shown good durability, such as the Harpoon missile, a minimum gage thickness of 0.06 in is considered a reasonable value.

Flight carriage impact on missile design is illustrated in Fig. 4.27. A comparison is shown of a representative distribution of missile free-flight maneuver loads versus launch platform carriage loads. The left section of the figure shows a typical free-flight maneuvering air-load distribution and the weight-load distribution on each bulkhead. The missile free-flight loads are usually higher than the carriage loads because missile maximum maneuverability is often greater than that of aircraft (e.g., 30 vs 9 g). It is usually possible to get a fairly accurate prediction of the missile free-flight loads. Also, wind tunnel tests are usually conducted to determine free-flight air loads. The right section of the figure shows a typical maneuvering aircraft carriage air-load distribution, carriage weight-load distribution, and carriage suspension loads. The missile skin thickness is

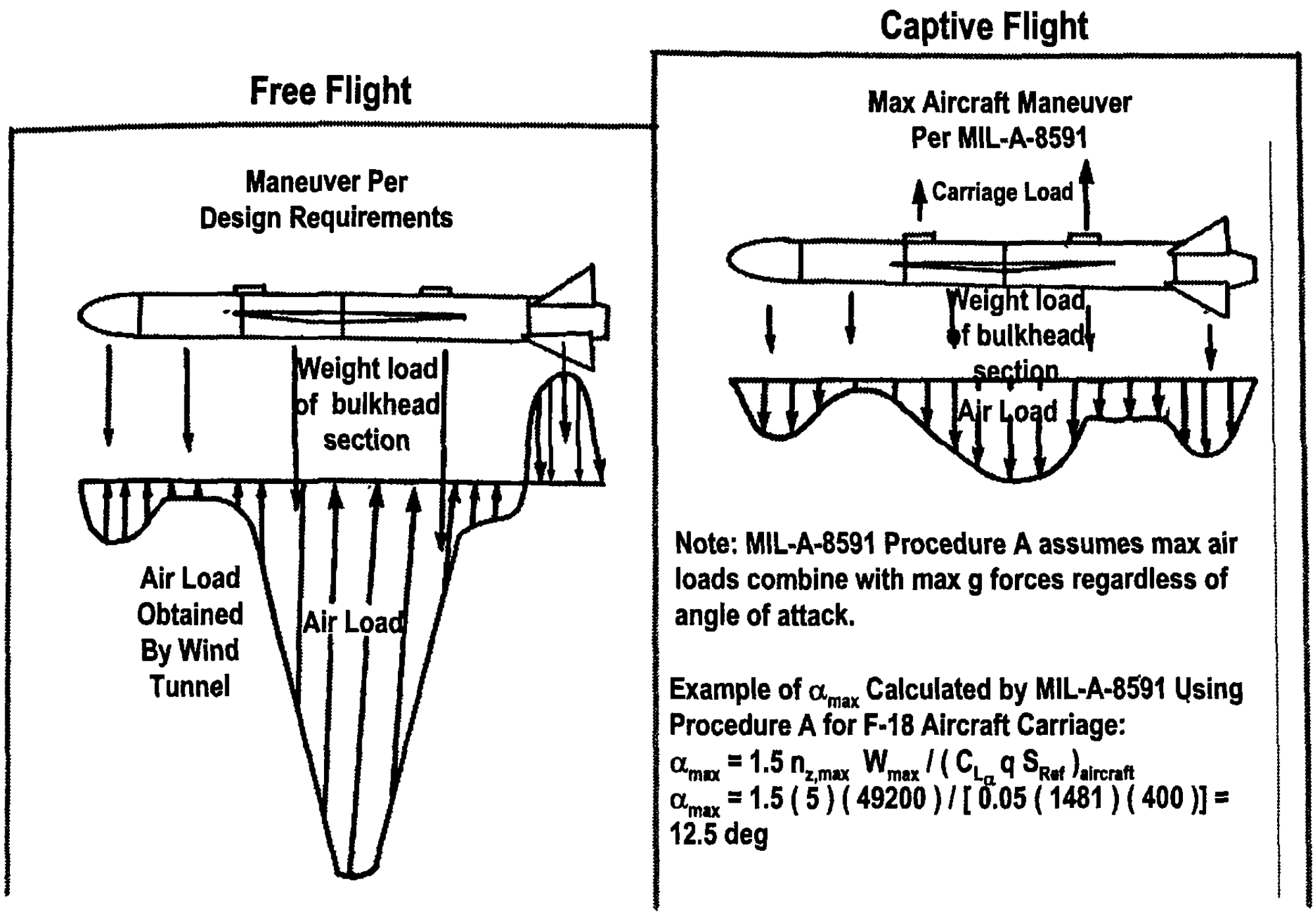

Fig. 4.27 Process for captive and free-flight loads calculation.

usually not sized by aircraft maneuver loads. As shown in the right section of the figure, carriage loads are taken out through a suspension system. It is difficult to accurately predict the two-body problem of a store in the flow field of the launch aircraft. In addition, it is difficult to get accurate wind tunnel data because of the small size of the missile model for aircraft carriage wind tunnel tests. As a result, the current conceptual design approach to estimating carriage loads is often based on the conservative process of Military Standard (MIL STD) MIL-A-8591. As missile loads estimation becomes more accurate in the future, there is a potential for structure weight savings based on improving the estimation accuracy for carriage loads.

MIL-A-8591 Procedure A assumes that the highest air loads combine with the highest inertial loads regardless of angle of attack. The maximum angle of attack from aircraft pitch maneuver, incremental angle of attack from aircraft roll rate, and the angle of sideslip from aircraft sideslip maneuver, using Procedure A of MIL-A-8591, are given by the respective equations:

$$\alpha_{\max} = [1.5 n_{z,\max} W_{\max} / (C_{L_\alpha} q S_{Ref})]_{aircraft} \tag{4.79}$$

$$\Delta\alpha_{\phi\max} = [0.0345 \dot{\phi}_{\max} y / (q)^{1/2}]_{aircraft} \tag{4.80}$$

$$\beta_{\max} = [1.5 n_{y,\max} W_{\max} / (C_{y_\beta} q S_{Ref})]_{aircraft} \tag{4.81}$$

As an example, assume an F-18 aircraft with the following characteristics:

$n_{z,max}$ = maximum normal maneuverability = 5 g
$n_{y,max}$ = maximum side maneuverability = 1 g
W_{max} = maximum weight = 49,200 lb
S_{Ref} = 400 ft^2
C_{L_α} = lift curve slope at maximum dynamic pressure = 0.050 per deg
C_{y_β} = side force curve slope at maximum dynamic pressure = 0.010 per deg
$\dot{\phi}_{max}$ = maximum roll rate at maximum dynamic pressure = 270 deg/s
y = lateral location of store from centerline of aircraft = 11.2 ft
q = dynamic pressure at store release = 1481 psf (Mach 1 at sea level)

Using the preceding parameters, the store maximum angle of attack from aircraft pitch maneuver, maximum incremental angle of attack from aircraft roll maneuver, and the maximum angle of sideslip from aircraft side maneuver are respectively:

$$\alpha_{max} = 1.5(5)(49200)/[0.050(1481)(400)] = 12.5 \text{ deg} \tag{4.82}$$
$$\Delta\alpha_{\phi max} = 0.0345(270)(11.2)/1481^{1/2} = 2.7 \text{ deg} \tag{4.83}$$
$$\beta_{max} = 1.5(1)(49200)/[0.010(1481)(400)] = 12.5 \text{ deg} \tag{4.84}$$

The preceding derived maximum angle of attack conditions are then used to compute the store loads.

Shown in Fig. 4.28 is a nomogram that calculates the bending moment M_B as a function of the applied load N, length l, and the type of loading c. The equation is

$$M_B = Nl/c \tag{4.85}$$

The scales of the nomogram cover the typical maximum/minimum ranges of the values of the parameters for tactical missiles. An advantage of using a nomogram is insight into the design drivers.

Referring again to the figure, note the shape of the typical load distributions, where w is the load per unit length. The load distributions are uniform loading ($c = 8$), linear loading increasing from the nose tip to the base ($c = 7.8$), linear loading increasing from the nose tip to the center of the missile and returning to zero at the base ($c = 6$), point loading (e.g., ejection load) at the center ($c = 4$), and point loading (e.g., control force) at the base ($c = 1$).

As an example for the 500-lb rocket baseline missile subjected to an ejection load of 20 g (10,000 lb load), the bending moment is calculated as

$$M_B = Nl/c = 10{,}000(144)/4 = 360{,}000 \text{ in-lb} \tag{4.86}$$

The bending moment is estimated in the nomogram by drawing a straight line from line 1 ($c = 4$) to line 2 ($l = 144$), to determine a turning point on line 3. A second straight line is drawn from line 4 ($N = 10{,}000$) through the

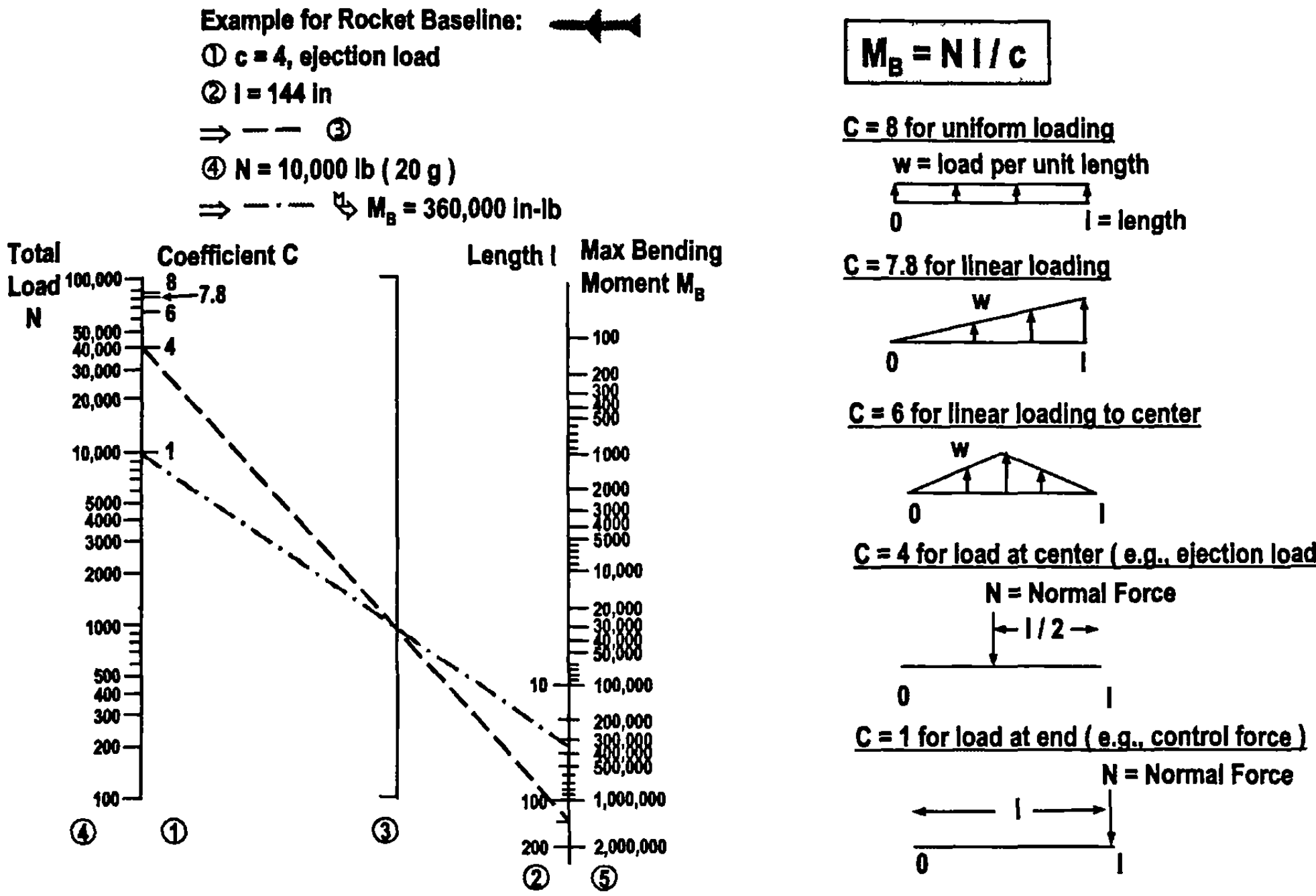

Fig. 4.28 Maximum bending moment depends upon load distribution.

turning point on line 3 to intersect the value of the bending moment on line 5 ($M_B = 360{,}000$ in-lb).

The simple nomogram shown in the figure is a throwback to the way engineering estimates were made 40 years ago, before the advent of high-speed computers. Although nomograms are still in use in areas such as medicine, they have fallen out of use in aerospace engineering. Up to about the year 1970, nomograms (including complex special slide rules with three or more sliders) were used in aerospace design and as an aerospace engineering teaching tool in universities.

An example is shown in Fig. 4.29 of the required thickness of the rocket baseline missile airframe to ensure that the bending moment stress is below the maximum allowable stress. The required thickness is calculated as a function of bending moment, airframe radius, maximum allowable stress, and FOS. The equation is

$$t = M_B(\text{FOS})/[\pi r^2 \sigma_{\text{Max}}] \tag{4.87}$$

Assumptions for the equation are a thin cylinder of circular cross section, solid skin, longitudinal bending moment, negligible axial (thrust and drag) stress, and negligible thermal stress. As noted in the previous discussion, the rocket baseline subjected to an ejection load of 20 g will have a bending moment $M_B = 360{,}000$ in-lb. Based on a FOS for an ultimate load of FOS = 1.5, an aluminum airframe structure ultimate stress $\sigma_{\text{ult}} = 65{,}000$ psi, and an airframe

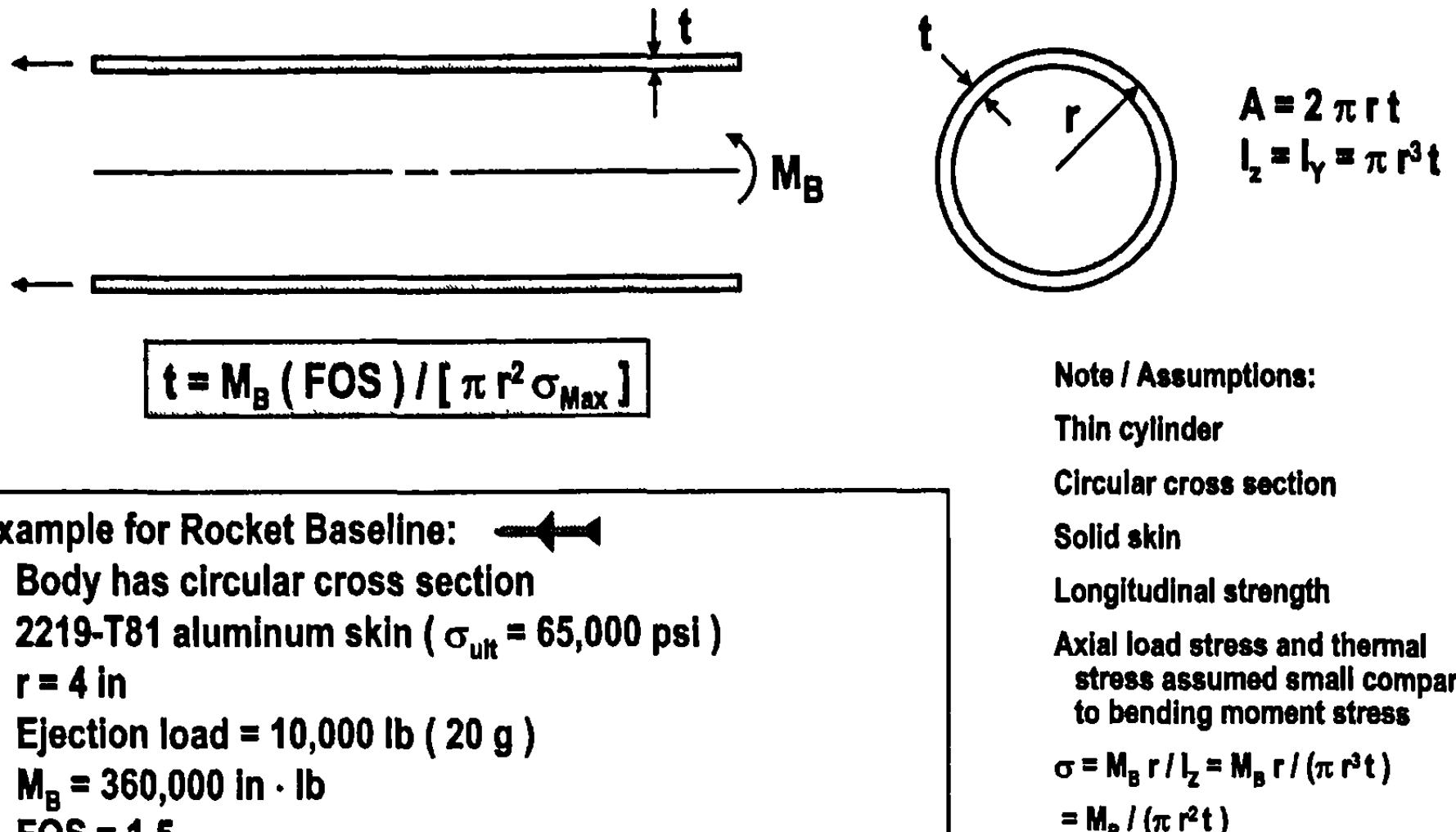

Fig. 4.29 Bending moment may drive body structure weight.

radius $r = 4$ in, the required airframe thickness is computed to be

$$t = 360000(1.5)/[\pi(4)^2(65000)] = 0.16 \text{ in.} \tag{4.88}$$

Figure 4.30 is a correlation of the propellant weight fraction of eight tactical missiles. The rocket motors range in weight from $W_M = 32$ to 4278 lb. The

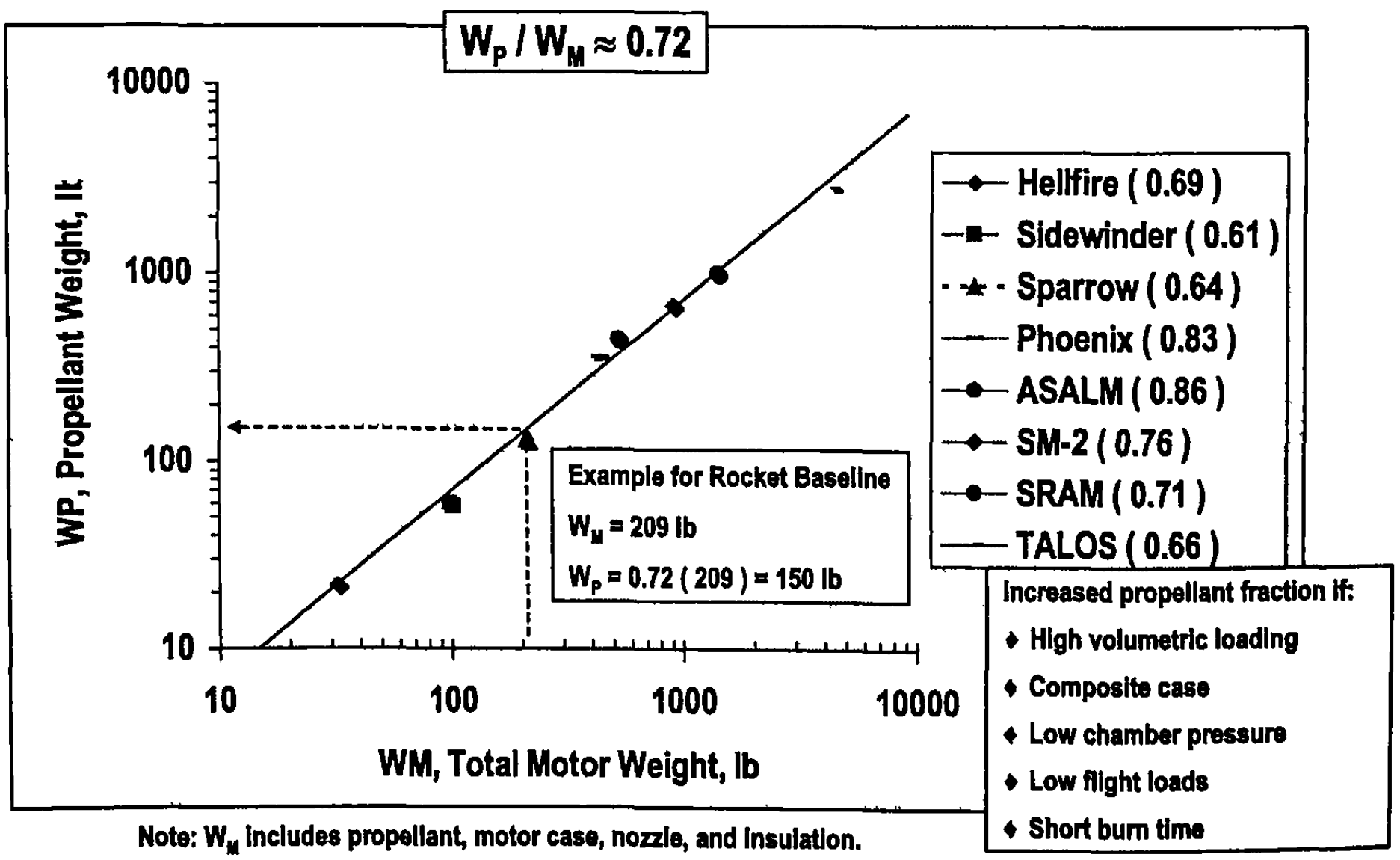

Fig. 4.30 Tactical missile propellant weight is about 72% of the rocket motor weight. Figure also in color section.

total motor weight includes the weight of the propellant, case, nozzle, and insulation. Note that the average propellant weight fraction is

$$W_P/W_M = 0.72 \tag{4.89}$$

A rocket motor with a high propellant weight fraction (i.e., greater than 72%) would tend to have high volumetric loading of propellant, a composite case, low chamber pressure, low flight loads, and a short burn time. Correspondingly, a rocket motor with a propellant weight fraction less than 72% would tend to have low volumetric loading, high chamber pressure, high flight loads, and a long burn time.

As an example, assume the rocket baseline, which has a motor weight $W_M = 209$ lb. The predicted propellant weight is $W_P = 0.72(209) = 150$ lb.

The rocket motor case is subjected to a variety of loads. The loads on the motor case include the internal pressure load produced during motor operation, thrust produced during motor operation, localized buckling, aerodynamic bending, thermal stress, and ground handling loads. Load conditions include handling, storage, launch platform carriage, ejection, and flight conditions.

The dominant load on the motor case is usually from the internal pressure. Figure 4.31 illustrates the motor case internal pressure and the resulting hoop stress and longitudinal stress. The stresses are a function of the internal pressure, case thickness, and the average radius. Hoop stress is the radial stress in the cylindrical section of the motor case. It is given by the equation

$$(\sigma_t)_{\text{HoopStress}} = pr/t \tag{4.90}$$

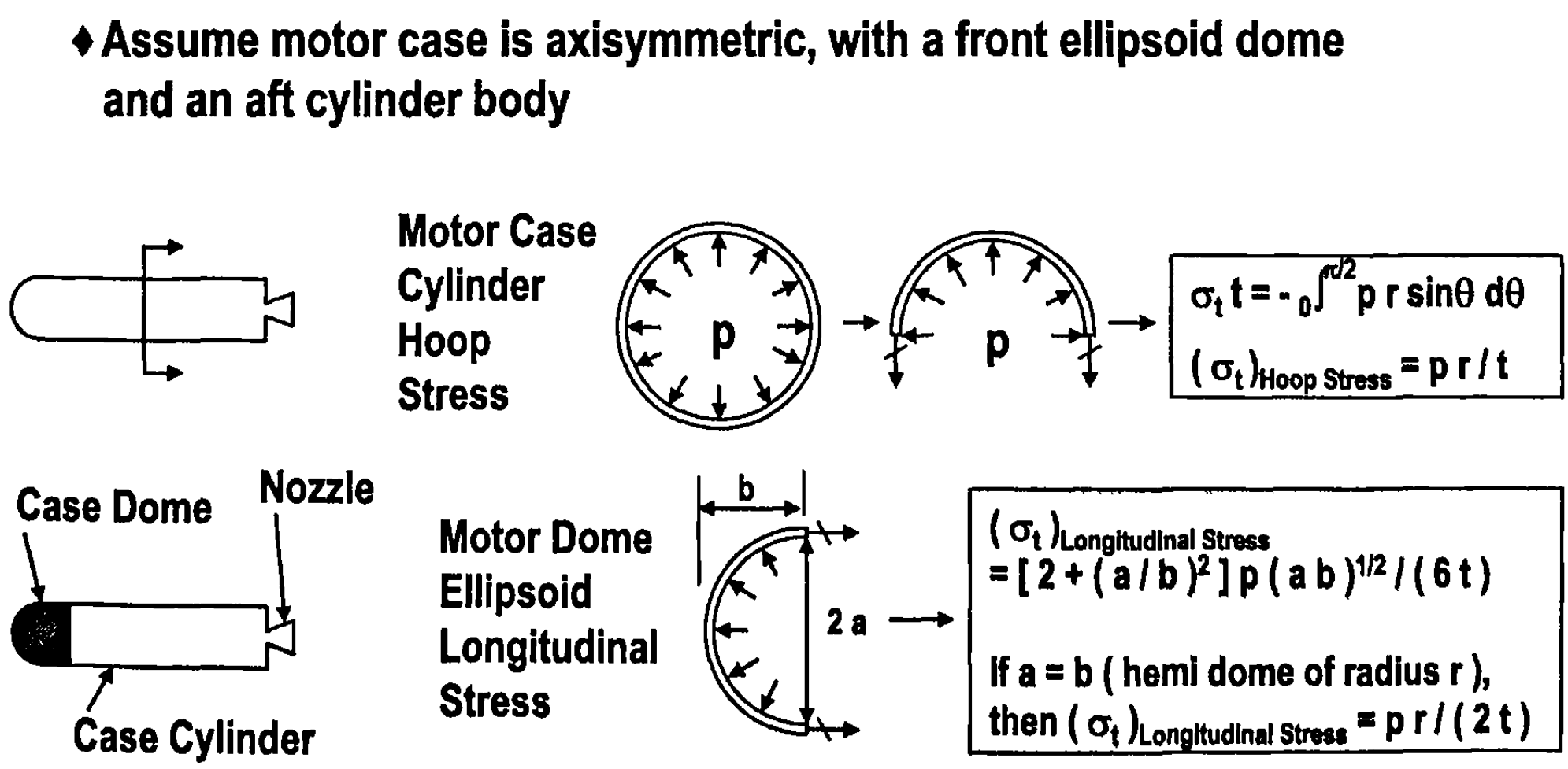

Fig. 4.31 Motor case weight is usually driven by stress from internal pressure.

The longitudinal stress is the tensile stress in the forward dome. For an ellipsoid dome, it is

$$(\sigma_t)_{\text{LongitudinalStress}} = [2 + (a/b)^2]p(ab)^{1/2}/(6t) \tag{4.91}$$

For a hemispherical dome ($a = b = r$), the equation is

$$(\sigma_t)_{\text{LongitudinalStress}} = pr/(2t) \tag{4.92}$$

Because tactical missiles are usually more volume limited than weight limited, most tactical missiles have an ellipsoid forward dome to reduce length. For a typical ellipsoid dome of $a/b = 3$, the thickness required for the dome longitudinal hoop stress is the same as the thickness required for the circular cylinder hoop stress.

A metal motor case has strength to react to both radial (internal pressure) stress and body bending stress. For a composite motor case, the case thickness that is set by the radial fibers to react the internal pressure usually also requires additional (longitudinal) fibers to react the body bending loads. However, because motor cases are usually driven much more by internal pressure than external loads, a composite motor case is usually much lighter.

The following example calculates the required thickness of the steel motor case of the rocket baseline as a function of pressure, FOS, radius, and the maximum allowable stress. The calculation shows the weight savings of a composite motor case over a steel motor case.

Step 1. Calculate maximum effective operating pressure (MEOP):

- $p_{\text{MEOP}} = p_{\text{Boost,RoomTemp}} \times e^{\pi_k \Delta T} \times$ (margin for ignition spike, welds, and other design uncertainty) (4.93)

- Assume rocket baseline: motor diam = 8 in; motor length = 55 in; ellipsoid dome with $a/b = 2$; $p_{\text{Boost,RoomTemp}} = 1769$ psi; $\pi_k = (\Delta p/\Delta T)/p_c = 0.14\%/°\text{F}$, where π_k = sensitivity of motor chamber pressure to temperature
- Assume hot day = 160° F, calculate $e^{\pi_k}\Delta^T = e^{0.0014\ (160-70)} = 1.134$. The uncertainty factor is 1.134, 1σ
- Assume that a 3σ uncertainty design margin is provided by $p_{\text{MEOP}} \approx 1769 \times 1.134^3 = 2{,}582$ psi

Step 2. Assume an ultimate FOS = 1.5.

Step 3a. First try the rocket baseline steel material for the motor case. The maximum allowable tensile ultimate stress of the 4130 heat-treated steel is $(\sigma_t)_{\text{ult}} = 190{,}000$ psi. Calculate:

- $t_{\text{Hoop}} = (\text{FOS}) \times p_{\text{MEOP}} \times r/\sigma_t = 1.5 \times 2582 \times 4.0/190{,}000 = 0.082\,\text{in}$ (4.94)

- $t_{\text{Dome}} = (\text{FOS}) \times p_{\text{MEOP}} \times (ab)^{1/2} \times [2 + (a/b)^2]/(6\sigma_t)$

  $= 1.5 \times 2582 \times [4 \times 2]^{1/2} \times [2 + 2^2]/[6 \times 190{,}000] = 0.058\ \text{in}$ (4.95)

- Weight $= W_{\text{Cylinder}} + W_{\text{Dome}} = \rho\pi d t_{\text{Hoop}} l + \rho(2\pi ab)t_{\text{Dome}} = 30.8 + 0.8 =$ 31.6 lb for a steel motor case (without attachments, aft dome, and insulation) (4.96)

Step 3b. Next, try an alternative composite graphite/epoxy material for the motor case. The maximum allowable stress in the graphite fiber is $\sigma_t =$ 450,000 psi yield/ultimate. Assume a 60% fiber/40% epoxy composite. Calculate:

- $t_{\text{Hoop}} = 1.5 \times 2582 \times 4.0/[450000(0.60)] = 0.057$ in radial fibers for internal pressure load (4.97)
- $t_{\text{Dome}} = 0.041$ in, for internal pressure load (4.98)
- Weight = 11.0 lb for composite case. Note that this is about one-third of the weight of the rocket baseline steel motor case. Attachments, an aft dome, and insulation would add additional weight.

We also need to add about 0.015 in of additional thickness of either longitudinal or helical wind fibers to react to body bending load.

Figure 4.32 shows the nondimensional structure weight of surfaces (e.g., wing, canard, tail.). The equation for the figure is

$$W_{\text{wing}}\sigma_{\max}^{1/2}/[\rho S N_{\max}^{1/2}] = [A(1+2\lambda)]^{1/2} \tag{4.99}$$

Assumptions are that the surface is composed of two panels, is monolithic (solid), has uniform loading, and its thickness is determined by bending moment stress. Note from the figure that a low aspect ratio wing with delta ($\lambda = 0$) planform is lightest weight. The equation for surface weight is

$$W_{\text{Surface}} = \rho S t_{\text{mac}} \tag{4.100}$$

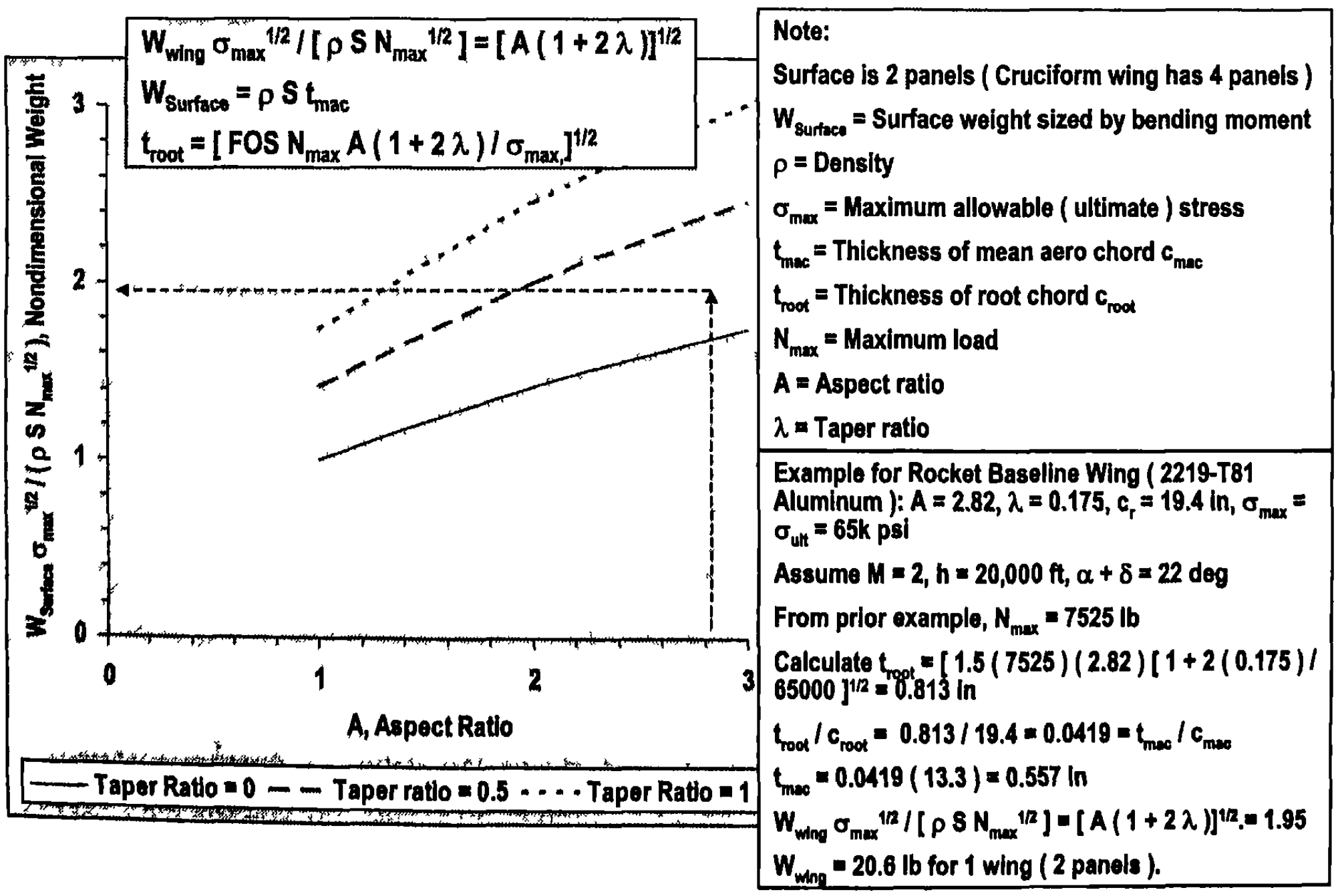

Fig. 4.32 A low aspect ratio delta wing allows lighter weight structure.

The terms in the above equation are ρ = material density, S = surface planform area, and t_{mac} = thickness of the mean aerodynamic chord (average thickness). The equation for surface root chord thickness is

$$t_{root} = (FOS)N_{max}A[1 + 2\lambda)/\sigma_{max}]^{1/2} \tag{4.101}$$

The terms in the above equation are FOS = factor of safety, N_{max} = maximum load, A = aspect ratio, λ = taper ratio, and σ_{max} = maximum stress.

An example calculation will be based on the rocket baseline wing. The wing material is 2219-T81 aluminum with a maximum allowable stress (ultimate stress) $\sigma_{max} = \sigma_{ult} = 65$ k psi and density $\rho = 0.101$ lb/in^3. The wing geometry has a surface area $=2.55$ ft$^2 = 367$ in^2, an aspect ratio $A = 2.82$, taper ratio $\lambda = 0.175$, and a root chord $c_{root} = 19.4$ in. Assume a flight condition of $M = 2$, 20,000 ft altitude, and $\alpha + \delta = 22$ deg. From a prior example, $N_{max} = 7525$ lb for this flight condition. Substitution gives

$$t_{root} = [1.5(7525)(2.82)[1 + 2(0.175)/65000]^{1/2} = 0.813 \text{ in} \tag{4.102}$$

Solving for the thickness ratio

$$t_{root}/c_{root} = t_{mac}/c_{mac} = 0.813/19.4 = 0.0419 \tag{4.103}$$

The average thickness of the mean aerodynamic chord is

$$t_{mac} = 0.0419(13.3) = 0.557 \text{ in} \tag{4.104}$$

Substituting into the wing weight equation, the weight for one surface with two panels is

$$W_{wing} = \rho S t_{mac} = 0.101(367)(0.557) = 20.6 \text{ lb} \tag{4.105}$$

The rocket baseline has two wings (cruciform), with a predicted weight of $2 \times 20.6 = 41.2$ lb.

4.14 Seeker Dome

Shown in Fig. 4.33 is a comparison of alternative dome materials for missile seekers. The dome materials are grouped based on their best applicability to multimode [radar frequency (RF)/IR], RF-only, and midwave IR-only seekers. Measures of merit are low dielectric constant, IR bandpass for combined midwave (3 to 5 μm)/long-wave (8 to 14 μm), high transverse strength, low thermal expansion, high erosion resistance, and high maximum temperature for short-duration flight. Dome materials that are especially suited for combined radar and infrared seekers are zinc sulfide and zinc selenide. Zinc sulfide and zinc selenide are also suitable for IR-only seekers. Zinc selenide has an advantage of high bandpass, with a transmission of about 70% over the wavelength from 0.8 μm to greater than 14 μm. Zinc sulfide has advantages in dielectric constant, transverse strength, and rain erosion. Ordinary zinc sulfide has a transmission of

Seeker Dome Material	Density (g / cm³)	Dielectric Constant	MWIR / LWIR Bandpass	Transverse Strength (10³ psi)	Thermal Expansion (10⁻⁶ / °F)	Erosion, Knoop (kg / mm²)	Max Short-Duration Temp (°F)
RF-IR Seeker							
Zinc Sulfide (Z_nS)	4.05	○ 8.4	● ◒	○ 18	○ 4	○ 350	○ 700
Zinc Selenide (Z_nS_e)	5.16	◡ 9.0	● ●	◡ 8	○ 4	○ 150	○ 600
Sapphire / Spinel	3.68	○ 8.5	● -	○ 28	○ 3	● 1650	● 1800
Quartz / Fused Silica (S_iO_2)	2.20	● 3.7	○ -	◡ 8	● 0.3	◒ 600	● 2000
Silicon Nitride (Si_3N_4)	3.18	◒ 6.1	◡ -	● 90	◒ 2	● 2200	● 2700
Diamond (C)	3.52	◒ 5.6	- ◡	● 400	● 1	● 8800	● 3500
RF Seeker							
Pyroceram	2.55	◒ 5.8	◡ -	○ 25	○ 3	◒ 700	● 2200
Polyimide	1.54	● 3.2	◡ -	○ 17	◡ 40	◡ 70	◡ 400
IR Seeker							
Mag. Fluoride (M_gF_2)	3.18	◒ 5.5	● ◡	◡ 7	◡ 6	◒ 420	◒ 1000
Alon ($Al_{23}O_{27}N_5$)	3.67	◡ 9.3	◒ -	◒ 44	○ 3	● 1900	● 1800
Germanium (Ge)	5.33	- 16.2	● ●	○ 15	○ 4	◒ 780	◡ 200

● Superior ◒ Above Average ○ Average ◡ Below Average - Poor

Fig. 4.33 Dome material is driven by the type of seeker and flight environment.

about 55% in the 3-to-5 μm range and about 65% in the 8-to-12 μm range. The transmission of zinc sulfide can be enhanced by a postdeposition hot isostatic press, which removes the zinc hydrides from the crystal lattice. The transmission of zinc sulfide for a single crystal-like structure is about 70% from 0.8 to 10 μm. Zinc sulfide is generally the multimode dome material of choice for supersonic missiles with Mach numbers up to 3. Zinc selenide is often selected for subsonic IR guided missiles. For Mach number greater than 3, new materials are required for multimode seekers. Candidate high-temperature materials include spinel/sapphire, quartz/fused silicon, silicon nitride, and diamond. A disadvantage is higher cost than zinc sulfide and zinc selenide. The high-temperature materials are also suitable for RF-only and millimeter wave (mmW) only seekers.

Diamond dome material is under development for missile defense applications. For a solid diamond dome, the material cost, which is about $200,000/lb, is very high. In addition to high material cost, diamond dome assembly cost is high. Diamond domes must be assembled as a built-up mosaic because the present manufacturing processes produce relatively small diamonds. Diamond can also be used as a coating over a conventional dome to provide erosion resistance. The coating can be deposited through a chemical vapor deposition (CVD) process.

For RF-only seekers, two popular radome materials are pyroceram and polyimide. Pyroceram is commonly used in supersonic missiles, such as Sparrow and the Patriot PAC-2. Polyimide radomes are used on relatively low speed,

low-cost missiles such as the mmW Brimstone. Polyimide radomes have excellent dielectric characteristics.

For midwave infrared (MWIR) only seekers, additional dome materials include magnesium fluoride and Alon. Although both are suitable for high supersonic missiles, Alon is less susceptible to rain and dust erosion and is capable of operating at higher Mach number. Germanium, another candidate material, is most suitable for subsonic/low-supersonic missiles with MWIR long-wave infrared (LWIR) seekers, such as AGM-130. Germanium has more than 50% transmission over the wavelength from 1.8 to 23 μm. Multispectral dome materials may also be used for MWIR-only and RF-only seekers. Mentioned previously, zinc sulfide is also suitable for MWIR-only seekers at supersonic Mach number. Spinel or sapphire domes may be used with MWIR-only seekers at high-supersonic/low-hypersonic Mach numbers. An example of a missile with a sapphire dome for its MWIR seeker is ASRAAM.

The required weight of a radome may be set by the thickness required for efficient transmission of the radar signal, rather than by structural design or handling considerations. As a result, a missile radome may have a structure FOS of 2 or more.

The weight of a dome is a function of the material density ρ, wetted or surface area S_{wet}, and thickness t. For a monolithic dome with constant thickness and neglecting the weight of the nose cap and aft attachment ring, the equation for dome weight for an optimum transmission thickness is

$$W_{\text{OptTrans}} = \rho S_{\text{wet}} t_{\text{OptTrans}} \tag{4.106}$$

Transmission efficiency of the radar signal through a radome is a function of the radome thickness t, the radar seeker wavelength in air λ_0, the dielectric constant ε, and the incidence angle of the radar signal with the radome surface θ_i. The equation for radome thickness based on optimum transmission is

$$t_{\text{OptTrans}} = 0.5n\lambda_0/(\varepsilon - \sin^2\theta_i)^{1/2} \tag{4.107}$$

There is a cyclic relationship ($n = 1, 2, \ldots$) of good transmission efficiency with radome thickness. For very low values of n (e.g., $n < 0.1$) there is good transmission efficiency, but the radome usually does not have sufficient structural integrity. Except for very high dynamic pressure or very high bending moment, the $n = 1$ solution for the optimum thickness usually results in an over designed structure. Poor transmission efficiency occurs in the cyclic relationship of $n = 0.5, 1.5, \ldots$ For a nonoptimum thickness and a high value of the dielectric constant, the transmission loss can be more than 60%.

Shown in Fig. 4.34 is the geometric relationship of θ_i with seeker look angle δ and radome surface angle θ. The equation is

$$\theta_i = 90 \text{ deg} - \delta - \theta \tag{4.108}$$

From an electromagnetic point of view, a hemispheric radome would be ideal. Because a hemispherical radome has zero incidence angle for all seeker look

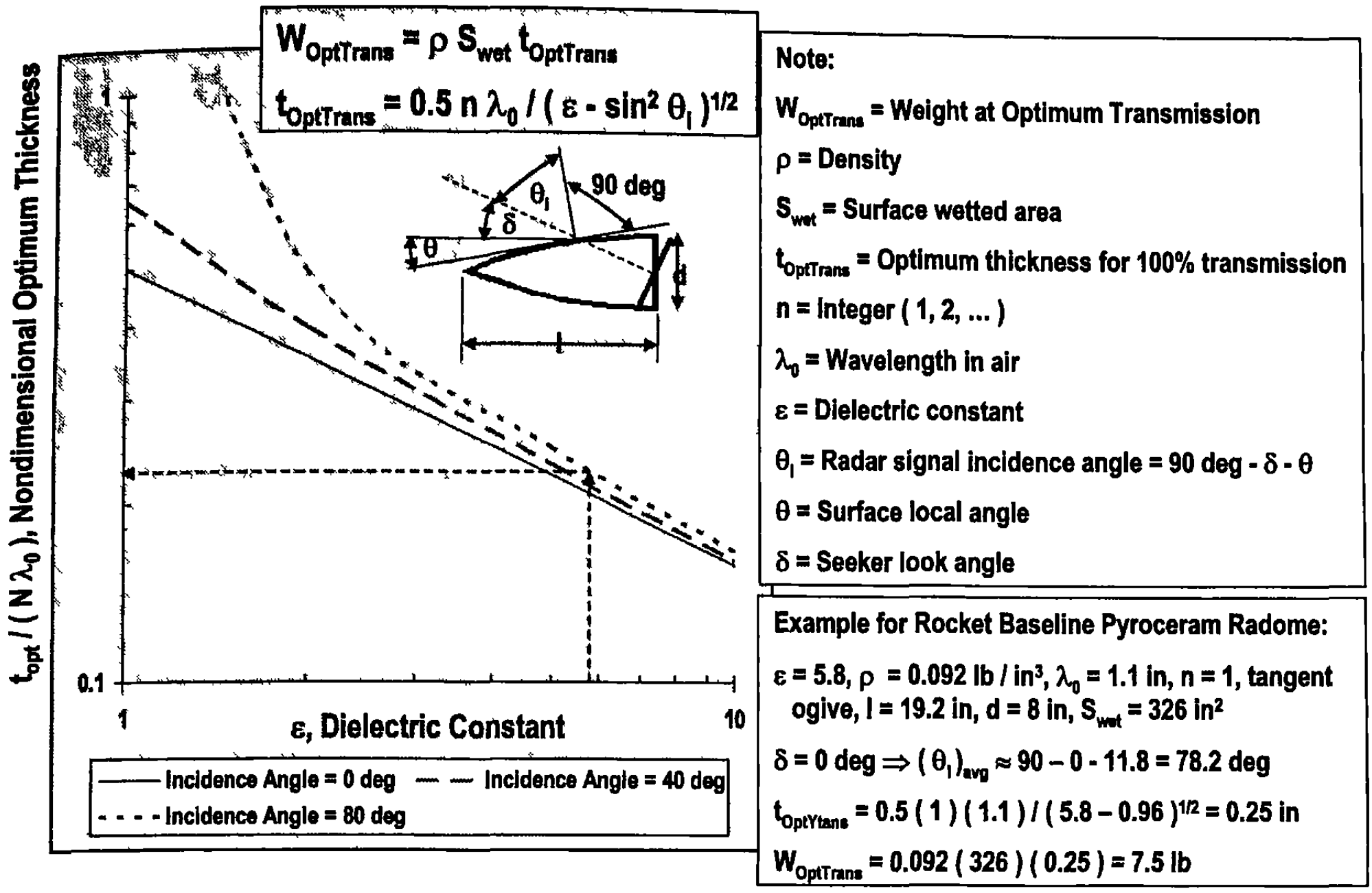

Fig. 4.34 Radome weight may be driven by the optimum thickness required for efficient transmission.

angles, the optimum thickness is constant. For a hemispherical radome with an ideal dielectric constant of $\varepsilon = 1$, the ideal thickness is equal to one-half the radar wavelength.

The application of a hemispherical radome is usually limited to subsonic missiles because of high drag at supersonic Mach number. A high-fineness radome is usually required at supersonic Mach number. A disadvantage of a high-fineness radome is the radar incidence angle changes with seeker look angle, resulting in a nonoptimum thickness for a typical low-cost missile radome, which is constant thickness. An optimized high-fineness radome requires expensive prescription tailoring, with smaller thickness near the nose and greater thickness near the airframe attachment.

As an example, the radome material of the rocket baseline missile is pyroceram. Pyroceram has a dielecric constant $\varepsilon = 5.8$ and a density $\rho = 0.092$ lb/in^3. The geometry of the baseline radome is a tangent ogive, with a length l, diameter d, and wetted area S_{wet} of 19.2 in, 8 in, and 326 in^2, respectively. The baseline seeker is an X-band radar seeker with a frequency of $f = 10$ GHz and a wavelength in air of $\lambda_0 = 1.1$ in. For a seeker looking straight ahead ($\delta = 0$ deg), the average incidence angle $(\theta_i)_{avg} = 90 - \delta - \theta \approx 90 - 0 - \tan^{-1}[(d/2)/l] = 90 - 0 - \tan^{-1}[(8/2)/19.2] = 90 - 0 - 11.8 = 78.2$ deg. Substituting into the optimum thickness equation $t_{OptTrans} = 0.5n\lambda_0/(\varepsilon - \sin^2\theta_i)^{1/2}$, the smallest thickness with efficient transmission ($n = 1$) results in

$$t_{OptTrans} = 0.5(1)(1.1)/(5.8 - 0.96)^{1/2} = 0.25 \text{ in} \tag{4.109}$$

Substituting into the weight equation, the weight of the optimum transmission thickness radome is

$$W_{\text{OptTrans}} = \rho S_{\text{wet}} t_{\text{OptTrans}} = 0.092(326)(0.25) = 7.5 \text{ lb} \tag{4.110}$$

Note that required radome thickness for high transmission efficiency should be checked to see if there is sufficient thickness for structural integrity. If additional thickness is required for structural integrity, then the next largest value of n (e.g., $n = 2$) should be used to provide good transmission efficiency combined with structural integrity.

4.15 Power Supply and Actuators

Missile electrical power supply provides the electrical energy required for the seeker, autopilot, navigation system, flight control actuators, and fuses. Shown in Fig. 4.35 is a comparison of the alternative approaches of a generator, lithium battery, and a thermal battery for electrical power supply. Measures of merit are the storage life (typically a maximum of about 20 years), cost, weight per energy in kg/kW-s, weight per power in kg/kW, and voltage stability. The weight per energy and weight per power are typical values based on the relatively small power supply that is appropriate for missile applications. As an example, because missiles have a short time of flight, the weight of their batteries is relatively large because of the relatively larger cell hardware.

$$W = W_E E + W_P P$$

Measure of Merit	Power Supply		
	Generator	Lithium Battery	Thermal Battery
Storage Life	●	◡	●
Cost	◡	○	●
W_E, Weight / Energy (kg / kW-s)	● 0.0007	◒ 0.0012	◡ 0.0125
W_P, Weight / Power (kg / kW)	◒ 1.4	◡ 1.5	● 0.3
Voltage Stability	◒	●	◡

● Superior ◒ Above Average ○ Average ◡ Below Average

Example for Thermal battery: If E = 900 kW–s, P = 3 kW $\Rightarrow$ $W = W_E E + W_P P = 0.0125\,(900) + 0.3\,(3) = 12.2$ kg

Note: Generator provides highest energy with light weight for long time of flight (e.g., cruise missile).

Lithium battery provides nearly constant voltage suitable for electronics. Relatively high energy with light weight.

Thermal battery provides highest power with light weight (may be required for actuators).

Fig. 4.35 Missile electrical power supply alternatives.

Power supply must accommodate both the total energy required and the instantaneous power required. The weight of the power supply correlates with the equation

$$W = W_E E + W_P P \tag{4.111}$$

In the above equation W_E is the weight per energy and W_P is the weight per power. As an example, the weight of a thermal battery for a missile requiring 3 kW of power for 300 s of flight time is

$$W = W_E E + W_P P = 0.0125(900) + 0.3(3) = 12.2 \text{ kg} \tag{4.112}$$

For a long-range airbreathing cruise missile, a generator is usually the best approach for power supply. The generator can be efficiently powered by either the airflow through the inlet or, in the case of a turbojet engine, driven directly by the shaft of the turbojet.

For a shorter range tactical missile (e.g., time of flight less than 10 m), the electrical power to the seeker and autopilot may be best provided by a lithium battery. A lithium battery provides the nearly constant voltage required by electronics. A lithium battery is also efficient for energy storage; it provides relatively high power at light weight. For a short-duration time of flight, a lithium battery would be lighter than a generator. Also note that because the missile is used only once, the battery may not need to be rechargeable. However, a rechargeable battery is desirable for periodic maintenance test surveillance. The weight per energy and the weight per power values shown in the figure are based on relatively high performance lithium ion polymer batteries. This type of lithium battery is attractive for missile application because in addition to its high performance, the extrusion process adapted from the plastics industry results in relatively low cost.

For a shorter range tactical missile, the electrical power for electromechanical (EM) flight control actuators is usually best provided by a thermal battery. A thermal battery efficiently provides the high power density required by actuators. Another advantage is that it can be stored almost indefinitely. An electrical energy impulse from a squib activates the thermal battery by igniting the pyrotechnic materials inside the battery, which melt the electrolyte. Most thermal batteries use an iron disulfide cathode and a lithium alloy anode (e.g., lithium/iron sulfide).

A typical tactical missile may have two batteries—a lithium battery providing the nearly constant voltage required by the electronics and a thermal battery providing the high power required by the flight control actuators.

Flywheels, capacitors, and fuel cells are other potential sources of power supply. However, their technologies are relatively immature and they have not yet been applied to operational missiles.

Shown in Fig. 4.36 is a comparison of the missile actuator alternatives of electromechanical (EM), cold gas pneumatic, and hydraulic. EM actuators are attractive because they have superior reliability and weight and do not have any serious weaknesses. EM actuators are usually the best choice for most

$W = W_T T_S$

Measure of Merit	EM	Cold Gas Pneumatic	Hydraulic
W_T, Weight / Stall Torque (lb / in-lb)	● 0.0025	◡ 0.0050	○ 0.0034
Rate (deg / s)	○ Up to 800	◡ Up to 600	● Up to 1000
Bandwidth (Hz)	○ Up to 40	◡ Up to 20	● Up to 60
Reliability	●	○	◡
Cost	○	●	◡

● Superior ◒ Above Average ○ Average ◡ Below Average

Note:

- Actuation system weight based on four actuators.
- Cold gas pneumatic actuation weight includes actuators, gas bottle, valves, regulator, and supply lines.
- Hydraulic actuation weight includes actuators, gas generator or gas bottle, hydraulic reservoir, valves, and supply lines.
- Stall torque ≈ 1.5 maximum hinge moment of single panel.

Schematic of Cold Gas Pneumatic Actuation

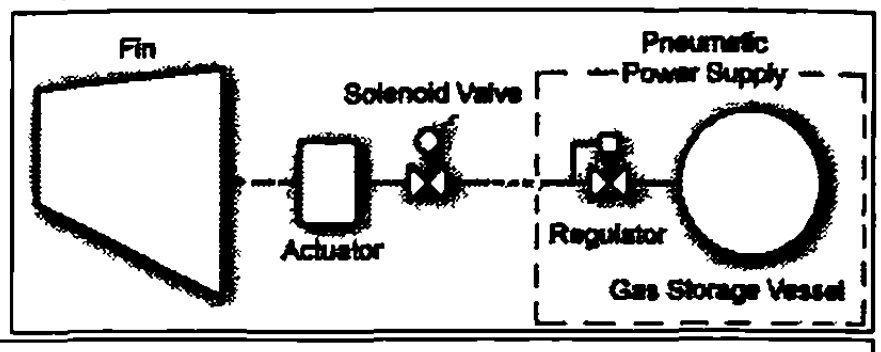

Example weight for rocket baseline hydraulic actuation at Mach 2, 20,000 ft altitude with max control deflection of wing (δ = 13 deg) ⇒ Hinge moment of one panel = 11,500 in-lb. T_S = 1.5 (11500) = 17,250 in-lb ⇒ $W = W_T T_S$ = 0.0034 (17250) = 59 lb

Fig. 4.36 Electromechanical actuators are lightweight and reliable.

tactical missiles. A cold gas pneumatic actuation system is lowest cost but has disadvantages of weight per torque (W_T), rate, and bandwidth. In the bottom right section of the figure is a schematic of the components of a cold gas pneumatic actuation system, which includes the actuators, gas bottle, valves, regulator, and supply lines. Cold gas pneumatic actuators are most applicable to small, low-cost, and lower performance missiles. Higher performance warm gas (approximately 1000° F) and hot gas (approximately 5000° F) pneumatic actuation systems have also been developed but have seen much less application than cold gas pneumatic because of their higher cost. The SM-3 Standard Missile third stage rocket motor (TSRM) has a warm gas control actuation system. Finally, a hydraulic actuation system has superior rate and bandwidth but is higher cost and has lower reliability. The components of a hydraulic actuation system include the actuators, gas generator or gas bottle pressurization, hydraulic reservoir, valves, and supply lines. Hydraulic actuators are most applicable to large, high-cost, high-performance missiles.

The weight of the actuation system is given by the equation

$$W = W_T T_S \tag{4.113}$$

In the above equation W_T is the weight per stall torque and T_S is the stall torque. The equation is based on an actuation system with four actuators. As a design practice, the stall torque should be about 50% larger than the maximum hinge moment to allow sufficient design margin and bandwidth.

As an example, the rocket baseline missile has a hydraulic actuation system. As shown previously, at a burnout condition of Mach 2 and 20,000 ft altitude, the

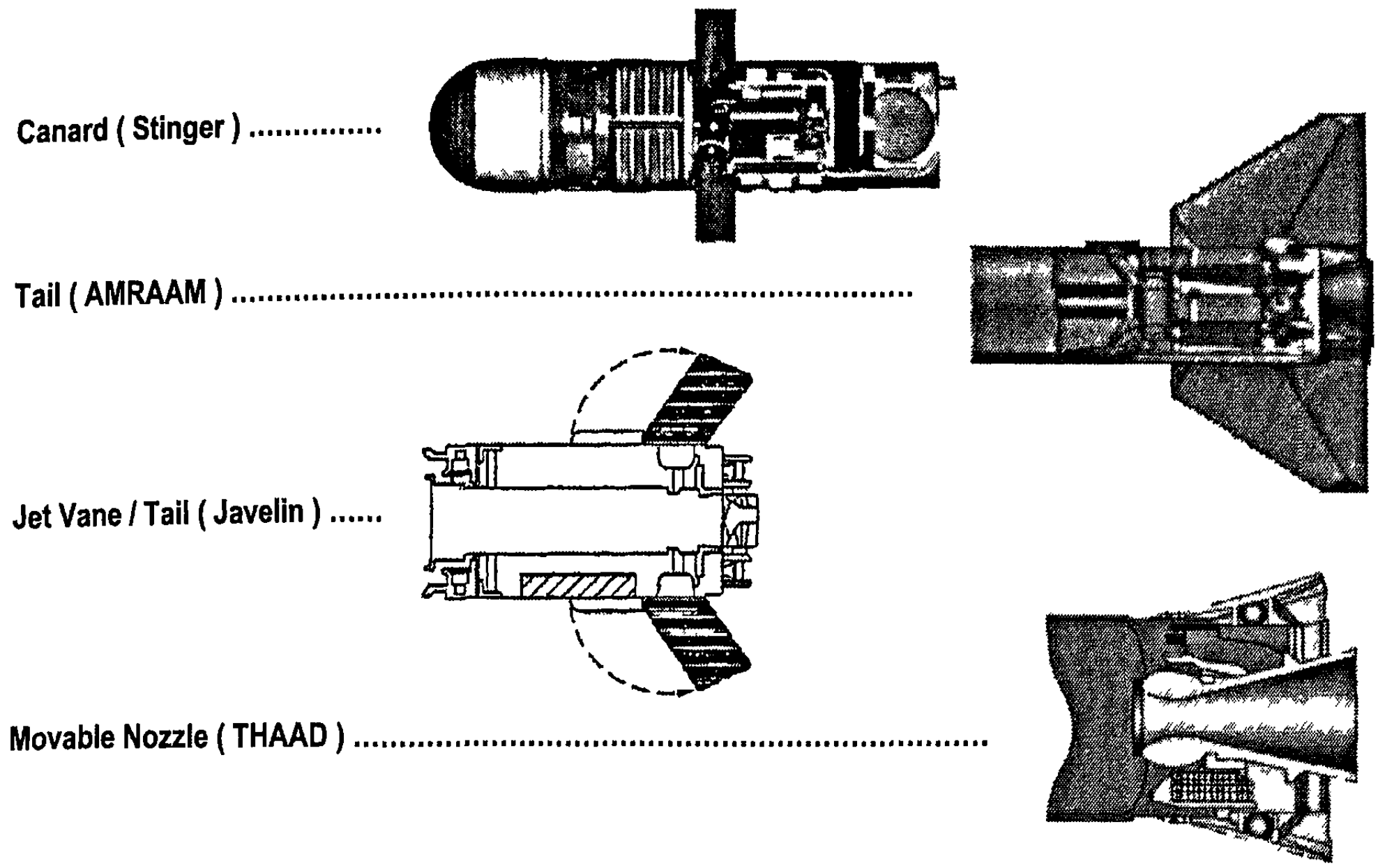

Fig. 4.37 Examples of electromechanical actuator packaging.

maximum hinge moment for a maximum control deflection of $\delta = 13$ deg plus an angle of attack $\alpha = 9$ deg is a total of 23,000 in-lb for the two panels that comprise the wing. The hinge moment on a single panel is $23000/2 = 11{,}500$ in-lb. The design stall torque of the actuator is

$$T_S = 1.5(11{,}500) = 17{,}250 \text{ in-lb} \tag{4.114}$$

Substituting into the weight equation for a hydraulic actuation system gives

$$W = W_T T_S = 0.0034(17{,}250) = 59 \text{ lb} \tag{4.115}$$

Figure 4.37 shows examples of the packaging of EM actuators. The nozzle blast tube is an efficient location for packaging flight control actuators. In the figure, note the inboard profile of the canard actuator packaging of Stinger compared with the aft control actuator packaging for the tail control AMRAAM, jet vane/tail control Javelin, and the movable-nozzle TVC THAAD. The canard actuator packaging of Stinger increases the length of the missile, while aft actuator packaging around the blast tubes of AMRAAM, Javelin, and THAAD can be accommodated with less impact on missile length.

4.16 Summary

This chapter addressed design methods, manufacturing processes, design considerations, and the technologies for lightweight, low-cost tactical missiles.

Design methods included missile system weight prediction; center-of-gravity and moment-of-inertia prediction; FOS, aerodynamic heating prediction; and the weight considerations for structure, dome, propulsion, insulation, power supply, and actuators. Manufacturing processes included low parts count/ low-cost processes such as precision castings, vacuum-assisted resin transfer molding, pultrusion, extrusion, and filament winding. Design considerations included airframe material alternatives, insulation material alternatives, seeker dome material alternatives, power supply and actuator alternatives, thermal stress, and aerodynamic heating. Finally, new technologies were identified for lightweight missiles. These include micromachined electromechanical systems (MEMS) diagnostic technology, composites, titanium alloys, high-density insulation, high energy and power density power supply, and high torque density actuators.

Problems

4.1. Propulsion system and structure weight are driven by f_____ o_ s_____ requirements.

4.2. For a ballistic range greater than about 200 nm, a t__ s____ missile is usually lighter weight.

4.3. Tactical missile weight is proportional to v_____.

4.4. Subsystem d_____ for tactical missiles is about 0.05 lb/in^3.

4.5. Modeling weight, balance, and moment of inertia are based on a buildup of s_____.

4.6. Missile structure factor of safety for free flight is usually about 1.25 for ultimate loads and about 1.10 for y____ loads.

4.7. Manufacturing processes that can allow low parts count include vacuum-assisted resin transfer molding of composites and c_____ of metals.

4.8. Low-cost airframe materials are usually based on aluminum and steel while lightweight airframe materials are usually based c_____ materials.

4.9. Graphite fiber has high strength and high m_____ o_ e_____.

4.10. The recovery factors of stagnation, turbulent boundary layer, and laminar boundary layer are 1.0, 0.9, and ___ respectively.

4.11. The most popular types of insulation for temperatures greater than 4000 R are charring insulators based on p_____ composites.

4.12. Tactical missiles experience transient heating, and with increasing time the temperature approaches the r_____ temperature.

4.13. The inner wall temperature is nearly the same as the surface temperature for a t_____ t___ structure.

4.14. A thermally thick surface is a good i_____.

4.15. A low-conductivity structure is susceptible to thermal s_____.

4.16. The minimum gauge thickness is often set by the m_____ process.

4.17. A very thin wall structure is susceptible to localized b_____.

4.18. Ejection loads and flight control loads often result in large b_____ moment.

4.19. An approach to increase the tactical missile propellant/motor weight fraction over the typical value of 72% would be c_____ motor case.

4.20. The required rocket motor case thickness is often driven by the combustion chamber p_____.

4.21. A low aspect ratio delta wing has reduced w_____.

4.22. For low-speed missiles, a popular infrared dome material is z___ s_____.

4.23. A thermal battery provides high p____.

4.24. The most popular type of actuator for tactical missiles is an e_____ actuator.

5
Flight Performance Considerations in Tactical Missile Design

5.1 Introduction

This chapter addresses the conceptual design modeling and prediction of missile flight performance. It is oriented toward predicting the missile flight range, velocity, time to target, and off-boresight maneuvering. Flight performance considerations include the flight performance envelope, equations of motion modeling, driving parameters, trajectory shaping, intercept lead angle and velocity, and comparison with requirements. Analytical prediction methods are developed for alternative modes of flight, including cruise (Breguet range equation), steady state, turning (turn radius and turn rate prediction), coast, ballistic, and boost.

Figure 5.1 illustrates the next step in the missile configuration synthesis process, flight trajectory evaluation. Evaluations of the forward and off-boresight flight trajectories are conducted to determine maximum/minimum range envelopes, velocity, time to target, off-boresight envelope, and maneuverability limits. Alternative flight trajectories are compared with the flight performance requirements to develop an effective flight trajectory.

5.2 Flight Performance Envelope

The missile flight envelope may be characterized by the maximum and the minimum flight ranges in forward and off-boresight flight. In the example shown in Fig. 5.2, the missile has a large off-boresight capability, up to $+/-180$ deg off boresight. Illustrated in the figure are the maximum and minimum ranges for straight-ahead flight and off-boresight flight. The maximum coast range for a supersonic missile in straight-ahead flight is often driven by the zero-lift drag coefficient. A supersonic missile at 1 g and at low altitude flies near zero angle of attack. The maximum effective range may also be established by the speed and maneuverability required for an intercept. It was discussed previously that higher missile speed and higher maneuverability are required against a maneuvering target. The maximum effective range may also be set by miss distance. The maximum effective range is degraded by the miss distance from a maneuvering target. Another consideration for the maximum effective range is the intercept altitude. A boost-coast rocket usually has lower velocity and maneuverability for a high-altitude intercept than

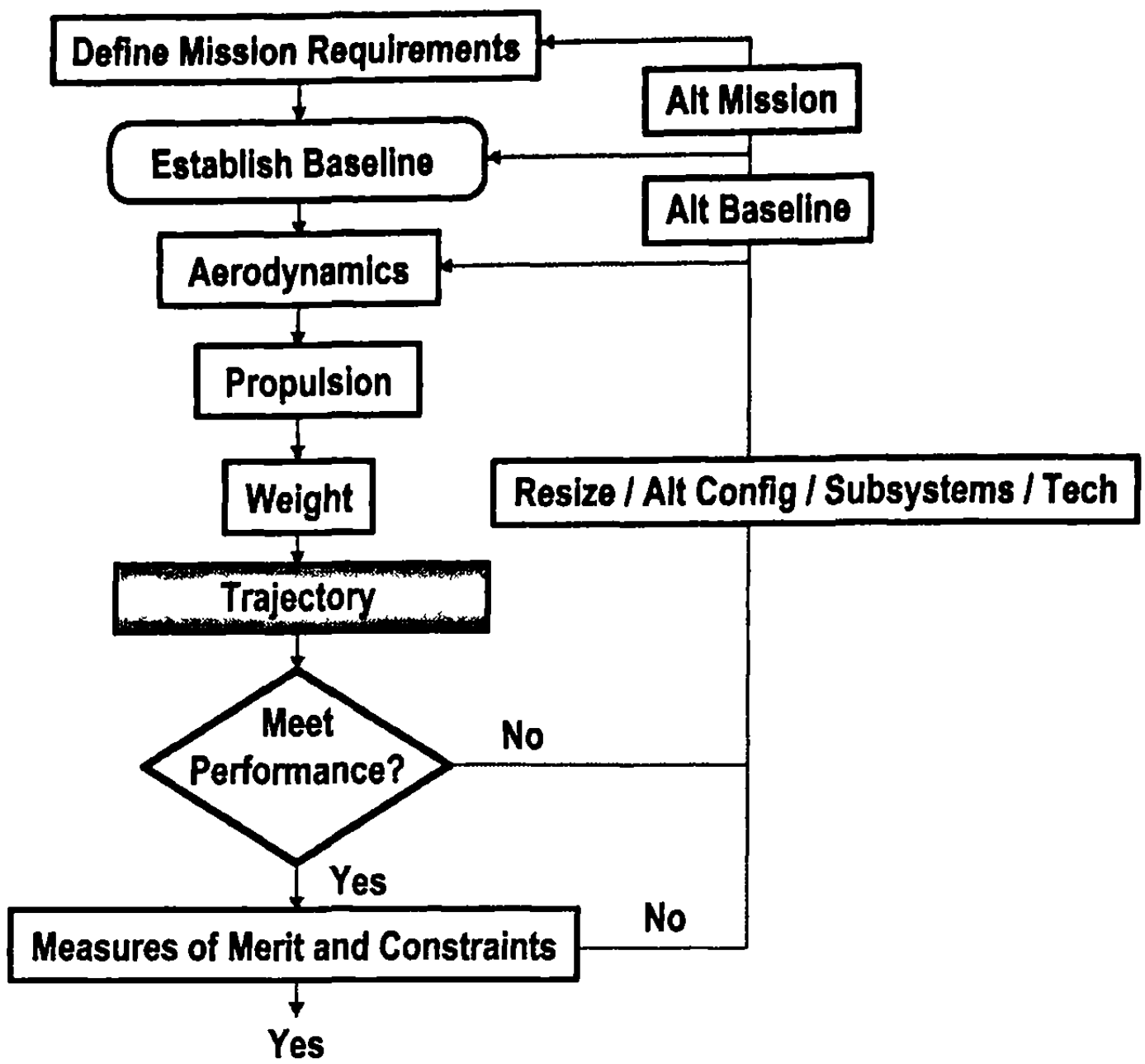

Fig. 5.1 Missile concept synthesis requires evaluation of alternatives and iteration.

for a low-altitude intercept. Other constraints on the maximum range include the fire control system maximum range, fire control system off-boresight capability, time-of-flight limits for the missile (e.g., battery duration), and the minimum closing velocity to arm the warhead and capture an evading target. The fire control system range should usually be at least twice the missile range.

For the off-boresight envelope, the minimum range may be established by the maneuverability required to correct an initial heading error. For a beam flight

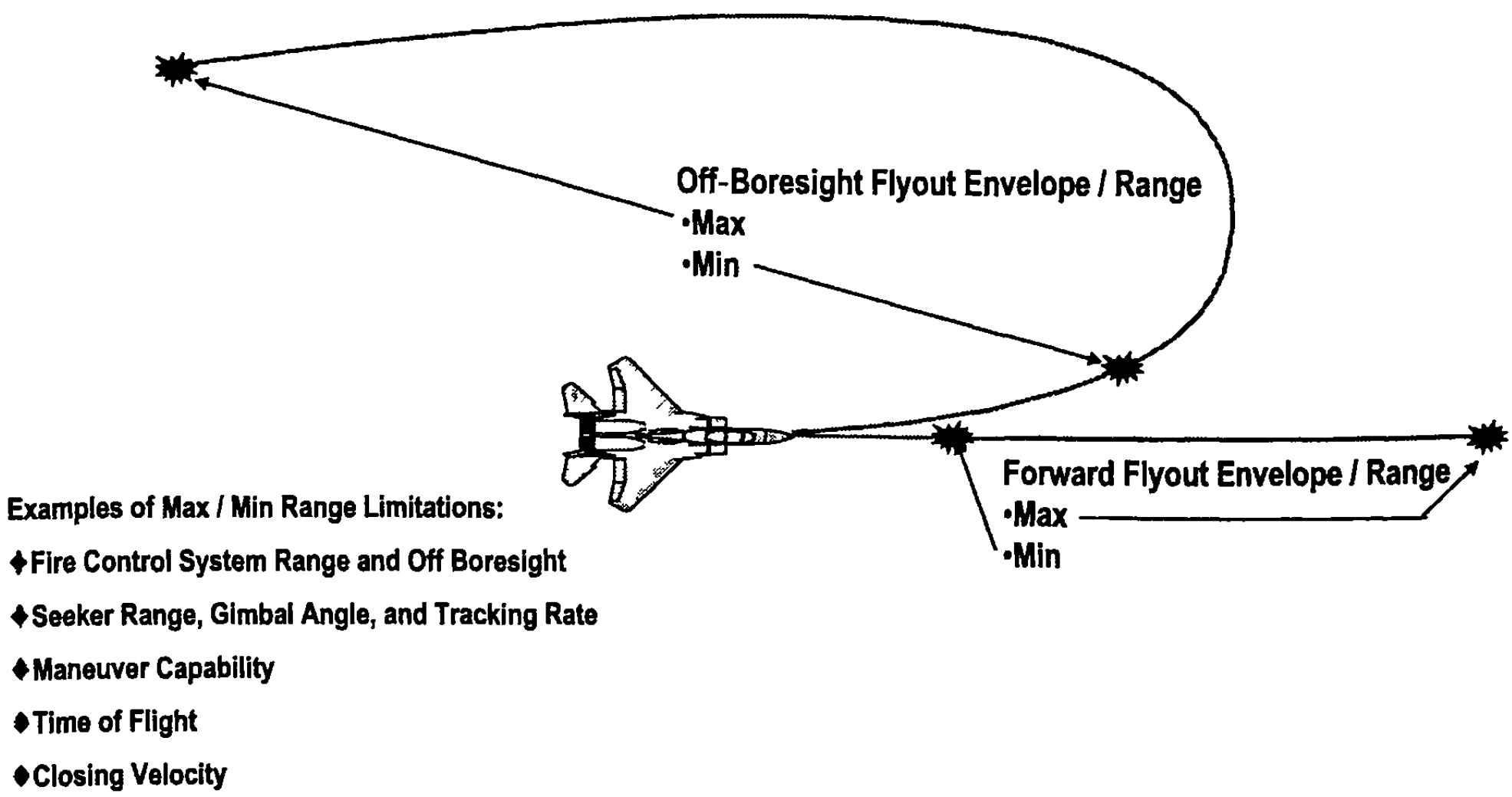

Fig. 5.2 Missile flight envelope should have a large maximum range, small minimum range, and large off boresight.

trajectory to the side of the launch platform, the missile must operate at high angle of attack to rapidly turn the velocity vector to 90 deg off boresight. The time to arm the warhead based on establishing a safe standoff from the launch platform may also set the minimum range. Other limitations are the seeker gimbal angle and tracking rate, which may set the minimum range in off-boresight maneuvers. The maximum/minimum range for a beam intercept may be driven by a combination of parameters, such as the seeker gimbal angle and tracking limits, maneuverability, stability, and the drag due to lift. For flight to the rear of the launch platform, the missile must make a heading change of 180 deg. The drivers for a rear intercept may be a combination of parameters such as zero-lift drag and the drag due to lift.

If practical, the missile should have a large maximum range, a small minimum range, and a large off-boresight capability. This provides robustness for long-range, short-range, and off-boresight targets.

5.3 Equations of Motion Modeling

The flight trajectory evaluation activity during missile concept synthesis requires consideration of the degrees of freedom (DOF) to be simulated. Figure 5.3 compares the simulation modeling DOF that are usually used in conceptual design with the DOF that are appropriate for preliminary design. As discussed previously, conceptual design is the rapid evaluation of a large range of alternatives. It requires that the design methods be fast, be easy to use, and have a broad range of applicability. The simplest model, often acceptable for the conceptual design of high-speed missiles, is one DOF. One-DOF modeling requires only the zero-lift drag coefficient, thrust, and weight.

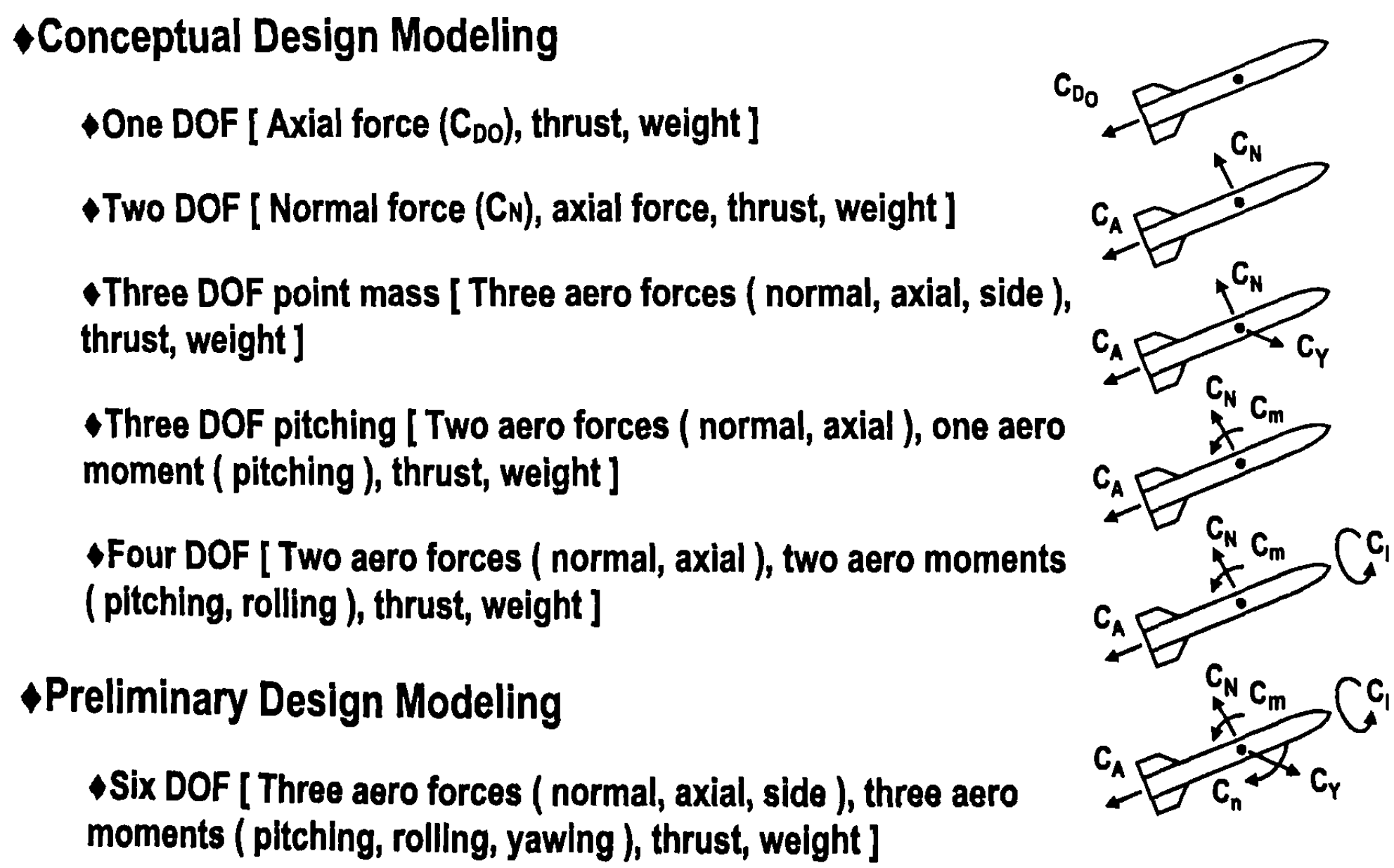

Fig. 5.3 Conceptual design modeling versus preliminary design modeling.

Analytical equations can be used to model a one DOF simulation. Other models used for conceptual design are two-DOF point-mass modeling; three DOF, with point-mass modeling; three DOF, with pitch modeling; and four DOF, with roll modeling. In the four-DOF roll modeling the normal force, axial force, pitching moment, rolling moment, thrust, and weight are modeled for a rolling-airframe missile. Finally, missile simulation during preliminary design is usually modeled in six DOF. The six-DOF simulation includes three aerodynamic forces (normal force, axial force, side force), three aerodynamic moments (pitching moment, rolling moment, yawing moment), thrust, and weight. For a thrust vector control or a reaction jet control missile, the propulsion vector forces and moments must be included. Missile DOF greater than six DOF describe the structure-bending modes. Because most tactical missiles are relatively stiff, modeling at greater than six DOF is usually not required for aerodynamic control missiles but may be required for impulse reaction jet control missiles.

The one-DOF coast equation is compared in Fig. 5.4 with the more accurate two-DOF coast equation. Results are for the rocket baseline missile coasting in horizontal flight at Mach 2 and 20,000 ft altitude, following motor burnout. Note that the one-DOF coast equation for the rocket baseline has less than 10% error in the deceleration $\dot{V}$ for angles of attack up to about 3 deg. For the rocket baseline, the angle of attack for the example 1-*g* flight is only 0.3 deg. The one-DOF coast equation provides sufficient accuracy for conceptual design assessment of the 1-*g* flight trajectory of the rocket baseline missile. Other high-performance missiles operating at high dynamic pressure could also be evaluated with sufficient accuracy using the one-DOF coast equation.

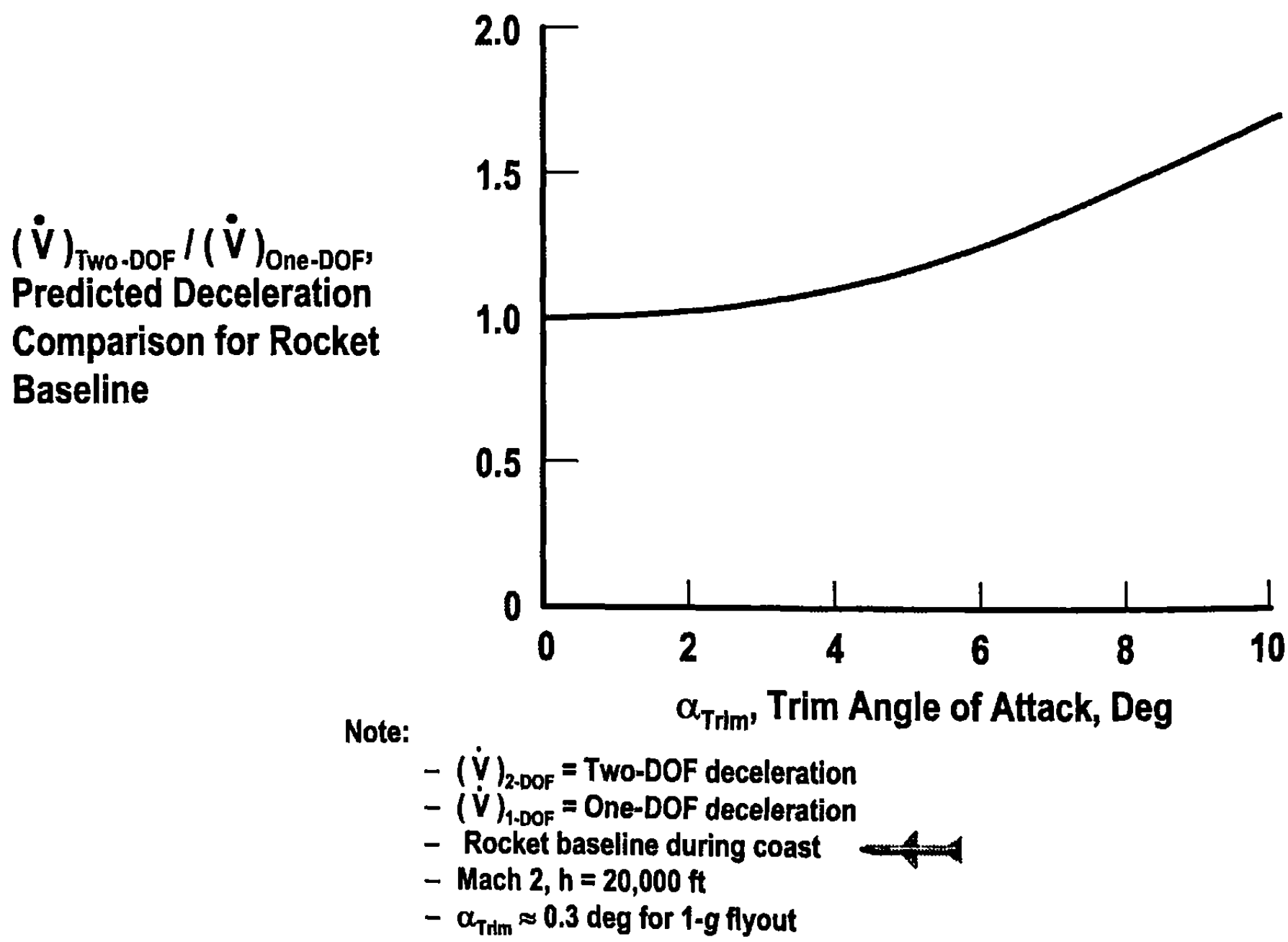

Fig. 5.4 The one-DOF coast equation may have good accuracy near zero angle of attack.

5.4 Driving Parameters for Flight Performance

It is instructive to examine the equations of motion for missile design drivers. Figure 5.5 shows the simplified equations of motion for three DOF with pitch modeling. Aerodynamic control is assumed. The equations describe the missile angular acceleration $\theta^{\cdot\cdot}$, rate of change in the flight path angle $\gamma^{\cdot}$, and the rate of change in the velocity $V^{\cdot}$. The configuration sizing implication from examining the angular acceleration equation shows the importance of control effectiveness

$$I_y\theta^{\cdot\cdot} \approx I_y\alpha^{\cdot\cdot} \approx qS_{\mathrm{Ref}}dC_{m_\alpha}\alpha + qS_{\mathrm{Ref}}dC_{m_\delta}\delta \tag{5.1}$$

High control effectiveness is provided by high pitching moment control effectiveness C_{m_δ}, low static stability C_{m_α}, small moment of inertia I_y, and large dynamic pressure q. A small moment of inertia is a characteristic of a lightweight missile. The second equation shows the design drivers for missile maneuverability

$$(W/g_c)V\gamma^{\cdot} \approx qS_{\mathrm{Ref}}C_{N_\alpha}\alpha + qS_{\mathrm{Ref}}C_{N_\delta}\delta - W\cos\gamma \tag{5.2}$$

High maneuverability is the capability to make large and rapid changes in the flight path angle. This occurs for large normal force coefficient C_N, lightweight W, low velocity V, and high dynamic pressure q. Large C_N is achievable through large values of C_{N_α}, α, C_{N_δ}, and δ. The preceding equation describes vertical climb maneuvers. The term $W\cos\gamma$ is the weight component in the

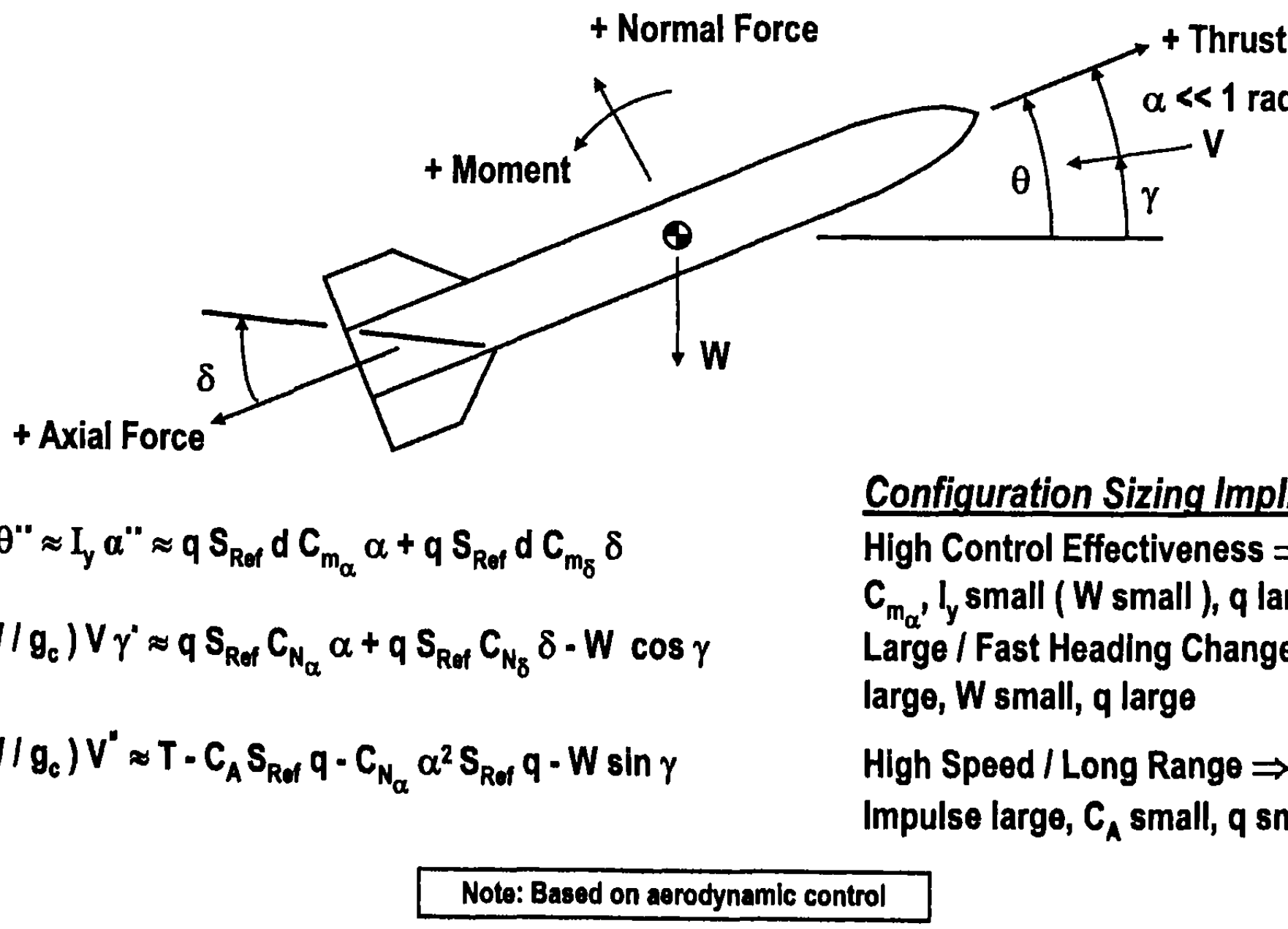

Fig. 5.5 Three-degrees-of-freedom simplified equations of motion show the drivers for configuration sizing.

vertical plane. For horizontal plane maneuvers, the term $W\cos\gamma$ is not included. Implications of the third equation are the missile speed and range

$$(W/g_c)V^{\cdot} \approx T - C_A S_{Ref} q - C_{N_\alpha} \alpha^2 S_{Ref} q - W \sin\gamma \tag{5.3}$$

High speed and long range are provided by a large total impulse, which is the integral of thrust for the burn time duration ($\int T dt$). There is also payoff for flight range in using high-density propellant/fuel. High-density propellant/fuel increases the total impulse of a volume-limited propulsion system. The third equation also shows that low axial force coefficient C_A and low dynamic pressure q provide longer range. Axial force coefficient is approximately equal to the zero-lift drag coefficient C_{D_0}. The term $W\sin\gamma$ in the preceding equation is the weight component in the horizontal plane. For horizontal flight, $\gamma = 0$ and $W \sin\gamma = 0$.

5.5 Cruise Flight Performance

The Breguet range equation provides an estimate of the missile flight range during cruise flight. Assumptions in the derivation of the Breguet range equation are constant velocity, constant lift-to-drag ratio, and constant specific impulse. The derivation is as follows:

The missile flight range is the time integral of velocity

$$R = \int V \, dt \tag{5.4}$$

Incremental time dt is related to fuel flow rate, thrust, and specific impulse by

$$dW/dt = T/I_{SP} \tag{5.5}$$

For nonaccelerating flight, lift equals weight and thrust equals drag. Therefore

$$L/D = W/T \tag{5.6}$$

Substitution and integration give the Breguet cruise range equation

$$R = (VI_{sp})(L/D) ln[W_{BC}/(W_{BC} - W_P)] \tag{5.7}$$

Note that the Breguet cruise range equation is a function of the missile weight at the beginning of cruise W_{BC}, propellant weight W_P, aerodynamic efficiency L/D, specific impulse I_{sp}, and velocity V. Figure 5.6 shows the maximum cruise range for a typical rocket, a typical axisymmetric ramjet, and a typical subsonic turbojet with a wing. The bottom curve is based on a typical maximum value of the rocket propulsion parameter of

$$VI_{sp}(L/D) = 2 \times 10^6 \text{ ft} \tag{5.8}$$

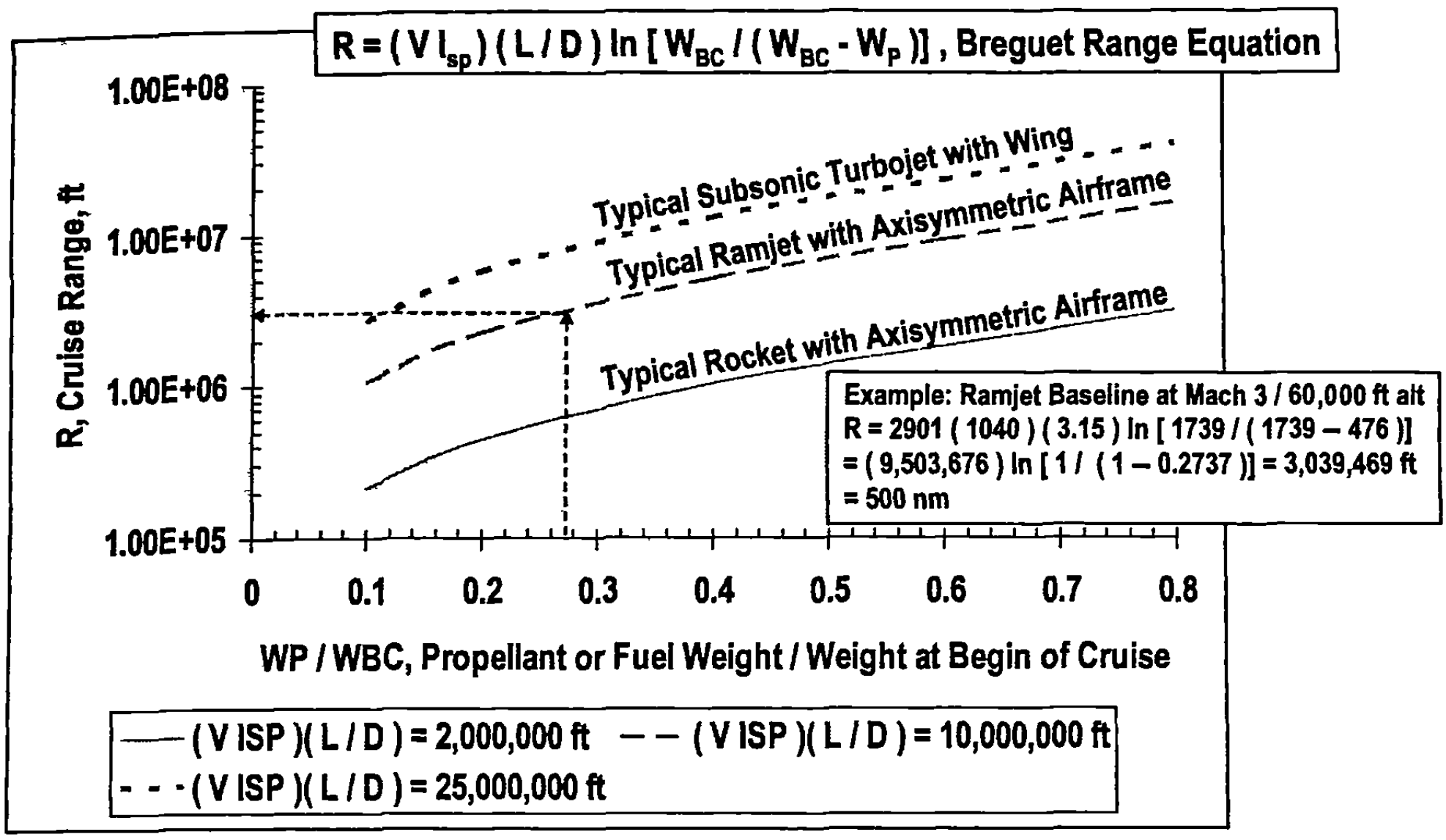

Note: R = cruise range, V = cruise velocity, I_{SP} = specific impulse, L = lift, D = drag, W_{BC} = weight at begin of cruise, W_P = weight of propellant or fuel

Fig. 5.6 For long-range cruise, maximize VI_{sp}, L/D, and the weight fraction of fuel/propellant.

The middle curve is based on a typical maximum value of the ramjet propulsion parameter for an axisymmetric, low L/D airframe of

$$VI_{sp}(L/D) = 10 \times 10^6 \text{ ft} \tag{5.9}$$

The top curve is based on a typical maximum value for a subsonic turbojet with a wing of

$$VI_{sp}(L/D) = 25 \times 10^6 \text{ ft} \tag{5.10}$$

The curves are a function of the fuel or propellant fraction of the missile weight at the beginning of cruise (W_P/W_{BC}). Note from the figure that for the same fuel/propellant weight fraction the subsonic turbojet with a wing has the longest cruise range while the rocket has the shortest cruise range. However, as mentioned previously, the rocket usually has a longer range in ballistic or semiballistic flight than in constant altitude cruise flight and for the same total missile weight the rocket usually has a larger propellant weight fraction.

For supersonic missiles in low-altitude flight, the dynamic pressure is high. One-g flight (lift equals weight) at high dynamic pressure results in a cruise L/D that is usually much lower than $(L/D)_{Max}$. The lower L/D results in shorter range.

As an example of the Breguet range equation, the ramjet baseline is evaluated at Mach 3, 60,000 ft altitude. At Mach 3 the ramjet baseline has a velocity $V = 2901$ ft/s, specific impulse $I_{sp} = 1040$ s, and an aerodynamic efficiency $L/D = 3.15$. At the beginning of cruise the missile weight $W_{BC} = 1739$ lb and

the fuel weight $W_P = 476$ lb. Computing the range for Mach 3 cruise at 60,000 ft altitude gives

$$R = 2901(1040)(3.15)ln[1739/(1739 - 476)] = 3.0 \times 10^6 \text{ ft or } 500 \text{ n miles}$$

5.6 Steady-State Flight

The steady-state level flight, steady climb, and steady dive relationships from Chin[4] are shown in Fig. 5.7. In steady-state level flight at low angle of attack, the lift L is approximately equal to the weight W and the thrust T is approximately equal to the drag D. Note that the thrust required for steady-state level flight is the missile weight divided by the aerodynamic efficiency

$$T = W/(L/D) \tag{5.11}$$

High L/D and light weight have the benefit of reducing the required thrust, resulting in a lower fuel flow rate. Note from the steady climb equation in the figure, the flight path angle γ_c and climb velocity V_c are proportional to the excess thrust $(T - D)$. High thrust and low drag provide higher climb angle and higher climb velocity. The horizontal flight range in a steady climb is given by the equation

$$R_c = \Delta h/\tan\gamma_c = \Delta h(L/D) \tag{5.12}$$

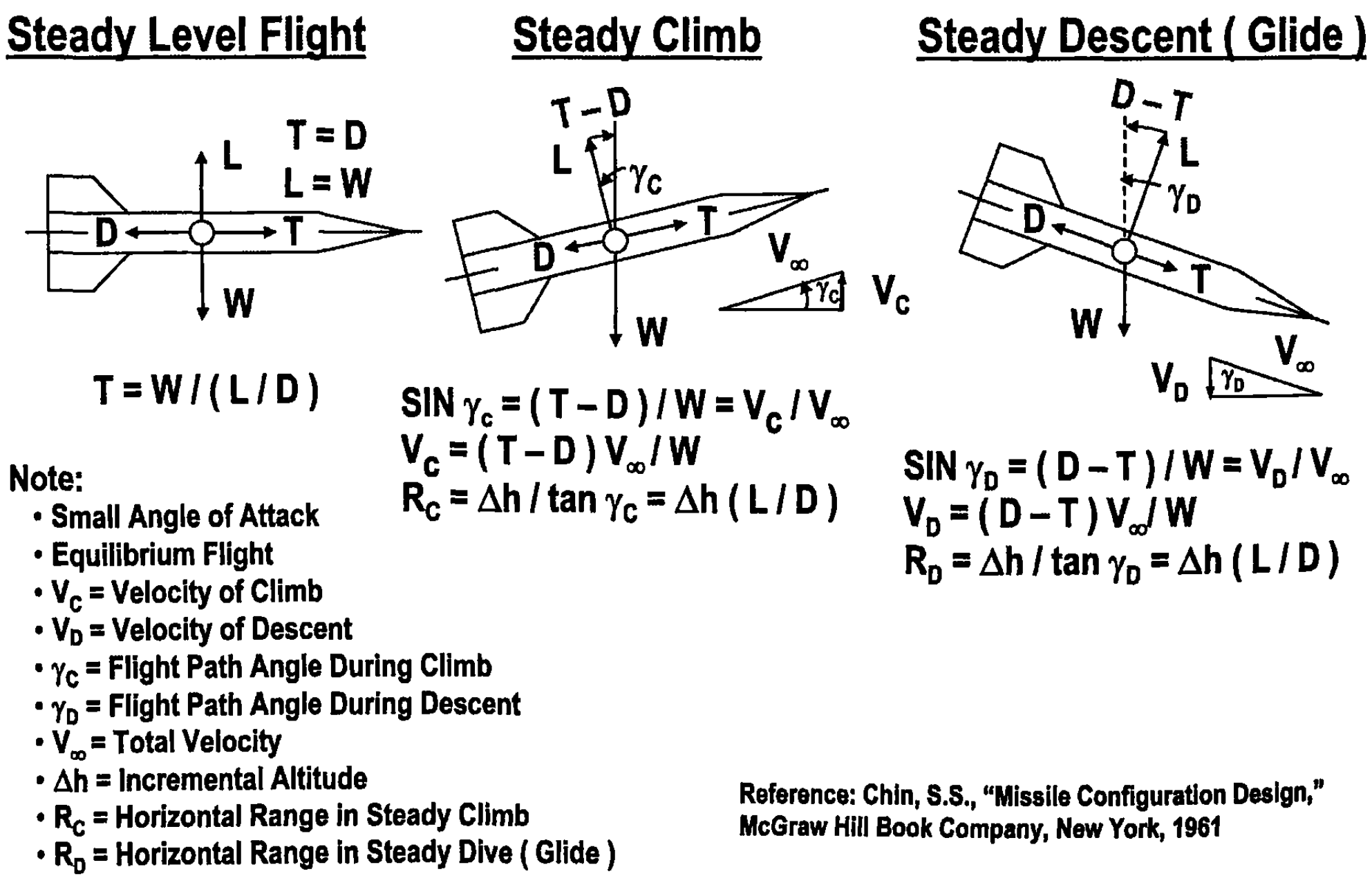

Fig. 5.7 Efficient steady flight is enhanced by high L/D and light weight.

Similarly, in a steady dive (glide) the flight path angle γ_D and dive velocity V_D are proportional to the excess drag $(D - T)$. Low drag allows a shallow glide angle after burnout $(T = 0)$, providing an extended glide range. The horizontal flight range in a steady dive is

$$R_D = \Delta h / \tan \gamma_D = \Delta h (L/D) \tag{5.13}$$

5.7 Flight Trajectory Shaping

Figure 5.8 illustrates the extended range advantage of missiles that use flight trajectory shaping. Flight trajectory shaping is particularly beneficial for high-performance supersonic missiles, which have large propellant or fuel weight fraction. To take advantage of flight trajectory shaping, the missile must rapidly pitch up and climb to an efficient flight altitude. During the climb, the angle of attack should be small to minimize drag. The missile initial thrust-to-weight ratio should be high $(T/W \approx 10)$ for safe separation, followed by a relatively low (≈ 2) thrust-to-weight during the climb. A thrust-to-weight ratio greater than about 2–3 will result in a high dynamic pressure, which increases missile drag. After reaching higher altitude, the missile benefits from an improved lift-to-drag ratio, such as $(L/D)_{Max}$. Dynamic pressure for efficient flight of a high-performance supersonic missile is on the order of $q = 500$ to 1000 psf. Following burnout, the missile can have extended range through glide at a dynamic pressure of about 700 psf, providing an aerodynamic efficiency approximately equal to $(L/D)_{Max}$.

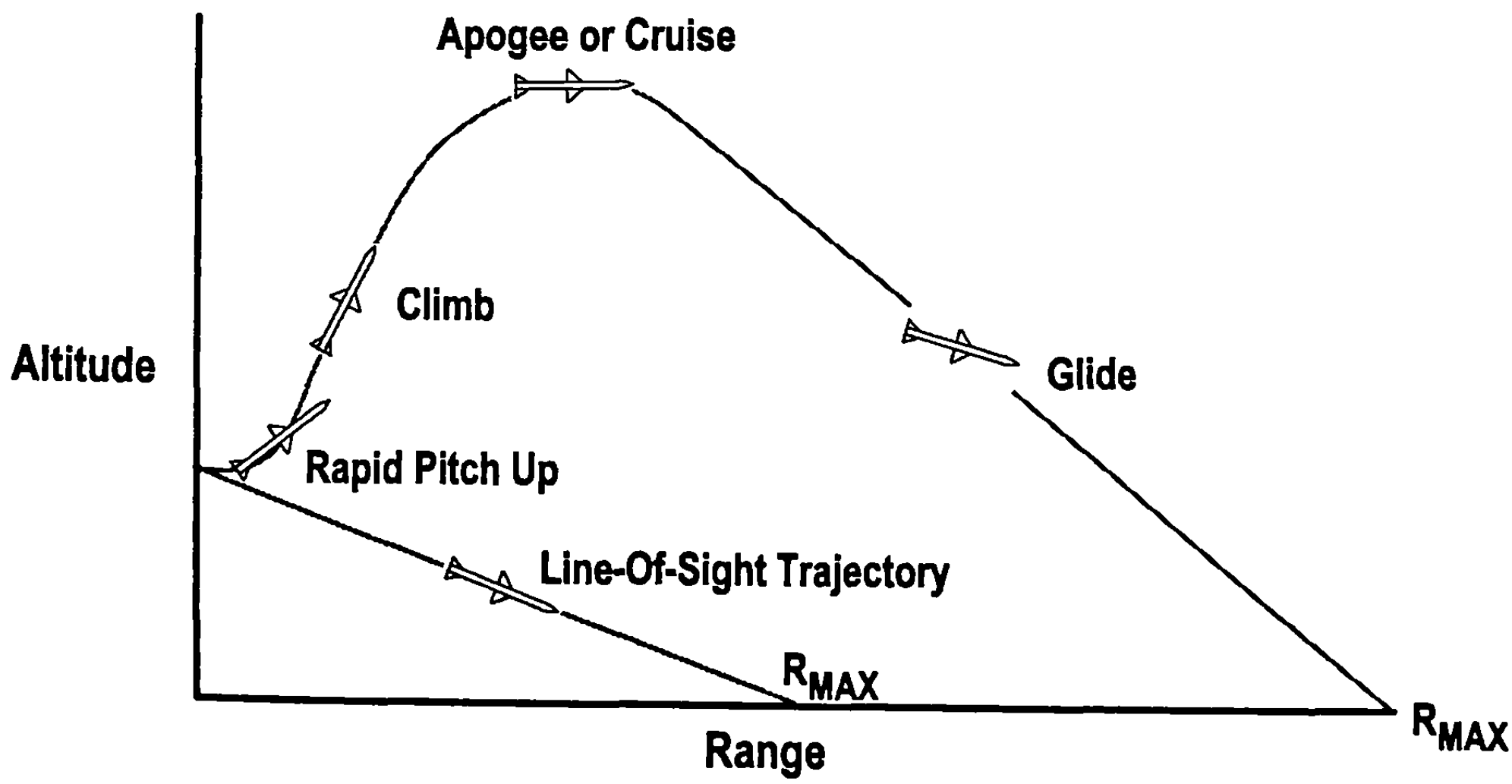

Lofted Trajectory Design Guidelines for Horizontal Launch:
- High thrust-to-weight ≈ 10 for safe separation
- Rapid pitch up minimizes time / propellant to reach efficient altitude
- Climb at $\alpha \approx 0$ deg with thrust-to-weight $T/W \approx 2$ and $q \approx 700$ psf to minimize drag / propellant
- Apogee at $q \approx 700$ psf, followed by either $(L/D)_{MAX}$ cruise or $(L/D)_{MAX}$ glide

Fig. 5.8 Flight trajectory lofting/shaping provides extended range.

5.8 Turn Performance

Figure 5.9 shows an example of missile instantaneous turn radius using aerodynamic control of the flight path. The turn radius of the missile should be less than the turn radius of the target for small miss distance. The equation of motion for a vertical maneuver turn, relating the rate of change in the flight path angle $\gamma^{\cdot}$ to the forces on the missile, is

$$(W/g_c)V\gamma^{\cdot} = qS_{\mathrm{Ref}}C_{\mathrm{N}} - W\cos\gamma \tag{5.14}$$

Also, the instantaneous turn radius R_{T} is a function of $\gamma^{\cdot}$ and velocity V, by the equation

$$R_{\mathrm{T}} = V/\gamma^{\cdot} \tag{5.15}$$

If the missile is maneuvering in a horizontal turn or is in a vertical turn such that the aerodynamic normal force ($N = qS_{\mathrm{Ref}}C_{\mathrm{N}}$) is much larger than the missile weight W, then

$$R_{\mathrm{T}} \approx 2W/(g_c C_{\mathrm{N}} S_{\mathrm{Ref}}\rho) \tag{5.16}$$

Note that the instantaneous turn radius is a function of missile weight W, normal force coefficient C_{N}, reference area S_{Ref}, and the atmospheric density ρ. The term g_c in the equation is the gravitational constant for English units ($g_c = 32.2$).

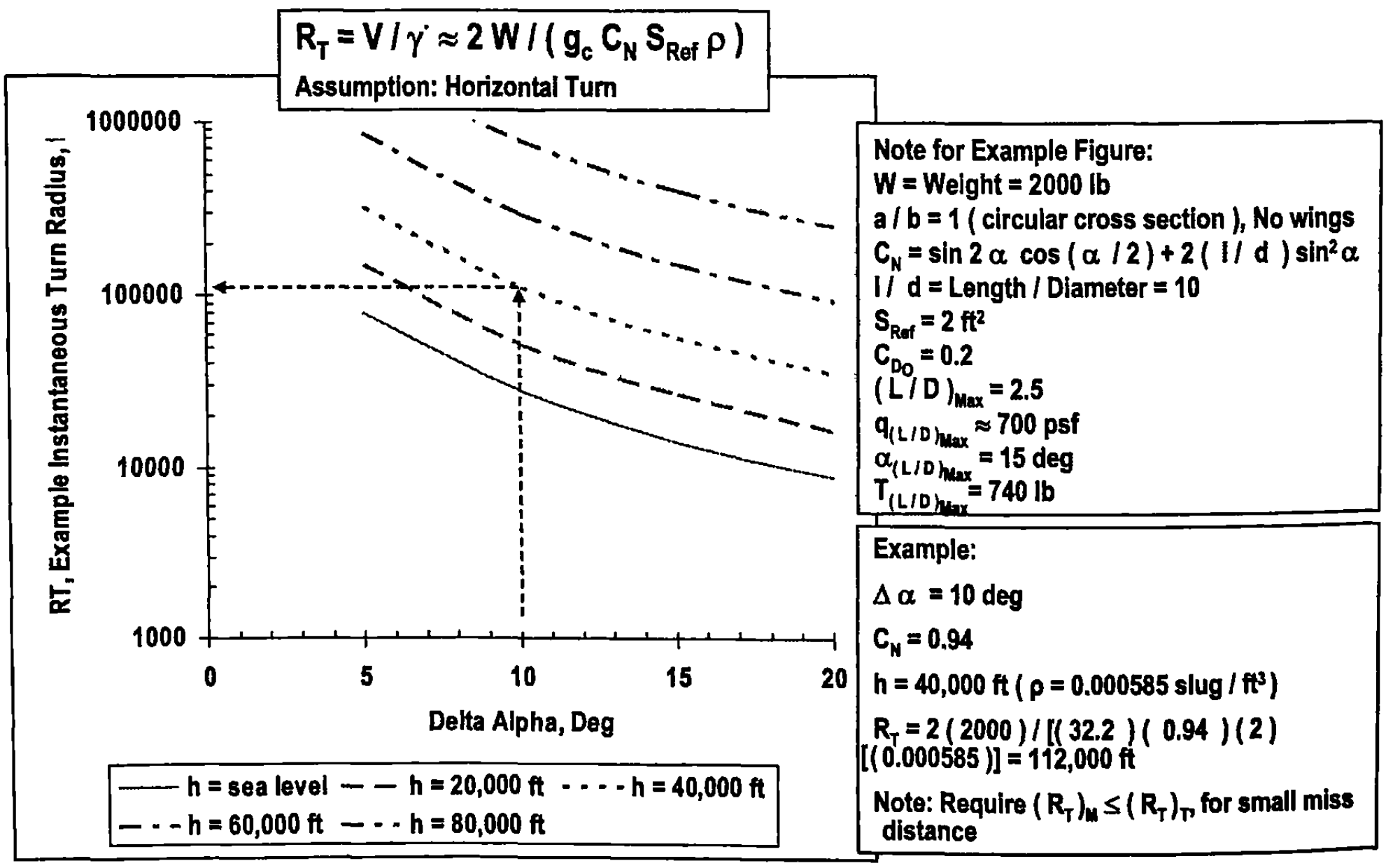

Fig. 5.9 Small turn radius using aero control requires high angle of attack and low altitude flight.

An example is shown in the figure for a wingless missile with a circular body cross section. Results are based on combining slender body theory (Ref. 7) with cross-flow theory (Ref. 8). The example missile has a weight $W = 2000$ lb, length that is 10 times the diameter ($l/d = 10$), cross-sectional area $S = 2$ ft^2, and zero-lift drag coefficient $C_{D_0} = 0.2$. Note from the figure that the instantaneous turn radius increases rapidly as the altitude increases. For example, assume an altitude of 40,000 ft ($\rho = 0.000585$ slug/ft^3) and a horizontal turn with an incremental angle of attack $\Delta\alpha = 10$ deg. Calculating the normal force coefficient

$$\begin{aligned} C_N &= \sin(2\alpha)\cos(\alpha/2) + 2(I/d)\sin^2\alpha \\ &= \sin[2(10)]\cos[10/2] + 2(10)\sin^2(10) = 0.94 \end{aligned} \tag{5.17}$$

Substituting, the instantaneous turn radius is

$$R_T = 2(2000)/[32.2(0.94)(2)(0.000585)] = 112{,}000 \text{ ft} \tag{5.18}$$

Note that the turn radius of a wingless missile with a circular cross-sectional body is very large. Adding a wing or shaping the missile into an elliptical body cross section would provide higher normal force capability, resulting in smaller turn radius.

For the example wingless axisymmetric missile, $(L/D)_{Max} = 2.5$ and $\alpha_{(L/D)Max} = 15$ deg. The dynamic pressure required to fly in 1-g horizontal steady flight at $(L/D)_{Max}$ for the wingless missile is $q_{(L/D)Max} \approx 700$ psf. The thrust required for 1-g steady-state horizontal flight of the wingless missile at $(L/D)_{Max}$ is $T_{(L/D)Max} = 740$ lb. Note the required thrust is 37% of the missile weight.

The capability to rapidly make a heading change in the flight path angle γ is an important consideration for missile maneuverability. The approximate equation shown previously, which is based on using aerodynamic control in a horizontal turn, is

$$\gamma^{\cdot} = g_c C_N \rho V S_{Ref}/(2W) \tag{5.19}$$

In the preceding equation the units of $\gamma^{\cdot}$ are rad/s. Figure 5.10 shows an example of the rate of change in flight path angle $\gamma^{\cdot}$ for a lifting body at an altitude $h = 20{,}000$ ft as a function of angle of attack α and velocity V. Note that high turn rate for a lifting body is achieved for large values of angle of attack and velocity.

As an example, assume a lifting body missile conducting a horizontal maneuver at an angle of attack $\alpha = 15$ deg, velocity $V = 2000$ ft/s, and altitude $h = 20{,}000$ ft. Assume a missile weight $W = 2000$ lb, a circular cross-sectional body ($a/b = 1$), no wings, negligible tail lift, neutral static stability, $S_{Ref} = 2$ ft^2, and $l/d = 10$. Calculate the normal force coefficient

$$\begin{aligned} C_N &= \sin(2\alpha)\cos(\alpha/2) + 2(l/d)\sin^2\alpha \\ &= \sin[2(15)]\cos(15/2) + 2(10)\sin^2(15) = 1.835 \end{aligned} \tag{5.20}$$

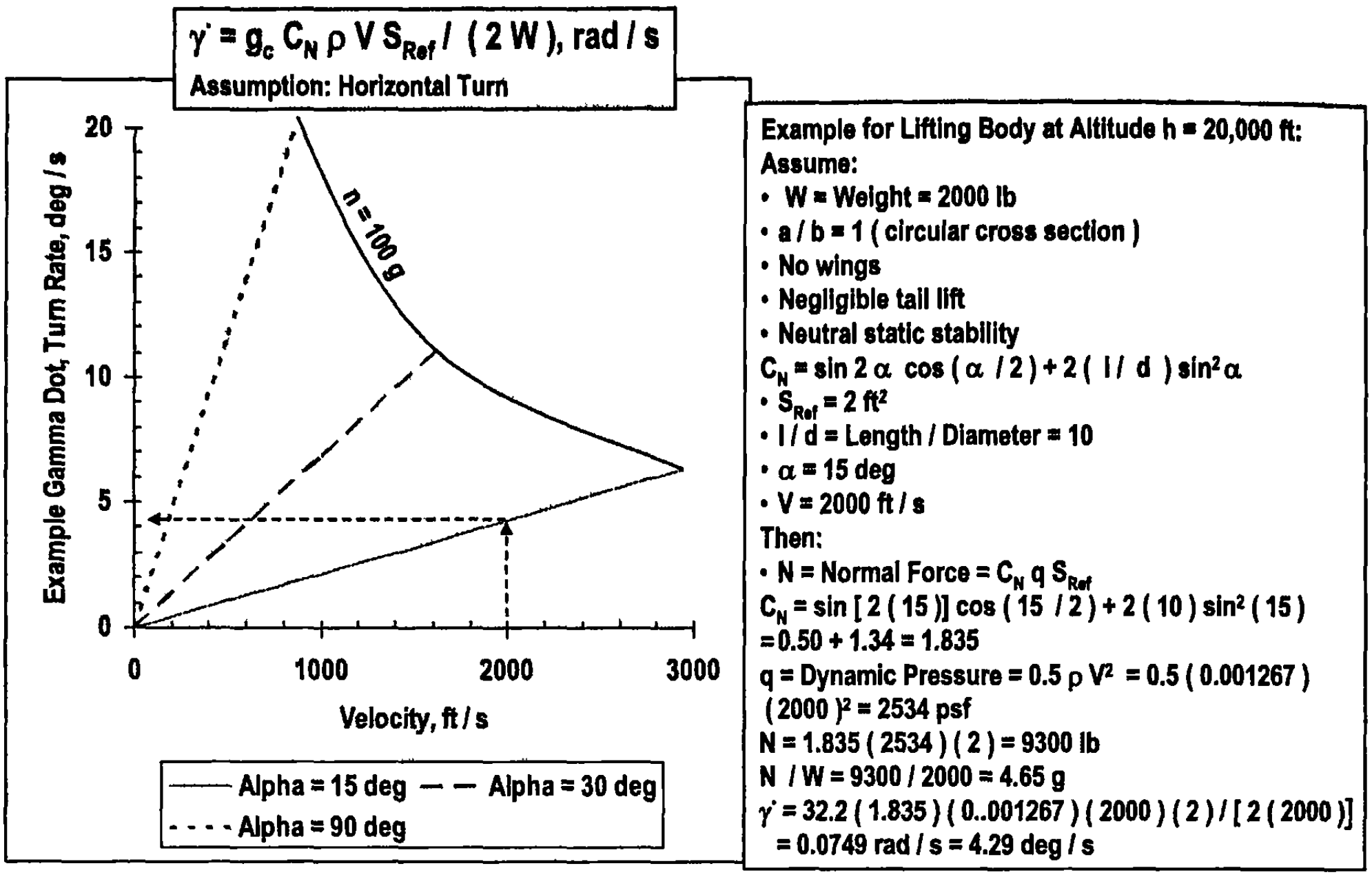

Fig. 5.10 High turn rate requires high maneuverability.

The dynamic pressure $q = 0.5\rho V^2 = 0.5(0.001267)(2000)^2 = 2534$ psf. Substituting, the normal force is

$$N = C_N q S_{\text{Ref}} = 1.835(2534)(2) = 9300 \text{ lb} \tag{5.21}$$

The maneuver acceleration is

$$N/W = 9300/2000 = 4.65\ g \tag{5.22}$$

Finally, the turn rate is

$$\begin{aligned}\dot{\gamma} &= 32.2(1.835)(0.001267)(2000)(2)/[2(2000)] = 0.0749 \text{ rad/s} \\ &= 4.29 \text{ deg/s}\end{aligned} \tag{5.23}$$

Note from the preceding result that a conventional body configuration has relatively low turn rate. Approaches to improve the turn rate include thrust vector control, adding wings, and the application of an elliptical cross-sectional lifting body.

Another example of a requirement for turn rate performance is the capability of an antiaircraft missile to at least match the turn rate of the target for a successful intercept. For manned combat aircraft, typical air-to-air combat maneuvering conditions are a normal acceleration of about $n = 9\ g$ (pilot limit) and a velocity of about $V = 1000$ ft/s. Substitution into the turn rate equation gives a typical maximum turn rate of a manned aircraft of about

$$\dot{\gamma} = 32.2(9)/1000 = 0.290 \text{ rad/s or } 16.6 \text{ deg/s} \tag{5.24}$$

Because the missile must have a speed advantage to intercept the aircraft, it must also have higher maneuverability to match the turn rate of the aircraft. For example, a missile with a velocity $V = 3000$ ft/s must have 27-g maneuverability to achieve a turn rate of $\gamma^{\cdot} = 16.6$ deg/s.

The rocket baseline missile and its data from Chapter 7 will be used to illustrate the drivers for turn rate performance. Assume that a climb maneuver is commanded for a typical launch condition of Mach 0.8 and 20,000 ft altitude. At this flight condition the velocity $V = 830$ ft/s, dynamic pressure $q = 436$ psf, launch weight $W_L = 500$ lb, and the launch center of gravity $x_{cg} = 84.6$ in from the nose tip. The trim angle of attack and the control surface deflection based on the launch center of gravity are derived from the wind tunnel data of Chapter 7. Based on the reference center of gravity for the wind tunnel data of 75.7 in, the maximum trimmed angle of attack α and control surface deflection δ for the launch center of gravity are computed from

$$\begin{aligned}(C_{m_\alpha})_{x_{cg}=84.6} &= (C_{m_\alpha})_{x_{cg}=75.7} + C_{N_\alpha}(84.6 - 75.7)/d \\ &= -0.40 + 0.68(8.9)/8 = 0.36 \text{ per deg}\end{aligned} \tag{5.25}$$

$$\begin{aligned}(C_{m_\delta})_{x_{cg}=84.6} &= (C_{m_\delta})_{x_{cg}=75.7} + C_{N_\delta}(84.6 - 75.7)/d \\ &= 0.60 + 0.27(8.9)/8 = 0.90 \text{ per deg}\end{aligned} \tag{5.26}$$

Note that the missile is statically unstable at launch ($C_{m_\alpha} > 0$) and requires negative wing control deflection to trim. The control effectiveness is given by

$$\alpha/\delta = -C_{m_\delta}/C_{m_\alpha} = -0.90/0.36 = -2.5 \tag{5.27}$$

The maximum wing local angle of attack $|\alpha'| = |\alpha + \delta| < 22$ deg. For a maximum angle of attack of the body of $\alpha = 30$ deg, the trim control deflection is $\delta = -12$ deg. Compute

$$\begin{aligned}\gamma^{\cdot} = g_c n/V &= [qSC_{N_\alpha}\alpha + qSC_{N_\delta}\delta - W\cos\gamma]/[W/g_c V] \\ &= [436(0.349)(0.68)(30) + 436(0.349)(0.27)(-12) \\ &\quad - 500(1)]/[(500/32.2)(830)] \\ &= 0.164 \text{ rad/s or } 9.4 \text{ deg/s}\end{aligned} \tag{5.28}$$

For a postburnout flight condition of Mach 2 at 20,000 ft altitude, the missile has a higher turn rate. The missile is statically stable, with $\alpha/\delta = 0.75$. The turn rate

$$\begin{aligned}\gamma^{\cdot} &= [2725(0.349)(0.60)(9.4) + 2725(0.349)(0.19)(12.6) \\ &\quad - 367(1)]/[(367/32.2)(2074)] \\ &= 0.31 \text{ rad/s or } 18 \text{ deg/s}\end{aligned} \tag{5.29}$$

The faster turn rate after burnout is from the higher dynamic pressure $q = 2725$ psf, positive wing control deflection to trim the missile, and lighter weight.

A metric for missile response time is the angle of attack sensitivity to turn rate, or $\alpha/\gamma^{\cdot}$. For the rocket baseline at Mach 0.8 launch and 20,000 ft altitude,

$$\alpha/\gamma^{\cdot} = 30/9.4 = 3.2\,\text{s} \tag{5.30}$$

As a comparison, the response time metric for Mach 2 at 20,000 ft altitude is better

$$\alpha/\gamma^{\cdot} = 9.4/18 = 0.52\ \text{s} \tag{5.31}$$

It will be shown in Chapter 6 that values of $\alpha/\gamma^{\cdot} < 0.5$ s are required for a small miss distance.

5.9 Coast Flight Performance

Coast velocity and the coast range are shown in Fig. 5.11 as a function of the coast time, weight, atmospheric density, reference area, zero-lift drag coefficient and the initial velocity. It is based on the one-DOF equation of motion with the assumptions of constant flight path angle (γ = constant) and low angle of attack ($\alpha \approx 0$ deg). The simplified equation of motion is

$$dV/dt = -g_c C_{D_0} S_{Ref} q/W - g_c \sin\gamma \tag{5.32}$$

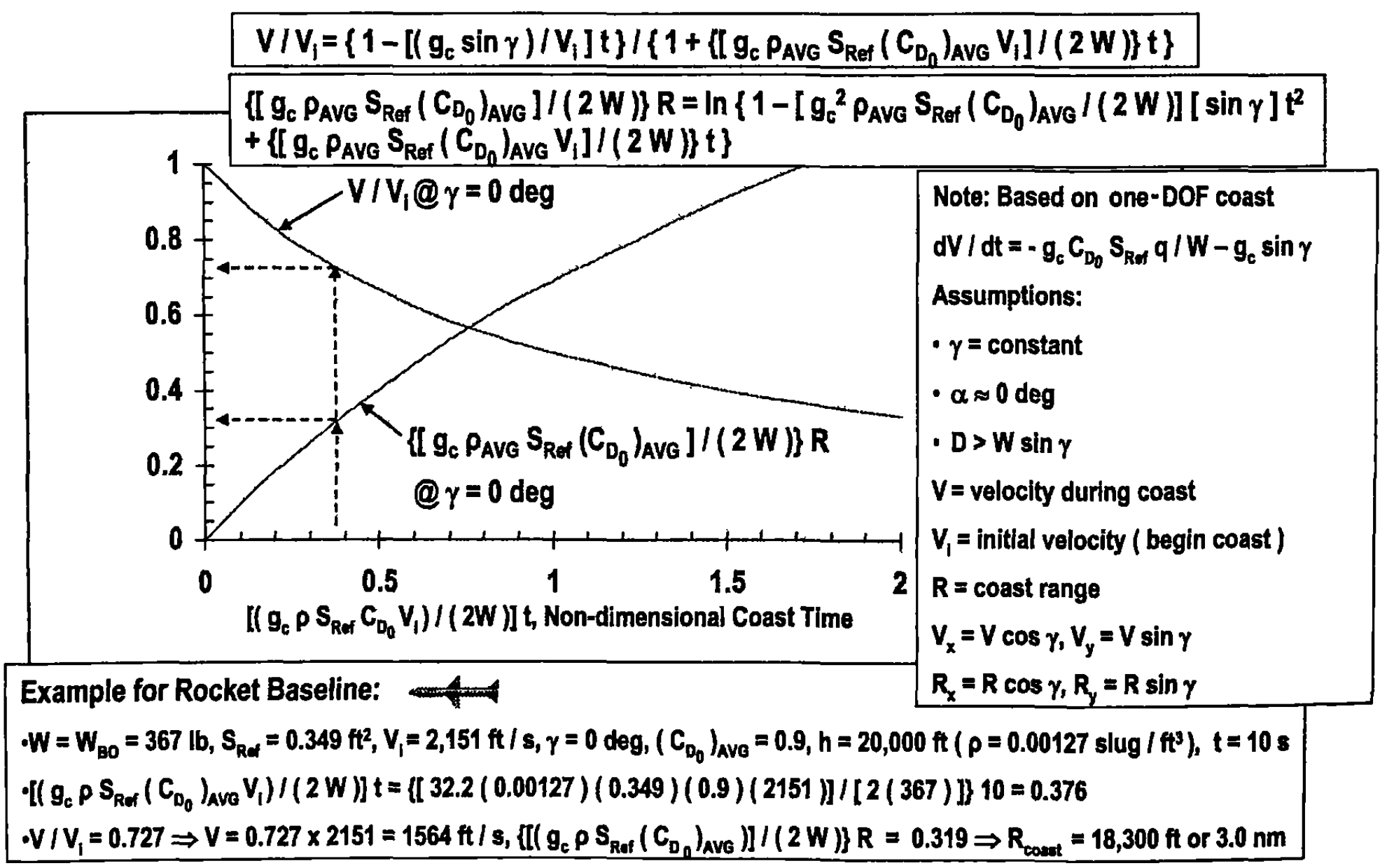

Fig. 5.11 For a long-range coast, maximize the initial velocity and altitude and minimize the drag coefficient.

Integrating, the equation for coast velocity is

$$V = V_i\{1 - [(g_c \sin\gamma)/V_i]t\}/\{1 + \{[g_c\rho_{AVG}S_{Ref}(C_{D_0})_{AVG}V_i]/(2W)\}t\} \quad (5.33)$$

Integrating again, the incremental flight range during coast is given by

$$R = \{2W/[g_c\rho_{AVG}S_{Ref}(C_{D_0})_{AVG}]\}\ln\{1 - [g_{c^2}\rho_{AVG}S_{Ref}(C_{D_0})_{AVG}/(2W)] \times [\sin\gamma]t^2 + \{[g_c\rho_{AVG}S_{Ref}(C_{D_0})_{AVG}V_i]/(2W)\}t\} \quad (5.34)$$

Examining the equations shows that the contributors to a long-range coast include high initial velocity, low zero-lift drag coefficient, and high altitude (low atmospheric density) flight.

The zero-lift drag coefficient C_{D_0} will vary during the coast because of the variation in Mach number. An approach to estimate the average value of the zero-lift drag coefficient $(C_{D_0})_{AVG}$ is to first compute the end-of-coast condition based on the initial value of C_{D_0}. $(C_{D_0})_{AVG}$ is the average of the initial and the end-of-coast estimate of C_{D_0}. Similarly, the atmospheric density ρ will vary for changes in altitude. The average density ρ_{AVG} is assumed to be the average of the initial and the end-of-coast estimate of density.

The computed coast velocity can be resolved into horizontal and vertical components by the equations

$$V_x = V\cos\gamma \quad (5.35)$$

$$V_y = V\sin\gamma \quad (5.36)$$

Similarly, coast range can be resolved into $R_x = R\cos\gamma$

$$R_y = R\sin\gamma \quad (5.37)$$

As an example for the rocket baseline missile, the coast (burnout) weight $W = W_{BO} = 367$ lb and the reference area $S_{Ref} = 0.349$ ft^2. Assume a constant altitude coast ($\gamma = 0$ deg). For a burnout flight condition of Mach 2.1 at 20,000 ft altitude ($\rho = 0.00127$ slug/ft^3), the zero-lift drag coefficient $C_{D_0} = 0.9$ and the beginning of coast velocity $V_{BO} = 2151$ ft/s. The end-of-coast velocity after 10 s of coast is computed to be

$$V = 2151\{1 - [(32.2\sin 0)/2151]10\}/\{1 + \{[32.2(0.00127) \times (0.349)(0.9)(2151)]/[2(367)]\}10\} = 1564 \text{ ft/s} \quad (5.38)$$

The incremental range during coast is

$$
\begin{aligned}
R_{\text{coast}} &= \{2(367)/[32.2(0.00127)(0.349)(0.9)]\} \\
&\quad \times ln\{1 - \{32.2^2(0.00127)(0.349)(0.9)/[2(367)]\}[\sin 0]10^2 \\
&\quad + \{[32.2(0.00127)(0.349)(0.9)(2151)]/[2(367)]\}10\} \\
&= 18{,}300 \text{ ft or } 3.0 \text{ n mile}
\end{aligned}
\tag{5.39}
$$

5.10 Ballistic Flight Performance

Ballistic flight velocity and range are shown in Fig. 5.12 as a function of the time, weight, atmospheric density, reference area, zero-lift drag coefficient, initial velocity, and the initial flight path angle. The figure is based on the one-DOF equation of motion with the assumptions of no thrust ($T = 0$), zero angle of attack ($\alpha = 0$ deg), drag force greater than the component of weight along the drag axis ($D > W\sin\gamma$), and negligible error from the curvature of the earth. The simplified equation for the horizontal component of velocity is

$$V_x = V_i \cos\gamma_i / \{1 + \{[g_c \rho_{AVG} S_{Ref} (C_{D_0})_{AVG} V_i]/(2W)\}t\} \tag{5.40}$$

The vertical component of velocity is

$$V_y = V_i \sin\gamma_i / \{1 + \{[g_c \rho_{AVG} S_{Ref} (C_{D_0})_{AVG} V_i]/(2W)\}t\} - g_c t \tag{5.41}$$

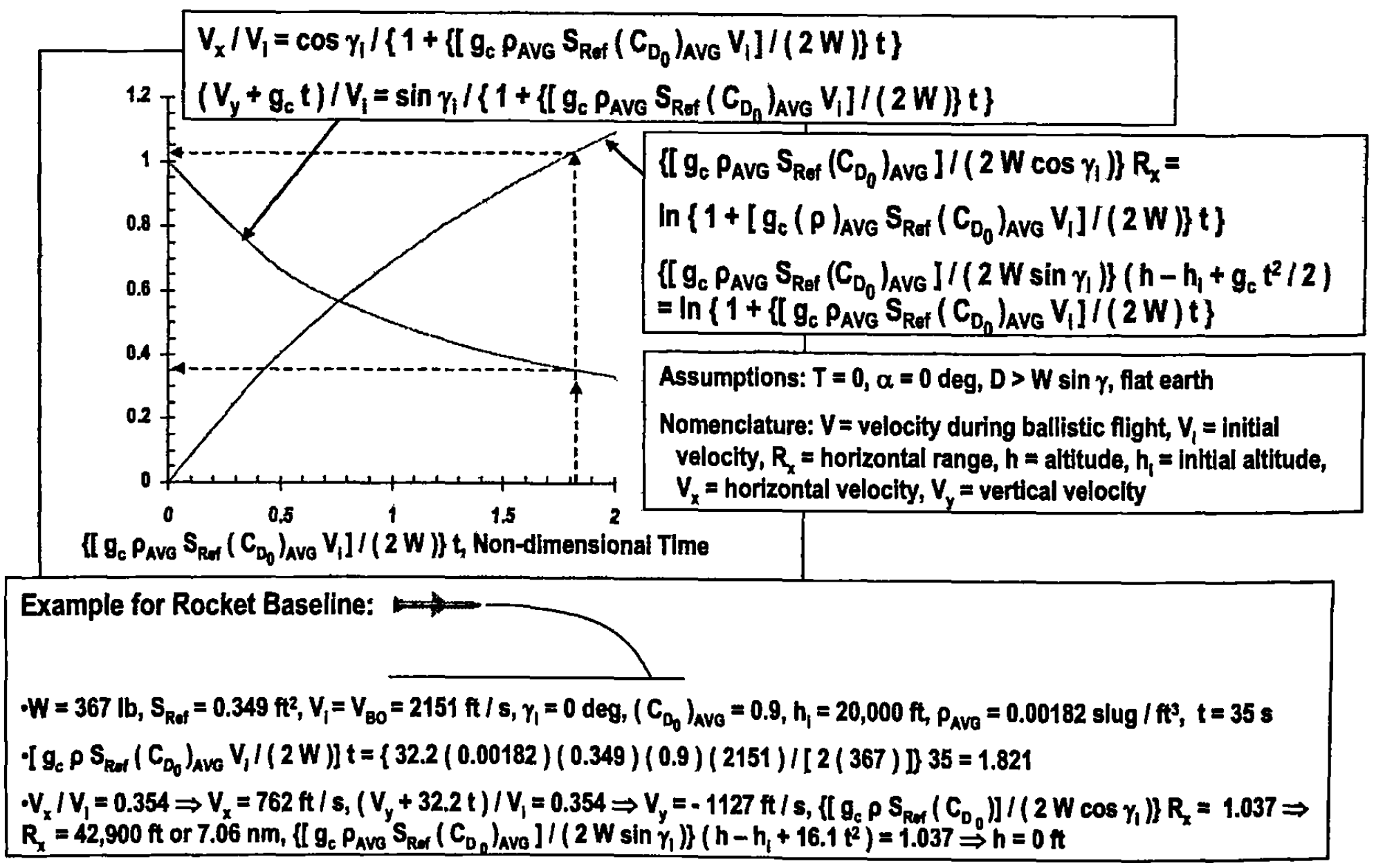

Fig. 5.12 For long-range ballistic flight, maximize the initial velocity, optimize the launch angle, and minimize the drag coefficient.

Horizontal flight range during ballistic flight is given by

$$R_x = \{2W\cos\gamma_i/[g_c\rho_{AVG}S_{Ref}(C_{D_0})_{AVG}]\} \times ln\{1 + \{[g_c\rho_{AVG}S_{Ref}(C_{D_0})_{AVG}V_i]/(2W)\}t\} \quad (5.42)$$

The altitude during ballistic flight is given by

$$h = h_i + \{(2W\sin\gamma_i)/[g_c\rho_{AVG}S_{Ref}(C_{D0})_{AVG}]\} \times ln\{1 + \{[g_c\rho_{AVG}S_{Ref}(C_{D0})_{AVG}V_i]/(2W)\}t - 16.1t^2\} \quad (5.43)$$

Examining the above equations shows that the contributors to a long-range ballistic flight include high initial velocity, low zero-lift drag coefficient, an optimum launch angle, and high-altitude (low atmospheric density) flight.

The zero-lift drag coefficient C_{D_0} will vary during ballistic flight because of the variation in Mach number. An approach to estimate the average value of the zero-lift drag coefficient $(C_{D_0})_{AVG}$ is to first compute the end-of-flight condition based on the initial value of C_{D_0}. $(C_{D_0})_{AVG}$ is the average of the C_{D_0} at the initial Mach number and the C_{D_0} at the end-of-flight Mach number. Similarly, the atmospheric density ρ will vary because of changes in altitude. The average density ρ_{AVG} is assumed to be the average of the density at the initial altitude and the density at the end-of-flight altitude.

An example is given for the rocket baseline missile, which has a burnout weight $W = 367$ lb and a reference area $S_{Ref} = 0.349$ ft^2. Assume an initial horizontal flight path angle ($\gamma_i = 0$ deg). For a burnout flight condition of Mach 2.1 at 20,000 ft altitude ($\rho = 0.00127$ slug/ft^3), the zero-lift drag coefficient $C_{D_0} = 0.9$ and the beginning-of-coast velocity $V_{BO} = 2151$ ft/s. The missile impacts the ground ($h = 0$) at a time $t = 35$ s. The average atmospheric density is the average of the atmospheric densities at the launch ($h = 20{,}000$ ft) and impact (sea level) altitudes

$$\rho_{AVG} = (0.00127 + 0.00238)/2 = 0.00182 \text{ slug/ft}^3 \quad (5.44)$$

The horizontal component of velocity, V_x, after 35 s of ballistic flight is computed to be

$$V_x = 2151\cos 0/\{1 + \{[32.2(0.00182)(0.349)(0.9)(2151)]/[2(367W)]\}35\} = 762 \text{ ft/s} \quad (5.45)$$

The vertical component of velocity, V_y, at impact after 35 s of flight is

$$V_y = 2151\sin 0/\{1 + \{[32.2(0.00182)(0.349)(0.9)(2151)]/[2(367)]\}35\} - 32.2(35) = 0 - 1127 = -1127 \text{ ft/s} \quad (5.46)$$

The impact angle γ is

$$\gamma = \tan^{-1}(V_y/V_x) = \tan^{-1}(-1127/762) = \tan^{-1}(-1.479) = -55.9\,\text{deg} \quad (5.47)$$

Finally, the horizontal range R_x for 35 s of ballistic flight is

$$\begin{aligned} R_x &= \{[2(367)\cos 0]/[32.2(0.00182)(0.349)(0.9)]\} \\ &\quad \times \ln\{1 + \{[32.2(0.00182)(0.349)(0.9)(2151)]/[2(367)]\}35\} \\ &= 42{,}886\ \text{ft or } 7.1\ \text{n miles} \end{aligned} \quad (5.48)$$

5.11 Boost Flight Performance

Incremental velocity from the rocket motor burn is shown in Fig. 5.13 as a function of propellant weight fraction, specific impulse, average drag, and thrust. Based on assumptions of low angle of attack ($\alpha \approx 0$ deg), constant flight path angle (γ = constant), and the thrust larger than the weight component along the thrust axis ($T > W\sin\gamma$), the equation is

$$\Delta V/(g_c I_{SP}) = -[1 - (D_{AVG}/T) - (W_{AVG}\sin\gamma/T)]ln(1 - W_p/W_i) \quad (5.49)$$

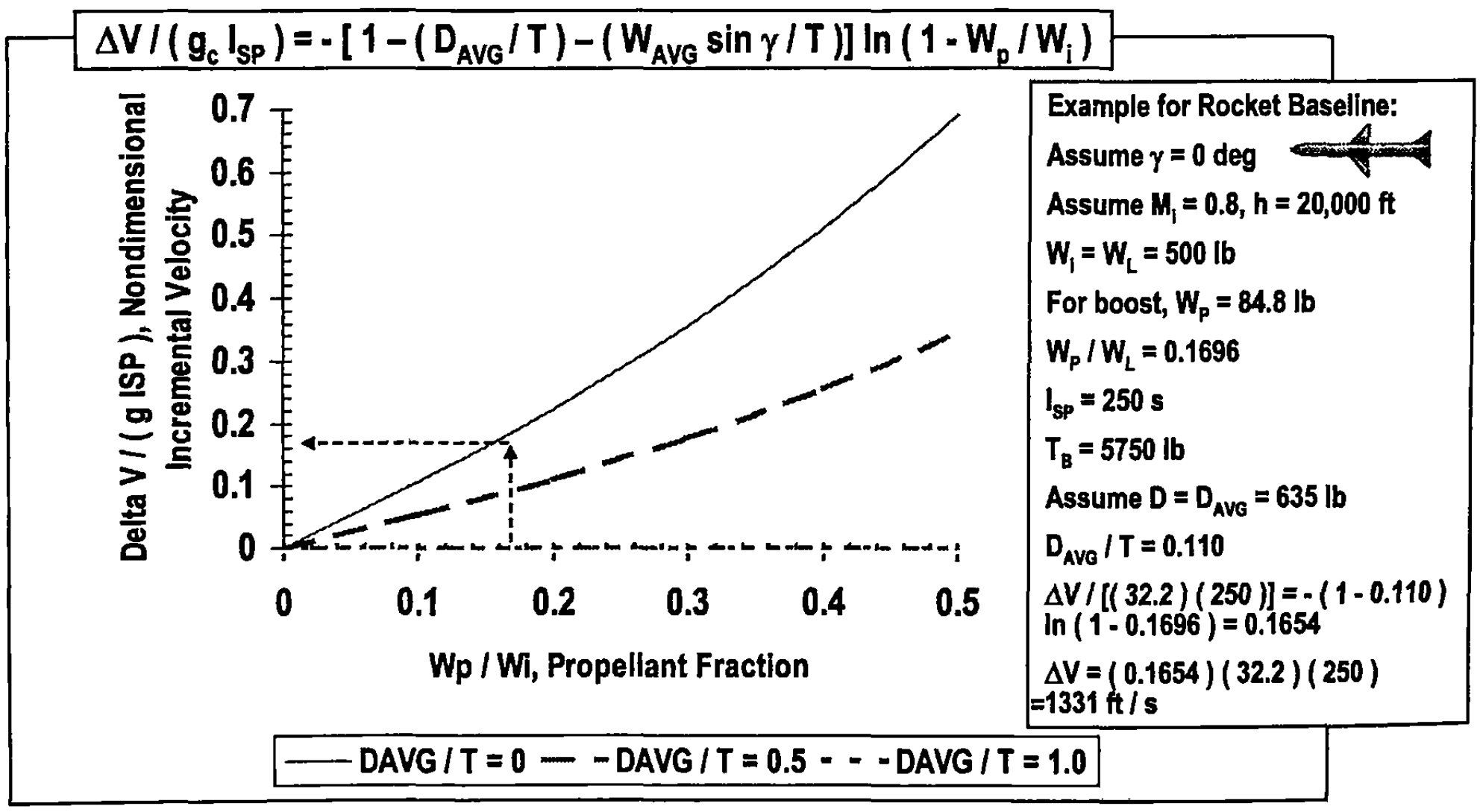

Note: One-DOF Equation of Motion with $\alpha \approx 0$ deg, γ = constant, W_i = initial weight, W_{AVG} = average weight, W_P = propellant weight, I_{SP} = specific impulse, T = thrust, M_i = initial Mach number, h = altitude, D_{AVG} = average drag, ΔV = incremental velocity, g_c = gravitation constant, $V_x = V\cos\gamma$, $V_y = V\sin\gamma$, $R_x = R\cos\gamma$, $R_y = R\sin\gamma$

Note: $R = (V_i + \Delta V/2)\,t_B$, where R = boost range, V_i = initial velocity, t_B = boost time

Fig. 5.13 High propellant weight, high thrust, and low drag provide high burnout velocity.

High incremental velocity from the motor burn is provided by a high propellant weight fraction of the missile initial weight (W_P/W_i), low average drag D_{AVG}, high thrust T, high specific impulse I_{sp}, and a diving flight trajectory ($\gamma < 0$).

The incremental range during boost is given by the equation

$$R = (V_i + \Delta V/2)t_B \tag{5.50}$$

In the above equation V_i is the initial velocity and t_B is the boost time.

As an example, the incremental boost velocity is calculated for the rocket baseline missile, which has an initial (launch) weight $W_i = 500$ lb, boost propellant weight $W_P = 84.8$ lb, boost specific impulse $I_{sp} = 250$ s, and boost thrust $T = 5750$ lb. The assumed launch condition of Mach 0.8, 20,000 ft altitude provides an initial (launch) velocity of $V_i = 820$ ft/s. It is also assumed that the missile flies at constant altitude ($\gamma = 0$ deg). After iterating, using an initial estimate of end-of-boost drag based on the theoretical end-of-boost velocity with no drag, the average drag between launch and the end of boost is found to be $D_{AVG} = 635$ lb. The incremental velocity from boost is computed to be

$$\begin{aligned}\Delta V &= -32.2(250)[1 - (635/5750) - 457.6\sin 0/5750)]ln(1 - 84.8/500)\\ &= 1331 \text{ ft/s}\end{aligned} \tag{5.51}$$

The end-of-boost velocity is $V_{EOB} = V_i + \Delta V = 820 + 1331 = 2151$ ft/s. Including the effect of drag results in an end-of-boost velocity that is 93% of the theoretical (no drag) velocity (2151 vs 2316 ft/s). The incremental range for horizontal flight during boost is computed to be

$$R = (V_i + \Delta V/2)t_B = (820 + 1331/2)3.69 = 5481 \text{ ft} \tag{5.52}$$

5.12 Intercept Lead Angle and Velocity

The average missile velocity and the lead angle required for intercept are shown in Fig. 5.14 as a function of target aspect and velocity. The equation is

$$V_M \sin L = V_T \sin A \tag{5.53}$$

The above equation is based on homing guidance. An assumption is that the seeker look angle is equal to the missile lead angle. The assumption is most applicable for constant altitude intercepts at a low angle of attack flight trajectory. Note from the figure that high average missile velocity is required to intercept a target at an aspect angle $A = 90$ deg (beam shot). Increasing the maximum lead angle/seeker gimbal angle reduces the required missile velocity for intercept.

As an example, assume a target with an aspect angle $A = 45$ deg. Also assume that the maximum allowable lead angle is $L = 30$ deg, a typical gimbal limit for a

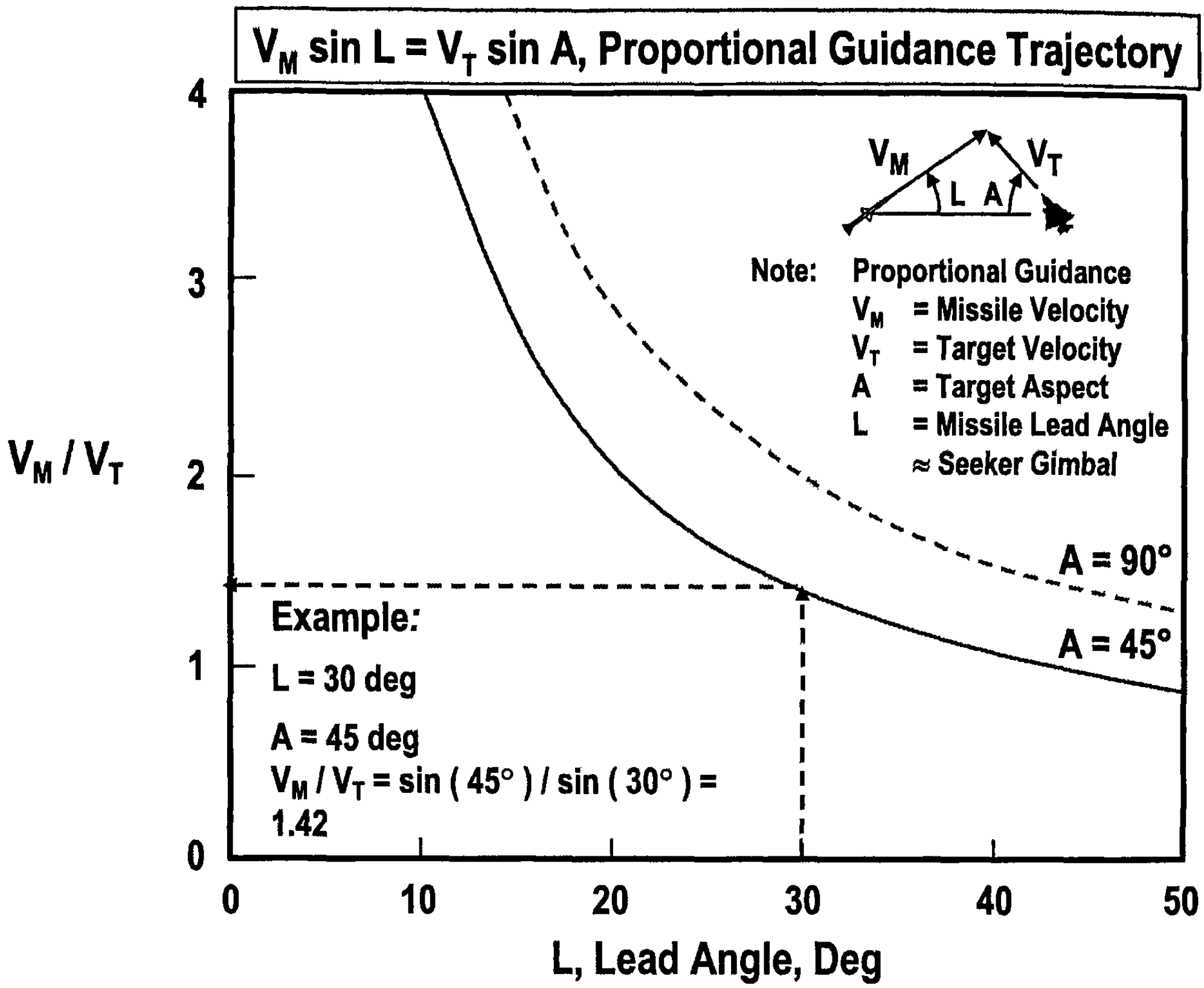

Fig. 5.14 High missile velocity and lead are required to intercept high-speed crossing targets.

seeker. Compute

$$V_M/V_T = \sin 45°/\sin 30° = 1.42 \tag{5.54}$$

For these assumptions, the missile must have an average velocity that is 42% greater than the velocity of the target to achieve an intercept.

5.13 Comparison with Performance Requirements

As shown in Fig. 5.15, after completing the missile flight performance computation, the next step in the missile configuration synthesis process is to compare the candidate missile design flight performance (e.g., range, velocity, time to target, off boresight) with the mission requirements for flight performance. If the candidate missile has insufficient flight performance, changes are made in the aerodynamic configuration, propulsion, structure, subsystems, and/or flight trajectory to improve the flight performance. The refined/resized missile is then sent through another cycle of evaluation. The iteration continues until there is an optimum design convergence that meets the flight performance requirements.

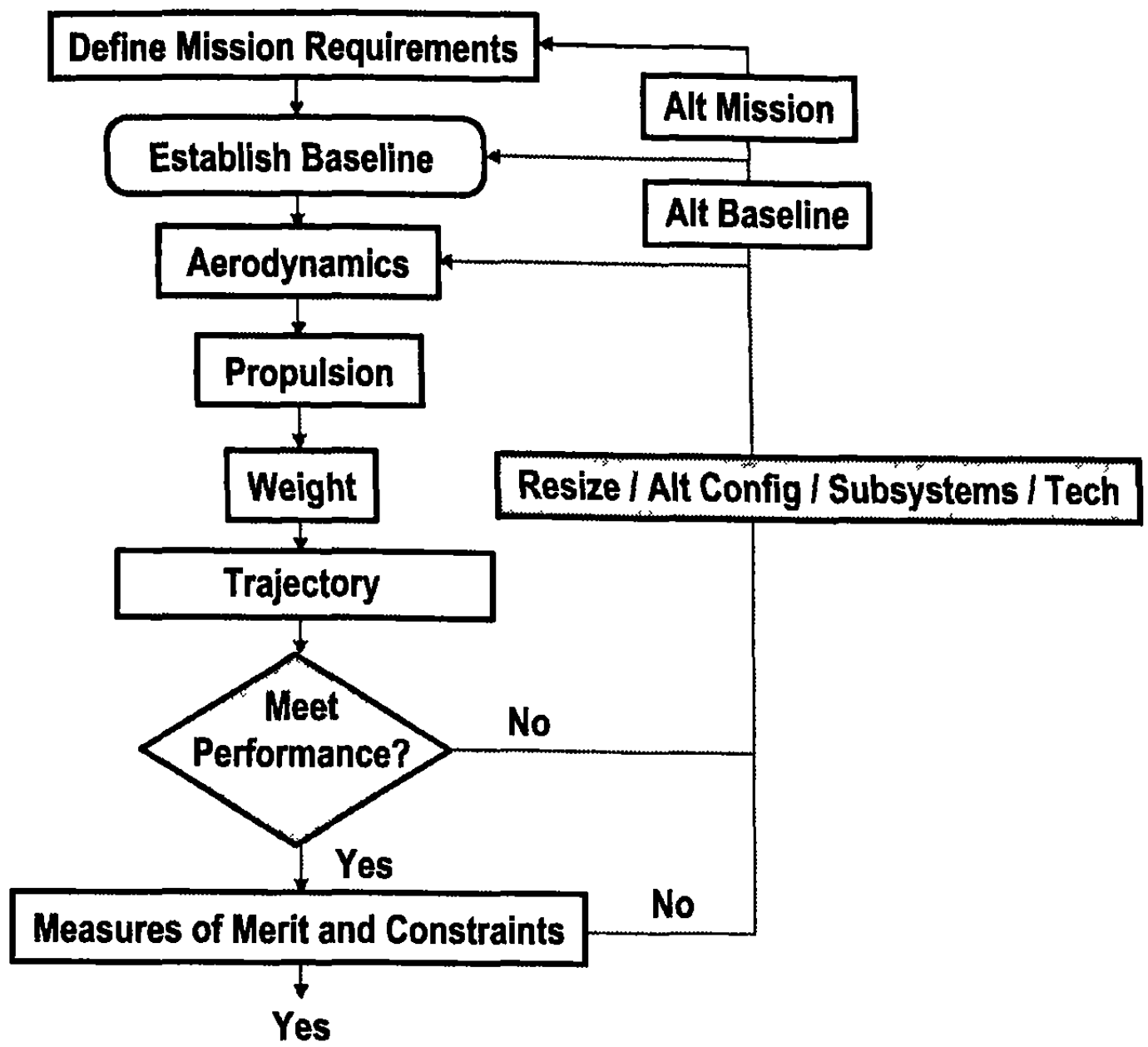

Fig. 5.15 Missile concept synthesis requires evaluation of alternatives and iteration.

5.14 Summary

Flight performance consideration in tactical missile design is oriented toward flight trajectory computation and comparison with the missile flight performance requirements. Flight performance requirements include range, velocity, time to target, and off-boresight capability. This chapter presented equations of motion modeling, examples of flight performance drivers, typical flight performance for propulsion alternatives, steady-state flight relationships, and proportional homing lead angle requirements. It also provided simplified equations for predicting steady climb, steady glide, cruise, boost, coast, turn, and ballistic flight performance. Tactical missile flight phases (e.g., boost, cruise, glide) can be patched together to compute a complete flight trajectory. Much of the impact of changes in the missile aerodynamics, propulsion, and weight is in the area of flight performance. Converging to a design that harmonizes the aerodynamics, propulsion, and weight while also satisfying the flight performance requirements is a primary activity in missile configuration design.

Problems

5.1. Flight trajectory calculation requires input from aero, propulsion, and w_____.

5.2. Missile flight envelope can be characterized by the maximum effective range, minimum effective range, and o__ b_____.

5.3. Limitations to the missile effective range include the fire control system, seeker, time of flight, closing velocity, and m_____ capability.

5.4. One-DOF simulation requires modeling only the thrust, weight, and a____ f____.

5.5. A three-DOF simulation that models three aero forces is called p____ m___ simulation.

5.6. A simulation that includes three aero forces (normal, axial, side), three aero moments (pitch, roll, yaw), thrust, and weight is called a_DOF simulation.

5.7. The pitch angular acceleration $\dot{\theta}$ is approximately equal to the second time derivative of the a____ o_ a_____.

5.8. Cruise range is a function of velocity, specific impulse, L/D, and f___ fraction.

5.9. If thrust is equal to drag and lift is equal to weight, the missile is in s_____ l____ flight.

5.10. Turn rate is a function of normal force, weight, and v_____.

5.11. Coast range is a function of initial velocity, weight, drag, and the t___ of flight.

5.12. Incremental velocity from boost is a function of I_{SP}, drag, and p_____ weight fraction.

5.13. To intercept a high-speed crossing target requires a high-speed missile with a high g_____ angle seeker.

5.14. An analytical model of a rocket in coaltitude, nonmaneuvering flight can be developed by patching together the flight phases of boost and c____.

5.15. An analytical model of a rocket in a short range, off-boresight intercept can be developed by patching the flight phases of boost and t___.

5.16. An analytical model of a guided bomb in nonmaneuvering flight can be developed from the flight phase of a steady d___.

5.17. An analytical model of an unguided weapon can be developed from the b_____ flight phase.

5.18. An analytical model of a ramjet in coaltitude, nonmaneuvering flight can be developed by patching the flight phases of boost and c_____.

6
Measures of Merit and Launch Platform Integration

6.1 Introduction

Measures of merit and launch platform integration considerations in tactical missile design include robustness, warhead lethality, miss distance, carriage and launch observables, other survivability considerations, reliability, cost, and launch platform integration/firepower. Examples of the measures of merit, launch platform integration, and conceptual design prediction methods are given in this chapter.

As shown in Fig. 6.1, the last step in missile configuration sizing is optimizing the missile design against the measures of merit requirements and any constraints, such as system of systems command, control, and communication (C^3) and launch platform compatibility. If the missile design is optimized against the measures of merit and constraints, the design has converged, and we are finished. If not, the designer selects alternative configurations, subsystems, technologies, baseline missiles, or mission requirements and the design is reiterated until it is optimized against the measures of merit and constraints.

Figure 6.2 illustrates the considerations of measures of merit and constraints for a balanced missile design. The aeromechanics performance of tactical missiles must be harmonized with other measures of merit such as robustness, warhead lethality, miss distance, carriage and launch observables, other survivability considerations, reliability, and cost as well as constraints such as launch platform integration and firepower requirements.

6.2 Robustness

The first measure of merit to be discussed is robustness. Tactical missiles must have sufficient robustness to handle effects such as adverse weather, clutter, local climate, flight environment variations, uncertainty, countermeasures, and electromagnetic interference/electromagnetic pulse (EMI/EMP). This section of the text provides examples of requirements and technologies for robustness.

Adverse weather capability is a driving concern for tactical missiles. Cloud cover is a particular concern for target sensors because clouds are pervasive worldwide. As shown in the National Oceanic and Atmospheric Administration (NOAA) typical satellite image in Fig. 6.3, clouds cover a large portion of the

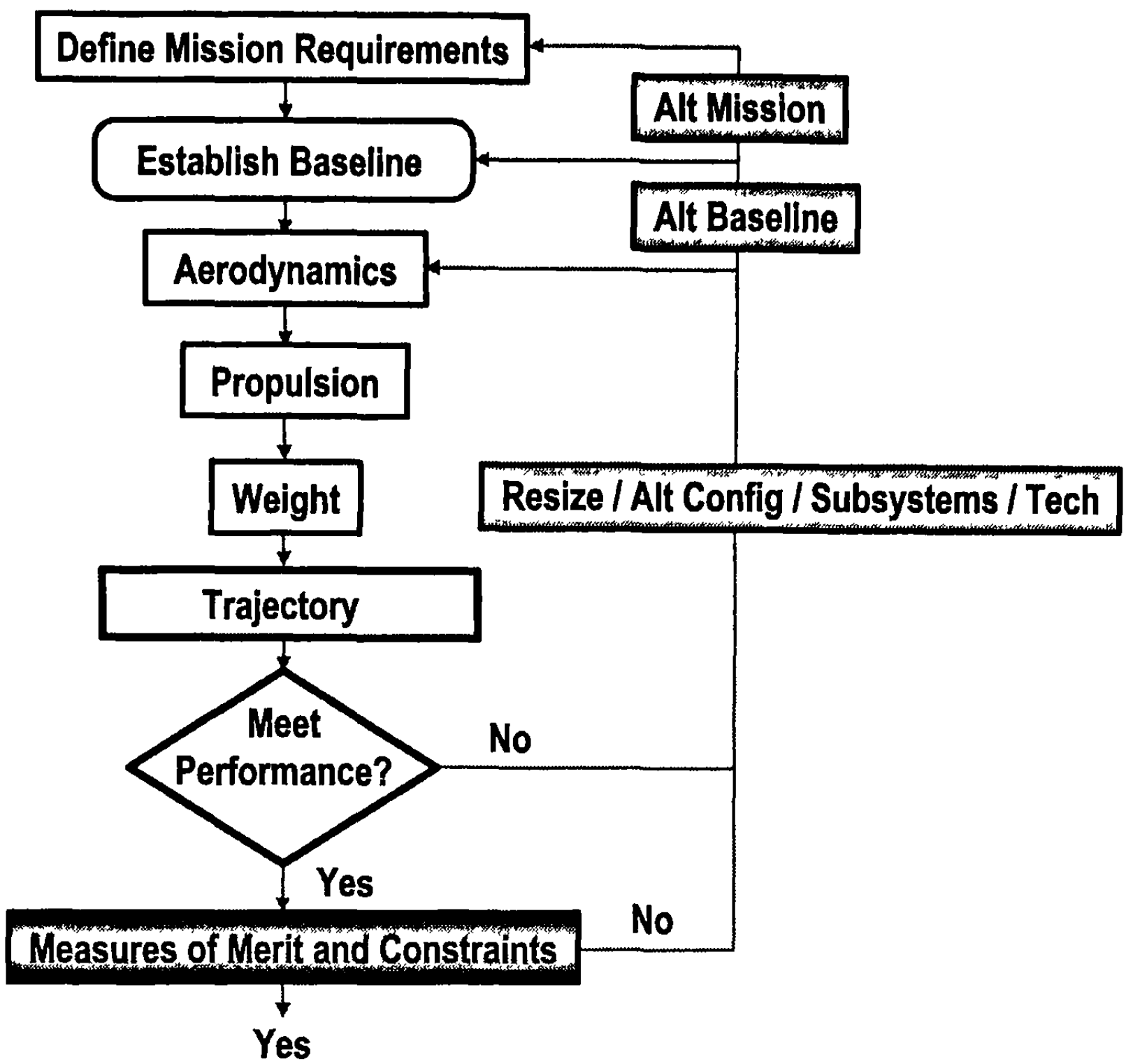

Fig. 6.1 Missile concept synthesis requires evaluation of alternatives and iteration.

earth. The figure shows that the global average annual cloud cover is about 61%. The average cloud cover over land is about 52% and the average cloud cover over the oceans is about 65%. The figure is based on Ref. 18. Clouds tend to occur between 3000 and 20,000 ft elevation. Clouds may be thick; in some cases the thickness may be greater than 6000 ft. The average annual cloud cover shown in the figure is based on weather observers around the world. It is a composite of averages that vary widely with geographical location, season, and time of day.

An example of a geographical cloud system that changes regularly with the season and the time of day is the low-level, layered stratus cloud cover over much of the world's oceans. Stratus clouds are more frequent during the summer months of the Eastern Pacific and the Eastern Atlantic and in the hours before sunrise.

Another example of a geographical cloud system that changes regularly with the season and the time of day is cumulonimbus. Cumulonimbus clouds are large columnar clouds that can extend to high altitude. These clouds are concentrated where surface temperatures are high and there is a general upward movement of the air. An example is a zone known as the Inter-Tropical Convergence Zone (ITCZ). In the ITCZ the trade winds of the Northern Hemisphere converge with those of the Southern Hemisphere. Cumulonimbus clouds have high concentrations of droplets and ice crystals, which can grow to a large size. Cumulonimbus clouds are often responsible for the frequent summer afternoon

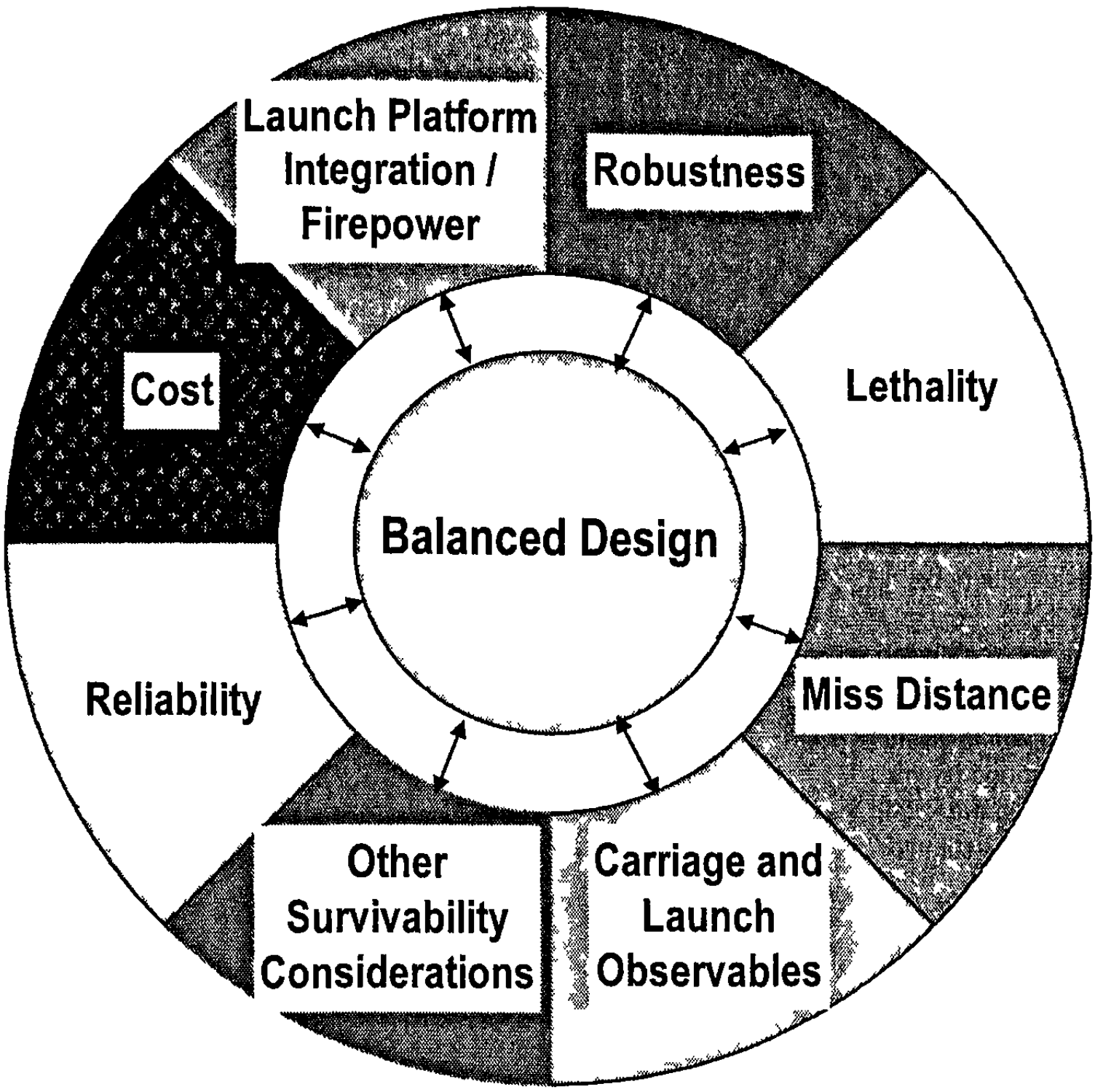

Fig. 6.2 Measures of merit and launch platform integration should be harmonized.

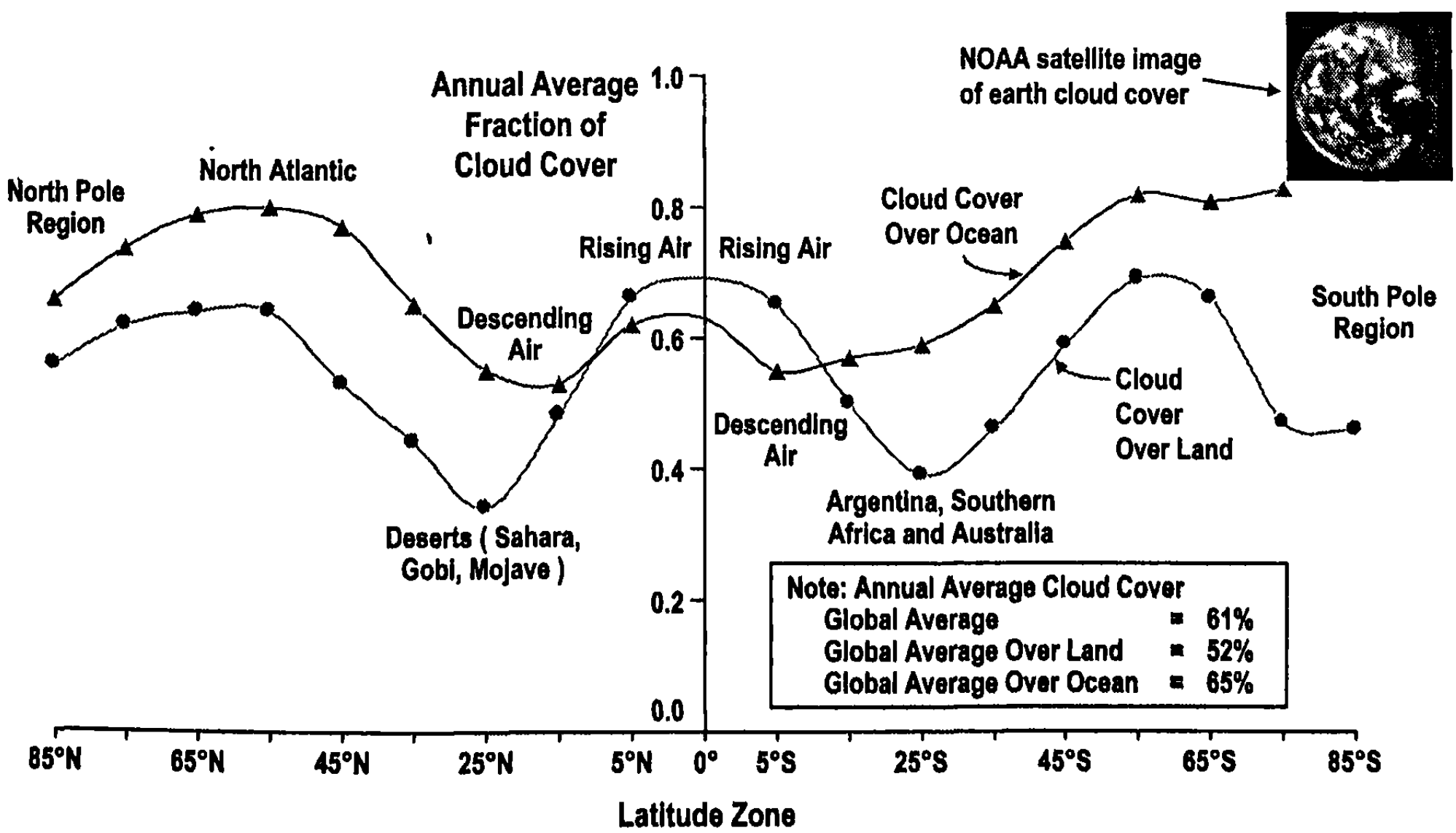

Reference: Schneider, Stephen H. *Encyclopedia of Climate and Weather.* Oxford University Press, 1996.

Fig. 6.3 Adverse weather and could cover are pervasive.

rainfall of Southeast Asia, North America, and Europe and the rainfall of the Amazon basin during December, January, and February.

For the purpose of conceptual design, an assumed cloud maximum base height of 5 km, cloud maximum thickness of 2 km, and a maximum rain rate of 4 mm/h are considered to be cost effective (e.g., 3σ) environmental requirements for tactical missile sensors. In a wet tropical climate the probability that the rain rate is currently exceeding 4 mm/h is less than 1%. In a desert environment the probability is less than 0.1%. It would be unnecessarily restrictive to require tactical target sensors to operate in 100% weather conditions, such as severe thunderstorms.

The relative locations of the missile and its target have an effect on target signal attenuation. For example, a high-altitude missile with a downward looking seeker may have larger signal attenuation in rain than that of a low-altitude missile. This is because of a longer rain path.

Shown in Fig. 6.4, based on Ref. 19, is the signal attenuation versus wavelength for a representative atmospheric environment of cloud droplet density, rain rate, and humidity level. Note that although passive electro-optical (EO) sensors have one-way transmission through rain of about 50% per km, there is almost no transmission of an EO signal through clouds. Cloud droplets are small, about 5 to 20 μm in diameter, with dimensions comparable to the EO wavelength. The concentration is high, about 50 to 500 droplets per cm^3. EO wavelengths are strongly diffracted around cloud droplets because of Mie electromagnetic (EM) scattering, which provides a concentration of the scatter in the forward direction. However, raindrops are about 2 to 6 mm in diameter (much larger than EO wavelengths) and cause less attenuation of an EO signal. Rain

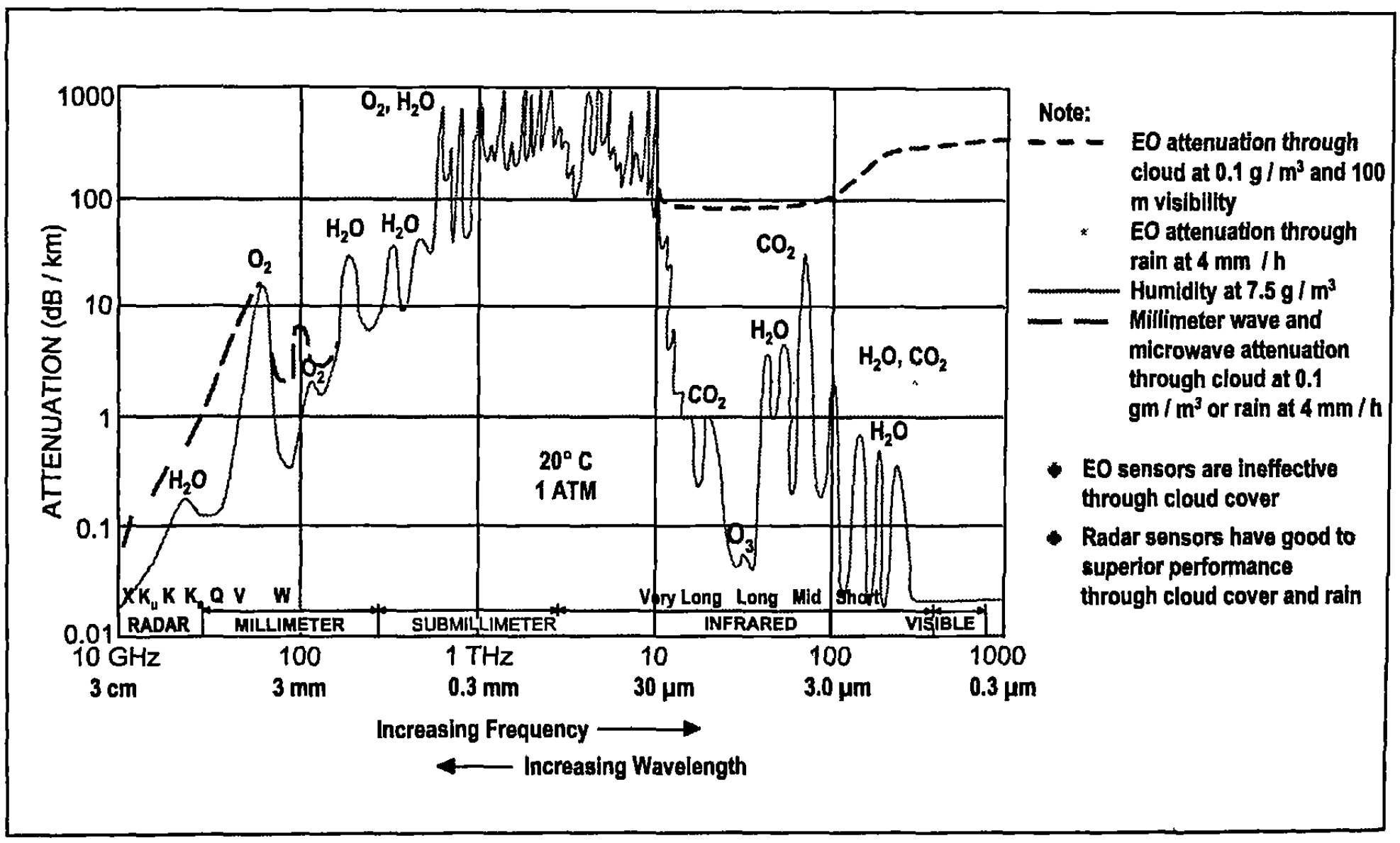

Source: Klein, L.A., *Millimeter-Wave and Infrared Multisensor Design and Signal Processing*, Artech House, Boston, 1997

Fig. 6.4 Radar seekers are robust in adverse weather. Figure also in color section.

rate attenuation is primarily from optical scattering. EO transmission through rain is a function of the size of the raindrops, rain rate, and the path length through the rain. EO passive sensors are limited from about 2 to 5 km of path length through the rain. EO focal plane array sensors for tactical missiles cover the wavelength range from ultraviolet (UV) through long-wave infrared (LWIR).

The best sensors for looking through cloud cover and rain are radar sensors. Radar sensors have negligible atmospheric attenuation at frequencies below 10 GHz. At higher frequencies, millimeter wave (mmW) sensors operating in cloud cover and rain are limited to about 2 to 5 km of path length through the clouds and rain, with the same implications as those discussed in the previous paragraph. Cloud droplets, which are much smaller than mmW wavelengths, absorb mmW radiation (much like a microwave oven). A different mechanism is responsible for the attenuation of a mmW signal through rain or snow. Raindrops and snowflakes are comparable in size to mmW wavelengths and cause Rayleigh and Mie EM scattering attenuation. Lower frequency radars, such as Ku-band radars, are less affected by cloud cover and rain rate.

As shown in Fig. 6.5, most clouds occupy elevation heights between 3000 and 20,000 ft, which is much of the altitude of interest for tactical missiles. Also, as shown previously, cloud cover is a frequent occurrence. Because of the extent and frequency of cloud cover, EO sensors are often limited in their applications. The Low Cost Autonomous Attack System (LOCAAS) and the Brilliant Anti-Tank (BAT) submunitions minimize the problem of cloud cover by operating at low altitude under most clouds. LOCAAS and BAT also fly at low velocity to maximize the time available for target lock-on and homing under the constraint of a shallow look-down angle. The "under the weather" operation is effective for

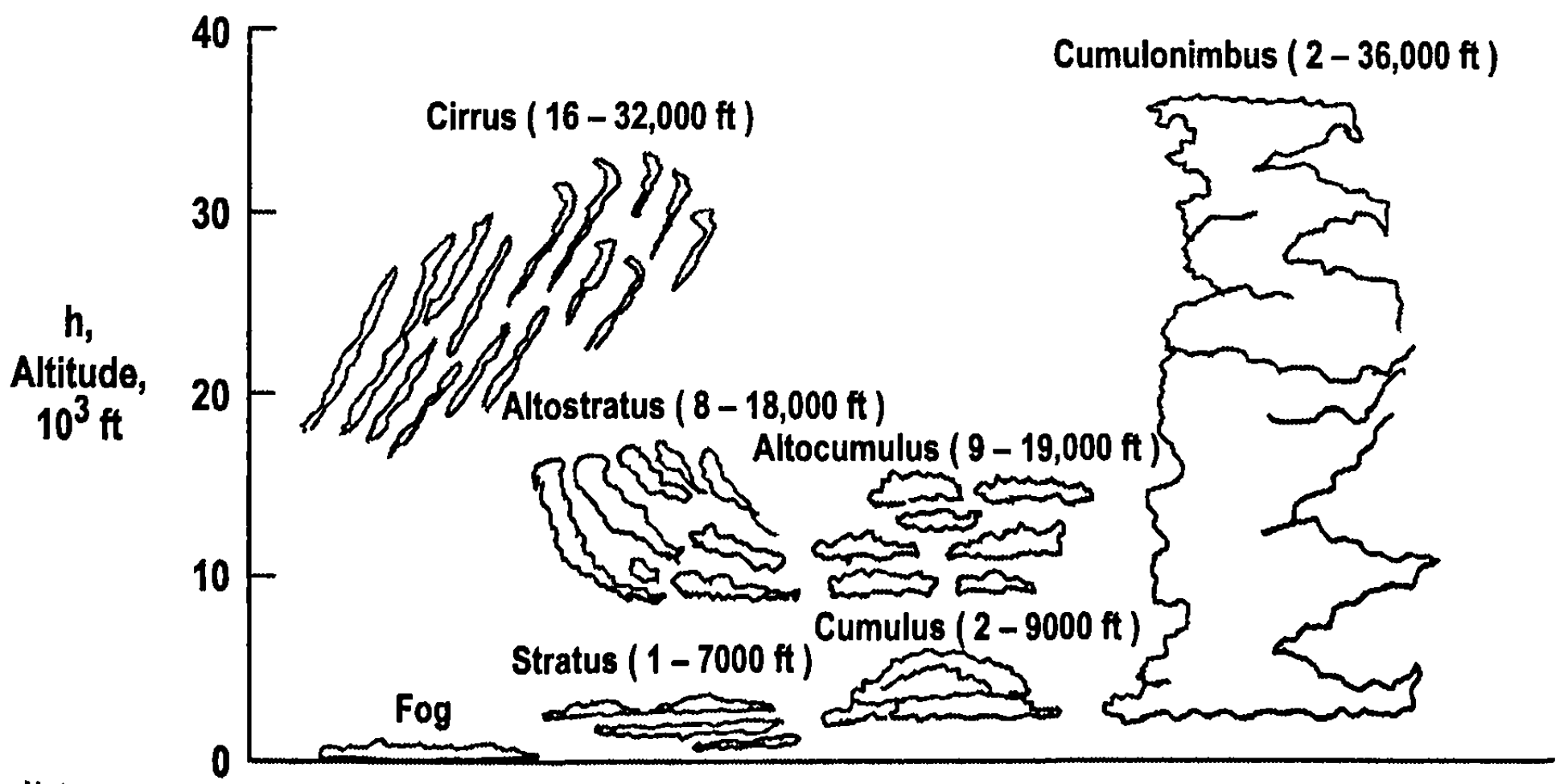

Note:
- IR seeker may be able to operate "Under the Weather" at elevations less than 2000 ft using GPS / INS midcourse guidance
- IR attenuation through cloud cover greater than 100 dB per km. Cloud droplet size (0.1 to 50 μm) causes resonance.
- mmW has ~ 2 dB/km attenuation through rain. Typical rain drop size (~ 4 mm) is comparable to mmW wavelength.

Fig. 6.5 Radar seekers are desirable for robust operation within the troposphere cloud cover.

most conditions except for the occurrence of fog, heavy rain, and obscurants. The search capability operating at low altitude is improved by adding an additional wide field of view (FOV) sensor, such as passive imaging IR. For example, a wide FOV sensor could cue a narrow FOV sensor, such as a laser detection and ranging (LADAR) sensor, for target recognition, acquisition, and fine tracking. However, as stated previously, for most missiles operating in adverse weather, especially supersonic missiles, the most robust sensors are radar sensors.

A comparison of sensor alternatives for precision strike missiles is shown in Fig. 6.6. The measures of merit are: 1) performance in an adverse weather environment such as cloud cover, rain, snow, or dust, 2) automatic target recognition (ATR)/automatic target acquisition (ATA) performance in ground clutter, 3) sensor range, 4) performance against moving targets, 5) volume search cycle time to cover the required FOV/field of regard, 6) compatibility with a dome suitable for hypersonic application, 7) diameter required, 8) weight/cost, and 9) technology maturity.

Synthetic aperture radar (SAR) is a potential sensor with many performance advantages for a precision strike missile. SAR has the flexibility required to cover an area search for single-cell target detection and then switch to high resolution for target identification and targeting. SAR sensors can also provide high-accuracy profiling of the terrain features around the target to provide a reference for deriving global positioning system (GPS) coordinates of the target. Polarization provides a SAR sensor with the capability to extract information on the physical shape characteristics of the target. Other discriminates that improve the ATR performance of SAR include motion detection and

Sensor	Adverse Weather Impact	ATR / ATA in Clutter	Range	Moving Target	Volume Search Time	Hypersonic Dome Compat.	Diameter Required	Weight and Cost	Maturity
• SAR	●	◒	●	○	◒	●	○	-	-
• Active Imaging mmW	◒	○	◒	●	○	●	○	-	-
• Passive Imaging mmW	◒	●	-	○	○	●	-	○	-
• Active Imaging IR (LADAR)	-	●	○	◒	-	○	●	◒	◒
• Active Non-image IR (LADAR)	-	○	○	◒	◒	○	◒	●	●
• Active Non-image mmW	◒	-	◒	◒	●	●	●	○	●
• Passive Imaging IR	-	◒	◒	○	◒	-	●	◒	◒
• Acoustic	●	◒	-	○	●	-	-	●	◒
• GPS / INS / Data Link	●	●	●	-	●	●	●	●	◒

Note: ● Superior ◒ Good ○ Below Average - Poor

Fig. 6.6 Precision strike missile target sensors are complemented by GPS/INS/data link sensors.

three-dimensional imagery. The weight and cost of SAR sensors have been reduced in recent years. However, SAR technology is relatively immature for tactical missiles. There are no current SAR missiles.

Active imaging mmW is another potential sensor for future missiles. Cost and technology maturity are limitations. PAC-3 has a pseudo-imaging capability for target aim-point selection.

A passive imaging mmW sensor is another sensor with potential application to future precision strike missiles. Passive imaging mmW has an advantage over EO in the capability to see through cloud cover and its high contrast of metal objects in the mmW spectrum. Advantages over active radar sensors include lower observables (passive), lower noise, and avoidance of radar glint. The cold sky temperature is about 35 K and is reflected by metal objects at mmW frequencies. The temperature of terrestrial object clutter is about 300 K and is not reflected. There are no current passive imaging mmW missiles.

Other sensors for precision strike include active imaging IR based on LADAR, passive imaging staring or scanning IR, active nonimaging mmW or centimeter wave (cmW) radar, active nonimaging LADAR, passive nonimaging IR, visible, and acoustic/seismic. Sensors cover the range of acoustic to visible. Because sensors have limitations in one or more areas, multimode sensors using sensor data fusion will be developed for future missiles. Multidimensional orthogonal discriminants that are likely to be used in sensor data fusion include angular resolution, range resolution, contrast, polarization, temporal, multispectral, and gas composition signatures of the target. Because of the importance of operating in adverse weather, radar sensors are projected to have increased usage for future precision strike missiles.

GPS/inertial navigation system (INS)/data link guidance is an enabling capability for precision navigation and the fusion of target sensor data in a clutter environment. GPS/INS accuracy for a tightly coupled system in the Wide Area GPS Enhancement (WAGE), differential, or relative modes has sensor hand-off error less than 3 m, allowing precision guidance against a fixed target without having to use a seeker. A tightly coupled GPS/INS system corrects the navigation error through Kalman filtering. A typical Kalman filter has about 23 states, correcting measurements such as the missile position error (3 states for x, y, and z location), velocity error (3 states), attitude error (3 states), accelerometer bias (3 states), gyro bias (3 states), GPS receiver clock bias (1 state), GPS receiver clock drift (1 state), data link radar misalignment (3 states), and launch position error (3 states). The enhanced accuracy from GPS coordinates of the target facilitates seeker lock-on in clutter. Clutter is particularly high in an urban environment.

A data link allows a target location update during missile flight, which is particularly useful against a movable target. A real-time data link has the potential to eliminate the seeker, reducing missile cost. In the case of a data link with sufficient bandwidth (approximately 100 Mb/s) to provide target image data, transmitting an image of the target prior to impact reduces the possibility of collateral damage and provides battle damage indication (BDI) information. At the present time a limitation for data links is their capability against moving targets. Real-time data links that could replace seekers are currently limited to slowly moving targets, such as surface moving targets.

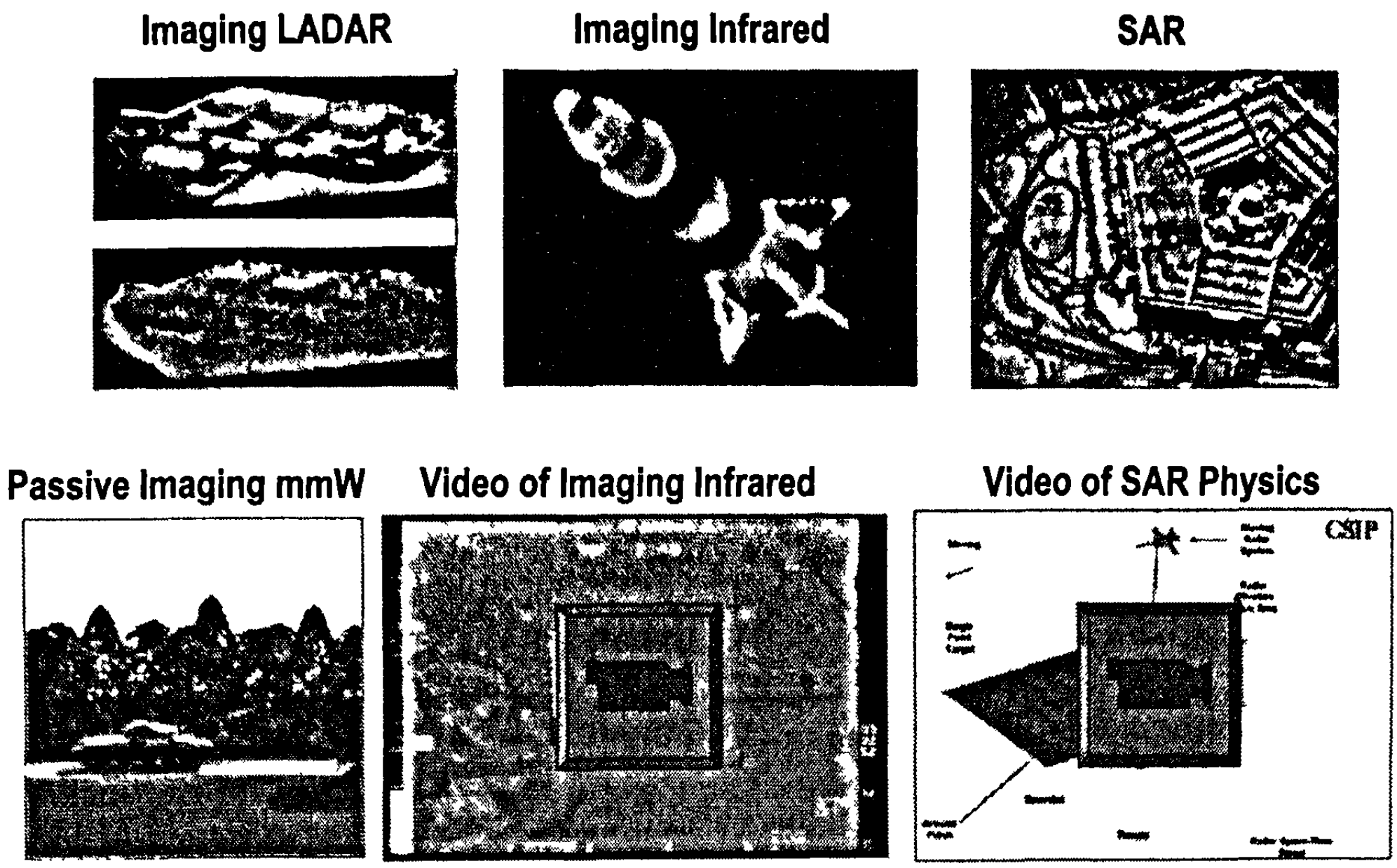

Fig. 6.7 Imaging sensors enhance target acquisition/discrimination. Figure also in color section. Videos are in the CD included with this textbook.

Shown in Fig. 6.7 are examples of the resolution for tactical missile imaging sensors. An example of the resolution of a LADAR sensor is shown in the upper left corner of the figure. A LADAR sensor has the best resolution for target discrimination. It also provides three-dimensional imagery, enhancing ATR. The next best resolution is a passive imaging IR sensor. The top middle image shows the resolution of the SM-3 Standard Missile 256 × 256 imaging IR seeker against a Lance missile target. IR sensors are in development with resolution up to 1000 × 1000 pixels. The upper right image is from a SAR sensor. SAR has a resolution of about 0.3 m, independent of range. At very long range a SAR sensor has higher resolution than the other sensor alternatives. The bottom left image is from a passive imaging mmW sensor. Passive imaging mmW has relatively low resolution. Array sizes up to 60 × 75 elements have been produced, with apertures sizes down to 0.4 meter in diameter. The frequency and frame rate demonstrated to date are 89 GHz and 30 Hz respectively. Passive imaging mmW is a relatively immature technology, and the resolution is expected to improve in the future.

The bottom center section of the figure is a video from a 256 × 256 imaging IR seeker. The AGM-130 missile is attacking a bridge in Kosovo. The initial phase of flight before seeker lock-on is provided by GPS/INS. Note the initially low contrast and high clutter for the GPS/INS-guided portion of the flight. As the missile closes on the target in the final (seeker guided) portion of the flight there are higher contrast, less clutter, and higher resolution.

The bottom right section of the figure is a video demonstration of the physics of SAR. The video is courtesy of the Georgia Tech Center for Signal and Image Processing (CSIP). Shown is a flight vehicle with a fixed side-looking SAR

sensor operating in a strip map mode. Along the flight path the SAR sensor and computer measure and process the amplitude, phase, and frequency of the back-scattered signal. The SAR computer stores the received signals at each point in time and files them as to position, amplitude, and phase. As an example in the video, at time zero the target is at the edge of the effective beam area of the SAR sensor. There is a relatively long time delay in receiving the return from the target from the large downrange and lateral offset distances. At the next time the time delay is smaller, because the distances are smaller. This continues until the target is in the center of the radar effective beam area, with a minimum time delay in the return signal. As the vehicle continues, the target moves out of the center of the radar effective beam area, and the time delay increases. Summing up the radar space-time signals provides the location of the target. An alternative approach to strip map SAR, which has a relatively long dwell time because of the time for a point on the ground to travel through the antenna beam, is scanning SAR. For scanning SAR, the dwell time is the time required to scan one beam width. Although scanning SAR has less resolution than strip map SAR, scanning SAR is more often used because it provides a relatively high search rate. SAR requires accurate velocity measurement and motion compensation to support the signal processing. A precision inertial navigation system is required, which is one reason why SAR is relatively expensive.

Next, design considerations in the tradeoff of a passive midwave IR seeker versus a passive long-wave infrared seeker will be illustrated by examining the detection range equation. The equation for detection range is

$$R_{\mathrm{D}} = \left\{(I_{\mathrm{T}})_{\Delta\lambda}\eta_{\mathrm{a}}A_{\mathrm{o}}\left\{D^{*}/(\Delta f_{\mathrm{p}}^{1/2}A_{\mathrm{d}}^{1/2})\right\}(S/N)_{\mathrm{D}}^{-1}\right\}^{1/2} \tag{6.1}$$

As shown in the equation, there are seven drivers for IR seeker range: radiant intensity of the target within the upper and lower wavelength cutoffs of the seeker $(I_{\mathrm{T}})_{\Delta\lambda}$, atmospheric transmission efficiency for the total distance from the target to the seeker η_{a}, seeker optics aperture area A_{o}, pixel specific detectivity D^{*}, pixel detector bandwidth Δf_{p}, detector total area A_{d}, and signal-to-noise ratio required for detection $(S/N)_{\mathrm{D}}$.

Referring to the first term in the preceding equation for seeker range, the radiant intensity of the target for a gray body radiator is given by the equation

$$(I_{\mathrm{T}})_{\Delta\lambda} = \varepsilon L_{\lambda}(\lambda_2 - \lambda_1)A_{\mathrm{T}} \tag{6.2}$$

In the preceding equation ε is the emissivity of the target, L_{λ} is the spectral radiance, λ_2 is the upper wavelength cutoff of the seeker, λ_1 is the lower wavelength cutoff of the seeker, and A_{T} is the target planform area viewed by the seeker (assumed to be a Lambertian source at long distance). Radiant intensity is the power emitted per unit solid angle from an isotropic radiator, a theoretical point source that radiates equally in all directions in three-dimensional space. The units of radiant intensity are $W\mathrm{sr}^{-1}$. Inspecting the first term of the equation for $(I_{\mathrm{T}})_{\Delta\lambda}$, the value of ε is between 0 (perfect polished mirror) and 1 (blackbody radiator/absorber). Emissivity is a function of the target material, surface roughness, and temperature. As an example, the emissivity of aluminum is less than 0.3

while the emissivity of carbon is greater than 0.7. The second term in the $(I_T)_{\Delta\lambda}$ equation is spectral radiance L_λ. Spectral radiance is given by Planck's law, which states

$$L_\lambda = 3.74 \times 10^4 / \{\lambda^5 \{e^{[1.44\times10^4/(\lambda T_T)]} - 1\}\} \tag{6.3}$$

Units are $W cm^{-2} sr^{-2} \mu m^{-1}$. It can be seen from Planck's law that higher spectral radiance occurs at shorter wavelength and higher temperature. The third term in the $(I_T)_{\Delta\lambda}$ equation is the upper wavelength cutoff λ_2 of the seeker. It is a design consideration that includes tradeoffs such as maximizing the energy collected at longer wavelengths, maximizing the atmospheric transmission, maximizing the quality of the optics design, and minimizing background clutter. The lower wavelength cutoff λ_1 has similar tradeoffs, including minimizing stray solar radiation. Finally, the area of the target A_T is an obvious design driver; a smaller target has less radiant intensity than a larger target.

Referring to the seeker range equation, the second term is atmospheric transmission efficiency η_a. It accounts for the attenuation over the total distance from the target to the seeker. The transmission can range from perfect transmission ($\eta_a = 1$) for exo-atmospheric conditions to almost no transmission ($\eta_a \approx 0$) through clouds. The effect of atmospheric transmission on detection range was illustrated previously in Chapter 2.

The third term in the seeker range equation is the seeker optics aperture area. As discussed in the second chapter of this text, optics diameter is a major design parameter. A larger aperture delivers more optical energy to the detectors, providing longer detection range. It also provides better resolution.

The fourth term in the seeker range equation is specific detectivity D^*, which is the sensitivity performance of the detector material. D^* allows a comparison of different detector materials on a material basis only. The units are $cm Hz^{1/2} W^{-1}$. D^* represents the signal-to-noise (S/N) ratio when 1 W of radiation is incident upon a detector with a sensitive area of 1 cm^2 and the noise is measured at an electrical bandwidth of 1 Hz. D^* for an IR detector varies widely, with values ranging from as low as 10^9 to greater than 10^{12}, depending upon the detector material, detector cooling temperature, and wavelength. As a reference, the human eye has a D^* of 10^{14} in the visible wavelengths. A low-cost detector such as bolometer thermal detector has a relatively low value of D^*, about 10^9. A high-performance detector such as $Hg_{0.67}Cd_{0.33}Te$ has a value of D^* of about 8×10^{11} at a detector temperature of 77 K (liquid nitrogen) when it is optimized for midwave IR (e.g., 4 μm) application. The strong impact of detector cooling on D^* can seen from the theoretical D^* equation for a bolometer thermal detector as

$$D^* = (8\pi\sigma k T^5)^{-1/2}$$

Substituting for the Stephan–Boltzman constant $\sigma = 5.67 \times 10^{-12}\ W cm^{-2} K^{-4}$ and Boltzman's constant $k = 1.3807 \times 10^{-23}\ W s K^{-1}$ gives a theoretical maximum

$$D^* = 7.02 \times 10^4\, T^{-5/2} \tag{6.4}$$

As an example, for an uncooled bolometer at room temperature (e.g., $T = 300$ K), the theoretical $D^* = 1.44 \times 10^{10}$ is lower than that of a bolometer detector cooled to liquid nitrogen temperature ($T = 77$ K), which has a theoretical $D^* = 4.32 \times 10^{11}$.

Referring back to the seeker range equation, the fifth term is the pixel detector bandwidth Δf_p. Selecting the pixel detector bandwidth and integration time is a tradeoff of signal versus noise. The pixel detector signal increases approximately linearly with the integration time while random noise increases with the square root with time. Pixel detector bandwidth is related to integration time by the equation

$$\Delta f_p = 2\pi t_{\text{integ}} \tag{6.5}$$

The pixel integration time, also called dwell time, can be selected to optimize the detector signal-to-noise ratio. For HgCdTe detectors, the optimum integration time typically varies from about 0.5 to about 8 ms. A background with high temperature/noise requires a shorter dwell time for an optimum signal-to-noise ratio. A low noise detector with low noise electronics in a low background temperature/noise environment provides a higher S/N ratio with longer dwell time. Note that either the pixel detector electron well capacity of a HdCdTe detector or the guidance update rate, or frame rate, may set an upper limit on the pixel dwell time. As an example, for a fast guidance update rate of 100 Hz (10 ms), the pixel dwell time must be less than 10 ms.

The sixth term in the IR seeker range equation is the active area of the detector A_d. For a focal plane array it is the active area of a single pixel multiplied by the total number of pixels in the FPA. A small size pixel (e.g., 12 μm) has advantages of longer detection range and better resolution while a large size pixel (e.g., 60 μm) has an advantage of lower manufacturing cost. A large focal plane array (e.g., 1024×1024) has an advantage of a large FOV while a smaller FPA (e.g., 128×128) has advantages of lower manufacturing cost and higher reliability.

The final term in the seeker range equation is the S/N ratio that is required for detection. The S/N ratio required for detection of a noise limited system can be as low as $(S/N)_D = 1$ or as high as $(S/N)_D = 5$, depending upon the sophistication of the signal processing and the background noise. For a target in a background where the temperature of the background is comparable to the temperature of the target, detection may be background limited rather than detector noise limited. A higher value of S/N ratio (e.g., $S/N > 10$) is required for a low signature target in clutter.

As an example, the detection range will be calculated for a 5-in aperture seeker in an exo-atmospheric intercept. The seeker is assumed to operate over a wavelength range of 3.0 to 5.0 μm, with an average wavelength of $\lambda = 4$ μm. The target characteristics are 2 ft diameter ($A_T = 2919\ \text{cm}^2$), temperature $T_T = 300$ K, and emissivity $\varepsilon = 0.5$. The spectral radiance of the target is computed to be

$$\begin{aligned} L_\lambda &= 3.74 \times 10^4 / \{4^5 \{e^{\{1.44 \times 10^4/[4(300)]\}} - 1\}\} \\ &= 0.000224\ W\text{cm}^{-2}\text{sr}^{-2}\mu\text{m}^{-1} \end{aligned} \tag{6.6}$$

Substituting into the equation for target radiant intensity gives

$$(I_T)_{\Delta\lambda} = 0.5(0.000224)(5.0 - 3.0)(2896) = 0.643\ W\text{sr}^{-1} \tag{6.7}$$

The detector is assumed to be a diffraction limited 256 × 256 focal plane array with 40 μm pixels. Detector area is $A_d = 256(256)(0.004)^2 = 1.049\ \text{cm}^2$. A $Hg_{0.67}Cd_{0.33}Te$ detector is assumed, which has a value of D^* of about 8×10^{11} at a detector temperature of 77 K (liquid nitrogen) when it is optimized for midwave IR (e.g., 4 μm) application. The pixel detector bandwidth for best S/N ratio is assumed to be $\Delta f_p = 50$ Hz and the S/N for detection is assumed to be $(S/N)_D = 5$. Substituting into the IR seeker range equation gives

$$\begin{aligned} R_D &= \{(I_T)_{\Delta\lambda}\eta_a A_o\{D^*/(\Delta f_p^{1/2}A_d^{1/2})\}(S/N)^{-1}\}^{1/2} \\ &= \times\{0.0643(1)(0.01267)\{8 \times 10^{11}/[(50)^{1/2}(1.049)^{1/2}]\}(5)^{-1}\}^{1/2} \\ &= 13{,}420\ \text{m} \end{aligned} \tag{6.8}$$

Next, the detection range will be calculated for a LWIR seeker with consistent assumptions that were applicable to the midwave IR seeker. The unique assumptions for the LWIR seeker are a nominal wavelength of $\lambda = 10$ μm, an upper cutoff wavelength $\lambda_2 = 13$ μm, a lower cutoff wavelength $\lambda_1 = 7$ μm, and an $Hg_{0.80}Cd_{0.20}Te$ detector that is optimized for best performance at $\lambda = 10$ μm and 77 K detector cooling. The specific detectivity $D^* = 5 \times 10^{10}\ \text{cm}^{1/2}\ \text{Hz}^{1/2}\text{W}^{-1}$. Again, the equation for detection range is $R_D = \{(I_T)_{\Delta\lambda}\eta_a A_o\{D^*/(\Delta f_p^{1/2}A_d^{1/2})\}(S/N)_D^{-1}\}^{1/2}$, the equation for radiant intensity is $(I_T)_{\Delta\lambda} = \varepsilon\ L_\lambda(\lambda_2 - \lambda_1)A_T$, and the equation for spectral radiance is $L_\lambda = 3.74 \times 10^4/\{\lambda^5\{e^{[1.44\times10^4/(\lambda T_T)]} - 1\}\}$. Substituting,

$$L_\lambda = 0.00310\ W\text{cm}^{-2}\text{sr}^{-2}\mu\text{m}^{-1} \tag{6.9}$$

Substituting for L_λ gives

$$(I_T)_{\Delta\lambda} = 26.7\ W\text{sr}^{-1} \tag{6.10}$$

$$\begin{aligned} \text{Then}\quad R_D &= \{(26.7)(1)(0.01267)\{(5 \times 10^{10})/[(50)^{1/2}(1.049)^{1/2}]\}(5)^{-1}\}^{1/2} \\ &= 21{,}600\ \text{m} \end{aligned} \tag{6.11}$$

Note that the LWIR seeker has 61% more range than the midwave infrared (MWIR) seeker for the example against a low-temperature target. This illustrates that target temperature is often a driving consideration in selecting the best seeker wavelength. Most of the spectral radiance of low temperature targets is in the long-wave region (e.g., 8 to 12 μm) while for high-temperature targets most of the spectral radiance is at midwave (e.g., 3 to 5 μm). Figure 6.8 shows the wavelength for maximum spectral radiance $\lambda_{(L_\lambda)_{max}}$ at a given target temperature T_T. The

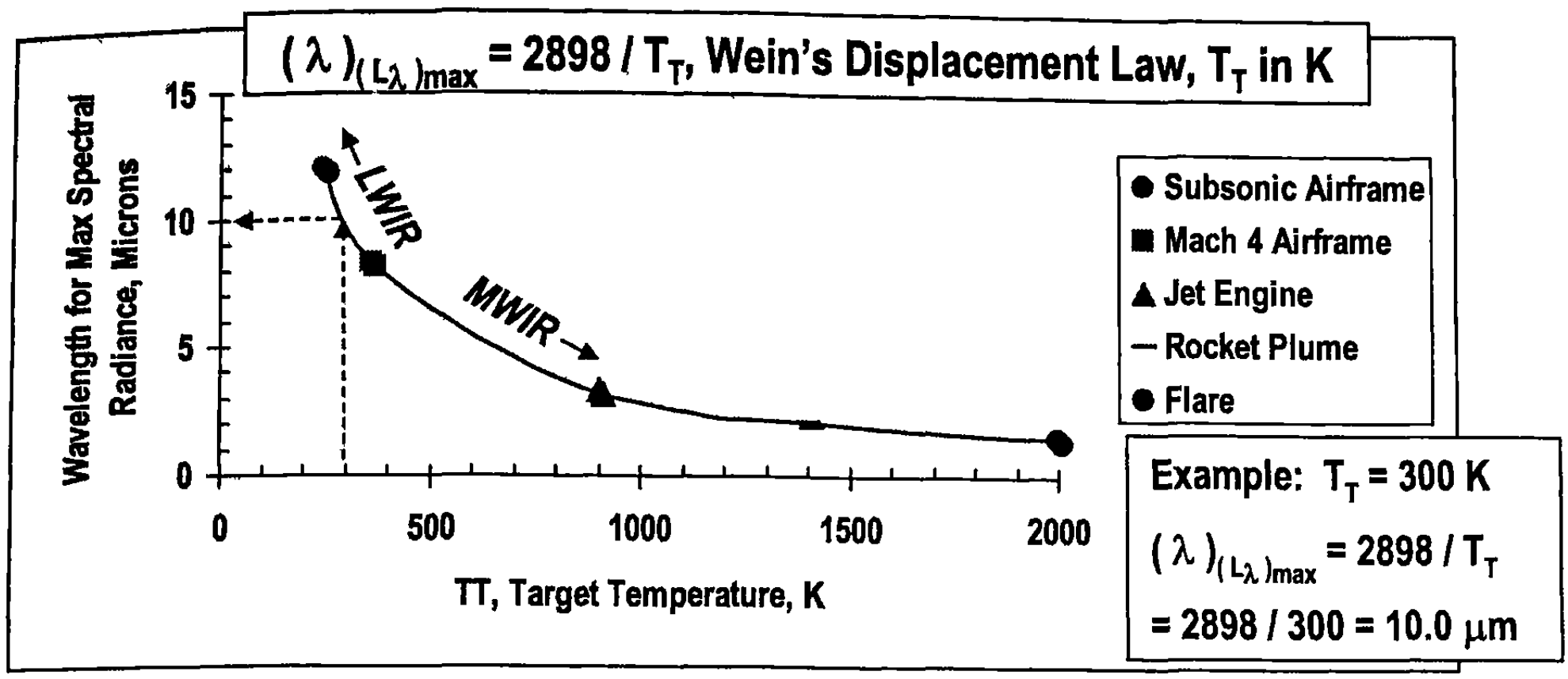

Fig. 6.8 Longwave versus midwave infrared seeker selection depends upon target temperature.

equation is based on Wein's Displacement Law, which states

$$\lambda_{(L_\lambda)_{\max}} = 2898/T_{\mathrm{T}} \tag{6.12}$$

In the above equation T_{T} is the target temperature in K. Note from Fig. 6.8 that an LWIR seeker is probably best for homing against a relatively cold airframe target while an MWIR seeker is probably best for homing against a relatively hot jet engine or rocket plume target. As an example, assume a cold target with $T_{\mathrm{T}} = 300$ K. The wavelength for maximum spectral radiance is $\lambda_{(L_\lambda)_{\max}} = 2898/T_{\mathrm{T}} = 2898/300 = 10.0\ \mu\mathrm{m}$.

Figure 6.9 illustrates the benefit of precision GPS/INS guidance. The example is a bridge target in adverse weather and in a high clutter environment consisting of a river and rolling terrain. In this example a high-resolution (640 pixels × 480 pixels) strapdown imaging infrared (IIR) seeker provides terminal homing. The aimpoint is the center pier of the bridge. Note that even for a relatively large target such as the bridge in the figure, at the initial range of 850 m there is a large amount of clutter in the seeker FOV. The 20-deg FOV seeker provides a 300 m × 230 m scene. However, GPS/INS precision accuracy (3 m), allows delay of seeker lock-on and terminal guidance until the missile is closer to the target. As the missile closes to the ranges of 500 m and 250 m, note that there is less and less clutter. Finally, at a range-to-go of 125 m, note that there is almost no clutter within the seeker FOV. The GPS/INS accuracy of 3 m is comparable to the tracking accuracy of the seeker, allowing a smooth transition from GPS/INS midcourse guidance to seeker terminal guidance. For a typical closing velocity of 300 m/s and guidance update rate of 60 Hz, there are up to 25 guidance updates available to conduct ATR when the weapon is at a range-to-go of 125 m. At this point the terminal accuracy is driven more by airframe response than seeker tracking error. As a result of the GPS/INS precision guidance, the missile has high probability of hitting the center pier aim point and dropping the center span of the bridge. A GPS/INS guided missile can be treated almost

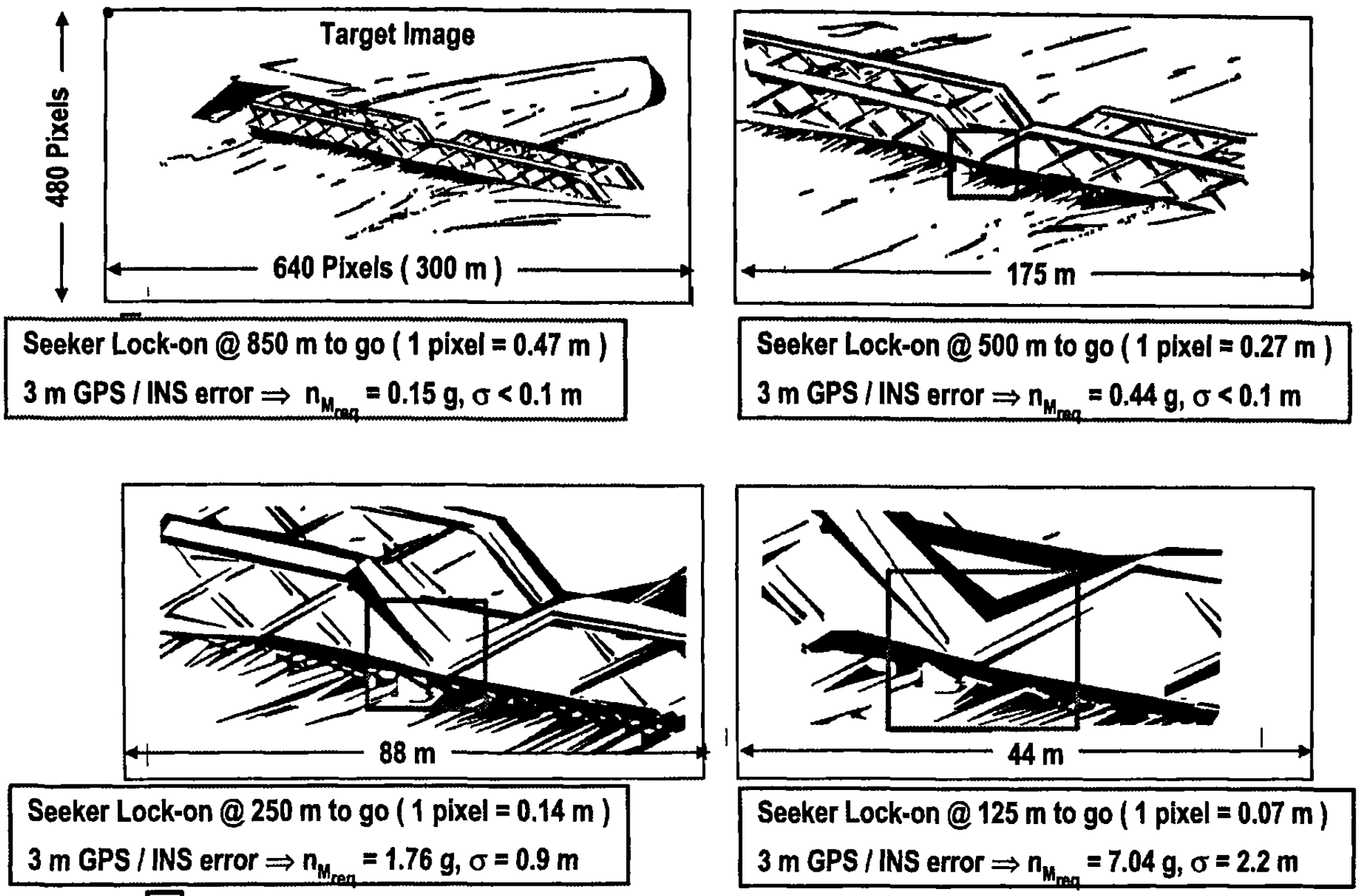

Fig. 6.9 GPS/INS provides robust seeker lock-on in adverse weather and clutter.

like an artillery projectile, with a high probability of impacting in the target area and a low probability of collateral damage.

Benefits of tightly coupled integration of the INS with the GPS for navigation include high-precision position and velocity measurement and reduced jamming susceptibility. The availability of GPS to continuously update the inertial system allows the design trades to consider a lower precision and less-expensive INS, while maintaining good navigation accuracy and anti-jam (A/J) performance.

Advanced GPS/INS receivers are based on a centralized Kalman filter that processes the raw data from all of the sensors (e.g., SAR seeker, GPS receiver, INS). Tightly coupled GPS/INS is more robust against jamming because it is able to make pseudorange measurements from three, two, or even one satellite if one or more of the satellites are lost.

Also shown in the figure is the missile maneuverability requirement to correct the heading error at seeker lock-on. Because of the accuracy of GPS/INS the maneuverability required is very low at long range and becomes significant (e.g., greater than 2 g) only if the seeker lock-on range is less than 200 m.

A data link that provides an update of a moving target location during the missile fly-out facilitates seeker lock-on. The target error (TE) at seeker lock-on is a function of the target location error (TLE) at an update, target velocity V_T, and the target latency time $t_{Latency}$. Target latency is the time between the last update and seeker lock-on, given by the equation

$$t_{Latency} = t_{Seeker} - t_{Update} \tag{6.13}$$

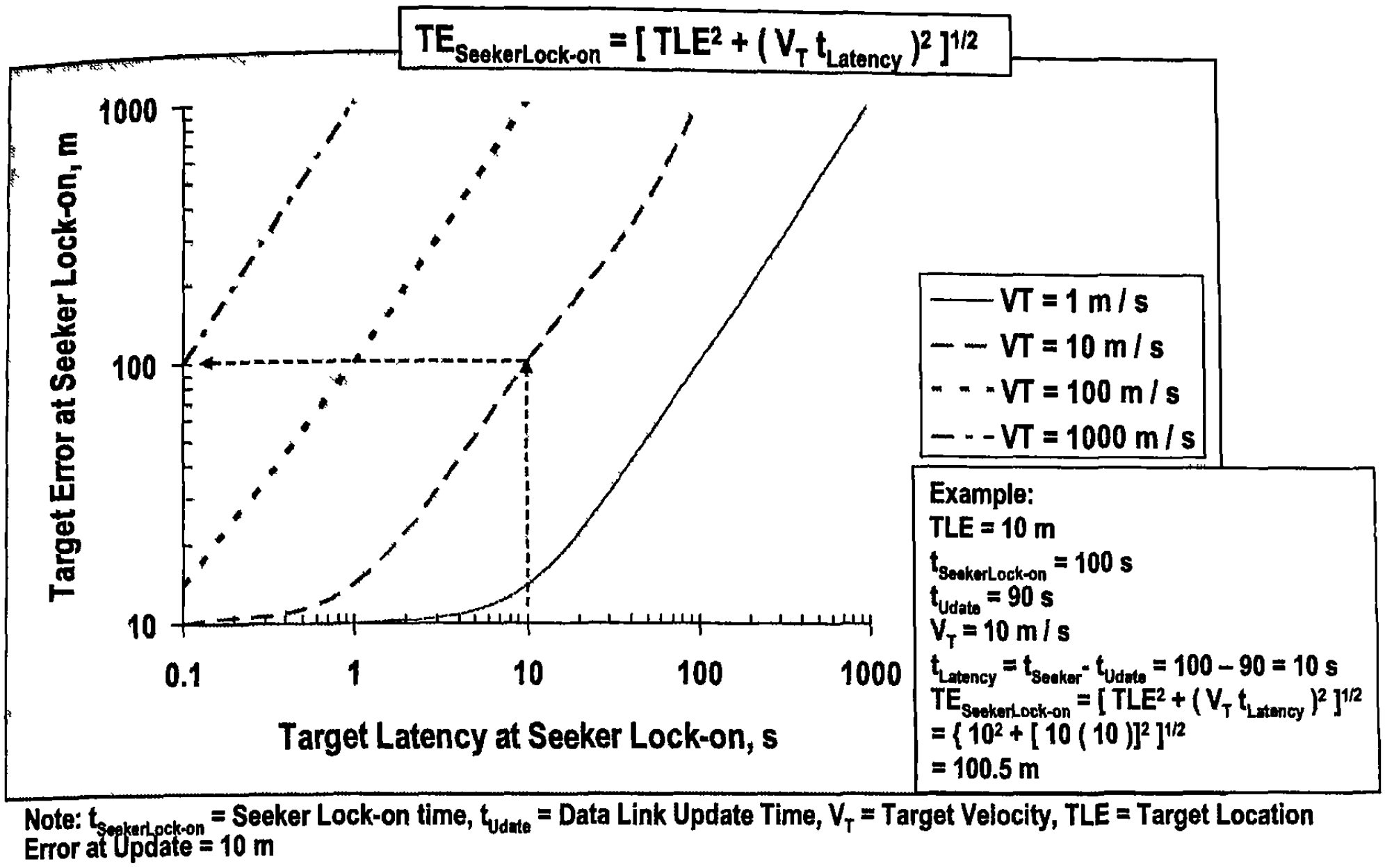

Fig. 6.10 Data link update at seeker lock-on reduces moving target error.

In the above equation t_{Seeker} = seeker lock-on time and t_{Update} = datal link update time. Assuming errors in TLE and TE are uniformly random, the root sum of squares (RSS) equation is

$$TE_{\text{SeekerLock-on}} = [TLE^2 + (V_{\text{T}} t_{\text{Latency}})^2]^{1/2} \tag{6.14}$$

Figure 6.10 shows the rapid growth in target error at seeker lock-on if the target latency is large or if the target has high velocity.

As an example, assume $TLE = 10$ m, $t_{\text{Seeker}} = 100$ s (seeker lock-on 100 s after launch), $t_{\text{Update}} = 90$ s (target location update 90 s after launch), and $V_{\text{T}} = 10$ m/s. Calculate

$$t_{\text{Latency}} = t_{\text{Seeker}} - t_{\text{Update}} = 100 - 90 = 10 \text{ s} \tag{6.15}$$

Substituting into the target error equation gives

$$\begin{aligned} TE_{\text{SeekerLock-on}} &= [TLE^2 + (V_{\text{T}} t_{\text{Latency}})^2]^{1/2} = \{10^2 + [10(10)]^2]\}^{1/2} \\ &= 100.5 \text{ m} \end{aligned} \tag{6.16}$$

From the preceding, note that a target update latency of 10 s prior to seeker lock-on provides a large target error. A near real-time (e.g., $t_{\text{Latency}} \sim 1$ s) data link is required to have a target error at seeker lock-on that would be comparable to the TLE.

Figure 6.11 shows the optimum cruise flight environment for tactical missiles. Note that there is a large variation in dynamic pressure as a function of Mach

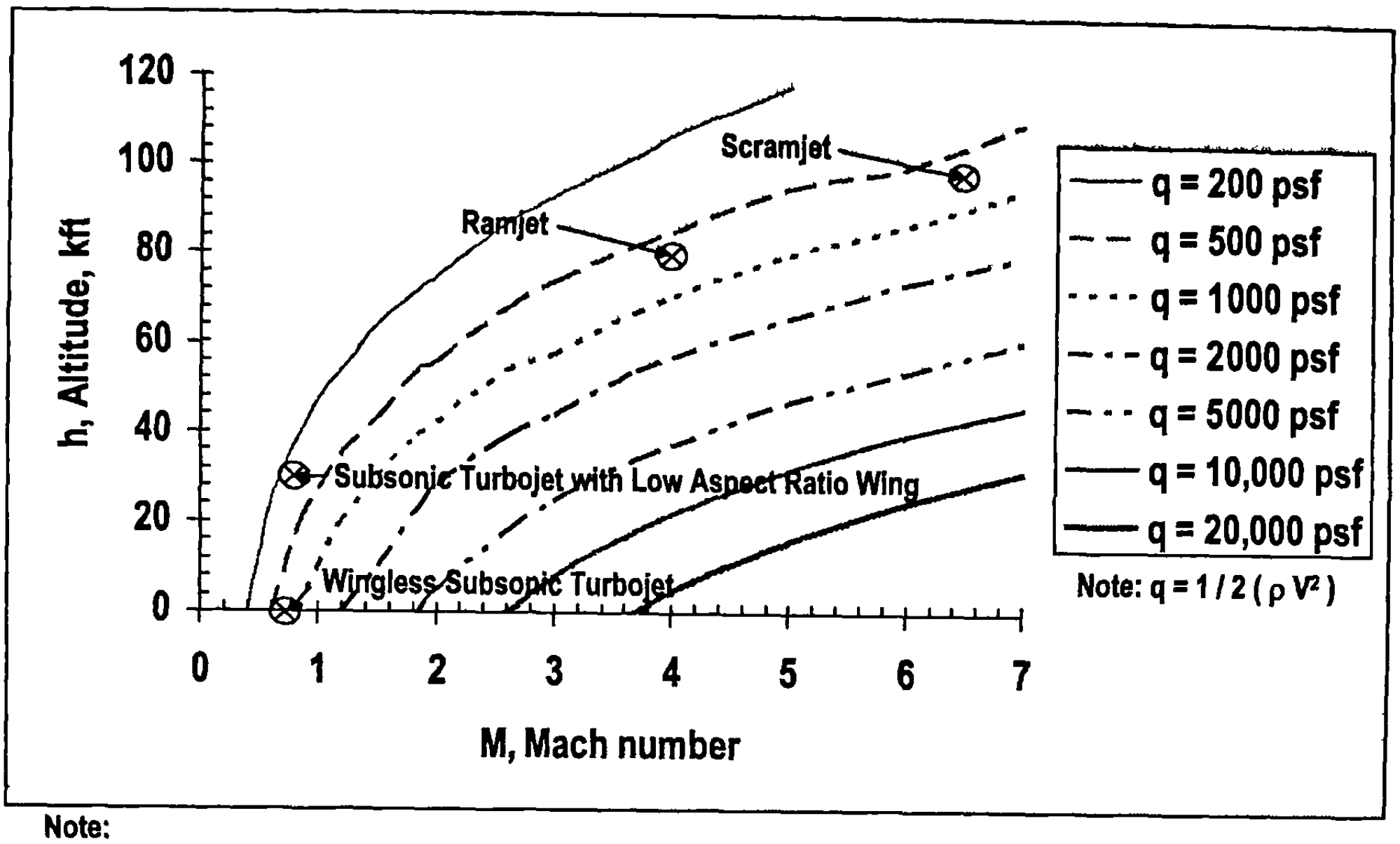

Note:
- U.S. 1976 Standard Atmosphere
- For Efficient Cruise, $(L/D)_{Max}$ for Cruising Lifting Body Typically Occurs for $500 < q < 1{,}000$ psf
- $(L/D)_{Max}$ for Cruise Missile with Low Aspect Ratio Wing Typically Occurs for $200 < q < 500$ psf
- $q \approx 200$ psf lower limit for aero control

Fig. 6.11 Optimum cruise is a function of Mach number, altitude, and planform geometery.

number and altitude. For a given Mach number the dynamic pressure decreases rapidly with altitude. Most wingless missiles have their best aerodynamic efficiency $(L/D)_{Max}$ at a dynamic pressure of about 700 psf. The figure shows the flight envelope of the optimum dynamic pressure as a function of Mach number and altitude. For a wingless turbojet flying at about Mach 0.8 (e.g., subsonic wingless cruise missile), the optimum flight altitude is sea level. Adding wings to a subsonic cruise missile results in an altitude for optimum aerodynamic efficiency that is higher. As shown in the figure, for a wingless ramjet missile flying at Mach 4, the optimum cruise altitude is about 80,000 ft. For a wingless scramjet missile flying at Mach 6.5, the optimum cruise altitude is about 100,000 ft.

There is a lower limit of dynamic pressure (approximately 200 psf) for sufficient aerodynamic control effectiveness to provide stabilization and maneuverability. For $q < \approx 200$ psf, either thrust vector control or reaction jet control is required.

Shown in Fig. 6.12 is an example of the broad range in the flight environment that can be encountered by a complex high-performance missile such as a ramjet. An air-launched ramjet is usually ejection launched at a subsonic Mach number. It is subjected to high angles of attack during ejection. If the missile has compressed carriage surfaces, these must be deployed as soon as possible to minimize the angle of attack divergence from the static instability. After safe separation from the launch platform, the missile then conducts a pitch-up maneuver at high angle of attack. It then begins a climb at an efficient flight path angle.

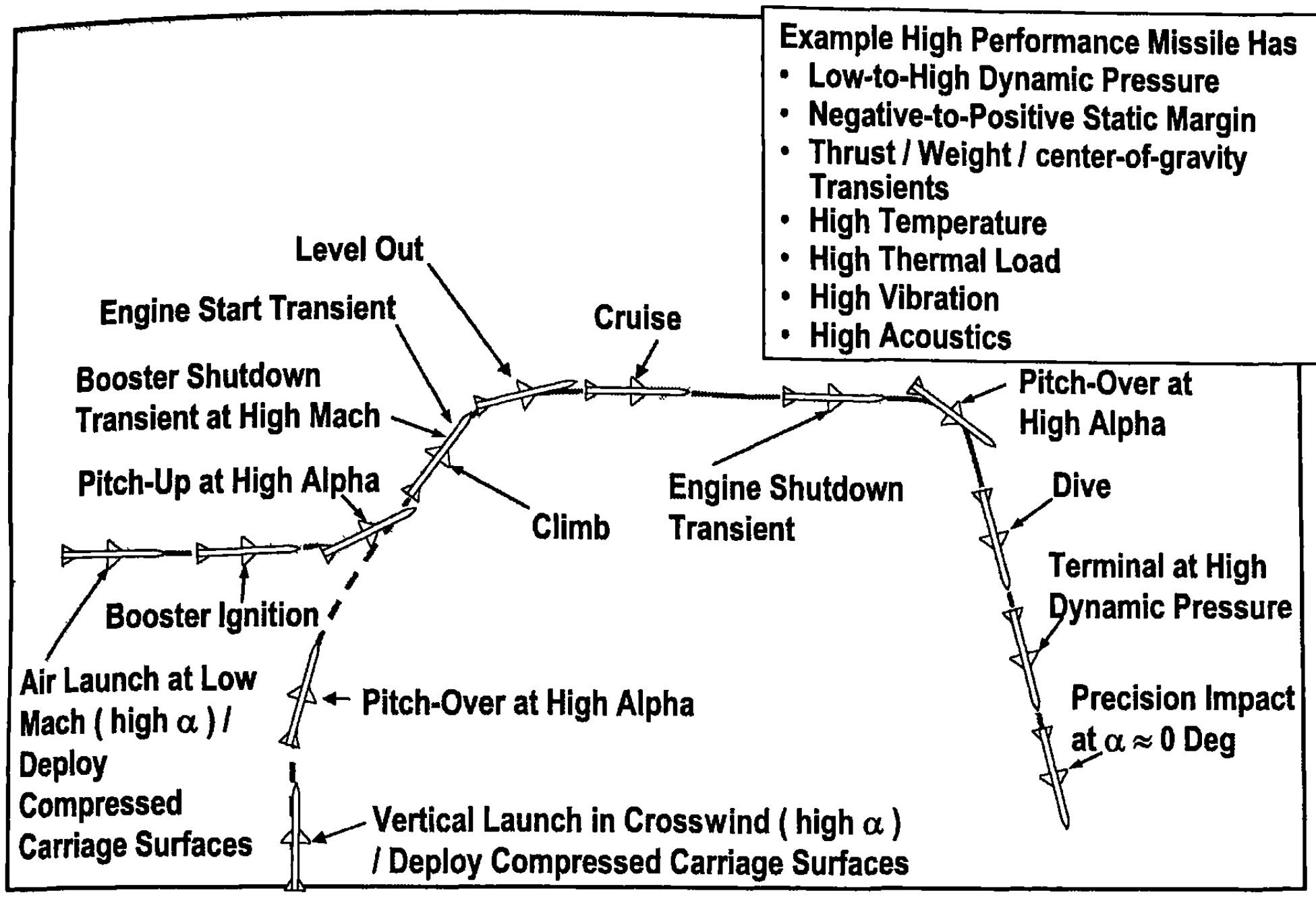

Fig. 6.12 Missile guidance and control must be robust for changing events and flight environment.

A surface-launched ramjet is usually vertically launched in a cross wind, resulting in a high angle of attack during launch platform separation. If the missile has compressed carriage surfaces, these must be deployed as soon as possible. Following launch, the surface-launched ramjet pitches over at a high angle of attack. It then begins a climb at an efficient flight path angle. Both the air-launched and the surface-launched ramjets are boosted to a supersonic Mach number while climbing. Following booster shutdown during the climb, the ramjet is ignited and the missile continues to climb under ramjet propulsion. As the missile approaches the optimum altitude for ramjet cruise, a pitch-over maneuver is conducted to level off for cruise flight. The missile cruises at an optimum altitude until it approaches the target area. The engine may be shut down at the end of cruise, or if there is sufficient fuel, the engine may continue to operate to maximize the speed during the dive. At the end of cruise a pitch-over maneuver at high angle of attack is initiated, and the missile dives toward the target. During the dive through the lower atmosphere the dynamic pressure reaches a maximum. For a deeply buried target, the impact angle of attack must be tightly controlled, usually to less than one deg, to avoid breaking up the warhead.

A modern control autopilot is required to handle the broad range of events, flight phases, and the flight environment of a high-performance missile. The autopilot is the brain of the missile. It provides flight control commands based on input data from the seeker, navigation, and stabilization sensors. Gains are multidimensional functions of complex parameters and are selected to maintain stable gain and phase margins. Special attention is given to the different flight phases. The autopilot design allows for sequencing between flight phases

and fading in the different control gains for each phase. The flight phases may have low-to-high dynamic pressure, negative-to-positive static margin, and thrust/weight/center-of-gravity transients. Another consideration is designing robust subsystem hardware to handle a severe thermal, vibration, and acoustic environment.

Design robustness is impacted by the variation in the flight environment design parameters with flight altitude. Figure 6.13 shows the variation of atmospheric temperature, pressure, density, and speed of sound as a function of altitude. Within the troposphere, the temperature and speed of sound decrease with increasing altitude up to about 36,000 ft. Based on the U.S. 1976 Standard Atmosphere, an equation for the troposphere temperature T at an altitude h compared to the sea level temperature T_{SL} is

$$T/T_{SL} = 1 - 6.875 \times 10^{-6} h \tag{6.17}$$

Note that atmospheric pressure and density decrease rapidly with altitude. The standard atmosphere ratios of the troposphere pressure p and density ρ to their sea level values are given by

$$p/p_{SL} = (T/T_{SL})^{5.2561} \tag{6.18}$$

$$\rho/\rho_{SL} = (T/T_{SL})^{4.2561} \tag{6.19}$$

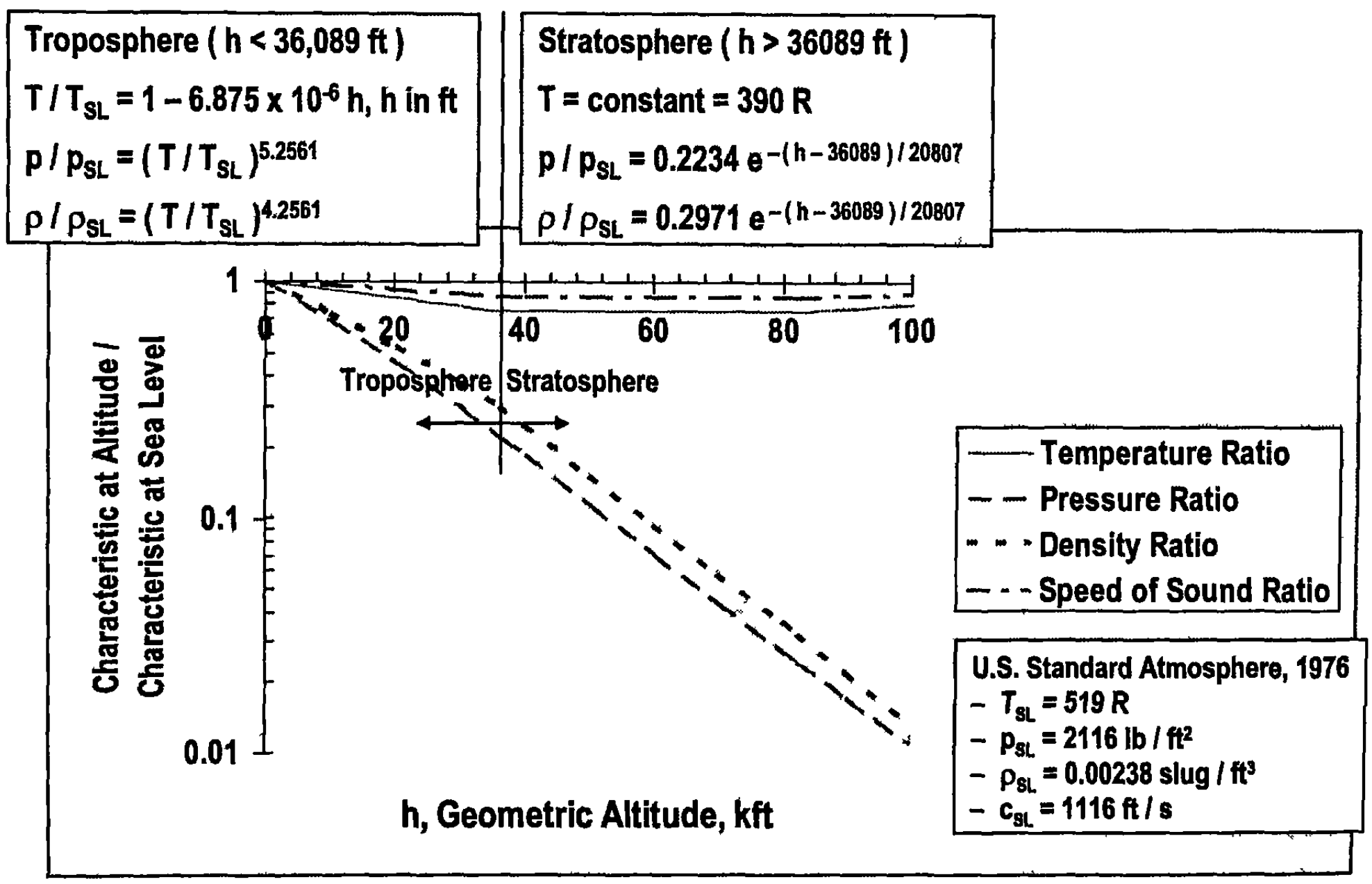

Note: T_{SL} = Temperature at sea level, p_{SL} = pressure at sea level, ρ_{SL} = density at sea level, c_{SL} = speed of sound at sea level, h = altitude in ft.

Fig. 6.13 Design robustness requires consideration of flight altitude.

For a given velocity, there is a slight increase in Mach number with increasing altitude for flight within the troposphere from the slight decrease in the speed of sound with altitude. Because weather and clouds are driven by changes in temperature, the troposphere has active weather and clouds. Above the troposphere is the stratosphere. For flight within the stratosphere, above about 36,089 ft, temperature and speed of sound are nearly constant. The temperature in the stratosphere for the U.S. 1976 Standard Atmosphere is

$$T = 390\,\mathrm{R} \tag{6.20}$$

Similar to the troposphere, the atmospheric pressure and density decrease rapidly with altitude in the stratosphere. The standard atmosphere ratios of the stratosphere pressure and density to their sea level values are given by the equations

$$p/p_{\mathrm{SL}} = 0.2234\, e^{-(\mathrm{h}-36089)/20807} \tag{6.21}$$

$$\rho/\rho_{\mathrm{SL}} = 0.2971\, e^{-(\mathrm{h}-36089)/20807} \tag{6.22}$$

Note from the figure that for an altitude of 36,089 ft, the pressure in only 22% of the sea level value and the density is only 30% of the sea level value. Because dynamic pressure, aerodynamic heating, and airbreathing propulsion thrust are a function of atmospheric density, for a given velocity they also decrease rapidly with altitude. Rocket motor thrust for a typical (underexpanded) nozzle increases with altitude because of the decreasing atmospheric pressure.

The values of the atmospheric properties vary with different atmospheric models. The standard atmospheric model used for many design activities is the U.S. 1976 Standard Atmosphere. However, the worldwide weather and climate can provide significant differences in parameters such as temperature, density, and speed of sound. Shown in Fig. 6.14 are comparisons of cold, hot, polar, and tropic atmospheric models with the standard atmospheric model. Note that the values of the parameters can vary by up to 30% from the standard atmospheric model. The design of subsystems such as the rocket motor requires consideration of off-nominal design conditions, such as extreme hot and extreme cold atmospheric temperatures.

Examples of typical design uncertainties of tactical missiles are illustrated in Fig. 6.15. A probability density function is usually used to represent the design uncertainties that have a normal, symmetrical distribution. The probability density function is given by the equation

$$PDF = \{1/[\sigma(2\pi)^{1/2}]\}e^{\{[(x-\mu)/\sigma]^2/2\}} \tag{6.23}$$

The design uncertainty in system development and demonstration (SDD), formerly known as engineering and manufacturing development (EMD), should ideally be small, for low risk in meeting the mission requirements. Design uncertainty in SDD is usually a symmetrical, normal distribution of uncertainty with a relatively small deviation (e.g., $+/-5\%$, 1 σ). Usually there is a single set of technologies for SDD based on a prior downselect of the technology alternatives.

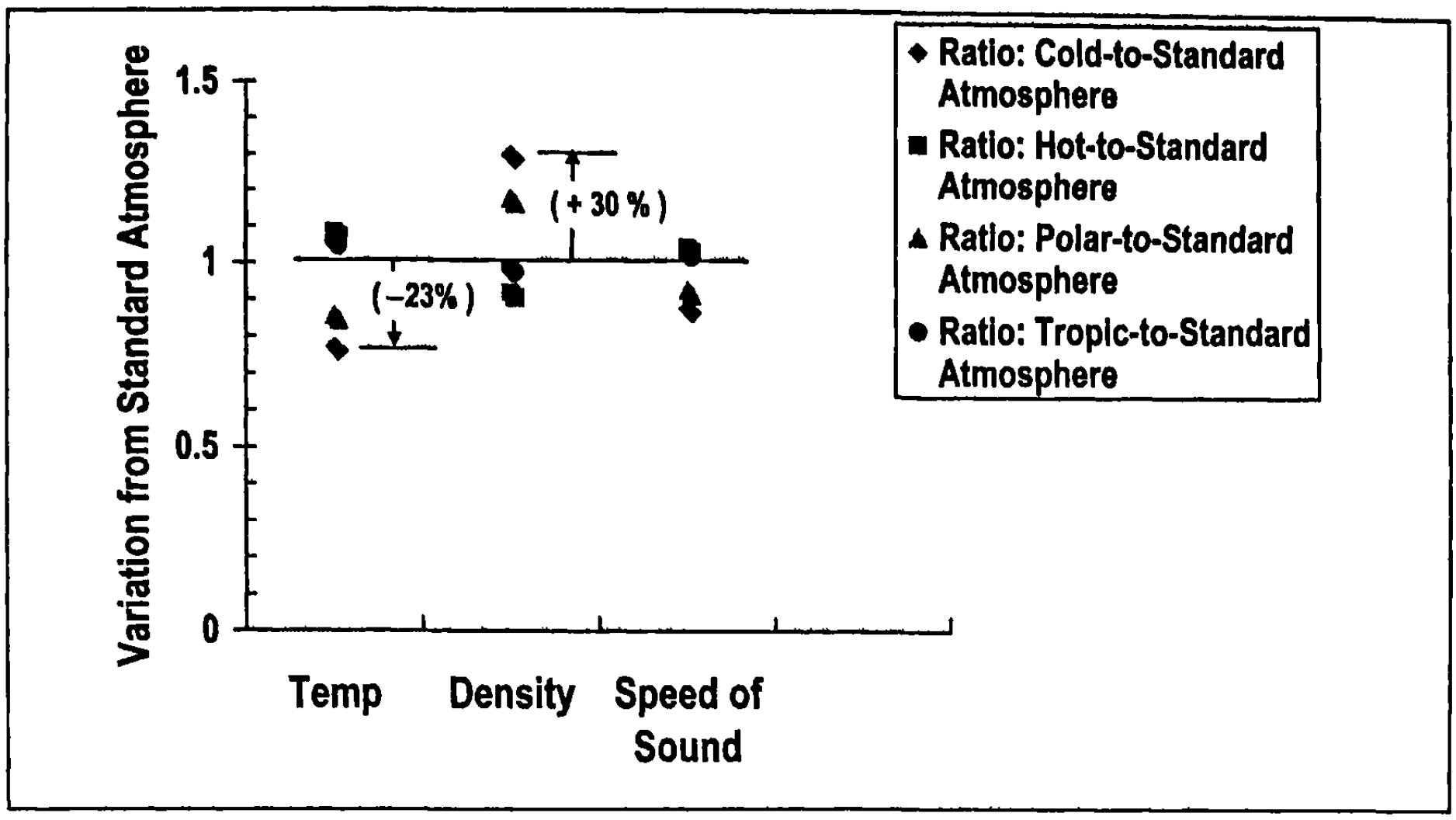

Note:

- Based on properties at sea level
- U. S. 1976 Standard Atmosphere: Temperature = 519 R, Density = 0.002377 slug / ft³, Speed of sound = 1116 ft / s

Fig. 6.14 Design robustness requires consideration of cold and hot atmospheres.

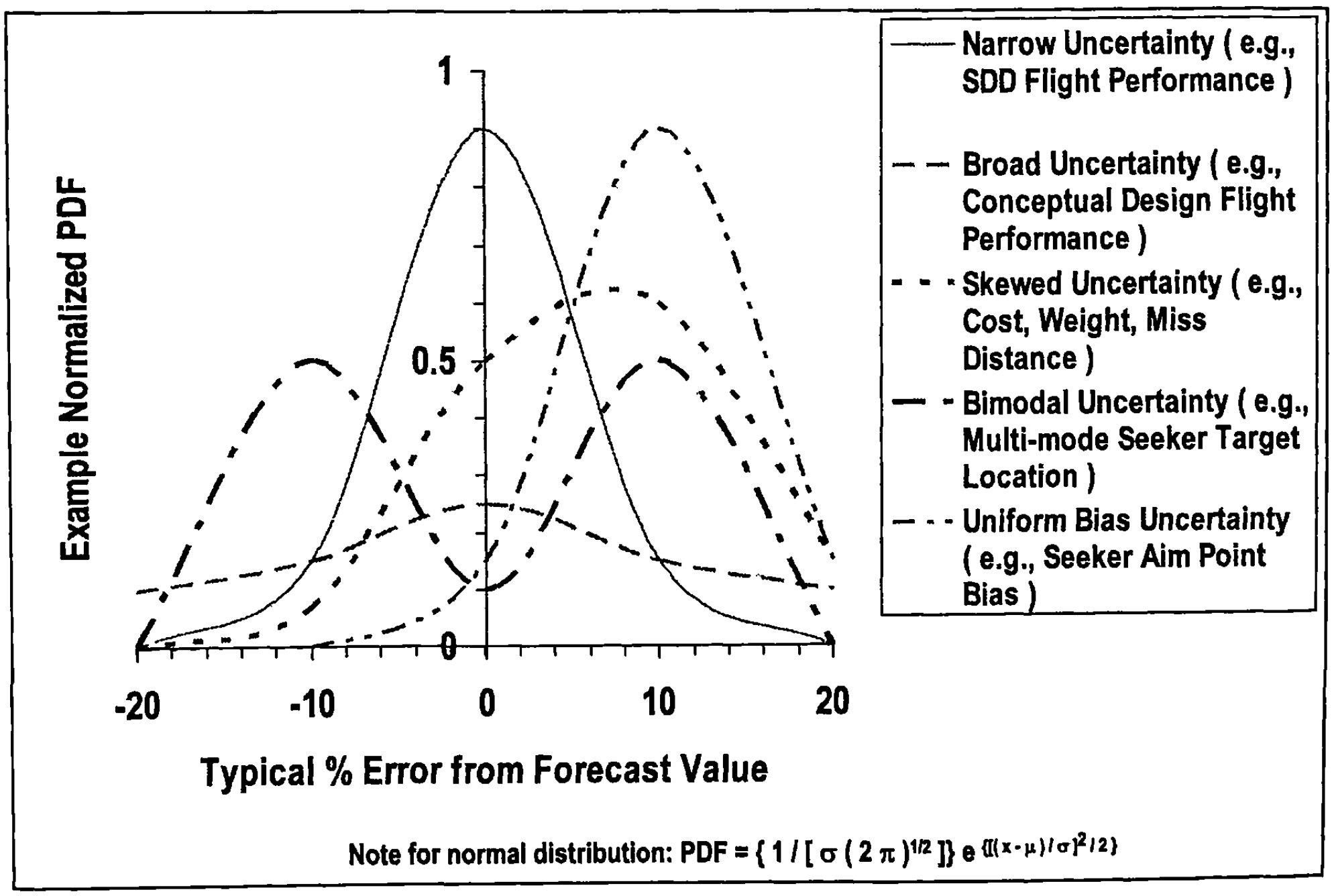

Fig. 6.15 Design robustness is required to handle uncertainty.

Note that the typical design uncertainty in conceptual design flight performance is much larger (e.g., $+/-15\%$, 1 σ). The elements that contribute to conceptual design flight performance can have even larger uncertainty. For example, the uncertainty in the static margin of a nearly neutrally stable missile may be more than 100%. As a result of the larger uncertainty in conceptual design, alternative technology solutions must be explored and developed. Different technologies have the potential to satisfy the mission requirements, but some have higher probability of success than others. The benefit of investment in the technology alternatives to quantify their performance and reduce their uncertainty is to reduce the missile system design uncertainty and mature the design. Prior to entering SDD there is usually sufficient confidence to select the preferred technology from the set of alternatives.

Because of the large design uncertainty in conceptual design, it is important to evaluate the robustness of the conceptual design and the associated technology alternatives. Insufficient design robustness may be a factor in not selecting a technology that may have higher potential performance or lower potential cost but is highly sensitive to uncertainty and there is insufficient funding or time to reduce the uncertainty.

The most important requirements (MIRs) may have design values that are specified as a threshold, a standard, and a goal. The threshold value represents marginal utility, with less capability than the standard (e.g., -3σ). The standard value is the nominal, expected utility. The goal is typically represented as an enhancement over the standard (e.g., $+3\sigma$).

Some uncertainty distributions are not a normal distribution. The third curve in the figure is a skewed uncertainty distribution. Examples of skewed distributions are cost, weight, and miss distance uncertainty. Usually the actual cost, weight, and miss distance measured during SDD tend to be higher than the original predictions. The design maturation process, such as testing, usually shows that the initial conceptual design predictions are optimistic. An approach used during conceptual design to compensate for the optimistic prediction methods is to provide design margin for robustness. For example, during conceptual design the warhead lethal radius may be sized for a large (e.g., 3σ) miss distance. The fourth curve in the figure is a bimodal distribution. As an example of a bimodal distribution, a dual-mode seeker (e.g., mmW/IR) could measure two different locations of the target, with uncertainty in the target location from each sensor. The final curve in the figure is a distribution that is similar to a normal distribution, except for a bias. An example is a seeker that has an aim point bias, such as the IR seeker of an air intercept missile that homes on the hot plume aft of the target aircraft instead of the airframe centroid of the aircraft.

Another consideration for design robustness is the robustness against countermeasures. Examples of countermeasures to missiles are shown in Fig. 6.16. These are 1) electro-optical countermeasures (EOCM) against an IR missile seeker, such as directed energy lasers, flares, and smoke; 2) radar frequency countermeasures (RFCM) against a radar missile seeker or GPS, such as active radar (e.g., angle error) electronic countermeasures (ECM), jammers, and chaff; 3) decoys, such as towed decoys to induce homing on the decoy false target; 4) low observables, including reduction in the contrail, radar cross section (RCS) and IR signature of the target; 5) high-speed flight, to defeat the missile seeker

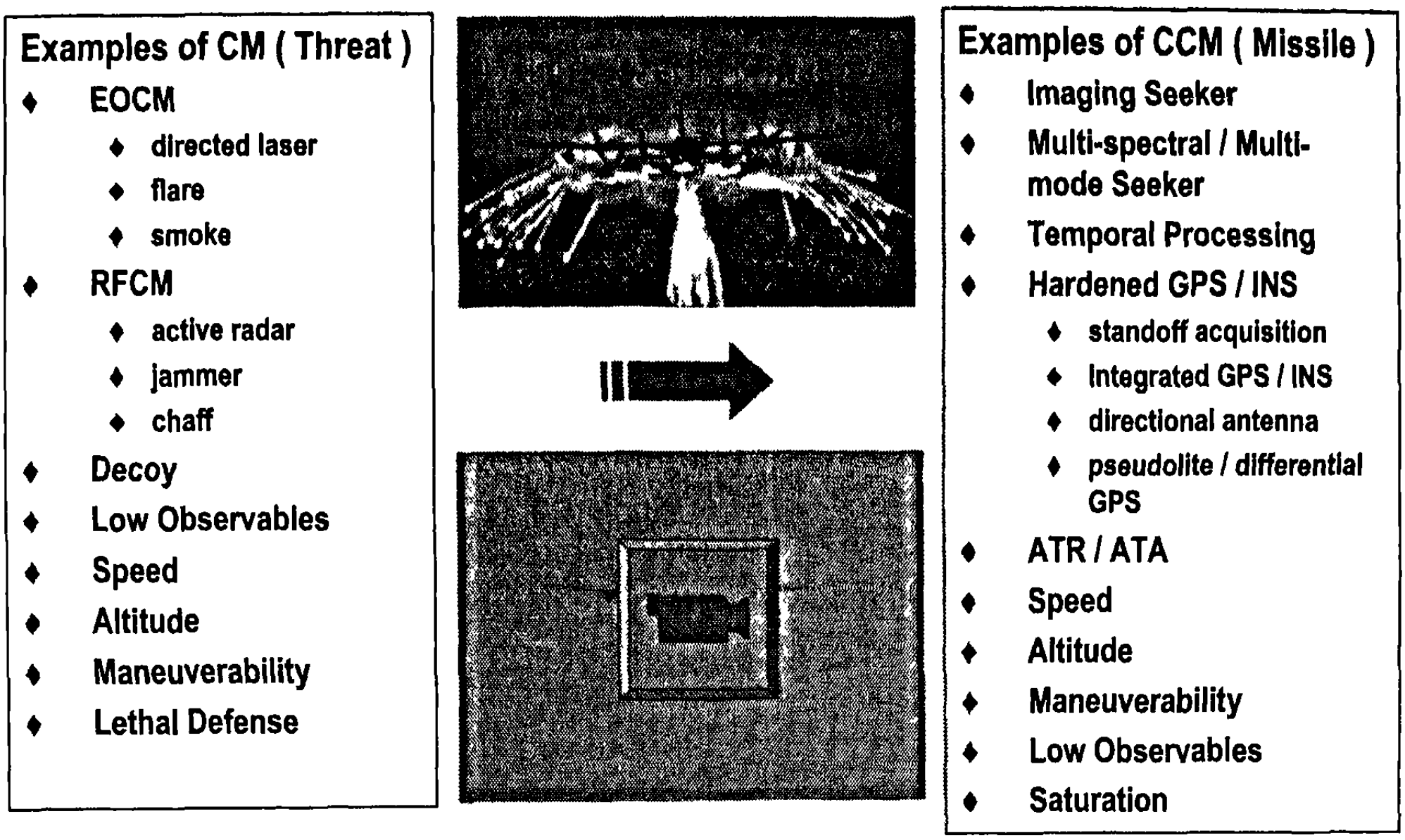

Fig. 6.16 Counter-countermeasures by missile enhance design robustness. Figure also in color section. Video is in the CD included with this textbook.

tracking and the warhead fusing; 6) high-altitude flight, to prevent missile seeker lock-on and exceed the missile flight envelope; 7) high maneuverability, to induce missile miss distance; and 8) lethal defense, to destroy the missile in flight.

Robust counter-countermeasures (CCMs) may use new technology that was not envisioned when the countermeasure was originally developed by the threat. Examples of robust CCM are 1) imaging seeker, to provide the resolution required to separate the target from ejected or towed countermeasures; 2) multi-spectral/multimode seeker, to provide broadband discrimination of the target signature; 3) temporal processing to identify the time varying characteristics of the target; 4) hardened GPS/INS, to maintain a high S/N in a jamming environment through approaches such as lock-on at a standoff range and altitude (this forces the jammer to break GPS code track, which requires about 20 dB more jammer power), an integrated GPS/INS, directional antenna aimed toward the satellites/away from the threat jammer, and pseudolites/differential GPS consisting of high-power transponders with corrected accuracy; 5) ATR/ATA, to pull the target out of the countermeasures; 6) high speed, to minimize the exposure time to countermeasures; 7) high-altitude flight, to avoid detection and exceed the threat flight envelope; 8) high maneuverability, to minimize miss distance from countermeasures; 9) low observable missile plume visual, RCS, and IR signatures, to avoid detection by the threat; and 10) saturation, to overwhelm the threat by the simultaneous use of more than one missile.

Also shown in the figure are a photograph and a video of dispensed flare countermeasures to missiles. Examples of CCMs that are used by missiles against flares include 1) a high-resolution imaging seeker with a sufficient number of pixels to maintain tracking of the larger target compared to the smaller flare(s);

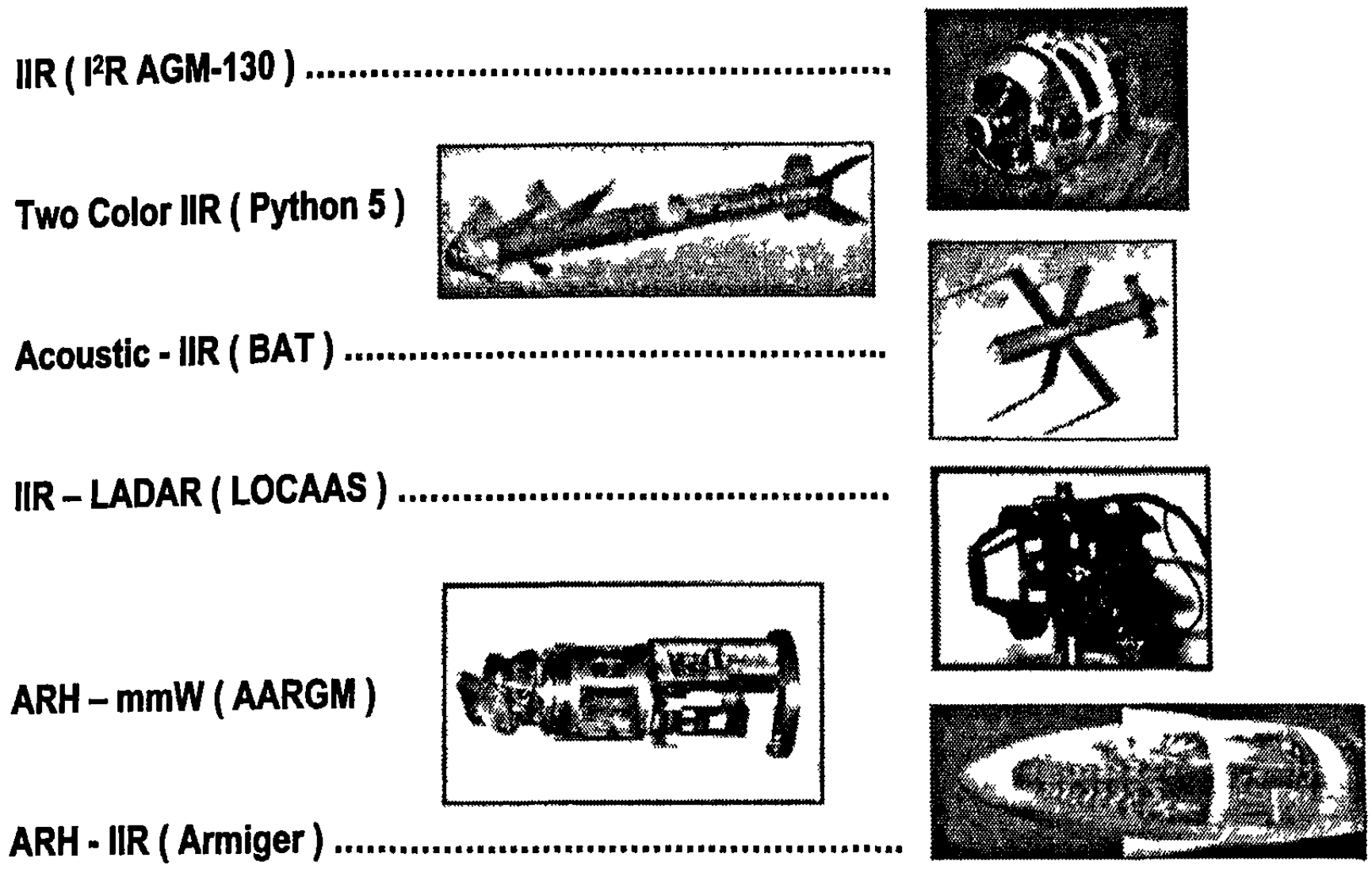

Fig. 6.17 Examples of countermeasure-resistant seekers. Figure also in color section.

2) a multispectral/multimode seeker to distinguish the energy distribution of the hot flare compared to that of the relatively cool target; 3) temporal processing of successive frames of the seeker to separate the relatively high frequency intensity fluctuations of the flare from the relatively low frequency of the target airframe; and 4) GPS/INS to maintain a target heading if the seeker is jammed.

Figure 6.17 shows examples of missiles that have countermeasure-resistant seekers. Examples are imaging IR (AGM-130), two-color imaging IR (Python 5), acoustic/imaging IR (BAT), imaging IR/LADAR (LOCAAS), antiradiation homing/active mmW (AARGM), and antiradiation homing/imaging IR (Armiger).

6.3 Warhead Lethality

The second measure of merit to be discussed is warhead lethality. Warhead lethality addressed in this text emphasizes blast fragmentation and kinetic energy warheads because of their impact on missile configuration design and the availability of unclassified information. Warheads that are not addressed include shaped charge, continuous expanding rod, thermobaric, and directed energy warheads, such as EMP and high power microwave (HPM) warheads.

A driving design consideration for warhead design is the target size and hardness. For example, a small size, hard target such as a tank is best defeated by either a small shaped charge warhead, an explosively formed penetrator warhead, or a kinetic energy warhead. A deeply buried target, such as a bunker, requires a two-stage warhead: a kinetic energy warhead for penetration, followed by a blast fragmentation warhead. Another example is a large size surface target, such as a building, which requires a large blast fragmentation warhead.

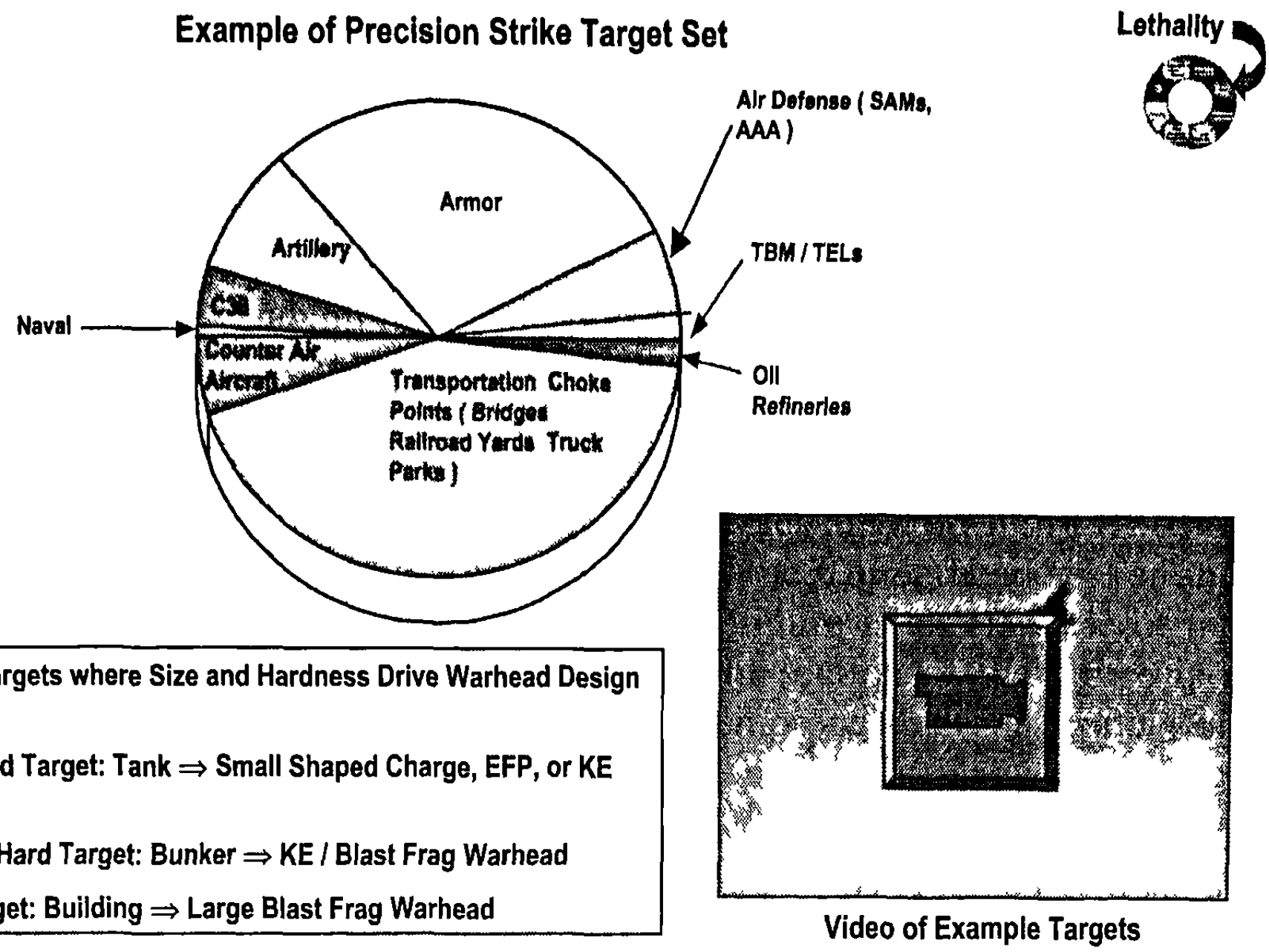

Fig. 6.18 A target set varies in size and hardness. Video is in the CD included with this textbook.

Shown in Fig. 6.18 is a typical surface target set. Armor targets and transportation choke points are usually the largest number of targets. New precision strike missiles should ideally have a capability against more than one type of target. An example is a combined capability to engage and defeat hardened buried targets in addition to fixed and mobile surface targets. Benefits of producing a multipurpose missile that is effective against a broad range of targets include reduced unit production cost from a larger production run and reduced logistic cost because of a simplified logistics organization.

Shown in the video are nine examples of different precision strike missiles used against nine different targets. The missions are to defeat 1) airfield runways; 2) aircraft shelters; 3) bunkers; 4) buildings; 5) tanks; 6) tank columns; 7) fixed surface-to-air missile (SAM) sites; 8) mobile SAMs; and 9) ships. The first example is an Apache missile dispensing runway cutting submunitions. In the second example, a Diamond Back Small Diameter Bomb penetrates an aircraft shelter. The third example is a bunker defeat using a GBU-24 laser guided bomb with the BLU-109 penetrator warhead. In the fourth example, a laser-guided bomb attacks a large building target of concrete/steel construction. The fifth example is a Maverick missile attacking a within-visual-range tank target. A sixth example is the Brimstone missile conducting a beyond-visual-range salvo attack against a column of tanks, using an autonomous mmW seeker with ATR. The seventh example is a HARM antiradiation homing missile attacking a fixed SAM site. An eighth example is a Diamond Back Small Diameter Bomb using a standoff warhead against a mobile SAM site. Finally, the ninth example is a Harpoon missile attacking a ship.

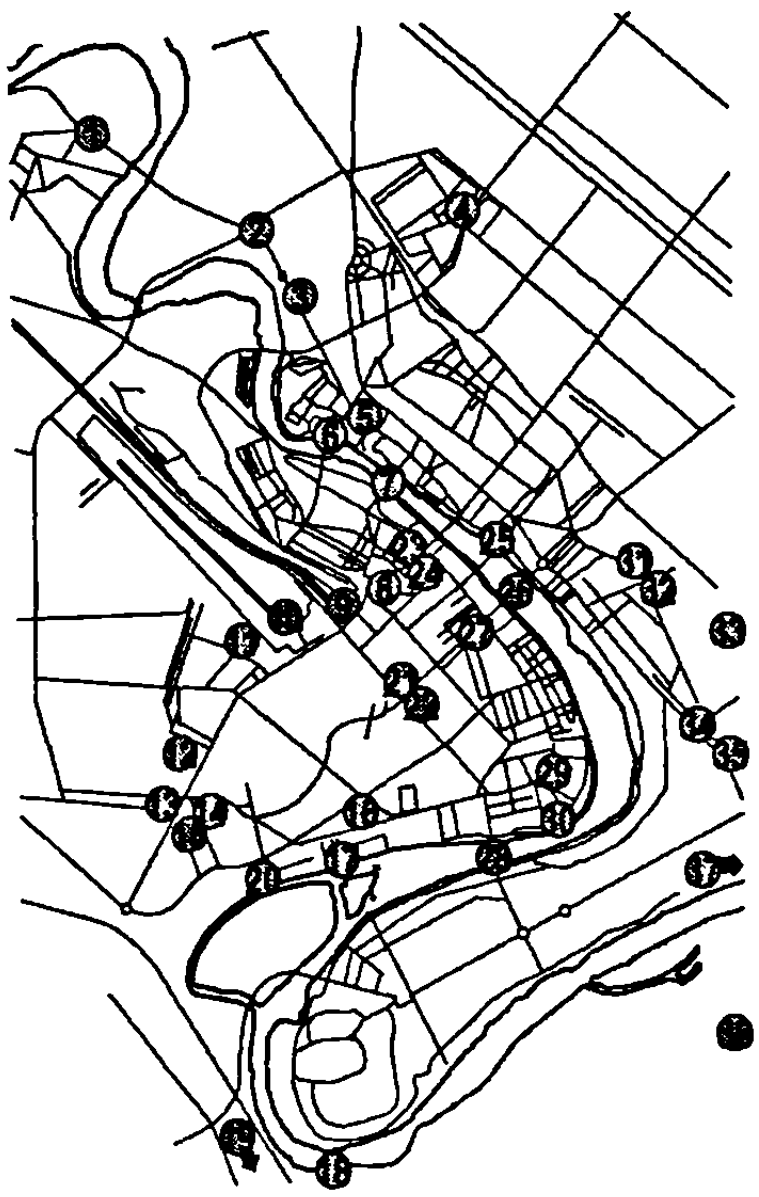

Targets: 1. Directorate of Military Intelligence; 2, 5, 8, 13, 34. Telephone switching stations; 3. Ministry of Defense national computer complex; 4. Electrical transfer station; 6. Ministry of Defense headquarters; 7. Ashudad highway bridge; 9. Railroad yard; 10. Muthena airfield (military section); **11. Air Force headquarters; 12. Iraqi Intelligence Service; 14. Secret Police complex;** 15. Army storage depot; **16. Republican Guard headquarters; 17. New presidential palace; 18. Electrical power station;** 19. SRBM assembly factory (Scud); **20. Baath Party headquarters; 21. Government conference center;** 22. Ministry of Industry and Military Production; **23. Ministry of Propaganda; 24. TV transmitter; 25, 31. Communications relay stations;** 26. Jumhuriya highway bridge; **27. Government Control Center South;** 28. Karada highway bridge (14th July Bridge); **29. Presidential palace command center; 30. Presidential palace command bunker; 32. Secret Police headquarters; 33. Iraqi Intelligence Service regional headquarters; 35. National Air Defense Operations Center;** 36. Ad Dawrah oil refinery; **37. Electrical power plant**

Source: AIR FORCE Magazine, 1 April 1998

Fig. 6.19 76% of Baghdad targets struck first night of Desert Storm were C^3 time-critical targets. Figure also in color section.

Time-critical targets (TCTs) are the highest priority targets in the opening round of a war. Taking out the threat C^3 is particularly important. An example is shown in Fig. 6.19 derived from Air Force magazine dated 1 April 1998. It shows the Baghdad targets that were struck on the first night of Desert Storm. TCTs are noted with a bold font. Note that the greatest emphasis (76%) was on TCTs, particularly C^3 targets.

Figure 6.20 is an example of surface target types and the characteristics of current precision strike missiles for the target types. The missions for precision strike missiles cover a broad range of targets, including fixed targets, radar sites, ships, armor, and buried targets. Most of the missile configurations shown in the figure are from Ref. 1.

In the case of **fixed targets** (which usually are of large size with hardness ranging from soft to hard), a blast fragmentation warhead or dispensed cluster submunitions are usually used. The current missiles for use against fixed targets are relatively large, with wings for efficient subsonic flight. Current missiles in this category include AGM-154 JSOW, Storm Shadow/Scalp/Apache, KEPD-350, BGM-109 Tomahawk, and AGM-142 Popeye/Have Nap.

The second target category is **radar sites**. Radar sites are relatively soft and can usually be defeated by a relatively small blast fragmentation warhead. Antiradar missiles have an antiradiation homing (ARH) seeker and generally fly at high supersonic Mach number, for launch aircraft survivability in a SAM engagement and to minimize threat radar shutdown before missile impact. Current missiles in this category include AGM-88 HARM, AS-11 Kilter/Kh-58, ARMAT, Armiger, and ALARM. In the event that the threat radar shuts down prior to

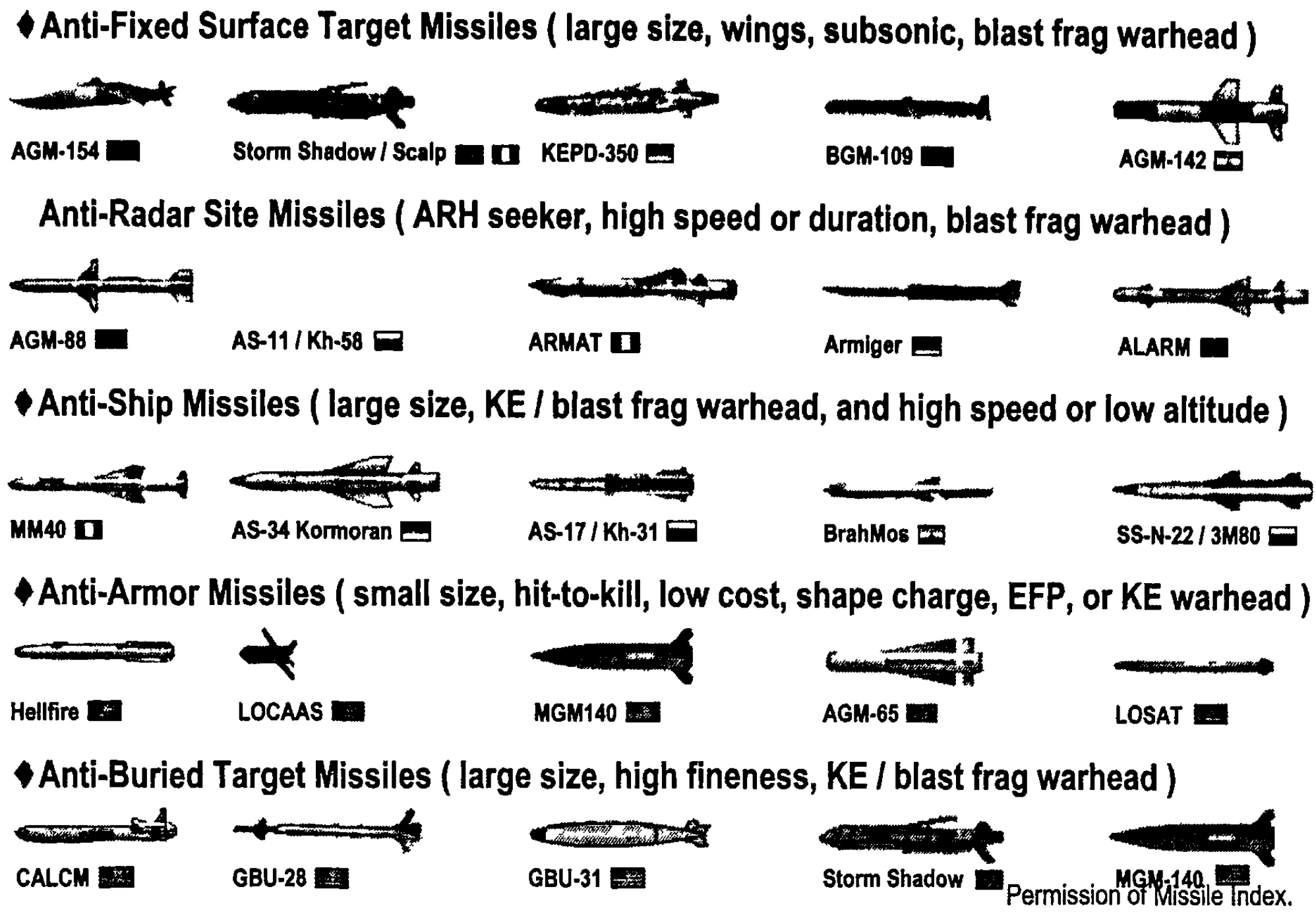

Fig. 6.20 Type of target drives precision strike missile speed, cost, seeker, and warhead. Figure also in color section.

impact, most modern missiles use GPS/INS to maintain the heading course toward the target. In addition to GPS/INS, Armiger has a dual-mode radar/IIR seeker that allows IR acquisition of the target in the event of target radar shutdown. Another advantage of Armiger is the high average velocity and long range from the boron fuel ducted rocket propulsion. Another unique missile is ALARM. ALARM can go into a loiter mode in the event of threat shutdown. If the threat radar comes back online during loiter, ALARM reacquires the target and reinitiates homing.

A third target category is **ship targets**. Ships are relatively hard targets and usually require a kinetic energy penetrating warhead, followed by blast fragmentation after penetration of the hull. Antiship missiles are generally large in size and have a large warhead. Antiship missiles are designed to survive ship defenses, relying on high speed, high altitude, or low altitude/clutter to survive. Current antiship missiles include MM40 Exocet, AS-34 Kormoran, AS-17 Krypton/Kh-34, BrahMos, and SS-N-22 Sunburn/3M80.

A fourth category is **armor targets**. This includes tanks, armored personnel carriers, and other armored combat vehicles. Armor targets are small in size, mobile, and hard. Typical antiarmor warheads include shaped charge, explosively formed projectile (EFP), and kinetic energy penetrator. Most antiarmor missiles are small size, have hit-to-kill accuracy, and are low cost. Examples are Hellfire/Brimstone, LOCAAS, AGM-65 Maverick, and LOSAT. An exception is MGM-140 ATACMS, which is a relatively large missile that uses submunitions to defeat an array of armor targets. Antiarmor warheads may also be

effective against larger area, relatively soft targets. For example, the Hellfire shaped charge warhead may also be effective against targets such as radar sites, bunkers, small buildings, and small ships.

A final category is **buried targets**. The current penetration capability against buried targets is typically about 5 to 20 ft of concrete, depending upon the warhead characteristics and the impact velocity. Most missiles used against buried targets have a high fineness kinetic energy/blast fragmentation warhead. Some missiles have a forward shape charge warhead followed by a kinetic energy/blast fragmentation warhead. Buried targets include underground command posts and bunkers. The current missiles in this category (CALCM, GBU-28, GBU-31 JDAM, Storm Shadow, MGM-140) are large and heavy. A technical concern is the maneuverability precision of the flight control system at impact to avoid breaking up the warhead. Design considerations for the warhead include the nose shape, weight, case material, and diameter. A challenge for explosives and fuses is survival at high deceleration. Another challenge for fusing is the ability to sense changes in deceleration during passage through earth, concrete, and rooms in order to detonate the warhead at the proper time.

Examples of lightweight, air-launched multipurpose precision strike weapons and their system considerations are shown in Fig. 6.21. The selected examples are relatively lightweight air-launched missiles because of the importance of firepower. Firepower is especially important for light weight fighter aircraft, helicopters, and unmanned combat air vehicles (UCAVs) which may have a firepower limitation because of a store weight limit. Current operational air-launched

Weapon	Fixed Surface Targets(1)	*Moving Targets(2)*	*Time-Critical Targets(3)*	*Buried Targets(4)*	*Adverse Weather(5)*	*Firepower(6)*
Example New Missile	●	●	●	●	●	◒
AGM-65	●	○	○	○	–	○
Small Diameter Bomb	●	–	–	○	●	●
AGM-88	◒	–	◒	–	●	–
Hellfire / Brimstone / Longbow	○	●	○	–	●	●
LOCAAS	○	●	◒	–	○	●

(1) – Multimode warhead desired. GPS / INS provides precision (3 m) accuracy.
(2) - Seeker or high bandwidth data link required for terminal homing.
(3) - High speed with duration required ⇒ High payoff of high speed / loiter and powered submunition.
(4) - KE penetration warhead required ⇒ High impact speed, low drag, high density, long length.
(5) - GPS / INS, SAR seeker, imaging mmW seeker, and data link have high payoff.
(6) - Light weight required. Light weight also provides low cost

Note:
● Superior
◒ Good
○ Average
– Poor

Fig. 6.21 Examples of lightweight air-launched multipurpose precision strike weapons.

precision strike missiles that are relatively lightweight include AGM-65 Maverick, Small Diameter Bomb, AGM-88 HARM, Brimstone/Longbow/Hellfire, and LOCAAS. Measures of merit shown are the effectiveness against the broad range of fixed-surface targets, effectiveness against moving targets, effectiveness against TCTs, effectiveness against buried targets, effectiveness in adverse weather, and the firepower loadout on the launch aircraft. Note that no one operational missile is superior in all areas. The Small Diameter Bomb is a small GPS/INS-guided bomb that has good effectiveness against fixed-surface targets; has moderate effectiveness against buried targets; is capable of operation in adverse weather; and is relatively light weight (about 250 lb), providing high firepower. In addition to GPS/INS, new technologies for the Small Diameter Bomb include compressed carriage lattice fins and compressed carriage diamond back wing. However, the Small Diameter Bomb is relatively ineffective against moving targets and TCTs. A new lightweight precision strike missile that combines the attributes of a small smart bomb with the capability to handle moving targets and TCTs would be more robust. Examples of technologies that provide robustness to handle a broad range of targets include GPS/INS precision guidance, SAR seeker, mmW seeker, and high-bandwidth data link for adverse weather homing and moving targets; ducted rocket propulsion for TCTs; turbine propulsion and powered submunition for loiter duration and targeting flexibility; multimode kinetic energy/blast fragmentation warhead for deeply buried and surface targets; and lightweight subsystems for lighter weight missiles that allow higher firepower.

Figure 6.22, based on Ref. 20, shows the overpressure scaling for an explosive charge as a function of the charge weight c and the distance from the charge to the

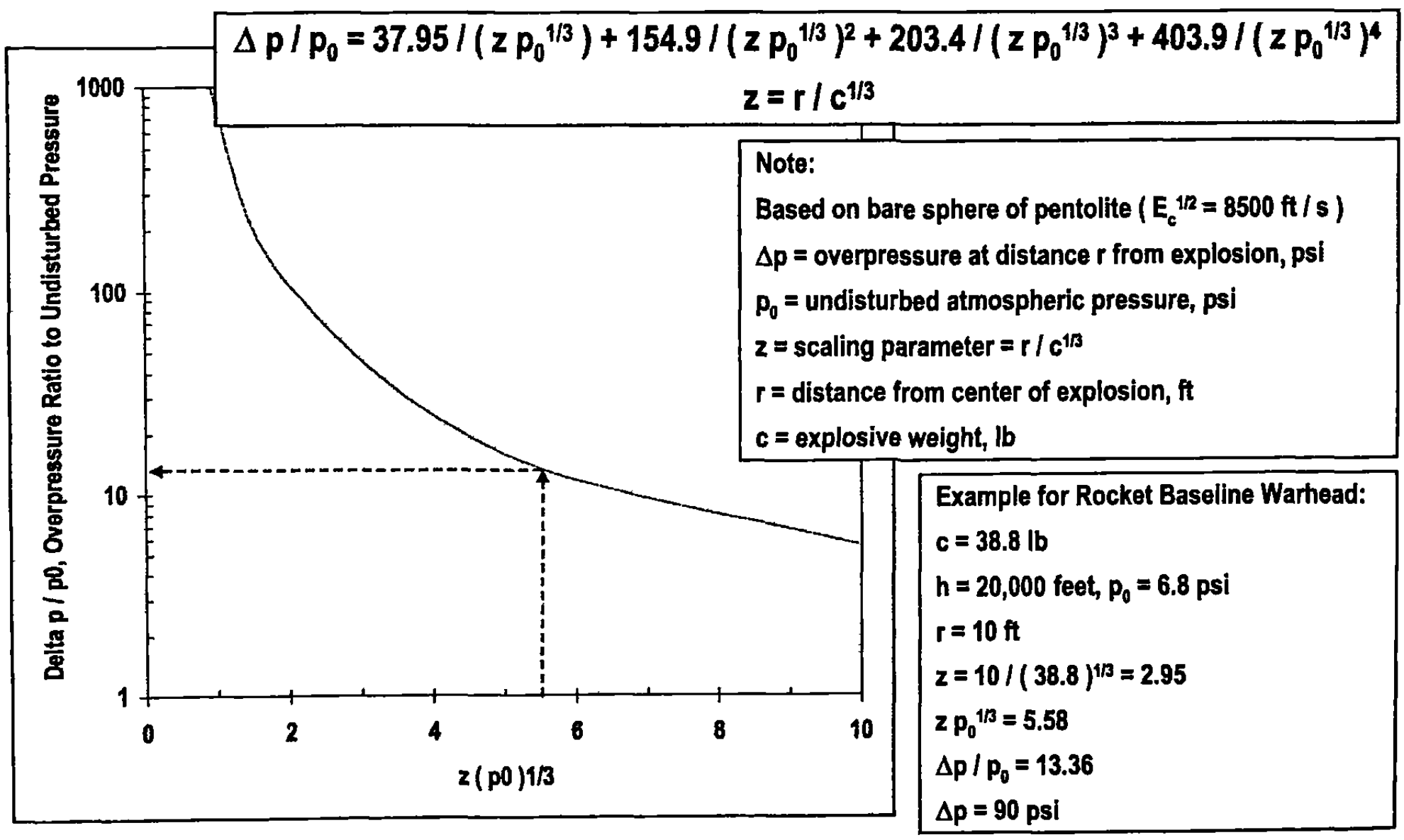

Reference: U.S. Army Ordnance Pamphlet ORDP-2—290-Warheads, 1980

Fig. 6.22 Blast is effective at small miss distance.

target (r). Blast overpressure is given by the equation

$$\Delta p/p_0 = 37.95/(zp_0^{1/3}) + 154.9/(zp_0^{1/3})^2 + 203.4/(zp_0^{1/3})^3 + 403.9/(zp_0^{1/3})^4 \tag{6.24}$$

The example is for a bare sphere of pentolite charge. Pentolite consists of 50% TNT ($C_7H_5N_3O_6$) and 50% PETN ($C_5H_8N_4O_{12}$). The scaling parameter is

$$z = r/c^{1/3} \tag{6.25}$$

The preceding equation is used to relate overpressure to distance and charge weight. Note that the overpressure is driven more by distance from the charge than by charge weight.

As an example, the rocket baseline warhead charge weight of 38.8 lb at a distance of 10 ft provides a maximum overpressure of 90 psi (six atmospheres). The scaling parameter z is computed to be 2.95. Comparing a smaller (10-lb) charge for the same value of z, the distance is 6.4 ft to achieve the same overpressure of 90 psi. A 36% reduction in miss distance has the same effect as a 290% increase in warhead weight! Because decreasing miss distance is more important to enhance lethality than increasing warhead weight, highly accurate missiles can have high lethality that is also combined with lighter weight, higher firepower, less collateral damage, and lower cost.

The kill and damage envelope from a blast/fragmentation warhead against a typical aircraft target is shown in Fig. 6.23. The kill envelope is based on

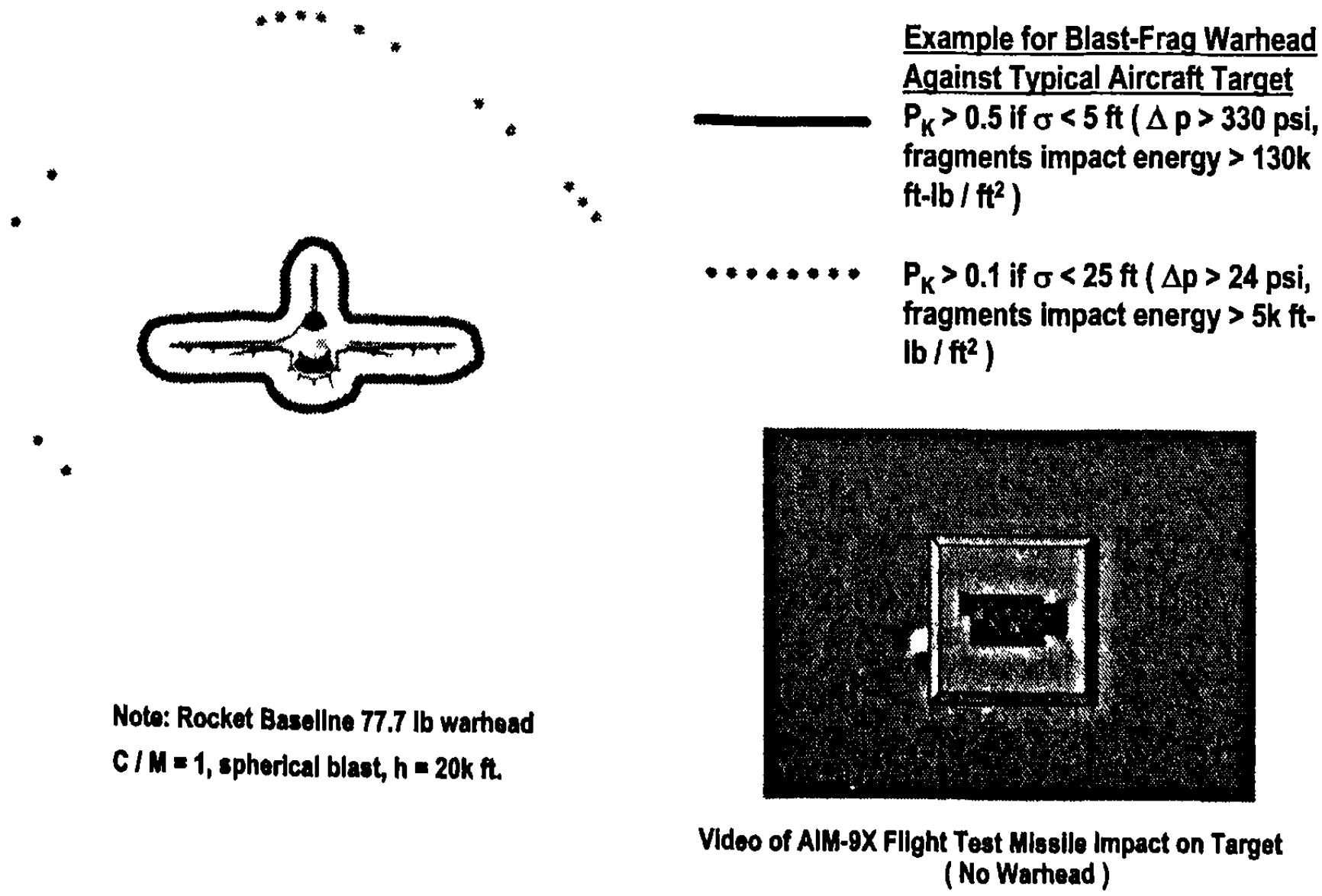

Fig. 6.23 Guidance accuracy enhances lethality. Video is in the CD included with this textbook.

predicting the effects of the rocket baseline 77.7-lb warhead with an assumed spherical blast and a charge-to-metal ratio of 1. The altitude is assumed to be 20,000 ft. Other assumptions are that the minimum blast overpressure and the fragments impact kinetic energy to kill the target are 330 psi (22 atmospheres) and 130,000 ft-lb/ft^2, respectively. For the 77.7-lb warhead, the kill overpressure and kill fragment impacts occur at a miss distance of about 5 ft. The outer envelope, where there is still significant damage, is a miss distance of about 25 ft. At 25 ft miss distance the blast overpressure and the kinetic energy from fragment impact are reduced to values of 24 psi and 5000 ft-lb/ft^2, respectively. For miss distance greater than 25 ft, there is a low probability of kill or even damage to the aircraft. Note from the figure that a highly accurate missile has a high kill probability, while a slightly less accurate missile has low kill probability.

Shown at the bottom of the figure is a video of a drone aircraft that is destroyed by an AIM-9X Sidewinder flight test missile. The flight trajectory results in a small miss distance, with the missile impacting the target. The warhead on the flight test missile has been replaced with telemetry. However, the impact kinetic energy alone is sufficient to destroy the target.

The photographs in the top section of Fig. 6.24 show the fireball and fragments from warhead detonations. The left section of the figure is the Hellfire missile warhead, which weighs about 24 lb. Hellfire has a shaped charge warhead with a naturally fragmenting case. Note that the fireball and fragment coverage are larger than the 8 ft (2.4 m) witness plate. In the right section of the figure is a

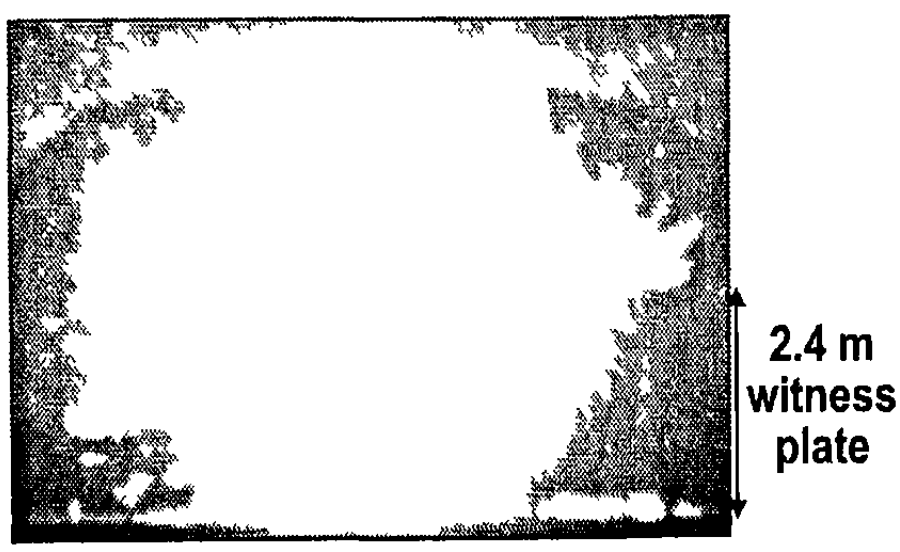

Hellfire 24 lb shaped charge warhead
fragments are from natural fragmenting case

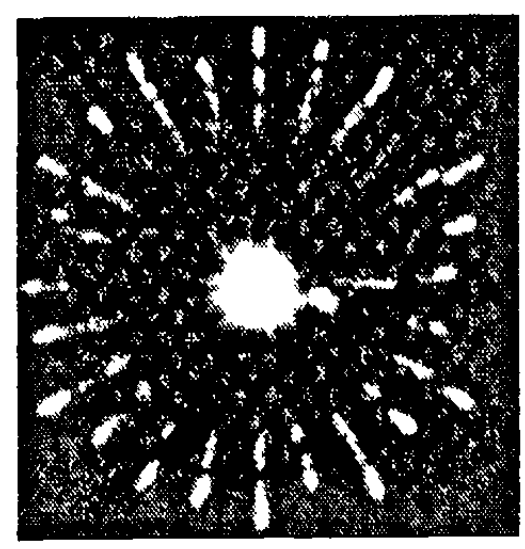

Roland 9 kg explosively formed warhead
multi-projectiles are from preformed case

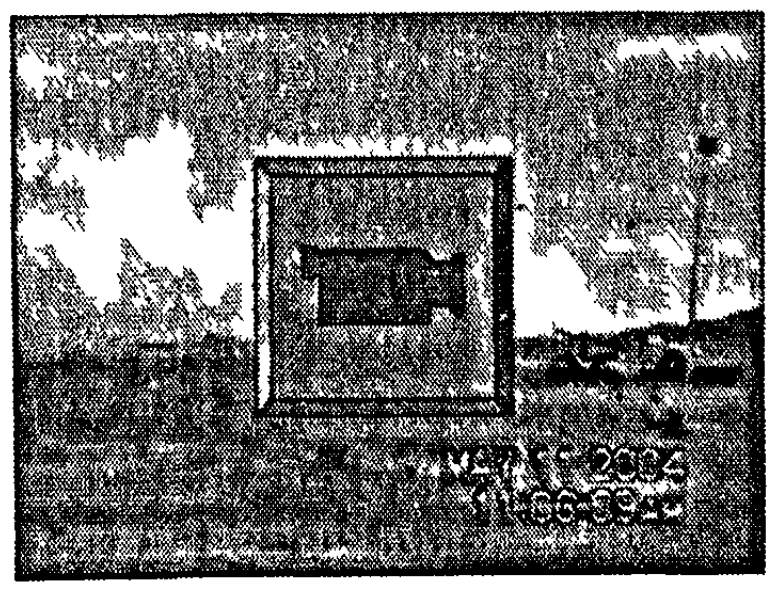

Video of Guided MLRS 180 lb blast fragmentation warhead

Fig. 6.24 Warhead blast and fragments are effective at small miss distance. Figure also in color section. Video is in the CD included with this textbook.

detonation of the Roland warhead (9 kg weight) against a helicopter drone target. Roland has a multiprojectile warhead. Dimples in the side of the warhead case provide explosively formed projectiles. Note that the tight fragment distribution extends beyond the target. The bottom section of the figure is a video of the blast and debris from warhead detonation of a guided unitary multiple launch rocket system (MLRS). The MLRS unitary warhead weight is 180 lb. Note the relatively large area and long time duration extent of debris from the blast.

Figure 6.25 shows the total kinetic energy of a blast fragmentation warhead as a function of charge-to-metal ratio. Total kinetic energy is given by the equation

$$\mathrm{KE} = (1/2)M_{\mathrm{m}}V_{\mathrm{f}}^2 = E_{\mathrm{c}}M_{\mathrm{c}}/(1 + 0.5\,M_{\mathrm{c}}/M_{\mathrm{m}}) \tag{6.26}$$

Results are based on the Gurney equation for a cylindrical warhead, from Ref. 21. Maximizing the total kinetic energy of the fragments is an optimization of the warhead charge-to-metal case mass ratio ($M_{\mathrm{c}}/M_{\mathrm{m}}$). A small value of charge-to-metal ratio has low kinetic energy because the small charge cannot accelerate the metal fragments to a high velocity. Charge-to-metal ratio greater than 1 provides high kinetic energy. However, a very large value of the charge-to-metal ratio may not be optimum. Although metal fragments are accelerated to high velocity, there are fewer fragments available to impact the target. The optimum value for maximum kinetic energy is usually about

$$M_{\mathrm{c}}/M_{\mathrm{m}} \approx 1 \tag{6.27}$$

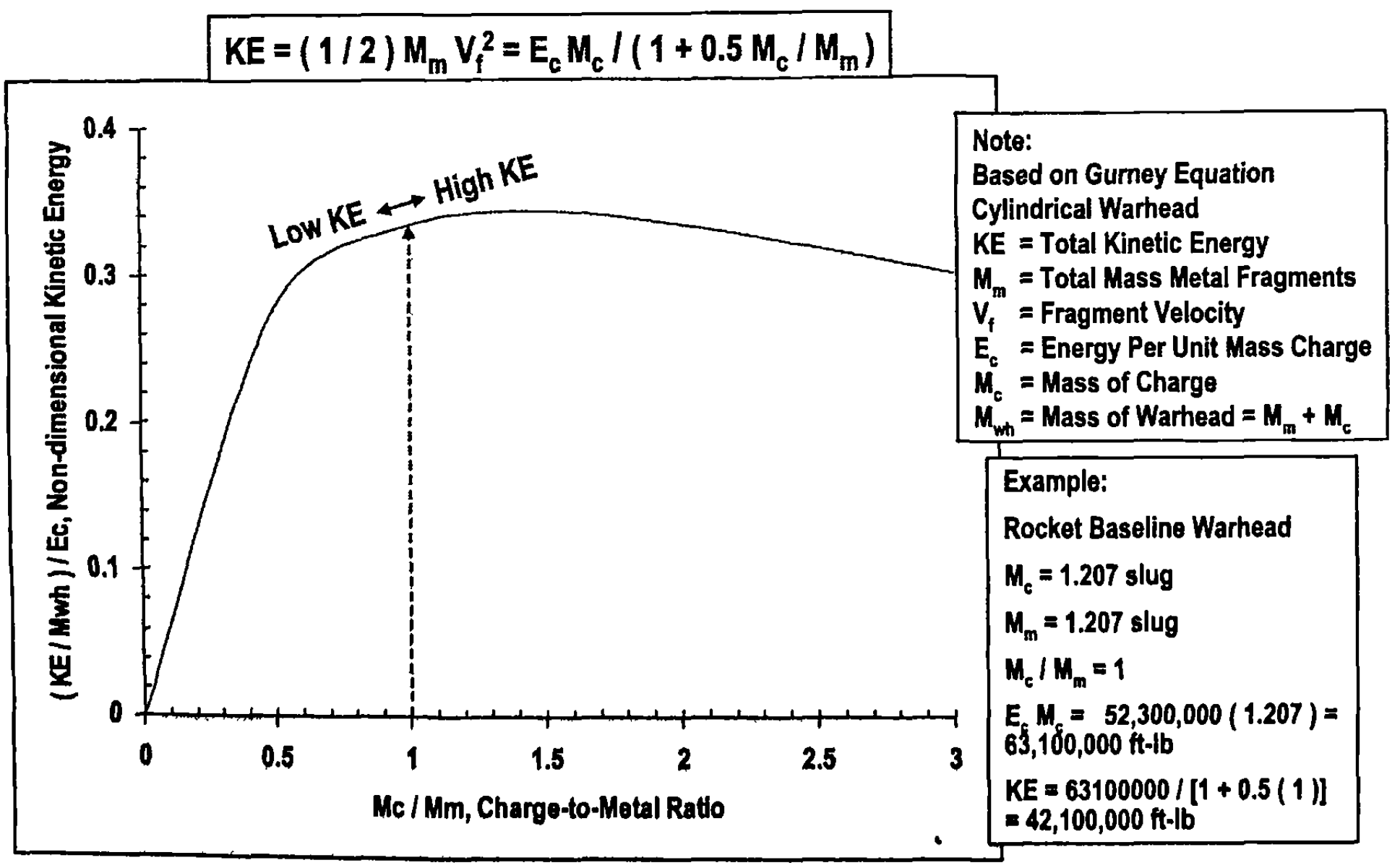

Reference. Carleone, Joseph (Editor), *Tactical Missile Warheads* (Progress in Astronautics and Aeronautics, Vol 155), AIAA, 1993.

Fig. 6.25 Maximum total fragment kinetic energy requires high charge-to-metal ratio.

As an example, the rocket baseline warhead has a total weight $M_{wh} = M_m + M_c = 77.7$ lb and a charge-to-metal mass ratio $M_c/M_m = 1$. The Her Majesty's Explosive (HMX) explosive charge has an energy per unit mass of $E_c = 52{,}300{,}000\ \text{ft}^2/\text{s}^2$. The total charge energy for a charge mass of $M_c = 1.207$ slug is 63,100,000 ft-lb. The total kinetic energy of the fragments is computed to be KE = 42,100,000 ft-lb. Approximately 67% of the charge energy is converted into kinetic energy. Again, note from the figure that the rocket baseline warhead charge-to-metal ratio $M_c/M_m = 1$ maximizes the total kinetic energy.

For a target kill by warhead fragments, probability of kill P_K is a function of the number of hits on the target and the fractional area of the target that is vulnerable. For a single hit, the probability of kill is the fractional area of the target that is vulnerable

$$P_K = A_V/A_{tp} \tag{6.28}$$

If the kill probability of a second hit is independent of the first hit, then the probability of kill for two hits is

$$P_K = 1 - (1 - A_V/A_{tp})^2 \tag{6.29}$$

For n hits, the general equation is

$$P_K = 1 - (1 - A_V/A_{tp})^{n_{hits}} \tag{6.30}$$

Figure 6.26 shows the probability of kill from fragments impacting a target with low vulnerable area ($A_V/A_{tp} = 0.1$), a target with a moderate vulnerable

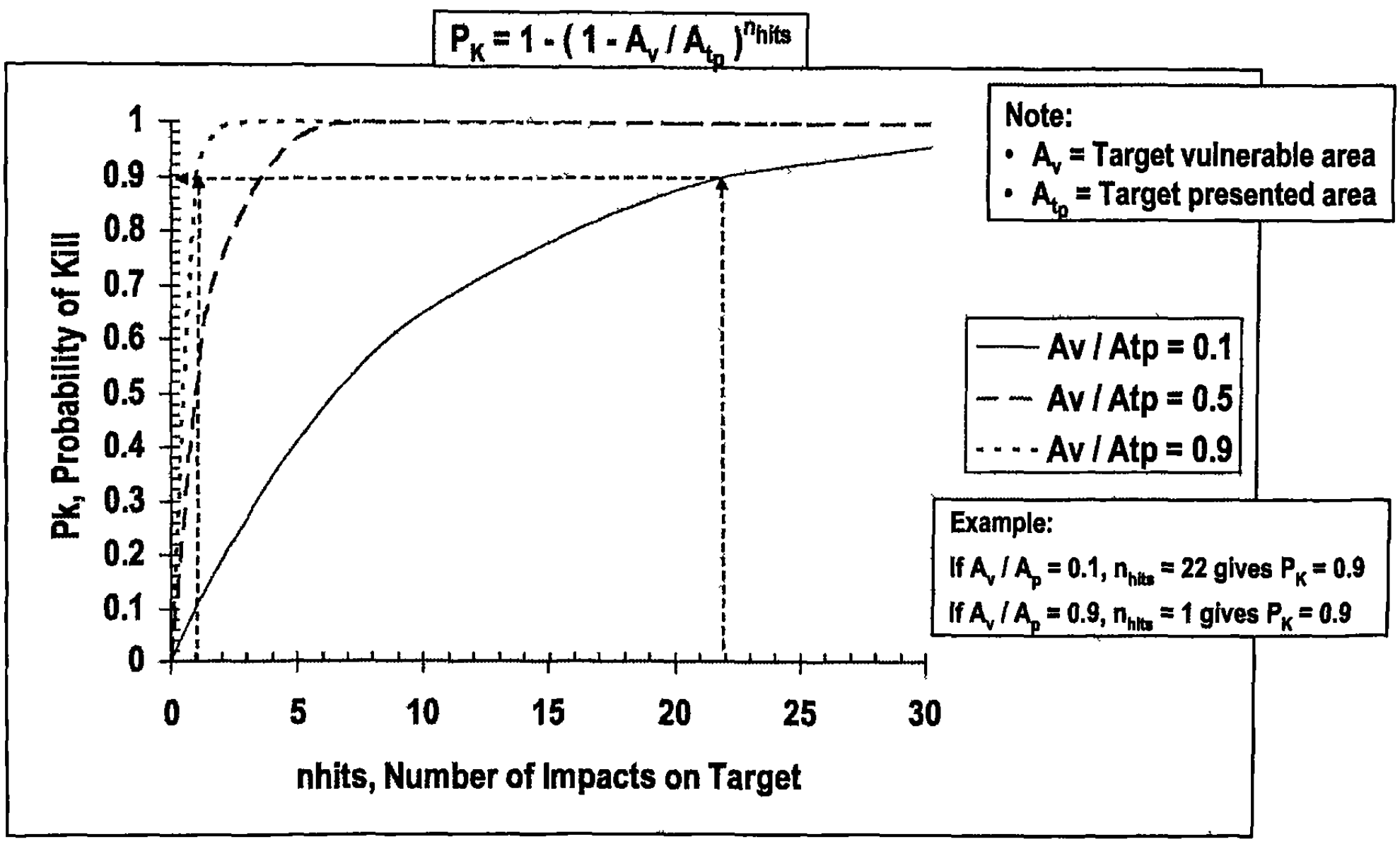

Fig. 6.26 Multiple impacts are effective against threat vulnerable area subsystems.

area ($A_V/A_P = 0.5$), and a target with a large vulnerable area ($A_V/A_{tp} = 0.9$). Note that only a few warhead fragments are required to kill a soft target with a large vulnerable area, while many fragment impacts are required to kill a hard target with a relatively small vulnerable area.

As an example for a kill probability of 0.9, 22 hits are required on a hard target with a vulnerable area that is 10% of the presented area. However, only one hit is required against a soft target with a vulnerable area that is 90% of the presented area.

The number of fragment hits on the target is shown in Fig. 6.27 as a function of miss distance and warhead weight. It is based on the equation

$$n_{\text{Hits}} = n_{\text{Fragments}}[A_P/(4\pi\sigma^2)] \tag{6.31}$$

The assumptions are a spherical blast with uniformly distributed fragments, charge-to-metal ratio equal to 1, an average fragment weight equal to 50 grains (3.2 g), and a target presented area equal to 20 ft^2. The warhead and target characteristics are representative of an air target engagement. Again, note the value of guidance accuracy. At a small miss distance less than 10 ft, even a small 5-lb warhead will have multiple fragment hits on the target.

Technology may be used to focus warhead energy to provide a greater density of fragments than that available from a uniform spherical distribution. Examples are aimed cylindrical warheads and mass focus warheads. Disadvantages are the requirement for more sophisticated fusing and increased risk that the warhead energy may not be focused toward the target.

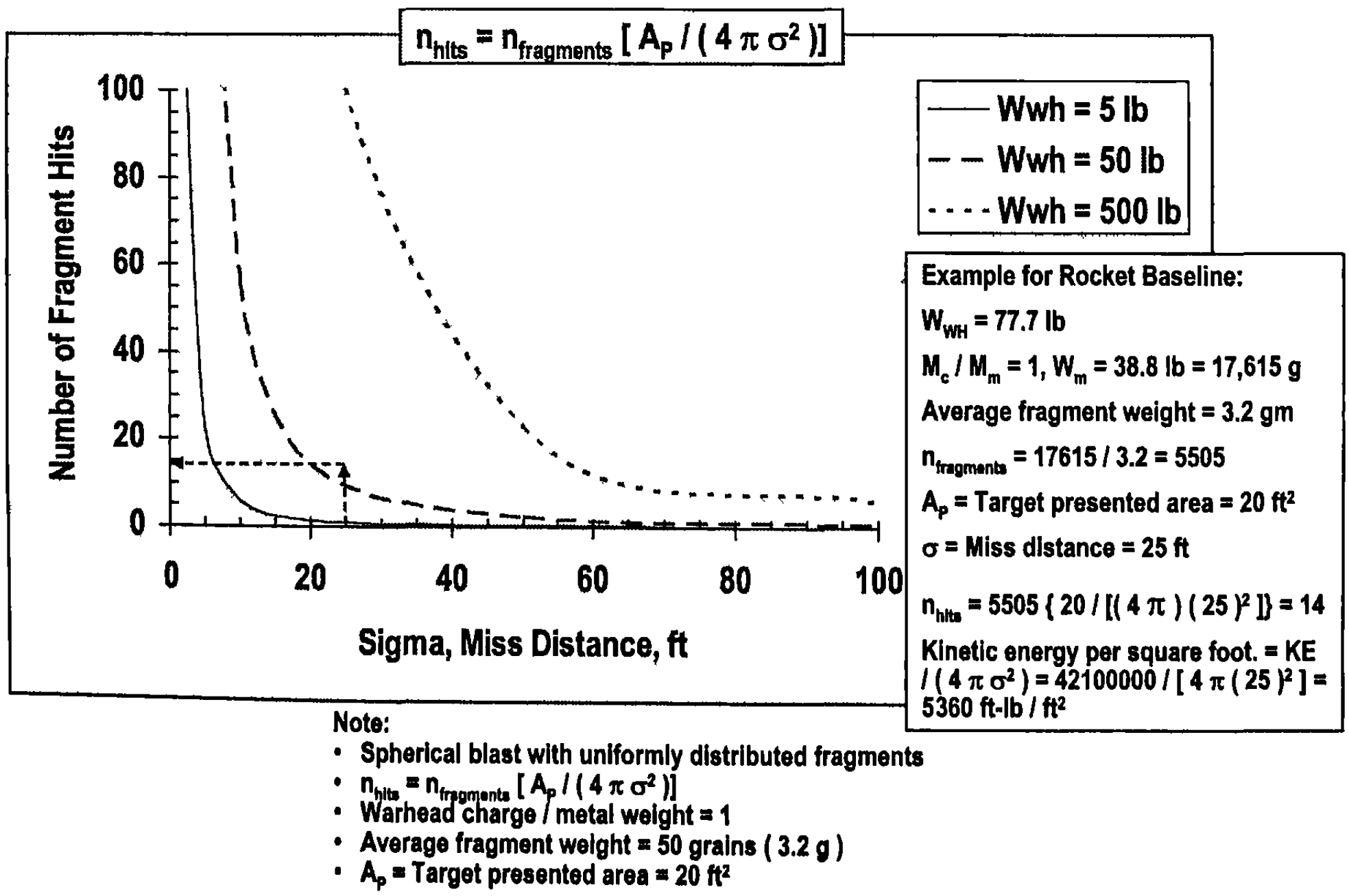

Fig. 6.27 Small miss distance improves the number of warhead fragment hits.

As an example of warhead fragment impacts, the rocket baseline 77.7-lb warhead has a charge-to-metal ratio of 1, providing a total fragment weight of 38.8 lb or 17,615 g. For an average fragment weight of 3.2 g there are $n_{\text{fragments}} = 17615/3.2 = 5505$ fragments. For an assumed spherical blast with a miss distance of 25 ft, 14 fragments will impact a target with a presented area of 20 ft^2. The kinetic energy density of the fragments impacting on the target is 5360 ft-lb/ft^2.

Fragment initial velocity is a function of charge energy and the charge-to-metal-ratio (M_c/M_m). Figure 6.28, based on the Gurney equation for a cylindrical warhead, shows the fragment initial velocity for a relatively modern explosive (HMX, $C_4H_8N_8O_8$) compared to that of TNT ($C_7H_5N_3O_6$). The Gurney equation for the fragment velocity of a cylindrical warhead is

$$V_f = (2E_c)^{1/2}[(M_c/M_m)/(1 + 0.5M_c/M_m)]^{1/2} \tag{6.32}$$

HMX provides higher fragment velocity because it has 35% more explosive energy than TNT [$(2E_C)^{1/2} = 10{,}230$ ft/s vs 7,600 ft/s]. Note from the figure that very high fragment velocity V_f requires that $M_c/M_m > 1$.

As an example, the baseline rocket has a cylindrical warhead with HMX explosive and $M_c/M_m = 1$. The fragment velocity is computed

$$V_f = 10230[1/1 + 0.5(1)]^{1/2} = 8353 \text{ ft/s} \tag{6.33}$$

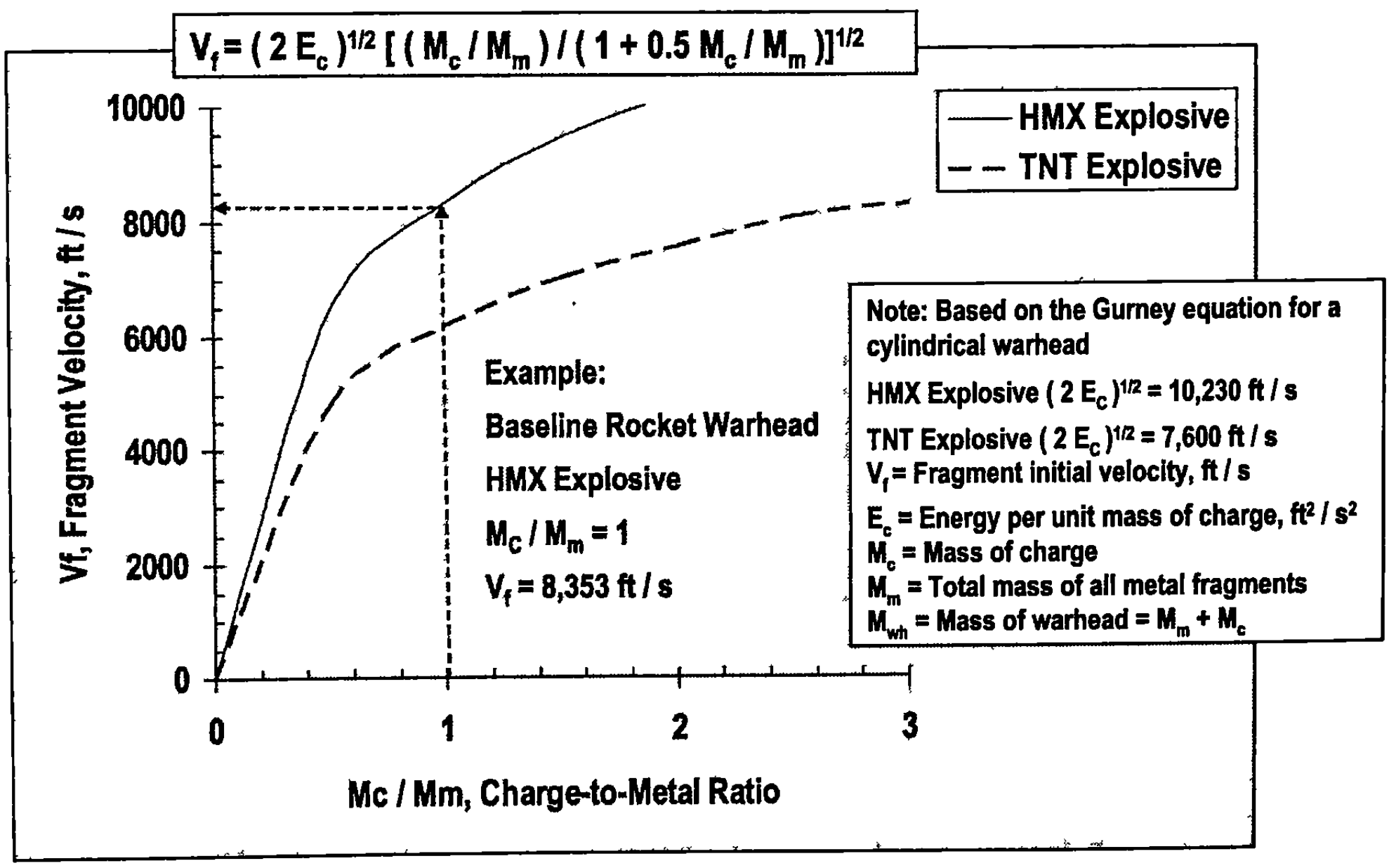

Fig. 6.28 High fragment velocity requires high charge-to-metal ratio.

A more general form of the Gurney equation may be used to predict the fragment velocity of more general warhead configurations. The equation is

$$V_f = (2E_c)^{1/2}\{(M_c/M_m)/\{1 + [n/(n+2)]M_c/M_m\}\}^{1/2} \tag{6.34}$$

In the preceding equation $n = 1$ for a flat sandwich of explosive between two flat plates, $n = 2$ for a cylindrical warhead, and $n = 3$ for a spherical warhead. Note that for the same value of M_c/M_m and $2E_c$, a flat plate warhead provides the highest fragment velocity while a spherical warhead provides the lowest fragment velocity.

Penetration of the fragments from a blast fragmentation warhead is shown in Fig. 6.29 as a function of the miss distance and the fragment weight. Again, the value of small miss distance is apparent: fragments have much greater penetration at small miss distance. Warhead fragments are chunky, with high drag, and the fragment velocity decays rapidly with distance. In the example, a fragment that travels 10 ft has about four times the penetration compared to a fragment that travels 100 ft. The data for the figure are based on a fragment initial velocity of 5000 ft/s, sea level test, average fragment weight of 50 grains (3.2 g), and maximum fragment weight of 150 grains (9.7 g). The average fragment weight for a typical air-to-air blast fragmentation warhead that uses preformed fragments is about 50 grains. Less than 0.3% of the fragments of a nominal 50-grain air-to-air blast fragmentation warhead with preformed

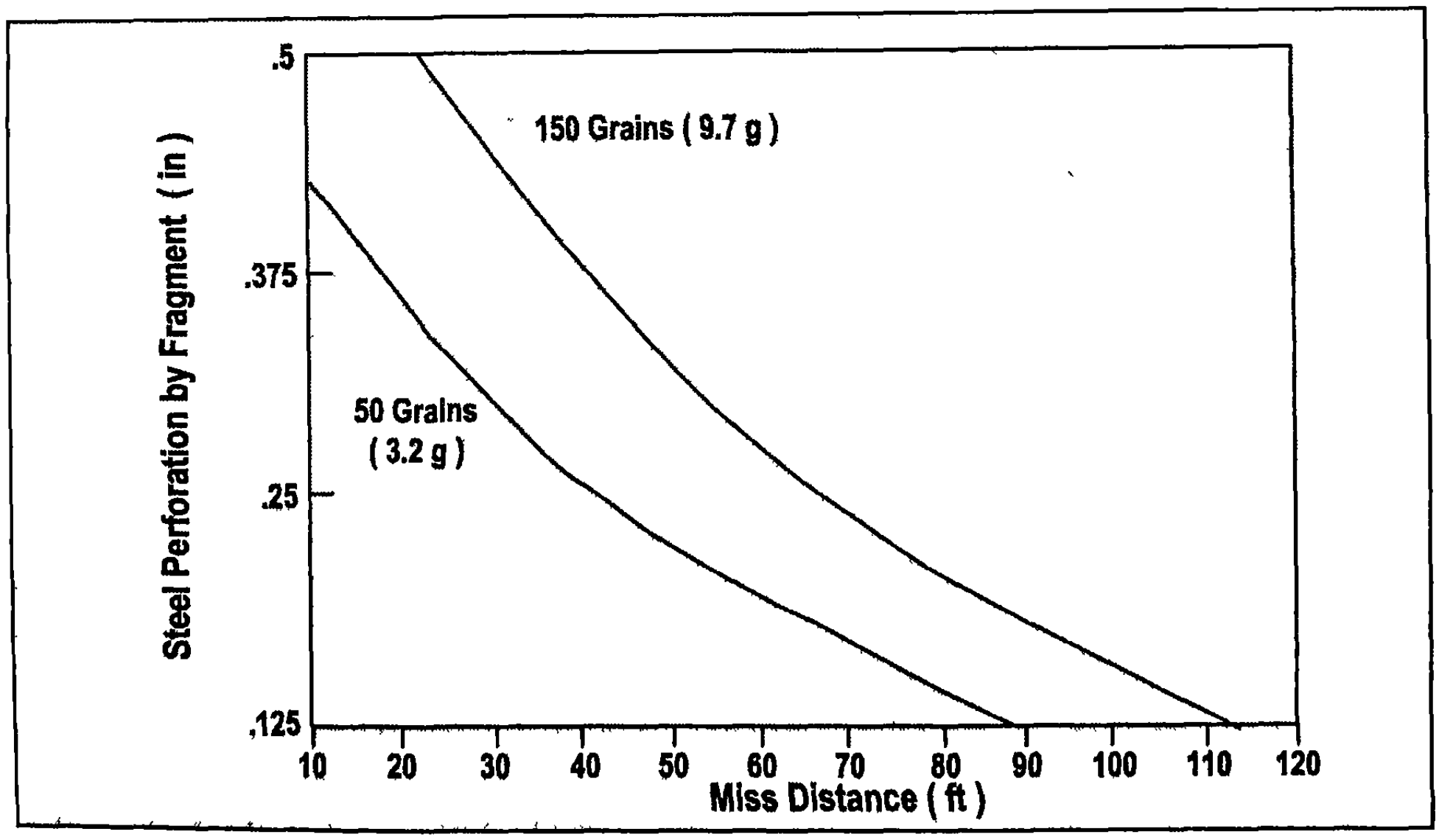

Note: Typical air-to-air missile warhead
- Fragments initial velocity 5000 ft / s
- Sea level
- Average fragment weight 3.2 g
- Fewer than 0.3% of the fragments weigh more than 9.7 g for nominal 3.2 g preformed warhead fragments
- Small miss distance gives less reduction in fragment velocity, enhancing penetration

Fig. 6.29 Small miss distance improves fragment penetration.

fragments weigh more than 150 grains. Preformed and multiprojectile blast fragmentation warheads for air targets have been developed with a broad range of fragment weight, ranging from 4 to 200 grains. The optimum fragment weight is a function of missile accuracy, target size, target hardness, and the type of kill requirements.

The nondimensional total energy on target from a missile impact is given by the equation

$$E_T/E_C = [(1/2)(W_{Missile}/g_c)V^2 + E_C(W_C/g_c)]/[E_C(W_C/g_c)] \tag{6.35}$$

The total energy E_T is assumed to be the sum of the warhead charge energy E_c plus the missile kinetic energy $(1/2)(W_{Missile}/g_c)V^2$. Note from Fig. 6.30 that for a supersonic missile with a missile weight much larger than the warhead charge weight (e.g., $W_{missile}/W_C > 20$), more of the total energy is from the missile kinetic energy than the warhead charge energy. The warhead charge energy in the figure is based on an HMX explosive. At a hypersonic closing velocity the missile kinetic energy is sufficiently large so that for missiles that impact the target, a warhead charge may not be required.

As an example, consider a direct hit intercept by the rocket baseline missile. The rocket baseline has a burnout weight of 367 lb and a warhead charge weight of 38.8 lb. The missile weight is 9.46 times the warhead charge weight. At a relatively slow closing velocity of 2000 ft/s (e.g., 1200 ft/s missile velocity +800 ft/s head-on target velocity), the kinetic energy is $(1/2)(367/32.2)(2000)^2 = 22.8 \times 10^6$ ft-lb. The warhead explosive charge energy is based on

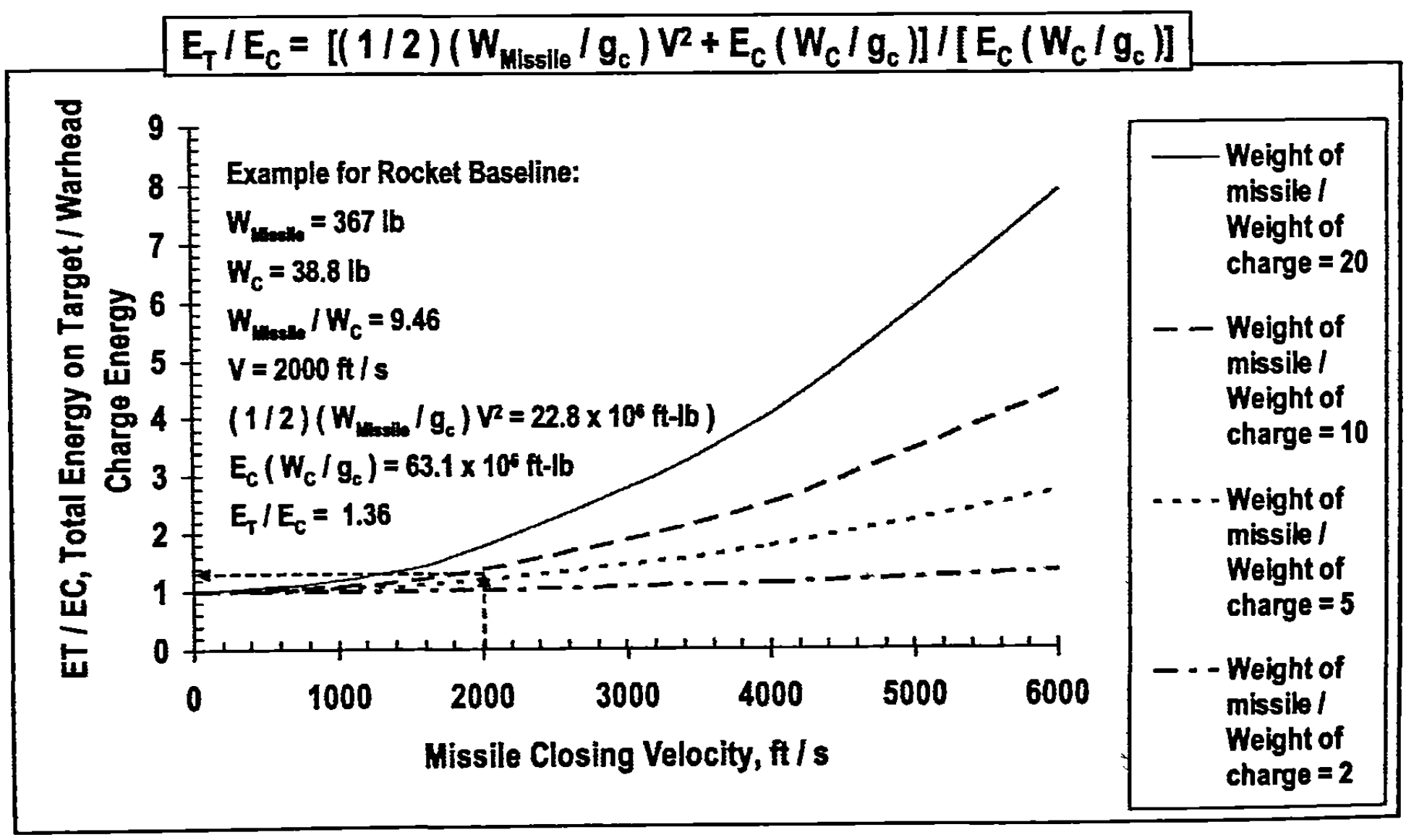

Note: Warhead explosive charge energy based on HMX, $(2E_C)^{1/2}$ = 10,230 ft / s.

1 kg weight at Mach 3 closing velocity has kinetic energy of 391,000 J ⇒ equivalent chemical energy of 0.4 lb TNT.

Fig. 6.30 Hypersonic hit-to-kill enhances the energy on target for missiles with small warheads.

HMX, in which a unit energy of $E_C = 52.3 \times 10^6$ ft^2/s^2. For a warhead charge weight $W_c = 38.8$ lb, the warhead charge energy is

$$E_C(W_C/g_c) = 52.3 \times 10^6 \text{ ft}^2(38.8/32.2) = 63.1 \times 10^6 \text{ ft-lb} \tag{6.36}$$

The ratio of total energy to warhead charge energy is

$$E_T/E_C = (22.8 \times 10^6 + 63.1 \times 10^6)/(63.1 \times 10^6) = 1.36 \tag{6.37}$$

Note that the kinetic energy of the rocket baseline missile adds an additional 36% to the energy of the warhead charge.

As a reference, 1 kg of weight at Mach 3 has a kinetic energy of 391,000 J. This is the equivalent of the chemical energy of 0.4 lb of TNT.

Fig. 6.31, based on Ref. 22, gives an example of kinetic energy warhead penetration distance through a target. It is based on the equation

$$P/d = [(l/d) - 1](\rho_P/\rho_T)^{1/2} + 3.67(\rho_P/\rho_T)^{2/3}[(\rho_T V^2)/\sigma_T]^{1/3} \tag{6.38}$$

Assumptions for the equation are impact velocity $V > 1000$ ft/s, penetrator length-to-diameter $l/d > 2$, and a nondeforming penetrator. A nondeforming penetrator has the properties of high hardness, high strength, and a sharp nose. Note that kinetic energy penetration is a function of the penetrator length, diameter, density, and velocity as well as the target density and ultimate stress. Target penetration increases with penetrator length, diameter, density, and velocity. Penetration is also greater for a low density target with a low value of ultimate stress.

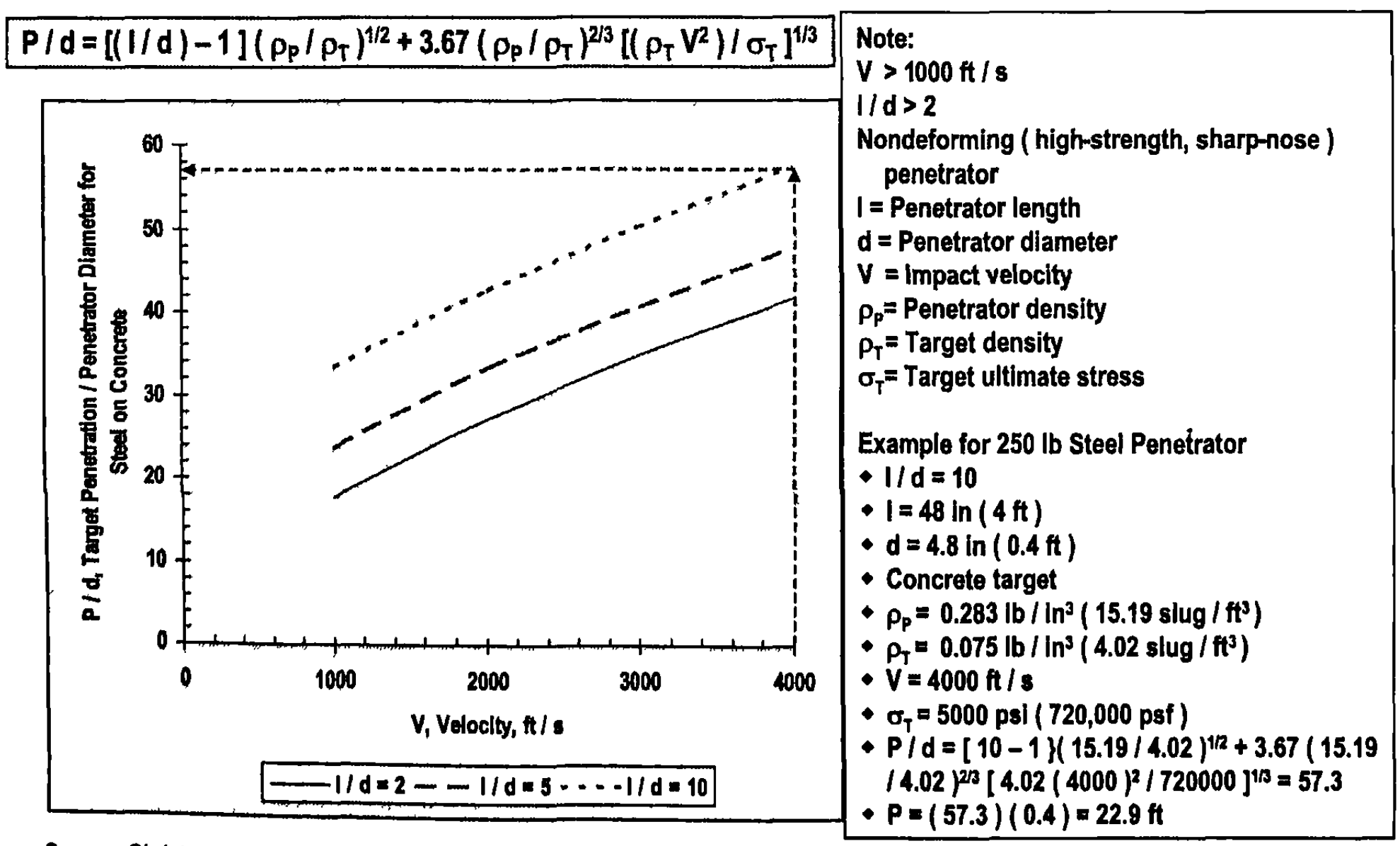

Source: Christman, D.R., et al, "Analysis of High-Velocity Projectile Penetration," Journal of Applied Physics, Vol 37, 1966

Fig. 6.31 Kinetic energy warheads with high density, long length, and high velocity have enhanced penetration.

As an example, assume a 250-lb steel penetrator that has density $\rho_P = 0.283\ \text{lb/in}^3 = 15.19\ \text{slug/ft}^3$, length $l = 48\ \text{in} = 4\ \text{ft}$ and a diameter $d = 4.8\ \text{in} = 0.4\ \text{ft}$. Assume a vertical impact at a velocity $V = 4000\ \text{ft/s}$ of a concrete target of $\sigma_T = 5000\ \text{psi} = 720{,}000\ \text{psf}$ strength and $\rho_T = 0.075\ \text{lb/in}^3 = 4.02\ \text{slug/ft}^3$ density. Substituting, the penetration is

$$P = 0.4\{[(4/0.4) - 1](15.19/4.02)^{1/2} + 3.67(15.19/4.02)^{2/3}[4.02(4000)^2/720000]^{1/3}\} = 22.9\ \text{ft} \tag{6.39}$$

A higher density penetrator such as a tungsten carbide ($\rho = 0.540\ \text{lb/in}^3$) rod has advantages of greater penetration and smaller packaging volume. A 250-lb tungsten carbide penetrator with the same fineness ratio ($l/d = 10$) as the previous example has a length $l = 38.9$ in and a diameter $d = 3.89$ in. The penetration through concrete for an impact velocity $V = 4000\ \text{ft/s}$ is $P = 27.7$ ft. The tungsten carbide rod has 21% greater penetration than the steel rod (27.7 vs 22.9 ft). Because a tungsten carbide rod has greater hardness, it has less surface damage and deformation during penetration. The tungsten carbide rod also has better packaging, with 19% smaller diameter (3.9 vs 4.8 in) and 24% shorter length (38.9 vs 48 in).

Examples of kinetic kill missiles are shown in Fig. 6.32. These missiles have no warhead charge; the kinetic energy of the hypersonic missile provides the kill mechanism.

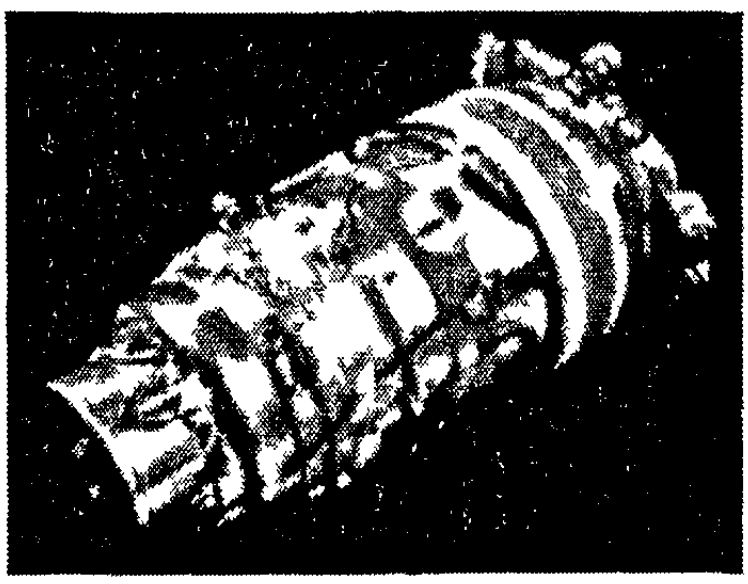

Standard Missile 3 (NTW)

PAC-3

THAAD

LOSAT

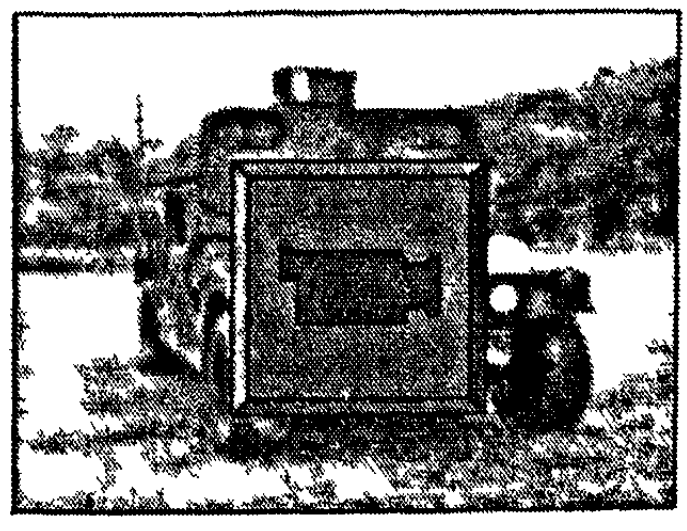

LOSAT Video

Fig. 6.32 Examples of kinetic-kill missiles. Figure also in color section. Video is in the CD included with this textbook.

In the upper left corner of the figure is a drawing of the U.S. Navy Standard Missile 3 kinetic kill warhead. The SM 3 kinetic kill warhead replaces the current warhead and seeker of the Standard Missile 2. It is part of the Navy Theater Wide (NTW) upper-tier, sea-based capability for missile defense. The SM 3 kinetic kill warhead includes a third-stage kick motor, strapdown imaging 256 × 256 LWIR seeker, guidance, autopilot, and solid propellant reaction jet control.

The upper center photograph is the U.S. Army Patriot Advanced Capability (PAC-3) missile. PAC-3 is a lower tier missile defense system. Hit-to-kill accuracy is provided by a high-resolution mmW seeker and impulse reaction jet control.

In the upper right section of the figure is a photograph of the U.S. Army Theater High Altitude Area Defense (THAAD) missile. THAAD is an upper-tier, land-based missile defense system. Hit-to-kill accuracy is provided by a high-resolution IIR seeker and reaction jet control. THAAD has four divert thrusters (up, down, left, right) and eight attitude control thrusters (two for clockwise roll, two for counterclockwise roll, pitch up, pitch down, yaw right, and yaw left).

The bottom left photograph is the U.S. Army hypersonic Line-of-Sight Anti-Tank (LOSAT) missile. LOSAT provides kinetic energy on target that exceeds that of a tank round, without requiring the heavy weight of a tank gun. It is particularly suitable for rapidly deployed, light forces. The LOSAT system can be deployed using a C-130 aircraft, while an M-1 tank cannot be carried on a C-130 aircraft. Hit-to-kill accuracy is provided by the launch platform projecting a narrow beam laser spot on the target. LOSAT has laser beam rider guidance and impulse reaction jet control.

In the bottom right section of the figure is a video of the LOSAT missile. Shown in the video are the lightweight transportation vehicle and demonstrations of hit-to-kill firings against tank targets.

The United States is arguably the world leader in kinetic kill missile technology.

6.4 Miss Distance

The third measure of merit to be discussed is miss distance. Missile miss distance is important in missile configuration development because it impacts the required flight performance and the required volume/weight for an appropriately matched warhead.

The definition of how miss distance relates to circular error probable (CEP) is shown in Fig. 6.33 from Ref. 23. The CEP is the radius of a circle within which 50% of the flight trajectories with the closest distance to the target (e.g., miss distance) are expected to occur. If the miss distance is a normal distribution (a common assumption for conceptual design), then the probability that the miss distance is less than the 1σ value of the normal distribution is 68%. A common assumption for conceptual design, consistent with design accuracy, is to use the terminology of CEP and 1σ miss distance interchangeably. The probabilities that the miss distance is less than 2 and 3σ are 95 and 99.7% respectively. A typical, usually conservative approach to blast fragmentation warhead

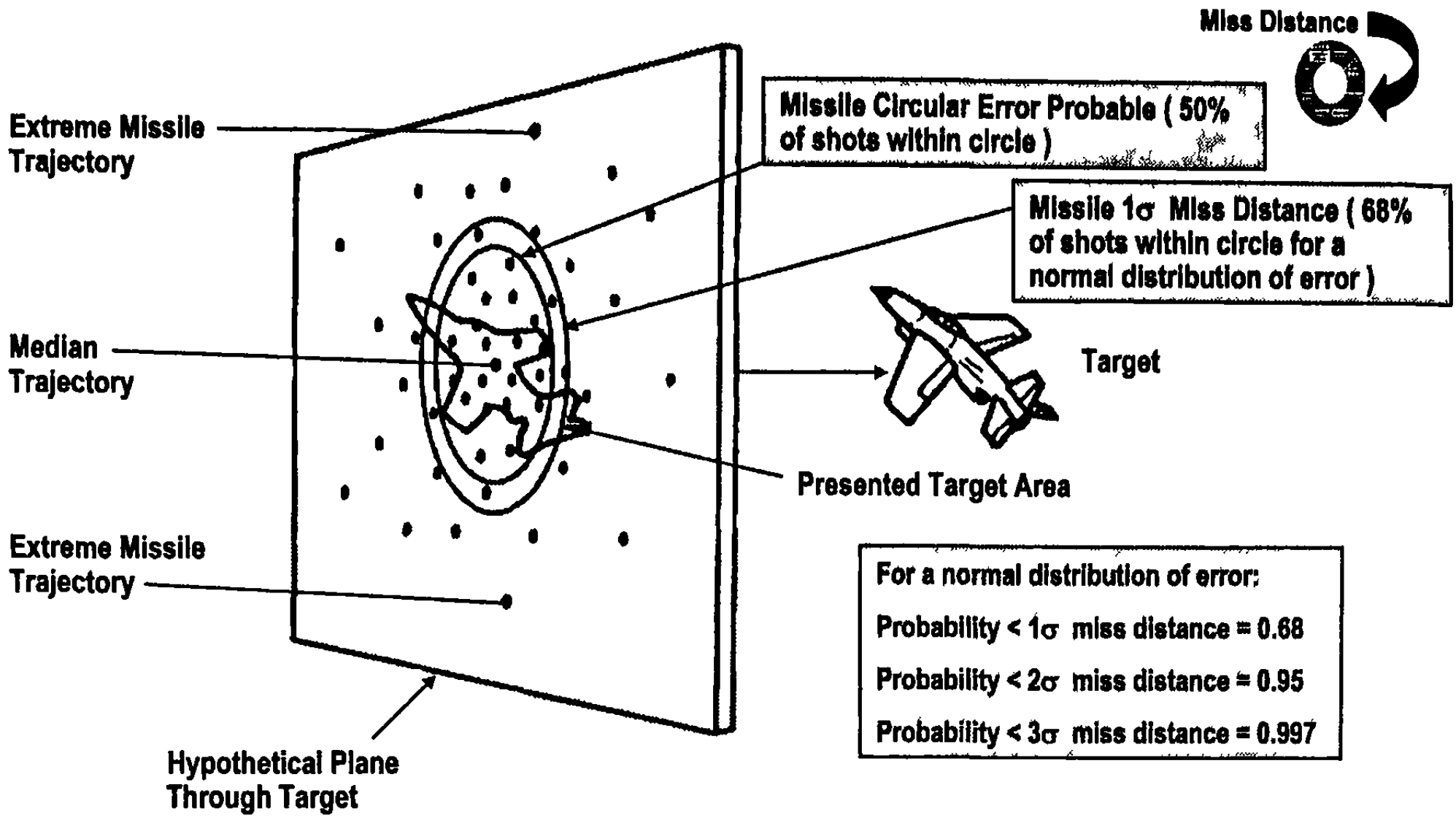

Source: Heaston, R.J. and Smoots, C.W., "Introduction to Precision Guided Munitions," GACIAC HB-83-01, May 1983.

Fig. 6.33 CEP is approximately equal to the 1σ miss distance.

conceptual design is to set the warhead lethal radius equal to the guidance estimate of the 3σ miss distance to provide a design margin for miss distance uncertainty.

Figure 6.34 compares an overshooting miss trajectory with a collision intercept trajectory. An assumption is a constant velocity and nonmaneuvering

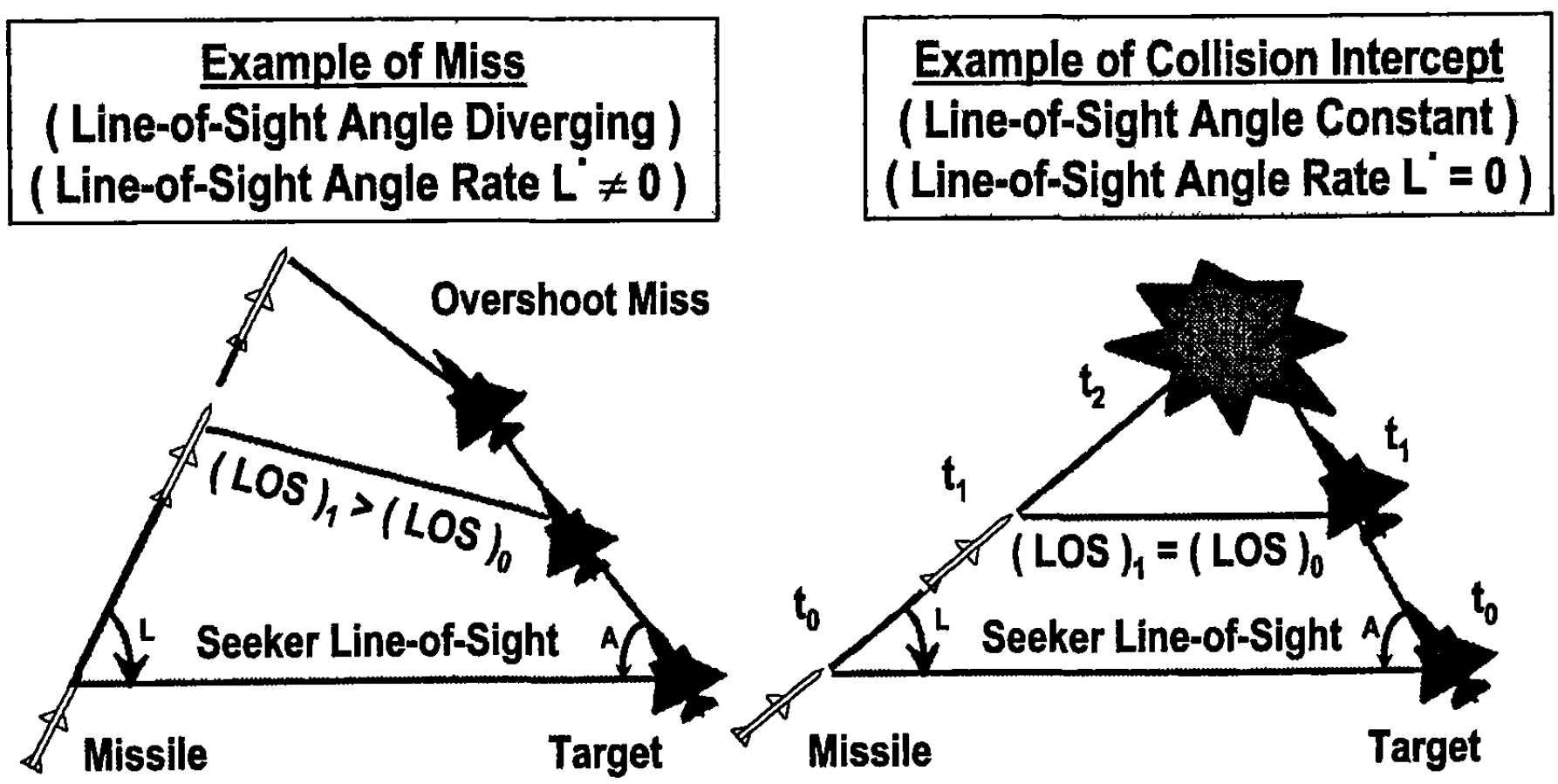

Note: L = Missile Lead
A = Target Aspect

Fig. 6.34 A collision intercept has constant bearing against a constant velocity, nonmaneuvering target.

target. An efficient flight trajectory can be followed in terminal guidance by directing the missile with sufficient lead to a predicted intercept. A constant line-of-sight trajectory, or constant-looking course, is known as proportional guidance. In the left section of the figure, the line-of-sight angle between the missile and the target is increasing, resulting in an overshoot miss. In the right section of the figure, the line-of-sight angle between the missile and the target is constant, resulting in a collision intercept. Proportional guidance terminal homing is based on adjusting the rate of change in the missile velocity heading γ, proportional to the rate of change in the seeker line-of-sight angle $L^{\bullet}$. The objective is to make $L^{\bullet} = 0$. For most tactical missiles, the turning rate correction in the missile heading is usually designed to be three-to-five times the line-of-sight angle rotation rate.

The trajectory equation for the missile flight path against a maneuvering target and the trajectory equation for the missile flight path from an initial heading error are shown in Fig. 6.35 from Jerger[4]. A target maneuver or an initial heading error will result in a missile flight path deviation from a collision course. Note that the equation of motion of the missile flight trajectory against the maneuvering target and the equation of motion for an initial heading error have a discontinuity of the term $(t_0 - t)$ in their denominators. For a flight trajectory attempting to follow proportional guidance, as the time t approaches the total time of flight t_0, the missile deviates from proportional guidance, resulting in a miss distance.

Effective navigation ratio N' accounts for the navigation ratio N, missile velocity V_M, target velocity V_T, and target aspect A. The navigation ratio N relates the flight path angle rate $d\gamma/dt$ to the line of sight rate dL/dt. The equation

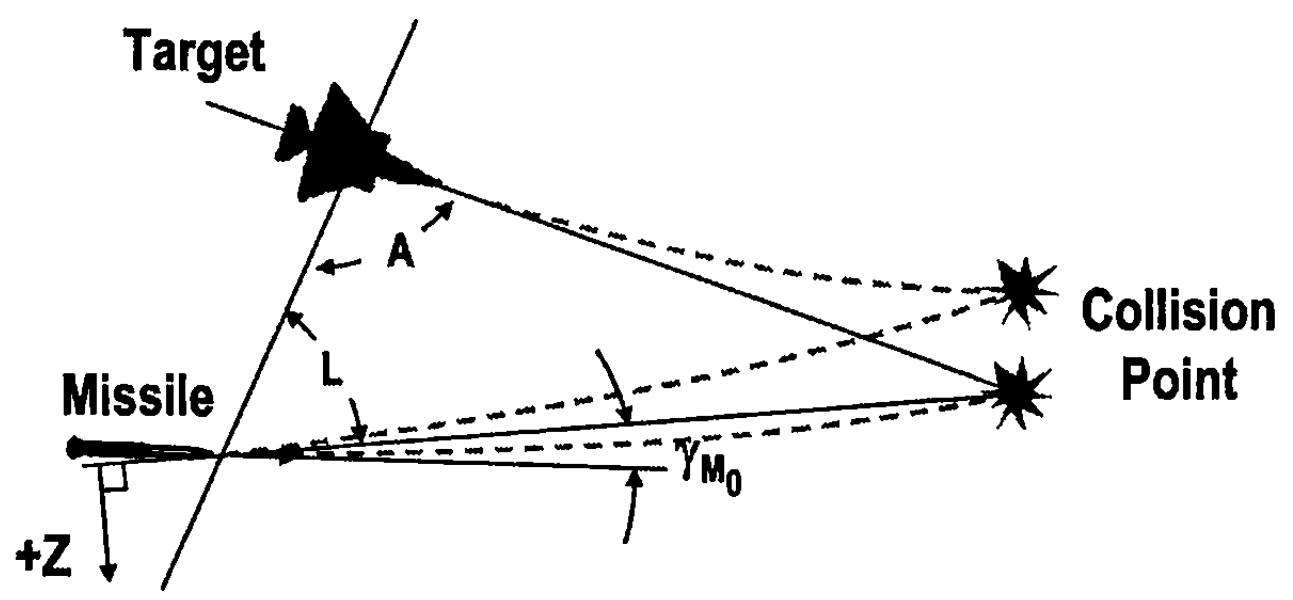

Maneuvering Target: $$\tau \frac{d^2Z}{dt^2} + \frac{dZ}{dt} + N' \frac{Z}{t_0 - t} = \frac{-N'}{t_0 - t} \frac{\cos A}{\cos L} \frac{1}{2} a_T t^2$$

Initial Heading Error: $$\tau \frac{d^2Z}{dt^2} + \frac{dZ}{dt} + N' \frac{Z}{t_0 - t} = -V_M \gamma_{M_0}$$

Note: $t_0 - t = 0$ at intercept, causing discontinuity in above equations.
N' = Effective navigation ratio = $N\,[V_M / (V_M - V_T \cos A)]$
N = Navigation ratio = $(d\gamma / dt) / (dL / dt)$
τ = Missile time constant, V_M = Velocity of missile, γ_{M_0} = Initial flight path angle error of missile, t_0 = Total time of flight, a_T = Acceleration of target, V_T = Velocity of target

Reference: Jerger, J.J., *Systems Preliminary Design Principles of Guided Missile Design*, D. Van Nostrand Company, Inc., Princeton, New Jersey, 1960

Fig. 6.35 A maneuvering target and initial heading error cause miss.

for the navigation ratio is

$$N = (d\gamma/dt)/(dL/dt) \tag{6.40}$$

The equation for the effective navigation ratio is

$$N' = N[V_M/(V_M - V_T \cos A)] \tag{6.41}$$

For conceptual design, the miss distance is usually evaluated for a constant maneuvering target and for an initial heading error at seeker lock-on. It may also be necessary to evaluate the miss distance from smart target dynamic maneuvers such as sinusoidal maneuvers and corkscrew maneuvers. Also, for conceptual design, the miss distance is usually evaluated using proportional guidance. Augmented proportional guidance and modern guidance laws often provide smaller miss, particularly if the missile has an active, low noise seeker that provides additional target information such as range, range rate, and target maneuver acceleration.

Figure 6.36 shows the definition of time constant τ that is used in this text. The contributors to time constant τ are assumed to be from the flight control effectiveness τ_δ, flight control system dynamics (e.g., actuator rate limit) $\tau_{\delta^\cdot}$, and the seeker dome error slope τ_{Dome}. The time constant from guidance and control filters τ_{Filter}, other guidance and control (G&C) contributors (gyro dynamics, accelerometer dynamics, digital processor latency, etc), and seeker errors (resolution, latency, blind range, tracking dynamics because of actuator bandwidth and rate limits, noise, glint, amplitude) are not usually evaluated in conceptual design because they usually have a lower impact on missile configuration design.

- τ is a measure of missile ability to respond to target condition changes
- τ equals elapsed time from input of target return until missile has completed 63% or ($1 - e^{-1}$) of corrective maneuver ($t = \tau$)
- τ also called "rise time"
- Contributions to time constant τ
  - Control effectiveness (τ_δ)
  - Control dynamics (e.g., actuator rate) ($\tau_{\delta^\cdot}$)
  - Dome error slope (τ_{Dome})
  - Guidance and control filters (τ_{Filter})
  - Other G&C dynamics (gyro dynamics, accelerometer, processor latency, etc)
  - Seeker errors (resolution, latency, blind range, tracking, noise, glint, amplitude)
- Approach to estimate τ
  - $\tau = \tau_\delta + \tau_{\delta^\cdot} + \tau_{Dome}$

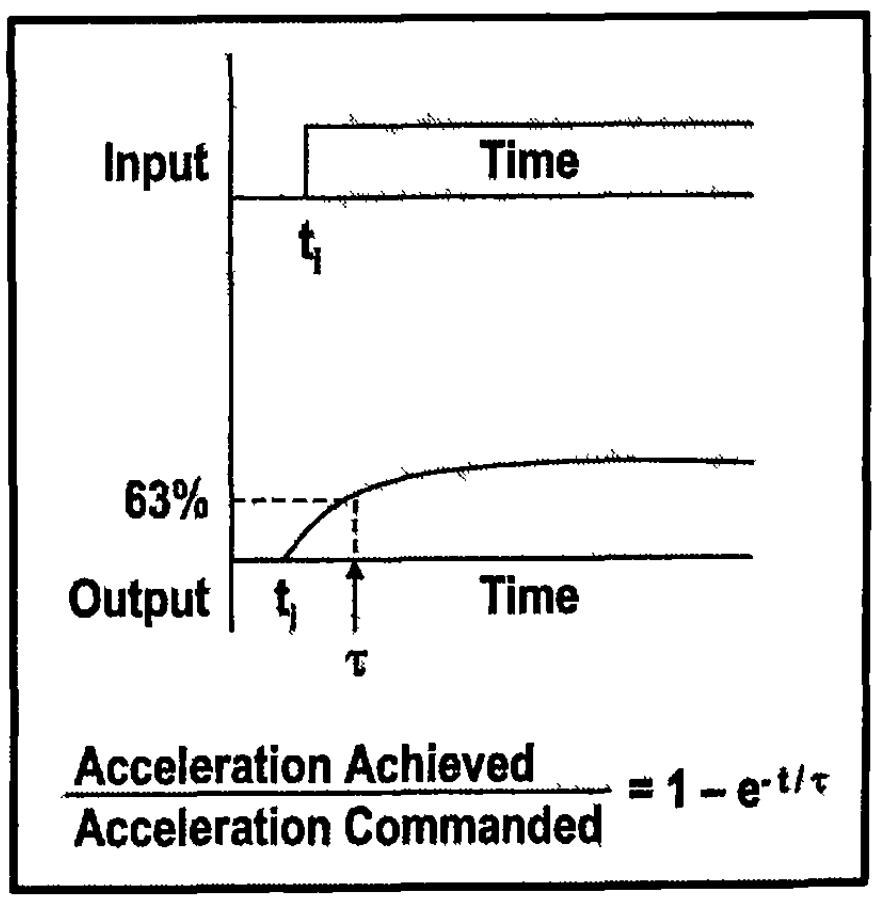

Example for Rocket Baseline:
M = 2, h = 20,000 ft, coast
$\tau = \tau_\delta + \tau_{\delta^\cdot} + \tau_{Dome}$
$= 0.096 + 0.070 + 0.043 = 0.209$ s

Fig. 6.36 Missile time constant causes miss distance.

Missile time constant is an aggregate measure of the ability of the missile to respond to target condition changes. It is equal to the elapsed time from receiving an input for a required target correction until the missile has completed an exponential convergence to 63% or $(1 - e^{-1})$ of the required corrective maneuver. Missile time constant is also called "rise time." For this text it is assumed that the missile time constant is the sum of the contributors

$$\tau = \tau_\delta + \tau_{\dot{\delta}} + \tau_{\text{Dome}} \tag{6.42}$$

As an example for the rocket baseline missile coasting at Mach 2 and 20,000 ft altitude, the missile time constant is

$$\tau = \tau_\delta + \tau_{\dot{\delta}} + \tau_{\text{Dome}} = 0.096 + 0.070 + 0.043 = 0.209\,\text{s} \tag{6.43}$$

For a 10-g command, the missile requires a time $t = \tau = 0.209$ s to achieve 63% (or 6.3 g) of the command $[10(1 - e^{-1}) = 6.3]$. At a time $t = 4\tau = 0.836$ s, the missile achieves 98% (or 9.8 g) of the command $[10(1 - e^{-4}) = 9.8]$.

The time constant from control effectiveness is usually driven by the missile static margin. The effect of limited pitching moment on control effectiveness is illustrated in Fig. 6.37. Assume that the flight control surface is deflection limited, operating in a race-break deflection profile (see figure). The assumption is valid if the flight control actuator is very fast ($\dot{\delta}_{\text{ideal}} \to \infty$) and the missile has near-neutral static stability. The equation of motion for one-degree of freedom (DOF) is

$$\ddot{\alpha} = [\rho V^2 S d C_{m_\delta}/(2I_y)]\delta_{\text{Max}} \tag{6.44}$$

- Assumptions for τ_δ
  - Control surface deflection limited
  - Near neutral stability
- Equation of motion is
  - $\ddot{\alpha} = [\rho V^2 S d C_{m_\delta} / (2 I_y)] \delta_{Max}$
- Integrate to solve for α_{Max}
  - $\alpha_{Max} = [\rho V^2 S d C_{m_\delta} / (8 I_y)] \delta_{Max} \tau_\delta^2$
- τ_δ is given by
  - $\tau_\delta = [8 I_y (\alpha_{Max} / \delta_{Max}) / (\rho V^2 S_{Ref} d C_{m_\delta})]^{1/2}$
- Contributors to small τ_δ
  - Low fineness (small $I_y / (S_{Ref} d)$)
  - High dynamic pressure (low altitude / high speed)
  - Large C_{m_δ}

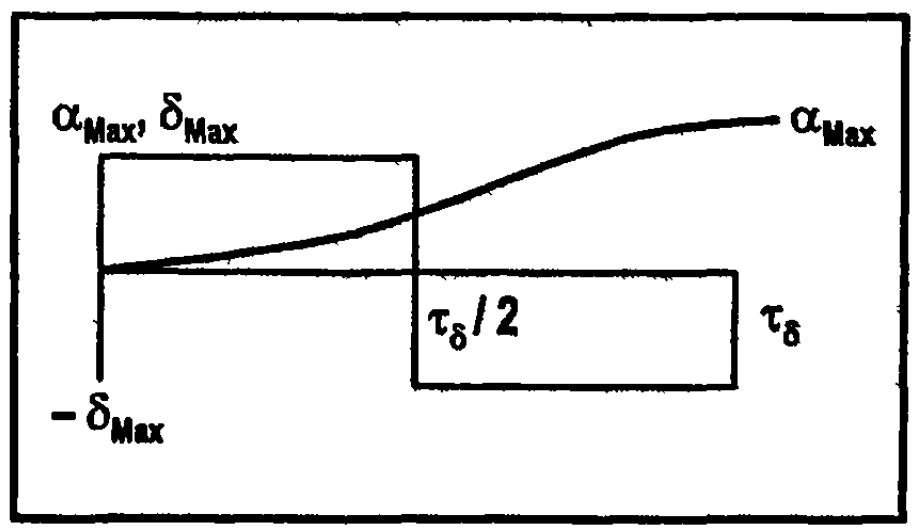

Example for Rocket Baseline:
W = 367 lb, d = 0.667 ft, S_{Ref} = 0.349 ft², I_y = 94.0 slug-ft²,
M = 2, h = 20,000 ft (ρ = 0.001267 slug / ft³),
α_{Max} = 9.4 deg, δ_{Max} = 12.6 deg, C_{m_δ} = 51.6 per rad,
τ_δ = { 8 (94.0) (9.4 / 12.6) / [0.001267 (2074)² (0.349) (0.667) (51.6)]$^{1/2}$ = 0.096 s

Fig. 6.37 Time constant τ_δ for control effectiveness is driven by static margin.

Integrating the above equation to solve for α_{Max} gives

$$\alpha_{Max} = [\rho V^2 S d C_{m_\delta}/(8I_y)]\delta_{Max}\tau_\delta^2 \tag{6.45}$$

τ_δ is given by

$$\tau_\delta = [8I_y(\alpha_{Max}/\delta_{Max})/(\rho V^2 S_{Ref} d C_{m_\delta})]^{1/2} \tag{6.46}$$

The contributors to a small value of τ_δ are low fineness [small $I_y/(S_{Ref}d)$], high dynamic pressure (low altitude/high speed), and a large pitching moment control effectiveness C_{m_δ}.

As an example of the time constant from limited pitching moment control effectiveness, the rocket baseline missile has a burnout weight $W = 367$ lb, diameter $d = 8$ in (0.667 ft), reference area $S_{Ref} = 0.349\ \text{ft}^2$, and burnout pitch moment of inertia $I_y = 94.0$ slug-ft^2. At an intercept Mach number and altitude of $M = 2$ and $h = 20{,}000$ ft respectively, the maximum allowable angle of attack $\alpha_{Max} = 9.4$ deg, the maximum control deflection $\delta_{Max} = 12.6$ deg, and the pitching moment control effectiveness derivative $C_{m_\delta} = 51.6$ per rad. The time constant from limited pitching moment control effectiveness is computed to be

$$\begin{aligned}\tau_\delta &= \{8(94.0)(9.4/12.6)/[0.001267(2074)^2(0.349)(0.667)(51.6)\}^{1/2}\\ &= 0.096\,\text{s}\end{aligned} \tag{6.47}$$

We will next evaluate the time constant for flight control system dynamics. The time constant for flight control system dynamics is usually driven by the actuator response, the slowest component of the flight control system. Actuator rate dynamics (e.g., $\tau_{\dot\delta}$ from actuator rate limit) are illustrated in Fig. 6.38. Assume that the flight control surface is rate limited ($\dot\delta = \dot\delta_{Max}$) and that the missile has near-neutral stability. The one-DOF equation of motion for $\dot\delta = +/-\dot\delta_{Max}$ is

$$\dddot\alpha = [\rho V^2 S d C_{m_\delta}/(2I_y)]\dot\delta_{Max} \tag{6.48}$$

As a comparison, the equation of motion from a "perfect" response $\dot\delta = \infty$, $\delta = +/-\delta_{Max}$ is

$$\ddot\alpha = [\rho V^2 S d C_{m_\delta}/(2I_y)]\delta_{Max} \tag{6.49}$$

$\tau_{\dot\delta}$ is the difference between the actual response to α_{Max} and the "perfect" τ_δ response to α_{Max}.

Then

$$\tau_{\dot\delta} = 2\delta_{Max}/\dot\delta_{Max} \tag{6.50}$$

As an example for the rocket baseline missile, the maximum wing control surface deflection rate $\dot\delta_{Max} = 360$ deg/s and the maximum wing control

- Assumptions for $\tau_{\delta^{\cdot}}$
  - Control surface rate limited ($\delta^{\cdot} = \delta^{\cdot}_{Max}$)
  - Near neutral stability
- Equation of motion for $\delta^{\cdot} = +/-\delta^{\cdot}_{Max}$
  - $\alpha^{\cdots} = [\rho V^2 S d C_{m\delta} / (2 I_y)] \delta^{\cdot}_{Max}$
- Equation of motion for "perfect" response $\delta^{\cdot} = \infty$, $\delta = \delta_{Max}$
  - $\alpha^{\cdot\cdot} = [\rho V^2 S d C_{m\delta} / (2 I_y)] \delta_{Max}$
- $\tau_{\delta^{\cdot}}$ is difference between actual response to α_{Max} and "perfect" (τ_δ) response
- Then
  - $\tau_{\delta^{\cdot}} = 2\, \delta_{Max} / \delta^{\cdot}_{Max}$

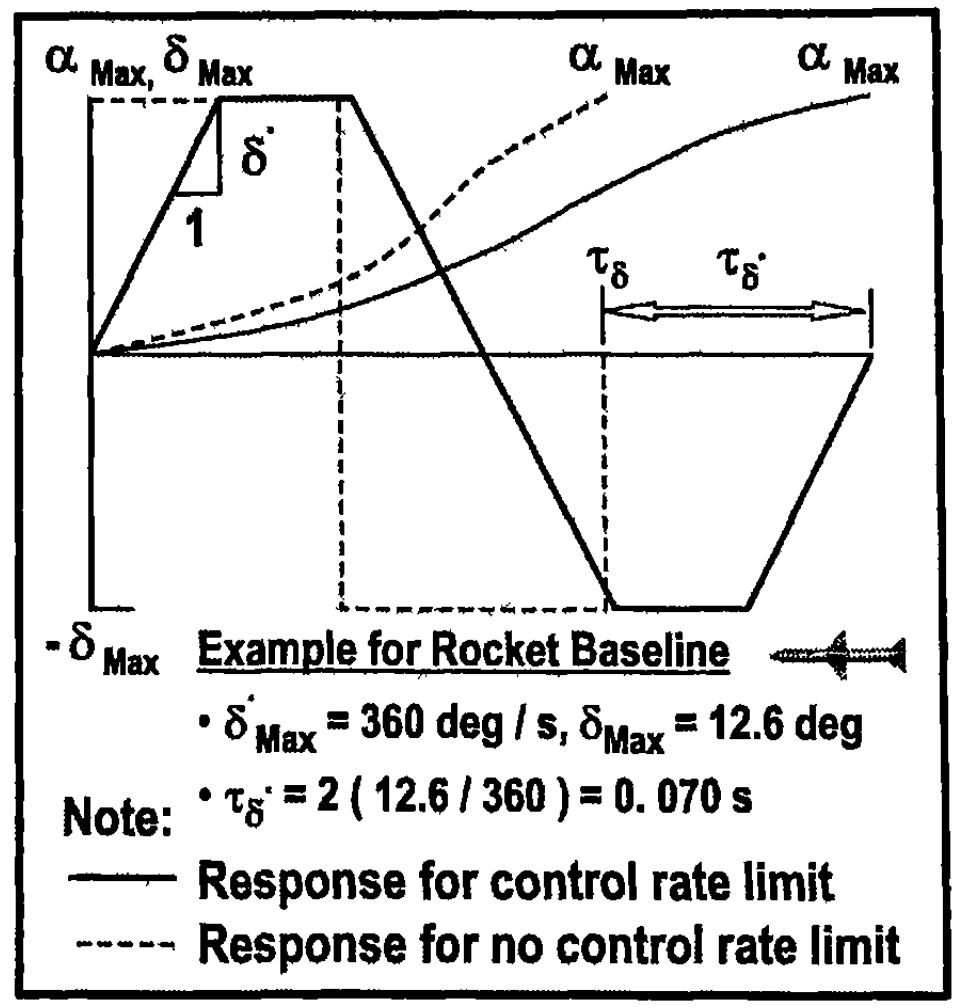

Fig. 6.38 Time constant $\tau_{\delta^{\cdot}}$ for the flight control system is driven by actuator rate dynamics.

surface deflection $\delta_{Max} = 12.6$ deg. The maximum wing control surface deflection occurs at wing stall, which has a maximum local angle of attack $\alpha' = \alpha + \delta = 22$ deg. For a nominal static margin of $\alpha/\delta = 0.75$, $\alpha = 9.4$ deg and $\delta = 12.6$ deg. The time constant from pitching moment control rate dynamics is computed to be

$$\tau_{\delta^{\cdot}} = 2(12.6/360) = 0.070 \text{ s} \tag{6.51}$$

The time constant from radome error slope is illustrated in Fig. 6.39. The seeker radome error slope for a typical high-fineness curved dome (e.g., tangent ogive single dome) is

$$|R| = 0.05(l_N/d - 0.5)[1 + 15(\Delta f/f)]/(d/\lambda) \tag{6.52}$$

The radome time constant τ_{Dome} is given by

$$\tau_{Dome} = N'(V_C/V_M)|R|(\alpha/\gamma) \tag{6.53}$$

The angle of attack sensitivity to turn rate is

$$\alpha/\gamma^{\cdot} = \alpha(W/g_c)V_M/\{qS_{Ref}[C_{N_\alpha} + C_{N_\delta}/(\alpha/\delta)]\} \tag{6.54}$$

Substituting for $\alpha/\gamma^{\cdot}$

$$\tau_{Dome} = N'WV_C|R|/\{g_c qS_{Ref}[C_{N_\alpha} + C_{N_\delta}/(\alpha/\delta)]\} \tag{6.55}$$

The contributors to a small value of τ_{Dome} are 1) low weight per cross-sectional area W/S_{Ref}, which implies a low value of body fineness ratio l/d; 2) low dome error slope $|R|$ such as the dome error slope of a hemispherical, faceted, window,

- $|R| = 0.05\,(l_N / d - 0.5)\,[1 + 15\,(\Delta f / f)] / (d / \lambda)$
- $\tau_{Dome} = N'\,(V_C / V_M)\,|R|\,(\alpha / \gamma')$
- $\alpha / \gamma' = \alpha\,(W / g_c)\,V_M / \{q\,S_{Ref}\,[C_{N_\alpha} + C_{N_\delta} / (\alpha / \delta)]\}$
- Substituting gives $\tau_{Dome} = N'\,W\,V_C\,|R| / \{g_c\,q\,S_{Ref}\,[C_{N_\alpha} + C_{N_\delta} / (\alpha / \delta)]\}$

Example for Rocket Baseline at M = 2, h = 20,000 ft, q = 2725 psf

Assume V_T = 1000 ft / s, giving V_C = 3074 ft / s

Assume N' = 4, f = 10 GHz or λ = 1.18 in, $\Delta f / f$ = 0.02

Configuration data are l_N / d = 2.4, d = 8 in, S_{Ref} = 0.349 ft², W = 367 lb, C_{N_α} = 40 per rad, C_{N_δ} = 15.5 per rad, α / δ = 0.75

Compute | R | = 0.05 (2.4 – 0.5) [1 + 15 (0.02)] / (8 / 1.18) = 0.0182 deg / deg

τ_{Dome} = 4 (367) (3074) (0.0182) / [32.2 (2725) (0.349) (40 + 15.5 / 0.75)] = 0.043 s

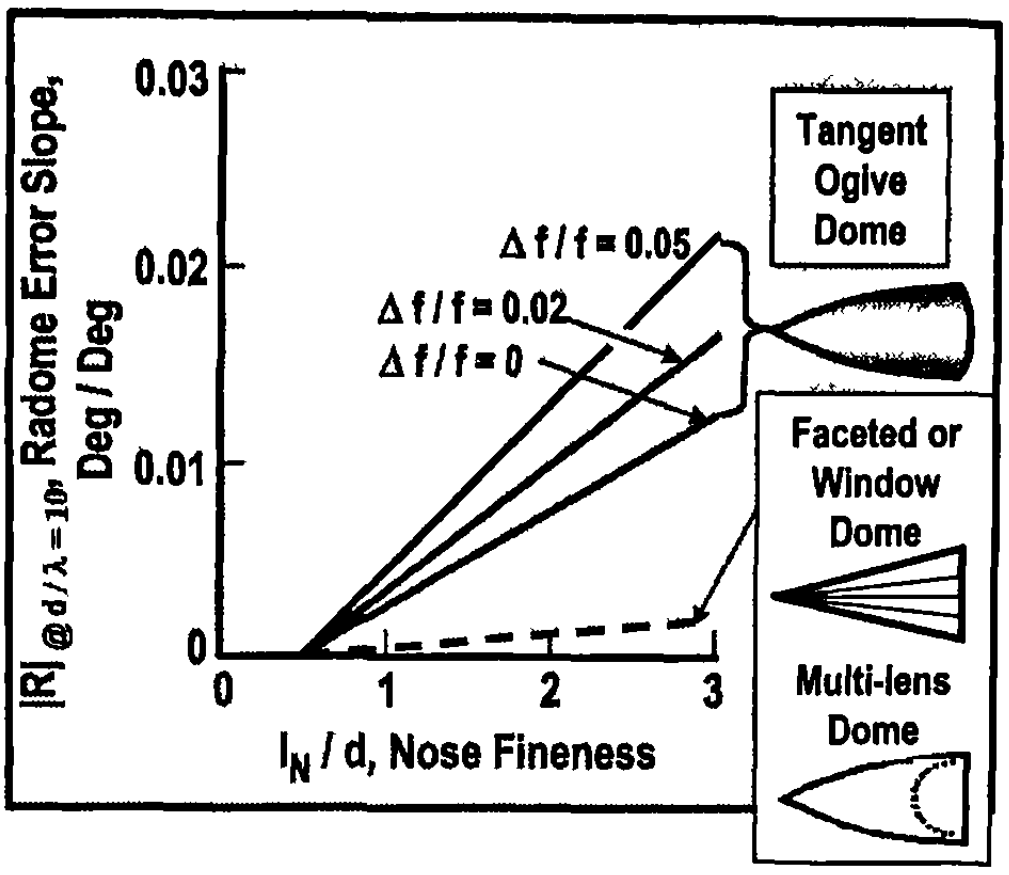

Fig. 6.39 Time constant τ_{Dome} for radome is driven by dome error slope.

or multilens dome; 3) low nose fineness l_N/d; 4) low change in angle of attack with control deflection α/δ, such as a statically stable missile with wing control; 5) low effective navigation ratio N'; 6) low closing velocity V_C, such as a tail chase intercept; 7) small frequency bandwidth $\Delta f/f$ of the seeker transmitter frequency; 8) high frequency f of the seeker transmitter, such as a mmW radar; 9) high normal force coefficient derivative from angle of attack C_{N_α}, such as a missile with a high aspect ratio, large wing; 10) high normal force coefficient derivative from control deflection C_{N_δ}, such as wing control; and 11) high dynamic pressure q, such as low-altitude/high-speed flight.

As an example for the rocket baseline missile, consider a head-on intercept of a target flying at an altitude of 20,000 ft and a velocity of $V_T = 1000$ ft/s. The assumed missile Mach number is $M = 2$, providing a dynamic pressure $q = 2725$ psf and a closing velocity $V_C = 3074$ ft/s. The seeker and guidance parameters are a frequency $f = 10$ GHz, frequency bandwidth $\Delta f/f = 0.02$, and effective navigation ratio $N' = 4$. Configuration data are a tangent ogive nose fineness ratio $l_N/d = 2.4$, seeker diameter $d = 8$ in, reference area $S_{Ref} = 0.349$ ft^2, burnout weight $W = 367$ lb, normal force coefficient angle of attack derivative $C_{N_\alpha} = 40$ per rad, normal force control deflection coefficient derivative $C_{N_\delta} = 15.5$ per rad, and angle of attack sensitivity $\alpha/\delta = 0.75$.

Computing the dome error slope and the dome time constant

$$|R| = 0.05(2.4 - 0.5)[1 + 15(0.02)]/(8/1.18) = 0.0182 \text{ deg/deg} \tag{6.56}$$

$$\tau_{Dome} = 4(367)(3074)(0.0182)/\{32.2(2725)(0.349)(40 + 15.5/0.75)\} = 0.043 \text{ s} \tag{6.57}$$

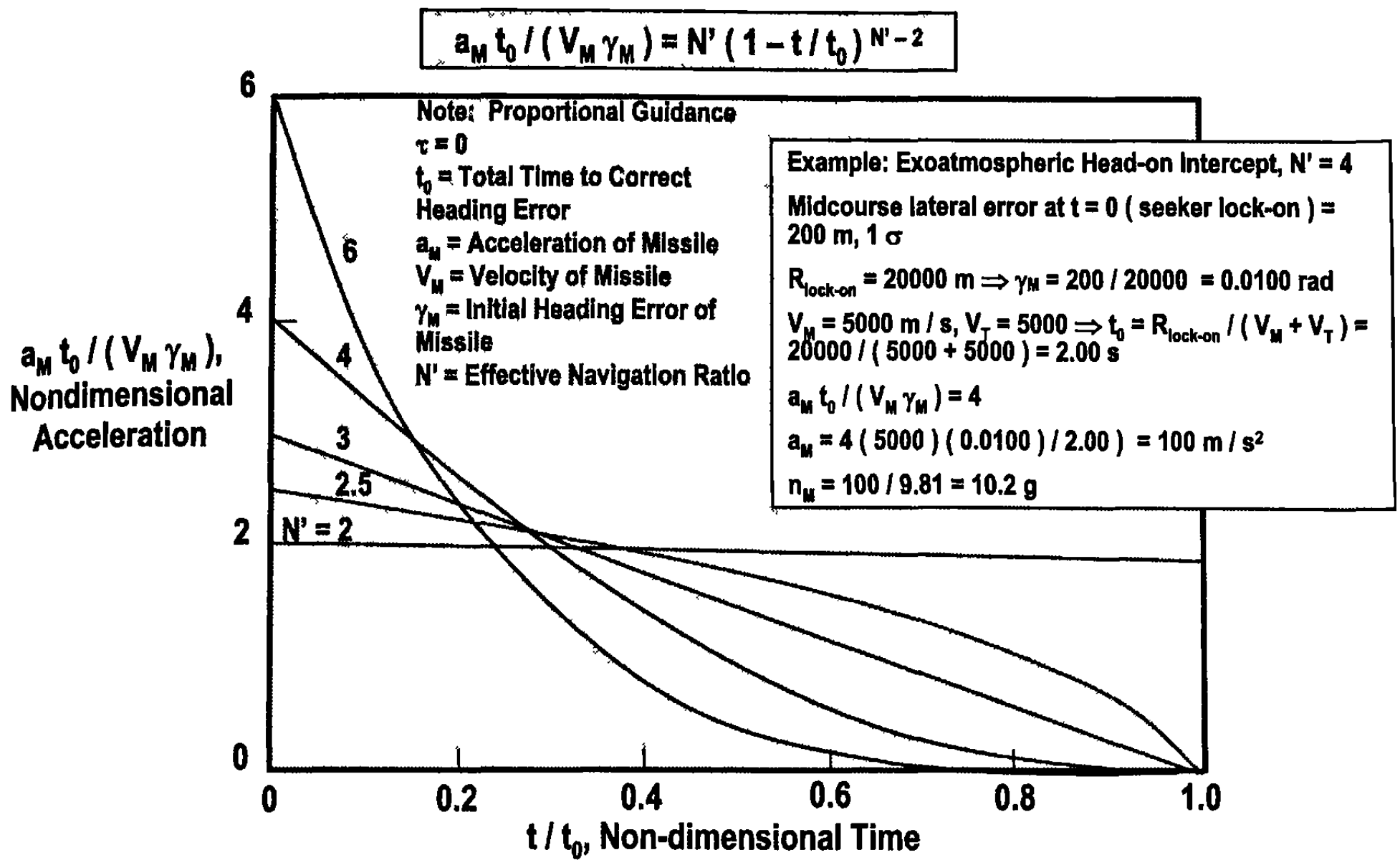

Fig. 6.40 High initial acceleration is required to eliminate a heading error.

Note from the figure that an approach to reduce the dome error slope would be to use either a hemispherical, faceted, window, or multilens dome. The reduced error slope would enhance the missile seeker tracking accuracy, reduce the missile time constant, and reduce the miss distance.

Figure 6.40 shows the missile maneuver acceleration that is required to eliminate an initial heading error for an ideal missile. It is based on proportional homing guidance for an ideal missile with zero time constant ($\tau = 0$). The equation is

$$a_M = (V_M \gamma_M N'/t_0)(1 - t/t_0)^{N'-2} \tag{6.58}$$

The required maneuverability to correct a heading error is a function of the effective navigation ratio N', the time elapsed since the initiation of guidance correction t, the total time available to correct the heading error t_0, the missile velocity V_M, and the initial heading error γ_M. Note from the figure that for $N' > 2$, the missile maneuver acceleration to eliminate a heading error is largest at the initiation of the correction and decreases with time. A large value of the effective navigation ratio N' provides large initial missile acceleration and the acceleration decreases rapidly with time. A large value of N' has an advantage of providing a larger off-boresight intercept capability. For exo-atmospheric missile defense, a large N' reduces the total impulse requirement for the divert thrusters, allowing more efficient use of the divert propellant. Note that for a limiting small value of $N' = 2$ (not a practical case), the theoretical missile acceleration is constant.

For proportional homing guidance for a theoretical missile with no lags in the system ($\tau = 0$) and no saturation in the commanded acceleration, there is

theoretically no miss distance. However, as mentioned previously, for a real missile the lags in the system will cause a time constant and miss distance.

Consider an example of an exo-atmospheric missile interceptor correcting an initial heading error against a ballistic missile target at an assumed seeker lock-on range $R_{\text{lock-on}} = 20{,}000$ m. Assume that the target midcourse error is 200 m, 1σ. Also assume a head-on intercept with an interceptor velocity $V_M = 5000$ m/s and a target velocity $V_T = 5000$ m/s. Then the total time available to correct the initial heading error is $t_0 = R_{\text{lock-on}}/(V_M + V_T) = 2.00$ s. For an assumed seeker lock-on range of $R_{\text{lock-on}} = 20{,}000$ m, the initial heading error $\gamma_M = 200/20{,}000 = 0.0100$ rad. For an assumed missile effective navigation ratio $N' = 4$, the initial required maneuver acceleration

$$a_M = (V_M \gamma_M N'/t_0)(1 - t/t_0)^{N'-2} = 5000(0.0100)(4)(1-0)^{4-2}/2.00$$
$$= 100 \text{ m/s}^2, \text{ or } n_M = 10.2\,\text{g}. \tag{6.59}$$

Consider another example of correcting an initial homing error against a fixed ground target. Based on a previous example, assume that the GPS/INS midcourse guidance has an error of 3 m, 1σ at $t = 0$ s (seeker lock-on). For an assumed seeker lock-on range $R_{\text{lock-on}} = 125$ m, the initial heading error $\gamma_M = 0.024$ rad. Assume a missile velocity $V_M = 300$ m/s. Then the total time available to correct the initial heading error is $t_0 = 0.417$ s. For a missile effective navigation ratio $N' = 4$, the required maneuver acceleration is

$$a_M = 69.1 \text{ m/s}^2, \text{ or } n_M = 7.04 \text{ g} \tag{6.60}$$

Miss distance from heading error is a function of the time available to correct the error t_0, missile time constant τ, heading error γ_M, missile velocity V_M, and the effective navigation ratio N'. The adjoint method of References 24 and 25 gives the miss distance as

$$\sigma_{HE} = V_M \gamma_M t_0 e^{-(t_0/\tau)} \sum_{j=1}^{N'-1} \{(N'-2)![-(t_0/\tau)]^j/[(j-1)!(N'-j-1)!]\} \tag{6.61}$$

$$\text{If } N' = 3,\ \sigma_{HE} = V_M \gamma_M t_0 e^{-(t_0/\tau)}[(t_0/\tau) - (t_0/\tau)^2/2] \tag{6.62}$$

$$\text{If } N' = 4,\ \sigma_{HE} = V_M \gamma_M t_0 e^{-(t_0/\tau)}[(t_0/\tau) - (t_0/\tau)^2 + (t_0/\tau)^3/6] \tag{6.63}$$

$$\text{If } N' = 5,\ \sigma_{HE} = V_M \gamma_M t_0 e^{-(t_0/\tau)}[(t_0/\tau) - (3/2)(t_0/\tau)^2 + (t_0/\tau)^3/2 - (t_0/\tau)^4/24] \tag{6.64}$$

$$\text{If } N' = 6,\ \sigma_{HE} = V_M \gamma_M t_0 e^{-(t_0/\tau)}[(t_0/\tau) - 2(t_0/\tau)^2 + (t_0/\tau)^3 - (t_0/\tau)^4/6 + (t_0/\tau)^5/120] \tag{6.65}$$

Figure 6.41 shows an envelope of the adjoint miss distance for effective navigation ratios of $N' = 3$, 4, and 6. Note that the miss distance is smaller for large values of navigation ratio. The figure also shows that the peak miss distance

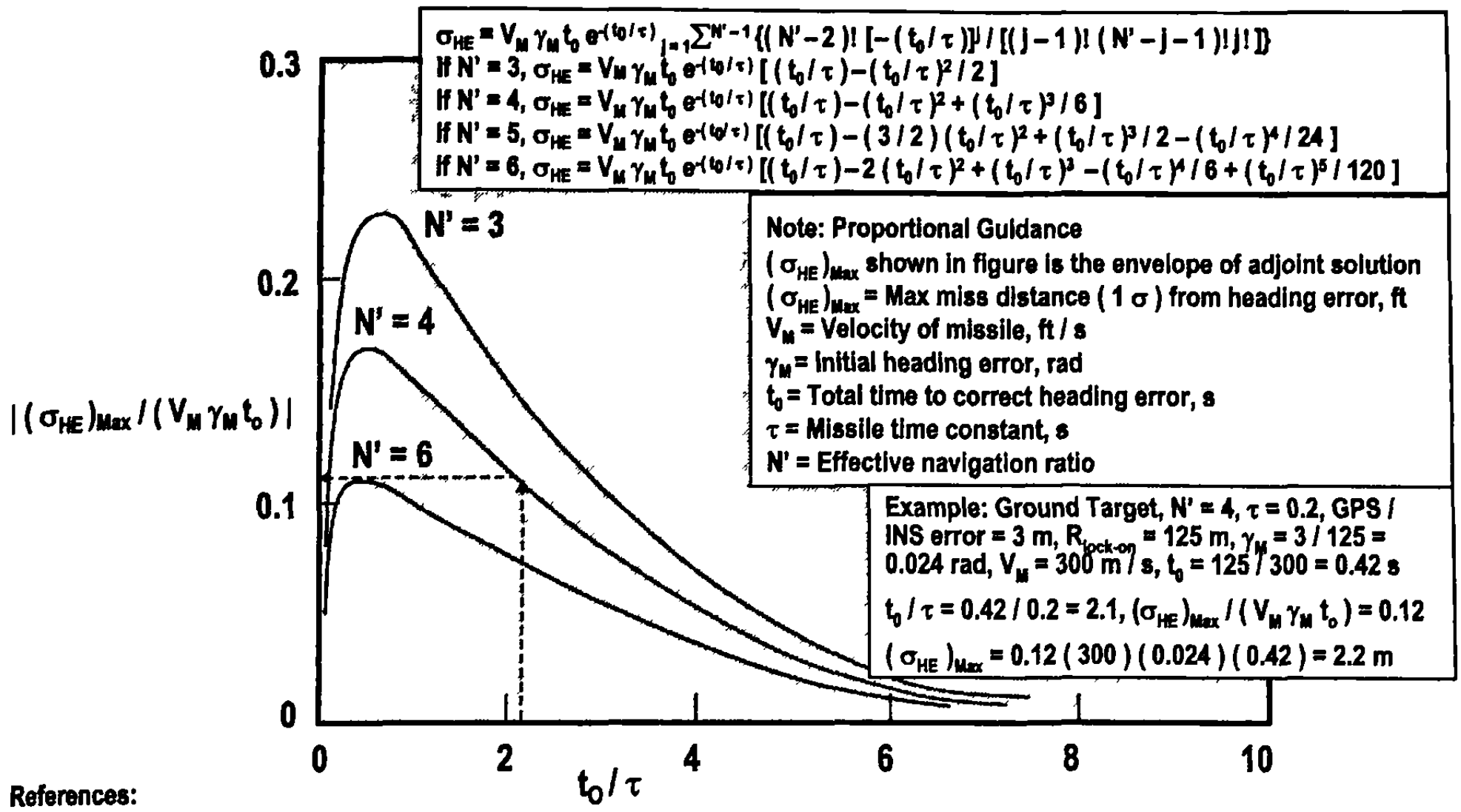

Fig. 6.41 Missile minimum range may be driven by the four to eight time constants required to correct an initial heading error.

occurs if the guidance to correct the heading error is initiated at about one time constant before intercept. If guidance is initiated at about four to eight time constants prior to intercept, the miss distance is negligible.

As an example, assume the same conditions as those from the previous figure. These are 1) an initial heading error against a ground target; 2) GPS/INS mid-course guidance with an error of 3 m at $t = 0$ s (seeker lock-on); 3) seeker lock-on range $R_{\text{lock-on}} = 125$ m; 4) missile velocity $V_M = 300$ m/s; 5) effective navigation ratio $N' = 4$; and 6) missile time constant $\tau = 0.2$ s. Then the initial heading error is $\gamma = 3/125 = 0.024$ rad and total time available to correct the heading error is $t_0 = 125/300 = 0.417$ s. Compute the number of available time constants to correct the heading error as

$$t_0/\tau = 0.417/0.2 = 2.1 \tag{6.66}$$

Compute the envelope (maximum value) of the missile miss distance from heading error

$$(\sigma_{HE})_{Max} = 2.2 \text{ m} \tag{6.67}$$

For this example, the miss distance of 2.2 m using seeker homing guidance is almost as large as the uncorrected heading error of 3 m. Seeker lock-on at a longer range would provide a smaller miss distance because of the longer time available for seeker homing guidance.

Figure 6.42 shows the ideal missile maneuver acceleration required against a constant maneuvering target. It is based on proportional homing guidance for

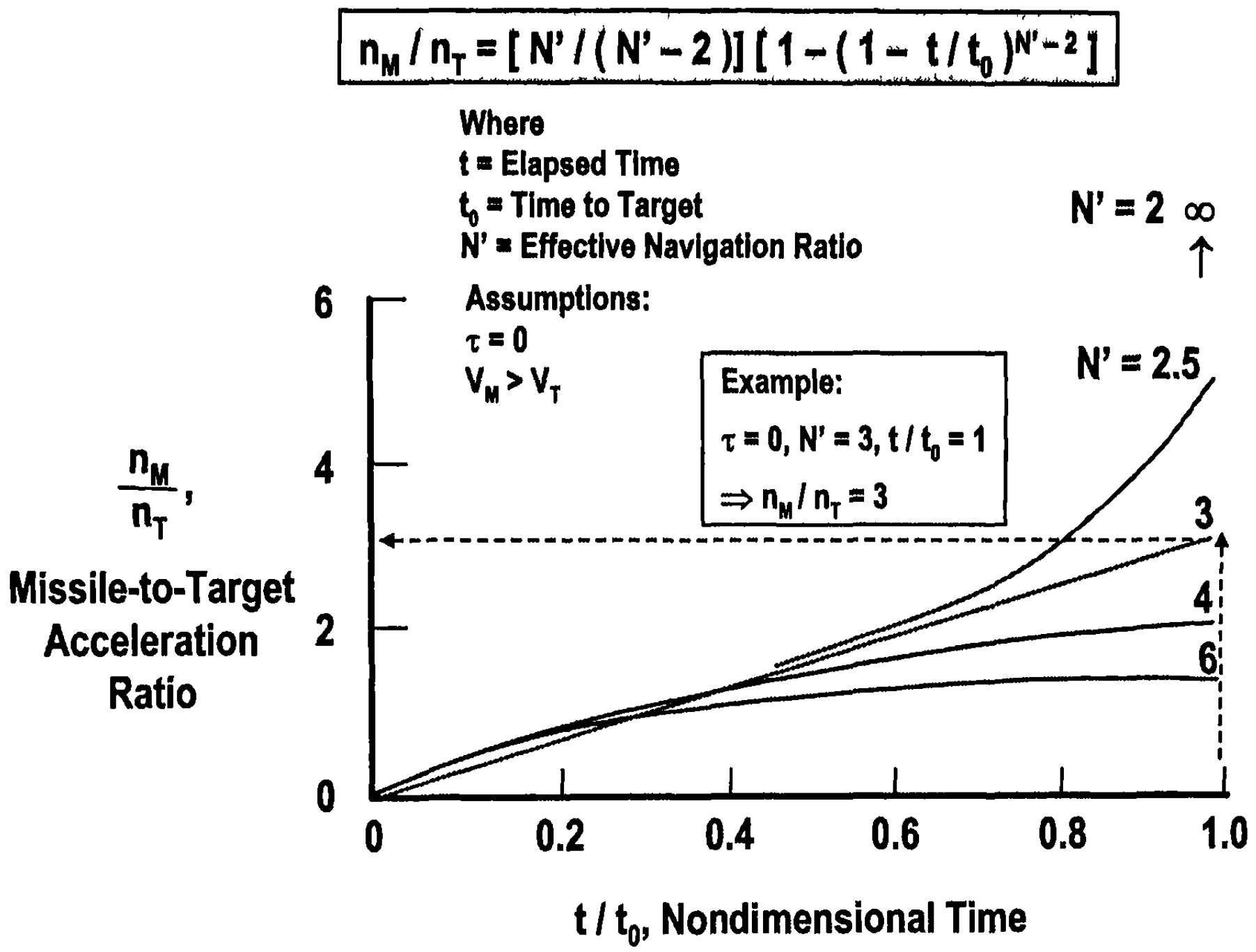

Fig. 6.42 Required maneuverability is about 3× the target maneuverability for an ideal $\tau = 0$ missile.

a missile with the assumptions of a negligibly small time constant ($\tau = 0$) and the velocity of the missile greater than the velocity of the target. The equation is

$$n_M = n_T[N'/(N'-2)][1-(1-t/t_0)^{N'-2}] \tag{6.68}$$

The required maneuverability against a maneuvering target is a function of the effective navigation ratio N', time after the target initiates maneuvering t, and the total time to the target intercept t_0. Note from the figure that the missile maneuver acceleration against a maneuvering target increases with time and has the largest value at intercept. A large value of the effective navigation ratio N' results in less required maneuverability at intercept.

As an example, assume a "perfect" system with a time constant $\tau = 0$ and a typical effective navigation ratio $N' = 3$. Then against a maneuvering target, the ratio of missile maneuverability to target maneuverability at intercept ($t = t_0$) must be equal to $n_M/n_T = 3/(3-2)[1-(1-1)^{3-2}] = 3$. As a rule of thumb, the missile maneuverability must be about three times the maneuverability of the target. To intercept a highly maneuverable 9-g fighter aircraft requires about 30-g maneuverability for the missile.

Miss distance against a maneuvering target is a function of the time to go t_0, missile time constant τ, target maneuverability n_T, and the effective navigation ratio N'. Based on the adjoint method of References 23 and 24, the equation

for miss distance is

$$\sigma_{\mathrm{MAN}} = g_c n_T \tau^2 e^{-(t_0/\tau)} \times \sum_{j=1}^{N'-1} \{(N'-3)![-(t_0/\tau)]^j/[(j-2)!(N'-j-1)!j!]\} \tag{6.69}$$

Substituting typical values for N' into the above equation gives for

$$N' = 3,\ \sigma_{\mathrm{MAN}} = g_c n_T \tau^2 e^{-(t_0/\tau)}[(t_0/\tau)^2/2] \tag{6.70}$$

$$N' = 4,\ \sigma_{\mathrm{MAN}} = g_c n_T \tau^2 e^{-(t_0/\tau)}[(t_0/\tau)^2/2 - (t_0/\tau)^3/6] \tag{6.71}$$

$$N' = 5,\ \sigma_{\mathrm{MAN}} = g_c n_T \tau^2 e^{-(t_0/\tau)}[(t_0/\tau)^2/2 - (t_0/\tau)^3/3 + (t_0/\tau)^4/24] \tag{6.72}$$

$$N' = 6,\ \sigma_{\mathrm{MAN}} = g_c n_T \tau^2 e^{-(t_0/\tau)}[(t_0/\tau)^2/2 - (t_0/\tau)^3/2 + (t_0/\tau)^4/8 - (t_0/\tau)^5/120] \tag{6.73}$$

Shown in Fig. 6.43 is the envelope of the adjoint miss distance for effective navigation ratios of $N' = 3$, 4, and 6. Note that the peak miss distance occurs if the target initiates a constant acceleration maneuver at about two time constants prior to intercept. Also note that a high value of navigation ratio gives smaller miss distance. The figure also shows that the missile has negligible miss distance if the target initiates a maneuver at six to ten time constants prior to intercept.

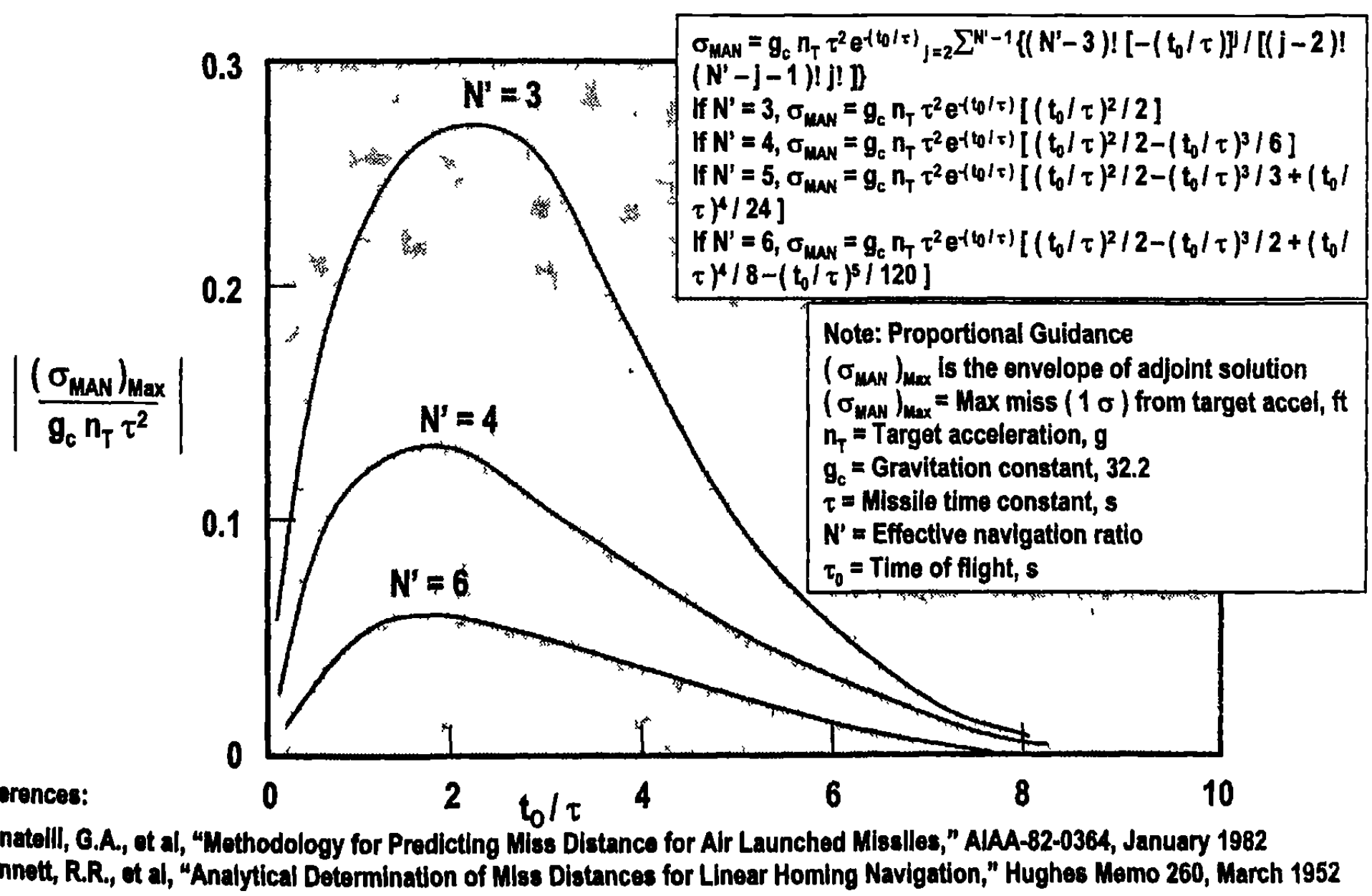

References:
•Donatelli, G.A., et al, "Methodology for Predicting Miss Distance for Air Launched Missiles," AIAA-82-0364, January 1982
•Bennett, R.R., et al, "Analytical Determination of Miss Distances for Linear Homing Navigation," Hughes Memo 260, March 1952

Fig. 6.43 Target maneuvers require 6 to 10 time constants to settle out miss distance.

The adjoint results for both the initial heading error case and the maneuvering target case showed that a high value of effective navigation ratio gives the smallest miss distance. However, a high value of effective navigation ratio increases the time constant from dome error slope, contributing to miss distance. Also, a high value of effective navigation ratio makes the missile more sensitive to seeker noise and seeker tracking error, such as glint. A missile that has a seeker with low noise and high resolution, such as a LADAR or an imaging IR seeker, may be able to operate effectively at a high value of effective navigation ratio (e.g., $N' = 6$). However, most current tactical missile seekers have relatively high noise and relatively low resolution. Most of the current tactical missiles, especially radar missiles, operate most effectively at $3 < N' < 5$.

Figure 6.44 shows the effect of intercept altitude and target maneuverability on the miss distance of the aerodynamic control rocket baseline. Assumptions are proportional guidance, effective navigation ratio $N' = 4$, Mach 2 coasting flight, head-on intercept of a target traveling at $V_T = 1000$ ft/s, target maneuver initiated at a time to go for maximum miss distance ($t_0/\tau = 2$), and negligible contributors to miss distance from guidance filters, seeker noise, and target glint. The equation for miss distance is

$$(\sigma_{\mathrm{MAN}})_{\mathrm{Max}} = 0.13 g_c n_T \tau^2 @ N' = 4, \quad t_0/\tau = 2 \tag{6.74}$$

Note from the figure that the miss distance increases with altitude. For the same velocity, a higher altitude results in lower dynamic pressure, which results in a larger time constant. The missile miss distance also increases with

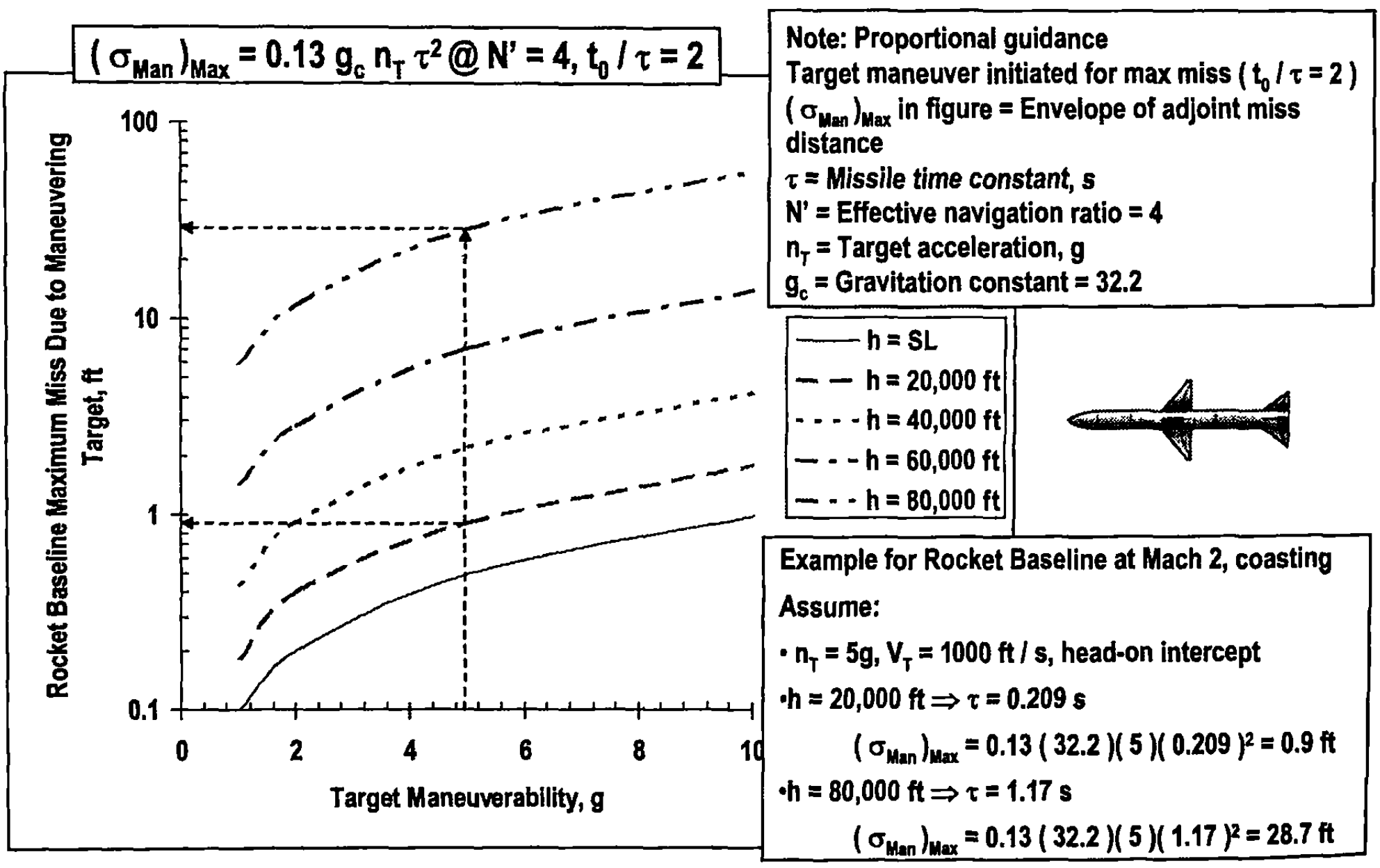

Fig. 6.44 An aero control missile has reduced miss distance at low altitude/high dynamic pressure.

target maneuverability. As an example, at an intercept altitude of $h = 20{,}000$ ft, the rocket baseline has a time constant of $\tau = 0.209$ s. If the target conducts a maneuver of $n_T = 5\ g$, the maximum miss distance is

$$(\sigma_{MAN})_{Max} = 0.13(32.2)(5)(0.209)^2 = 0.9\,\text{ft} \tag{6.75}$$

However, at an intercept altitude of 80,000 ft, for the same target maneuver the maximum miss distance is

$$(\sigma_{MAN})_{Max} = 0.13(32.2)(5)(1.17)^2 = 28.7\,\text{ft} \tag{6.76}$$

The increased miss distance is because of an increased time constant, $\tau = 1.17$ s. The time constant contributions from limited control effectiveness and dome error slope are much larger at 80,000 ft altitude ($\tau_\delta = 0.38$ s, $\tau_{Dome} = 0.72$ s). For a high-altitude intercept with hit-to-kill accuracy, unconventional flight control (e.g., reaction jet control) and a low error slope dome (e.g., window dome) would be required.

Glint noise can be a driver for miss distance, particularly for missiles that do not have good seeker resolution, are low time constant, and have high navigation ratio. Glint is also more of a problem in intercepting a large target. The reflections from multiple scattering centers on the target combine in a complex manner to give an error in the target location. In some cases the scattering centers can combine to give an apparent target location that is outside the actual target. Seeker glint, or angular noise, is the angular error from the wander of the apparent center of the target signal across the seeker field of view. Glint is generally one of the largest contributors to miss distance of a radar missile. Because radar missiles are particularly sensitive to glint, it is often used as a countermeasure. An IIR seeker, which has a high resolution, usually has negligible glint compared to a radar seeker and typically has a smaller miss distance. A mmW radar seeker (e.g., 39 GHz) will also have lower glint than a conventional radar seeker (e.g., 10 GHz) because of its smaller FOV and higher resolution.

The Ref. 24 equation for proportional guidance adjoint miss distance from glint is

$$\sigma_{Glint} = K_{N'}(W/\tau)^{1/2} \tag{6.77}$$

In the above equation $K_{N'} = 0.5(2K_{N'=4})^{N'/4}$. For a typical effective navigation ratio of $N' = 4$, $K_{N'=4} = 1.206$

The equation for the spectral density of glint noise is

$$W = (b_t)^2_{Res}/(3\pi^2 B) \tag{6.78}$$

Terms in the above equations are σ_{Glint} = miss distance from glint noise, ft; W = glint noise spectral density from uniformly distributed target scatterers across the seeker span resolution of the target, ft^2/Hz; τ = missile time constant, s; N' = effective navigation ratio; $(b_T)_{Res}$ = seeker resolution of target span at

the seeker blind range, ft; and B = noise bandwidth, Hz. The noise bandwidth typically is over a range of

$$1 < B < 5 \text{ Hz}$$

Figure 6.45 shows the rocket baseline miss distance from glint noise. A typical noise bandwidth of $B = 2$ Hz is assumed in the figure. Note that the miss distance from glint is lower for large values of time constant τ and low values of effective navigation ratio N'.

Assume as an example the rocket baseline, which has a radar seeker with relatively poor target resolution. Assume an intercept condition of Mach 2 and $h = 20{,}000$ ft altitude. It was previously shown that for this condition the time constant $\tau = 0.209$ s. Also assume 1) $N' = 4$, 2) $B = 2$ Hz, 3) $f = 10$ GHz ($\lambda = 0.03$ m), 4) $d = 8$ in $= 0.203$ ft, 5) $t_{\text{blind}} = \tau = 0.209$ s, 6) $b_T = 40$ ft (aircraft target with 40 ft wing span), and 7) $V_T = 1000$ ft/s. Calculate

$$V_c = V_M + V_T = 2074 + 1000 = 3074 \text{ ft/s} \tag{6.79}$$

$$R_{\text{blind}} = V_c t_{\text{blind,}} = 3074(0.209) = 642 \text{ ft} \tag{6.80}$$

For a radar seeker the resolution is limited by the seeker beam width. Calculating the seeker beam width

$$\theta_{3\text{dB}} = 1.02\,\lambda/\text{d} = 1.02(0.03)/0.203 = 0.1503 \text{ rad} = 8.6 \text{ deg} \tag{6.81}$$

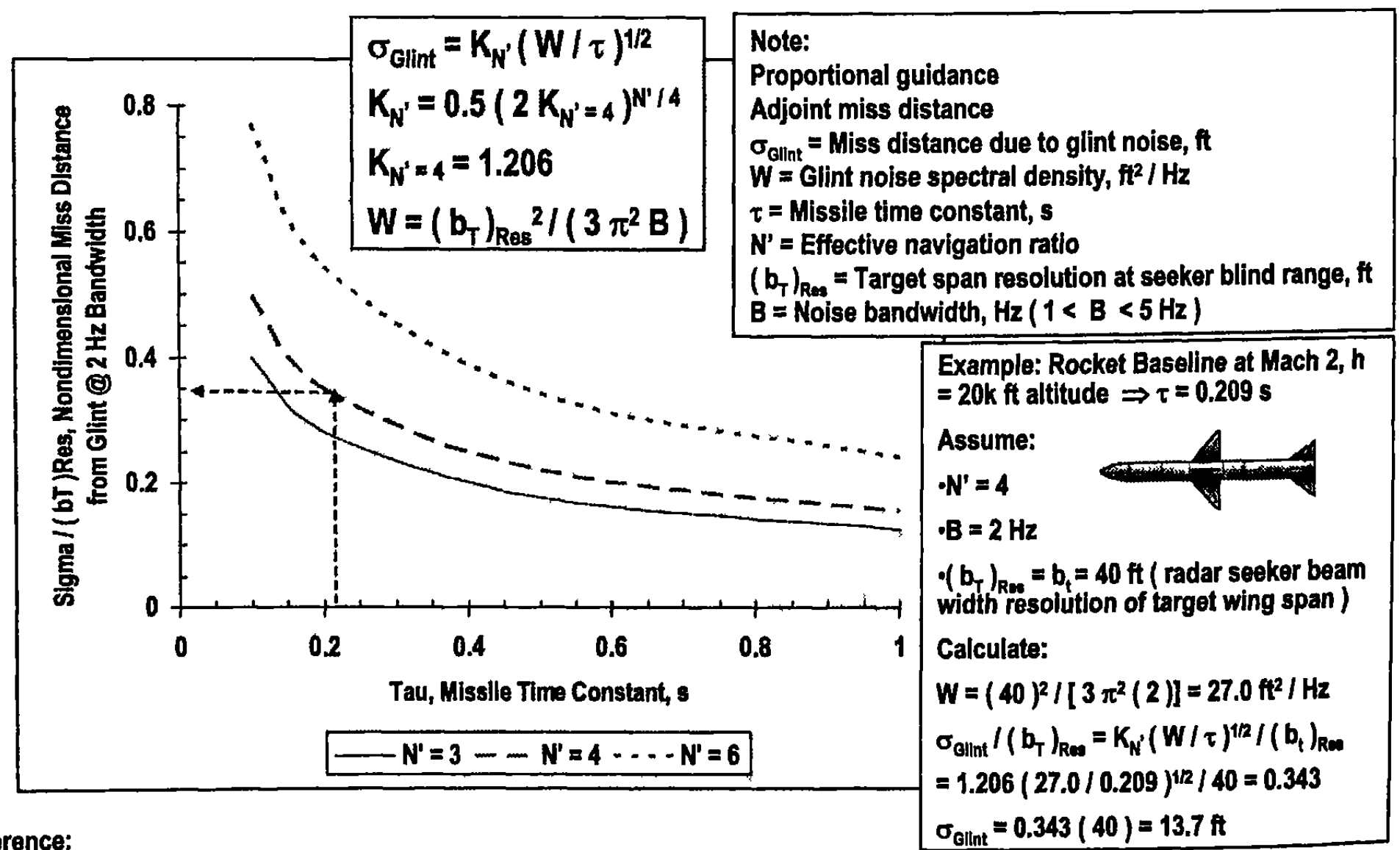

Reference:
Bennett, R.R., et al, "Analytical Determination of Miss Distances for Linear Homing Navigation," Hughes Memo 260, March 1952

Fig. 6.45 Glint miss distance is driven by seeker resolution, missile time constant, and navigation ratio.

The seeker resolution width is then

$$R_{\text{blind}} \tan \theta_{3\text{dB}} = 642(0.1512) = 97\,\text{ft} \tag{6.82}$$

Comparing the seeker resolution width to the target span gives

$$(b_{\text{Res}})_{\min} = \text{Min}[R_{\text{blind}} \tan \theta_{3\text{dB}},\ \text{b}_\text{T}] = 40\,\text{ft} \tag{6.83}$$

Substituting, the glint noise spectral density is

$$W = (40)^2/[3\pi^2(2)] = 27.0\,\text{ft}^2/\text{Hz} \tag{6.84}$$

Substituting into the above equation, the nondimensional miss distance from glint is

$$\sigma_{\text{Glint}}/b_\text{t} = 1.206(27.0/0.209)^{1/2}/40 = 0.343 \tag{6.85}$$

Finally, substituting the target span into the above equation gives

$$\sigma_{\text{Glint}} = 0.343(40) = 13.7\,\text{ft} \tag{6.86}$$

Minimizing missile miss distance for a missile that is susceptible to glint requires a tradeoff of the optimum time constant and navigation ratio. Figure 6.46 shows the root mean square (RMS) miss distance from target

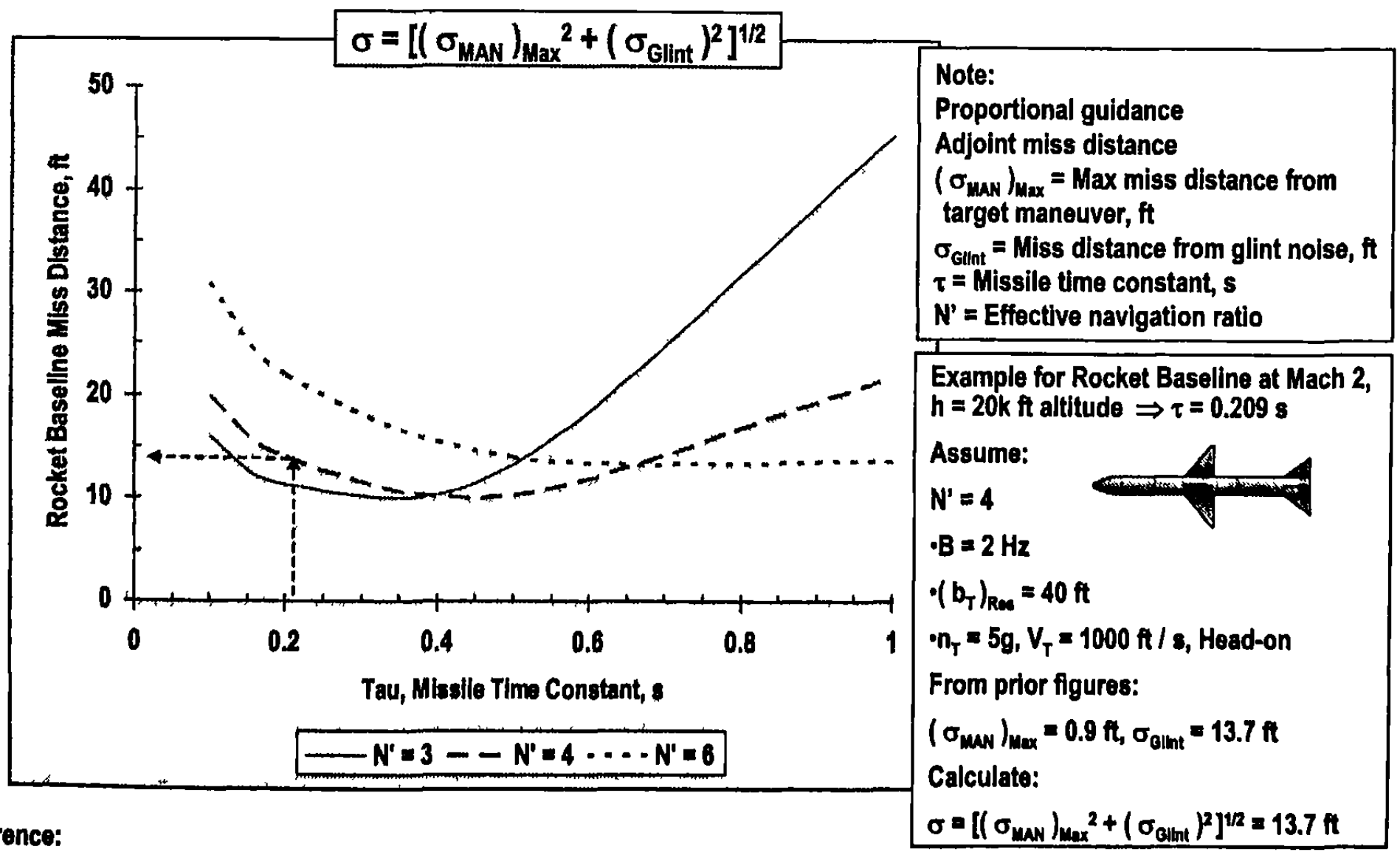

Reference:
Bennett, R.R., et al, "Analytical Determination of Miss Distances for Linear Homing Navigation," Hughes Memo 260, March 1952

Fig. 6.46 Minimizing miss distance with glint requires optimum time constant and navigation ratio.

maneuverability $(\sigma_{MAN})_{Max}$ and seeker glint noise σ_{Glint}, given by the equation

$$\sigma = [(\sigma_{MAN})^2_{Max} + (\sigma_{Glint})^2]^{1/2} \tag{6.87}$$

Note that there is an optimum time constant τ and an optimum effective navigation ratio N' for minimum miss distance. The values of τ and N' for minimum miss distance from target maneuvers are at cross purposes with the values for minimum miss distance from glint. For this example, glint is the dominant source of miss. An approach to reduce glint miss distance is a high-resolution seeker, such as an IIR seeker.

As an example, assume proportional guidance and an adjoint miss distance for the rocket baseline at Mach 2, $h = 20{,}000$ ft altitude. For this condition the time constant $\tau = 0.209$ s. Based on the previous examples assume a maneuvering target with glint noise. The previous parameters are $N' = 4$, $B = 2$ Hz, $(b_T)_{Res} = 40$ ft, $n_T = 5$ g, $V_T = 1000$ ft/s, and a head-on intercept. From the prior examples,

$$(\sigma_{MAN})_{Max} = 0.9\,\text{ft} \tag{6.88}$$

$$\sigma_{Glint} = 13.7\,\text{ft} \tag{6.89}$$

Calculate

$$\sigma = (0.9^2 + 13.7^2)^{1/2} = 13.7\,\text{ft} \tag{6.90}$$

6.5 Carriage and Launch Observables

The fourth measure of merit to be discussed is carriage and launch observables. Missile carriage and launch observables impact the survivability of the launch platform. Two areas of concern are the RCS for carriage on the launch platform and the missile plume visual signature. Missile carriage alternatives based on the consideration of observables are 1) internal carriage, which has the lowest RCS in carriage; 2) conformal carriage, which provides reduced RCS in carriage; and 3) conventional external pylon or rail carriage, which has high RCS in carriage. The missile plume alternatives based on the consideration of visual observables are 1) minimum smoke motor, which has the lowest visual observables during launch (H_2O contrail); 2) reduced smoke motor, which has reduced observables during launch (e.g., HCl contrail); and 3) high smoke motor, which has high observables during launch (e.g., Al_2O_3 smoke).

As stated previously, the alternative approaches for missile carriage on aircraft include conventional external carriage, conformal carriage, and internal carriage. Conventional external carriage has disadvantages of high RCS, high carriage drag, and potentially adverse aeroelastic, stability, and control interactions with the aircraft platform. An advantage of external carriage is high firepower load-out because of the large number of possible store attachment locations on the aircraft body and wings. Conformal carriage has an advantage of reduced RCS and lower drag compared to conventional carriage. A disadvantage is a

need for specialized store and aircraft attachments for each type of aircraft. Internal carriage has the lowest carriage RCS and the lowest drag. A disadvantage of internal carriage is a span constraint, which results in a reduction in firepower by factors of up to two to four.

Figure 6.47 shows examples of internal carriage and load-outs for low observable fighters, bombers, and helicopters. In the upper left is shown the F-22 internal center bay. The F-22 center bay typically has a partition for air-to-air weapons (e.g., AMRAAM) and a partition for air-to-surface weapons (e.g., JDAM). LAU-142/A pneudraulic (pneumatic plus hydraulic) ejection launchers are provided for the AMRAAM. The LAU-142 has a 9-in stroke that ejects an AMRAAM from the bay at a velocity of 25 ft/s. The peak ejection acceleration is 40 *g*. Advantages of pneudraulic ejection compared to conventional pyrotechnic cartridge ejection include less logistics, faster turnaround for weapon loading, and a more nearly constant ejection force that allows a shorter ejection stroke. A conventional BRU-46/A bomb rack is provided for the GBU-32 JDAM (1000-lb class weapon). Examples of typical mixed weapon load-outs in the F-22 center bay are 1) two AIM-120B AMRAAMs (without compressed carriage) plus one 1000-lb JDAM or 2) three AIM-120C compressed carriage AMRAAMs plus one 1000-lb JDAM. The F-22 center bay can also be set up for air-to-air weapons only, such as four AIM-120B conventional AMRAAMs (without compressed carriage) or six AIM-120C compressed carriage AMRAAMs. The F-117 internal weapons bay is shown in the top center of the figure. The F-117 weapons bay is similar to that of the F-22, except that it has about twice the payload weight capability. A typical load-out for the F-117 is two Paveway guided bombs

Fig. 6.47 Examples of weapon bay internal carriage and load-out. Figure also in color section. Video is in the CD included with this textbook.

(2000-lb class). Shown in the figure foreground is the GBU-27 laser-guided bomb. Its warhead is based on the BLU-109 hardened structures penetrator bomb. In the background is the GBU-10 laser-guided bomb. Its warhead is either the general-purpose Mk-84 bomb or the BLU-109 penetrator bomb. The B-1 bomber weapons bay is shown in the upper right of the figure. The B-1 has three bays. Each bay has a rotary launcher for ejection of missiles and bombs. An ejector rack assembly is provided for each weapon that is attached to the rotary launcher. The ejector rack assembly has a 30-in spacing of the ejectors. Shown in the figure is a standard load-out of eight AGM-69 SRAM missiles per bay. The lower left section is a video of loading an AMRAAM missile into the center bay of the F-22 aircraft. In the lower center of the figure is a photograph of an F-22 side bay. The F-22 has two side carriage bays. Each bay is capable of carrying a single Sidewinder missile on a LAU-141/A trapeze rail launcher. A trapeze launcher is required for lock-on-before-launch missiles. During the launch sequence the trapeze launcher extends the missile away from the aircraft, the missile seeker acquires the target, and the missile is launched. Following missile launch, the trapeze launcher retracts into the weapons bay and the bay doors are closed. The LAU-141/A launcher has a deflector surface to keep the motor plume from entering the weapon bay. Finally, the lower right section of the figure is a photograph of the RAH-66 Comanche helicopter. The Comanche has two side bays with rail launchers. Each bay has a typical mixed mission (combined air-to-surface/air-to-air) load-out of one Hellfire missile plus two Stinger missiles plus four Hydra 70 rockets. For an air-to-surface-only mission, each bay can carry three Hellfire missiles, giving the Comanche a total bay load-out of six Hellfire missiles. As shown in the figure, the Comanche can also carry an additional eight Hellfire missiles externally, at the expense of increased RCS.

Illustrated in Fig. 6.48 are the plume observables of high-smoke, reduced-smoke, and minimum-smoke propellants. The relatively old Sparrow missile rocket motor is a representative high-smoke motor. The high-smoke plume is shown in the upper left corner of the figure. The Sparrow has high-smoke Al_2O_3 particles from aluminum fuel. Shown in the upper center of the figure is an example of a reduced-smoke rocket motor. The AMRAAM is a more recent missile with a reduced-smoke motor. It still has a contrail of HCl from the ammonium perchlorate oxidizer. The HCl contrail occurs if the atmospheric temperature is less than $-10°$ F, corresponding to altitudes greater than about 20,000 ft. Finally, the far upper right photograph is an example of a minimum-smoke rocket motor. The Javelin is a recent missile with a minimum-smoke motor. It has almost no smoke from either the launch motor or the flight motor, enhancing the survivability of the gunner. Minimum-smoke propellants can have an H_2O (ice) contrail if the atmospheric temperature is less than $-35°$ F, corresponding to altitudes greater than about 27,000 ft.

The bottom left section of the figure shows typical contrails for high-smoke, reduced-smoke, and minimum-smoke motors. The high-smoke motor solid particles are visible immediately behind the nozzle under all atmospheric conditions. The contrail from a reduced-smoke motor occurs farther downstream of the nozzle. For an ammonium perchlorate oxidizer, it is produced when the HCl gas from the reduced-smoke motor is absorbed by water and then freezes at

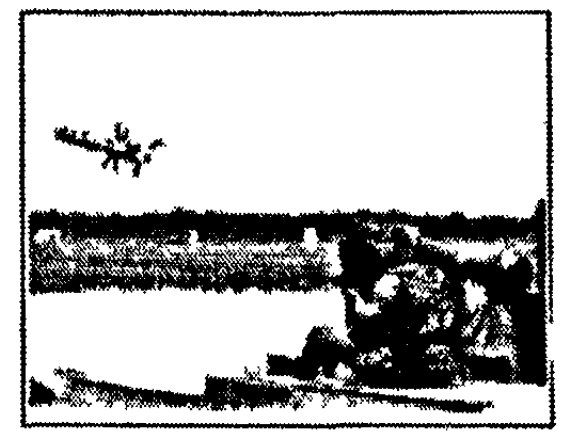

High Smoke Example: AIM-7

Particles (e.g., metal fuel) at all atmosphere temperature.

Reduced Smoke Example: AIM-120

Contrail (HCl from AP oxidizer) at < -10° F atmospheric temperature.

Minimum Smoke Example: Javelin

Contrail (H_2O) at < -35° F atmospheric temperature.

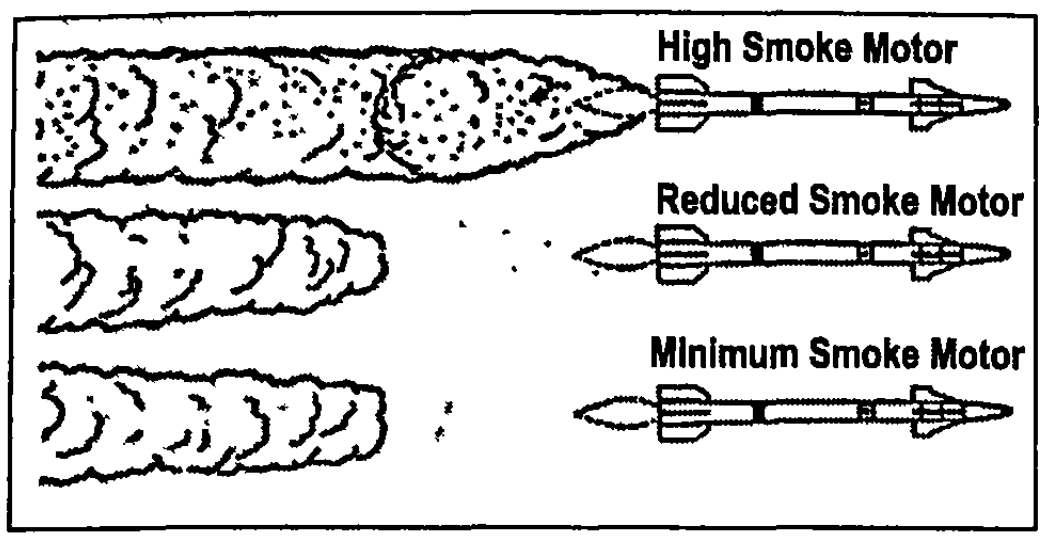

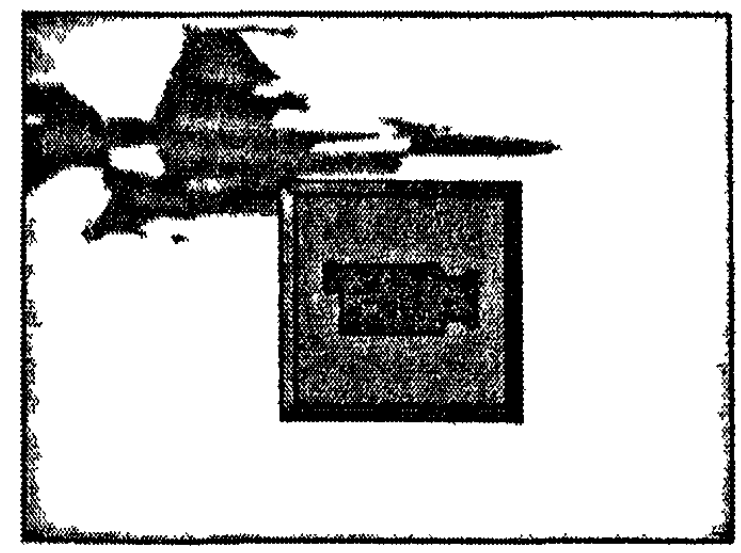

Fig. 6.48 Minimum smoke propellant has low observables. Figure also in color section. Video is in the CD included with this textbook.

low atmospheric temperature. Finally, water vapor from a minimum-smoke motor can also freeze farther downstream of the nozzle to produce a contrail at low atmospheric temperature. The bottom right section of the figure contains a video of missile systems with high-smoke (Sparrow), reduced-smoke (AMRAAM, Hellfire I), and minimum-smoke (Javelin, Hellfire II) propellants.

6.6 Other Survivability Considerations

The fifth measure of merit to be discussed is other survivability considerations. Missile RCS, standoff distance from threat defenses, mission planning for threat avoidance, and insensitive munitions are design considerations.

Shown in Fig. 6.49 is an example of the detection range by a ground-based radar threat. Two approaches are illustrated for survivability, RCS and standoff range. The target has three different values of RCS and is flying at altitudes from 22,000 to 90,000 ft. Results are based on the radar range equation discussed previously, with an assumed S/N for detection of $(S/N)_{Detect} = 1$. Another assumption is that there is an unobstructed line of sight to the target. The equation is

$$P_t = (4\pi)^3 P_r R^4 / (G_t G_r \sigma \lambda^2) \tag{6.91}$$

The assumed values of the ground radar parameters for transmitted power P_t, received power P_r, transmitter gain G_t, receiver gain G_r, and wavelength λ are given in the figure. Note the dramatic increase in the required power of the

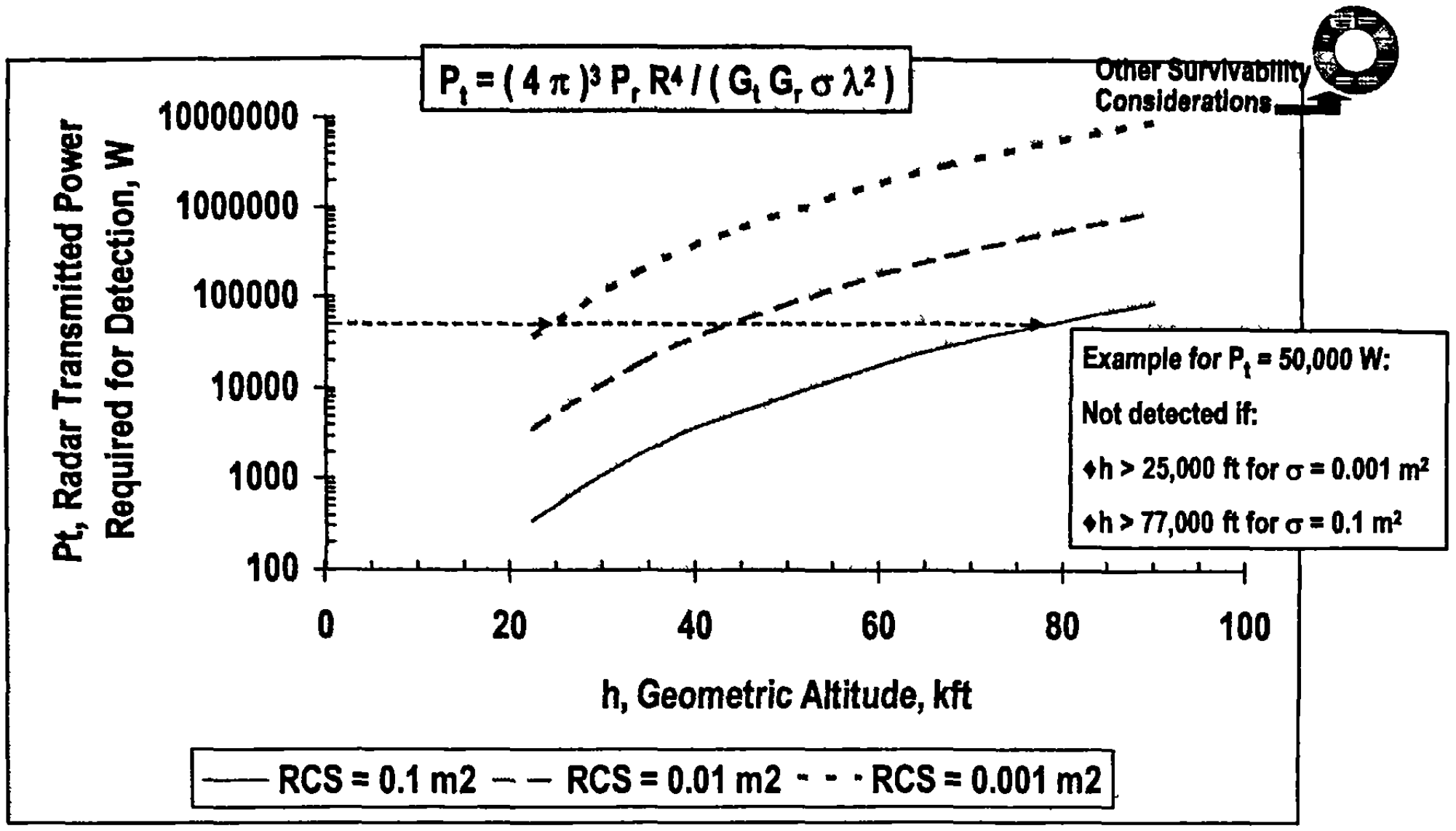

Note:
- Range Slant Angle = 20 deg, G_t = Transmitter Gain = 40 dB, G_r = Receiver Gain = 40 dB, λ = Wavelength = 0.03 m, P_r = Receiver Sensitivity = 10^{-14} W, σ = radar cross section (RCS)
- Based on Radar Range Equation with $(S/N)_{Detect} = 1$ and Unobstructed Line-of-Sight

Fig. 6.49 High-altitude flight and low RCS enhance survivability.

ground radar to detect the missile if the missile flies at high altitude, which results in a large value of slant range R. Reducing the RCS also results in a large increase in the power required for the ground radar. A tradeoff is the missile required flight altitude versus RCS to avoid detection. As an example, assume that a typical threat fire control radar has a transmitted power of 50,000 W and is looking up at 20-deg elevation angle. A missile with a low RCS ($\sigma = 0.001$ m^2) is not detected if it flies above 25,000 ft altitude. Similarly a missile with a much larger RCS ($\sigma = 0.1$ m^2) is not detected if it flies above 77,000 ft altitude.

Another consideration for survivability is mission planning. Mission planning to minimize the exposure to known threats has high payoff in survivability. Exposure times less than about 15 s provide survivability because the human reaction time of the typical threat is about 15 s.

Shown in the left portion of Fig. 6.50 is the nondimensional exposure time to a SAM threat. It is based on the equation

$$t_{\text{exp}} = 2(R_{\text{Max}}/V)\cos[\sin^{-1}(y_{\text{offset}}/R_{\text{Max}})] - t_{\text{react}} \tag{6.92}$$

The parameters are exposure time t_{exp}, maximum detection range by the SAM threat R_{max}, flyby velocity V, flyby offset y_{offset}, and the reaction time of the SAM site t_{react}. The SAM site reaction time is the time from initial detection to launch. An assumption is that the flyby is with constant altitude and heading. It is also assumed that the SAM site has an unobstructed line of sight.

Shown in the upper right portion of the figure is a sketch illustrating the flyby of the threat SAM site. The circle is the envelope of detection by the SAM site.

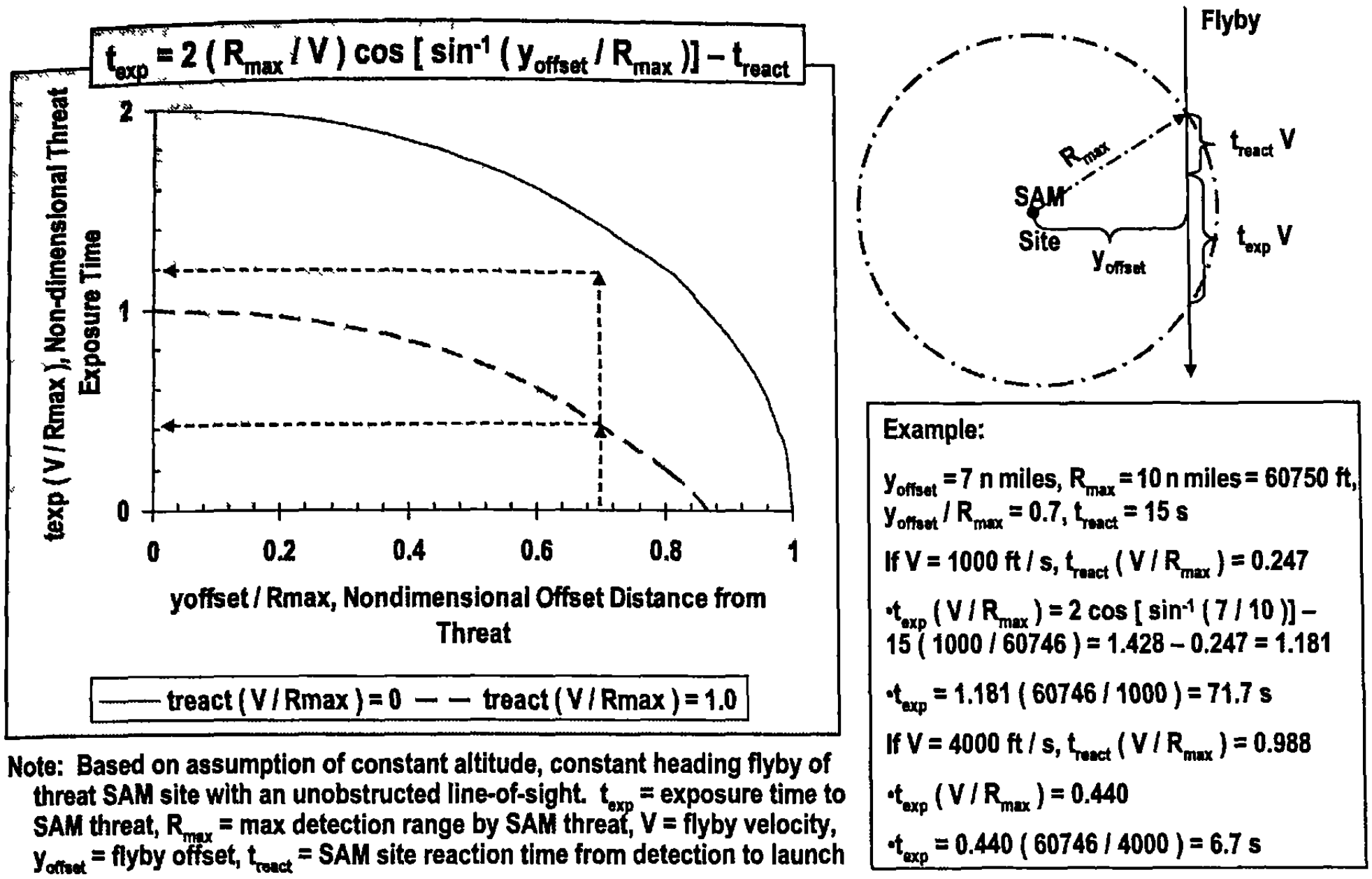

Note: Based on assumption of constant altitude, constant heading flyby of threat SAM site with an unobstructed line-of-sight. t_{exp} = exposure time to SAM threat, R_{max} = max detection range by SAM threat, V = flyby velocity, y_{offset} = flyby offset, t_{react} = SAM site reaction time from detection to launch

Fig. 6.50 Mission planning and high speed enhance survivability.

The maximum time available for a SAM to engage the flyby would be a direct overflight of a SAM site. A lateral offset flyby enhances survivability by reducing the exposure time. This is illustrated in the flyby trajectory on the upper right portion of the figure.

The detection range by the threat is reduced by low observables, such as low RCS. For an overflight of a "perfect" SAM site that has no delay in reacting from detection to launch, the exposure time is given by the equation $t_{\text{exp}} = 2(R_{\text{Max}}/V)$. As an example, if $R_{\text{Max}} = 10$ nm and $V = 1000$ ft/s, then $t_{\text{exp}} = 2(60746/1000) = 121$ s. The SAM site would have about 60 s for a shot at the incoming trajectory. It would also have about 60 s for a shot at the outgoing trajectory. More than one shot would probably be possible in both the closing and retreating trajectories. Because the exposure time is so large and multiple shots are possible, survivability is a concern for an overflight trajectory. An approach to enhance survivability for an overflight trajectory would be to reduce the observables such that the reduced detection range would result in a low exposure time. As an example, an exposure time of 15 s would require a reduction in the detection range by the SAM threat to $15/121 = 0.124$ of the nominal range. For a radar threat, the 88% reduction in detection range to minimize the exposure time to 15 s would require an RCS that is −36 dB compared to the nominal RCS.

In the bottom right portion of the figure is an example calculation based on a lateral offset $y_{\text{offset}} = 7$ nm, maximum detection range by the SAM site $R_{\text{Max}} = 10$ n miles, and SAM site reaction time from detection to launch $t_{\text{react}} = 15$ s. For a low speed flyby representative of a subsonic cruise missile with $V = 1000$ ft/s, the exposure time is large, $t_{\text{exp}} = 71.7$ s. For a very high

speed flyby, such as a ramjet missile with $V = 4000$ ft/s, the exposure time is only 6.7 s, a reduction of 91%.

Another approach to survivability is to fly at low altitude and exploit terrain masking, clutter, and transmission line-of-sight limitations. Figure 6.51 shows the payoff of low-altitude flight in reducing the line-of-sight range of a surface-to-air threat. Disadvantages of low-altitude flight may include increased fuel consumption, higher probability of terrain clobber, and exposure to an increased number of IR threats.

The equation for the required altitude to provide masking from a surface-to-air threat is

$$h_{\text{mask}} = h_{\text{obstacle}}(R_{\text{los}}/R_{\text{obstacle}}) + (R_{\text{los}}/7113)^2 \tag{6.93}$$

The above equation is based on the assumptions that the obstacle height is larger than the threat height above the terrain and that the earth has spherical curvature. Parameters are h_{mask} = altitude that allows the obstacle and the earth curvature to mask exposure to surface threat LOS, ft; h_{obstacle} = height of the obstacle above the terrain, ft; R_{los} = line-of-sight range to the surface threat, ft; and R_{obstacle} = range from the surface threat to the obstacle, ft. Terrain obstacles have the following typical heights above the terrain 1) height of low hill or tall tree ≈ 100 ft; 2) height of moderate hill ≈ 200 ft; 3) height of high hill ≈ 500 ft; and 4) height of mountain ≈ 1000 ft.

As an example, assume an obstacle height of h_{obstacle} = 200 ft, range from the threat to the obstacle of R_{obstacle} = 5.0 nm = 30,395 ft, and line-of-sight range

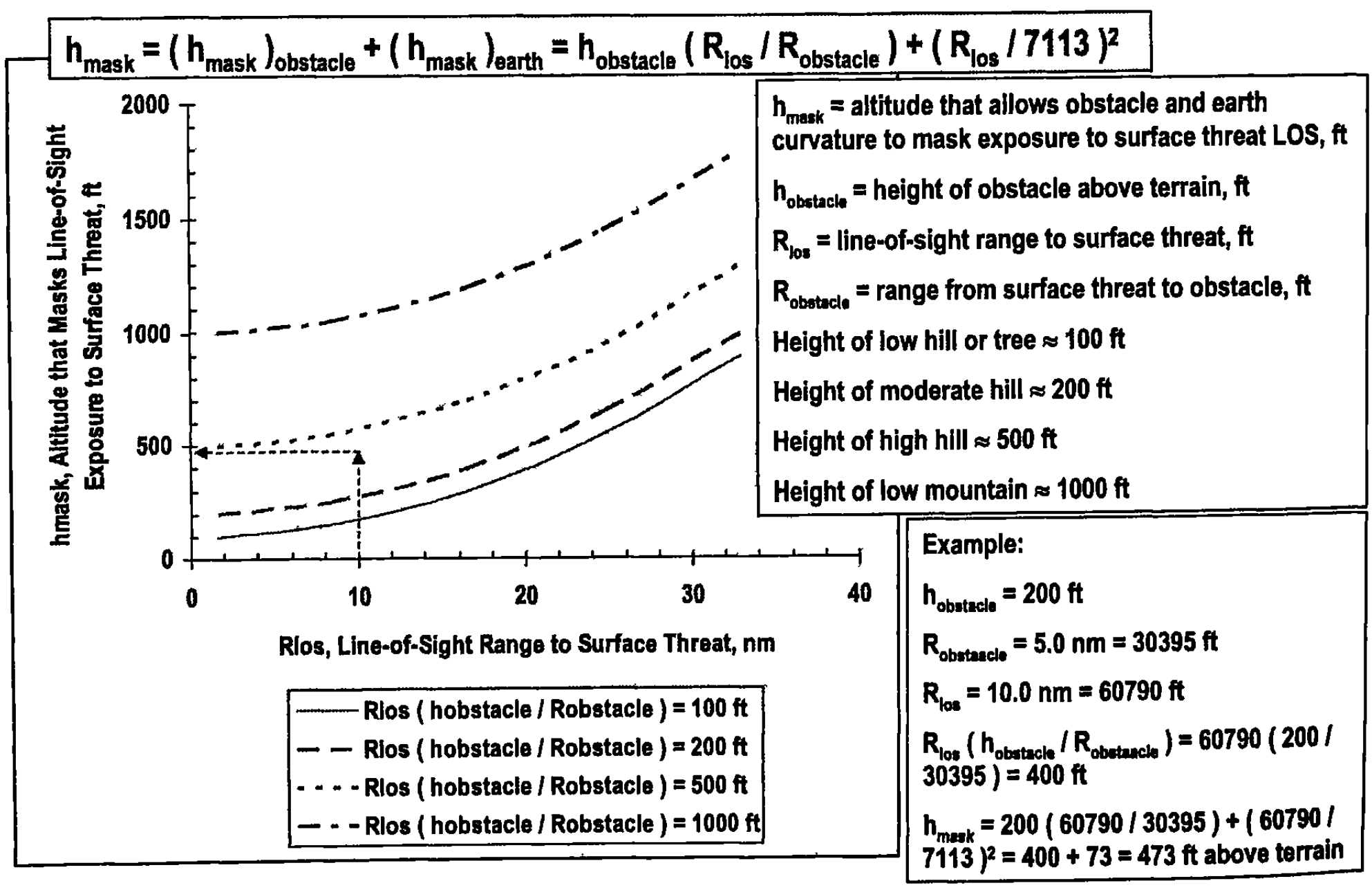

Fig. 6.51 Low-altitude flight and terrain obstacles provide masking from threat.

for exposure to the threat of $R_{los} = 10.0$ nm = 60,790 ft. The parameter

$$R_{los}(h_{obstacle}/R_{obstacle}) = 60790(200/30395) = 400\,\text{ft} \tag{6.94}$$

Substituting into the equation for h_{mask} gives

$$h_{mask} = 200(60{,}790/30{,}395) + (60{,}790/7113)^2 = 400 + 73 = 473\,\text{ft} \tag{6.95}$$

Insensitive munitions have payoff in improving launch platform survivability. The critical energetic subsystems are the rocket motor, engine fuel, and the warhead. Other energetic subsystems include fuses, batteries, and gas bottles. An example of a missile that has received high emphasis in the area of insensitive munitions is JASSM.

In terms of hazard severity, detonation (Type 1) is considered the most severe because of the high power output. A detonation has a rise time of about 2 μs. The power output during a detonation is more than six orders of magnitude greater than the power output during normal rocket motor combustion. The decreased severity ranking for other hazard concerns are partial detonation (Type 2, rise time about 0.1 ms), explosion (Type 3, rise time about 1 ms), deflagration or burning (Type 4, rise time about 0.1 s), and burning (Type 5, rise time greater than 1 s).

In the United States the design and test considerations for insensitive munitions are based on military standard (MIL-STD)-2105C, Hazard Assessment Tests for Non-Nuclear Munitions. MIL-STD-2105C includes considerations of hardening against threat weapons, fast and slow cookoff fires, dropping the weapon, extremes in environmental temperature, missile vibration, and operation off an aircraft carrier. Hardening against threat weapons includes considerations of fragment impact, bullet impact, and blast. Hardening also requires avoiding sympathetic detonation of adjacent weapons. Cookoff from a fire requires consideration of the type of fire (slow cookoff, fast cookoff) and the warhead or rocket motor reaction to the fire (e.g., burning, detonation). Drop shock sensitivity consideration is a particular concern for ground maintenance personnel dropping the missile during handling. The environmental temperature extremes range from very low temperatures that could damage the rocket motor (e.g., crack the propellant grain) to very high temperatures that could cause detonation of the warhead. Missile vibration consideration includes the dynamic acceleration imparted during store carriage on the launch platform. Aircraft carrier operation includes the shock of aircraft landing sink rates as high as 18 ft/s.

6.7 Reliability

The sixth measure of merit to be discussed is reliability. Because missiles usually do not have redundancy and each subsystem must function reliably for success, the missile system reliability is approximately a product of the individual subsystem reliabilities. Figure 6.52 shows representative system and subsystem reliabilities for a tactical missile. For an operational missile, the system reliability is usually between 90 and 99%, depending upon the parts count and the type of

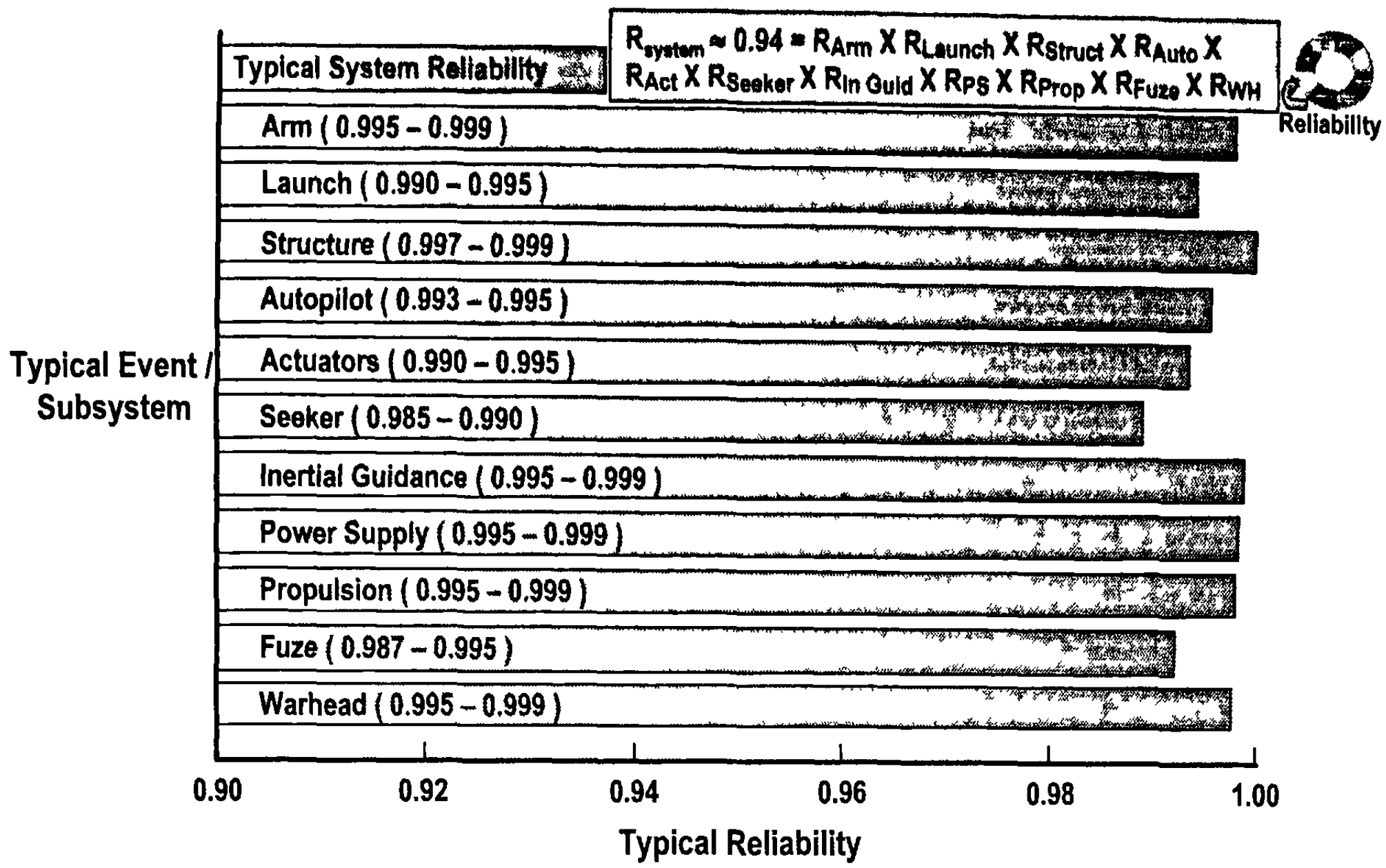

Fig. 6.52 High system reliability is provided by high subsystem reliability and low parts count.

subsystems/parts. Moving parts tend to be less reliable than nonmoving parts. For a typical missile an individual subsystem failure rate should be about 1/10 the system design failure rate to provide a balance of emphasis in the individual subsystem reliabilities. As an example, a typical missile with 90% system reliability and having 10 subsystems would require about 99% reliability ($0.9 = 0.99^{10}$) for each subsystem. The requirement for component reliability is even higher. A typical missile may have about 10 components in each subsystem, giving a total of 100 components. A system reliability of 90% would require very high component reliability, about 99.9% reliability ($0.9 = 0.999^{100}$) for each component. Design considerations for high reliability are to minimize the number of subsystems, minimize components/parts count, minimize moving parts, and minimize the complexity of the subsystems. In recent years the electronic subsystems and components have become much more reliable, as the manufacturing processes have reduced the effective parts counts. A computer chip may be the equivalent of millions of transistors, but the manufacturing process provides high reliability. Note that in recent years software reliability has replaced mechanical reliability as a major contributor to failure.

The example of the figure has an overall reliability of 0.94. If the allocation of subsystem reliabilities were equally allocated, then each of the 11 subsystems would have a reliability of 0.994 (i.e., $0.994^{11} = 0.94$). However, the cost of achieving a reliability of 0.994 for some subsystems (e.g., seeker) would be too high. A less expensive subsystem (e.g., structure) would be allocated a reliability requirement greater than 0.994 to compensate for the lower reliability of the seeker.

6.7 Cost

The seventh measure of merit to be discussed is cost. The relative importance of subsystems to missile cost is shown in Fig. 6.53. The seeker is usually the highest cost subsystem for a tactical missile, usually exceeding 25% of the missile production cost. The guidance and control system is also high cost, usually exceeding 10% of the missile production cost. A difference in the cost of airbreathing missiles compared to rockets is the cost of the propulsion system and structure. The propulsion system and structure parts count/cost of airbreathing missiles are usually higher than that of rockets. The propulsion system of an airbreathing missile is very high, exceeding 25% of the missile production cost, while the propulsion system of a rocket-powered missile is usually between 10 and 25%. The relatively complex structure cost of an airbreathing missile is usually between 5 and 10% of the missile production cost, while the structure cost of a rocket-powered missile is usually less than 5%. The cost of the dome varies widely, depending upon the accuracy and speed requirement. For a low-speed missile with a chemical energy warhead, the cost of the dome is about 5 to 10% of the missile cost. However, for a hypersonic hit-to-kill missile, the cost of the dome usually exceeds 10% of the missile cost. The cost of the warhead and fusing also vary widely. A blast fragmentation or shaped charge warhead with contact fusing is usually inexpensive. At the other extreme, a multipurpose warhead with smart fusing can be expensive. System assembly and system test are about 10% of the missile production cost for a moderately complex missile. For a complex missile, system assembly and system test may

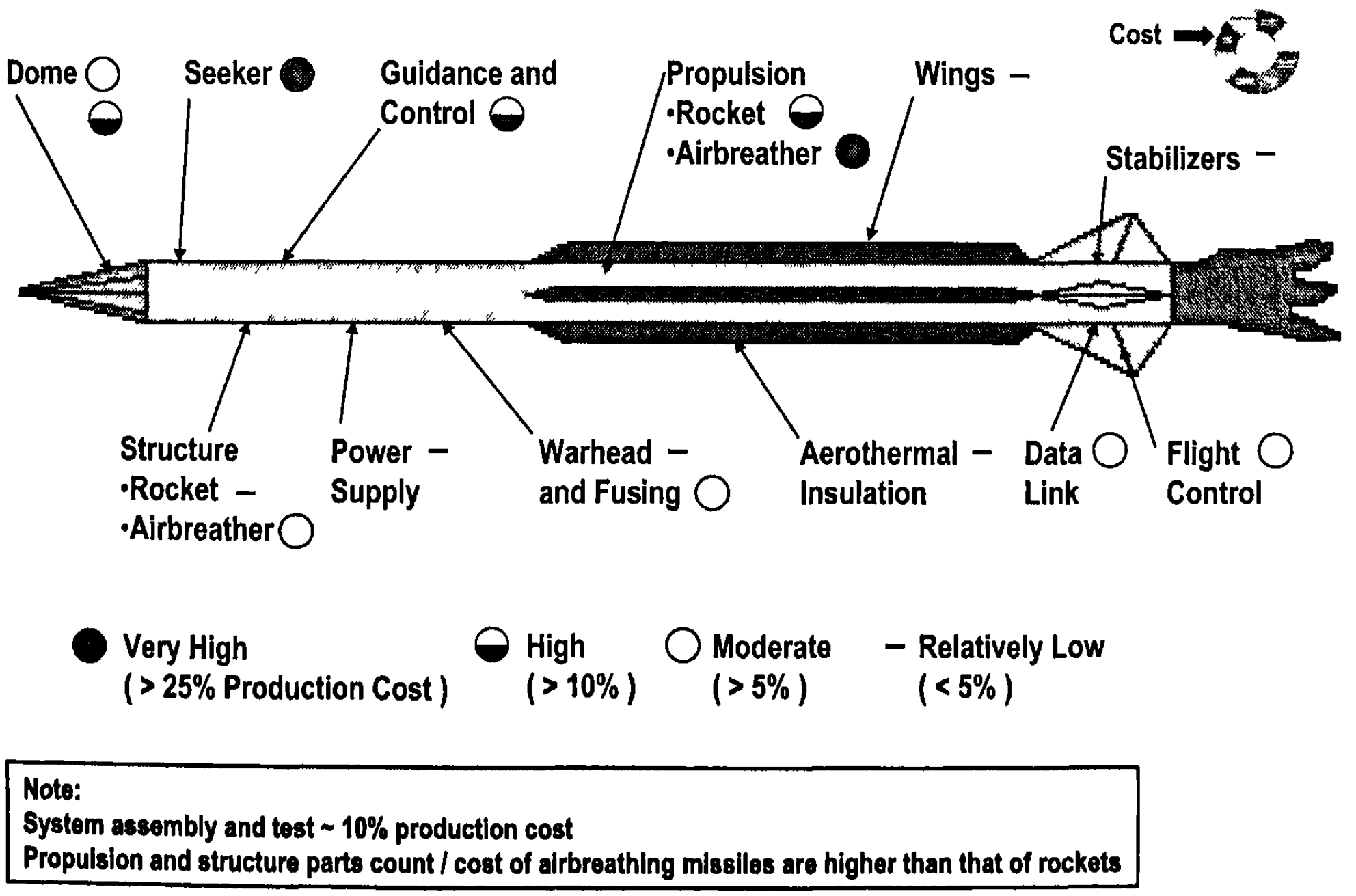

Fig. 6.53 Sensors, electronics, and propulsion drive missile production cost.

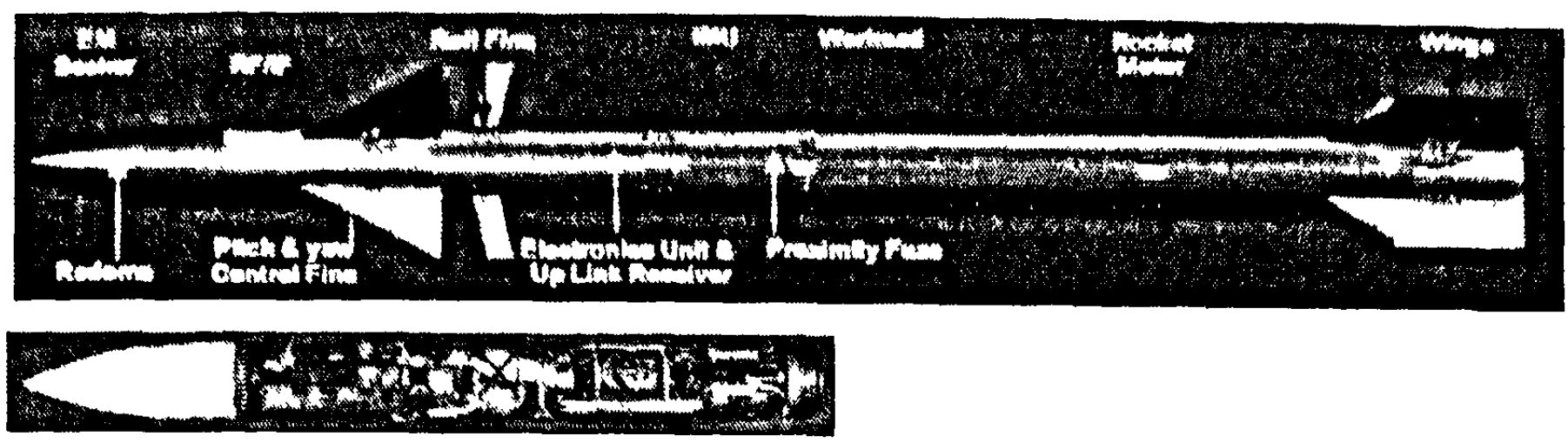

Source: http://www.israeli-weapons.com/weapons/missile_systems/air_missiles/derby/Derby.html

Fig. 6.54 Sensors and electronics occupy a large portion of a high-performance/ high-cost missile. Figure also in color section.

be more than 15% of the missile production cost. For a simple missile, system assembly and test may be as low as 5% of the missile production cost.

Figure 6.54 illustrates the emphasis on sensors and electronics for high-performance, high-cost missiles. Note that about 40% of the volume of the Derby/R-Darter missile is devoted to sensors and electronics. In addition to the radome, radar seeker, inertial navigation system, proximity fuse, autopilot, and four flight actuators for pitch/yaw control, the Derby/R-Darter also has two additional actuators for roll control and a data link.

The total life cycle cost of a missile system includes the cost of SDD, cost of production, and the cost of logistics. SDD cost may be predicted fairly accurately, based on data from previous missile programs. There is always some risk after completing the SDD program, which can impact the production cost and require follow-on development to fix problems. Production cost is often difficult to predict accurately, particularly for complex missiles with new types of subsystems and technology. Also, there may be pressure to provide optimistic predictions of production cost to sell the missile program. Finally, although logistics cost is a major component of the missile life cycle cost, historically there has been little incentive for the contractor to design and develop a missile with reduced logistics cost, especially if the reduced logistics cost results in increased development or production cost. In recent years logistic cost has received more emphasis because of environmental considerations, including disposal. The following figures will provide more information on design considerations for SDD, production, and logistics cost.

The culture of the strategic missile community, the unmanned air vehicle (UAV) community, and the aircraft community are different from that of the tactical missile community. For example, the tactical missile community usually puts more emphasis on reducing cost with less emphasis on performance, reliability, and the organization structure. In the other aerospace vehicle communities the emphasis on performance, reliability, and a large organization structure is usually greater than the emphasis on reducing cost. A tactical missile may have 90% of the performance and reliability of a comparable strategic missile at $\frac{1}{2}$ the cost and $\frac{2}{3}$ of the development time. Another example of culture is the customer's

expectations on the application of military standards. If the customer allows the relaxed and tailored use of military standards, there is usually a more cost-effective design. Also, customer participation in the design development through a team process, such as integrated product and process development (IPPD), allows a more cost-effective design. Another attribute by the customer that could allow a more cost-effective design is the view toward profit. A profit incentive contract provides motivation for the contractor to reduce cost, which increases his profit.

Although it is not possible to provide specific examples in this text of how competition reduces cost, it is well known that competition drives down cost. Production buys with two competing contractors improve efficiency and may reduce the unit production cost by 50% compared to that of a sole-source contractor. Unfortunately, the downsizing of the number of contractors in the tactical missile community has reduced competition and many tactical missile programs are being absorbed into the strategic missile, UAV, and aircraft communities. As a result, the cost of tactical missiles is likely to increase in the future.

As a first-order estimate, the cost of an SDD program is a function of the duration of SDD. A low-risk SDD is usually less than four years duration. A moderate-risk SDD is usually four-to-six year duration. A high-risk SDD is usually longer than six years duration. Shown in Fig. 6.55 is the cost of 21 SDD programs. The source of the data is Ref. 26. The cost of SDD in FY 99 U.S. dollars is correlated as

$$C_{\mathrm{SDD}} = \$20{,}000{,}000\, t_{\mathrm{SDD}}^{1.90} \tag{6.96}$$

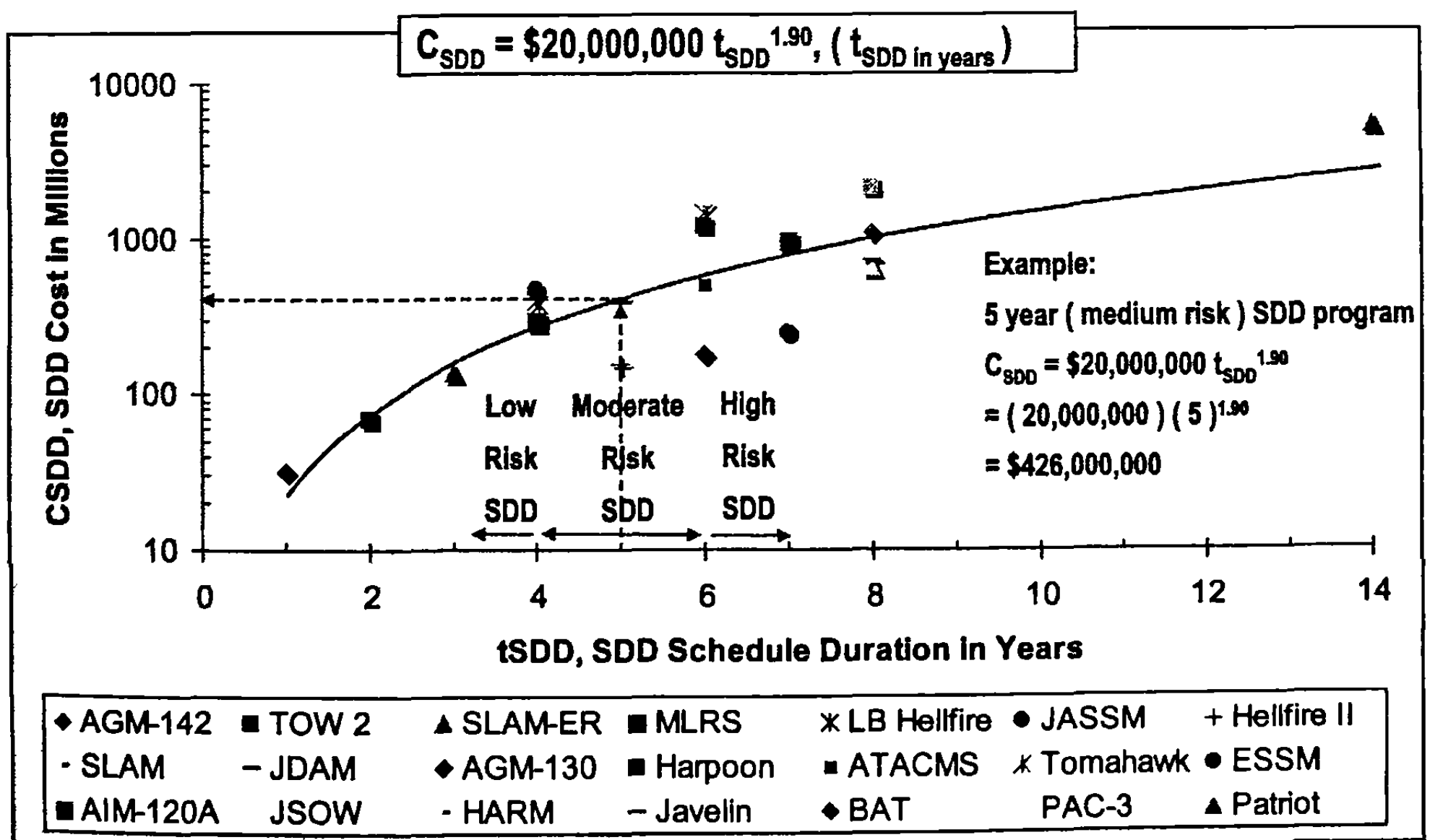

Note: SDD required schedule duration depends upon risk. Should not ignore risk in shorter schedule.
– Source of data: Nicholas, T. and Rossi, R., "U.S. Missile Data Book, 1999," Data Search Associates, 1999
– SDD cost based on 1999 US$

Fig. 6.55 SDD cost is driven by schedule duration and risk. Figure also in color section.

In the preceding equation t_{SDD} is duration of the SDD in years. Three SDD programs that cost significantly less than predicted by the equation are Hellfire II, AGM-130, and ESSM. Part of the reason for the relatively low SDD cost is that these programs were modifications of existing weapons, requiring relatively little development and test assets.

Sometimes management will force the engineers to accept an unrealistically short duration schedule. However, the risk will eventually catch up, and as a result overrun funding and schedule slippage will be probably be required to complete the program.

As an example of using the equation to predict SDD cost, a five-year, medium-risk SDD program cost is predicted to be

$$C_{SDD} = \$20{,}000{,}000(5)^{1.90} = \$426{,}000{,}000 \tag{6.97}$$

The average duration of SDD of the 21 missiles shown in the figure is six years. Average cost of SDD of the 21 missiles is \$822,000,000 in U.S. 1999 dollars.

An example of a short-duration and low-cost SDD program is the U.S. acquisition of the AGM-142 Raptor missile. The U.S. SDD program was low risk, short duration, and low cost because the missile had been previously developed by Israel. The U.S. SDD was primarily limited to integration of the missile on the B-52 and F-111 aircraft. At the other extreme is the long SDD development and high SDD cost of the PAC-2 Patriot missile. The long duration of SDD for Patriot was a combination of high risk and an annual shortage of funding, which resulted in extending the SDD program and adding additional total program cost.

As a first-order design consideration, production cost is a function of weight. The equation is

$$C_{1000} \approx \$6100 W_L^{0.758} \tag{6.98}$$

The preceding equation is based on correlating the data from Ref. 26. The derived cost of the 1000th missile C_{1000} is in U.S. 1999 dollars. Missile launch weight W_L is in lb. The correlation shown in Fig. 6.56 covers two orders of magnitude in missile weight, ranging from 27 lb for the lightweight, man-portable Javelin to 3200 lb for the Tomahawk.

As an example, the predicted unit production cost of the 1000th unit for a missile with a launch weight of 100 lb is $C_{1000th} \approx \$6100(100)^{0.758} =$ \$200,000. The cost of a total missile buy of 2000 units would be equal to the total number of missiles (2000) times the cost of the average (1000th) missile (\$200,000), or $2000 \times 200{,}000 = \$400{,}000{,}000$.

Note from the figure that the actual cost of Javelin is higher than predicted. Javelin is more complex than a typical lightweight missile. For example, it has both aerodynamic control and thrust vector control and has an expensive IIR seeker. Also note from the figure that the actual cost of MLRS and JSOW are less than predicted. MLRS is a less complex than most heavy missiles and has no seeker, relying on inertial guidance. JSOW is also less complex than most heavy missiles. JSOW has no propulsion; it is a guided glide bomb. For both

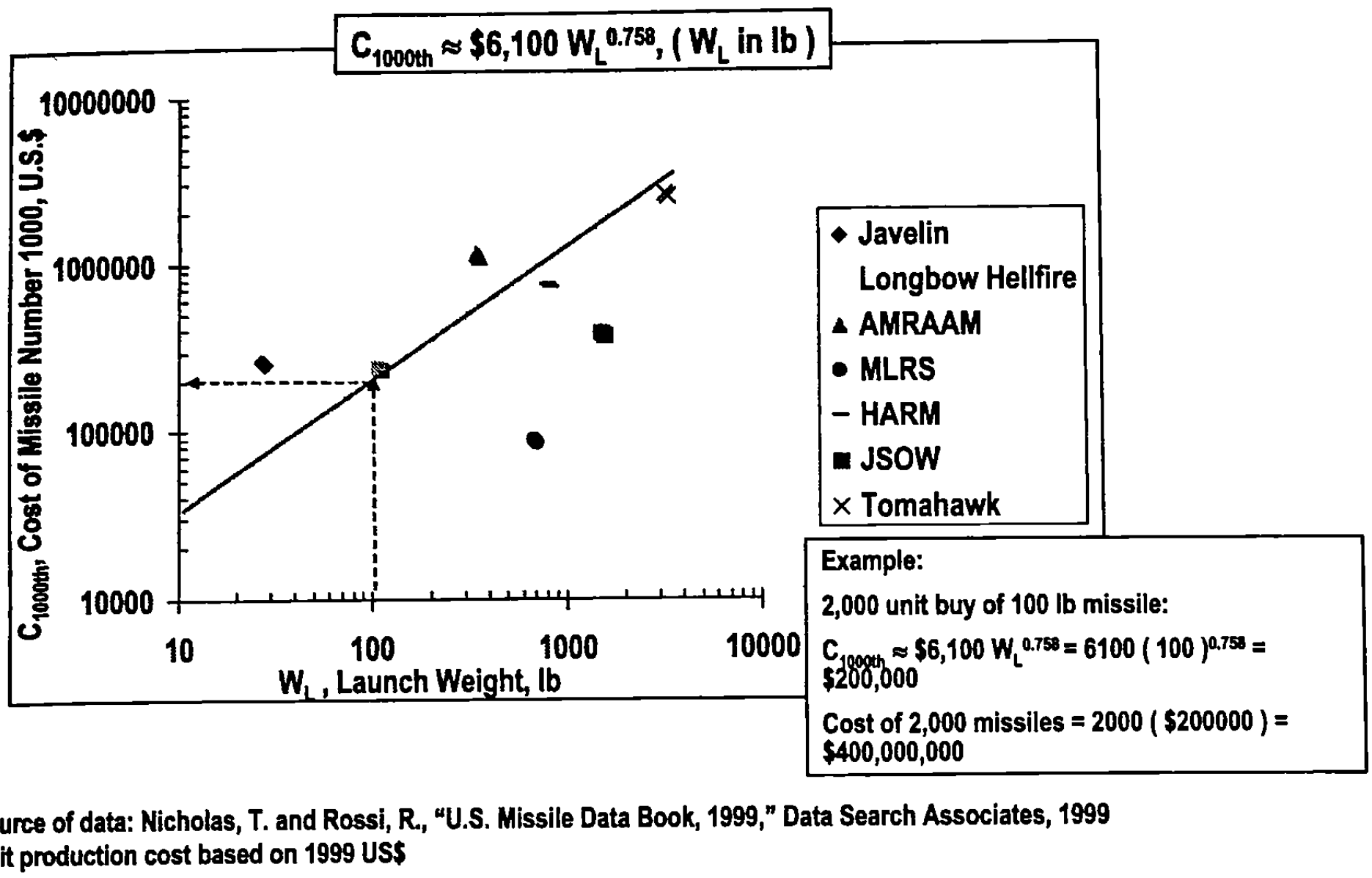

Fig. 6.56 Lightweight missiles have low unit production cost. Figure also in color section.

MLRS and JSOW, a relatively large fraction of the missile weight is the warhead, which is a relatively low cost subsystem.

A factor in manufacturing cost is controlled cleanliness. Clean rooms are necessary for optical manufacturing, inertial instrument manufacturing, EM manufacturing, thermal blankets, and electronics manufacturing (e.g., printed circuit boards). Optical, inertial, and EM manufacturing require a facility cleanliness standard of 100 (fewer than 100 particles per ft^3). Thermal blanket and electronics manufacturing require a standard of 10,000. Other manufacturing processes such as machining, mechanical assembly, plating, chemical treatment, composite forming, adhesive bonding, heat treatment, assembly tests, and system level tests do not need a clean room and are usually less expensive.

The unit production cost of a missile is dependent upon the learning curve from the past production of the missile, given by the equation

$$C_x = C_{1st} L^{\log_2 x} \tag{6.99}$$

In the preceding equation C_x is the unit cost of the current missile, C_{1st} is the unit cost of the first production missile, x is the number of missiles produced to date, and L is the coefficient of the learning curve. Another expression for the learning curve is the relationship of the cost to doubling the production, $C_{2x} = LC_x$. The learning curve is extensively used to predict production cost, not only in the aerospace industry but also in other industries such as the automotive industry. The contributors to the learning curve include labor efficiency, scrap, and the production process.

For a labor-intensive process such as building a developmental missile or a complex missile, the value of the coefficient of the learning curve is usually less than 0.8. For a machine-intensive process such as high rate production or a simple missile, the value of the coefficient of the learning curve is usually greater than 0.8.

Figure 6.57 illustrates the impact of the learning curve and the number of units produced on missile production cost. As an example, for a value of the learning curve coefficient of $L = 0.80$, the cost of the 1000th missile is 11% of the cost of the first missile. Changing a production process will change the learning curve. The production process (and its value of L) that is used for the first missile is different from the production process (and its value of L) that is used for the 1000th missile. The first missile is probably a developmental missile that is labor intensive and produced in the laboratory using soft tooling. The 1000th missile is probably a rate production missile produced in the factory using hard tooling.

Also shown in the figure is production cost as a function of units produced for operational missiles. The source of the data is Ref. 26. The data cover a broad range of learning curve, first unit cost, and year introduced. The learning curve coefficient varies from $L = 0.738$ for AMRAAM to $L = 0.817$ for Tomahawk. The MLRS learning curve data have a lot of scatter, indicating there have been changes in the manufacturing processes. The initial MLRS was just a simple unguided ballistic missile, with a large value of the learning curve coefficient. Later versions added the complexity of inertial guidance, which resulted in a lower value of the learning curve coefficient.

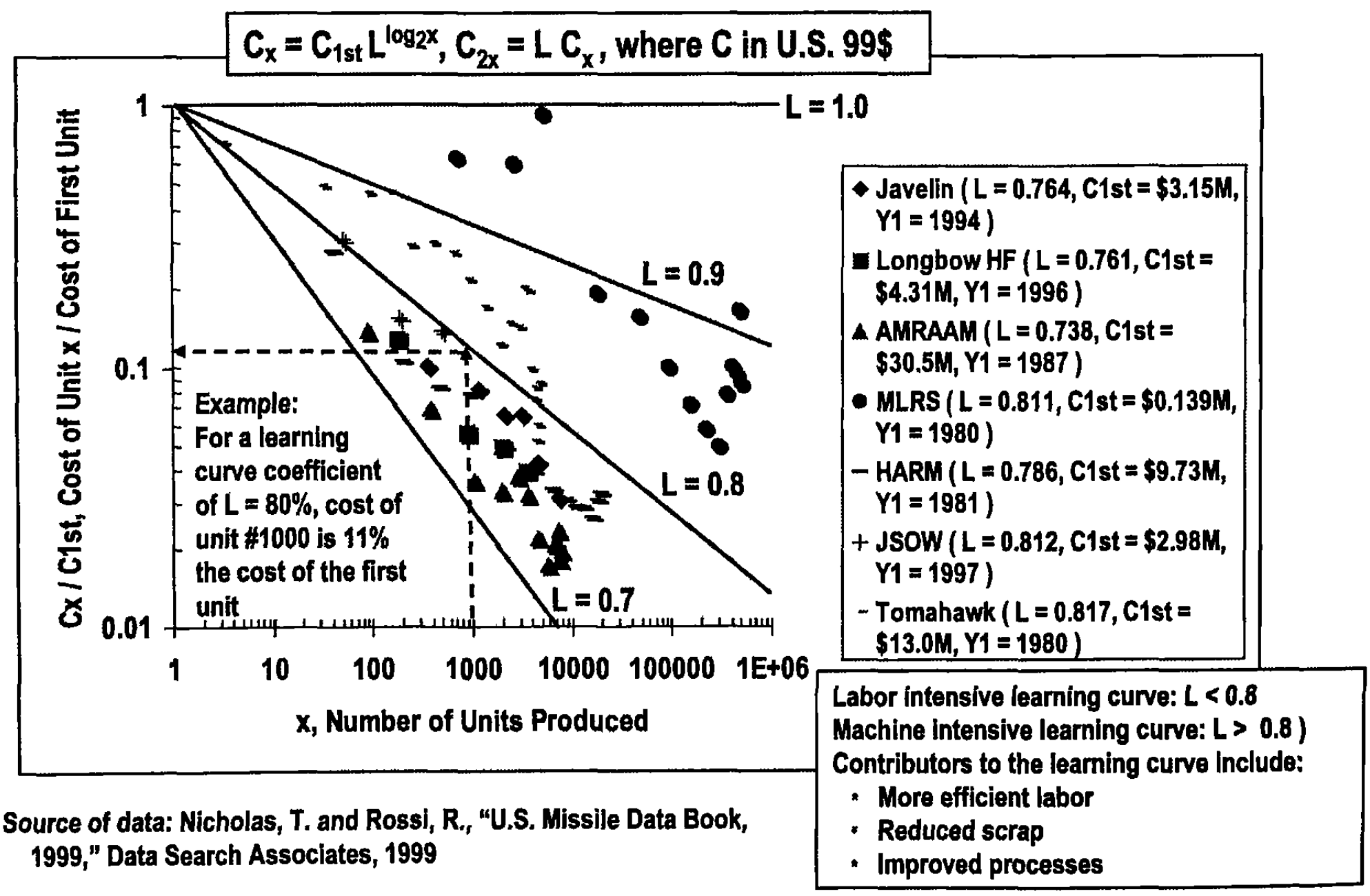

Fig. 6.57 Learning curve and large production reduce unit production cost. Figure also in color section.

Adjusted cost of the first missiles in the figure varies from $139,000 for MLRS to $30,500,000 for AMRAAM in U.S. 1999 dollars. Finally, the first year of production ranges varies from 1980 to 1997. The costs of missiles produced were adjusted to 1999 dollars. Note that the derived value of the learning curve coefficient for a typical tactical missile is $L \approx 0.8$. Production of a typical tactical missile requires balanced consideration of both labor and machine costs.

New technology is in development that will enhance the producibility and reduce the cost of weapons. Examples of recent precision strike weapons that include low-cost technologies include JDAM, JSOW, and JASSM. Technologies to reduce cost are also being introduced into existing weapons, with large savings. An example shown in Fig. 6.58 is Tactical Tomahawk, with an estimated unit production cost of $569,000 for 1300 missiles. It has a simple low-cost cast aluminum airframe (see figure) with extruded wings that results in greatly reduced parts count for the structure. Low-cost commercial parts are used for G&C and propulsion. The earlier Tomahawk has 11,500 parts, 2500 fasteners, 45 circuit cards, and 160 connectors and requires 610 assembly/test hours. The tactical Tomahawk is projected to have 35% fewer parts, 68% fewer fasteners, 51% fewer circuit cards, 72% fewer connectors, and 68% fewer assembly/test hours, resulting in a projected 50% reduction in cost. The tactical Tomahawk also has superior flexibility (e.g., shorter mission planning time, data link capability for in-flight targeting, data link capability for battle damage indication/battle damage assessment, modular payload) and higher reliability at the same launch weight and flight range (~1000 n miles) as the earlier Tomahawk.

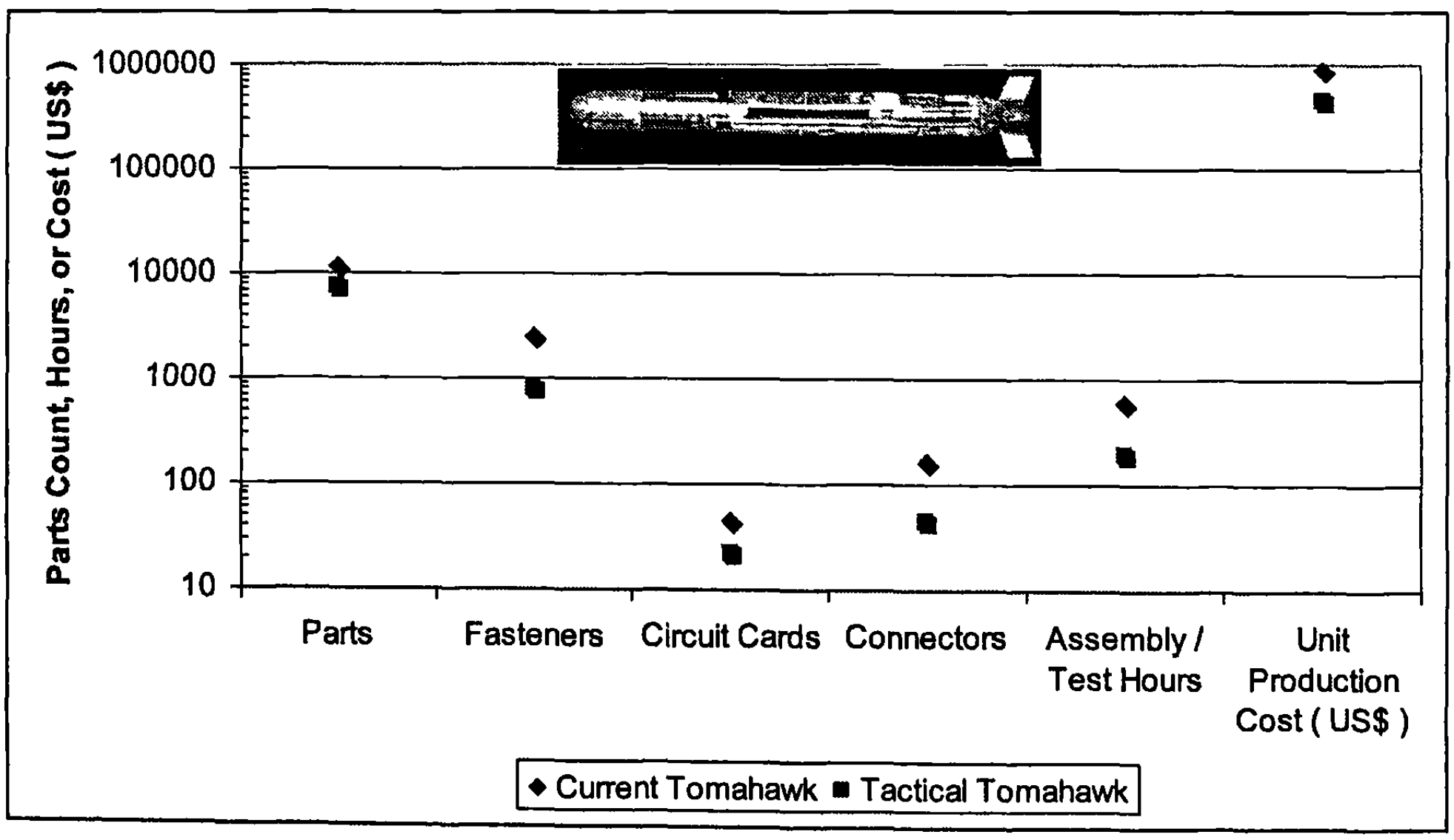

Note: Tactical Tomahawk has superior flexibility (e.g., shorter mission planning, in-flight retargeting, BDI / BDA, modular payload) at lower parts count / cost and higher reliability. Enabling technologies for low parts count include: casting, pultrusion / extrusion, centralized electronics, and COTS.

Fig. 6.58 Low parts count reduces missile unit production cost. Figure also in color section.

Missile production cost is sensitive to production rate. There is normally an economy of high-rate production. High-rate production allows hard tooling, which is usually more efficient. The work force is also usually more efficient in rate production.

A difference of the tactical missile culture compared to the related cultures of the strategic missile, UAV, and combat aircraft communities is the emphasis on low-cost manufacturing and high rate production. Tactical missile production rate may be more than 5000 missiles per year. This may be 10 times the production rate of a strategic missile and 100 times the production rate of a UAV or combat aircraft.

Examples of relatively high rate production processes are shown in Fig. 6.59. Shown in the left side of the figure is an example of the Copperhead seeker and electronics production. The top right section of the figure is an example of the Patriot flight control production. In the bottom right section of the figure is a video of the Hellfire seeker and electronics production processes. The production processes of the Copperhead, Patriot, and Hellfire weapons are labor intensive, with some automation of electronics, such as circuit boards. System assembly and system test are a significant portion of the production cost. A simpler missile that is produced at a very high rate, such as TOW, is less labor intensive. The production process for TOW is highly automated. There is relatively little assembly and testing. Missile system assembly and system tests are a relatively small portion of the TOW production cost. At the other extreme is the AMRAAM missile. AMRAAM is a more complex missile that is produced at a lower rate and is more labor intensive. The production process for AMRAAM has less automation. Missile subsystem, subsystem assembly, and system tests are a large portion of the AMRAAM production cost.

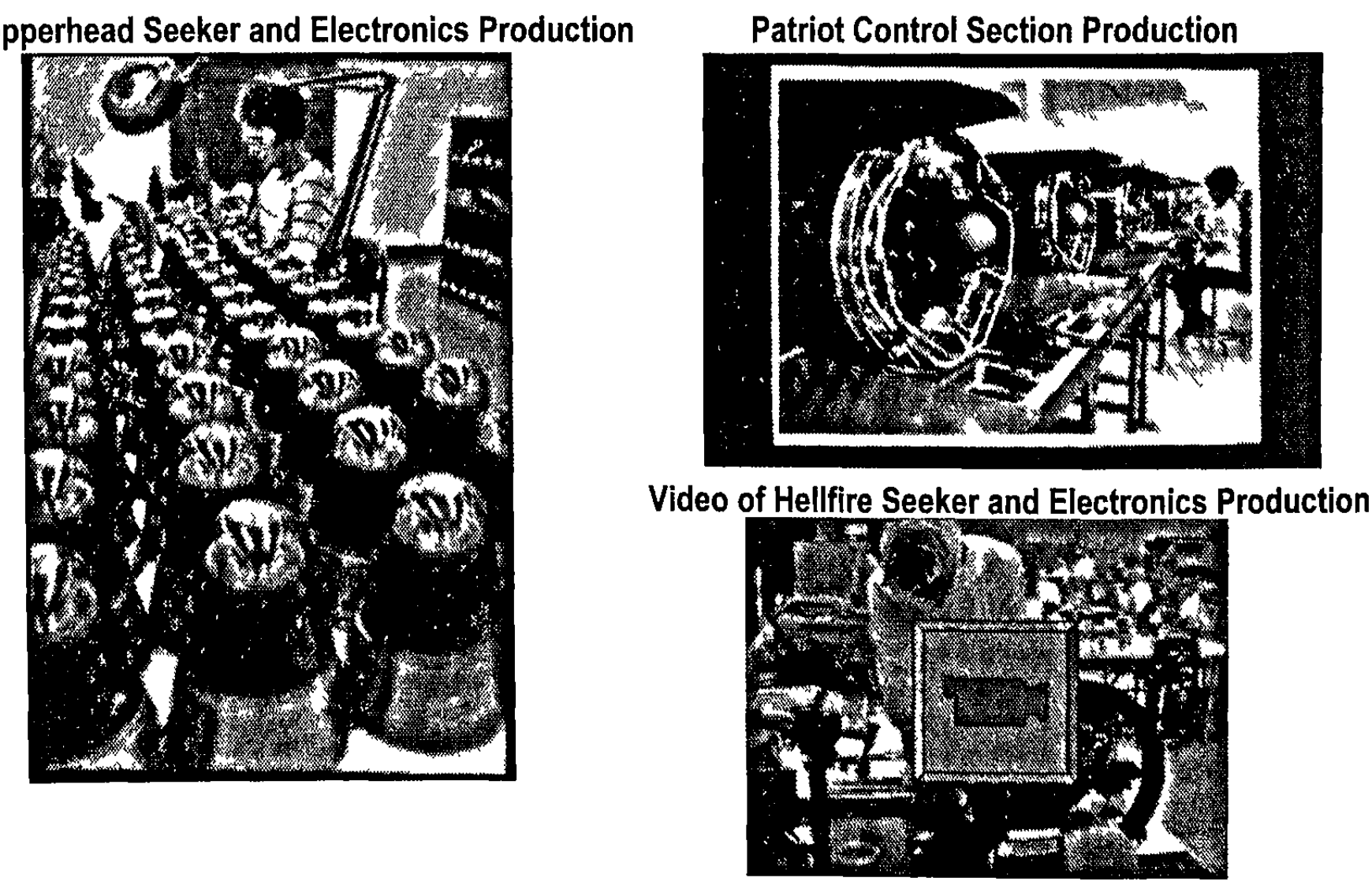

Fig. 6.59 Tactical missile culture is driven by rate production of sensors and electronics. Figure also in color section. Video is in the CD included with this textbook.

A skilled labor force is desirable for tactical missile production. Skilled production workers provide enhanced reliability and reduce the scrap/cost.

The logistics cost of the missile system over the years following production can be comparable to or even greater than the SDD and production costs. Note in Fig. 6.60 that logistics considerations can be grouped into two major categories of peacetime and wartime logistics. Design tradeoffs include the cost allocation to each category and the allocation of cost within each category.

Peacetime logistic considerations may be categorized as contractor post-production activity, storage, maintenance, and disposal.

Following the production of the missile, the contractor maintains and updates the training manuals for the military user. A technical data package that documents the weapon system characteristics is also usually maintained by the contractor. A configuration management system is used to provide order and accuracy for the data. Other maintenance activities following production include the six-DOF digital simulation, hardware-in-loop (HWL) simulation, and software. The prime contractor also provides engineering support if it is necessary to analyze and correct problems that develop after delivery of the missile. System engineering support provided by the prime contractor after production includes maintaining a capability for system analysis, launch platform integration, and requirements documents. Much of the system analysis capability emphasizes the G&C system, with validation conducted through the six-DOF and HWL simulations. Much of the work on launch platform integration emphasizes the impact of changes in the launch platform avionics on the missile. Much of the work on requirements documents addresses the flow down and allocation of new system and launch platform requirements. Finally, the prime contractor continues to coordinate with suppliers following production.

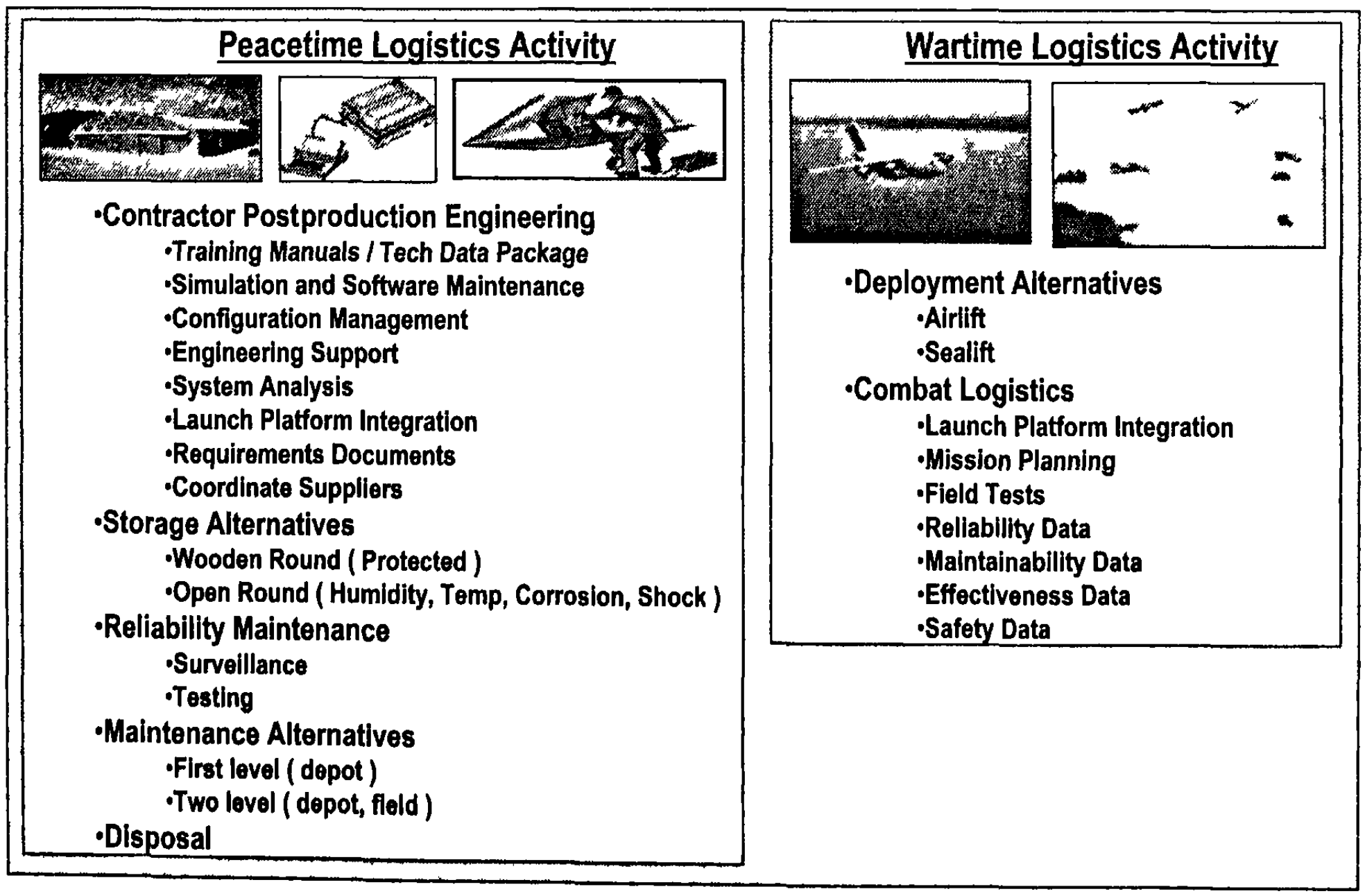

Fig. 6.60 Logistics cost considerations. Figure also in color section.

A typical tactical missile production provides more than a single load-out for the launch platforms. Most missiles are stored following production, awaiting deployment. For long-term storage, e.g., 10 years, a wooden round is cost effective. The missiles are stored in a sealed container, protected from humidity, shock, and corrosion. For short-term storage, a simple hinged container may provide sufficient protection from the environment.

The stockpile is periodically assessed for reliability through surveillance and testing. Two philosophies that apply to maintenance are first-level versus two-level maintenance. In first-level maintenance, all of the maintenance is conducted by a contractor at the depot. First-level maintenance is particularly applicable to naval weapons because ships and submarines have limited available space. Two-level maintenance is particularly applicable to Air Force and Army weapons. A field maintenance facility can be used for routine maintenance, for example, sealing gaps to ensure low observables. If sophisticated maintenance is required, the missile is shipped back to the central depot.

A final consideration during peacetime is disposal of obsolete missiles without harming the environment. The total number of tactical missiles in the U.S. inventory is relatively large, more than 500,000 missiles. However, only a fraction of the inventory will require disposal. Some may be used in wartime, others will be used for training, and some may be approved for foreign military sale. Typical disposal cost of a tactical missile varies from about $100 to about $2000, depending upon the number of hazardous components, type of hazard, environmental impact, the complexity of the missile, security classification, and the size of the missile. Disposal of most tactical missiles is at their depot storage. The disposal process of the warhead charge and rocket motor propellant usually consists of removal and destruction. After the removal of the guidance and control system, it is usually disposed, but sometimes parts are salvaged. The airframe and rocket motor case are usually salvaged.

Environmental impact and the avoidance of law suits have become increased concerns in recent years. Hazardous materials such as asbestos, mercury, and beryllium that were used in older missiles are no longer allowed. The application of new technologies for future missiles will be limited by environmental restrictions. For example, gel rocket motors will not be able to use toxic propellants such as hydrazine, nitrogen tetroxide, or nitric acid. Because environmental requirements are becoming stricter, current practices that are now deemed to be potentially hazardous, such as the use of lead solder in electronics and the use of thermal batteries for power supply, are likely to be replaced in the future by other approaches.

Wartime logistics may be categorized as deployment and combat considerations.

A tradeoff of deploying the missiles from the storage facility to the theater of operation is the cost and time required for deployment. Airlift is rapid but has limited capacity and is expensive. Sealift has a large capacity and is inexpensive but may take a month or longer to deliver a weapon from the storage facility to the theater.

After delivery to the theater of combat, the missiles are integrated with the launch platform for physical and electrical compatibility. Prior to launching the missile, mission planning and check-out tests are conducted. During

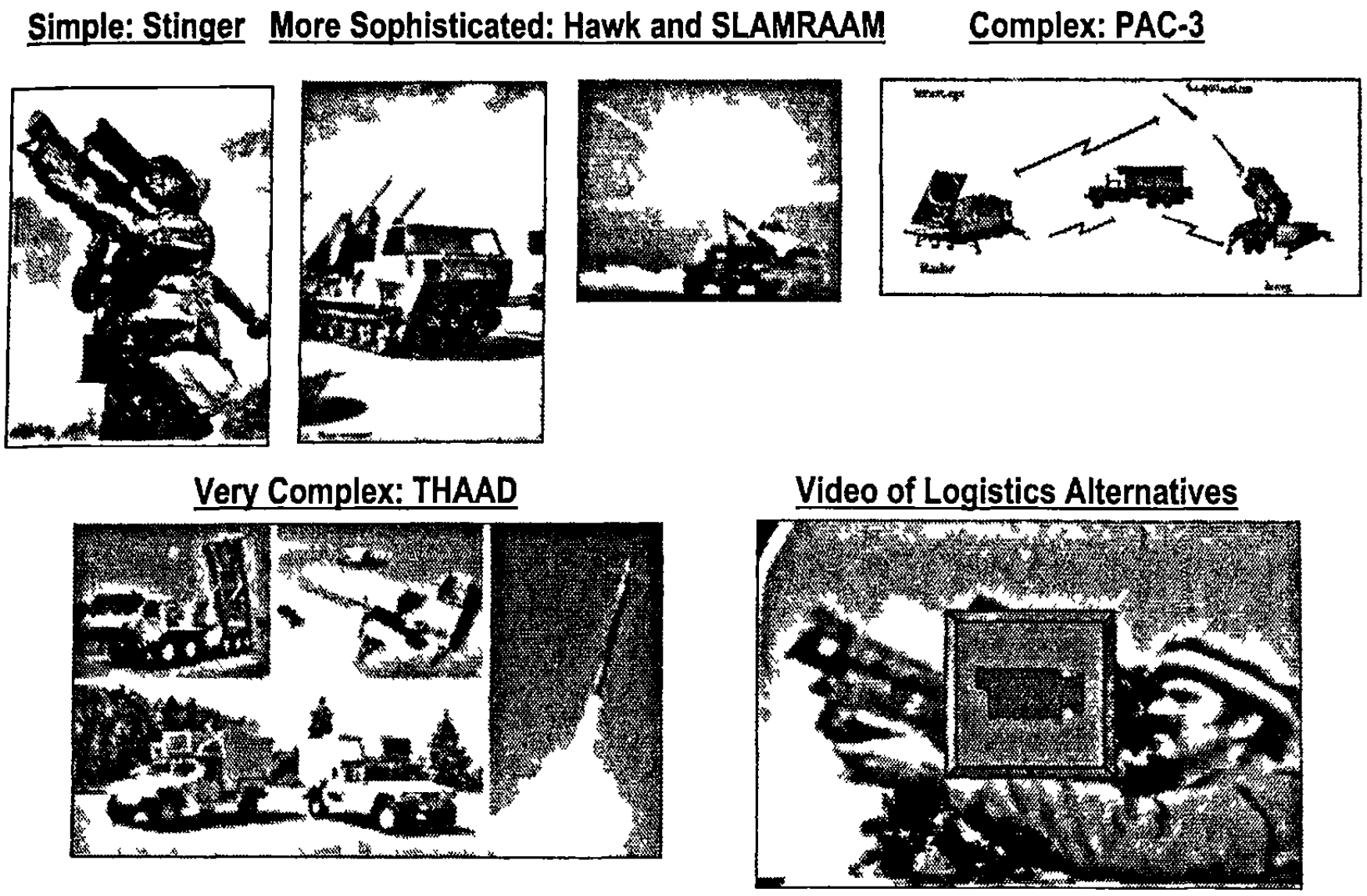

Fig. 6.61 Logistics cost is lower for simple missile systems. Figure also in color section. Video is in the CD included with this textbook.

combat, statistical data are acquired on the reliability, maintainability, effectiveness, and safety of the missile. These data are used to develop any necessary fixes and provide guidelines for future design.

Figure 6.61 compares a simple surface-to-air missile system (Stinger) that has low-cost, wooden round logistics to more sophisticated missile systems that include a launch vehicle and radar (Hawk and SLAMRAAM). Continuing with the comparison, shown in the top right section of the figure is a more complex missile system (PAC-3) that has higher cost logistics from three vehicles, a radar van, an engagement control station, and a missile launching station. Finally, the bottom left section of the figure illustrates a very complex missile system, THAAD, which has an entourage of vehicles and support personnel for transportation, maintenance, launch, fire control, and command and control.

Shown in the bottom right section of the figure is a video that compares the operational logistics of Stinger, Hawk, Surface Launched AMRAAM (SLAM-RAAM), PAC-3, and THAAD. Also shown in the video are firings, fly-outs, and intercepts against air targets.

Shown in Fig. 6.62 are examples of the impact of missile weight on the support manpower requirements for tactical missiles. A typical maximum lift requirement per person is between 50 and 100 lb. For a lightweight man-portable missile such as Predator, a single gunner can prepare and launch the missile. As an example of a moderately heavy missile, the 190-lb Sidewinder requires two to four personnel to install the missile on the launch aircraft. A heavier missile, such as a 500-lb Sparrow, requires additional support personnel plus ground support equipment. Finally, a very heavy weapon, such as a laser-guided bomb, requires specialized, heavy ground support equipment.

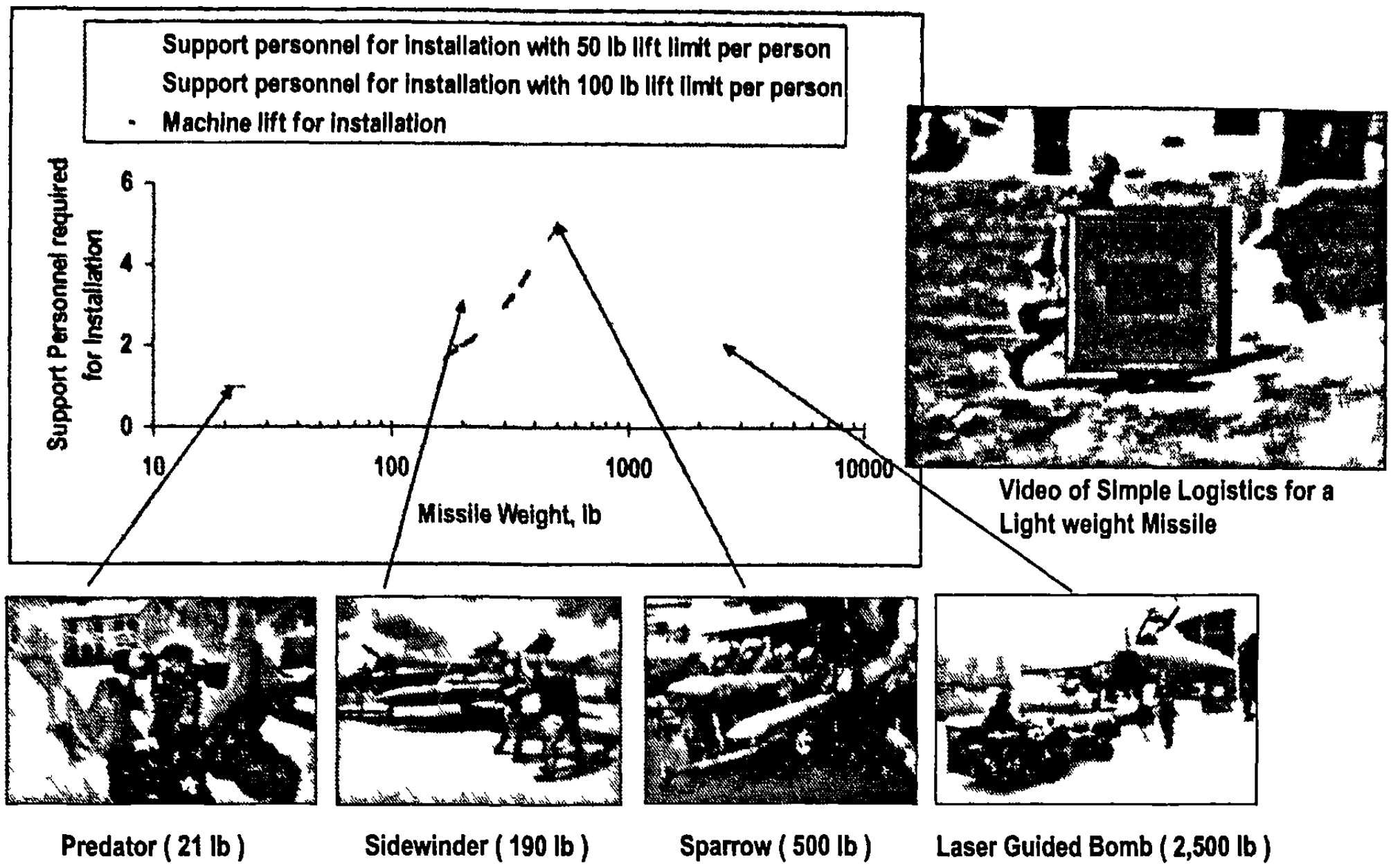

Fig. 6.62 Logistics is simpler for lightweight missiles. Figure also in color section. Video is in the CD included with this textbook.

The video in the upper right corner of the figure illustrates the logistics simplicity of a lightweight missile. The 21-lb Predator system (missile/launcher) is easily carried, set up, and fired by a single gunner in a broad range (e.g., open terrain, urban building) of battlefield engagements. Also shown in the video is the effectiveness of the Predator's explosively formed projectile (EFP) warhead and the top attack flyover trajectory against tank targets.

Predator's use of an EFP warhead in a top flyover trajectory allows a lightweight warhead to penetrate the relatively soft top armor of a tank. Also, Predator's simple top flyover trajectory minimizes the maneuvering requirement of the missile, allowing lighter weight/lower cost flight control actuators and gyros.

The application of micromachined electromechanical systems (MEMS) devices to logistics health monitoring after production will provide a more accurate assessment of the lifetime of each individual missile. This will greatly reduce logistics cost. MEMS devices would also have payoff during missile development. Because high-performance missiles such as ramjets are weight and volume limited, there is leverage in reducing weight. Reduced weight is consistent with reduced cost, improved performance, and improved launch platform compatibility. One approach to reduce missile weight is to reduce the required factors of safety. The higher confidence from MEMS data would allow weight reduction in the overdesigned areas of the structure.

MEMS devices are fabricated from a single piece of silicon by semiconductor manufacturing processes, resulting in a small size, low-cost package. Between 2000 and 5000 MEMS sensor devices can be produced from a single 5-in silicon wafer. An example of the small size of a MEMS device is shown in Fig. 6.63. Future tactical missiles could have low-cost/small-size MEMS

- ♦Micro-machined Electro-Mechanical Systems (MEMS)
  - ♦Small size / low cost semiconductor manufacturing process
  - ♦2000 to 5000 sensors on a 5 in silicon wafer
- ♦Wireless (RF) Data Collection and Health Monitoring
- ♦Distributed Sensors Over Missile
  - ♦Stress / strain
  - ♦Vibration
  - ♦Acoustics
  - ♦Temperature
  - ♦Pressure
- ♦Reduced Logistics Cost
  - ♦Health monitoring
- ♦Reduced Weight and Production Cost
  - ♦More Efficient Design

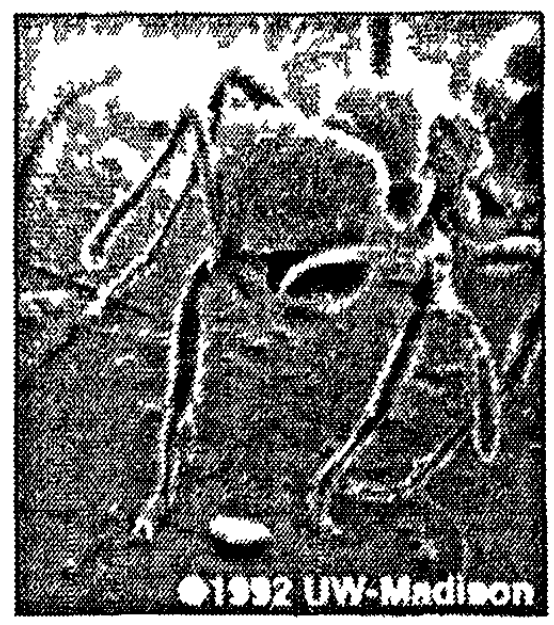

Fig. 6.63 Small MEMS sensors can provide health monitoring, reducing cost and weight.

sensors for data collection during missile development and for health monitoring after production. Localized stress/strain, vibration, acoustics, temperature, pressure, and other measurements could be monitored through many sensors distributed around the airframe.

6.9 Launch Platform Integration

Launch platform integration sets constraints on the missile that must be considered early in the development process. Moreover, the design process requires iteration to harmonize the outputs from the diverse areas of mission/scenario definitions, missile requirements, launch platform integration, missile concepts, and technologies. In a few cases it may be possible to modify a launch platform to accommodate a new missile, but in most cases this is not an option. Generally the launch platform is a constraint that drives the missile design. For example, AMRAAM was originally developed as a lightweight radar missile for carriage on the wing tips of the F-16, which has a 300-lb weight limit. Later, AMRAAM was modified to a compressed carriage configuration (clipped wings and tails) to better accommodate internal carriage in the F-22 center weapons bay. Missiles are driven as much by launch platform compatibility as other measures of merit. Cross-platform compatibility is desirable for a missile system. A larger total buy of missiles for cross-platform application has benefits of lower unit production cost. Weapon compatibility with multiple launch platforms also has payoff in the neckdown benefit cost savings of fewer missile logistics systems. Carriage constraints for missiles on U.S. surface ships, submarines, fighter/bomber aircraft, helicopters, UCAVs, and ground vehicles are shown in Fig. 6.64.

Launch Platform Integration / Firepower

US Launch Platform	Launcher	Carriage Span / Shape	Length	Weight
Surface Ships	VLS	~22" ~22"	263"	3400 lb
Submarines	CLS	22"	263"	3400 lb
Fighters / Bombers / UCAVs	Rail / Ejection	~24" x 24"	~168"	~500 lb to 3000 lb
Ground Vehicles	Launch Pods	~28" ~28"	158"	3700 lb
Helos	Rail	13" x 13"	70"	120 lb

Fig. 6.64 Missile carriage size, shape, and weight are driven by launch platform compatibility. Figure also in color section.

In the United States, the Vertical Launch System (VLS) is a standard sea carriage and launch system for many missiles (Tomahawk, Standard Missile, Sea Sparrow, ASROC) on surface ships such as cruisers and destroyers. The Arleigh Burke class destroyer has 90 VLS cells. The larger Ticonderoga class cruiser has 122 VLS cells. The VLS length constraint is approximately 263 in. The cross-sectional geometry constraint of the current standard canister is approximately 22 × 22 in. The maximum missile weight constraint for the current standard canister is approximately 3400 lb. A ship typically has two magazines of missiles, located fore and aft. As an example of a possible configuration, each magazine could have six modules, with eight launchers in each module, providing a total of 48 missiles per magazine, or 96 VLS-launched missiles per ship.

United States submarines have a missile launcher that is similar to the VLS but it has a circular cross section. The tactical submarine Canister Launch System (CLS) has a diameter constraint of 22 in and a length constraint of 263 in. Maximum missile weight for the CLS is the same as that of the VLS, 3400 lb. The VLS and CLS also have a maximum limit of the mass flow rate delivered in the event of a restrained launch to avoid burning through the launch platform structure. Some Trident missile launch tubes on strategic submarines (SSGM) have been adapted to launch conventional missiles such as Tomahawk and ATACMS, providing high firepower. As an example, a modified launch tube can store and launch up to seven Tomahawk missiles, allowing an SSGM to carry up to 154 missiles.

Fixed-wing aircraft launch platforms for missiles include tactical fighters, bombers, and UCAVs. Shown in the figure is an example of a fighter aircraft,

the F-18C. The F-18C carries weapons externally for pylon ejection launch and rail launch. The launcher photograph shows a rail-launched AMRAAM carried on the wing tip, an ejection-launched AMRAAM carried under the wing, and an ejection-launched HARM carried under the wing. Other aircraft, such as the F-22, F-35, B-1, and B-2 have an additional capability of internal carriage. Internal launchers include vertical ejection, rail trapeze, and rotary ejection. Missile span constraint for typical fixed-wing aircraft carriage is about 24 × 24 in. Length constraint for typical fixed-wing aircraft is about 168 in and the maximum allowable missile weight varies from about 500 to 3000 lb, depending upon the aircraft. There is a desire for lightweight missiles to maximize the firepower of small aircraft such as the F-18C fighter and UCAVs. As examples of this concern, about 50% of the U.S. Navy fleet combat aircraft in the year 2010 timeframe are expected to be F-18Cs and UCAVs will be assuming a greater role in weapon delivery in future years.

Most helicopters have rail launchers. Helicopters have severe integration constraints, with the Hellfire missile representing a typical constraint. A typical missile length constraint is about 70 in and a maximum allowable missile weight is about 120 lb.

An example of a ground-launch platform is the U.S. Army M270 Armored Vehicle, which is based on a modified M2 Bradley armored personnel carrier. It is the standard U.S. Army platform for surface-to-surface artillery rockets and missiles. The M270 has two launch pods. Either 12 MLRS rockets or 2 ATACM missiles can be launched from the M270. The MLRS rocket and ATACM payloads can be either submunitions or unitary warheads.

Technology for weapon aeromechanics compatibility and high firepower includes low-volume propulsion, ordnance, and airframe; store carriage and store separation wind tunnel tests; computational fluid dynamics (CFD) predictions; and finite element modeling (FEM) predictions.

In an ideal world new combat aircraft development would be conducted in concert with new missile development for a more cost-effective weapon system. Examples of system-level trades include aircraft maneuverability versus missile maneuverability and aircraft observables versus missile standoff range. The reality is that new aircraft are developed based on the current weapons with little consideration of the new weapons or the new missile technology that is in development. The lack of consideration of new weapons may be a concern of the aircraft developer that the consideration of new weapons may endanger the aircraft program funding.

Figure 6.65 illustrates how aircraft carrier bring-back load limits, day/night operation, firepower objectives, and weapons load-out impact the maximum allowable weight of a precision strike missile. Shown are examples for the F-18C and F-18E aircraft. Note that the F-18C aircraft has less capability than the F-18E in all load-out configurations. The figure shows a large difference in the maximum allowable missile weight for day operation versus night operation. The difference is because of the additional fuel that must be reserved for night operation off an aircraft carrier. The maximum weapon weight shown in the curves may be driven by the asymmetric carriage bring-back load limits (2500 lb maximum weight for inboard asymmetric carriage and 1500 lb maximum weight for outboard asymmetric carriage). Finally, note the reduction

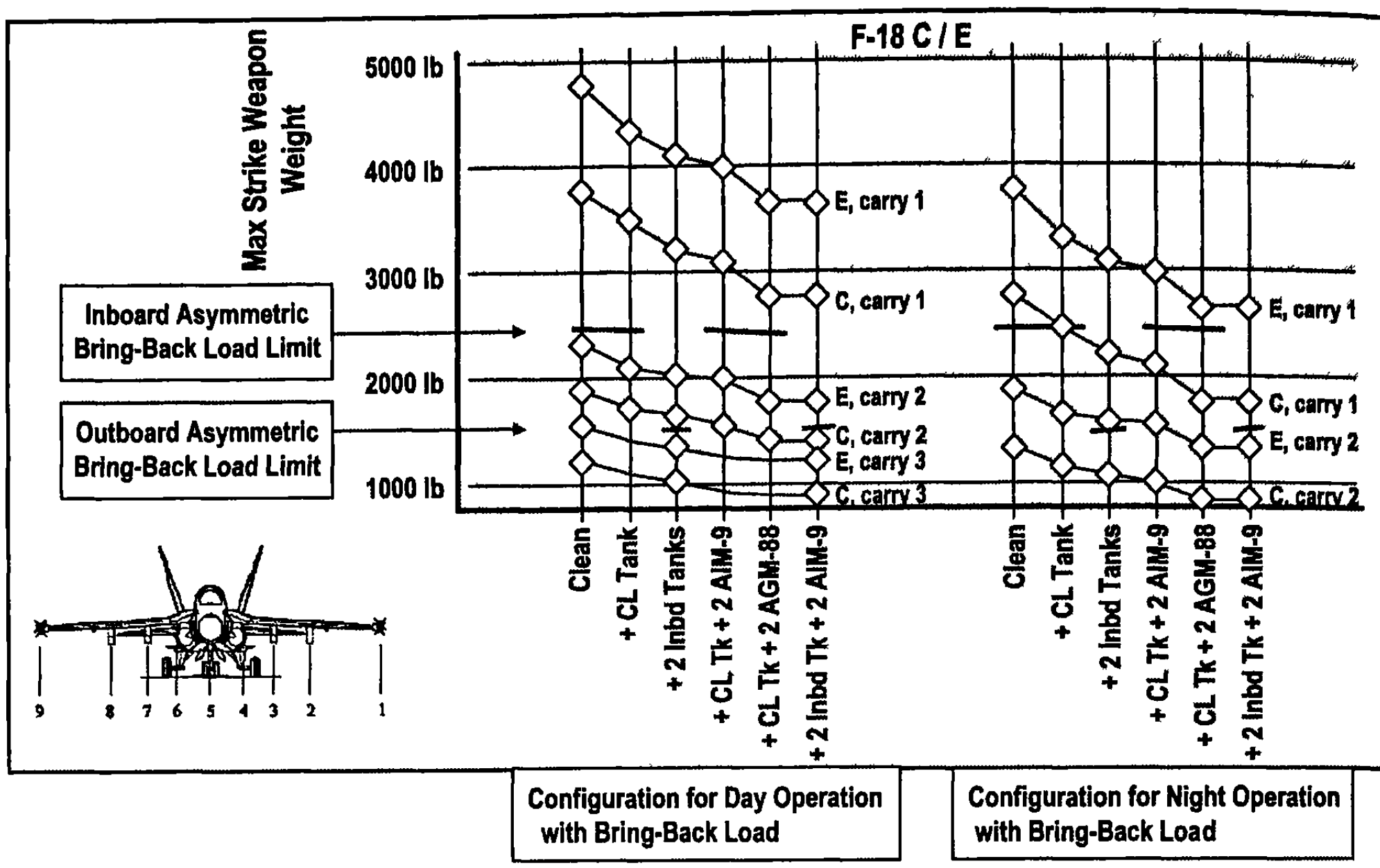

Fig. 6.65 Lightweight missiles enhance firepower.

in maximum allowable missile weight as the load-out configuration is changed from that of a clean aircraft carrying only precision strike missile(s) to other configuration load-outs. Five load-out configurations are the precision strike missile(s) plus either 1) a centerline fuel tank; 2) two inboard fuel tanks; 3) a centerline fuel tank plus two AIM-9 Sidewinder air-to-air missiles; 4) a centerline fuel tank plus two AGM-88 antiradiation missiles (ARM); or 5) two inboard fuel tanks plus two AIM-9 Sidewinders. Note that the maximum allowable weight of a single precision strike missile on the F-18E is about 4800 lb under ideal conditions. At the other extreme is an F-18C operating under more typical, limited conditions. For an F-18C operating at night with two inboard fuel tanks and two AIM-9 Sidewinders, the maximum allowable weight of a single precision strike missile is much lower, about 1800 lb. In the case of carriage of two precision strike missiles, the F-18E under ideal conditions can carry a missile weighing up to 2400 lb. At the other extreme for an F-18C load-out of two precision strike missiles, operating at night with the addition of two inboard fuel tanks and two AIM-9 Sidewinders requires that the precision strike missile weigh less than 900 lb. A precision strike missile weight of about 1400 lb is probably a good compromise for the example of F-18C/E aircraft integration. It allows two weapons on the F-18C for unrestricted day operation, two weapons on the F-18E for near-unrestricted night flight operation, and three weapons on the F-18E for day operation with two inboard fuel tanks.

In addition to firepower, weight, and fitment, other considerations in missile/launch platform integration include the launch envelope limitations from:

1) Missile seeker field of regard (FOR) obscured by the launch platform. As an example, the F-22 has a trapeze launcher that extends laterally from the side

bay. This enables the Sidewinder seeker to have a target lock-on before launch, without being obscured by the F-22 aircraft.

2) Minimum range limitations. Launch rail clearance may affect the minimum range. The missile has tip-off angular rates in pitch, yaw, and roll from the clearance between the missile hangers/shoes and the launcher rail. Launcher aeroelasticity may also affect the minimum range. Tip-off rates are imparted by a flexible launcher. A third example for helicopters is that the rotor downwash may affect the missile flight trajectory and the minimum range.

3) Safety. For rail-launched missiles, a safety concern is launcher rail retention to avoid an inadvertent release of the missile prior to launch. The launcher must also release the missile reliably during the motor firing to avoid a hangfire. Another safety concern is the launch platform local flow field (α, β) and its effect on the separation trajectory. As an example, a ship-launched missile during launcher separation must be controllable at high angle of attack from the crosswind. Launch platform maneuvering is another consideration of safe separation. Also, launch platform handling qualities with attached stores may be a safety concern. As an example, the changes in the aircraft flow field and center of gravity from a stores load-out may degrade the aircraft flying qualities. For internal carriage, the launch platform bay or canister acoustics and vibration may also be a safety concerns.

Aircraft store compatibility wind tunnel tests are conducted to determine store carriage loads and store separation forces, moments, and trajectories. Figure 6.66 shows examples of wind tunnel installations of aircraft and store models. Note that a typical aircraft store load-out has closely spaced stores. The local airflow

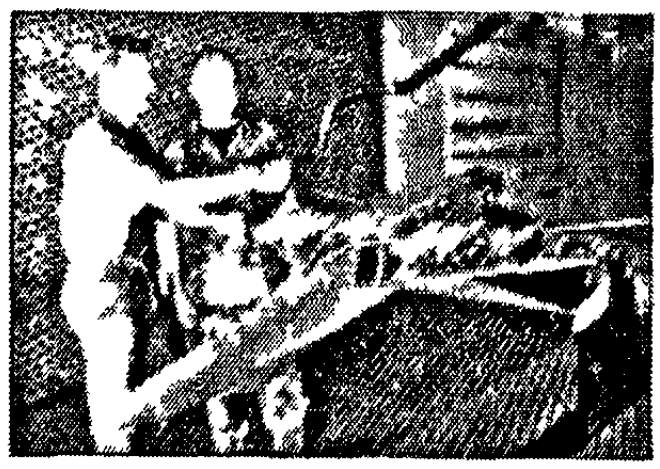

F-18 Store Compatibility Test in AEDC 16T

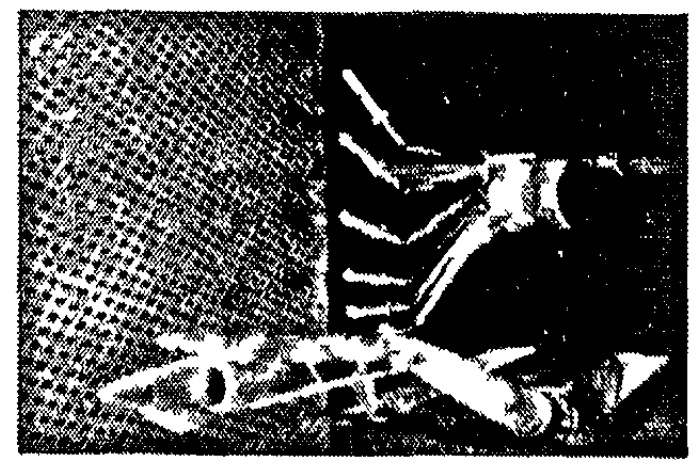

AV-8 Store Compatibility Test in AEDC 4T

Types of Wind Tunnel Testing for Store Compatibility
- Flow field mapping with probe
- Flow field mapping with store
- Captive trajectory simulation
- Drop testing

Example Stores with Flow Field Interaction: Kh-41 + AA-10

Fig. 6.66 Store separation wind tunnel tests are required for missile/aircraft compatibility. Figure also in color section.

around a store is difficult to predict. There is a complex flowfield interaction of a store with the aircraft and also with the adjacent stores.

The types of wind tunnel testing for store compatibility include:

1) Flowfield mapping underneath the aircraft with a pitot static pressure probe to measure the local values of the static pressure, total pressure, and angle of attack.

2) Flowfield mapping with an instrumented store model on a sting to measure the forces and moments on the store immersed in the aircraft flowfield.

3) Captive trajectory simulation of an instrumented store model on a sting.

4) Drop testing of store models. The store models are constructed of lead, tungsten, or even gold to provide weight scaling to simulate full-scale buoyancy in the wind tunnel test.

Shown in Fig. 6.67 are examples of missile carriage on U.S. standard rail and ejection launchers. The launcher provides the mechanical and electrical interface between the missile and the launch aircraft. The mechanical interface includes the attachment, structural support, and the launch mechanism. The electrical interface supports the cockpit controls and displays, enabling the pilot to launch the missile.

In the upper left of the figure is an AGM-114 Hellfire II missile on a helicopter rail launcher. Rail launchers are particularly suited to lightweight, high-thrust missiles such as the Hellfire. The Hellfire weighs about 100 lb, with a launch thrust-to-weight ratio of about 30:1. Hellfire has a semilaser seeker with a FOR of +/−30 deg.

Most precision strike missiles use ejection launch. In the upper right corner of the figure is an AGM-86 ALCM precision strike missile that is installed on a rotary launcher of a bomb bay. ALCM is ejected from the bay at an ejection

Example Rail Launcher: Hellfire / Brimstone

Example Ejection Launcher: AGM-86 ALCM

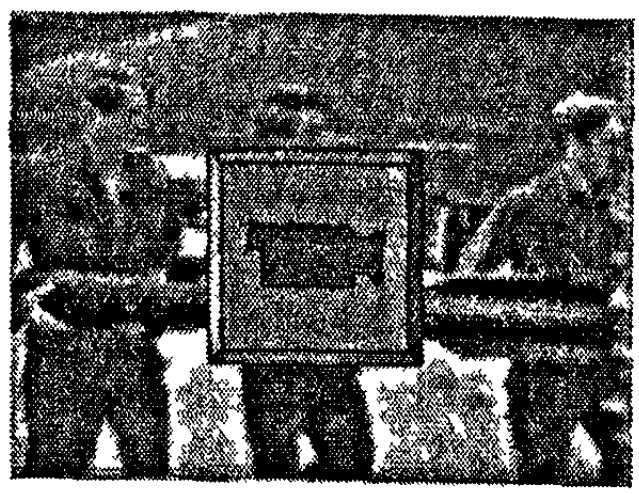

Video of Hellfire / Brimstone Carriage / Launch

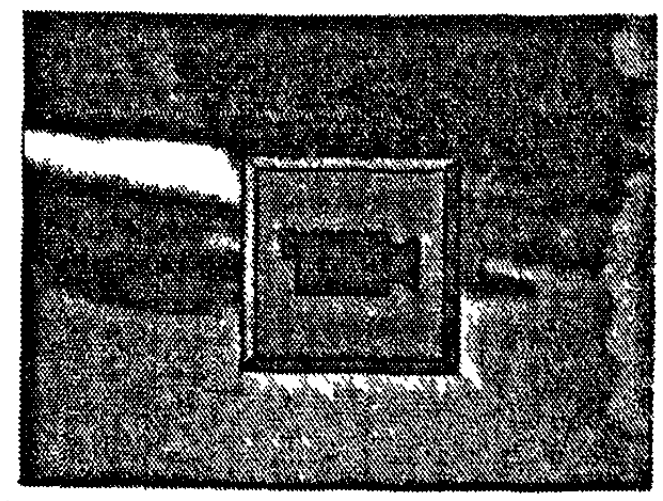

Video of AGM-86 Carriage / Launch

Fig. 6.67 Examples of rail-launched and ejection-launched missiles. Figure also in color section. Video is in the CD included with the textbook.

velocity of about 20 ft/s. The ejection stroke is about 12 in, providing an average acceleration of about 6 g. The ejection launcher contains cartridges that provide the downward velocity and a downward pitch rate to the missile at launch, aiding safe and accurate separation. Suspension of the missile is such that the missile center of gravity is midway between the ejectors. A concern during launch is the local angle of attack and the local angle of sideslip because of the proximity of the store to the aircraft and the effect on the missile flight trajectory, especially at high dynamic pressure. Up to eight ALCM missiles can be carried on a rotary launcher in each bay of the B-1, B-2, and B-52 bombers. The ALCM has compressed carriage (switchblade wing, folded tails), providing a high load-out in the bomb bay. The wing and tails are unfolded immediately after separation from the bay. Concerns for internal bay carriage include bay acoustics, bay vibration, flowfield angularities near the aircraft, and safe separation at high dynamic pressure.

The left bottom section of the figure is a video of the rail launcher loading of the Brimstone missile. The missile slides onto the rail and into a "shotgun" connector that interfaces with the aircraft avionics. The video also shows rail loading and launch of the Hellfire missile.

The right bottom section is a video of the loading, carriage, ejection launch, separation, and flight of the ALCM missile. Note the deployment of the compressed carriage switchblade wing and the folded tails.

Examples are shown in Fig. 6.68 of safe separation of a rail-launched AMRAAM from an F-16 and the clean separation of two laser-guided bombs

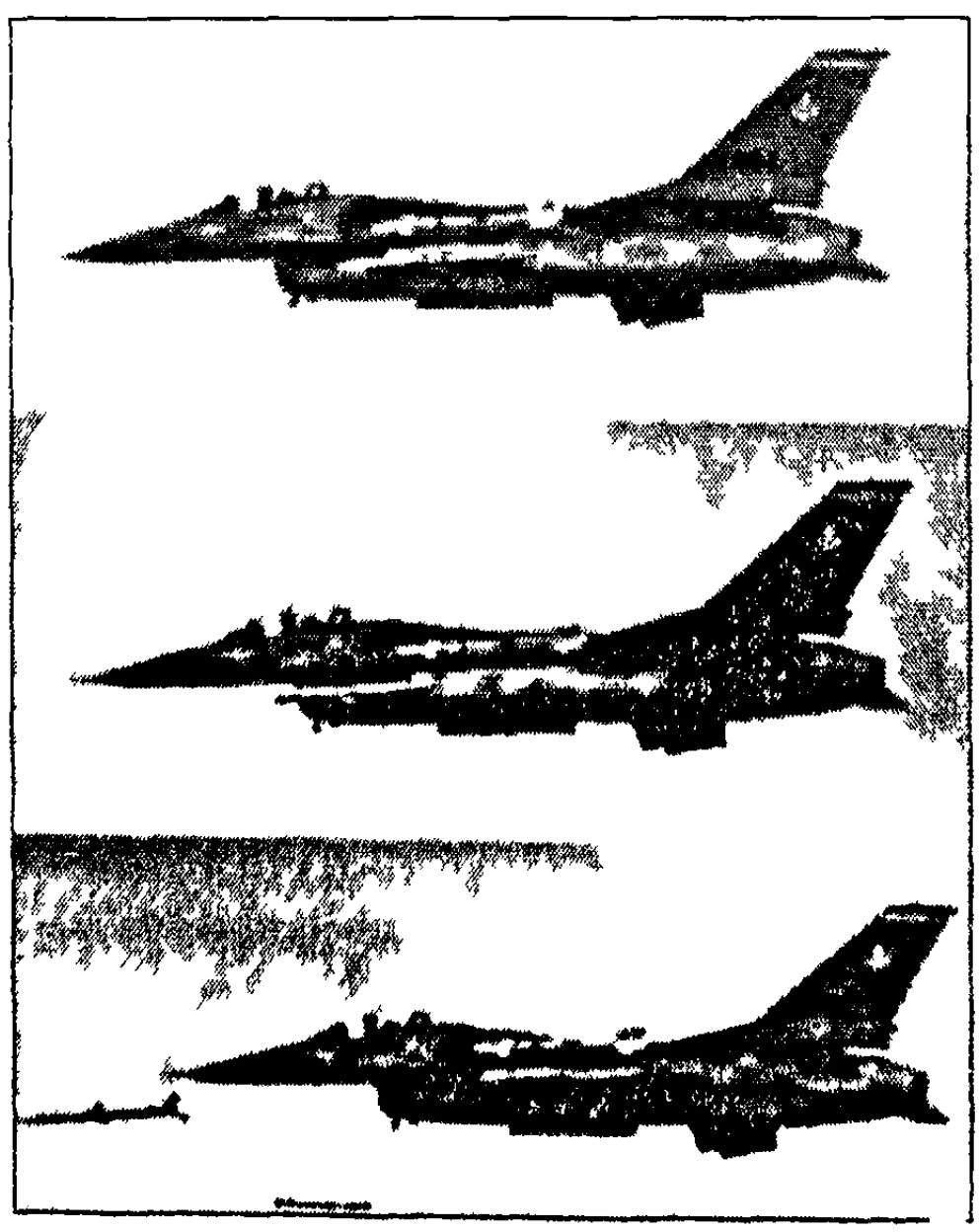

AMRAAM Rail Launch from F-16

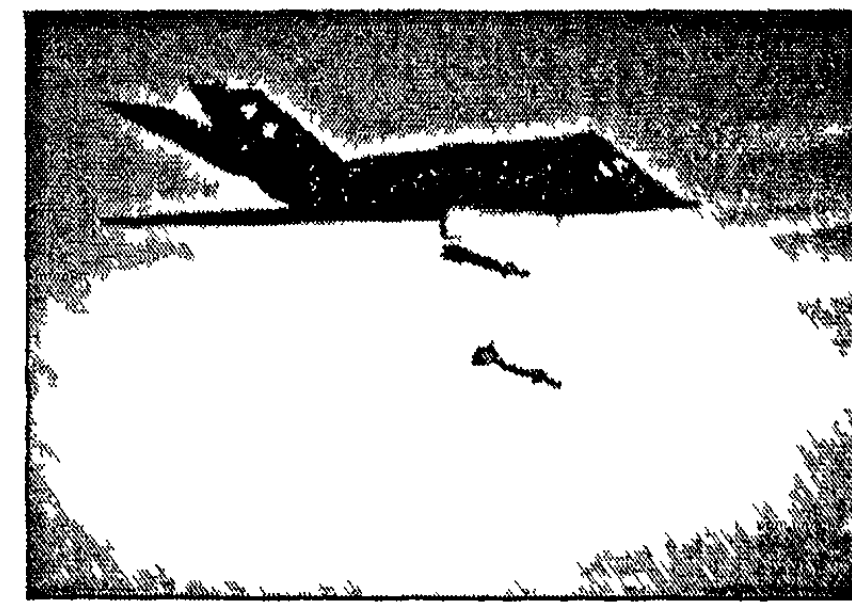

Laser Guided Bombs Drop from F-117

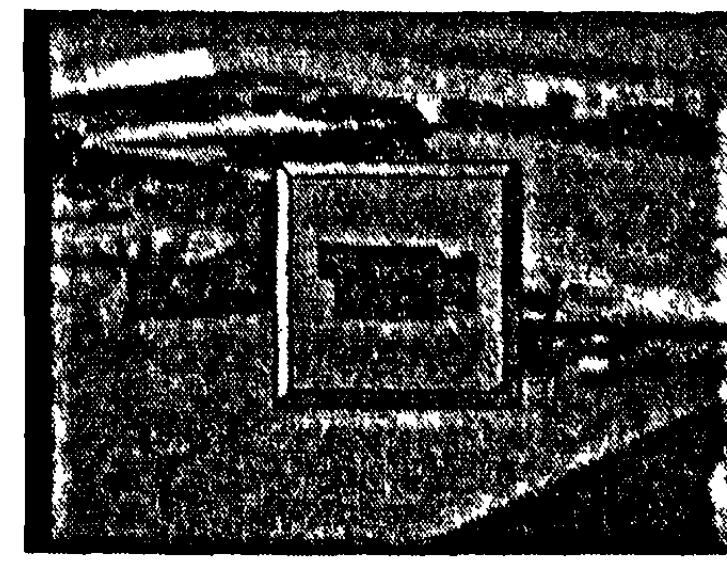

Video of Rapid Drop (16 Bombs) from B 2

Fig. 6.68 Examples of safe store separation. Figure also in color section. Video is in the CD included with this textbook.

dropped from an F-117. In the bottom right corner is a computer video from the Northrop Grumman Corporation, showing the clean separation of a rapid bomb drop (about one per second) from the B-2 bomber. A rapid bomb drop is desirable to minimize the exposure time with the high observables from the open weapon bay. An exposure time less than about 15 s is desirable to prevent threat radars from establishing a track file.

Figure 6.69 shows store compatibility problems of unsafe separation from the launch platform, missile hang-fire on the launcher, and aeroelastic instability of stores.

The top left portion of the figure illustrates an unsafe separation of a missile from an aircraft, with the missile impacting the aircraft. The bottom left video shows examples of unsafe store separation of fuel tanks, bombs, and missiles. Note that store separation problems tend to occur for large stores; buoyant stores (e.g., empty fuel tanks); and close proximity, multiple adjacent stores.

The top center portion of the figure shows an example of a rail launch retention system for a missile. Under a normal condition the missile is locked to the rail except for launch, as shown with the position of the latch. In a locked position, aft travel of the missile is blocked by the missile shoe pressing against an aft stop on the launcher. Forward travel is restrained by a latch on the launcher, which is pressed in front of the missile shoe. The latch is held in place by the compression force of spring. When the launch command is given by the pilot, a solenoid is activated, which pulls the latch away from the rail and unlocks the missile. The unlocked position of the latch is shown as the dashed line in the figure. The retention force on the unlocked missile is usually about 50% of the thrust of the rocket motor, which allows the missile thrust to overcome the retention force. If the missile does not leave the rail within a normal time period, the retention system is designed to automatically relock the missile to

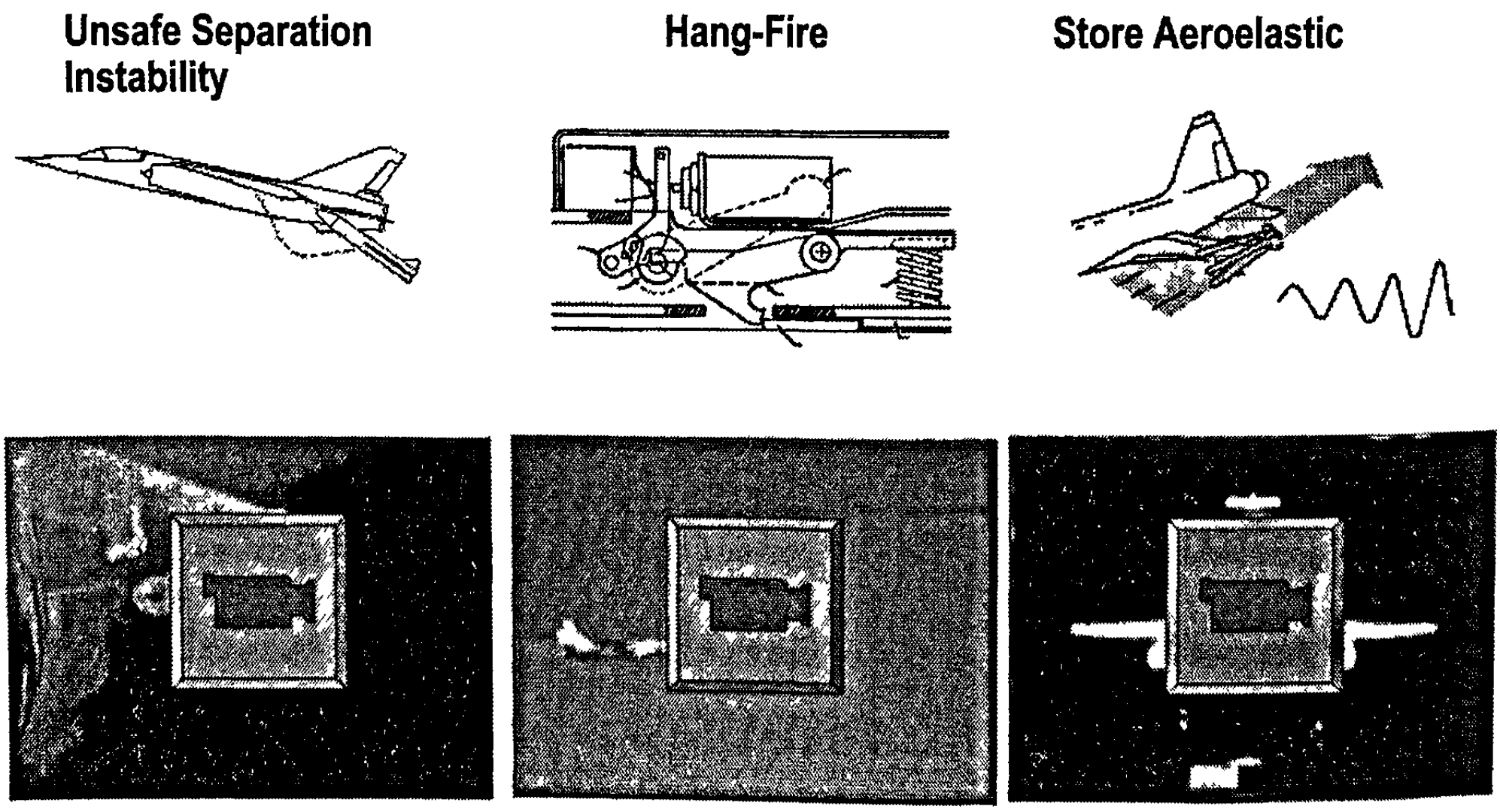

Fig. 6.69 Examples of store compatibility problems. Video is in the CD included with this textbook.

the rail. A hang-fire occurs if the retention system does not unlock the missile from the rail following the launch command. A concern of hang-fire is the hot rocket exhaust from the missile, which can damage the adjacent aircraft structure. Shown in the bottom center video is a hang-fire of a rocket motor, from the failure of the launcher retention system to unlock the missile from the rail.

Illustrated in the top right portion of the figure is the aeroelastic instability of a store on an aircraft. At low dynamic pressure with lightweight stores mounted on a stiff portion of the aircraft structure, aeroelasticity is not a problem. Under normal design conditions the amplitude of structural vibration is small and is damped out. However, for relatively heavy stores mounted on relatively flexible portions of the aircraft, such as the wing tips, flight at high dynamic pressure can induce vibrations that diverge. The divergence can damage the aircraft, degrade the flying qualities, and may even lead to the loss of the aircraft. Shown in the bottom right video is an example of aircraft aeroelastic instability from stores.

Store suspension requirements for ejection launchers, based on U.S. military standard MIL-A-8591, are summarized in Fig. 6.70. Shown are the store weight and the store dimension parameters for lightweight stores (up to 100 lb), medium-weight stores (101 to 1450 lb), and heavy-weight stores (over 1451 lb). Suspension alternatives are 30-in and 14-in suspension systems. For an ejected store weight up to 100 lb, only the 14-in suspension can be used. A lightweight (up to 100 lb) missile requires a lug height and an ejector pad area of 0.75 in and 4.0 × 26.0 in, respectively. For a medium-weight missile with a

Store Weight / Parameter	30 Inch Suspension	14 Inch Suspension
♦ Weight Up to 100 lb	Not Applicable	Yes
• Lug height (in)	↓	0.75
• Min ejector area (in x in)		4.0 x 26.0
♦ Weight 101 to 1450 lb	Yes	Yes
• Lug height (in)	1.35	1.00
• Min lug well (in)	0.515	0.515
• Min ejector area (in x in)	4. 0 x 36.0	4.0 x 26.0
♦ Weight Over 1451 lb	Yes	Not Applicable
• Lug height (in)	1.35	↓
• Min lug well (in)	1.080	
• Min ejector area (in x in)	4.0 x 36.0	

Ejection Stroke

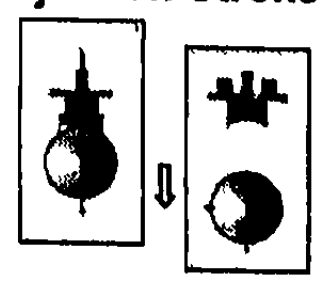

Fig. 6.70 MIL-STD-8591 Aircraft store suspension and ejection launcher requirements.

weight between 101 and 1450 lb, either the 14 or a 30-in suspension may be used. Medium-weight ejected stores have larger required lug height. They also require lug wells. The required lug wells could have a strong impact on the missile internal structure design. For example, in some cases the rocket motor overlaps the missile center of gravity. Accommodating the lug wells in the rocket motor case is difficult and expensive. A strong back may be required, similar to that of the AGM-69 SRAM missile. For a heavy missile with a weight that is over 1451 lb, only the 30-in suspension can be used. MIL-STD-8591 requires that the lugs have a deeper well if the missile weighs more than 1451 lb.

Examples of missile rail launchers that are compatible with MIL-STD-8591 are shown in Fig. 6.71. Rail launchers usually suspend the missile at two locations, a forward hanger and an aft hanger. Some rail launchers suspend the missile at three locations for added stiffness.

The launcher shown in the top of the figure is the LAU-7. The LAU-7 rail launcher has a store weight limit of 300 lb and a store diameter limit of 7 in. The LAU-7 is a standard launcher for the Sidewinder missile. It has forward and aft hangers with a shoe width of 2.26 in.

The LAU-117 rail launcher, shown in the bottom of the figure, has a store weight limit of 600 lb and a store diameter limit of 10 in. The LAU-117 is a standard launcher for the Maverick missile. It has a forward T-hanger with a shoe width of 1.14 in and an aft hanger with a shoe width of 7.23 in.

A missile that has reduced span surfaces during carriage allows closer spacing of the adjacent missiles on the launch platform. Approaches for compressed carriage include reduced span surfaces, folded surfaces, wraparound surfaces, and planar surfaces that extend (such as switchblade wings, Diamondback wings,

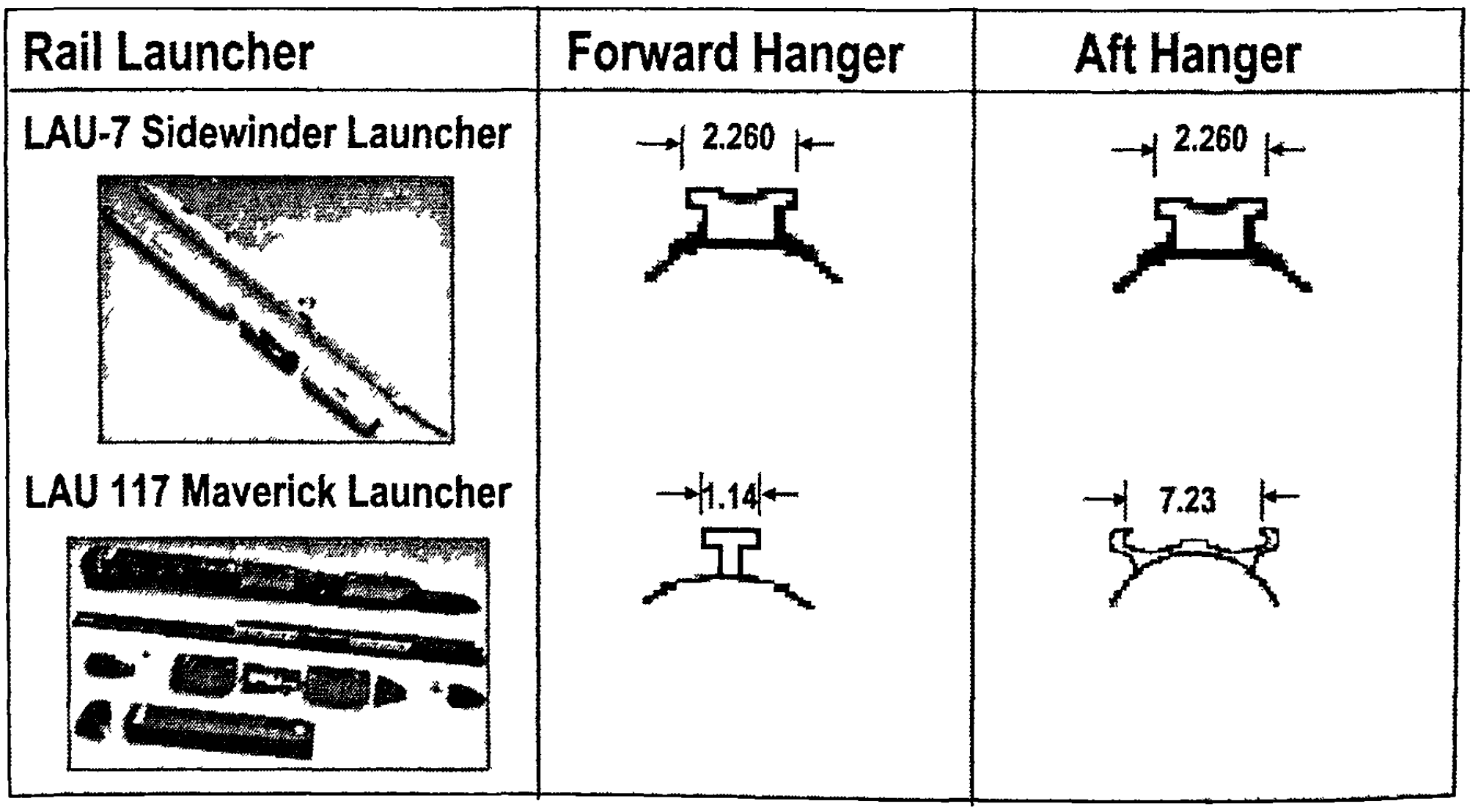

Note: Dimensions in inches.

• LAU 7 rail-launched store weight and diameter limits are ≤ 300 lb, ≤ 7 in

•LAU 117 rail-launched store weight and diameter limits are ≤ 600 lb, ≤ 10 in

Fig. 6.71 MIL-STD-8591 aircraft store rail launcher examples.

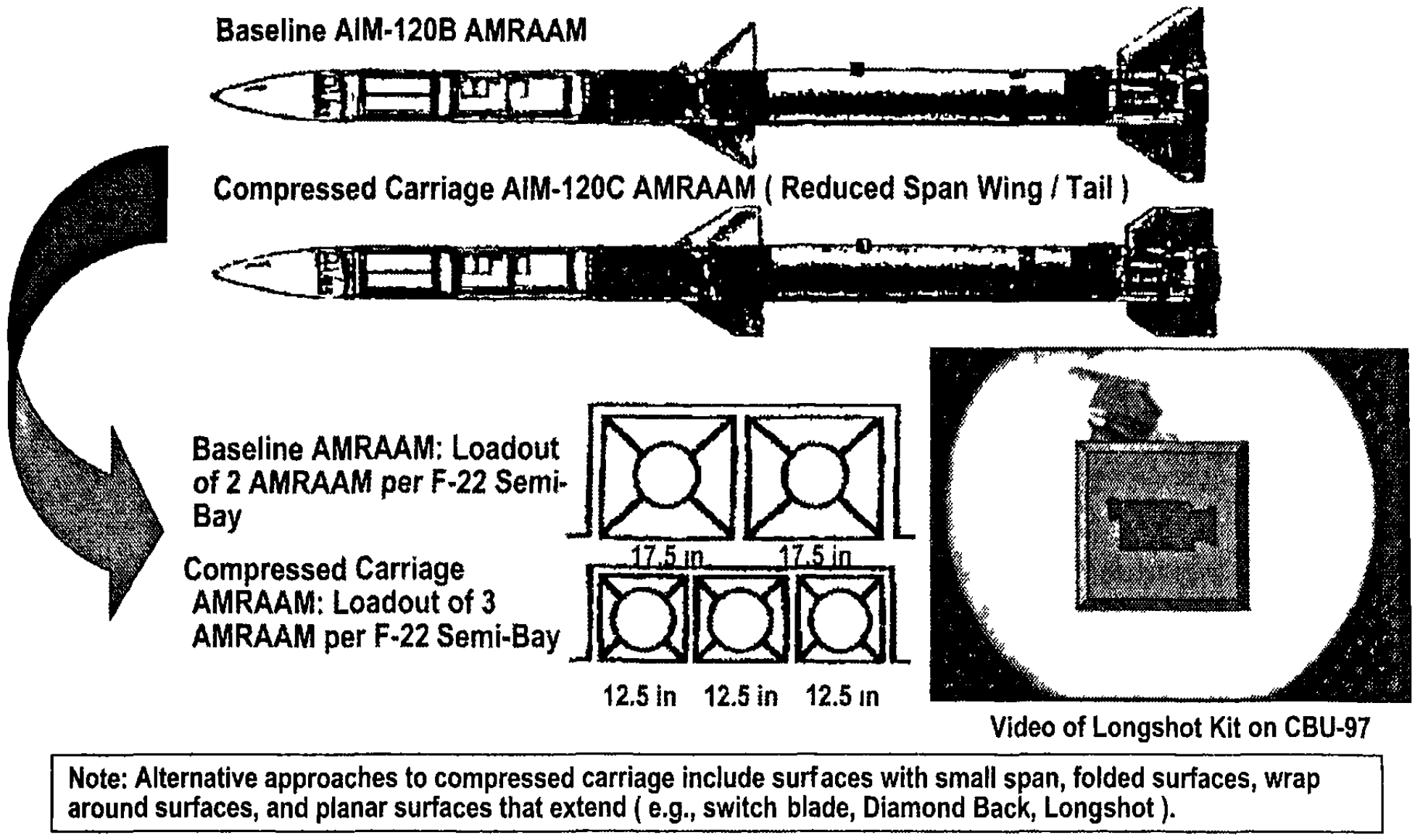

Fig. 6.72 Compressed carriage missiles provide higher firepower. Video is in the CD included with this textbook.

and the Longshot wings). Figure 6.72 illustrates the benefits of compressed carriage. The F-22 internal center weapons bay typically has two partitions, with one partition for air-to-air (e.g., AMRAAM) missiles. A baseline AMRAAM AIM-120B load-out in an F-22 center bay partition allows two missiles per partition. However, compressed carriage AMRAAM AIM-120C can be packaged three missiles per partition, a 50% increase in the firepower load-out. For an air-to-air mission only, both partitions of the F-22 center bay are allocated to air-to-air missiles, allowing a bay load-out of six compressed carriage AIM-120C.

It was noted previously in the aerodynamics chapter that missiles that use low aspect ratio surfaces, such as AMRAAM AIM-120C, usually have a larger supersonic hinge moment. This is from the larger variation in the aerodynamic center. However, an advantage of a low aspect ratio surface is a lower bending moment because of the reduced span. The lower bending moment reduces the required weight of the control surface shaft and the frictional bearing torque. Reduced frictional bearing torque improves the performance of the flight control actuator.

Another example of compressed carriage is in the video at the bottom right section of the figure. The Longshot wing and GPS guidance adaptor kit provide extended range and enhanced accuracy for dumb bombs, such as CBU-97. The compressed carriage wings and folded tails are deployed at launch.

Figure 6.73 shows an example of aircraft carriage and fire control interface. It is based on the ADM-141 TALD (Tactical Air-Launched Decoy). Shown are an electrical safety pin, which is removed just prior to aircraft takeoff; flight control access cover for maintenance check-out and tests; fire control/avionics umbilical connector to the aircraft store management computer and displays in the

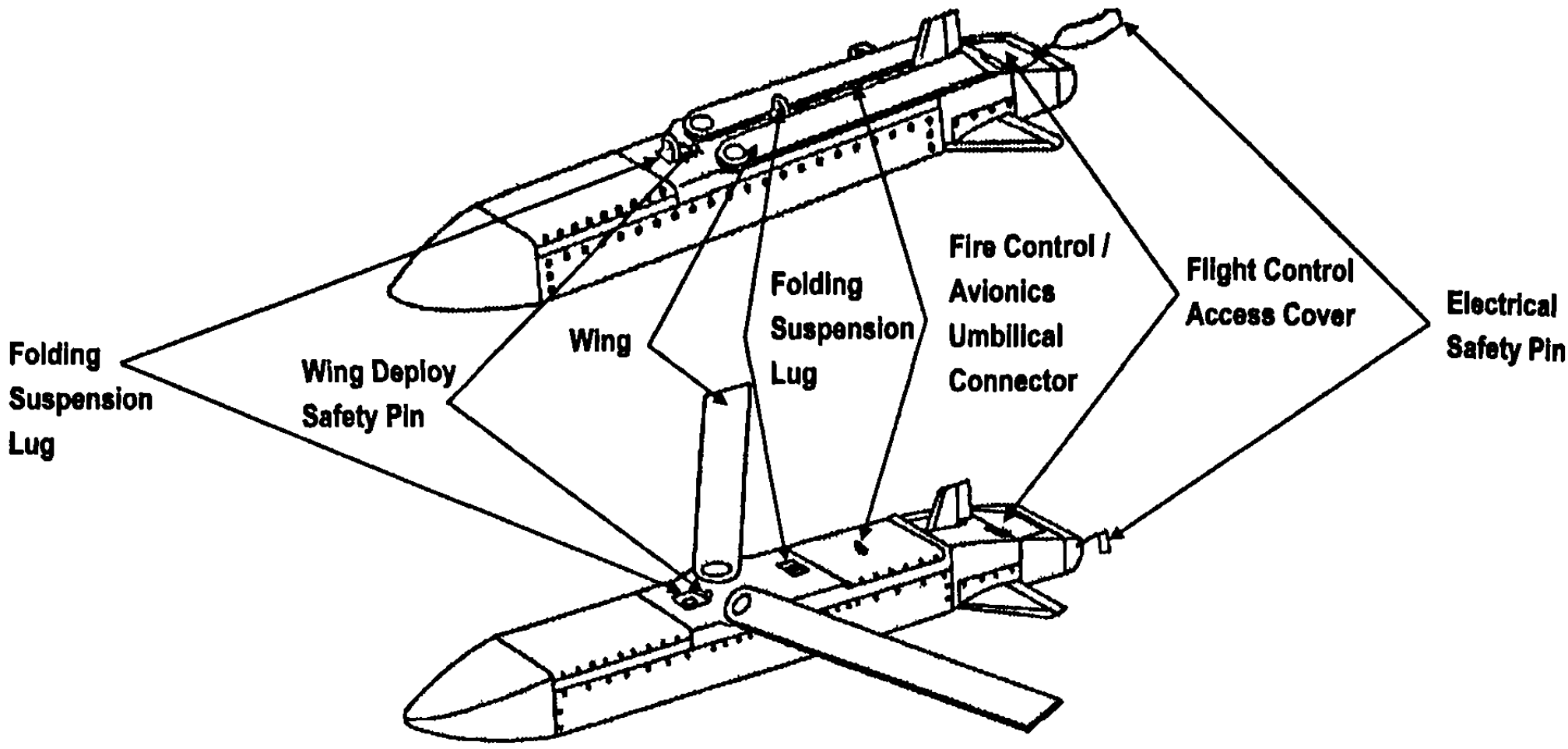

Example: ADM-141 TALD (Tactical Air-Launched Decoy)
Carriage and Fire Control Interfaces

Fig. 6.73 Example of aircraft carriage and fire control interfaces.

cockpit; folding suspension lugs; deployable wings after launch; and safety pin to prevent wing deployment prior to launch.

Figure 6.74 shows an example of a ship weapon carriage and launcher, the Mk41 VLS. VLS is a standard missile launcher for U.S. Navy ships. In the

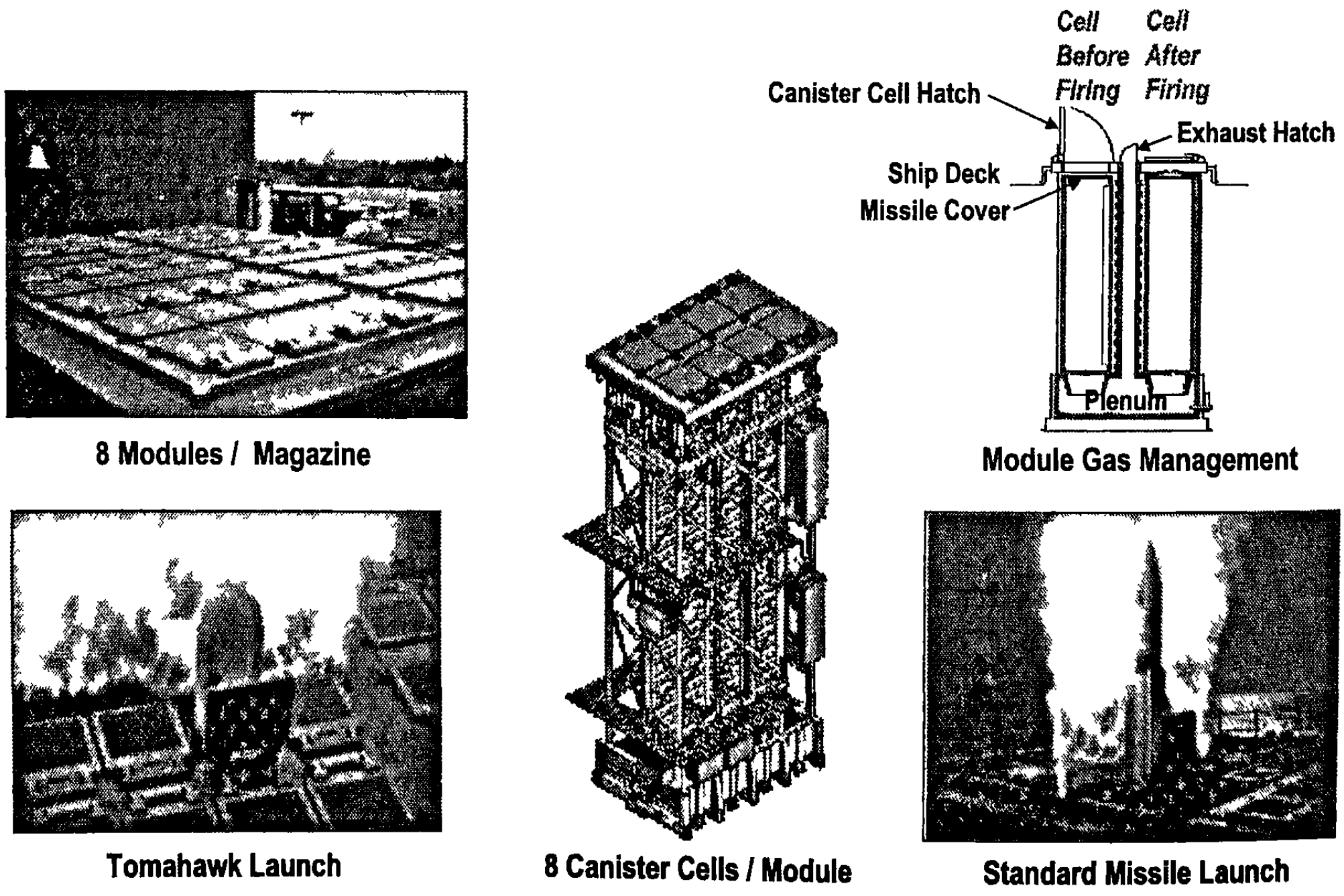

Fig. 6.74 Example of ship weapon carriage and launcher, Mk41 VLS. Figure also in color section.

upper left section of the figure is a photograph of a magazine consisting of eight modules. The center of the figure is a schematic of a module. There are eight canister cells in the module. The top right section of the figure shows an internal view of a canister before and after a missile firing. Also shown in the figure are photographs of Tomahawk and Standard missile launches. The VLS specifications for missile launch include a temperature range of −18 to 144° F, roll angle up to 29 deg, crosswind up to 75 knot, maximum gas flow rate up to 200 lb/s, and maximum gas flow rate increase 2000 lb/s/s.

Missiles must have sufficient robustness in their design to accommodate a broad environment during storage, shipping, and launch platform carriage. Figure 6.75 has examples of environmental requirements for temperature, humidity, rain, wind, salt fog, vibration, shock, and acoustics. Examples of concern at the temperature extremes are the propulsion and the warhead safety, reliability, and performance. Another concern is the effect of high rain rate, such as seeker dome erosion during carriage at high aircraft velocity. A typical requirement for missiles that are carried externally on aircraft is 1000 h of external carriage. A third example of an environmental concern is corrosion from salt fog, particularly for naval operation. An advantage of internal bay carriage over external carriage is that many of the carriage environment concerns are alleviated. However, some carriage environment concerns could be greater for internal carriage than that of external carriage. Examples for aircraft internal carriage are high vibration and acoustic loads when the internal carriage bay doors are open at a flight condition with high dynamic pressure.

MIL-HDBK-310 (Global Climatic Data for Developing Military Products) and the earlier MIL-STD-210 (Military Standard of Climatic Extremes for

Environmental Parameter	Typical Requirement
♦Surface Temperature	-60° F* to 160° F
♦Surface Humidity	5% to 100%
♦Rain Rate	120 mm / h**
Surface Wind	100 km / h steady***
	150 km / h gusts****
Salt fog	3 g / mm^2 per year
♦Vibration	10 g rms at 1000 Hz: MIL STD 810, 648, 1670A
Shock	Drop height 0.5 m, half sine wave 100 g / 10 ms: MIL STD 810, 1670A
Acoustic	160 dB

Video: Ground / Sea Environment

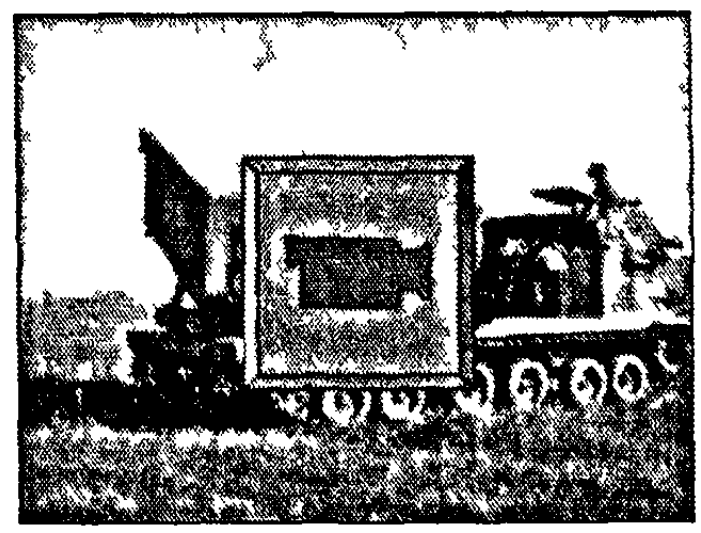

Note: MIL-HDBK-310 and earlier MIL-STD-210B suggest 1% world-wide climatic extreme typical requirement.

* Lowest recorded temperature = -90° F. 20% probability temperature lower than -60° F during worst month of worst location.

** Highest recorded rain rate = 436 mm / h. 0.5% probability greater than 120 mm / h during worst month of worst location.

*** Highest recorded steady wind = 342 km / h. 1% probability greater than 100 km / h during worst month of worst location.

**** Highest recorded gust = 378 km / h. 1% probability greater than 150 km / h during worst month of worst location.

Fig. 6.75 Robustness is required for carriage, shipping, and storage environment. Video is in the CD included with this textbook.

Military Equipment) were developed to provide data on the extremes of climate of global conflict in the areas north of 60 deg south latitude and less than 15,000 ft elevation. The extremes have near zero probability of being exceeded in the natural environment. It provides sets of climatic extremes for land, sea, and air operation.

It would not be cost effective to design a tactical missile for the worldwide climate extremes such as the lowest recorded temperature (−90° F), highest recorded wind speed (177 knots steady and 196 knots gust), and highest recorded rain rate (436 mm/h). A typical approach is to design a missile for operation in the 1% worldwide climatic extreme. An exception is the surface low temperature requirement, where the 20% extreme of −60° F is typically used because combat is less likely to occur in extremely cold areas of the world. The cold temperature requirement often varies depending upon the missile program emphasis of cost versus performance. As an example, the emphasis on developing a low-cost motor and seeker for Hellfire led to the selection of −40° F for the minimum temperature requirement. At the other extreme, the SRAM missile has a minimum temperature requirement of −80° F because of less emphasis on cost and high emphasis on low-temperature reliability and performance. Another exception to the 1% guideline is the rain rate requirement, where the 0.5% extreme is typically used. The 0.5% extreme of 120 mm/h is typically used because periods of high rain rate typically extend over more than one month each year and areas with high rain rate are also often areas of combat. Wind steady state and gust velocities are based on the 1% climatic extreme values of 100 km/h and 150 km/h, respectively. For a sea-launched missile, a steady wind speed of 100 km/h (54 knots) is representative of the upper boundary of a storm (wind speed 48–55 knots, sea state 10, and a wave height 29 ft). A violent storm would be sea state 11, with a steady wind speed of 56–63 knots and a wave height of 37 ft.

Air-launched missiles that are externally carried at high altitude may be subjected to very low carriage temperature. For example, Mach 0.6 external carriage at 50,000 ft altitude with a MIL-HDB-310 1% cold day results in a recovery temperature of −95° F. Also, air-launched missiles that are externally carried at high speed may be subjected to very high carriage temperatures. As an example, Mach 1.2 external carriage at sea level with a MIL-HDBK-310 hot day results in a recovery temperature of 310° F.

Designing a missile for worldwide expeditionary warfare requires more consideration of climatic extremes. Missiles that are designed for use in a smaller geographic area usually have more relaxed environmental requirements.

The video in the upper right corner of the figure illustrates the carriage and launch environments for the ground vehicle-launched MLRS, surface ship-launched Standard Missile, and surface ship/submarine-launched Tomahawk missile. For the MLRS, in addition to natural environment considerations such as temperature and rain, the tracked propulsion M270A1 and the wheeled propulsion high-mobility artillery rocket systems (HIMARS) launchers also subject the MLRS to a severe vibration and shock environment. For the Standard Missile, the sea salt corrosive environment is a particular concern. For submarine launch of the Tomahawk missile, the initial underwater environment is a concern.

6.10 Summary

This chapter addressed the broad considerations of measures of merit and launch platform integration. Considerations for robustness included the effectiveness of alternative sensors operating in adverse weather and clutter, the capability in off-design flight conditions, changes in performance with uncertainty, and the performance in countermeasures. Considerations for warhead lethality included warhead effectiveness against a broad range of targets, synergy with guidance accuracy, and the type of warhead (e.g., blast fragmentation, kinetic energy). Considerations for miss distance included the miss distance because of an initial heading error at seeker lock-on, miss distance because of a maneuvering target, miss distance from glint noise, and the contributions to the missile time constant by limited control effectiveness, flight control dynamics, and seeker dome error slope. Included in the considerations for carriage and launch observables were launch platform carriage RCS and missile plume visual signature for reduced observables. Other survivability considerations included missile radar cross section, missile flight altitude, mission planning, speed, terrain masking, and insensitive munitions. Considerations for reliability included the number of subsystems, parts count, types of parts, and subsystem complexity. Cost considerations included the types of subsystems, weight, system development duration and risk, production quantity/learning curve, parts count, logistics, production rate, culture/processes, and competition. Considerations for launch platform integration included firepower, weight, and fitment; launch envelope limitations; store separation; launch platform handling qualities; aircraft aeroelasticity; hangfire; vibration; compatibility with standard launchers; compressed carriage; avionics interface; and the carriage/storage environment.

Problems

6.1. IR signal attenuation is greater than 100 dB per km through a c____.

6.2. GPS/INS enhances seeker lock-on in adverse weather and ground c_____.

6.3. A data link can enhance missile seeker lock-on against a m_____ target.

6.4. An example of a missile counter-counter measure to flares is an i_____ i_____ seeker.

6.5. Compared to a midwave IR seeker, a long-wave IR seeker receives more energy from a c___ target.

6.6. High-fineness kinetic energy penetrators are required to defeat b_____ targets.

6.7. For the same lethality, a small decrease in miss distance allows a large decrease in the required weight of the w_____.

6.8. For a blast/frag warhead, a charge-to-metal ratio of about one is required to achieve a high total fragment k_____ e_____.

6.9. A blast fragmentation warhead tradeoff is the number of fragments versus the individual fragment w_____.

6.10. Kinetic energy penetration is a function of the penetrator diameter, length, density, and v_____.

6.11. In proportional homing guidance, the objective is to make the line-of-sight angle rate equal to z___.

6.12. Aeromechanics contributors to missile time constant are the flight control effectiveness, flight control system dynamics, and the seeker dome e____ s____.

6.13. Miss distance from heading error is a function of missile navigation ratio, velocity, time to correct the heading error, and the missile t___ c_____.

6.14. A missile must have about t_____ times the maneuverability of the target.

6.15. Minimizing the miss distance from radar glint requires a high-resolution seeker, an optimum missile time constant, and an optimum n_____ r____.

6.16. Weapons on low observable launch platforms use i_____ carriage.

6.17. Weapons on low observable launch platforms use m_____ smoke propellant.

6.18. For an insensitive munition, burning is preferable to detonation because it releases less p____.

6.19. Missile system reliability is enhanced by subsystem reliability and low p____ count.

6.20. High-cost subsystems of missiles are sensors, electronics, and p_____.

6.21. Missile SDD cost is driven by the program duration and r___.

6.22. Missile unit production cost is driven by the number of units produced, learning curve, and w_____.

6.23. First-level maintenance is conducted at a d____.

6.24. A standard launch system for U.S. Navy ships is the V_____ L____ S_____.

6.25. Most lightweight missiles use rail launchers while most heavy weight missiles use e_____ launchers.

6.26. Higher firepower is provided by c_____ carriage.

6.27. The typical environmental requirement from MIL-HDBK-310 is the _% worldwide climatic extreme.

7
Sizing Examples

7.1 Introduction

This chapter presents examples of sizing missile configurations and examples of computer-aided sizing tools for conceptual design. The topics presented are 1) sizing examples for the rocket baseline missile; 2) sizing examples for the ramjet baseline; 3) computer-aided sizing tools; and 4) an example of a "hands on" design, build, and fly activity. The rocket baseline missile sizing examples address air-to-air standoff range requirement, wing sizing requirement, multiparameter harmonization, and lofted range comparison. Ramjet baseline missile sizing examples are range robustness, propulsion and fuel alternatives, and velocity control. The computer-aided sizing tools for conceptual design that are addressed are a DOS-based code and a spreadsheet code. The design, build, and fly sizing example is based on the student developing a soda straw rocket.

7.2 Standoff Range Requirement

The rocket baseline missile will be used to illustrate the establishment and substantiation of an air-to-air missile standoff range requirement, wing sizing for maneuverability, multiparameter harmonization of missile weight/miss distance, and lofted trajectory range comparison with conventional trajectories. The first example is sizing the rocket baseline missile to meet an air-to-air standoff range requirement.

The air-to-air missile flight range in this example is derived from the speed and range required for standoff survivability of the launch aircraft. The assumed requirement is to provide an F-pole range that allows a kill of a head-on threat outside the threat weapon launch range. For air-to-air combat, the visual detection range by the threat is $R_D \approx 3.3$ n miles for a typical aircraft contrast of $C = 0.18$. We will assume that the threat fire control system does not have a beyond-visual-range engagement capability. The maximum launch range of the threat missile is assumed to be the visual detection range. This sets the required F-pole range of 3.3 n miles. The assumed altitude and speed of the launch aircraft (blue), target aircraft (red, threat), and the launch aircraft missile (blue) for this analysis are $h = 20{,}000$ ft, $V_L = 820$ ft/s (Mach 0.8), $V_T = 820$ ft/s, and $V_M = 2\,V_T = 1640$ ft/s respectively.

The assumed air-to-air scenario is shown in Fig. 7.1. The required launch range R_L and F-pole range $R_{F\text{-}Pole}$ are functions of the missile average velocity

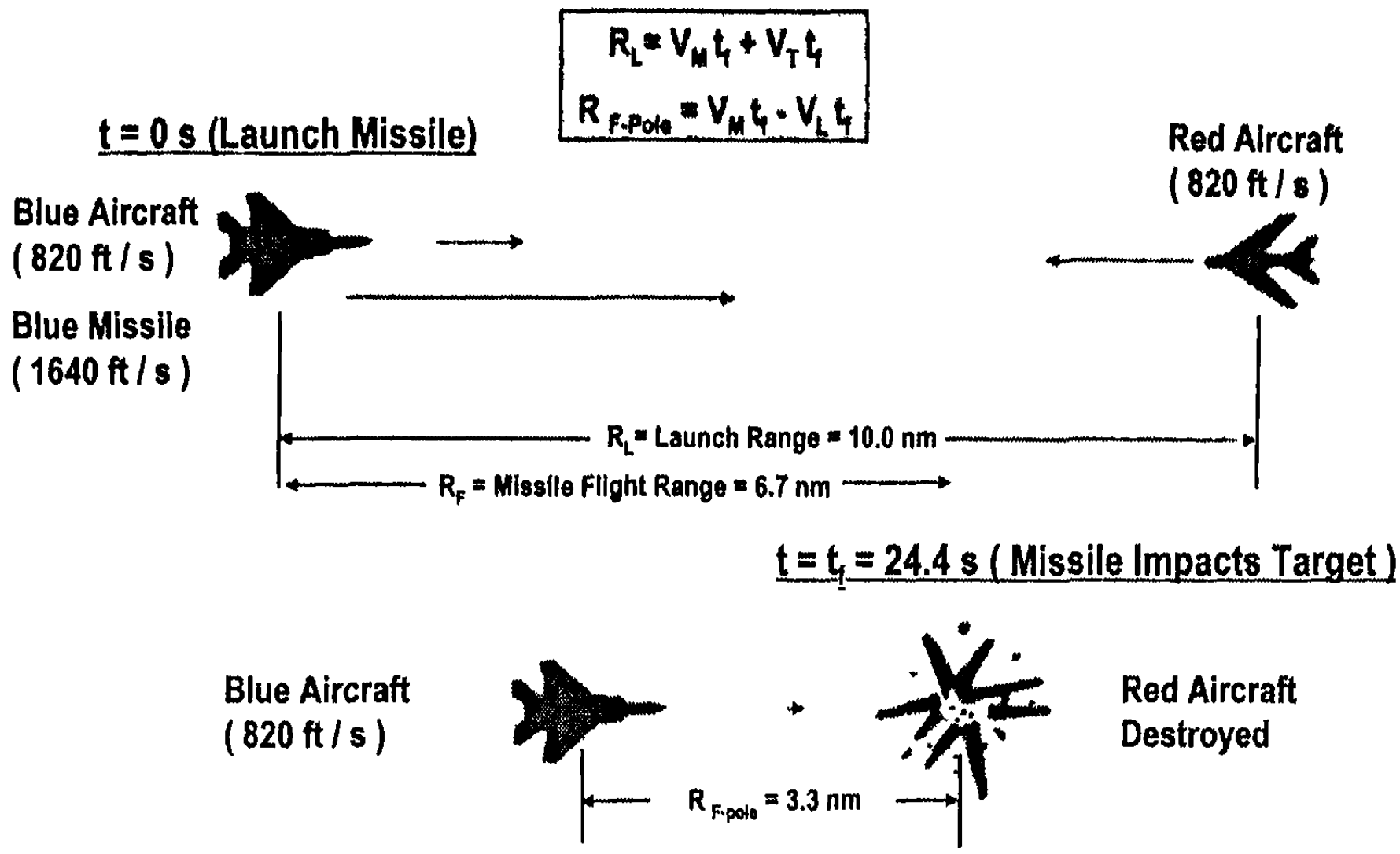

Fig. 7.1 Assumed air-to-air engagement scenario for head-on intercept. Figure also in color section.

V_M, missile time of flight t_f, and the target average velocity V_T. The equations are

$$R_L = V_M t_f + V_T t_f \tag{7.1}$$

$$R_{F\text{-Pole}} = V_M t_f - V_L t_f \tag{7.2}$$

Referring to Fig. 7.1, note that to provide an $R_{F\text{-Pole}} = 3.3$ n miles, the rocket baseline missile must be launched at 10.0 n miles from the target and have a flight range of 6.7 n miles within 24.4 s. Because the launch range is greater than the visual detection range, noncooperative target identification (NCTID) capability is required for the launch aircraft fire control system to avoid fratricide to friendly or neutral aircraft.

A simplified model of the typical ranges at which a pilot can detect and recognize a typical aircraft target is shown in Fig. 7.2. The detection range and the recognition range are assumed to be primarily driven by the target contrast C, target presented area A_{tp}, and the threshold contrast C_T. The equation for visual detection range is

$$R_D = 1.15[A_{tp}(C - C_T)]^{1/2} \tag{7.3}$$

The equation for visual recognition range is

$$R_R = 0.29\, R_D \tag{7.4}$$

The assumptions are a 50% probability of detection and recognition, visual fovial angle of 0.8 deg, pilot glimpse time during search of 1/3 s, and clear weather. Referring to Fig. 7.2, note that the detection range is reduced as the contrast is reduced. A design consideration for aircraft integration of tactical

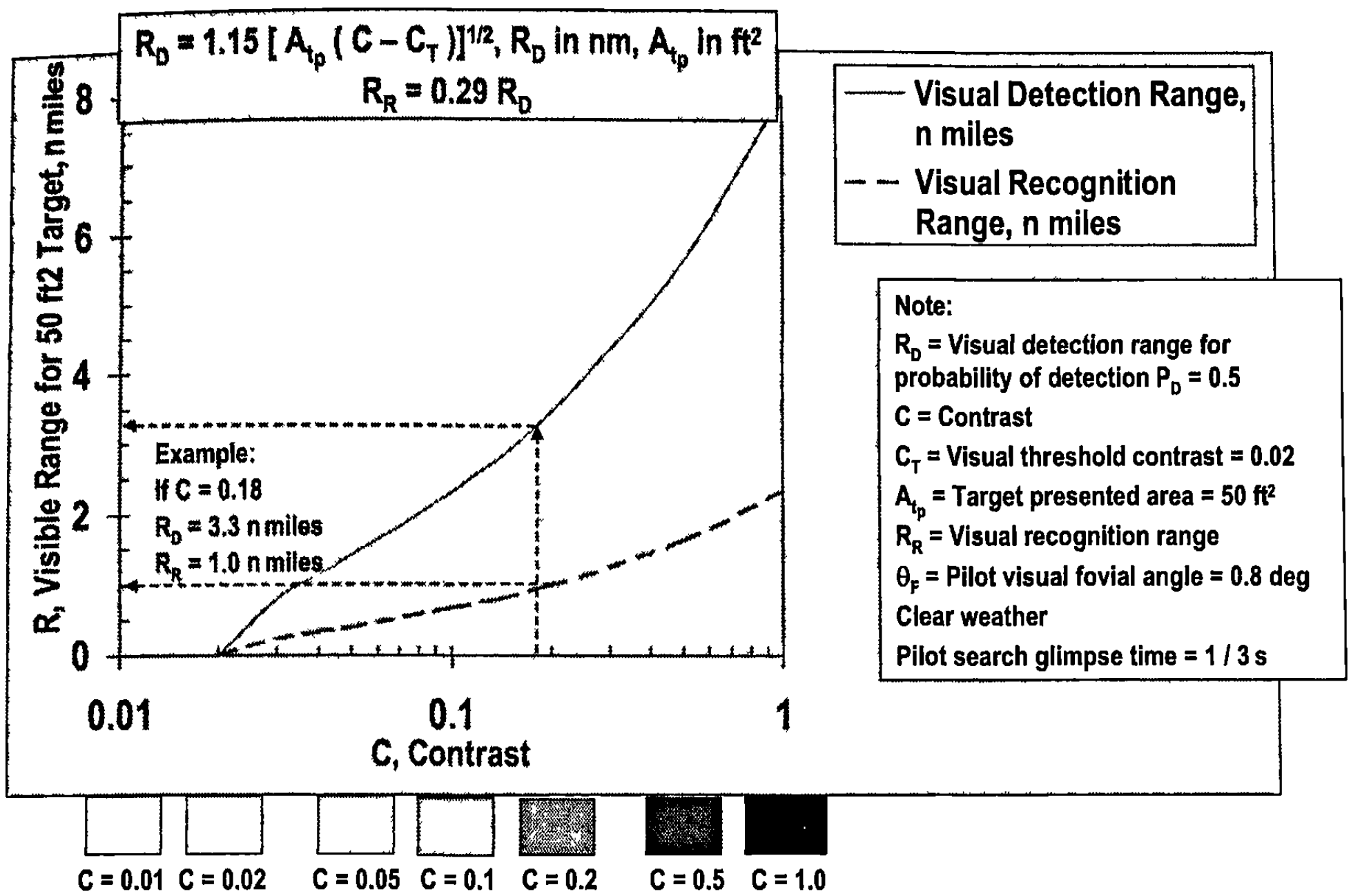

Fig. 7.2 Target contrast and size drive visual detection and recognition range.

missiles is to use a paint scheme for the missile (e.g., gray) that matches the paint scheme of the launch aircraft. Note from the figure that for an assumed target contrast $C = 0.18$, target presented area $A_{tp} = 50\ \text{ft}^2$, and threshold contrast $C_T = 0.02$, the visual detection range is $R_D = 3.3$ n miles. The visual recognition range is 29% of the detection range, giving $R_R = 0.29R_D = 1.0$ n miles. Assumptions for the analysis of this example are:

1) The threat does not have NCTID or a beyond-visual-range missile.
2) The threat will launch a within-visual-range missile (e.g., Sidewinder type) when it is within visual detection range.
3) Probability of detection by the threat is $P_D = 0.5$.
4) Threat pilot visual acuity angle θ_F (fovial angle of the eye) = 0.8 deg.
5) The weather is clear.
6) Threat pilot uses an optimum glimpse time for an air-to-air search ($\approx$1/3 s).

At the bottom of the figure is a grayscale of contrast ranging from $C = 0.01$ to 1.0. Note that it is difficult to distinguish the difference between the contrast and the white background for $C = 0.02$. Visual detection is also influenced by other parameters such as color, relative motion, and scintillation.

Figure 7.3 shows the relative standoff range $R_{\text{F-Pole}}$ between the launch platform and the target at missile intercept. $R_{\text{F-Pole}}$ is a function of missile velocity V_M, threat aircraft velocity V_T, and the launch platform velocity V_L. The equation is

$$R_{\text{F-Pole}}/R_L = 1 - (V_T + V_L)/(V_M + V_T) \tag{7.5}$$

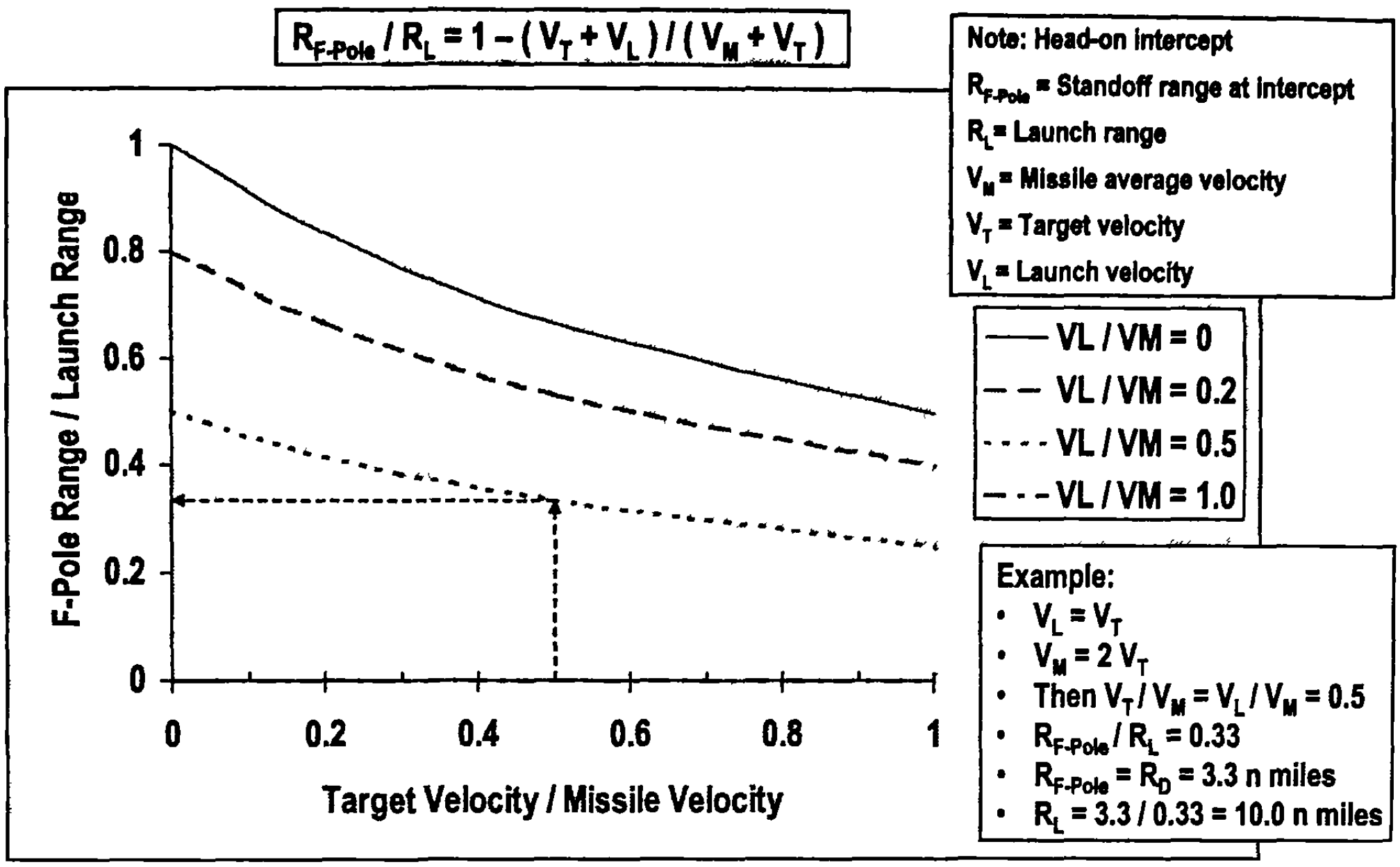

Fig. 7.3 High missile velocity improves standoff range.

An assumption is a head-on intercept engagement. Note that the longest F-pole range is for a missile velocity that is much greater than the threat target velocity.

As an example, assume that the average missile velocity is twice that of the target ($V_M/V_T = 2$). Also assume that the launch platform is an aircraft with the same velocity as the target aircraft ($V_L/V_T = 1$). Then $V_T/V_M = 0.5$ and $V_L/V_M = 0.5$. If the F-pole range is required to be the same as the detection range, then $R_{F\text{-Pole}} = R_D = 3.3$ n miles. Substituting into the above equations, the missile launch range is calculated to be $R_L = 10.0$ n miles.

As shown in Fig. 7.4, the missile flight range R_F that is required to intercept a target is a function of the launch range R_L, missile velocity V_M, target velocity V_T, and the target aspect (i.e., head-on, tail chase). The equations are

$$(R_F/R_L)_{\text{Head-on}} = (V_M/V_T)/[(V_M/V_T) + 1] \tag{7.6}$$

$$(R_F/R_L)_{\text{TailChase}} = (V_M/V_T)/[(V_M/V_T) - 1] \tag{7.7}$$

Note from the figure that a higher speed missile reduces the required flight range for a tail chase intercept and increases the required flight range for a head-on intercept.

As an example using the rocket baseline flight missile range, assume the head-on intercept engagement discussed previously. For an average missile velocity $V_M = 1640$ ft/s and an average target velocity of $V_T = 820$ ft/s, the flight range is 67% of the launch range. For a launch range $R_L = 10.0$ n miles, the required missile flight range $R_F = 6.67$ n miles.

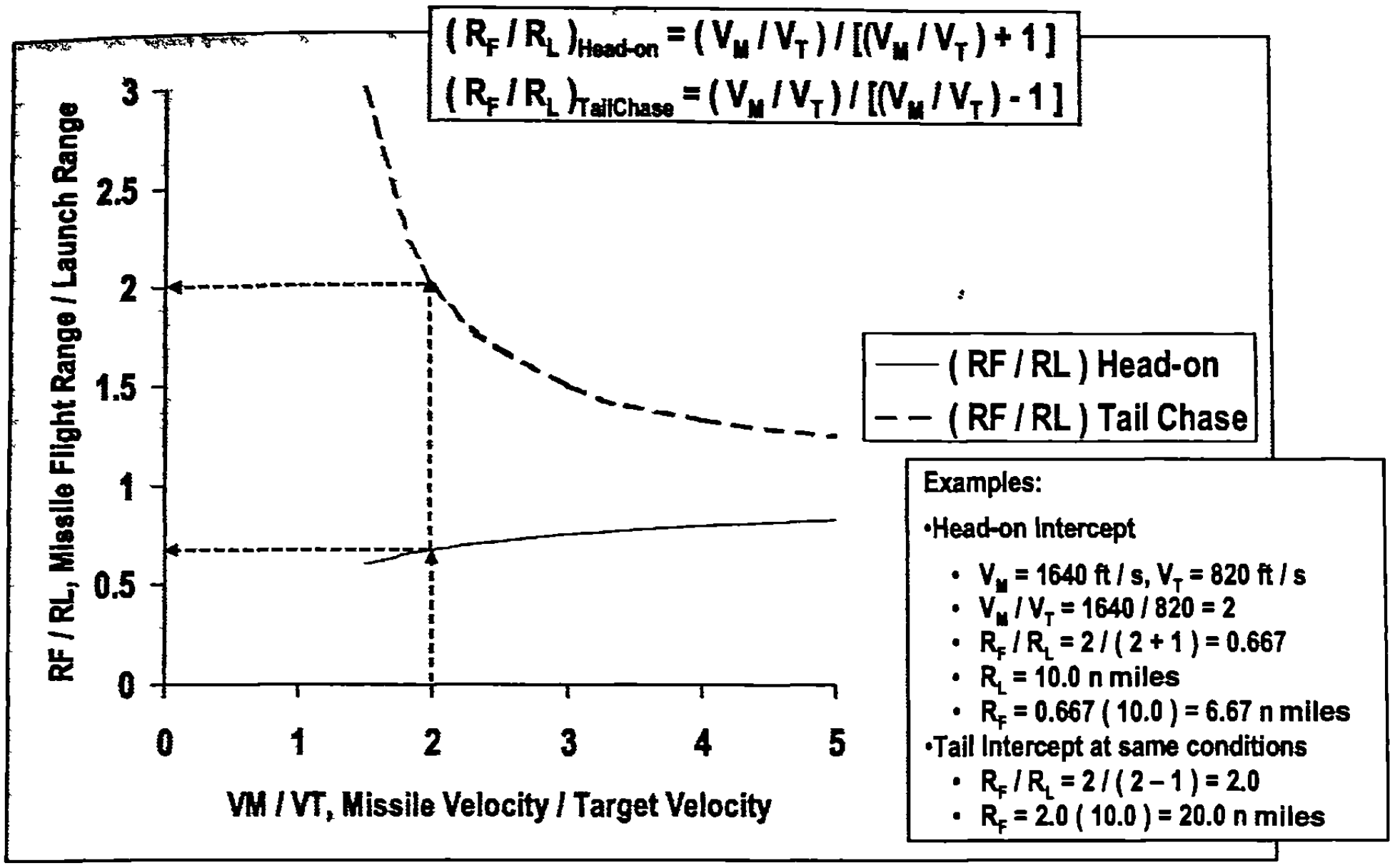

Fig. 7.4 Missile flight range requirement is greatest for a tail chase intercept.

Note from the figure that the missile flight range requirement is greatest for a tail chase intercept. If the target in the engagement discussed previously were retreating from the launch aircraft, for the same assumptions of launch range ($R_L = 10.0$ n miles), missile average velocity ($V_M = 1640$ ft/s), and target average velocity ($V_T = 820$ ft/s), the required flight range of the missile is increased by 200% (20.0 vs 6.67 n miles).

A configuration drawing of the rocket baseline missile, which is similar to the Sparrow missile, is shown in Fig. 7.5 from Ref. 27. The rocket baseline is a radar-guided missile. It has a design flight range of about 7 n miles when launched at an altitude of 20,000 ft. The missile uses cruciform wings as control surfaces. Fixed cruciform tail surfaces provide static stability. Missile launch weight is 500 lb, including 133 lb of propellant. The rocket motor has a boost-sustain thrust profile with 32,272 lb-s total impulse. The motor grain configuration is an internal burner type with three radial slots, aft-end longitudinal slots, and a center web grain. The nozzle has a 1.81-in^2 throat area and provides an expansion ratio of 6.2.

Note from the figure that the missile diameter $d = 8$ in, total wing span $b_w = 40.2$ in, and length $l = 143.9$ in. Shown are the length of the rocket motor and the section lengths/bulkhead locations. The missile is divided into nose, forebody, payload bay, midbody, aftbody, and the tailcone sections. The wing geometry in the figure includes the wing span, sweep angle, location of the mean aerodynamic chord, length of the root chord and its location, and the length of the tip chord. The tail geometry shown in the figure includes the tail span, sweep angle, location of the mean aerodynamic chord, length of the root chord, and the location of the root chord.

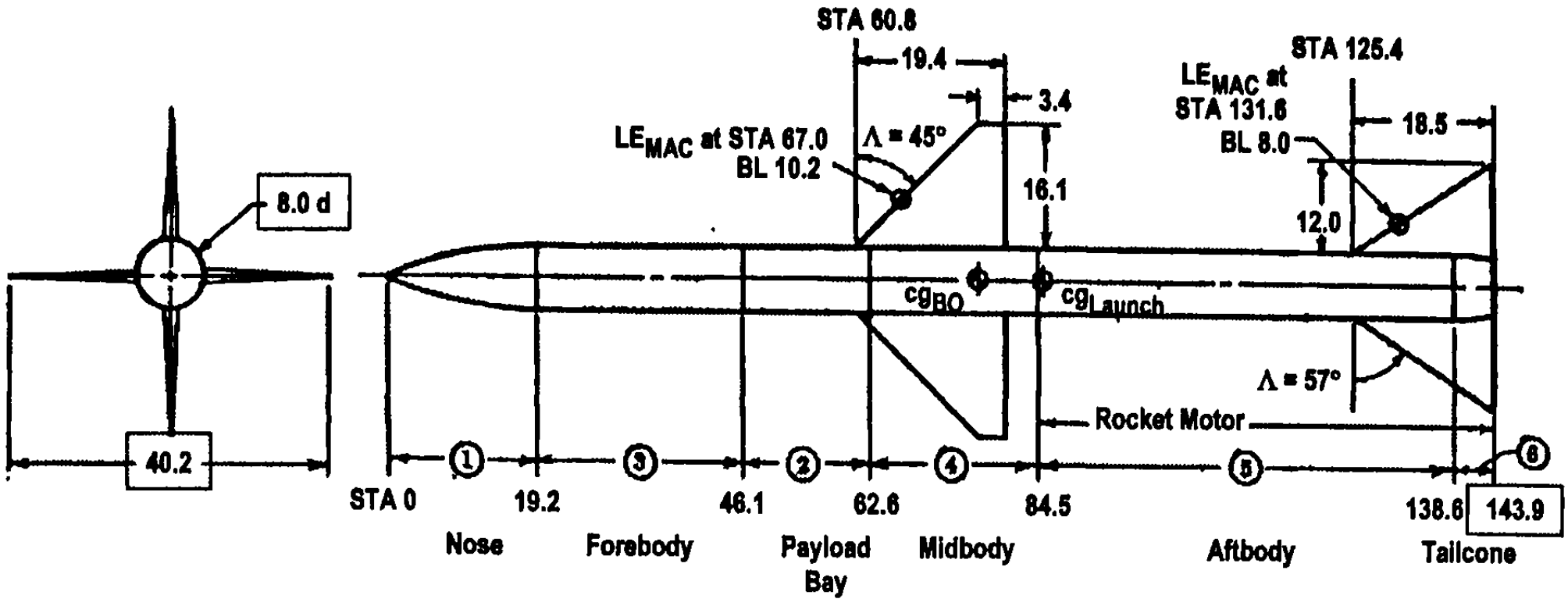

Note: Dimensions in inches

Source: Bithell, R.A. and Stoner, R.C., "Rapid Approach for Missile Synthesis, Vol. 1, Rocket Synthesis Handbook," AFWAL-TR-81-3022, Vol. 1, March 1982.

Fig. 7.5 Drawing of rocket baseline missile configuration.

The rocket baseline missile weight and balance statement is given in Table 7.1, derived from Ref. 27. Note that the burnout weight $W_{BO} = 367$ lb, the launch weight $W_L = 500$ lb, and the propellant weight $W_P = 133$ lb. The center-of-gravity location is 84.6 in from the nose tip at launch and 76.2 in from the nose tip at burnout. There is a large forward movement (1.05 diam) in the center of gravity during motor burn, resulting in excess static margin.

Table 7.1 Mass properties of rocket baseline missile

Component	Weight, lb.	C.G. STA, in.
① Nose (Radome)	4.1	12.0
③ Forebody structure	12.4	30.5
Guidance	46.6	32.6
② Payload Bay Structure	7.6	54.3
Warhead	77.7	54.3
④ Midbody Structure	10.2	73.5
Control Actuation System	61.0	75.5
⑤ Aftbody Structure	0.0	–
Rocket Motor Case	47.3	107.5
Insulation (EDPM-Silica)	23.0	117.2
⑥ Tailcone Structure	6.5	141.2
Nozzle	5.8	141.2
Fixed Surfaces	26.2	137.8
Movable Surfaces	38.6	75.5
Bumout Total	367.0	76.2
Propellant	133.0	107.8
Launch Total	500.0	84.6

The total weight of the aluminum airframe structure, wing and tail surfaces, and the steel motor case is 30% of the missile launch weight.

Reference 27 provides the rocket baseline missile geometric data, material data, configuration reference data, and propulsion data. Table 7.2, based on Ref. 27, shows data on the body and movable wing surfaces. The material for the body, wing, and tail structure is Aluminum 2219-T81. The radome is pyroceram.

Continuing with Table 7.2, additional information is provided on the movable wings, fixed aft stabilizers, and the configuration reference values. The configuration reference area for the rocket baseline missile is $S_{\text{Ref}} = 0.349$ ft^2. It is the body cross-sectional area. The configuration reference length of the rocket baseline missile is $l_{\text{Ref}} = d = 8$ in (0.667 ft). It is the body diameter.

Also shown in Table 7.2 are additional configuration reference values, rocket motor performance data, and propellant characteristics. The pitch/yaw moment of inertia is 117.0 slug-ft^2 at launch and 94.0 slug-ft^2 at burnout. The rocket motor boost thrust and boost burn time are 5750 lb and 3.69 s respectively. The sustain thrust and sustain burn time are 1018 lb and 10.86 s respectively. The assumed altitude and temperature are 20,000 ft and 70° F respectively. Boost and sustain propellant weight are 84.8 lb and 48.2 lb respectively.

The conclusion of Table 7.2 provides data on the rocket motor case and nozzle. The structural material for the rocket motor case and the nozzle housing is 4130 heat treated steel. It has a yield and ultimate tensile strength of 170,000 psi and 190,000 psi respectively. The rocket motor case length is 59.4 in and the cylindrical case thickness is 0.074 in. The nozzle has an expansion ratio of 6.2. Nozzle length is 4.9 in.

A graph of the rocket baseline simplified thrust-time history is shown in Fig. 7.6. The boost thrust is 5.6 times the sustain thrust (5750 vs 1018 lb). The sustain burn time is 2.9 times longer than the boost burn time (10.86 vs 3.69 s). The boost and sustain thrust profiles shown in the figure are a simplified approximation of the actual thrust profiles. The thrust time matches the total impulse $\int T dt$ of the actual rocket motor. Because thrust is much larger than drag during boost, the incremental velocity during boost is driven by the boost total impulse $\int T dt = 21{,}217$ lb-s. The total impulse during sustain is $\int T dt = 11{,}055$ lb-s.

Figure 7.7a from Ref. 27 shows the rocket baseline missile pitching moment C_m and normal force coefficient C_N as a function of angle of attack and Mach number. The figure is based on undeflected control surfaces ($\delta = 0$ deg). Note that the pitching moment coefficient and normal force coefficient decrease with increasing supersonic Mach number. The reference center-of-gravity location for the aerodynamic data is $x_{CG} = 75.7$ in from the nose tip, slightly forward of the burnout center of gravity.

Figure 7.7b shows other aerodynamic data consisting of the rocket baseline missile normal force coefficient derivative from control surface deflection C_{N_δ}, zero-lift drag coefficient ($C_{D_0} = C_A$ at $\alpha = 0$ deg), corrections to the axial force coefficient because of control surface deflection and angle of attack (K_1, K_2), and the pitching moment coefficient derivative from control surface deflection C_{m_δ}. The power-off (coast) drag coefficient is higher because of the additional drag from the base pressure. Note the decrease in the aerodynamic coefficients and derivatives with increasing supersonic Mach number.

Table 7.2 Rocket baseline missile definition

Body	
Dome Material	Pyroceram
Airframe Material	Aluminum 2219-T81
Length, in	143.9
Diameter, in	8.0
Airframe thickness, in	0.16
Fineness ratio	17.99
Volume, ft^3	3.82
Wetted area, ft^2	24.06
Nozzle exit area, ft^2	0.078
Boattail fineness ratio	0.38
Nose fineness ratio	2.40
Nose bluntness	0.0
Boattail angle, deg	7.5
Movable surfaces (forward)	
Material	Aluminum 2219-T81
Planform area, ft^2 (2 panels exposed)	2.55
Wetted area, ft^2 (4 panels)	10.20
Aspect ratio (2 panels exposed)	2.82
Taper ratio	0.175
Root chord, in	19.4
Tip chord, in	3.4
Span, in (2 panels exposed)	32.2
L.E. sweep, deg	45.0
M.A.C., in	13.3
Thickness ratio	0.044
Section type	Modified double wedge
Section leading edge total angle, deg	10.01
X MAC, in	67.0
Y MAC, in (from root chord)	6.2
Actuator rate limit, deg/s	360.0
Fixed surfaces (aft)	
Material	Aluminum 2219-T81
Modulus of elasticity, 10^6 psi	10.5
Planform area, ft^2 (2 panels exposed)	1.54
Wetted area, ft^2 (4 panels)	6.17
Aspect ratio (2 panels exposed)	2.59
Taper ratio	0.0
Root chord, in	18.5
Tip chord, in	0.0
Span, in (2 panels exposed)	24.0
L.E. sweep, deg	57.0
M.A.C., in	12.3
Thickness ratio	0.027

(Continued)

Table 7.2 Rocket baseline missile definition (Continued)

Section type	Modified double wedge
Section leading edge total angle, deg	6.17
X MAC, in	131.6
Y MAC, in (from root chord)	4.0
References values	
Reference area, ft^2	0.349
Reference length, ft	0.667
Pitch/Yaw Moment of inertia at launch, slug-ft^2	117.0
Pitch/Moment of inertia at burnout, slug-ft^2	94.0
Rocket Motor Performance (altitude = 20,000 ft, temp = 70° F)	
Burning time, sec (boost/sustain)	3.69/10.86
Maximum pressure, psi	2042
Average pressure, psi (boost/sustain)	1769/301
Average thrust, lbf (boost/sustain)	5750/1018
Total impulse, lbf-s (boost/sustain)	21217/11055
Specific impulse, lbf-s/lbm (boost/sustain)	250/230.4
Propellant	
Weight, lbm (boost/sustain)	84.8/48.2
Flame temperature @ 1000 psi, °F	5285/5228
Propellant density, lbm/in^3	0.065
Characteristic velocity, ft/s	5200
Burn rate @ 1000 psi, in/s	0.5
Burn rate pressure exponent	0.3
Burn rate sensitivity with temperature, %/°F	0.10
Pressure sensitivity with temperature, %/°F	0.14
Rocket Motor Case	
Yield/ultimate strength, psi	170,000/190,000
Material	4130 Steel
Modulus of elasticity, psi	29.5×10^6 psi
Length, in	59.4
Outside diameter, in	8.00
Thickness, in (minimum)	0.074
Burst pressure, psi	3140
Volumetric efficiency	0.76
Grain configuration	Three slots + web
Dome ellipse ratio	2.0
Nozzle	
Housing material	4130 Steel
Exit geometry	Contoured (equiv. 15°)
Throat area, in^2	1.81
Expansion ratio	6.2
Length, in	4.9
Exit diameter, in	3.78

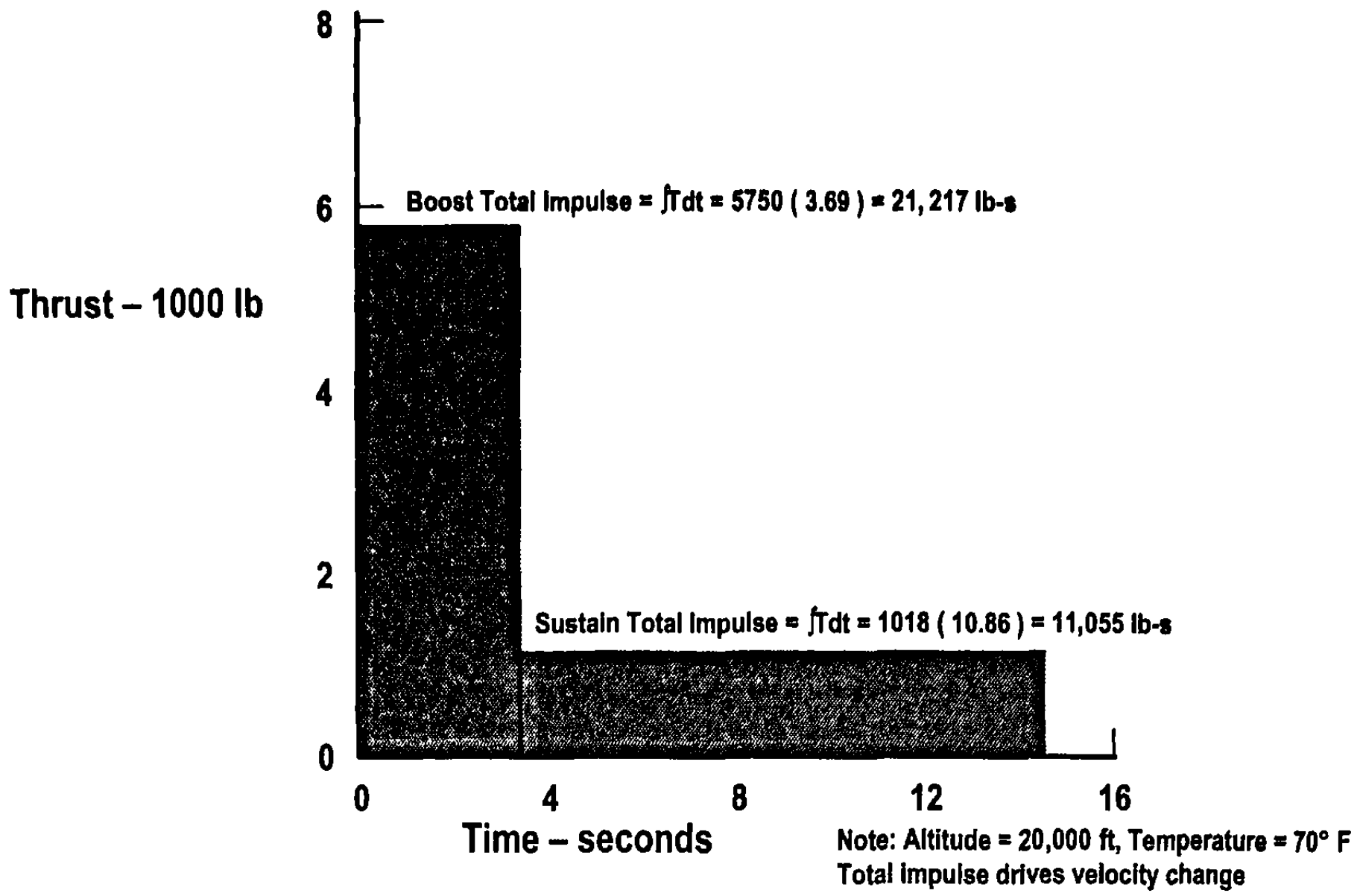

Fig. 7.6 Rocket baseline missile has boost-sustain thrust-time history.

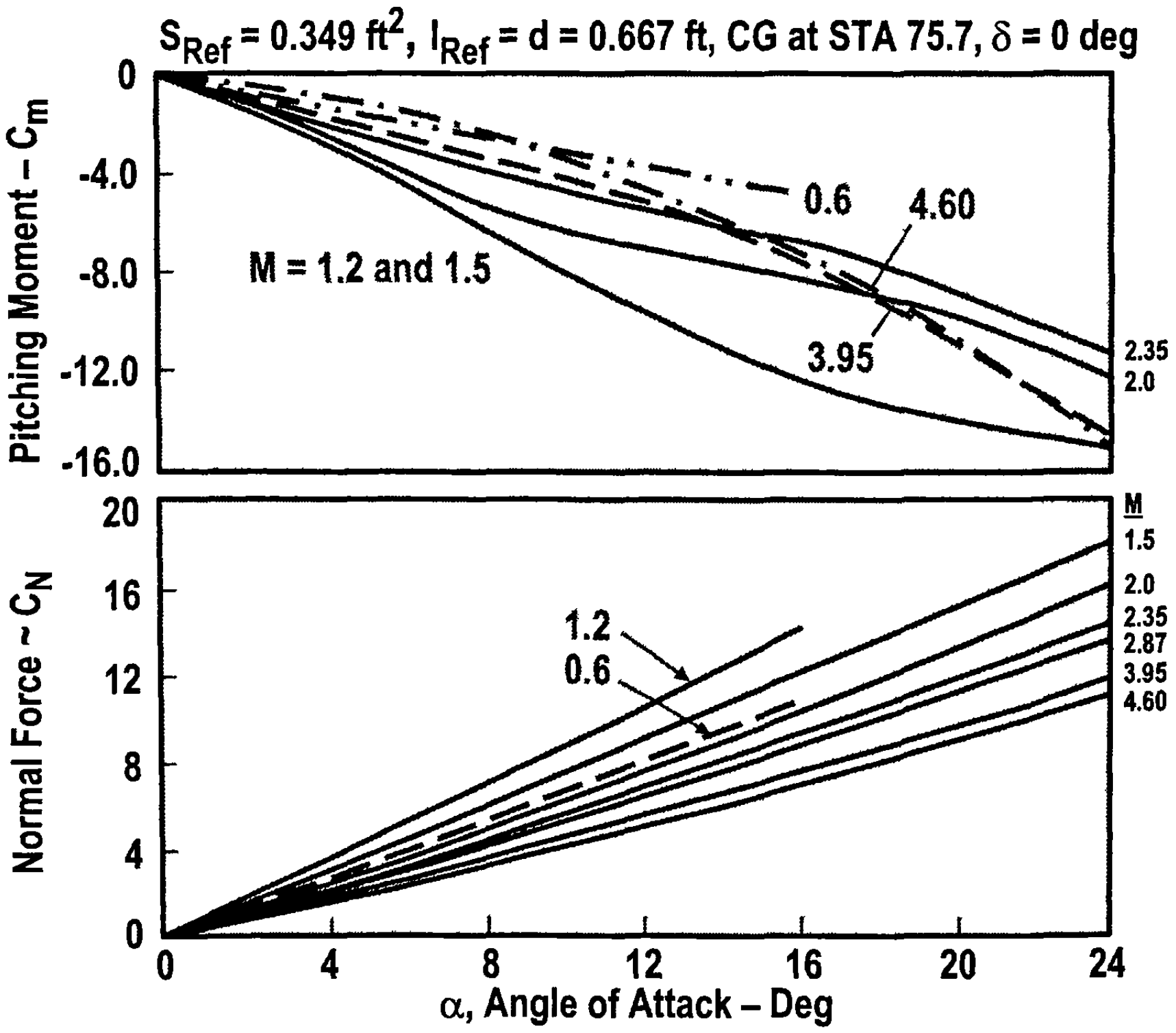

Fig. 7.7a Rocket baseline missile aerodynamic characteristics: pitching moment and axial force.

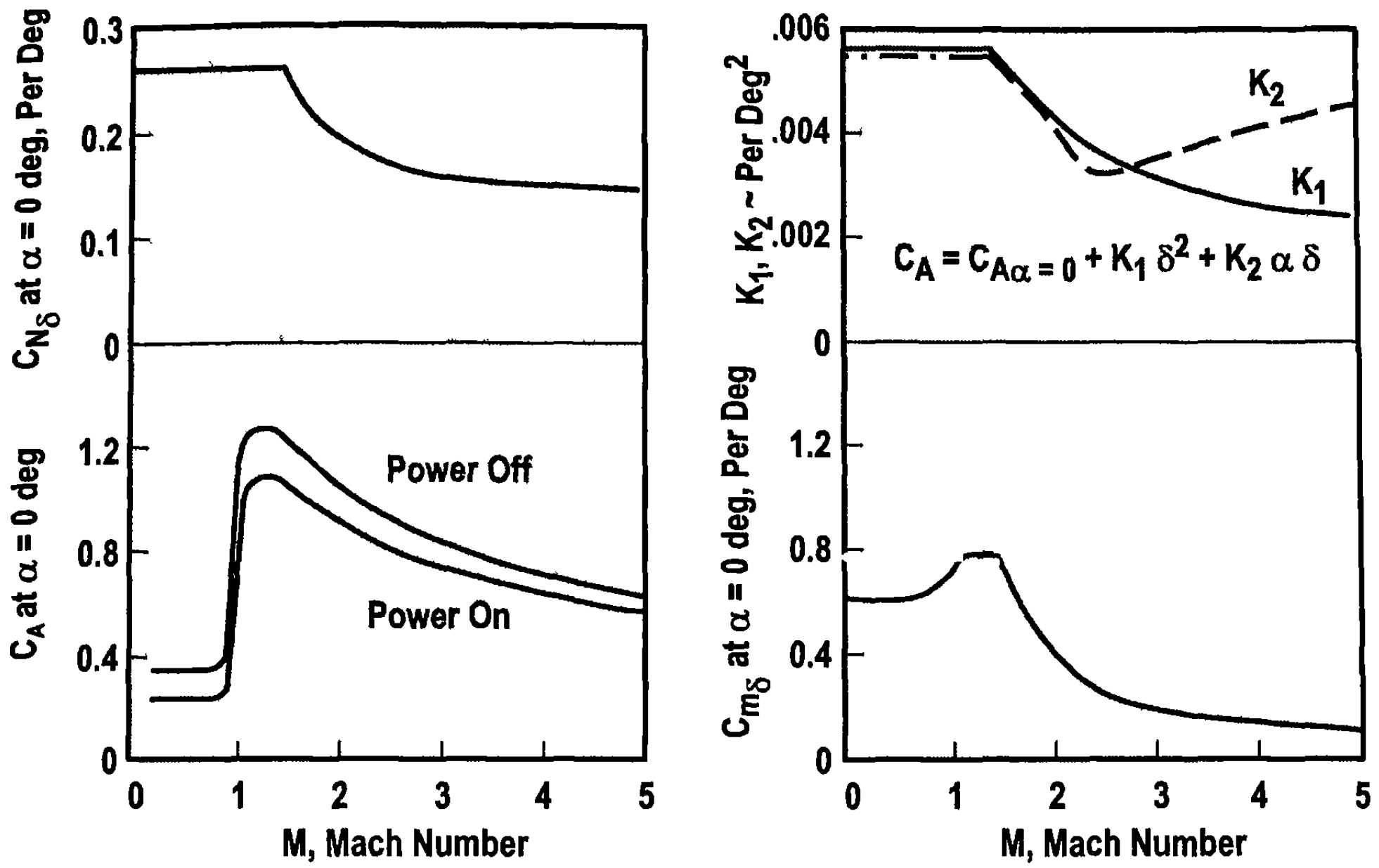

Fig. 7.7b Rocket baseline missile aerodynamic characteristics: other aerodynamic characteristics.

The maximum forward flight-range performance for an assumed Mach 0.7 launch and Mach 1.5 termination is shown in Fig. 7.8, based on Ref. 27. The flight range increases with high-altitude launch because of the lower drag and higher L/D at high altitude. For sea-level flight the sustain thrust Mach number is Mach 1.5, the same as the end-of-boost Mach number.

Off-boresight maneuverability performance of the rocket baseline missile is shown in Fig. 7.9 from Ref. 27. The best turn performance is at low altitude with high angle of attack. Note that the missile envelope shown in the figure is an ideal, unconstrained envelope. A typical seeker gimbal angle limit (e.g., $+/-30$ deg) and a requirement for lock-on before launch would limit the missile off-boresight envelope to about $+/-30$ deg. A seeker with high gimbal angle (e.g., $+/-90$ deg) and a lock-on after launch capability facilitate a large off-boresight envelope.

A flight performance Paredo sensitivity study was conducted of the rocket baseline missile to determine the most significant parameters and the required accuracy for prediction methods. Note from Fig. 7.10 that the flight range is most sensitive to changes in specific impulse, propellant weight, zero-lift drag coefficient, drag due to lift, and static margin. In the Paredo, these provide more than 90% of the sensitivity. The sensitivity study was conducted at a nominal flight condition of an altitude $h_L = 20{,}000$ ft, launch Mach number $M_L = 0.7$, and an end-of-coast Mach number $M_{EC} = 1.5$. The nominal flight range is $R_{@M_L=0.7,\ h_L=20{,}000\ \text{ft}} = 9.5$ n miles.

As an example, note from the figure that a 10% increase in propellant weight provides an 8.8% increase in flight range.

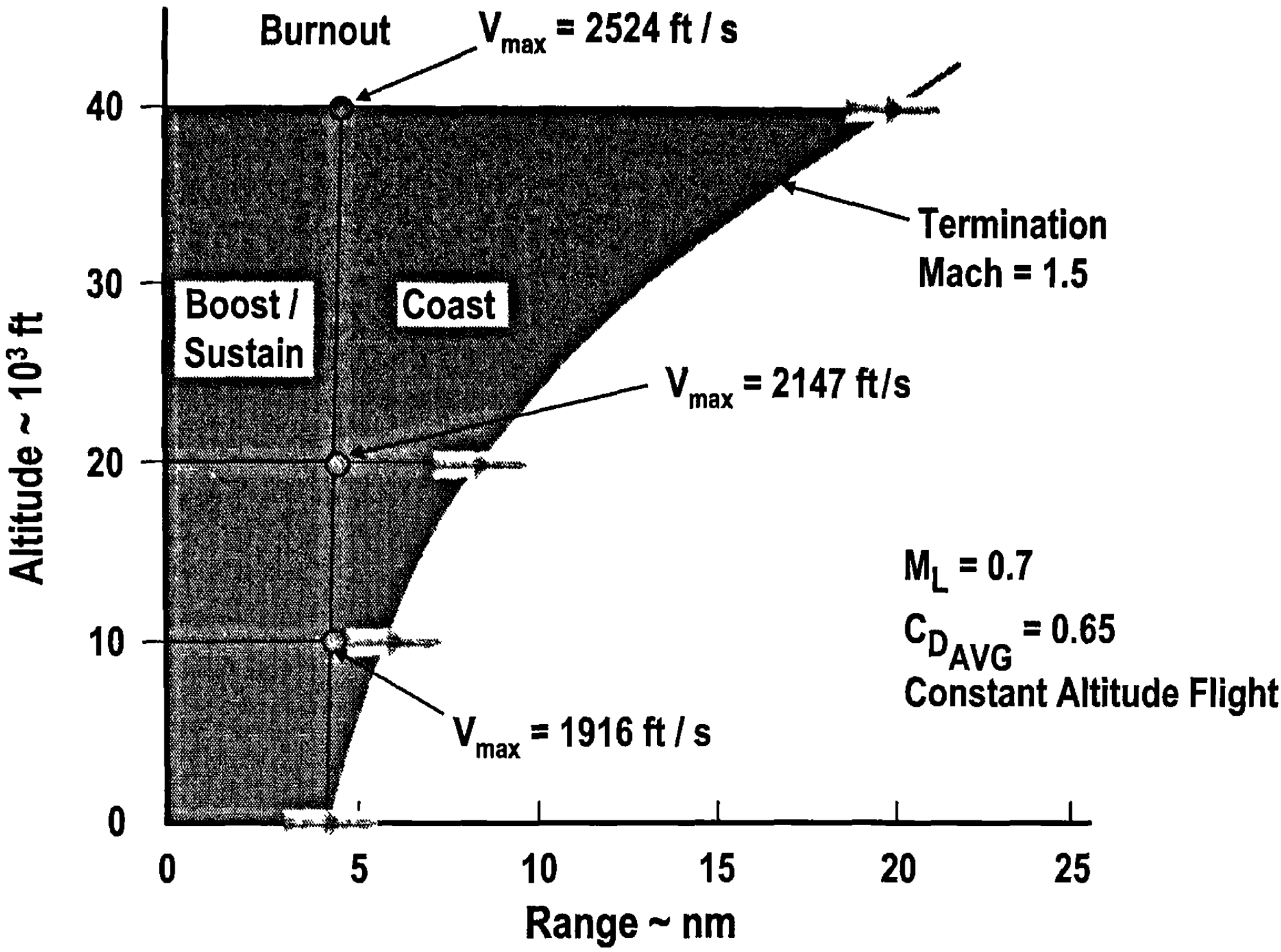

Fig. 7.8 High-altitude launch enhances rocket baseline range.

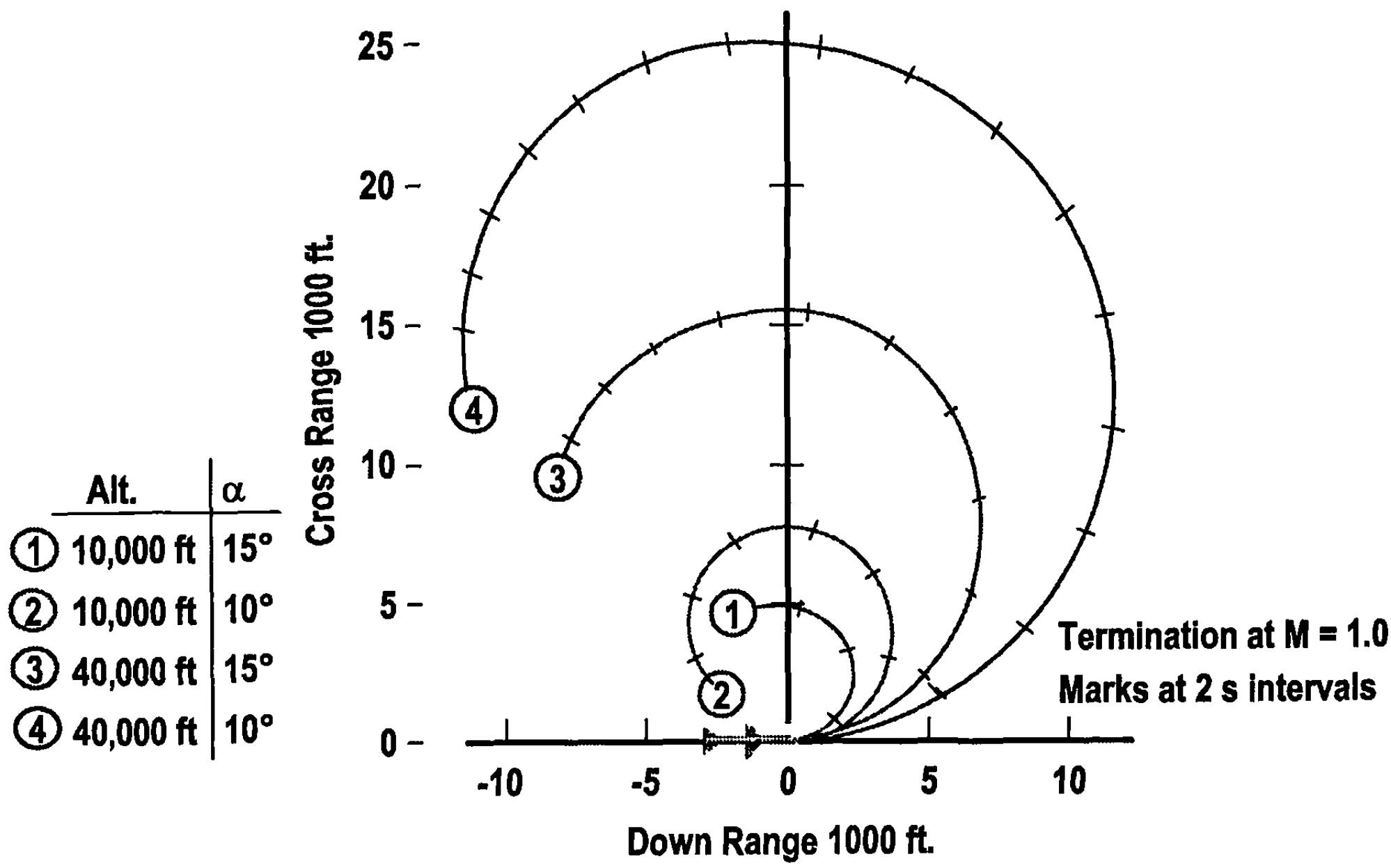

Note: Off-boresight envelope that is shown does not include the rocket baseline seeker field-of-regard limit (30 deg).

Fig. 7.9 Low-altitude launch and high alpha maneuvers enhance rocket baseline turn performance.

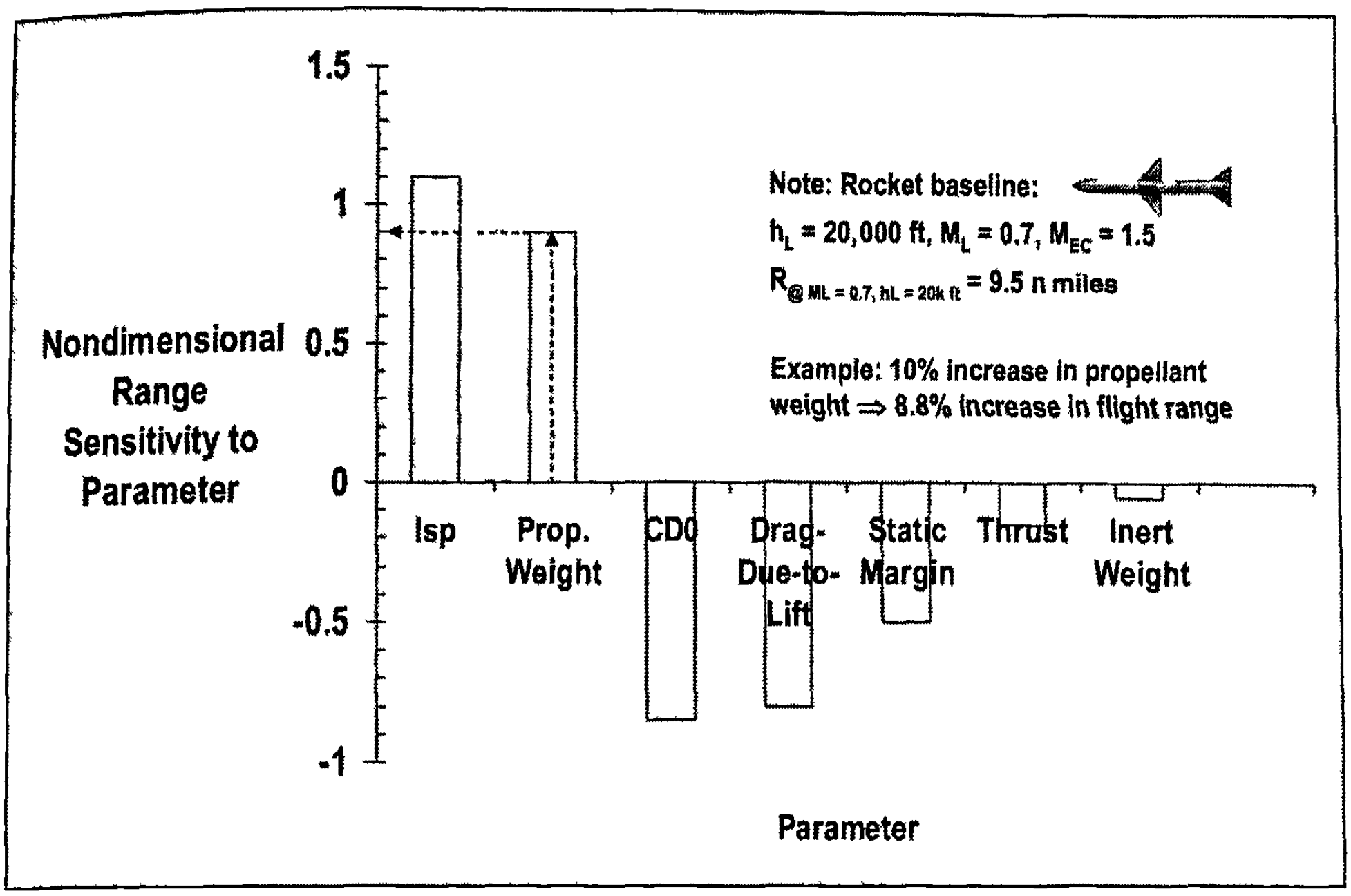

Fig. 7.10 Paredo sensitivity shows range of rocket baseline is driven by specific impulse, propellant weight, drag, and static margin.

The prediction methods for specific impulse, zero-lift drag coefficient, and drag due to lift usually have sufficient accuracy (e.g., $+/-5\%$, 1 σ) for conceptual design. However, there is often large uncertainty in predicting the subsystem packaging volume available for the propellant weight and predicting the static margin. Inboard profile drawings and wind tunnel tests are required to reduce the design uncertainty.

The assumptions for the conceptual design analysis of the boost-sustain flight trajectory are one degree of freedom (DOF) and constant altitude. The simplified equation for axial acceleration based on thrust, drag, and weight is

$$n_X = (T - D)/W \tag{7.8}$$

Missile weight varies with burn rate and time

$$W = W_L - W_P t/t_B \tag{7.9}$$

Missile drag is approximated by

$$D = C_{D_0} q S \tag{7.10}$$

Figure 7.11 shows the rocket baseline missile axial acceleration during the boost, sustain, and coast phases of flight. As mentioned previously, the equation

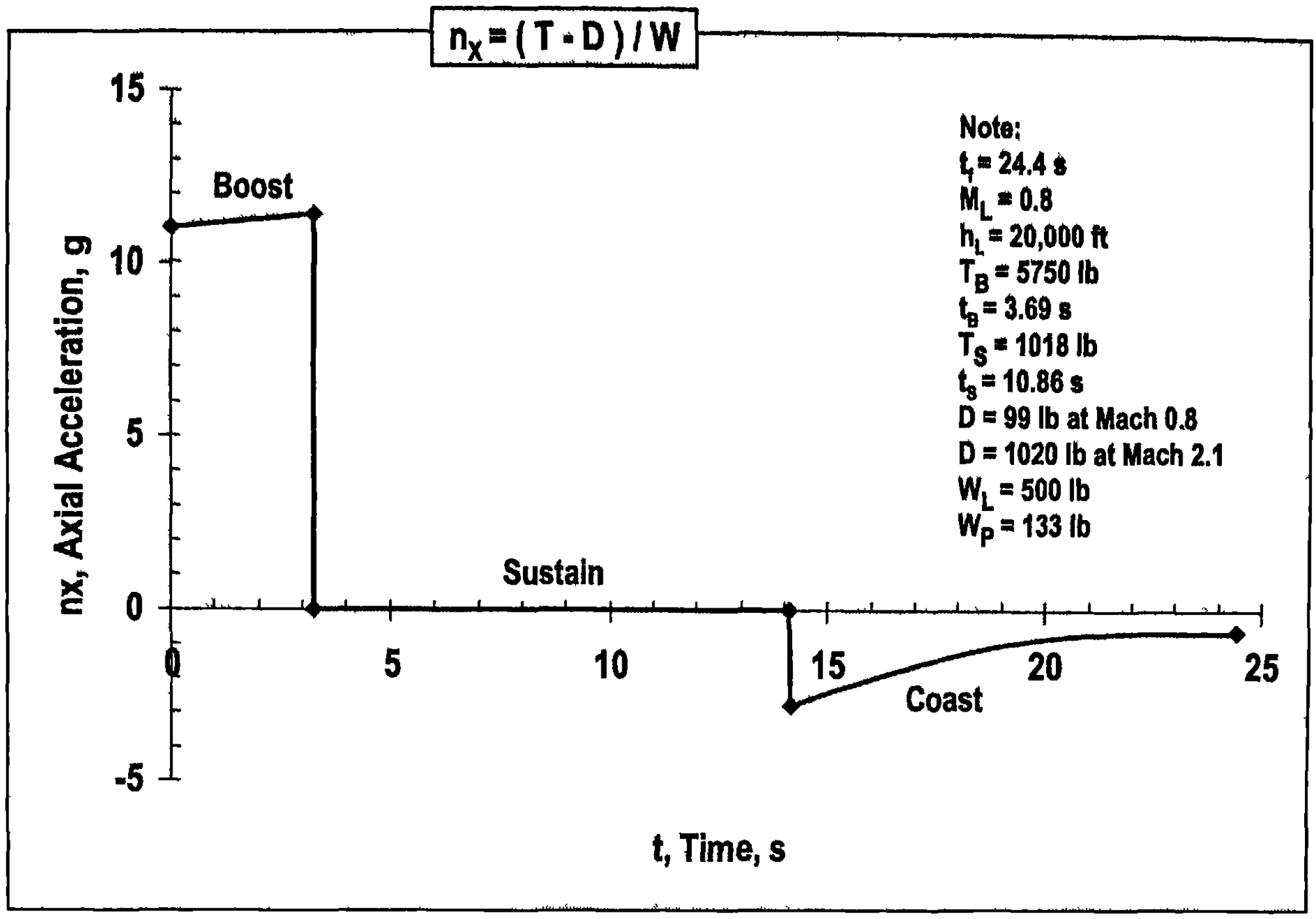

Fig. 7.11 Example of rocket baseline axial acceleration.

for axial acceleration is $n_X = (T - D)/W$. During boost the acceleration is positive (increasing flight velocity), during sustain the acceleration is nearly zero (nearly constant flight velocity), and during coast the acceleration is negative (decreasing flight velocity). The assumed flight conditions are:

1) Total time of flight $t_f = 24.4$ s (required to provide F-pole range)
2) Launch Mach number $M_L = 0.8$
3) Launch altitude $h_L = 20{,}000$ ft
4) Boost thrust $T_B = 5750$ lb
5) Boost time $t_B = 3.69$ s
6) Sustain thrust $T_S = 1018$ lb
7) Sustain time $t_S = 10.86$ s
8) Drag $D = 99$ lb at launch (Mach 0.8)
9) Drag $D = 1020$ lb during sustain (Mach 2.1)
10) Launch weight $W_L = 500$ lb
11) Propellant weight $W_P = 133$ lb

The aerodynamic efficiency of the rocket baseline missile is relatively low for most of the flight conditions shown in the figure. For the 1-g constant altitude flyout, the lift is equal to the missile weight. At the Mach 0.8, 20,000-ft-altitude launch condition, the L/D is relatively high ($L/D \approx 500/99 = 5.1$). At the end of the Mach 2.1 sustain, the L/D is very low ($L/D \approx 367/1020 = 0.36$). For most of the flight the L/D is much lower than $(L/D)_{Max}$. The rocket baseline missile would have to fly at much higher altitude and nearly constant (cruise) velocity to fly a trajectory at $(L/D)_{Max}$.

From Chapter 5, the nondimensional incremental velocity equation during boost-sustain is

$$\Delta V/(g_c I_{SP}) = -(1 - D_{AVG}/T) ln(1 - W_p/W_i) \tag{7.11}$$

ΔV is a function of the initial weight W_i, propellant weight W_P, thrust T, average drag D_{AVG}, and specific impulse I_{SP}. Also from Chapter 5, the nondimensional velocity at the end of coast is

$$V/V_{BO} = 1/\{1 + t/\{2W_{BO}/[g_c \rho_{AVG} S_{Ref} (C_{D_0})_{AVG} V_{BO}]\}\} \tag{7.12}$$

V is a function of the begin-of-coast (burnout) velocity V_{BO}, burnout weight W_{BO}, average atmospheric density ρ_{AVG}, reference area S_{Ref}, average zero-lift drag coefficient $(C_{D_0})_{AVG}$, and coast time t_C. Figure 7.12 shows the rocket baseline missile velocity versus time history for the flight phases of boost, sustain, and coast. The launch conditions are Mach 0.8, 20,000 ft altitude. The peak (sustain) velocity is 2151 ft/s. The velocity at the end of 24.4 s time of flight is 1588 ft/s. Note that the missile has a rapid velocity increase during boost, nearly constant velocity during sustain, and a velocity decay during coast.

The rocket baseline missile flight range is shown in Fig. 7.13 as a function of time. The launch conditions are Mach 0.8, 20,000 ft altitude. Note that the flight range at a time of flight $t_f = 24.4$ s exceeds the requirement by 16% (7.8 vs 6.7 n miles). The rocket baseline achieves the required flight range of 6.7 n miles at a time that is 14% shorter than the required time of flight (21 vs 24.4 s).

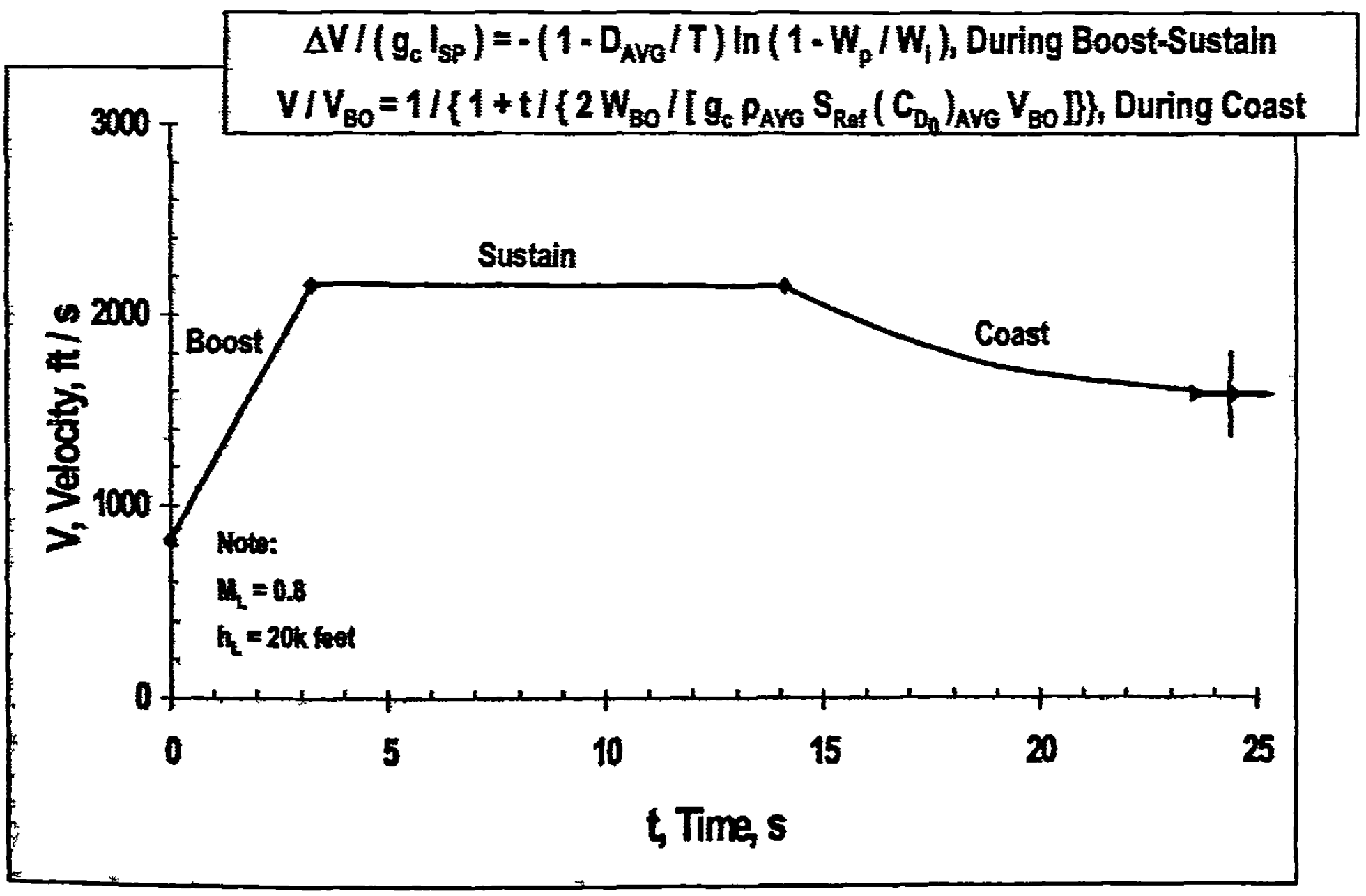

Fig. 7.12 Example of rocket baseline missile velocity versus time.

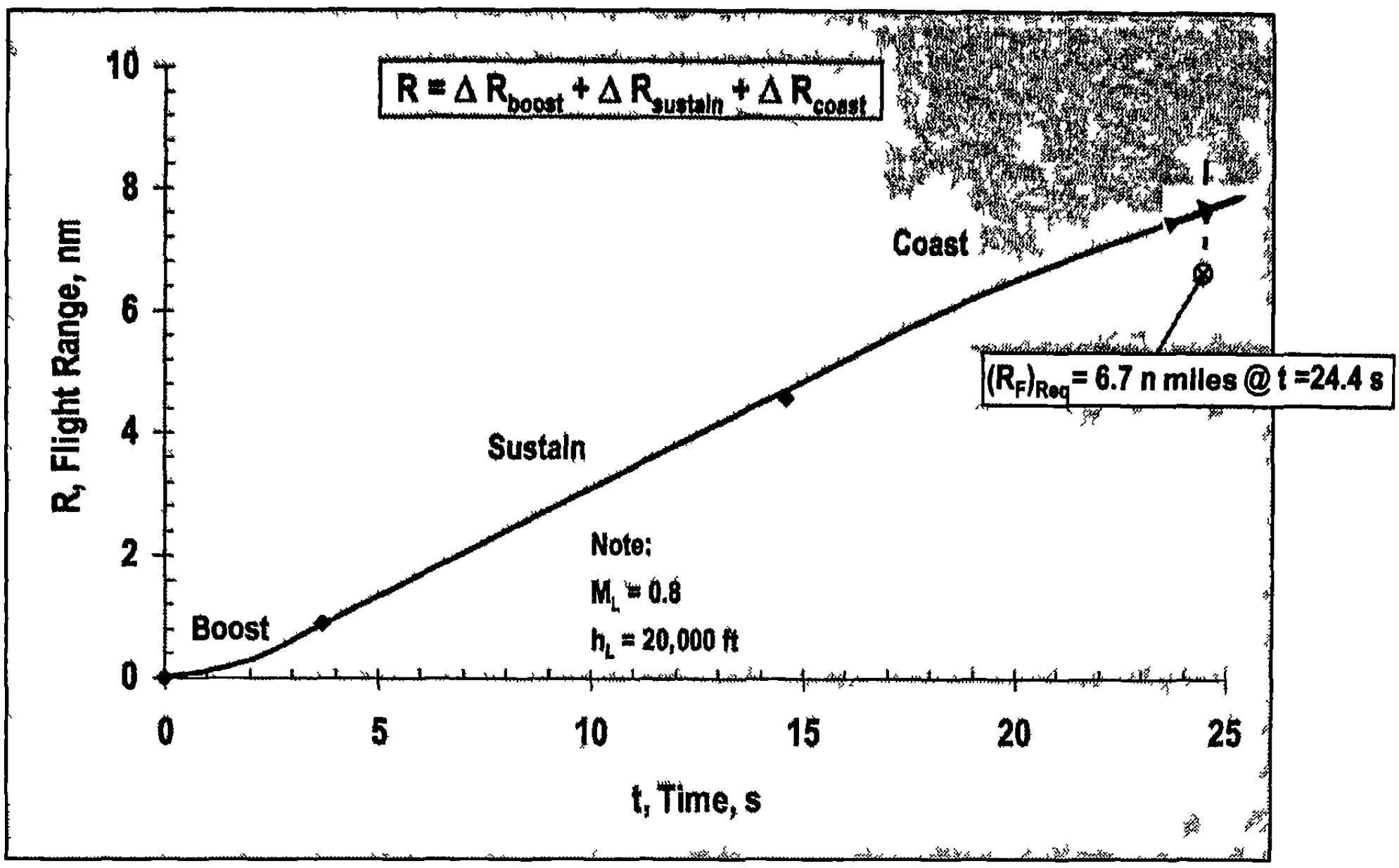

Fig. 7.13 Range and time to target of rocket baseline missile meet requirements.

The total flight range R is the sum of the incremental flight ranges during boost ΔR_{boost}, sustain $\Delta R_{\text{sustain}}$, and coast ΔR_{coast}. The incremental range during boost is a function of the propellant weight W_{P}, launch weight W_{L}, specific impulse I_{SP}, thrust T, average drag D_{AVG}, launch velocity V_{L}, and the boost time t_{B}. The equation for the incremental range during boost and the example result are

$$\begin{aligned}\Delta R_{\text{boost}} &= (V_{\text{L}} + \Delta V/2)t_{\text{B}} \\ &= \{V_{\text{L}} + [-g_{\text{c}}I_{\text{SP}}(1 - D_{\text{AVG}}/\text{T})ln(1 - W_{\text{p}}/W_{\text{L}})]/2\}t_{\text{B}} \\ &= \{820 + [-32.2(250)(1 - 635/5750)ln(1 - 84.8/500)]/2\}(3.69) \\ &= 5481\,\text{ft} = 0.90\,\text{nm} \qquad (7.13)\end{aligned}$$

Similarly, the incremental range during sustain $\Delta R_{\text{sustain}}$ is a function of the propellant weight W_{P}, missile weight at the beginning of sustain W_{BS}, specific impulse I_{SP}, thrust T, average drag D_{AVG}, velocity at the beginning of sustain V_{BS}, and the sustain burn time t_{S}. The equation for the incremental range during sustain and the example result are

$$\begin{aligned}\Delta R_{\text{sustain}} &= (V_{\text{BS}} + \Delta V/2)t_{\text{S}} \\ &= \{V_{\text{BS}} + [-g_{\text{c}}I_{\text{SP}}(1 - D_{\text{AVG}}/\text{T})ln(1 - W_{\text{p}}/W_{\text{BS}})]/2\}\,(t_{\text{S}}) \\ &= [2151 - 32.2(230.4)(1 - 1020/1018)ln(1 - 48.2/415.2)/2](10.86) \\ &= 23{,}350\,\text{ft} = 3.84\,\text{nm} \qquad (7.14)\end{aligned}$$

The incremental range during coast ΔR_{coast} is a function of the begin-of-coast velocity V_{BC}, burnout weight W_{BO}, atmospheric density ρ, reference area S_{Ref}, zero-lift drag coefficient C_{D_0}, and the coast time t_C. From Chapter 5, the equation for the incremental range during coast and the example result are

$$\begin{aligned}\Delta R_{coast} &= [2W/(g_c\rho S_{Ref}C_{D_0})]ln\{1 + t_C/[2W/(g_c\rho S_{Ref}C_{D_0}V_{BC})]\}\\ &= \{2(367)/[(32.2)(0.00127)(0.349)(0.9)]\}\\ &\quad \times ln\{1 + 10.28/\{(2)(367)/[(32.2)(0.00127)(0.349)(0.9)(2150)]\}\}\\ &= 18{,}685\,\text{ft} = 3.07\,\text{n miles}\end{aligned} \tag{7.15}$$

Finally, the total flight range for 24.4 s of flight is

$$R = \Delta R_{boost} + \Delta R_{sustain} + \Delta R_{coast} = 0.90 + 3.84 + 3.07 = 7.8\,\text{n miles} \tag{7.16}$$

7.3 Wing Sizing Requirement

The next sizing examples for the rocket baseline missile are wing sizing to meet a maneuverability requirement and the missile turn performance.

In this example, the wing size is evaluated against an assumed maneuverability requirement of 30 g, required for small miss distance against a 9-g maneuvering target. Also assume flight conditions of Mach 2, 20,000 ft altitude, and 367 lb weight (burnout).

The maximum local angle of attack of the rocket baseline missile movable wing is 22 deg, established by wing stall. The relationship of the local wing angle of attack to the body angle of attack is

$$\alpha_{Wing} = \alpha'_{Max} = (\alpha + \delta)_{Max} = 22\,\text{deg} \tag{7.17}$$

The rocket baseline missile trim angle of attack for a nominal static margin is $\alpha = 0.75\delta$, giving

$$\alpha = \alpha_{Body} = \alpha_{Tail} = 9.4\,\text{deg} \tag{7.18}$$

Using the results from a prior example in Chapter 2, the incremental maneuverability contribution from the isolated body is

$$\begin{aligned}\Delta(n_Z)_{Body} &= qS_{Ref}(C_N)_{Body}/W = 2725(0.349)(1.28)/367\\ &= 3.3\,\text{g (from body)}\end{aligned} \tag{7.19}$$

Also based on the prior result in Chapter 2, the aerodynamic contribution from the tail at Mach 2, with an angle of attack $\alpha_{Tail} = 9.4$ deg is $(C_N)_{Tail}(S_{Ref}/S_{Tail}) = 0.425$. The incremental maneuverability contribution from the isolated tail is

$$\begin{aligned}\Delta(n_Z)_{Tail} &= qS_{Tail}[(C_N)_{Tail}(S_{Ref}/S_{Tail})]/W = 2725(1.54)(0.425)/367\\ &= 4.9\,\text{g (from tail)}\end{aligned} \tag{7.20}$$

The wing must be designed to meet the shortfall in maneuverability. Compute

$$\Delta(n_Z)_{Wing} = (n_Z)_{Required} - \Delta(n_Z)_{Body} - (n_Z)_{Tail} = 30 - 3.3 - 4.9$$
$$= 21.8\,g \tag{7.21}$$

Based on the Chapter 2 example, the aerodynamic contribution from the wing at Mach 2, with an effective angle of attack of $\alpha_{Wing} = 22$ deg is $(C_N)_{Wing}(S_{Ref}/S_{Wing}) = 1.08$. The required wing area is therefore

$$S_W = \Delta(n_Z)_{Wing} W/\{q[(C_N)_{Wing}(S_{Ref}/S_{Wing})]\}$$
$$= 21.8(367)/\{(2725)(1.08)\} = 2.72\,\text{ft}^2 \tag{7.22}$$

Note that the wing area of the rocket baseline missile $(S_W)_{Rocket\ Baseline} = 2.55\ \text{ft}^2$. The rocket baseline requires about 7% additional wing area to satisfy the maneuverability requirement of 30 g at Mach 2, 20,000 ft altitude. Although a 7% larger wing would also increase the missile wing weight by 7% (38.6 to 41.2 lb) and the missile weight by about 1% (367 to 369.6 lb), the increased weight of 2.6 lb would have a negligible effect on missile maneuverability, speed, and flight range.

The video in the top right corner of Fig. 7.14 illustrates the air-to-air missile maneuverability requirement against a maneuvering target. Note that the missile must lead the target, have high velocity, have a high turn rate, and have a small turn radius to intercept the target.

Turn rate performance is the capability to make a rapid rate of change in the flight path angle γ. From Chapter 5, the equation for turn rate using aerodynamic control is

$$\dot{\gamma} = g_c n/V = [qSC_{N_\alpha}\alpha + qSC_{N_\delta}\delta - W\cos\gamma]/[(W/g_c)V] \tag{7.23}$$

An example of a requirement for turn rate performance is the capability of an antiaircraft missile to match the turn rate of the target, which is necessary for a successful intercept. As discussed in Chapter 5, for manned combat aircraft, typical air-to-air combat maneuvering conditions are a normal acceleration of about n = 9 g (pilot limit) and a velocity of about $V = 1000$ ft/s. Substitution into the turn rate equation gives a typical maximum turn rate of a manned aircraft of

$$\dot{\gamma} = 32.2(9)/1000 = 0.290 \text{ rad/s or } 16.6\,\text{deg/s} \tag{7.24}$$

Because the missile must have a speed advantage to intercept the aircraft, it requires higher maneuverability to match the turn rate of the aircraft. For example, a missile with a velocity $V = 3000$ ft/s requires about 27-g maneuverability to achieve a turn rate $\dot{\gamma} = 16.6$ deg/s.

The aerodynamically controlled rocket baseline missile and its data and the prior example in Chapter 5 will be used to illustrate the drivers for turn rate. Assume that a vertical climb maneuver is commanded for a typical

- Size Wing for the Assumptions
  - $(n_Z)_{Required}$ = 30 g to counter 9 g maneuvering target)
  - $(n_Z) = \Delta(n_Z)_{Wing} + \Delta(n_Z)_{Body} + \Delta(n_Z)_{Tail}$
- Rocket Baseline @
  - Mach 2
  - 20,000 ft altitude
  - 367 lb weight (burnout)
- From Prior Example, Compute

$\alpha_{Wing} = \alpha'_{Max} = (\alpha + \delta)_{Max}$ = 22 deg for rocket baseline

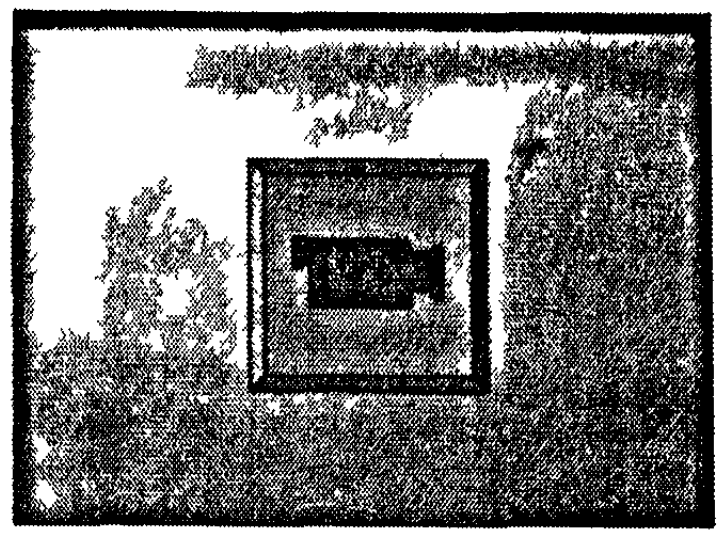

Video of Intercept of Maneuvering Target

$\alpha = 0.75\delta$, $\alpha_{Body} = \alpha_{Tail}$ = 9.4 deg

$\Delta(n_Z)_{Body} = q\, S_{Ref}\, (C_N)_{Body} / W = 2725\,(0.349)\,(1.28) / 367 = 3.3$ g (from body)

$\Delta(n_Z)_{Tail} = q\, S_{Tail}\, [(C_N)_{Tail}\,(S_{Ref}/S_{Tail})] / W = 2725\,(1.54)\,(0.425) / 367 = 4.9$ g (from tail)

$\Delta(n_Z)_{Wing} = (n_Z)_{Required} - \Delta(n_Z)_{Body} - \Delta(n_Z)_{Tail} = 30 - 3.3 - 4.9 = 21.8$ g

$(S_W)_{Required} = \Delta(n_Z)_{Wing}\, W / \{ q\, [(C_N)_{Wing}\,(S_{Ref}/S_{Wing})]\} = 21.8\,(367) / \{(2725)\,(1.08)\} = 2.72\ ft^2$

Note: $(S_W)_{RocketBaseline} = 2.55\ ft^2$

Fig. 7.14 Example of wing sizing to satisfy required maneuver acceleration. Video is in the CD included with this textbook.

post burnout intercept condition of Mach 2, 20,000 ft altitude, and horizontal flight. The maximum wing local angle of attack $|\alpha'| = |\alpha + \delta| < 22$ deg. The rocket baseline is statically stable, with $\alpha/\delta = 0.75$. The turn rate

$$\begin{aligned}\dot{\gamma} = {} & [2725(0.349)(0.60)(9.4) + 2725(0.349)(0.19)(12.6) \\ & - 367(1)]/(367/32.2)(2074) = 0.31 \text{ rad/s or } 18 \text{ deg/s}\end{aligned} \tag{7.25}$$

Thus, the rocket baseline wing provides sufficient turn rate capability to counter a typical highly maneuverable aircraft.

A metric for missile response time is the angle of attack sensitivity to turn rate, or $\alpha/\dot{\gamma}$. For the rocket baseline at Mach 0.8 launch and 20,000 ft altitude,

$$\alpha/\dot{\gamma} = 30/9.4 = 3.2\,\text{s} \tag{7.26}$$

As a comparison, the response time metric for Mach 2 coast at 20,000 ft altitude is better,

$$\alpha/\dot{\gamma} = 9.4/18 = 0.52\,\text{s} \tag{7.27}$$

An advantage of a thrust vector control (TVC) missile is the capability of high turn rate at a low dynamic pressure, such as launch. A TVC missile at launch can have a much higher turn rate than an aerodynamically controlled missile.

Another concern in sizing the wing for maneuverability is the required turn radius capability. To achieve an intercept, the missile turn radius must be less than the turn radius of a maneuvering target. As an example, assume a maneuvering aircraft target with $\dot{\gamma} = 18$ deg/s $= 0.314$ rad/s, $V = 1000$ ft/s. Compute the instantaneous turn radius using the Chapter 5 equation

$$(R_T)_{\text{Target}} = V/\dot{\gamma} = 1000/0.314 = 3183\,\text{ft} \tag{7.28}$$

Also, assume the intercept missile is the rocket baseline at Mach 2, 20,00 ft altitude, and 367 lb weight (burnout). From the prior example, $\dot{\gamma} = 18$ deg/s. Compute

$$(R_T)_{\text{RocketBaseline}} = V/\dot{\gamma} = 2074/0.314 = 6602\,\text{ft} \tag{7.29}$$

Note that $(R_T)_{\text{RocketBaseline}} > (R_T)_{\text{Target}}$. Because the rocket baseline turn radius is larger than the target, it can be countermeasured by the maneuverable target in a tight turn. Candidate counter-countermeasure approaches for the rocket baseline include a larger wing, higher angle of attack capability, a longer burn motor with TVC.

7.4 Multiparameter Harmonization

The next example of sizing for the rocket baseline missile is multiparameter harmonization of weight/miss distance.

A sensitivity study was conducted to determine which parameters have the greatest impact on weight and miss distance for the rocket baseline missile. Baseline sensitivities to parametric changes are shown in Table 7.3 from Ref. 28. If an increase in the value of a subsystem parameter results in an increase in the value of a measure of merit parameter (weight, miss distance), the value of the measure of merit sensitivity parameter will be positive. The measure of merit sensitivity parameters are:

$$W^* = (\Delta W/W)/(\Delta P/P) = \text{weight sensitivity} \tag{7.30}$$

$$\sigma^* = (\Delta\sigma/\sigma)/(\Delta P/P) = \text{miss distance sensitivity} \tag{7.31}$$

In the above equations $\Delta P/P$ represents a relative change in a parameter.

The table shows that there is moderate-to-strong synergistic benefit in reducing both weight and miss distance by increasing the nozzle expansion ratio and increasing the motor volumetric efficiency. For example, a 10% increase in motor volumetric efficiency (0.76 to 0.84) reduces the missile weight by 14% (500 to 432 pounds) and reduces the miss distance by 45% (62 to 34 feet). Other sensitivities that have a moderate-to-strong impact on either weight or miss distance but not a significant impact on both are reducing the number of tails, reducing the number of wings (bank-to-turn), reducing the static margin, increasing the wing sweep, increasing the nose fineness ratio, decreasing the boattail fineness ratio, increasing the sustain thrust, and moving the wing forward.

Table 7.3 Rocket baseline missile strongest drivers for combined weight and miss distance are nozzle expansion ratio and motor volumetric efficiency

Parameter	Baseline	Sensitivity variation	W*	σ^*
Fixed surface number of panels	4	3	+0.054	+0.100
Movable surface number of panels	4	2	+0.071	+0.106
Design static margin at launch	0.40	0.30	+0.095	+0.167
Wing movable surface sweep (deg)	45.0	49.5	−0.205	+0.015
Tail fixed surface sweep (deg)	57.0	60.0	+0.027	+0.039
Wing movable surface thickness ratio	0.044	0.034	+0.041	+0.005
Nose fineness ratio	2.4	2.6	−0.016	−0.745
Rocket chamber sustain pressure (psi)	301	330	−0.076	−0.045
Boattail fineness ratio (length/diameter)	0.38	0.342	+0.096	+0.140
Nozzle expansion ratio	6.2	6.82	−0.114	−0.181
Motor volumetric efficiency	0.76	0.84	−0.136	−0.453
Propellant density (lb/in^3)	0.065	0.084	−0.062	+0.012
Boost thrust (lb)	5,750	6,325	+0.014	−0.018
Sustain thrust (lb)	1,018	1,119	+0.088	+0.246
Characteristic velocity (ft/s)	5,200	5,720	−0.063	−0.077
Wing location (percent total length)	47.5	42.75	+0.181	−0.036

Baseline: Weight = 500 lb, Miss distance = 62.3 ft
W* = weight sensitivity for parameter variation = $\Delta W/W$
σ^* = miss distance sensitivity for parameter variation = $\Delta\sigma/\sigma$
Note: Strong impact with synergy
Strong impact
Moderate impact with synergy
Moderate impact

Missile parameters were selected that resulted in the lightest weight and smallest miss distance missiles without exceeding the state of the art. A design of experiment (DOE) selection of a lightest weight missile and a smallest miss distance missile led to a harmonized missile. These parameters and their values for the four missiles (baseline, lightest weight, smallest miss distance, and harmonized missile) are shown in Table 7.4 from Ref. 28. The harmonized missile compared to the baseline missile has the following characteristics:

1) higher fineness nose (2.6 vs 2.4)
2) higher expansion nozzle (15 vs 6.2)
3) higher sustain pressure (1000 vs 301 psi)
4) smaller boattail fineness (0.21 vs 0.38)
5) fewer wing panels (two vs four)
6) fewer tail panels (three vs four)
7) higher wing leading edge sweep (55 vs 45 deg)
8) smaller static margin at launch (0 vs 0.4 diam)
9) higher propellant density (0.084 vs 0.065 lb/in^3)
10) higher propellant loading for higher motor volumetric efficiency (84 vs 76%).

Table 7.4 A harmonized missile can have smaller miss distance and lighter weight

Parameter	Baseline value	Missile configured for minimum: Weight	Miss distance	Harmonized
Judicious changes				
Boost thrust (lb)	5750	3382	3382	3382
Wing location (percent missile length to 1/4 mac)	47.5	47	44	46
Wing taper ratio	0.18	0.2	0.2	0.2
Nose fineness ratio	2.4	3.2	2.55	2.6
Nose blunting ratio	0.0	0.05	0.05	0.05
Nozzle expansion ratio	6.2	15	15	15
Sustain chamber pressure (psi)	301	1000	1000	1000
Boattail fineness ratio	0.38	0.21	0.21	0.21
Tail leading edge sweep (deg)	57	50	50	50
Technology limited changes				
No. wing panels	4	2	2	2
No. tail panels	4	3	3	3
Wing thickness ratio	0.044	0.030	0.030	0.030
Wing leading edge sweep (deg)	45	55	55	55
Static margin at launch (diam)	0.4	0.0	0.0	0.0
Propellant density (lb/in^3)	0.065	0.084	0.084	0.084
Motor volumetric efficiency	0.76	0.84	0.84	0.84
Measures of merit				
Total weight (lb)	500	385.9	395.0	390.1
Miss distance (ft)	62.3	63.1	16.2	16.6
Time to target (s)	21.6	23.8	23.6	23.8
Length (in)	144	112.7	114.7	114.9
Mach no. at burnout	2.20	2.08	2.09	2.07
Weight of propellant (lb)	133	78.3	85.4	85.9
Wing area (in^2)	368.6	175.5	150.7	173.8
Tail area (in^2)	221.8	109.1	134.5	112.0

*Note: ☐ Value of driving parameter

The measures of merit comparison of the harmonized missile with the baseline missile shows that the harmonized missile has lighter weight (390 vs 500 lb), smaller miss distance (17 vs 62 ft), and shorter length (115 vs 144 in). A comparison of the harmonized missile with the minimum weight missile shows that the harmonized missile is only slightly heavier (390 vs 386 lb). It is also slightly longer (115 vs 113 in). Comparing the harmonized missile with the minimum miss distance missile shows that the harmonized missile has only

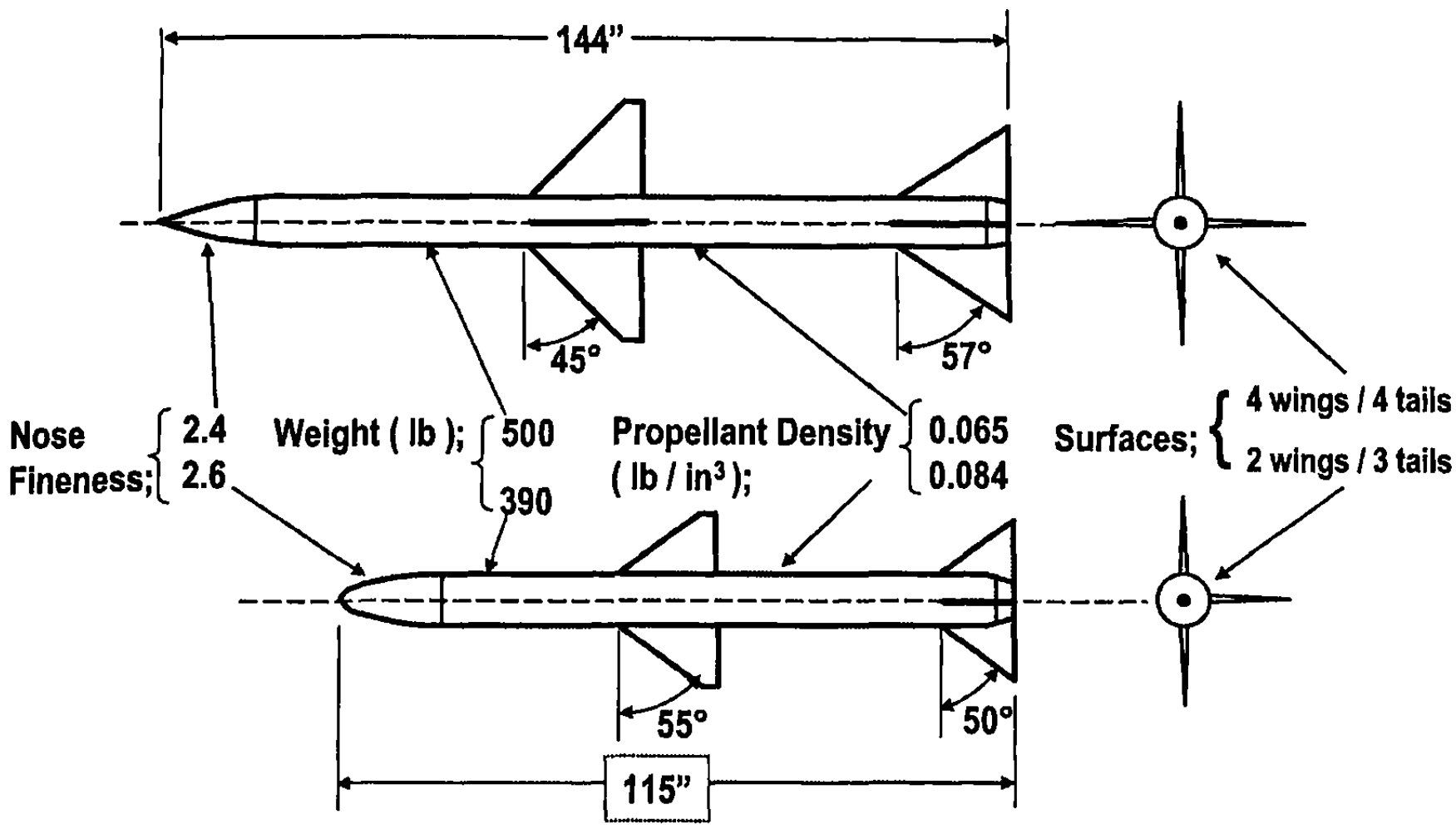

Fig. 7.15 Baseline missile versus harmonized missile.

slightly larger miss distance (17 vs 16 ft). The harmonized missile was selected based on synergistic parameters for weight and miss distance that are within the state of the art.

The configuration of the harmonized missile, which has lighter weight and smaller miss distance, is compared with the baseline missile in Fig. 7.15 from Ref. 28. Note the 22% smaller size of the harmonized missile compared to the baseline. The harmonized missile is also 22% lighter in launch weight and has a 73% reduction in miss distance. A slight disadvantage for the harmonized missile is 10% longer time of flight for a flight range of 6.7 n miles. However, the time of flight of the harmonized missile still meets the F-Pole requirement of 24.4 s to 6.7 n miles.

7.5 Lofted Range Comparison

The final example of sizing for the rocket baseline missile shows the range advantage of a lofted launch-coast-glide trajectory compared to alternatives of a lofted launch-ballistic trajectory and a constant altitude trajectory.

Surface launch ($h = 0$ ft) is assumed with an initial inclination angle of 45 deg. A constant flight path angle ($\gamma = 45$ deg) is assumed during boost and sustain. From the Chapter 5 equation, the velocity at the end of the initial boost is

$$\begin{aligned}\Delta V &= -g_c I_{SP}[1 - (D_{AVG}/T) - (W_{AVG}\sin\gamma)/T]ln(1 - W_p/W_i)\\ &= -32.2(250)[1 - (419/5750) - 458(0.707)/5750]ln(1 - 84.8/500)\\ &= 1303\ \text{ft/s}\end{aligned} \tag{7.32}$$

The distance traveled at the end of the initial boost is

$$\Delta R = (V_i + \Delta V/2)t_B = (0 + 1303/2)3.69 = 2404\,\text{ft} \tag{7.33}$$

The horizontal range at the end of the initial boost is

$$\Delta R_x = \Delta R\cos\gamma_i = 2404(0.707) = 1700\,\text{ft} \tag{7.34}$$

Similarly, the altitude at the end of the initial boost is

$$h = h_i + \Delta R_y = 0 + \Delta R\sin\gamma_i = 1700\,\text{ft} \tag{7.35}$$

Similarly, the velocity, horizontal range, and altitude at the end of motor sustain (burnout) are

$$\begin{aligned}\Delta V &= -g_c I_{SP}[1 - (D_{AVG}/T) - (W\sin\gamma)/T]ln(1 - W_p/W_i)\\ &= -32.2(230.4)[1 - (650/1018) - 391(0.707)/1018]\\ &\quad \times ln(1 - 48.2/415.2) = 81\,\text{ft/s}\end{aligned} \tag{7.36}$$

$$V_{BO} = 1303 + 81 = 1384\,\text{ft/s} \tag{7.37}$$

$$\Delta R = (V_i + \Delta V/2)t_B = (1303 + 81/2)10.86 = 14{,}590\ \text{ft} \tag{7.38}$$

$$\Delta R_x = \Delta R\cos\gamma_i = 14{,}590(0.707) = 10{,}315\,\text{ft} \tag{7.39}$$

$$\Delta R_y = \Delta R\sin\gamma_i = 14{,}590(0.707) = 10{,}315\,\text{ft} \tag{7.40}$$

$$h = h_i + \Delta R_y = 1700 + 10{,}315 = 12{,}015\,\text{ft} \tag{7.41}$$

Following motor burnout, the missile is assumed to coast at a flight path angle of $\gamma = 45$ deg. Coast continues until the missile reaches an altitude of maximum aerodynamic efficiency $h_{@(L/D)max}$. This occurs after 21 s of coast. The velocity, incremental coast horizontal range, and incremental coast altitude using the equations of Chapter 5 are

$$\begin{aligned}V_{coast} &= V_i\{1 - [(g_c\sin\gamma)/V_i]t\}/\{1 + \{[g_c\rho_{AVG}S_{Ref}(C_{D_0})_{AVG}V_i]/(2W)\}t\}\\ &= 1384\{1 - [32.2(0.707)/1384]21\}/\{1 + \{[32.2(0.001338)(0.319)\\ &\quad \times (0.7)(1384)]/(2(367))\}21\} = 674\,\text{ft/s}\end{aligned} \tag{7.42}$$

$$R_{\text{coast}} = \{2W/[g_c\rho_{\text{AVG}}S_{\text{Ref}}(C_{D_0})_{\text{AVG}})]\}ln\{1 - [g_c^2\rho_{\text{AVG}}S_{\text{Ref}}(C_{D0})_{\text{AVG}}/(2W)]$$
$$\times [\sin\gamma]t^2 + \{[g_c\rho_{\text{AVG}}S_{\text{Ref}}(C_{D0})_{\text{AVG}}V_i]/(2W)\}t\}$$
$$= \{2(367)/[32.2(0.001338)(0.319)(0.7)]$$
$$\times ln\{1 - [(32.2)^2(0.001338)(0.319)(0.7)/(2(367))][0.707](21)^2$$
$$+ \{[32.2(0.001338)(0.319)(0.7)(1384)]/(2(367))]21\} = 17{,}148\text{ft} \quad (7.43)$$
$$(R_x)_{\text{coast}} = (R_y)_{\text{coast}} = R_{\text{coast}}\sin\gamma = 17{,}148(0.707) = 12{,}124\text{ ft} \quad (7.44)$$

The flight conditions at the end of coast are

1) $t = 35$ s
2) $V = 674$ ft/s
3) $h = 24{,}189$ ft
4) $q = 251$ psf
5) $M = 0.66$
6) $(L/D)_{\max} = 5.22$
7) $\alpha_{(L/D)\max} = 5.5$ deg

At the end of coast ($h = 24{,}189$ ft), the angle of attack is set to

$$\alpha = \alpha_{(L/D)\max} = 5.5\text{ deg} \quad (7.45)$$

Incremental horizontal range at the end of the $(L/D)_{\max}$ glide, using the equation in Chapter 5, is

$$\Delta R_x = (L/D)\Delta h = 5.22(24{,}189) = 126{,}267\text{ ft} \quad (7.46)$$

Finally, the total horizontal range for the elevated launch-coast-glide trajectory is

$$R_x = \Sigma\Delta R_x = \Delta R_{x,\text{Boost}} + \Delta R_{x,\text{Sustain}} + \Delta R_{x,\text{Coast}} + \Delta R_{x,\text{Glide}}$$
$$= 1700 + 10{,}315 + 12{,}124 + 126{,}267 = 150{,}406\text{ ft} = 24.8\text{ n miles} \quad (7.47)$$

Figure 7.16 compares a lofted launch-coast-glide trajectory versus lofted ballistic and coaltitude flight trajectories. For lofted flight, the initial launch angle is assumed to be 45 deg and during motor burn the flight path angle is held constant at 45 deg. The missile continues at 45 deg flight path angle following motor burnout, coasting until it reaches an apogee altitude of $h = 24{,}189$ ft, which occurs 35 s after launch. After reaching the apogee, where lift approximately equals weight, the rocket baseline begins a glide at maximum aerodynamic efficiency. The angle of attack is maintained at $\alpha = \alpha_{(L/D)\max} = 5.5$ deg during the glide. The dynamic pressure during the $(L/D)_{\max}$ glide is relatively constant at $q \approx 285$ psf. Impact occurs after 298 s of flight. The impact velocity is 459 ft/s. The impact angle is −10.8 deg. Impact range is 24.8 n miles.

The ballistic trajectory alternative has an apogee of 21,590 ft, which occurs at 35 s after launch. For a ballistic trajectory after apogee, impact occurs at 68 s,

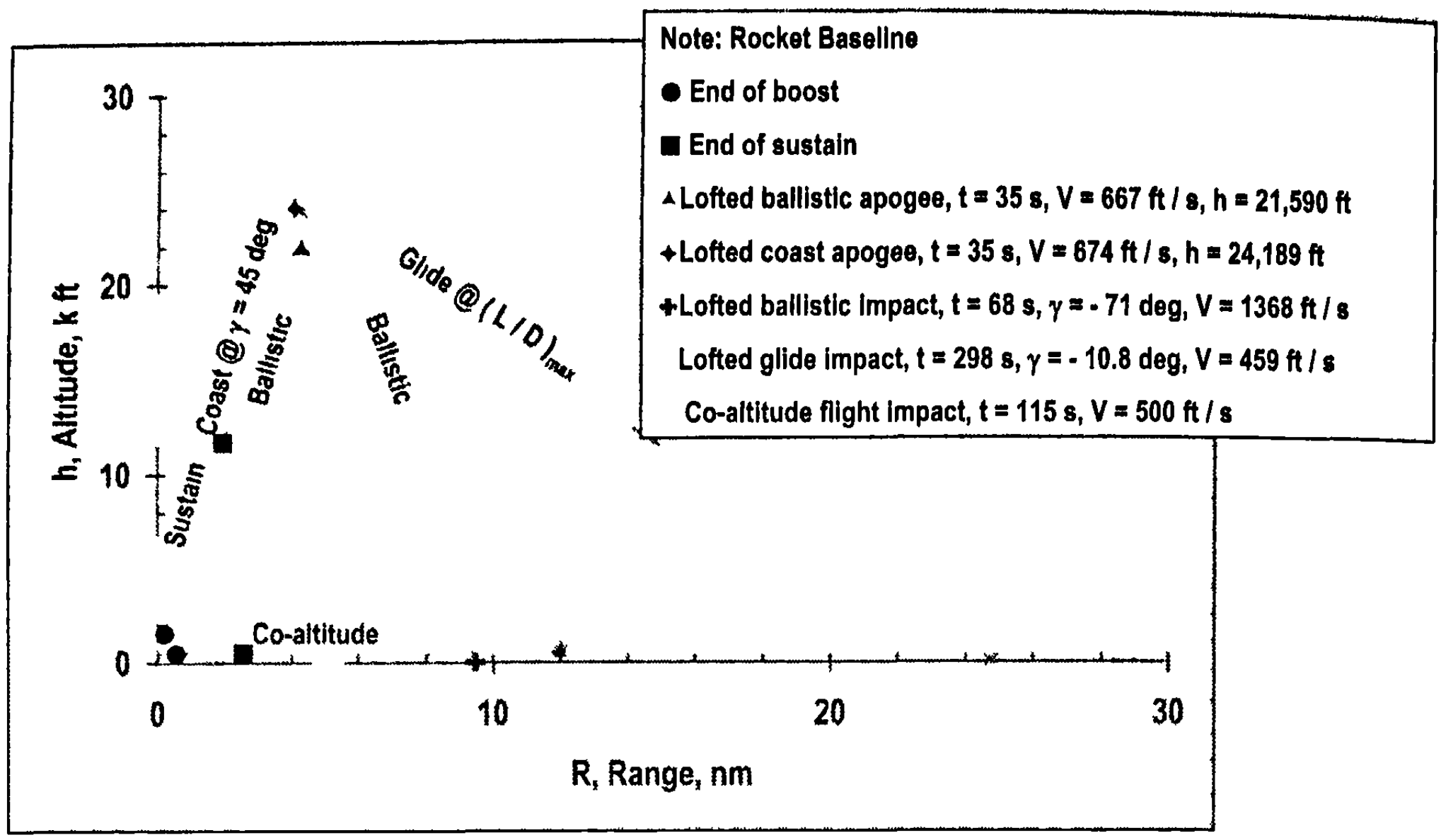

Fig. 7.16 Lofted glide trajectory provides extended range.

with an impact velocity of 1368 ft/s and an impact angle of −71 deg. The ballistic trajectory has a flight range of 9.6 n miles. Note from the figure that a gliding flight trajectory after apogee provides greatly extended range, while a ballistic flight trajectory provides a higher velocity impact.

As a comparison, a coaltitude flight has a range of 12 n miles, which is longer than a ballistic trajectory but much shorter than a lofted glide trajectory.

In addition to range, other design considerations in selecting an optimum trajectory include time to target, survivability, and buried target penetration. The low-altitude trajectory may benefit from terrain masking survivability. The ballistic trajectory has a supersonic impact velocity, which improves penetration of buried targets and may enhance survivability.

7.6 Ramjet Missile Range Robustness

A generic baseline of a ramjet missile, derived from the Advanced Strategic Air Launched Missile (ASALM), is used to illustrate the typical characteristics of ramjet powered missiles. Sizing examples are presented for flight range robustness, alternative propulsion systems, alternative fuels, and surface impact velocity.

The baseline ramjet engine is sized for cruise at Mach numbers up to Mach 4.0 at 80,000 ft altitude and up to Mach 3.0 at sea level. An integral solid rocket motor boosts the missile to a ramjet thrust takeover Mach number of about 2.5. After rocket motor burnout, the rocket motor case becomes the ramjet combustor. Unlike the rocket missile baseline, the ramjet missile baseline is able to

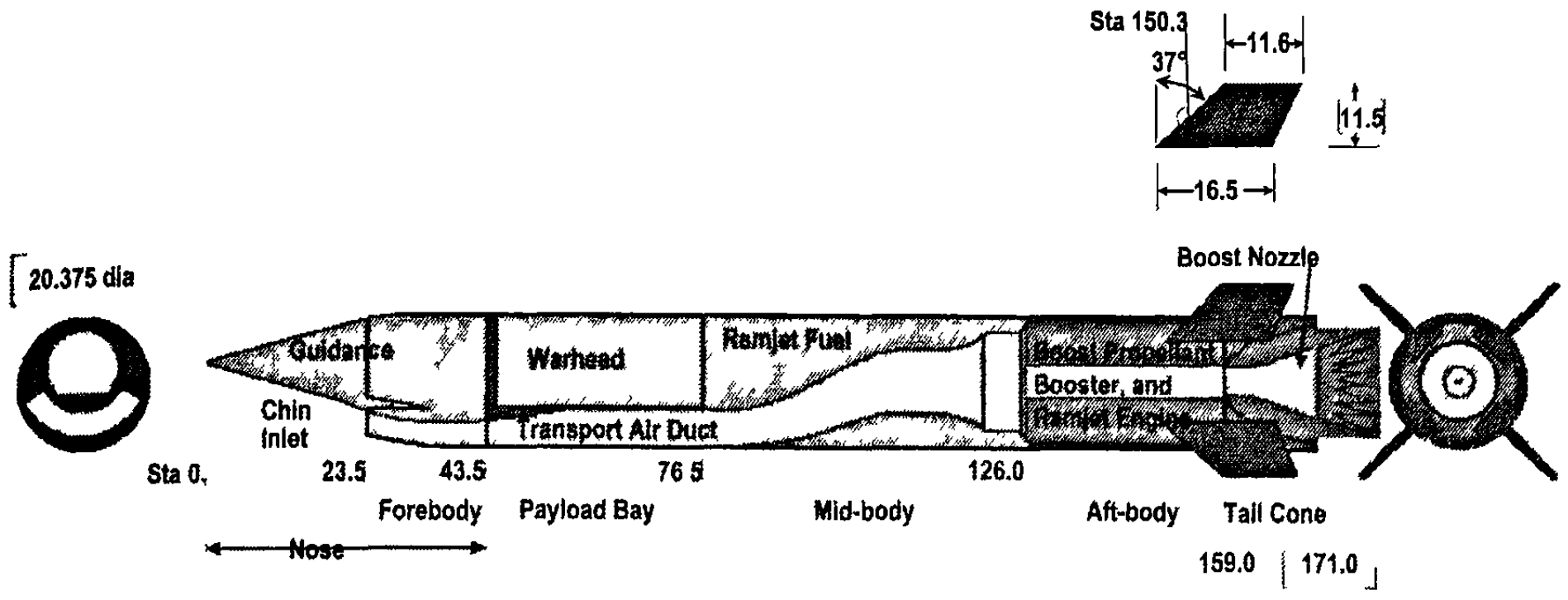

Note: Dimensions are in inches

Source: Bithell, R.A. and Stoner, R.C. "Rapid Approach for Missile Synthesis", Vol. II, Air-breathing Synthesis Handbook, AFWAL TR 81-3022, Vol. II, March 1982.

Fig. 7.17 Ramjet baseline is a chin inlet integral rocket ramjet (IRR). Figure also in color section.

cruise at constant velocity and high altitude, providing an aerodynamic efficiency near $(L/D)_{\text{Max}}$.

The baseline ramjet configuration is shown in Fig. 7.17. It is a chin inlet integral rocket ramjet based on Ref. 27. The aerodynamic configuration has a conical forebody with a half-angle of 17.7 deg, followed by a nearly circular cross-sectional body. From the body station 23.5 in to body station 43.5 in, the nose diameter gradually increases. The fineness ratio of the nose is $f_N = 43.5/20.375 = 2.13$. Downstream of body station 43.5 in, the average diameter $d = 20.375$ in. The ASALM diameter and length were set by the diameter and length constraints to efficiently package eight ASALM missiles within the B-1 rotary launcher/weapon bay. Flight control is provided by four tail surfaces. The tails are folded for compressed carriage in the weapons bay. Tail span after deployment is 41.4 in. The missile uses bank-to-turn maneuvering to minimize the sideslip air flowing into the inlet. The fuel is liquid hydrocarbon RJ-5 fuel, packaged in a fuel tank around the inlet duct. Shown in the figure are the section bulkhead locations and lengths for the nose, forebody, payload bay, midbody, aftbody, and tail cone sections. Also shown are frontal and aft views of the nose and tail sections. A planform view is provided of the tail geometry, showing the tail leading edge sweep, root chord location and length, tip chord length, and the exposed tail semi-span.

Shown in Table 7.5 from Ref. 27 is a weight and balance statement of the ramjet baseline. The launch weight $W_L = 2230$ lb and the end of cruise weight $W_{EC} = 1263$ lb. The fuel weight $W_f = 476$ lb and the booster propellant weight $W_P = 449$ lb. There is a small forward movement (0.07 diameter) in the center of gravity during the ramjet cruise portion of flight. The center of gravity at the start of cruise is 83.2 in from the nose tip. The center of gravity at the end of cruise is 81.8 in from the nose tip. Most of the missile structure is titanium.

Table 7.5 Mass properties of the ramjet baseline missile

Component	Weight, lb	CG Sta, in
Nose	15.9	15.7
Forebody Structure	42.4	33.5
Guidance	129.0	33.5
Payload Bay Structure	64.5	60.0
Warhead	510.0	60.0
Midbody Structure	95.2	101.2
Inlet	103.0	80.0
Electrical	30.0	112.0
Hydraulic System for Control Actuation	20.0	121.0
Fuel Distribution	5.0	121.0
Aftbody Structure	44.5	142.5
Engine	33.5	142.5
Tailcone Structure	31.6	165.0
Ramjet Nozzle	31.0	165.0
Flight Control Actuators	37.0	164.0
Fins (4)	70.0	157.2
End of Cruise	1262.6	81.8
Ramjet Fuel (11900 in^3)	476.0	87.0
Start of Cruise	1738.6	83.2
Boost Nozzle (Ejected)	31.0	164.0
Frangible Port	11.5	126.0
End of Boost	1781.1	84.9
Boost Propellant	449.0	142.5
Booster Ignition	2230.1	96.5

The total weight of the titanium airframe, inlet, and fins is 17% of the launch weight.

The ramjet baseline geometric and material definition of the inlet, body, and tails are shown in Table 7.6 from Ref. 27. The inlet is a mixed compression type with a total of four compressions prior to the normal shock, consisting of 1) the shock wave on the conical nose; followed by 2) the shock wave on the ramp leading to the cowl; followed by 3) the shock wave on the cowl; and finally 4) a series of nearly isentropic internal contraction shock waves leading to a normal shock. The missile has a hot structure. The body structure and inlet are uninsulated titanium with internal insulation to protect the subsystems. The tails are made of a titanium built-up structure. A ballistic actuator located inside each tail unfolds the tail after the missile separates from the launch aircraft. The combustor is constructed from Inconel super alloy with internal insulation. The dome material is silicon nitride.

Also shown in the table are data on the missile reference geometry parameters. The ramjet baseline missile reference area $S_{\text{Ref}} = 2.264\ \text{ft}^2$ is based on the body cross-sectional area. The reference length $l_{\text{Ref}} = d_{\text{Ref}} = 1.698$ ft is based on an equivalent circular diameter of the body cross-sectional area.

Table 7.6 Ramjet baseline missile definition

Inlet	
Type	Mixed compression
Material	Titanium
Conical forebody half angle, deg	17.7
Ramp wedge angle, deg	8.36
Cowl angle, deg	8.24
Internal contraction ratio	12.2 Percent
Capture area, ft^2	0.79
Throat area, ft^2	0.29
Body	
Dome Material	Silicon nitride
Airframe Material	Titanium
Combustor Material	Insulated Inconel
Length, in	171.0
Diameter, in	20.375
Fineness ratio	8.39
Volume, ft^3	28.33
Wetted area, ft^2	68.81
Base area, ft^2 (cruise)	0.58
Boattail fineness ratio	N/A
Nose half angle, deg	17.7
Nose length, in	23.5
Tail (Exposed)	
Material	Titanium
Planform area (2 panels), ft^2	2.24
Wetted area (4 panels), ft^2	8.96
Aspect ratio (2 panels exposed)	1.64
Taper ratio	0.70
Root chord, in	16.5
Span, in. (2 panels exposed)	23.0
L.E. sweep, deg	37.0
M.A.C., in	14.2
Thickness ratio	0.04
Section type	Modified double wedge
Section leading edge total angle, deg	9.1
X MAC, in	150.3
Y MAC, in (from root chord)	5.4
Reference values	
Reference area, ft^2	2.264
Reference length, ft	1.698

Definitions of the propulsion parameters and the flowpath are shown in Fig. 7.18 based on Ref. 27. The ramjet baseline inlet captures the air that flows over the bottom one-third of the nose (120 deg). In the thrust-drag accounting system the nose corrected drag accounts for the air captured by the inlet. It is

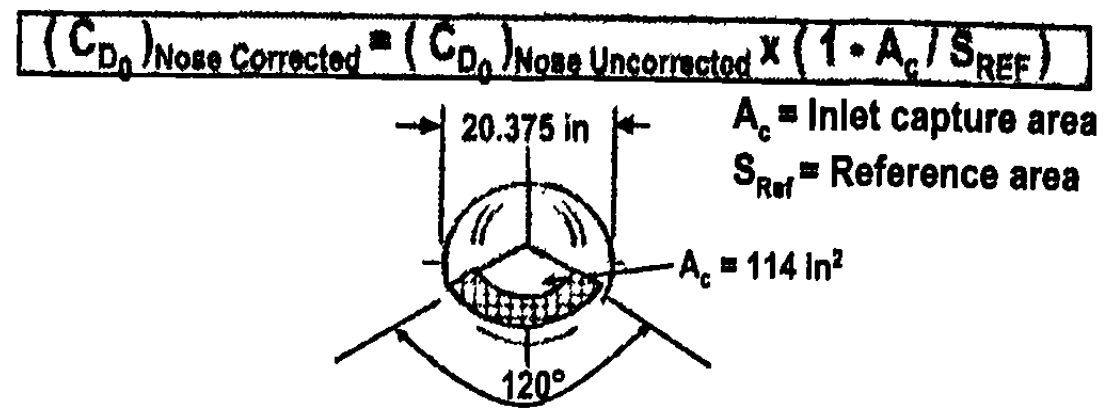

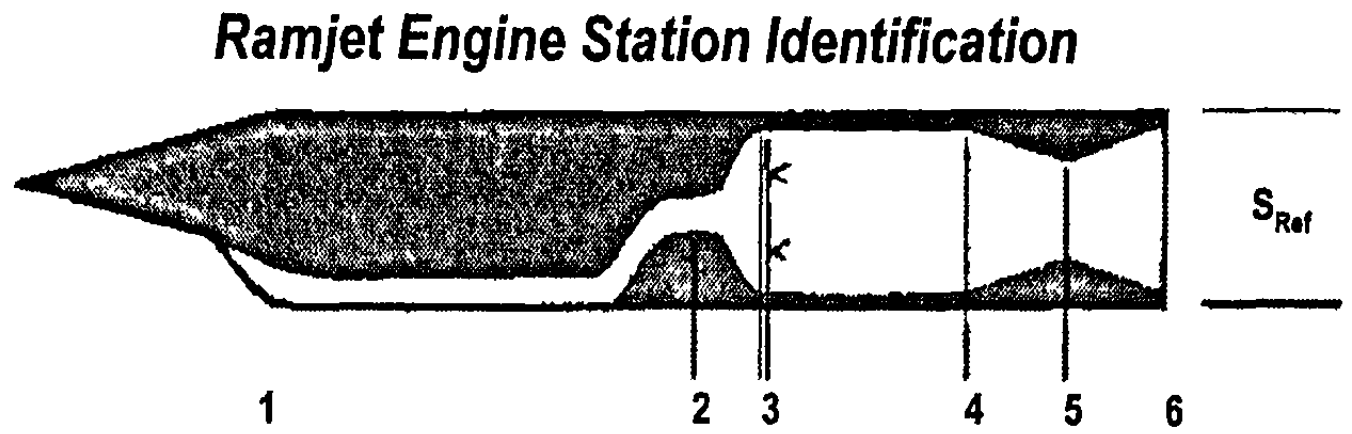

Subscripts

0	Freestream flow into inlet (Example, Ramjet Baseline at Mach 4, α = 0 deg $\Rightarrow A_0$ = 104 in². Note: A_c = 114 in²)
1	Inlet throat (Ramjet Baseline $A_1 = A_{IT}$ = 41.9 in²)
2	Diffuser exit (Ramjet Baseline A_2 = 77.3 in²)
3	Flame holder plane (Ramjet Baseline A_3 = 287.1 in²)
4	Combustor exit (Ramjet Baseline A_4 = 287.1 in²)
5	Nozzle throat (Ramjet Baseline A_5 = 103.1 in²)
6	Nozzle exit (A_6 = 233.6 in²)
Ref	Reference Area (Ramjet Baseline Body Cross-sectional Area, S_{Ref} = 326 in²)

Fig. 7.18 Engine nomenclature and flowpath geometry for ramjet baseline. Figure also in color section.

given by the equation

$$(C_{D_0})_{\text{Nose Corrected}} = (C_{D_0})_{\text{Nose Uncorrected}} \times (1 - A_c/S_{REF}) \tag{7.48}$$

Flowpath is described by the stations number 1 (freestream conditions) through number 6 (nozzle exit). The largest flowpath areas are located at the subsonic combustion stations 3 (flame holder plane) and 4 (combustor exit), each having an area of 287.1 in^2. The other areas of the flowpath are the inlet throat (41.9 in^2), diffuser exit (77.3 in^2), ramjet nozzle throat (103.1 in^2), and the ramjet nozzle exit (233.6 in^2). The smallest area in the flowpath is the inlet throat, which is 15% of the combustor area.

At station number 0 the freestream flow conditions apply. The capture area A_c is the theoretical flow area into the inlet if there were no shock wave in front of the inlet. A_0 is the actual flow area into the inlet in the presence of the forebody. As an example, referring to Chapter 3, at Mach 4 with angles of attack of 0 deg and 10 deg, respectively, the capture ratios of the ramjet baseline baseline are $A_0/A_c = 0.91$ and 0.61, respectively.

The axial force, normal force, and pitching moment aerodynamics of the ramjet baseline are presented in Fig. 7.19 from Ref. 27. Aerodynamics for the ramjet baseline were developed using an early version (year 1974) of the computer program from Ref. 32.

Axial force C_A and normal force C_N coefficients are presented as a function of Mach number and angle of attack in Fig. 7.19a. Note the decrease in the

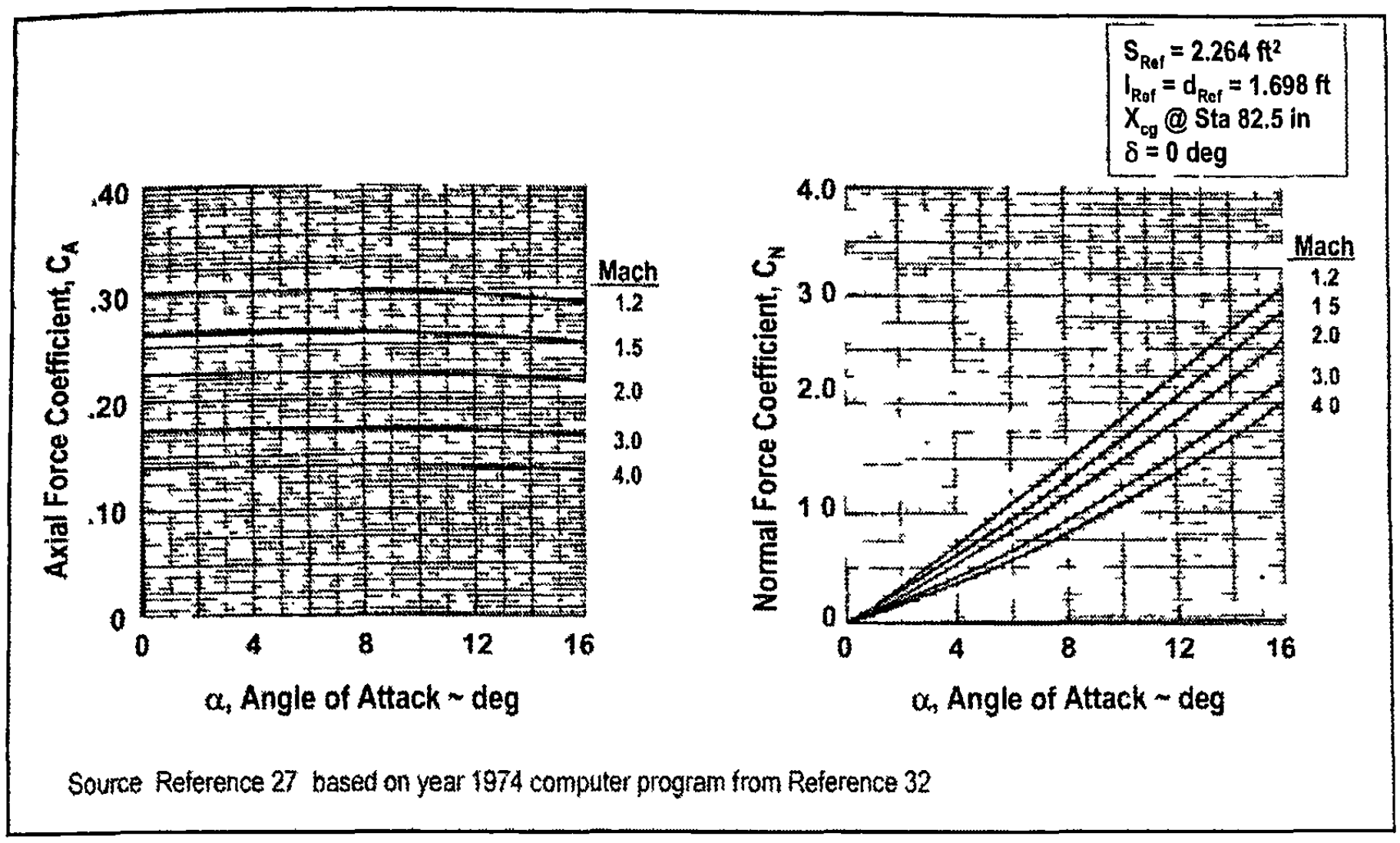

Source Reference 27 based on year 1974 computer program from Reference 32

Fig. 7.19a Aerodynamic characteristics of the ramjet baseline missile: axial and normal force coefficients.

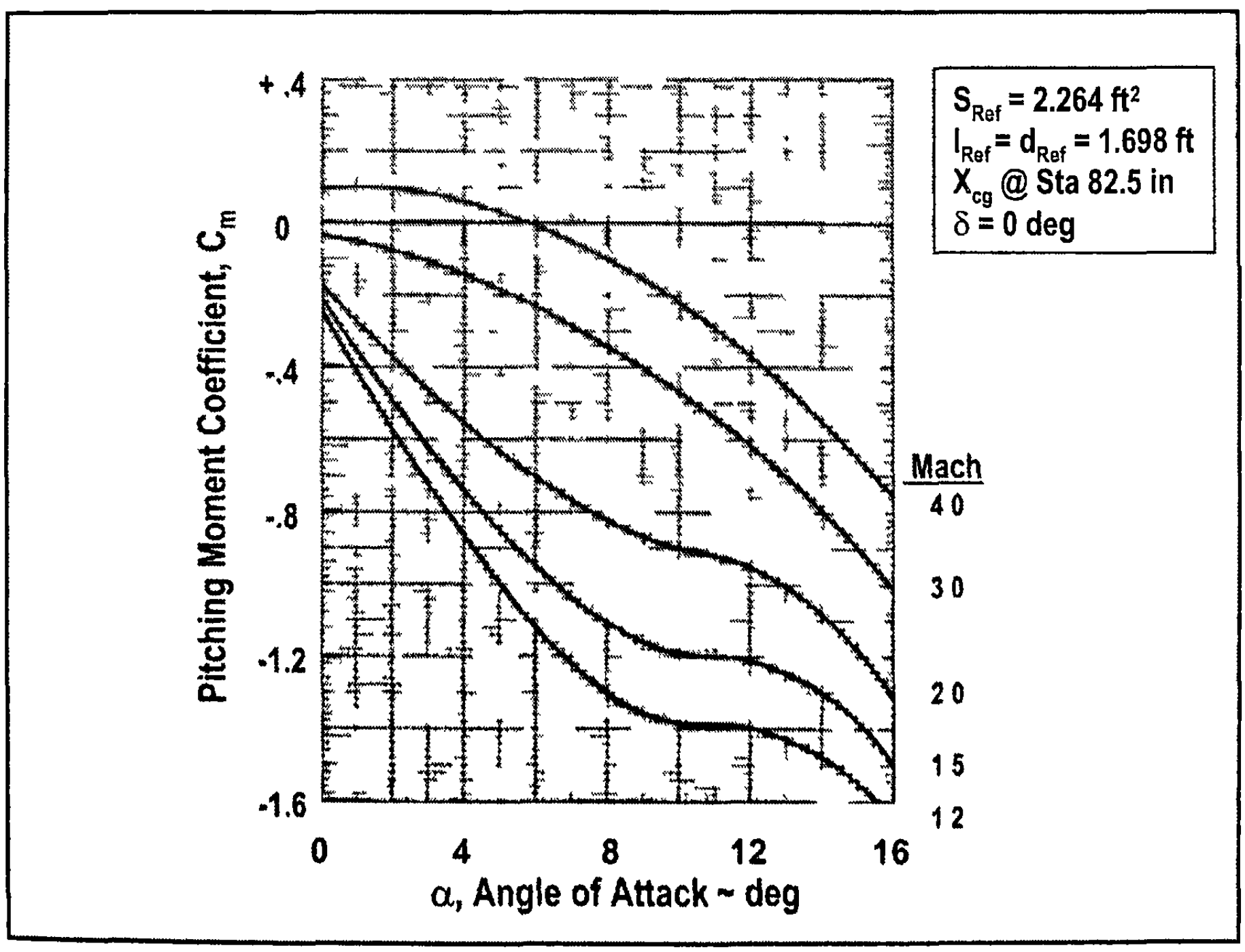

Source: Reference 27, based on year 1974 computer program from Reference 32.

Fig. 7.19b Aerodynamic characteristics of the ramjet baseline missile: pitching moment coefficient.

c)

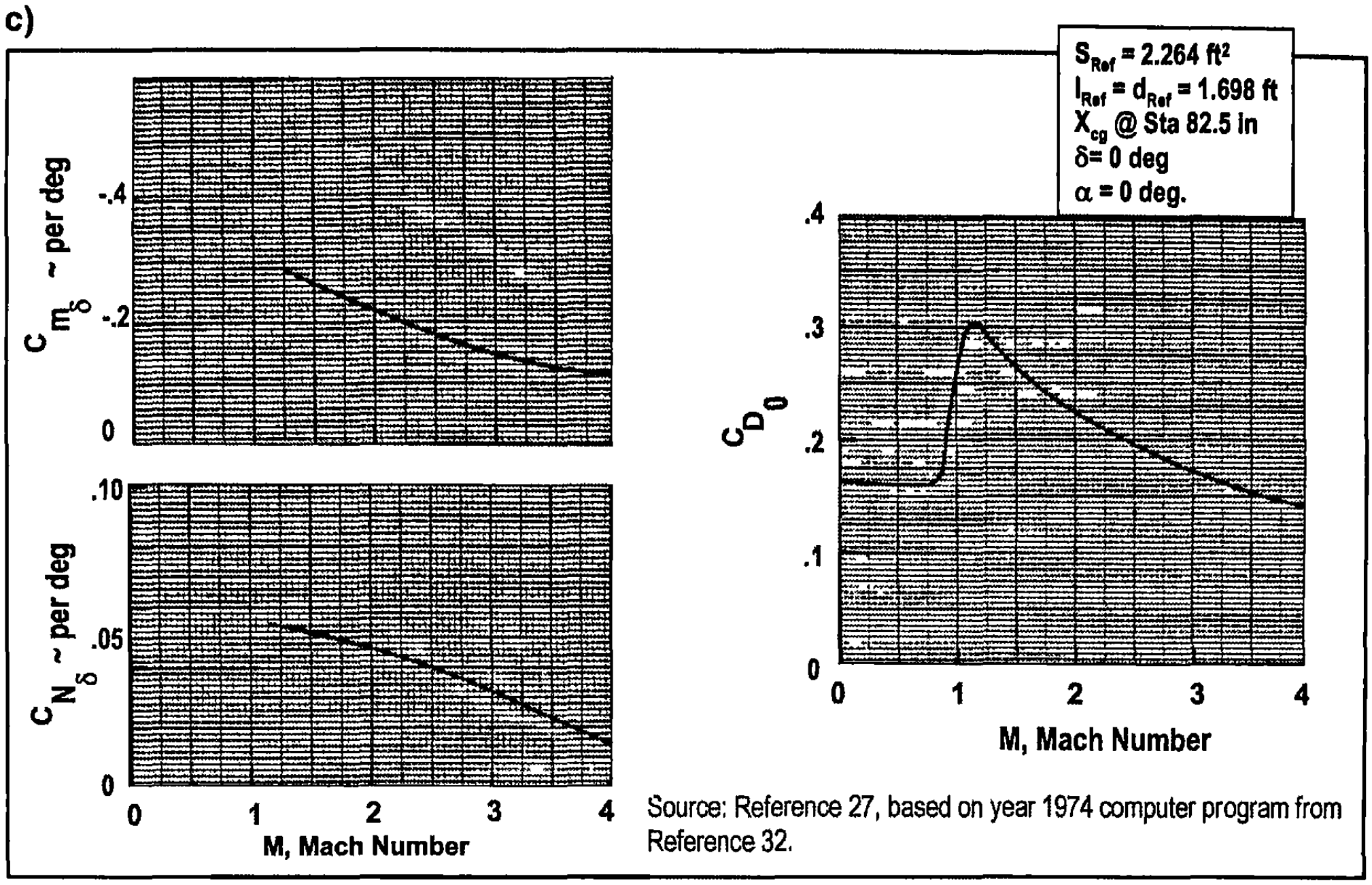

Fig. 7.19c Aerodynamic characteristics of the ramjet baseline missile: other aerodynamic characteristics.

aerodynamic coefficients with increasing supersonic Mach number. Also note that the axial force is nearly equal to the zero-lift drag coefficient. The reference center of gravity for the aerodynamic data is 82.5 in from the nose tip, representative of the cruise center of gravity.

Pitching moment coefficient C_m with undeflected controls is presented in Fig. 7.19b. Pitching moment is a function of Mach number and angle of attack. Again, the reference center-of-gravity location for the aerodynamic data is 82.5 in from the nose tip. Note the small value of pitching moment and the relatively small variation with angle of attack and Mach number. This enhances the control effectiveness and reduces the trim drag of the missile.

Zero-lift drag coefficient C_{D_0} and the stability and control derivatives C_{m_δ} and C_{N_δ} are presented in Fig 7.19c as a function of Mach number. The zero-lift drag coefficient is based on power-on flight. Note the decrease of the zero-lift drag coefficient and the stability and control derivatives with increasing supersonic Mach number. The zero-lift drag coefficient shown in the figure includes a correction to account for inlet capture. $(C_{D_0})_{Nose}$ is based on a flowing inlet, which reduces the drag.

Net thrust of the ramjet baseline is shown in Fig. 7.20 as a function of Mach number and altitude for standard atmospheric conditions. The assumed equivalence ratio is $\phi = 1$ (i.e., 100%, stochiometric combustion), which corresponds to a fuel-to-air ratio $f/a = 0.0667$. The assumed angle of attack is $\alpha = 0$ deg. The figure is not based on data, but was generated based on the computer program of Ref. 27. The Mach number range is 2 to 4 and the altitude range is sea level to 80,000 ft. Note that the peak thrust is produced at about Mach 3.5. For conceptual

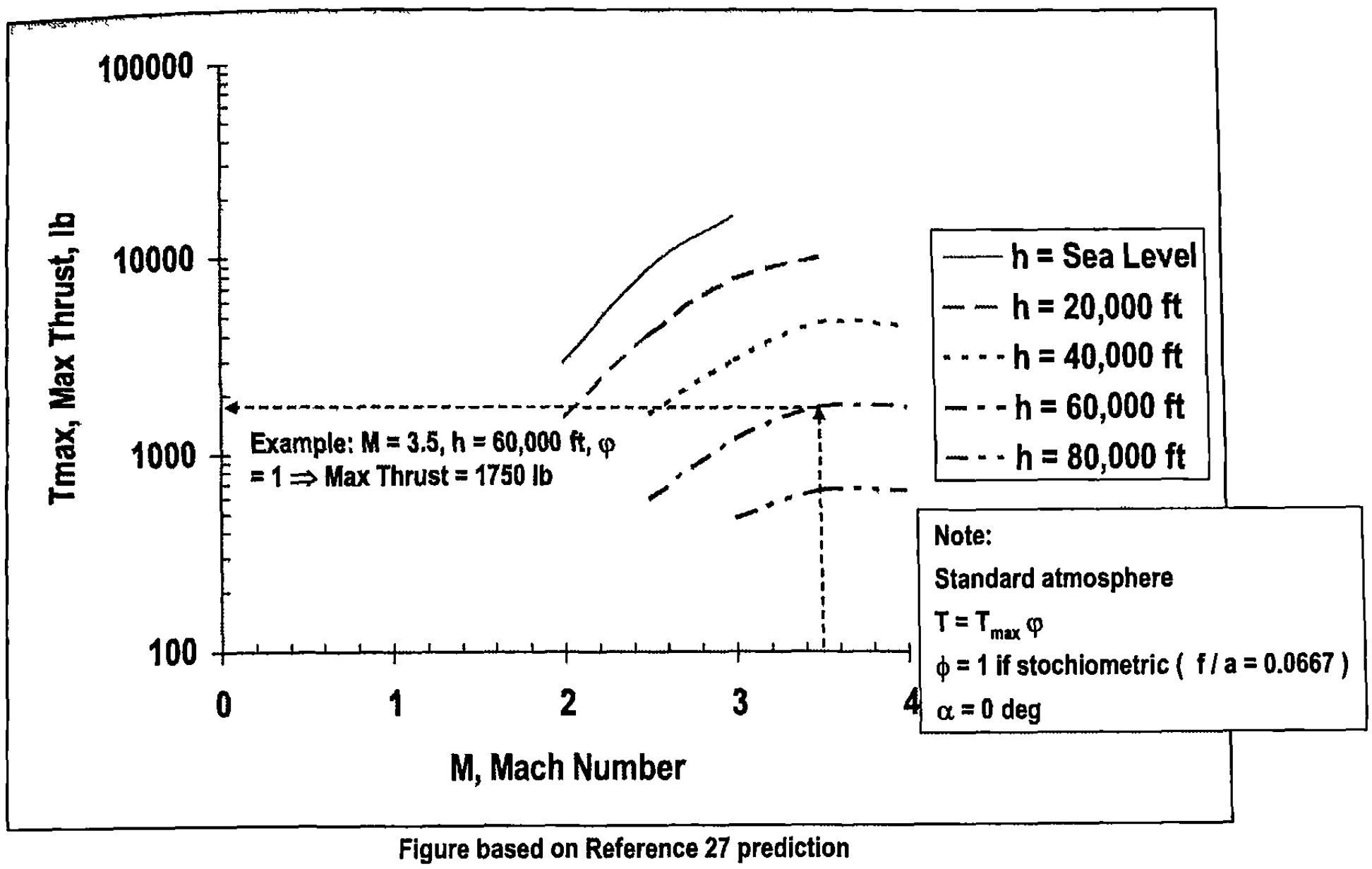

Fig. 7.20 Thrust modeling of ramjet baseline.

design purposes, it is assumed that thrust is proportional to equivalence ratio for values of $\varphi < 1$.

As an example, at Mach 3.5 and 60,000 ft altitude the maximum thrust ($\varphi = 1$) is

$$T_{\max} = 1750\,\text{lb} \tag{7.49}$$

Note that it may not be possible to achieve maximum thrust if there is a combustor temperature limit. From Chapter 3, the combustor temperature for Mach 3.5/60,000 ft/$\varphi = 1$ is

$$\begin{aligned} T_4 &\approx T_0\{1 + [(\gamma_0 - 1)/2]M_0^2\} + (H_f/c_p)(f/a) \\ &= 390\{1 + [(1.4 - 1)/2]\}(3.5)^2\} + (14{,}525/0.302)(0.0667) = 1345 + 3208 \\ &= 4553\ \text{R} \end{aligned} \tag{7.50}$$

Specific impulse of the ramjet baseline is shown in Fig. 7.21 as a function of Mach number for standard atmospheric conditions. The figure is based on the computer predictions of Ref. 27 for fuel-to-air ratio less than or equal to stochiometric. Note that the peak value of specific impulse occurs at a Mach number of about Mach 3.5. The specific impulse of the ramjet baseline is nearly independent of altitude if the equivalence ratio is less than or equal to stochiometric.

As an example, the figure shows that the specific impulse at Mach 3.5 is

$$I_{SP} = 1120\,\text{s} \tag{7.51}$$

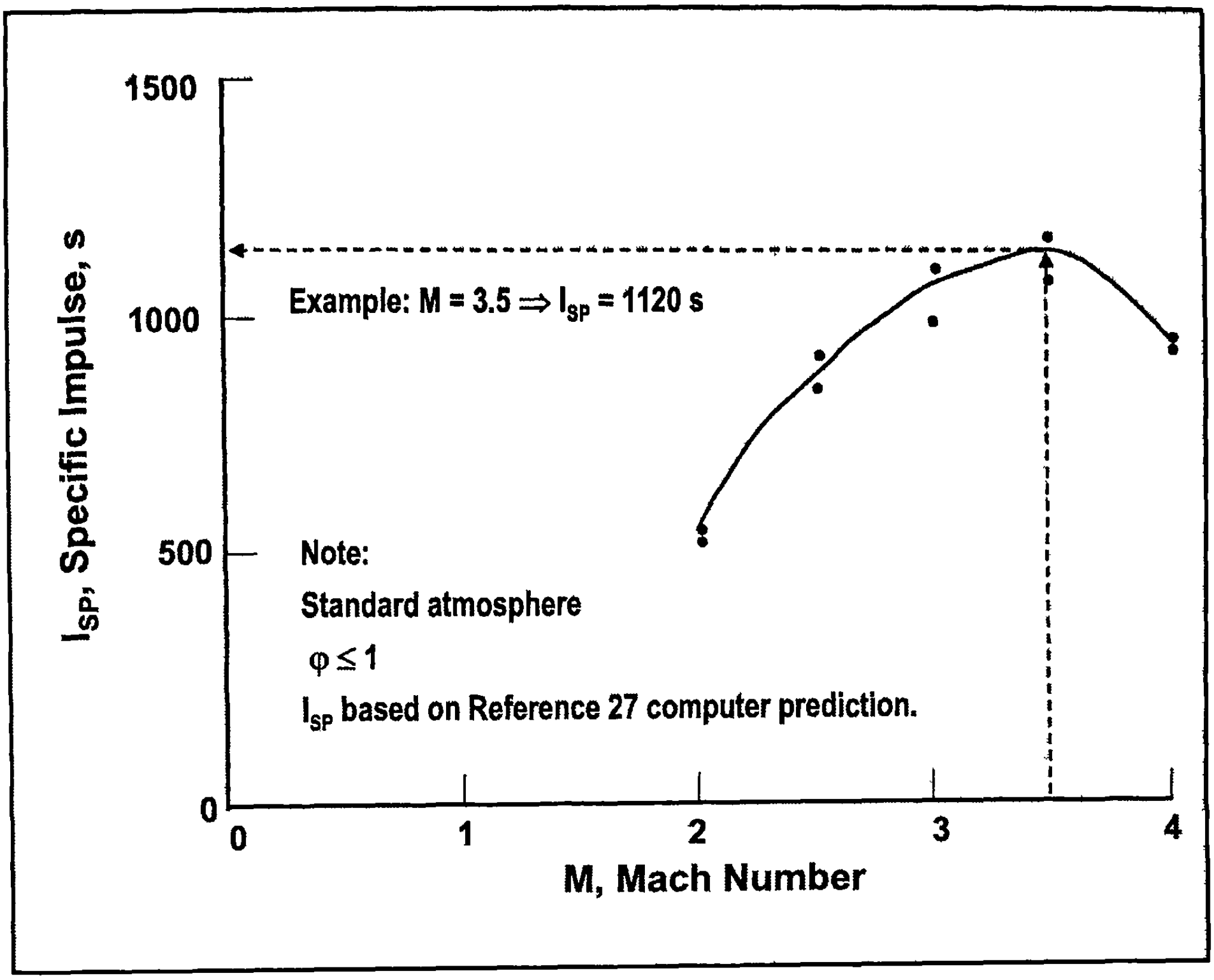

Fig. 7.21 Specific impulse modeling of ramjet baseline.

The standard atmosphere performance of the rocket boost motor is shown in Fig. 7.22 from Ref. 27. The booster thrust and burn time are 22,000 lb and 5.05 s, respectively. The booster thrust-to-launch-weight ratio is 9.9:1. A high thrust-to-weight ratio is required to provide safe separation from the launch aircraft and to minimize the propellant that is required for boost to the ramjet thrust takeover Mach number (about Mach 2.5). The incremental flight range during boost is about 1.3 n miles for a launch Mach number of 0.8. The end-of-boost burnout Mach number varies from Mach 2.3 to 2.7, depending upon the launch altitude.

Flight-range performance for constant altitude flight is shown in Fig. 7.23 from Ref. 27. Note that the ramjet baseline is much more efficient in high-altitude flight than in low-altitude flight.

As an example, for a Mach 3/60,000 ft fly-out, the range is 445 n miles. As a comparison, the Chapter 5 Breguet range prediction is

$$\begin{aligned} R &= VI_{SP}(L/D)ln[W_{BC}/(W_{BC} - W_f)] \\ &= 2901(1040)(3.15)ln(1739/(1739 - 476)) = 3{,}039{,}469\,\text{ft or } 500\,\text{nm} \end{aligned} \tag{7.52}$$

Note that the predicted range is 10% greater than baseline missile data.

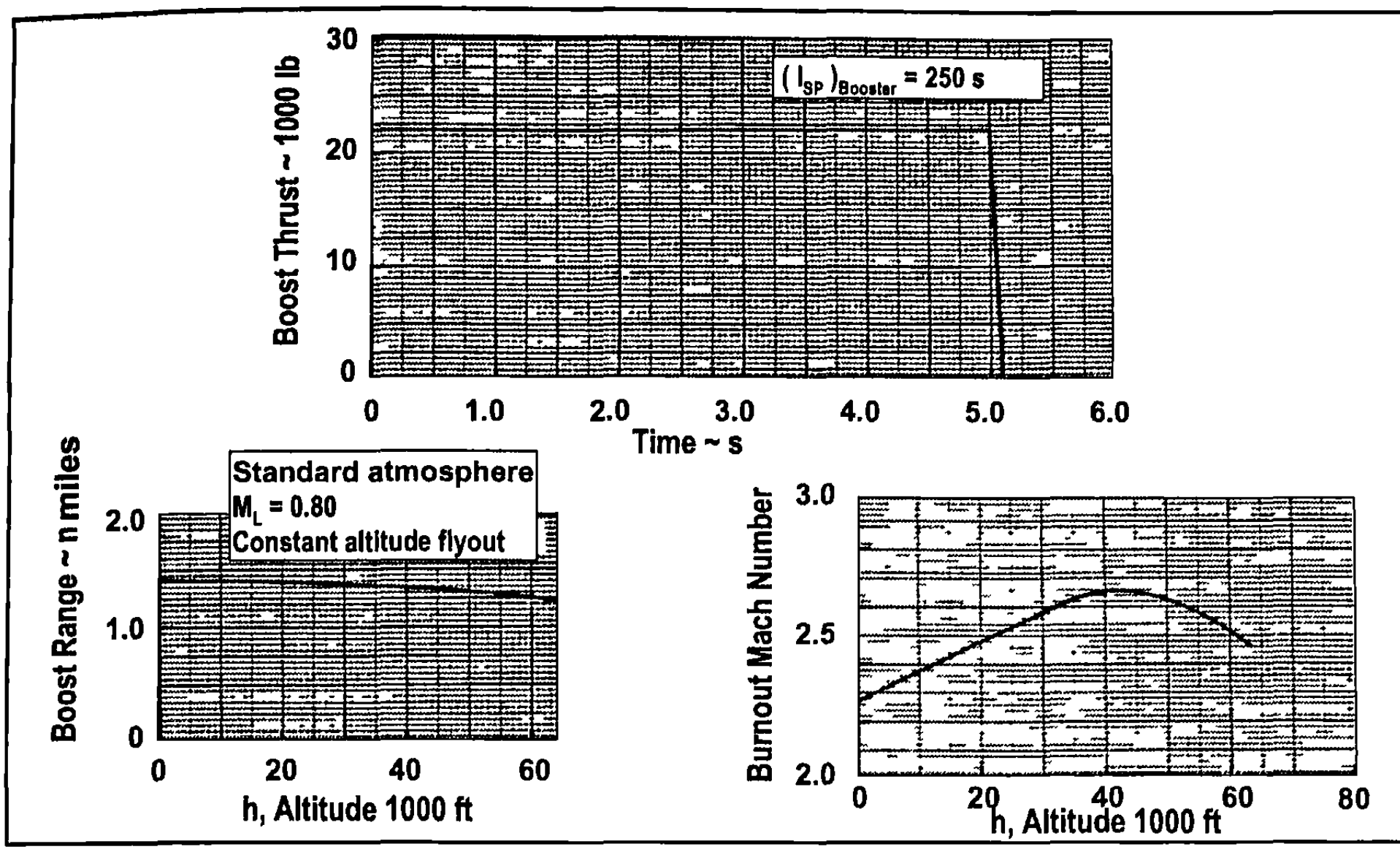

Fig. 7.22 Rocket booster acceleration/performance of ramjet baseline.

A Paredo sensitivity study was conducted to define the ramjet baseline most significant parameters for flight range and the required accuracy for prediction methods. Note from Fig. 7.24 that flight range is most sensitive to the ramjet specific impulse, fuel weight, ramjet thrust, and zero-lift drag coefficient.

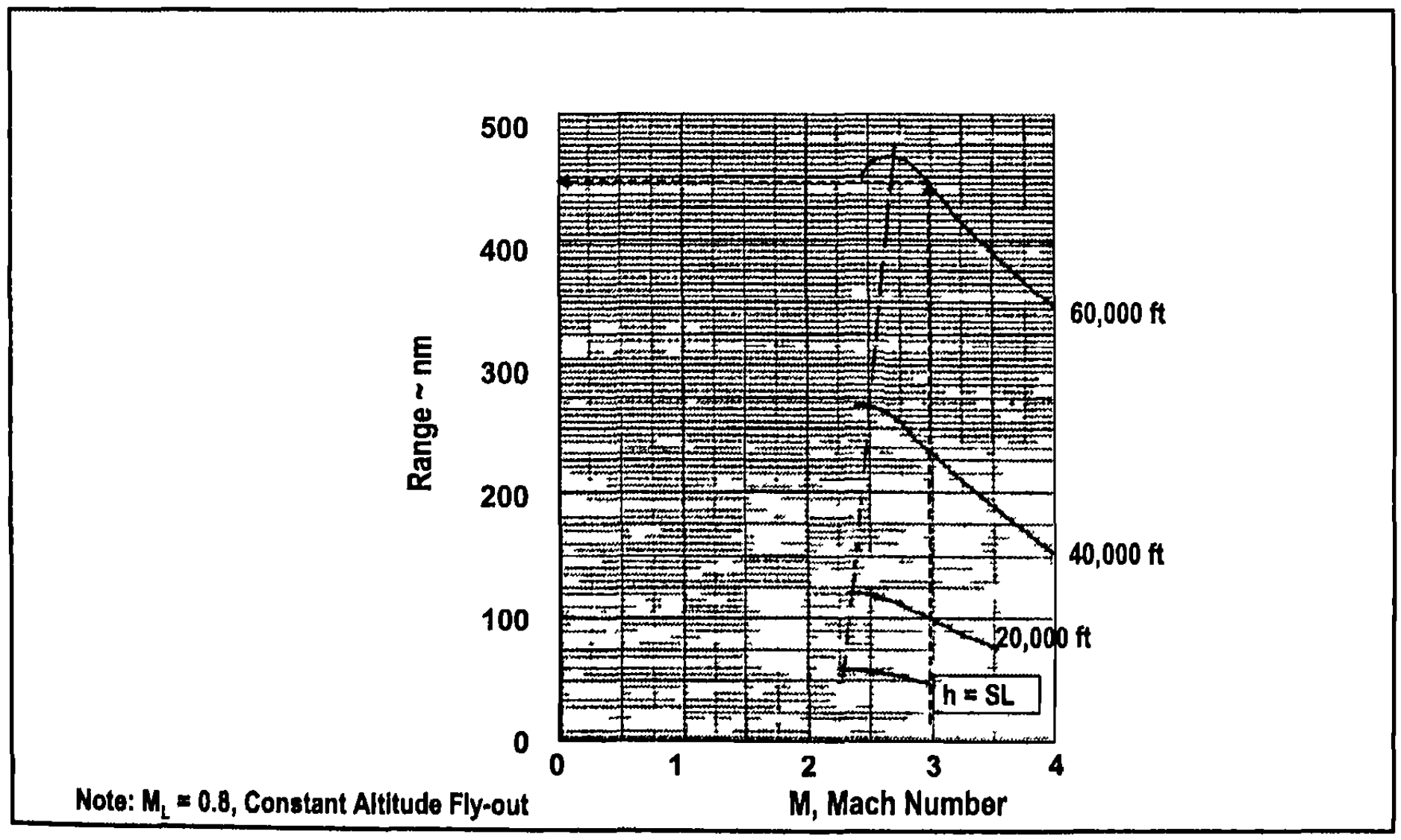

Example, Mach 3 / 60,000 ft flyout ⇒ 445 n miles. Breguet Range Prediction is $R = V\, I_{SP} (L / D) \ln [W_{BC} / (W_{BC} - W_f)] = 2901 (1040) (3.15) \ln (1739 / (1739 - 476)) = 3{,}039{,}469$ ft or 500 n miles. Predicted range is 10% greater than baseline missile data.

Fig. 7.23 Ramjet baseline has best performance at high altitude.

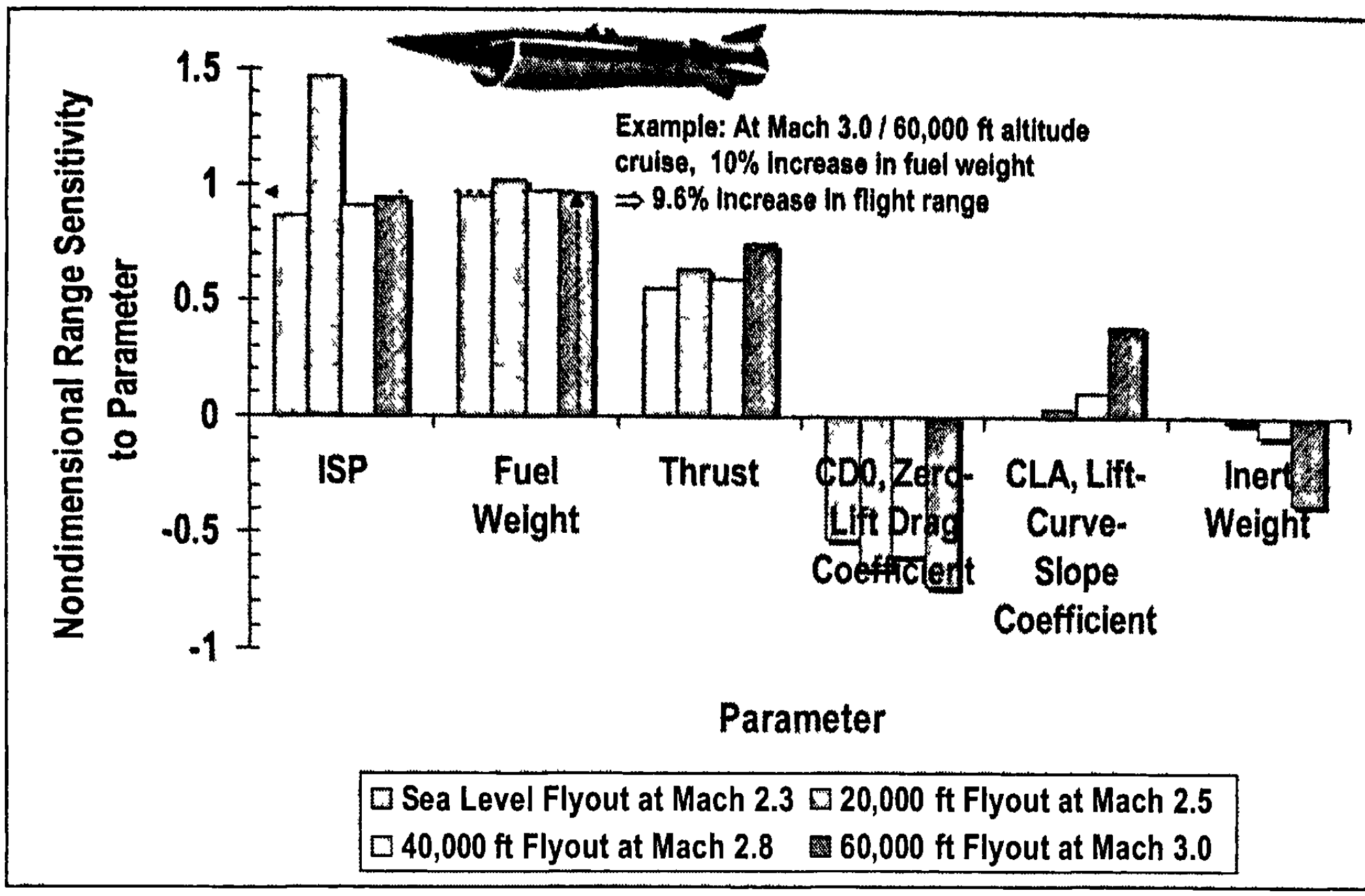

Fig. 7.24 From Paredo sensitivity, ramjet baseline range is driven by specific impulse, fuel weight, thrust, and zero-lift drag coefficient. Figure also in color section.

The flight range is relatively insensitive to inert weight and lift curve slope, especially for low-altitude flight (high dynamic pressure).

As an example, note from the figure that a 10% increase in fuel weight for a Mach 3/60,000 ft altitude cruise provides a 9.6% increase in flight range.

The prediction methods for ramjet specific impulse, zero-lift drag coefficient, and ramjet thrust usually have sufficient accuracy (e.g., $+/-5\%$, 1 σ) for conceptual design. However, there is often large uncertainty in predicting the subsystem packaging volume available to package the fuel, providing uncertainty in the fuel weight. Inboard profile drawings of subsystem packaging are required in the design process to reduce the uncertainty in the available fuel volume/weight.

The uncertainties of the values of the ramjet baseline parameters that define the cruise flight range can be used to determine the uncertainty in flight range, as shown in Table 7.7. The assumed cruise flight condition is Mach 3.0 at 60,000 ft altitude. It was previously shown that the parameters affecting flight range, in order of their Paredo sensitivity, are

1) Specific impulse
2) Ramjet fuel weight
3) Cruise thrust ($\phi = 0.39$)
4) Zero-lift drag coefficient
5) Lift curve slope coefficient
6) Inert weight

The level of maturity of the ramjet baseline used in this text is based on an advanced technology demonstration (ATD) of a flight prototype of the

Table 7.7 Ramjet baseline flight range uncertainty is +/−7%, 1σ

Parameter	Baseline value at Mach 3.0/60,000 ft	Uncertainty in parameter	ΔR/R from uncertainty
1. Specific Impulse	1040 s	+/−5%, 1σ	+/−5%, 1σ
2. Ramjet Fuel Weight	476 lb	+/−1%, 1σ	+/−0.9%, 1σ
3. Cruise Thrust ($\phi = 0.39$)	458 lb	+/−5%, 1σ	+/−2%, 1σ
4. Zero-Lift Drag Coefficient	0.17	+/−5%, 1σ	+/−4%, 1σ
5. Lift Curve Slope Coefficient	0.13/deg	+/−3%, 1σ	+/−1%, 1σ
6. Inert Weight	1205 lb	+/−2%, 1σ	+/−0.8%, 1σ

- Level of Maturity Based on Flight Demo of Prototype, Subsystem Tests, and Integration
  - Wind tunnel tests
  - Direct connect, freejet, and booster firing propulsion tests
  - Structure test
  - Mock-up
  - Hardware-in-loop simulation
  - Flight Test
- Total Flight Range Uncertainty at Mach 3.0/60,000 ft Flyout
  - $\Delta R/R = [(\Delta R/R)_1^2 + (\Delta R/R)_2^2 + (\Delta R/R)_3^2 + (\Delta R/R)_4^2 + (\Delta R/R)_5^2 + (\Delta R/R)_6^2]^{1/2} = +/-6.9\%, 1\sigma$
  - R = 445 nm +/−31 nm, 1σ

ASALM missile. Subsystem technology tests included wind tunnel tests; direct connect, inlet, and freejet propulsion tests; booster firings; and structure tests. Integration included a mock-up and hardware-in-loop simulation.

Based on the above tests, for the assumed cruise flight condition of Mach 3, 60,000 ft altitude, the ramjet baseline parameters are assumed to have the following values and uncertainties: specific impulse: 1040 s +/−5%, 1 σ; ramjet fuel weight: 476 lb +/−1%, 1 σ; cruise thrust: 458 lb ($\phi = 0.39$) +/−5%, 1σ; zero-lift drag coefficient: 0.17 +/−5%, 1 σ; lift curve slope coefficient 0.13/deg +/−3%, 1 σ; and inert weight: 1205 lb +/−2%, 1σ. The effect of uncertainty of each parameter on flight range was obtained by multiplying the uncertainty in the value of the parameter times the Paredo sensitivity of the parameter. The ranking of parameter uncertainty on flight range, in order of importance, is

1) Specific impulse: +/−5%, 1 σ
2) Zero-lift drag coefficient: +/−4%, 1 σ
3) Cruise thrust ($\phi = 0.39$): +/−2%, 1σ
4) Lift curve slope coefficient: +/−1%, 1σ
5) Ramjet fuel weight: +/−0.9%, 1 σ
6) Inert weight: +/−0.8%, 1 σ

Uncertainty analysis is an aid in planning the development program. As an example, to meet the flight range requirement based on the above ranking, the development program should give more emphasis to reducing the uncertainty in specific impulse than in reducing the uncertainty in inert weight. The uncertainty in specific impulse has more than six times the impact on flight range than that of inert weight (+/−5% vs +/−0.8%).

The ramjet baseline total flight range uncertainty for the Mach 3.0/60,000 ft cruise condition is assumed to be the root mean square (RMS) of the contributors

$$\Delta R/R = +/-[(\Delta R/R)_1^2 + (\Delta R/R)_2^2 + (\Delta R/R)_3^2 + (\Delta R/R)_4^2 + (\Delta R/R)_5^2 + (\Delta R/R)_6^2]^{1/2}$$
$$= +/-6.9\%, 1\sigma \tag{7.53}$$

The ramjet baseline missile cruise flight range with uncertainty is therefore

$$R = 445\,\text{n miles} +/- 31\,\text{n miles}, 1\sigma \tag{7.54}$$

From above, the prediction gives a 99% confidence (3σ) that the ramjet baseline range would exceed 352 n miles. However, if the customer requires that the ramjet baseline achieve a range of 400 n miles with 99% confidence, the missile would not satisfy the requirement. The program manager would have to either develop a missile with a nominal range greater than 445 n miles or reduce the uncertainty with more development testing.

Note that because the engine burnout is at 60,000 ft altitude, the missile has additional range available in gliding from the high altitude.

7.7 Ramjet Propulsion/Fuel Alternatives

The second example of ramjet missile sizing is the effect of propulsion system alternatives and fuel alternatives on the missile flight range. Shown in Fig. 7.25 is a comparison of the baseline liquid-fuel ramjet with the propulsion/fuel alternatives of low-smoke ducted rocket, high-performance ducted rocket, solid-fuel ramjet, and slurry-fuel ramjet propulsion. The assumed cruise condition is Mach 3.5 at an altitude of 60,000 ft. The comparison is conducted for a volume-limited missile. Note that the solid hydrocarbon ducted rocket has 75% of the range of the liquid-fuel ramjet because of lower specific impulse and less available fuel volume. Although a solid hydrocarbon ducted rocket has less range than a liquid-fuel ramjet, other attributes such as simpler logistics and higher acceleration capability may make it attractive for some missions. The high-performance boron ducted rocket has 94% of the range of the liquid-fuel ramjet. A tradeoff could be made of the simpler logistics and higher acceleration of the ducted rocket versus the lower observables of the liquid-fuel ramjet plume. The solid boron fuel ramjet has 27% longer range than the liquid-fuel ramjet (496 vs 390 n miles). Although boron fuel has much higher volumetric performance and density than liquid hydrocarbon fuel, some of the potential performance benefit is lost in the reduced fuel volume from design integration. As shown in the figure, a grain cavity must be provided for the burn area, reducing the volumetric efficiency of the solid-fuel ramjet. The solid-fuel ramjet has disadvantages of increased plume observables and the lack of a throttle capability compared to the liquid hydrocarbon fuel baseline. Finally, the slurry-fuel ramjet (40% JP-10, 60% boron carbide) has almost two times the range of the liquid-fuel ramjet. The adverse characteristic of the high observables of the plume of the slurry-fuel ramjet must be traded off with the outstanding range performance. Another

Propulsion / Configuration	Fuel Type / Volumetric Performance (Btu / in3) / Density (lb / in3)	Fuel Volume (in3) / Fuel Weight (lb)	ISP (s) / Cruise Range at Mach 3 5 60,000 ft (nm)
Liquid Fuel Ramjet	RJ-5 / 581 / 0.040	11900 / 476	1120 / 390
Ducted Rocket (Low Smoke)	Solid Hydrocarbon / 1132 / 0.075	7922 / 594	677 / 294
Ducted Rocket (High Performance)	Boron / 2040 / 0.082	7922 / 649	769 / 366
Solid Fuel Ramjet	Boron / 2040 / 0.082	7056 / 579	1170 / 496
Slurry Fuel Ramjet	40% JP-10, 60% boron carbide / 1191 / 0.050	11900 / 595	1835 / 770

Note: Flow Path Available Fuel $R_{cruise} = V I_{SP} (L / D) \ln [W_{BC} / (W_{BC} - W_f)]$

Fig. 7.25 Slurry fuel and efficient packaging provide extended range ramjet. Figure also in color section.

design consideration is the need for a higher performance fuel pump because of the highly viscous slurry fuel.

In addition to the benefit of high density and high specific impulse fuel, this example illustrates the benefit of packaging efficiency to provide fuel volume. It is important to develop good drawings and packaging in the design process to have confidence in the resulting performance.

7.8 Velocity Control

The last example of ramjet missile sizing are the thrust and fuel flow rate requirements to achieve a high-velocity impact on a surface target. It illustrates the process of matching thrust and fuel flow rate to the required values for flight performance. Figure 7.26 illustrates the benefit of ramjet fuel control as a means of velocity control. The previous cruise performance data for the ramjet baseline showed that the liquid-fuel ramjet has a low thrust and a low fuel flow rate requirement in the efficient cruise at high altitude. The thrust for efficient cruise at Mach 3, 60,000 ft altitude is $T = 458$ lb. At Mach 3, 60,000 ft altitude the dynamic pressure q, fuel flow rate $w^{\cdot}$, and equivalence ratio φ are 945 psf, 0.46 lb/s, and 0.39, respectively. The liquid-fuel ramjet can also provide the higher thrust that is required for a high-impact speed on a surface target. As an example, assume an impact Mach number $M_1 = 4$ at an

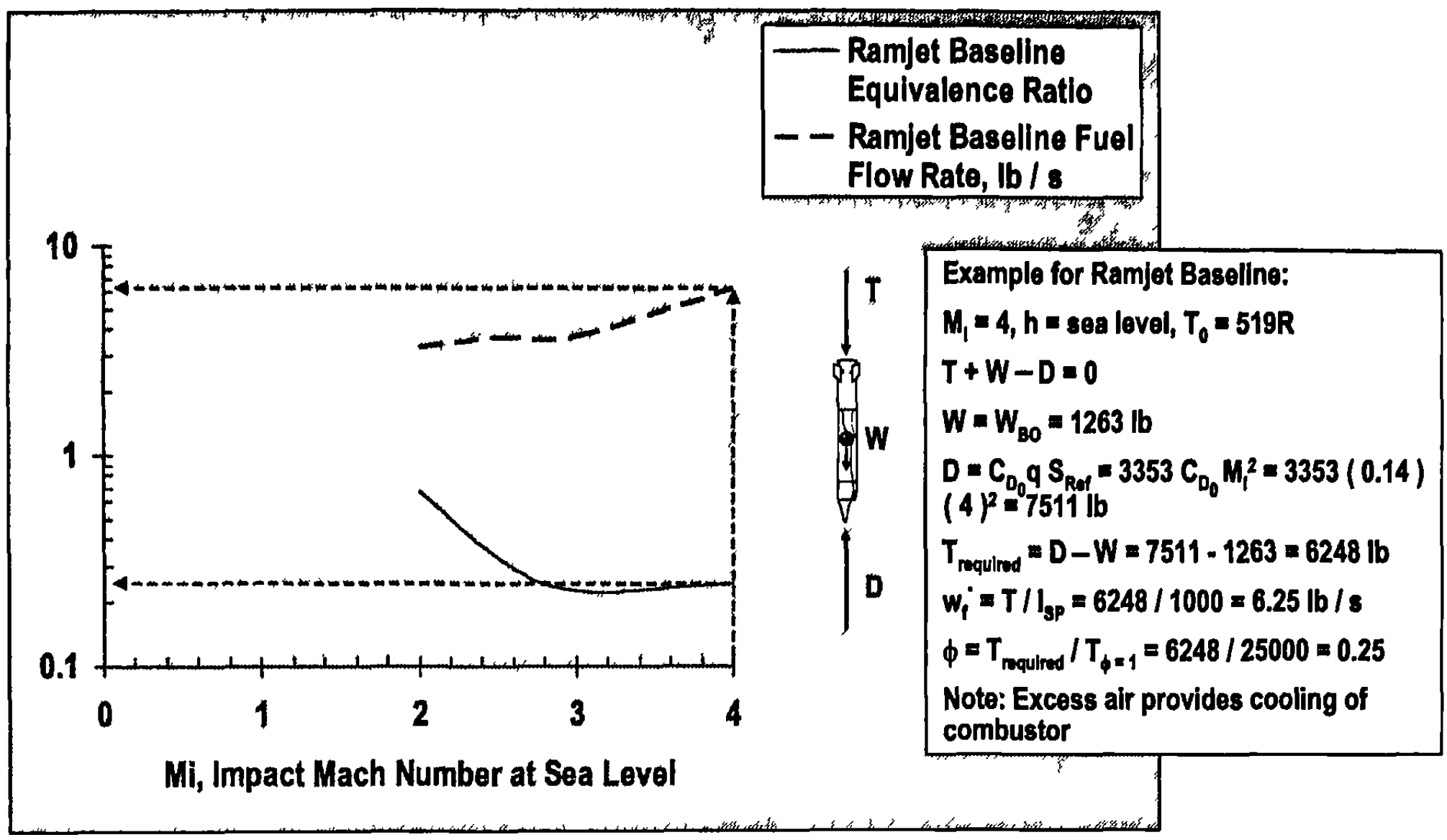

Note: Ramjet baseline, vertical impact at sea level, steady state velocity at impact, T = thrust, W = weight, D = drag, W_{BO} = burnout weight, C_{D_0} = zero-lift drag coefficient, M_I = impact Mach number, $T_{required}$ = required thrust for steady state flight, $w_f^{\cdot}$ = fuel flow rate, I_{SP} = specific impulse, ϕ = equivalence ratio ($\phi = 1$ stochiometric)

Fig. 7.26 Example of ramjet velocity control through fuel control.

impact altitude h = sea level ($T_0 = 519$ R). For a vertical impact at constant velocity, the summation of forces is

$$T + W - D = 0 \tag{7.55}$$

The weight at burnout is

$$W = W_{\mathrm{BO}} = 1263\ \mathrm{lb} \tag{7.56}$$

Drag is

$$\begin{aligned} D &= C_{\mathrm{D}_0} q S_{\mathrm{Ref}} = C_{\mathrm{D}_0}[(1/2)\rho M^2 c^2] S_{\mathrm{Ref}} \\ &= C_{\mathrm{D}_0}[(1/2)(0.002377) M^2 (1116)^2](2.264) \\ &= 3353 C_{\mathrm{D}_0} M_{\mathrm{I}}^2 = 3353(0.14)(4)^2 = 7511\ \mathrm{lb} \end{aligned} \tag{7.57}$$

Substituting for the required thrust

$$T_{\mathrm{required}} = D - W = 7511 - 1263 = 6248\ \mathrm{lb} \tag{7.58}$$

The fuel flow rate is

$$w^{\cdot} = T / I_{\mathrm{SP}} = 6248/1000 = 6.25\ \mathrm{lb/s} \tag{7.59}$$

Calculating equivalence ratio

$$\varphi = T_{\mathrm{required}} / T_{\phi=1} = 6248/25{,}000 = 0.25 \tag{7.60}$$

The thrust required for a Mach 4 vertical impact on a sea-level target is much larger than the thrust required for high-altitude cruise. At Mach 4, sea-level impact, the dynamic pressure is $q = 23{,}700$ psf, fuel flow rate $w^{\cdot} = 6.25$ lb/s, and $\phi = 0.25$. The fuel-to-air ratio at Mach 4 impact is $f/a = 0.25(0.0667) = 0.0167$. Note that the equivalence ratio is much less than stochiometric for both the low-thrust/high-altitude cruise and the high-thrust/sea-level impact flight conditions. The ramjet baseline takes on more air than is nominally required for high efficiency in aerodynamics and propulsion. For the Mach 4 impact condition, the combustor exit temperature using the equation from Chapter 3 is calculated to be

$$\begin{aligned} T_4 &\approx T_0\{1 + [(\gamma - 1)/2]M_0^2\} + (H_f/c_p)(f/a) \\ &= 519\{1 + [(1.29 - 1)/2](4)^2 + (14525/0.30)(0.0167) \\ &= 1723 + 809 = 2{,}532\,\mathrm{R} \end{aligned} \tag{7.61}$$

The excess air has a benefit of cooling the combustor.

Operating the ramjet engine over the broad range of throttle ratio (13.6 to 1) is pushing the state of the art in combustion stability technology and fuel pump technology. Also, the baseline ramjet missile was also designed for cruise at Mach 3.0, sea-level flight. A heavier structure would be required for Mach 4, sea-level flight.

7.9 Examples of Computer-Aided Conceptual Design Sizing Tools

The next sizing examples are examples of computer-aided conceptual design sizing tools. Two fundamental requirements for computer programs used in conceptual design are fast turnaround time and ease of use. Fast turnaround is necessary to search a broad solution space with a sufficient number of iterations for design convergence to an optimum design. A good design code connects the missile physical parameters directly to a trajectory code that calculates flight performance. The conceptual design methods should be simple physics-based methods, incorporating only the most important driving parameters. A simple physics-based code with only a few, driving parameters allows easier insight into the relationships of the parameters. Paredo analysis shows that the top four most sensitive parameters usually provide greater than 80% of the design drivers. Another advantage of a simple, analytical code is that the computation is usually more stable than a detailed design and analysis code. Baseline missile data should be imbedded in the code to facilitate startup.

More detailed computational methods are used later in preliminary design when the number of alternative geometric, subsystem, and flight parameters have been reduced to a smaller set of possibilities. As an example, it is usually inappropriate to use computational fluid dynamics (CFD) in conceptual design. The mathematical considerations of CFD (e.g., mesh size, time interval, numerical stability, turbulence modeling, smoothing) are impediments to the fast turnaround time that is required for conceptual design. Similarly, a six-DOF trajectory simulation is inappropriate during conceptual design for the convenient

evaluation of guided flight. The development of the required autopilot for six-DOF guided flight is time consuming, diverting emphasis from other more appropriate considerations. Similarly, missile optimization codes are generally inappropriate for conceptual design. Optimization in conceptual design is best left to the creativity and the intuition of the designer. Optimization codes work best when there is a continuous smooth variation in parameters, which is usually not the case in conceptual design. For example, optimization codes do not work well in comparing ramjet propulsion versus rocket propulsion. The CFD, six-DOF guided flight trajectory simulations and optimization codes have seductive "precision." However, more often than not their accuracy in conceptual design is worse than simpler methods. Simple aerodynamic, propulsion, weight, and flight trajectory methods combined with a well-defined baseline missile and the designer's creativity and intuition are a preferable approach for alternatives selection, sizing, and optimization. They are invariably more accurate and more robust and provide better insight into the relationships of the driving parameters. References 28 and 29 are examples of conceptual design computer-aided sizing methods that are fast and usually have sufficient accuracy for the relative screening of missile concept alternatives. Finally, it is important that the designer, not the computer, make the creative decisions. A computer program, even an adaptive program such as genetic algorithms, lacks the creativity to consider a novel concept (e.g., lattice fins).

The following discussion of the Advanced Design of Aerodynamic Missiles (ADAM) missile simulation program (Ref. 29) is provided as an example of a computer program that generally meets the conceptual design criteria of fast turnaround, ease of use, and applicability to a broad range of configurations and flight conditions. ADAM is a DOS code that runs on a personal computer. A disadvantage of ADAM is that it may have compatibility problems with high-speed computers. It may require a compatible timing hardware emulation setting to reduce the rate at which the computer's timer sends timing calls. The aerodynamics predictions are based on References 7 and 8. The aerodynamic methods cover subsonic to hypersonic Mach numbers and angles of attack up to 180 deg. The ADAM aerodynamics module calculates force and moment coefficients, static and dynamic stability derivatives, trim conditions, control effectiveness, and center-of-pressure location. Modeling of the equations of motion can be in three, four, five, or even six-DOF (unguided flight). The three-DOF flight trajectory model runs faster than real time. As an example, a 30-s time of flight requires about 8 s of run time. The six-DOF flight trajectory simulation is used to analyze the nutation/precession modes of missiles during their unguided portion of flight as well as unguided bombs and unguided projectiles. It requires longer run time. For homing missiles, proportional guidance can be used as well as other guidance laws. The input to the flight trajectory module is provided automatically by the aerodynamics module, simplifying the user input. The benchmark missiles used in the aerodynamics module have corrected coefficients and derivatives based on wind tunnel data. Greater than 50 input parameters are available. The input default is the baseline missile parameters, simplifying the input data preparation.

The baseline missiles in ADAM include air-to-air (e.g., Archer), surface-to-air (e.g., Patriot), air-to-surface (e.g., Hellfire), and surface-to-surface (e.g., ATACMS) missiles. The aerodynamic modeling of the body includes the

diameter, nose configuration (geometry, fineness, bluntness), body bulge, boattail, and length. The body cross section may be circular or elliptical. Up to three surfaces (stabilizers, wings, and controls) can be specified. The geometric modeling of each surface includes the location, leading edge root and tip station, span, trailing edge root and tip station, thickness, control surface deflection limit, and the number of surfaces. The program models the missile center-of-gravity variation from launch to burnout. For propulsion, the thrust is modeled as a two-value thrust profile of a given time duration. The propellant weight of each thrust-time phase can also be specified. The target can be fixed or moving. Down range and cross range of the target are specified as well as the target altitude and velocity. Launch conditions for the missile are specified, including altitude, velocity, launch angle, and the guidance law. The output of the three-DOF pitch simulation modeling includes a drawing of the missile geometry with dimensions, aerodynamic coefficients and derivatives, center-of-pressure location, flight performance parameters (velocity, trim angle of attack, acceleration, range, trim control surface deflection) versus time, and missile miss distance.

A second computer technique suitable for conceptual design is spreadsheet analysis. Figure 7.27 shows the design parameters of the Tactical Missile Design (TMD) spreadsheet included with this textbook. The current spreadsheet is based on the methods and data that were developed for the first edition of the *Tactical Missile Design* textbook, circa 2001. More recent methods and data

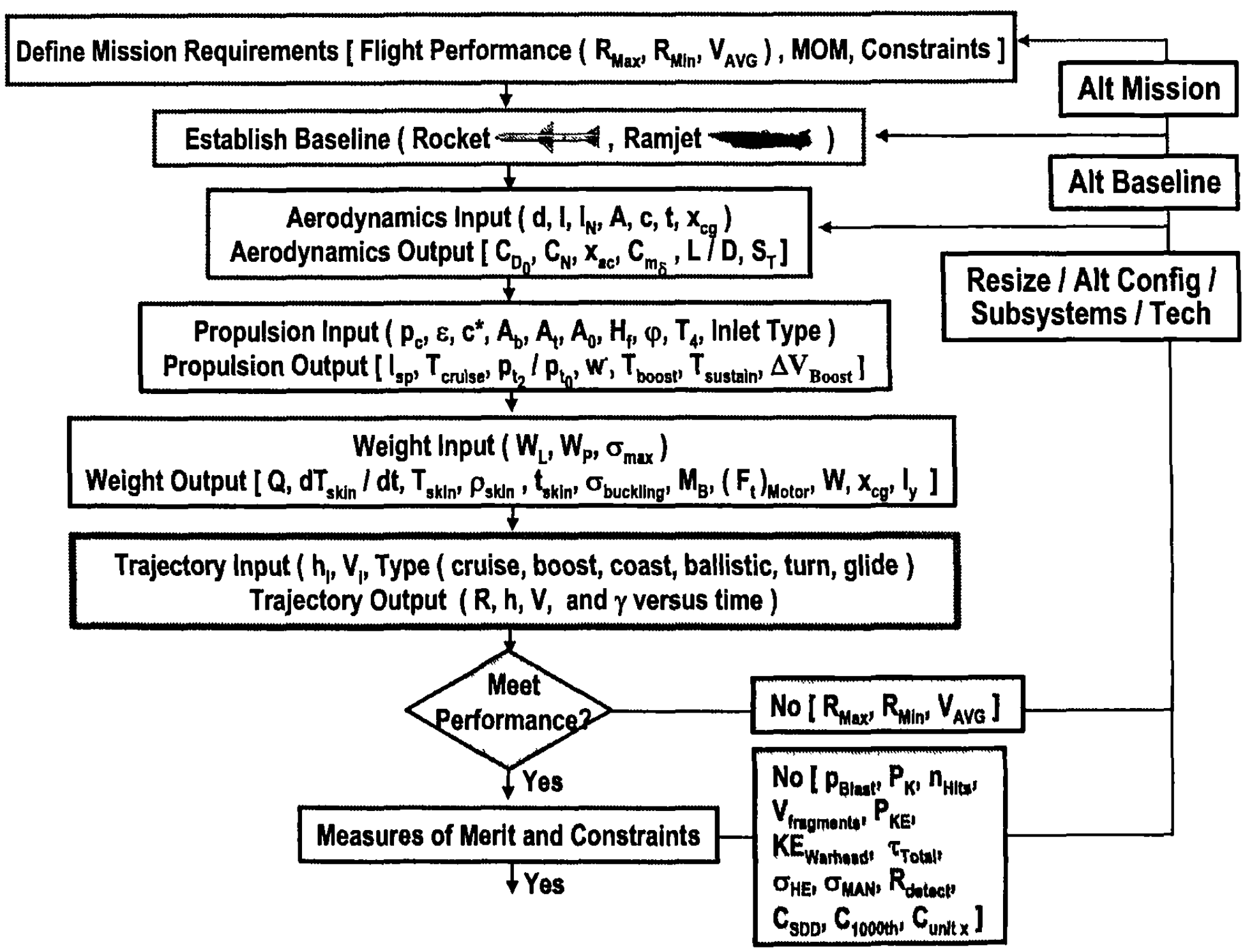

Fig. 7.27 Example of spreadsheet based conceptual sizing computer code, TMD spreadsheet.

developed for the 2nd edition of the textbook have not yet been incorporated in the spreadsheet. However, it is anticipated that the spreadsheet software will be periodically updated with future printings of the textbook. The spreadsheet software is Windows Excel, which has wide availability for personal computers. The following description of the TMD spreadsheet is based on the current text in the anticipation of future revisions of the spreadsheet.

Aerodynamics of the missile body is from slender body theory[7] and crossflow theory[8]. The fixed and movable surface aerodynamic predictions are based on linear wing/slender wing theory[7,9] and Newtonian impact theory[8]. The methods are applicable to low aspect ratio wing and wingless configurations at angles of attack up to 90 deg and Mach number from subsonic to hypersonic.

For a ramjet-powered missile, the propulsion module output includes the inlet total pressure recovery, specific impulse, and thrust.[11,13,14] The ramjet thrust and specific impulse predictions include the oblique and normal shock losses in total pressure. The rocket motor thrust and specific impulse are based on the isentropic flow equations adjusted for the change in specific heat ratio with temperature.

The system and subsystem weight scaling (i.e., density scaling) and material data (e.g., stress-strain vs temperature) in the TMD spreadsheet weight module are from this text. Predictions of aerodynamic heating and temperatures from Refs. 4, 16, and 17 are used to evaluate structure and insulation thickness/weight. The body localized buckling stress from bending moment and axial loads, motor case stress, and the required motor case and airframe thickness are based on the methods used in this text. Methods from this text are also used to predict the weight of the missile dome, power supply, and actuators.

Flight trajectory methods are based on closed-form analytical methods. Cruise range prediction is the Breguet range equation. The thrust required for steady cruise, steady climb, and steady dive is based on Jerger[4]. Turn radius, turn rate, boost velocity, coast velocity, coast range, ballistic flight velocity, ballistic range, missile homing lead angle, launch range, and F-pole range are based on the methods used in this text.

Warhead blast pressure is based on Ref. 20. Fragment velocity, kill probability, number of warhead fragments impacting the target, kinetic energy warhead penetration, and penetrator kinetic energy are based on Ref. 21 and the methods used in this text. Kinetic energy penetration depth is based on Ref. 22. In the area of guidance, miss distance prediction and parameters (e.g., missile time constant, heading error, maneuvering target acceleration) are based on this text, Ref. 24, and Ref. 25. Survivability detection range and other design considerations for survivability are based on this text. Finally, production cost due to weight and the learning curve and system development and demonstration (SDD) cost are based on this text, using data from Ref. 26.

Reference 30 presents a more detailed discussion of the TMD spreadsheet.

Following definition of mission requirements such as range and velocity and selection of a baseline configuration (either rocket or ramjet), the aerodynamics module is exercised. Aerodynamic data input to the aerodynamics module includes the missile diameter d, missile length l, nose length l_N, surfaces aspect ratio A, surfaces chord c, surfaces thickness t, and the missile center of

gravity x_{cg}. The aerodynamics module then calculates the zero-lift drag coefficient C_{D_0}, normal force coefficient C_N, aerodynamic center location x_{ac}, pitching moment control effectiveness C_{m_δ}, lift-to-drag ratio L/D, and the required tail stabilizer surface area S_T. Although the TMD spreadsheet can size the tails for neutral stability at a specified Mach number flight condition, it is important to check a number of flight conditions to make sure that the tails provide sufficient stability at the worse case flight condition. The worse case flight condition for stability is often the highest Mach number. However, because the highest Mach number may occur at burnout with a forward location of the center of gravity, it is important to also check the stability at the launch condition, which usually has a more aft location of the center of gravity. It is also necessary to check that the missile has sufficient control effectiveness. The output of the aerodynamics module, along with the default data of the baseline missile, is an input into the propulsion module.

Propulsion data input to the propulsion module for the rocket includes motor chamber pressure p_c, nozzle expansion ratio ε, characteristic velocity c^*, burn area A_b, and throat area A_t. For a ramjet engine, the input data also include the inlet capture area A_0, heating value of the fuel H_f, equivalence ratio ϕ, combustor exit temperature T_4, and the type of inlet. The propulsion module output for a rocket motor includes incremental velocity ΔV, thrust T, and specific impulse I_{SP}.

A weight module is next used to revise the missile weight. Input data include the missile launch weight W_L, propellant weight W_p, and the maximum allowable stress σ_{max} of the structure materials. The weight module provides an estimate of aerodynamic heating, surface and inner wall temperatures, required airframe and motor case thickness, localized buckling stress, bending moment, motor case stress, total weight, center of gravity, moment of inertia, and the density/weight of subsystems.

The flight trajectory spreadsheet has closed-form, analytical equations for one- and two-DOF trajectories. Closed-form, analytical equations provide design insight into the driving parameters and usually eliminate instabilities, which can be a problem for a more sophisticated time marching numerical integration of the equations of motion. The input includes the initial altitude, initial velocity, and the type of flight profile (e.g., cruise, boost, coast, ballistic, turn, glide). The output of the flight trajectory spreadsheet includes flight range, altitude, velocity, and flight path angle versus time.

Finally, the designer compares the output of the flight trajectory spreadsheet against the mission flight performance requirements. If the missile design does not meet the performance requirements, the process is repeated until the requirements are satisfied. The modularity of the spreadsheet and the default baseline missile data reduce the time required for data input in the next iteration.

Once flight performance requirements are met, the measures of merit (e.g., lethality, miss distance, survivability, cost) and launch platform constraints are evaluated. For example, the warhead lethality parameters include the blast pressure and kinetic energy penetration. Miss distance parameters include time constant and the miss distances from heading error and maneuvering target. Costs are provided for SDD cost, production cost of the 1000th missile, and the unit production cost of other missile quantities. Again, the design is iterated until the measures of merit and constraints are satisfied.

The verification process of a computer sizing code includes comparing the source code with the original algorithms, comparing results with another computer code, and when possible comparing the results with test data. Verification of the TMD spreadsheet was based on comparing the source code with the equations from this text, comparing results with the ADAM code, and comparing the results with the text examples. The rocket and ramjet baselines, which are based on test data, were used in the verification of the TMD spreadsheet. A limited validation of the TMD spreadsheet has been accomplished based on comparisons with Sparrow and ASALM test data. A complete validation of the TMD spreadsheet has not been accomplished because the broad range of applicability of the TMD spreadsheet requires an extensive comparison with a large set of test data.

As an example, assume the air-to-air range requirement discussed previously in this chapter. The launch condition is Mach 0.8 launch at 20,000 ft altitude. In the example the rocket baseline missile flies straight ahead at constant altitude. Based on the F-pole requirement, the missile must fly 6.7 n miles in less than 24.4 s. In this example the time of flight to 6.7 n miles based on wind tunnel data is 21 s. The ADAM computer program gives a time of flight of 18 s. The TMD spreadsheet gives a time of flight of 19 s. As discussed previously, the flight range of the rocket baseline is most sensitive to the parameters of specific impulse, propellant weight, zero-lift drag coefficient, drag-due-to-lift, and static margin. Results may also be sensitive to the modeling assumptions for the equations of motion. In this example, specific impulse, weight, and static margin were specified. An examination of the two solutions shows that the major contributor to the difference in time of flight is attributable to the difference in zero-lift drag coefficient C_{D_0}. For example, at Mach 2, the ADAM prediction of zero-lift drag coefficient during coast is $(C_{D_0})_{coast} = 0.53$. The TMD spreadsheet prediction is slightly higher, $(C_{D_0})_{coast} = 0.57$. However, wind tunnel data for the rocket baseline is a much larger value, $(C_{D_0})_{coast} = 1.05$. Because the uncertainty in the predicted value of zero-lift drag coefficient has an impact on flight range and time to target, it is desirable to correct the TMD spreadsheet with wind tunnel data to reduce the uncertainty. The wind tunnel data on a baseline missile can be used to reduce the uncertainty.

7.10 Soda Straw Rocket Design, Build, and Fly

The final sizing example is a "hands on" process for the student to conduct a soda straw rocket design, build, and fly activity.

Examples of postulated customer requirements for this activity include the objective, availability of furnished property, use of furnished material, launch conditions, and the requirement to compare predictions with test. The general objective is to design, build, and fly a soda straw rocket that meets customer requirements of flight range (e.g., greater than 90 ft) and weight (e.g., less than 2 g).

The furnished property includes a launch system and a measuring wheel to measure the flight range. It may also include weight scales, micrometer scales, engineer's scales, and scissors.

Furnished material includes a large diameter soda straw for the rocket body, strip tabbing for the tails, an ear plug for the nose, and a smaller diameter straw for the launch tube. The rocket body is a "giant" soda straw of 0.28 in diameter, 7.75 in length, and 0.6 g weight. Strip tabbing for construction of the tails, available at office supply stores, is $\frac{1}{2}$ in width by 6 in length, with a weight of 1.4 g. A flexible ear plug for the nose is 0.33 to 0.45 in diameter by 0.9 in length, with a weight of 0.6 g. Finally, a "super jumbo" soda straw for the launch tube is slightly smaller diameter (0.25 in) and at the same length (7.75 in) compared to the soda straw rocket.

The specified launch tube length after inserting the launch straw inside the launcher pipe fitting exit is 6 in. A typical (adjustable) launch pressure is 30 psi and a typical (adjustable) launch angle is 40 deg (for maximum range). Finally, a comparison should be conducted of predicted range with the flight test result.

The soda straw rocket launcher is compact size, allowing storage/carriage in a travel case for use in the Tactical Missile Design short course. Shown in Fig. 7.28 is a photograph of the launcher and its components. A small bicycle pump (1) pressurizes an air supply tank (2). An air hose (3) leads from the air supply tank to a pressure gauge (4) that has a maximum reading of 60 psi. Pushing the launch button (5) activates a fast responding (0.025 s) solenoid valve (6a) that allows the air to flow. An inclinometer (7) sets the angle of the launch tube (8) and rocket (9). In the event that electricity is not available, an alternative air flow path is provided through a manual valve (6b), which has a slower response time (about 0.1 s). Also shown in the figure is a laser pointer as a targeting device (10) to measure dispersal and (11) a collection of some of the rockets that have been previously built by students.

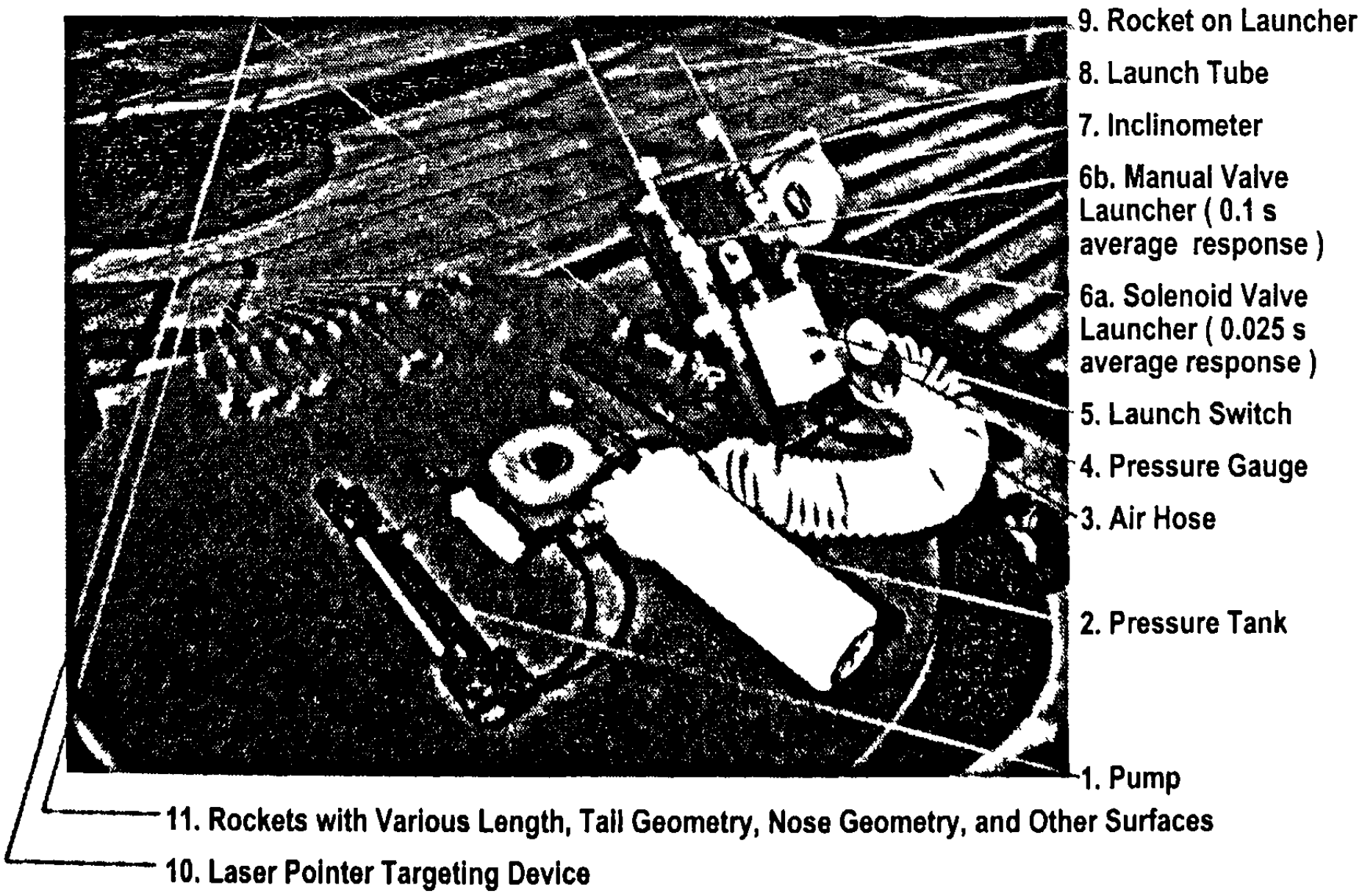

Fig. 7.28 Soda straw rocket launcher and targeting. Figure also in color section.

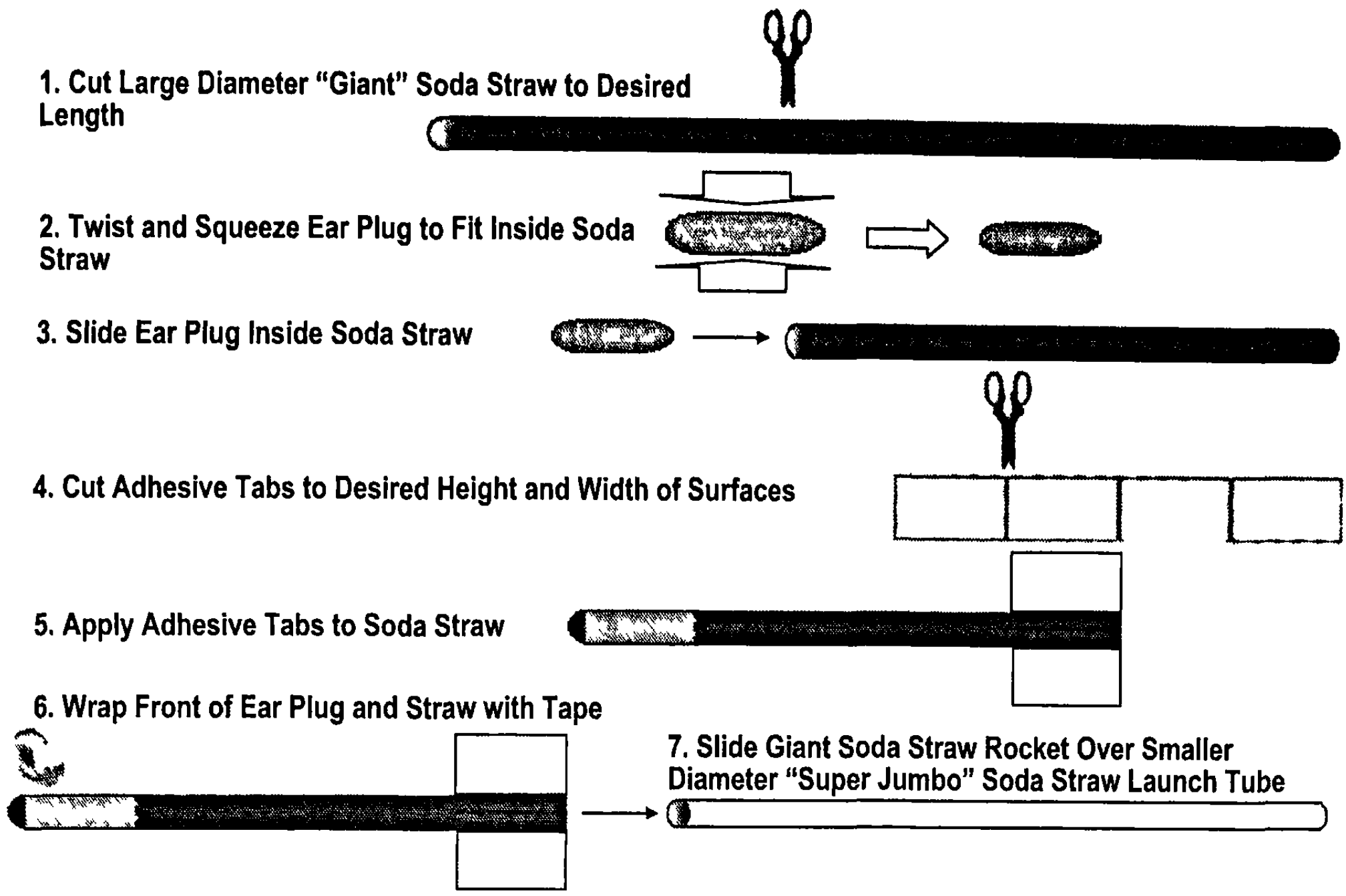

Fig. 7.29 It is easy to make a soda straw rocket.

It takes about 15 to 30 m to make a soda straw rocket. The steps for construction are shown in Fig. 7.29. The rocket body consists of a large diameter "giant" soda straw, which is cut (1) to a desired length. Next, a flexible ear plug is squeezed (2) to reduce its diameter and then inserted (3) into the front of the soda straw. Tails are made from adhesive filing tabs cut (4) to the desired size and shape. The adhesive tabs are then attached to the rear of the soda straw (5) to complete the rocket. Next (6) wrap the front of the ear plug and straw with tape to prevent the ear plug from blowing out of the straw. The soda straw rocket slides over the smaller diameter launch tube (7).

The baseline soda straw rocket configuration is shown in Fig. 7.30. It is a body-tail design consisting of a nose plug, soda straw body, and four strip tabs

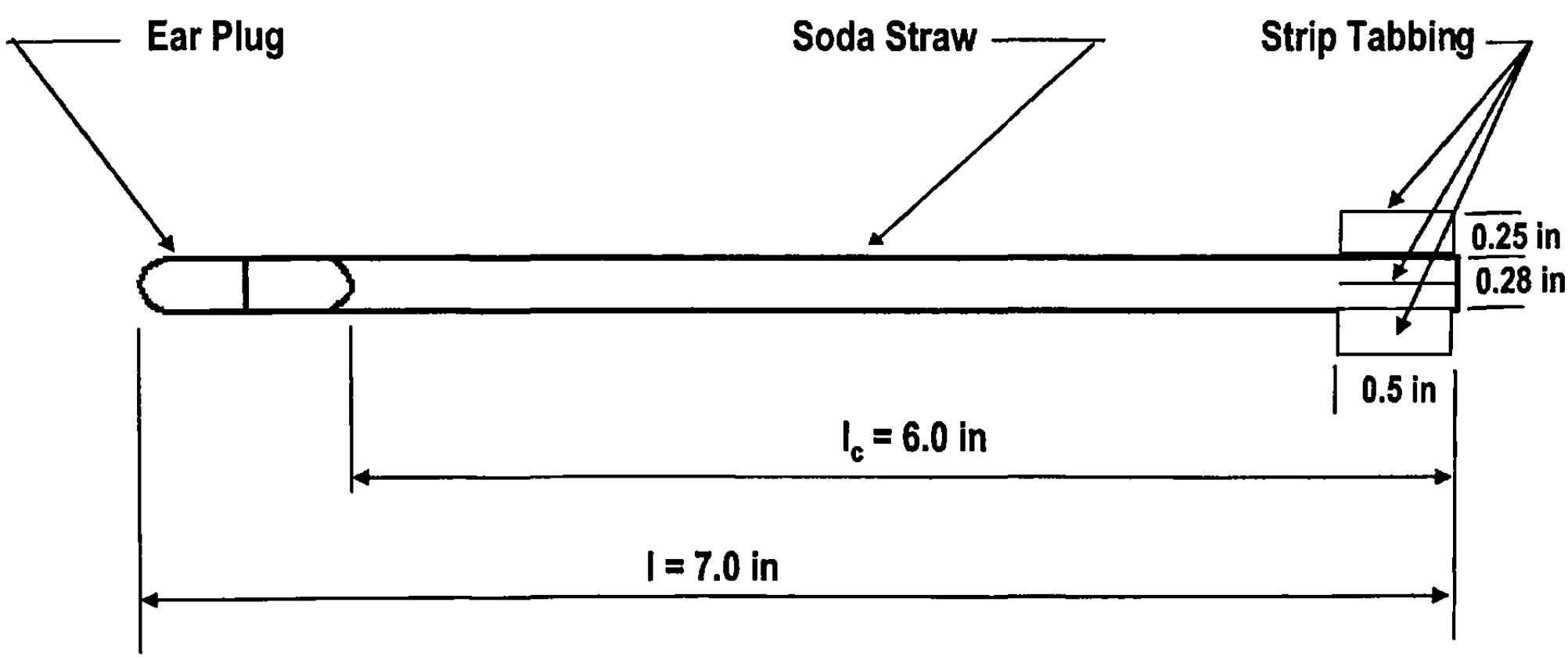

Fig. 7.30 Soda straw rocket baseline configuration.

for tails. The baseline has a diameter of 0.28 in and a length of 7.0 in. The inside chamber length is 6.0 in to maximize the total impulse from the 6.0 in length launcher. The cruciform tails are 0.25 in exposed semi-span × 0.5 in chord.

Note that the baseline soda straw rocket was selected as a representative but not an optimum configuration. It is anticipated that the student can design a lighter weight, longer range configuration.

Table 7.8 is a weight and balance statement for the baseline soda straw rocket. The 0.9-in nose plug weighs 0.6 g. The nose-plug center of gravity is located approximately in its middle, 0.5 in from the beginning of the nose. The soda straw body weighs 0.5 g, with its center of gravity located in the middle of the body, 3.5 in from the nose. Total weight of the four tails is 0.5 g. Center of gravity of the tails is 6.75 in from the nose. Total weight of the soda straw rocket is 1.6 g, which satisfies the requirement that the weight be less than 2 g. The soda straw rocket center of gravity is located approximately in the middle, 3.39 in from the nose.

Table 7.9 is a description of the soda straw rocket geometry, structure materials, and propulsion. The body is made of a thin wall (0.004 in) high-density polyethylene (HDPE) plastic soda straw. Nominal ultimate stress is $\sigma_{\text{ult}} = 4600$ psi. According to the hoop stress equation, the soda straw should theoretically withstand a gauge pressure of

$$p = \sigma_{\text{ult}} t/r = 4600(0.004)/0.14 = 131 \text{ psi} \tag{7.62}$$

Tests have been conducted for gauge pressures up to a maximum of 120 psi without failure. However, soda straw rockets have experienced side wall failure about 10% of the time at a gauge pressure of 60 psi. This is probably because of a variation in the wall thickness and voids from the extruded plastic manufacturing process. A safe gauge pressure that allows multiple launches without failure/exceeding the yield limit is 40 psi.

The fins are also made of thin wall plastic, with self-adhesive tabs for attachment to the body. The fin geometry was selected as a tradeoff of weight, stability, and drag. The nose plug is a 0.9-in length soft foam earplug with a density of $\rho = 0.012$ lb/in^3. The nose plug is inserted inside the soda straw and reinforced by tape to prevent a blowout during launch.

Reference diameter and area are based on the body diameter and cross-sectional area respectively. Nominal thrust for a 30 psi gauge pressure is $T = 1.47$ lb. The thrust rise time constant from the response time required to open the solenoid valve is $\tau = 0.025$ s.

Table 7.8 Soda straw rocket baseline weight and balance

Component	Weight, g	cg Station, in
Nose (Plug)	0.6	0.5
Body (Soda Straw)	0.5	3.5
Fins (Four)	0.5	6.75
Total	1.6	3.39

Table 7.9 Soda straw rocket baseline definition

Body	
Material Type	HDPE Plastic
Material density, lb/in^3	0.043
Material strength, psi	4,600
Thickness, in	0.004
Length, in	7.0
Diameter, in	0.28
Fineness ratio	25.0
Nose fineness ratio	0.5
Fins	
Material	Plastic
Planform area, in^2 (2 panels exposed)	0.25
Wetted area, in^2 (4 panels)	1.00
Aspect ratio (2 panels exposed)	1.00
Taper ratio	1.0
Chord, in	0.5
Span (exposed), in	0.5
Span (total including body), in	0.78
Leading edge sweep, deg	0
X_{mac}, in	6.625
Reference Values	
Reference area, in^2	0.0616
Reference length, in	0.28
Thrust Performance	
Inside cavity length, in	6.0
Pressure, psi	30
Maximum thrust, lb	1.47
Time constants, s (standard temperature)	0.025

Figure 7.31 illustrates the process to calculate the static margin prediction of the soda straw rocket baseline. For the body-tail geometry, static margin given by the equation from Chapter 2,

$$\begin{aligned}(x_{AC} - x_{CG})/d = -\{&(C_{N\alpha})_B\{[x_{CG} - (x_{AC})_B]/d\} \\ &+ (C_{N\alpha})_T\{[x_{CG} - (x_{AC})_T]/d\}(S_T/S_{Ref})\}/[(C_{N\alpha})_B \\ &+ (C_{N\alpha})_T S_T/S_{Ref}]\end{aligned} \tag{7.63}$$

The input data for the baseline soda straw configuration are $x_{CG} = 3.39$ in, $d = 0.28$ in, $(C_{N\alpha})_B = 2$ per rad, $S_T = 0.25$ in^2, and $S_{Ref} = 0.0616$ in^2. Compute the aerodynamic center of the body

$$(x_{AC})_B = [(x_{AC})_B/l_N]l_N = 0.63(0.14) = 0.09 \text{ in} \tag{7.64}$$

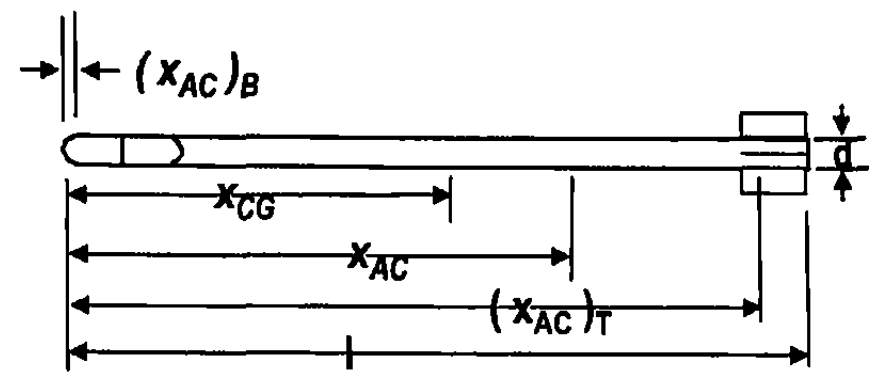

- For body-tail geometry, static margin given by
  - $(x_{AC} - x_{CG}) / d = -\{(C_{N_\alpha})_B \{[x_{CG} - (x_{AC})_B] / d\} + (C_{N_\alpha})_T \{[x_{CG} - (x_{AC})_T] / d\}(S_T / S_{Ref})\} / [(C_{N_\alpha})_B + (C_{N_\alpha})_T S_T / S_{Ref}]$
- For baseline soda straw configuration
  - $x_{CG} = 3.39$ in, $d = 0.28$ in, $(C_{N_\alpha})_B = 2$ per rad, $S_T = 0.25$ in^2, $S_{Ref} = 0.0616$ in^2
  - $(x_{AC})_B = [(x_{AC})_B / l_N]\, l_N = 0.63\,(0.14) = 0.09$ in
  - $(C_{N_\alpha})_T = \pi A_T / 2 = \pi (1) / 2 = 1.57$
  - $(x_{AC})_T = 6.5 + 0.25\,(c_{mac})_T = 6.63$
- Substituting
  - $(x_{AC} - x_{CG}) / d = -\{2(3.39 - 0.09)/0.28 + [1.57(3.39 - 6.63)/0.28][(0.25)/0.0616]\} / [2 + 1.57(0.25)/0.0616] = 6.00$ (statically stable)
  - $x_{AC} = 6.00\,(0.28) + 3.39 = 5.07$ in from nose

Fig. 7.31 Soda straw rocket baseline static margin.

The normal force coefficient of the tail, from the slender wing equation in Chapter 2, is

$$(C_{N_\alpha})_T = \pi A_T/2 = \pi(1)/2 = 1.57 \tag{7.65}$$

Compute the aerodynamic center location of the tail

$$(x_{AC})_T = 6.5 + 0.25(c_{mac})_T = 6.63 \text{ in} \tag{7.66}$$

Substituting, the static margin of the baseline soda straw rocket is

$$\begin{aligned}(x_{AC} - x_{CG})/d = &-\{2(3.39 - 0.09)/0.28 \\ &+ [1.57(3.39 - 6.63)/0.28][(0.25)/0.0616]\}/ \\ &[2 + 1.57(0.25)/0.0616] \\ = &\ 6.0 \text{ (statically stable)}\end{aligned} \tag{7.67}$$

Note from the above result the baseline soda straw rocket has a static margin of 6.0 diameters. A soda straw rocket with less static margin would probably have better performance. It would be lighter weight resulting in a higher launch velocity and longer range. It would also be less likely to weather cock, resulting in less dispersal and longer range in a crosswind.

The location of the aerodynamic center is $x_{AC} = 6.00(0.28) + 3.39 = 5.07$ in from the nose.

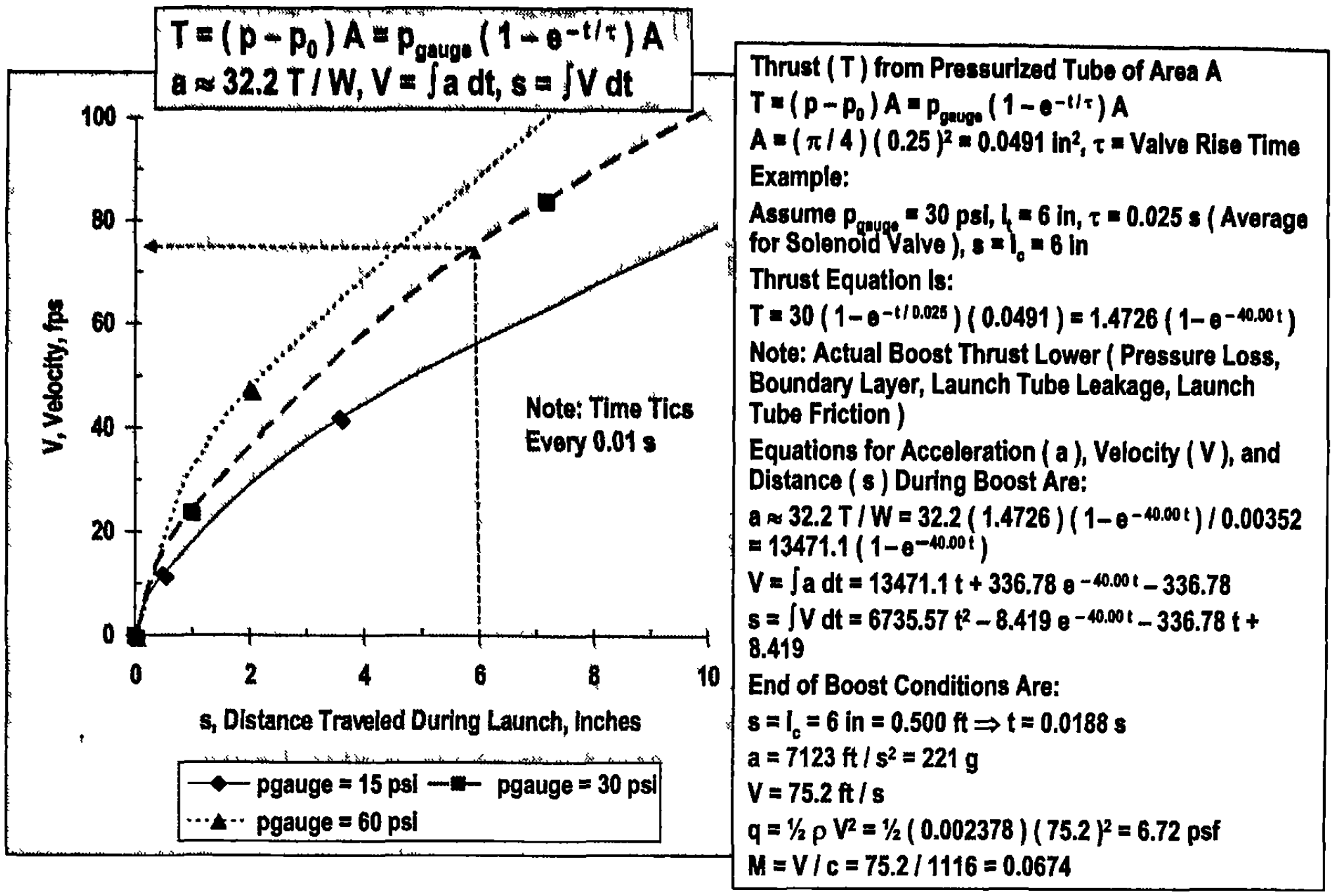

Fig. 7.32 Soda straw rocket has high acceleration boost performance.

Figure 7.32 describes the prediction method for boost velocity and an example of the performance of a baseline soda straw rocket. Thrust is assumed to be equal to the differential pressure in the launch tube multiplied by the cross-sectional area of the launch tube. The equation is

$$T = (p - p_0)A \tag{7.68}$$

The pressure in the launch tube is assumed to have the same rise time as that of the solenoid valve and exponentially rises to the gauge pressure, giving

$$T = p_{\text{gauge}}\,(1 - e^{-t/\tau})A \tag{7.69}$$

The actual force is less than the theoretical thrust because of the pressure loss in the line, boundary layer restriction of the effective flow area, launch tube leakage around the soda straw rocket, and launch tube friction. Drag can be neglected during boost because the thrust force is relatively large, more than two orders of magnitude larger than the drag. Therefore, from Newton's Laws, the equation for acceleration of a baseline rocket of weight W is

$$a \approx 32.2T/W \tag{7.70}$$

Integrating the acceleration gives the velocity during boost ($V = \int a\ dt$) and distance traveled ($s = \int V dt$). The graph shows velocity as a function of time during boost. It is based on a launch soda straw diameter of 0.25 in

[area $A = (\pi/4)(0.25)^2 = 0.0491$ in^2], soda straw rocket baseline weight $W =$ 1.6 g $=$ 0.00352 lb, and a solenoid valve average rise time $\tau = 0.025$ s.

As an example, for a gauge pressure of 30 psi and a launch length of 6 in,

$$T = 30(1 - e^{-t/0.025})(0.0491) = 1.4726(1 - e^{-40.00t}) \tag{7.71}$$

The equations for acceleration (a), velocity (V), and distance (s) during boost are

$$a \approx 32.2T/W = 32.2(1.4726)(1 - e^{-40.00t})/0.00352$$
$$= 13471.1(1 - e^{-40.00t}) \tag{7.72}$$

$$V = \int a\,dt = 13471.1\,t + 336.78\,e^{-40.00t} - 336.78 \tag{7.73}$$

$$S = \int V\,dt = 6735.57\,t^2 - 8.419\,e^{-40.00t} - 336.78\,t + 8.419 \tag{7.74}$$

Finally, the end-of-boost conditions are

$$s = l_c = 6 \text{ in} = 0.500 \text{ ft} \Longrightarrow t = 0.0188 \text{ s} \tag{7.75}$$

$$a = 7123 \text{ ft/s}^2 = 221\,g \tag{7.76}$$

$$V = 75.2 \text{ ft/s} \tag{7.77}$$

$$q = \tfrac{1}{2}\rho\,V^2 = \tfrac{1}{2}(0.002378)(75.2)^2 = 6.72 \text{ psf} \tag{7.78}$$

$$M = V/c = 75.2/1116 = 0.0674 \tag{7.79}$$

Figure 7.33 shows the soda straw rocket drag coefficient based on summing the contributions from body skin friction drag, base drag, and tail skin friction drag

$$C_{D_0} = (C_{D_0})_{\text{Body,Friction}} + (C_{D_0})_{\text{Base,Coast}} + (C_{D_0})_{\text{Tail,Friction}} \tag{7.80}$$

The Chapter 2 equation for the body skin friction drag coefficient from Jerger[4] is

$$(C_{D_0})_{\text{Body,Friction}} = 0.053(l/d)[M/(ql)]^{0.2} \tag{7.81}$$

Note from the equation that body skin friction drag is primarily driven by body fineness ratio. The assumption of a turbulent boundary layer is in error for the very low Mach number of the soda straw rocket. The Chapter 2 base drag equation for coasting flight at subsonic Mach number is

$$(C_{D_0})_{\text{Base,Coast}} = 0.12 \tag{7.82}$$

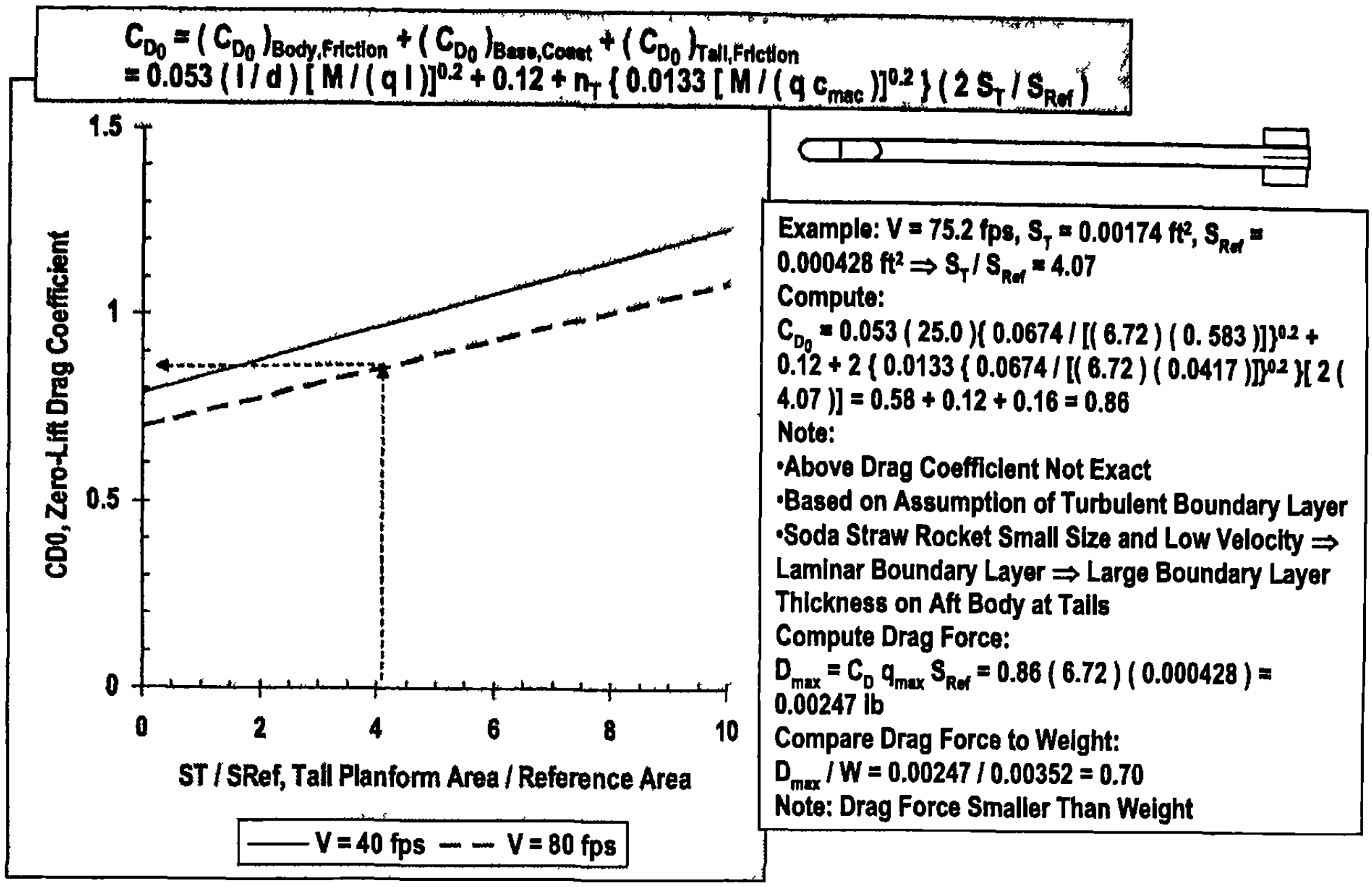

Fig. 7.33 Most of the soda straw rocket drag coefficient is from body skin friction.

The Chapter 2 tail skin friction drag prediction based on Jerger[4] is the equation

$$(C_{D_0})_{\text{Tail, Friction}} = n_T[0.0133[M/(qc_{mac})]^{0.2}](2S_T/S_{Ref}) \tag{7.83}$$

In the equation the units of dynamic pressure q and mean aerodynamic chord c_{mac} are lb/ft^2 and ft respectively. Major contributors to the tail skin friction drag are the number of tails n_T and the tail planform area S_T. The total wetted area for tail skin friction drag is equal to $2n_TS_T$. Tail skin friction drag is a weak function of Mach number, dynamic pressure, and the length of the mean aerodynamic chord. Again, an error in using this equation is the assumption of a turbulent boundary layer. A laminar boundary layer with larger thickness would probably have higher drag. Note from the figure that for a typical tail size, the major contributor to the zero-lift drag coefficient is from the body, with a lesser contribution from the tails.

As an example, assume that the baseline soda straw rocket is launched at 30 psi launch pressure, which results in an end-of-boost velocity of 75.2 ft/s. The baseline tail area is $S_T = 0.00174$ ft^2 and reference area is $S_{Ref} = 0.000428$ ft^2, providing a ratio of tail-area-to-reference-area of $S_T/S_{Ref} = 4.07$. Then for a sea-level launch, the zero-lift drag coefficient is computed to be

$$\begin{aligned} C_{D_0} &= 0.053(25.0)\{0.0674/[(6.72)(0.583)]\}^{0.2} \\ &\quad + 0.12 + 2\{0.0133\{0.0674/[(6.72)(0.0417)]\}^{0.2}\}[2(4.07)] \\ &= 0.58 + 0.12 + 0.16 = 0.86 \end{aligned} \tag{7.84}$$

The maximum total drag force will occur at launch, which is maximum velocity. Computing

$$D_{\max} = C_D q_{\max} S_{\text{Ref}} = 0.86(6.72)(0.000428) = 0.00247 \text{ lb} \tag{7.85}$$

Comparing the drag force to weight

$$D_{\max}/W = 0.00247/0.00352 = 0.70 \tag{7.86}$$

Note that the drag is comparable to the weight but somewhat smaller. Although the rocket follows a nearly ballistic trajectory, it has somewhat shorter range than that of an ideal (no drag) trajectory.

The ballistic trajectory shown in Fig. 7.34 is a function of the time, weight, atmospheric density, reference area, zero-lift drag coefficient, initial velocity, and the initial flight path angle. It is based on the one-DOF equation of motion with the assumptions of no thrust ($T = 0$) after launch, zero angle of attack ($\alpha = 0$ deg), and drag force greater than the component of weight along the drag axis ($D > W \sin\gamma$).

Horizontal flight range during ballistic flight is given by the Chapter 5 equation

$$R_x = \{2W\cos\gamma_i/[g_c\rho S_{\text{Ref}} C_{D_0}]\} ln\{1 + t/\{2W/[g_c\rho S_{\text{Ref}} C_{D_0} V_i]\}\} \tag{7.87}$$

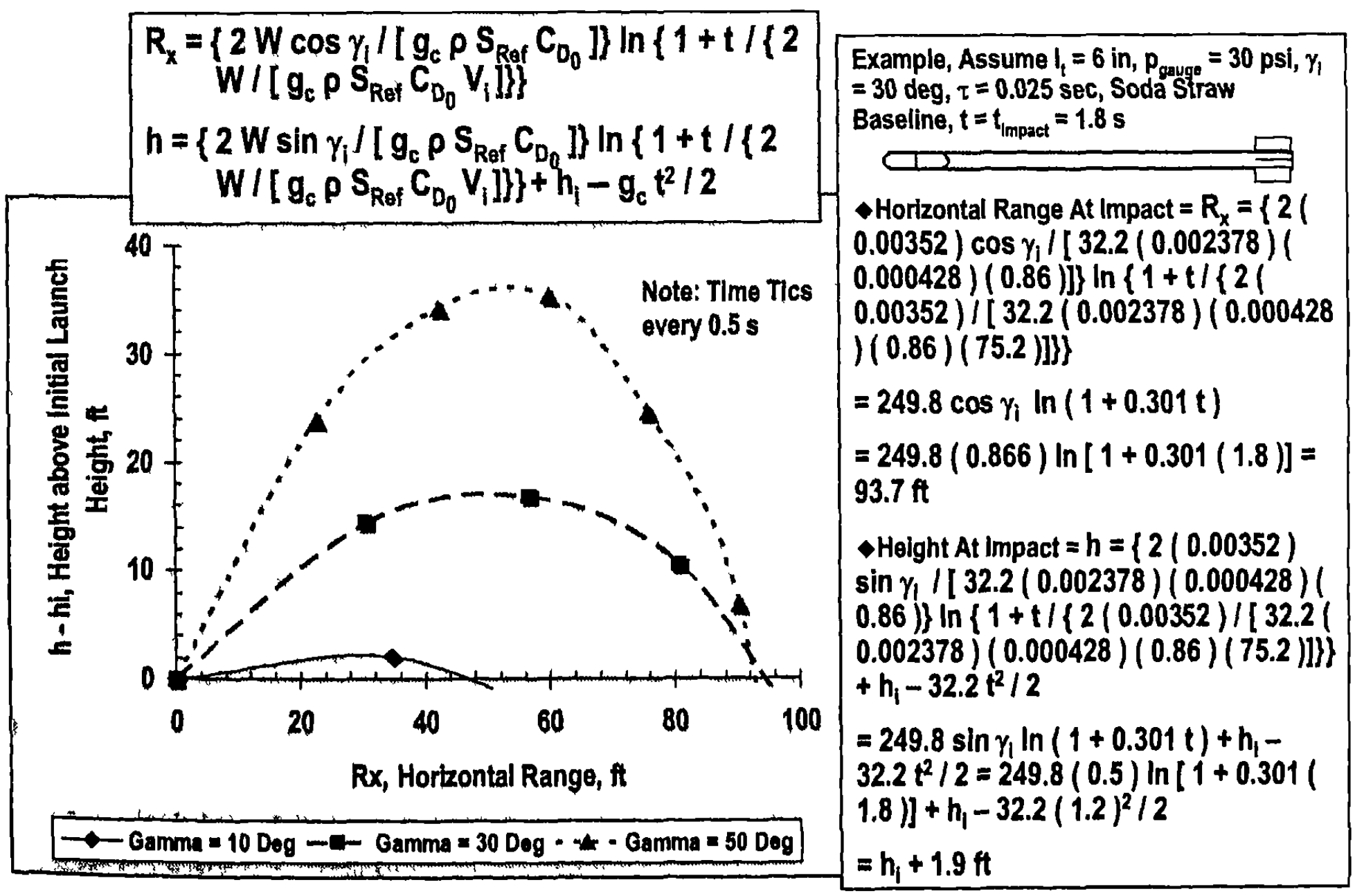

Fig. 7.34 Soda straw rocket baseline has a ballistic flight range greater than 90 ft.

In the above equation the term g_c is the gravitational constant, with $g_c = 32.2$. The altitude during ballistic flight is given by the Chapter 5 equation

$$h = h_i + \{2W \sin\gamma_i/[g_c \rho S_{Ref} C_{D_0}]\} ln\{1 + t/\{2W/[g_c \rho S_{Ref} C_{D_0} V_i]\}\} - g_c t^2/2 \tag{7.88}$$

Examination of the equations above shows that the contributors to long-range ballistic flight include high initial velocity, low zero-lift drag coefficient, an optimum launch angle, and high-altitude (low atmospheric density) flight.

Note from the figure that launches at $\gamma_i = 30$ deg and 50 deg provide almost the same range. A delay in the launch time of about 0.7 s would result in a nearly simultaneous impact time. It can be shown that the maximum range, including drag, is at launch angle of about 40 deg. For ideal ballistic flight with zero drag, the launch angle for maximum range would be 45 deg.

As an example, assume $l_t = 6$ in, $p_{gauge} = 30$ psi, $\gamma_i = 30$ deg, $\tau = 0.025$ s, soda straw rocket baseline, and $t = t_{impact} = 1.8$ s. Then the predicted horizontal range at impact is

$$\begin{aligned} R_x &= \{2(0.00352)\cos\gamma_i/[32.2(0.002378)(0.000428)(0.86)]\} ln \\ &\quad \times \{1 + t/\{2(0.00352)/[32.2(0.002378)(0.000428)(0.86)(75.2)]\}\} \\ &= 249.8 \cos\gamma_i ln(1 + 0.301t) = 249.8(0.866) ln[1 + 0.301(1.8)] \\ &= 93.7 \text{ ft} \end{aligned} \tag{7.89}$$

Similarly, the height at impact ($t = 1.8$ s) is

$$\begin{aligned} h &= \{2(0.00352)\sin\gamma_i/[32.2(0.002378)(0.000428)(0.86)]\} ln \\ &\quad \{1 + t/\{2(0.00352)/[32.2(0.002378)(0.000428)(0.86)(75.2)]\}\} \\ &\quad + h_i - 32.2\, t^2/2 \\ &= 249.8 \sin\gamma_i ln(1 + 0.301\ t) + h_i - 32.2\ \ t^2/2 \\ &= 249.8(0.5) ln[1 + 0.301(1.8)] + h_i - 32.2(1.2)^2/2 \\ &= h_i + 1.9 \text{ ft} \end{aligned} \tag{7.90}$$

As stated previously, the customer requirements for the soda straw rocket are assumed to be a flight range greater than 90 ft and a weight less than 2 g. A Paredo sensitivity study (Fig. 7.35) was conducted of the soda straw rocket baseline to determine the most important drivers and the required accuracy for prediction methods. Note from the figure that more than 80% of the sensitivity in flight range is from the inside chamber length and launch angle. The most sensitive parameter is the inside chamber length l_c. If the chamber length decreases, the boost time and total impulse also decrease, resulting in a decrease in the launch velocity. Note that there is no increase in range for a chamber length greater than 6 in because the launcher length is also 6 in. Another significant parameter is the

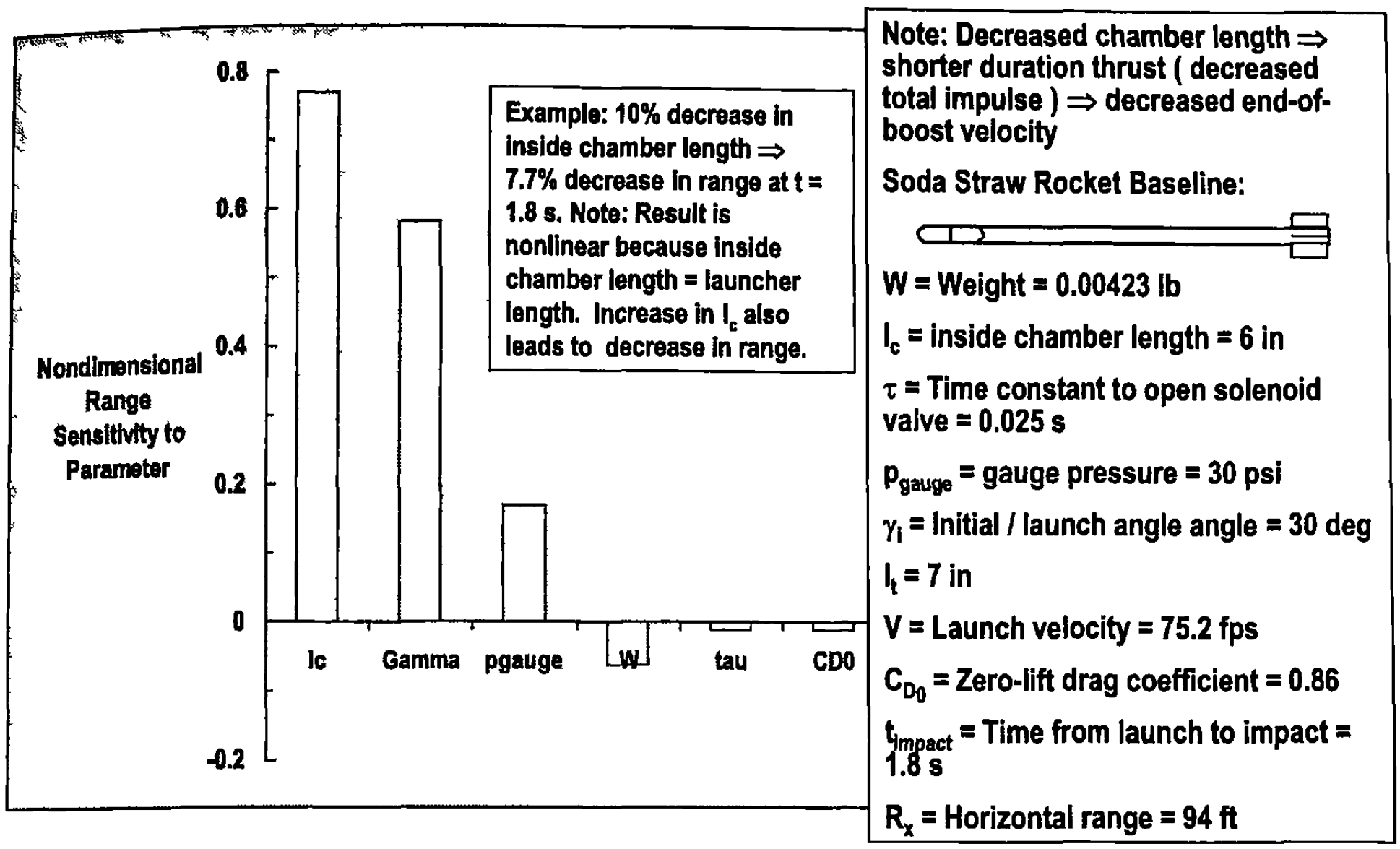

Fig. 7.35 Paredo sensitivity shows soda straw rocket range is driven by inside chamber length and launch angle.

initial flight path angle γ_i, which is the launch angle. The baseline launch angle was assumed to be 30 deg. Increasing the launch angle provides increased range for launch angles up to 40 deg. A launch angle of $\gamma_i = 40$ deg provides 21% greater range than a launch angle of 30 deg (114 vs 94 ft). For launch angles greater than 40 deg, the range decreases. Also shown in the figure is the sensitivity to changes or uncertainties in other parameters that have less impact on range. Shown are the sensitivities from gauge pressure p_{gauge}, weight W, solenoid valve opening time τ, and zero-lift drag coefficient C_{D_0}. An increase in gauge pressure increases the thrust, resulting in an increase in the launch velocity, which increases range. For weight, an increase in weight results in lower acceleration during boost and therefore a lower launch velocity. For the solenoid valve, an increase in the valve opening time results in a slower rise in thrust, which results in a decrease in the launch velocity, which decreases the flight range. The nominal opening time of the baseline solenoid valve is 0.025 s. As a comparison, the nominal valve opening time of the manual valve is much longer, about 0.1 s. A manual, hand-operated valve is limited by the typical human muscular response time. The use of the faster responding baseline solenoid valve (0.025 vs 0.1 s) results in a 44% greater launch velocity (75 vs 52 ft/s), providing longer range. Finally, note that zero-lift drag coefficient C_{D_0} has only a small influence on range. The relatively low drag of the soda straw rocket is because of the low velocity and dynamic pressure. As a result, the flight trajectory of the relatively low speed soda straw rocket is dominated more by inertial forces rather than aerodynamic forces. The soda straw rocket follows a nearly ballistic flight trajectory of somewhat shorter range than the ideal (no drag) ballistic trajectory.

The engineering parameters that are under the control of the designer are the inside chamber length, weight, and zero-lift drag. In this case, it is assumed that the launch angle, gauge pressure, and solenoid value time constant are fixed by the customer and are not under the control of the designer. As previously discussed, the most important design characteristic is the inside chamber length.

The uncertainties of the values of the soda straw rocket baseline parameters are used to determine the uncertainty in flight range, as shown in Table 7.10. Assumed launch conditions are a gauge pressure of 30 psi and a launch angle of 30 deg. The parameters are:

1) Inside chamber length
2) Launch angle
3) Gauge pressure
4) Weight
5) Solenoid valve time constant
6) Zero-lift drag coefficient

The estimated levels of maturity/uncertainty in the parameters of the soda straw rocket baseline are based on conducting tests and prediction. Ground tests included wind tunnel test, thrust static test, and weight measurement.

Total flight range uncertainty for a 30 psi/30 deg launch is assumed to be the RMS of the contributors

$$\begin{aligned}\Delta R/R &= +/-[(\Delta R/R)_1^2 + (\Delta R/R)_2^2 + (\Delta R/R)_3^2 + (\Delta R/R)_4^2 \\ &\quad + (\Delta R/R)_5^2 + (\Delta R/R)_6^2]^{1/2} \\ &= +/-2.4\%,\ 1\sigma \end{aligned} \tag{7.91}$$

The soda straw rocket baseline flight range with uncertainty is therefore

$$R = 94\ \text{ft} +/- 2.3\ \text{ft},\ \ 1\sigma \tag{7.92}$$

Table 7.10 Soda straw rocket baseline flight range uncertainty is +/−2.4%, 1

Parameter	Baseline value	Uncertainty in parameter	ΔR/R due to uncertainty
1. Inside Chamber Length	6 in	$+/-2\%,\ 1\sigma$	$+/-1.5\%,\ 1\sigma$
2. Launch Angle	30 deg	$+/-3\%,\ 1\sigma$	$+/-1.7\%,\ 1\sigma$
3. Gauge Pressure	30 psi	$+/-3\%,\ 1\sigma$	$+/-0.5\%,\ 1\sigma$
4. Weight	1.6 g	$+/-6\%,\ 1\sigma$	$+/-0.4\%,\ 1\sigma$
5. Solenoid Time Constant	0.025 s	$+/-20\%,\ 1\sigma$	$+/-0.2\%,\ 1\sigma$
6. Zero-Lift Drag Coefficient	0.86	$+/-20\%,\ 1\sigma$	$+/-0.2\%,\ 1\sigma$

- Estimate of Level of Maturity/Uncertainty of Soda Straw Rocket Baseline Parameters Based on
  - Wind tunnel test
  - Thrust static test
  - Weight measurement
  - Prediction methods
- Total Flight Range Uncertainty for 30 psi launch at 30 deg
  - $\Delta R/R = [(\Delta R/R)_1^2 + (\Delta R/R)_2^2 + (\Delta R/R)_3^2 + (\Delta R/R)_4^2 + (\Delta R/R)_5^2 + (\Delta R/R)_6^2]^{1/2} = +/-2.4\%,\ 1\sigma$
  - $R = 94\ \text{ft} +/- 2.3\ \text{ft},\ 1\sigma$

From above, there is a predicted 99% confidence (3σ) in achieving a range exceeding 87 ft. If a 99% confidence is required for the customer requirement of a 90-ft range, options to satisfy the customer requirement include 1) conduct more accurate testing, measurement, and/or prediction to reduce the uncertainty; 2) request customer approval of a deviation in the specified launch conditions, such as a higher launch angle (the optimum launch angle for maximum range is about 40 deg); or 3) develop a new design concept.

Figure 7.36 shows the house of quality process applied to the soda straw rocket. It is made up of seven rooms, with each room contributing to the task of mapping customer requirements to engineering design characteristics. Because the process of populating these rooms requires brainstorming, discussion with the customer, and analysis by the design team, a benefit of the house of quality is a better understanding of the problem. The house of quality should not be a static document. It should continue to evolve as the design progresses.

The first room of the house of quality is *Customer Requirements.* It is frequently referred to as the ***whats*** of the house of quality. Customer requirements can fall into three categories

1) Formal requirements directly indicated by the customer organization

2) Unspoken requirements or "hidden" requirements of the customer's implicit needs

3) Exciters or "softer" customer requirements that can be traded off against other needs

The customer requirements may be derived from formal sources such as the request for proposal (RFP) and technical requirements document (TRD) as well as informal discussions with customer. The informal discussions with the

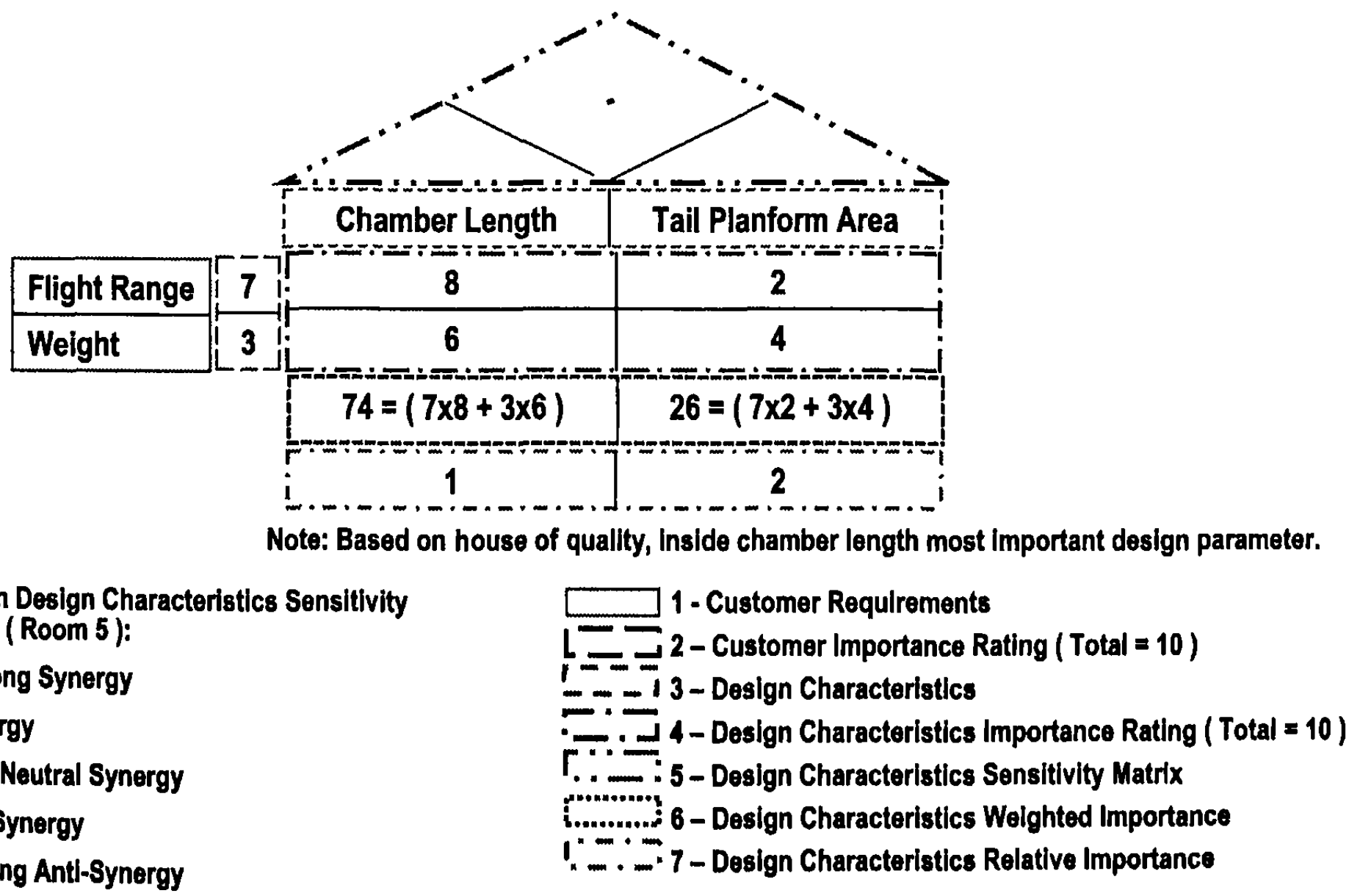

Fig. 7.36 House of quality translates customer requirements into engineering emphasis. Figure also in color section.

customer may provide further insight into the formal requirements as well as implied requirements, such as safety, preferred technologies, and launch platform compatibility. Informal discussions with the customer organization may also indicate contradictory desires from different members of the customer organization. As an example of customer requirements for the soda straw rocket, the flight range must be greater than 90 ft and the weight must be less than 2 g.

The second room, just to the right of customer requirements, is the *Customer Importance Rating*. It shows the relative importance of each customer requirement. It is at this stage, above all others, where clear customer input is required to accurately map the customer needs. Ideally, the customer is present in the discussion of the customer importance rating and concurs with the rating. Often the summation of the values of the rating for each requirement is set equal to 10. This forces a relative priority ranking of each of the customer requirements. As an example, the soda straw rocket flight range is considered by the customer to be more important than weight (rating of 7 vs 3).

The third room of the house of quality is *Design Characteristics*. These are frequently referred to as the ***hows*** of the house of quality. Design characteristics are a translation of customer needs into engineering product or process attributes. They identify how the customer requirements can be satisfied. The design characteristics are based on the important engineering design parameters that can be controlled and measured. Engineering insight and sensitivity analysis of a baseline design are ideally used in selecting the design characteristics. For example, we know from analyzing the soda straw rocket baseline that the end-of-boost velocity drives the flight range, and the end-of-boost velocity increases with increasing inside chamber length until the chamber length is equal to the launcher length. Also, much of the weight of the soda straw rocket is because of the inside chamber length. It is therefore expected that inside chamber length would be an important design parameter, with a maximum reasonable length less than the launcher length. Another design parameter is the tail planform area. Benefits of a small tail planform area are less weight and drag, providing longer range. However, some tail area is required for neutral stability. At the other extreme, too much tail area results in excess stability, causing the soda straw rocket to weathercock (and lose range) in a crosswind. The values of the engineering design characteristics are derived from a baseline design sensitivity study that is used to initiate the design process. For a soda straw rocket baseline with specified values of launch angle, launch length, launch gauge pressure, and solenoid valve response time, the sensitivity of flight range to the engineering design characteristics is from the inside chamber length and tail planform area. Similarly, the sensitivity of the weight is from the inside chamber length and tail planform area.

Room four is the engineering *Design Characteristics Importance Rating*. It is here that the quantifiable metrics, controllable by the designer, are defined. The design characteristics importance rating identifies the correlation between the customer requirements and the engineering design characteristics. Engineering design characteristics are assigned quantitative values that depend upon their impact on the customer requirements. The total for each customer requirement is often set to 10 to force a ranking of importance. An empty column indicates that an engineering characteristic that was previously thought to be significant does

not have a significant impact on any of the customer requirements and therefore should probably be eliminated as a design parameter. An empty row shows that a customer requirement is not being properly addressed with the current set of engineering characteristics and therefore additional engineering design characteristics should be added to accommodate it. The goal of this matrix is to match the important engineering associations with customer requirements. As stated above, the sensitivity study of the baseline found that the flight range is driven about 80% by inside chamber length and about 20% by tail planform area, while the weight is driven about 60% by inside chamber length and about 40% by tail planform area. These values were used as the basis for the design characteristics importance rating.

The fifth room of the house of quality is the *Design Characteristics Relationship Matrix.* It identifies the sensitivities that exist among the engineering design characteristics. Five different sensitivities are often used: strong synergy, synergy, near neutral, antisynergy, and strong antisynergy. A synergistic sensitivity means that a beneficial change in the value of an engineering design characteristic also benefits another engineering characteristic. An antisynergy sensitivity means that a beneficial change in the value of an engineering design characteristic unfortunately degrades another engineering characteristic, requiring a design tradeoff. Areas requiring the most attention are those with strong sensitivities that can lead to either strong synergy or require major design tradeoffs. For the soda straw rocket, there is a moderately antisynergistic sensitivity between the inside chamber length and tail area (i.e., an increase in chamber length requires an increase in tail area). The reason is an increase in chamber length moves the body normal force farther forward, resulting in a decrease in static stability. As a result, the tail planform area must be increased to maintain static margin.

The two lowest rooms (six and seven), represent the outcome of the house of quality process. They focus on the most important engineering design characteristics. Room six is the *Design Characteristics Weighted Importance.* It indicates which engineering design characteristics are most important in meeting the customer requirements. The design characteristics weighted importance matrix is obtained by multiplying the design characteristic importance rating by the corresponding customer requirements rating and summing the results. For the soda straw rocket, the weighted importance of the inside chamber length ($74 = 7 \times 8 + 3 \times 6$) is considered to be more important than the weighted importance of the tail planform area ($26 = 7 \times 2 + 3 \times 4$). Finally, room seven, *Design Characteristics Relative Importance*, facilitates the quick identification of the most important engineering characteristics by providing a ranking of the design characteristics. The most important design characteristics should receive the greatest attention during the design study. In the case of the soda straw rocket, the inside chamber length receives the highest ranking and should receive the greatest attention in the design.

Shown in Fig. 7.37 is a DOE applied to the soda straw rocket. DOE develops a reasonably small set of alternatives within the large possible design space of practical solutions. It is instructive to select a set of concepts that illustrate the practical limits of the driving engineering characteristics and the driving customer requirements. For the soda straw rocket, the driving engineering

Design Space for Design of Experiments (DOE)

Engineering Characteristics Range	l_c, Inside Chamber Length, in	S_T, Tail Planform Area, in^2
Lower Value	4	0.125
Upper Value	6	0.25

Full Factorial DOE Based on Upper / Lower Values of k = 2 Parameters: Number of Combinations = $2^k = 2^2 = 4$

Concept	Sketch	l_c, Inside Chamber Length, in	S_T, Tail Planform Area, in^2
"Big Kahuna"		6	0.25
"Shorty"		4	0.25
"Stiletto"		6	0.125
"Petite"		4	0.125

Note: DOE concepts should emphasize customer driving requirements and the driving engineering characteristics.

Fig. 7.37 DOE explores the broad possible design space with a reasonably small set of alternatives.

characteristics are the inside chamber length and the tail planform area. As an example, the "Big Kahuna" concept has a long chamber length and relatively large tails. The long chamber length provides high boost velocity, which enhances range. Its relatively large tails provide static stability. However, the Big Kahuna is heavy. The "Shorty" concept has a short chamber length and relatively large tails for static stability. The short chamber length reduces weight (at the expense of launch velocity and range). The third concept, "Stiletto", has a long chamber length and relatively small tails. It is relatively lightweight and could have good range in still air. However, Stiletto may not have sufficient stability, especially in a crosswind. Angle of attack oscillations could lead to divergence and increased drag, resulting in decreased range. Finally, "Petite" is the lightest weight concept. However, it has the shortest range. It is anticipated that an optimum "Harmony" concept would have an inside chamber length and tail area that are intermediate from these four extremes.

Developing a DOE set of alternatives is not just a mathematical exercise but is also based on engineering experience. The design space should be an envelope of reasonable solutions. As an example, the reasonable design space for the soda straw rocket is bounded by the following considerations:

1) Soda straw rocket must fit the launcher.

2) Inside chamber length should be no longer than the launch tube length. Maximum launch velocity will occur when the inside chamber length is equal to the launch tube length.

3) Three or four small tails are best for stability.

4) Tails that are too small may result in unstable flight.

5) Tails that are too large add weight and cause trajectory dispersal in a cross wind.

As an Example, Soda Straw Rocket Geometry Should Be Comparable to an Operational Rocket with Near-Neutral Static Stability (e.g., Hydra70)

Concept	Sketch	l / d, Total Length / Diameter	b / d, Total Tail Span / Diameter	c / d, Tail Chord / Diameter
"Big Kahuna"		25	2.79	2
"Shorty"		17.9	2.79	2
"Stiletto"		25	1.89	2
"Petite"		17.9	1.89	2
Hydra 70		15.1	2.66	1

Note: For a subsonic rocket with the center-of-gravity in the center of the rocket, slender body theory and slender surface theory give total tail span and chord for neutral stability of $b_{NeutralStability} \approx 2$ d and $c_{NeutralStability} > \approx$ d respectively.

Fig. 7.38 Engineering experience should guide the DOE set of alternatives and preferred design.

6) Canards would require that the tails be larger for stability, increase weight, and cause ballistic dispersal.

7) Wings would add weight, drag, and ballistic dispersal.

The characteristics of operational free-flight unguided rockets such as the Hydra-70 can be used as a guide in developing the DOE set of alternatives and a preferred design. Figure 7.38 compares the total length-to-body diameter ratio (fineness ratio), tail span-to-body diameter ratio, and tail chord-to-diameter ratio of the Hydra-70 to the DOE set of alternatives. Because free-flight rockets such as Hyda-70 are designed to be near neutrally stable, the tail geometry should be somewhat similar. For a neutrally stable rocket, the destabilizing moment from the body is equal to the stabilizing moment from the tail. Because the moment arm from the body is located at the nose and is approximately equal to the moment arm from the tail, the normal force derivative of the body should be approximately equal to the normal force derivative of the tail. Based on slender body theory[7], subsonic slender wing theory[9] (low aspect ratio), and an assumed center of gravity near the center of the rocket, the total span and chord of the tail should be about $b_{\text{NeutralStability}} \approx 2d$ and $c_{\text{NeutralStability}} > \approx d$, respectively. Note from the figure that the Hydra-70 total tail span is 2.66 times the body diameter and the tail chord is equal to the body diameter, providing a sanity check.

After setting up the DOE set of alternatives, students then develop an optimum design that reflects the customer requirements emphasis (e.g., range, weight), with a balanced design emphasis of the most important engineering characteristics (e.g., inside chamber length, tail planform area/span).

7.11 Summary

Chapter 7 provided examples of the sizing process. Examples were shown for a rocket-powered missile, a ramjet-powered missile, computer programs for

conceptual design, and a soda straw rocket. The Sparrow missile was used as a baseline missile to illustrate 1) the flight performance sizing to meet an air-to-air standoff range requirement; 2) wing sizing to meet maneuverability, turn rate, and turn radius requirements; 3) multiparameter harmonization of weight and miss distance; and 4) ballistic versus lofted glide flight range. A ramjet missile based on the ASALM was used to illustrate 1) the robustness in the uncertainty of the cruise flight range; 2) propulsion and fuel alternatives; and 3) surface target impact velocity. Examples were shown of computer-aided sizing codes for conceptual design. ADAM is a DOS-based aerodynamic sizing code that includes a time-marching numerical solution of the equations of motion. TMD spreadsheet is a Windows-based sizing code consisting of a spreadsheet based on the analytical methods of this text. Finally, a soda straw rocket design, build, and fly project was presented. Predictions of static margin, drag, and flight performance were shown. A sensitivity study identified the most important driving parameters. A House of Quality was developed to illustrate the interface of customer requirements to engineering design characteristics. Finally, a DOE was conducted to illustrate candidate design concepts and an efficient process to evaluate the design space.

Problems

7.1. Required flight range is shorter for a head-on intercept and it is longer for a t___ c____ intercept.

7.2. The rocket baseline center of gravity moves f_____ with motor burn.

7.3. The rocket baseline is an a_____ airframe.

7.4. The rocket baseline thrust profile is b____ s_____.

7.5. The rocket baseline motor case and nozzle are made of s____.

7.6. The rocket baseline flight range is driven by I_{SP}, propellant weight fraction, drag, and s_____ m_____.

7.7. Contributors to the maneuverability of the rocket baseline are its body, tail, and w___.

7.8. Although the rocket baseline has sufficient *g*'s and turn rate to intercept a maneuvering aircraft, it needs a smaller turn r_____.

7.9. Compared to a coaltitude trajectory, the rocket baseline has extended range with a l_____ glide trajectory.

7.10. The ramjet baseline has a c___ inlet.

7.11. The Mach 4 ramjet baseline has a t_____ airframe.

7.12. Although the ramjet baseline combustor is a nickel-based super alloy, it requires insulation because of high temperature. The super alloy is i_____.

7.13. The flight range of the ramjet baseline is driven by I_{SP}, weight, thrust, zero-lift coefficient, and the weight fraction of f___.

7.14. Extended range for the ramjet baseline would be provided by more efficient packaging of subsystems and the use of s_____ fuels.

7.15. A conceptual design sizing code should be based on the simplicity, speed, and robustness of p_____ based methods.

7.16. The house of quality room for design characteristics weighted importance indicates which engineering design characteristics are most important in meeting the c_____ r_____.

7.17. Paredo sensitivity identifies the design parameters that are most i_____.

7.18. DOE concepts should emphasize the customer driving requirements and the envelope of the driving e_____ characteristics.

7.19. If the total tail span (including body diameter) is twice the body diameter, the missile is approximately n_____ s_____.

8
Development Process

8.1 Introduction

The relationship of tactical missile design to the development process is presented in this chapter. It addresses the areas of technology assessment/roadmap, phases of development and the relationship to design, technology readiness level (TRL), frequency of and rationale for new missile system follow-on programs, integration of missile subsystems development with the missile system development, examples of development tests and facilities, example of technology development, examples of missile state-of-the-art advancement, and new technologies for tactical missiles.

8.2 Technology Assessment/Roadmap

Technology assessment and road mapping identify the key, enabling, high-payoff technologies; technology drivers; key decision points; critical paths; facility requirements; and the resource needs for technology development. The purpose of a technology roadmap is to establish the time-phase relationships that are required for the missile technology development activity. This includes 1) development of plans for technology development and validation; 2) identification of the technology options; 3) setting time-phased technology goals; and 4) development of a plan for technology transition. The technology plan provides an approach in maturing the missile technology through the development phases. As a result of technology development, the level of maturity will move from that of exploratory development, to advanced technology development, to a prototype demonstration. For most new missiles, a technology development, risk reduction, and maturity demonstration activity is required prior to entering system development and demonstration (SDD).

An optimum allocation of funding for technology investment is a difficult task. Some technologies may have the potential to satisfy the requirements but may be highly immature. There may be insufficient time or insufficient funding available to mature the technology to the required level of performance/cost or confidence. As a result, the highly immature technologies would not be included in the technology roadmap for a specific missile. Other technologies may be mature, with high confidence in their performance/cost. However, the technologies may fall short of meeting the requirements, and a funding investment may do little to improve the performance/cost. As a result, the mature technologies would not

be included in the technology roadmap. Technologies that would be included in the technology roadmap are those that have high potential payoff and can mature within the available time and funding.

8.3 Phases of Development/Design Maturity

Summarized in Fig. 8.1 is the technology development and design validation process for tactical missile systems developed by the United States. Technology development is focused on the key enabling technologies that are driven by the requirements but are in need of additional development and demonstration for a required level of maturity. The technology development program addresses alternative approaches and risk mitigation. It has exit criteria for each phase and an exit plan in the event of failure. The technology development and demonstration activities lead to a level of readiness for entry into SDD.

Early technology work addresses laboratory tests and demonstrations of a critical component of a subsystem in a representative environment but not necessarily a full-scale, environment. The next step of technology development is a laboratory or a flight demonstration of a subsystem in a representative, but not a full-scale, environment. This is followed by either a laboratory demonstration or a flight advanced technology demonstration (ATD) of a subsystem in a full-scale environment. Finally, there is a flight demonstration based on either an advanced concept technology demonstration (ACTD) or a program definition and risk reduction (PDRR) of a full-scale prototype missile in a full-scale environment. This is required for a missile to enter into SDD.

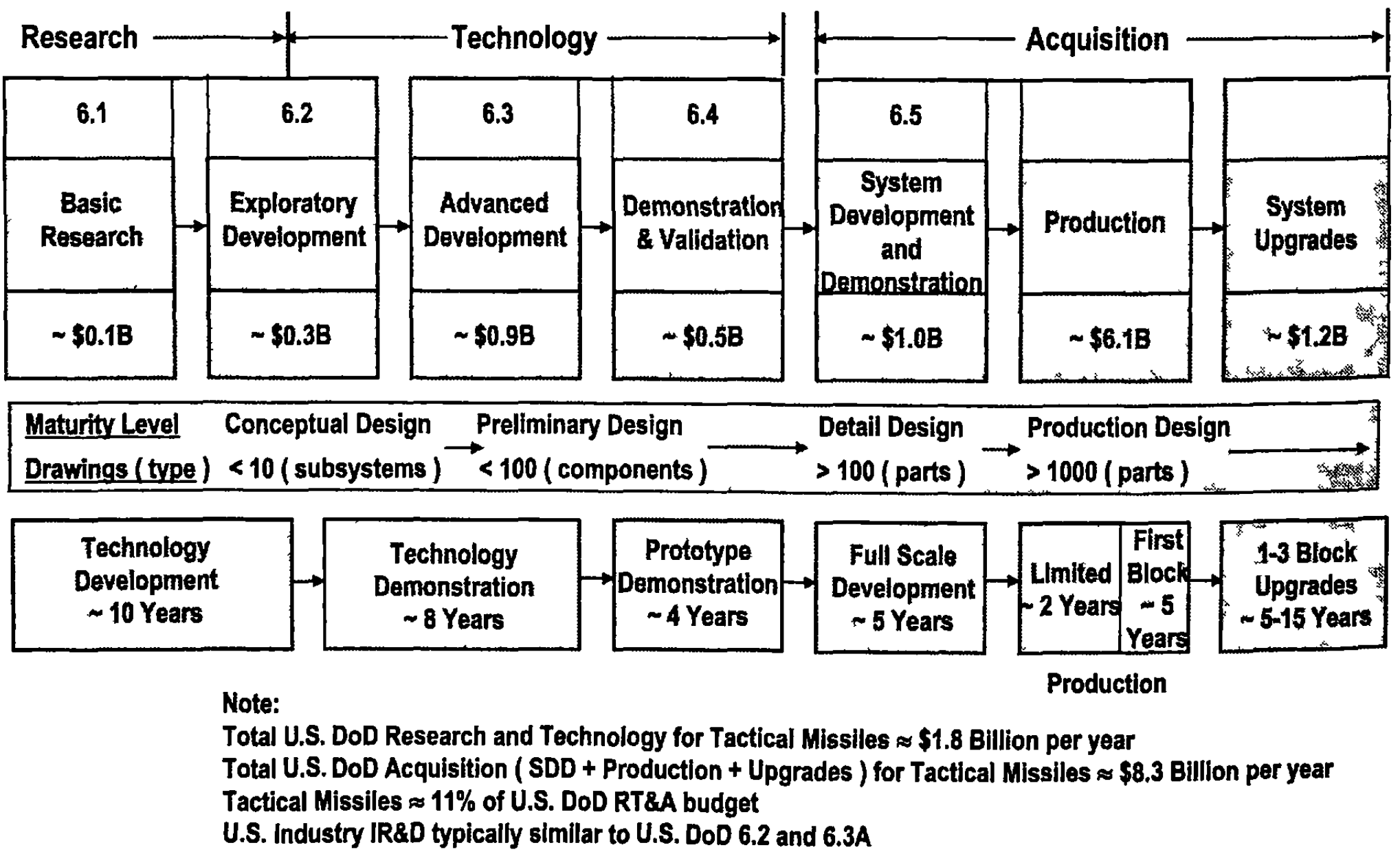

Fig. 8.1 Relationship of the design maturity to the U.S. Research, Technology, and Acquisition process.

The figure also shows the relationship of missile design to the development process of research, technology, and acquisition. Conceptual design is most often conducted during the exploratory development phase of missile development. A primary objective of exploratory development is to investigate and evaluate technology alternatives. Research and technology funds are allocated to promising alternatives as a hedge against uncertainties and risk. The next phase, advanced technology development, is intended to mature the enabling technologies of key subsystems. Although conceptual design may also be conducted later during advanced development, preliminary design methods are usually more appropriate during advanced development. The concept risk is reduced during preliminary design through the use of the more sophisticated prediction methods, parameter optimization, and testing. Preliminary design continues during advanced development demonstration of the prototype missile. Following successful demonstration of a prototype, the program moves into SDD. At this point more detail design methods are appropriate for the operational missile. However, the assessment of possible future block upgrades may require the reintroduction of preliminary design and conceptual design activities.

Conceptual design and sensitivity studies should be conducted early in the exploratory development process and continued into advanced development. Many of the cost and performance drivers may be locked in during the conceptual design phase. It is important to evaluate quickly a large number of alternatives that cover the feasible design solution space as part of the downselect process.

Figure 8.2 relates the maturity of a subsystem or a technology for application to a missile system. The technology levels that characterize the type of funding

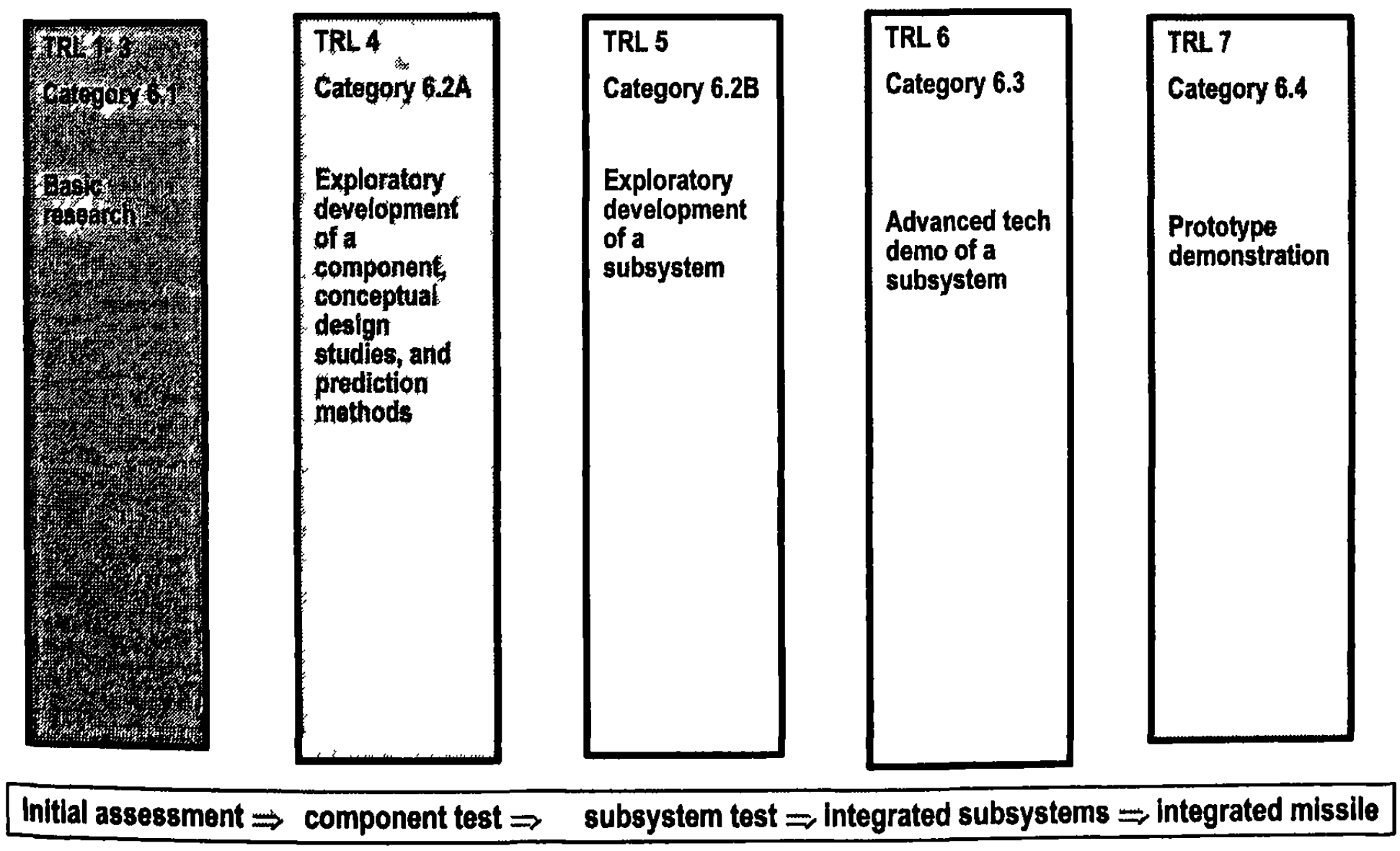

Fig. 8.2 Technology Readiness Level (TRL) indicates the maturity of technology.

are derived from the TRL model, developed by NASA. TRLs for tactical missile technology may be characterized as follows:

1) TRL 1–3 is basic research. The category of funding is 6.1. The technology goals for this category generally have limited consideration of the constraints of other component interactions or a specific application for the technology. An example of a basic research program is determining the basic strength characteristics of a high-temperature composite material, which may have numerous applications (e.g., missiles, aircraft, spacecraft). The differences of TRL 1–3 are the degree of consideration of the interaction with the other components of the subsystem and the depth of consideration of applications.

2) TRL 4 is laboratory development and laboratory test demonstration of a component. The category of funding is 6.2A exploratory development. In this category a component is usually tested in a representative, but not a full-scale, environment. The component usually has general application (e.g., follow-on to AMRAAM, follow-on to JASSM). Conceptual design and analysis studies are also conducted in this category. These set the technology into a military context. Analytical prediction methods are usually developed under this category of funding. The accuracy of the analytical predictions is established by the laboratory experiments under this category.

3) TRL 5 is laboratory development or demonstration of a subsystem. The subsystem usually has full-scale components and is tested in a representative, but not full-scale, environment. The category of funding is 6.2B exploratory development category.

4) TRL 6 is laboratory or flight ATD of a full-scale subsystem in a full-scale environment with integration of some of the other subsystems and some of the other new technologies of a follow-on missile system. This is the concept definition phase of program development. The category of funding is 6.3 advanced development.

5) TRL 7 flight demonstration is either an ACTD or a PDRR full-scale prototype in a full-scale environment. The category of funding is 6.4 demonstration and validation. All of the new critical technologies and subsystems are demonstrated. A driving consideration is to assure the system engineering and the development of management confidence in the technologies. TRL 7 is normally performed when the technology and/or subsystem application is critical and high risk. The technology availability date (TAD) for entry into SDD is based on successfully completing TRL 7.

Indicators of design maturity include the number of drawings that describe the design and the number of alternative concepts that are currently under consideration. These are shown in Fig. 8.3. Conceptual design may be characterized by approximately five drawings for each concept, describing perhaps five subsystems. A large number of alternative missile system concepts, perhaps 10, are in evaluation during conceptual design. Conceptual design drawings include the overall dimensions of the missile, major subsystems layout, and the major subsystems mass properties. The next step is preliminary design. Preliminary design drawings of a prototype missile are usually characterized by up to 100 drawings with greater detail and showing up to 100 components. Preliminary design drawings have fully dimensioned subsystems, inboard layouts showing the subsystems, individual subsystem and component drawings, and dimension

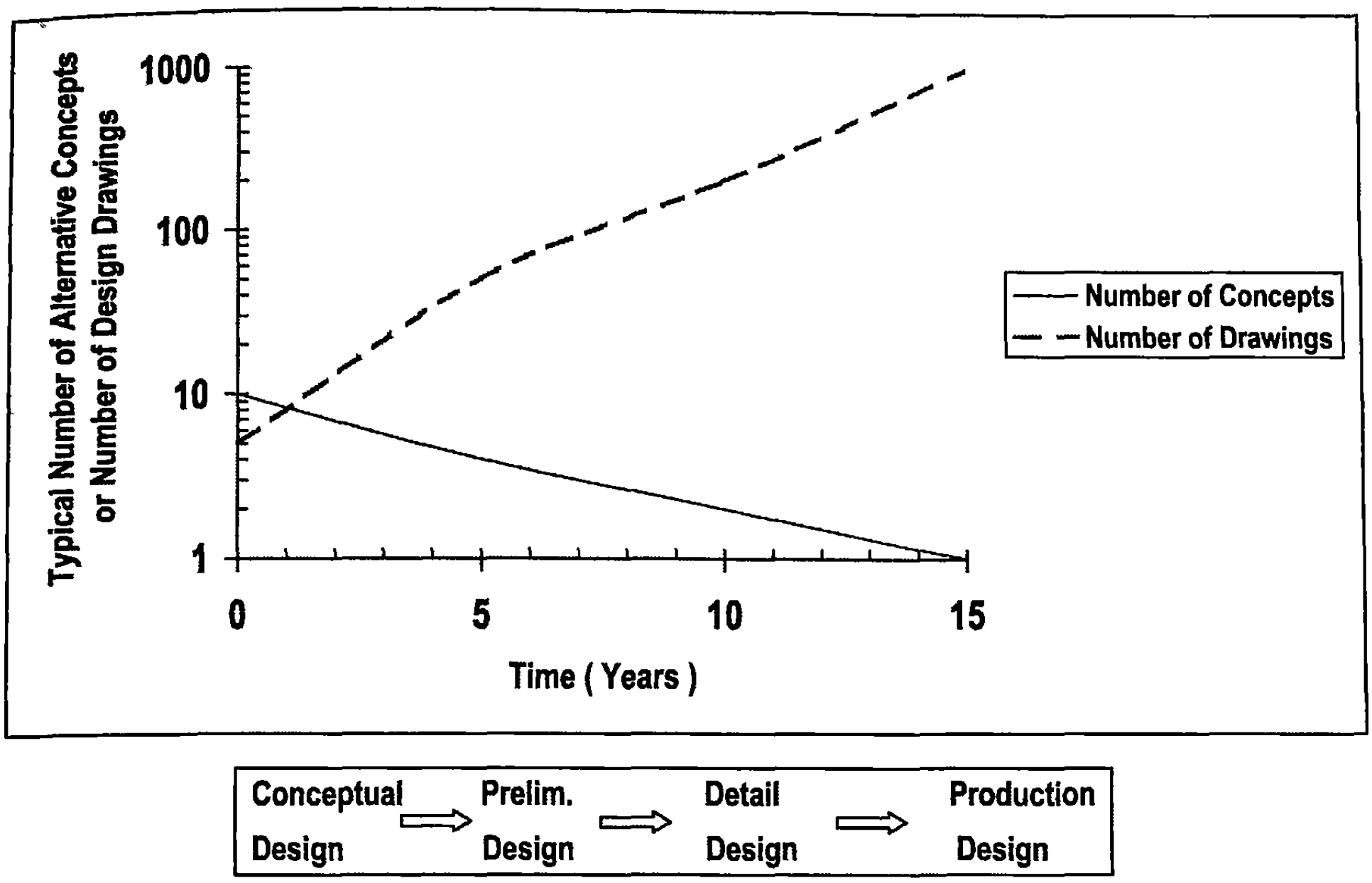

Fig. 8.3 Conceptual design has broad alternatives while detail design has high definition.

tolerances. A fewer number of alternative missile system concepts, perhaps four, are under evaluation during preliminary design. Following preliminary design, the next step is detail design. Detail design for SDD usually requires more than 100 drawings and often has more than 1000 drawings. Production drawings have even more detail, including drawings of each part, detailed work assembly instructions and descriptions of the manufacturing processes. During SDD and production there is usually only one design concept (e.g., sole source contractor) or perhaps at most two similar design concepts (two competitive contractors).

8.4 Tactical Missile Follow-on Programs

Figure 8.4 shows that the frequency of a follow-on program to a tactical missile is about every 24 years for U.S. missiles. Once a missile is in production, it usually has a long lifetime, including block upgrades. Block upgrades are often necessary to incorporate the rapidly emerging new technologies in electronics and sensors. Block upgrades are also often necessary for launch platform integration. However, eventually a capability is needed that is not easily achievable through a block upgrade, requiring a follow-on missile development. Examples are shown in the figure of the driving requirements in the follow-on missile programs. These are the improved maneuverability of AIM-9X; improved speed and range of AIM-120 and AGM-88; improved accuracy of PAC-3; higher gunner survivability (lower observables, launch and leave), lethality, and lighter weight of Javelin; reduced radar cross section (RCS) of AGM-129;

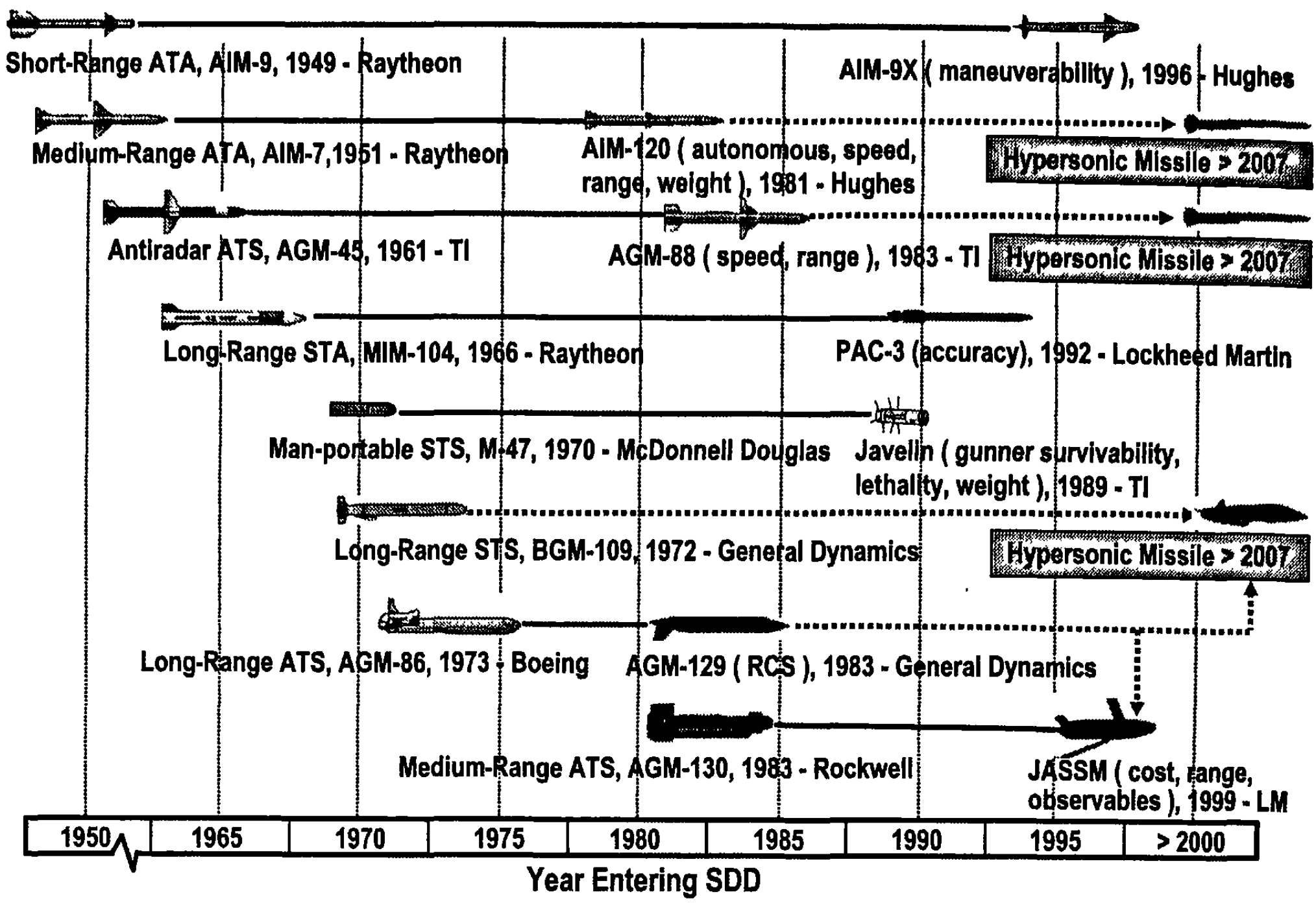

Fig. 8.4 U.S. tactical missile follow-on programs occur about every 24 years.

and the combined robustness of lower cost, longer range, and reduced observables for JASSM. It is interesting to note that in almost no case does a missile follow-on program go to the incumbent contractor of the current missile.

There may be opportunities for a new start for a U.S. hypersonic airbreathing missile in the post-2007 year timeframe. A hypersonic airbreathing missile provides faster time-to-target and may also provide longer range (compared to an endo-atmospheric rocket). Opportunities include follow-on programs for the air-to-air AIM-120 AMRAAM, air-to-surface defense suppression AGM-88 HARM, and cruise missiles (BGM-109 Tomahawk, AGM-86 CALCM).

8.5 Subsystem Integration

Figure 8.5 shows the design validation and technology development process for tactical missiles. A primary integration tool for the design validation/development process is missile system simulation. The initial simulations used in conceptual and preliminary design are digital simulations. As missile guidance and control hardware becomes available, a hardware-in-loop (HWL) simulation is also developed. HWL simulation incorporates the missile guidance and control hardware (e.g., seeker, gyros, accelerometers, actuators, autopilot). It also includes a simulated target signal for the seeker to track. Either an all-digital or a hybrid computer may be used in HWL simulation. In the case of hybrid HWL simulation, fast analog computers simulate the rapidly changing parameters, such as the flight trajectory equations of motion. Digital computers

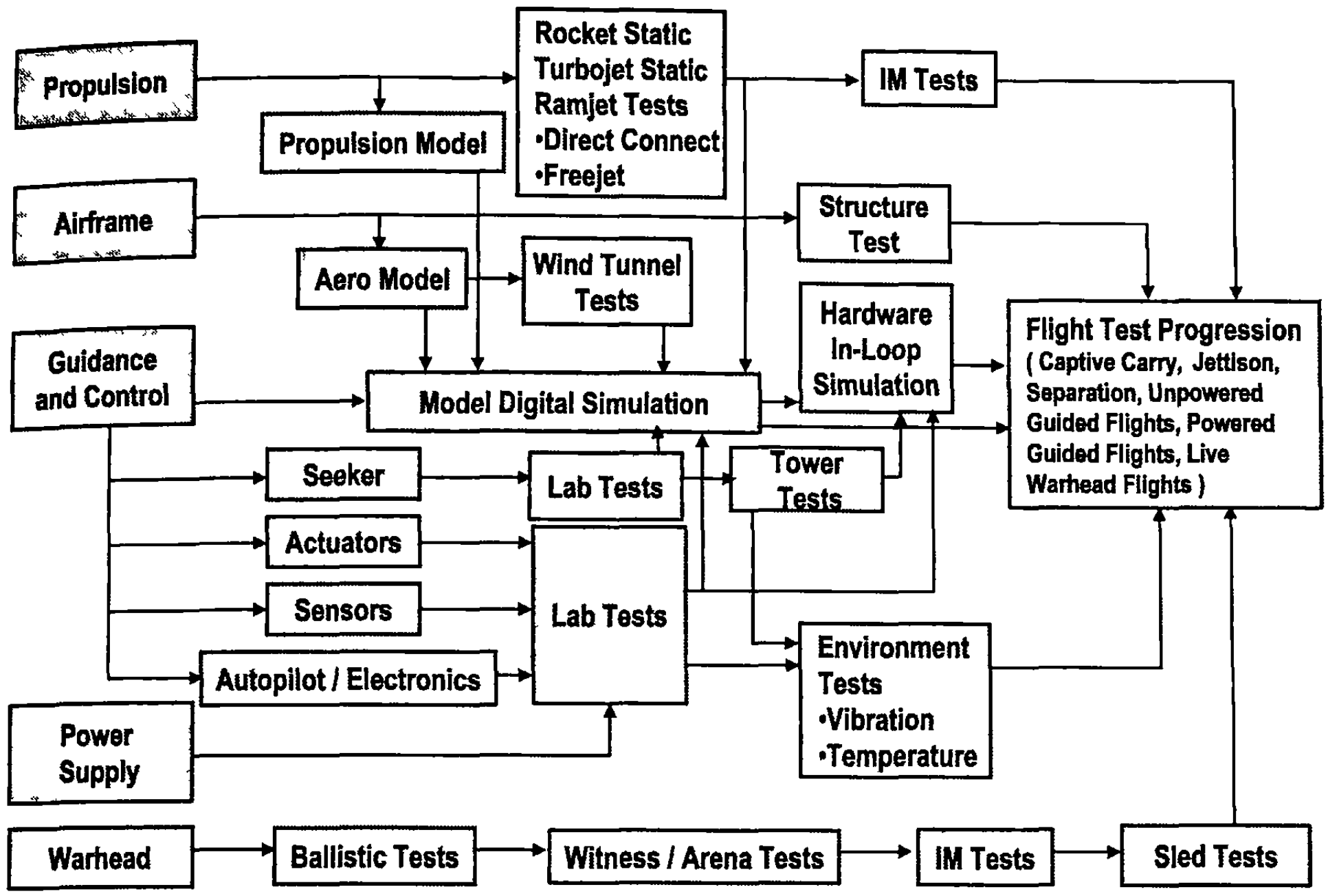

Fig. 8.5 Missile design validation/technology development is an integrated process.

for a hybrid HWL simulation are used for the more slowly changing parameters, such as the forces and moments from aerodynamics and propulsion. More modern HWL simulation is based on an all-digital computer that is sufficiently fast to model the rapidly changing dynamics. As an example, the required update rate for solving the equations of motion may be less than a ms to provide sufficient accuracy to the simulation. HWL and digital simulations are the primary system analysis tools used during missile development and flight tests. For example, simulation results based on wind tunnel data are validated with flight test results. HWL and digital simulations are also used to determine the cause of flight test anomalies. In recent years the number of required flight tests has reduced because of the increased confidence in the HWL and digital simulations. HWL and digital simulations are cost-effective complements to flight test. The approximately $4 million per year cost to maintain HWL and digital simulations is relatively small compared to the cost of the flight test program. Also, the time required to initiate and complete an HWL evaluation is relatively short (e.g., ~weeks) compared to the time required to initiate and complete a flight test program (e.g., ~months).

Launch platform integration is considered from the start of the subsystems development activities, continuing as they evolve into a missile system. In the propulsion area, static firings and insensitive munition tests are conducted before a missile with a live rocket motor is fired from a launch platform. For the airframe, wind tunnel configuration development tests are conducted. Store separation wind tunnel tests are also conducted for an air-launched missile. In the guidance and control area, laboratory tests are conducted in a simulated

ground and flight environment for the missile seeker, navigation, data link, flight control gyros and accelerometers, flight control actuators, and electronics. The laboratory tests include environmental tests that simulate the conditions such as the operational temperature, humidity, rain rate, shock, and vibration. The missile modeling and simulation activities include safe separation analysis. The flight control system sensors, actuators, and electronics are analyzed to ensure safe separation as part of a missile modeling and simulation activity. Similar to the propulsion area, the warhead has insensitive munition tests prior to firing a missile with a live warhead from the launch platform. For the missile system, flight test validation is a progressive activity of increasing complexity. The objective of progressively complex testing is to minimize risk and enhance safety in the flight test activity. For example, a typical progression of flight demonstration for an air-launched missile begins with captive carriage of the missile and ends with launches of the missile with a live warhead. Intermediate flight tests may include store jettison tests, safe separation tests, unpowered guided flights with an inert warhead, and powered guided flights with an inert warhead.

Examples of missile development tests and test facilities are shown in Figures 8.6a to d. Figure 8.6a gives examples of aerodynamics and propulsion tests and facilities. The top right photograph is an example of a wind tunnel test of a ramjet missile model in the ONERA wind tunnel facility. The wind tunnel test may acquire six component aerodynamic force and moment data, surface pressure data, and flowfield data across the Mach number, angle of attack, angle of roll, and control surface deflection envelope. The next example is a propulsion test static rocket motor firing with thrust vector control (TVC). Measurements are made of thrust versus time. Measurements also include side forces and

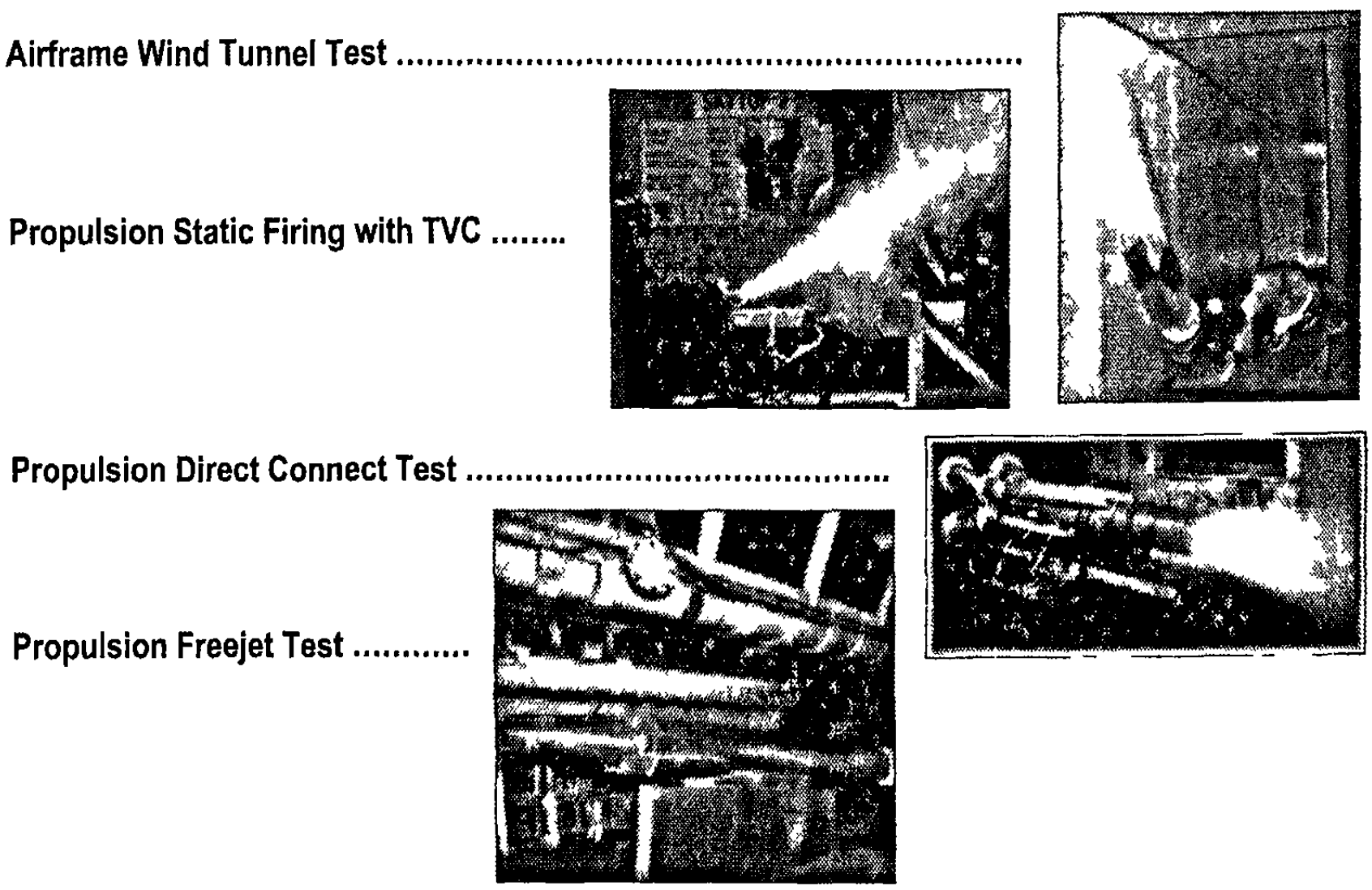

Fig. 8.6a Examples of missile development tests and facilities: aerodynamics and propulsion. Figure also in color section.

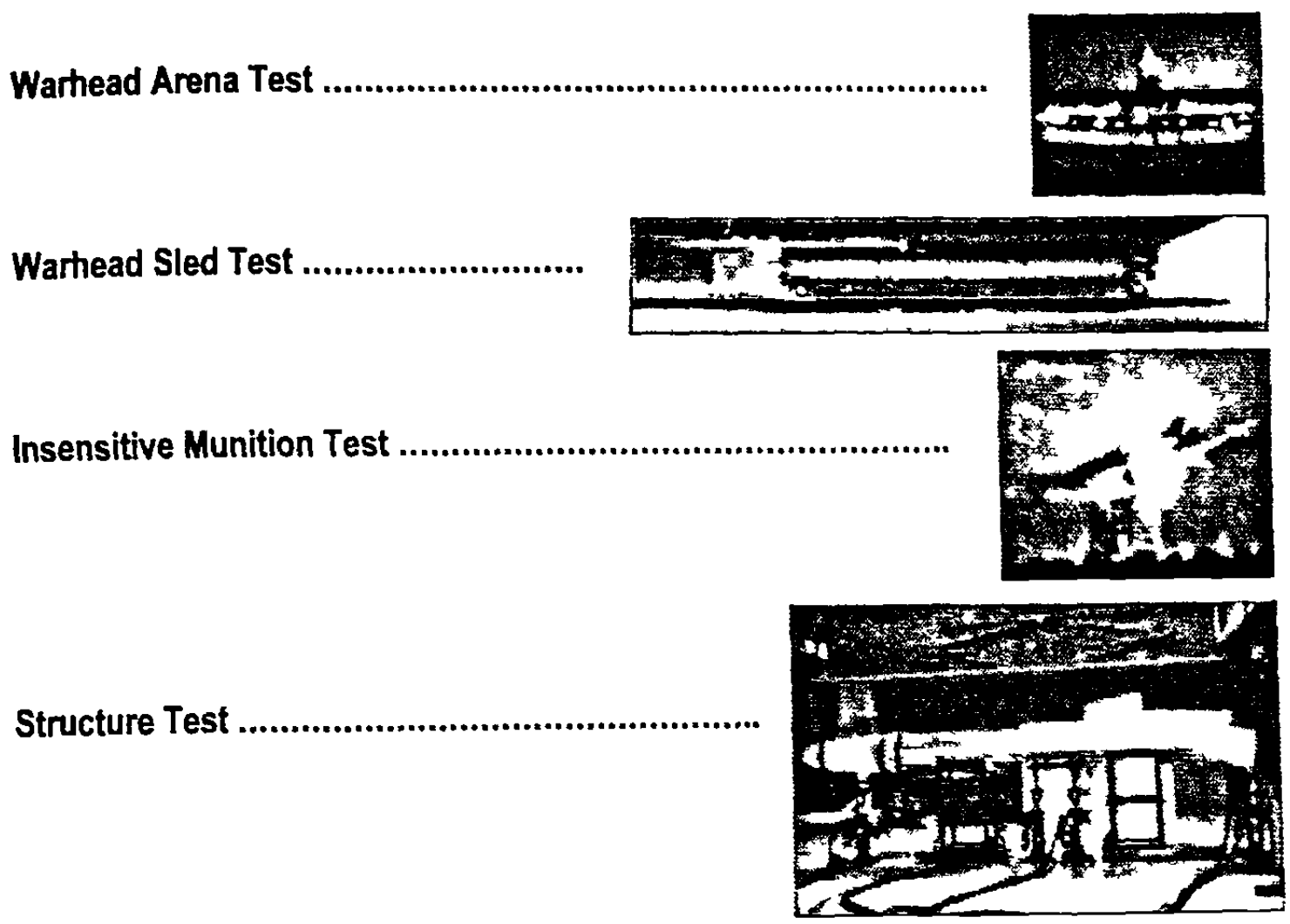

Fig. 8.6b Examples of missile development tests and facilities: warhead and structure. Figure also in color section.

moments to evaluate thrust misalignment. Also, for a missile with TVC, measurements are made of the six forces and moments provided by the TVC. The bottom right photograph shows an example of a direct connect test, in this case the Armiger ducted rocket missile. In the left side of the photograph are four pipes that supply preheated air to simulate the inlet flow into the combustor. Actual hardware can be tested for the gas generator, combustor, and nozzle. Finally,

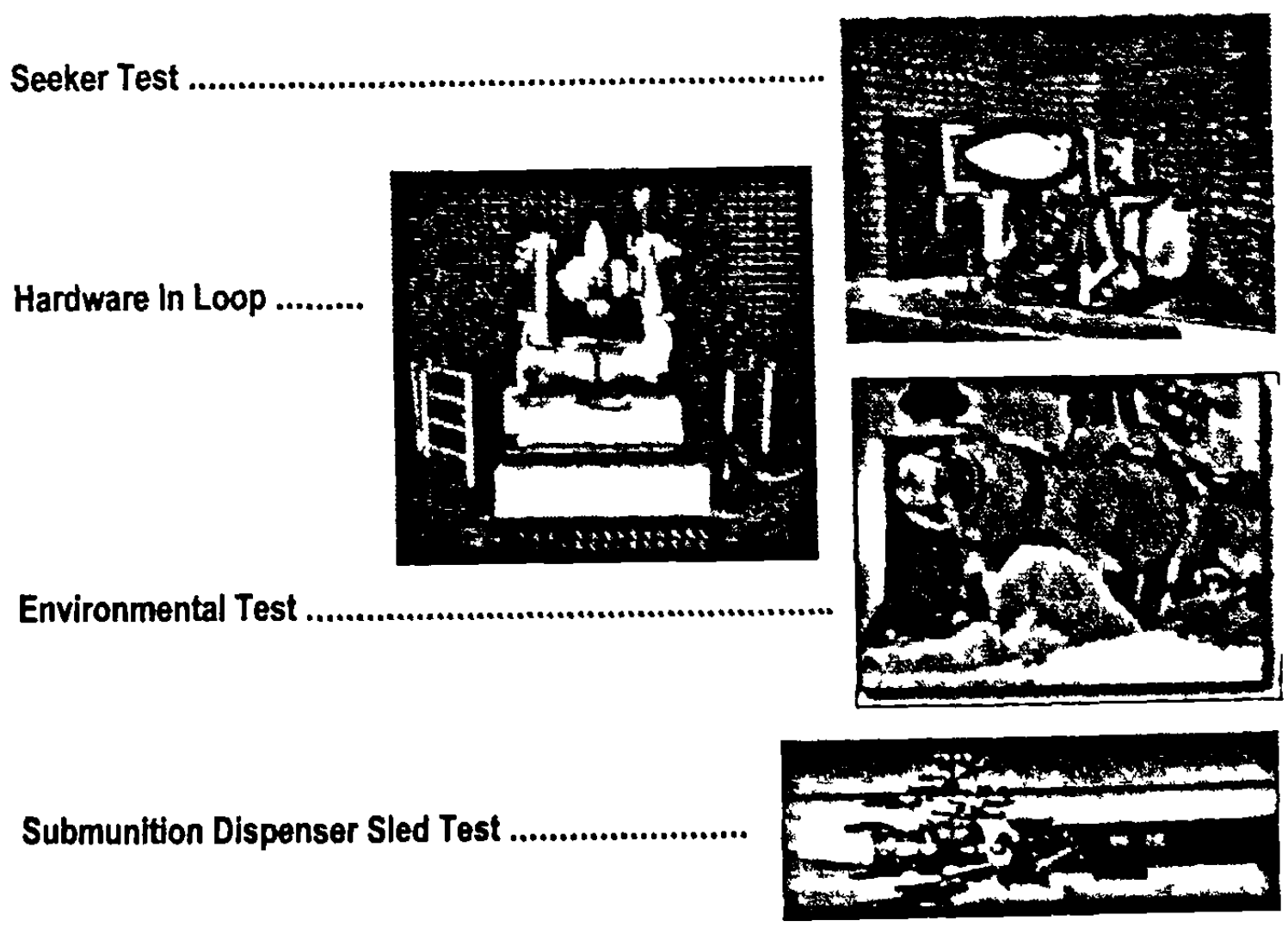

Fig. 8.6c Examples of missile development tests and facilities: seeker, hardware-in-loop, environmental, and submunition. Figure also in color section.

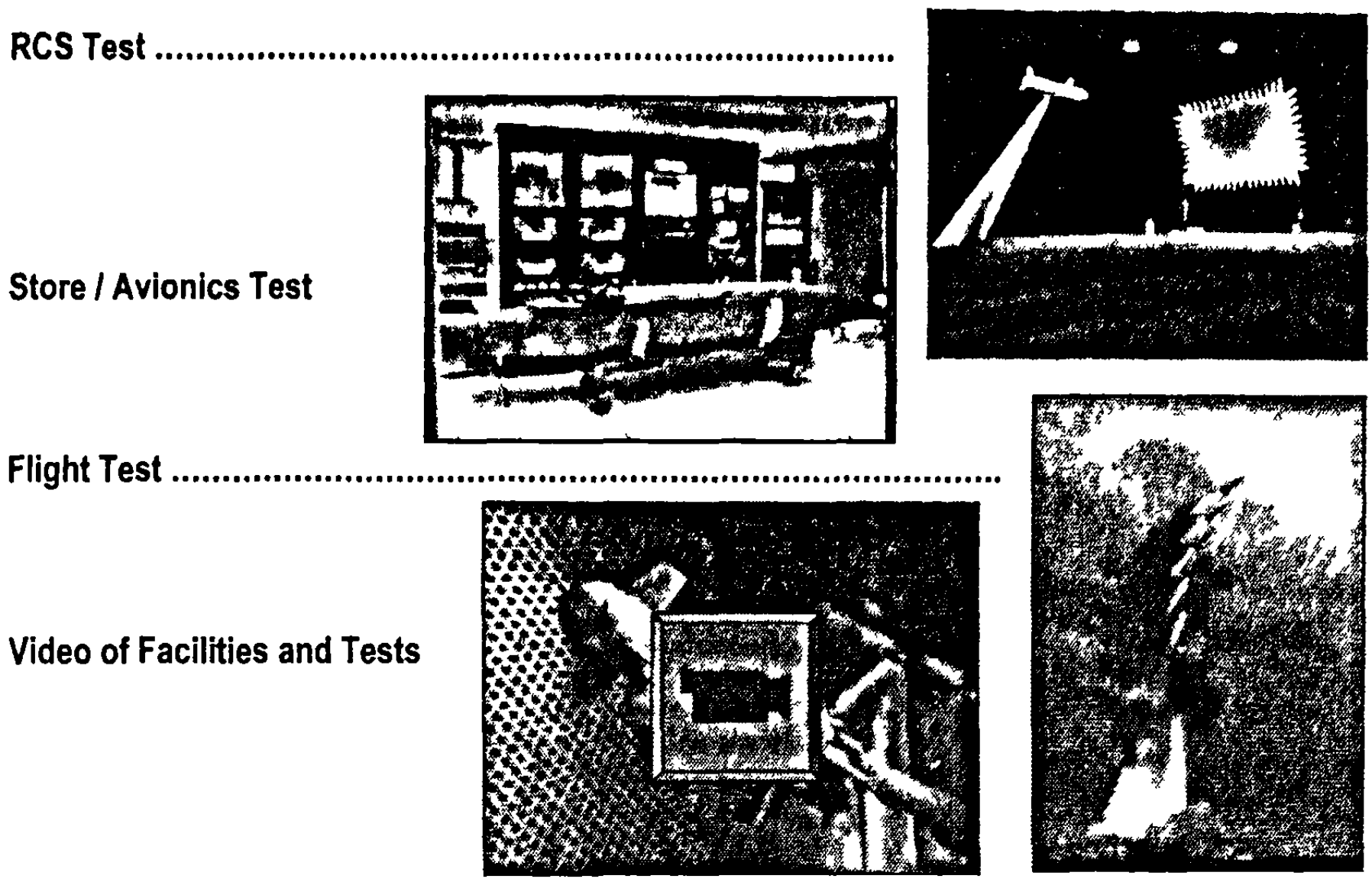

Fig. 8.6d Examples of missile development tests and facilities: RCS, avionics integration, flight test, summary video. Figure also in color section. Video is in the CD included with this textbook.

the bottom left photograph is a freejet test of the HyFly Dual Combustor Ramjet-Scramjet (DCR). The freejet test operates the entire propulsion system, including the inlet, over the angle of attack, Mach number, and altitude envelope.

Figure 8.6b shows examples of warhead and structure tests and facilities. The top photograph is a warhead arena test conducted at the Naval Air Warfare Center, China Lake, California. The warhead fragments that penetrate the witness plates provide information on the size and distribution of the fragments. The next photograph shows a sled test of a warhead. Warhead sled tests are conducted to evaluate the warhead effectiveness in a dynamic environment. Sled tests provide data on the warhead performance as function of the velocity and orientation at impact. The third photograph is an insensitive munitions live fire test. Insensitive munition tests are conducted with fragment impact, blast, fire cook-off, and other hostile environments. The photograph shows an insensitive munition test against a missile impact. The insensitive munition tests provide measurements of the hazard severity of the warhead and the propulsion. Hazard severity measurements may require instrumentation capable of very short time measurements. For example, the rise time in detonation is about 2 μs. The bottom photograph in the figure shows a structure test. Structure tests of the missile airframe are conducted using hydraulic actuators to provide simulated loads. Testing may be conducted at elevated temperature. The missile structure is instrumented with strain gauges to measure the strain, structural displacement, and structural failure mode conditions. Structure tests are usually conducted only on high-cost, long-range missiles, such as the Storm Shadow cruise missile.

Figure 8.6c shows examples of missile seeker, HWL, environmental, and submunition dispenser tests and facilities. The upper right photograph is a seeker test of the Standard Missile. The seeker performance against a simulated target is evaluated, along with its interfaces with the guidance section. The left photograph is a rate table for AMRAAM guidance and control HWL simulation. The rate table provides simulated flight trajectory pitch, yaw, and roll rates for rate-sensitive guidance and control hardware such as missile gyros and actuators. The rate table requires high-performance actuators, usually hydraulic, to move at the required rates and bandwidth. The AMRAAM seeker in the figure is surrounded by an anechoic chamber that contains the simulated target. Shown in the middle right photograph is an AGM-130 environmental test to demonstrate the reliability and performance of guidance and control hardware at low temperature. The bottom right photograph shows a submunition dispenser test to evaluate the flight trajectory pattern of submunitions. Accurate dispensing of submunitions is a challenge, particularly at high dynamic pressure, because of the complex aerodynamic interactions of the submunitions. High-speed sleds may be used in the development of a submuntion dispenser.

Figure 8.6d shows concluding examples of missile system integration testing and test facilities. In the top right of the figure is a JSOW RCS test at the Naval Air Warfare Center, Weapons Division Bi-static Anechoic Chamber. In the top left section of the figure is a photograph of an aircraft store/avionics integration laboratory test at the Naval Air Warfare Center, China Lake. Tests are conducted to determine the launch platform avionics compatibility with the weapon. The bottom right photograph is an example of a flight test of a surface-to-air missile. The Aster FSAF 15 missile is demonstrating stability and control and maneuverability at high angles of attack over the Mach number and altitude flight envelope. Finally, the bottom left section of the figure is a video of development facilities and testing for tactical missiles. Included are examples of a wind tunnel test, rocket motor static test including radiography measurement, TVC static test, reaction jet control hover flight test demonstration, propellant development, warhead arena test, warhead sled test, insensitive munitions tests, HWL simulation, environmental test, submunition dispense test, aircraft avionics/store integration laboratory test, and TVC flight demonstration tests.

New facilities may be required to accommodate future missiles. As an example, the current hypersonic facilities for aerodynamic and propulsion testing have limited capability to simulate the Mach number and altitude of large hypersonic missiles. A benefit of conceptual design activities is the timely identification of new facility requirements for future missiles.

Figure 8.7 is an example of a missile flight test validation program. It is based on the ASALM propulsion test validation (PTV) flight test program for the ramjet missile baseline. A flight test demonstration should progress from an initial low-risk demonstration of nominal performance to an evaluation of the limits of the flight envelope. Note from the figure that the areas of concern for the ASALM PTV flight test were booster transition to ramjet thrust takeover, aerodynamic maneuver performance, cruise performance at high dynamic pressure, engine operation and cruise at low dynamic pressure, structural integrity at high aerodynamic heating, and high L/D cruise performance. The objective of Flight 1 was to simply conduct a nominal launch and operate in the middle of

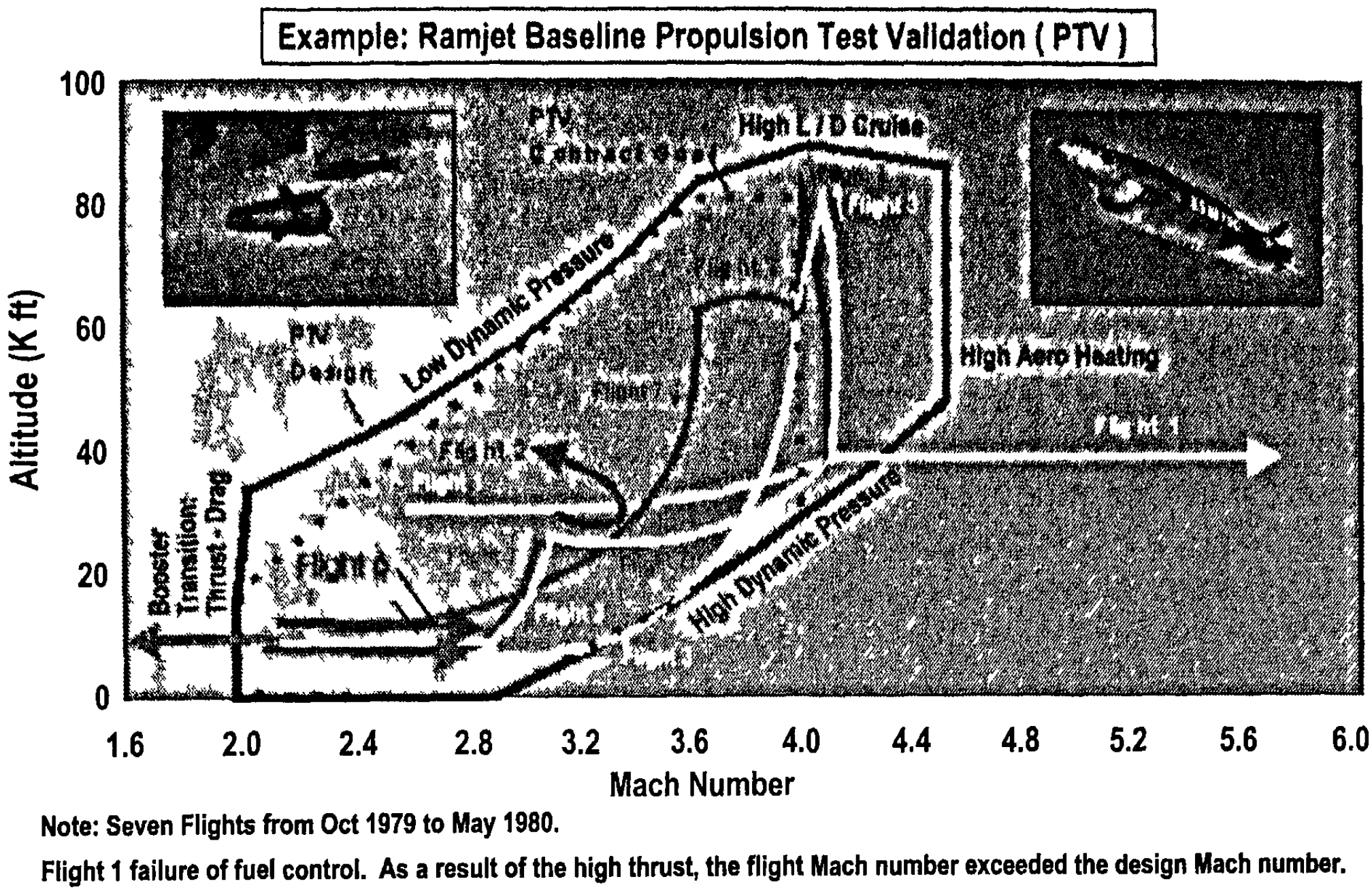

Fig. 8.7 Missile flight test should cover the extremes of the flight envelope. Figure also in color section.

the flight envelope. However, the missile did not operate in accordance with the plan. In this case, the fuel control stuck, driving the missile outside of the design flight envelope. Flight 1 accidentally went Mach 5.7, exceeding the design requirement for Mach number, dynamic pressure, and temperature. Fortunately, the missile did not fail. The next flight, Flight 2, operated in accordance with the plan. It demonstrated high angle of attack maneuverability. ASALM was designed for both an air-to-surface mission and an air-to-air mission. The air-to-air bomber defense mission required the capability to make a heading change up to 180 deg for an intercept of an aircraft target. The next flight, Flight 3 demonstrated operation in the high dynamic pressure environment of low-altitude supersonic cruise. It also demonstrated operation in the low dynamic pressure at an altitude of 90,000 ft. Flights 4, 5, and 6 demonstrated acceleration at low supersonic Mach number (Mach 2) and low altitude (5000 ft) cruise range. The last flight, Flight 7 demonstrated the high Mach number cruise range.

8.6 Example of Technology Development

An example of a technology development activity will be presented for the area of aerodynamics. It illustrates the maturity development and risk reduction activities of missile aerodynamics. Conceptual design is usually based on predicted aerodynamics using simple methods such as the methods described in this text, without the benefit of test data for the configuration. Preliminary design may also be initially based on prediction, using more sophisticated codes. The accuracy is improved when wind tunnel data become available.

Relatively low fidelity simulation [e.g., three degrees of freedom (DOF) digital] is conducted during conceptual design to provide an initial estimate of flight performance and stability and control. The six-DOF digital simulation and the HWL simulation are usually initiated during preliminary design, continuing with refinement through flight test. The six-DOF simulation provides integration of aerodynamics with flight control and other subsystems.

Examples of preliminary design aerodynamic prediction codes are Missile DATCOM, MISL3, SUPL, and AP98. The Missile DATCOM (DATa COMpendium) is a Fortran 90 computer code (Ref. 31) that was developed under the sponsorship of the Air Force Research Laboratory, Wright–Patterson Air Force Base, Ohio. It is available at low cost. The generalized methods are applicable to wing-body-tail configurations with circular and noncircular body cross section at any angle of attack. It can model inlets and protuberances. Surfaces may be at arbitrary roll orientation and deflection. Missile DATCOM is more applicable to preliminary design because of the large number of input parameters and the time required to prepare input data and to analyze output. Missile DATCOM is a complex computer program, with 405 subroutines.

The Nielsen Engineering and Research (NEAR) MISL3 computer code (Ref. 10) is based on the equivalent angle of attack method developed by NEAR. It includes the effects of vortex shedding, configuration geometry, and Mach number. MISL3 is applicable to wing-body-tail configurations at high angles of attack, arbitrary roll angle, and arbitrary control surface deflection. Bodies may have conical changes in diameter, modeling flares and boattails. Surfaces may be inline or interdigitated. The output includes static and dynamic forces and moments, loads, hinge moments, bending moments, and dynamic stability derivatives. The code is more applicable to preliminary design because it does not automatically transfer output data to a flight trajectory code.

The NEAR MISDL computer code (Ref. 10) is a subsonic and supersonic panel method that models up to two different surfaces at different locations, including the effect of fin-body interference. The body and fin separation vortices are tracked aft of the separation point. Either two-dimensional shock expansion theory or Newtonian impact theory can be selected to provide lifting surface pressure calculations. Surface pressures are integrated to provide loads, forces, and moments. MISDL is limited to relatively low angles of attack and control surface deflection. The code handles arbitrary surface geometry and roll angle. It is more applicable to preliminary design because of the time required to model the surface panels.

The Naval Surface Warfare–Dahlgren Aeroprediction Code AP02 (Ref. 32) includes bodies of elliptical cross section, high angles of attack, arbitrary control surface deflection, arbitrary roll angle, and base bleed. It has been periodically updated over the years. The output includes forces and moments, dynamic stability derivatives, pressure distribution, load distribution, the airframe temperature response, and a three-DOF flight trajectory simulation. It is user friendly for preliminary design. The integrated three-degree-of-simulation expedites design convergence.

Computational fluid dynamics (CFD) provides a physics-based prediction that is suitable for complex flow fields and configuration geometry. Disadvantages of CFD include a long setup time and usually a requirement for parallel processing.

However, CFD is useful as a check of a few selected cases of results from the more traditional approaches to aerodynamic prediction. As an example of CFD, Georgia Tech has a relatively user friendly/relatively fast CFD program that runs on a personal computer work station.

Examples of preliminary design optimization techniques are the response surface methods and probabilistic analysis developed by Georgia Tech. Response surface methods provide a polynomial approximation of the results from running a more sophisticated aerodynamic prediction code. Only the most important, Paredo-type, driving parameters are included in the polynomial approximation. This allows a rapid assessment of the available design space and the use of probabilistic analysis to evaluate design robustness. Probabilistic analysis provides an assessment of the robustness of the design-to-design uncertainty in areas such as cost and performance.

Wind tunnel testing develops the aerodynamic configuration and verifies the conceptual and preliminary design prediction. Wind tunnel testing is a progressive series of tests of increasing complexity. The initial tests are simple body buildup evaluations of aerodynamic configuration alternatives. Data are six component forces and moments with undeflected control surfaces. An objective is to define a baseline configuration that has low drag, high lift, and a small variation in aerodynamic center. Following body buildup tests, a missile baseline configuration is selected and a wind tunnel test is conducted to determine flight control effectiveness and the control surface hinge moment. In the control effectiveness test the control surfaces are systematically deflected in "pure" pitch, yaw, or roll and asymmetric combined pitch, yaw, and roll configurations over their limits for the Mach number, angle of attack, and roll attitude envelope. The combined control deflections measure cross coupling forces and moments. The control surface hinge moment measurements focus on the flight conditions of high dynamic pressure, high angle of attack, and high control surface deflection, where the maximum hinge moment is likely to occur.

Additional wind tunnel tests may be required, depending upon the missile type. Examples are store compatibility, flowfield, pressure distribution, plume, heat transfer, dynamic stability, and inlet wind tunnel tests. Aircraft store carriage and separation wind tunnel tests were discussed previously. The flowfield test investigates the quality of the flow over the missile. Areas of concern include flow separation and shock wave-boundary layer interaction. Flowfield measurements may be made using a laser velocimeter, wind tunnel model paint, oil flow over the model, smoke, water bubbles (for a water tunnel test), or schlierens. The pressure distribution test provides surface pressure data that are used for the air loads prediction. Pressure distribution may be obtained using either pressure taps or pressure-sensitive paint. Areas of particular interest are separated flow and shockwave-boundary layer interaction. The other wind tunnel tests such as thrust plume, reaction jet plume, heat transfer, and dynamic stability testing are usually not required, depending upon the missile and flight characteristics. Plume measurements may be required at high angle of attack (e.g., $\alpha > 30$ deg). Cold gas air is usually used to simulate the plume, with momentum flux scaling to full-scale conditions. Heat transfer measurements are usually required for Mach numbers greater than 4. Heat transfer may be measured

using either gages or temperature-sensitive paint. Dynamic stability testing of roll damping (C_{l_p}) is usually required for rolling airframe missiles. Similarly, inlet tests would be required only for airbreathing missiles.

The aerodynamic data from the wind tunnel tests are used to provide increasing confidence in the digital and HWL simulations. During conceptual design only a few (typically fewer than 50) aerodynamic parameters are required. However, for detail design more than 200 aerodynamic parameters may be required in the simulation. A potential problem in more detailed computer simulation is that the interaction of the large number of parameters may lead to computer instability.

The flight test missile may have about 50 channels available for telemetry data. Aerodynamic data of interest include missile acceleration, angle of attack, Mach number, altitude, roll attitude, control surface deflection, hinge moment, and surface temperature. Ideally, the flight test would include a correlation of the flight test aerodynamic data with the wind tunnel data and aerodynamic prediction. Unfortunately, this rarely happens.

8.7 Examples of State-of-the-Art Advancement

Examples will be shown of the missile state-of-the-art advancement in the areas of air-to-air missile maneuverability and supersonic airbreathing missile cruise Mach number.

An assessment of the state-of-the-art advancement in air-to-air missile maneuverability is shown in Fig. 8.8. The figure is based on the maximum angle of attack of air-to-air missiles at the date of their initial operational capability (IOC). Note that there is a trend of increased angle of attack capability, especially for short-range air-to-air missiles. Aerodynamic control missiles are limited by technology to about 35-deg angle of attack. For very high angles of attack, unconventional flight control (i.e., TVC, reaction jet/jet interaction control) is required. Examples of modern highly maneuverable missiles with unconventional flight control are the Archer AA-11, Mica, and AIM-9X.

Ramjet propulsion has been investigated as early as the 1940s and has been used on several production missile systems in the United States, United Kingdom, France, Russia, China, Taiwan, and India. Figure 8.9 shows a history of most of the ramjet Mach number demonstrations over the last 50 years. As shown in the figure, the Mach 4.31 ramjet cruise Mach number demonstration in the year 1953 by the X-7 has had little advancement over the last 50 years. The ASALM demonstration of Mach 5.5 in the year 1979 probably represents the practical limit of subsonic combustion ramjet technology. A future flight demonstration of a Dual Combustor Ramjet-scramjet (DCR) engine may demonstrate Mach 6.5 cruise in the year 2006 timeframe. The Scramjet Engine Demonstrator (SED) may demonstrate a "pure" scramjet in the year 2008 timeframe. In recent years, France, Russia, and the United Kingdom have maintained a steady commitment to ramjet propulsion technology and have ramjet missile systems that are currently deployed. France, Russia, and the United Kingdom are arguably the world leaders in ramjet missiles.

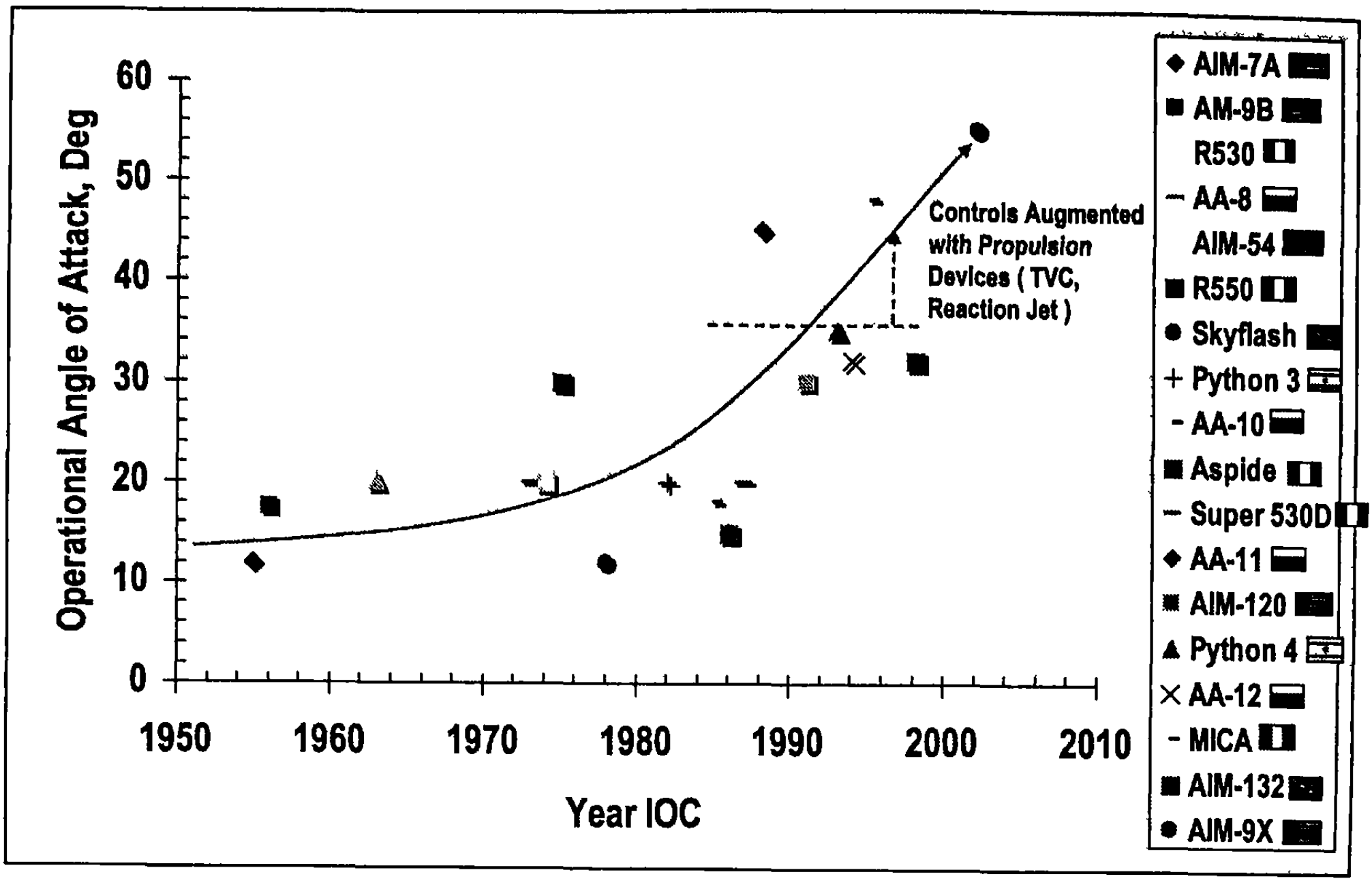

Fig. 8.8 Example of missile technology state-of-the-art advancement: air-to-air missile maneuverability. Figure also in color section.

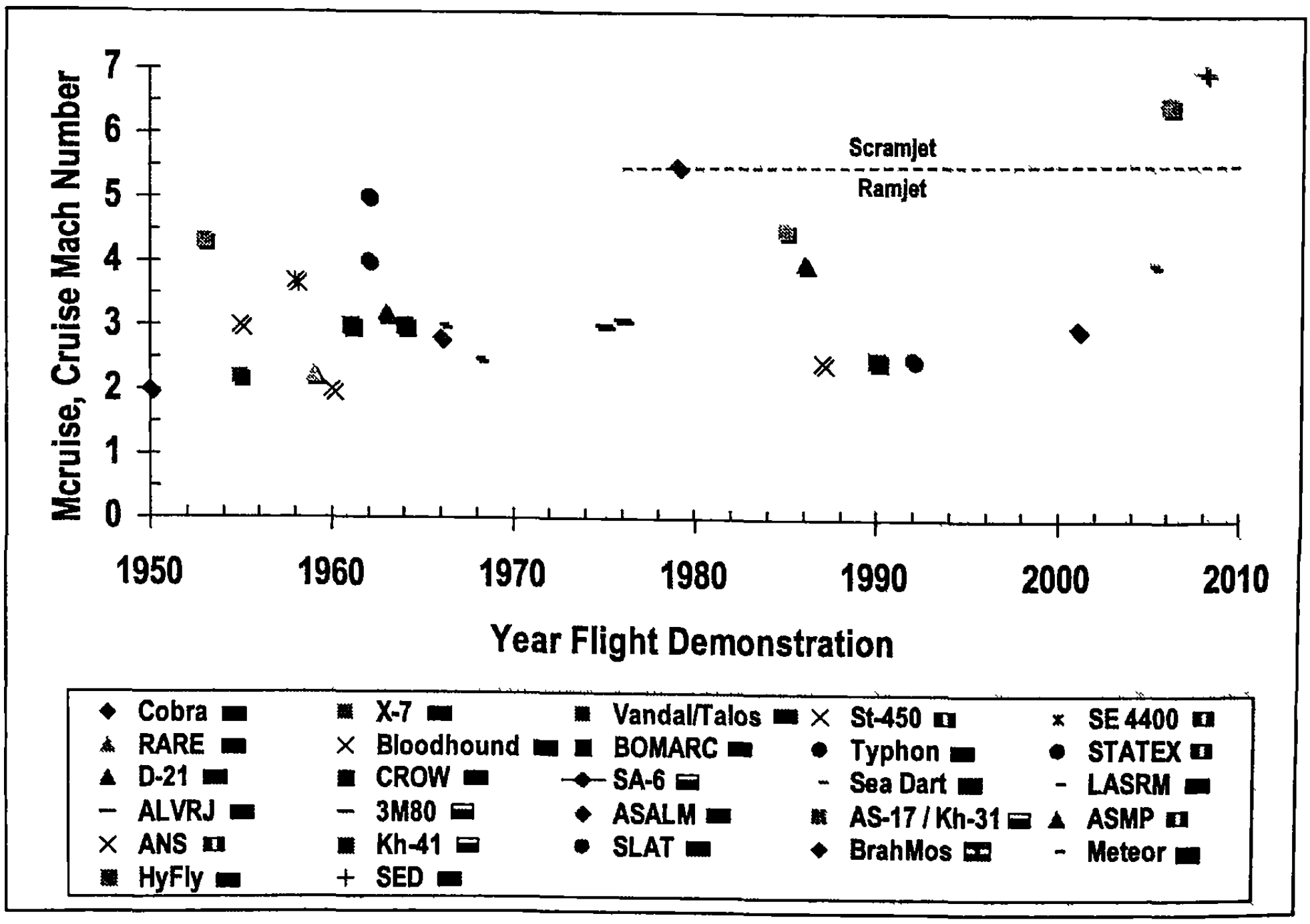

Fig. 8.9 Example of missile technology state-of-the-art advancement: ramjet propulsion. Figure also in color section.

8.8 New Technologies for Tactical Missiles

Figure 8.10 is a summary of the high-payoff, enabling technologies for tactical missiles that were presented in this text. High-payoff technologies are as follows.

1) **Dome**. Faceted/window and multilens domes have reduced dome error slope, resulting in improved guidance accuracy, low observables, and low drag at supersonic speed. Multimode and multispectral domes will also be developed.

2) **Seeker**. Multispectral/multimode imaging seekers enhance performance for automatic target recognition (ATR) in countermeasures and clutter. Synthetic aperture radar (SAR) seekers have good effectiveness in adverse weather and ground clutter. Strapdown and uncooled infrared (IR) seekers reduce parts count/cost. High gimbal seekers enhance off-boresight capability.

3) **Guidance and Control (G&C)**. Integrated global positioning system/inertial navigation system (GPS/INS) permits precision guidance of a low-cost seekerless missile against fixed targets. Using inflight digital trajectory flight prediction and derived flight conditions from the GPS/INS, missiles will continuously optimize the flight trajectory to maximize performance parameters. Advancements in ATR technology will provide new capabilities of near-real-time ATR and lower false alarm rate.

4) **Electronics**. Processing capability is ceasing to be a limitation for the application of processors to sensor data fusion and near-real-time trajectory optimization to missiles. Commercial off-the-shelf (COTS) electronics and a single central processor provide lower cost.

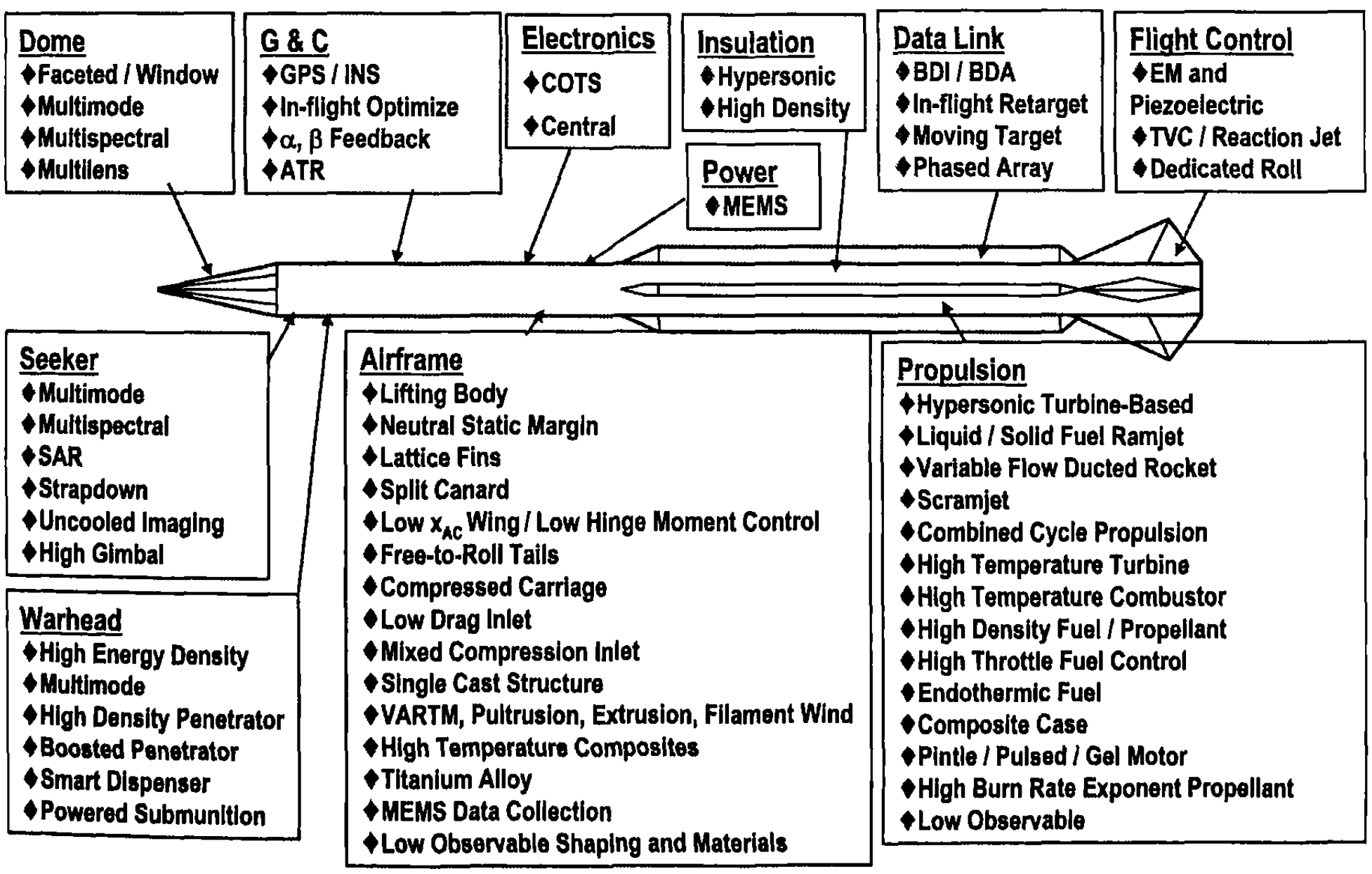

Fig. 8.10 Enabling technologies for tactical missiles.

5) **Airframe**. Lifting body airframes provide enhanced maneuverability and efficiency. Enhancements are also provided by configurations that maintain near-neutral static margin over the flight envelope. Split canard control and free-to-roll tails also enhance maneuverability. Aerodynamic surface planform shaping can reduce the shift of static margin with Mach number and minimize hinge moment. Lattice fins have advantages of smaller hinge moment and higher control effectiveness. Compressed carriage aerodynamic surfaces will be developed for internal carriage. Low drag and higher pressure recovery inlets are in development for hypersonic missiles. Increased usage will be made of castings, vacuum-assisted resin transfer molding, pultrusion, extrusion, and filament winding to reduce parts count/cost. Composite and titanium materials will be used in hypersonic missiles. Low-cost/small-size micromachined electromechanical systems (MEMS) sensors will be used in data collection and health monitoring. Airframe shaping and composite materials technology will provide reduced observables.

6) **Power**. A MEMS microturbine generator is 5% of the weight of a conventional battery for the same power output.

7) **Warhead**. Higher energy density explosive warheads such as the U.S. Navy China Lake CL-20 will be developed. Modular multimode warheads will be developed. Kinetic energy warheads will be developed that have higher density and boosted penetrators for defeating hard and deeply buried targets. Smart submunition dispensers and autonomous submunitions will counter mobile, time-critical targets (TCTs).

8) **Insulation**. Higher density insulation will be developed to improve the volumetric efficiency for hypersonic missiles.

9) **Propulsion**. Turbojet, air turbo-rocket, ramjet, ducted rocket, scramjet, and combined-cycle propulsion will be developed for hypersonic missiles. High-temperature turbines and combustors will be developed. Higher density fuels and propellants will provide high volumetric performance. Endothermic fuels will provide higher specific impulse, shorter combustor length, and cooling for scramjets. Composites will reduce weight. Thrust management technologies will be developed for pintle, pulse, and gel motors. In the case of a pintle motor, high burn rate exponent propellant is an enabling technology to maintain high specific impulse over a broad range of thrust. Reduced observable propellants will continue development. Finally, kinetic kill missiles will use high-thrust motors to quickly accelerate to hypersonic speed.

10) **Data Link**. Battle damage indication/battle damage assessment (BDI/BDA) will be provided by a data link of target imagery. Inflight retargeting by a high-bandwidth data link will be developed for mobile and moving targets. A high-bandwidth data link will provide a seekerless missile with a hit-to-kill capability against moving targets. Phased array antennas will be developed for high data rate and mission flexibility.

11) **Flight Control**. High power density electromagnetic and piezoelectric actuators provide high bandwidth and high rate with reduced weight. TVC and reaction jet control will be developed for highly maneuverable and hit-to-kill missiles. Finally, dedicated roll control surfaces provide higher control effectiveness at high angle of attack and simplify the autopilot design.

8.9 Summary

Chapter 8 addressed the development process for tactical missiles. The areas of discussion included the application of a technology roadmap to the development process; the development activities and timeframe for the phases of basic research, exploratory development, advanced technology development, advanced development, and SDD; and the levels of design and drawing maturity as related to the stage of missile system development. Also discussed were missile follow-on program frequency and examples of follow-on programs. The process for the integration of missile subsystems (propulsion, airframe, G&C, power supply, warhead) development to the missile system development/integration activities (e.g., HWL simulation, environmental tests, launch platform compatibility) and the process leading to a flight demonstration of the missile system were presented. Examples were given of missile development tests and facilities. Examples were also given of state-of-the-art advancement for the areas of maneuverability and cruise Mach number. Finally, new technologies for tactical missiles were summarized.

Problems

8.1. A technology roadmap establishes the high-payoff technologies g____.

8.2. The levels of design maturity from the most mature to least mature are production, detail, preliminary, and c_____ design.

8.3. Technology transitions occur from basic research to exploratory development, to advanced development, to d_____ and v_____.

8.4. Approximately 11% of the U.S. research, technology, and acquisition (RT&A) budget is allocated to t____ m____.

8.5. In the United States, a tactical missile has a follow-on program about every _____ years.

8.6. Compared to the AIM-9L, the AIM-9X has enhanced m_____.

8.7. Compared to the AIM-7, the AIM-120 has autonomous guidance, lighter weight, higher speed, and longer r____.

8.8. Compared to the PAC-2, the PAC-3 has h____ t_ k_____ accuracy.

8.9. Guidance and control is verified in the h_____ in l_____ simulation.

8.10. Airbreathing propulsion ground tests include direct connect tests and f_____ tests.

8.11. Aerodynamic force and moment data are acquired in w__ t_____ tests.

9
Summary and Lessons Learned

9.1 Introduction

This final chapter is a summary of the material presented in this text, a reiteration of conceptual design criteria, and a discussion of lessons learned from the author's experience in the development of tactical missiles and their technologies. We will begin with a discussion of seventeen guidelines from lessons learned in the conceptual design of tactical missiles.

9.2 Evaluate Alternatives and Iterate the System-of-Systems Design

Again, Fig. 9.1 illustrates that the missile design process requires a broad assessment of alternatives and iteration at all levels. This figure was discussed in detail in Chapter 1. A common mistake is to select a design too quickly without sufficient consideration of the system-of-systems alternatives.

9.3 Exploit Diverse Skills

Figure 9.2 illustrates that the missile design activity is an opportunity to harmonize diverse inputs early in the development process. The military customer has the lead in providing the "requirements pull" initial input for the mission/scenario definition task and in providing the relative weighting for the most important requirements (MIRs). A useful tool in reaching a consensus on the most important requirements and their weighting is constructing a house of quality. In many cases it is not possible to put a single value on a requirements parameter. Instead, a requirements parameter may be specified with threshold, standard, goal values that are based on considerations such as cost, performance, risk, and the projected state of the art (SOTA). The mission/scenario definition, the relative weighting of the MIRs, and the values of the requirements parameters may be modified later based on the emerging results from the study. For example, the customer may change the requirements as a result of the "technology push" of the projected available capability in the timeframe of interest. The customer may also change the requirements to satisfy an unforseen sales opportunity. For example, if a design warhead weight and flight range are only slightly greater than the constraints of the Military Technology Control Regime (MCTR), the customer may ask that the warhead weight and the flight range be limited to

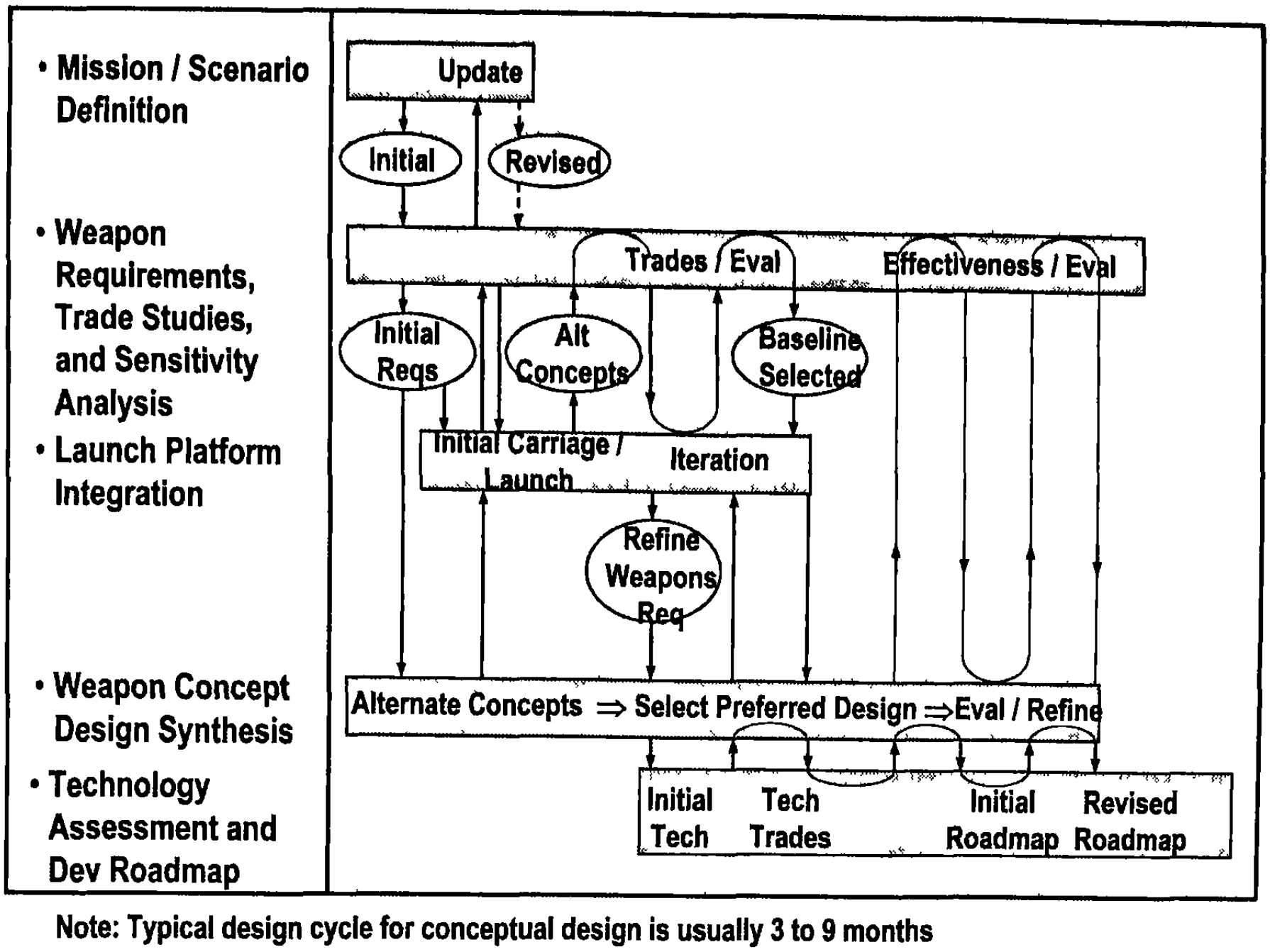

Fig. 9.1 Evaluate alternatives and iterate the system-of-systems design.

500 kg and 300 km to allow the possibility of future foreign sales. The system-of-systems weapon requirements [including command, control, and communication (C^3) targeting], trade studies, and sensitivity analysis are usually conducted by operations analysis personnel. System integration engineers usually lead the

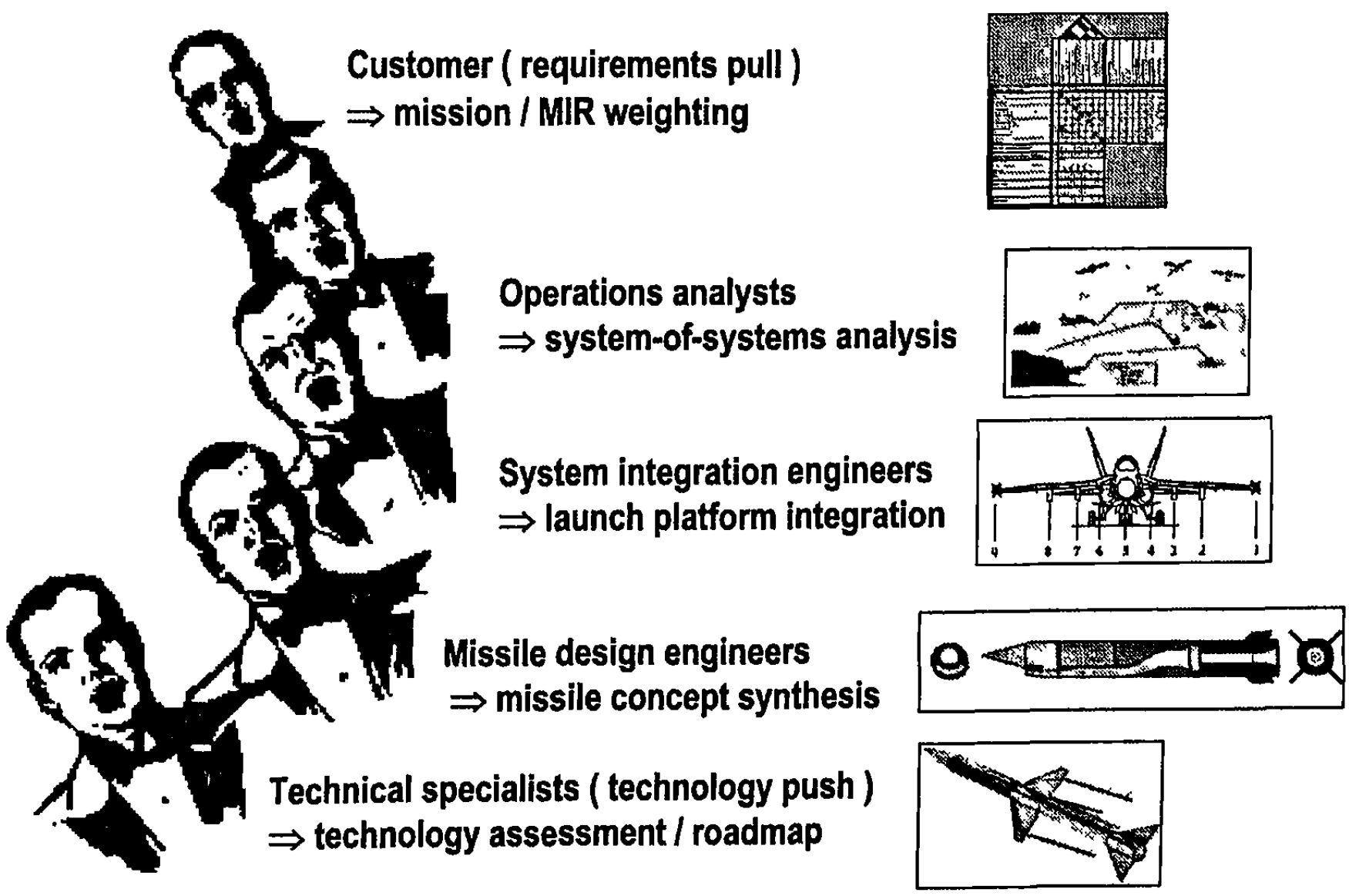

Fig. 9.2 Exploit diverse skills for a balanced design.

task to integrate the missile with the launch platform. Missile design engineers lead the task to synthesize the alternative missile concepts. Finally, technical specialists provide the lead input for the technology push of potentially available technical capability (e.g., enhanced aerodynamic prediction accuracy at high angles of attack) and the technology development roadmap.

9.4 Utilize Creative Skills

Missile design is a creative process that requires unique skills (Fig. 9.3). Missile design requires creative skills for 1) consideration of a broad range of alternatives; 2) questioning the basis of requirements and constraints to ensure that they are not artificially limiting the range of alternative approaches; 3) projecting into the future (e.g., 5–15 years) the SOTA, threat, scenarios, tactics, military doctrine, alternative concepts, and technology impact forecast; 4) recognizing and distilling the most important, key drivers from a large number of possibilities; 5) developing a missile concept that is synergistic within a system-of-systems; 6) developing a synergistic/balanced combination of high leverage subsystems and technologies.

9.5 Identify and Quantify the High-Payoff Measures of Merit

One objective of missile design is to identify and quantify the high-payoff measures of merit. Because missiles are cost constrained, it is not possible to use the latest SOTA for all areas. Measures of merit such as range, time to target, robustness, lethality, reliability, miss distance, survivability, observables, and weight impact the missile cost. As illustrated in Fig. 9.4, judicious selection must be made for a balanced cost-effective design.

- Use Creative Skills to Consider Broad Range of Alternatives
- Ask Why? of Requirements / Constraints
- Project into Future (e.g., 5 – 15 years)
  - State-of-the-Art (SOTA)
  - Threat
  - Scenario / Tactics / Doctrine
  - Concepts
  - Technology Impact Forecast
- Recognize and Distill the Most Important, Key Drivers
- Develop Missile Concept that is Synergistic within a System-of-Systems
- Develop Synergistic / Balanced Combination of High Leverage Subsystems / Technologies

Fig. 9.3 Utilize creative skills.

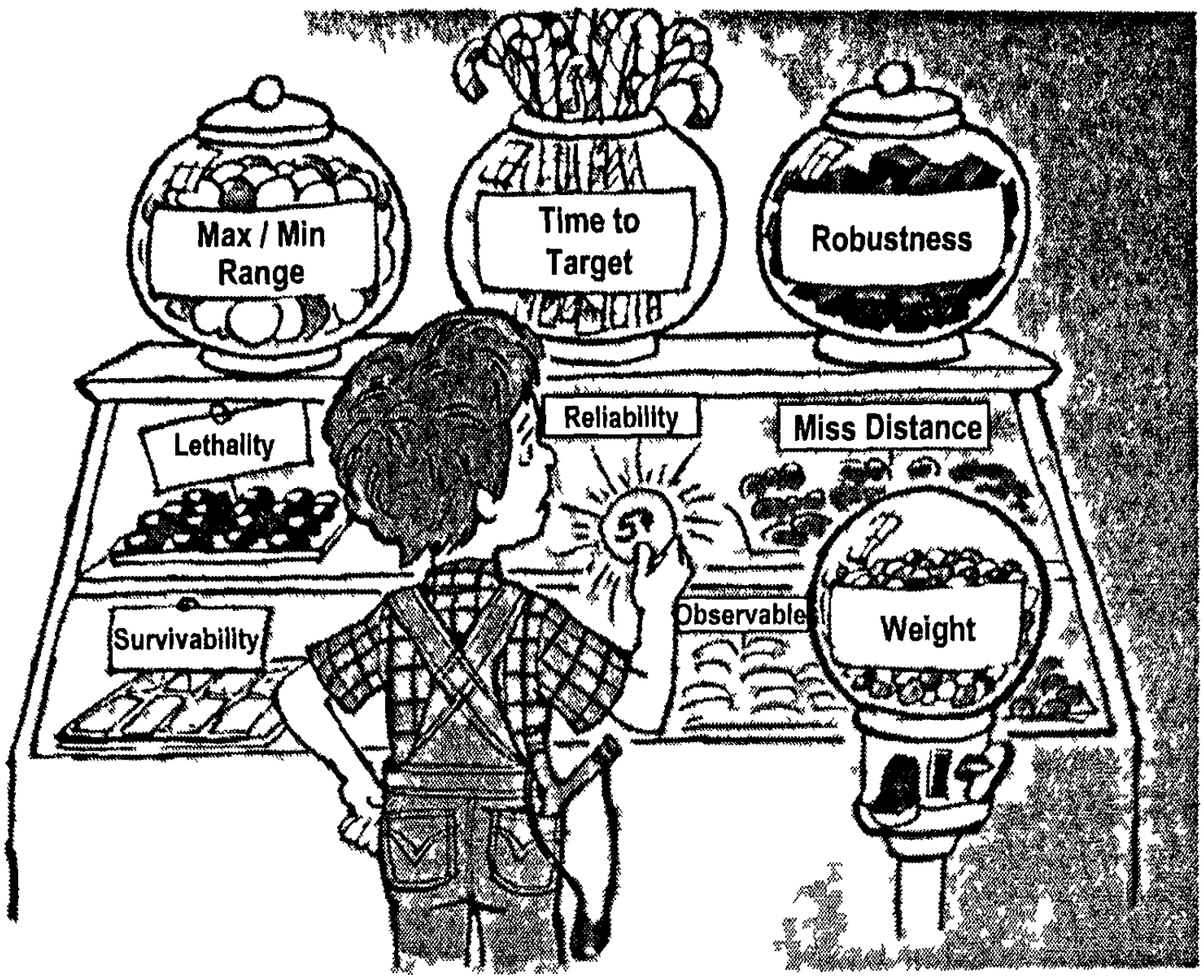

Fig. 9.4 Identify and quantify the high-payoff measures of merit.

Analysis techniques such as the house of quality and the design of experiments (DOE), discussed in Chapter 7, should be used in the design process. The house of quality provides a process for meeting customer requirements. The DOE provides a process for efficiently covering the design solution space. A DOE of the nine measures of merit illustrated in the figure requires $2^9 = 512$ design concepts to cover the solution space of cost based on minimum/maximum reasonable values for each measure of merit.

Participation by the military customer is required to obtain a consensus on the relative weighting of the MIRs/system measures of merit. As an example for a typical volume- and weight-limited missile, one contractor may overly emphasize the warhead lethality, and, as a result, develop a larger/heavier warhead at the expense of range. Another contractor may overly emphasize the launch platform survivability and, as a result, develop a longer range missile at the expense of warhead weight lethality. The customer preference of lethality versus launch platform survivability should be a driver in the relative weighting of the MIRs/system measures of merit.

9.6 Start with a Good Baseline Design

As discussed in Chapter 1, starting with a good baseline enhances the accuracy and speed of the design process. Figure 9.5 illustrates that the selection of a baseline missile should not be biased by previous experience. As an example, the Sparrow missile was a good baseline missile in the development of designs for a lightweight, active radar missile (which later became AMRAAM).

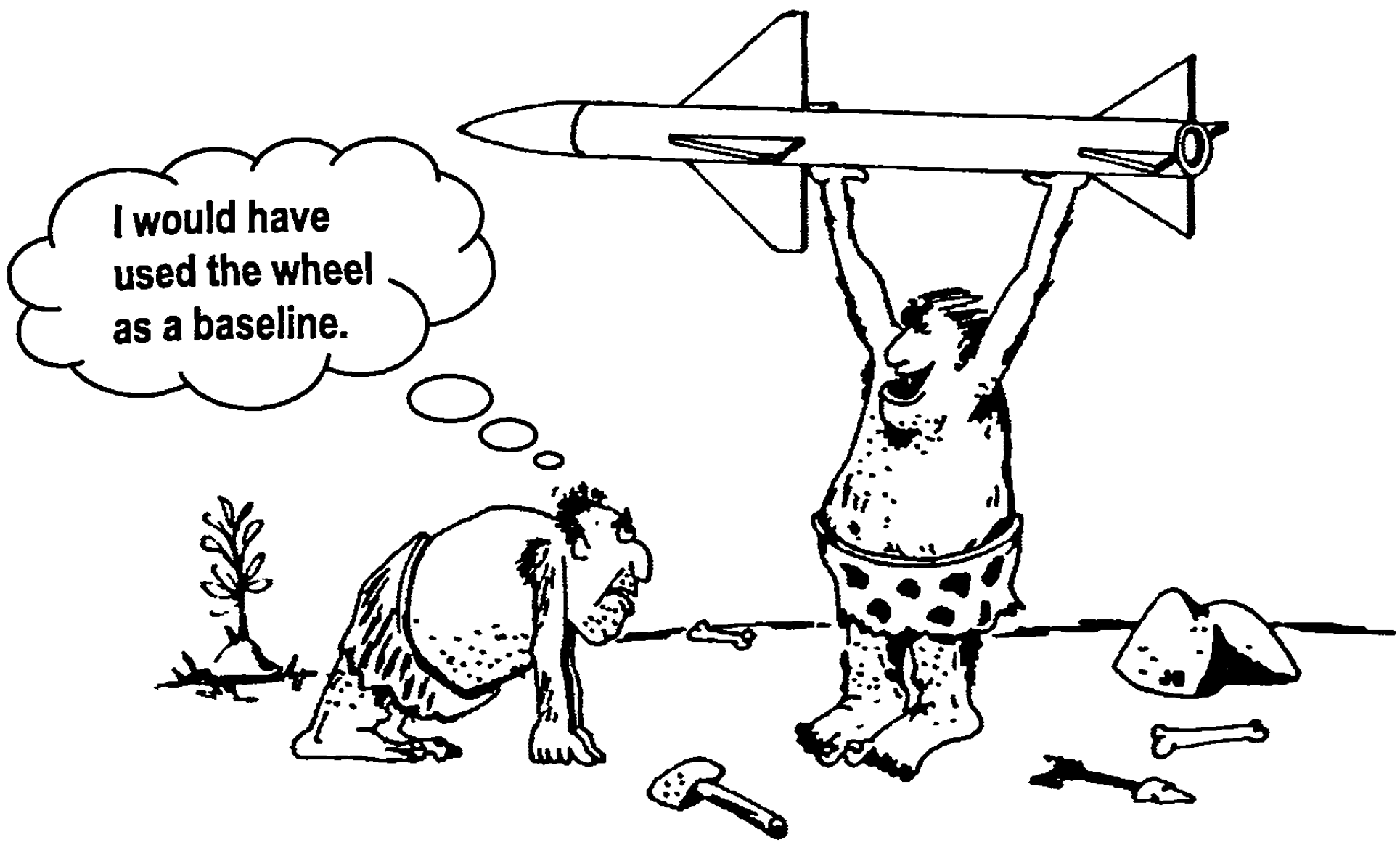

Fig. 9.5 Start with a good baseline.

9.7 Conduct Balanced, Unbiased Tradeoffs

As shown in Fig. 9.6, what is important is in the eye of the beholder. Based on experience, if a subsystem is taken to an extreme limit of its capability, it is usually at cross purposes to the other subsystems and results in a nonoptimum missile. The missile designer must harmonize the subsystems to create a cost-effective design.

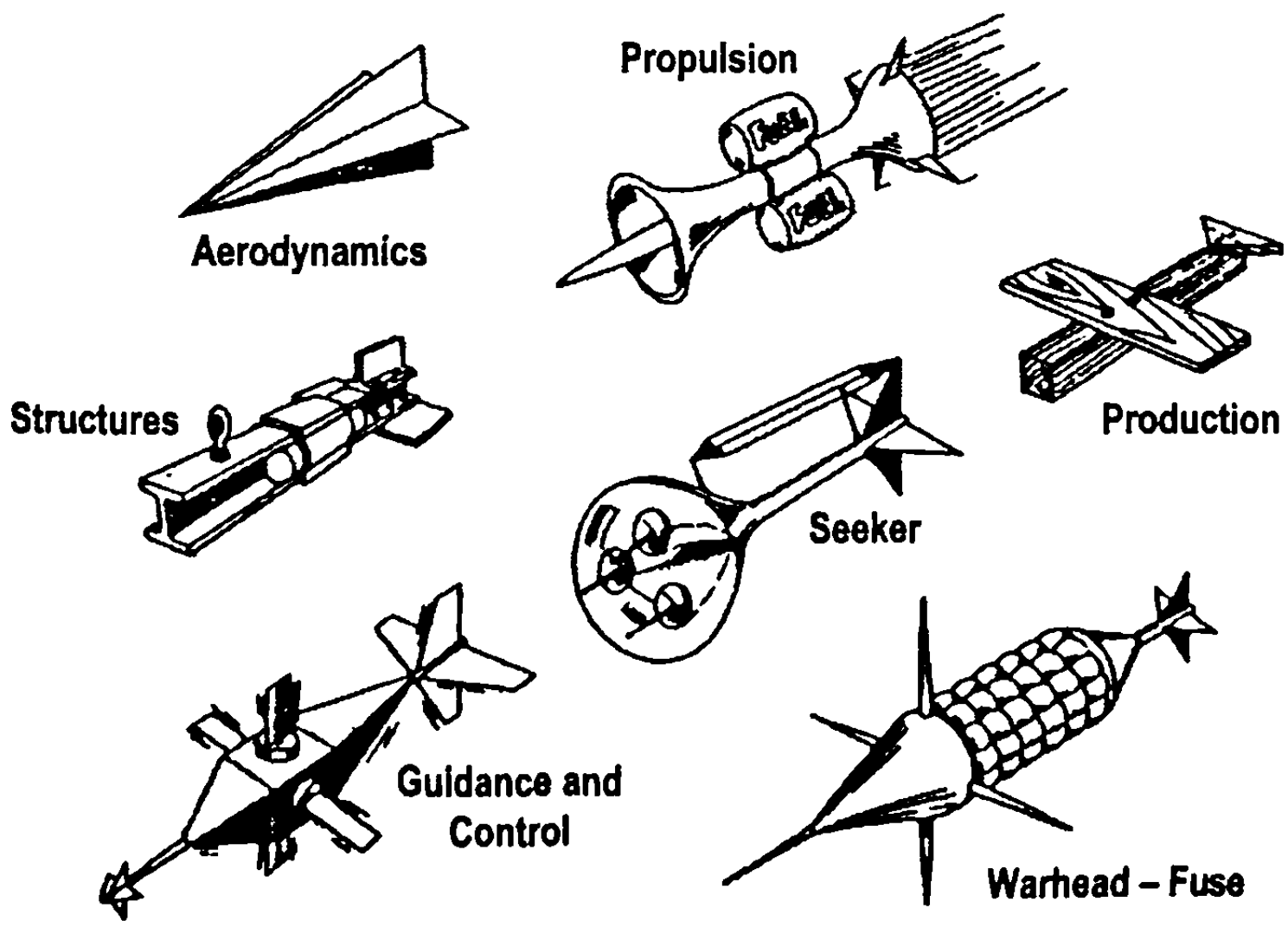

Fig. 9.6 Conduct balanced, unbiased tradeoffs.

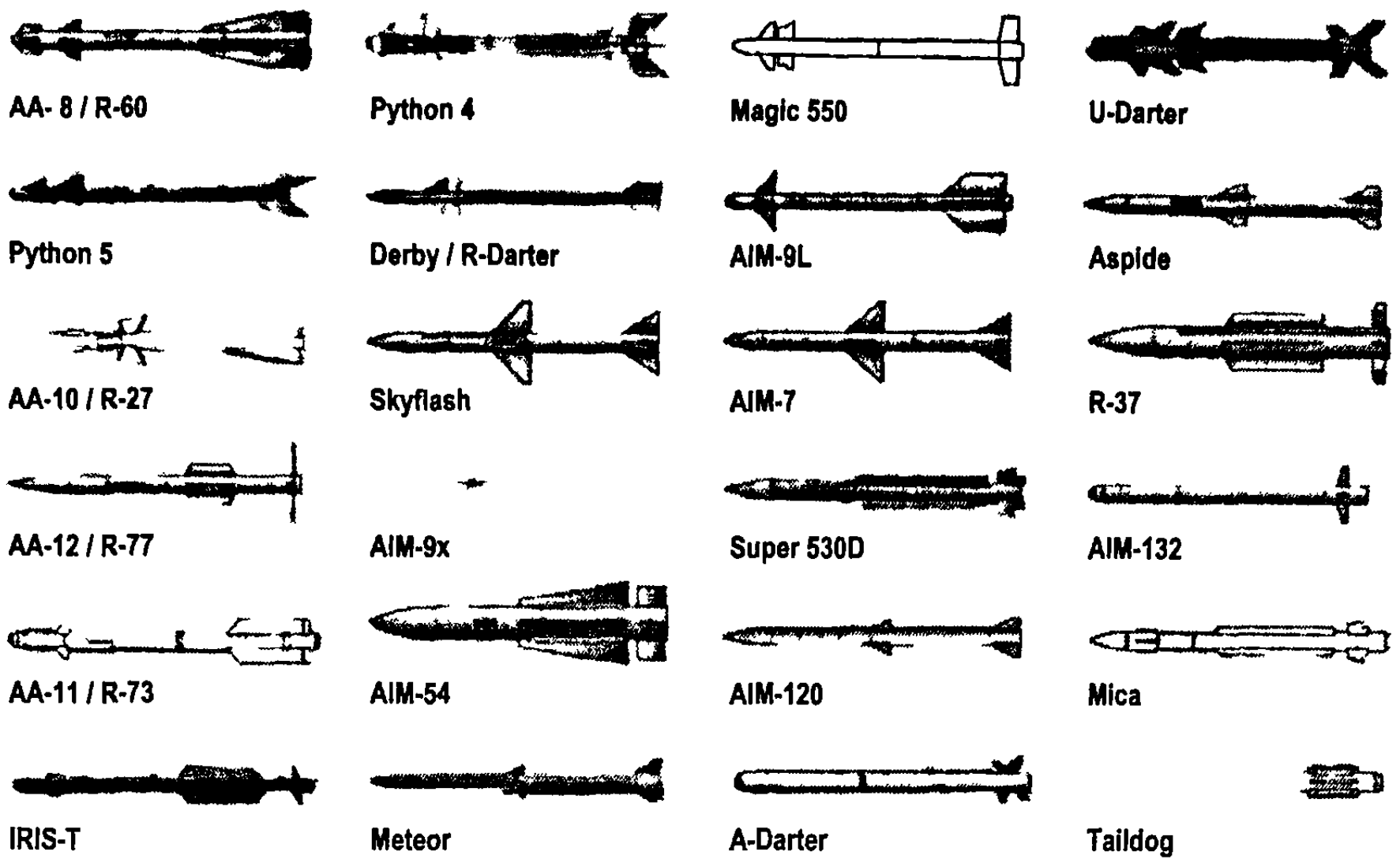

Note: Although all of the above are supersonic air-to-air missiles, they have different configuration geometry

Fig. 9.7 Evaluate many alternatives.

9.8 Evaluate Many Alternatives

There are many configuration candidates for a missile design. A balanced, optimum conceptual design requires the consideration of a broad range of alternatives. For example, Fig. 9.7 shows air-to-air missile alternatives that are very different in their aerodynamic configurations. As expected, aircraft launch platform constraints and supersonic flight consideration result in air-to-air missiles with high fineness ratio. Also, the relatively soft/small air target results in a relatively small warhead. Although all of the missiles have high maneuverability (e.g., 30 $+g$), the approach to surface area and geometry varies widely. Some missiles have wings, whereas others are wingless. Flight control alternatives include thrust vector control (TVC), tail control, canard control, and wing control. There are a variety of propulsion alternatives (e.g., rocket, ducted rocket, ramjet). The harmonization of measures of merit that may conflict, such as aircraft compatibility, maneuverability at low speed, turn radius, rate of turn, and velocity, will often drive the designer to different aerodynamic configurations.

9.9 Search a Broad Design Solution Space (Global Optimization Versus Local Optimization)

Figure 9.8 illustrates the problem of finding an optimum in a cluttered environment. Missile design is a complex problem consisting of many parameters. These measures of merit are interacting and are often conflicting. The optimum is not obvious. Prior experience may not necessarily be applicable and intuition may not necessarily lead in the correct direction. The best approach is usually to search the broadest possible solution space to the greatest depth in the available time.

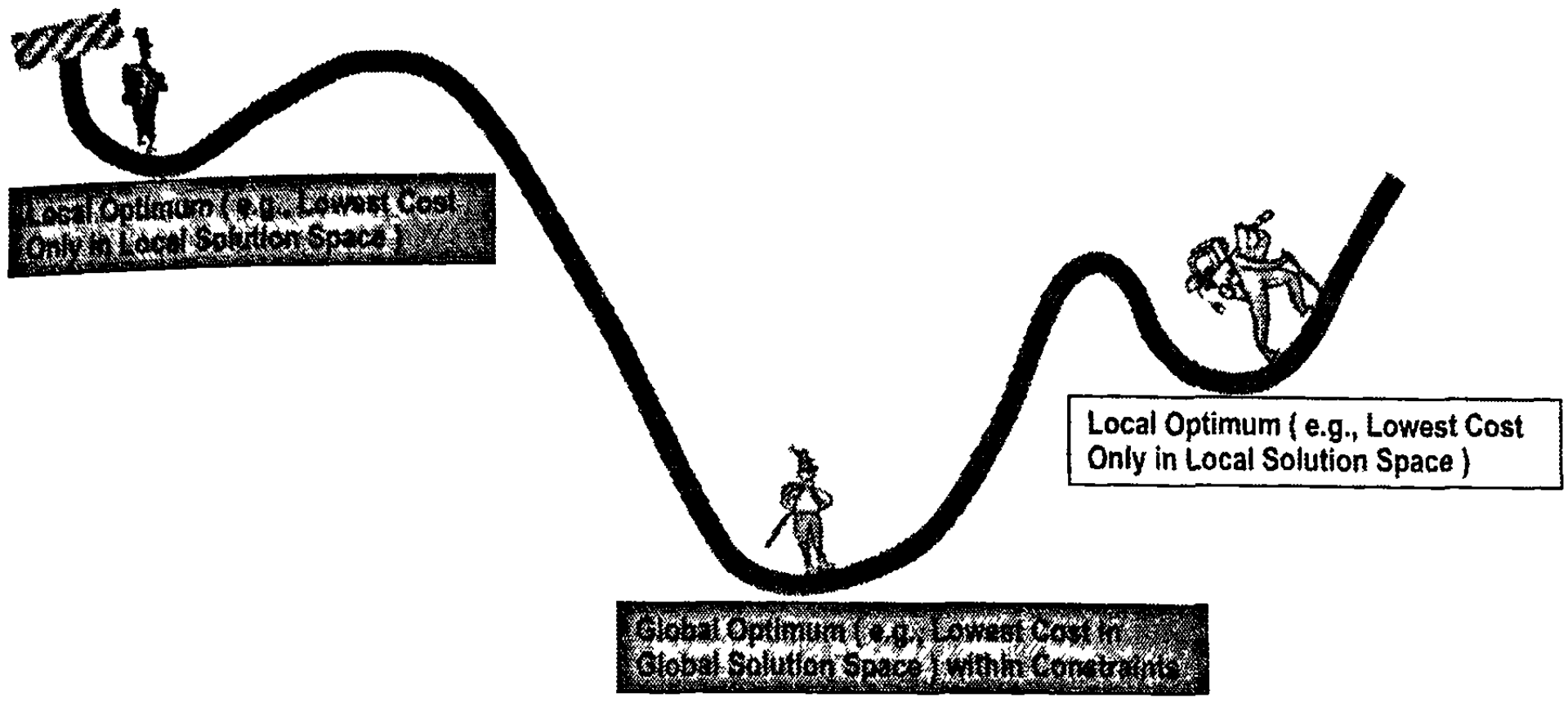

Fig. 9.8 Search a broad design solution space (global optimization vs local optimization).

9.10 Evaluate and Refine as Often as Possible

Figure 9.9 illustrates a natural bias from the developer of a missile that changes to the current missile are not necessary. The pride of authorship reflects the time and money that went into developing the missile. However, time does not stand still. The developer of a missile should not ignore new technologies,

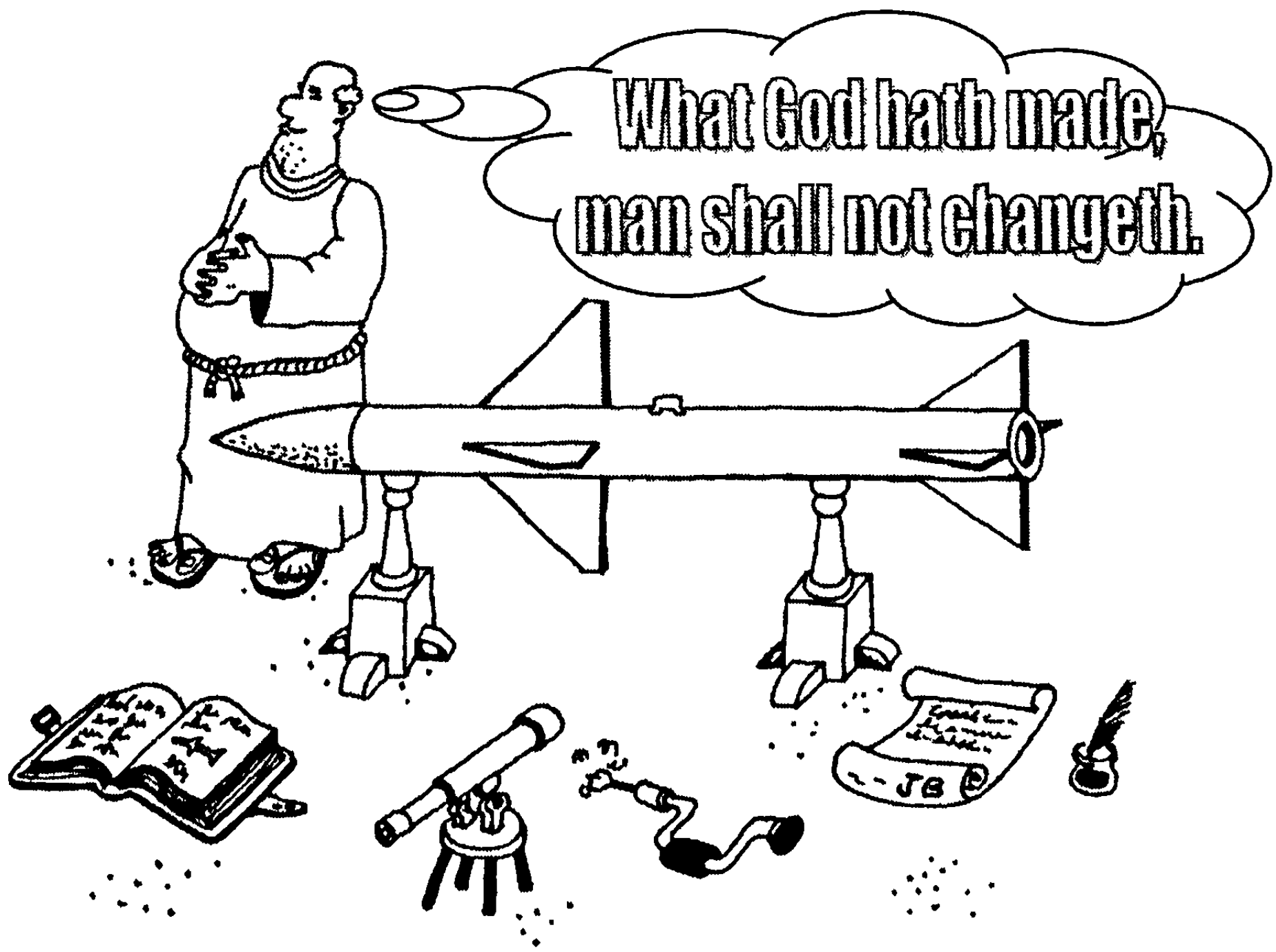

Fig. 9.9 Evaluate and refine as often as possible.

new capabilities, or new requirements because of a "not invented here" attitude. A good design should eventually be replaced by a better design.

9.11 Provide Balanced Emphasis of Analytical Versus Experimental

Aerospace engineering is by its nature a synthesis profession, requiring a balance of emphasis of analytical activity and experimental activity. Each has value, each has its advocates and role model examples (Fig. 9.10), and each can be a career path unto itself. Although the individual functional disciplines of aerospace engineering (e.g., propulsion, aerodynamics, structure, flight control) could be accommodated within a mechanical engineering program, one of the things that makes aerospace engineering unique is the requirement for synergistic synthesis of its disciplines into aerospace systems. This requires a system development process with feedback at each stage of the process.

9.12 Use a Design, Build, and Fly Process for Feedback that Leads to Broader Knowledge

Figure 9.11 illustrates the feedback and synergy of the design, build, and fly process. The initial stage, design synthesis, requires synergistic selection of subsystems, with prediction of subsystem and system performance and cost. Iteration is required for convergence of the design predicted characteristics to a balanced

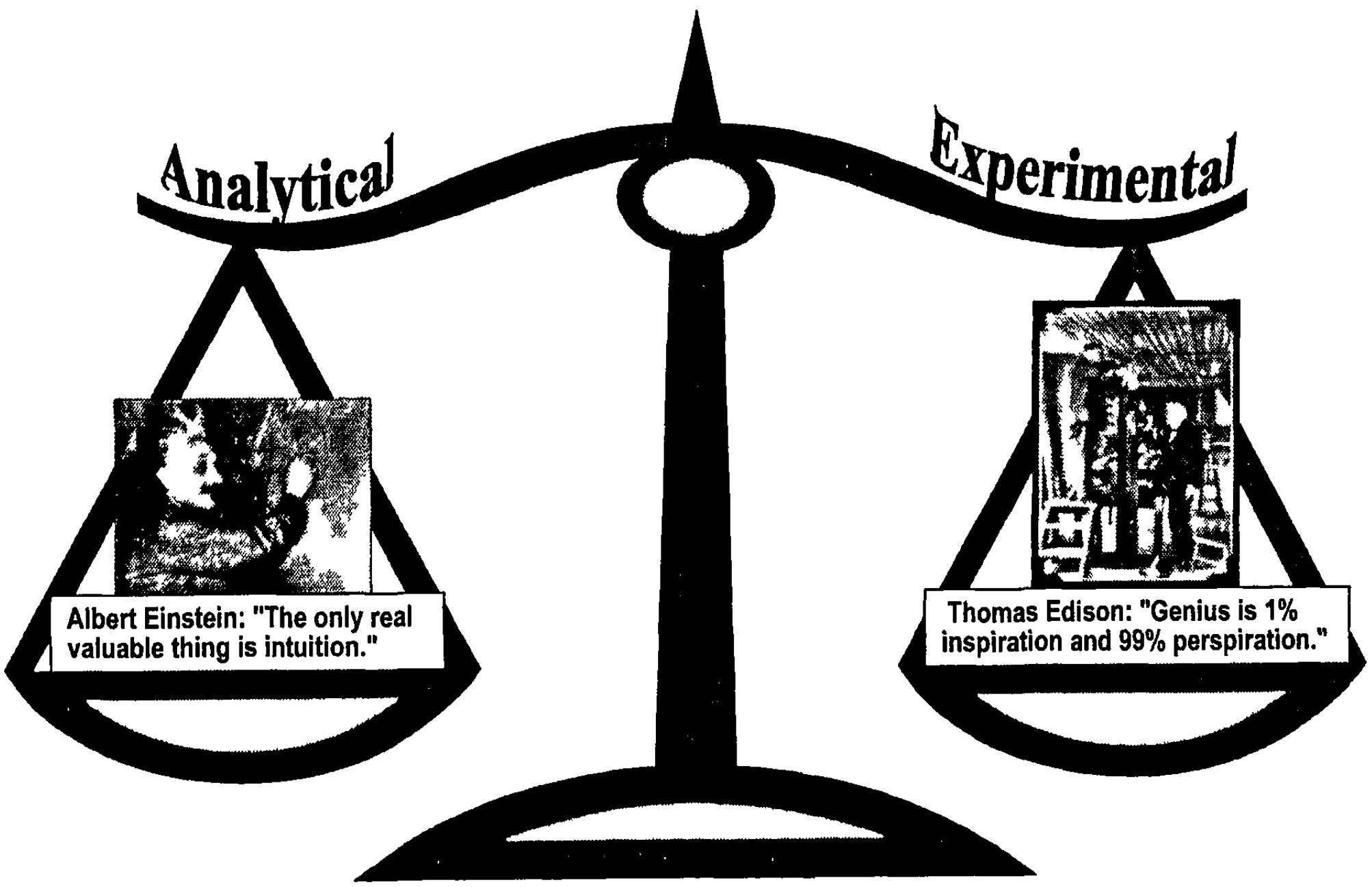

Fig. 9.10 Provide balanced emphasis of analytical vs experimental.

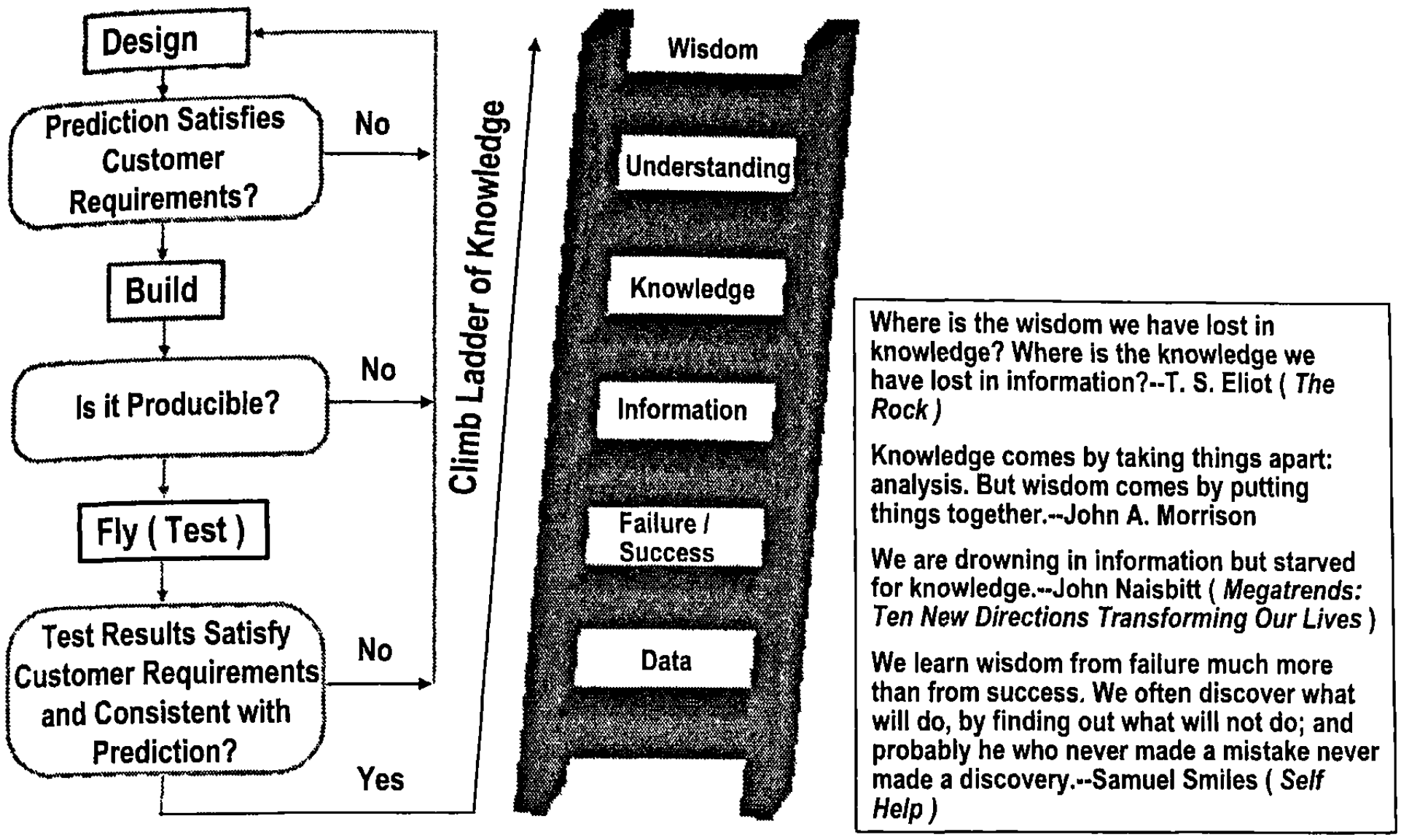

Fig. 9.11 Use a design, build, and fly process for feedback that leads to broader knowledge.

emphasis that is consistent with customer requirements. The next step is building the flight vehicle in accordance with the design drawings/work instructions. A lesson learned here is that the engineering drawings/work instructions need to be clear and producible. The third step is test. In the case of flight test, comparisons can be made of predicted range performance versus actual range performance. Often prediction does not match the data, and you have to explain possible reasons for the differences. Also, for repeat tests there are differences in the results, introducing the problem of probabilistic uncertainties.

Illustrated in the right side of the figure is the classical ladder of knowledge. Advancing up each step of the ladder of knowledge requires multiple and diverse experiences. Steps lead from collecting data to outcomes of failure/success to acquiring information to obtaining knowledge. Knowledge may (or it may not) lead to a more general understanding, which may finally lead to wisdom.

9.13 Evaluate Technology Risk

Immature technologies often have unknown and adverse interactions with other subsystems. Unfortunately the technical specialist will often present only the favorable features of a technology. A technology should not be inserted into a future system development and demonstration (SDD) or production program unless the technology is mature and the risk, performance, schedule, cost, and customer acceptance have been fully characterized. Figure 9.12 illustrates that there may be hidden, perhaps even disguised, problems of using a new, highly immature technology.

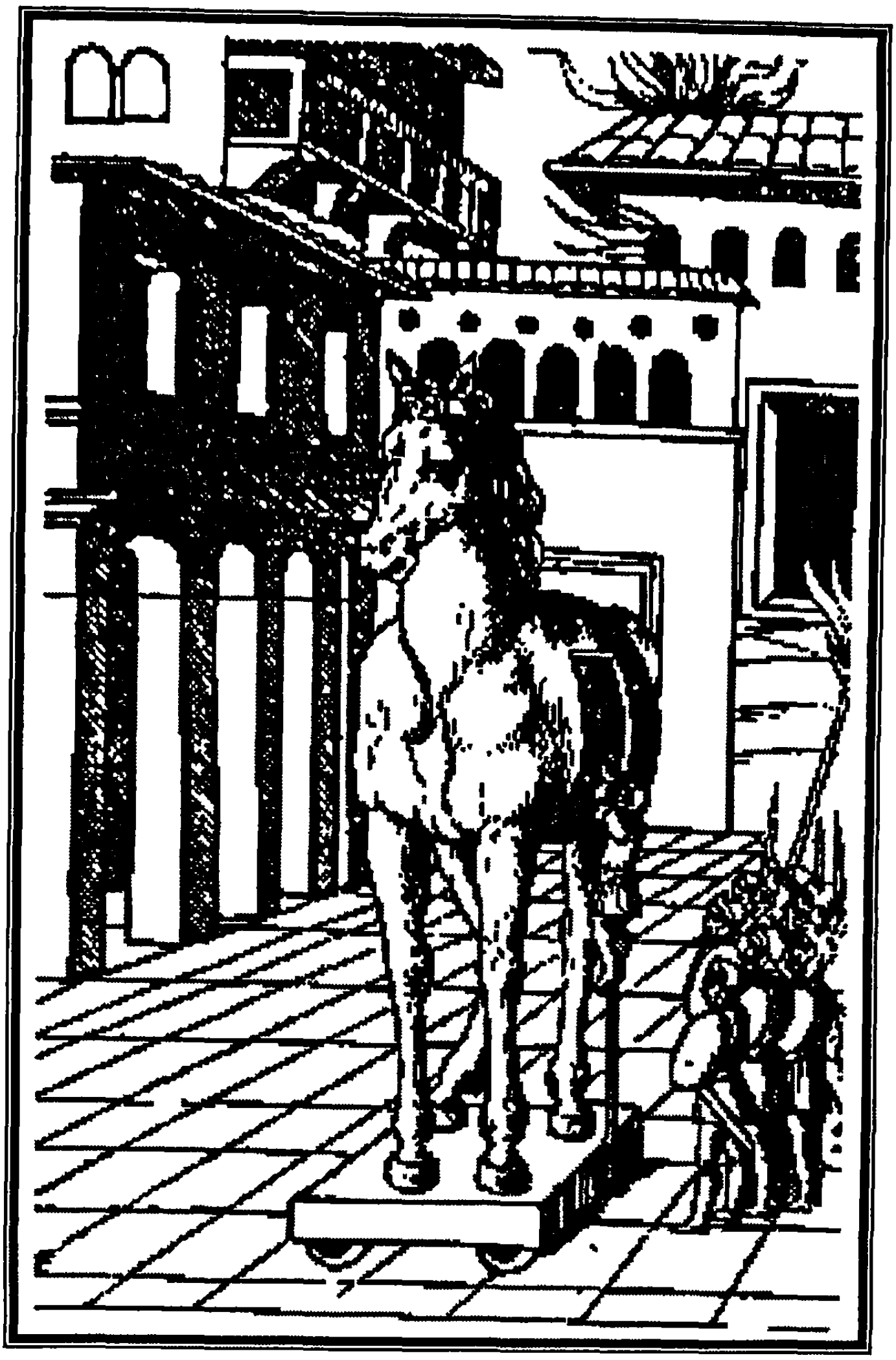

Fig. 9.12 Evaluate technology risk.

9.14 Maintain Real-Time Documentation

As illustrated in Fig. 9.13, it is good practice to maintain real-time documentation of the assumptions and results during the design process, rather than waiting until the end. A common mistake is to delay the documentation until the end of the study. However, key assumptions and results may be lost during the study unless there is timely and accurate documentation. Also, there may be insufficient time to complete the documentation before moving on to other activities.

9.15 Develop Good Documentation

Figure 9.14 is an example of documentation requirements for tactical missile conceptual design. Good documentation should provide a traceable flow-down of information from the system-level requirements to subsystem requirements to

Fig. 9.13 Keep track of assumptions and develop real-time documentation.

component performance to the technology rationale. An example output of a missile conceptual design process is the following:

1) MIRs/system measures of merit weighting. Meetings are held with the customer to develop a consensus on the most important requirements and their weighting. A house of quality is usually constructed to facilitate the process.

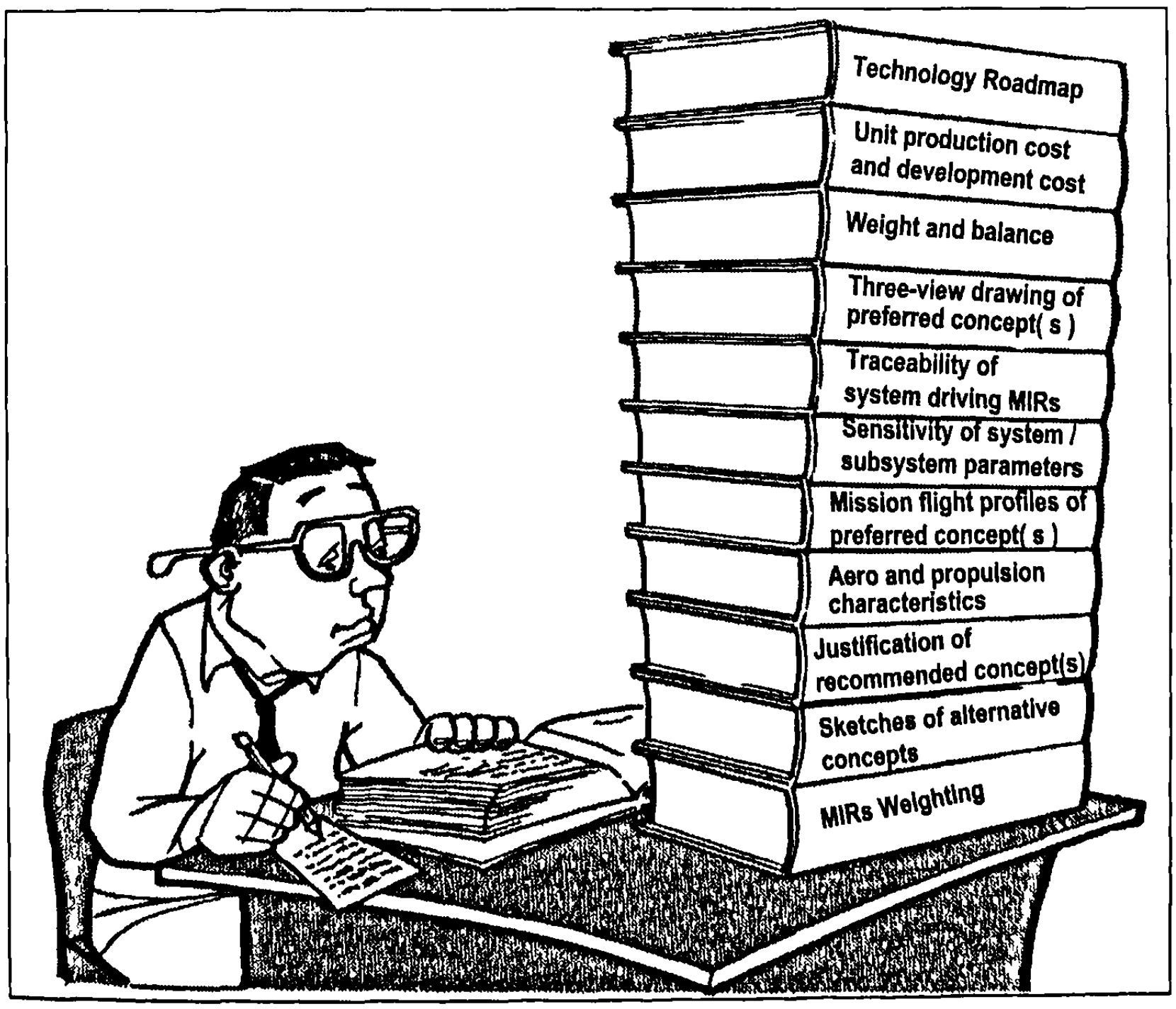

Fig. 9.14 Develop good documentation.

2) Sketches of alternative concepts.

3) Justification of the recommended concept(s), including reasons for the concept(s) being selected, measures of merit, design tradeoffs, criteria for selection, and advantages compared to alternative concepts. Measures of merit include maximum range, minimum range, maximum speed, and accuracy. A DOE should be conducted of alternative concepts.

4) Aerodynamics and propulsion characteristics, including aerodynamic stability, aerodynamic control effectiveness, normal force, axial force, specific impulse, thrust, weight of propellant/fuel, and the methods used for prediction.

5) Mission flight profiles of the preferred concept(s).

6) Sensitivity of the system/subsystem parameters to measures of merit.

7) Traceability of flowing down the system driving MIRs to concept performance, subsystem performance, and technology selection.

8) Three-view drawing of preferred concept(s), including an outboard profile showing external features and dimensions and inboard profiles showing subsystems and their dimensions.

9) Weight and balance statement, including subsystems weight, subsystems location, launch and burnout center of gravity, launch and burnout moments of inertia, and the methods used for weight and balance.

10) Unit production cost, including the number of units that are produced, the learning curve, and the basis for the learning curve.

11) Technology roadmap of technologies that require development to demonstrate maturity and readiness for an operational application. The technology roadmap includes the required schedule and milestones for timely insertion of technology into an operational system.

9.16 Utilize Group Skills

Tactical missile conceptual design is usually conducted by a small group of engineers in an advanced programs department. The advanced programs/conceptual design team is part of a larger organization. Overall management of the design activity is usually conducted by a program manager and a systems engineer. The program manager focuses on cost performance, schedule performance, and the outside customer interface. The systems engineer provides the inside technical interface with the engineering team and addresses the system engineering concerns. The conceptual design team consists of about 10 engineers, representing the key technical areas. It is important that the design team function as a synergistic group rather than a set of individuals with primary interests in promoting their individual technical areas.

Figure 9.15, based on Ref. 33, shows that the size of the conceptual design team is about 2% of the engineering organization. The size of the typical advanced programs/conceptual design organization is about 10–30 engineers, with about two engineers in each broad technical area (e.g., system design, aerodynamics, propulsion, structures, performance, flight control, guidance and navigation, sensors, warhead, system effectiveness, cost). Usually there is a senior engineer as a mentor for each junior engineer. Most of the junior engineers move out of the conceptual design organization after a few years. The junior

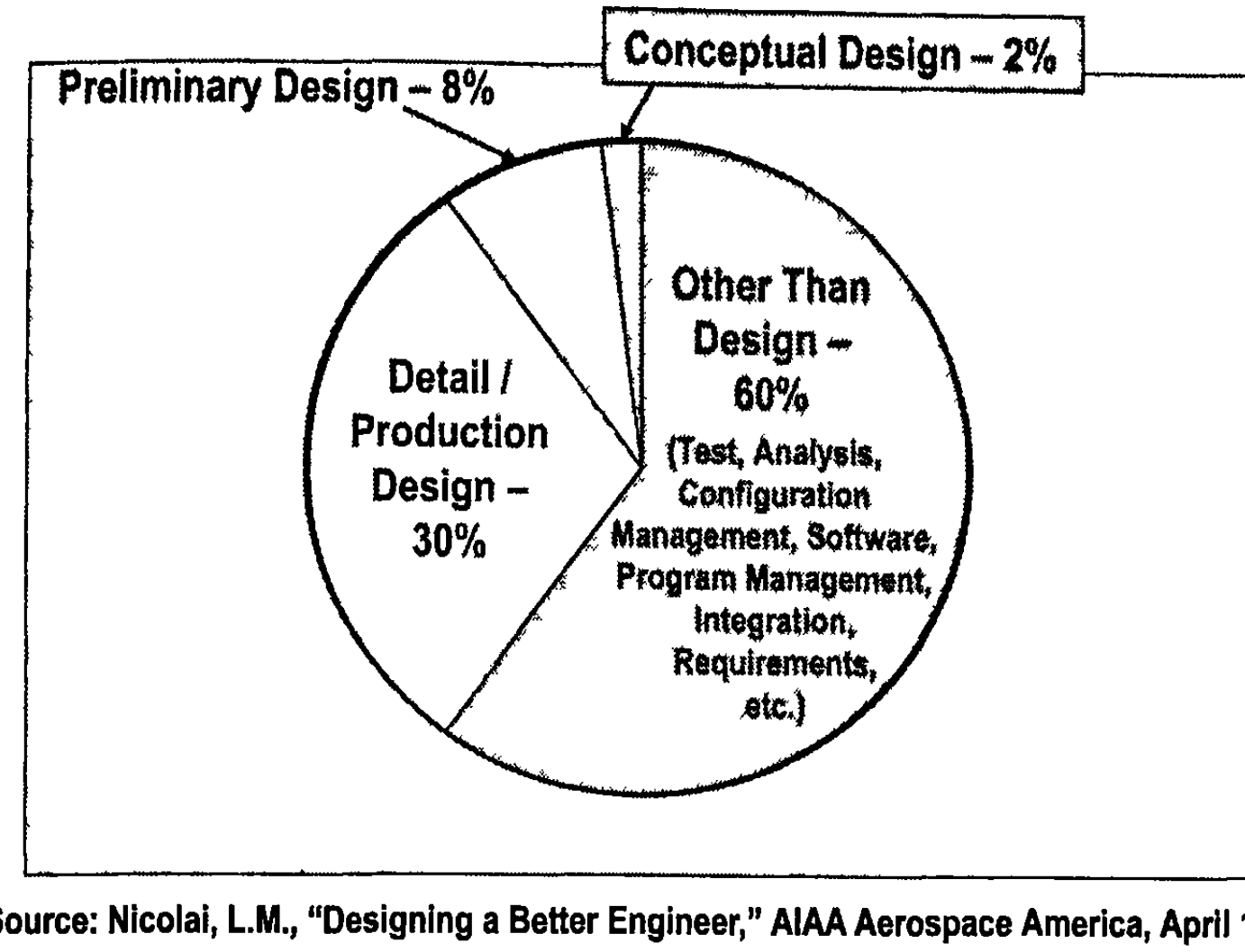

Fig. 9.15 Utilize group skills.

system engineers often become program managers, while the junior technical specialists may move on to either providing technical support to specific programs or to conducting more detailed work in their technical specialty.

9.17 Balance the Tradeoff of Importance Versus Priority

The advanced programs/conceptual design team works on future business opportunities that are important but usually have relatively low priority in comparison to the more near-term concerns of the larger organization. As illustrated in Fig. 9.16, it is important to be agile to survive in a dynamic environment of the

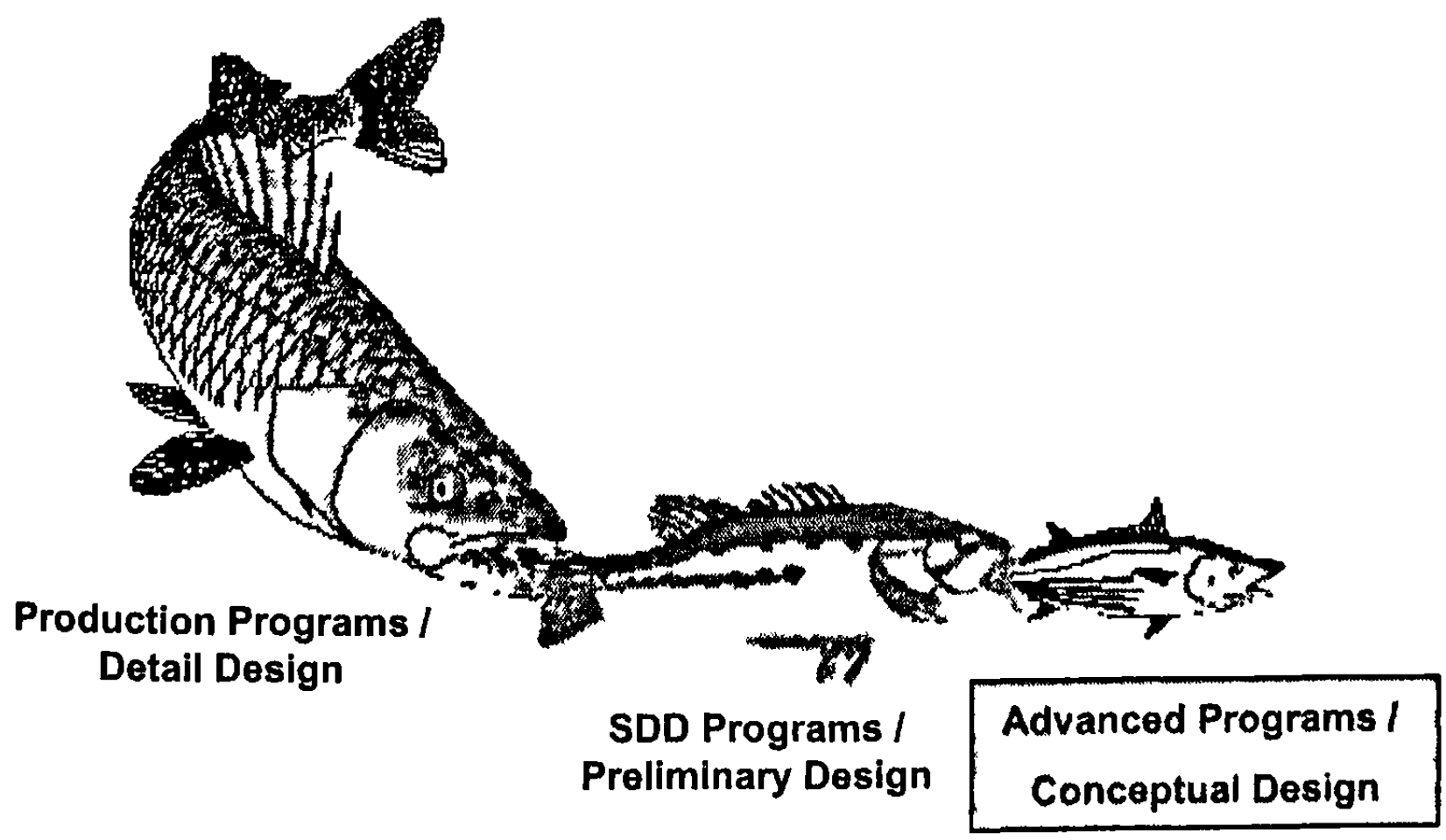

Fig. 9.16 Balance the tradeoff of importance vs priority.

shifting priority for the SDD and production programs. When the large programs get into trouble, there is a tendency to "mortgage the future" or "eat the seed corn" by taking away the funding and personnel in advanced programs. The large current programs may also view advanced programs as a threat to their future long-term survival and a competitor for discretionary funding. In many organizations the senior engineering managers and program managers began their careers in advanced programs/conceptual design. There may be unspoken management support for conceptual design and advanced programs in spite of the relatively low priority and the lack of a short-term return on investment.

9.18 Iterate the Configuration Design

Figure 9.17 was repeated in each of the first six chapters of this text. It is shown here for one last time. The point is that the conceptual design sizing process is an evaluation of a broad range of alternatives that requires iteration, iteration, and iteration. A conceptual design is only as good as the number of iterations and the number of alternatives considered.

9.19 Configuration Sizing Conceptual Design Guidelines

Table 9.1 shows conceptual design configuration sizing guidelines that were presented in this text. The table has 10 design guidelines related to the area of aeromechanics and 10 guidelines related to the area of guidance and control.

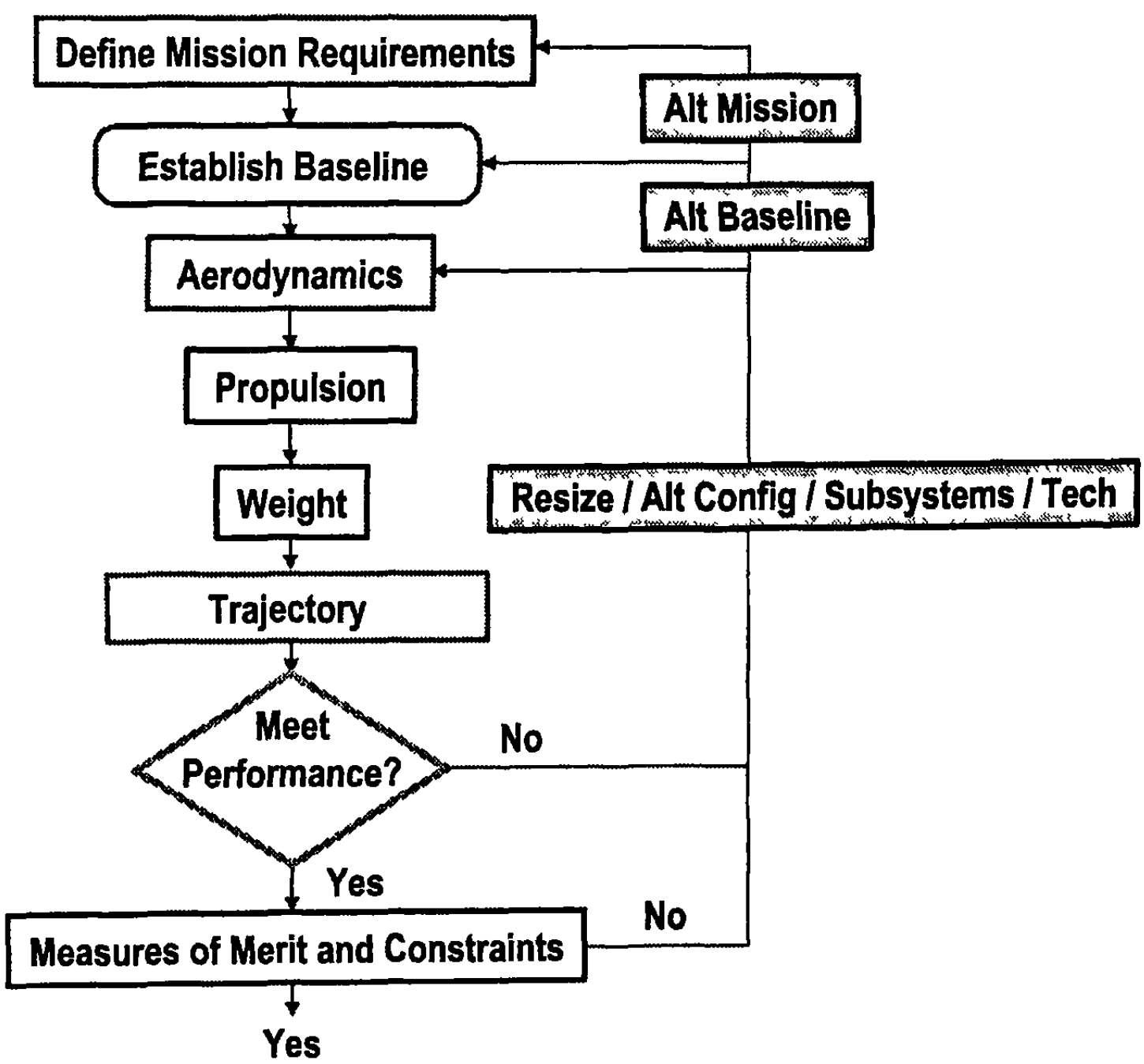

Fig. 9.17 Evaluate alternatives and iterate the configuration design.

Table 9.1 Configuration sizing conceptual design criteria

Configuration Sizing Parameter	Aeromechanics Design Guideline
(a) Aeromechanics	
◆ Body fineness ratio	$5 < l/d < 25$
◆ Nose fineness ratio	$l_N/d \approx 2$ if $M > 1$
◆ Boattail or flare angle	<10 deg
◆ Efficient cruise dynamic pressure	q < 1000 psf
◆ Missile homing velocity	$V_M/V_T > 1.5$
◆ Ramjet combustion temperature	>4000° F
◆ Oblique shocks prior to inlet normal shock to satisfy MIL-E-5008B	>2 oblique shocks/compressions if $M > 3.0$, >3 shocks/compressions if $M > 3.5$
◆ Inlet flow capture	Shock on cowl lip at M_{max} cruise
◆ Ramjet minimum cruise Mach number	$M > 1.2 \times M_{InletStart}$, $M > 1.2\ M_{MaxThrust=Drag}$
◆ Subsystems packaging	Maximize available volume for fuel/propellant
(b) Guidance and control	
◆ Body bending frequency	$\omega_{BB} > 2\omega_{ACT}$
◆ Trim control power	$\alpha/\delta > 1$
◆ Neutral stability tail-body	If low aspect ratio, $b/d \approx 2$, $c/d > \approx 1$
◆ Stability and control cross coupling	< 30%
◆ Airframe time constant	$\tau < 0.2$ s
◆ Missile maneuverability	$n_M/n_T > 3$
◆ Proportional guidance ratio	$3 < N' < 5$
◆ Target span resolution by seeker	$< b_{target}$
◆ Missile heading rate	$\gamma_M > \gamma_T$
◆ Missile turn radius	$R_{T_M} < R_{T_T}$

Configuration design guidelines related to aeromechanics include missile body fineness ratio, nose fineness ratio, boattail or flare angle, efficient cruise dynamic pressure, missile homing velocity, ramjet combustion temperature, oblique shocks prior to the inlet normal shock, inlet flow capture, ramjet minimum cruise Mach number, and subsystem packaging. A design guideline for the missile body fineness ratio (length-to-diameter ratio) is that it should be between 5 and 25 to harmonize tradeoffs of drag, subsystem packaging available volume, launch platform integration, seeker and warhead effectiveness, and body bending. The nose fineness (nose length-to-diameter ratio) for supersonic missiles should be approximately $l_N/d = 2$ to avoid high drag at high speed while maintaining acceptable seeker performance. Boattail or flare angle should be less than 10 deg to avoid flow separation. This is particularly important for

supersonic missiles to avoid increased drag at high speed. A design guideline for efficient cruise flight is that the dynamic pressure be less than 1000 psf. For a missile with a relatively large wing, the optimum dynamic pressure is somewhat lower. Missile velocity should be at least 50% greater than the target velocity to capture the target. Ramjet combustion temperature should be greater than 4000° F for high specific impulse and thrust at Mach numbers greater than 3.5. This requires high temperature insulation for the combustor. Efficient inlet integration for supersonic missiles to satisfy MIL-E-5008B requires more than two oblique shocks/compressions prior to the inlet normal shock for good inlet total pressure recovery at Mach numbers greater than 3.0. For Mach numbers greater than 3.5, more than three oblique shocks/compressions prior to the inlet normal shock are desirable for inlet total pressure recovery. Also, the forebody shock wave should impact the inlet cowl lip at the highest Mach number cruise condition to maximize the air flow capture and thrust. It also minimizes the spillage drag at lower Mach number. A concern for a ramjet is a sufficiently high cruise Mach number for the inlet to swallow the shock, avoiding inlet buzz, and having sufficient thrust to overcome drag. Design criteria are $M > 1.2 \times M_{\text{InletStart}}$ and $M > 1.2\ M_{\text{MaxThrust=Drag}}$. Finally, subsystems should be synergistically and efficiently packaged to maximize the available volume for fuel or propellant. Unlike aircraft, missiles are more volume limited than weight limited.

Configuration design guidelines related to guidance and control include the flight control actuator frequency, trim control power, tail span/chord for neutral stability, stability and control derivatives cross coupling, airframe time constant, missile maneuverability, proportional guidance ratio, target span resolution by the seeker, missile heading rate capability, and missile turn radius capability. Body bending frequency in the first mode should be greater than twice the flight control actuator frequency, if possible, to avoid the complication and risk of notch filters. Trim control power (trim-angle-of-attack-to-control-surface-deflection ratio) should be greater than 1 for maneuverability. For a neutrally stable body-tail missile (no canard), the total tail span (including body diameter) of a low aspect ratio tail should be approximately twice the body diameter and the tail chord length should be larger than the body diameter. Stability and control derivatives cross coupling should be less than 30% for efficient dynamics. The missile airframe time constant should be less than 0.2 s for precision accuracy (3 m). Contributors to a low value of the airframe time constant include high maneuverability capability, neutral static margin, high rate control surface actuators, low dome error slope, and a low noise seeker. Missile maneuverability should be at least three times the target maneuverability for small miss distance. The proportional guidance ratio should be between 3 and 5 to minimize miss distance. Values less than 3 will result in excessive time to correct heading error and target maneuver error, while values greater than 5 make the missile overly sensitive to glint noise input from the seeker and the dome error slope. The seeker should be capable of resolving the target geometry to a fraction of the target span to minimize the miss distance from glint. The missile heading rate capability should be greater than that of the target in order to achieve an intercept. Finally, the missile turn radius capability should be less than that of the target in order to achieve an intercept.

9.20 Wrap-Up

Missile design is a creative and iterative process that includes system-of-systems considerations, missile sizing, and flight trajectory evaluation. Because many of the cost and performance drivers may be "locked in" early during the design process, the emphasis of this text has been on conceptual design.

Missile design is an opportunity to harmonize diverse inputs early in the missile development process. The military customer, operations analysts, system integration engineers, conceptual design engineers, technical specialists, and others work together in harmonizing the mission/scenario definition, system-of-systems requirements, launch platform integration, missile concept synthesis, and technology assessment/roadmaps.

Missile conceptual design is a highly integrated process requiring synergistic compromise and tradeoffs of many parameters. The synthesis of an effective compromise requires balanced emphasis in subsystems, unbiased tradeoffs, efficient packaging of subsystems, and the evaluation of many alternatives. It is important to keep track of assumptions to maintain traceable results. It is necessary to be aware not only of the current SOTA but also to conduct a technology impact forecast for the projected SOTA in the timeframe of interest. Starting with a well-defined baseline that has similar propulsion and performance expedites design convergence and provides a more accurate design.

Conceptual design is an open-ended problem and has no single right answer. The available starting point information is never sufficient to provide only one solution. The design engineer makes assumptions in coming up with candidate concepts, subsystems, and technologies to satisfy mission requirements and cover the solution space. Weighting of the most important measures of merit is required in coming up with a cost-effective solution. The military customer buy-in is important in achieving a consensus weighting of the most important measures of merit. Trade studies are conducted to investigate the impact of design parameters. Sensitivity analyses are also conducted to evaluate the effects of uncertainty in the design and the benefit of new technology. The missile is designed for robustness to handle risk and uncertainty of both a deterministic and a stochastic nature.

Finally, a good conceptual design code is a physics-based code that connects the missile geometric, physical, and subsystem performance parameters directly into a flight trajectory evaluation. Good conceptual design codes do not automatically change the design or resize automatically. It is best that the missile designer make the creative decisions.

Appendix A
Homework Problems/Classroom Exercises

These homework problems/classroom exercises are designed to complement the problems at the end of each chapter. The problems at the end of the chapters can be posed as verbal questions to the students. They provide an indication that the students were listening to the lecture. The following homework problems/classroom exercises are designed provide a more in-depth learning reinforcement. Points associated with each homework problem/classroom exercise indicate the degree of difficulty as a consideration in assigning the student's grade for the problem.

1 (20 points). Chapter 1 (Introduction/Key Drivers in the Design Process)
Compare measures of merit for the following alternative concepts to destroy threat ballistic missiles during their boost phase:

- Space-based interceptors
- Space-based lasers
- Airborne laser
- Air-launched interceptors
- Ship-launched interceptors
- Ground-launched interceptors

2 (10 points). Chapter 1 (Introduction/Key Drivers in the Design Process).
Develop a state-of-the-art (SOTA) comparison of tactical missile characteristics with the current SOTA of unmanned combat air vehicles (UCAVs). Show examples where missiles are driving technology. Also show examples where missiles are not driving technology.

3 (10 points). Chapter 1 (Introduction/Key Drivers in the Design Process).
For the examples shown of air-launched and surface-launched missiles, which have been applied to more than one mission?

4 (20 points). Chapter 2 (Aerodynamic Considerations in Tactical Missile Design).
Based on the example, calculate radar seeker detection range and 3-dB beamwidth for a target cross section $\sigma = 1\ \mathrm{m}^2$, millimeter wave (mmW) transmitter frequency $f = 35 \times 10^9$ Hz, transmitted power $P_t = 100$ W, and antenna diameter $d = 4$ in.

5 (20 points). Chapter 2 (Aerodynamic Considerations in Tactical Missile Design).

Based on the example, calculate imaging infrared (IR) seeker detection range and instantaneous field of view for rainfall at 4 mm/hr and optics diameter $d_o = 2$ in.

6 (10 points). Chapter 2 (Aerodynamic Considerations in Tactical Missile Design).

Based on the example, calculate the first-mode body bending frequency for a missile weight of 367 lb.

7 (10 points). Chapter 2 (Aerodynamic Considerations in Tactical Missile Design).

In the example, what is the required diameter of the flare to provide neutral stability at launch?

8 (20 points). Chapter 2 (Aerodynamic Considerations in Tactical Missile Design).

What are the strengths and weaknesses of the China SD-10/PL-12 tail planform?

9 (10 points). Chapter 2 (Aerodynamic Considerations in Tactical Missile Design).

Calculate the rocket baseline wing normal force coefficient $(C_N)_{Wing}$ at Mach 1.1, $\delta = 13$ deg, $\alpha = 9$ deg.

10 (40 points). Chapter 2 (Aerodynamic Considerations in Tactical Missile Design).

Calculate C_{D_0}, C_N, and C_m for the ramjet baseline at Mach 2.5 end-of-cruise and Mach 4.0 end-of-cruise. Compare with the aerodynamic data of Chapter 7. Why is it difficult to accurately predict (or even obtain accurate data) for C_m?

11 (20 points). Chapter 2 (Aerodynamic Considerations in Tactical Missile Design).

What are the dynamic pressures at cruise $(L/D)_{max}$ for a circular cross section and an $a/b = 2$ lifting body cross section missile if the weight $W = 500$ lb, cross-sectional reference area $S_{Ref} = 0.5$ ft^2, length-to-diameter ratio $l/d = 10$, and zero-lift drag coefficient $C_{D_0} = 0.2$?

12 (20 points). Chapter 2 (Aerodynamic Considerations in Tactical Missile Design).

Calculate hinge moment for the ramjet baseline at the initiation of a pitch-over dive. Flight conditions are Mach 4.0, $h = 80{,}000$ ft altitude, end-of-cruise, $\delta_e = -30$ deg control deflection, and $\alpha = \alpha_{max}$ angle of attack.

13 (30 points). Chapter 3 (Propulsion Considerations in Tactical Missile Design).

Calculate the total pressure ratios entering the combustor for the ramjet baseline cruising at Mach 2.5, sea level and at Mach 4.0, 80,000 ft. The inlet is a mixed compression type with a total of four compressions prior to the normal shock, consisting of 1) the shock wave on the conical nose; followed by 2) the shock wave on the ramp leading to the cowl; followed by 3) the shock wave

on the cowl; and finally 4) a series of nearly isentropic internal contraction shock waves leading to a normal shock. Compare with the maximum available total pressure ratio from four optimum compressions.

14 (20 points). Chapter 3 (Propulsion Considerations in Tactical Missile Design).

For the turbojet example ($T_4 = 3000$ R, $A_0 = 114$ in^2, RJ-5 fuel, $M = 2$, $h = 60{,}000$ ft) show the impact on maximum ideal thrust and specific impulse of $+/-10\%$ uncertainty in specific heat ratio.

15 (30 points). Chapter 3 (Propulsion Considerations in Tactical Missile Design).

For an ideal turbojet, calculate thrust, specific impulse, equivalence ratio, and nozzle exit area for the following conditions/assumptions: liquid hydrocarbon fuel, freestream Mach number = 2, angle of attack = 0 deg, altitude = 60,000 ft, compressor pressure ratio for maximum thrust, turbine maximum temperature = 2000 R, and inlet capture area = 114 in^2. Compare with the text example.

16 (30 points). Chapter 3 (Propulsion Considerations in Tactical Missile Design).

Calculate the thrust, specific impulse, equivalence ratio, and nozzle exit area of an ideal ramjet for the following conditions/assumptions: liquid hydrocarbon fuel, freestream Mach number = 2.5, angle of attack = 0 deg, altitude = 60,000 ft, ramjet combustor maximum temperature 4000 R, and inlet capture area = 114 in^2. Compare with the ramjet baseline data of Chapter 7.

17 (40 points). Chapter 3 (Propulsion Considerations in Tactical Missile Design).

The corrected specific impulse of a ramjet is a function of the individual efficiencies of the combustor, nozzle, and inlet. Assuming that the driving parameter for the efficiencies is the total pressure recovery, derive an expression for correcting theoretical specific impulse.

18 (100+ points). Chapter 3 (Propulsion Considerations in Tactical Missile Design).

Derive the one-dimensional equations for thrust and specific impulse for an ideal scramjet. Calculate thrust, specific impulse, combustor area, and nozzle exit area for the following conditions/assumptions: hydrocarbon fuel, freestream Mach number = 6.5, angle of attack = 0 deg, altitude = 100,000 ft, Mach 3 initial combustion, thermal choking limit, combustor maximum temperature = 4000 R, and inlet capture area = 114 in^2. How is a scramjet similar to a ramjet? How is it different?

19 (10 points). Chapter 3 (Propulsion Considerations in Tactical Missile Design).

In the example, what is the inlet start Mach number if the inlet throat area $A_{IT} = 0.4$ ft^2? Is there a problem in having a large area for the inlet throat?

20 (100+ points). Chapter 3 (Propulsion Considerations in Tactical Missile Design).

Derive the one-dimensional equations for thrust and specific impulse for an ideal ducted rocket. Calculate thrust, specific impulse, equivalence ratio,

inlet throat area, and diffuser exit area for the following conditions/assumptions: 40% boron fuel, 8% aluminum fuel, 27% binder fuel, 25% ammonium perchlorate oxidizer, freestream Mach number = 4, angle of attack = 0 deg, altitude = 80,000 ft, gas generator pressure = 1000 psi, combustor maximum temperature = 4000 R, combustor area = 287 in^2, and inlet capture area = 114 in^2.

21 (20 points). Chapter 3 (Propulsion Considerations in Tactical Missile Design).

Calculate the rocket baseline thrust at altitudes of sea level, 20,000 ft, and 50,000 ft. Compare results with Chapter 7.

22 (20 points). Chapter 3 (Propulsion Considerations in Tactical Missile Design).

If the rocket baseline throat area were reduced by 50%, with the propellant, burn area, and nozzle expansion ratio the same, what would be the resulting boost/sustain chamber pressure, thrust, specific impulse, and propellant weight flow rate?

23 (30 points). Chapter 3 (Propulsion Considerations in Tactical Missile Design).

Assume a propellant burn rate exponent $n = 0.9$. Assuming the same nominal propellant burn rate $r_{p_c} = 1000$ psi, propellant characteristic velocity c^*, propellant density ρ, nozzle geometry, and thrust profile as the rocket baseline, calculate the chamber pressures and burn areas for boost/sustain. Compare with the rocket baseline chamber pressures and burn areas.

24 (20 points). Chapter 4 (Weight Considerations in Tactical Missile Design).

The baseline rocket propellant grain is a slotted tube with a propellant volumetric efficiency of 90%. For the same volume of the motor case, what is the boost propellant weight and end-of-boost velocity for a grain with a propellant volumetric efficiency of 80%?

25 (20 points). Chapter 4 (Weight Considerations in Tactical Missile Design).

A typical strategic ballistic missile motor has a much larger propellant fraction than a typical tactical ballistic missile, resulting in longer range. Assume a strategic ballistic missile has a typical inert weight fraction of 0.1 of the propellant weight. Also assume a payload weight of 1000 lb. Calculate the maximum range of a three-stage 100,000-lb missile with specific impulse of $I_{SP} = 250$ s (Minuteman-type solid propellant). As a comparison, calculate the maximum range of a two-stage 100,000-lb missile with specific impulse of $I_{SP} = 300$ s (Titan-type liquid propellant). Discuss the tradeoff of the number of stages versus type of propellant/specific impulse.

26 (20 points). Chapter 4 (Weight Considerations in Tactical Missile Design).

Calculate the center of gravity and pitch/yaw moment of inertia of the rocket baseline if the propellant density were increased by 50%, assuming the same

weights for subsystems (e.g., motor case) in Chapter 7. Compare with the data in Chapter 7.

27 (30 points). Chapter 4 (Weight Considerations in Tactical Missile Design).

Based on an average heat transfer coefficient, estimate the rocket baseline airframe temperature at the end-of-flight trajectory of Chapter 7.1 (Mach 0.8 launch at 20,000 ft altitude, 3.26 s boost, 10.86 s sustain, 9.85 s coast).

28 (30 points). Chapter 4 (Weight Considerations in Tactical Missile Design).

Estimate the ramjet baseline internal insulation required thickness to maintain warhead temperature less than 160° F for 10 m time of flight at Mach 4/80,000 ft.

29 (40 points). Chapter 4 (Weight Considerations in Tactical Missile Design).

For the ramjet baseline, compare the weight of an aluminum airframe with external microquartz insulation to that of the baseline uninsulated titanium airframe.

30 (30 points). Chapter 4 (Weight Considerations in Tactical Missile Design).

Using the baseline ramjet inlet geometry and material data of Chapter 7, estimate the required inlet thickness and the required inlet weight based on an inlet start at Mach 2.5, sea level altitude. Compare with the inlet weight of Chapter 7.

31 (20 points). Chapter 4 (Weight Considerations in Tactical Missile Design).

Calculate motor case weight for the rocket baseline if the case were titanium, with a forward dome ellipse ratio of 3 and a cylindrical cross section aftbody. Compare with the example calculation for a steel motor case and the data in Chapter 7.

32 (20 points). Chapter 4 (Weight Considerations in Tactical Missile Design).

Calculate required tail thickness and the resulting weight of the rocket baseline. Assume a flight condition of Mach 2, altitude = 20,000 ft, motor burnout, angle of attack = 9.4 deg, and an ultimate stress factor of safety = 1.5. Compare result with the data of Chapter 7.

33 (20 points). Chapter 4 (Weight Considerations in Tactical Missile Design).

Calculate radome weight for the rocket baseline if the radome were silicon nitride with an optimum transmission thickness. Compare with the example calculation for a pyroceram radome and the data in Chapter 7.

34 (20 points). Chapter 4 (Weight Considerations in Tactical Missile Design).

Calculate the required thickness and the resulting weight of the rocket baseline radome to withstand the load from Mach 2, 20,000 ft altitude, and angle of

attack = 9.4 deg for an ultimate stress factor of safety = 1.5. Compare with the Chapter 4 example of optimum transmission thickness and the data of Chapter 7.

35 (10 points). Chapter 4 (Weight Considerations in Tactical Missile Design).

Calculate actuation system weight for the rocket baseline if the actuators were electromechanical. Compare with the example calculation and the data in Chapter 7.

36 (10 points). Chapter 5 (Flight Performance Considerations in Tactical Missile Design).

Calculate the Mach 2.5, sea level cruise range of the ramjet baseline, using data from Chapter 7. Compare with the range in Chapter 7.

37 (10 points). Chapter 5 (Flight Performance Considerations in Tactical Missile Design).

Calculate the steady state rate of climb and the climb flight path angle for the ramjet baseline at Mach 2.5, sea level, maximum thrust. Use data from Chapter 7.

38 (20 points). Chapter 5 (Flight Performance Considerations in Tactical Missile Design).

Calculate turn radius and turn rate of the ramjet baseline for horizontal and pitch-over turns at Mach 4, h = 80,000 ft altitude, end of cruise, angle of attack $\alpha = 15$ deg. Use data from Chapter 7.

39 (20 points). Chapter 5 (Flight Performance Considerations in Tactical Missile Design).

Calculate booster burnout Mach number and ramjet acceleration capability following booster burnout at sea level for the ramjet baseline. Compare with the performance data of Chapter 7.

40 (20 points). Chapter 5 (Flight Performance Considerations in Tactical Missile Design).

Calculate the velocity and range of the rocket baseline after 10 s of coast at a flight path angle of 30 deg for an initial velocity of 2151 ft/s and an initial altitude of 20,000 ft.

41 (10 points). Chapter 5 (Flight Performance Considerations in Tactical Missile Design).

Assuming a nonaccelerating target at Mach 0.8, h = 20,000 ft altitude, and 30 deg aspect, what is the required missile lead angle for a Mach 3 fly-out at h = 20,000 ft?

42 (10 points). Chapter 6 (Measures of Merit and Launch Platform Integration).

For fog cover of 20 m height over the target, what is the required look-down angle to achieve less than 5 dB attenuation of a passive IR seeker?

43 (20 points). Chapter 6 (Measures of Merit and Launch Platform Integration).

Assume an initial target location error (TLE) = 10 m, targeting latency time $t_{\text{Latency}} = 20$ s, and target maximum lateral velocity $V_T = 10$ m/s. For a

strapdown semiactive laser seeker, what are the required field of view and the detection range?

44 (20 points). Chapter 6 (Measures of Merit and Launch Platform Integration).

Compare the performance of an medium-wave infrared (MWIR) seeker versus long-wave infrared (LWIR) seeker using the data of the example, but with a target temperature of 500 K.

45 (10 points). Chapter 6 (Measures of Merit and Launch Platform Integration).

For the example, what is the blast overpressure Δp at a distance from the center of explosion of r = 5 ft and an altitude h = sea level?

46 (20 points). Chapter 6 (Measures of Merit and Launch Platform Integration).

Calculate the required miss distance requirement of a 5-lb warhead with $C/M = 1$ to achieve a lethality of 0.5 for a typical air target vulnerability (overpressure $\Delta p = 330$ psi, fragments impact energy = 130,000 ft-lb/ft^2).

47 (10 points). Chapter 6 (Measures of Merit and Launch Platform Integration).

Compare the text example of penetration through concrete with the penetration of the same penetrator through granite of density $\rho = 0.0897$ lb/in^3 and ultimate strength $\sigma = 20{,}000$ psi.

48 (30 points). Chapter 6 (Measures of Merit and Launch Platform Integration).

Assume a missile defense interceptor has a time constant of $\tau = 0.05$ s, a navigation ratio of $N' = 4$, and the target glint noise bandwidth is $B = 2$ Hz. What is the miss distance from glint for the imaging IR seeker example in Chapter 2?

49 (10 points). Chapter 6 (Measures of Merit and Launch Platform Integration).

In the text example for survivability through high-altitude flight and low radar cross section (RCS), if the flight altitude h = 80,000 ft, what is the required RCS to avoid detection by a threat radar that has a transmitted power $P_t = 10^6$ W and a wavelength $\lambda = 0.01$ m?

50 (10 points). Chapter 6 (Measures of Merit and Launch Platform Integration).

Assuming a reliability of 98%, what is the missile circular error probable (CEP) that is required to provide a 95% probability of kill for a warhead lethal radius of 5 ft?

51 (10 points). Chapter 6 (Measures of Merit and Launch Platform Integration).

Calculate a typical system reliability of a missile that combines the autopilot, navigation sensors, and computer as a single subsystem and has no seeker. Compare with the text example.

52 (10 points). Chapter 6 (Measures of Merit and Launch Platform Integration).

For a seven-year development program of a 300-lb missile with a learning curve of 0.7, calculate the following for a total buy of 10,000 missiles:

- development cost
- total production cost
- average unit production cost
- unit production cost of missile number 10,000

53 (30 points). Chapter 7 (Sizing Examples).

Compare the rocket motor baseline motor case (see Chapter 7) with a higher strength motor case made of 4130 heat-treated steel with an ultimate tensile strength of 250,000 psi. Discuss design considerations such as brittleness, fracture sensitivity, material cost, motor case manufacturing cost (e.g., machining, welding), required case thickness, and required case weight. Is a higher strength 4130 motor case a good idea?

54 (10 points). Chapter 7 (Sizing Examples).

What are the visual detection and recognition ranges of a small UCAV target that has a presented area $A_P = 10\ \text{ft}^2$ and a contrast $C_T = 0.1$?

55 (60 points). Chapter 7 (Sizing Examples).

Using the rocket baseline air-to-air standoff range example, compare the results based on the one degree of freedom (one-DOF) analytical equations of motion of Chapter 5 with results from a numerical solution of the time marching equations of motion.

56 (30 points). Chapter 7 (Sizing Examples).

For the rocket baseline, what is the required wing area for 40 g maneuverability at Mach 3, burnout, and 20,000 ft altitude?

57 (40 points). Chapter 7 (Sizing Examples).

Conduct a design of experiment (DOE) to define the wind tunnel model configuration alternatives for the harmonized rocket baseline. Specify the nose, body, wing, and tail geometry options for a lightweight/small miss distance missile.

58 (40 points). Chapter 7 (Sizing Examples).

For the ramjet baseline, compare the inlet mass flow rate at Mach 2.5, sea level altitude with the mass flow rate at Mach 4.0, 80,000 ft altitude.

59 (10 points). Chapter 7 (Sizing Examples).

Based on the ramjet baseline data in Chapter 7 and the Breguet range equation, calculate the cruise range for Mach 4/80,000 ft altitude. Assume that all of the fuel is available for cruise.

60 (70 points). Chapter 7 (Sizing Examples).

Size an extended range ramjet that has 30% greater range than the ramjet baseline. Assume launch at Mach 0.8/sea level with cruise at Mach 2.3/sea level.

Size the design by extending the missile length while maintaining constant missile diameter and static margin. Compare the new body length, tail area, launch weight, and the individual weights of fuel, fuel tank, boost propellant, booster case, and tails with the ramjet baseline.

61 (40 points). Chapter 7 (Sizing Examples).

From the Request for Proposal given in Appendix B, develop a house of quality customer requirements/most important requirements (MIRs) and an importance rating of the MIRs. Expand the rows and columns of the house of quality. Give rationale for your selections and values.

62 (20 points). Chapter 7 (Sizing Examples).

For the soda straw rocket baseline, specify a tail geometry and area that provides neutral static stability.

63 (80 points). Chapter 7 (Sizing Examples).

Design, build, and fly a soda straw rocket that is optimized for maximum range at an assumed launch condition of 30 psi launch pressure. The rocket design must be compatible with a launch platform constraint of a "Super Jumbo" straw launcher of 0.25 in diameter and 6 in available launch length. You may base your rocket on the materials provided in class, or you may use your own materials as long as you satisfy the launch straw constraint (0.25 in diameter, 6 in available length). Provide the following information for your design:

- Geometric, weight, center-of-gravity, aerodynamic, and thrust-time characteristics and the rationale for their values
- Dimensioned drawing
- Velocity during boost as a function of time and distance
- Postboost flight trajectory height and horizontal range as a function of time
- Effect of $+/-10\%$ (1σ) prediction uncertainty of the drag coefficient on horizontal range
- Effect of $+/-10$ ft/s (1σ) horizontal head/tailwind velocity on horizontal range
- Comparison of predicted range with flight test

64 (60 points). Chapter 8 (Development Process).

Develop a technology roadmap for the Request for Proposal given in Appendix B.

65 (30 points). Chapter 8 (Development Process).

For the ASALM PTV flight envelope, what are the values of the booster transition thrust–drag, high dynamic pressure, high aero heating, high L/D cruise, and low dynamic pressure.

66 (20 points). Chapter 8 (Development Process).

For the ramjet baseline, compute the Mach number when thrust equals drag at an altitude h = 40,000 ft if equivalence ratio $\phi = 1$. Compare with the ASALM PTV flight test result.

67 (60 points). Chapter 9 (Summary and Lessons Learned).

Select one of the design case study presentations from the CD included with the textbook and conduct a review of the design case study. Provide a scoring/evaluation of the presentation, including rationale. The review should address the areas of technical content (35% weighting), organization and presentation (20% weighting), originality (20% weighting), and practical application and feasibility (25% weighting).

Appendix B
Example of Request for Proposal

American Institute of Aeronautics and Astronautics

2003/2004 Graduate Student

Team Missile Design Competition

Multimission Cruise Missile (MMCM)
Design and Analysis Study

Sponsored by the
Missile Systems Technical Committee
(MSTC)

Revised October 15, 2003

Table of Contents

INTRODUCTION

STATEMENT OF WORK (SOW)

SCORING/EVALUATION

AWARD

ADDITIONAL INFORMATION AND CLARIFICATIONS

Introduction

The Missile Systems Technical Committee (MSTC) of the American Institute of Aeronautics and Astronautics (AIAA) sponsors the graduate team missile design competition in order to further the understanding of the sciences associated with the design and development of missile systems. The competition is designed to allow a team of graduate level college engineering students to gain hands-on design and development experience in a real life competitive environment.

Statement of Work

Multimission Cruise Missile (MMCM) Design and Analysis Study

1.0 Statement of Need

This study addresses the opportunity of an advanced cruise missile to counter time critical targets (TCTs) as well as long-range surface targets of the year 2015 timeframe. Threat TCTs include 1) mobile theater ballistic missile (TBM) launchers; 2) surface-to-air (SAM) missile systems; 3) major command, control, and communication (C3) sites; 4) storage and support sites for weapons of mass destruction; and 5) other strategic targets such as bridges and transportation choke points. Mobile threat TBMs and SAMs are of particular interest because the stationary dwell time may be less than 10 minutes.

The Tomahawk subsonic cruise missile is a current baseline approach used by the U.S. Navy to counter long-range surface threats. However, because the location of TCTs is often uncertain or their appearance is sudden, the response capability of a subsonic cruise missile is often insufficient. An MMCM system with the combined capabilities of 1) fast response against TCTs; 2) subsonic cruise and extended range against other targets; and 3) loitering while waiting for retargeting would have operational and logistical advantages.

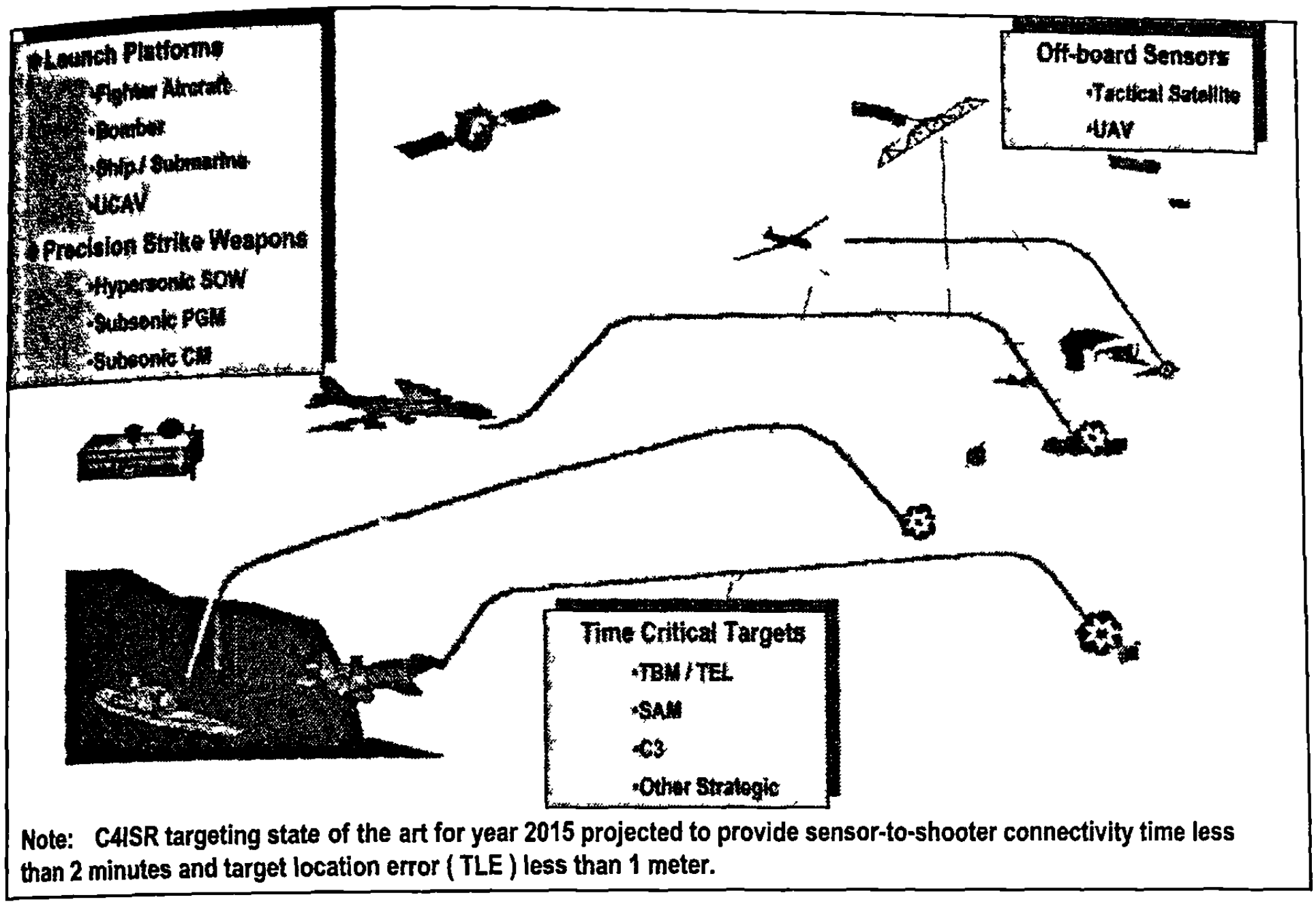

Fig. B.1 Example of C4ISR Architecture for Hypersonic Standoff Missile Systems.

An enabling synergistic capability for MMCM is the anticipated advancement of the command, control, communication, computers, intelligence, surveillance, reconnaissance (C4ISR) network projected for the year 2015 timeframe. It is anticipated that near-real-time, accurate targeting will be available from overhead tactical satellite and overhead unmanned air vehicle (UAV) sensors. Figure B.1 illustrates an example of a ground station, overhead satellite sensors and satellite relays, and overhead UAV sensor platform elements of the C4ISR architecture. The assumed C4ISR of the year 2015 is projected to have a capability for a target location error (TLE) of less than 1 meter (1 sigma) and an off-board sensor-to-shooter connectivity time of less than 2 minutes (1 sigma).

A second example of an enabling capability for MMCM is low-cost precision guidance available from global positioning system/inertial navigation system (GPS/INS). The assumed GPS/INS of the year 2015 is projected to have a guidance navigation error of less than 3 meters circular error probable (CEP).

A third example of an enabling capability is the application of high-bandwidth data link technology to a cruise missile, allowing target position updates, retargeting, and precision command guidance.

A fourth example of an enabling capability for MMCM is the recent cost reductions in standoff missiles, due in part to manufacturing processes such as castings that reduce parts count, the "spin on" application of commercial technologies (in areas such as electronics and materials), and the application of procurement reform. Examples include JDAM, JASSM, and Tactical Tomahawk.

Low cost, combined with high performance and operational flexibility, has the potential to allow MMCM to be used not only in TCT missions but also in other more traditional standoff missions. It could provide a neck-down benefit of a more simplified missile logistics system with fewer types of missiles.

Finally, a fifth example of an enabling capability for a multimission missile is the projected advances in turbine-based propulsion. It is anticipated that future turbine-based propulsion systems such as turbojet, turbo ramjet, and air turbo-rocket will be capable of higher compressor pressure ratio and higher turbine temperature and will be capable of operating at higher Mach number. By the year 2015 it is anticipated a turbine-based propulsion system could be operational that could provide the required specific impulse and thrust necessary to operate across a Mach number range from subsonic to about Mach 3 to 5.

2.0 Objective

The objective of this study is to evaluate alternative concepts and technologies for a subsonic to hypersonic standoff missile system that would be used against TCTs and other surface targets. The baseline requirements in sizing the missile concept and the selection of subsystems/technologies are given below.

- Maximum Mach number of 3 (threshold), 4 (standard), and 5 (goal). An objective is a counterforce response capability against short dwell targets such as TBMs within the projected state of the art (SOTA) of cost-effective technologies for the year 2010.
- Maximum subsonic cruise range against non-time-critical surface targets greater than 300 n miles (threshold), 600 n miles (standard), and 1000 n miles (goal).
- Response time against TCTs less than 30 minutes (threshold), 15 minutes (standard), and 5 minutes (goal). This includes the command and control (C&C) decision time.
- Subsonic loiter time greater than 45 minutes (threshold), 60 minutes (standard), and 90 minutes (goal).
- Maximum postloiter dash range after retargeting greater than 20 n miles (threshold), 50 n miles (standard), and 100 n miles (goal).
- Weight less than 3400 lb. The basis is vertical launch system (VLS) carriage on cruisers and destroyers.
- Length less than 256 in for compatibility with VLS.
- Cross section less than 22 in by 22 in for compatibility with VLS.
- Electrical compatibility with VLS.
- Launch exhaust gas compatibility with VLS.
- Multipurpose (blast/frag/penetrator) warhead payload with a weight of 250 lb.
- Average unit production cost less than $1,000,000, based on 4000 units produced over a 10-year timeframe.
- Wooden round with no shipboard maintenance and 15 year depot life.
- Satellite and UAV data link communication payload for retargeting and guidance.
- Guidance navigation error less than 3 meters CEP.

3.0 Tasks

A trade study will be conducted to evaluate alternative turbine-based missile concepts, their associated subsystems, and their associated technologies. The study will be based on projecting the current SOTA to a technology readiness level (TRL) of 7 for Fiscal Year (FY) 2010. TRL 7 represents the program definition and risk reduction (PDRR) phase of a full-scale prototype in a full-scale flight environment. PDRR is comparable to demonstration/validation (demval). Following PDRR, a baseline assumption is that system development and demonstration (SDD) will begin in FY 2010. The desired initial operational capability (IOC) is FY 2015.

Tasks to be performed under this conceptual design study are as follows:

- Alternative baseline concepts and subsystems definition
- Alternative baseline concepts and subsystems evaluation
- Recommended concept refinement
- Mission verification
- Technology roadmap
- Documentation

Task 1. Alternative Baseline Concepts and Subsystems Definition

At least three alternative turbine-based concepts and their appropriate subsystems will be defined based on the requirements of Section 2.0. The characteristics of the alternative baseline concepts will be determined using the Tactical Missile Design (TMD) methods of Georgia Tech or similar conceptual design tools. A "house of quality" based on an integrated product and process development (IPPD) will be developed with customer involvement for the relative weighting of the requirements. The turbine-based concepts will include at least the following:

- Turbojet
- Turbo ramjet
- Air turborocket

Task 2. Alternative Baseline Concepts and Subsystems Evaluation

The alternative baseline concepts and their subsystems will be evaluated against the requirements of Section 2.0, using the Georgia Tech TMD methods or similar conceptual design and analysis tools. Physics-based models will developed that show the transparent prediction of specific impulse and thrust. The robustness of the design subsystems/technologies uncertainties and risks will be evaluated. Based on the capability against the requirements and the design robustness, a recommended MMCM and its subsystems will be selected.

Task 3. Recommended Concept Refinement

The MMCM recommended concept and subsystems will be refined based on considerations of alternative technologies. More sophisticated preliminary design

and analysis tools will be used and results compared with the previous results from the conceptual design methods. Probabilistic/robust design, cost estimation, and optimization will be conducted. Design refinement will include:

- Turbine materials
- Compressor pressure ratio
- Inlet
- Fuels
- Insulation materials
- Airframe materials
- Aerodynamic configuration
- Forebody angles in front of the inlet
- Tail sizing
- Power supply
- Guidance, navigation, and control
- Data link
- Other subsystems and components
- Radar cross section and infrared signature

Task 4. Mission Verification

The MMCM concept will be evaluated in a three degree-of-freedom (three-DOF) digital computer simulation. The flight trajectory and thrust profile will be optimized for maximum range, maximum loiter, and minimum time-to-target scenarios.

Task 5. Technology Roadmap

A technology roadmap will be developed for MMCM. The technology roadmap will address key enabling technologies that are driven by the requirements but will require additional development and demonstration to provide a required TRL of 7 to support a required SDD decision. The technology roadmap will include the major milestones, alternative approaches, risk mitigation plan, exit criteria for each TRL phase, and exit plan for failures. The technology development and demonstration activities will consider the following TRLs, leading to a TRL of 7 and an assumed SDD start in FY 2010:

- TRL 4 laboratory test demonstration of a component in a representative, but not full scale, environment (6.2A exploratory development category funding).
- TRL 5 laboratory development or demonstration of a subsystem. The subsystem usually has full-scale components and is tested in a representative, but not full-scale, environment. The category of funding is 6.2B exploratory development category.
- TRL 6 laboratory or flight advanced technology demonstration (ATD) of a full-scale subsystem in a full-scale environment, with integration of some of the other subsystems and some of the other new technologies of a follow-on missile system. The category of funding is 6.3 advanced technology development.

- TRL 7 flight demonstration of either an advanced concept technology demonstration (ACTD) or a PDRR full-scale prototype in a full-scale environment. The category of funding is 6.4 demval. All of the new critical technologies and subsystems are demonstrated. A driving consideration is to assure the system engineering and management confidence in the technologies. TRL 7 is normally performed where the technology and/or subsystem application is critical and high risk. The assumed technology availability date (TAD) of year 2010 is based on successfully completing TRL 7.

Task 6. Documentation

The MMCM solution, rationale, and supporting technology will be documented. The documentation will be provided in a kickoff meeting, midterm review, final review, and final report.

- Kickoff Meeting. A presentation at the kickoff meeting will be given to the sponsor and customer representatives. It will be held in early December 2003. The kickoff meeting will address 1) "house of quality" weighting of the requirements; 2) clarification of requirements; 3) alternative concepts; and 4) the proposed plan for the study. A copy of the viewgraphs from the kickoff meeting will be provided.
- Midterm Review. A midterm review will be presented to the sponsor and customer at the completion of Task 2. It will be held in March 2004. Approval of the recommended concept will be required prior to the initiation of Task 3. A copy of the viewgraphs from the midterm review will be provided.
- Final Review. A final review will be presented to the sponsor and customer in late May 2004, after completing the study tasks. It will address the final results of the study. A copy of the viewgraphs from the final review will be provided.
- Final Report. Six copies of the final report will be delivered to the sponsor and customer for review and scoring no later than June 1, 2004. The size of the final report will be no more than 100 pages. It will include the following information shown in Table B.1:

Scoring/Evaluation

1. Technical Content (35 points)
   This addresses the correctness of theory, validity of reasoning used, apparent understanding and grasp of the subject, etc. Are all the major factors considered and a reasonably accurate evaluation of these factors presented?
2. Organization and Presentation (20 Points)
   The description of the design as an instrument of communication is a strong factor. Organization of written design, clarity, and inclusion of pertinent information are major factors.

Table B.1 Final Report Information

- **Table of contents**, with sections consistent with the tasks of this statement of work (i.e., Tasks 1, 2, 3, 4, 5).
- Literature review **bibliography**.
- Tabulation of MMCM design **requirements**.
- **House of quality** IPPD relative weighting of requirements.
- **Justification of MMCM concept**, including a comparison against the requirements, results of the design tradeoffs, robustness of the design and its technologies to uncertainties and risk, criteria used for selection, and advantages compared to alternative concepts.
- **Three-view drawing** of MMCM concept, with a layout showing the inboard profile of subsystems, including dimensions of the major subsystems. The center-of-gravity location at launch and burnout events will be shown on the drawing.
- Sketches of **alternative concepts**.
- Mission **flight profiles** of MMCM showing altitude, range, Mach number, weight, flight path angle, angle of attack, time, and major events such as booster ignition, surface deployments, booster burnout, booster separation, engine start, climb, cruise, descent, loiter, dash, dive, engine burnout, and impact.
- Operational **flight profiles** defining performance boundaries including altitude, speed, and maneuver *g* limits.
- **Aerodynamic, propulsion**, and **thermal characteristics** as a function of Mach number, angle of attack, angle of roll or sideslip, control surface deflection, and altitude.
- Airframe **structure** and **material** characteristics.
- **Sensitivity** of the system and subsystem parameters to requirements, with typical uncertainties.
- **Weight** and **balance** statement with subsystem weight, subsystem location (x,y,z), launch/burnout center-of-gravity locations, and launch/burnout moments-of-inertia.
- Discussion of **prediction methods** used to size the missile (e.g., aerodynamic configuration, propulsion system, guidance system, flight control system, structure, data link, power supply, other subsystems) and the methods used to predict the performance, cost, and constraint compliance. When practical, results will be verified as reasonable and consistent with other methods, available data, prior practice, and theory.
- Traceable **flow-down of system requirements** to subsystem and technology performance, cost, and constraints.
- Estimated **unit production cost** with units produced, production rate, learning curve, and basis for the learning curve.
- Estimated **SDD development cost** and schedule of SDD activities leading to production.
- Discussion of **VLS** integration.
- Discussion of the **year 2015 architecture** to support the areas of targeting, fire control, C4ISR, and GPS.
- **Technology roadmap** with a time-phased schedule of exploratory development and advanced development programs and milestones required to demonstrate key enabling technologies by the year 2010.
- Discussion of other **life cycle** considerations with any operational, environmental, social, and technological issues that may affect the fitness of the concept over the system life cycle.
- Discussion of **manufacturing**, with considerations of reduced parts count, ease of manufacturing, life-cycle cost, risk reduction, and compatibility with the logistics for the launch platforms.

3. Originality (20 points)
   The design proposal should avoid standard textbook information and should show the independence of thinking or a fresh approach to the project. Do the method and treatment of the problem show imagination? Does the method show an adaptation or creation of automated design tools?
4. Practical Application and Feasibility (25 points)
   The proposal should present conclusions or recommendations that are feasible and practical and not merely lead the evaluators into further difficult or insolvable problems. Is the project realistic from the standpoints of cost, hazardous materials, and commonality with future systems?

Award

Based on a review and scoring of the final report, a trip and an award plaque may be provided by the sponsor. The trip may consist of attending a missile launch, facility tour, or other aerospace related event. The sponsor may award up to $5000 toward travel expenses.

Additional Information and Clarifications

Questions regarding this competition can be referred to the AIAA MSTC Sponsor members presented below.

Jacqueline Murdock
MSTC Chair
Atlantic Research Corporation (ARC)
5945 Wellington Rd.
Gainesville, VA
Phone: (703) 754-5337
E-mail: murdock@arceng.com

Eugene L. Fleeman
Georgia Institute of Technology
School of Aerospace Engineering
P.O. Box 150
Atlanta, GA 30332-0150
Phone: (703) 697-2187
E-mail: Eugene.Fleeman@asdl.gatech.edu

Appendix C
Nomenclature

The figures and tables in this text are designed as a stand-alone set of information. In most cases it is possible to use a figure or table without referring to the text or referring to other figures and tables. When practical the symbols are defined in the figures and tables. As a complement, a list of symbols is provided in this section.

a	speed of sound
a_0	freestream speed of sound
A	target aspect angle or aspect ratio
A_0	freestream air flow area
A_1	inlet throat area
A_2	diffuser exit area
A_3	combustor flame holder entrance area
A_4	combustor exit area
A_5	nozzle throat area
A_6	nozzle exit area
A_b	propellant burn area
A^*	cross-sectional area of inlet or nozzle with Mach 1 flow
A_C	inlet capture area
A_d	detectors total area
A_{IT}	inlet throat area
A/J	antijam
Al	aluminum
a_M	acceleration of missile
AP	ammonium perchlorate
A_o	optics aperture area
A_{Ref}	reference area
A_t	throat area
A_{t_p}	presented area of threat or target
A_V	target vulnerable area
b	span
B	bandwidth, Boron, body, or billion
$(b_t)_{res}$	target span resolution by seeker
c	specific heat or thermal capacitance, type of loading, or warhead charge weight

C	canard, contrast, explosive charge weight, coefficient, chord length, carbon, control, or cost
C_1	cost of 1st unit
C_{1000th}	cost of 1000th missile
c^*	characteristic velocity
C_A	axial force coefficient
C/C_T	actual contrast-to-threshold contrast ratio
c_d	discharge coefficient
C_d	cadmium
C_D	drag coefficient
C_{D_0}	zero-lift drag coefficient
cg	center of gravity
cg_{BO}	center of gravity at burnout
cg_{Launch}	center of gravity at launch
Cl	chlorine
C_l	rolling moment coefficient
CL	centerline
C_L	lift coefficient
$CL\ Tk$	centerline tank carriage
C_{l_p}	rolling moment derivative from roll damping
C_{l_β}	rolling moment derivative from sideslip
$C_{l\delta a}$	rolling moment derivative from roll control deflection
$C_{l\delta r}$	rolling moment derivative from yaw control deflection
C_{l_ϕ}	rolling moment derivative from roll angle
C_m	pitching moment coefficient
c_{mac}	mean aerodynamic chord
C_{m_α}	pitching moment derivative from angle of attack
$C_{m_{\delta e}}$	pitching moment derivative from pitch control deflection
C_n	yawing moment coefficient
C_N	normal force coefficient
$C_{N\alpha}$	normal force derivative from angle of attack
$C_{N_{\delta e}}$	normal force derivative from pitch control deflection
C_{n_β}	yawing moment derivative from angle of sideslip
$C_{n_{\delta a}}$	yawing moment derivative from roll control deflection
$C_{n_{\delta r}}$	yawing moment derivative from yaw control deflection
C_{N_c}	normal force coefficient from control deflection
C_{Nc}	normal force coefficient on control surface
$C_{N_{Trim}}$	normal force coefficient at trim
c_p	specific heat at constant pressure
cp	center of pressure
c_R	root chord
C_{SDD}	cost of system development and demonstration
c_{skin}	specific heat ratio of skin (airframe) material
c_T	tip chord or threshold contrast
C_x	cost of unit x
d	diameter
D	drag force
D_0	zero-lift drag

dB	decibel
d_{BT}	diameter of boattail
d_{hemi}	diameter of hemisphere
d_o	optics diameter
d_p	pixel diameter
d_{Ref}	reference diameter
d_{spot}	spot diameter
dt	incremental time
D_t	target diameter
dz/dt	velocity in z-direction
d^2z/dt^2	acceleration in z-direction
D^*	specific detectivity
E	Young's modulus of elasticity or energy
E_c	energy per unit mass of charge
$erfc$	complementary error function
E_T	total energy
f	frequency
f/a	fuel-to-air ratio
F	force, flare, or noise factor
F_{CR}	critical force
f-number	aperture length/diameter
F-Pole	standoff range at missile intercept
F_T	tensile force
F_{TU}	ultimate tensile force
g	gravity
g_c	gravitational constant (32.2)
GHz	10^{12} Hz
G_r	gain of receiver antenna
G_t	gain of transmitter antenna
h	altitude, convection heat transfer coefficient, or inlet height
HCl	hydrogen chloride
H_f	heating value of fuel
h_i	initial altitude
h_f	final altitude
H_g	mercury
h_L	launch altitude
h_{mask}	mask altitude
$h_{obstacle}$	height of obstacle
I	moment of inertia
I_{sp}	specific impulse
I_t	total impulse
$(I_T)_{\Delta\lambda}$	target radiant intensity between λ_1 and λ_2
I_y	yaw moment of inertia
j	integer
J	Joule
k	thermal conductivity
K	Boltzman's constant, thousands, or thickness constant
kg	kilogram

km	kilometer
l	length
L	lift force, lead angle, learning curve, or loss factor
l_b	length of body
lb	pound
lbf	pound force (unit of force)
lbm	pound mass (unit of mass)
l_c	inside chamber length
$(l_{comb})_{min}$	minimum efficient combustor length
l/d	length/diameter
L/D	lift/drag
l_N	length of nose
l_N/d	nose fineness ratio
l_{Ref}	reference length
L_λ	spectral radiance (Plank's law)
m	meter
M	Mach number, moment, or warhead metal weight
$\dot{m}$	mass flow rate
M_0	freestream Mach number
$(M_3)_{TC}$	combustor entrance Mach number with thermal choking
$M_{\Lambda_{LE}}$	Mach number perpendicular to leading edge
M_∞	freestream Mach number
Max	maximum value
M_B	bending moment
M_C	mass of charge of warhead
M_g	magnesium
M_i	impact Mach number or initial Mach number
M_{IE}	inlet entrance Mach number
M_L	launch Mach number
M_m	mass of metal case of warhead
M_{wh}	mass of warhead
n	number of pulses integrated, integer, type of warhead geometry, or burn rate exponent
N	normal force, noise, navigation ratio, or Newton
N/A	not applicable
N'	effective navigation ratio
$n_{fragments}$	number of fragments
n_{hits}	number of hits
nm	nautical miles
n_M	missile maneuver acceleration g
N_{NU}	Nusselt number
n_T	target maneuver acceleration g
n_w	number of wings ($n_w = 1$ is planar, $n_w = 2$ is cruciform)
N_w	normal force on wing
n_x	acceleration g in longitudinal direction
n_z	acceleration g in vertical direction
O	oxygen
p	pressure

P	penetration, load, or power
p_0	freestream static pressure
p_2	compressor entrance pressure
p_3	compressor exit pressure
p_{5_t}	turbine exit total pressure
P_a	Pascal
$P_{B,C}$	parameter of baseline, corrected (based on actual data)
$P_{B,U}$	parameter of baseline, uncorrected
p_{blast}	blast pressure
p_c	chamber pressure
$P_{CD,C}$	parameter of conceptual design, corrected
$P_{CD,U}$	parameter of conceptual design, uncorrected
p_e	exit pressure
p_{gauge}	gauge pressure
P_K	probability of kill
P_{KE}	penetration of kinetic energy warhead
P_r	power received
psf	pounds per square foot
psi	pounds per square inch
p_t	total pressure
P_t	power transmitted
p_{t0}	total pressure of freestream
p_{t2}	total pressure after normal shock
q	dynamic pressure $= \frac{1}{2}\rho V^2$
Q	heat transfer rate per unit area
r	radius, recovery factor, or propellant burn rate
R	range, radius, dome error slope, or reliability
R_0	radar reference range
R_C	climb incremental range
R_D	detection range or descent incremental range
R_e	Reynolds number
R_F	flight range
$R_{F\text{-}Pole}$	standoff range at missile intercept
R_L	launch range
R_{LOS}	line-of-sight range
R_{max}	maximum range
$R_{obstacle}$	range to obstacle
R_R	recognition range
R_T	turn radius
R.T.	room temperature
RT&A	research, technology, and acquisition
R_{T_M}	radius of turn of missile
R_{T_T}	radius of turn of target
R_x	range in x-direction
R_y	range in y-direction
S	area or signal
S_{hemi}	cross-sectional area of hemisphere
S/N	signal-to-noise ratio

$(S/N)_D$	signal-to-noise ratio for detection
S_P	presented area
S_{Ref}	reference area
S_T	tail area
S_W	wing area
S_{wet}	wetted area
t	time or thickness
T	thrust, temperature, or tail
t_0	total time of flight
T_0	freestream temperature
t_0/τ	number of time constants for intercept
T_1	inlet entrance temperature
T_2	compressor entrance temperature
T_3	compressor exit temperature
T_4	combustor exit temperature or turbine entrance temperature
T_5	turbine exit static temperature
T_{5_t}	turbine exit total temperature
t/t_0	fraction of time to-go
t_B	rocket motor boost time
T_B	boost thrust
t_C	coast time
t/c	thickness-to-chord ratio
t_{comb}	time required for combustion
T_e	telluride
t_{exp}	exposure time
t_f	time of flight
THz	10^{15} Hz
t_i	initial time
Ti	titanium
t_{mac}	maximum thickness of mean aerodynamic chord
t_{react}	reaction time
t_S	rocket motor sustain time
T_S	stall torque of single actuator
t_{SDD}	time duration of system development and demonstration
T_T	target temperature
t_{wall}	thickness of wall material
T_Δ	temperature difference
V	velocity or vanadium
$\dot{V}$	time rate of change in velocity
V_{BC}	velocity at begin of coast
V_{BO}	velocity at burnout
V_C	velocity of climb or closing velocity
V_{comb}	combustion velocity
V_D	velocity of descent
V_e	exit velocity
V_{EB}	velocity at end of boost
V_{EC}	velocity at end of coast
V_f	fragment velocity

V_i	initial velocity
V_L	launch velocity
V_M	velocity of missile
V_T	velocity of target
V_x	velocity in x-direction
V_y	velocity in y-direction
V_∞	freestream velocity
w	load per unit length or wing
W	weight, wing, glint noise spectral density, or Watt
W_{BC}	weight at begin of cruise
W_{BO}	weight at burnout
W_c	weight of warhead charge
W_E	weight per unit energy
W_f	weight of fuel
$\dot{W}_f$	fuel flow rate
W_i	initial weight
W_L	launch weight
W_m	weight of warhead metal case (fragments)
W_P	propellant weight or weight per unit power
$\dot{w}_p$	propellant weight flow rate
W_T	weight per unit torque
W_s	structure weight
x_{AC}	aerodynamic center location
x_{cp}	center-of-pressure location
x_{CG}	center-of-gravity location
x_{HL}	hinge line location
y	lateral distance
Y_1	first year
y_{cp}	outboard center-of-pressure location
y_{offset}	lateral offset distance
z	warhead scaling parameter or vertical direction
z_{skin}	skin thickness
z_{max}	maximum value of z
α	angle of attack, thermal diffusivity, coefficient of thermal expansion
α'	local effective angle of attack
$\ddot{\alpha}$	angle of attack angular acceleration
α_{Trim}	trim angle of attack
α/δ	change in angle of attack with control deflection
$\alpha/\dot{\gamma}$	angle of attack sensitivity to turn rate
β	angle of sideslip
δ	control deflection, body angle, or seeker angle
$\dot{\delta}$	control surface defection rate
δ_{LE}	leading edge section angle
δ_{trim}	control deflection for trim
ε	nozzle expansion ratio (exit area/throat area), strain, dielectric constant, or emissivity coefficient

ϕ	equivalence ratio (actual fuel-to-air compared to stochiometric) or missile roll angle
ζ	damping coefficient
γ	specific heat ratio ($\approx$1.4 for ambient air, $\approx$1.2 for rocket motor) or flight path angle
γ_0	freestream specific heat ratio
γ_1	specific heat ratio at inlet entrance
γ_2	specific heat ratio at compressor entrance
γ_3	specific heat ratio at compressor exit or combustor entrance
γ_4	specific heat ratio at turbine entrance or combustor exit
γ_5	specific heat ratio at turbine exit
$\dot{\gamma}$	rate of change in flight path angle
γ_C	flight path climb angle
γ_D	flight path dive or descent angle
γ_i	initial flight path angle
γ_M	initial heading error of missile
η	efficiency ($n = 1$ is 100% efficient)
η_a	atmospheric transmission
λ	taper ratio (tip chord/root chord) or wavelength
μ	Mach angle
θ	missile pitch attitude, beam width, shock angle, radial angle, or surface angle
$\ddot{\theta}$	pitch attitude angular acceleration
θ_{BT}	boattail angle
θ_F	vision fovea angle of human eye that provides highest resolution
θ_i	incidence angle
ρ	density
ρ_∞	freestream density
ρ_M	missile average density
ρ_P	density of penetrator warhead
ρ_T	density of target
ρ_{wall}	density of wall material
σ	radar cross section, stress, standard deviation, or miss distance
σ_{Buckle}	buckling stress
σ_{glint}	miss distance from glint
σ_{HE}	miss distance from heading error
σ_{MAN}	miss distance from target maneuver acceleration
σ_{Max}	maximum stress
σ_t	tensile stress
σ_{TU}	target ultimate stress
σ_{TS}	thermal stress
σ_{yield}	yield stress
π_K	pressure sensitivity to temperature
τ	time constant
τ_δ	time constant from control effectiveness
$\tau_{\dot{\delta}}$	time constant from deflection rate limit
τ_{Dome}	time constant from radome error slope
$\omega_{Actuator}$	actuator bandwidth

ω_{BB}	first mode body bending frequency
Δ	incremental
Δf_p	pixel detector bandwidth
Λ	sweep angle
$\sum$	summation
!	factorial
$\lvert\ \rvert$	absolute value
$\approx$	approximately equal to
$\sim$	similar to
$<$	less than
$>$	greater than
$\perp$	perpendicular to
#	number
2a	major axis of ellipse
2b	minor axis of ellipse

Appendix D
Acronyms

1-DOF	one-degree-of-freedom
2-DOF	two-degrees-of-freedom
3-DOF	three-degrees-of-freedom
4-DOF	four-degrees-of-freedom
6-DOF	six-degrees-of-freedom
AAA	antiaircraft artillery
AAM	air-to-air missile
AARGM	Advanced Anti-Radiation Guided Missile
ACTD	advanced concept technology demonstration
ADAM	Advanced Design of Aerodynamic Missiles
AEDC	Arnold Engineering Development Center
AGM	air-to-ground missile
AIM	air intercept missile
AMRAAM	Advanced Medium Range Air-to-Air Missile
AoA	angle of attack or assessment of alternatives
ARH	antiradiation homing
ARM	antiradiation missile
ARRMD	Affordable Rapid Response Missile Demonstrator
ASALM	Advanced Strategic Air-Launched Missile
ATA	air-to-air or automatic target acquisition
ATD	advanced technology demonstration
ATM	atmosphere
ATR	automatic target recognition
ATS	air to surface
AVG	average
BAT	brilliant antitank
BDA	battle damage assessment
BDI	battle damage indication
BL	baseline or body line
BTT	bank-to-turn
Btu	British thermal unit
C^3	command, control, and communication
C^3I	command, control, communication, intelligence

C4ISR	command, control, communication, computers, intelligence, surveillance, reconnaissance
CBU	cluster bomb unit
CCM	counter-countermeasures
CEP	circular error probable
CFD	computational fluid dynamics
CLS	canister launch system
CM	cruise missile
COTS	commercial off-the-shelf
CPIA	Chemical Propulsion Information Agency
DATCOM	Data Compendium
DCR	Dual Combustor Ramjet-scramjet
DemVal	demonstration and validation
DoD	Department of Defense
DOE	design of experiment
DOF	degree of freedom
DOS	disk operating system
ECM	electronic countermeasures
EDPM	ethylene propylene diene monomer
EFP	explosively formed projectile
EM	electromechanical or electromagnetic
EMC	electromagnetic compatibility
EMD	engineering and manufacturing development
EMI	electromagnetic interference
EMP	electromagnetic pulse
EO	electro-optical
EOCM	electro-optical countermeasure
FEM	finite element model
FMRAAM	Future Medium-Range Air-to-Air Missile
FOS	factor of safety
FOV	field of view
fps	feet per second
G&C	guidance and control
GPS	global positioning system
HDBK	handbook
HE	high explosive or heading error
HL	hinge line
HM	hypersonic missile or hinge moment
HMX	Her Majesty's Explosive
HOQ	house of quality
HPM	high-power microwave
HTPB	hydroxyl-terminated polybutadiene binder
HWL	hardware in loop
IFOV	instantaneous field of view
IM	insensitive munition
IMU	inertial measurement unit
INS	inertial navigation system
IOC	initial operational capability

IPPD	integrated product and process development
IR	infrared
IIR	imaging infrared
IRR	integral rocket-ramjet
ITCV	Inter-Tropical Convergence Zone
JASSM	Joint Air-to-Surface Standoff Missile
JDAM	Joint Direct Attack Munition
JI	jet interaction
JSOW	Joint Standoff Weapon
KE	kinetic energy
LADAR	laser detection and ranging
LE	leading edge
LOCAAS	Low Cost Autonomous Attack System
LOS	line of sight angle
LRIP	low rate initial production
LWIR	long-wave infrared
mac	mean aerodynamic chord
MEOP	maximum effective operating pressure
MD	miss distance
MEMS	micromachined electromechanical systems
MIL STD	military standard
MIRs	most important requirements
mmW	millimeter wave
MOM	measure of merit
MRAAM	medium-range air-to-air missile
MWIR	medium-wave infrared
NEAR	Nielsen Engineering and Research
NOAA	National Oceanic and Atmospheric Administration
NSWC	Naval Surface Warfare Center
NTW	Navy Theater Wide
OP	operating pressure
PBX	plastic bonded explosive
PDRR	program definition and risk reduction
PGM	precision guided munition
P^3I	pre-planned product improvement
PS	power supply
PTV	propulsion test validation
RA	rolling airframe
RCS	radar cross section
RDX	Royal Demolition Explosive
RF	radar frequency
RFCM	radar frequency countermeasure
RFP	request for proposal
RJ	ramjet
RSS	root sum of squares
RT&A	research, technology, and acquisition
RTM	resin transfer molding
SAM	surface-to-air missile

SAR	synthetic aperture radar
SDD	system development and demonstration
SFW	Sensor Fused Weapon
SL	sea level
SLAM-ER	Standoff Land Attack Missile-Expanded Response
SM	static margin or Standard Missile
SOTA	state of the art
SOW	statement of work
STA	station or surface-to-air
STD	standard
STS	surface-to-surface
STT	skid-to-turn
SW	Sidewinder
TALD	Tactical Air-Launched Decoy
TBM	theater ballistic missile
TCT	time critical target
TE	trailing edge or target error
TEL	transporter, erector, launcher
THAAD	Theater High Altitude Area Defense
TK	tank
TLE	target location error
TM	telemetry
TMC	thrust magnitude control
TMD	Tactical Missile Design
TNT	trinitrotoluene
TRL	technology readiness level
TURB	turbulent
TVC	thrust vector control
UAV	unmanned air vehicle
UCAV	unmanned combat air vehicle
VARTM	vacuum-assisted resin transfer molding
VLS	vertical launch system
W/H	warhead
XLDB	cross-linked double base
w/o	without

Appendix E
Conversion Factors

Table E.1 Conversion of English to Metric Units

Parameter	English unit	To metric unit	Multiply by
Acceleration	ft/s^2	m/s^2	0.3048
Area	ft^2	m^2	0.09294
Area	in^2	m^2	6.452E-04
Density	lbm/in^3	kg/m^3	2.767E + 04
Density	lbm/ft^3	kg/ m^3	16.02
Density	$lbf\text{-}s^2/in^4$	kg/m^3	1.069E + 07
Density	$slug/ft^3$	kg/m^3	515.4
Energy	Btu	J or N-m	1055
Energy	ft-lbf	J or N-m	1.3557
Force	lbf	N	4.4484
Heat capacity	Btu/lbm/° F	J/kg/° C	4188
Heat transfer coefficient	$Btu/h/ft^2/°F$	$W/m^2/°C$	5.6786
Heat transfer coefficient	$Btu/s/ft^2/°F$	$W/m^2/°C$	2.044E + 04
Heat transfer rate	$Btu/ft^2/s$	W/m^2	1.135E + 04
Length	ft	m	0.3048
Length	in	m	0.0254
Length	mile	m	1609
Length	n mile	m	1853
Mass	lbm	kg	0.4535
Mass	$lbf\text{-}s^2/in$	kg	1200
Mass	slug	kg	14.59
Mass flow rate	lbm/h	kg/s	1.260E-04
Mass flow rate	lbm/s	kg/s	0.4535
Mass flow rate	slug/s	kg/s	14.59
Moment of inertia	$ft\text{-}lbf\text{-}s^2$	$kg\text{-}m^2$	1.3557
Moment of inertia	$in\text{-}lbf\text{-}s^2$	$kg\text{-}m^2$	0.113
Power	Btu/h	W	0.2931
Power	hp	W	745.71
Pressure	lbf/ft^2	Pa or N/m^2	47.89
Pressure	lbf/in2	Pa or N/m^2	6897

(Continued)

Table E.1 Conversion of English to Metric Units (Continued)

Parameter	English unit	To metric unit	Multiply by
Pressure	std atm	Pa or N/m^2	1.013E + 05
Specific heat	Btu/lbm/°F	J/kg/°C	4186
Temperature	°F	°C	(°F −32)0.5556
Temperature	°R	K	0.5556
Thermal conductivity	Btu/hr/ft/°F	W/m/°C	1.7307
Thermal conductivity	Btu/s/ft/°F	W/m/°C	6231
Thermal diffusivity	ft^2/s	m^2/s	0.09290
Torque	ft-lbf	N-m	1.3557
Torque	in-lbf	N-m	0.113
Torque	slug-ft^2/s	N-m	1.3557
Velocity	ft/s	m/s	0.3048
Velocity	knot or n miles/h	km/h	1.852
Viscosity—absolute	lbf-s/ft^2	N-s/m^2	47.87
Viscosity—absolute	lbm-s/ft	N-s/m^2	1.4881
Viscosity—kinematic	ft^2/s	m^2/s	0.09294
Volume	ft^3	m^3	0.02831
Volume	in^3	m^3	1.639E-05
Volume	U.S. gallons	m^3	0.003785

Appendix F
Example of a Syllabus

An example syllabus for a two-semester course on Tactical Missile Design is given below. This is a lecture-lab course that includes lectures, classroom team homework, individual homework problems, exams, student team design study/studies, customer reviews, and documentation. The first semester is 3 credit hours, consisting of 2 hours each week in the classroom plus design team participation outside the classroom. The second semester is 2 credit hours, consisting primarily of the design team study/studies, customer reviews, and documentation.

Summary: This is a self contained course on the fundamentals of tactical missile design. It provides a system-level, integrated method for the missile aerodynamic configuration/propulsion system design and analysis. The course addresses the broad range of alternatives in meeting missile performance, cost and system measures of merit/constraint requirements. The methods presented are generally simple closed-form analytical expressions that are physics-based, to provide insight into the primary driving parameters. Configuration sizing examples are presented for rocket-powered and ramjet-powered baseline missiles. Typical values of missile parameters and the characteristics of current operational missiles are presented. Also presented are the enabling subsystems and technologies for tactical missiles and the current/projected state-of-the-art of tactical missiles. During this course the students will size the configuration, size the propulsion system, estimate the weight, and estimate the flight performance for a conceptual tactical missile design, in accordance with the requirements of a Request for Proposal (RFP). The students will also include first order system measures of merit/constraints (such as miss distance, lethality, cost, and launch platform integration) for the conceptual design of a tactical missile, in accordance with the requirements of the RFP. Results will be presented to a customer review team at kickoff, midterm, and final reviews.

Textbook: Tactical Missile Design by Eugene L. Fleeman.

Prerequisites: Previous courses in flight vehicle aerodynamics, propulsion, structure, and performance.

Schedule:

Lectures: Weeks 1-15 of the first course, on Chapters 1-9 of the textbook.

Classroom Review of Textbook Problems: Upon completion of the lecture for each chapter of the textbook. The problems are at the end of the chapter.

Classroom Homework Problems: A classroom homework assignment will be given each week, from Appendix F of the textbook. The following week, a selected two-student team will present their solution in the classroom.

Individual Homework Problems: Individual homework assignments will be given each week, from Appendix F of the textbook. Homework is due the following week after the assignment.

Midterm Exam: Upon completion of the Chapter 5 lecture (Flight Performance Considerations in Tactical Missile Design). It is anticipated that the midterm exam will be given during week 9 of the first course.

Final Exam: Upon completion of the Chapter 9 lecture (Summary and Lessons Learned). It is anticipated that the Final Exam will given during week 15 of the first course.

Request for Proposal: The RFP provides the statement of work and deliverable requirements for the missile design study. An example of an RFP is shown in Appendix B of the textbook. The RFP will be provided prior to week 10 of the first course.

Student Design Team(s): The student design team(s) will be formed prior to week 10 of the first course. Each student design team will consist of about ten students. One of the students will be the program manager and one of the students will be the systems engineer. The other students will be responsible for functional areas such as propulsion, aerodynamics, structure, flight control, guidance and navigation, weight and balance, design layout, warhead, flight performance, cost, and launch platform integration.

Customer Reviews: Three reviews are held with the customer – A Kickoff Meeting during week 15 of the first course, a Midterm Review upon completion of a down-select to a preferred concept (about week 8 of the second course), and a Final Review (during week 13 of the second course). Dry runs will be held prior to the customer reviews.

Documentation: Documentation from the student design team(s) will include a final technical report of about 100 pages and slides from the customer reviews. The draft final report will provided 1 week following the Final Review. A paper may also be presented later at a technical conference. Drafts of the documentation will be reviewed prior to submittal to the customer(s).

Grading: Grades will be based on the exam scores, classroom team homework scores, individual homework scores, student team participation, classroom participation, presentation skills, the overall quality of the student team presentations, and the overall quality of the student team documentation.

References

[1]"Missile.index," http://missile.index.ne.jp/en/

[2]*AIAA Aerospace Design Engineers Guide*, AIAA, Washington, DC, 1993.

[3]Bonney, E. A., et al., *Aerodynamics, Propulsion, Structures, and Design Practice*, "Principles of Guided Missile Design," Van Nostrand, Princeton, NJ, 1956.

[4]Jerger, J. J., *Systems Preliminary Design Principles of Guided Missile Design*, "Principles of Guided Missile Design," Van Nostrand, Princeton, NJ, 1960.

[5]Chin, S. S., *Missile Configuration Design*, McGraw–Hill, New York, 1961.

[6]Mason, L. A., Devan, L., and Moore, F. G., "Aerodynamic Design Manual for Tactical Weapons," NSWCTR 81-156, 1981.

[7]Pitts, W. C., Nielsen, J. N., and Kaattari, G. E., "Lift and Center of Pressure of Wing-Body-Tail Combinations at Subsonic, Transonic, and Supersonic Speeds," NACA Rept. 1307, 1957.

[8]Jorgensen, L. H., "Prediction of Static Aerodynamic Characteristics for Space-Shuttle-Like, and Other Bodies at Angles of Attack from 0° to 180°," NASA TND 6996, Jan. 1973.

[9]Hoak, D. E., et al., "USAF Stability and Control DATCOM," AFWAL TR-83-3048, Global Engineering, Documents, Irvine, CA, 1978.

[10]"Nielsen Engineering and Research (NEAR) Aerodynamic Software Products," http://www.nearinc.com/near/software.htm

[11]Ashley, H., *Engineering Analysis of Flight Vehicles*, Dover, New York, 1974.

[12]Anderson, John D. Jr., *Modern Compressible Flow*, 2nd ed., McGraw–Hill, New York, 1990.

[13]Kinroth, G. D. and Anderson, W. R., "Ramjet Design Handbook," CPIA Pub. 319 and AFWAL TR 80-2003, June 1980.

[14]"Technical Aerodynamics Manual," North American Rockwell Corp., DTIC AD 723823, June 1970

[15]Oswatitsch, K. L., "Pressure Recovery for Missiles with Reaction Propulsion at High Supersonic Speeds," NACA TM-1140, 1947.

[16]Carslaw, H. S. and Jaeger, J. C., *Conduction of Heat in Solids*, Clarendon, Oxford, England, UK, 1988.

[17]Allen, J. and Eggers, A. J., "A Study of the Motion and Aerodynamic Heating of Ballistic Missiles Entering the Earth's Atmosphere at High Supersonic Speeds," NACA Rept. 1381, April 1953.

[18]Schneider, S. H., *Encyclopedia of Climate and Weather*, Oxford Univ. Press, Oxford, England, UK, 1996.

[19]Klein, L. A., *Millimeter-Wave and Infrared Multisensor Design and Signal Processing*, Artech House, Boston, 1997.

[20]U.S. Army Ordnance Pamphlet ORDP-20-290-Warheads, 1980.

[21]Carleone, J. (ed.), *Tactical Missile Warheads*, "AIAA Vol. 155, Progress in Astronautics and Aeronautics," AIAA, Washington, DC, 1993.

[22]Christman, D. R. and Gehring, J. W., "Analysis of High-Velocity Projectile Penetration Mechanics," *Journal of Applied Physics*, Vol. 37, 1966.

[23]Heaston, R. J. and Smoots, C. W., "Precision Guided Munitions," GACIAC Rept. HB-83-01, May 1983.

[24]Donatelli, G. A. and Fleeman, E. L., "Methodology for Predicting Miss Distance for Air Launched Missiles," AIAA Paper 82-0364, Jan. 1982.

[25]Bennett, R. R. and Mathews, W. E., "Analytical Determination of Miss Distances for Linear Homing Navigation Systems," Hughes Tech. Memo 260, Hughes Aircraft, 31 March 1952.

[26]Nicholas, T. and Rossi, R., *US Missile Data Book, 1996*, Data Search Associates, Orange County, CA, 1996.

[27]Bithell, R. A. and Stoner, R. C., "Rapid Approach for Missile Synthesis," AFWAL TR 81-3022, Vol. 1, March 1982.

[28]Fleeman, E. L. and Donatelli, G. A., "Conceptual Design Procedure Applied to a Typical Air-Launched Missile," AIAA Paper 81-1688, Aug. 1981.

[29]Hindes, J. W., "Advanced Design of Aerodynamic Missiles (ADAM)," Oct. 1993.

[30]Frits, A. P., et al., "A Conceptual Sizing Tool for Tactical Missiles," AIAA Missile Sciences Conf., November 2002.

[31]Bruns, K. D., Moore, M. E., Stoy, S. L., Vukelich, S. R., and Blake, W. B., "Missile DATCOM," AFWAL-TR-91-3039, April 1991.

[32]Moore, F. G., et al., "The 2002 Version of the Aeroprediction Code", Naval Surface Warfare Center, March 2002.

[33]Nicolai, L. M., "Designing a Better Engineer," *Aerospace America*, April 1992.

Bibliography

System Design

"Aircraft Stores Interface Manual (ASIM)," http://akss.dau.mil/software/1.jsp

"Advanced Sidewinder Missile AIM-9X Cost Analysis Requirements Description (CARD)," http://deskbook.dau.mil/jsp/default.jsp

Ashley, H., *Engineering Analysis of Flight Vehicles*, Dover, New York, 1974.

Ball, R. E., *The Fundamentals of Aircraft Combat Survivability Analysis and Design*, AIAA, New York, 1985.

"Conversion Factors by Sandelius Instruments," http://www.sandelius.com/reference/conversions.htm

"Defense Acquisition Guidebook," http://akss.dau.mil/dag/

Defense Technical Information Center, http://www.dtic.mil/

"Directory of U.S. Military Rockets and Missiles," http://www.designation-systems.net/

"DoD Index of Specifications and Standards," http://stinet.dtic.mil/str/dodiss.html

Eichblatt, E. J., *Test and Evaluation of the Tactical Missile*, AIAA, Washington, DC, 1989.

Fleeman, E. L. "Aeromechanics Technologies for Tactical and Strategic Guided Missiles," AGARD Paper, FMP Meeting, London, May 1979.

Fleeman, E. L., et al., "Technologies for Future Precision Strike Missile Systems," NATO RTO EN-018, July 2001.

Fleeman, E. L., "Tactical Missile Design," AIAA Short Course, AIAA, Reston, VA, March 2006.

Giragosian, P. A., "Rapid Synthesis for Evaluating Missile Maneuverability Parameters," *10th AIAA Applied Aerodynamics Conference*, AIAA, Washington, DC, June 1992.

Hogan, J. C., et al., "Missile Automated Design (MAD) Computer Program," AFRPL TR 80-21, March 1980.

Lee, R. G., (Ed.) *Guided Weapons*, Third Edition, Brassey's, London, 1998.

Lindsey, G. H. and Redman, D. R., "Tactical Missile Design," Naval Postgraduate School, Monterey, CA, 1986.

"Missile System Flight Mechanics," AGARD CP270, May 1979.

"National Defense Preparedness Association Conference Presentations," http://www.dtic.mil/ndia

NATO Research and Technology Organisation, http://www.rta.nato.int/

Nicolai, L. M., *Fundamentals of Aircraft Design*, METS, Inc., San Jose, CA, 1984.

"Periscope," http://www.periscope.usni.com

Rapp, G. H., "Performance Improvements with Sidewinder Missile Airframe," AIAA Paper 79-0091, Jan. 1979.

Raymer, D. P., *Aircraft Design, A Conceptual Approach*, AIAA, Washington, DC, 1989.

"The Ordnance Shop," http://www.ordnance.org/portal/

Wertz, J. R and Larson W. J., *Space Mission Analysis and Design*, Microprism Press and Kluwer Academic Publishers, Norwell, MA, 1999.

Aerodynamics

"1976 Standard Atmosphere Calculator," http://www.digitaldutch.com/atmoscalc/

"A Digital Library for NACA," http://naca.larc.nasa.gov/

Ashley, H. and Landahl, M., *Aerodynamics of Wings and Bodies*, Dover, New York, 1965.

Briggs, M. M., *Systematic Tactical Missile Design, Tactical Missile Aerodynamics: General Topics*, Vol. 141, Progress in Astronautics and Aeronautics, AIAA, Washington, DC, 1992.

Briggs, M. M., et al., "Aeromechanics Survey and Evaluation, Vol. 1-3," Naval Surface Warfare Center, NSWC/DL TR-3772, Dahlgren, VA, Oct. 1977.

Burns, K. A., Deters, K. J., Haley, C. P., and Kikiken, T. K. "Viscous Effects on Complex Configurations," WL-TR-95-3060, 1995.

"Compressible Aerodynamics Calculator," http://www.aoe.vt.edu/~devenpor/aoe3114/calc.html

Dillenius, M. F. E., et al., "Engineering-, Intermediate-, and High-Level Aerodynamic Prediction Methods and Applications," *Journal of Spacecraft and Rockets*, Vol. 36, No. 5, Sept.–Oct., 1999.

John, James E. A., *Gas Dynamics*, 2nd ed., Prentice–Hall, Upper Saddle River, NJ, 1984.

Lesieutre, D., et al., "Recent Applications and Improvements to the Engineering-Level Aerodynamic Prediction Software MISL3," AIAA-2002-0274.

Mendenhall, M. R. et al., *Proceedings of NEAR Conference on Missile Aerodynamics*, NEAR, Mountain View, CA, 1989.

"Missile Aerodynamics," NATO AGARD LS-98, Feb. 1979.

"Missile Aerodynamics," NATO AGARD CP-336, Feb. 1983.

"Missile Aerodynamics," NATO AGARD CP-493, April 1990.

"Missile Aerodynamics," NATO RTO-MP-5, Nov. 1998.

Moore, F. G., *Approximate Methods for Weapon Aerodynamics*, AIAA, Reston, VA, 2000.

Nielsen, J. N., *Missile Aerodynamics*, McGraw–Hill, New York, 1960.

Nielsen, J. N., "Missile Aerodynamics – Past, Present, Future," AIAA Paper 79-1818, 1979.

Nielsen, J. N., and Pitts, W. C., "Wing-Body Interference at Supersonic Speeds with an Application to Combinations with Rectangular Wings," NACA TN 2677, April, 1952.

Simon, J. M., et al., "Missile DATCOM: High Angle of Attack Capabilities," AIAA-99-4258.

Spreiter, J. R., "The Aerodynamic Forces on Slender Plane-and Cruciform-Wing and Body Combinations," NACA Report 962, 1950.

Zucker, Robert D., *Fundamentals of Gas Dynamics*, Matrix, 1977.

Propulsion

Bathie, W. W., *Fundamentals of Gas Turbines*, Wiley, New York, 1996.

Bonney, E. A., et al., "Propulsion, Structures and Design Practice," *Principles of Guided Missile Design*, Van Nostrand, Princeton, NJ, 1956.

Chemical Information Propulsion Agency, http://www.cpia.jhu.edu/

Durham, F. P., *Aircraft Jet Powerplants*, Prentice–Hall, Upper Saddle River, NJ, 1961.

Hill, P. G. and Peterson, C. R., *Mechanics and Thermodynamics of Propulsion*, Addison-Wesley, Reading, MA, 1970.

Humble, R. W., Henry, G. N., and Larson, W. J., *Space Propulsion Analysis and Design*, McGraw–Hill, New York, 1995.

Jenson, G. E. and Netzer, D. W., *Tactical Missile Propulsion*, AIAA, Reston, VA, 1996.

Mahoney, J. J., *Inlets for Supersonic Missiles*, AIAA, Washington, DC, 1990.

Mattingly, J. D., et al., *Aircraft Engine Design*, AIAA, New York, 1987.

St. Peter, J., *The History of Aircraft Gas Turbine Engine Development in the United States: A Tradition of Excellence*, ASME International Gas Turbine Institute, Fairfield, NJ, 1999.

Sutton, G. P., *Rocket Propulsion Elements*, Wiley, New York, 1986.

"Tri-Service Rocket Motor Trade-off Study, Missile Designer's Rocket Motor Handbook," Chemical Propulsion Information Agency CPIA 322, Columbia, MD, May 1980.

Materials

Budinski, K. G., and Budinski, M. K., *Engineering Materials Properties and Selection*, Prentice–Hall, Upper Saddle River, NJ, 1999.

Chapman, A. J., *Heat Transfer*, 3rd ed., Macmillan, New York, 1974.

Harris, D. C., *Materials for Infrared Windows and Domes*, SPIE Optical Engineering Press, 1999.

Incropera, F. P. and DeWitt, D. P., *Fundamentals of Heat and Mass Transfer*, 4th ed., Wiley, New York, 1996.

Kalpakjian, S., *Manufacturing Processes for Engineering Materials*, Addison Wesley, Reading, MA, 1997.

Mallick, P. K., *Fiber-Reinforced Composites: Materials, Manufacturing, and Design*, 2nd ed., Marcel Dekker, New York, 1993.

"Matweb's Material Properties Index Page," http://www.matweb.com

"Metallic Materials and Elements for Aerospace Vehicle Structures," MIL-HDBK-5J, Jan 2003.

"Metallic Material Properties Development and Standardization (MMPDS)," http://www.mmpds.org

"NASA Ames Research Center Thermal Protection Systems Expert (TPSX) and Material Properties Database," http://tpsx.arc.nasa.gov/tpsxhome.shtml

Guidance and Control

Blakelock, J. H., *Automatic Control of Aircraft and Missiles*, Wiley, New York, 1965.

Donati, S., *Photodetectors*, Prentice–Hall, Upper Saddle River, NJ, 2000.

Garnell, P., *Guided Weapon Control Systems*, Pergamon, Oxford, England, UK, 1980.

Jha, A. R., *Infrared Technology*, Wiley, New York, 2000.

Lawrence, A. L., *Modern Inertial Technology*, Springer, Verlag, New York, 1998.

Lecomme, P., Hardange, J. P., Marchais, J. C., and Normant, E., *Air and Spaceborne Radar Systems*, SciTech and William Andrew, 2001.

Locke, A. S., *Guidance*, "Principles of Guided Missile Design", Van Nostrand, Princeton, NJ, 1955.

Proceedings of AGARD G&C Panel Conference on Guidance & Control of Tactical Missiles, AGARD LS-52, May 1972.

Schlessinger, M., *Infrared Technology Fundamentals*, Marcel Dekker, New York, 1995.

Siouris, G. M., *Aerospace Avionics Systems*, Academic International Press, New York, 1993.

Stimson, G. W., *Introduction to Airborne Radar*, SciTech Publishing, 1998.

Wehner, D. R., *High-Resolution Radar*, Artech House, Boston, 1995.

Zarchan, P., *Tactical and Strategic Missile Guidance*, "Vol. 124, Progress in Astronautics and Aeronautics," Washington, DC, 1990.

Index

Acceleration
  initial heading error, 198
  longitudinal, 317
  maneuver, 6, 208
  maneuvering target, 197
  ramjet, 202
  rocket, 204
  turbojet, 202
Acquisition, 3, 380, 447, 449
Actuator, 190
Advanced concept technology demonstration, 380, 433, 447
Aerodynamic heating, 42–43, 162
Aerodynamic center, 40, 47, 363, 443
Aeroelasticity, 299
Aircraft integration, 298, 314
Airframe, 112
Air loads, 178–179
Air-to-air missile, 7, 313, 394, 404
Air-to-surface missile, 8
Air turbo rocket, 90–91
Altitude, 1, 11, 213, 222, 278, 336, 346
Aluminum, 134, 136, 227, 319, 437
Ammonium perchlorate, 122, 276, 437
Angular resolution, 27, 225
Annular inlet, 110–111
Antenna, 11, 24, 240, 396, 439
Advanced Strategic Air Launched Missile (ASALM), 15, 71, 338
Antiradiation homing (ARH), 242–243
Aspect ratio, 53, 60, 69, 185, 305, 437
Atmosphere, 236–237, 346, 447
Atmospheric attenuation, 25
Axial force, 202, 342, 344, 438
Axial load, 356

Bandwidth, 27–28, 39, 225, 272, 396, 429
Bank-to-turn, 54, 69, 339, 447
Base area, 32, 34
Base drag (base pressure), 31–32
Baseline missile, 6, 14, 23, 28, 40, 122, 181, 192, 209
Battery, 24, 190–191, 396
Battle damage indication (BDI), 11, 225, 289, 396
Beam range, 199
Beamwidth, 25, 417
Bending moment, 180
Binder, 120, 133
Blast, 21, 57
Blast tube, 136–137
Blunt nose, 33, 171
Boattail drag, 34
Body bending frequency, 28, 414
Body
  aerodynamic center, 40, 47, 53
  bending, 4, 28
  center of pressure, 53
  drag coefficient, 31–32
  normal force, 36
  weight, 16, 69, 100, 141
Boost, 125, 127, 129, 151, 214, 319
Boost-glide trajectory, 1
Booster, 105, 108, 235, 346
Boresight, 13, 197
Boundary layer, 47, 163
Breguet range equation, 84–85, 202–203
Buckling, 177, 356
Burn area, 122
Burn rate, 127

Canard, 44–49
Canister launch system (CLS), 296
Captive flight, 119, 386
Capture efficiency, 114–115, 117
Carbon, 121–122
Carriage, 274–277
Case, 134–135
Casting, 150–151, 153, 157, 429
Center of gravity, 146–147, 209

Center of pressure, 40, 53, 65, 76, 438, 443
Ceramic, 89, 153, 161
Chamber pressure, 122, 125–127, 137, 176, 357
Characteristic velocity, 123, 127, 238, *321*, 357
Charge, 246, 248–250, 254, 437–438, 443
Choked flow, 124
Circular error probable (CEP), 257, 423
Climb, 201, 204–205, 209, 330
Cloud, 219–220
Clutter, 225, 404
Coast, 130, 195, 200, 210, 336
Collision course, 259
Combustion chamber, 83, 91, 132
Command, control, communication (C^3), 11, 429, 477
Command, control, communication, computers, intelligence, surveillance, reconnaissance (C4ISR), 11, 429
Communication, 430, 433
Composite material, 52, 155, 157, 160
Composite propellant, 133–134
Compressed carriage, 17, 235, 304–305
Compressor, 86–88, 413
Computational fluid dynamics (CFD), 38, 353, 391
Computer-aided sizing, 313, 354, 376
Conceptual design, 4–7, 14–16, 40, 137, 141
Conductivity, 163, 170
Configuration buildup, 77–78
Configuration sizing, 1, 49, 201, 412, 453
Conical flow, 114
Conical nose, 114
Contrast, 13
Control effectiveness, 56, 61, 201, 209, 392
Control, axis
  pitch, 55–56, 69
  roll, 55–56, 72, 389
  yaw, 55–56, 69–72, 147, 299
Control, types of
  all movable, 55
  canard, 56–59, 61–62, 193, 375, 396
  flap, 55
  lattice, 60–61, 396
  tail, 56–66
  unconventional, 43, 57, 66–67
  wing, 56, 64–65, 263
Cost
  development, 3
  logistics, 11, 141, 284, 291–293
  production, 284, 286–288, 290, 356, 410
  system development and demonstration (SDD), 356
Counter-countermeasures, 240
Countermeasures, 239, 395
Cross coupling, 392
Crossflow, 36, 40
Cruciform design, 51, 72, 109–111, 317
Cruise missile, 3, 42, 52, 54, 56, 191
Cruise trajectory, 356

Damping characteristics, 393
Data link, 11, 225, 232–233, 396, 429,
Degrees of freedom, 199
Delta wing, 52–53
Demonstration and validation (Demval), 382
Density, 161–162, 202, 237, 245, 351, 396
Design,
  conceptual, 4–5, 7, 14–15, 40, 74, 76, 141
  criteria, 76–77, 79, 117, 413–414
  detailed, 83
  loads, 149, 176
  of experiments (DOE), 7, 333, 402, 424
  preliminary, 7, 78, 200, 353, 381–392
  validation, 380, 384–385
Detection range, 23–24, 26, 229–230, 277, 279
Development,
  facilities, 386
  process, 379, 381
  tests, 386–388
Diameter considerations, 245
Dielectric constant, 186
Diffuser, 16
Discharge coefficient, 123
Diving flight trajectory, 215
Documentation, 15, 408, 433, 454
Dome
  bandpass, 186
  error slope, 29–30, 64, 69, 71, 265, 395
  faceted, 29–30, 395

material alternatives, 141
multilens, 29–30, 395
stress, 172, 174
weight, 188–189
window, 29–31
Double base propellant, 133–134
Drag
base, 31–32, 34, 50
boattail, 34–35
components of, 212, 367
crossflow, 36, 40, 72, 356
definition of, 4, 22
skin friction, 31–32, 49–51
wave, 31–33, 49–51
Ducted rocket, 7–8, 71, 83, 97, 121–122
Dynamic pressure, 2, 22, 48, 203, 207
Dynamic stability, 393, 410

Effective navigation ratio, 259–261, 266, 268
Ejection launch, 300, 303
Electro-optical, 222, 239
End burning grain, 127, 129
Engine nomenclature, 342
Environment, 13, 150, 224, 307
Exit, 16, 85, 137
pressure, 91, 93
velocity, 85–86, 93
Expansion ratio, 125, 137, 319, 332, 357, 420, 443

Faceted dome, 29–30
Factor of safety, 149, 186
Field of regard, 30, 298
Field of view, 27, 224
Fineness ratio, 22, 27–28, 30, 339, 413
Fire control, 198, 306
Firepower, 3, 245, 303
Flap, 55
Flare, 41–43, 413
Flight loads, 178–179
Flight path angle, 122, 201, 259, 330, 337
Flight performance, 4, 6–7, 141–142, 146
Flow path geometry, 16, 342
Flow separation, 31, 50, 392
Flow types
laminar, 163
turbulent, 163
Forebody types
conical, 118
faceted, 29, 395
hemispherical, 33, 184, 188
tangent ogive, 28–29, 264
window, 29–30, 263, 395
Four degrees of freedom, 447
Fragment, 249, 356, 442
Free-to-roll tails, 54, 58
Freestream Mach number, 61, 98, 440
Frequency, 25, 29, 223, 226, 383, 414, 439, 445
Fuel
alternatives, 120, 350
density, 85, 120–121, 202
heating value, 18, 88, 97
observables, 133
Fuel-to-air ratio, 87–90, 100, 353
Full expansion nozzle, 124

Gain, 235, 277
Gas generator, 97, 122
Gel motor, 396
Glide trajectory, 83, 335, 338
Glint, 270–271
Global positioning system (GPS), 224
Grain configuration, 317
Graphite, 155, 162
Gravitational constant, 206
Ground handling loads, 149, 183
Guidance, 247, 414

Hardware in loop, 291, 349
Heading error 198, 232, 266, 414, 444, 484,
Heat capacity, 159
Heat flux, 172
Heat sink, 83, 173
Heat transfer, 136, 162–163, 392
Heating, aerodynamic, 141, 162, 175, 237, 356
Heating value of fuel, 88
Hemispherical nose, 33
Hinge moment, 48, 193, 392
Hoop stress, 183–184, 361
Horizontal flight, 122, 213, 215
House of quality, 5, 17, 371, 376, 409, 431
Hydroxyl-terminated polybutadiene binder (HTPB) 120
Hypersonic Mach number, 122, 354
Hypersonic missile, 1, 157, 161, 396

Imaging seeker, 210
Impulse
  specific, 16, 18, 72, 81–86, 94–98, 125
  total, 202, 319
Induced roll, 62, 64–66
Inert weight, 144
Inertia, moment of, 146–149, 201, 319, 439, 451
Inertial navigation system (INS) 225, 227, 395, 448
Infrared (IR) seeker, 25
Initial operational capability (IOC) 13, 431, 448
Inlet
  alternatives, 110
  capture efficiency, 114–115
  cowl, 109, 112
  integration, 112, 119, 414
  spillage, 113
  start, 116–118
  throat, 116, 437
In-line surfaces, 55–56, 391
Insensitive munition, 133, 388, 488
Instantaneous field of view (IFOV), 27, 448
Insulation, 135, 158–160, 396
Integral rocket-ramjet (IRR), 106, 449
Integrated product process development (IPPD), 285, 431, 449
Interdigited surfaces, 54–56, 391
Internal carriage, 275, 396
IR dome, 30, 172
Isentropic flow, 86, 92, 100, 356

Jet interaction, 43, 57, 67, 393
Jet vanes, 66, 68

Kill probability, 3, 248, 250
Kinetic energy, 136, 241, 255, 356

Laminar flow, 163
Lattice fins, 60–61
Launcher, 134, 275, 300, 304, 359
Launch platform integration, 1, 9, 56, 219–311
Launch range, 313, 356
Lead angle, 197, 215–216, 356
Learning curve, 287–288
Length considerations, 296
Lessons learned, 399–415
Lethality, 5, 13, 219
Lift, 16, 21, 348, 438, 440
Lifting body, 21, 34–38, 396
Lift-to-drag ratio, 21, 38, 202
Limit stress 184, 421
Linear wing theory, 44–45, 47, 76
Line of sight, 69–70
Load factor, 149
Load distribution, 178, 180
Loads, 38, 149, 176, 183
Local angle of attack, 44, 58, 209
Localized buckling, 134, 154, 178
Lofted trajectory, 69, 313
Logistics, 11, 71, 91, 291, 293
Low observables, 29, 38, 239

Mach angle, 114, 444
Maneuverability, 1, 7, 67, 78, 201, 414
Manufacturing process, 361
Mass ratio, 249–250
Material density, 186, 188
Material strength, 154, 156
Maximum angle of attack, 179–180, 209, 393
Maximum effective operating pressure, 149, 184, 449
Maximum lift coefficient, 34–36
Maximum range, 84, 199, 368, 441
Maximum speed, 122
Mean aerodynamic chord (MAC), 186, 366, 438, 449
Measures of merit, 10, 13, 186, 190, 219, 334
Micromachined electromechanical systems (MEMS), 194, 294, 396, 449
Military standard, 120, 449
Minimum range, 198–199, 299
Minimum smoke, 122, 133, 276–277
Miss distance, 71, 246, 248, 257, 266, 268, 357
Missiles, types of, 8, 145
Mission definition, 14, 356
Mission planning, 278–279
Mission requirements, 5, 10, 356
Modulus of elasticity, 28, 154, 439
Moment of inertia, 146–149, 201, 319
Monocoque construction, 150
Motor case
  chamber pressure, 178
  heating, 136
  materials, 134–135
  weight, 128–129

Natural frequency, 70–71
Navigation ratio, 259–260
Newtonian impact theory, 44–45, 391
Nitrocellulose, 133–134
Noise, 229, 271–274
Nomogram, 180–181
Normal distribution, 237, 239, 257
Normal force
  from angle of attack, 36, 46
  from control deflection, 73, 264
Normal force coefficient
  body, 36, 46, 78
  wing, 45–46
  tail, 46, 363
  total, 46, 363
Normal force curve slope, 36, 46
Nose geometry, 32
Nose fineness, 4, 9, 29, 413, 440
Nose inlet, 109, 111–112
Nozzle
  discharge coefficient, 121, 123, 438
  exit area, 32, 126, 437
  exit pressure, 91–95, 98–99
  exit velocity, 83, 85–86, 93–94
  expansion ratio, 123–124, 126, 319, 443
  materials, 68, 136
  throat, 125–126, 137

Oblique shock, 61, 109, 113, 117, 119–120
Observables, 38, 121, 133, 239, 274, 276
Off boresight, 13–14, 198, 323
One degree of freedom, 261, 447
Optimum
  climb, 234–235, 356
  cruise, 233–234
  design, 216, 353, 375
  dive, 234–235
  trajectory, 338

Paredo, 17, 323
Parts count, 150, 281
Penetration, 13, 241
Pintle motor, 85, 396
Pitching moment, 16, 38–41, 319
Pitot-static probe, 300
Planform, 21, 145, 339
Point load, 180
Power supply, 1, 190–193
Precision, 3, 354
  guided munition, 10, 11, 449
  strike accuracy, 3, 231, 414
  strike missile, 3, 10–11, 36, 224, 298
Preliminary design, 7, 78, 199, 381, 391, 431
Pressure, 2
  base, 34, 319
  chamber, 122, 125–126, 420, 441
  recovery, 110
Probability of kill, 248, 250, 441
Production process, 287–288, 290
Progressive thrust, 129
Propellant, 4–7, 128–130, 132–134
  burn area, 126, 137, 437
  cross section, 129
  extruded, 289, 361
  flow rate, 85, 97, 121
  fraction, 81, 123, 203
  grain, 97, 122, 128–130, 281
  minimum smoke, 123, 133, 276
  properties, 133
  reduced smoke, 132–133, 277
  selection, 333
  slotted, 128–129, 420
  web, 129
Proportional guidance, 259–260, 354, 414
Pulse motor, 130–131
Pultrusion, 150–152, 194, 396

Radar, 3, 8, 23, 186, 222
  beam width, 227, 272
  cross section, 3, 24, 30, 155, 239
  frequency, 186, 239, 449
  range, 23–24, 277
  resolution, 23–25, 224
Radial burn, 129, 130
Radiation, 156, 171, 223, 228, 447
Radome, 28, 166, 187, 189, 263
Rail launch, 276, 297, 304
Rain, 186, 188, 222, 386
Ramjet, 7, 16, 95–112
  engine-booster integration, 81, 105–108
  inlet, 81, 109–112
  length, 7, 97–98, 105
  specific impulse, 16, 81, 83, 97–98, 347, 348
  temperature limit, 100–105, 345
  thrust, 83, 98–100, 356, 389
Range, 3–19, 313–329, 338–350
  ballistic, 212–213, 368
  climb, 85

Range (*Continued*)
coast, 210–211
cruise, 13, 38, 203
detection, 5, 23–24, 26, 227, 356
dive, 205, 235, 356
launch, 313–314, 316–317, 356
maximum, 84, 144, 198, 410
minimum, 197–198, 267, 299, 410
recognition, 314–315, 441
sensitivity, 17, 24
standoff, 13, 240, 277, 297, 313–329, 376
Rate of climb, 422
Rate of dive, 39
Reaction jet, 43, 57, 69
Recovery factor, 158, 172, 441
Recovery temperature, 156, 158
Rectangular planform, 53
Reduced smoke, 132–133, 274
Regressive thrust, 128–129
Reliability, 122, 281–282
Risk, 3, 407
Robustness, 9, 199, 219–241, 338–350
Rocket motor, 7, 29, 90, 122–128
Roll, 72–73
attitude, 72, 77, 392, 393
control, 55–56, 58, 284
orientation, 21, 69, 72–73
stabilization, 56
Rolling airframe, 56, 70
Rolling moment, 54, 56, 200

Safety, 83, 132, 149–150
Scramjet, 81, 83, 234, 388, 419, 448
Seeker, 1, 29–30, 186–190
Seeker dome, 71, 141, 186–190
Surface-to-air missile, 9, 68, 242, 389
Semimonocoque construction, 150
Sensitivity, 5, 17, 141–142, 347, 410
Ship integration, 132
Shipboard launching, 430
Shock angle, 61, 115
Shock wave, 31, 50, 112, 340, 414
Sideslip, angle of, 69, 71, 179, 180, 301
Signal, 21, 25, 188, 441
Sizing, 1, 6, 9–10, 74–76, 313–377
Six degrees of freedom, 200, 291, 447
Skid-to-turn, 54, 69, 70
Skin friction drag, 31, 49, 365, 366
Slender body theory, 36, 76, 356
Slender wing theory, 45, 356, 375
Slotted propellant grain, 128
Smoke, 122, 133, 274
Solid propellant rocket, 83, 85, 145
Sound, speed of, 32, 49, 95, 137
Sparrow missile, 65, 163, 376, 402
Specific heat, 86–88, 101, 356
Specific impulse, 16, 83, 94–95, 348
ducted rocket, 83, 97, 121
ramjet, 16, 71, 97–98, 347–348
rocket, 81, 83
scramjet, 83
turbojet, 81, 94–95
Spillage, inlet, 81
Split canard, 13, 62
Spreadsheet, 313, 355–356
Stability, 1, 5, 38–40, 76–77
static, 21, 38–40, 72–73, 75
dynamic, 354, 391–393
neutral, 74, 262, 357
Stabilizer, 1, 41–43, 319
Stage, rocket, 90, 145, 192
Stagnation temperature, 158
Standard atmosphere, 163, 236, 346
Standard deviation, 444
State of the art, 1, 7–9, 393–394, 399
Static margin, 4, 13, 73, 236
Steady flight, 204, 207
Steady-state temperature, 162, 171–172
Steel, 28, 134, 136
Stiffeners, 150
Store, 39, 180, 299
carriage, 281, 297, 299, 392
separation, 39, 297, 299, 302
suspension, 303
Strength, 53, 150, 152, 154, 382
Stress, 32, 129, 141, 172–175, 295
Structure, 1, 28, 52, 149–150, 158–160
design, 141, 149, 150, 175–186
efficiency, 157
material, 156, 357, 361
weight, 141, 175, 185
Submarine integration, 295–296
Subsystems, 5, 14, 38, 141–142
Surface planform, 21, 46, 53, 396
Surface-to-air missile, 9, 68, 293
Surface-to-surface missile, 9
Survivability, 9, 11, 243, 277–281
Sustain flight, 124, 171, 325
Synthetic aperture radar (SAR), 224, 395
Synthesis, 5, 21, 141, 406

System analysis, 11, 291, 385
System development and demonstration (SDD), 237, 356, 379, 407, 431

Tactical Missile Design (TMD) spreadsheet, 355
Tail, 5, 7, 42, 56
  arrangement, 60
  control, 34, 56, 58
  force, 44, 46
  sizing, 74–76, 146
Tangent ogive nose, 264
Target, 3, 24
  acquisition, 3, 224, 226, 447
  aspect, 215, 259, 316
  damage, 11, 225
  detection, 24, 224, 229
  error (TE), 232–233
  kill, 3, 13, 250
  location error (TLE), 11, 232
  maneuver, 6, 259, 414
  recognition, 3, 224, 395
  types, 243
Technology, 1, 21, 86–92, 100–105
  assessment, 5, 379–380
  availability date (TAD), 382, 433
  development, 5, 11, 379, 390–393
  readiness level (TRL), 379, 381, 431
  roadmap, 5, 379–380, 410
Temperature, 18, 86–92
Tensile stress, 154, 184, 444
Terminal guidance, 231, 259
Test, 6, 283, 289–300, 358, 389
Thermal, 23, 83, 158, 162–172, 287
  choking, 83, 102–103
  conductivity, 135, 158–159, 170
  diffusivity, 159, 165, 443
  expansion, 131, 172, 174, 186
  stress, 141, 172–175
Thermally thick surface, 165, 167
Thermally thin surface, 162, 164
Thickness, 28, 47
  airframe, 163, 177, 182, 356
  motor case, 178, 357
  surface, 51, 53, 61, 356
Thin wall cylinder, 28
Threat radar, 61, 243, 244
Three degrees of freedom, 201, 391, 447
Throat, nozzle, 16, 125–126, 137, 342, 437
Thrust considerations, 81, 121
Thrust
  magnitude control (TMC), 81–85, 130–132
  ramjet, 83–86, *89*, 95–97, 100–105
  rocket, 7, 81, 121–128
  turbojet, 81, 86–92, 94–95, 396
Thrust vector control, 14, 43, 66, 286, 331
Time to climb, 442
Time constant, 43, 77, 260–265, *362*
Time critical target, 84, 243
Titanium, 151–157, 396
TNT, 247, 252, 255
Total impulse, 202, 265, 319
Trajectory
  ballistic, 197, 212, 266, 337
  boost-coast, 131, 197
  boost-sustain-coast, 130–131
  boost-glide, 83, 217
  climb, 83, 204–209, 235
  coast, 197, 210–212, 421
  cruise, 17, 197, 234, 418, 428
  dive, 235, 434, 444
  glide, 83, 205, 217, 286, 337
  lofted, 69, 313, 338
  turn, 206–209
Trapezoidal planform, 53
Triangular planform, 29
Tri-tail, 56
Trim angle of attack, 7, 73, 209, 414
Trim normal force coefficient, 46
Turbine, 81, 85, 92, 94, 246, 396
Turbojet
  compressor, 81, 83, 86
  engine, 191
  material, 89, 90
  specific impulse, 16, 91–96
  turbine, 89–90
  thrust, 56, 419, 442
Turbo ramjet, 89, 90
Turbulent flow, 163
Turn
  radius, 197, 207–209, 330
  rate, 207–210, 263, 330
Two degrees of freedom, 447

Ultimate strength, 319, *321*
Uncertainty, 63, 150, 184
Undamped natural frequency, 71
Underexpanded nozzle, 237
Uniform load, 180, 185
Unguided flight trajectory, 39, 354
Unit cost, 3, 287–288

Unmanned
air vehicle, 11, 26, 141, 245
combat air vehicle, 245
Unpowered flight, 386

Velocity, 122, 197–199, 452
ballistic, 144, 145, 212–214, 450
burnout, 143, 214, 327–329
climb, 204–205
coast, 210–213, 329, 356
cruise, 30, 326, 339
dive, 205, 235, 257
fragment, 21, 248, 252–253
sustain, 319, 327, 420, 442
Vertical launch system (VLS), 135, 296
Volumetric
efficiency, 38, 97, 129, 134–135, 420
loading, 96, 121, 129, 183
Vortices, 54, 65
Vulnerable area, 250, 251

Wall temperature, 166, 357
Warhead
blast fragmentation, *248*, 250–253, 257, 356
kinetic energy, 242, 257
Wave drag, 31–33, 49–51
Weather, 25, 219–221, 372
Weight
actuator, 52
airframe, 11, 28, 160, 188, 319
density, 212, 356, 357
dome, 141–144, 320
fuel, 81, *84*, 425, 439
inert, 144, 348–349, 420,
insulation, 356, 421
motor, 132, 183
power supply, 141, 144, 190–193, 356
propellant, 121–125, 128, 143, 183, 202, 318, 420
reduction, 7, 294
statement, 16, 146
structure, 1, 141, 179, 185
subsystems, 85, 144, 146, 309, 421
warhead, 399, 404
Wetted area, 32, 189, 366
Wind tunnel test, 38, 163, 178–179, 349, 385, 392
Window dome, 29–31, 271
Wing
aerodynamic center, 48, 76
area, 7, 45, 336
arrangement, 54
center of pressure, 40, 76
characteristics, 243, 251, 372
control, 48, 49, 54–56, 64
delta, 51–53
double delta, 52
drag, 438
forward swept, 51–52, 65, 79
location, 21, 75, 317, 422, 443
mean aerodynamic chord (MAC), 47–53, 186, 438
normal force, 16, 18, 21, 34–36, 200, 438
planform, 21, 38, 44–46
rectangular, 53
section, 43, 49–51, 317
size considerations, 21, 112
sizing, 313, 329–331, 335
trapezoidal, 51, 53
weight, 106, 141, 135
Wing-body-tail, 78, 391
Wing theory, 44, 49, 356
linear, 44, 76
Newtonian, 44–45, 49–50, 356
slender, 45, 49, 356

X tail, 56, 60

Yawing moment, 73, 77, 200
Yield strength, 178

Zero lift drag, 21, 51, 199
body, 32
tail, 51
total, 31, 51
wing, 51, 47